Joint Meeting

German and Italian Sections of The Combustion Institute

Sorrento

May 23-36, 2018

PROCEEDINGS

edited by

H. Bockhorn, F. Scala, M. Commodo, A. Tregrossi

Joint Meeting

German and Italian Sections of The Combustion Institute

41st Meeting of the Italian Section of The Combustion Institute

PROCEEDINGS

Sorrento
May 23-26, 2018

edited by
H. Bockhorn, F. Scala, M. Commodo, A. Tregrossi

Joint Meeting of the German and Italian Sections of The Combustion Institute
41st Meeting of the Italian Section of The Combustion Institute
Proceedings
ISBN 978-88-88104-22-5
Editors:
H. Bockhorn, F. Scala, M. Commodo, A. Tregrossi

ASICI - Associazione Sezione Italiana del Combustion Institute
P. Tecchio, 80, 80125 Napoli
Napoli, May, 2018

The Italian Section of The Combustion Institute
www.combustion-institute.it

Copyright ©, May 2018, ASICI - Associazione Sezione Italiana del Combustion Institute

All rights reserved. Parts of this paper may be reproduced with the permission of the author(s) and quoting the source.

SESSION I: TURBULENT FLAMES

A PARTIALLY STIRRED REACTOR MODEL FOR TURBULENT COMBUSTION CLOSURE USING DETAILED CHEMICAL TIME SCALES I1
E.Quadarella, A. Stagni, A. Cuoci, A. Parente, T. Faravelli, H.G.Im

THE TRANSITION FROM AUTOIGNITION TO PROPAGATION AT ELEVATED TEMPERATURES OBTAINED FROM 1-D FLAME SIMULATIONS I2
O. Schulz, N. Noiray

DIRECT NUMERICAL SIMULATION OF A LEAN, PREMIXED, STAGED COMBUSTOR WITH A FOCUS ON CO EMISSION I3
K. Kleinheinzc, L. Berger, A. Attili, H. Pitsch

A DIRECT NUMERICAL SIMULATION STUDY OF POST DISCHARGE PLASMA IGNITION OF JET FUEL IN ISOTROPIC TURBULENCE I4
G. Borghesi, A. Krisman, T. Lu, J.W. Park, J.H. Chen

EFFECT OF RADIANT TRANSFER OF ENERGY IN HIGH-PRESSURE OXY-COMBUSTION I5
E. Giacomazzi, D. Cecere, F.R. Picchia, N.M. Arcidiacono

FLOW AND 'ADDED' SMALL-SCALE TOPOLOGIES IN A TURBULENT PREMIXED FLAME I6
L. Cifuentes, A. Kempf, C. Dopazo

NUMERICAL AND EXPERIMENTAL INVESTIGATION OF THE NOISE GENERATION OF A TURBULENT FLAME I7
K. Pausch, S. Herff, H. Nawroth, C. O. Paschereit, W. Schröder

SPECTRAL RESPONSE OF DIFFERENT COMBUSTION MODELS IN LES OF DIRECT COMBUSTION NOISE I8
F. Zhang, T. Zirwes, H. Nawroth, N. Li, P. Habisreuther, H. Bockhorn, D. Trimis, C.O. Paschereit

REACTION ZONE IDENTIFICATION AND CHARACTERIZATION BASED ON RIDGE ANALYSIS I9
V. Bykov, R. Schießl

LARGE EDDY SIMULATION OF TURBULENT FLOW IN A FAN-STIRRED COMBUSTION VESSEL I10
F. Zhang, T. Zirwes, P. Habisreuther, N. Zarzalis, D. Trimis, H. Bockhorn

MIXING FIELD EFFECTS IN PARTIALLY PREMIXED TURBULENT FLAMES I11
S. Luca, A. Attili, F. Bisetti

QUASI-PROBABILITY APPROACH FOR MODELLING LOCAL EXTINCTION AND COUNTER-GRADIENT IN TURBULENT PREMIXED COMBUSTION I12
G. Pagnini, A. Trucchia

STATISTICAL ANALYSIS OF PULSATING METHANE FLAMES ISSUED INTO HOT CO-FLOW BY LES WITH FGM I13
E. Inanc, I. Wlokas, A. M. Kempf

DISSIPATION ELEMENT ANALYSIS OF PREMIXED JET FLAMES I14
D. Denker, A. Attili, S. Luca, F. Bisetti, H. Pitsch

MORPHOLOGY AND PROPAGATION OF LARGE SCALE PREMIXED FLAMES: COMPARISON OF 2D, 3D DNS AND EXPERIMENTS I15
R. Lamioni, P.E. Lapenna, G. TroianI, F. Creta

ON ENERGY AND DISSIPATION SPECTRA IN TURBULENT NON PREMIXED JETSWITH LOCAL EXTINCTION I16
A. Shamooni, A. Cuoci, A. Sadiki, T. Faravelli

HEAT RELEASE RATE MARKERS FOR TURBULENT MILD COMBUSTION FED BY CH4-H2 MIXTURE I17
D.Bascherinia,, M. Ferrarotti, C. Galletti, G. Bagheri, A. Parente

STABILIZATION OF A HIGH PRESSURE JET FLAME WITH HEAT LOSSES BY LES I18
P. Gruhlke, H. Janbazi, I. Wlokas, C. Beck, A. M. Kempf

CONSISTENT FLAMELET-BASED TURBULENT COMBUSTION MODELING FOR LIQUID ROCKET ENGINES I19
P. E. Lapenna, G. Indelicato, R. Amaduzzi, D. Durigon, R. Lamioni, F. Creta

FUEL PERFORMANCE DETECTION IN MICRO GAS TURBINE USING A NEW APPROACH BASED ON CHAOS DETECTION FROM COMBUSTION VIBRATIONS I20
C. Allouis, A. Amoresano, R. Pagliara, G. Langella, V. Niola, G. Quaremba

SESSION II: SOLID FUELS

MEASUREMENT OF BEECH WOOD PYROLYSIS KINETICS IN A FLUIDIZED BED REACTOR II1
S. Pielsticker, K. Schlögel, T. Kreitzberg, O. Hatzfeld, R. Kneer

EFFECTS OF CO2 ON PYROLYSIS OF WALNUT SHELLS AT HIGH TEMPERATURE AND HEATING RATE IN A HSR II2
O. Senneca, B. Apicella, C. Russo, F. Cerciello, L. Cortese, F. Stanzione, P. Salatino, A. Wütscher, M. Muhler, V. Scherer

SLOW PYROLYSIS OF POTASSIUM DOPED XYLAN: A COMPARISON BETWEEN TWO DOPING APPROACHES II3
P. Giudicianni, V. Gargiulo, M. Alfè, R. Ragucci

INVESTIGATION ON IGNITION BEHAVIORS OF PULVERIZED COAL PARTICLES IN A TUBULAR SWIRL BURNER II4
Y. Xu, S. Li

A NOVEL METHOD TO COUPLE DEM AND CFD TO SIMULATE TRANSPORT PHENOMENA IN SOLID BIOMASS FUEL BEDS II5
F. Buß, S. Wirtz, V. Scherer

THERMOANALYTICAL AND XPS SURFACE CHARACTERIZATION OF OXIDIZED CHARS II6
F. Cerciello, O. Senneca, A. Coppola, P. Salatino

EXPERIMENTAL AND NUMERICAL STUDY OF WOODCHIPS COMBUSTION IN AN UNDERFEED STOKER BOILER II7
G. Caposciutti, S. Patronelli, F. Barontini, M. Antonelli, U. Desideri, L. TognottI, C. Galletti

FLUIDIZED BED COMBUSTION OF PELLETIZED SEWAGE SLUDGE IN A PILOT SCALE REACTOR II8
A. Cammarota, F. Cammarota, R. Chirone, G. Ruoppolo, R. Solimene, M. Urciuolo

ENTRAINED FLOW GASIFICATION: EXPERIMENTS AND MATHEMATICAL MODELLING BASED ON RANS II9
M. Dammann, M. Mancini, S. Fleck, R. Weber, T. Kolb

FOOD WASTE GASIFICATION THROUGH HYDROTHERMAL CARBONIZATION PRE-TREATMENT II10
A. N. Izaharuddin, M. C. Paula, S. Theppitak, X. Dai, Kunio Yoshikawa

PARTICLE-WALL IMPACT EXPERIMENTS FOR ENTRAINED-FLOW BIOMASS GASIFIERS II11
M. Troiano, F. Montagnaro, R. Solimene, P. Salatino

DETAILED DEM SIMULATION OF PARTICLE-WALL INTERACTIONS UNDER COAL GASIFIER CONDITIONS II12
D.M. Balice, F. S. Marra, F. Montagnaro, P. Salatino

UNSTEADY THREE-DIMENSIONAL SIMULATION OF A FLUIDIZED BED FOR BIOMASS GASIFICATION II13
M.A. Uzair, S. Camporeale, F. Fornarelli, P. Oresta

REACTIVITY OF BIOCHAR GASIFICATION IN ATMOSPHERES OF STEAM, CARBON DIOXIDE AND THEIR MIXTURES II14
T. Kreitzberg, S. Pielsticker, O. Hatzfeld, R. Kneer

AN ASSESSMENT OF CARBON OXIDATION MECHANISM BY DYNAMIC OXIDATION/DESORPTION IN A LOOPING REACTOR II15
A. Coppola, O. Senneca, F. Cerciello, P. Salatino

PROGRESS AND CHALLENGES IN FLOW FIELD STUDIES OF 40 - 60 KW_{TH} PULVERIZED COAL FLAMES II16
D. Zabrodiec, J. Hees, A. Massmayer, O. Hatzfeld, R. Kneer

SESSION III: FUEL AND BIOFUEL PROCESSING AND UPGRADING

ON TORREFACTION OF AGRO-INDUSTRIAL RESIDUES: FROM LOW-VALUE WASTES TO HIGH-QUALITY ENERGY CARRIERS III1
P. Brachi, R. Chirone, F. Miccio, M. Miccio, G. Ruoppolo

TORREFACTION OF A LIGNIN-RICH RESIDUE IN A SOLAR FLUIDIZED BED REACTOR III2
C. Tregambi, F. Montagnaro, P. Salatino, R. Solimene

IMPROVING THE CATALYTIC PERFORMANCE OF Ni(Ru)/MgO IN THE CONVERSION OF ETHANOL TO BUTANOL BY DISPERSION ON γ-AL_2O_3 PELLETS. III3
J. Apuzzo, S. Cimino, L. Lisi

INTEGRATION OF ENZYMATIC PROCESSES FOR DELIGNIFICATION AND HYDROLYSIS OF AGRO-FOOD WASTES III4
S. Niglio, A. Procentese, M.E. Russo, F. Raganati, A. Marzocchella

SOLAR THERMOCHEMICAL CO_2 SPLITTING OVER $La_{0.6}Sr_{0.4}MnO_3$ PEROVSKITES III5
G. Luciani, C. Imparato, G. Landi, A. Aronne, A. Di Benedetto

PROCESS MODELLING OF AN INNOVATIVE POWER TO LNG DEMONSTRATION PLANT III6
E. A. Morosanu, S. Bensaid, R. Pirone

TORREFACTION OF HEAVY METALS CONTAMINATED BIOMASSES III7
C.M. Grottola, P. Giudicianni, F. Stanzione, J.B. Michel, R. Ragucci

A PRELIMINARY STUDY OF FLUIDIZED BED SORPTION-ENHANCED METHANATION BY CaO III8
A. Coppola, F. Massa, P. Salatino, F. Scala

SESSION IV: SOOT, NANOPARTICLES AND PAHs

OXIDATION BEHAVIOR AND RAMAN SPECTROSCOPIC ANALYSIS OF DIESEL SOOT AND PROPANE SOOT IV1
C. Zöllner, D. Brüggemann

EXPERIMENTAL INVESTIGATION OF SOOT OXIDATION UNDER WELL-CONTROLLED CONDITIONS IN A HIGH-TEMPERATURE FLOW-REACTOR IV2
T. Bierkandt, P. Oßwald, M. Köhler

SECONDARY TAR REACTIONS AND SOOT FORMATION IN PYROLYSIS OF COAL IV3
C. Russo, O.Senneca, F. Cerciello, F. Stanzione, L. Cortese, A. Ciajolo, S. Heuer, V. Scherer, B. Apicella

DECONVOLUTION OF SOOT PARTICLE SIZE DISTRIBUTIONS IV4
H. Mätzing, P. Vlavakis, M. Sentko, A. Loukou, B. Stelzner, D. Trimis, D. Stapf

HOW TO VALIDATE NUMERICAL RESULTS ON PRIMARY PARTICLE DIAMETER TO EXPERIMENTAL DATA FROM LAMINAR SOOTING FLAMES IV5
A. Bodor, A. Cuoci, B. Franzelli

SOOT MODELING OF ETHYLENE COUNTERFLOW DIFFUSION FLAMES IV6
W. Pejpichestakul, A. Frassoldati, A. Parente, T. Faravelli

FLAME AEROSOL SYNTHESIS OF TIO2 NANOPARTICLE COATINGS WITH ADVANCED ANTIBACTERIAL AND HYDROPHILIC PROPERTIES IV7
G. De Falco, C. Almini, R. Ciardiello, M. Commodo, P. Del Gaudio, P. Minutolo, A. Porta, A. D'Anna

THE IMPACT OF TEMPERATURE AND FLAME CHEMISTRY ON THE DEGRADATION OF METAL OXIDE NANOPARTICLES IV8
N. Teuscher, W. Baumann, M. Hauser, J. Mahl, H.-R. Paur, D. Stapf

EELS AND HRTEM OF ETHYLENE SOOT IV9
B. Apicella, A. Tregrossi, A. Ciajolo, J. Abrahamson, R.L. Vander Wal, C. Russo

SOOT PREDICTION IN A MODEL AERO ENGINE COMBUSTOR WITH MULTIPHYSICS APPROACH IV10
S. Paccati, D. Bertini, S. Puggelli, L. Mazzei, A. Andreini

MODELLING OF SOLAR RADIATION ON SOOT FORMATION IN DIFFUSION FLAME IV11
M. Sirignano, A. D'Anna

STUDY OF SOOT PARTICLES NANOSTRUCTURE EVOLUTION IN A LAMINAR PREMIXED FLAME BY RAMAN AND EPR SPECTROSCOPY IV12
F. Picca, M. Di Serio, G. De Falco, M. Commodo, G. Vitiello, G. D'Errico, P. Minutolo, A. D'Anna

SESSION II: INTERNAL COMBUSTION ENGINES

EXPERIMENTAL INVESTIGATION OF DIFFERENT COMBUSTION MODES IN A SINGLE-CYLINDER DUAL-FUEL CI ENGINE V1
M. Korkmaz, B. Jochim, J. Beeckmann, H. Pitsch

STUDY OF LIQUID AND VAPOUR PHASES OF A GDI SPRAY V2
A. Montanaro, L. Allocca

PARTICLE FORMATION AND EMISSIONS FROM DUAL FUELED CNG DI AND GASOLINE PFI SI RESEARCH ENGINE V3
F. Catapano, S. Di Iorio, P. Sementa, B. M. Vaglieco

MODELING VIRTUAL FUELS FOR HCCI-LIKE INTERNAL COMBUSTION ENGINES DEVELOPMENT V4
P. Miceli, D. Fino, M. Chiodi

EXPERIMENTAL STUDY ON GLOBAL AND LOCAL TURBULENT PREMIXED FLAME CHARACTERISTICS OF ALCOHOLS V5
J. Trabold, S. Walther, S. Hartl, A. Dreizler, D. Geyer

ANALYSIS OF ENGINE CONTROL PARAMETERS EFFECT TO MINIMIZE GHG EMISSIONS IN A DUAL FUEL NG/DIESEL LIGHT DUTY ENGINE V6
C. Beatrice, V. Fraioli, C. Guido, P. Napolitano

EXERGO-ECONOMIC ANALYSIS OF AN HCCI-ENGINE POLYGENERATION SYSTEM V7
D. Schröder, A. Güngör, R. Hegner, B. Atakan

COMPUTATIONALLY AEFFICIENT COMBUSTION PROGRESS VARIABLE (CPV) APPROACH FOR ENGINE APPLICATIONS V8
A. Werner, C. Netzer, H. Lehtiniemi, A. Borg, A. Matrisciano, L. Seidel, F. Mauss

SESSION VI: REACTION KINETICS

A COMPREHENSIVE DETAILED KINETIC MECHANISM FOR THE SIMULATION OF GAS-OLINE FUELS VI1
M. Mehl, K. Zhang, S.W. Wagnon, G. Kukkadapu, C.K. Westbrook, W.J. Pitz, Y. Zhang, H.J. Curran, M.J. Al Rashidi, N. Atef, S.M. Sarathy

DRG AND GQL REDUCTION METHODS FOR A H2/AIR AUTO-IGNITION PROBLEM VI2
C. Yu, F. Minuzzi, V. Bykov, U. Maas

DEVELOPMENT OF A MECHANISM FOR DUAL FUEL COMBUSTION VI3
S. Schuh, J. Frühhaber, F. Winter

INSIGHTS INTO OXIDATION BEHAVIOR OF POTENTIAL GASOLINE ADDITIVES: 2-METHYLFURAN AND 2-METHYLTETRAHYDROFURAN VI4
R. Tripathi, U. Burke, A. K. Ramalingam, C. Lee, R. X. Fernandes, K. A. Heufer, S. M. Sarathy, H. Pitsch

DEVELOPMENT OF A KINETIC MECHANISM FOR NOx FUEL INTERACTION VI5
K. P. Shrestha, L. Seidel, F. Mauß, T. Zeuch

COMPARISON OF DIFFERENT DIAGNOSTIC TECHNIQUES FOR THE ASSESSMENT OF COAL PYROLYSIS RATE VI6
S. Krusch, V. Scherer, R. Solimene, G. Ruoppolo, F. Cerciello, S. Pielsticker, R. Kneer, K. Schlögel, O. Senneca

PLUG-FLOW REACTOR STUDY OF THE PARTIAL OXIDATION OF METHANE AND NATURAL GAS AT ULTRA-RICH CONDITIONS VI7
D. Kaczmarek, T. Kasper, B. Atakan

ADVANCEMENT ON HEAT TRANSFER MODELLING OF OXIDATION PROCESSES IN JET STIRRED FLOW REACTORS VI8
L. Acampora, M. Lubrano Lavadera, P. Sabia, R. Ragucci, M. de Joannon, F.S. Marra

A COMPARISON OF NUMERICAL FRAMEWORKS FOR MODELLING HOMOGENOUS REACTORS AND LAMINAR FLAMES VI9
R. Langer, A. Cuoci, L. Cai, U. Burke, C. Olm, H. Curran, T. Turány, H. Pitsch

INVESTIGATION OF S2 + AIR COMBUSTION VI10
N. Sebbar, T. Zirwes, P. Habisreuther, H. Bockhorn, D. Trimis

SESSION VII: FORMATION AND CONTROL OF POLLUTANTS AND GREENHOUSE GASES

CALCIUM LOOPING WITH AIR POLLUTION CONTROL RESIDUES FROM MUNICIPAL SOLID WASTE INCINERATORS: A PRELIMINARY SCREENING VII1
A. Dal Pozzo, A. Armutlulu, M. Rekhtina, C.R. Müller, V. Cozzani

EMBEDDING GRAPHENE-LIKE LAYERS IN HYBRID METAL ORGANIC FRAMEWORKS: THE EFFECT ON CO_2 CAPTURE VII2
M. Alfè, R. Rea, V. Gargiulo, M. Minelli, L. Lisi, M. G. De Angelis

THERMODYNAMIC AND KINETIC STUDY OF CO_2 ADSORPTION ON A FINE ACTIVATED CARBON IN A SOUND ASSISTED FLUIDIZED BED VII3
F. Raganati, R. Chirone and P. Ammendola

PRELIMINARY CHARACTERIZATION OF THE EMISSIONS FROM SCENTED TEA-LIGHT CANDLES VII4
E. Oddo, M. Derudi

COMPARISON BEHAVIOUR OF COMMERCIAL ACTIVATED CARBON AND COAL-DERIVERED CHAR IN HOT SYNGAS CLEANING VII5
F. Parrillo, G. Ruoppolo, U. Arena

INSIGHTS INTO THE MECHANISM OF H_2S REACTIVE ADSORPTION OVER ZNO–CUO DISPERSED ONTO ACTIVATED CARBON VII6
G. de Falco, F. Montagnaro, M. Balsamo, A. Erto, F.A. Deorsola, L. Lisi, S. Cimino

THE INFLUENCE OF H_2O AND SO_2 ON CO_2 UPTAKE IN FLUIDIZED BED CALCIUM LOOPING VII7
A. Coppola, F. Montagnaro, A. Esposito, F. Scala, P. Salatino

CO_2 ADSORPTION DATA ON DIFFERENT SORBENTS UNDER DYNAMIC CONDITIONS: AN OVERVIEW VII8
V. Gargiulo, M. Alfè, F. Raganati, P. Ammendola, R. Chirone

A DESCRIPTIVE MODEL FOR A PILOT-SCALE WET ELECTROSTATIC SCRUBBER VII9
M. Esposito, C. Carotenuto , A. Lancia, M. Giavazzi, E. Di Benedetto, F. Di Natale

SESSION VIII: DETONATIONS, EXPLOSIONS AND SUPERSONIC COMBUSTION - SPRAY AND DROPLETS

SHOCKLESS FLAME ACCELERATION AND DDT IN OPEN CHANNELS DRIVEN BY HYDRAULIC RESISTANCE VIII1
M. Kuznetsov, J. Yanez, V. Bykov

CHANGE IN FLAME GEOMETRY OF AN ETHANOL SPRAY FLAME BY VARYING THE INJECTION FREQUENCY VIII2
F. C. C. Galeazzo, N. K. Fukumasu, J. A. Denev , G. C. Krieger Filho

AN EXPERIMENTAL INVESTIGATION OF EMULSIFICATION EFFECT ON HEAVY FUEL OIL DROPLET COMBUSTION VIII3
P. Guida, W. L. Roberts

A CFD FRAMEWORK FOR EVAPORATING FUEL DROPLETS IN A GRAVITY FIELD VIII4
A.E. Saufi, A. Cuoci, A. Frassoldati, T. Faravelli

EXPERIMENTAL AND NUMERICAL EVALUATIONS ON THE CHARACTERISTICS OF VENTED METHANE EXPLOSION VIII5
L. Zhen-min, S. Bin, W. Tao, C: Fang-ming, Z. Jing-yu

FLASH POINT OF BINARY MIXTURES VIII6
V. Di Sarli, R. Sanchirico, A. Di Benedetto

EXPERIMENTTAL STUDY ON THE EFFECTS OF CRUDE OIL ON SPONTANEOUS COMBUSTION: A CASE STUDY VIII7
J. Deng, S.X. Fan, K. Wang, Y.N. Zhang, C.P. Wang, J.Y. Zhao

SESSION IX: LAMINAR FLAMES

EXPERIMENTAL INVESTIGATION OF FUEL-SPECIFIC SPECIES FORMATION IN BLENDED PREMIXED FLAMES IX1
J. Wullenkord, M. Zeng, M. Salamanca, I. Graf, S. Schmitt, L. Ruwe, K. Kohse-Höinghaus

A NUMERICAL STUDY ON THE EFFECT OF TEMPERATURE AND COMPOSITION ON THE FLAMMABILITY OF SOUR GAS IX2
G. Pio, V. Palma, E. Salzano

NON-LINEAR EVOLUTION OF THERMODIFFUSIVELY UNSTABLE LEAN PREMIXED HYDROGEN FLAMES IX3
L. Berger, K. Kleinheinz, A. Attili, H. Pitsch

FLAME FOLDING AND WRINKLING FACTOR FOR 2D AND 3D HYDROGEN-AIR FLAMES IX4
M. Kuznetsov, N. Chaumeix, J. Yanez, S. Tengah

THE EFFECT OF EQUIVALENCE RATIO VARIATION ON THE FLAME STRUCTURES OF LAMINAR LOW-PRESSURE TETRAMETHYLSILANE/HYDROGEN FLAMES IX5
Y. Karakaya, T. Kasper

NUMERICAL AND EXPERIMENTAL STUDIES OF LAMINAR COUNTER-FLOW DIFFUSION FLAMES USING BIOMASS-BASED GASEOUS FUELS IX6
M.-T. Scharl, D. Greenhalgh, A. Diéguez Alonso, F. Behrendt

CH_4/AIR-FLAME IMPINGEMENT HEAT TRANSFER TO A CYLINDRICAL SURFACE IX7
P.O. Oketch, U. Bergmann, B. Atakan

SESSION X: NOVEL CONCEPTS, TECHNOLOGIES AND SYSTEMS

ON THE INFLUENCE OF THE EFFECTIVE FOCAL LENGTH ON LASER IGNITION WITH A PASSIVELY Q-SWITCHED LASER X1
M. Bärwinkel, D. Brüggemann

A LOW POWER LIQUID FUELED BURNER USING A NOVEL ATOMIZATION CONCEPT X2
T. Müller, A. Goßmann, J. Kühn, M. Etzold, B. Stelzner, N. Zarzalis, F. Durst, D. Trimis

ASSESSMENT OF COMBUSTION PARADIGMS FOR MODELING A CYCLONIC BURNER UNDER MILD COMBUSTION CONDITIONS X3
M. Ferrarotti, S. Patronelli, G. Ceriello, G. Sorrentino, C. Galletti, A. Parente

EVALUATION OF FUEL FLEXIBILITY IN A CYCLONIC BURNER. X4
P. Sabia, G. Sorrentino, P. Bozza, R. Ragucci, M. de Joannon

CATALYTIC COMBUSTION OF METHANOL OVER NANO-STRUCTURED CeO_2-Pt/FECRALLOY FOAM CATALYSTS X5
S. Cimino, L. Lisi, M. Musiani, E. Verlat

USE OF SOLAR ENERGY TO SUSTAIN LIMESTONE CALCINATION FOR ORDINARY PORTLAND CEMENT PRODUCTION X6
C. Tregambi, R. Solimene, F. Montagnaro, P. Salatino, M. Marroccoli, N. Ibris, A. Telesca

THE COMBUSTION INSTITUTE
1954

SESSION I

Turbulent flames

A partially stirred reactor model for turbulent combustion closure using detailed chemical time scales

E.Quadarella[*,], A. Stagni[**], A. Cuoci[**], A. Parente[***], T. Faravelli[**], H.G.Im[*],**

alessandro.stagni@polimi.it

[*]*Clean Combustion Research Center,*
King Abdullah University of Science and Technology (KAUST), Thuwal, Saudi Arabia
[**]*Politecnico di Milano, Department of Chemistry,*
Materials and Chemical Engineering "G.Natta", Milano, Italy
[***]*Université Libre De Bruxelles, Ecole Polytechnique de Bruxelles,*
Aero-Thermo-Mechanics Laboratory, Bruxelles, Belgium

Abstract

The closure of the reaction term in modeling turbulent combustion systems is crucial when dealing with the Reynolds-averaged Navier-Stokes (RANS) approaches. The partially-stirred reactor model (PaSR), that explicitly includes the characteristic chemical time of the system in the expression of the mean reactive term is one of the most commonly used approaches in the description of turbulence-chemistry interaction. The model showed limitations in predicting some key phenomena, such as Nitrogen Oxides (NO_x), which have distinct characteristic time scales compared to that of the main combustion process. The present study proposes a refined PaSR model with incorporating detailed chemical time scales in the description of the reaction source term closure. A stochastic reactor is used as a representation of the target turbulent combustion system and its results are compared with data given by a perfectly stirred reactor whose reactive term is modeled according to the proposed formulation of PaSR. The model is tested with reaction schemes describing different common kinetic pathways. Overall, good agreement is found between PaSR and the stochastic reactor.

Introduction

The computational simulation of turbulent reacting flows is a challenging problem due to the extremely large number of solution variables and a large spectrum of length and time scales involved. For many engineering applications, the Reynolds-averaged Navier-Stokes (RANS) approach is most commonly used as a means to provide the statistical average behavior of the system. In particular for reacting flows, the proper closure of the mean reaction source terms is a great challenge, due to their strong nonlinearity associated with chemical reactions (with vastly different time scales) and their interaction with turbulent flows which also have a range of flow time scales. The partially-stirred reactor (PaSR) model [1], which has been

widely used in engineering computational fluid dynamic (CFD) simulations, allows a systematic way to account for various chemical and flow time scales. Most existing forms of the implementation of PaSR, however, represent the complex chemical reaction processes with a single characteristic time scale, thus limiting its fidelity in predicting a wide variety of key observables, such as the NO_x formation. The present study aims to improve on this limitation of the PaSR approach by systematically incorporating key chemical time scales depending on the targeted objectives, by employing the numerical procedure based on the computational singular perturbation (CSP) theory [2]. In the following, the proposed model is described and its implementation into the PaSR model is validated against the stochastic reactor model results, which represent an idealized turbulent combustion system. Results of different test cases are presented and discussed.

The partially-stirred reactor (PaSR) model

The partially-stirred reactor model (PaSR) [1], is based on the assumption that each computational cell can be divided into two fractions: a reactive portion (characterized by a concentration $\boldsymbol{c}$) and a non-reactive one where species are characterized by the initial concentration $\boldsymbol{c}_0$. Due to the mixing, these two portions interact and exchange mass giving an outlet composition $\boldsymbol{c}_1$. It was shown [1] that the mean reactive term can be expressed as:

$$\boldsymbol{\Omega}(\mathbf{c}) = \gamma\, \boldsymbol{\Omega}(\boldsymbol{c}_1) \tag{1}$$

$$\gamma = \tau_c/(\tau_c + \tau_{mix}) \tag{2}$$

In PaSR model the formation rate of a certain species is then defined according to the γ factor. In fact, when the mixing time τ_{mix} is smaller than the chemical characteristic time of the system τ_c ($\tau_{mix} < \tau_c$), γ is close to unity, meaning that mixing is efficient, and the final composition is mainly determined by chemistry. Contrarily, when $\tau_c < \tau_{mix}$, γ is close to zero and mixing controls the system. The model is then able to well correlate the chemical phenomena with the mixing one due to turbulence. The chemical characteristic time is related to a reference species and can be calculated from the eigenvalues of the Jacobian matrix. Generally, the largest chemical time is selected because it is supposed to be most limiting one. However, this is the main limitation of the model, and makes it unable to describe systems where chemical times are very different from each other (e.g. formation of thermal NO_x in combustion systems). In order to take into account for all the chemical time scales, a different approach should be used, and it is the focus of this work. To this purpose, reactions chemical times can be exploited. According to Lam [2] they can be expressed as:

$$\tau_{c,j} = 1/\left(\frac{\partial r_j}{\partial \boldsymbol{c}_0}\,\boldsymbol{\alpha}_j\right) \tag{3}$$

where j is the number of reactions and r_j and α_j are, respectively, the reaction rate and the vector of stoichiometric coefficient of the j-th reaction. In this way, it is possible to assess a γ_j for each reaction that directly scales the value of the corresponding reaction rate. Then the formation rate of each species i is computed:

$$\Omega_i = \sum_{j=1}^{NR} \gamma_j r_j \alpha_{i,j} \tag{4}$$

Stochastic reactor

The validation of the proposed methodology is performed by means of a stochastic reactor [3]. It describes the effects of the partial mixing assuming fluids not perfectly diffusing one into each other at a molecular level but considering mean thermo-chemical properties to be spatially homogeneous. The reactor is then composed of many fluid particles that interact statistically and diffuse into each other according to the imposed mixing. The statistic events are chosen from the stochastic ensemble. Then, the mixing is modeled according to the modified coalescence and dispersion model [4]. The mixing events occur with a frequency which is characteristic of turbulence mixing. If $\tau_{mix} = 0$ the stochastic reactor becomes a perfectly stirred reactor (PSR), while if $\tau_{mix} = \infty$ the particles are completely segregated. Finally, chemistry is solved inside each particle which is treated like a batch reactor. Mass inside the reactor can be assumed constant since the mass entering the reactor is equal to the one at the exit. The stochastic reactor can be then considered like a single cell inside a complex computational domain. It is able to faithfully reproduce the real behavior of the system since the only phenomena which is modeled is the mixing. Its results are compared with those coming from a perfectly stirred reactor whose reactive term is modeled according to the new formulation of PaSR.

Results on test cases

In order to fully understand the effects of the introduction of chemical reaction times, different simple test cases are investigated. All simulations are run with arbitrary, temperature-independent kinetic parameters and fictitious species. The first inlet stream is composed by pure A while the other has B diluted in an inert
species I. The molar ratio between B and A is equal to 2. Residence time is fixed equal to $0.1\ s$. All reactions are elementary and non-reversible.

Monomolecular reactions

The sample reaction first considered is:

A→B ($k_1 = 10^5\ [1/(s)]$)

From Figure 1a it is possible to note that if γ is calculated with the (2), PaSR is not able to reproduce the stochastic results. However, the monomolecular reaction is not

influenced by the mixing, because A converted into B without needing to mix with other species.

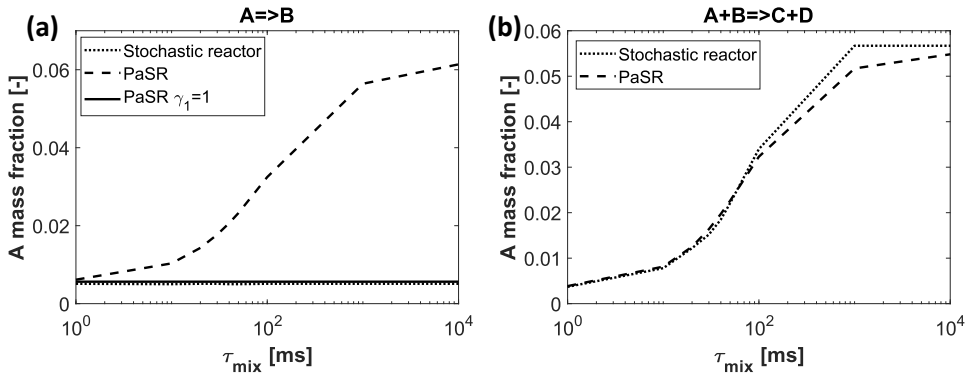

Figure 1: Mass fraction of A varying with mixing time for (a) a monomolecular and (b) a bimolecular reaction.

Consequently, if γ is fixed equal to one, PaSR gives the same results as the stochastic reactor.

Bimolecular reaction

The simple, bimolecular reaction investigated is:

A+B→C+D ($k_1 = 10^5$ $[m^3/(s\,mol)]$)

Figure 1b shows that the PaSR faithfully reproduces the curve from the stochastic reactor because in this case the mixing is crucial to make species react.

Bimolecular and monomolecular reactions

According to the results obtained, a kinetic scheme made up of a combination of bimolecular and monomolecular reactions is studied:

A+B→C+D ($k_1 = 10^5$ $[m^3/(s\,mol)]$)

C→E ($k_2 = 10^4$ $[1/(s)]$)

D→F ($k_2 = 10^4$ $[1/(s)]$)

Results from Figure 2 confirm that monomolecular reactions have to be treated with a γ which is always unitary, while the reaction rate associated to bimolecular reactions must be properly scaled with the γ calculated as in (2).

Parallel reactions

The behaviour of PaSR modelling with respect to the following parallel reactions scheme is analyzed:

A+B→C+D ($k_1 = 10^5$ $[m^3/(s\,mol)]$)

A+B→E+F ($k_2 = 10^4$ $[m^3/(s\,mol)]$)

From Figure 3 it can be noted that the production of species E is largely overestimated by PaSR and also species A and C show consistent discrepancies when γ_1 and γ_2 are computed as in (2). This is due to the fact that once the two reactants mix, their transformation into products is driven only by chemistry. Thus,

the two reactions must be characterized by the same γ, corresponding to the fastest reaction.

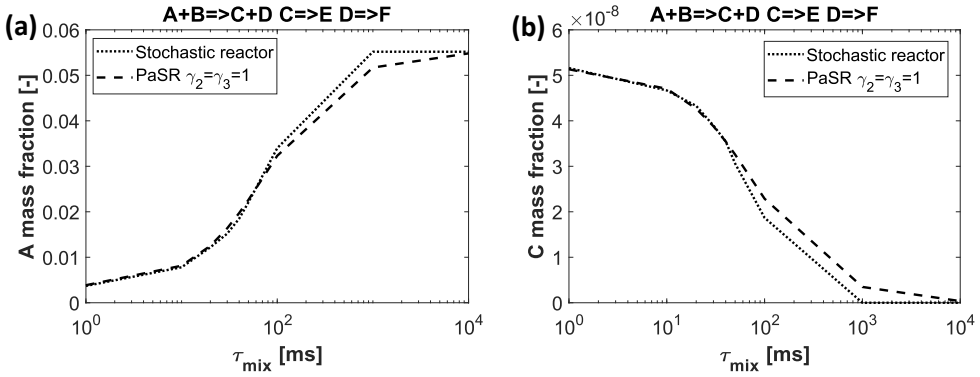

Figure 2: Mass fractions of (a) A and (b) C varying with the mixing time for a combination of monomolecular and bimolecular reactions.

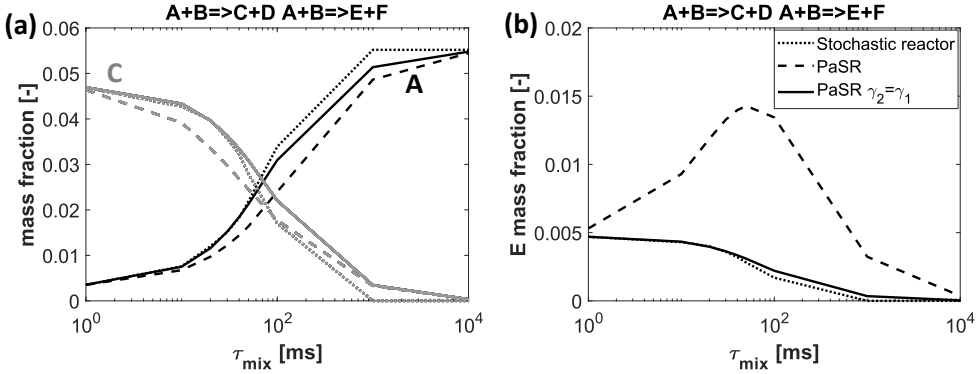

Figure 3: Mass fractions of (a) A, C and (b) E varying with the mixing time for parallel reactions

Reactions in series

The following two reactions in series are finally analyzed:

A+B→C+D ($k_1 = 10^5$ $[m^3/(s\,mol)]$)

C+D→E+F ($k_2 = 10^4$ $[m^3/(s\,mol)]$)

Figure 4 shows that species A is well reproduced by PaSR while differences appear in the curves related to species C and D. This is caused by the fact that C and D are produced from the first reaction, so they are present in the same particle of fluid and then partially mixed. It is easily understandable that the issue is related in general to the premixing of reactants. Reactions may happen not only because reactants are mixed by turbulence but also because they are already in contact (similarly for monomolecular reactions). This suggests that, in order to make the model

comprehensive, the inhomogeneous mixing of premixed reactants has to be considered.

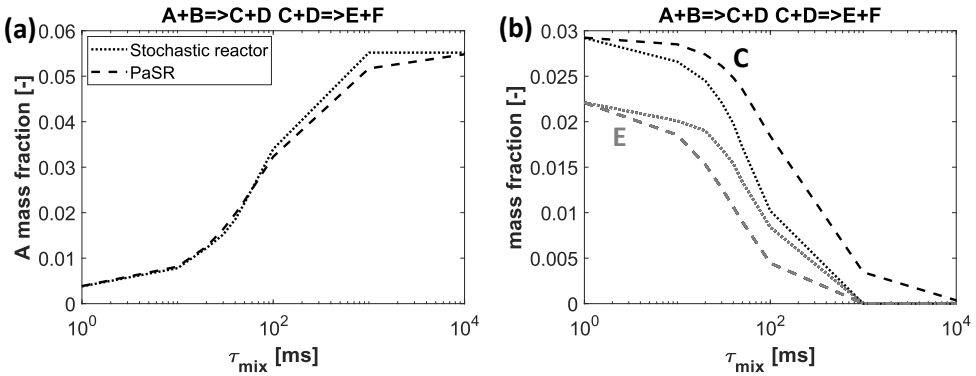

Figure 4: Mass fractions of (a) A and (b) C and E varying with the mixing time for series reactions.

Conclusions and future works

The new formulation of PaSR that includes chemical reaction times involved in a reactive system shows promising results. Its effectiveness has been investigated by comparing the results of a stochastic reactor and a Perfectly Stirred Reactor whose reactive term has been modeled through the newly introduced algorithm. Several test cases representing common kinetic pathways have been investigated. Overall, PaSR is able to well reproduce the behavior of the system. However, several peculiar aspects have been highlighted. With parallel reactions, the γ_j corresponding to the fastest reaction dominates the mixing of the two reactants, thus the process becomes controlled only by kinetics and both reactions must be characterized by the γ_j of the faster one. Moreover, premixing of reactants has a strong impact on the final results. For monomolecular reactions it is enough to impose $\gamma = 1$ but bimolecular reactions deserve further attention, because the inhomogeneous mixing of premixed reactants should be considered.

References

[1] P. A. Nordin, *Complex chemistry modeling of diesel spray combustion*, Chalmers University of Technology, 2001

[2] S. H. Lam, "Model reductions with special csp data", *Combustion and Flame* 160 (12) (2013) 2707–2711

[3] Chen, J-Y. "Stochastic modeling of partially stirred reactors." *Combustion Science and Technology* 122.1-6 (1997): 63-94.

[4] Janicka, J., W. Kolbe, and W. Kollmann. "Closure of the transport equation for the probability density funcfion of turbulent scalar fields." *Journal of Non-Equilibrium Thermodynamics* 4.1 (1979): 47-66.

The transition from autoignition to propagation at elevated temperatures obtained from 1-D flame simulations

O. Schulz* and N. Noiray**
*oschulz@ethz.ch, **noirayn@ethz.ch
CAPS Laboratory, Department of Mechanical and Process Engineering, ETH Zurich, Zurich 8092, Switzerland

Abstract
This study investigates the transition from autoignition to flame propagation at elevated temperatures and atmospheric pressure with 1-D flame simulations. These simulations were performed for mixtures of methane, and vitiated gas at 1000 K to 1600 K. The examined conditions are relevant for the operation of the second stage of sequential combustors. Steady-state simulations with varying flame positions and mixture compositions identify the boundaries between three combustion regimes: (i) autoignition, (ii) flame propagation assisted by autoignition, and (iii) pure flame propagation. The effect of varying the temperature of the reactants on the three regimes is investigated. A transient 1-D flame simulation with an inlet mixture at 1400 K was performed. Results show that the mixture auto-ignites and subsequently, a flame propagates towards the inlet of the computational domain. All of the three combustion regimes are present in this simulation.

Introduction

Autoignition and flame propagation are two different mechanisms that can stabilize flames in high temperature flows. There exist many studies that report flame stabilization due to autoignition (e.g. [1], [2]), flame propagation (e.g. [3], [4]) or a mix between the two (e.g. [5], [6], [7]).

This paper investigates the transition between the two regimes using canonical 1-D flames at conditions that are relevant for sequential combustion system [6]. Sequential combustors [8] represent a significant technology change for gas turbine combustor architectures towards pollutant emission reduction and higher performance [8]. Such systems feature two flames in series. The first flame is a "classical" turbulent-premixed propagating flame. The second one auto-ignites after fuel injection into a hot vitiated crossflow and it can subsequently stabilize via flame propagation [6], which is the topic of the present work.

The first part of the study introduces the combustion regimes maps that were obtained from steady-state 1-D flame simulations. It also investigates the effect of varying the mixture temperature. Finally, a transient 1-D flame simulation that features three distinct combustion regimes is presented.

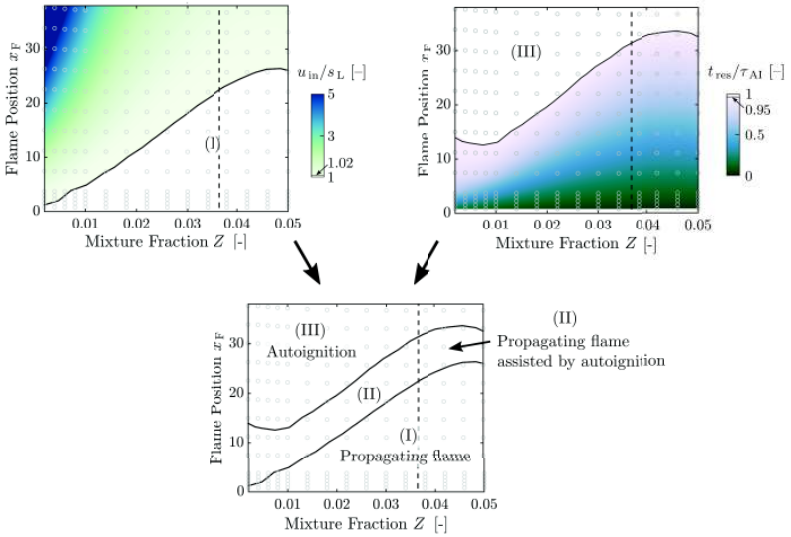

Figure 1. Top: contours of inlet velocity u_{in} normalized by the laminar flame speed s_L (left), and flame residence time t_{res} normalized by the autoignition delay τ_{AI} (right), extracted from 0-D reactor simulations. Bottom: combustion regime map created from the top contours. Vitiated gas temperature at 1450 K.

Combustion regimes maps obtained from steady-state simulations

We performed 1-D flame simulations using Cantera with the detailed GRI-Mech 3.0 mechanism to investigate the boundaries between autoignition and flame propagation at atmospheric pressure.

In [6] and [8], fuel is injected substantially upstream of the high heat release rate region, where the "visible" second stage flame is located. This is because the autoignition time of lean mixtures at relevant pressure and temperatures is long enough (couple of ms) in order to ensure good mixing of the fuel with the vitiated flow, before the former is consumed. This architecture is particularly suited for very low NOx emissions and homogeneous hot gas temperature distribution. In general, it falls into the category of partially premixed combustion. Therefore, in this work, the effect of varying mixture fraction Z on the combustion mode is investigated.

Here, Z describes the mixing between two streams: (i) vitiated gas with a certain vitiated gas temperature (1000 K - 1600 K) coming from the first stage operated at $\varphi = 0.75$, and (ii) methane at ambient temperature. For more details about species composition and the sequential combustor configuration, one can refer to [6]. Figure 1 shows two contour plots (top) that were used to obtain a combustion

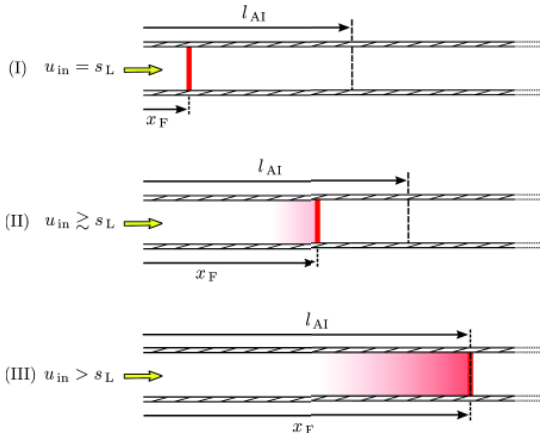

Figure 2. Sketch of three 1-D steady-state flames: (I) – pure propagating flame, (II) – propagating flame assisted by autoignition and (III) – autoignition flame (compare with Fig. 1). The red contour depicts heat release rate q.

regimes map (bottom) for varying flame position x_F and mixture fraction Z. Each circle represents one 1-D flame simulation. For a single simulation, Cantera provides a solution in which the flame is located between one fourth and half of domain length L_d. We varied L_d between 2 and 100 mm, resulting in a change of the flame position x_F. Cantera solves an eigenvalue problem in which the inlet velocity u_{in} is the solution. For a freely propagating flame, u_{in} equals the laminar flame speed s_L. The top left plot of Fig. 1 shows the inlet velocity u_{in} normalized by the laminar flame speed s_L. Here, s_L is assumed to be the inlet velocity for a simulation with the shortest domain length and therefore the smallest flame position. We define a region (I) in which u_{in} changes $\leq 2\%$ compared to s_L and which represents flame propagation; this region is colored in white. For x_F above (I), the influence of autoignition chemistry starts leading to an increase of u_{in}.

The top right contour plot in Fig. 1 shows the flame residence time t_{res} normalized by the autoignition delay τ_{AI}. The flame residence time was computed with a velocity that was integrated from the inlet of the domain to x_F. The autoignition delays were computed with 0-D Cantera reactor simulations at the respective Z. Here, we define a region (III) in which the flame residence time is $\geq 95\%$ of τ_{AI} and which represents autoignition; this region is colored in white. A combined representation of the two zones is shown in the bottom plot. In between (I) and (III), another zone (II) is defined. It represents propagating flames that are assisted by autoignition chemistry upstream of the actual flame front.

Figure 2 presents sketches of three flames located in (I), (II) and (III). We assume that all flames have the same Z and therefore also the same equivalence ratio.

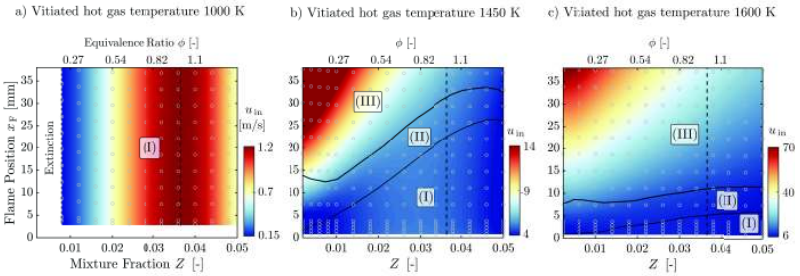

Figure 3. The effect of inlet temperature on combustion regimes maps obtained from 1-D simulations. Contours of inlet velocity u_{in} for three vitiated gas temperatures: (a) 1000 K, (b) 1450 K and (c) 1600 K. Lines highlight the regimes boundaries shown in Fig. 1.

For (II), the flame stabilizes for an inlet velocity that is slightly higher than s_L. Therefore, the theoretical autoignition length l_{AI} moves downstream compared to (I). The red contour sketches a moderate q upstream of x_F.

In case (III), the flame stabilizes with an inlet velocity that can be significantly higher than s_L. Therefore, l_{AI} and the onset of moderate q are shifted further downstream compared to (II). Here, the flame stabilizes at l_{AI} and therefore, the flame residence time t_{res} equals the autoignition delay time τ_{AI}.

Figure 3 compares the inlet velocity u_{in} maps with regime boundaries for three different vitiated gas temperatures: (a) 1000 K, (b) 1450 K and (c) 1600 K. As in Fig. 1, the axis are flame position x_F and mixture fraction Z. Each circle represents one Cantera 1-D flame simulation. The contour colorbar scale is changed from (a) to (c). For 1000 K in (a), only freely propagating flame solutions were obtained within the domain (regime (I)). For any x_F, u_{in} does not change, and therefore, a unique laminar flame speed $s_L = u_{in}$ is determined. For $Z < 0.008$, Cantera did not converge to a solution due to flame extinction. As the vitiated gas temperature is increased to 1450 K (b) (same case as in Fig. 1), autoignition chemistry becomes important and the three regimes can coexist depending on x_F and Z. As the vitiated gas temperature is further increased (c), only a small region (I) with pure flame propagation is identified. Flame residence times approach τ_{AI} even for small flame positions and fast autoignition of the mixtures dominates.

The transient from autoignition to flame propagation

Figure 4 shows the transient evolution from an unburned mixture to a propagating flame. The unburned gas has a temperature of 1400 K and an equivalence ratio at stoichiometry. The 1-D simulation was performed with the time advancement solver AVBP. The velocity at the inlet of the computational domain (x = 0 mm) fixed at u_{in} = 2 m/s. The starting point of the simulation is at t = 0.

Figure 4a shows temperature profiles that were obtained from the simulation at

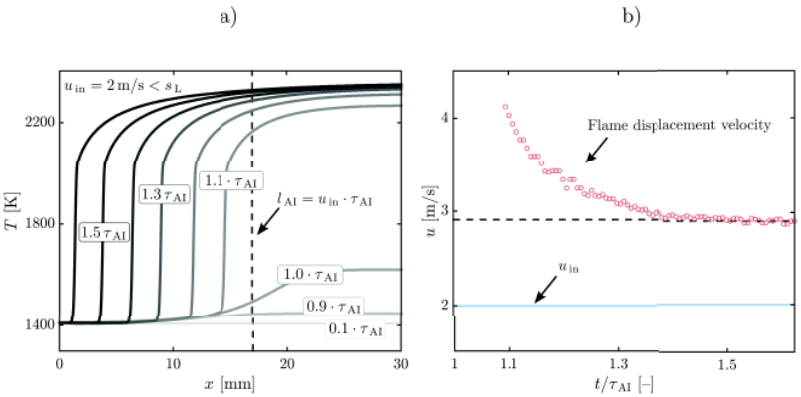

Figure 4. a) Temperature profiles of a transient 1-D simulation at varying instants of time. The mixture auto-ignites at τ_{AI} = 8.5 ms, and subsequently, a flame propagates towards the domain inlet. b) Transient flame displacement velocity from t = 1.1 τ_{AI} to t = 1.6 τ_{AI} obtained from the same simulation as in (a).

different instants of time. The unburned mixture has the property to auto-ignite at the autoignition time τ_{AI} = 8.5 ms, which was computed with a 0-D reactor simulation. The autoignition length l_{AI} is marked with a dashed vertical line. Indeed, one can observe a rapid increase of temperature T, as shown at instants from 0.9 τ_{AI} to 1.1 τ_{AI}. Afterwards, from 1.1 τ_{AI} to 1.5 τ_{AI}, the flame propagates against the incoming flow. The inlet velocity u_{in} = 2 m/s is smaller than the laminar flame speed s_L = 5.0 m/s, which leads to a continuous flame displacement towards the inlet of the domain. The flame displacement velocity u_d is shown in Fig. 4b starting from 1.1 τ_{AI}. Close to l_{AI}, the displacement speed reaches values of 4 m/s and further downstream it approaches a constant value of ≈ 3 m/s. The increase of u_d is due to autoignition chemistry in the unburned gases, corresponding to the "flame propagation assisted by autoignition" regime (II) in Fig. 1. Consequently, also the fresh gas temperature upstream of the pre-ignition zone increases, which is shown in Fig. 4a. At approximately 1.4 τ_{AI}, the effect of upstream autoignition chemistry vanishes, which leads to a constant u_d (regime (I)).
These results show that all three regimes can exist in reactants at elevated temperatures. After autoignition, a propagating type flame assisted by autoignition can evolve. Further downstream, the effect of autoignition chemistry upstream of the flame front vanishes and we observe a purely propagating type flame.

Outlook
Ongoing work extends the regimes maps for high-pressure conditions and makes use of these maps to predict dominant flame stabilization combustion regimes at

varying operating conditions. These predictions are validated with 3-D large eddy simulations of the second stage sequential combustor [6]. More specifically, the ignition sequence of a sequential combustor at atmospheric and high-pressure is investigated. These results show that, similar to the canonical transient simulation of this work (Fig. 4), a transition from autoignition to flame propagating also occurs in the highly turbulent and partially premixed conditions of sequential combustor. Further ongoing work focuses on the transition from steady operation with pure autoignition stabilization to a condition driven only by flame propagation. This transient is induced by a relatively small change of vitiated gas temperature (ΔT = 150 K), which can also have a strong influence on the thermoacoustic stability [9, 10] of such a systems.

References

[1] Schulz, O., Jaravel, T., Poinsot, T., Cuenot, B., Noiray, N. "A criterion to distinguish autoignition and propagation applied to a lifted methane–air jet flame", *Proc. Combust. Inst.* 36 (2017) 1637 - 1644.

[2] Yoo, C. S., Sankaran, R., Chen, J.H., "Three-dimensional direct numerical simulation of a turbulent lifted hydrogen jet flame in heated coflow: flame stabilization and structure", *J. Fluid Mech.* 640 (2009) 453 - 481.

[3] Deng, S., Zhao, P., Mueller, M.E., Law, C.K., "Stabilization of laminar nonpremixed DME/air coflow flames at elevated temperatures and pressures", *Combust. Flame* 162 (2015) 4471 - 4478.

[4] Karami, S., Hawkes, E.R., Talei, M., Chen, J.H., "Stabilisation mechanisms in a turbulent lifted slot-jet flame at a low lifted height", *J. Fluid Mech.* 777 (2015) 633 - 689.

[5] Wagner, J., Renfro, M., Cetegen, B., "Premixed jet flame behavior in a hot vitiated crossflow of lean combustion products", *Combust. Flame* 176 (2017) 521 - 533.

[6] Schulz, O., Noiray, N., "Autoignition flame dynamics in sequential combustors", *Combust. Flame* 192 (2018) 86 - 100.

[7] Krisman, A., Hawkes, E.R., Chen, J.H., "The structure and propagation of laminar flames under autoignitive conditions", *Combust. Flame* 188 (2018) 399 - 411.

[8] Pennell, D.A., Bothien, M.R., Ciani, A., Granet, V., Singla, G., Thorpe, S., Wickstroem, A., "An introduction to the Ansaldo GT36 constant pressure sequential combustor", *ASME Turbo Expo* (2017), pp. GT2017 - 64790.

[9] Poinsot, T. "Prediction and control of combustion instabilities in real engines", *Proc. Combust. Inst.* 36 (2017) 1 - 28.

[10] Schulz, O., Doll, U., Ebi, D., Droujko, J., Bourquard, C., Noiray, N. "Thermoacoustic instability in a sequential combustor: large eddy simulation and experiments", submitted to *37th International Symposium on Combustion*

DIRECT NUMERICAL SIMULATION OF A LEAN, PREMIXED, STAGED COMBUSTOR WITH A FOCUS ON CO EMISSION

K. Kleinheinz[c,]*, L. Berger*, A. Attili*, H. Pitsch*
[c]Corresponding author: k.kleinheinz@itv.rwth-aachen.de
*Institute for Combustion Technology, RWTH Aachen,
Templergraben 64, 52064 Aachen, Germany

Abstract
In stationary gas turbines under part load conditions, CO emissions can increase drastically and limit the load range. To reach low load limits, staged combustion is one common operational strategy, for which the fuel load in an array of jets is varied from one jet to another. The interaction of these jets can influence CO related chemistry and lead to the increased concentration in the exhaust gas. In this work, a Direct Numerical Simulation (DNS) study is carried out featuring the key characteristics of this operational strategy. Three cases with one turbulent lean flame and varying levels of interaction with neighboring air jets are compared to a reference case with three turbulent flames. The cases are compared in terms of the global flame stability, CO emissions in the exhaust gas, as well as its formation and consumption process. It is found that stronger interaction and increased mixing of reactive fluids and air lead to reduced CO consumption and consequently higher CO concentration in the exhaust gas.

Introduction
For the development of next generation gas turbine combustors, the reduction of pollutants plays a major role to meet increasingly strict emission limits. Within this process, numerical simulations can strongly contribute to reduce design cost and to accelerate the development, but further improvement of the predictive quality of combustion and emission models is necessary.
In stationary gas turbines, the most relevant pollutants are nitrogen oxides (NO_x) and carbon monoxide (CO). The former is less relevant under part load conditions, which are typically in line with very lean combustion and relatively low peak temperatures. However, at these conditions CO emissions can increase strongly and, therefore, limit the load flexibility. One operational strategy at this load range is staged combustion. In an array of combustors, fuel injection is omitted for selected burners while neighboring burners receive the fuel and are operated under lean yet stable conditions. Although the overall fuel conversion in the combustion process may be affected only marginally, the interaction of reactive and disconnected burners can result in a perturbation of the oxidation process of CO to CO_2 and, possibly, increased CO emissions. In this work, a series of DNS is performed in a simplified

configuration, which represents the interaction of staged combustors and exhibits increased levels of CO. These simulations are analyzed to improve the understanding of the physical and chemical processes involved in the formation and consumption of CO in turbulent combustion under part load conditions of stationary gas turbines.

Description of DNS database

The layout of the simulation domain has been designed to represent the significant features of the model combustor of a stationary gas turbine, which has been used in several experimental studies by Lückerath et al. [1]. Figure 1 shows a sketch of this model combustor. In this combustor, an array of eight burners is arranged circularly around a central pilot flame. This setup is transformed into a linear, periodic arrangement, which is shown in Figure 2. In the simulation domain, the inlet is located at the left side and the outlet on the right side. The domain is periodic in the y and z directions. The inlet consists of three jets with a slot width of $H_j = 1.2\ mm$, which are aligned parallel and alternate with the pilot slot. The slot width of the pilot is varied between $H_p = 1.0\ H_j\ and\ 1.5\ H_j$ for the different cases. The Cartesian grid has a constant spacing of $dx = 20\ \mu m$ and depending on the case the number of grid points varies between $260 \cdot 10^6$ and $430 \cdot 10^6$. All simulations are carried out using the in-house code CIAO [2] with finite rate chemistry and employing a skeletal mechanism for lean premixed methane/air combustion, derived from GRI3.0 [3] by Luca et al. [4] (16 species and 72 reversible reactions).

The turbulent jets feature a bulk exit velocity $u_j = 100\ m/s$ and the resulting Reynolds number is $Re_j = u_j\ H_j/\nu = 5500$, where ν denotes the viscosity of the unburnt mixture. The pressure of the simulations is $p = 4\ atm$. The unburnt temperature and the equivalence ratio of the reactive jets are $T_u = 673\ K$ and $\phi = 0.7$, which corresponds to typical gas turbine conditions at part load. The pilot, consisting of burnt gases of these initial conditions, has an exit velocity of $u_p = 20\ m/s$.

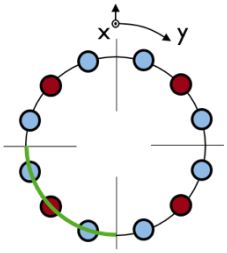

Figure 1. Layout of the model combustor with circular arrangement

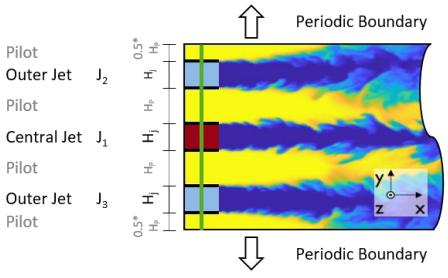

Figure 2. Simulation domain

Four different cases are presented. The cases differ in the number of reactive jets and in terms of the pilot slot width H_p. Case names are composed of a unique letter, the

number of fueled jets, and the ratio of the pilot slot width to the width of the turbulent jets. For the first case A-3F-HP1.0, which is regarded as the reference case, all three jets J_1, J_2, and J_3, are loaded with the reactive methane/air mixture and the combustion process is undisturbed from dilution with air. For the remaining three cases, only the central jet J_1 is loaded with the reactive methane/air mixture with the outer two jets J_2 and J_3 being pure air at $T_u = 673\ K$. For cases A-3F-HP1.0 and B-1F-HP1.0, the slot width of the pilot is equal to the jet slot width. It is increased for cases C-1F-HP1.2 and D-1F-HP1.5 to $H_p = 1.25\ H_j$ and $H_p = 1.5\ H_j$, respectively.

Both parameters influence the ratio $\mathrm{CH}_{4,\mathrm{jet}}/\ (\mathrm{CH}_{4,\mathrm{jet}} + \mathrm{CH}_{4,\mathrm{pilot}})$, which relates the injected unburnt fuel $\mathrm{CH}_{4,\mathrm{jet}}$ to the total fuel issued in the turbulent jets as well as the fuel necessary for the pilots $\mathrm{CH}_{4,\mathrm{pilot}}$. Figure 3 shows this fraction for all four cases as a function of the pilot slot width. This fraction is obviously higher for case A-3F-HP1.0 with three flames. For the remaining three cases, the fraction decreases with increasing pilot width.

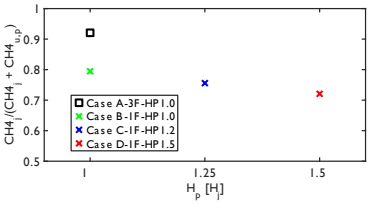

Figure 3. Fuel fraction injected unburnt within the slot jets.

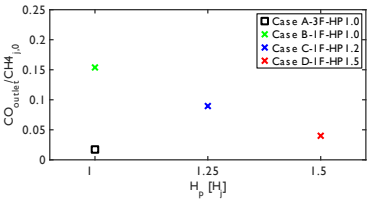

Figure 4. Time averaged mass flux of CO at the outlet – normalized by injected methane mass flux.

Global Flame Statistics

The two parameters, which are varied, influence the intensity of interaction between the different jets. This impacts the flame length and the amount of fuel consumed within the simulation domain. Figure 5 shows the normalized, integrated mass flux of CH_4 in the axial direction. Two important observations are drawn from this plot. First, all fuel is consumed in the reference case A-3F-HP1.0, while some fraction of the fuel persists at the outlet for the three remaining cases. This is below 2% of the injected fuel mass flux for cases C-1F-HP1.2 and D-1F-HP1.5 and it is about 5% for case B-1F-HP1.0. Furthermore, the flame length of the cases is different. For all cases, the axial location, where 50% of the fuel remains is around $x/H_j \approx 14$. However, the location at which only 20% of the fuel remains varies significantly between $x/H_j \approx 19\ and\ 24$ for cases A-3F-HP1.0 and B-1F-HP1.0.

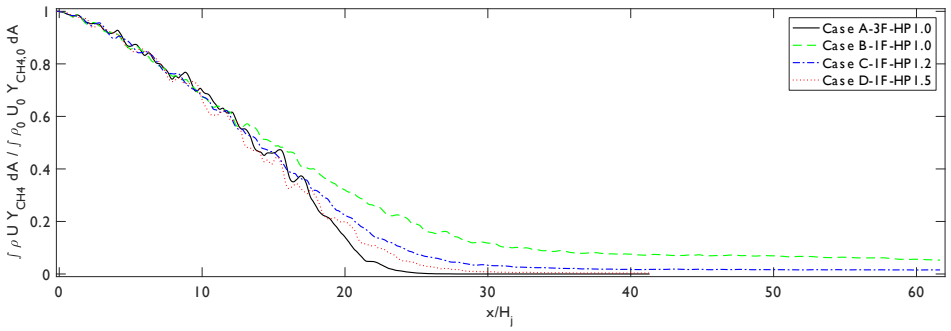

Figure 5. Mean integrated mass flux of methane normalized by the inlet methane mass flux

Analysis of CO formation and consumption

In Figure 6, the time averaged, integrated CO mass flux is shown. It is normalized by the fuel mass flux injected into the domain. This quantity exhibits the same qualitative behavior for all cases. In the first part of the simulation domain, the mass flux increases until it reaches its peak at around $x/H_j \approx 20$. The magnitude of this peak, is very similar for all four cases. The decrease of CO beyond this point is stronger the more stable the combustion process is. CO consumption is fastest for the reference case A-3F-HP1.0 and converges towards the equilibrium value of adiabatic flame temperature conditions. For the remaining three cases, the level of CO mass flux at the outlet increases inversely proportional to the pilot width and flame stability. For a more quantitative comparison, Figure 4 shows the normalized CO mass flux at the outlet. While some of the higher amount in case B-1F-HP1.0 might be related to the incomplete combustion of hydrocarbons, the level of unburnt hydrocarbons is similarly low for cases C-1F-HP1.2 and D-1F-HP1.5. However, the level of CO mass flux is considerably higher for case C-1F-HP1.5, in which the interaction of turbulent flame with the two outside air jets is stronger than for case D-1F-HP1.5.

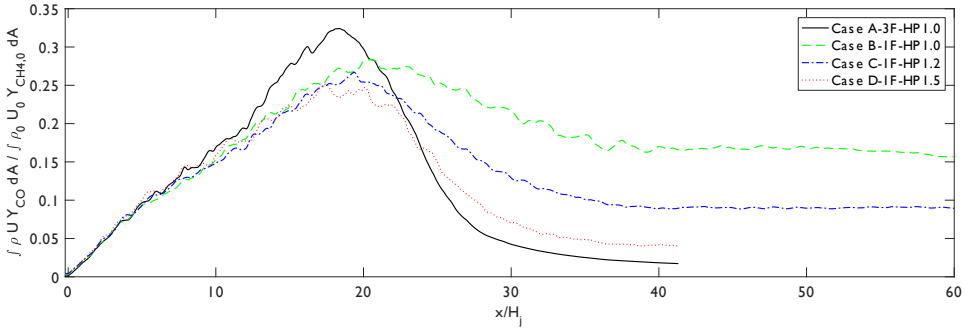

Figure 6. Mean Integrated Mass Flux CO normalized by the methane mass flux at the inlet

Figure 7 shows the joint PDF of the CO mass fraction Y_{CO} and the progress variable for cases A-3F-HP1.0 and C-1F-HP1.2 at four different axial intervals. The red line indicates the solution for an unstretched, one-dimensional laminar flamelet at the same thermochemical conditions of the DNS. For case A-3F-HP1.0, the joint pdf and the conditional mean coincide very well with the reference flamelet. The entire process of CO increase in early flame stages and the decrease at later flame stages is observed. In this case, there is no mixing with air from other jets and the fluctuations stem only from the interaction between chemistry and turbulence. At the last location, the joint pdf is reduced to the point of the equilibrium value of the adiabatic flame temperature. For the case C-1F-HP1.2, the behavior becomes more complex. At the very early location, $x / H_j = 0 \; to \; 5$, the joint pdf is split into two branches. The top branch is related to the outside of the central jet, where combustion is initiated in regions of undisturbed premixed combustion. The lower branch, with Y_{CO} close to zero, can be associated to mixing of the air jets with adjacent pilots. Further downstream, at $x / H_j = 25 \; to \; 30$ all streams mix and the CO mass fraction is covers the entire probabilistic space. The CO mass fraction shows no clear correlation to the progress variable and it cannot be described by the undisturbed flamelet neither by the branch associated with mixing. An additional modeling parameter like a mixture fraction is necessary to account for the local composition. At the last location, $x / H_j = 35 \; to \; 40$, methane combustion is complete and the integrated mass flux of CO remains constant beyond this point. The wide range of progress variable values is associated to the range of mixture fraction. It is worth noting that the CO mass fraction is significantly higher than the corresponding equilibrium values.

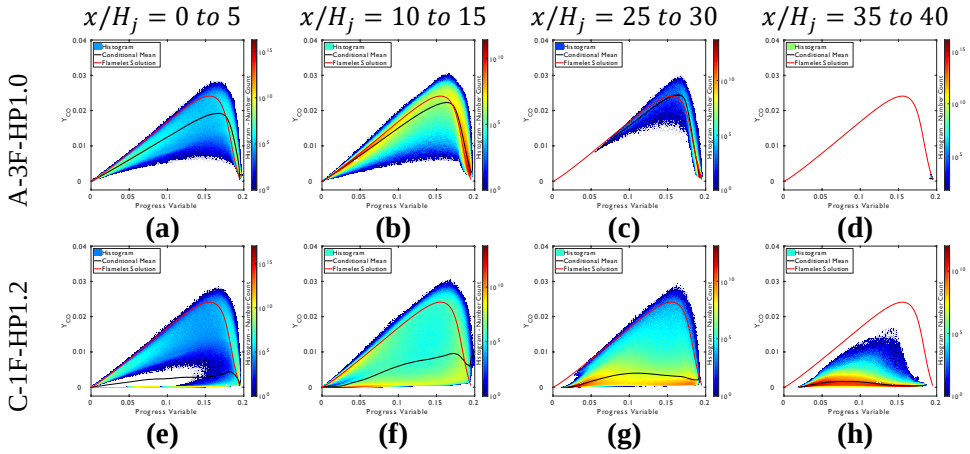

Figure 7. Joint PDF of the mass fraction Y_{CO} and progress variable for cases A-3F-HP1.0 and C-1F-HP1.2

Conclusion

In this work, a set of four different direct numerical simulations (DNS) of turbulent, lean premixed combustion is presented. This study is carried out to investigate CO emissions and its formation and consumption process under conditions typical for gas turbines at part load. In these simulations lean premixed jets are located next to turbulent jets of pure air. For the four cases, the intensity of the interaction between the different jets is varied to reach different levels of CO emissions.

The stability of the combustion process is compared for the different cases and it is found that the CO concentration in the exhaust gas increases with decreasing flame stability. Differences in the concentration become apparent in the late stages of the flame and in the region where fuel reactions are completed. It is assumed that especially the consumption of CO is affected by the increased dilution with unreactive, cold air.

The distribution of CO within the combustion process is compared for two cases, the reference case for which no air is injected into the domain and another case for which all fuel is consumed but CO emissions are considerably increased. While the CO mass fraction reaches its equilibrium value for the reference case, it is significantly larger in the disturbed case.

Acknowledgement

Generous support of the Deutsche Forschungsgemeinschaft (DFG) and the Research Association for Combustion Engines (FVV) under grant numbers PI 368/6-2 (DFG) and 6012390 (FVV) for K. K. and L. B. is gratefully acknowledged. A. A. and H. P. gratefully acknowledge generous support of the European Research Council (ERC) under the European Union's Horizon 2020 research and innovation program (grant agreement No. 695747). Computational resources have been provided by the Gauss Centre for Supercomputing/Leibniz Supercomputing Centre in Munich.

References

[1] Lückerath, R., Lammel, O., Stöhr, M., Boxx, I., Stopper, U., Meier, W., Janus B., Wegner, B., "Experimental Investigations of Flame Stabilization of a Gas Turbine Combustor", *Proceedings of ASME Turbo Expo 2011*, Vancouver, British Columbia, Canada, paper GT2011-45, pp. 725-736 (2011).

[2] Desjardins, O., Moureau, V., Pitsch, H., "High order conservative finite difference scheme for variable density low Mach number turbulent flows", *Journal of Computational Physics* 227: 8395-8416 (2008).

[3] Smith, G., Golden, D., Frenklach, M., Moriarty, N., Eiteneer, B., Goldenberg M., Bowman, C., Hanson, R., Song, S., Gardiner, W., Lissianski V., Qin, Z, GRI-Mech.

[4] Luca, S., Al-Khateeb, A. N., Attili, A., Bisetti, F., Journal of Propulsion and Power 1-8 (2017).

A direct numerical simulation study of post discharge plasma ignition of jet fuel in isotropic turbulence

Giulio Borghesi*, Alex Krisman, Tianfeng Lu*** and Ji-Woong Park*** and Jacqueline H. Chen***

jhchen@sandia.gov

*Combustion Research Facility, Sandia National Laboratories, Livermore, CA 94550, USA

**FM Global Research Corporation, Norwood, MA, USA

*** University of Connecticut, Storrs, CT 06269-3139, USA

Abstract

Direct numerical simulations are performed for post discharge plasma ignition kernels of a jet surrogate fuel in fully developed isotropic turbulence at a turbulent Reynolds number, $Re_t = 2872$, at cold ambient conditions. The success or failure of the ignition kernel to ignite the reactant mixture is studied and the ignition sensitivity to the transit time through a non-flammable inert air layer before mixing with the reactants is determined. In addition to turbulence-chemistry interactions, variations to jet fuel chemistry are studied including differences induced by variations in fuel volatility and low-temperature chemistry.

Introduction

Aviation gas turbines operate over a broad range of altitudes and must be able to relight successfully following a blow-out (global extinction) event for the safe operation of the aircraft. If blow-out occurs, the temperature and pressure within the combustion chamber will decrease due to the absence of the flame and the loss of power to the compressor. This condition is exacerbated at high-altitude where the ambient air is cold and rarefied. To successfully relight, the liquid fuel stream has to undergo atomization and evaporation in order to prepare an ignitable fuel-air premixture in the vicinity of the ignition source. The ignition source must then be able to transition to a rapidly-expanding flame kernel in order to achieve a stabilized flame and, ultimately, successful relight.

There exist two central challenges in the high-altitude relight problem: (1) mixture preparation, and (2) interactions between the ignition source and the prepared mixture.

1. Mixture preparation is essential to produce locally well-mixed parcels at the required equivalence ratio. At high-altitude relight conditions, the atomization of the liquid fuel stream is impeded by the reduced momentum of the air stream, and the increased surface tension of the fuel stream. Once atomized, evaporation is affected by both the reduced pressure which favors vaporization, and the reduced temperature which lowers the fuel

volatility and impedes vaporization. Once in the fuel is in the vapor phase, it is mixed with ambient air in a turbulent environment. The combination of these mixture preparation processes will ultimately determine the distribution of fuel in the vicinity of the ignition source. A necessary condition for successful relight is that this fuel-air mixture is ignitable.

2. The ignition source, usually supplied by a spark, generates a plasma which rapidly decays to a hot gas as it expands and entrains ambient air. The interaction between the post-discharge plasma ignition source, the ambient air, and the fuel, governs the onset of combustion chemistry and the overall success of the ignition event. The ignition source must therefore deliver a sufficiently energetic impulse to a sufficiently reactive fuel-air mixture. At high altitude, the mass-density of the fuel vapor is reduced, which lowers the heat release rate due to combustion and therefore impedes the growth and stabilization of an incipient flame. Variations in fuel chemistry may also play an important role due to differences in the laminar burning rate in addition to turbulence-chemistry interactions.

Configuration and Physical Parameters

To investigate these dynamics, we performed direct numerical simulations (DNS) in a configuration inspired by the experimental facility at the Georgia Institute of Technology (Georgia Tech.), see Fig. 1 [1-3]. This experiment introduces a plasma ignition kernel into a stratified cross-flow consisting of an inert layer below a flammable reactants layer. The kernel is impulsively ejected into the inert layer, entrains ambient air and cools as it travels to the flammable layer.

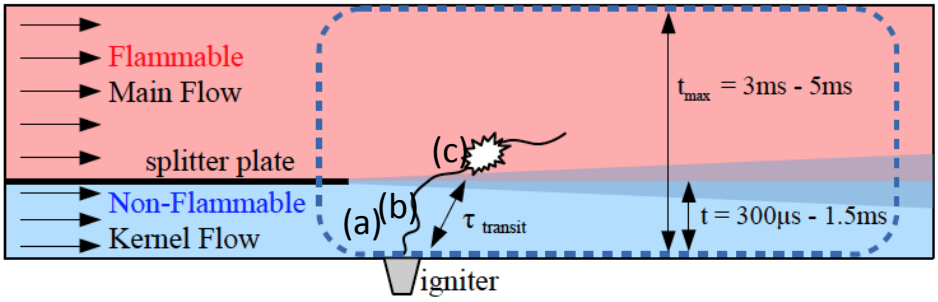

Figure 1:Overview of the experimental test facility at Georgia Tech [1]

The computational expense of performing DNS of this experimental configuration is prohibitive. Hence, we devised a canonical configuration that encapsulates the main dynamics of the experiment in a computationally tractable manner. A box of isotropic, decaying turbulence evolving in time will model the spatial development of the ignition impulse as it traverses the inert layer to the flammable layer. This

will be achieved by decomposing the overall process into several stages summarized in Fig. 2. In the first stage denoted as (a) in Figs. 1 and 2, a mixture corresponding to the ambient non-flammable mixture undergoes linear forcing [4] to establish a physically accurate field of fully-developed isotropic turbulence. In the second stage denoted as (b) in Figs. 1 and 2, a sphere of ionized air at 3300K, determined from reduced order modeling of the spark plasma discharge [1-3], is introduced into the center of the domain, representing the post-discharge plasma ignition impulse. The DNS domain will then be evolved in time, in the absence of turbulent forcing, in order to represent the mixing of the ignition kernel that occurs during the transit time from the igniter to the flammable layer. The initial rms velocity of the turbulence is taken to be ~26 m/s. The turbulence integral scale and the initial spark diameter are 3.5 mm. The 3D computational domain size is 15 mm per side, and the computational grid size is 832 x 832 x 832. Subsequently in stage 3 denoted as (c) in Figs. 1 and 2, a uniform premixture of fuel/air at unity equivalence ratio is introduced into the decaying turbulence and chemical reactions are activated. The turbulence-chemistry interactions are evolved until ignition success or failure is determined.

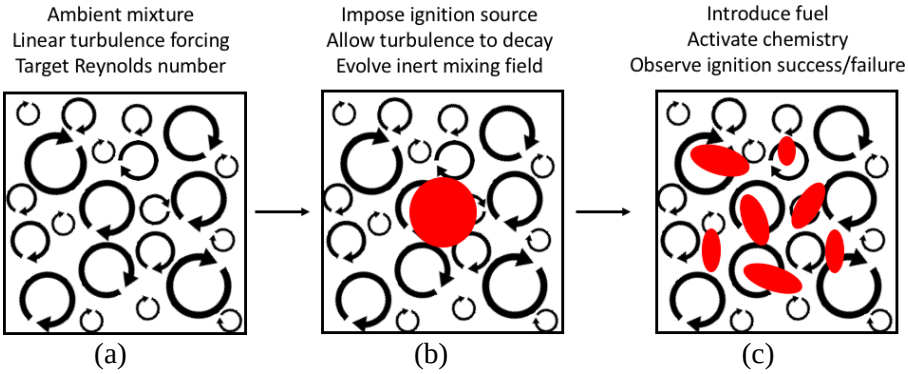

Figure 2: DNS configuration sequence of simulations.

The design of this DNS experiment sacrifices the spatial structure of the plasma impulse/cross-flow interactions, which are considered not to be of leading order importance. This claim is justified by the relatively low Reynolds number of the cross-flow and the relatively small interface between the non-flammable and flammable layers in the channel. The advantage of this configuration is the small number of design parameters and the relatively low computational cost, which allows for a parametric investigation of the key physics.

A series of DNS investigations will be presented to consider both the effects of mixture preparation and the interactions between the ignition source and the prepared mixture. As a first step, the conditions of the Georgia Tech. experiment will be presented for a selected equivalence ratio, which corresponds to ground-

level ambient conditions (or moderately compressed and heated conditions at high altitude). This will allow for validation against known experimental and LES results where the risk of failing to successfully ignite the mixture is low.

Following this baseline, variations are performed for the fuel chemistry and mixture preparation by varying:

1. The definition of the fuel stream and the governing chemical kinetics (high- and low-temperature chemistry submodels)
2. The transit time through the inert nonflammable air layer.
3. The ambient air condition, measured by the altitude above ground level for a standard atmosphere.

The description of the jet fuel chemistry is provided by the HyChem model by Hai Wang *et al.* [5]. In HyChem high-temperature chemistry of multi-component real fuels is modeled by decoupling fuel pyrolysis from the oxidation of the fuel pyrolysis products. The fuel pyrolysis is modeled by 7 lumped reactions where the stoichiometric and reaction rate coefficients are determined experimentally. The oxidation of the pyrolysis products is based on the foundational chemistry of hydrocarbon fuels obtained from USC Mech II. Here, we consider the conventional jet fuels (JetA(A2), and JP5(A3)) modeled with extensive validation including ignition delay times, laminar flame speeds and nonpremixed flame extinction strain rates. HyChem also predicts negative temperature coefficient (NTC) behaviors of jet fuels.

In the present study, three chemical models A2, A2a and A3, were selected to explore a range of jet fuel chemistries. A2a models a highly volatile fuel with high levels of low-temperature chemistry, whereas A2 is the same as A2a with the exception that it has more moderate NTC activity. A3 on the other hand is a low volatile fuel with low levels of low-temperature chemistry. Furthermore, the influence of low-temperature chemistry may be isolated for all three fuel models by neglecting the low-temperature chemistry submodel. In a future study we plan to also investigate the role of fuel volatility in the evaporation of a liquid fuel. The present study considers only gaseous fuel mixtures.

Numerical method

The DNS code S3D [6] is used to solve the compressible Navier-Stokes, total energy, and species continuity conservation equations. S3D uses higher order accurate numerical methods that are eighth-order in space and fourth-order in time.

The species thermodynamic and transport properties are evaluated using mixture-averaged properties and the chemistry is described by the HyChem surrogate jet fuel model [5] that has been reduced to 35 species for A2, 36 species for A2a, and 37 species for A3 with dynamic stiffness reduction in S3D including thermal NO chemistry.

Evolution of Inert Mixing Field

The fully developed turbulence field is shown in Fig. 3a for the u component of the velocity fluctuations and the imposed spherical ignition source of ionized air superimposed on the fully developed isotropic turbulence field is shown in Fig. 3b. After 30 microseconds the kernel has been wrinkled by the turbulence as the turbulence decays and evolves the inert air field as shown in Fig. 3c. In the final step the wrinkled kernel will be imposed in a field of uniform reactants and evolved by the turbulence until ignition success or failure is observed.

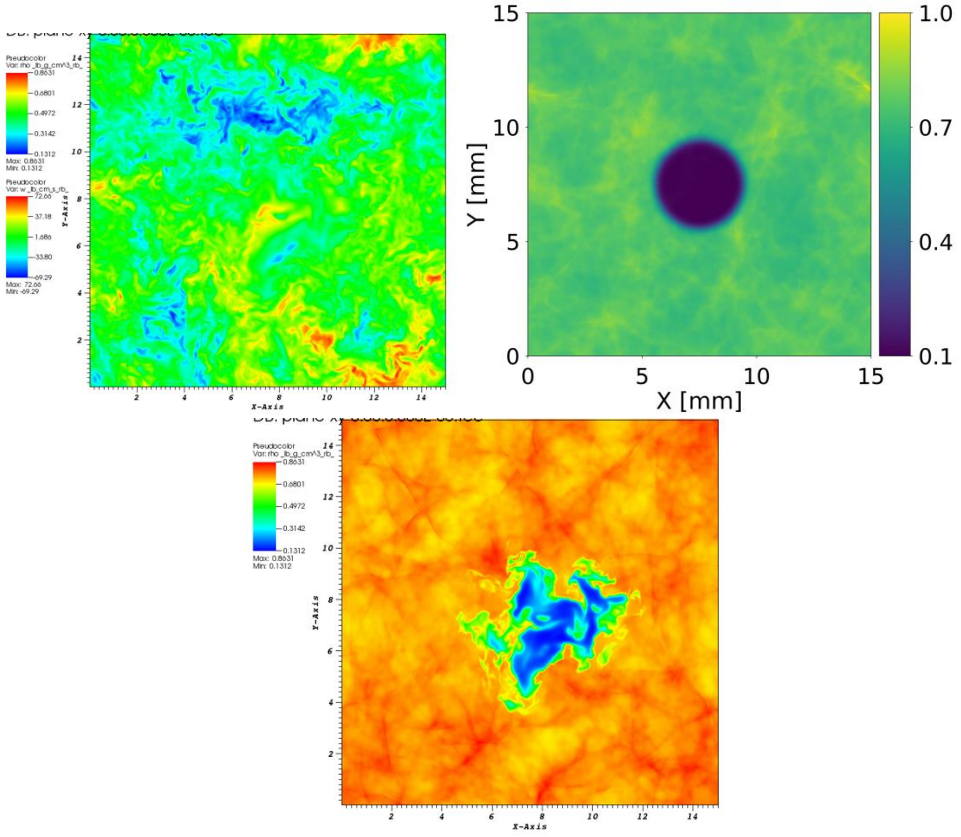

Figure 3. a) u component of velocity fluctuation from fully-developed turbulence prior to spark; b) initial density field of the ionized gas; and c)

density field in isotropic turbulence after 30 microseconds of inert mixing.

References

[1] Jaravel, T., Labahn, J., Sforzo, B., Seitzman, J. and Ihme, M., "Numerical study of the ignition behavior of a post-discharge kernel in a turbulent stratified crossflow", *Center for Turbulence Research Annual Research Briefs*. 176: 63-76 (2017).

[2] Sforzo, B. A., "High energy spark ignition in non-premixed flowing combustors", Ph.D. Thesis, Georgia Institute of Technology (2014).

[3] Sforzo, B. A., Kim, J., Jagoda, J. and Seitzman, J., "Ignition probability in a stratified turbulent flow with a sunken reigniter", *J. Eng. Gas Turb. Power* 137, 011502 (2014).

[4] Rosales, C. and Meneveau, C., "Linear forcing in numerical simulations of isotropic turbulence: physical space implementations and convergence properties", *Physics of Fluids* 17 (2005).

[5] Xu, R., Wang, K., Banerjee, S., Shao, J., Parise, T., Zhu, Y., Wang, S., Moaghar, A., Lee, D. J., Zhao, R., Han, X., Gao, Y., Lu, T., Brezinsky, K., Egolfopoulos, F., Davidson, D., Hanson, R., Bowman, C., and Wang, H., "A Physics-based approach to modeling real-fuel combustion chemistry – II. Reaction kinetic models of jet and rocket fuels", submitted to *Combustion and Flame* (2018).

[6] Chen, J.H., Choudhary, A., de Supinski, B., DeVries, M., Hawkes, E.R., Klasky, S., Liao, W.K., Ma, K.L., Mellor-Crummey, J., Podhorski, N., Sankaran, R., Shende, S., Yoo, C.S., "Terascale direct numerical simulations of turbulent combustion using s3d," *Computational Science and Discovery* 2 (2009).

EFFECT OF RADIANT TRANSFER OF ENERGY IN HIGH-PRESSURE OXY-COMBUSTION

E. Giacomazzi, D. Cecere, F.R. Picchia, N.M. Arcidiacono
eugenio.giacomazzi@enea.it
*DTE-PCU-IPSE, ENEA

Abstract
The aim of this work is to investigate the role of radiant transfer of energy in turbulent non-premixed methane oxy-combustion in an atmosphere rich in CO_2 at supercritical conditions by means of Large Eddy Simulation. A simple shear-layer configuration typical of slot burners is considered: the fuel is CH_4 and flows through the central slot, the oxidant O_2/CO_2 (90% O_2 by mass) mixture flows on both sides of the slot, and a pilot flame is imposed at the inlet between the two streams of reactants to force ignition. Another CO_2 stream coflows.
Fully compressible Navier-Stokes equations coupled to the Peng-Robinson cubic equation of state for real gases in its improved translated volume formulation are solved adopting the Large Eddy Simulation approach. The dynamic Smagorinsky and the LTSM subgrid scale models are used for turbulence and combustion closures. Among the diffusive mechanisms only the Dufour effect is neglected; transport properties are accurately calculated. The M_1 radiant transfer of energy model is adopted without considering turbulence-radiation interactions.

Introduction
The Radiative Transfer of Energy (RTE) is a very important mechanism in several applications. At industrial furnace and combustion chamber temperatures the gaseous species that absorb and emit significantly are CO_2, H_2O, CO, SO_2, NO, and CH_4. Other gases, such as N_2, O_2 and H_2, are transparent to infrared radiation and do not emit significantly; however, they become important absorbing/emitting contributors at very high temperatures. A non-negligible contribution to radiation is also provided by hot carbon (soot) particles within the flame and from suspended particulate material (as in pulverized-coal combustion).
Emission and absorption coefficients of gases increase proportionally to the concentration of the participating species, and hence to the mixture pressure for a given species mass or molar fraction. Besides, the spectral coefficients vary with temperature but also with pressure. Increasing pressure results in spectral line broadening, mainly due to molecular collisions (since the gas density increases) [1], up to wider and more overlapping lines than at lower pressures: the result is that the gas becomes ”grayer” (opaque).
When the total emission from a volume element of absorbing medium is to be calculated, the appropriate mean absorption coefficient is the Planck mean

absorption coefficient, k_P. The Planck mean is convenient since it depends only on the local properties and it can be tabulated. Values have been estimated in the past, but these are today known to be seriously in error, especially at higher temperatures and pressures.
This work is devoted to numerical simulation of methane oxy-combustion in supercritical carbon dioxide at 300 bar. Although adopting a simple chemical scheme, simplifying assumptions on the radiative transfer of energy and a two-dimensional computational domain, some interesting observations are highlighted, and needs for future work identified.

Physical and Numerical Models
The compressible Navier-Stokes equations are solved for a reacting real gas flow at supercritical conditions for which the Peng-Robinson cubic equation of state in its improved volume translated formulation is assumed. The mathematical models adopted are derived for a Newtonian fluid with the Stoke's assumption of N_S chemical species. The mass diffusion constitutive law assumed takes into account the Hirschfelder and Curtiss law for multi-component mixtures, the baro-diffusion and Soret effects. The heat diffusion flux takes into account the Fourier law and the mass diffusion fluxes, neglecting the Dufour effect.
Molecular transport properties for individual species are accurately modelled through NIST models for viscosity and thermal conductivity. The diffusion coefficient D_i of the i-th species into the rest of mixture is modelled according to the Hirschfelder and Curtiss expression, where the required binary diffusion coefficient is calculated by means of kinetic theory. The thermo-diffusion coefficient D_T is estimated by means of the EGLIB routines.
A simplified chemical mechanism consisting of 4 reactions and 6 species developed for oxycombustion is adopted [2, Table 2]. Since main radical species are not included in the mechanism, temperature is overestimated by more than 300 K. This is a first step before facing a more complex kinetics.
The transport equations are solved in the framework of Large Eddy Simulation. Unclosed turbulent combustion subgrid terms of the filtered compressible Navier-Stokes equations are modelled through the dynamic Smagorinsky model and the authors' LTSM (Localised Turbulent Scale Model) [3] turbulent combustion model.
The radiant transfer of energy is also taken into account by means of the M_1 diffusive model. For the time being, turbulence-radiation interaction is neglected, although it is expected to play an important role in flame cooling at the high-pressure conditions of the present simulations. Another simplification is the adoption of the individual species' Planck mean absorption coefficients typically used at atmospheric pressure. Since they are expected to increase by increasing pressure, the effect of multiplying them by 1000 is investigated. In the future they will be accurately calculated by using high-resolution spectroscopic databases.

The numerical simulations are performed by means of the in-house parallel code HeaRT and ENEA's supercomputing facility CRESCO [4]. The HeaRT code solves the compressible Navier- Stokes equations discretised through staggered finite-difference schemes. A second-order accurate centered scheme is adopted for diffusive fluxes; convective terms are modelled through the AUSM$^+$-up method coupled with a third/fifth-order accurate WENO interpolation to reduce spurious oscillations (strongly experienced using centered schemes in high-pressure tests); such numerical spatial scheme was extensively tested by the present authors proving its robustness and accuracy. The low-storage third-order accurate Runge-Kutta method of Shu-Osher is used for time integration. The total energy is defined as sum of internal (thermal) and kinetic energy only. The authors found this choice mandatory to avoid, or at least reduce, unphysical energy and temperature oscillations, mainly driving to the divergence of calculation. No spurious waves were experienced in previous simulations of premixed flames, when the total energy was defined including the chemical formation contribution.
Non-reflecting boundary conditions are implemented at open boundaries in their extended form to take into account the effect of variable transport properties, local heat release and real gas effects. It is observed that in previous and present real gas simulations the authors had to impose a higher value of the relaxation constant in the partially non-reflecting treatment of the outlet with respect to the ideal gas theoretical value (1.5 against 0.27) to avoid unphysical pressure drift in the whole computational domain. A synthetic turbulence generator is adopted at flow inlets.

The Numerical Experiment

The numerical experiment here simulated has a nominal pressure around 300 bar and consists in a simple shear-layer; the flow is confined by means of two no-slip adiabatic walls (at left and right of the domain). At the bottom of the computational domain there is the inlet, while the outlet is located at the top. Simulations are perfomed in a two-dimensional framework to reduce computational time. The domain Y x Z is 8 x 10mm, Y and Z being the transversal and the streamwise dircetions, respectively: it is discretised by means of 396 x 700 nodes.
The fuel is CH_4 and is injected centrally at 50m/s and 388K; its width is 4 x 10^{-4} m. The oxidant O_2/CO_2 mixture flows on both sides of the methane, and a pilot flame is imposed at the inlet between the two streams of reactants to force ignition. Each oxidant jet flows at 100m/s and 450K; their width is 1.95 x10^{-4} m. The pilot flames imposed at the inlet exhibit a temperature distribution ranging from 900 to 2049K and a coherent distribution of chemical species; such data come from separate calculations previously performed; these hot gases flow at 5m/s and are 10^{-4} m widen. Adjacent to each of the oxidant streams, there is a coflowing stream of CO_2 at 50m/s and 973K. The (isotropic) turbulence characteristics of the jets are specified in terms of velocity fluctuations and auto-correlation length-scales: $u' = 5$m/s and $l_y = 3 \times 10^{-5}$ m for the methane jet; $u' = 1$m/s and $l_y = 5 \times 10^{-5}$ m for the pilot flames; $u' = 10$m/s and $l_y = 5 \times 10^{-5}$ m for the oxidant jets; $u' = 5$m/s and l_y

ranging from 2 to 6 x 10^{-5} m for the CO_2 coflowing streams. The length-scale l_y is the (transversal) scale on the inlet plane, while the orthogonal one is $l_z = 2l_y$. The methane jet Reynolds number (based on its bulk velocity and diameter) is nearly 142500 while its turbulent counterpart (based on the imposed velocity fluctuation and length-scale) is around 1070. The oxidant jet Reynolds number is nearly 141500, while its turbulent counterpart ($Re_{t\,Ox}$) is around 3600. The smallest dissipative scale expected comes from the $Re_{t\,Ox}$ and is nearly 10^{-7} m.
Three simulations are performed. The first, without considering the radiant transfer of energy (case NO-RTE); the second, switching on the M1 model with two different levels of absorption: in the case named 1 x k_P the individual species Planck mean absorption coefficients used at atmospheric pressure are adopted, while in the case 10^3 x k_P they are intensified by a factor 10^3.

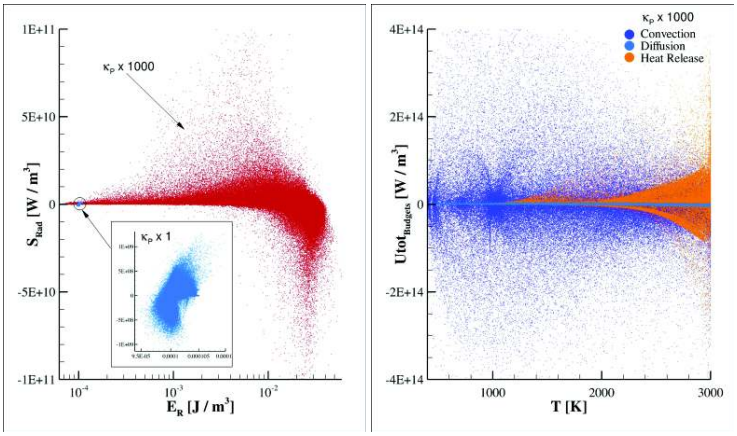

Figure 1. Instantaneous distributions of the radiative source term in the total energy transport equation versus the radiant energy density for two intensifying factors of the Planck mean absorption coefficient k_P (left). Instantaneous distributions of energy budgets related to convection, diffusion and heat release terms contributing to the total energy transport equation (right); contributions from viscous and gravity force works are lower and hence not reported.

Effect of Radiant Transfer of Energy

Comparing results obtained without considering the RTE model with those obtained using different intensification factors of the Planck mean absorption coefficients, very little differences appear in the flame. This happens despite the large differences in the radiation source/sink term of the energy transport equation shown in Fig. 1 (left). This behaviour can be easily understood by comparing the energy budgets of the different terms contributing to the total energy transport and shown in Fig. 1 (right). The order of magnitude of the work done by the gravity

force is 10^5W/m^3; the viscous work is of the order of 10^8W/m^3; since they are order of magnitudes lower than the other terms, they are not shown. Then, in the ordered list of budgets there is the radiative source term with 10^{10}W/m^3, followed by the heat diffusion term with 10^{11}W/m^3. It can be concluded that in the present simulation the effect of radiant transfer of energy is negligible even with the intensifying factor 10^3 for the k_P . However, accurate calculation of the Planck mean absorption coefficients from high-resolution spectroscopic databases is necessary to really understand if the intensification factor 10^3 here adopted is justifiable, sufficient or not. Besides this, it is reminded that turbulence/radiation interaction has not been taken into account in this work, although its contribution is expected to be enhanced in high-pressure combustors [5, 6].

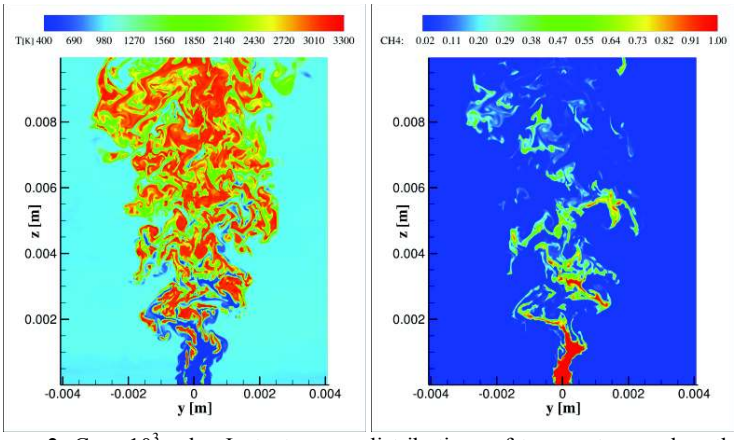

Figure 2. Case 10^3 x k_P. Instantaneous distributions of temperature and methane mass fraction.

It is observed that radiation cooling is active in the hottest regions of the flame but it produces a negligible effect, i.e., peak temperatures do not decrease due to radiation transport. As a matter of fact, the competition between the enhanced radiative cooling expected and the enhanced chemical kinetics (both due to the high pressure) is here dominated by chemistry, in agreement with the heat release budget that is four order of magnitudes greater than the radiative budget. Instantaneous distributions of the radiative source/sink term show that it is localized in thin layers. Although not shown, the results evidenced that radiative cooling (associated to negative values of S_{rad}) in this flame is limited to a very thin layer localized around the stoichiometric mixture fraction and it is more frequent in the hot products side ($Z < Z_{st}$).
Once clarified that in the present simulations the effect of radiation is negligible, let's examine the structure of the flame. The flame is stably anchored, showing

small reacting pockets mainly aligned in the streamwise direction close to the injection, and evolving into larger scale reacting regions moving downstream, as revealed by the temperature snapshot in Fig. 2 (left). The reacting structures are thinner than those typically encountered at lower pressures: this is due to the accelerated chemical kinetics promoted by the high-pressure condition. The methane distribution associated to the same instant is reported in Fig. 2 (right) showing that the jet is corrugated by turbulence without exhibiting any laminar region on its boundaries. High-momentum O_2 ligaments penetrate the methane jet as well as CH_4 fingers also develop into the coflowing stream, thus producing isles of fuels later developing in reacting pockets.

Conclusions

The present real gas simulations prove the robustness of the numerical schemes implemented in the HeaRT code to simulate high-pressure oxy-combustion in s-CO_2 atmosphere. Neglecting turbulence-radiation interaction and with the simplified assumptions on the k_P, it was shown that RTE is negligible; in the future high-resolution spectroscopic databases will be adopted. A further improvement will be a chemical mechanism with radical species.

References

[1] J.R. Howell, R. Siegel, and M.P. Menguc. Thermal Radiation Heat Transfer. CRC Press, Taylor & Francis Group, 5th edition, 2010.

[2] Andersen J., Rasmussen C.L., Giselsson T., and Glarborg P. Global combustion mechanisms for use in CFD modelling under oxy-fuel conditions. Energy & Fuels, 23:1379–1389, 2009.

[3] Giacomazzi E., Cecere D., Picchia F.R., and Arcidiacono N. Sviluppo di un Modello LES per Fiamme Turbolente Premiscelate / Development of an LES model for turbulent premixed flames. PAR2013, Ricerca di Sistema, Accordo di Programma tra ENEA ed il Ministero dello Sviluppo Economico RdS/2013/255, ENEA (UTTEI-COMSO), Roma - Italy, October 2014.

[4] Ponti G. et al. The role of medium size facilities in the HPC ecosystem: the case of the new CRESCO4 cluster integrated in the ENEAGRID infrastructure. In Proceedings of the 2014 International Conference on High Performance Computing and Simulation, volume HPCS 2014, pages 1030–1033, 2014.

[5] J.B. Moss and C.D. Stewart. Spectrally Resolved Measurements of Radiative Heat Transfer in a Gas Turbine Combustor. Experimental Thermal and Fluid Science, 28(6):575–583, 2004.

[6] T. Ebara, N. Iki, S. Takahashi, and W.H. Park. Effect of Radiation Reabsorption on Laminar Burning Velocity of Methane Premixed Flame Containing with Steam and Carbon Dioxide. JSME International Journal Series B - Fluids and Thermal Engineering, 49(2):260–264, 2006.

Flow and 'added' small-scale topologies in a turbulent premixed flame

L. Cifuentes*, A. Kempf* and C. Dopazo**
luis.cifuentes@uni-due.de
*University of Duisburg-Essen, Chair of Fluid Dynamics, Duisburg - Germany
**University of Zaragoza, Fluid Mechanics Area, Zaragoza - Spain

Abstract
The relative motion of two points on adjacent iso-surfaces is examined in terms of local flow topologies of a turbulent premixed flame. The three invariants of the gradients of the flow velocity and of the 'added' normal displacement speed vector are calculated. Joint probability density functions of second and third invariants show comparable magnitudes for the flow and 'added' small-scale topologies. Flow and 'added' enstrophies are obtained to examine the behavior of focal small-scale topologies across the iso-scalar surfaces.

Introduction

Flame topologies are of a fundamental interest in premixed turbulent combustion [1-3]. A number of previous studies have used Direct Numerical Simulation (DNS) data of turbulent premixed flames [4-5] to analyze statistical behaviors of the local flow topologies based on the invariants of the velocity-gradient tensor A_{ij} [6]. However, the motion of a premixed flame can be significantly influenced by molecular diffusion and reaction rates, which create small-scale topologies and affect the geometries of the iso-scalar surfaces.

The present study analyzes the flow topologies in the neighborhood of the enstrophy interface and detects nodal and focal topologies due to the flow and to the displacement speed of the iso-scalar surfaces. This study aims at exploring the general classification of small-scale 'flame' structures based on the invariants of A_{ij} and the 'added' velocity-gradient tensor A_{ij}^{a}. The physical insights obtained from this study will help to understand how molecular diffusion and chemical reaction rates might substantially contribute to the relative motion of two points on adjacent iso-surfaces. Enstrophies ascribed to the flow and 'added' vorticity components are also examined and yield further insight of focal small-scale topologies within a turbulent flame.

Mathematical formalism

In premixed flames, the total velocity v_i^c of a point $\mathbf{x}$ at time t on an iso-surface $c(\mathbf{x}, t) = \Gamma$ is expressed as [7]:

$$v_i^c(\mathbf{x}, t) = v_i(\mathbf{x}, t) + S_d(\mathbf{x}, t) n_i(\mathbf{x}, t) \quad (1)$$

In Eq. (1), v_i is the fluid velocity, S_d is the normal propagating speed relative to the fluid, and $n_i = -(\partial c/\partial x_i)/|\nabla c|$ is the unit vector normal to the iso-scalar surface. The time rate of change of an infinitesimal non-material vector, connecting point **x** on $c(\mathbf{x},t) = \Gamma$ and point **x**+**r** on $c(\mathbf{x},t) = \Gamma + \Delta\Gamma$, is:

$$\frac{dr_i}{dt} = [v_i^c(\mathbf{x}+\mathbf{r},t) - v_i^c(\mathbf{x},t)] = r_j \frac{\partial v_i^c}{\partial x_j} = A_{ij}^c r_j \tag{2}$$

In Eq. (2), the term $\partial v_i^c/\partial x_j = A_{ij}^c$ is the ij component of the total velocity-gradient tensor, which can be decomposed as:

$$A_{ij}^c = \frac{\partial v_i^c}{\partial x_j} = \frac{\partial v_i}{\partial x_j} + \frac{\partial (S_d n_i)}{\partial x_j} = A_{ij} + A_{ij}^a \tag{3}$$

The term $A_{ij} = \partial v_i/\partial x_j$ is the flow velocity-gradient tensor, and $A_{ij}^a = \partial(S_d n_i)/\partial x_j$ is the 'added' velocity-gradient tensor due to the spatial variations of the displacement velocity vector $S_d n_i$.
Consequently, Eq. (2) can be recast as:

$$\frac{d\,r_i}{dt} = S_{ij}\, r_j + \frac{1}{2}\varepsilon_{ijk}\,\omega_j r_k + S_d \frac{\partial n_i}{\partial x_j} r_j + \frac{1}{2}\left(n_i \frac{\partial S_d}{\partial x_j} + \frac{\partial S_d}{\partial x_i} n_j\right) r_j + \frac{1}{2}\varepsilon_{ijk}\omega_j^a\, r_k \tag{4}$$

In Eq. (4), the term S_{ij} is the flow strain rate tensor, ε_{ijk} is the Levi-Civita alternating tensor, $\omega_i = \varepsilon_{ijk}(\partial v_k/\partial x_j)$ is the flow vorticity vector, $\partial n_i/\partial x_j$ is the curvature tensor and $\omega_i^a = \varepsilon_{ijk}(\partial S_d/\partial x_j) n_k$ is the 'added' vorticity vector [7].
The first term on the right side of Eq. (4) includes linear dilatation and angular deformation rates due to the flow, whereas the second one represents solid body rotation of **r**. The third term contains the stretch rate of an area element on the iso-surface, the fourth one accounts for rates of separation or approach of two adjacent iso-surfaces, and the fifth term is the solid body rotation with ω_i^a.
The total enstrophy corresponding to the total vorticity vector $\omega_i^c = \omega_i + \omega_i^a$ is:

$$E^c = \frac{1}{2}\omega_i^c \omega_i^c = \frac{1}{2}\omega_i \omega_i + \frac{1}{2}\omega_i^a \omega_i^a + \omega_i \omega_i^a = E + E^a + \omega_i \omega_i^a \tag{5}$$

The total enstrophy aggregates the flow and 'added' enstrophies plus the scalar product of flow and 'added' vorticity vectors.
Perry and Chong [6] characterized the small-scale flow motions of point $\mathbf{x}+\mathbf{r}$ about point **r** in terms of the three invariants (P, Q, R) of A_{ij}. Nodal and focal topologies of a turbulent flow emerge depending on the dominance of strain or rotation. If **r** is not a material vector, the previous methodology can be extended by further examining the invariants (P^a, Q^a, R^a) of A_{ij}^a. The contributions of A_{ij} and

A_{ij}^a are additive $\left(A_{ij}^c = A_{ij} + A_{ij}^a\right)$. Hence, apart from the small-scale flow topologies, point $\mathbf{x} + \mathbf{r}$ will undergo an additional motion with respect to point $\mathbf{r}$ due to the gradient of the normal displacement speed $\partial(S_d n_i)/\partial x_j$. A general analysis can be performed examining the invariants $(P^c\ Q^c, R^c)$ of A_{ij}^c, and those of A_{ij} and A_{ij}^a.

Direct numerical simulation

The three-dimensional DNS analyzed was performed by Proch with the in-house code PsiPhi [8-9]. The Schmidt number is 0.7 and the Lewis number is unity for all species. The chemistry is tabulated with the Premixed Flamelet Generated Manifolds (PFGM) approach. Viscosity, thermal conductivity, and mass diffusion coefficients are given functions of the temperature. The geometry is described by an immersed boundary technique. The DNS computes the Cambridge stratified burner [9], which consists of a central bluff-body surrounded by two co-annular premixed methane-air streams at ambient conditions and a co-flow of air (see Fig. 1a). The computational domain consisted of $1120 \times 1200 \times 1200$ equidistant cells and a grid of 1.6 billion cells with a resolution of 100μm. Numerical values of the variables and dimensionless parameters for this simulation are presented in Table 1.

Table 1. DNS dimensional variables and dimensionless parameters.

Variables and dimensionless parameters	**Inner stream**	**Outer stream**
Integral length scale, l (mm)	0.5	0.5
Velocity fluctuations rms, u' (m/s)	0.9	1.8
Kolmogorov length micro-scale, η (μm)	40.9	24.3
Non-stretched laminar flame speed, S_L (m/s)	0.212	0.212
Laminar flame thickness, δ_L (mm)	0.565	0.565
Turbulent Reynolds number, Re	28.1	56.3
Damköhler number, Da	0.2	0.1
Schmidt number, Sc	0.7	0.7
Lewis number, Le	1.0	1.0

Results

Figure 1 shows the interaction between the instantaneous enstrophy field, the enstrophy interfaces and the iso-lines $c = 0.1$ and $c = 0.9$ for the premixed turbulent annular jet flame. The normalized progress variable based on temperature $c = (T - T_{\min})/(T_{\max} - T_{\min})$ is used to characterize the scalar interface of interest. The progress variable is zero in the fresh reactants and unity in the fully burnt products. Enstrophy structures are less convoluted near the nozzle and they curve and radially grow between the inner and outer interfaces downstream, as a result of engulfment and entrainment. This widening of the vortical region could be explained by the behavior of the large flow structures, which grow downstream and engulf large fluid packages from the irrotational region into the rotational zone.

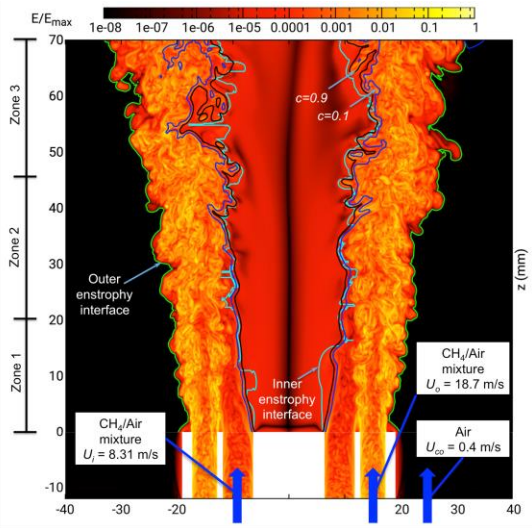

Figure 1. Instantaneous enstrophy field, progress variable iso-lines $c = 0.1$ and $c = 0.9$, and iso-lines defining the enstrophy inner $E/E_{max} = 7.0 \times 10^{-5}$ and outer $E/E_{max} = 1.0 \times 10^{-7}$interfaces.

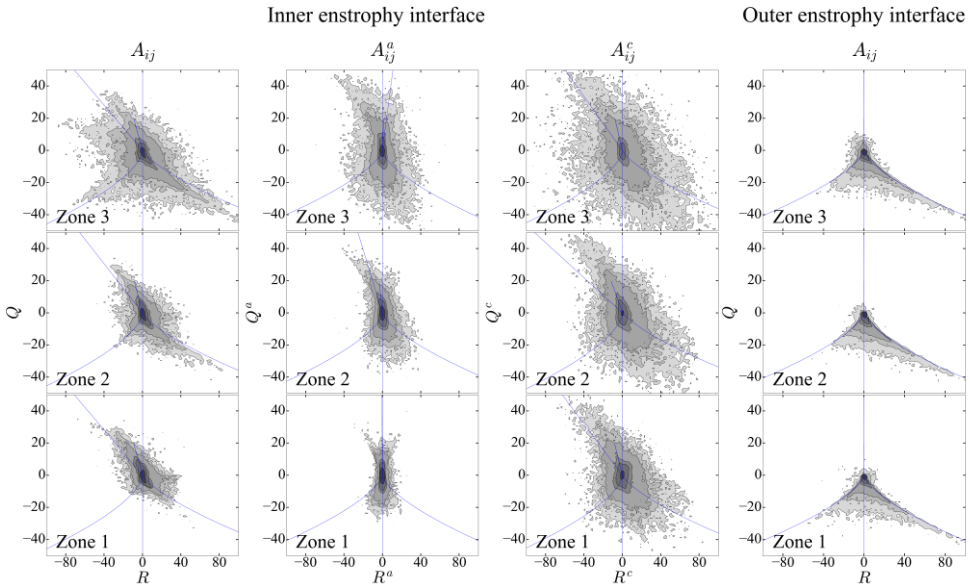

Figure 2. JPDFs of the invariants: Q and R of A_{ij}; Q^a and R^a of A^a_{ij}; and Q^c and R^c of A^c_{ij}.

Figure 2 shows the joint probability density functions (JPDFs) of the second and third invariants of the velocity-gradient tensor A_{ij}, of the 'added' velocity-gradient

tensor A_{ij}^{a} and of the total velocity-gradient tensor A_{ij}^{c} for the layers at the inner and outer enstrophy interfaces. The statistics has been performed at different axial locations above the burner, namely, *Zone 1* (0-20mm), *Zone 2* (20-45mm) and *Zone 3* (45-70mm), as illustrated in Fig. 1. Data were analyzed for ten cross-stream planes $x - z$ in the burner midsection, considering grid points in a region ± 5 mm in the radial direction from the enstrophy inner and outer interfaces. It is interesting to note in Fig. 2 that the universal teardrop shape typical of constant-density turbulent flows disappears at both interfaces. In the case of the inner enstrophy interface, the statistical distributions are displaced towards the left side, which is consistent with positive local dilatation rate close to the flame region.

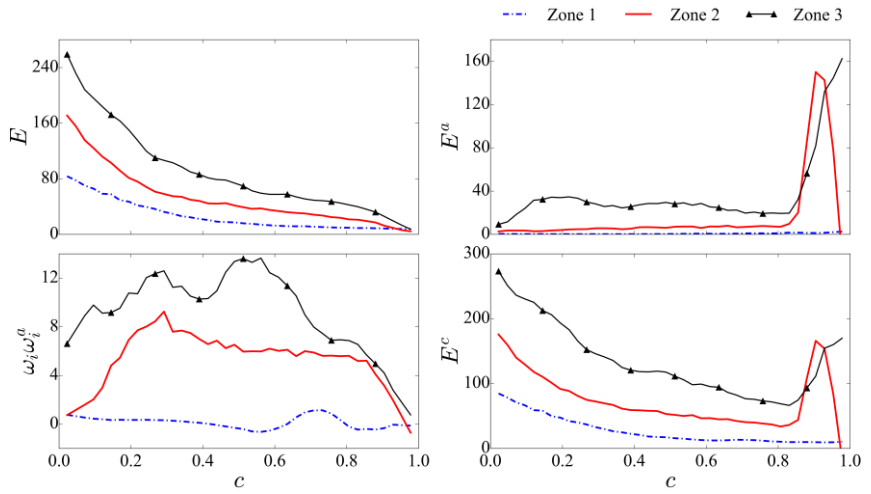

Figure 3. Mean values of the flow E and 'added' E^a enstrophies, scalar product $\omega_i\omega_i^a$ and total enstrophy E^c across the progress variable c.

Figure 3 depicts the average of the flow E and 'added' E^a enstrophies, scalar product $\omega_i\omega_i^a$ and the total enstrophy E^c across the progress variable c. For $c > 0.80$, namely, in the burning and hot product regions, the 'added' enstrophy grows significantly, whereas the flow enstrophy remains approximately constant and becomes much smaller as the reaction progress variable increases. This behavior implies that flow focal topologies govern in the fresh gases and tend to disappear, in favor of 'added' focal topologies, towards the burning region and hot products. It is worth stressing that the magnitudes of flow and 'added' enstrophies are comparable in the present case, which confirms that the rotation of **r**, as a solid body with an angular velocity ω_i^a, creates enstrophy by flame.

Conclusions

Contributions to the relative motion of two points on adjacent iso-surfaces can be examined in terms of small-scale flow and 'added' topologies. The later are

classified using the gradient of the displacement speed normal vector, related to molecular diffusion and reaction rates. The magnitudes of the 'added' invariants, Q^a and R^a, are comparable to those of the turbulent flow, Q and R. Alternative decomposition of A_{ij}^a can explicitly include area stretch rates and contributions to 'flame' thickening or thinning. The 'added' enstrophy is as important as the flow enstrophy, which indicates that a share of the total enstrophy is generated by flame.

Acknowledgments
The authors are grateful to Jülich Supercomputing Centre (JSC) for computational support. This project has received funding from the European Union's Horizon 2020 research and innovation program under grant agreement No 706672 - ITPF.

References
[1] Günther, R., Lenze, B., "Exchange coefficients and mathematical modelsof jet-diffusion flames", In Symposium (International) on Combustion. Vol. 14, No. 1, 1973, pp. 675-687.
[2] Driscoll, J.F., Gulati, A., "Measurement of various terms in the turbulent kinetic energy balance within a flame and comparison with theory", Combust. Flame, 72(2): 131-152 (1988).
[3] Steinberg, A.M., Driscoll, J.F., "Straining and wrinkling processes during turbulence-premixed flame interaction measured using temporally-resolved diagnostics", Combust. Flame, 156(12): 2285-2306 (2009).
[4] Cifuentes, L., Dopazo, C., Martin, J., Jimenez, C., "Local flow topologies and scalar structures in a turbulent premixed flame", Phys. Fluids, 26: 065108, (2014).
[5] Wacks, D.H., Chakraborty, N., Klein, M., Arias, P. G., Im, H.G., "Flow topologies in different regimes of premixed turbulent combustion: A direct numerical simulation analysis", Physical Review Fluids, 1(8): 083401, (2016).
[6] Chong, M.S., Perry, A.E., Cantwell, B.J., "A general classification of three-dimensional flow fields", Physics of Fluids A: Fluid Dynamics, 2(5): 765-777 (1990).
[7] Dopazo, C., Cifuentes, L., Martin, J., Jimenez, C., "Strain rates normal to approaching iso-scalar surfaces in a turbulent premixed flame", Combust. Flame, 162(5): 1729-1736 (2015).
[8] Kempf, A.M., Geurts, B.J., Oefelein, J.C., "Error analysis of large-eddy simulation of the turbulent non-premixed sydney bluff-body flame", Combust. Flame, 158(12): 2408-2419 (2011).
[9] Proch, F., Domingo, P., Vervisch, L., Kempf, A.M., "Flame resolved simulation of a turbulent premixed bluff-body burner experiment. Part I: Analysis of the reaction zone dynamics with tabulated chemistry", Combust. Flame, 180: 321-339 (2017).

Numerical and Experimental Investigation of the Noise Generation of a Turbulent Flame

K. Pausch*, S. Herff*, H. Nawroth, C. O. Paschereit**, W. Schröder***
k.pausch@aia.rwth-aachen.de
*Institute of Aerodynamics, RWTH Aachen University, Wüllnerstraße 5a, 52062 Aachen, Germany
**Chair of Fluid Dynamics - Hermann-Föttinger-Institut, Technische Universität Berlin, Müller-Breslau-Straße 8, 10623 Berlin, Germany

Abstract
The acoustic emission of a generic unconfined turbulent jet flame is studied numerically using a hybrid large-eddy simulation / computational aeroacoustics (LES/CAA) approach and compared with experimental data. To accurately reproduce the turbulent flow field of the experiment, the LES domain includes the full experimental burner plenum with its annular gas injection. The broadband acoustic spectrum predicted by solving the acoustic perturbation equations whose source terms are determined the LES data is in good agreement with the experimental measurements. The numerical data will be used to analyze the acoustic sources and their near-field characteristics.

Introduction
Since jet noise and fan noise are reduced through recent technological progress [1], combustion noise becomes an increasingly important contributor to the overall sound emission of jet aero engines. Furthermore, a deeper understanding of combustion noise source mechanisms is required for the development of highly efficient low-emission gas turbines, since the lean-premixed regime is prone to thermoacoustic instabilities. Such instabilities are characterized by the amplified interaction between acoustic pressure and the flame's unsteady heat release and can ultimately lead to the structural failure of the burner assembly. [2]
Two distinct mechanisms define the generation of combustion noise [1]: Direct combustion noise generated in the combustion chamber and indirect combustion noise generated due to the acceleration of entropy inhomogeneities, i.e., hot spots convected through a nozzle or a turbine stage [3–5]. The spectral shape of direct combustion noise from open flames has been studied experimentally [6, 7] with respect to fuel, flow parameters, and the burner geometry, numerically [8] and empirically [9]. Still, the mechanisms of the sound generation remain unknown and further detailed studies on the acoustic source terms are necessary. In classical theory, the sound generation is often associated with the flame's unsteady rate of heat release acting as a distribution of monopole sound sources, [10], [11] but there is no general justification that this is the dominant sound source independent from the gas mixture, flow conditions, or burner geometry.

Nawroth et al. [12] have designed a generic experimental setup to fundamentally investigate the generation of combustion noise of lean-premixed turbulent flames in an unconfined environment. This setup is studied numerically with a hybrid LES/CAA approach by solving the acoustic perturbation equations (APE) [13], which have been extended [14, 15] for the analysis of combustion noise based on LES data. The flow solver and the acoustic solver have been recently used for the hydrodynamic and acoustic analysis of laminar [16, 17] and turbulent flames [8,18–20]. Previous investigations have shown a sensitivity of the acoustic spectrum on the inflow turbulence [19]. It was concluded that an accurate numerical prediction of combustion noise requires a detailed numerical representation of the experimental domain with well-defined boundary conditions. Therefore, to accurately reproduce the experimental inflow turbulence, an LES including the full burner plenum was set up. Based on an experimental validation of the numerically predicted acoustics, the numerical data can be used to analyze the acoustic source mechanisms and their near-field radiation in detail.

Numerical Setup

The hybrid concept defines the numerical analysis. In the first step, the compressible Navier-Stokes equations for a three-dimensional unsteady reacting flow are solved by means of large-eddy simulation coupled with a combined G-equation progress variable approach by Moureau et al. [21] to model the combustion process. The flame speed varies with the flame surface curvature [22, 23]. A modeling approach for the subgrid turbulent flame speed by Pitsch et al. [24] is used. For a more detailed description of the combustion solver and the used LES model the reader is referred to [8, 18, 25]. The combustion model has been shown to satisfactorily capture the dynamics of the flame surface for several canonical problems, e.g., flame-vortex interaction [21, 25], Darrieus-Landau instability [16], mean heat release rate distribution, and mean turbulent mass consumption speed [18].

An unstructured Cartesian grid flow solver based on a strictly conservative finite-volume methodology [25–27] is used for the numerical solution. The convective terms are discretized by a second-order accurate modified low-dissipation AUSM scheme and the viscous terms are approximated by second-order accurate central differences. Time-integration is done by a third-order total-variation diminishing (TVD) Runge-Kutta scheme [18]. A conservative cut-cell technique captures arbitrary embedded boundaries [28, 29].

In the second step, the acoustic field is computed using the acoustic perturbation equations by Ewert and Schröder [13]. The left-hand side corresponds to the filtered linearized Euler equations extended for a non-uniform mean flow field describing acoustic wave propagation into the far field. The right-hand side consists of the source terms resulting from the linearization of the governing equations of viscous flow and determines the acoustic emission.

The acoustic perturbation equations are discretized in space using a 9-point 6th-order dispersion-relation preserving summation by parts scheme (SBP-DRP). [30] The temporal integration is done by an alternating 5-6 stage low-dispersion low-dissipation Runge-Kutta scheme (LDDRK) [31]. A radiation boundary condition is used on the domain boundaries to avoid reflections [32].

Burner Configuration

The experimental setup of the turbulent Bunsen-type burner and the computational domain of the LES are shown in figure 1. The experiments are conducted by TU Berlin by means of acoustic pressure measurements using condenser microphones in an anechoic room, flow diagnostics using particle image velocimetry (PIV), and flame diagnostics using an intensified camera for OH* chemiluminescence imaging. The burner setup consists of a combined fuel and air injection at the far upstream to premix methane and air. For PIV measurements, seeding can be added at this location. The combined injection is connected to an annular injection manifold, which feeds the mixture into the plenum of constant diameter. A converging nozzle follows this segment providing a top hat-like velocity profile at the outlet with a diameter d = 0.035m. To achieve high Reynolds numbers at lean equivalence ratios, a pilot ring burner encompasses the rig downstream of the nozzle. Both main and pilot flames use the same mixture with pure methane as fuel instead of natural gas to provide a constant chemical composition of the mixture at an equivalence ratio of φ = 0.7. The Reynolds number based on the burner exit diameter is Re_d = 10,000.

Figure 1. Sketch of the burner setup and the computational domain.

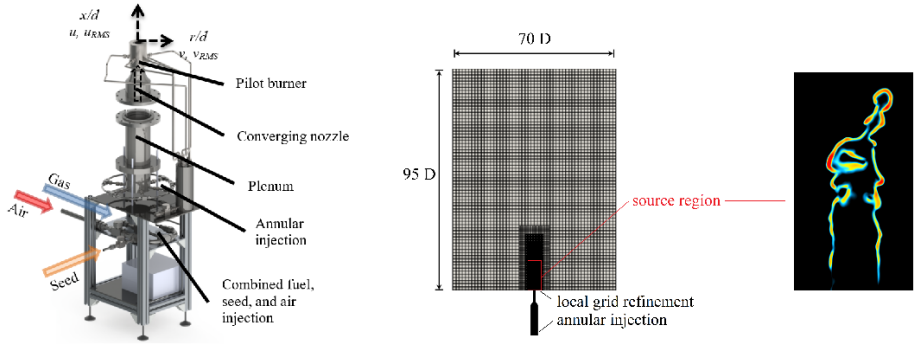

The computational LES domain consists of 87 million grid points. To accurately reproduce the experimental turbulent flow field, the full burner plenum with the radial injection of the methane-air mixture is included. Local refinement in the burner plenum and the jet region leads to an isotropic cell spacing of 0.0187d. The

acoustic source terms are computed in the source region of the LES and interpolated on the CAA grid for the subsequent acoustic computation.

Results

In a previous study [19] the flow statistics of the cold jet was shown to be in good agreement with the experimental data and the full plenum computation of the cold jet revealed the existence of acoustic modes within the burner plenum. The current study extends the analysis from acoustics of the cold flow to the acoustics of the reacting flow. In figure 2 the acoustic far-field spectrum obtained by the CAA simulation at the microphone position x = 0D; r = 30D is compared with the LES pressure spectrum inside the burner plenum. The far-field spectrum shows several peaks at the frequencies f = 60Hz, f = 360Hz, and f = 720Hz. Similar peaks are also observed in the Fourier transformed LES pressure inside the plenum. It is concluded that acoustic modes within the burner plenum excite the flame leading to the peaks observed in the far-field spectrum. The experimental results also show peaks at f = 360Hz and f = 720Hz, however, there is no distinct mode found at f = 60Hz. The overall broadband acoustic spectra of the experiment and CAA simulation are quantitatively in good agreement. The numerical data will be used for a detailed analysis of the acoustic source mechanisms and near-field radiation characteristics.

Figure 2. CAA pressure spectrum at x/d=0, r/d=30 (left), LES pressure spectrum in burner plenum (right)

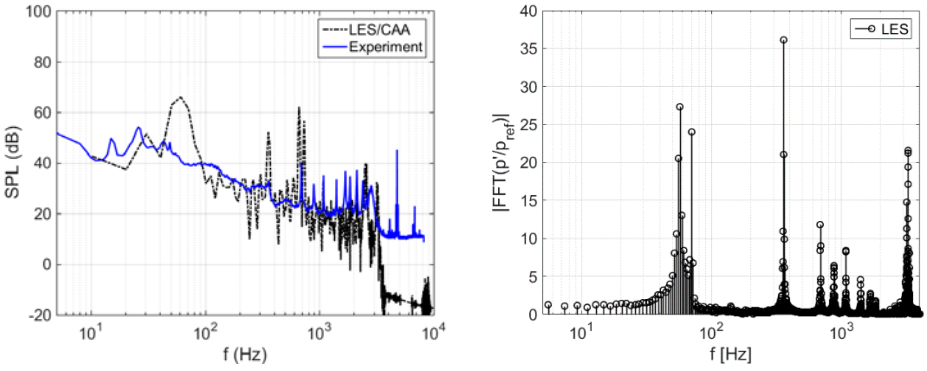

References

[1] Dowling, A. P. and Mahmoudi, Y., “Combustion noise”, *P. Combust. Inst.* 35:65-100 (2015)

[2] Lieuwen, T. and Yang, V., Combustion Instabilities in Gas Turbine Engines: Operational Experience, Fundamental Mechanisms, and Modeling, Vol. 210,

AIAA, 2005
[3] Strahle, W., "Combustion noise", *Prog. Energy Combust. Sci.* 4:157-176 (1978)
[4] Marble, F. and Candel, S., "Acoustic disturbance from gas non-uniformities convected through a nozzle", *J. Sound Vibr.* 55 (1977)
[5] Bake, F., Richter, C., Mühlbauer, B., Kings, N., Röhle, I., Thiele, F., and Noll, B., "The entropy wave generator (EWG): a reference case on entropy noise", *J. Sound Vib.* 326:574-598 (2009)
[6] Kotake, S. and Takamoto, K., "Combustion noise: effects of the shape and size of burner nozzle", *J. Sound Vib.* 112:345-354
[7] Rajaram, R. and Lieuwen, T., "Acoustic radiation from turbulent premixed flames", *J. Fluid Mech.* 637:357-385 (2009)
[8] Schlimpert, S., Koh, S. R., Pausch, K., Meinke, M., and Schröder, W., "Analysis of combustion noise of a turbulent premixed slot jet flame", *Combust. Flame* 175:292-306 (2017)
[9] Tam, C. K. W., "The spectral shape of combustion noise", *International Journal of Aeroacoustics* 14:431-456 (2015)
[10] Thomas, A. and Williams, G. T., "Flame noise: sound emission from spark-ignited bubbles of combustible gas," *Proceedings of the Royal Society of London. Series A. Mathematical and Physical Sciences* 294:449-466 (1966)
[11] Hurle, I., Price, R., Sugden, T., and Thomas, A., "Sound emission from open turbulent premixed flames," *Proceedings of the Royal Society of London A: Mathematical, Physical and Engineering Sciences* 303:409-427 (1968)
[12] Nawroth, H. and Paschereit, C. O., "High-speed flow field measurements of turbulent jet flames undergoing shear layer manipulation", AIAA Paper 2016-1841 (2016)
[13] Ewert, R. and Schröder, W., "Acoustic perturbation equations based on flow decomposition via source filtering", *J. Comput. Phys.* 188:365-398 (2003)
[14] Bui, P. T., Meinke, M., Schröder, W., Flemming, F., Sadiki, A., and Janicka, J., "A hybrid method for combustion noise based on LES and APE", AIAA Paper 2005-3014 (2005)
[15] Koh, S., Geiser, G., and Schröder, W., "Reformulation of acoustic entropy source terms", AIAA Paper 2011-2927 (2011)
[16] Schlimpert, S., Hemchandra, S., Meinke, M., and Schröder, W., "Hydrodynamic instability and shear layer effect on the response of an acoustically excited laminar premixed flame", *Combust. Flame* 162:345-367 (2015)
[17] Schlimpert, S., Meinke, M., and Schröder, W., "Nonlinear analysis of an acoustically excited laminar premixed flame", *Combust. Flame* 163:337-357 (2016)
[18] Schlimpert, S., Feldhusen, A., Grimmen, J. H., Roidl, B., Meinke, M., and Schröder, W., "Hydrodynamic instability and shear layer effects in turbulent premixed combustion", *Phys. Fluids* 28 (2016)

[19] Herff, S., Pausch, K. Nawroth, H., Schlimpert, S., Paschereit, C., and Schröder, W., "Impact of turbulent inflow distributions on combustion noise of lean-premixed flames", AIAA Paper 2017-3219 (2017)
[20] Pausch, K., Herff, S., Schlimpert, S., Meinke, M., and Schröder, W. "Acoustic flame response of a round and a slot burner", AIAA Paper 2017-3360 (2017)
[21] Moureau, V., Fiorina, B., and Pitsch, H., "A level set formulation for premixed combustion LES considering the turbulent flame structure", *Combust. Flame* 156:801-812 (2009)
[22] Markstein, G., "Nonsteady flame propagation", Pergamon Press 75 (1964)
[23] Poinsot, T., Echekki, T., and Mungal, M. G., "A study of the laminar flame tip and implications for premixed turbulent combustion", *Combust. Sci. Technol.* 81:45-73 (1992)
[24] Pitsch, H., "A consistent level set formulation for large-eddy simulation of premixed turbulent combustion", *Combust. Flame*, 143:587-598 (2005)
[25] Hartmann, D., Meinke, M., and Schröder, W., "A level-set based adaptive-grid method for premixed combustion", *Combust. Flame* 158:1318-1339 (2011)
[26] Hartmann, D., Meinke, M., and Schröder, W., "An adaptive multilevel multigrid formulation for cartesian hierarchical grid methods", *Comp. Fluids* 37:1103-1125 (2008)
[27] Hartmann, D., Meinke, M., and Schröder, W., "The constrained reinitialization equation for level set methods", *J. Comp. Phys.* 229:1514-1535 (2010)
[28] Schneiders, L., Hartmann, D., Meinke, M., and Schröder, W., "An accurate moving boundary formulation in cut-cell methods", *J. Comput. Phys.* 235:786-809 (2013)
[29] Schneiders, L., Günther, C., Meinke, M., and Schröder, W., "An efficient conservative cut-cell method for rigid bodies interacting with viscous compressible flows", *J. Comp. Phys.* 311:62-68 (2016)
[30] Johansson, S., "High order finite difference operators with the summation by parts property based on DRP schemes", 2004
[31] Hu, F., Hussaini, M., and Manthey, J., "Low-dissipation and low-dispersion Runge-Kutta schemes for computational acoustics", *J. Comput. Phys.* 124:177-197 (1996)
[32] Tam, C. K. W. and Webb, J. C., "Dispersion-relation-preserving finite difference schemes for computational acoustics", *J. Comput. Phys.* 107:262-281 (1993)

Spectral response of Different Combustion Models in LES of Direct Combustion Noise

F. Zhang*, T. Zirwes, H. Nawroth***, N. Li*, P. Habisreuther*, H. Bockhorn*, D. Trimis*, C.O. Paschereit*****

Feichi.Zhang@kit.edu

* Engler-Bunte-Institute, Division of Combustion Technology, Karlsruhe Institute of Technology, Engler-Bunte-Ring 1, 76131 Karlsruhe, Germany

** Steinbuch Centre for Computing (SCC), Karlsruhe Institute of Technology, Hermann-von-Helmholtz-Platz 1, Karlsruhe, Germany

*** Institute of Fluid Dynamics and Technical Acoustics, Technische Universität Berlin,Müller-Breslau-Straße 8, 10623 Berlin, Germany

Abstract

This work presents compressible large eddy simulation (LES) of a turbulent premixed methane/air jet flame along with two commonly used combustion models, the turbulent flame-speed closure (TFC-class) and the dynamically thickened flame (DTF) model. The mean and rms statistics of the flow velocity calculated with both TFC and DTF models show a reasonable agreement. However, DTF-LES predicts a higher sound pressure level compared to the TFC-LES, the reason is that the flame is thinner in the DTF-LES compared to TFC-LES, leading to a stronger flame-turbulence interaction and heat release rate fluctuation. In the DTF model, mean reaction rates are based on an Arrhenius-like model, whereas the current implementation of the TFC model postulates the mean rate as a parabolic function of the reaction progress variable. The difference between sound spectra calculated with DTF- and TFC-LES has been found to be dependent on the frequency range. The dependence is weak in the low and high frequency range and large in an intermediate range. This reflects the different spectral response behavior of TFC and DTF models to turbulent flow, which is essential when using compressible LES for calculating thermo-acoustics such as combustion noise.

1. Introduction

The reduction of noise emission has become an increasing important issue for industrial combustion devices such as aircraft engines or gas turbines [1, 2]. In low-Mach number flows, the transient fluctuations of the local heat release rate due to flame-turbulence interactions represent the main source of noise, which is known as direct combustion noise. Its generation mechanism is described by the unsteady generation of gas volume through thermal expansion, which leads to a temporal density fluctuation. Direct combustion noise exhibits a broadband distribution in the spectral domain, which correlates to the spectrum of turbulent kinetic energy due to the mutual interaction between heat release and turbulent fluctuations [3, 4]. Computational fluid dynamics (CFD) is widely used to study

combustion noise and its formation mechanisms. Among the different CFD approaches, the LES technique is viewed as a compromise between computing effort and accuracy and has found widespread use for the simulation of combustion and combustion noise in the last decade [2, 4, 5]. A variety of combustion models exists [6, 7, 8], where the treatment of flame-turbulence interactions is described with different physical aspects. For example, the level-set approach [7, 8] is derived by assuming an infinitely thin flame and tracking solely the dynamic movement of the respective flame surface due to the turbulent flow and flame's propagation. In the artificially thickened flame model [9], the flame is thickened in order to resolve it on a coarse grid. Therefore, the resolved flame structure as well as its response to the turbulent flow are affected by using different modeling concepts. The effects and consequences of two commonly used combustion models on noise formation will be demonstrated here by means of LES of a premixed turbulent jet flame.

2. Combustion Modeling

2.1 Turbulent Flame-speed Closure (TFC) Model

For the current implementation of the TFC class model, a transport equation for the Favre-filtered progress variable $\tilde{c}$ is solved [4]:

$$\frac{\partial \bar{\rho}\,\widetilde{c}}{\partial t} + \frac{\partial \bar{\rho}\tilde{u}_i\,\widetilde{c}}{\partial x_i} = \frac{\partial}{\partial x_i}\left(\frac{\mu_l + \mu_t}{Sc_t}\frac{\partial\,\widetilde{c}}{\partial x_i}\right) + \bar{\dot{\omega}}_c \qquad (1)$$

where $\bar{\cdot}$ denotes a filtered and $\tilde{\cdot}$ a Favre-filtered value. μ_l and μ_t are the laminar and turbulent viscosity. Sc_t is the turbulent Schmidt number. Focus of the model is to represent the source term $\bar{\dot{\omega}}_c$ with the turbulent flame speed S_t, which considers the effect of flame-turbulence interactions [10]:

$$\bar{\dot{\omega}}_c = \rho_0 \frac{S_t^2}{D_l + D_t}\,\widetilde{c}\,(1 - \widetilde{c}), \qquad \frac{S_t}{S_l} = \frac{u'}{S_l}\left(1 + {D_a}^{-2}\right)^{-\frac{1}{4}} \qquad (2)$$

ρ_0 is the density of the unburnt gas, S_l the unstretched laminar flame speed, u' the turbulence intensity, D_l and D_t the laminar and turbulent diffusivity. The Damköhler number Da is evaluated by the ratio of turbulent to chemical time scales $D_a = \tau_t/\tau_c \propto (L_t/u')/(a_0/S_l^2)$ with the turbulent length scale L_t and the thermal diffusivity of the unburnt gas a_0. In the context of LES modeling, the turbulence parameters u', L_t, $D_t = u' \cdot L_t$ are calculated from the sub-grid scale turbulence model. S_t represents in this case an effective burning velocity, which depends on the grid resolution. Structures of the flame zones are pre-computed by simulating unstrained 1D flames. The species mass fractions are then projected onto the c-space. In this work, c is calculated with the chemically bound oxygen.

2.2 Dynamically Thickened Flame (DTF) Model

The DTF model is based on thickening the actual flame front artificially while keeping the flame speed constant [9, 11]. It also introduces an efficiency parameter to account for the attenuated flame-turbulence interactions caused by a reduced Da

through the thickening procedure. A transport equation is solved for each species:

$$\frac{\partial \bar{\rho}\tilde{Y}_k}{\partial t} + \frac{\partial \bar{\rho}\tilde{u}_i\tilde{Y}_k}{\partial x_i} = \frac{\partial}{\partial x_i}\left((EF\frac{\mu_l}{Sc_k})\frac{\partial \tilde{Y}_k}{\partial x_i}\right) + \frac{E}{F}\bar{\dot{\omega}}_k \quad (3)$$

where $\tilde{Y}_k$ is the Favre-filtered mass fraction and Sc_k the Schmidt number of the *k*-th species. The filtered mean reaction rate $\bar{\dot{\omega}}_k$ is evaluated from the reaction rates of the respective species with the rate coefficient is given by an Arrhenius temperature dependency. The thickening factor F and the efficiency factor E are given by [9, 11]:

$$F = max\left(\frac{n\Delta}{\delta_l}, 1\right), \qquad E = \frac{1 + \alpha\Gamma\left(\frac{\Delta_e}{\delta_l}, \frac{u'}{S_l}\right)\frac{u'}{S_l}}{1 + \alpha\Gamma\left(\frac{\Delta_e}{\delta_l^1}, \frac{u'}{S_l}\right)\frac{u'}{S_l}} \quad (4)$$

with the grid size Δ, the laminar flame thickness δ_l and n the number of grid cells used to resolve the thickened flame. The computation of F is only active within the reaction zone and F is equal to 1 elsewhere. E takes into account the increase of mean reaction rates due to turbulent fluctuations, for example, through wrinkling of the flame surface. Γ indicates a functional operator and Δ_e the local filter size. δ_l^1 is the resolved flame thickness, i.e., $\delta_l^1 = F\delta_l = n\Delta$. α is a model constant that scales with $Re^{-1/2}$. The required turbulence parameters in both TFC and DTF models like u' and L_t are evaluated from the sub-grid turbulence modeling.

3. Numerical Setup

The above described methods are applied to a turbulent premixed methane/air jet flame operated at atmospheric conditions ($T_0 = 293$ K, $p_0 = 1$ atm) [12, 13], using two equivalence ratios $\phi = 0.7$ and $\phi = 0.9$. The Reynolds number based on the nozzle diameter D and the bulk velocity is $Re = 15{,}000$. The computational domain consists of the convergent nozzle part and a large cylindrical domain with an extension of 80 D in axial and radial direction, containing approx. 11.2 million hexahedral grid cells. The grid is systematically refined along the burner wall and the shear layer with a smallest grid size of 0.3 mm.

OpenFOAM [14] has been used to solve the governing equations with the finite volume method in a fully implicit compressible formulation [15]. We implemented the TFC and DTF models described in Sec.2 into this code. For the DTF model, $n = 2.5$ is used to resolve the flame, along with a two-step reaction mechanism and prescribed Sc_k for each species individually [11]. The GRI-3.0 [16] mechanisms is used for the chemistry tabulation in the TFC model. The Smagorinsky Model [17] has been used for sub-grid scale (SGS) turbulence modeling.

4. Results

Figure 1 shows instantaneous (left) and time-mean (right) contours of temperature calculated from LES using the TFC and the DTF model for the case of $\phi = 0.9$. The resolved flame is thinner and more heavily wrinkled with DTF compared to

TFC. This is attributed to the evaluation of the mean reaction rates by a parabolic shape-function $\widetilde{c}\,(1-\widetilde{c}\,)$ in the TFC model (see Eq.(2)). This approach alters the internal flame structure by broadening the evolution of $\overline{\dot{\omega}}_c$ spatially. For the DTF model, the flame thickness is prescribed by the thickening factor and the reaction rate is evaluated with the kinetic rate expression scaled by E/F (see Eq.(3)), which results in a thinner flame and hence, a more intense flame-turbulence interaction compared to the TFC model.

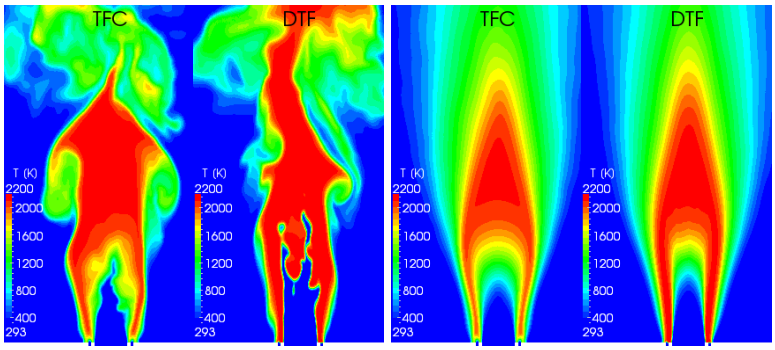

Figure 1. Comparison of instantaneous (left) and (right) time-mean temperature calculated with TFC and DTF combustion models.

In Fig.2, the time mean and root mean square (rms) values of the axial and radial velocities calculated with TFC and DTF are compared with experimental data for different streamwise locations: $x/D = 0.4$ to $x/D = 4$. The mean values (1st and 2nd column) obtained from TFC and DTF show a good agreement and also compare well to the measured data. The predicted resolved rms values (3rd and 4th column) are however higher in DTF-LES compared with TFC-LES. This is due to the resolved thinner flame by the DTF-LES compared to TFC-LES, which leads to a stronger wrinkling of the flame surface and fluctuation of velocity at the flame front.

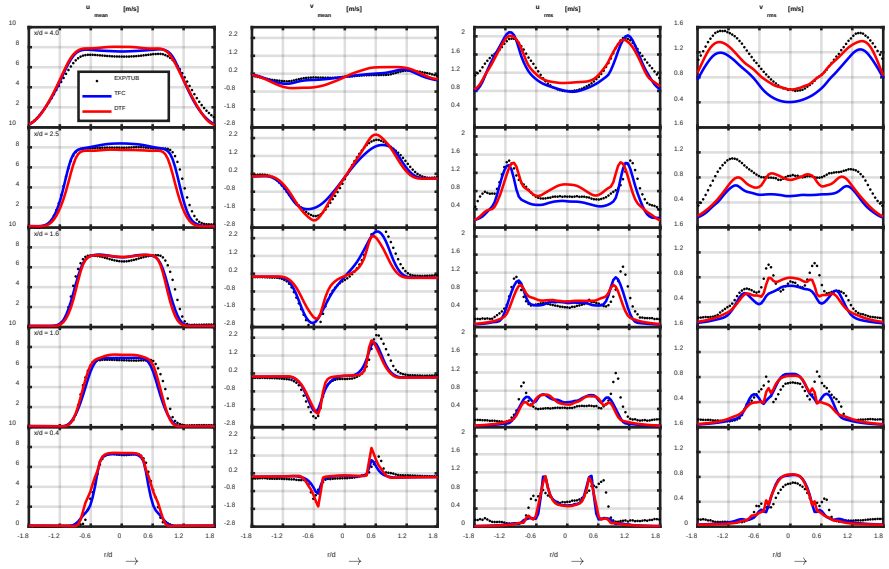

Figure 2. Comparison of calculated and measured mean and rms velocities.

Fig.3 at the top depicts calculated and measured sound pressure L_p for a far field monitor point ($x/D = 15, r/D = 30$), and at the bottom the spectra of total heat release rate $\dot{Q}_t$. In both cases with $\phi = 0.7$ (left) and $\phi = 0.9$ (right), L_p from TFC and DTF agree well with each other in the low frequency range ($f < 20$ Hz). With increasing frequency however, L_p from TFC is smaller than L_p from DTF, because a thicker flame is resolved by TFC-LES compared to DTF-LES, so that the resolved flame is less sensitive to high-frequency turbulent fluctuations. The TFC-LES shows better agreement with the experiment than DTF-LES in the range with $f < 100$ Hz. For higher frequencies, L_p is over-predicted by DTF-LES and under-predicted by TFC-LES. Corresponding to the results obtained for L_p, the spectra of $\dot{Q}_t$ are higher with DTF-LES than TFC-LES and the deviations between DTF and TFC are dependent on the frequency range. The results indicate a differently resolved flame response to turbulent fluctuations due to the use of different combustion models.

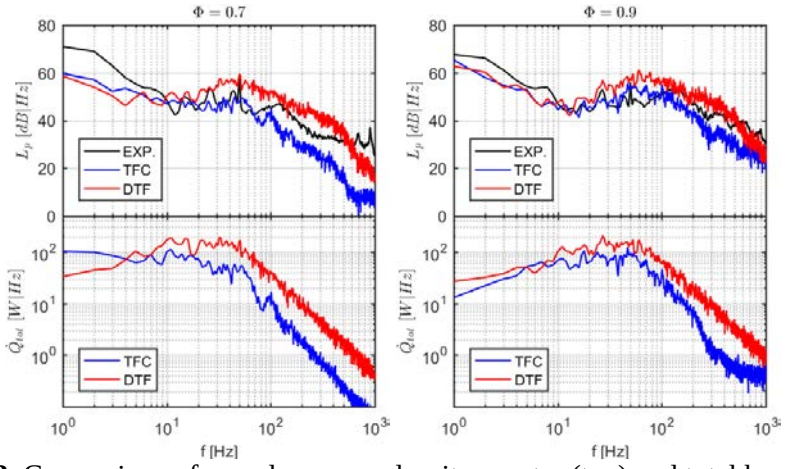

Figure 3. Comparison of sound pressure density spectra (top) and total heat release rate (bottom) calculated with TFC- and DTF-LES.

5. Conclusion

Two commonly used combustion models, the TFC and DTF approaches, are applied to LES of a turbulent premixed methane/air jet flame. Focus of this work lies on evaluating the ability of these combustion models to resolve the heat release rate and sound pressure in the spectral domain. The results reveal in which frequency range the heat release rate fluctuations can be correctly predicted by these models. As it has been elaborated in this work, the TFC shows better agreement with experiments than the DTF model in the low frequency range (see Fig.3), indicating that the DTF model is not always better suited than TFC for thermo-acoustic calculations.

Acknowledgements

The authors thank for the financial support by the German Research Council (DFG) through Research Units Bo 693/26-2 and DFG-PA920/12 "Combustion Noise". This work utilizes computational resources from the High Performance Computing Center Stuttgart (HLRS) and the Steinbuch Centre for Computing (SCC) at KIT.

References

[1] Dowling, A.P., Mahmoudi, Y., "Combustion noise", *Proc. Combust. Inst.* 35: 65-100 (2015).

[2] Bailly, C., Bogey, C., Candel, S., "Modelling of Sound Generation by Turbulent Reacting Flows", *Int. J. Aeroacoust.* 9: 461-490 (2010).

[3] Rajaram, R. Lieuwen, T., "Acoustic radiation from turbulent premixed flames", *J. Fluid Mech.* 637: 357-385 (2009).

[4] Zhang, F., Habisreuther, P., Bockhorn, H., Nawroth, H., Paschereit, C. O., "On Prediction of Combustion Generated Noise with the Turbulent Heat Release Rate ", *Acta. Acust. united with Ac*. 99: 940-951 (2013).

[5] Zhang, F., Habisreuther, P., Hettel, M., Bockhorn, H., "Numerical Computation of Combustion Induced Noise Using Compressible LES and Hybrid CFD/CAA Methods", *Acta. Acust. united with Ac*. 98: 120-134 (2012).

[6] Poinsot, T., Veynante, D., *Theoretical and numerical combustion*, Edwards Inc., Philadelphia, U.S.A., 2005.

[7] Peters, N., *Turbulent Combustion*, Cambridge University Press, Cambridge, U.K., 2000.

[8] Pitsch, H., "A consistent level set formulation for large-eddy simulation of premixed turbulent combustion", *Combust. Flame* 143: 587-598 (2005).

[9] Colin, O., Ducros, F., Veynante, D., Poinsot, T., "A thickened flame model for large eddy simulations of turbulent premixed combustion", *Phys. Fluids* 12: 1843-1863 (2000).

[10] Schmid, H., Habisreuther, P., Leuckel, W., "A model for calculating heat release in premixed turbulent flames", *Combust. Flame* 113: 79-91 (1998).

[11] Legier, J.P., Poinsot, T., Veynante, D., "Dynamically thickened flame LES model for premixed and non-premixed turbulent combustion", *Center for Turbulence Research, Proceedings of the Summer Program* 2000, p. 157.

[12] Nawroth, H., Paschereit, C.O., Zhang, F., Habisreuther, P., Bockhorn, H., "Flow Investigation and Acoustic Measurements of an Unconfined Turbulent Premixed Jet Flame", AIAA Paper, pp 2013-2459 (2013).

[13] Zhang, F., Zirwes, T., Nawroth, H., Habisreuther, P., Bockhorn, H., Paschereit, C.O., "Combustion-Generated Noise: An Environment-Related Issue for Future Combustion Systems", *Energy Technol*. 5: 1045-1054 (2017).

[14] OpenFOAM, The Open Source CFD Toolbox, User Guide (2014).

[15] Ferziger, J.H., Perić , M., *Computational methods for fluid dynamics*, Springer-Verlag Berlin Heidelberg, Germany, 2002.

[16] Smith, G., Golden, D.,Frenklach, M., Moriarty, N., Eiteneer, B., Goldenberg, M., Bowman, C., Hanson, R., Song, S., Gardiner, W., Lissianski, V., Qi, Z., Gri 3.0 reaction mechanism.

[17] Fröhlich, J., *Large Eddy Simulation turbulenter Strömungen*, Teubner Verlag, Germany, 2006.

REACTION ZONE IDENTIFICATION AND CHARACTERIZATION BASED ON RIDGE ANALYSIS

V. Bykov, R. Schießl
robert.schiessl@kit.edu
Institute of Technical Thermodynamics, Karlsruhe Institute of Technology (KIT)

Abstract
We introduce a novel method for identifying and characterizing reaction zones in combustion. The method is based on the general concept of ridges, i.e., regions where a given spatial field has local directional maxima in directions of its curvature eigenvectors. By identifying the reaction zone with ridges of a suitable reaction strength field allows us to describe the zone in a fully generic way. Firstly, low-dimensional spatial structures that "form the center" of the front can be defined in a natural way. These central regions may locally have different dimension, giving rise to patch-, filament- or sheet-like reaction zones. Secondly, in addition to localizing the central region, one can also infer information about the extent (the "thickness") of the zone from the analysis. This highly generic way of identifying and describing reaction fields can be applied to a wide spectrum of combustion cases, including premixed, non-premixed and partially premixed flames, laminar and turbulent, spanning different regimes (flame-like combustion, broken reaction zones, patch-like structures). As a first demonstration, the method is applied to a Direct Numerical Simulation (DNS) sample of a non-premixed diluted hydrogen/air turbulent flame, using the chemical entropy production rate field as indicator for reaction strength. It is shown that the topology of the central region can strongly differ from the classical "flame sheet" concept. In particular, we find that the filament-type reaction zone geometry is represented frequently in the DNS data set.

Introduction
Many concepts in combustion theory and modeling rely on the notion of a reaction zone [1-3]. A special type of reaction zone is a flame, classically a thin layer where combustion reactions occur, and which propagates by a combination of reaction and diffusive processes. Other types of reaction zone can occur as well, e.g., distributed combustion, or even bulk, volumetric combustion (e.g., after auto-ignition in a homogeneous system).
Existing concepts are widely applied to their respective type of combustion systems (e.g., premixed, non-premixed flames). However, it is unclear how they could be extended to include other systems, like partially premixed flames, or reaction zones which are generally not well described by a flame concept, e.g., zones of auto-ignition.

In view of the rapidly increasing variety of combustion applications, and the tendency to use extreme combustion regimes in technical applications, situations where a clear assignment of a system to one of the traditional paradigms (premixed or non-premixed, flame-like combustion or auto-igniting zones) is no more possible, become increasingly frequent and significant. It is desirable to have a systematic way of describing reaction zones available, which can be applied to a generic combustion system.

In this work, we propose to use the concept of *ridges* for the purpose. Loosely speaking, ridges are regions where a given spatial field has elevated values relative to its neighborhood; a more precise definition based on curvature analysis and directional maxima is given and used in this paper. We apply the ridge concept to a reaction intensity field of a combustion system. The chemical entropy production rate is used as a proxy for the reaction "strength".

The method is applied to three-dimensional DNS of a turbulent, non-premixed hydrogen/air flame. It is found that the reaction zone features aspects that are not covered by the classical notion of a flame-sheet. In particular, when turbulence and reaction interact strongly, the reaction front at some locations is no more a two-dimensional surface, but rather has characteristics of a one-dimensional, filament-like structure. Samples of these structures, which we propose to call flame worms, or shorter *florms*, due to their characteristic appearance, are shown, and some statistics on the front geometry in the DNS data are presented.

The findings can be used to more accurately quantify an effective flame surface of a turbulent flame, and therefore, for improved models of the flame propagation velocity in turbulent combustion. The exact relation of the filament-like structures to turbulence-chemistry interaction, as well as to other one-dimensional turbulence structures, still needs to be investigated.

Methodology

DNS simulation data

A turbulent non-premixed planar flame at atmospheric pressure, where nitrogen-diluted hydrogen (75/25 N2/H2 by mole) flows counter an air stream (79/21 N2/O2 by mole), both at 298 K was simulated by 3D-DNS. Details of the DNS are given in previous papers [4,5]. The data from this DNS was used to apply the concept for reaction zone identification.

Chemical entropy production rate as reaction intensity field

A reaction front is identified in the DNS data as a post-processing step. Several scalars could be employed as reaction front markers, e.g., the chemical source term of some species, or the heat release rate (HRR). However, a single specie's source term does not necessarily monitor the overall chemical activity, and the magnitude of the HRR can be small, even in presence of strong chemical activity, since the effects of exothermic and endothermic reactions may cancel. A quantity that is positive for any chemical activity in a combustion system is the rate of chemical entropy production; the second law of thermodynamics guarantees this positivity.

We used this field in our analysis. Therefore, first the mass-specific chemical entropy production rate (CEPR, in W/(kg· K)) ω_s was computed for every spatial point in the DNS data set. The CEPR is computed by:

$$\omega_S = \sum_{i=1}^{N} \omega_{Y_i} s_i + \frac{\omega_{th}}{T} = \sum_{i=1}^{N} \omega_{Y_i} \left(s_i + \frac{h_i}{T} \right) \quad (1)$$

With index *i* running from 1 to the number of chemical species *N*, ω_{Y_i} denotes the chemical source term of species *i* in a mass-fraction scale, s_i denotes its specific entropy, c_p is the specific heat capacity at constant pressure of the mixture, *T* its temperature, and ω_{th} the temporal rate of temperature change induced by chemical reaction. c_p and s_i are temperature- and composition dependent. The chemical source terms were computed from the species mass fractions, temperature and pressure. using the same reaction mechanism and thermodynamic data that had also been used in the preceding DNS calculations. For illustration, various scalar fields from a sample DNS data set are depicted in Fig.1.

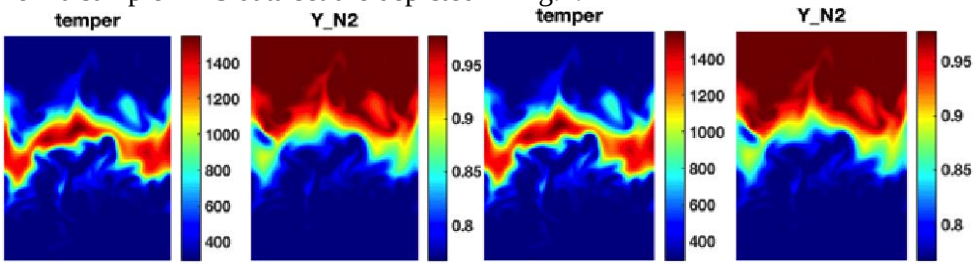

Figure 1. Different scalar fields on the same 2D-slice (size 1 cm × 1.2 cm) from a DNS snapshot. «temper» is the temperature in K, Y_N2 and Y_OH are N_2 and OH masss fractions, and sprod is the chemical entropy production rate ω_s in W/(kg·K). The 2D-slice is perpendicular to the average flame.

It is seen that OH mass fraction (Y_OH) can be large in regions where the local reaction activity is practically zero (e.g., near the right edge of the frames in Fig. 1). The appearance of the ω_s field roughly matches the heat release (not shown here); local differences exist, however. Strong reaction (as indicated by large values of the ω_s field) does not necessarily coincide with high temperatures or large OH mass fractions (Y_OH); large values of T and OH may prevail even if practically no reaction is proceeding (e.g., near the right edge of the frames in Fig. 1). The ω_s field will be used as a proxy for the reaction strength in the following.

Ridge and curvature analysis

A quantitative description of the reaction zone location and its geometry is possible based on the principal curvatures of the three-dimensional CEPR-field.

For this, the Hessian **H** (the matrix of all second spatial derivatives) of CEPR is determined at the spatial point which is to be analyzed. **H** is a real-valued, symmetric matrix, which contains information about the curvature of the three-dimensional ω_S-field. The local structure of the reaction field can be characterized

by an eigenvalue decomposition of the Hessian

$$\mathbf{H} = \mathbf{A}\Sigma\mathbf{A}^{-1} \tag{2}$$

where **A** is a 3×3 matrix containing eigenvectors as columns, and $\sum$ is a 3×3 diagonal matrix of eigenvalues σ_i (i=1,2,3). That is, $\sum$ and **A** have the form:

$$\Sigma = \begin{pmatrix} \sigma_1 & 0 & 0 \\ 0 & \sigma_2 & 0 \\ 0 & 0 & \sigma_3 \end{pmatrix}, \quad \mathbf{A} = \begin{pmatrix} \mathbf{u} & \mathbf{v} & \mathbf{w} \\ | & | & | \end{pmatrix}. \tag{3}$$

The mutually orthonormal vectors **u**, **v** and **w** correspond to directions of principal curvatures of the ω_S-field, and the associated σ_i are the principal curvatures in **u**, **v**, and **w** direction, respectively. The matrices $\sum$ and **A** can be rendered into a form where the eigenvalues are arranged in order of decreasing magnitude ($|\sigma_1|>|\sigma_2|>|\sigma_3|$) along the diagonal; then, the eigenvector **u** corresponds to the direction of strongest curvature (regardless of sign), and eigenvector **w** to the weakest.

A *ridge* is a region where the field has local directional maxima along the eigenvectors [6]. In particular, a point $\mathbf{x}=(x_1, x_2, x_3)$ is on a one-dimensional ridge of the ω_s field if the first two principal curvatures at **x** are negative and ω_s has zero directional derivatives at **x** on the plane spanned by eigenvectors **u** and **v:**

$$\sigma_1 < \sigma_2 < 0 \quad \text{and} \quad \text{grad}_{\mathbf{uv}}\omega_s = 0$$

where $\text{grad}_{\mathbf{uv}}\omega_s$ is the two-dimensional vector formed by the directional derivatives of ω_s along the **u**,**v**-subspace. The zero directional derivative is a necessary, but not sufficient condition for a directional extremum. The negative eigenvalues ensure the local directional maximum. Note again that the eigenvalues are arranged in order of increasing magnitude; for negative eigenvalues, this means that $\sigma_1 < \sigma_2$.

Likewise, **x** is on a two-dimensional ridge (a locally planar structure) if the first principal curvature at **x** is negative and ω_s has a local directional maximum at **x** along **u**: $\sigma_1<0$ and $\text{grad}_{\mathbf{u}}\omega_s = 0$, where $\text{grad}_{\mathbf{u}}\omega_s$ is the directional derivative of ω_s along **u**. Finally, even the degenerate case of a zero-dimensional ridge can occur, namely if **x** is a local maximum in any direction.

Results and Discussion

Depending on the on the different principal curvatures' magnitude, different paradigms for the local geometry of the reaction zone result. Figure 2 sketches these paradigms:

(I) One eigenvalue is dominant over the other two. This corresponds to a two-dimensional reaction front: There is strong curvature of the ω_s field (large magnitude of eigenvalue σ_1) in **u**-direction, and no or only negligible curvature in the other two spatial directions (given by the vectors **v** and **w**). The central region is a two-dimensional object (sheet). The classical two-dimensional flame sheet belongs to this paradigm, with the flame sheet being tangential to the **v**,**w**-plane, and **u** as the local flame-normal direction.

(II) Two eigenvalues are dominant over the third one; the curvature of the ω_s field in two directions (**u** and **v**) is strong, but weak in the third (**w**)-direction. The central region is a one-dimensional object (a curve). This results in a locally cylindrical, filamentary shape of the reaction zone.

(III) All three eigenvalues have the same order of magnitude. Then, the reaction zone has no distinguished local direction, but has a patch-like, roughly spherical shape. The central region is a point.

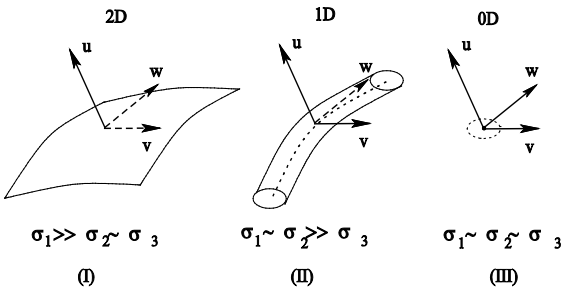

Figure 2. Classification of reaction zone shapes based on magnitudes of principal curvatures, leading to three geometrical paradigms. The dimensions of the underlying ridge structures (central region) are given.

This classification is local and in a combustion system, different paradigms might be encountered at different locations and times. The local shape can be expressed in a quantitative way by defining the ratios $r_{12}=|\sigma_1|/(|\sigma_1|+|\sigma_2|)$ and $r_{23}=|\sigma_2|/(|\sigma_2|+|\sigma_3)|$. Recalling that the σ_i are ordered in decreasing magnitude ($|\sigma_1|>|\sigma_2|>|\sigma_3|$), one can associate the case $r_{12} \sim 1$ to paradigm (I), $r_{12}\sim 0.5$ with simultaneously $r_{23} \sim 1$ to paradigm (II), and $r_{12} \sim 0.5$ with simultaneously $r_{23} \sim 0.5$ to paradigm (III).

In our data set, we frequently found structures corresponding to paradigm (II). An example is depicted in fig. 3.

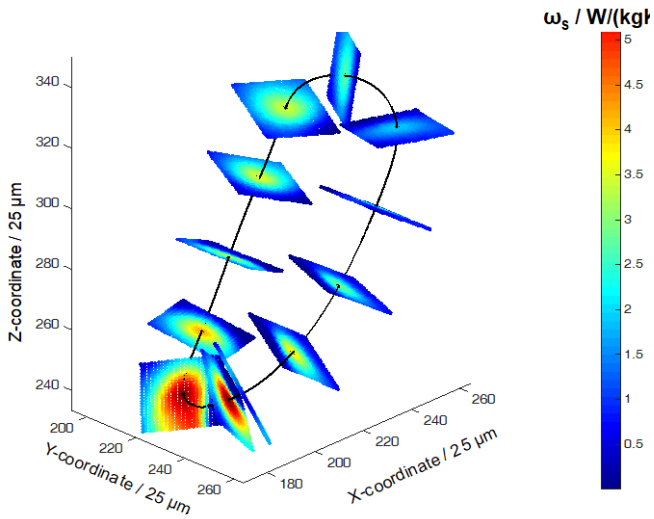

Figure 3. Sample of a reaction structure which is close to paradigm (II) (a flame worm or "florm") in the DNS data set.
Black curve: Tracked central region (a one-dimensional ridge)
Slices: local cut-outs (on planes spanned by the **u** and **v** eigenvectors of the Hessian) of the 3D field ω_S, depicted as false color contour plots.

Conclusions

In this paper, we introduce and demonstrate a generic method for characterizing reaction zones in combustion. It uses the related concepts of *ridges* and curvature analysis of a reaction intensity marker field (the chemical entropy production rate was used for this purpose) to identify two characteristics of the reaction zone: A low-dimensional central region in space, and the spatial extent ("thickness") of the zone. The method is applied to 3D DNS of a turbulent, non-premixed hydrogen/air flame. It is found that the reaction zone in the DNS features aspects that are not covered by the classical notion of a flame-sheet. In particular, when turbulence and reaction interact strongly, the reaction front at some locations is no more a two-dimensional sheet, but rather has characteristics of a one-dimensional, filament-like structure. These structures, which we propose to call flame worms, or shorter *florms*, are expected to bear considerable significance for turbulent combustion modeling. In particular, considering the inclusion of the *florm*-like reaction zone paradigm might extend models relying on flame surface density.

Acknowledgements

Financial support by the German Research Foundation (DFG) within the project SFB/TRR 150 is gratefully acknowledged. The research group of Prof. Thevenin has kindly provided DNS data samples; their support is also acknowledged.

References

[1] Echekki, T., Mastorakos, E. (2011). Turbulent Combustion Modeling, Advances, New Trends and Perspectives, Springer-Verlag, Berlin, Heidelberg, New York.

[2] Peters N. Laminar Flamelet Concepts in Turbulent Combustion. Proc Comb Inst.21:1231–50, (1986).

[3] Warnatz, J., Maas, Ulrich, Dibble, Robert W., Combustion, 4th edition, Springer, (2006), ISBN-10 3-540-25992-9

[4] Schießl R, Bykov V, Maas U, Abdelsamie A, Thévenin D. Implementing multi-directional molecular diffusion terms into Reaction Diffusion Manifolds (REDIMs). Proc Combust Inst. 2017;36(1):673–9.

[5] Abdelsamie, A., Fru, G., Oster, T., Dietzsch, F., Janiga, G., Thévenin D. (2016). Comput. Fluids 131: 123.

[6] Eberly, D., (1996). *Ridges in Image and Data Analysis*, Series on Computational Imaging and Vision, Kluwer Academic Publishers, September ISBN 0-7923-4268-2.

Large Eddy Simulation of Turbulent Flow in a Fan-Stirred Combustion Vessel

F. Zhang*, T. Zirwes, P. Habisreuther*, N. Zarzalis*, D. Trimis*, H. Bockhorn***

Feichi.Zhang@kit.edu

* Engler-Bunte-Institute, Division of Combustion Technology, Karlsruhe Institute of Technology, Engler-Bunte-Ring 1, 76131 Karlsruhe, Germany

** Steinbuch Centre for Computing (SCC), Karlsruhe Institute of Technology, Hermann-von-Helmholtz-Platz 1, Karlsruhe, Germany

Abstract

The turbulent flow field within a fan-stirred combustion vessel is numerically calculated by means of large eddy simulation (LES). Objective of the work is to explore application of high fidelity numerical methods for a more detailed insight into the turbulence characteristics prevailing prior to ignition of fuel/air mixtures, which lead to turbulent flame propagation due to flame-turbulence interactions. The LES have been preformed with the code OpenFOAM for a laboratory-scale test rig, along with the moving mesh technique for considering the rotational motion of fans. Totally 8 fans are considered at varying rotating speeds. The calculated root mean square flow velocities showed a reasonably good agreement with measured data and exhibit a linear increase with the rotating speed of the fans. The integral length scale evaluated from the LES agrees well with the measured value too, which increases slightly with the rotation speed of the fans. The proposed method in this work is able to reproduce the essential characteristics of the turbulent flow field prevailing in a fan-stirred bomb.

1. Introduction

The mutual interaction between flame propagation and turbulent flow plays a key role for the efficiency, stability and emission characteristics of energy conversion through combustion [1]. One of the commonly applied experimental configurations for studying this effect is the constant-volume, fan-stirred combustion bomb [2, 3, 4]. Homogeneous, isotropic turbulence conditions can be generated by applying a number of symmetrically arranged fans mounted within the vessel. Moreover, the setup can be operated at varying thermodynamic conditions like elevated pressure, temperature and mixture composition, which are of significant importance for industrial applications [5, 6, 7]. The overall consumption rate in terms of the turbulent burning velocity and the wrinkling rate of the flame surface depend on the underlying turbulence characteristics, such as the turbulence intensity and the turbulent length scales. The initial flame kernel is small compared to the integral length, and hence the initial flame kernel is not exposed to the full spectrum of turbulence in the early stage after ignition, and, therefore remains laminar. As the

flame surface grows, it is wrinkled by larger, energy-containing vortices. Thus, a thorough characterization of the turbulent flow represents a prerequisite for the subsequent analysis of the flame-turbulence interaction in this setup.
Although a number of experimental works have been performed to study the turbulent flow field in such explosion vessel, for example in [2, 8, 9], the flow velocities can only be measured on a 2D plane with limited ranges and resolutions, so that temporal and spatial fluctuations of small-scale motions cannot be captured correctly. The objective of the present work is the detailed analysis of the underlying turbulence characteristics by the application of high fidelity numerical simulations for the turbulent flow generated in a fan-stirred combustion vessel. Highlight of the work lies in considering the rotational movement of several fans for this commonly used experimental configuration by employing moving numerical grids for the fans. The reliability of the results are validated by comparison with corresponding measured data [2].

2. Numerical Setups

The test rig consists of an explosion vessel with 8 fans mounted on the inner wall of the vessel, which generate an almost homogeneous and isotropic turbulent flow field in the core region [2]. The fans are located at the corners of a cube inscribed into the spherical vessel; the axes of the fans are collinear to the diagonals of the cube. The vessel is assumed as a sphere with a diameter of 16 cm, the axial distance from one single fan to the opposite one is 133 mm. Each fan has a diameter of 45 mm and consists of 6 blades of 6 mm depth and 3.6 mm thickness; the surfaces of the blades are flat (without curvature), having a slanted angle of 22.5°. The computational domain covers the internal volume of the vessel along with the 8 fans. Tetrahedral elements have been used to build up the grid cells. As shown in Fig.1 on the left, the average cell length in the zones I, II, III are specified to 0.5 mm, 1 mm and 2 mm respectively. The regions enclosing the fans has an average resolution of 1 mm, see Fig.1 on the right. In total, the computational mesh consists of 8.6 million cells.

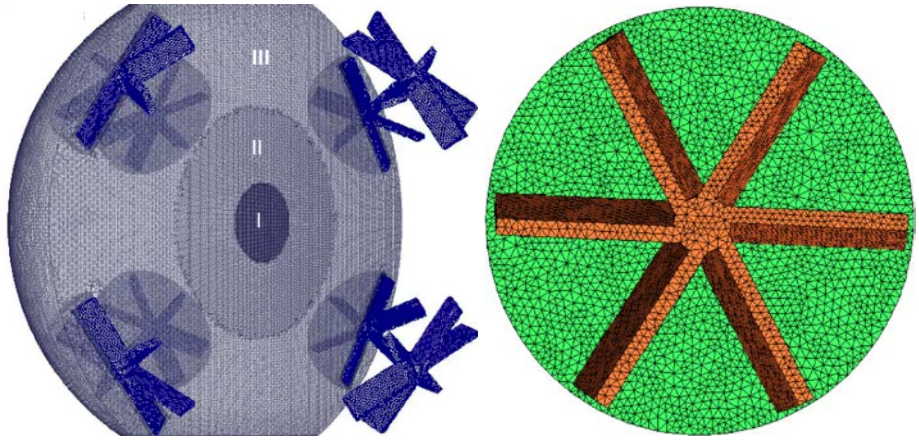

Figure 1. Surface meshes used for the LES of a fan-stirred bomb.

The open-source code OpenFOAM [11] has been used to solve the Navier-Stokes equations in the incompressible formulation by means of the finite volume method [12]. A constant kinematic viscosity of 1.58e-5 m^2/s for air at the condition of 298 K and 1 bar is assigned. The dynamic mesh implementation available in OpenFOAM has been applied to represent the rotational motion of the fans. The arbitrary mesh interface is used for exchanging data across adjacent mesh domains, in this case between the rotational zones including the fans and the remaining sphere volume. The motion of the mesh is accomplished by an automatic mesh motion solver, which is based on solving a mesh motion equation with prescribed boundary motion [12].

The solution procedure employs a fully implicit scheme of second order for the time derivative (three point backward) and a second order discretization scheme for the convective and diffusive terms [12]. A transport equation for the SGS turbulent kinetic energy [14] is applied in order to calculate the sub-grid scale (SGS) Reynolds stresses. The LES have been performed for four rotating speeds of the fans: ω = 2500, 5000, 7500, 10000 rpm (rounds per minute). The surface of the spherical vessel is set as no-slip wall. All simulations have been run for different physical times of 4.8 s, 2.4 s, 1.8 s, 1.2 s for ω = 2500, 5000, 7500, 10000 rpm (approx. 400,000 time steps) to gather time mean and rms (root mean square) statistics.

3. Simulation Results

3.1. Instantaneous Flow Field

Figure 2 shows instantaneous contours of the magnitude of flow velocity u for the cases with ω = 5000 rpm (left) and ω = 10000 rpm (right), for a slice through the center point of the vessel. For all cases, the highest flow velocities are given by the moving speed of the fan blades at their maximum radii. Therefore, the maximum value of u almost increases linearly with ω. It is largest near the fans and smallest at the axes of symmetry and in the core region of the vessel, because the flow the ventilators generate the flow in opposite directions.

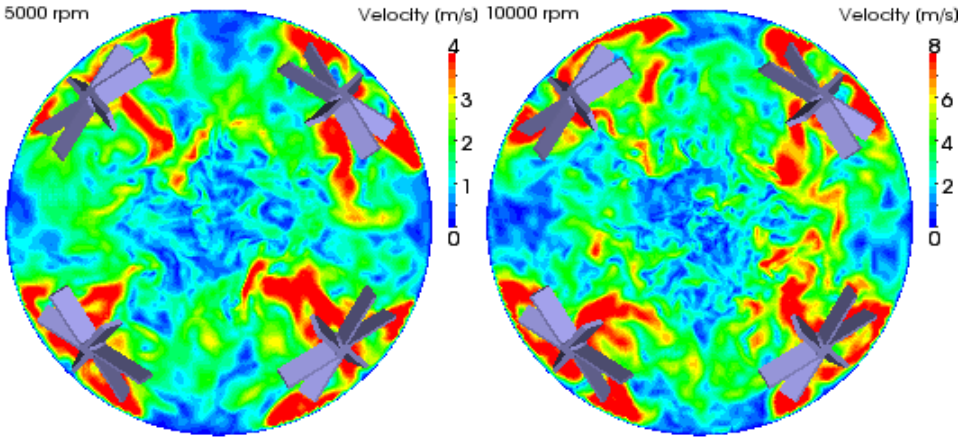

Figure 2. Instantaneous contours of the magnitude of flow velocity u for different fan rotating speed: ω = 5000 rpm (left) and 10000 rpm (right).

3.2. Mean and RMS Velocities

Figure 3 depicts contours of the time mean (left) and rms (right) values of the magnitude of flow velocity $\bar{u}$ and u' for the case of ω = 10,000 rpm, which increase from the center of the vessel towards the fans. $\bar{u}$ is zero in the center point, whereas u' is non-zero there due to the turbulent fluctuations. In addition, $\bar{u}$ and u' are not evenly distributed along the circumferential direction, they are larger in the diagonal planes across the fans (white lines) compared to the vertical and horizontal symmetric planes (black lines). Contours of $\bar{u}$ and u' are not mirrored perfectly regarding the symmetry axes, because the simulated physical time of 1.2 s may not be sufficient to smooth out long-term turbulent fluctuations. Results for other rotation speeds are qualitatively similar, $\bar{u}$ and u' however vary linearly with ω.

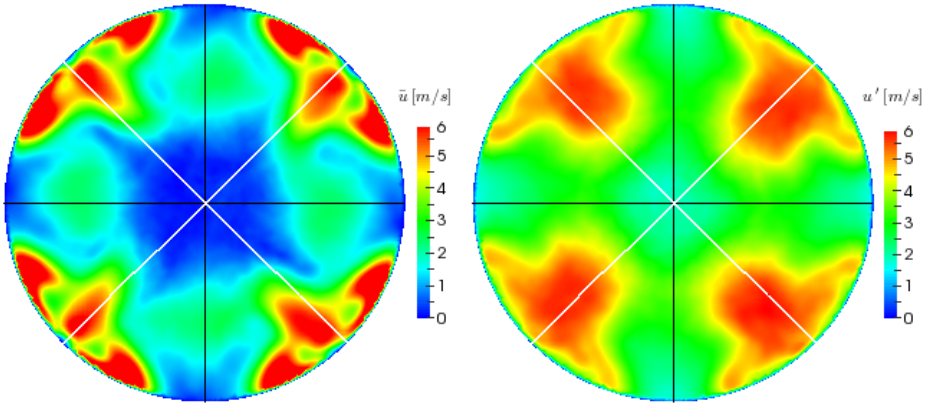

Figure 3. Contours of time-mean (left) and rms (right) velocities calculated by LES for the rotation speed of fan at ω = 10000 rpm.

In Fig. 4 on the left, the calculated and measured profiles of u' along the horizontal axis are compared for different ω, which increase with the radius from the center to

a maximum value and decreases while approaching the vessel wall. A larger ω leads to an increase in u', so that the turbulent kinetic energy increases with ω too. On the right hand side of Fig.4, u' shows a quasi-linear increase with ω at different radial positions. The calculated data (solid line) and the slopes of the curves are slightly lower than the data from LDA measurement (circles). The coarse grid resolution used for LES may lead to a higher numerical diffusion and hence, an attenuated turbulent fluctuation. In addition, the k-Eqn SGS model used in this work is strictly dissipative and suffers from the eddy viscosity assumption. The deviations of geometrical setups as well as the experimental uncertainties may also contribute to this difference. For instance, the shape of the vessel is assumed to be spherical, whereas other installations such as holders for the fans and windows (for the optical measurement) are present in the experiment. Despite these differences in the simulation and the measurement, the achieved results may be regarded as satisfactory, due to the complexity of the configuration by considering the full scale of the explosion vessel and including 8 rotating fans.

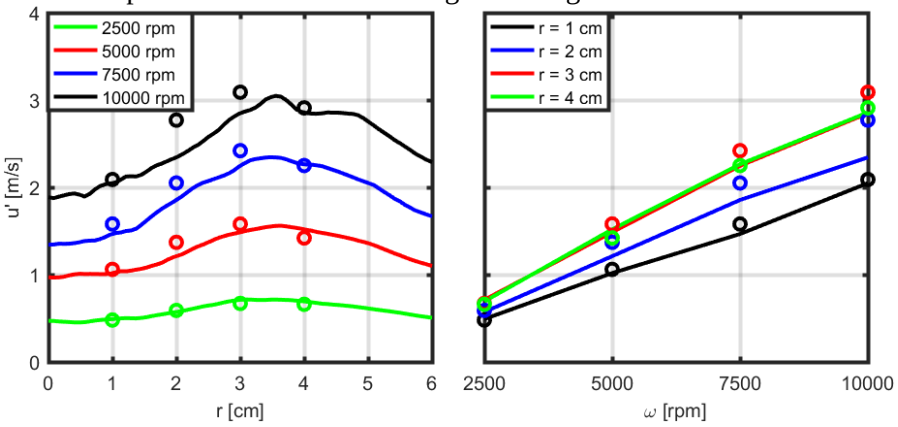

Figure 4. Comparison of calculated and measured profiles of rms velocity against the radial direction (left) and the rotation speed of the fan (right).

Based on the simulation results, the turbulent kinetic energy and eddy dissipation rate k and ε are evaluated by

$$k = \frac{1}{2}\left(\overline{u_i' u_i'}\right), \varepsilon = 2\nu\left(\overline{S_{ij}' S_{ij}'}\right)^2, \; S_{ij}' = \frac{1}{2}\left(\frac{\partial u_i'}{\partial x_j} + \frac{\partial u_j'}{\partial x_i}\right) \quad (1)$$

with the strain rate tensor S_{ij}' [15]. $\bar{\cdot}$ and $\cdot'$ indicate time mean and instantaneus fluctuations. By using these parameters the integral length scale L_t is calculated with $L_t = C_\mu^{3/4} k^{3/2}/\varepsilon$, which shows a homogenous distribution in the core region and compares well with the measured data of $L_t \approx 4\,mm$ [2]. L_t from LES has been found to be slightly increasing with ω, whereas it was found to be independent of ω in previous experimental studies [2, 8, 9]. The turbulent Reynolds number $Re_t = u' L_t/\nu$ consequently increases with ω or u', leading to a smaller Kolmogorov length due to $\eta \propto Re_t^{-3/4}$. The decrease of η with increasing Re_t has been verified by evaluating η from LES by $\eta = (\nu^3/\varepsilon)^{1/4}$. Results for L_t and η, as

well as the spectra of turbulent kinetic energy will be shown in the final presentation.

4. Conclusion

This work presents large eddy simulations (LES) of the turbulent flow in a fan-stirred explosion vessel, including several rotating fans using a moving mesh approach. The predicted turbulence field is nearly homogeneous and isotropic in the core region. The calculated rms velocities agree well with the measured data, which increase linearly with the rotation speed of the fans. The calculated integral length scale compares well with the measured value, which increases slightly with the rotation speed of the fans. Therefore, the proposed method is able to reproduce the turbulence characteristics generated in the fan-stirred bomb. The influence of turbulent flows on the flame propagation will be studied in future work.

Acknowledgements

The authors thank for the financial support by the Helmholtz Association of German Research Centres (HGF) for funding through the Research Unit EMR. This work utilizes computational resources from the High Performance Computing Center Stuttgart (HLRS) and the Steinbuch Centre for Computing (SCC) at KIT.

References

[1] Poinsot, T., Veynante, D., *Theoretical and numerical combustion*, Edwards Inc., Philadelphia, U.S.A., 2005.

[2] Weiß, M., Zarzalis, N., Suntz, R., "Experimental study of Markstein number effects on laminar flamelet velocity in turbulent premixed flames", *Combust. Flame* 154, 671-691 (2008).

[3] Abdel-Gayed, R.G., Al-Khishali, K.J., Bradley, D., "Turbulent burning velocities and flame straining in explosions", *Proc R Soc Lond A* 391: 393-414 (1984).

[4] Bradley, D., Haq, M.Z., Hicks, R.A., Kitagawa, T., Lawes, M., Sheppard, C.G.W., Woolley, R., "Turbulent burning velocity, burned gas distribution, and associated flame surface definition", *Combust Flame* 133: 415-430, (2003).

[5] Lipatnikov, A., Chomiak, J., "Global stretch effects in premixed turbulent combustion", *Proc Combust Inst* 31: 1361-1368 (2007).

[6] Bradley, D., Lawes, M., Mansour, M.S., "Explosion bomb measurements of ethanol-air laminar gaseous flame characteristics at pressures up to 1.4 MPa", *Combust. Flame* 156: 1462-1470 (2009).

[7] Liu, C., Shy, S., Chen, H., Peng, M., "On interaction of centrally-ignited, outwardly propagating premixed flames with fully-developed isotropic turbulence at elevated pressure", *Proc Combust Inst* 33: 1293-1299, (2011).

[8] Galmiche, B., Mazellier, N., Halter, F., Foucher, F., "Turbulence characterization of a high-pressure high-temperature fan-stirred combustion

vessel using LDV, PIV and TR-PIV measurements", *Exp. Fluids* 55: 1636 (2014).

[9] Fansler, T.D., Groff, E.G., "Turbulence characteristics of a fan-stirred combustion vessel", *Combust Flame* 80: 350-354 (1990).

[10] Sick, V., Hartman, M.R., Arpaci, V.S., Anderson, R., "Turbulent Scales in a Fan-stirred Combustion Bomb", *Combust Flame* 127: 2119-2123 (2001).

[11] OpenFOAM, The Open Source CFD Toolbox, User Guide (2014).

[12] Ferziger, J.H., Perić , M., *Computational methods for fluid dynamics*, Springer-Verlag Berlin Heidelberg, Germany, 2002.

[13] Moving Mesh Solver: https://www.slideshare.net/fumiyanozaki96/openfoam, http://web.student.chalmers.se/groups/ofw5/Advanced_Training/DynamicMesh.pdf.

[14] Fröhlich, J., *Large Eddy Simulation turbulenter Strömungen*, Teubner Verlag, Germany, 2006.

[15] Pope, S.B., *Turbulent Flows*, Cambridge University Press, Cambridge, U.K., 2000.

MIXING FIELD EFFECTS IN PARTIALLY PREMIXED TURBULENT FLAMES

S. Luca*, A. Attili, F. Bisetti*****
stefano.luca@kaust.edu.sa
* King Abdullah University of Science and Technology, Saudi Arabia
** RWTH Aachen University, Germany
*** University of Texas at Austin, USA

Abstract
Direct Numerical Simulations of three-dimensional lean methane/air flames in a spatially developing turbulent slot Bunsen burner are performed. This configuration is of interest as it retains selected characteristics of real devices, such as turbulent production by mean shear. The jet consist of a methane/air mixture with equivalence ratio 0.7 and temperature of 800 K. The simulations are performed at 4 atm. The coflow is composed of Argon at the temperature of the combustion products. The flame is in the thin-reaction zone regimes and the Reynolds number based on the jet width and velocity is 5600. A supporting simulation is performed to generate the inflow conditions for the jet. Chemistry is treated with a new skeletal chemical mechanism developed specifically for the DNS and consists of 33 species. The macroscopic and microscopic characteristics of the flame are analyzed. Due to the inert coflow, the flame starts from a location few millimeters above the nozzle. The flame structure is similar to the one-dimensional premixed flame, while the heat release rate is found to be affected by the mixing field.

Configuration & Numerical Methods
The flame configuration considered is a slot turbulent premixed jet flame surrounded by a coflow of Argon at high temperature. This arrangement is similar to piloted flames used in experiments [1] and to the configuration of a previous study from the authors [2].
The jet consist of a methane/air mixture with global equivalence ratio 0.7 and temperature of 800 K. The background pressure is 4 atm. The temperature in the coflow corresponds to the temperature of the equilibrium state of the unburnt reactive mixture (2218 K). The choice of the coflow is made in order to stabilize the flame with the hot gas, without affecting NO_x production with a coflow containing hot nitrogen and nitrogen oxides. The bulk jet velocity is U_b=100 ms, while the coflow has a uniform velocity of U_c=15 ms. The slot width is H=1.2 mm, and the resulting jet Reynolds number based on the slot width and the jet bulk velocity is U_bH/ν=5600 (ν is the kinematic viscosity of the reactants).
The size of the computational domain is 24H in the streamwise (x), 16H in the crosswise (y), and 4.3H in the spanwise (z) direction. The jet and the coflow

streams are separated at the inlet by walls of thickness H/10. The domain is periodic in z, open boundary conditions are prescribed at the outlet in x and no-slip conditions are imposed at the boundaries in y. The inlet conditions for the velocity field are obtained from four auxiliary simulations of fully developed turbulent channel flow. The mesh is uniform in all three directions with a resolution δ_x=20 μm, resulting in 1440x960x256=350M grid points. The resolution is such that the laminar flame thickness to grid size ratio $\delta_L/\Delta x$~6 and in a cell size to Kolmogorov scale ratio of $\Delta x/\eta_{min}$<2.

A supporting simulation is performed to generate the inflow conditions of the central jet. The velocity field is extracted from a fully developed turbulent channel simulation. The 2D field is sampled at a selected streamwise location in the channel and used as the inflow conditions for the main slot burner simulations. The simulation is performed using the NGA code. The gas phase hydrodynamics are modeled with the reactive, unsteady Navier-Stokes equations in the low Mach number limit [3]. The species obey the ideal gas equation of state and all transport properties are computed with a mixture-average approach [4]. Combustion is modeled using a new skeletal mechanism developed targeting lean premixed methane-air flame. The skeletal mechanism has 33 species and 181 reactions. It is obtained from the application of the directed relation graph (DRG [5]) method on the GRI-3.0 [6] detailed mechanism and is tailored to the lean conditions of the DNS. The mechanism has been validated for flame speed and flame structure for the target unburnt mixture conditions and good agreement was obtained.

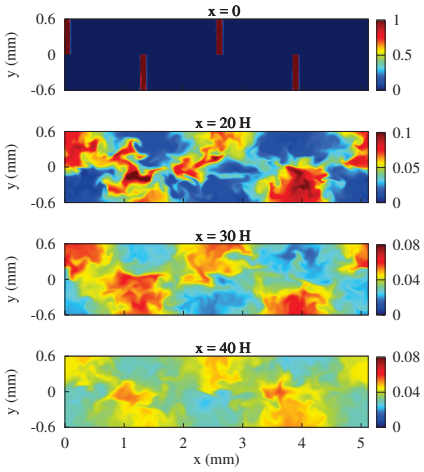

Figure 1: Contour plots of methane mass fraction at four different axial locations in the channel flow simulation. The fields at x=20H, 30H, 40H, are used as inlet conditions for the PPL, PPM, and PPH cases.

Each simulation required 3 million CPU hours on 16384 cores of the CRAY XC40 supercomputer ``Shaheen'' available at King Abdullah University of Science and Technology.

Results

Four simulations with different level of premixing have been performed. The first flame has a fully premixed inlet, while the other three have increasing level of

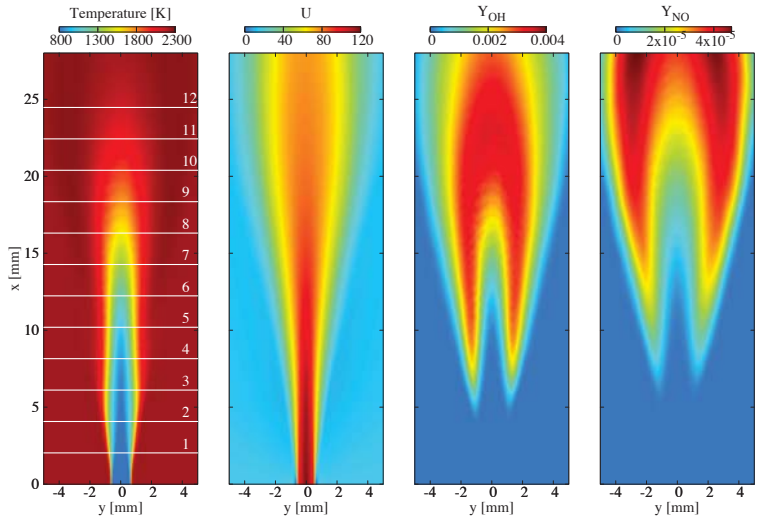

Figure 2: Contour plot of select mean quantities in the XY plane for the fully premixed flame.

partial premixing (PPL: low, PPM: medium, PPH: high).

The flame is initially planar near the jet nozzle and shows significant development and wrinkling with downstream distance. The flame is strongly wrinkled and the scales of wrinkling are characterized by a wide range of sizes.

Figure 2 shows the contour plots of the mean fields of temperature, axial velocity U and OH and NO mass fractions. The analysis of these simulations is carried out at selected axial locations: in this way it is possible to reduce the amount of data to post-process. These axial locations are showed in Fig. 2 superimposed on the temperature contour.

Due to the inert coflow the flame starts few millimeters above the nozzle exit as seen from the mean field of Y_{OH}. Where the flame is completely developed, it shows the same features of a flame with a coflow composed of burnt product [2], hence justifying the use of pure Argon in the coflow to avoid entrainment of NO_x that would be present in a coflow based on fully burned products.

An important factor in partially premixed flames is mixing. To account for the different inlets, two mixture fractions have been defined, and a characterization of the mixing process is somehow necessary. Two mixing processes can be identified: (i) one due to the intrinsic nature of the spatially evolving Bunsen configuration, where the mixing happens between the jet and the coflow and (ii) one introduced by the partially premixed jet inlet where the mixing happens between fuel and oxidizer contained in the jet mixture. Figure 3 shows a schematic of these

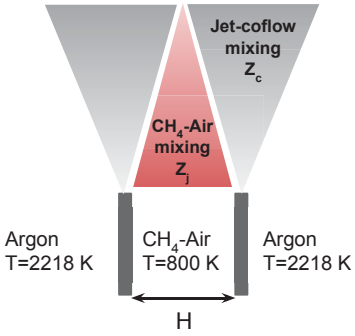

Figure 4: Sketch of the mixing fields and mixture fractions definitions.

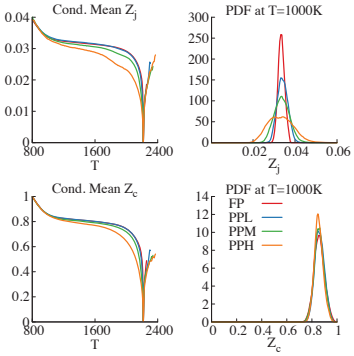

Figure 3: Conditional mean and conditional PDF of mixture fractions Zj and Zc at the axial location 6.

processes. The mixture fractions are defined in order to isolate the mixing effects when needed: Z_j is defined based on the fuel mass fraction at the inlet ($Z_j = Y_{CH4}$ at the inlet); and Z_c is 1 in the jet and zero in the coflow.

In order to understand the influence of the partially mixed jet on the overall mixing field, the conditional means and PDF of the mixture fractions at the axial location 6 are shown in Fig. 4. The jet mixture fraction (Z_j) conditional mean indicates that increasing the level of partial premixing the average mixture fraction decreases, in particular at the flame location (T=1800 K); this implies that the average mixture is leaner. The PDF is broader and peaks at lower values when increasing the inhomogeneities of the mixture, meaning also that the inlet characteristic is still affecting the flow at this axial location. The jet-coflow mixture fraction (Z_c) conditional means show a similar trend, but the PDF result almost unchanged.

The joint probability density functions of heat release rate (HRR) and temperature in Fig. 5 show that decreasing the level of premixing the fluctuations of HRR increase, but the conditional mean of the heat release rate decreases. Moreover the conditional means are almost identical to the HRR in a laminar freely propagating flame, indicating that the turbulent premixed flames belong to the thin reaction zone regime.

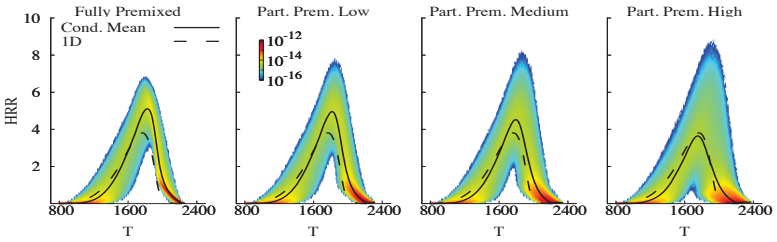

Figure 5: Joint PDF of heat release rate and temperature for the four flames at the axial location 6.

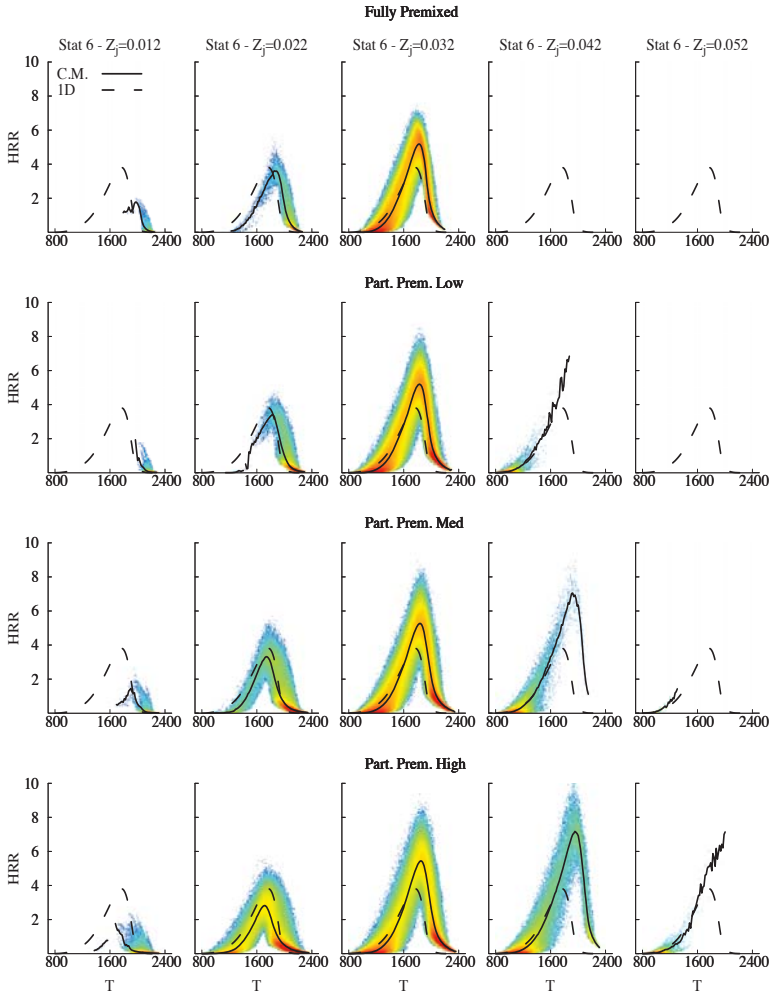

Figure 6: Joint PDF of HRR and temperature conditioned at different values of Zj for the four flames at the axial location 6. One-dimensional solutions are computed with PREMIX [7].

The fluctuations of HRR can be traced back to the inlet inhomogeneities: regions with different local equivalence ratio, which can be tracked using Z_j will produce

higher and lower heat release rate. Fig. 6 shows the heat release rate and temperature joint PDF conditioned at values of Z_j at the axial location 6. For the fully premixed flame, the heat release happens mainly at Z_j=0.032, which is the mean value of Z_j at T=1000 K; it is worth noting that the equivalence ratio 0.7 at the inlet correspond to Z_j=0.03927, and this decrease of Z_j is due to the mixing between jet and coflow. Increasing the level of partial premixing, the heat release rate grows also at different values of Z_j. For the PPH flame it is clear that low values of heat release rate at temperature greater than 800 K are due to mixture at Z_j=0.022, while high values of HRR happen for Z_j=0.042, i.e. a richer mixture.
It is worth noting that even if samples at Z_j=0.012 are present for the fully premixed flame, the heat release rate still follows the 1D profile; this doesn't happen increasing the level of partial premixing.

References

[1] Filatyev, S. A., Driscoll, J. F., Carter, C. D., and Donbar, J. M., "Measured properties of turbulent premixed flames for model assessment, including burning velocities, stretch rates, and surface densities", *Combustion and Flame* 141:1-21 (2005).

[2] S. Luca, A. Attili, and F. Bisetti. "Direct Numerical Simulation of Turbulent Lean Methane-Air Bunsen Flames with Mixture Inhomogeneities", *54th AIAA Aerospace Sciences Meeting*, AIAA SciTech, (AIAA 2016-0189). http://dx.doi.org/10.2514/6.2016-0189

[3] Desjardins, O., Blanquart, G., Balarac, G., Pitsch, H., "High order conservative finite difference scheme for variable density low Mach number turbulent flows", *Journal of Computational Physics*, 227:7125-7159 (2008).

[4] Attili, A., Bisetti, F., Mueller, M. E., Pitsch, H., "Effects of non-unity Lewis number of gas-phase species in turbulent nonpremixed sooting flames", *Combustion and Flame*, *166*:192-202 (2016).

[5] Lu, T., Law, C. K., "A directed relation graph method for mechanism reduction", *Proc. Comb. Inst.* 30:1333-1341 (2005).

[6] Smith, G. P., Golden, D. M., Frenklach, M., Moriarty, N. W., Eiteneer, B., Goldenberg, M., Bowman, C. T., Hanson, R. K., Song, S., Gardiner Jr, W. C., et al., "GRI-Mech 3.0" (1999).

[7] Kee, R. J., Grcar, J. F., Smooke, M., Miller, J., Meeks, E., "PREMIX: a Fortran program for modeling steady laminar one-dimensional premixed flames", *Sandia National Laboratories Report*, 1985.

QUASI-PROBABILITY APPROACH FOR MODELLING LOCAL EXTINCTION AND COUNTER-GRADIENT IN TURBULENT PREMIXED COMBUSTION

G. Pagnini*^, A. Trucchia*¨
gpagnini@bcamath.org
*BCAM- Basque Center for Applied Mathematics,
Alameda de Mazarredo 14, E-48009 Bilbao, Basque Country - Spain
^Ikerbasque, Calle de María Díaz de Haro 3, E-48013 Bilbao, Basque Country - Spain
¨Department of Mathematics, University of the Basque Country UPV/EHU,
Apartado 644, E-48080 Bilbao, Basque Country - Spain

Abstract
In opposition to standard probability distributions, quasi-probability distributions can have negative values which highlight nonclassical properties of the corresponding system. In quantum mechanics, such negative values allow for the description of the superposition of two quantum states. Here, we propose the same approach to model local extinction and counter-gradient in turbulent premixed combustion. In particular, the negative values of a quasi-probability correspond to the local reversibility of the progress variable, which means that a burned volume turns to be unburned and then the local extinction together with the counter-gradient interpretation follows. We derive the Michelson-Sivashinsky equation as the average of random fronts following the G-equation, and their fluctuations in position emerge to be distributed according to a quasi-probability distribution displaying the occurrence of local extinction and counter-gradient. The paper is an attempt to provide novel methods able to lead to new theoretical insights in combustion science.

Introduction
Turbulent premixed combustion requires a set of governing equations and a rich phenomenology follows. The set of governing equation includes: mass and momentum conservation, equation of state for gases, energy and species conservation. The nonlinearity of the problems requires closures and modelling. Self-extinction and counter-gradient are phenomena occurring in premixed combustion that require non-standard modelling approach or *ad hoc* modelling when standard approaches are adopted. Here we proceed with a research program presented in the last years at the Meetings of the Italian Section of the Combustion Institute [1,2,3]. The aim is to provide novel methods able to lead to new theoretical insights in combustion science. In particular, in the following we briefly report the derivation of the Michelson-Sivashinsky equation as the average of

random fronts following the G-equation [2,3], and we discuss that, since their fluctuations in position emerge to be distributed according to a quasi-probability distribution, then local extinction and counter-gradient are displayed by negative values of the quasi-probability emerging from such modelling approach. In the next section the main equations are derived, discussion and conclusion are reported in a further and ending section.

Statistical derivation of the Michelson-Sivashinsky equation

This section is based on [2,3] and it is here included for highlighting the role of the emerging quasi-probability into the proposed modelling approach.

Let the scalar function $G(x,t), x \in \mathbb{R}^n$, be a level surface that represents the front which splits the considered domain into burned and unburned sub-domains. Let x_c be a point on the level surface $G=c$ at the instant t_0 . The level surface propagates with a consumption speed given by the laminar burning velocity s_L in the normal direction ***n*** relative to the mixture element and its evolution is described by the following Hamilton-Jacobi equation where the flow velocity field is ***u***

$$\frac{\partial G}{\partial t} + u \cdot \nabla G = s_L \|\nabla G\| \quad , \quad n = -\frac{\nabla G}{\|\nabla G\|} \quad . \tag{1}$$

Let the front motion be described by the random process $X_c^{\omega}(\hat{x},t)$ where ω labels any independent realization and the mean value of X_c^{ω} be denoted by $\langle X^{\omega}(\hat{x},t)\rangle = \hat{x}(t)$, then if $P_c(x_c;t|\hat{x})$ is the corresponding PDF, with initial condition $P_c(x_c;t_0|\hat{x}) = \delta(x-x_0)$, the mean flame position is given by the integral

$$\langle x_c \rangle = \int_{\mathbb{R}^n} x_c P_c(x_c;t|\hat{x})\, d x_c = \hat{x}(t) \quad . \tag{2}$$

Introducing $\check{G}(\hat{x},t)$,with $\check{G}(\hat{x},t_0) = \check{G}(x_0,t_0) = c$, as the implicit formulation of the mean flame position $\hat{x}$, the ensemble averaging of (1) gives [5]

$$\frac{\partial \check{G}}{\partial t} + \hat{u} \cdot \nabla \check{G} = \widehat{s_L n} \cdot \nabla \check{G}. \tag{3}$$

Since the G-equation can be derived on the basis of considerations about symmetries, there is a unique model for the RHS term of equation (3) providing a relation between the laminar burning velocity s_L and the turbulent burning

velocity s_T [5], i.e.

$$\widehat{s_L n} = s_T \check{n} \quad , \qquad \check{n} = -\frac{\nabla \check{G}}{\left\| \nabla \check{G} \right\|} s \quad . \tag{4}$$

Finally, combining equation (3) and (4), the *G*-equation that describes the surface motion along the mean flame position results to be

$$\frac{\partial \check{G}}{\partial t} + \hat{u} \cdot \nabla \check{G} = s_T \left\| \nabla \check{G} \right\| \quad . \tag{5}$$

The one-dimensional Michelson-Sivashinsky equation reads [6]

$$\frac{\partial g}{\partial t} = \frac{\partial^2 g}{\partial x^2} - \left(\frac{\partial g}{\partial x} \right)^2 - D_x^1 g \quad , \tag{10}$$

where D_x^1 is the fractional derivative of order 1 in the Riesz-Feller sense with Fourier symbol $-|\xi|$, which differs from the classical first derivative, and it is related to the Hilbert transform by the formula

$$D_x^1 g = \frac{1}{\pi} \frac{d}{dx} \int_{-\infty}^{+\infty} \frac{g(x')}{(x' - x)} dx' . \tag{11}$$

Let us introduce the field $g(x,t)$ in analogy with [7], i.e.,

$$g(\mathrm{x},\mathrm{t}) = \int \check{G}(\hat{x},\mathrm{t}) P_c(x - \hat{x},\mathrm{t}) \, \mathrm{d}\hat{x} . \tag{12}$$

It is well-known that the dispersion relation of equation (10) is

$$e^{-\xi^2 t + |\xi| t} . \tag{13}$$

This suggests the following fractional differential equation for the PDF of the fluctuations of the front position:

$$\frac{\partial P_C}{\partial t} = \Delta \mathrm{P}_C + (-\Delta)^{1/2} P_C , \quad P_C(x,0) = \delta(x) . \tag{14}$$

Actually, the dispersion relation (13) is the Fourier transform of the Green function of (14). It is here highlighted that the PDF of fluctuations which solves (14) emerges to be a quasi-probability distribution showing negative values that requires high care, see Figure.

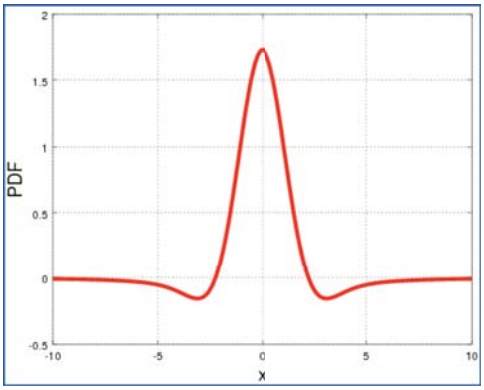

Figure: Quasi-probability distribution solution of (14).

The evolution equation of the function $g(x,t)$ results to be:

$$\frac{\partial g}{\partial t}=\frac{\partial^2 g}{\partial x^2}-D_x^1 \mathrm{g}+\int s_T(\hat{x},\mathrm{t})\,P_C(x-\hat{x},\mathrm{t})\,\mathrm{d}\hat{x}. \tag{15}$$

Comparing (10) and (15) we have

$$-\left(\frac{\partial g}{\partial x}\right)^2=\int s_T(\hat{x}\,\mathrm{t})\,P_C(x-\hat{x},\mathrm{t})\,\mathrm{d}\hat{x}\equiv\omega, \tag{16}$$

that in Fourier domain reads

$$\widetilde{\omega}=\widetilde{s_T}\,\widetilde{P_c}=\widetilde{s_T}\exp\left(-\xi^2 t+|\xi|t\right) \quad , \tag{17}$$

and the turbulent burning velocity turns out to be

$$s_T(x,t)=\frac{1}{2\pi}\int \exp(-i\xi x)\exp\left(\xi^2 t-|\xi|t\right)\widetilde{\omega}(\xi,t)\,d\xi \quad . \tag{18}$$

Discussion and conclusion

In the previous section we showed that when the Michelson-Sivashinsky equation is derived as the ensemble average of random fronts governed by the G-equation, then the spatial fluctuations of the positions of the random fronts are distributed accordingly to a quasi-probability. Quasi-probability distributions display negative values, see Figure, that require high care in their interpretation. In particular, by using Fourier inverse transformation, the quasi-probability that solves (14) can be written in the following integral form

$$P_c(x,t)=\frac{1}{2\pi}\int \exp(-i\xi x)\exp\left(-\xi^2 t+|\xi|t\right)d\xi, \tag{19}$$

such that it results to be close to the representation of the Wigner quasi-distribution for quantum optics.

The negative values highlight where statistically the fraction of burned mixture is replaced by unburned mixture. In fact, if we integrate (12) in space we have that in correspondence of the negative values of the quasi-probability there is a reduction of the mass amount. The propagation of the front is slowed. For this reason, we propose that these negative values can be interpreted as due to local extinction and counter-gradient phenomena. Local reversibility of the value of the progress variable occurs because of the entering of fresh mixture into a volume just now fully burned. This effect can be ascribed first to the local extinction, that stops the propagation of the combustion, and then to the so-called counter-gradient, which is generated by the density difference between reactants and products, that pushes back the front of the burned mixture.

In formulae, this interpretation can be stated as follows. Let $C=|C|e^{iQ}=C_R+iC_I$ be the progress variable with real and imaginary part. Then it holds $C_R^2=|C|^2-C_I^2$, and if the $g(x,t)$ defined in (12) corresponds to the real part, i.e. $g=C_R$, then we have

$$g=|C|+F(C_I), \tag{20}$$

where

$$|C|=\int_{P_c>0}\check{G}(\hat{x},\mathrm{t})P_c(x-\hat{x},\mathrm{t})\,\mathrm{d}\hat{x}, \tag{21}$$

$$F(C_I)=\int_{P_c<0}\check{G}(\hat{x},\mathrm{t})P_c(x-\hat{x},\mathrm{t})\,\mathrm{d}\hat{x}<0. \tag{22}$$

The imaginary part results to be

$$C_I=e^{i(Q-\pi/2)}\int_{P_c>0}\check{G}(\hat{x},\mathrm{t})P_c(x-\hat{x},\mathrm{t})\,\mathrm{d}\hat{x}+i\int\check{G}(\hat{x},\mathrm{t})P_c(x-\hat{x},\mathrm{t})\,\mathrm{d}\hat{x}. \tag{23}$$

Acknowledgments

This research is supported by the Basque Government through the BERC 2014-2017 program and by the Spanish Ministry of Economy and Competitiveness MINECO through BCAM Severo Ochoa excellence accreditation SEV-2013-0323 and through project MTM2016-76016-R ”MIP”. AT is supported by the PhD grant ”La Caixa 2014”.

References

[1] Pagnini, G., Akkermans, R.A.D., Buchmann, N., Mentrelli, A., “Reaction-diffusion equation and G-equation approaches reconciled in turbulent premixed combustion”, *Proceedings/Extended Abstract Book (6 pages) of the XXXVIII Meeting of the Italian Section of the Combustion Institute*, Lecce, Italy, September 20–23, 2015. ISBN 978-88-88104-25-6. Paper doi: 10.4405/38proci2015.I4

[2] Pagnini, G., “From G-equation to Michelson–Sivashinsky equation in turbulent premixed combustion modelling”, in M. Commodo, W. Prins, F. Scala, A. Tregrossi (Eds.): *Proceedings/Extended Abstract Book (6 pages) of the XXXIX Meeting of the Italian Section of the Combustion Institute*, Naples, Italy, July 4–6, 2016. ISBN 9788888104171. Paper doi: 10.4405/39proci2016.II3

[3] Pagnini G., Trucchia A., Front curvature evolution and hydrodynamics instabilities, in F. Scala, M. Valorani, M. Commodo, A. Tregrossi, H.G. Im, P. Glarborg (Eds) *Proceedings/Extended Abstract Book (6 pages) of the XL Meeting of the Italian Section of the Combustion Institute*, Rome, Italy, June 7–9, 2017. ISBN 9788888104188.

[4] Pagnini, G., Trucchia, A., “Darrieus-Landau instabilities in the framework of the G-equation”, *Digital proceedings of the 8th European Combustion Meeting*, Dubrovnik, Croatia, April 18-21, 2017. ISBN 978-953-59504-1-7 , Paper M_371, pages 1678-1683

[5] Oberlack, M.,Wenzel, H., Peters, N., “On symmetries and averaging of the G-equation for premixed combustion”, *Combust. Theor. Model.* 5:363-383 (2001).

[6] Creta, F, Matalon, M, “Propagation of wrinkled turblent flames in the context of hydrodynamic theory”, *J. Fluid Mech.* 680:225-264 (2011).

[7] Pagnini, G., Bonomi, E., “Lagrangian formulation of turbulent premixed combustion”, *Phys. Rev. Lett.* 107:044503 (2011).

Statistical Analysis of Pulsating Methane Flames issued into Hot Co-flow by LES with FGM

E. Inanc, I. Wlokas, A. M. Kempf
eray.inanc@uni-due.de
Chair of Fluid Dynamics, Institute for Combustion and Gas Dynamics (IVG), University of Duisburg-Essen, Germany

Abstract
This work presents a statistical analysis of an auto-igniting impulsively started jet flame issuing into hot and vitiated co-flowing oxidizer. This analysis uses data from a high-fidelity Large-Eddy Simulation with multidimensional detailed tabulated chemistry. The results are first validated against the (statistically) steady jet experiment from the German Aerospace Center, then the computed ignition delay times and spots are cross-checked with the same experiment, but now for a transient injection. A good agreement is achieved between the LES and the experiments, convincing to go further with the statistical analysis. For the statistics, the probability density functions and conditional means of temperature and important species-concentrations are evaluated during the pulses. Initial observations yield that the ignition-related species HO_2 and CH_2O show different properties than the flame related species OH. The probability of finding a high concentration of the ignition-related species increases until the flame becomes stabilized then decreases afterward. It is observed that these high species-concentrations first appear in the most-reactive mixture fraction before the ignition, later are visible towards the stoichiometry. After the flame stabilizes, mostly low-concentrations of these species are found in the fuel-rich zones.

Introduction
Direct injection and ignition play a significant role in many combustion systems including Diesel and gasoline engines. The ongoing chemistry in these systems is governed by ignition and mixing dynamics. Even small perturbations of temperature, pressure, turbulence intensity, gas composition and scalar dissipation rate influence ignition, hence the combustion [1]. This leads that the ignition dynamics determine the efficiency and the safety of the combustor. A detailed overview of studies on AI is given in the review paper by Mastorakos [1].
The studies showed that the self-driven ignition, or auto-ignition (AI), takes place in the form of local ignition kernels emerging at the most-reactive mixture fraction, away from stoichiometry, at low scalar dissipation rates (SDR) [2]. This work combines the high-fidelity flow fields that are obtained from high-resolution Large-Eddy Simulation (LES) with advanced tabulated chemistry approach Flamelet Generated Manifolds (FGM) [3], which enables an accurate description of the AI in a transient jet flame.

In the present work, the experiment from DLR (German Aerospace Center) [4-5] is reproduced. The objectives are; i. to validate the models by comparing the LES data against the experimental ones for (statistically) steady jet, and by cross-checking the predicted and measured ignition delay and flame stabilization times for transient jet; ii. to present a time-history of a transient flame's statistical behavior during an injection-cycle.

Modeling

For the combustion model, eight auto-igniting unsteady one-dimensional counter-flow flames (flamelets) are precomputed with the GRI-3.0 mechanism [6] using FlameMaster by Pitsch [7]. Flamelet simulations consider methane on the fuel side and hot and vitiated hydrogen/air mixture on the oxidizer side and vary the Scalar Dissipation Rates (SDR) in a range from 0.1 to 1000 1/s. These selected SDRs are chosen such that the S-curve is correctly described. The Lewis number is assumed to be unity. The ignition history is used to fill the manifold's composition and progress spaces controlled by the mixture fraction Z and the progress variable $Y_p = Y_{CO2}+Y_{CO}+Y_{HO2}$, and the third dimension includes the local effect of SDR on AI.

The pressure dependency is considered in the manifold by analytical functions [8], where the fit parameters of these functions are first pre-computed from the reference and perturbed flamelet simulations, then are re-computed in the LES simulations to adjust temperature, gas constant, heat conductivity and reaction source terms. In the perturbed flamelet simulation, the oxidizer and the fuel inlet temperatures are increased by 500 K and 100 K, respectively.

The manifold is accessed in the subsequent LES calculations by the transported mixture fraction, progress variable, total energy, and the computed SDR. The sub-grid fluctuations of Favre-filtered mixture fraction are considered via the top-hat filtered density function (FDF) method [9]. The flame is thickened to the order of the LES grid size by the artificial thickened flame (ATF) method [10].

Setup

In the experiment by Papageorge et al. [4-5], a high-velocity fuel (U_f = 177 m/s) emanates into a laminar co-flowing oxidizer of hot exhaust products of a lean hydrogen/air mixture (U_{co} = 4 m/s) at atmospheric pressure. The injector nozzle has a 1.5 mm diameter, leading to a jet-Reynolds number of 16,000 and a local-Mach number of 0.65. Further information is given in Table 1.

Table 1. Boundary conditions for the fuel and the oxidizer.

Fuel		Oxidizer				
Z_{st}	T_f [K]	T_o [K]	X_{N2}	X_{O2}	X_{H2O}	X_{OH}
0.034	290	1495	0.719	0.102	0.178	0.001

Experimentalists [4-5] measured the mixture fraction and temperature fields for 300 injections-cycles using high-speed Rayleigh scattering. They determined the AI delay times and ignition kernels for each realizations.

In-house LES and DNS solver PsiPhi [11,12] has been used for the LES in this work. Favre-filtered governing equations are solved with a low-storage explicit Runge-Kutta scheme. Convective fluxes of momentum are treated with a central differencing scheme blending over into a TVD scheme (MUSCL [13]) for Mach numbers greater than 0.2, and the rest with total variation diminishing (TVD) scheme.

The computations use an 80x45x45 mm^3 domain, which consists 48 Million equidistant cells with 0.15 mm spacing. The simulation requires 0.2 million compute hours per pulse cycle using 1296 cores in parallel through MPI.

The unresolved fluxes in momentum and scalars are estimated from eddy-viscosity and eddy-diffusivity approaches at a Turbulent Schmidt number of 0.7, respectively. Turbulent viscosity is determined by Nicoud's σ-model [14], and the Lewis number is assumed to be unity.

Results

The simulated (statistically) steady jet flame with the experimental line-plots have been initially compared. Then, the transient jet flame has been validated by comparing the ignition delay and flame stabilization times of simulations over 20 pulse-cycles to the experiments. In both cases, a good agreement between the predictions and the experiments has been observed, providing evidence that this model is suitable for this study.

For the statistical analysis, the second injection cycle is selected for post-processing. The hydroperoxyl HO_2 and formaldehyde CH_2O are chosen to study the ignition since they indicate the start and the progress of the AI. The time-history of the joint-Probability Density Function (JPDF) of the simulated normalized Y^*_{CH2O} over the mixture fraction is shown in Fig. 1. The Y^*_{CH2O} peaks in the stoichiometric mixture fraction, however, the probability of this species is highest in the lean-mixture, which coincides with the most-reactive mixture fraction, which has a value of 0.021. After the AI at 2.3 ms, the probability of this species increases towards the stoichiometry. It is also observed that the Y^*_{CH2O} shows an increase in its probability on the rich-zones just after the flame stabilizes at 4 ms.

The flame front can be identified by the mass fraction of hydroxyl OH. In the LES, the flame and ignition show quite distinctive statistical behavior. This can be seen in Fig. 1 from the time-history of the JPDF for the computed normalized Y^*_{OH} and the mixture fraction. Contrary to the Y^*_{CH2O}, the probability of high OH concentrations is observed on much leaner-mixture than the most-reactive one. This probability increases until the flame stabilized, then remains constant, however, on a wider mixture fraction spectrum.

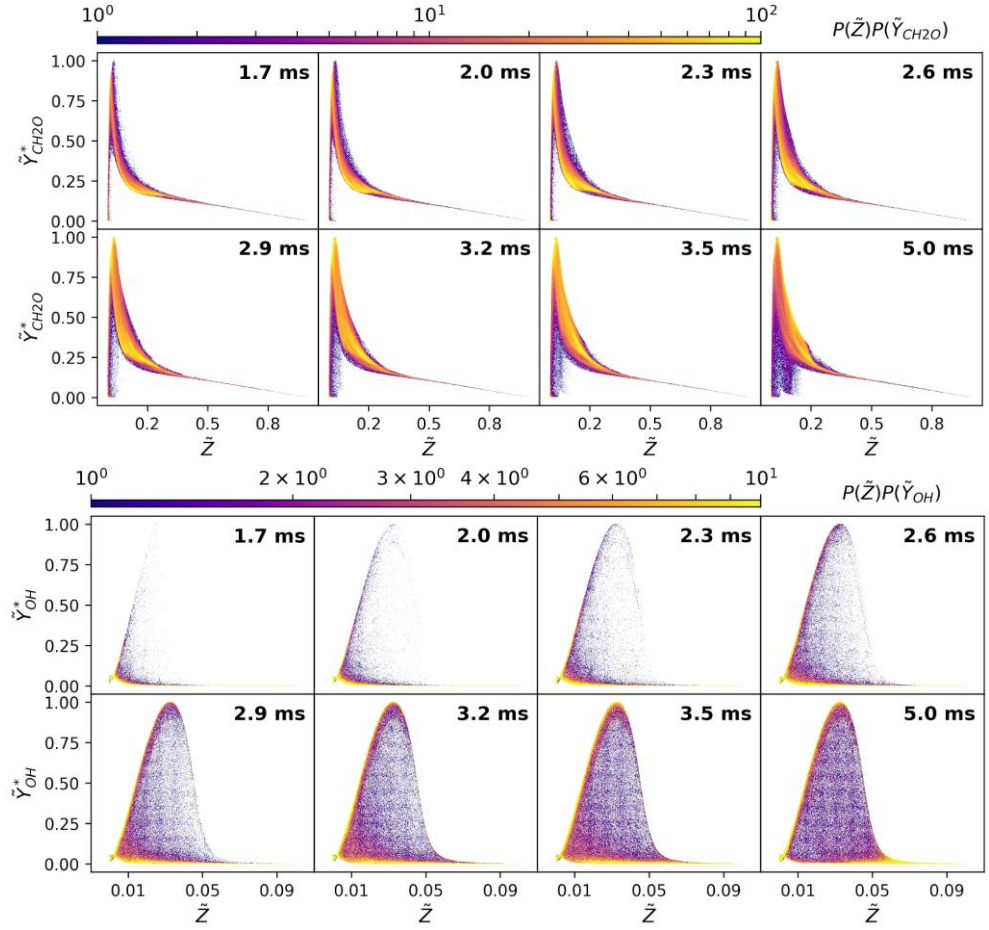

Figure 1. The time-history of normalized Y^*_{CH2O} (top) and Y^*_{OH} (bottom) over the mixture fraction colored by their JPDF.

The time-history of the PDFs of the predicted temperature, ignition related species Y_{HO2} and Y_{CH2O} and flame related species Y_{OH} are given in Fig. 2a. The highest temperature probability decreases until the AI, meanwhile, the distribution of the probability becomes wider over time. At the same time, similarly, the probability of higher Y_{OH} increases and is available on wider mixture fraction spectrum. On the other hand, the probability of finding high concentrations of ignition related species HO_2 and CH_2O increases until the flame stabilizes then decreases afterward.

It should be noted that the ignition-related species form even after the AI since the freshly injected gas must also ignite. However, the quantity of the ignition spots that form during the steady injection is fewer than the spots that form during the transient injection, which is due to the vortex pinch-off. Hence, the ignition-related species-concentrations could not maintain their high-values at later times.

Figure 2b shows the scatter plots of the temperature over the mixture fraction at several times of a pulse, colored by the distance from nozzle-exit. It can be seen that a temperature increase is visible even before the AI, however, this increase is not enough to trigger AI. Before the AI, the high-temperature values emerge on the most-reactive mixture fraction at an axial distance of x=30 mm. During the ignition, the AI kernel expands from this mixture to the richer zones. After a stable flame is established, the clustered high temperatures move to further downstream positions of x>60 mm.

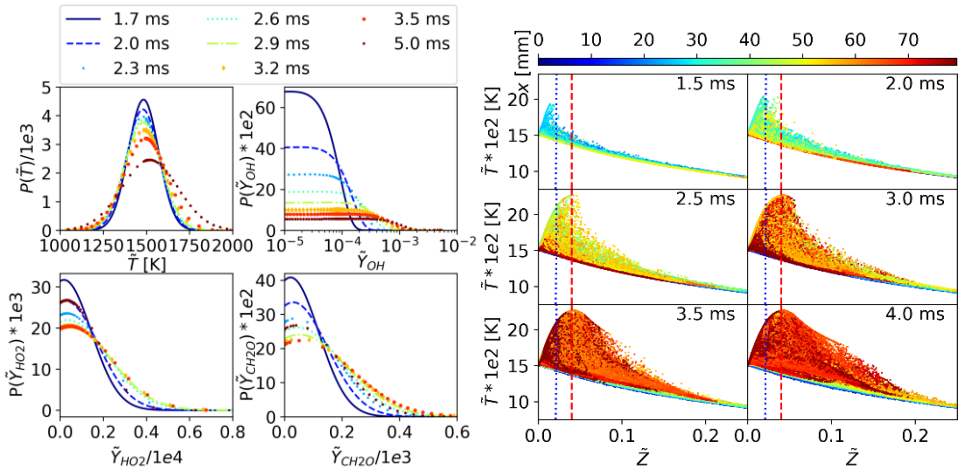

(a) (b)

Figure 2. The time-evolutions of PDFs of the temperature and relevant species (a), and of the temperature over the mixture fraction, colored by the distance from the nozzle-exit (b) during an injection. Dotted and dashed lines denote most-reactive and stoichiometric mixture, respectively

Conclusions

A good agreement was obtained between the LES and the experiments of the (statistically) steady and pulsed auto-igniting jet flames. The tested combustion model performed reasonably well, imposing low computational costs. The estimated AI delay times and ignition kernels were in a good agreement with the experiments, which normally require more costly combustion models.

Statistics showed that the ignition-related species HO_2 and CH_2O started forming at lean-zones, then formed at the richer-zones after the flame became stabilized. These species also form in a much larger quantity at the initial injection phase than the steady injection phase.

The authors gratefully acknowledge the financial support by the state North-Rhine-Westphalia, Germany, and the computing time grated on magnitUDE (DFG grant INST 20876/209-1 FUGG).

References

[1] Mastorakos, E., "Ignition of turbulent non-premixed flames", *Prog. Energy Comb. Sci.* 35.1: 57-97 (2009)

[2] Echekki, T., Jacqueline H. C., "Direct numerical simulation of autoignition in non-homogeneous hydrogen-air mixtures", *Comb. Flame* 134.3: 169-191 (2003)

[3] Oijen, J. A. v., de Goey, L. P. H., "Modelling of premixed laminar flames using flamelet-generated manifolds", *Comb. Sci. Tech.* 161.1: 113-137 (2000)

[4] Papageorge, M. J., Arndt, C., Fuest, F., Meier, W., Sutton, J. A., "High-speed mixture fraction and temperature imaging of pulsed, turbulent fuel jets auto-igniting in high-temperature, vitiated co-flows", *Exp. Fluids 55*.7: 1763 (2014)

[5] Papageorge, M. J., Arndt, C., Fuest, F., Meier, W., Sutton, J. A., "Erratum to: High-speed mixture fraction and temperature imaging of pulsed, turbulent fuel jets auto-igniting in high-temperature, vitiated co-flows", *Exp. Fluids 57*.1: 14 (2016)

[6] Smith, G. P. et al., "GRI-3.0", *combustion.berkeley.edu/gri-mech*: (2000)

[7] Pitsch, H., "FlameMaster: A C++ Computer Program for 0D Combustion and 1D Laminar Flame Calculations", *web.stanford.edu/group/pitsch/FlameMaster.htm*: (1998)

[8] Saghafian, A., "High-fidelity simulations and modeling of compressible reacting flows", *Ph.D. thesis in Stanford University*: (2014)

[9] Legier, J. P., Poinsot, T., Veynante, D., "Dynamically thickened flame LES model for premixed and non-premixed turbulent combustion", *Proc. Summer Prog. 2000*, pp 157-168

[10] Butler, T. D., O'rourke P. J., "A numerical method for two dimensional unsteady reacting flows", *Symp. (Int.) Comb 16.1*, pp 1503-1515

[11] Kempf, A. M., Geurts, B. J., Oefelein, J. C, "Error analysis of Large-Eddy Simulation of the turbulent non-premixed Sydney bluff-body flame", *Comb. Flame* 158.12: 2408-2419 (2011)

[12] Inanc, E., Nguyen, M. T., Kaiser, S., Kempf, A. M., "High-resolution LES of a starting jet", *Comp. Fluids* 140: 435-449 (2016)

[13] Camarri, S., Salvetti, M. V., Koobus, B., Dervieux, A., "A low-diffusion MUSCL scheme for LES on unstructured grids", *Comp. Fluids* 33: 1101-1129 (2004)

[14] Nicoud, F., and Toda, H. B., Cabrit, O., Bose, S., Lee, J., "Using singular values to build a subgrid-scale model for large eddy simulations", *Phy. Fluids* 23.8: 085106 (2011)

DISSIPATION ELEMENT ANALYSIS OF PREMIXED JET FLAMES

D. Denker*, A. Attili*, S. Luca, F. Bisetti*** and H. Pitsch***
d.denker@itv.rwth-aachen.de
*RWTH Aachen University, Germany
**King Abdullah University of Science and Technology, Saudi Arabia
***The University of Texas at Austin, USA

Abstract
Dissipation element analysis is a method for analyzing scalar fields in turbulent flows. Dissipation elements are defined as a coherent region, in which all gradient trajectories of a scalar field reach the same extremal points. Therefore, the scalar field can be compartmentalized in monotonous space filling regions.
The dissipation element analysis is applied to a set of spatial evolving premixed jet flames at different Reynolds numbers. The simulations feature finite rate chemistry with 16 species and 73 reactions. The jet consists of a methane/air mixture with an equivalence ratio $\varphi = 0.7$.
Marginal statistics of dissipation element parameters are shown and compared to those of a DNS of a non-reacting spatial jet. In addition, the correlation between the local flame structure and dissipation elements is investigated.

Introduction
In turbulent combustion, various regimes exist which pose different implications to the accompanying modeling procedure. For premixed combustion, the so-called "regime-diagram" exists [1], where turbulent scales, such as the Kolmogorov length are compared to different scales of the flame. To test the underlying theory of the combustion diagram by means of direct numerical simulations (DNS), a set of simulations of spatially evolving jet flames situated in the thin reaction zone regime was conducted by Luca et al. [2]. To achieve a meaningful comparison between the local turbulent and chemical scales, a procedure is required that employs a space-filling decomposition to assure that all interactions are being considered.
A method for obtaining the local turbulent scales in a turbulent scalar field is the dissipation element (DE) analysis [3,4]. DEs are constructed by tracing gradient trajectories in a scalar field in the ascending direction until a maximum is reached and in the descending direction, until the gradient trajectory terminates at a local minimum. All grid points whose gradient trajectories reach the same extremal points are grouped into a single DE. DEs can be statistically described by two parameters, namely the Euclidean distance between their extremal points ℓ and

their scalar difference in these points $\Delta\psi$. The joint probability density function of these two parameters is expected to suffice for a statistical reconstruction of the scalar field.
DE analysis was originally applied to scalar fields in isotropic turbulence [3,4,5], later to free shear flows [6] and verified in experiments [7]. More recently, the DE analysis was applied to a non-premixed jet flame [8].
In the scope of this work, the DE analysis is applied to the temperature fields of two DNS whose details will be outlined in the section below. Since the temperature can be interpreted as a progress variable in the context of premixed combustion, the gradient trajectories used in forming a DE can be interpreted as a grouping of flamelets, which share the same start and end points in space.

Configurations
The DE analysis was applied to two DNS of spatially evolving methane jet flames of the Bunsen burner configuration. This configuration is illustrated in Fig. 1, where the atomic oxygen mass fraction in the *x*-*y* center plane of the two DNS is shown.

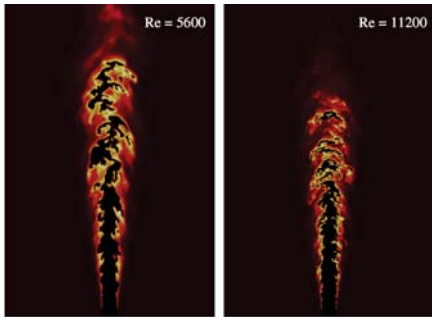

Figure 1. Atomic oxygen mass fraction in the x-y center-plane of the two DNS cases investigated here. The yellow colored regions corresponds to high values of the mass fraction, and brown colored regions to low values [2].

The jet Reynolds number is set to 5,600 and 11,200 for the low *Re* case and the high *Re* case, respectively. The jet Reynolds number is varied by changing the slot width *H* while keeping the jet bulk velocity constant. In this fashion, the turbulent small scales remain approximately constant while the integral scales are changed.
The DNS feature lean premixed methane/air flames with an equivalence ratio of $\varphi = 0.7$ and a temperature of $T = 800$K, as it is commonly found in stationary gas turbines. The temperature and species concentrations in the co-flow correspond to the equilibrium state of the burned mixture.
The laminar burning velocity is $s_L = 1.01$ ms^{-1} and the temperature gradient based flame thickness is $\delta_L = 110$ µm. This places the cases in the regime of the thin

reaction zone.

The DNS are performed in the low Mach number limit using finite rate chemistry with a skeletal mechanism with 16 species and 73 elementary reactions [9]. Additional details regarding the DNS are summarized in Tab. 1.

Table 1. Summary of the details of the DNS investigated with the DE analysis.

	Low *Re* case	High *Re* case
Jet Reynolds number *Re*	5,600	11,200
Jet bulk velocity *U*	100 ms^{-1}	100 ms^{-1}
Slot with *H*	1.2 mm	2.4 mm
Grid size ($n_x \times n_y \times n_z$)	1440 × 960 × 256	2880 × 1920 × 512

Dissipation Element Parameter Statistics

The DE analysis is applied to the temperature fields of the previously outlined DNS approximately 4*H* - 10*H* downstream from the nozzle, where the turbulence is already sufficiently evolved, but the flame front has not begun to close in on itself.

The corresponding DE analysis is shown in Fig. 2 for the *x*-*y* center plane of the temperature fields. On the top part of the figure, the temperature fields are shown as well as a black contour indicating the iso line of the temperature where the heat release peaks as an indicator for the position of the turbulent flame front. On the bottom part of Fig. 1, the DE analysis is shown in a mirrored fashion. The DE are colored individually and encompassed in a black contour. For the sake of orientation, the iso-line of the temperature of the maximum heat release is again shown in white. One observes that, compared to the jet thickness in cross-stream direction, the DEs of the high *Re* flame are a lot smaller in scale than in the low *Re* flame. Another observation to be pointed out are the various shapes and sizes of the DEs intersecting the flame front, which indicates a wide range of local turbulent scales interacting with the flame.

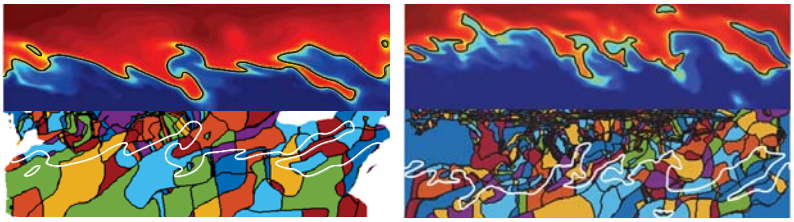

Figure 2. Top part: *x*-*y* center plane of the temperature fields in two DNS of spatially evolving methane jet flames. Red colored regions correspond to high temperatures, blue color to low temperature regions. The black contour indicates the iso-surface of the maximum heat release. Bottom: corresponding DE analysis of the temperature, mirrored. The DE are colored individually and encompassed in

a black contour. Left: low *Re* case, right: high *Re* case.

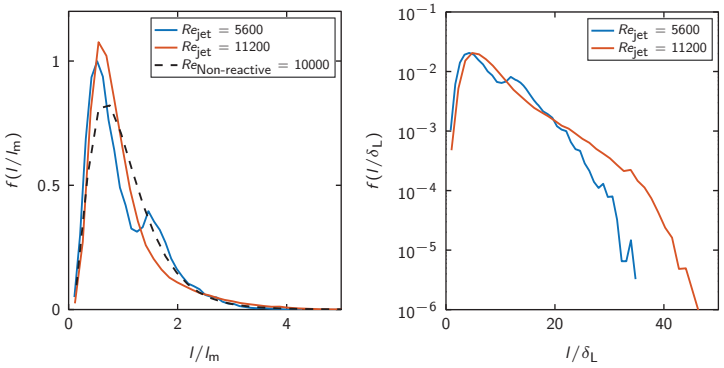

Figure 3. PDFs of normalized separation length ℓ. Left: normalization with the mean length ℓ_m. Right: normalization with flame thickness δ_L.

An important characteristic of DE statistics of the separation length ℓ is its invariance towards changes in Reynolds numbers when normalized with the mean length ℓ_m. The probability density functions (PDF) of the normalized separation length $P(\ell/\ell_m)$ are shown on the left of Fig 3. The solid blue and the red line correspond to the PDF of the low and high *Re* case, respectively. As a reference, the DE analysis of the passive scalar field in a non-reacting jet with a jet Reynolds number of *Re* = 10,000 is shown by the dashed line. For all three cases, for the short elements, a linear increase of the PDFs is observed. This linear increase is caused by the diffusive drift of the extremal points [2]. After a maximum, a exponential decrease of the PDF for longer DEs is observed, which is attributed to the Poisson process of random cutting and connecting of the DEs by turbulent eddies. Here, the PDF of the low *Re* case differs. A second, local maximum of the PDF is situated at $\ell/\ell_m \approx 1.6$. This second maximum is a signature of a length scale induced at the nozzle that has not been sufficiently mixed out at this stream-wise location due to the low level of turbulence in this case.

On the right hand side of Fig. 3, the normalization of ℓ is performed with the flame thickness δ_L to achieve the originally proposed comparison of turbulent and chemical scales. The PDFs display good agreement for the short DEs. For the longer elements, the PDF of the high *Re* displays a higher probability density than that of the low *Re* case, which is a result of the larger scale separation induced by the difference in the Reynolds number. In addition, this validates the original intent of the numerical experiments of keeping the small scales constant while changing the large scales. The assumption of the regime of the "thin reaction zone" is reflected by the PDFs as well. While being larger than the flame thickness δ_L, the

vast majority of the DEs are of a comparable length.

Influence of Dissipation Elements Parameters on the Flame Structure

To gain insight into the flame structure, the mean temperature conditioned on the distance to the flame front $\langle T|s\rangle$ is shown on the left of Fig. 4.

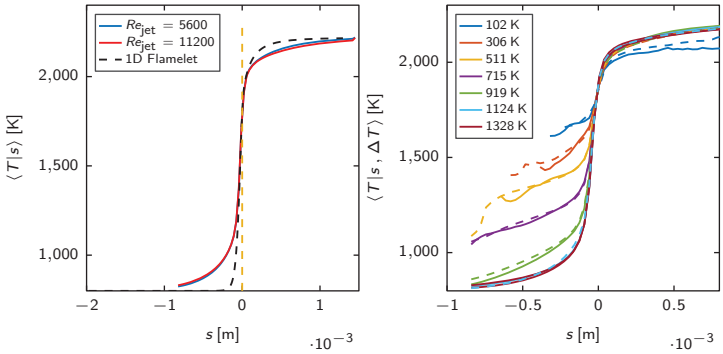

Figure 4. Left: Mean temperature conditioned on the distance to the flame front $\langle T|s\rangle$. Right: Mean temperature conditioned on the distance to the flame front and the DE temperature difference $\langle T|s,\Delta T\rangle$, solid lines correspond to the low *Re* case, dashed lines correspond to the high *Re* case.

The flame front is defined as the iso-surface of the maximum heat release of T = 1800 K. The distance s is obtained by using gradient trajectories in the temperature field to assure the shortest possible path from the unburned to the burned side. The unstretched 1D flamelet solution for the simulated conditions is indicated as the black dashed line. The conditional temperatures for the jet flames are indicated by the solid lines, which show a perfect collapse for all distances. For negative values of s, the jet flames show distinctly higher temperatures than the flamelet solution. This is due to turbulent mixing in the preheating zone. Close to the reaction zone all three lines collapse, indicating an unbroken inner reaction zone. In the oxidation zone, for positive values of s, the jet flames display slightly lower values of the temperature. All these findings are highly consistent with the expected flame structure in the "thin reaction zone" regime.

To achieve a more local comparison of scales as well as investigate the correlation between the DE parameters and the flame structure, the temperature is additionally conditioned on the DE temperature difference $\langle T|s,\Delta T\rangle$. This is shown on the right of Fig. 4. The solid lines and the dashed lines correspond to the low and the high *Re* case, respectively, and the colors indicate different ΔT. For decreasing values of ΔT and therefore smaller indicated turbulent scales, the temperature in the preheating zone increases, which is caused by more intense turbulent transport

from the inner reaction zone. For very small values of ΔT, a significant influence on the oxidation zone can be observed as well.

Conclusions

DE analysis was performed on the temperature fields of the DNS of two spatially evolving methane jet flames. The invariance of the normalized statistics of ℓ towards changes in *Re* observed in scalar fields in non-reacting flows was retained in the reacting cases. The marginal statistics showed a high consistency with the assumptions regarding the general setup of the DNS and the regime of the thin reaction zones. Additionally the correlation between the DE parameter ΔT and the flame structure was demonstrated.

References

[1] N. Peters. *Turbulent Combustion*. Cambridge University Press, 2000.

[2] S. Luca, Attili, A., E. Lo Schiavo, F. Creta, and F. Bisetti. “On the statistics of flame stretch in turbulent premixed jet flames in the thin reaction zone regime at varying Reynolds number”. In: *Proc. Combust. Inst.* (under review).

[3] L. Wang and N. Peters. “The length scale distribution function of the distance between extremal points in passive scalar turbulence”. In: *J. Fluid Mech.* 554 (2006), pp. 457– 475.

[4] L. Wang and N. Peters. “The scale distribution functions and conditional means for various fields in turbulence”. In: *J. Fluid Mech.* 608 (2008), pp. 113–138.

[5] N. Peters. “Turbulence statistics along gradient trajectories”. In: *ZAMM* 92 (2012), pp. 4 – 7.

[6] M. Gampert, P. Schaefer, J.H. Goebbert, and N. Peters. “Decomposition of the field of the turbulent kinetic energy into regions of compressive and extensive strain”. In: *Physica Scripta* 155.014002 (2013).

[7] M. Gampert, P. Schaefer, and N. Peters. “Experimental investigation of dissipation-element statistics in scalar fields in a jet flow”. In: *J. Fluid Mech.* 724 (2013), pp. 337–366.

[8] A. Scholtissek, F. Dietzsch, M. Gauding and C. Hasse. “In-situ tracking of mixture fraction gradient trajectories and unsteady flamelet analysis in turbulent non-premixed combustion”, In: *Comb. and Flame.* 175 (2017), pp 243 - 258.

[9] S. Luca, A. N. Al-Khateeb, Attili, A., and F. Bisetti. “Comprehensive Validation of Skeletal Mechanism for Turbulent Premixed Methane–Air Flame Simulations”. J. Prop. Power 34.1 (2018), pp. 153–160.

Morphology and propagation of large scale premixed flames: comparison of 2D, 3D DNS and experiments

R. Lamioni*, P.E. Lapenna*, G. Troiani, F. Creta***
rachele.lamioni@uniroma1.it
*Dept. of Mechanical and Aerospace Engineering,
Sapienza University of Rome, Italy
**ENEA C.R., Casaccia, Rome, Italy

Abstract
A comparison between experiments, 2D and 3D numerical simulations of large scale premixed flames in moderately turbulent flow fields is presented. Experiments are carried out using a Bunsen configuration with different burner sizes and a range of propane-air mixtures. Direct numerical simulations are performed using a slot burner configuration in both 2D and 3D settings using a simplified one-step chemistry. The range of parameters investigated by both the experiments and the numerical simulations are chosen by means of linear stability analysis ensuing from the asymptotic hydrodynamic theory of premixed flames. This feature is of particular relevance in the study of large scale premixed flames that can be influenced by Darrieus-Landau (DL) or hydrodynamic instability. The latter is characterized by a long wavelength nature and, therefore, it is expected to be ubiquitous in large scale combustion devices. Similar statistical trends, in terms of morphology and propagation, are found in both experiments and 2D/3D numerical simulations for hydrodynamically unstable flames.

Introduction
The interaction between a reactive flame front and a turbulent flow field are commonly investigated by means of experiments and numerical simulations. The common objective of such approaches is improve both the current knowledge and to improve the limited predictive capabilities of the currently available combustion models [1-3]. In this context, direct numerical simulation (DNS), even if limited by the extremely high computational costs, is a fundamental tool for the study of turbulent premixed combustion [4]. Nowadays many research groups are capable of investigating turbulent premixed flame using 3D DNS in realistic configurations and, concurrently, using detailed chemical kinetic mechanisms [5-7]. This has prompted an ever increasing interest toward DNS-oriented experiments, i.e. experimental configurations that can be simulated by means of currently available DNS codes and high performance computing (HPC) infrastructures.
Substantial differences in the morphological and propagative properties of large-scale compared to small scale flames have been unveiled in recent investigations. The DL instability in large scale flames was observed in both laminar and turbulent settings in multiple experimental [8,9] and numerical [10,11] studies. The DL induced morphology was found to be associated to an increase in flame area and to a consequent increase in laminar as well as turbulent propagation speed.

In the present work we utilize numerical simulations as well as experiments to collect statistics on flame curvature and propagations highlighting DL-induced large scale effects on the investigated premixed flames. The qualitative comparison between the experiments and 2D/3D DNS shows some common trends and similar DL-induced effects.

Theoretical and Numerical Approach

To study large scale premixed flames subject to DL instability, we adopt a one-step irreversible Arrhenius reaction model in which the reaction rate is determined by a deficient reactant. The use of the deficient reactant model enables the coherent use of results obtained within the asymptotic hydrodynamic theory of premixed flames developed in [12] and in particular the linear stability properties of flames derived therein. Operatively we non-dimensionalize spatial variables with respect to a critical hydrodynamic wavelength λ_c, which can be estimated from linear stability analysis [13], while time is non-dimensionalized by λ_c/S_{L0}.
A modified version [14,15] of the highly parallel, spectral element, incompressible and low-Mach number code *nek5000* [16] is used to solve numerically the discretized system.

Morphology and global propagation

Figure 1(a) shows the instantaneous snapshot of 3D simulations for the small, SB (left panel) and large, LB (right panel) domain of the slot bunsen, while Figure 1(b)

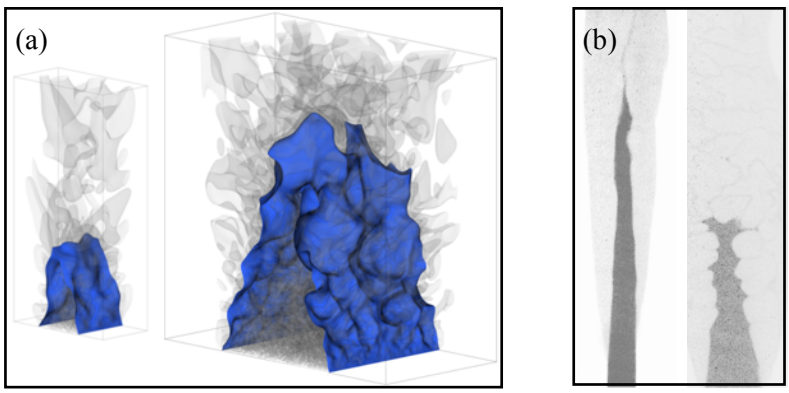

Figure 1: Overview of flames computational domains (a) and experiments (b), from left to right: small (SB) and large (LB) scale slot bunsen flame.

shows the experimental flames for two different burner sizes, small (SB) in the left panel and large (LB) in the right panel. Figure 2 shows the mean progress variable fields for 2D and 3D DNS. In particular the small scale flames with $\lambda_c/L=0.5$ are shown in the top panels of Fig. 2, where the flame brushes are comparable for 2D

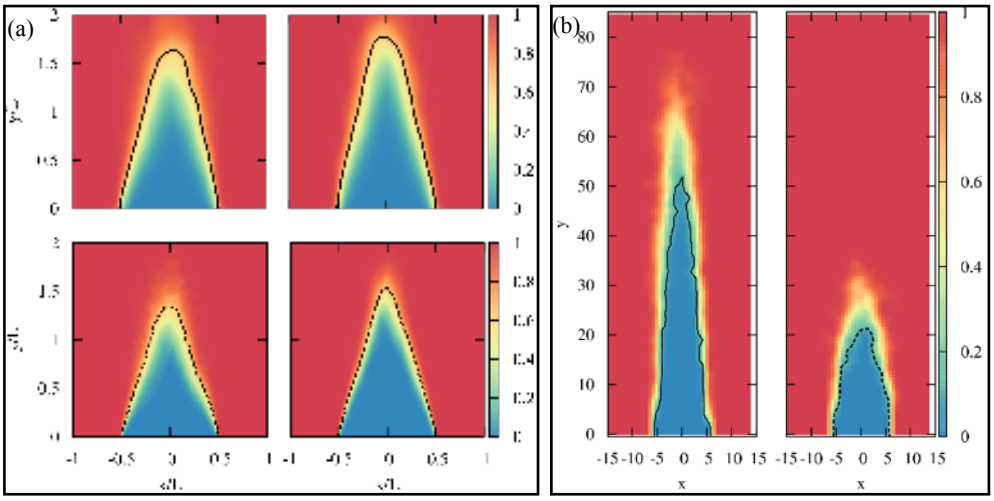

Figure 2: Panel (a): mean progress variable fields for large scale (bottom panels) and small scale (top panels) flames, left panel 2D and right panel 3D DNS. Panel (b): mean progress variable fields for experiments, left panel Φ=0.75 and right panel Φ=1.5.

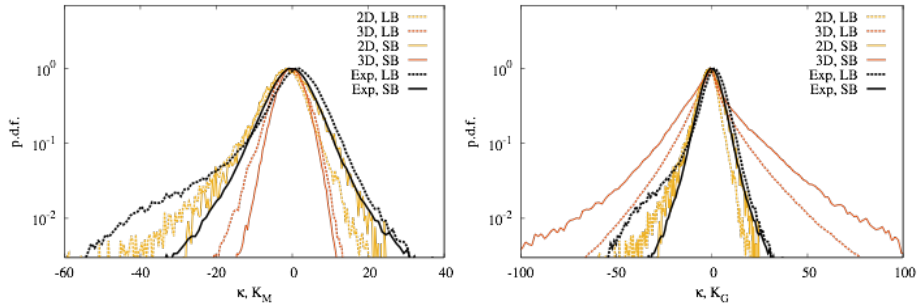

Figure 3: Curvature, Mean and Gaussian curvature p.d.f.s for 2D, 3D simulations and experiments. Dashed lines are the large scale flames (LB) and solid lines are the small scale flames (SB).

and 3D simulations. The slightly different area of the same progress variable iso-line (c=0.64), produce a difference in the global consumption speed $S_{T,GC}$, for 3D $S_{T,GC}/S_{L0}$=1.13 and for 2D $S_{T,GC}/S_{L0}$=1.14. A similar result is also observed for the large scale flames with λ_c/L=2, where the difference of the $S_{T,GC}$ is, for 3D $S_{T,GC}/S_{L0}$=1.29 and for 2D $S_{T,GC}/S_{L0}$=1.35.

In two dimensional simulations [11] cusp-like formations were detected in terms of localized bursts of negative flame curvature (flame normal oriented toward burnt gases) conversely moderately positive curvature values were found along the troughs. The skewness of the flame curvature was thus identified as an unambiguous marker of the presence of the DL-instability [11]. In the three dimensional scenario

similar considerations are expected to hold in terms of the mean curvature K_M, and Gaussian curvature, K_G defined as:

$$K_M = (\kappa_1 + \kappa_2)/2 \qquad K_G = \kappa_1 \cdot \kappa_2 \tag{1}$$

Figure 3 shows the curvature p.d.f.'s for experiments and 2D/3D numerical simulations. In the left panel of Fig. 3 the mean curvature p.d.f.'s are in qualitative agreement with the experiments and 2D results. In the right panels of Fig. 3 the Gaussian curvature p.d.f.'s show a qualitative difference with respect experiments ann 2D statistical results due to that the Gaussian curvature provides information on the overall 3D structure of the surface.

Local Propagation

The displacement speed S_d concept [17] conveniently describes the local flame propagation. This important characteristic of premixed combustion can be defined as the propagation speed of a flame relative to the gas and it can be derived from the motion of a scalar field isoline described by a level set equation. Using the progress variable as scalar field, S_d can be expressed as follows:

$$S_d = \frac{1}{|\nabla c|}\frac{Dc}{Dt}\bigg|_{c=c^*} = \frac{1}{\rho|\nabla c|}\left[\frac{\dot{\omega}}{\delta} + \frac{\delta}{Le}\nabla^2 c\right]_{c=c^*} \tag{2}$$

where the values are conditioned to the $c = c^*$ isoline. The displacement speed in Eq. (2) is dependent on the choice of c^* and can be rendered independent through a normalization with respect to the local density ratio [17], $S_d = S_d\, \rho/\rho_u$. In addition S_d can be analyzed [18] by splitting it into a reaction rate and a diffusion contribution. The diffusion term can be further decomposed into a normal and a tangential contribution, respectively S_n and S_t, being S_r the reactive component:

$$S_r = \frac{1}{\rho|\nabla c|}\left[\frac{\dot{\omega}}{\delta}\right]\bigg|_{c=c^*}; \quad S_n = \frac{1}{\rho|\nabla c|}\mathbf{n}\cdot\nabla\cdot[\delta\mathbf{n}\nabla c]|_{c=c^*}; \quad S_t = -\delta\kappa; \tag{3}$$

In order to investigate the statistical behavior of the displacement speed for both 2D and 3D flames, the p.d.f.'s of S_d and its components are analyzed. All terms are conditioned to the c^*=0.84 isoline, which corresponds to the progress variable location in which the reaction rate peaks for an unstretched laminar flame with the same mixture properties.

Figure 4, in left panel, shows the S_d p.d.f.'s for both 2D and 3D simulations, the behavior of the local propagation is the same for 3D and 2D DNS. However, some three dimensional effects can be observed in terms of a wider p.d.f.'s on both sides. The skewed shape of the p.d.f.'s can be attributed to the above unity Lewis number resulting in a positive Markstein length, as shown in a dedicated DNS analysis [18]. The right panel of Fig.4 shows the reaction component of S_d, which is the major contributor to S_d, due to the choice of the c-isoline. Figure 4 shows the others contributions to the displacement speed, S_n (left panel) and S_t (right panel).

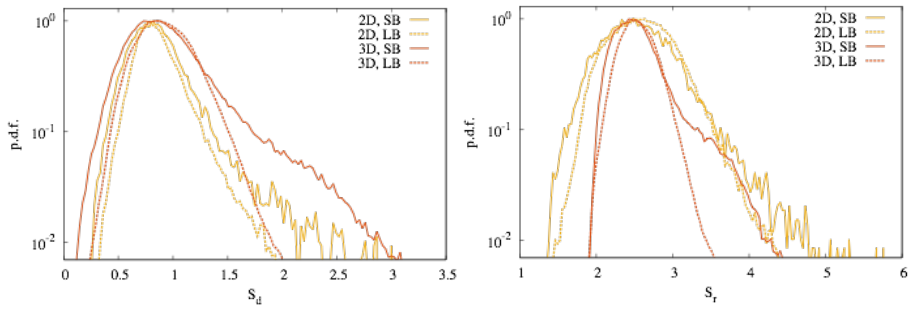

Figure 4: Displacement speed S_d and reaction component S_r p.d.f.'s for 2D and 3D simulations. Dashed lines are the large scale flames (LB) and solid lines are the small scale flames (SB).

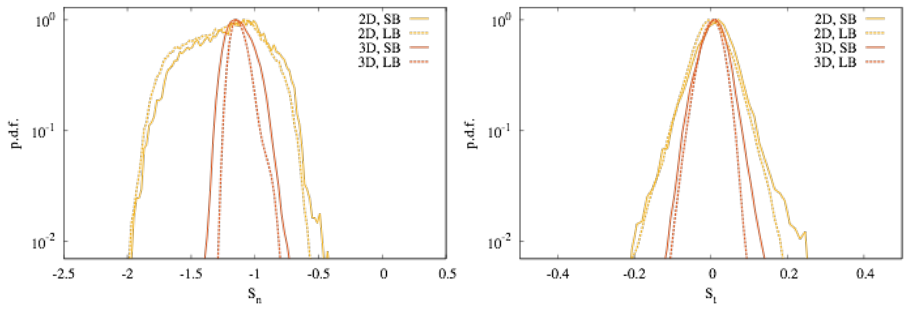

Figure 5: Normal component of the displacement speed p.d.f.'s for 2D and 3D simulations. Dashed lines are the large scale flames (LB) and solid lines are the small scale flames (SB).

Substantial differences are found for the reaction and normal diffusion components between 2D and 3D simulations. This suggests that progress variable scalar gradients and dissipation rates can influence the flame local propagation in a 3D setting.

Conclusion

The 3D computational results are compared with the experiments and 2D results. Curvature statistics obtained from both 2D and 3D DNS, show qualitative agreement with the experiments, suggesting that 3D effects on flame curvature and global propagation are not pronounced in the investigated conditions.

Regarding the local propagation for both the 2D and 3D cases, the tangential diffusion component of S_d is shown to be smaller than the reaction, S_r , and normal diffusion, S_n. The values of S_r and S_n in the 2D simulations are found to be larger than those in the 3D cases. This effect can be attributed to the evolution of reaction progress variable scalar gradients.

References

[1] R.W. Bilger, S.B. Pope, K.N.C Bray, and J.F. Driscoll., "Paradigms in turbulent combustion research", *Proc. Combust. Inst.* 30(1):21–42, (2005)

[2] A.,Lipatnikov, "*Fundamentals of premixed turbulent combustion*", (2012)

[3] C., K. Law, "*Combustion physics*", Cambridge university press, 2010.

[4] T. Poinsot, D. Veynante. "*Theoretical and numerical combustion*". RT Edwards, Inc., (2005).

[5] S., Luca, A., Attili, F., Bisetti. "Direct numerical simulations of nox formation in spatially developing turbulent premixed bunsen flames with mixture inhomogeneity". *55th AIAA Aerospace Sciences Meeting*, (2017).

[6] P., Trisjono, H., Pitsch. "A direct numerical simulation study on no formation in lean premixed flames". *Proc. Combust. Inst.*, 36(2):2033–2043, (2017).

[7] R., Yu, X-S, Bai, A. N., Lipatnikov. "A direct numerical simulation study of interface propagation in homogeneous turbulence". *Jour. Fluid Mech.*, 772:127–164, (2015).

[8] C. Almarcha, B. Denet, J. Quinard,. "Premixed flames propagating freely in tubes". *Combust. Flame,* 162 (4), 1225–1233, (2015).

[9] G., Troiani, F., Creta, M., Matalon. "Experimental investigation of Darrieus–Landau instability effects on turbulent premixed flames". *Proc. Combust. Inst.*, 35(2):1451–1459, (2015).

[10] F., Creta, N., Fogla, M., Matalon. "Turbulent propagation of premixed flames in the presence of Darrieus–Landau instability". *Combust. Theo. Model.*, 15(2):267–298, (2011).

[11] F., Creta, R., Lamioni, P. E., Lapenna, G., Troiani. "Interplay of Darrieus-Landau instability and weak turbulence in premixed flame propagation". *Phys. Rev. E*, 94(5):053102, (2016).

[12] M., Matalon, B. J., Matkowsky. "Flames as gasdynamic discontinuities". *Jour. Fluid Mech.*,124:239–259,(1982).

[13] P. E, Lapenna, R., Lamioni, G., Troiani, F., Creta, "Large scale effects in weakly turbulent premixed flames". *Proc. Combust. Inst.*, (under review - 2018).

[14] P. E, Lapenna, R., Lamioni, P. P. Ciottoli, F., Creta, "Low-Mach number simulations of transcritical flows". *AIAA Paper 2018-0346,* (2018).

[15] P. E, Lapenna, F., Creta, "Mixing under transcritical conditions: an a-priori study using direct numerical simulation". *Jour. Supercr. Fluid,* 128 263-278, (2017).

[16] P. F., Fischer, J. W., Lottes, S. G., Kerkemeier. nek5000 web page. *http://nek5000.mcs.anl.gov*, (2008).

[17] G.K., Giannakopoulos, A., Gatzoulis, C. E., Frouzakis, M., Matalon, A. G., Tomboulides. "Consistent definitions of flame displacement speed and markstein length for premixed flame propagation". *Combust. Flame* 162:1249–1264 (2015).

[18] Chakraborty, N., Cant, R., "Influence of lewis number on curvature effects in turbulent premixed flame propagation in the thin reaction zones regime", *Phys. Fluid* 17:105105 (2005)

ON ENERGY AND DISSIPATION SPECTRA IN TURBULENT NON-PREMIXED JETS WITH LOCAL EXTINCTION

A. Shamooni*,, A. Cuoci**, A. Sadiki*, T. Faravelli****
ali.shamooni@polimi.it
* Energy and Power Plant Technology Department, Technische Universität Darmstadt
**Department of Chemistry, Materials, and Chemical Engineering, Politecnico di Milano

Abstract
The turbulent kinetic energy (TKE) and its dissipation spectra are analyzed using a DNS database of temporally evolving non-premixed jet flame experiencing high level of local extinction. It is found out that when scaled using Favre averaged turbulent dissipation rate ($\tilde{\varepsilon}$) and the cutoff scale (λ_β) corresponding to the Batchelor scale, both TKE and its dissipation spectra collapse well in different planes across the flame in both low-medium and high wave number dissipative ranges. Further, the spectra are compared with the model spectra, it is found that again using the previous scaling laws the agreement is better than the classical scaling laws for spectra involving Kolmogorov scale, especially in high wave number regions.

Introduction
The analysis of velocity and scalar spectra in reactive flows is of great importance both in experiments and numerics. In experiments, one needs to know the true resolution requirements to scalar gradients. Many numerical models also rely on these scaling laws to evaluate constants or to justify assumptions. Knowing that the chemistry mostly occurs in small scales, the kinetic energy and dissipation spectra in high wave number range are of great importance.
In [1] Sandia flames C, D, and E are used to study the scalars spectra of non-premixed jets. A cutoff scale (λ_β) was introduced as the inverse of the wave number at which 2% peak dissipation spectrum occurs. It is found that, when normalized by λ_β, the dissipation spectra of temperature and mixture fraction nearly collapse. However, due to increased noise level in the measured data, there is no evidence of the behavior in high wave number range. In [2] the effect of heat release on the velocity and scalar spectra obtained by DNS of temporally evolving reacting shear layer is studied. Surprisingly, they found that the effect of heat release can be well scaled out by using Favre averaged turbulence quantities in velocity and mixture fraction spectra. In [3] the energy spectra of a premixed flame are studied. They found out that in agreement with [2], in the inertial range, classical scaling laws using Favre averaged quantities are applicable. In the high wavenumber range the laminar flame thickness (δ_L) produces a better collapse while disrupts the collapse in the inertial range. Recently, in [4] in the study of dissipation spectra of a premixed jet, it is found that they collapse when normalized by the corresponding Favre mean

dissipation rate and λ_β scale proposed in [1]. However, in contrast to [1] and [2], they saw that normalized dissipation spectra in all the cases deviate noticeably from those predicted by classical scaling laws for constant- density turbulent flows.
The purpose of the present study is to analyze the scaling laws in both inertial range and dissipative range of velocity spectra and to compare them with the model spectra proposed for non-reacting flows, but typically used in reacting flows (usually as a part of LES model development). The focus is on the effect of local extinction on the spectral behavior of velocity, which is missing in the literature. A DNS database of a temporally evolving non-premixed jet (introduced in next section) is used.

Computational setup

The numerical experiment is provided by DNS of temporal evolution of a non-premixed syngas (CO/H_2 as a fuel and air as an oxidizer) jet flame [5]. This flame experiences first extinction up to $20t_j$, with $t_j = 5\ \mu s$ the normalized time, and then reignition (as evident from Figure 1a). The domain is periodic in streamwise (x) and spanwise (z) directions. These are denoted as statistically homogenous directions. The time instant analyzed is $20t_j$, when the flame experiences maximum local extinction. In Figure 1b, the planes selected to carry out the analyses are introduced. Planes P^1 and P^2 are x-z planes with maximum density and temperature fluctuations. P^3 is a plane with maximum Favre averaged OH mass fraction and P^4 is a plane of maximum Favre averaged turbulent kinetic energy (TKE). P^0 is the center plane.

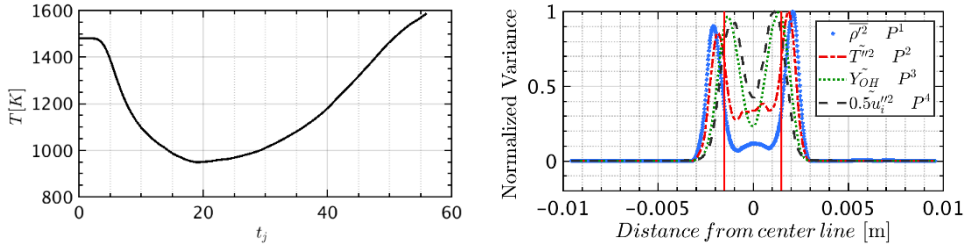

(a) **(b)**

Figure 1. (a) Maximum of Favre averaged temperature; **(b)** Reynolds averaged density fluctuation, Favre averaged temperature fluctuation, mean OH mass fraction and Favre RMS of velocity, normalized by their own maximum values. Vertical lines locate the planes of mean stoichiometric mixture fraction.

Results

The 3-dimensional spectra of velocity are extracted from the database. The term "3-dimensional" here refers to a line spectrum computed by adding the spectra of 3 components of velocity vector. Temporally evolving turbulence have been used before in the literature to analyze spectra [2-4]. The spectra are computed from a fixed temporal snapshot, using the data in each statistically homogenous x-z plane. Recently, in [3] the compressible form of spectrum function is proposed as:

$$E_{u_i}(\kappa) = \frac{1}{2\bar{\rho}}\left(\frac{1}{N_Z}\sum_{j=1}^{N_z}\mathcal{F}_j(\rho u_i")\mathcal{F}_j^*(u_i") + \mathcal{F}_j(u_i")\mathcal{F}_j^*(\rho u_i")\right) \quad (1)$$

where $\mathcal{F}_j$ and $\mathcal{F}_j^*$ are the Fourier transform and its complex conjugate, respectively. N_Z is the number of data points in z direction and κ is the wave number vector length. Using 1-D spectra for each velocity component, the 3-D spectrum is defined as:

$$E(\kappa) = \frac{1}{2}(E_{u_1} + E_{u_2} + E_{u_3}) \quad (2)$$

The dissipation spectra can be constructed using the relations in non-reacting homogenous isotropic turbulence as [6], but with Favre averaged viscosity:

$$D(\kappa) = 2\tilde{\nu}k^2E(\kappa) \quad (3)$$

Scaling laws

In [2], turbulent kinetic energy spectra are studied using a DNS of a non-premixed flame in a temporally evolving shear layer, a configuration nearly similar to the present study. They found a very good scaling of the spectra when normalized using Favre averaged Kolmogorov length scale ($\tilde{\eta}$) and turbulent dissipation rate ($\tilde{\varepsilon}$). They suggested that spectra in reacting flows follow the conventional Kolmogorov scaling in terms of Favre averaged quantities. The normalized spectrum is defined as:

$$E(\kappa)_{normal} = E(\kappa)/\left(\tilde{\eta}^{5/3}\tilde{\varepsilon}^{2/3}\right) \quad (4)$$

The normalized velocity dissipation spectrum using $\tilde{\eta}$ and $\tilde{\varepsilon}$ is defined as:

$$D(\kappa)_{normal} = D(\kappa)/\left(\tilde{\eta}\tilde{\varepsilon}\right) \quad (5)$$

We examine this scaling by plotting the normalized turbulent kinetic energy (TKE) and velocity dissipation spectra in different planes introduced in the previous section at time $20t_j$ where the flame experiences maximum local extinction. As shown and also in agreement with [2] and [3] the TKE spectra (Figure 2a) collapse well in the inertial range. However, in contrast to [2], in high wave number range the collapse is not good. In Figure 2b it is seen that in low wave number range the dissipation spectra is well collapsed, in agreement with [2]. In [2], the effect of heat release rate in non-premixed jets is studied. The one-way coupling is obtained by limiting the utilizing flame-sheet approximation and they eliminate flame structure changes and dynamics. So it seems that the dynamics of the flame, changed locally due to high level of local extinction, has an effect on high wave number range of both TKE and

dissipation spectra. However, inertial range remains unaffected and the conventional Kolmogorov scaling laws in Favre averaged form holds.

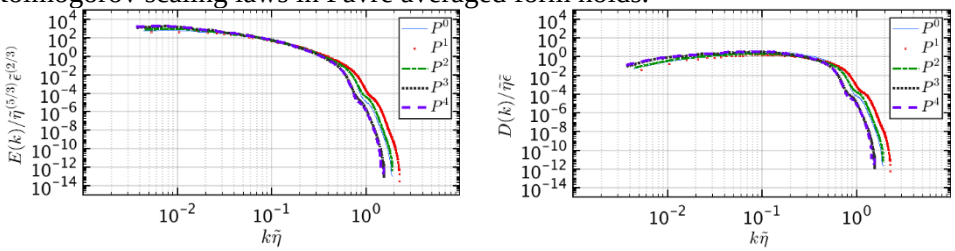

(a) **(b)**

Figure 2. Normalized energy **(a)** and dissipation **(b)** spectra in log-log axis in different planes, normalized using Favre averaged turbulence quantities $\tilde{\varepsilon}$ and $\tilde{\eta}$.

In [1], a cutoff scale (λ_β) was introduced, and used for normalization, as the inverse of the wave number at which 2% peak dissipation spectrum occurs. The dissipation spectra of scalars (i.e. temperature and mixture fraction) in non-premixed turbulent jets were normalized by λ_β. It is found that the normalized dissipation spectra of temperature and mixture fraction nearly collapse. However, due to increased noise level in the measured data, there is no evidence of that in high wave number range. Further, the TKE and its dissipation spectra are not provided. Here, in Figs 3a and 3b, the TKE and dissipation spectra normalized by λ_β instead η (shown in Figure 2) are reported. Compared to Figure 2, interestingly it is seen that both spectra well collapsed for all considered planes and nearly all wave number range.

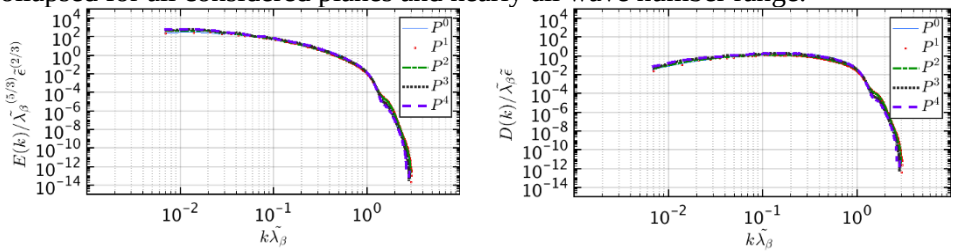

(a) **(b)**

Figure 3. Normalized energy **(a)** and dissipation **(b)** spectra in log-log axis in different planes normalized using the cutoff scale λ_β.

Model spectrum

The model spectrum of Pope [6] is proposed for non-reacting flows as:

$$E(\kappa)^{Model} = C_k \varepsilon^{\frac{2}{3}} \kappa^{-\frac{5}{3}} f_L(\kappa L) f_\eta(\kappa\eta) \tag{6}$$

where $f_L(\kappa L) = \left((\kappa L)/((\kappa L)^2 + c_L)\right)^{5/3+p_0}$ and $f_\eta(\kappa\eta) = \exp(-\beta[(\kappa\eta)^4 + c_\eta^4]^{\frac{1}{4}} + \beta c_\eta)$, with constants $C_k = 1$, $c_L = 6.78$, $p_0 = 2$, $c_\eta = 0.4$. In [2], for a non-premixed temporal jet without extinction, it is found that when scaled with Favre averaged $\tilde{\eta}$ and $\tilde{\varepsilon}$, spectra of different planes collapse and well follow the model spectrum of Pope [6]. Here we examine this scaling by plotting the energy spectra obtained by DNS and the model, normalized by Favre averaged turbulence quantities in Figure 4a and comparing it with normalization using cutoff scale (λ_β) in Figure 4b. The two spectra are computed in plane P^3. It is seen that using the cutoff scale (λ_β) for normalization, the model spectrum collapses well in inertial range compared to Figure 4a. Further, it is seen that in high wave number region, the agreement of the model spectra in both normalization methods are not good.

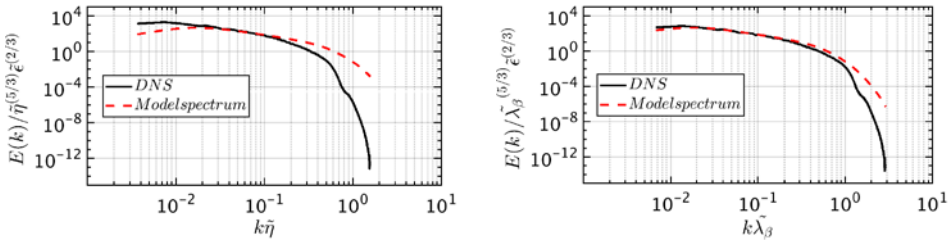

(a) **(b)**

Figure 4. Normalized energy spectrum in log-log axis in Plane P^3 compared to model spectrum of Pope [6] with different normalization scales; **(a)** using Favre averaged turbulence quantities $\tilde{\varepsilon}$ and $\tilde{\eta}$; **(b)** using the cutoff scale λ_β.

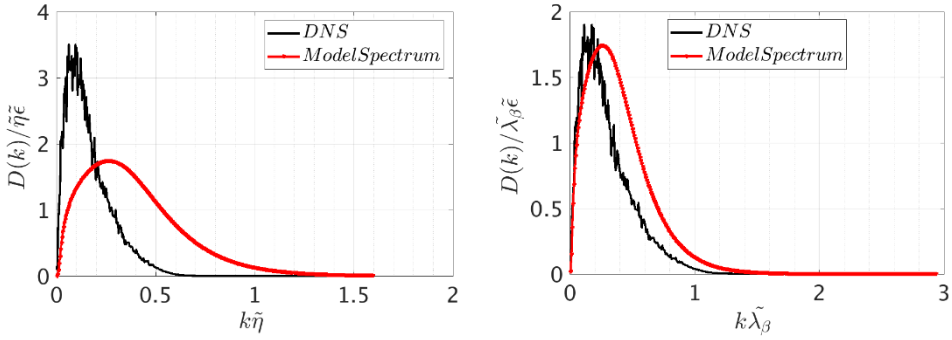

(a) **(b)**

Figure 5. Normalized dissipation spectrum in linear-linear axis in Plane P^3 compared to model spectrum of Pope [6] with different normalization scales; **(a)** using Favre averaged turbulence quantities $\tilde{\varepsilon}$ and $\tilde{\eta}$; **(b)** using the cutoff scale λ_β.

The effect of normalization is also studied in Figure 5 in linear-linear plots. Similar to energy spectra, normalization with λ_β is preferred. The normalized model dissipation spectrum peaks at $\kappa\tilde{\eta} \approx 0.26$ in Figure 5a. However, in agreement with

[4] the peak of the normalized dissipation spectrum is at lower wave number, around $\kappa\tilde{\eta} \approx 0.1$. Using the cutoff scale λ_β, the peak of dissipation spectrum of DNS shifts closer to the model spectrum ($\kappa\tilde{\eta} \approx 0.19$ instead of $\kappa\tilde{\eta} \approx 0.1$) in Figure 5b.

Conclusion

The velocity spectra of a non-premixed temporal jet flame at the instant of maximum local extinction are studied using a DNS database. The turbulent kinetic energy and velocity dissipation spectra are computed using a compressible formulation in different x-z planes of the computational domain corresponding to maximum of TKE, mean OH mass fraction, temperature, and density fluctuations and the central plane. The cutoff scale (λ_β) is defined as the inverse of wave number at which the dissipation spectrum reaches 2% of its peak at each plane. It is found that when scaled with λ_β, both velocity dissipation and TKE spectra computed in different planes collapse. The collapse in low-medium wave numbers including the inertial range is very good. In high wave number region, the collapse is much better than the case normalized with Favre averaged turbulence quantities. It seems that the large amount of local extinction has an effect on high wave number range of both TKE and dissipation spectra and inertial range remains unaffected and the conventional Kolmogorov scaling laws in Favre averaged form holds. Further, it is found that the agreement with the model spectrum is better if λ_β and $\tilde{\varepsilon}$ are used for scaling.

Acknowledgements

This project has received funding from the European Union's Horizon 2020 research and innovation programme under the Marie Sklodowska-Curie grant agreement No 643134.

References

[1] Wang, G., Karpetis, A.N., Barlow, R.S., "Dissipation length scales in turbulent nonpremixed jet flames", *Combust. Flame.* 148: 62–75 (2007).

[2] Knaus, R., Pantano, C., "On the effect of heat release in turbulence spectra of non-premixed reacting shear layers", *J. Fluid Mech.* 626: 67-109 (2009).

[3] Kolla, H., Hawkes, E.R., Kerstein, A.R., Swaminathan, N., Chen, J.H., "On velocity and reactive scalar spectra in turbulent premixed flames", *J. Fluid Mech.* 754: 456–487 (2014).

[4] Kolla, H., Zhao, X.-Y., Chen, J.H., Swaminathan, N., "Velocity and Reactive Scalar Dissipation Spectra in Turbulent Premixed Flames", *Combust. Sci. Technol.* 188: 1424–1439 (2016).

[5] Hawkes, E.R., Sankaran, R., Sutherland, J.C., Chen, J.H., "Scalar mixing in direct numerical simulations of temporally evolving plane jet flames with skeletal CO/H2 kinetics", *Proc. Combust. Inst.* 31: 1633–1640 (2007).

[6] Pope, S.B., *Turbulent Flows*, 1st Editio. Cambridge University Press, 2000, p. 233.

Heat release rate markers for turbulent MILD combustion fed by CH_4-H_2 mixture

D.Bascherini[a,*], M. Ferrarotti[b,c,d], C. Galletti[e], G. Bagheri[b,f], A. Parente[b,d]

*d.bascherini@studenti.unipi.it

[a]Department of Energy Engineering, Systems, Land and Buildings, University of Pisa, Italy
[b]Service d'Aero-Thermo-Mécanique, Université Libre de Bruxelles, Bruxelles, Belgium
[c]Service de thermique et de combustion, Université de Mons, Mons, Belgium
[d]Université Libre de Bruxelles and Vrije Universiteit Brussel, Combustion and Robust Optimization Group (BURN), Bruxelles, Belgium
[e]Department of Civil and Industrial Engineering, University of Pisa, Italy
[f] Department of Chemistry, Materials and Chemical Engineering "G. Natta", Politecnico di Milano, Italy

Abstract

The results of two-dimensional Reynolds-Averaged Navier-Stokes (RANS) numerical simulation of the Adelaide Jet in Hot Coflow (JHC) configuration involving Moderate or Intense Low oxygen Dilution (MILD) combustion are analyzed to investigate the correlation between Heat Release Rate (HRR) and spatial species distribution, with a fuel mixture of CH_4 and H_2. Correlations show a good agreement for O, OH, OH* concentrations at high HRR values.

Introduction

Numerous studies [1,2] on conventional combustion focus on visualization techniques of the reaction zone such as Planar Laser-Induced Fluorescence (PLIF) technologies or chemiluminescence imaging. PLIF measurements of OH and CH_2O were conducted also for MILD combustion [3,4] in past studies [5,6]. However, few investigations focused on the applicability of these chemical markers to capture the HRR region [7] in such a combustion regime.

Minamoto et al. [7] evaluated the PLIF signals of the markers OH, CH_2O and CHO by means Direct Numerical Simulations (DNS) of turbulent MILD combustion fed with methane (cases A and B in [7]). They found that LIF signals of OH and CH_2O well correlate with HRR in the MILD combustion of CH_4, although lower correlations were observed for low heat release regions. Another result of this study suggests also that MILD combustion is not a fully homogenous reactive mixture, but instead presents some thin reaction zones that macroscopically give the impression of a distributed reaction zone. These results are consistent with the ones reported in [6,8].

Sidey et al. [6] experimentally investigated methane jet flame autoigniting in a turbulent cross-flow, at MILD combustion conditions. Differences between OH* mean images and OH-PLIF mean images were observed, demonstrating the presence of OH radical in areas without OH*. The authors considered this feature as a possible mismatch between presence of OH and heat release region.

Nikolaou et al. [9] re-examined the validity of the rate of the reaction OH+CH2O←→HCO+H2O as a flame marker for both traditional and diluted methane-air combustion. Results suggest that the rate of the reaction $H+CH_2O \leftarrow\rightarrow HCO+H_2$ may be a more reliable HRR marker for the diluted case. It was also shown that the correlation between HRR and reactions rates of different reactions depends both on the equivalence ratio and the HRR intensity itself. Hence, the optimal flame marker can change according to them.
The local heat release rate is given by:

$$HRR = \sum_{\alpha}^{N} \dot{\omega}_{\alpha} \, h_{f,\alpha}^{0} \qquad (1)$$

where *N* is the number of species involved in the oxidation of the fuel species, $h_{f,\alpha}^{0}$ is the standard enthalpy of formation for species α, and $\dot{\omega}_{\alpha}$ is its reactions rate [9].
The choice of different scalars as HRR markers, such as different species concentrations, is fuel mixture specific. Therefore, an analysis to indicate which may be the best markers should be carried out for various possible conditions of non-conventional combustion regimes. As reported in [7], very few studies investigated the applicability of HRR markers for methane MILD combustion, and even less for MILD combustion with different fuel mixtures.
In the present work, the applicability of different chemical species as HRR markers is investigated for the Adelaide Jet in Hot Co-flow (JHC), fed with a mixture of methane and hydrogen [10]. To this goal, the correlations between HRR and species distributions at increasing axial locations from the burner are estimated.

Validation data set and modelling

The JHC is a nonconfined flame in air, fed through a central circular nozzle (ID=4.25 mm) using a mixture of CH_4 and H_2 (50/50 by vol.) at a temperature of 305K and velocity of 58.74 m/s. The jet issues into a hot and diluted co-flow, made up of CO_2, H_2O, O_2 and N_2, with a temperature of T = 1300 K and velocity of 3.2 m/s. A wind tunnel feeds room temperature air at 3.3 m/s. More details on the JHC burner can be found in [10-12].
RANS numerical simulations were carried out using the ANSYS FLUENT 18.0 CFD commercial code. A two-dimensional, steady-state simulation was carried out, considering the system symmetry. The computational domain is 1.4 m in the axial direction and 0.21 m in the radial direction from the symmetry axis. The mesh is structured and non-uniform with about 55,000 cells. Two additional meshes, one coarser and one finer, were considered to evaluate the Grid Convergence Index (GCI), which gives a measure of deviation from the asymptotic numerical value [13]. A GCI value less than 3% was obtained for temperature and major species, using the GRI-2.11 chemical mechanism [14] and the Partially Stirred Reactor model [15]. Velocity-inlet boundary conditions are specified at the inlets, while pressure-outlet conditions are applied at the boundaries assuming ambient air back-flow conditions. The inlet turbulence levels were set according to Aminian et al [16]. Two different

O_2 concentrations in the co-flow, 3% and 9% (by wt.) were tested. The former, 3%, corresponds to MILD conditions, for which operative definition was discussed by both Cavaliere and de Joannon [4] and Dally et al. [10]. Turbulence, combustion and radiation are modeled with the modified k-ε model (the $C_{\varepsilon 1}$ constant is increased from 1.44 to 1.6), the PaSR turbulent combustion model, and the discrete ordinate (DO) method together with Weighted-Sum-of-Gray-Gases (WSGG) model.
To consider the influence of kinetics on species distribution, four different mechanisms were used after modifying them by adding the species OH*. The four base mechanisms are: KEE-58 [17], GRI-2.11 [14], a reduced kinetic mechanism (34 species, 255 reactions) derived for the conditions of interest from the POLIMI-1407 [18], using the procedure described in [19], and a modification of this last, indicated as POLIMI-M [20], optimized for MILD conditions.
The electronically excited species OH($A^2\Sigma^+$) sub mechanism was added of the four above schemes. The OH* sub-mechanism consists of twelve reactions: eleven taken from Doan et al. [21] (reactions 47, 49-58 in table A4 of [21]) and one from Panoutsos et al. [22] (reaction 1 of Mechanism 7 in [22]). The resulting sub-mechanism utilizes reactions rate constants from Carl et al. [23], Kathrotia et al. [24] and collisional quenching data from Tamura et al. [25].

Results
Molar concentrations (X_i) and HRR values were sampled at several radial locations, to study the correlation between HRR and spatial species distribution, as reported in Table 2. Each sample is averaged along a 50mm radius, starting from the symmetry axis, and the species and HRR statistics are used to compute the metric shown in Figure 2.
Equation (2) [7], computes an error measure, $Z(X_i)$, that gives an idea on how well a normalized species mole fraction reproduces the spatially matched normalized HRR:

$$Z(X_i) = \sum_{n=1}^{np} \left(\frac{|HRR_n|}{max_r(|HRR|)} - \frac{|X_{i,n}|}{max_r(|X_i|)} \right)^2 \qquad (2)$$

In Equation (2), n indicates the number of sample points to compute average HRR and molar fractions, i is the species index, and $max_r(|HRR|)$ and $max_r(|X_i|)$ indicate the maximum values of HRR and X_i for the considered sample. The species showing the lowest value of Z are the ones that better correlate with HRR, and they can be considered optimal markers. The values of Z are shown in Figure 1, while Figure 2 reports the correlation between selected species and the HRR, at a location of 0.18m from the burner. The three top species markers, related numerical values of Z and correlations coefficients, are reported in Table 2 for Y_{O2} = 3% case, using the GRI-2.11 as chemical mechanism.

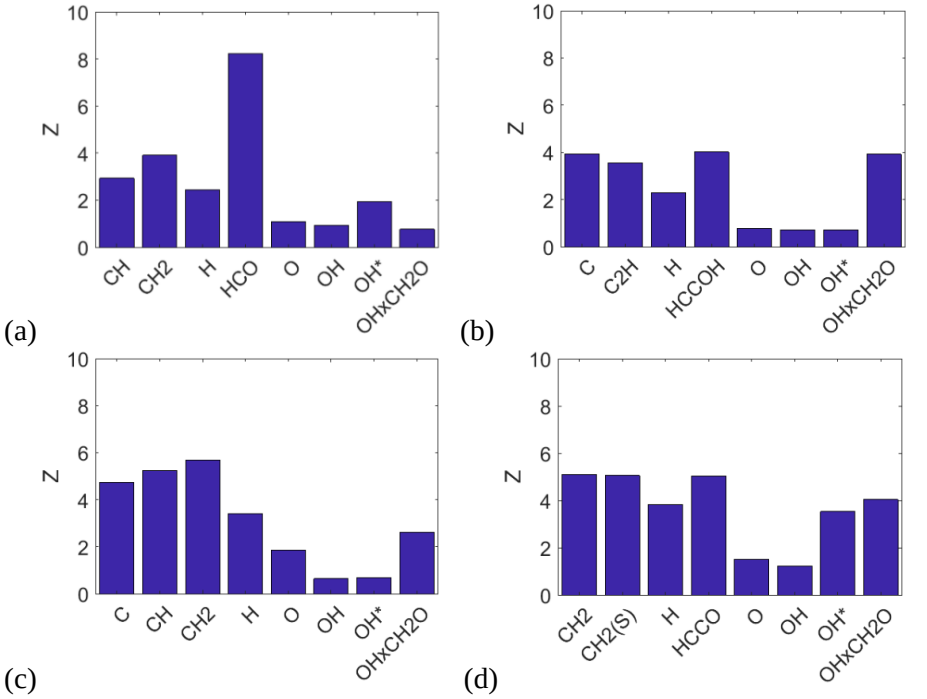

Figure 1. Eight lowest Z values obtained 0.18m from the burner, using four kinetic mechanisms: (a) KEE, (b) GRI2.11, (c) reduced POLIMI, (d) reduced POLIMI-M. O2 in the coflow: 3%.

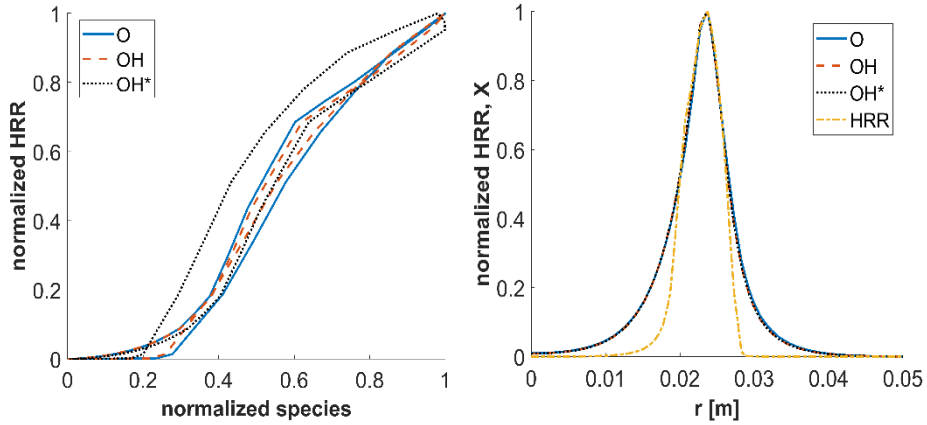

Figure 2. (a) Normalized HRR versus the normalized top three species-markers (according to the Z values in Table 2), 0.18m from the burner, for the YO_2 = 3% case and using the GRI2.11 mechanism; (b) radial profiles of normalized HRR and top three species-markers mole fractions 0.18m from the burner.

Discussion

Table 2 shows the top three HRR markers species and the associated values of the Pearson correlation coefficients and the metric Z, at different axial locations, for Y_{O2}=3% and using the GRI 2.11 mechanism. Concentrations of O, OH, OH* show very good correlation with HRR between 0.12 m and 0.35 m from the burner, that is the region of the flame where a higher HRR is observed. No significant differences are visible in this range among the correlations of the three species, with a slightly lower matching for OH* at the range edge, where the intensity of the heat of reactions decreases. Figure 1 reports the Z values of the first eight top related species for the four different chemical mechanisms at location of 0.18m. Apart from the KEE mechanism, that shows a good Z metric for the species product $OHxCH_2O$, all the other mechanisms confirm the choice of O, OH, OH* markers. In Figure 2(a), a non-fully linear trend among species and HRR is visible, indicating a low correlation between all markers and HRR, for low values of the normalized HRR, for both the burnt and unburnt region of the reaction zone, as confirmed by the trends in Fig.2(b). Similar difficulties at low heat release values are observed in [7] but only on the burnt side. Test cases with an oxygen concentration of 9% in the co-flow give the same three species as reliable HRR-markers without significative differences. Moving further along the flame, the metric Z increases rapidly, 0.5 m after the burner. Correspondingly, very low correlations factors are obtained, until any correlation is observed between the species and HRR.

In summary, for a turbulent MILD flame fed with an equimolar mixture of CH_4 and H_2, the correlation between different species concentration distributions and heat release rate (HRR) has been studied to investigate the applicability of different visualization techniques of the reaction zone, such as PLIF imaging and chemiluminescent imaging. Good agreement between concentration of O, OH, OH* and HRR is reported for high HRR levels, while poor or no correlations are found for these flame markers at lower HRR. Further investigations should be carried out to better understand the relationship with other thermochemical quantities, detect a method to reduce the error of prediction of these markers near-zero value of HRR.

Table 2. Best HRR-markers and respective correlation factors and minimum Z values at different axial location (test case with GRI 2.11, YO2=3% in the co-flow)

z [m]	0.030 m	0.120 m	0.180 m	0.250 m	0.350 m	0.450 m
Marker	O/H/OH	O/OH/OH*	O/OH/OH*	O/OH/OH*	O/OH/OH*	O/OH/OH*
R^2	0.92/0.90/ 0.90	0.96/0.95/ 0.88	0.97/0.97/ 0.96	0.96/0.97/ 0.96	0.90/0.90/ 0.84	0.72/0.68/ 0.53
Z	0.84/1.07/ 1.25	0.74/0.83/ 1.83	0.78/0.70/ 0.71	1.14/1.05/ 1.11	3.20/3.32/ 3.84	9.45/10.25 /11.52

References

[1] Nguyen Q.V., Paul P.H., *Proc. Combust. Inst*. 26: 357-364(1996)
[2] Paul P.H., Najm H.N., *Proc. Combust. Inst*. 27: 43-50(1998)
[3] Wünning J.A., Wünning J.G., *Prog. Energy Combust. Sci*. 23: 81-94 (1997).
[4] Cavaliere A., de Joannon M., *Prog. Energy Combust. Sci*. 30: 329-366 (2004);
[5] Duwig C., Li B., Li Z.S., Aldén M., *Combust. Flame* 159: 306-316 (2012)
[6] Sidey J., Mastorakos E., *Proc. Comb. Institute.* 35: 3537-3545 (2015)
[7] Minamoto Y., Swaminathan N., *Combust. Flame* 161: 1063-1075 (2014)
[8] Minamoto Y., Dunstan T.D., Swaminathan N., Cant R.S., *Proc. Comb. Institute.* 34: 3231-3238 (2013)
[9] Nikolaou Z.M., Swaminathan N., *Combust. Flame* 161: 3073-3084 (2014)
[10] Dally B.B., Karpetis A.N., Barlow R.S., *Proc. Comb. Inst.* 29: 1147-54 (2002)
[11] Parente A., Malik M.R., Contino F., Cuoci A., Dally B.B., *Fuel* 163: 98-111 (2016)
[12] Li Z., Cuoci A., Sadiki A., Parente A., *Energy* 139: 555-570 (2017)
[13] Roache P.J. *Verification and validation in computational science and engineering*. Hermosa Publishers, 1998.
[14] Bowman C., Hanson R., Davidson D., Gardiner J.W.C., Lissianski V., Smith G., et al. "GRI-Mech 2.11" (1995).
[15] J. Chomiak, *Combustion: a study in theory, fact and application*, Abacus Press/Gorden and Breach Science Publishers, United States, 1990.
[16] Aminian, J., Galletti, C., Shahhosseini, S., Tognotti, L. *Appl. Therm. Eng.* 31: 3287-3300 (2011)
[17] Bilger R., Starner S., Kee R., *Combust. Flame.* 80:135-49 (1990)
[18] Ranzi E., Sogaro, A., Gaffuri P., Pennati G., Faravelli T., *Comb. Sci. Tech.* 96: 279-325 (1994)
[19] Stagni A., Frassoldati A., Cuoci A., Faravelli T., Ranzi E., *Comb. Flame* 163: 382-393 (2016)
[20] Furst M., Sabia P., Lavadera M.L., De Joannon M., Frossoldati A., Parente A., "An optimization study of chemical kinetics for MILD combustion" *Energy&Fuel.* Under review.
[21] Doan N.A.K., Swaminathan N., Minamoto Y., *Comb. Flame* 189: 173-189 (2018)
[22] Panoutsos C.S., Hardalupas Y., Taylor A.M.K.P., *Comb. Flame* 156: 273-291 (2009)
[23] Carl S.A., Van Poppel M., Peeters J., *J. Phys. Chem.* 107: 11001-11007 (2003)
[24] Kathrotia T., Fikri M., BozkurtM., Hartmann M., Riedel U., Schulz C., *Combust. Flame* 157: 1261-1273 (2010)
[25] Tamura M., Berg P., Harrington J., Luque J., Jeffries J., Smith G., Crosley D., *Combust. Flame* 114: 502-514 (1998)

STABILIZATION OF A HIGH PRESSURE JET FLAME WITH HEAT LOSSES BY LES

P. Gruhlke*, H. Janbazi*, I. Wlokas*, C. Beck, A. M. Kempf***

pascal.gruhlke@uni-due.de

*Chair of Fluid Dynamics, Institute for Combustion and Gasdynamics (IVG), University of Duisburg-Essen, Carl-Benz-Straße 199, 47057 Duisburg, Germany

**Siemens AG, Mellinghofer Straße 55, 45473 Mülheim an der Ruhr, Germany

Abstract

Large-eddy simulations (LES) of a lean preheated high pressure jet flame are presented, comparing a premixed flamelet generated manifolds (PFGM) and a finite rate chemistry (FRC) approach, with dynamic flame thickening in either case. The impact of the combustion models on the stabilization of the flame is investigated. The PFGM tables are calculated from the detailed GRI 3.0 reaction mechanism. For the FRC combustion model, both a compact skeletal mechanism and the DRM19 mechanism extended by an OH* sub-mechanism have been tested. In the simulations, heat losses due to chamber cooling are considered by estimating and applying isothermal wall temperatures. The significant flame lift was predicted by the FRC and PFGM combustion models applying non-adiabatic boundary conditions. Simulation results of the flame stabilization improved using the DRM19 reaction mechanism. The correlation of heat release and OH* species was found to be insufficient in the present case for comparing flame lift-off monitored by OH* to flame lift-off determined by heat-release.

Introduction

Incomplete CO burnout becomes critical at gas turbine part-load operation. At the same time, more efficient baseload operation requires increasing combustor outlet temperature, potentially increasing NO_x emissions. Large-eddy simulations have proven to be suitable for combustion chamber development. For the investigation of the CO and NO_x pollutant formation, numerous methods have been used to model combustion [1,2] including the artificial flame thickening approach (ATF) [3,4]. In the FRC approach, the reaction progress is solved during runtime and combustion kinetics are directly considered. In the PFGM method, chemistry is tabulated from adiabatic 1-D premixed flames prior to the simulations and looked up during runtime based on control variables. This approach reduces the computational cost in comparison to direct chemistry, while additional effects such as strain or heat losses need to be modelled [5]. Large-eddy simulations coupled with ATF have proven to be a promising method with both finite rate chemistry [3,6] and premixed flamelet generated manifolds (PFGM) [4,5]. A reliable prediction of CO and NO_x necessitates the correct description of the flow field, flame shape and stabilization. A challenge for numerical modelling is presented by

lifted flames, where the stabilization is affected by different mechanisms such as quenching, auto-ignition delay [7,8] or high reactant flow rates [6]. In a new lean preheated high pressure jet flame examined by Lammel, Severin, Ax and co-workers [9,10], heat losses were found to have an impact on the flame stabilization at baseload operation as OH*-chemiluminescence indicated a lifted burning flame.
In the present work, FRC and PFGM and different reaction mechanisms are applied and their impact on the prediction of the flame stabilization is investigated.

Modelling Approach

With FRC, the laminar and turbulent Prandtl and Schmidt numbers are 0.7 and a unity Lewis assumption is made. Sutherland's law for air determines the transport properties. Favre-filtered transport equations are solved for the mixture fraction, absolute total enthalpy and species. To keep computational costs low, a skeletal mechanism has been developed for the limited range of conditions studied in this work. The mechanism was developed from the H_2/O_2 branch of the C1 mechanism by Li et al. [11], the CH_4/O_2 branch of the methane combustion mechanism by Cremer [12], and the C/N/O branch of GRI 3.0 [13]. Thermodynamic and transport properties were taken from GRI 3.0. A genetic algorithm [14,15] was used for the reduction and optimization, where GRI 3.0 was used as a reference. Optimization targets were the laminar flame speed, temperature and CO and NO_x species, potentially allowing for pollutant predictions in future studies. The new reaction mechanism includes 20 species and 35 reactions. The validation against GRI 3.0 indicated very good agreement for the limited operational range the mechanism has been developed for. In order to examine the skeletal mechanism's quality and applicability, the more detailed and established reaction mechanism DRM19 [16] was used and extended by an 11-step sub-mechanism [17] to include OH* species for direct comparison against experimental data.
The PFGM combustion model has been implemented by Dederichs et al. [18] and Mahiques et al. [19]. Prior to simulations, look-up tables are generated from 1-D laminar, premixed, freely propagating flames using Cantera with GRI 3.0. Control variables for table access are the mixture fraction Z and enthalpy h_t and the normalized progress variable c. The latter is defined as $c = Y_{CO_2}(\tilde{Z}, \tilde{h}_t)/Y_{CO_2}^{max}(\tilde{Z}, \tilde{h}_t)$ and is determined from the CO_2 mass fraction Y_{CO_2} and $Y_{CO_2}^{max}$ at equilibrium for a given mixture fraction and enthalpy. Favre-filtered transport equations are solved for the mixture fraction, absolute total enthalpy and progress variable. Heat losses are considered in the PFGM table generation by calculating flamelets at different enthalpy levels. This is achieved by lowered fresh gas temperatures.
In order to resolve the thin flame front on the numerical grid, an artificial flame thickening (ATF) approach is used, following Dederichs et al. [18]. Thickening is applied to the species transport equation for FRC and to the progress variable transport equation in PFGM. Unphysical thickening outside the flame region is avoided by applying a flame sensor. The thickening of the flame reduces the

wrinkling of the flame, which is compensated by applying the modified Charlette model [20].

Experiments and numerical setup

The chamber geometry and the inlet conditions are shown in Fig. 1. The lean partially-premixed CH_4-air mixture at 8 bar enters the combustion chamber with a jet Reynolds number of $6 \cdot 10^5$ and a bulk velocity of 120 m/s. The turbulent fluctuations and integral length-scale are approximately 10 m/s and 2.8 mm. Laser measurement techniques were applied in the experiments as the chamber is optically accessible and the flame shape and stabilization has been determined from OH* chemiluminescence (OH*-CL). More details on the experiments can be found in the work of Lammel, Severin, Ax and co-workers [9,10]. The combustor quartz glass walls were cooled in the experiments causing severe heat losses to the flame. We calculated heat transfer coefficients using coolant mass flows and temperatures (Lammel and Ax, personal communication, July 2016) and LES data. The estimations confirmed a burner baseplate temperature of 600 K [10] and temperatures of {920, 1000, 980, 960} K in the zones of {0−0.1, 0.1−0.2, 0.2−0.4, 0.4−0.84} m within the chamber.

The LES was performed using OpenFOAM. The temporal discretization blends explicit and implicit contributions, weighted at 0.3 and 0.7, with a convective CFL number of 0.3. Convection is discretized by a TVD scheme, it should be kept in mind that such schemes are more dissipative than one would wish for LES. The mesh consists of 8.1M hexahedral cells with 1.0 mm cell size in the flame region.

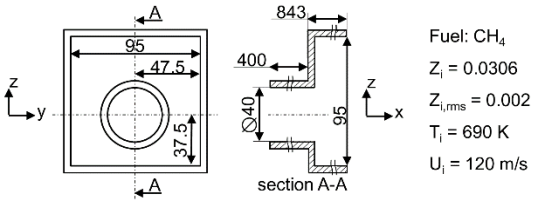

Figure 1. Chamber geometry and inlet conditions.

Results

In the experiments, OH*-CL has been used as an indicator for the flame heat release and thus to determine the flame shape and stabilization. It has been shown that the flame tends to burn asymmetrically and lifted as presented in Fig. 2a. The line-averaged (in z-direction) mean carbon dioxide source term from PFGM, the mean reaction heat release from FRC and the mean OH* mass fractions from FRC simulations applying the extended DRM19 mechanism are used for comparison against the experimentally obtained OH*-CL. These quantities are closely related and often used to compare chemiluminescence images from experiments to simulation results. In the experiments, a flame lift is observed at the upper side of the chamber which intensifies at the lower side. The PFGM model with chemistry tabulated from GRI 3.0 (Fig. 2b) and the FRC model with the new skeletal reaction

mechanism (Fig. 2c) show a qualitatively similar flame shape and lift-off. Figure 2d presents the mean OH* mass fraction from FRC simulations with DRM19 which shows very good agreement with the experimentally determined OH*-CL. The prediction of the asymmetric flame shape is significantly improved, and the lift-off height is in better agreement with the experiments.

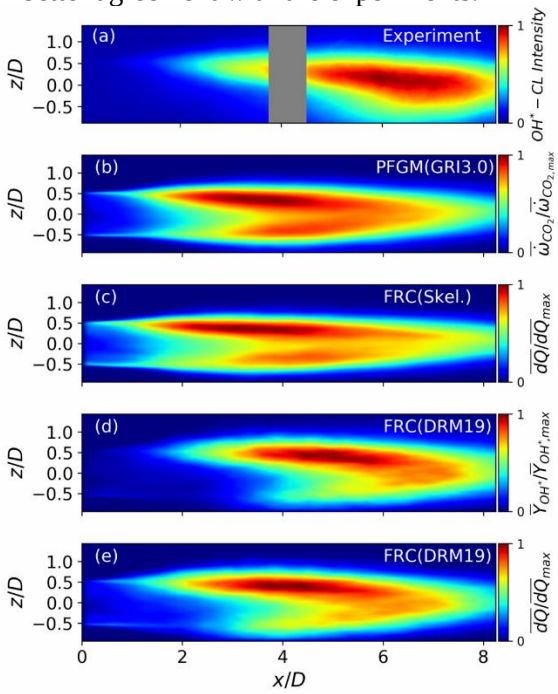

Figure 2. Line-averaged (in z-direction) mean normalized experimental OH*-CL a), CO_2 source term from PFGM b), reaction heat release rate from FRC using the skeletal mechanism c), OH* mass fraction for FRC using DRM19 mechanism d) and reaction heat release rate from FRC using DRM19 mechanism e).

The reaction heat release rate based on DRM19 (Fig. 2e) indicates lower heat release at the lower side of the chamber in comparison to PFGM and the FRC with the skeletal mechanism. Furthermore, local heat release rates of around 50% at the lower side of the chamber are observed for PFGM and FRC simulations using the skeletal mechanism, while only around 20% are identified from simulations applying DRM19. PFGM results might improve by considering strain effects which are not accounted for yet. Discrepancies from simulations using the skeletal mechanism in the prediction of the flame stabilization might be attributed to shortcomings in the choice of optimization targets while mechanism development. The identification of species and reactions which are significant for the prediction of the flame stabilization in a non-adiabatic environment may improve the mechanism. Deviations between the mean Y_{OH^*} and heat release rate are identified comparing Figs. 2d and 2e. The heat release rate indicates a similar flame shape as

OH* while a smaller lift-off height is observed. Interestingly, reduced but still considerable large heat release rates are found at x/D<3, which indicates that the flame is not fully lifted as suggested by the OH* mass fraction. This confirms that OH* is not an adequate indicator of local extinction [21] and is only partially agreeing with work that considers OH* a direct marker for the heat release rate.

Conclusion

Large-eddy simulations of the flame stabilization in a pressurized jet flame have been performed and different combustion models and reaction mechanisms were compared. An asymmetric and lifted flame was observed in the experiments which was also predicted by PFGM and FRC. Simulation results with an extended DRM19 reaction mechanism including OH* species were directly compared to the experimentally observed OH* chemiluminescence and showed very good agreement. The correlation of heat release and OH* species was shown to be insufficient for the present study as a distinct flame lift was found for the OH* species mass fraction while reduced but significant heat release rates were observed.

References

[1] Jella S., Gauthier, P., Bourque, G., Berthorson, J., Bulat, G., Rogerson, J., Sadasivuni, "Large Eddy Simulations of a Pressurized, Partially-Premixed Swirling Flame With Finite-Rate Chemistry", *ASME Turbo Expo* (2017).

[2] Bulat, G., Jones, W. P., & Marquis, A. J., "NO and CO formation in an industrial gas-turbine combustion chamber using LES with the Eulerian sub-grid PDF method", *Combust. Flame*, 161(7), 1804-1825 (2014).

[3] Schmitt, P., Poinsot, T., Schuermans, B., & Geigle, K. P., "Large-eddy simulation and experimental study of heat transfer, nitric oxide emissions and combustion instability in a swirled turbulent high-pressure burner", *J. Fluid Mech.*, 570, 17-46 (2007).

[4] Gruhlke, P., Proch, F., Kempf, A. M., Mahiques, E. I., Dederichs, S., & Beck, C., "Prediction of CO and NOx Pollutants in a Stratified Bluff Body Burner", *ASME Turbo Expo* (2017).

[5] Proch, F., & Kempf, A. M., "Modeling heat loss effects in the large eddy simulation of a model gas turbine combustor with premixed flamelet generated manifolds", *Proc. Comb. Inst.*, 35(3), 3337-3345 (2015).

[6] Legier, J. P., Poinsot, T., & Veynante, D, "Dynamically thickened flame LES model for premixed and non-premixed turbulent combustion", *Proc. of the summer program*, pp. 157-168 (2000).

[7] Cabra, R., Myhrvold, T., Chen, J. Y., Dibble, R. W., Karpetis, A. N., & Barlow, R. S., "Simultaneous laser Raman-Rayleigh-LIF measurements and numerical modeling results of a lifted turbulent H2/N2 jet flame in a vitiated coflow", *Proc. Comb. Inst.*, 29(2), 1881-1888 (2002).

[8] Domingo, P., Vervisch, L., & Veynante, D., "Large-eddy simulation of a

lifted methane jet flame in a vitiated coflow", *Combust. Flame*, 152(3), 415-432 (2008).

[9] Lammel, O. et al.,"High Momentum Jet Flames at Elevated Pressure: A—Experimental and Numerical Investigation for Different Fuels", *ASME Turbo Expo* (2017).

[10] Severin, M., et al. "High Momentum Jet Flames at Elevated Pressure: B—Detailed Investigation of Flame Stabilization With Simultaneous PIV and OH-LIF", *ASME Turbo Expo* (2017).

[11] Li, J., Zhao, Z., Kazakov, A., Chaos, M., Dryer, F. L., & Scire, J. J., "A comprehensive kinetic mechanism for CO, CH2O, and CH3OH combustion", *Int. J. Chem. Kin.*, 39(3), 109-136 (2007).

[12] Cremer, H., „Zur Reaktionskinetik der Methan- Oxidation", *Chemie-Ing.Technik*, 44(1- 2), 8-15 (1972).

[13] Smith, G. P. et al. *http://www.me.berkeley.edu/gri_mech/* (2000).

[14] Sikalo, N., Hasemann, O., Schulz, C., Kempf, A., & Wlokas, I., "A Genetic Algorithm- Based Method for the Automatic Reduction of Reaction Mechanisms", *Int. J. Chem. Kin.*, 46(1), 41-59 (2014).

[15] Sikalo, N., Hasemann, O., Schulz, C., Kempf, A., & Wlokas, I., "A Genetic Algorithm–Based Method for the Optimization of Reduced Kinetics Mechanisms", *Int. J. Chem. Kin.*, 47(11), 695-723 (2015).

[16] Kazakov, Andrei, and Michael Frenklach. "Reduced reaction sets based on GRI-Mech 1.2.", *http://www.me.berkeley.edu/drm* (1994).

[17] Kathrotia, T., Riedel, U., Seipel, A., Moshammer, K., & Brockhinke, A., "Experimental and numerical study of chemiluminescent species in low-pressure flames", *Applied Physics B*, 107(3), 571-584 (2012).

[18] Dederichs, S., Zarzalis, N., & Beck, C., "Validation of a novel LES approach using tabulated chemistry for thermoacoustic instability prediction in gas turbines", *ASME Turbo Expo* (2015).

[19] Mahiques, E. I., Dederichs, S., Beck, C., Kaufmann, P., & Kok, J. B. W., "Coupling multicomponent droplet evaporation and tabulated chemistry combustion models for large-eddy simulations", *Int. J. Heat Mass Transfer*, 104, 51-70 (2017).

[20] Wang, G., Boileau, M., & Veynante, D., "Implementation of a dynamic thickened flame model for large eddy simulations of turbulent premixed combustion", *Combust. Flame*, 158(11), 2199-2213 (2011).

[21] Najm, H. N., Paul, P. H., Mueller, C. J., & Wyckoff, P. S., "On the adequacy of certain experimental observables as measurements of flame burning rate", *Combust. Flame*, 113(3), 312-332 (1998).

Consistent flamelet-based turbulent combustion modeling for liquid rocket engines

P. E. Lapenna, G. Indelicato, R. Amaduzzi, D. Durigon, R. Lamioni and **F. Creta**
pasquale.lapenna@uniroma1.it
*Sapienza University of Rome, Department of Mechanical and Aerospace Engineering, via Eudossiana 18, Rome, Italy

Abstract
In this work we present a consistent flamelet-based framework for turbulent combustion modeling in liquid rocket engines. This approach is based on the low-Mach number approximation of the governing equations and on the tabulation of all the thermochemical properties by means of steady laminar flamelets. The proposed framework features the possibility to accommodate, in a computationally efficient manner, real gas thermodynamics and to account for non-adiabatic combustion in the presence of wall heat transfer. Such capabilities are tested separately on two well-established experimental configurations consisting in methane-oxygen flames at elevated pressures, by means of unsteady Reynolds averaged Navier Stokes simulations.

Introduction
Space propulsion is one of the most extreme applications of energy conversion by means of combustion since it usually occurs at high pressure, such as those encountered in liquid rocket engines (LRE) combustion chambers. For these devices the most significant technological trend over the years was increasing the thrust levels, which directly promoted a significant increase of the operating chamber pressure in order to improve performances and allowing engines to remain reasonably sized [1].
This rise in the operating pressure causes at least two technological drawbacks. Firstly wall heat transfer in combustion chamber of a LRE scales almost linearly with pressure, thus causing additional loads for both structures and cooling system. Secondly, typical operating pressures are above the critical pressure of a large part of the propellant combinations which are typically used by LRE therefore they will most likely behave like complex fluids rather than an ideal gas or liquid and poses serious challenges to the physical understanding and the numerical modeling [2].
Despite the great experimental and theoretical/numerical effort in the past decades, supercritical mixing and combustion processes in LRE combustion chambers are still to be completely understood [3], motivating a substantial research effort toward reliable computational fluid dynamics (CFD) tools.
In this contribution we present a consistent framework to simulate the subsonic part of LRE combustion chambers, i.e. the injector plate near field where the mixing and combustion occur in order to achieve elevated combustion efficiencies [1].

This consideration in conjunction with recent direct numerical simulations results [4] motivate the adoption, in this context, of a low-Mach number approximation of the governing equations.
In the low-Mach number limit, flamelet based tabulation methods for turbulent non-premixed combustion are well-posed [5], and provide a properly filtered/ averaged treatment of a real fluid equation of state (EoS) [6]. The ensuing flamelet generated thermodynamic manifolds can be extended to account for non-adiabatic flows due to wall heat transfer. Although non-adiabatic tabulation strategies have been successfully developed in the context of premixed combustion, the inclusion of enthalpy losses for high pressure non-premixed flames is less studied. A pragmatic approach to this issue is to adopt enthalpy defect methods developed for sooting non-premixed flames which are influenced by radiative heat transfer [7].
The mentioned key capabilities, namely the efficient inclusion of real gas EoS and wall heat transfer, are separately assessed by means of two LRE-oriented experimental configurations featuring methane-oxygen flames at elevated pressures. In particular the inclusion of real gas effects is tested on a reference cryogenic liquid oxygen (LOx) and gaseous methane (GCH4) using the configuration and thermodynamic conditions of the G2 test case of described in [8]. On the other hand, the modeling of non-adiabatic effects is tested simulating a model gaseous oxygen (GOx)-GCH4 single injector combustion chamber [9] for which experimental results are available in terms of wall heat transfer at the chamber wall. All the simulations presented in this work are based on an unsteady Reynolds averaged Navier Stokes approach in order to capture, with reasonably computational costs, the low frequency unsteadiness of the combustion process.

Theoretical and numerical framework

Flamelet based combustion models for non-premixed combustion lay the foundations on the assumption that a turbulent non-premixed flame can be treated as an ensemble of thin laminar diffusion flames, namely the *flamelets*. This flamelet assumption is justified as long as the chemical reaction region remain thin compared to small scales vortices [10]. These requirements are usually met by high pressure flames in both subcritical and supercritical pressure environments [11].
The main advantage of such formulation lies in the fact that, irrespective of the thermodynamic model used, laminar flamelet solutions are obtained as steady state solutions of one dimensional laminar problems (flamelet equations or counterflow flames) at a given constant thermodynamic pressure p_0 [5]. The ensuing laminar flame structures, which can be referred to as thermodynamic manifolds, can be expressed, for non-adiabatic non-premixed flame, as:

$$\psi = \psi(Z; \chi_{st}, \phi_H)$$

where ψ is a generic thermodynamic variable, Z is the mixture fraction, χ_{st} is the scalar dissipation rate of the mixture fraction at stoichiometric conditions and ϕ_H is the enthalpy defect. The latter is defined as the difference between the actual or

transported enthalpy and the enthalpy of an adiabatic mixture characterized by the same value of the mixture fraction [7].
The Favre averaged mean values which are needed by the CFD solver are obtained through multi-variate probability density function (p.d.f.) which represent the turbulence-chemistry interactions at a sub grid scale (SGS) level:

$$\widetilde{\psi} = \int_{-\infty}^{+\infty} \int_{0}^{\infty} \int_{0}^{1} \psi(Z, \chi_{st}, \phi_H)\, p(Z, \chi_{st}, \phi_H)\; dZ\; d\chi_{st}\; d\phi_H$$

where the joint p.d.f. is usually approximated, assuming statistical independence, using Bayes theorem as the product of single-variate p.d.f. of the variables. The three ensuing p.d.f.s are then modeled using a presumed p.d.f. approach, with a beta-p.d.f. for the mixture fraction distribution, a log-normal p.d.f for the scalar dissipation rate and Dirac delta for the enthalpy defect [7]. In particular the beta-p.d.f. is constructed starting from the first two statistical moments of the mixture fraction, namely its mean and variance, the latter represents the unresolved SGS fluctuations of *Z*. As a result the full thermodynamic manifold, composed of the mean quantities can be expressed, with the following expression, as a look-up table which can be efficiently accessed during the simulation [12]:

$$\widetilde{\psi} = \widetilde{\psi}(\widetilde{Z}, \widetilde{Z''^2}, \widetilde{\chi_{st}}, \widetilde{\phi_H})$$

Noteworthy of mention is the fact that this manifold includes a consistent averaging of the EoS via density tabulation [5,6]. It is important to remark that the generation of thermodynamic manifolds is strictly case dependent since it is constructed starting from the thermodynamic boundary conditions of the test case.
In this work we use the low-Mach URANS solver `FlameletPimpleSMOKE` [13] developed in the context of the open source `OpenFOAM` framework which implements a classical non-adiabatic steady flamelet formulation [12]. It solves the Favre averaged RANS equations for mass and momentum coupled with three additional transport equations for the mean mixture fraction its variance and the mean enthalpy. In order to access the thermodynamic manifold the scalar dissipation rate and the enthalpy defect are obtained through an algebraic models [12,13]. The system is closed with a standard two equation $k - \varepsilon$ turbulence model with the adoption of wall functions in order to blend the grid requirements imposed by boundary layers [14].

Transcritical flame
The reference LOx-GCH4 flame used in this work is taken from the G2 case of the Mascotte test bench at ONERA described in [8]. The configuration consists in a prismatic test chamber (dimensions: 50x50x400 mm^2) maintained at an operative chamber pressure of p_0 = 56.1 bar. This pressure level is supercritical for both the fuel and the oxidizer, which is injected by the central part of a co-axial injector in a transcritical state (T_{LOX} = 120 K) of elevated density and viscosity, while methane

is injected by the outer part of the injector in a supercritical state (T_{GCH4} = 288 K) of lower density and, as a result, greater injection velocity.
The URANS simulation uses a 2D axy-symmetric computational domain, whose dimension have been chosen to reproduce the hydraulic diameter of the chamber, similarly to other RANS studies [15]. The computational domain is discretized with 30000 finite volumes, which have shown to correctly capture the main flow fields patterns. The case dependent thermodynamic manifold, which is adiabatic in this simulation, is generated using the `OpenSMOKE++` [13] framework and the GRI 3.0 chemical kinetic mechanism. Real fluids effects are including via multi-fluid-mixing (MFM) model [16], that has been recently validated for this case [6].

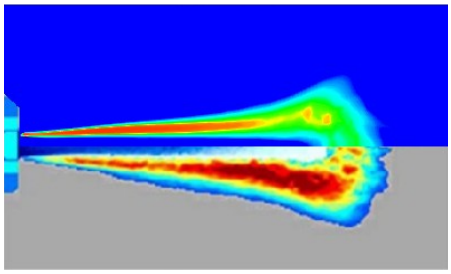

Figure 1. Structure of the LOx-methane flame of the G2 case [8]. Qualitative comparison between time averaged OH mass fraction of the simulation (top half) and the averaged experimental Abel transformed OH emission image (bottom half).

The top half of Fig.1 displays the structure of the cryogenic flame in terms of time averaged OH mass fraction, which has been obtained averaging the URANS simulation. The bottom half of the same figure display the averaged experimental OH emission, Abel transformed image, taken from [8]. The numerical result are in good qualitative agreement with the limited experimental informations available. The simulation capture well the main morphological features of the flame, which are the flame length and its abrupt termination after a sudden expansion, in accordance with recent LES results [17].

Wall heat transfer
Along with the mixing and combustion at high pressure, another key aspect of LRE design is the characterization of combustion chamber wall heat loads. The latter determines both the sizing and operative parameters of the regenerative cooling system and is generally tackled separately from the mixing and combustion of the propellants. In this context, the numerical simulation of both the mixing/ combustion phenomena and wall heat loads can provide useful physical insights on the reacting flow field in the combustion chamber and, more practically, actively supports the design process.
For these reason we perform numerical simulations focused on wall heat loads of a single-element GCH4/GOX experimental configuration. This experimental configuration has been recently described by Celano et al. [9], and provides

measurements of wall heat transfer under conditions relevant for LREs. The operative pressure is 20 bar and GOX and GCH4 are respectively injected at 278 K and 269 K. Following [7] the non-adiabatic thermodynamic manifold has been discretized with at least 100 enthalpy defect shelves in the flamelet libraries.

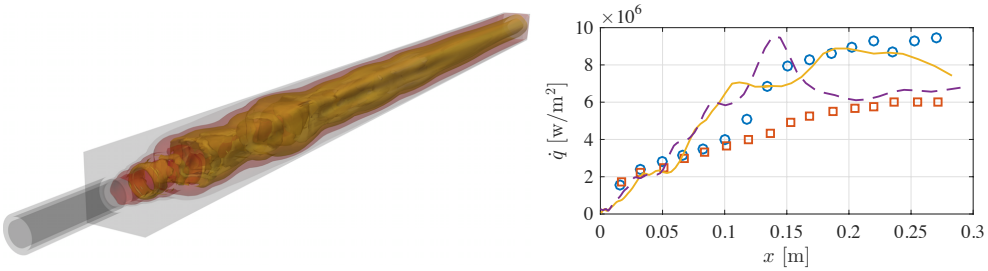

Figure 2. Left panel: instantaneous temperature representative iso-surfaces inside the single element combustion chamber in the 3D URANS simulation. Right panel: Axial distribution of heat flux along the chamber wall. Symbols represent the experimental values using two different approaches, continuos and dashed lines denote, respectively 2D and 3D results.

In this case we have conducted both 2D and 3D simulations with similar grid resolution (smallest finite volume with characteristic dimension of 0.1 mm) and flamelet libraries. An instantaneous temperature field overview is shown in the left panel of Fig.2. The results in terms of wall heat transfer time averages are displayed in the right panel of Fig.3 for both 3D and 2D URANS simulations. The trends show that both the simulations well-capture the experimental results, even if some differences can be observed between the 2D and 3D profiles. Since the resolution of the computational grid is similar the observed differences can be attributed to the interaction between the conical shape of the diffusive flame in the injector near field region and the square shaped combustion chamber.

Conclusion and perspective

A consistent flamelet-based framework for turbulent combustion modeling in LRE has been presented using the low-Mach number approximation of the governing equations. All the thermochemical and transport properties have been calculated by means of steady laminar flamelets using a detailed chemical mechanism and transport properties. The proposed framework features the possibility to accommodate, in a computationally efficient manner, real gas thermodynamics and to account for non-adiabatic combustion in the presence of wall heat transfer. These capabilities have been tested on two experimental configurations featuring methane-oxygen flames at elevated pressures, which of technological relevance for LRE applications. Simulations have been carried out using an URANS approach and in both cases, a cryogenic flame and a non-adiabatic single element combustion chamber, the numerical results are in a fairly good agreement with experiments.

Future efforts will be devoted to explore the eddy dissipation concept EDC

combustion model and to employ the presented framework in realistic multi injectors geometries.

References

[1] G. P. Sutton, “History of Liquid Propellant Rocket Engine”, AIAA, Reston, VA, 2005.
[2] V. Yang, “Modeling of supercritical vaporization, mixing, and combustion processes in liquid-fueled propulsion systems”, Proc. Combust. Inst. 28 (2000) 925–942.
[3] D. Banuti, M. Raju, P. C. Ma, M. Ihme, J.-P. Hickey, “Seven questions about supercritical fluids-towards a new fluid state diagram”, AIAA-paper (2017) 2017-1106.
[4] P. E. Lapenna, F. Creta, “Mixing under transcritical conditions: an a-priori study using direct numerical simulation”, Jour. of Supercr. Fluids 128 (2017) 263–278.
[5] P. E. Lapenna, R. Lamioni, P. P. Ciottoli, F. Creta, “Low-mach number simulations of transcritical flows”, AIAA-paper (2018) 2018-0346.
[6] P. E. Lapenna, G.Indelicato, R. Lamioni, F. Creta, “Modeling the equation of state using a flamelet approach in LRE-like conditions”, Acta Astr. (under review).
[7] B. Marracino, D. Lentini, “Radiation modelling in non luminous non premixed turbulent flames”. Combust. Sci. Tech. 128 (1997), 23-48.
[8] G. Singla, P. Scouflaire, C. Rolon, S. Candel, “Transcritical oxygen/ transcritical or supercritical methane combustion”, Proc. Combust. Inst. 30 (2005) 2921–2928.
[9] M. P. Celano, S. Silvestri, G. Schlieben, C. Kirchberger, O. J. Haidn and O. Knab, “Injector characterization for a gaseous oxygen-methane single element combustion chamber” Prog. in Prop. Phys. 8 (2016) 145-164
[10] N. Peters, “Turbulent Combustion”, University Press, Cambridge, UK, 2000.
[11] G. Lacaze, J. C. Oefelein, “A non-premixed combustion model based on flame structure analysis at supercritical pressures”, Combust. Flame 159 (2012) 2087–2103.
[12] T. Poinsot, D. Veynante, “Theoretical and numerical combustion”, RT Edwards Inc., Philadelphia, PA, 2005.
[13] A.Cuoci, A.Frassoldati, T.Faravelli, E.Ranzi, “Opensmoke++: An object-oriented framework for the numerical modeling of reactive systems with detailed kinetic mechanisms”, Comp. Phys. Commun. 192 (2015) 237–264.
[14] D.C. Wilcox, “Turbulence modeling for CFD”. DCW industries, 1993.
[15] L. Cutrone, P. De Palma, G. Pascazio, M. Napolitano, “A RANS flamelet–progress-variable method for computing reacting flows of real-gas mixtures”, Comput. Fluids 39 (3) (2010) 485– 498.
[16] D. T. Banuti, V. Hannemann, K. Hannemann, B. Weigand, An efficient multi-fluid-mixing model for real gas reacting flows in liquid propellant rocket engines, Combustion and Flame 168 (2016) 98–112.
[17] H. Muller, M. Pfitzner,”A flamelet model for transcritical LOX/GCH4 flames”, Jour. of Phys.: Conf. Series 821 (1) (2017) 012010.

Fuel Performance Detection in Micro Gas Turbine Using a New Approach Based on Chaos Detection from Combustion Vibrations

C. Allouis*, A. Amoresano, R. Pagliara*, G. Langella**, V. Niola**, G. Quaremba****

allouis@irc.cnr.it

* Istituto di Ricerche sulla Combustione - CNR, via Claudio 21, 81025, Naples, Italy
**Dipartimento di Ingegneria Industriale – Università degli Studi di Napoli Federico II, via Claudio 21, 80125, Naples, Italy.

Abstract

The use of pure vegetable oils in Micro Gas Turbine can damage the injection system or the combustion chamber causing undesired vibrations. An ideal solution would consist in having an available tool able to forecast and/or follow in real time the vibrational state of the combustion device. The present paper describes tests performed on a low emission Micro Gas Turbine for power generation, fueled with different liquid fuels, including commercial diesel oil and its blends with pure rapeseed oil. A particular attention was paid both on the emissions and on the measurements of the micro vibrational distributions and their correlation under the different fueling conditions using a new signal processing based on a nonlinear method and chaos analysis. We observed that the overall behavior of the MGT fueled with the blends was good, and the emission concentrations of CO, NOx and Total Particle Matter were comparable to the pure diesel oil ones. Moreover, the chaos analysis and the proposed methodology came out as a possible tool for the real-time characterization of the combustion process of the MGT and to individuation of the fuel supplied. Equations should be separated from text by one line, and may be referred to by equation number. All symbols should be printed in italics or otherwise according to conventional practice, both in the equations and in the text. An example of how italics and equation numbers should be used is given here in referring to the force *F* in above.

Introduction

There is a growing concern that the use of fossil fuels and the associated carbon dioxide emissions are contributing to global warming. The Energy Information Administration estimates that world carbon dioxide emissions from energy production will increase by 51% by 2030, namely from 28.1 billion metric tons in 2005 to 42.3 billion metric tons in 2030 [1]. As energy use grows, concerns over global warming may lead to imposing limits on greenhouse gas emissions from fossil fuel plants. This has stimulated extensive research on the subject of carbon capture and sequestration and an increase of renewable sources. Even though, the future renewable fuels of 3rd generation are not available yet, the use of 1st

generation biofuel, pure vegetable oils, is still of interest as an alternative fuel [2,3], and is commonly used both for transportation and energy production. Many studies are available about fuel preparation and emission characterization of systems fully or partially fueled with pure vegetable oils [4-8]. The use of pure vegetable oils can damage the injection system or the combustion device [4] causing undesired vibrations. The ideal solution would consist in having an available tool able to forecast and/or follow in real time the vibrational state of the combustion device. This objective could be partially solved applying recent mathematical algorithms based on chaos [9]. The purpose of this work is to describe an application of recent nonlinear signal processing method to distinguish the regularity of micro-vibration shown by micro gas turbine (for short, MGT) due to mixed fuels at fixed speed of rotation. The reason of such an approach is because the turbine is a dynamical system extremely balanced, so the vibrational morphodynamics due to the use of very similar fuels, are difficult to determine. This creates then a challenge in applied dynamical systems. The signal processing are usually performed by means of classic approach [10] (e.g., spectral analysis) or by applying the most advanced methods based on the wavelet transform or thermography [11-14]. Most of the techniques that have been developed for the analysis of both linear and nonlinear systems are observations of a stationary random process. The difficulty, of course, is identifying when it is appropriate to treat the data as stationary. As a working definition, we may therefore term stationary process to be one in which the measure of interest associated (e.g., pdfs) with collections of observations is not changing in time [15]. Recently, a new test approach for distinguishing regular from chaotic dynamics in deterministic dynamical systems was proposed [16]. The present paper describes tests performed on a low emission MGT for power generation, providing electrical power up to 30kWe. Different liquid fuels, including commercial diesel oil, blends of diesel oil with pure rapeseed oil, were tested under fixed load. Primarily attention has been focused on the measures of the micro vibrational distributions and their correlation with gas turbine fueling.

Experimental Set-Up and Method

Experimental set-up

The Micro Turbine Capstone C30 is a turbine of last generation system with a maximum power output of 30kWe with 26% electrical efficiency and up to 90% combined heat power efficiency. It is widely used in the aeronautical field; in particular, as energy provider for the aircrafts on parking. It can be also operated with different liquid fuels. The fuel supply system is composed of three nozzles (one main and two auxiliaries). In this paper, diesel as fuel and its blend with rapeseed oil at 1%v/v (for short, Diesel 1%) and 3%v/v (for short, Diesel 3%) were used. The choice of the rapeseed oil as an additive present in a small percentage is to verify an eventual difference between fuels in terms of machine performance. The turbine rotation was set at 85.000rpm close to maximum speed (i.e.,

90.000rpm) for all the fuels. All parameters of the turbine (i.e., rotational speed of the turbine, power output, exhaust gas temperature, etc.) were continuously acquired every two seconds by means of a PC and analyzed at the end of test. The vibrational signals were acquired by means of two unidirectional micro accelerometers, model PCB 352 C22. The acquired data through the accelerometers have been synchronized with each other and were stored in the computer. Synchronization here means that the accelerometer signals were acquired in parallel and aligned on a time basis through a LMS SCADAS data acquisition system. Hence, no electromechanical synchronization system was used for each accelerometer signal (e.g., tachometer signal). Front and side views of the turbine and the location of the accelerometers are shown in Figure 1.

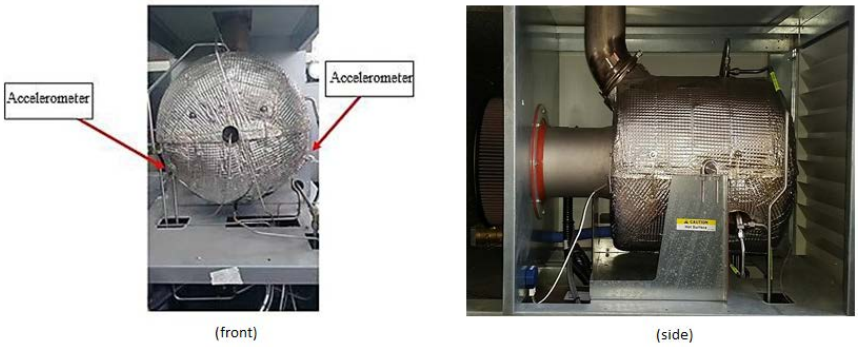

Figure 1 Turbine with location of accelerometers: front and side view

Methods

The proposed method for distinguishing regular from chaotic dynamics is successful if the noise-level is sufficiently small but also because the balanced dynamics of turbine are essentially stationary and deterministic. Many methods desensitize the test performed on noisy signals but damps the ability to detect slow growth of the features as well as the signature for time series data of moderate length. For such a reason each accelerometric signal was sampled at 102.400Hz for 10s, for a total of 1.025.024 sampled points. The calculations were performed by using the MATLAB® software. The nonlinear method introduced in this work consists primarily in the decomposition of the accelerometric signal into two mutually orthogonal components [18] for projecting them on a plane other than phase space [16-19]. This plane can be obtained by using the following equations

$$\chi_\omega(m) = \sum_{j=1}^{m} x_j \cos(j\omega) \qquad (1)$$

$$\zeta_\omega(m) = \sum_{j=1}^{m} x_j \sin(j\omega) \qquad (2)$$

where xj, j=1,2,..,N is a time series (e.g., accelerometric signal) , $\omega\epsilon(0,\pi]$ and m=1,2,...,N, N length of time series. The functions (1) and (2) are two orthogonal projectors and are useful to determine the “signature” of the vibration. For instance, a qualitative information on the regularity or not of the time series may be acquired

by observing the development of $\chi_\omega$vs ζ_ω. [20].

Results And Discussion

Since the quantity of added rapeseed oil was not important, any mechanical modifications of the MGT were done. The overall behavior of the MGT fueled with the blends was good and the emission concentrations, averaged over one hour, of CO, NOx and Total Particle Matter were comparable to the pure diesel oil ones as showed in tab.1. The procedures and the standards used for sampling are better described in ref. [5].

Table 1 - Emissions of the different fuels at 85.000rpm

	O_2 %	**NO_X** ppm (mg/Nm^3)@15%O_2	**CO** ppm (mg/Nm^3)@15%O_2	**Particle Matter** mg/Nm^3
Diesel oil	18,6	16 (34)	10 (12)	0,92
Diesel oil + 1%v/v Rapeseed oil	18,6	17 (36)	7 (9)	0,93
Diesel oil + 3% v/v Rapeseed oil	18,5	16 (34)	8 (10)	0,95

The accelerometric signals were simultaneously acquired for each fuel. An example of the acquired raw signals for each fuel is reported in Fig.2. One clearly observes the different shapes of the raw signals. The one generated by the combustion of diesel oil is periodical and relatively clean, while the other signals became noisier while increasing rapeseed oil concentration. These different vibrational behaviors are probably due the different combustion kinetic times of diesel oil and its blends because of the presence of rapeseed oil. The further chaos analysis leads to a comparison of the Kω and FFT concerning the frequencies of interest viz., 0÷30.000Hz. The accelerometric signal derived from pure diesel combustion has been characterized by the diagram Kω vs ω; the (fig.3, Top) compares three sequences randomly selected from raw accelerometric signal of length 150.000 points, roughly 1.46s. Let us observe that no statistical inference was done for a given combination of rotational speed and fuel. In fact, from a practical point of view we found that repeated sampling of the vibrations does not greatly alter the computed value of Kω. The interest is concentrated on the window where Kω assumes very stable and regular values of the accelerometric signal, i.e., 1.7 <ω <2.2 rad, corresponding to the frequency range 27700 ÷ 35850Hz (fig. 3, bottom). The choice of such a spectrum window is because any modification of the vibrational turbine morphodynamics, caused by the use of blended fuel, results in the occurrence of an easily identifiable frequency on a very "spurious" spectral range that can be assumed as reference spectrum or “baseline”. This eventuality will be evidenced with the trend of Kω vs ω and χω vs ζω.

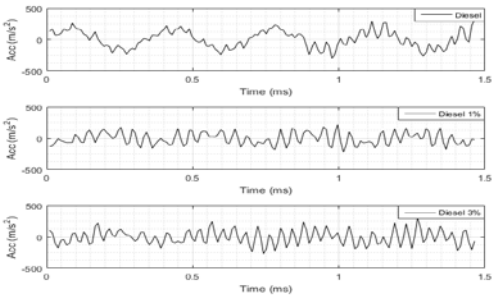

Figure 2: Accelerometric raw signals for different fuels

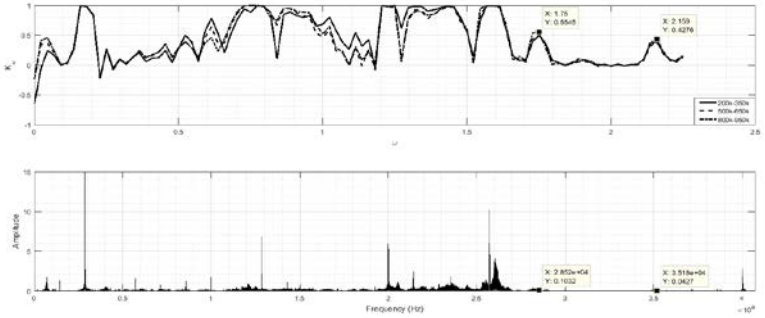

Figure 3: Comparison of trend Kω vs ω and corresponding spectrum diagram

A Fast Fourier Transform (FFT) of raw signals was performed to characterize the mean frequencies shown by the MGT for the different fuels and several common frequencies for the different fuels with different peak intensity are detectable namely 3.000Hz, 13.000Hz, 20.000Hz and 25.500Hz. While the peak intensities for diesel oil and its blend at 1%v/v are comparable, they drastically increase for the blend at 3%v/v. Moreover, a new peak intensity appears at around 28.200Hz. This last high frequency is probably due to the major concentration of oxygenated compounds formed during rapeseed oil combustion. In fact, the oxygen content of the pure rapeseed oil increases flame length but decrease soot and Polycyclic Aromatic Hydrocarbon formation, then leading to a faster combustion. These results are presented in figure 4 for the different fuels. One clearly observes that the chaos index, Kω, increases while increasing the rapeseed oil concentration. This indicates that the combustion is getting more chaotic as well as more irregular.

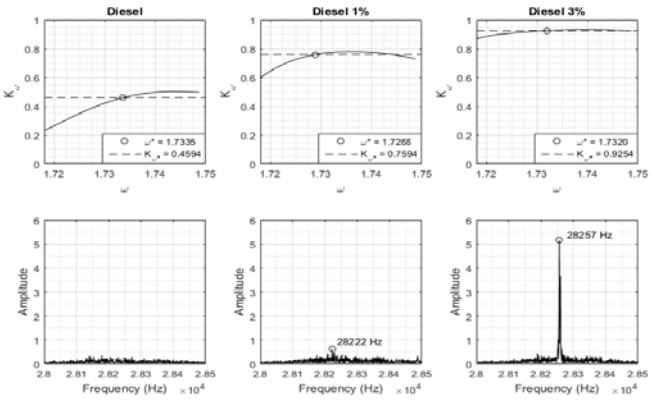

Figure 4: Comparison of Kω and FFT, the * stand for the median value of radius of cluster corresponding to the median value of Kω

This tendency is becoming clearer if we plot the map of ξ vs ς and of Mω vs m. The results are represented in figure 5. The symbols circle, cross, and star, stand for the centroids of plotted clusters. The chaotic behavior appear more highlighted in figure 5 where for the case of pure diesel oil the clusters are concentrated around the zero position and thus representing any chaos tendency.

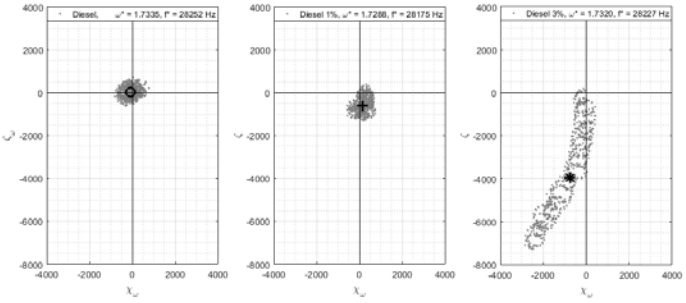

Figure 5: Maps of ξ vs ς for ω=ω* for each blend

On another hand, the higher the rapeseed oil is in the blends, the higher is the chaotic index, namely the centroid get far from zero position. The results presented in figure 5 represent a combustion fingerprint of each fuel.

Conclusion

Gas concentration and vibrational measurements were performed on a low emission Micro Gas Turbine for power generation supplied with commercial diesel oil and its blends with pure rapeseed oil under fixed load without any significant trouble. Chaos Analysis of vibrational according to the proposed methodology came out as an interesting tool for the real-time characterization and control of the combustion process of the MGT.

References

[1]. Energy Information Administration. International Energy Outlook 2008, report DOE/EIA-0484 (2008). Washington, DC: U.S. Department of Energy, 2008.
[2]. Lawlor V., Olabi A.G., Review of scientific research regarding PPO, tallow and RVO as diesel engine fuel, Fuel, 2015,145:25-38.
[3]. Kleinová A., Vailing I., Lábaj J., Mikulec J., Cvengroš J., Vegetable oils and animal fats as alternative fuels for diesel engines with dual fuel operation, Fuel Processing Technology, 2011, 92(10):1980-1986.
[4]. ACREVO. Advanced combustion research for energy from vegetable oils [ACREVO] final report [FAIR-CT95-0627]. http://www.biomatnet.org/secure/Fair/F484.htm .
[5]. Chiariello F., Allouis C., Reale F., Massoli P., Gaseous and particulate emissions of a micro gas turbine fuelled by straight vegetable oil-kerosene blends, Experimental Thermal and Fluid Science, 2014, 56, 16-22.
[6]. Allouis C., Romano M., Beretta F., Viegas L., D'Alessio A., Particulate formation from the spray combustion of heavy oil and biofuel, Combustion Science and Technology, 1998, 134, 1-6, pp. 457-476.
[7]. Daho T., Vaitilingom G., Sanogo O., Ouiminga S. K., Zongo A. S., Pirioud B., . Koulidiati J., Combustion of vegetable oils under optimized conditions of atomization and granulometry in a modified fuel oil burner, Fuel, 2014, 118(5):329-334.
[8]. D. C. Rakopoulos, C. D. Rakopoulos, E. G. Giakoumis, "Impact of properties of vegetable oil, bio-diesel, ethanol and n-butanol on the combustion and emissions of turbocharged HDDI diesel engine operating under steady and transient conditions", Fuel, 156:1-19, (2015).
[9]. V. Niola, G. Quaremba, "New Approach of Detecting Chaos in Deterministic Dynamical System", International Journal of Applied Engineering Research, Volume 11 (18):9576-9583(2016).
[10]. C.M.Harris, A.G. Piersol: Shock and vibration handbook. 5th Ed., McGraw-Hill (2002).
[11]. Amoresano A., Avagliano V., Niola V., Quaremba G., The assessment of the in-cylinder pressure by means of the morpho-dynamical vibration analysis - Methodology and application, International Review of Mechanical Engineering, 2013, 7 (6), 999-1006.
[12]. Amoresano A., Niola V., Quaremba G., A sensitive methodology for the EGR optimization: A perspective study. International Review of Mechanical Engineering, 2012, 6 (5), 1082-1088.
[13]. Niola V., Quaremba G., Avagliano V., Vibration monitoring of gear transmission, In Proceeding of 9th WSEAS Int. Conf. Simulation, Modelling and Optimization, SMO '09, pp. 74-79 2009.
[14]. Niola V., Quaremba G., Amoresano A., A study on infrared thermography processed through the wavelet transform. In Proceedings of the 8th WSEAS International Conference on System Science and Simulation in Engineering, ICOSSSE '09, pp. 57-62 2009.
[15]. Abarbanel H.D.I., Analysis of observed chaotic data, Springer-Verlag, New York, 1996.
[16]. Gottwald G.A., Melbourne I., A new test for chaos in deterministic systems. Proc. R. Soc. London, 2004, A 460:603-611.

SESSION II

Solid fuels

MEASUREMENT OF BEECH WOOD PYROLYSIS KINETICS IN A FLUIDIZED BED REACTOR

S. Pielsticker*, K. Schlögel, T. Kreitzberg*, O. Hatzfeld*, R. Kneer***
pielsticker@wsa.rwth-aachen.de
*Institute of Heat and Mass Transfer (WSA), RWTH Aachen University,
Augustinerbach 6, 52056 Aachen, Germany
**Unit of Technologies of Fuels (TEER), RWTH Aachen University,
Wüllnerstraße 2, 52062 Aachen, Germany

Abstract
Detailed experimental data for pyrolysis kinetics of pulverized solid fuels at high heating rates for temperatures below 1000 K is essential for the validation of reaction mechanisms in complex pyrolysis network models. The present study demonstrates the capability of a fluidized bed reactor setup to provide experimental data in the temperature range from 523 to 973 K carried out with pulverized beech wood. A comparison with simple 1- and 2-step models has shown plausible results.

Introduction

For the simulation of pulverized fuel boilers, modeling of devolatilization behavior plays an important role to describe ignition, volatile combustion and pollutant formation. With increasing computational power, typically used single first order models are replaced with more complex models e.g. network models like Chemical Percolation Devolatilization (CPD), Flashchain or Functional-Group, Depolymerization, Vaporization, Cross-linking Model (FG-DVC). Necessary validation data for those models are typically provided by drop tube reactors (DTR) at high temperatures and high particle heating rates. A fluidized bed reactor (FBR) is capable to extend the validation data set to lower temperatures in combination with high particle heating rates. Furthermore, a continuous analysis of the reaction products like in the FBR allows for more data points than the analysis at discrete time steps in the DTR. The higher number of data points is helpful to prove the plausibility of possible reaction mechanisms in network models. The present study demonstrates the capability of an FBR to determine pyrolysis kinetics in the temperature region from 523 to 973 K.

Experimental Setup

For determination of pyrolysis kinetic data, a small-scale fluidized bed reactor with a diameter of d = 55 mm is used. Reactor temperature is controlled with an electrical heated furnace around the reactor (see Figure 1). The main part of the reactor consists of two axial Al_2O_3 pipes, mounted in a stainless steel reactor head. The annular gap between the pipes serves as heat up zone for the fluidizing gas

flow (150–300 slph N_2 depending on temperature), while the inner part encloses the fluidized bed consisting of Al_2O_3 particles (d_{50} = 116 µm).

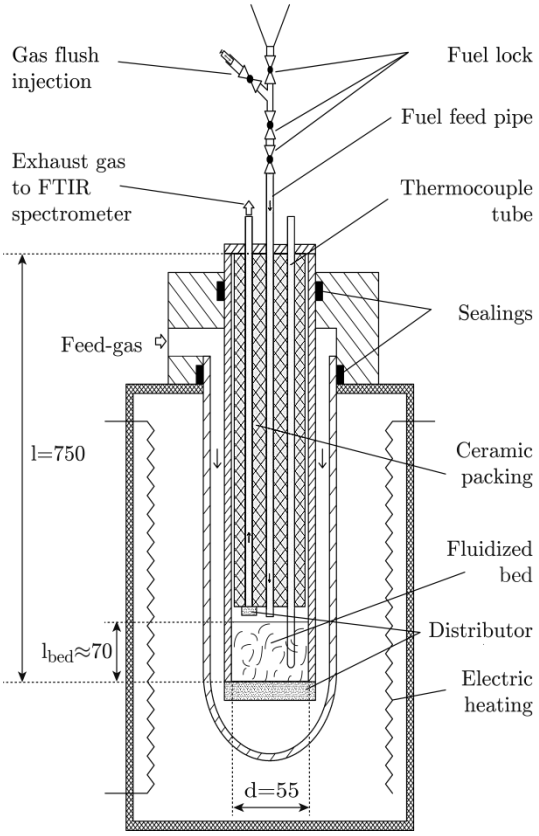

Figure 1. Scheme of the fluidized bed reactor (dimensions in mm)

Fuel samples (15–50 mg depending on temperature) are supplied to the reactor in batches. Particle transport from the fuel lock to the bed is forced with a gas flush from (10 ml N_2) to achieve fast heating rates of approximately 10^4 K/s [1]. Product gases are captured just above the bed and then transported to an FTIR spectrometer. The sampling line is heated to 453 K to avoid condensation of H_2O and tar components. The ceramic packing reduces dead volume, while the distributor in front of the gas sampling line allows for higher volume flows without particle entrainment. Both increase the gas exchange rate, which was identified to be the limiting factor in the determination of reaction rates of solid fuel particles [2]. Time dependent gas concentrations $c_i(t)$ are measured with an Agilent Cary 670 FTIR spectrometer, which analyzes in the wavenumber range from 600 to 6500 cm^{-1}, a spectral resolution of 4 cm^{-1} and a sampling frequency of 10 Hz. More detail on construction, operation and error analysis is given elsewhere [1–3].

For the present investigation pulverized and pre-dried beech wood particles from a sieving mesh size of 125–160 µm are used. Corresponding results from proximate and ultimate analysis are given in Table 1.

Table 1. Fuel properties based on ultimate and proximate analysis for investigated beech wood samples (mesh size: 125–160 µm)

Ultimate analysis	**C (daf)**	**H (daf)**	**N (daf)**	**S (daf)**	**O (daf)**
	48.83 %	5.64 %	0.23 %	0.02 %	45.24 %
Proximate analysis	**Moisture (raw)**		**Ash (dry)**		**Volatiles (daf)**
	7.28 %		0.36 %		85.34 %

Evaluation and Modeling

In the first step of the evaluation procedure for determining pyrolysis kinetic parameters, the experimentally derived rate of released gases $\mathrm{d}Y_{\mathrm{Gas,exp}}/\mathrm{d}t$ is calculated according to equation (1) from the measured FTIR gas concentrations c_i of 21 different gas species (including CO, CO_2, $C_xH_yO_z$, SO_2 and NO_x). Concentration of H_2O was ignored to avoid interferences with underlying drying processes.

$$\frac{\mathrm{d}Y_{\mathrm{Gas,exp}}}{\mathrm{d}t} = \frac{\rho_{\mathrm{N_2}} \cdot \dot{V}_{\mathrm{N_2}}}{m_\mathrm{F} \cdot M_{\mathrm{N_2}}} \cdot \frac{\sum_{i=1}^{n} c_\mathrm{i} \cdot M_\mathrm{i}}{1 - \sum_{i=1}^{n} c_\mathrm{i}} \tag{1}$$

Herein m_F is the injected fuel mass, $\dot{V}_{\mathrm{N_2}}$ the fluidizing volume flow of nitrogen, $\rho_{\mathrm{N_2}}$ the density and M_i the molar mass of each measured species.

In the second step, the experimentally derived gas release rate $\mathrm{dY_{Gas,exp}/dt}$ is approximated with a model derived one. In the present study, two different model approaches are presented, a 1-step model and a 2-step model. Characteristic parameters of both models are evaluated by the method of least squares. Effects of gas transportation and mixing in reactor and sampling line have been considered with a convolution transfer function as described in detail in [3].

In the 1-step model, the rate of released gases during pyrolysis is captured with

$$\frac{\mathrm{d}Y_{\mathrm{Gas}}}{\mathrm{d}t} = r \cdot \left[Y_{\mathrm{Solid}}(t) - Y_{\mathrm{Solid},\infty}\right], \tag{2}$$

where r is the characteristic reaction rate and Y_{Solid} represents the mass fraction of solid material, unconsidering the chemical transformation process from coal to char. $Y_{\mathrm{Solid},\infty}$ is the final char yield after pyrolysis is completed. Amount of solid material can be calculated from a coupled integration of equation (2) and a mass balance (equation (3)) with the assumption, that all released volatiles are captured in the gas phase:

$$Y_{\mathrm{Solid}}(t) = 1 - Y_{\mathrm{Gas}}(t) \tag{3}$$

In the 2-step model, primary and secondary pyrolysis reactions are considered in the model formation. During primary pyrolysis, the model assumes the release of gaseous products ($Y_{\mathrm{Gas,prim}}$) as well as tar (Y_{Tar}). Fraction of released tar from the overall amount of released volatiles is given by the factor f_{Tar}. Corresponding rate equations are given by equation (4) and (5).

$$\frac{\mathrm{d}Y_{\mathrm{Gas,prim}}}{\mathrm{d}t} = (1 - f_{\mathrm{Tar}}) \cdot r_{\mathrm{prim}} \cdot \left[Y_{\mathrm{Solid}}(t) - Y_{\mathrm{Solid},\infty}\right] \tag{4}$$

$$\frac{\mathrm{d}Y_{\mathrm{Tar}}}{\mathrm{d}t} = f_{\mathrm{Tar}} \cdot r_{\mathrm{prim}} \cdot \left[Y_{\mathrm{Solid}}(t) - Y_{\mathrm{Solid},\infty}\right] - r_{\mathrm{sec}} \cdot Y_{\mathrm{Tar}} \tag{5}$$

Despite the formation of tar, also decomposition during secondary pyrolysis with the reaction rate r_{sec} is considered in the last term of equation (5). The decomposed tar reacts into secondary gas $Y_{\mathrm{Gas,sec}}$ according to equation (6).

$$\frac{\mathrm{d}Y_{\mathrm{Gas,sec}}}{\mathrm{d}t} = r_{\mathrm{sec}} \cdot Y_{\mathrm{Tar}} \tag{6}$$

For the comparison with experimental data, primary and secondary gas release rates are summed, as there is no possibility to distinguish between primary and secondary gas species during the experimental evaluation.

$$\frac{\mathrm{d}Y_{\mathrm{Gas}}}{\mathrm{d}t} = \frac{\mathrm{d}Y_{\mathrm{Gas,prim}}}{\mathrm{d}t} + \frac{\mathrm{d}Y_{\mathrm{Gas,sec}}}{\mathrm{d}t} \tag{7}$$

Analogous to equation (3), yield of remaining solid is calculated via a mass balance:

$$Y_{\mathrm{Solid}}(t) = 1 - Y_{\mathrm{Gas}}(t) - Y_{\mathrm{Tar}}(t) \tag{8}$$

Results

Figure 2 gives a comparison between the experimentally derived gas release rate $\mathrm{d}Y_{\mathrm{Gas,exp}}/\mathrm{d}t$ (dots) and the two model derived fitted curves for 1- and 2-step model. Data corresponds to a single batch experiment at 873 K. Both models can capture the overall profile. Especially the maximum peak height is almost identical to the experimental values. Offside the peak, different behaviors of the two models are observable. While the 2-step model captures the experimental curve for all times very well, the 1-step model shows deviations in particular on the falling edge of the profile. Further investigations are thus only performed with the 2-step model.

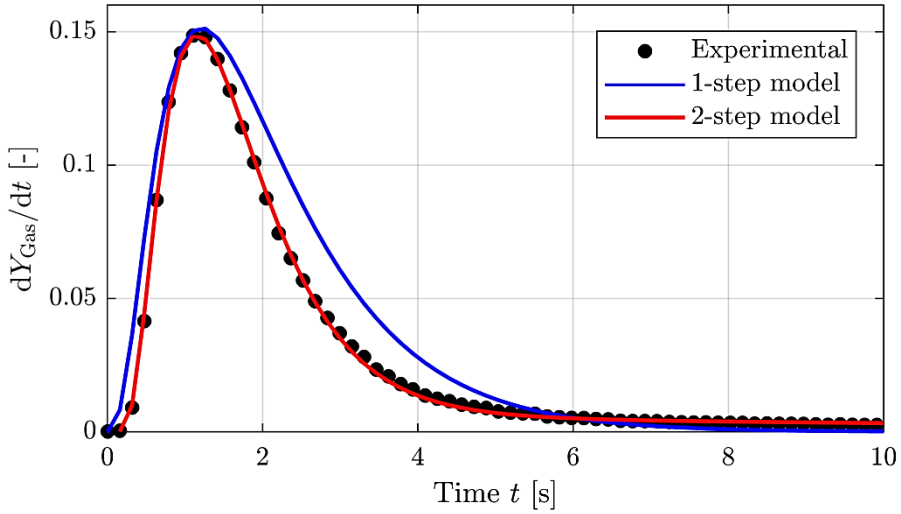

Figure 2. Comparison of experimentally derived gas release rate and corresponding model fit for 1- and 2-step model (single experiment at 873 K)

The above shown 2-step model curve is based on the following parameter set: $r_{\mathrm{prim}} = 1.656\ \mathrm{s}^{-1}$, $r_{\mathrm{sec}} = 0.0575\ \mathrm{s}^{-1}$, $f_{\mathrm{Tar}} = 0.235$ and $Y_{\mathrm{Solid},\infty} = 0.629$. Analogous, parameter sets are derived via least squares fits for all investigated temperatures from 523 K to 1473 K. Figure 3 shows an Arrhenius diagram, where the primary reaction rate r_{prim} is plotted over inverse temperature. Two main aspects are observable. In the low temperature region below ≈973 K, the reaction rate shows a linear trend according to an Arrhenius law

$$r = A \cdot \exp\left(-\frac{E_{\mathrm{a}}}{\mathcal{R}T}\right), \tag{9}$$

where A is the pre-exponential factor, E_{a} the activation energy, $\mathcal{R}$ the universal gas constant and T the temperature. For the investigated beech wood, $E_{\mathrm{a}} = 48.74\ \mathrm{kJ/mol}$ and $A = 1.27 \cdot 10^{3}\ \mathrm{s}^{-1}$ are found as kinetic parameters. In the high temperature range, detection limit of the reactor has been reached as it was theoretically predicted in [2].

Conclusion

The study has shown that the small-scale fluidized bed reactor is capable to derive pyrolysis kinetic parameters in the temperature range from 523 to 973 K. For the exemplary chosen beech wood, a 2-step model including primary and secondary pyrolysis reactions was well suited to capture the experimentally derived gas release. Furthermore, the fitted parameters show consistent behavior within the investigated temperature range.

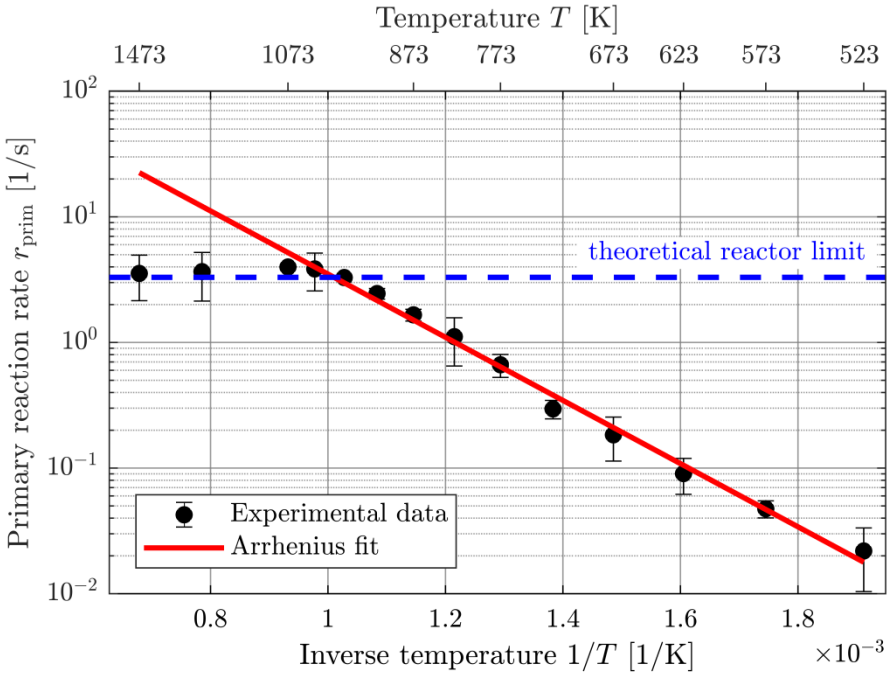

Figure 3. Arrhenius diagram for primary reaction rate

Acknowledgements
The authors would like to thank the German Research Foundation (DFG) for funding Stefan Pielsticker and Thobias Kreitzberg within the SFB/Transregio 129 "Oxyflame".

References

[1] Pielsticker, S., Gövert, B., Kreitzberg, T., Habermehl, M., Hatzfeld, O., Kneer, R., "Simultaneous investigation into the yields of 22 pyrolysis gases from coal and biomass in a small-scale fluidized bed reactor", *Fuel* 190: 420–434 (2017).

[2] Pielsticker, S., Gövert, B., Kreitzberg, T., Habermehl, M., Hatzfeld, O., Kneer, R., "Development of a rapidly responding fluidized bed reactor by theoretical and experimental evaluation of combustion reactions", *Fuel* 223: available online (2018).

[3] Gövert, B., Pielsticker, S., Kreitzberg, T., Habermehl, M., Hatzfeld, O., Kneer, R., "Measurement of reaction rates for pulverized fuel combustion in air and oxyfuel atmosphere using a novel fluidized bed reactor setup", *Fuel* 201: 81–92 (2017).

Effects of CO_2 on pyrolysis of walnut shells at high temperature and heating rate in a HSR

O. Senneca[*], B. Apicella[*], C. Russo[*], F. Cerciello[*], L. Cortese*, F. Stanzione*, P. Salatino[**], A. Wütscher[***], M. Muhler[***], V. Scherer[****]

o.senneca@irc.cnr.it

[*]Istituto di Ricerche sulla Combustione, C.N.R., Naples, Italy
[**]DICMAPI Università degli Studi di Napoli Federico II, Napoli, Italy
[***]Laboratory of Industrial Chemistry, Ruhr-University, Bochum, Germany
[****]Department of Energy Plant Technology, Ruhr-University, Bochum, Germany

Abstract

Previous studies have addressed the effects of carbon dioxide (CO_2) rich atmospheres, as those established in oxy-firing of solid fuels, on the properties of chars produced from pyrolysis of biomass. The present work complements previous investigation with experiments carried out under high heating rate/high temperature conditions in a purposely designed heated strip reactor (HSR). Walnut shell samples have been heat treated in the HSR in N_2 and CO_2 at temperatures of 1573-2073 K with holding times of 3s. Primary tar has been analyzed by GC-MS, char has been analyzed by thermogravimetric analysis and Raman spectroscopy. The effect of substitution of N_2 with CO_2 during heat up of biomass is not straightforward, as it can result in either an enhancement or reduction of char reactivity and structural order depending on the temperature. At 1573 K, CO_2 chars are less reactive and more graphitized than N_2 chars. In contrast, when the temperature is increased to 2073 K, CO_2 chars turn out to be more porous, less graphitized and more reactive than N_2 chars. The behavior is discussed within the frame of the competition of pyrolysis, gasification and thermal annealing.

1. Introduction

The classical approach for the prediction and modeling of the combustion or gasification of solid fuel particles is to assume a purely sequential course of drying, pyrolysis and heterogeneous combustion/gasification. Oxy-combustion is a case of practical relevance where the overlapping of purely thermally activated processes (pyrolysis, thermal annealing) and heterogeneous gasification occurs [1].

In oxy-combustion, fuel particles undergo devolatilization in CO_2 enriched atmospheres. Some recent studies investigated the course of pyrolysis of biomass in CO_2 rich atmospheres in different experimental setups. The authors reported cases in which the composition of the pyrolysis atmosphere affected the quality of the resulting chars, suggesting the existence of mutual interactions between the purely pyrolytic process and the heterogeneous reaction with CO_2, and cases in which this effect was negligible [2,3]. The current study investigates the influence of CO_2 atmosphere on the chars produced under more severe pyrolysis conditions than those previously examined. To this end a heated strip reactor described in previous publications [4,5] has been used. The reactor can be operated in N_2 and

CO_2. It can be heated up to 2100 K in approximately 0.1s and allows holding times of the order of seconds.

2. Experimental description

Biomass fuel

Experiments have been carried out on Walnut Shells (WS) whose properties are summarized in Table 1. Notably WS is a biomass where the lignin component prevails over the cellulosic/hemicellulosic ones with a ratio in the order 2:1. Samples have been pyrolyzed in atmospheres of N_2 and CO_2 of chromatographic grade.

Table 1. Standardized analyses of the examined fuel

Fuel	**Moisture** raw wt%	**Ash** dry wt%	**Volatiles** dry wt%	**C** daf[a], wt%	**H** daf[a], wt%	**N** daf[a], wt%	**S** daf[a], wt%	**O** daf[a], wt%	**HHV** daf[a], MJ/kg
WS	4	0.4	81.1	52.15	5.77	0.28	0.02	41.78	20.514

[a] dry and ash free

Pyrolysis apparatus

The reactor used for pyrolysis, depicted in Fig. 1, is a special heated grid device, where the usual metal grid, used as sample holder, is replaced by a pyrolytic graphite strip thermally stabilized for use up to 2773 K [4,5].

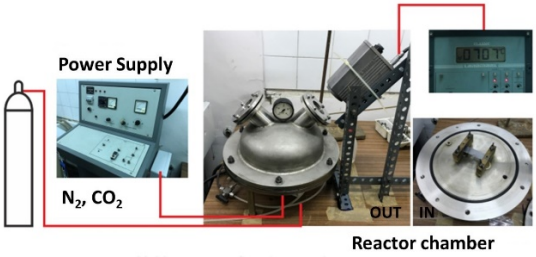

Figure 1. Heated strip pyrolysis reactor.

The apparatus is enclosed in a stainless-steel vessel which can be pressurized up to 12 bar. The temperature of the strip is set by changing the value of the voltage at the two ends of the strip. Due to the very high heating rate of the HSR, the strip can be considered isothermal for the entire duration of the test. For each test about 100 mg of fine WS particles (diameter approx. 130 μm), have been placed on the strip in a thin layer. The reactor is flushed with the test gas (either N_2 or CO_2) for 10 min with a high flow rate to remove any oxygen traces. The strip has then been heated up to 1573 or 2073 K. The total reaction time was 3s. Due to the very small size, the particles heated up by contact with the strip and could be considered at the

same temperature as the strip. Details on equipment and heating rate profiles are provided in [4,5]. The char samples were collected from the strip. A pyrex support is positioned above the strip and tar samples were recovered by washing the support located with acetone in ultrasonic bath.

Product analysis methods

The tar sample solutions were analysed by gas chromatography-mass spectrometry (GC-MS, AGILENT GC 7890 - MSD 5975C).

Char samples were investigated by thermogravimetric analysis (TGA), Raman spectroscopy and scanning electron microscopy (SEM). TGA analysis was carried out in Perkin-Elmer Pyris 1 Thermogravimetric Analyzer. Approximately 1-2 mg were used for each test. After a dehumidification step, samples were heated up to 1073 K in a flow of air of 50 ml/min (STP) at constant heating rate of 5 K/min. The weight loss data measured during combustion experiments have been worked out to obtain instantaneous rates of reaction *df/dt*.

Raman spectra were measured by means of a Horiba XploRA Raman microscope system with an excitation wavelength of λ = 532 nm (frequency doubled Nd:YAG-solid state laser, laser power on the sample less than 1mW). SEM analysis was performed using a FEI INSPECT S.

3. Results and Discussion

Figure 2 reports the results of GC-MS analysis on tar produced in N_2 and CO_2 environment. The area% of the peaks and the corresponding chemical species associated with each peak are shown. In particular PAH compounds are marked with*. The effect of exposure to CO_2 on tars during fast pyrolysis in HSR at 2073 K is remarkable. PAH compounds appear predominantly in CO_2, while monocyclic oxygenated compounds are more abundant in N_2

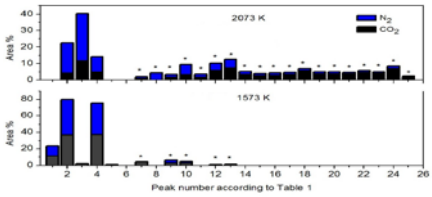

1) Aliphatic acid	8) Acenaphthene*	15) Methylpyrene*	21) Benzo(b)fluoranthene*
2) Benzendiol	9) Fluorene*	16) Benzo[de]anthracene	22) Benzo(k)fluorathene*
3) Naphthalenol	10) Phenanthrene	17) Benzo[gh]fluoranthene	23) Benzo[j]fluoranthene*
4) Vanillin	11) Anthracene*	18) Cyclopenta[cd]pyrene*	24) Benzo(a)pyrene*
5) Biphenylene	12) Fluoranthene	19)Benzo(a)anthracene*	26) Perylene*
6) Naphthalene*	13) Pyrene*	20) Crisene*	27) Indeno(cde)pyrene*
7) Acenaphthylene*	14) Benzo[a]fluorene*		

Figure 2. GC-MS analysis on tar samples.

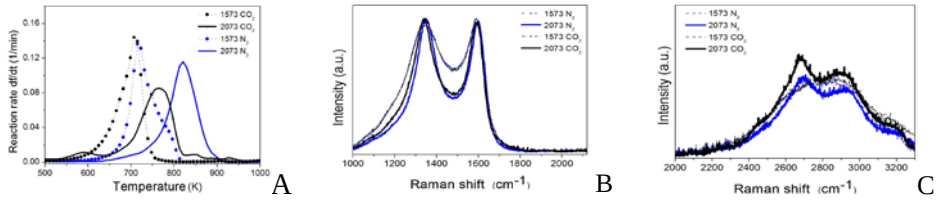

Figure 3. A) TG analysis of chars in air; Raman spectra of chars: B) 1st order, C) 2nd order.

The results of the TG analyses carried out on chars are summarized in Fig. 3A.
The DTG curves show that 1573 CO_2 char is the most reactive among the char samples. It features a DTG curve with a single well-defined peak at T_{max}= 710 K. The DTG peak of the 1573 N_2 char occurs at a moderately higher temperature (T_{max}= 720 K, with a shoulder at 770 K) suggesting that the CO_2 char is moderately more reactive than the N_2 char prepared at the same temperature of 1573 K. The DTG curve of the 2073 CO_2 char still features a single peak, but in this case the peak occurs at T_{max}= 760 K, indicating a more remarkable effect of the temperature of heat treatment on the char reactivity. The least reactive of the four chars is the one prepared in N_2 at 2073 K. In this case, a DTG peak appears at T_{max}= 820 K. The values of the residual weight from TG curves are reported in Table 2. Notably the ash content in the CO_2 chars is higher than in the N_2 chars, suggesting the occurrence of heterogenous gasification. This effect is more remarkable at the higher temperature of 2073 K and is confirmed by SEM analysis (Fig. 4) of the samples which shows a clear occurrence of pitting on the surface of chars prepared in CO_2 at 1573 K. Surface pitting was not detected on the surface of the N_2 chars and is attributed to gasification effects.

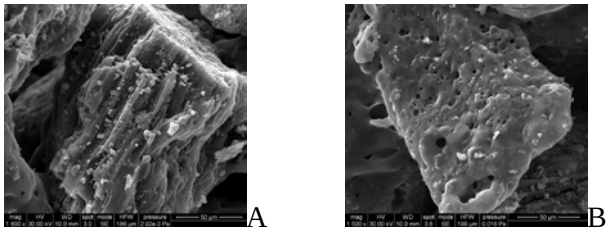

Figure 4. SEM of char: A)1573 N_2, B) 1573 CO_2.

Results of Raman analysis are reported in Figs. 3B-C. The two most remarkable spectral modes of the Raman spectra are the G peak (at about 1600 cm^{-1}) and the D peak (at about 1350 cm^{-1}). The accurate quantification of Raman spectra by a systematic procedure is necessary to derive reliable spectral parameters. The deconvolution procedure and the peak attribution were already described in a previous study [6]. The ratio of the D to the G peak intensities, *I(D)/I(G)*, reported in the Table 2, is commonly used to express the order/disorder quantification.

Table 2. Results of characterization of the char samples by Raman spectroscopy and TG analysis.

Sample	I(D)/I(G)	FWHM (D), cm^{-1}	DTG peaks T_{max} (K)	TG residue, w%
1573 N_2	0.92	156.50	720	5.8 ± 1
2073 N_2	1.00	121.04	820	5.4 ± 1
1573 CO_2	1.01	163.81	710	8.8 ± 2
2073 CO_2	0.97	122.35	760	17 ± 2

However, in this case the I(D)/I(G) ratio seems not to be representative of the differences that can be visually appreciated in Figs. 3-4. This is due to the non monomodal character of the *I(D)/I(G)* ratio with the size of the graphitic clusters *La* [7]. Indeed, Tuinstra and Koenig [8] showed that *I(D)/I(G)* varied inversely with the aromatic layer size *La*. Later on, Ferrari and Robertson [18] found that the Tuinstra-Koenig equation is no longer valid for small crystallite (L_a < ~2 nm) and showed that in such case the D band intensity is proportional to the area of the aromatic domains. To overcome this ambiguity, as the D band is usually very strong and easy to fit in the case of pyrocarbons, the full width at half maximum of the D band (*FWHM(D)*) is often chosen as a reliable structural order parameter, specifically, it is found to decrease as the order increases [9]. The Raman spectra of the samples at 1573 K are all characterized by a *FWHM(D)* around 145-155cm^{-1}. However, they can be compared on the basis of the *I(D)/I(G)* ratio since the absence of a well-defined second order means that they are in the range of L_a < 2 nm. In fact, they present a small modulated bump from 2400 to 3100 cm^{-1}. Instead, the samples with a *FWHM(D)* around 120 cm^{-1} (2073 N_2/CO_2 chars) present a well-defined second-order Raman peaks, confirming the strong aromatization they underwent at 2073 K.

4. Conclusion

Pyrolysis of high-lignin biomass samples in a high-temperature/high heating rate heated strip reactor has been scrutinized. Experiments were carried out in either CO_2-rich or N_2-rich atmospheres, representative of oxy-fuel or conventional combustion conditions at two peak temperature levels and 3 s holding time. The results confirm that char reactivity decreases as the severity of heat treatment is increased, and this is well correlated with increased microstructural order assessed via Raman spectroscopy. The effect of the CO_2 vs. N_2 atmosphere on the reactivity of the resulting char is not straightforward, as it results from conflicting effects of CO_2-char interaction. At moderate temperature, CO_2 apparently fosters pyrolysis, promotes structural order and reduces char reactivity. At higher temperatures, exposure to CO_2 enhances char reactivity, a feature that is explained based on the progress of CO_2 gasification and activation of the char.

The effect of exposure to CO_2 on tars during fast pyrolysis in HSR at 2073 K is remarkable. PAH compounds appear predominantly in CO_2, while monocyclic oxygenated compounds are more abundant in N_2

Acknowledgments
This work has been financed by the German Research Foundation (DFG) within the framework of the SFB/Transregio 129 "Oxyflame". We acknowledge Ruhr-University Bochum (RUB) Research School for awarding O. Senneca with an International Visiting Professor Grant (VIP_4_2016_02).

References

[1] Senneca, O., Scala, F., Chirone, R., Salatino, P., "Relevance of structure, fragmentation and reactivity of coal to combustion and oxy-combustion", *Fuel* 201:65-80 (2017).

[2] Senneca, O., Cerciello, F., Cortese, Heuer, S., Schiemann M., Scherer, V., "Effects of oxy-fuel conditions on walnut shells pyrolysis in a drop tube reactor", *10th Mediterranean Combustion Symposium*, Naples, Italy 2017.

[3] Senneca, O., Cerciello, F., Heuer, S., Ammendola, P., "Slow pyrolysis of walnut shells in nitrogen and carbon dioxide", *10th Mediterranean Combustion Symposium*, Naples, Italy 2017.

[4] Senneca, O., Allouis, C., Chirone, R., Russo, S., "Set up of an experimental apparatus for the study of fragmentation of solid fuels upon severe heating", *Exp. Therm Fluid Sci*, 34:366-372 (2010).

[5] Senneca, O., Urciuolo, M., Chirone, R., Cumbo, D., "An experimental study of fragmentation of coals during fast pyrolysis at high temperature and pressure", *Fuel* 90:2931–2938 (2011).

[6] Apicella, B., Senneca, O., Russo, C., Heuer, S., Cortese, L., Cerciello, F., Scherer, V., Schiemann, M., Ciajolo, A., "Separation and characterization of carbonaceous particulate (soot and char) produced from fast pyrolysis of coal in inert and CO_2 atmospheres", *Fuel* 201:118-123 (2017).

[7] Tuinstra, F., Koenig, J.L., "Raman Spectrum of Graphite" J. *Chem. Phys*. 53:1126-1130 (1970).

[8] Ferrari, A.C., Robertson, J., "Interpretation of Raman spectra of disordered and amorphous carbon" *Phys. Rev. B* 61:14095-14107 (2000).

[9] Vallerot, J.M., Bourrat, X., Mouchon, A., Chollon, G., "Quantitative structural and textural assessment of laminar pyrocarbons through Raman spectroscopy, electron diffraction and few other techniques", *Carbon* 44:1833-1844 (2006).

SLOW PYROLYSIS OF POTASSIUM DOPED XYLAN: A COMPARISON BETWEEN TWO DOPING APPROACHES

Paola Giudicianni, Valentina Gargiulo, Michela Alfè, Raffaele Ragucci
giudicianni@irc.cnr.it
Istituto di Ricerche sulla Combustione (IRC-CNR), P.le Tecchio 80, 80125 Napoli, Italy

Abstract
In this study, the effect of potassium ions on the slow pyrolysis of hemicellulose is assessed using xylan as a representative of hardwood hemicellulose. Thermogravimetric and pyrolysis tests, up to 973 K at a heating rate of 7 K/min, were conducted on different xylan samples: commercial xylan (X), demineralized xylan (DX), potassium doped xylan (DX_K) samples. Commercial xylan was demineralized through a cation exchange resin in order to reduce the presence of inherent inorganics. Subsequently, the demineralized sample was doped with a controlled amount of K ions (ca 1 wt%) by using two different approaches: wet impregnation and cation-exchange resin.
The results show that the wet impregnation doping procedure affected negligibly the pyrolytic behavior of the demineralized sample, and thus it is not suitable for the study of the effect of salts ions on xylan pyrolysis.
By comparing the results obtained from X, DX and _K doped DX through cation exchange method, it can be inferred that, overall, the presence of metal ions favored the gas production at the expense of pyrolysis liquids and the release rate of permanent gases (mainly CO_2 and CO) along the temperature is greatly altered too.

Introduction
The interest in the exploitation of biomass as fuel source increased in the last decades due to biomass neutrality with respect to CO_2 emissions. At the same time, the need of a correct disposal of vegetal residues raised the interest in exploring new routes for residual biomasses valorization [1].
Energy carriers and added-value products can be obtained through biomass thermochemical conversion [2]. Products yield and characteristics are strongly affected by the relative content of organic and inorganic biomass components [1].
There are several studies focused on the effect of the inorganic matter on biomass pyrolysis showing that the presence of alkali and earth alkali metals (AAEMs) causes an increase in the yields of char and gas at the expense of pyrolysis liquids (favoring dehydration, demethoxylation, decarboxylation reactions).
A wide literature is available on the effect of AAEMs on pyrolysis of biomass and cellulose, whereas only few works reported about the effect of metals on hemicelluloses pyrolysis [3,4]. However, hemicelluloses constitute about 20–30%

of the total mass of annual and perennial plants and the comprehension of their thermal behavior is important for determining the characteristics of biomass char and even more of torrefied biomass. Recent experiments conducted on xylan under slow pyrolysis conditions in presence of steam confirmed the role of AAEMs in favoring char and gas production, but highlighted that the formation of light oxygenates via ring scission is preferred instead of dehydration reaction [4].
In order increase the comprehension of the effect of metal ions on hemicellulose pyrolysis behavior and to pave the way for the formulation of possible decomposition mechanisms a study on the effect of K ions (one of the main components of inorganic matter in biomass) on xylan slow pyrolysis was carried out. To this aim a complete demineralization of commercial beechwood xylan was performed. After that the demineralized xylan was doped with about 1 wt.% of K^+ ions by using two different approaches: wet impregnation and cation-exchange resin. The resulting samples, the commercial and the demineralized xylan samples were subjected to pyrolysis tests up to 973 K under an inert atmosphere of nitrogen at a heating rate of 7 K/min and the products yields and gas composition were compared.

Experimental section

Materials. Beechwood xylan (Sigma–Aldrich X4252) was used as hemicellulose representative. Raw xylan (X) was demineralized as described in [4]. A significant removal of the metal ions in the demineralized sample (DX) was obtained through the demineralization procedure (the ash content decreased from 4.4% to 0.3%).
DX was doped with a controlled amount of K^+ ions (~1 wt.%) in two different ways. The first procedure was to pass the DX sample through a K+ form cation-exchange resin: 5 g of DX were dissolved in 100 mL of distilled water and passed through 10 mL of K^+ form resin. Then, the sample was dried at 50 °C for 24 hours.
The second doped sample was prepared according to the wet impregnation procedure: the appropriate amount of KCl (about 191 mg) was dissolved in 100 mL of deionized water and added to 5 g of DX. The suspension was stirred for 30 min at ambient temperature to obtain a well-mixed slurry and dried in an oven at 50 °C for 24 hours.
Thermogravimetric tests. The thermal behavior of the samples was studied in a thermogravimetric (TG) apparatus (STA 449 F5 Jupiter) by heating the sample (2-10 mg) from 323 K up to 973 K, at atmospheric pressure under an inert environment (N_2, 50 mL/minat a heating rate of 7 K/min.
Pyrolysis tests. Commercial, demineralized and K^+ doped samples were pyrolysed at 7 K/min up to 973 K in the reactor described in detail elsewhere [4-6]. Brefly, it consists of a steel jacketed prismatic chamber in which the sample (4-6 g) is spread in thin layers (approximately 1 mm thick) over 4 sample trays, placed uniformly along the rectangular cross-section of the reaction chamber. A superheater placed before the jacketed reactor heats the carrier gas to the programmed temperature via a PID controller. Carrier gas flows into the jacket at a constant gas mass flow rate

(3.09 Nl/min) and then its flow is reversed so that it enters the reaction environment through a ceramic flow straightener. The residence time of the gas in the reaction chamber is 2 s, thus limiting the secondary reactions of the volatiles evolving from the primary decomposition of the feedstock. Temperature is monitored using N-type thermocouples along the main dimension of the rectangular sample trays. The gaseous stream that exits the reaction chamber passes through a condensation device. The non-condensing gases are fed to a micro gas chromatograph, equipped with a thermal conductivity detector (Agilent 3000 Quad) to obtain temporal profiles of the release rates of all the gaseous species evolving from the pyrolysis tests (CO, CO_2, H_2, CH_4, C_2H_4, C_2H_6 and N_2). The yields of the gaseous products were calculated by integrating the measured rate curves along the test duration. At the end of each experimental test char yield was determined gravimetrically, with respect to the fed sample. The liquid yield was evaluated as the amount needed to complete the mass balance.

Result and discussion

Thermogravimetric results. Figure 1 shows the experimental TG profiles of the samples and the corresponding DTG curves.

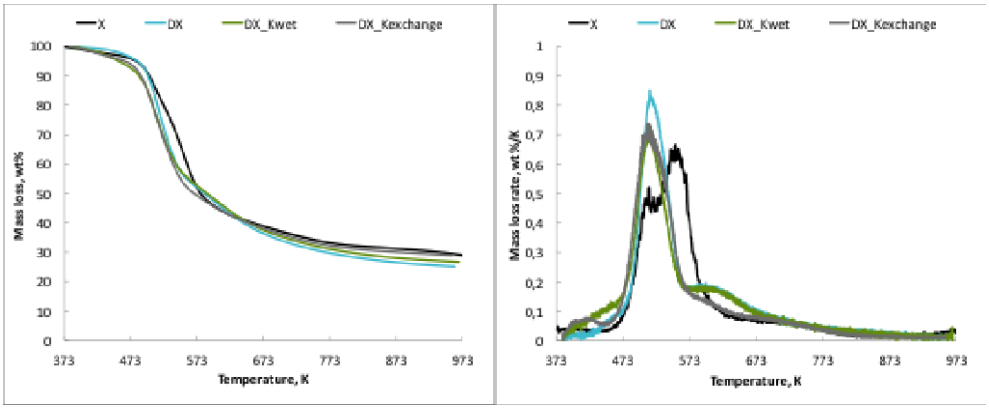

Figure 1. TG (left) and DTG (right) profiles of the samples.

As indicated by the TG profile, X decomposed between 473 K and 623 K, and two distinct peaks can be detected at 510 K and at 550 K, respectively. Demineralized xylan decomposed over a narrower temperature range (473–573 K) with the main peak occurring at 517 K. A second small peak is detected between 560 and 660 K. As concerns the char yields, in the case of the X sample, a higher amount of solid residue compared to the DX sample was obtained (29.7 wt.% for X and 25.5 wt.% for DX). The doped sample obtained by wet impregnation (DX_K_{wet}) decomposed following the same TG profile of DX with a main event peaked at 513 K and small event detected between 560 and 660 K. The char yield was 26.8 wt.%, but the slight difference with respect to X char yield is within the experimental error. The DTG profile of the doped sample obtained by cation-exchange ($DX_K_{exchange}$)

resembled the DX profile except for the absence of the second event between 560 and 660 K. The char yield was 29 wt.%, higher than that of DX and DX_K_{wet}.
Pyrolysis products distribution. Figure 2 shows the pyrolysis product yields of all the xylan based samples.

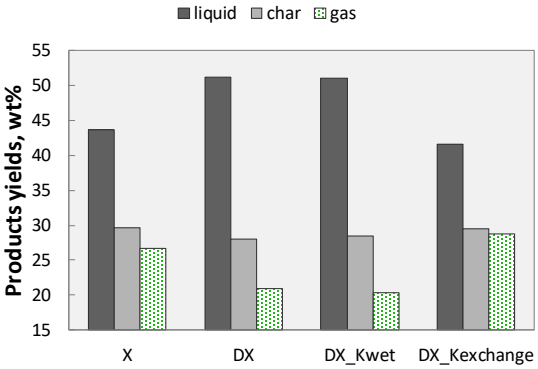

Figure 2. Pyrolysis products yields.

As expected, the demineralization process clearly favored the liquid production at the expense of gas (the gas yield decreased from 26.7 in X to 20.9 wt% in DX, while the liquid yield increased from 43.7 in X to 51.1 wt.% in DX) and affected slightly char production (the char yield passes from 29.6 in X to 28 wt.% In DX).
K doping through wet impregnation did not produce noticeable changes in the product yields compared to DX. On the contrary, char and gas production at the expense of the liquid was promoted in DX_$K_{exchange}$ in agreement with previous literature findings on the effect of K^+ ions on cellulose pyrolysis [6].
It is likely that K^+ promoted the ring-scission and rearrangement reactions (formation of non-condensable gases, light oxygenates, and char) in competition with depolymerization and dehydration reactions leading to higher molecular weight species retaining the xylan pyranose structure (xylose and xylose dehydratation products) [3]. In order to get useful insights into the effect of K^+ ions on xylan decomposition mechanisms, the evolution of the gaseous species along the pyrolysis temperature was studied. The release rate curves of the main gaseous species (CO_2, CO, H_2 and CH_4) are shown in Figure 3.
For all the samples, CO_2 and CO were the main gaseous species, even though the production of CO_2 was predominant with respect to CO. CO_2 mainly resulted from decomposition of side acetyl groups and carboxylic groups, whereas CO derives from the carbonyl ending groups left from the dehydration reactions of the side chain groups [3].
For the X sample, CO_2 curve was characterized by two overlapped events in the lower temperature region (470-600 K), whereas two distinct events can be detected for DX sample: the first one between 423 and 580 K and the second one in the 580-873 K temperature range.
The release of CO from X sample exhibited a main release peak centered at 558 K,

whereas in the case of DX sample two overlapped events in the same temperature ranges as CO_2 were detected, but the first one is a shoulder on the increasing branch of the second main peak.

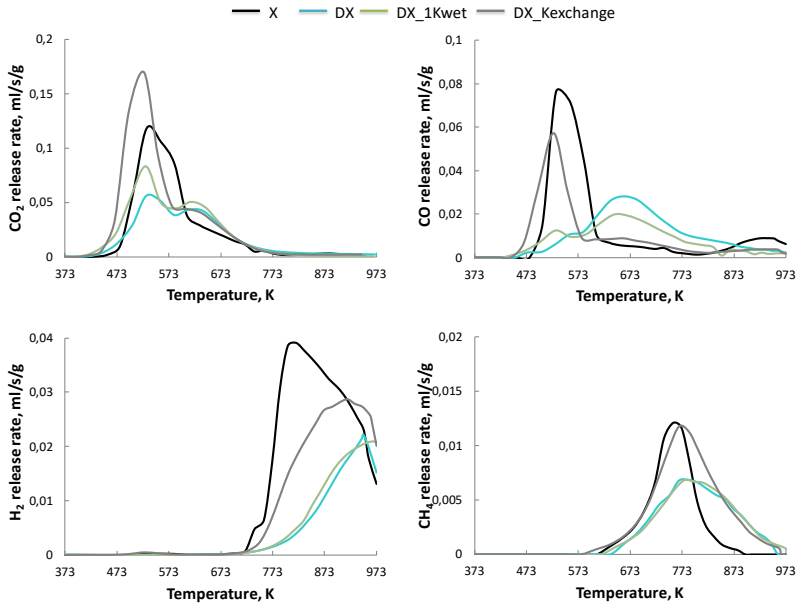

Figure 3. Release rate profiles along the temperature of the main gaseous species produced from the different xylan samples.

The introduction of K^+ ions into the demineralized sample by wet impregnation did not induce great modifications on the decomposition mechanism of DX except for a slight enhancement of the first peak of CO_2 release rate. On the contrary, the K^+ doping through cationic exchange resin induced great modifications on the release rate of all the detected gaseous species. In both CO_2 and CO release rate curves the enhancement of the first event in the 423-580 K temperature range was observed, whereas only for CO release rate curve the depression of the second peak occurred.
For all the samples, minor species such as H_2 and CH_4 were released at higher temperature, at about 750 and 650 K, respectively, probably derived from reactions occurring after the opening of the xylan ring. Both for X and DX_$K_{exchange}$ samples the release of these two species is slightly anticipated with respect to DX and DX_K_{wet} sample.
Overall, the presence of metal ions in X and K^+ in DX_$K_{exchange}$ samples favored the release of all the gases with particular effect on CO_2, H_2 and CH_4. The enhanced release of H_2 and CH_4 denote a slight catalytic effect of K^+ also on secondary reaction pathways.
The structural features of xylan can clarify the contrasting results obtained with the two doping procedures used in this study. The xylan is an acidic polysaccharide

containing one glucruronic unit approximately for ten xylan units, so the cation-exchange procedure allowed the complete exchange between the H^+ and K^+ transforming the COOH groups of glucruronic unit in COO^-K^+ form. In this way the K^+ ions are tightly linked to xylan polysaccharide and can properly exploit their catalytic effect. On the contrary, the wet impregnation procedure with KCl does not allow the exchange between the H^+ and K^+ and thus the catalytic effect is lowered.

Conclusions

In the present paper the influence of K^+ ions on hemicellulose pyrolysis was studied using commercial xylan as proxy compound. The thermal behavior of commercial, demineralized xylan and K^+ doped samples obtained with two different doping procedures was investigated in a pyrolysis reactor in nitrogen atmosphere at atmospheric pressure under slow pyrolysis conditions (HR= 7 K/min). The demineralization process clearly favored the liquid production at the expense of gas and slightly reduced char production. The two doping approaches produced contrasting results. Doping through wet impregnation did not produce noteworthy modifications either on product yields or gas release rate. On the contrary, sample doped through cation exchange resin produced higher gas yield at the expense of liquid yield similarly to what observed for commercial xylan rich in inorganic matter. In this case also the mechanisms responsible of the release of the main gaseous species where greatly affected by the presence of K^+.

In the case of xylan the wet impregnation is not the suited doping procedure, probably because of the chemical nature of the polysaccharide (low molecular weight and rich in COOH).

Overall, the results obtained in this work about the K^+ effect encourage future researches for the production of a database useful for the improvement of the predictive capabilities of pyrolysis kinetic models also in presence of metal ions.

Acknowledgments

The financial support of Piano Annuale della Ricerca Mise-CNR was acknowledged.

References

[1] Naik S. N., Goud V. V., Rout P. K., Dalai A. K. *Renew. Sustain. Energy Rev.* 142: 578-597 (2010)

[2] Kambo H.S., Dutta A. Renew. Sustain. Energy Rev. 45: 359-378 (2015)

[3] Patwardhan P.R., Brown R.C., Shanks B.H., *ChemSusChem* 4: 636-643 (2011)

[4] Giudicianni P., Gargiulo V., Grottola C.M., Alfè M., Ragucci R. *Fuel* 216: 36-43 (2018)

[5] Gargiulo V., Giudicianni P., Alfè M., Ragucci R. *J. Anal. Appl. Pyrol.* 112: 244-252 (2015)

[6] Ferreiro A.I., Rabaçal M., Costa M., Giudicianni P., Grottola C.M., Ragucci R. *Fuel* 215: 57-65 (2018)

Investigation on ignition behaviors of pulverized coal particles in a tubular swirl burner

Yang Xu, Shuiqing Li*

lishuiqing@tsinghua.edu.cn

Key laboratory for Thermal Science and Power Engineering of Ministry of Education, Department of Energy and Power Engineering, Tsinghua University, Beijing, 100084, China

Abstract

This paper focuses on the investigation of ignition behavior of pulverized coal particles in a specially-designed tubular swirl burner. The temperature and flow field of the newly-developed burner was simulated by computational fluid dynamics (CFD), and further verified by advanced optical measurements. A digital camera was used to capture the combustion behaviors of coal particles in different ambiences. Combined with the CFD simulation, the ignition delay time of coal particles was then estimated and compared with that in the laminar flat-flame Hencken burner. The turbulence effect on the ignition delay time in different ignition modes was specially discussed.

1. Introduction

In a foreseeable future, the role of coal as one of major energy sources in China has gained renewed interest because of its reliability/stability in both supplies and prices [1]. However, public concerns over the coal combustion generated issues, like the emission of particulate matter and greenhouse gases, have led to mounting efforts on fundamental studies of coal combustion characteristics [2-6].

As a crucial step during the early stage of coal combustion, ignition process determines the combustion stability and safety. Studies on the ignition behaviors of isolated coal particles have already aroused substantial attention. Considering the ultra-high heating rate which is similar to that in practical combustor, the most widely used bench-scale devices for laboratory ignition studies are drop tube furnace (DTF) and flat-flame burner. Based on existing researches, coal ignition behaviors are demonstrated to depend on the coal rank, particle size, heating rate, oxygen mole fraction, diluents, *etc*. [2-6]. However, it should be noted that the existing apparatus can only provide a laminar flow field with low Reynold number for the ignition study, which makes it reasonable to omit the turbulence effect on the local combustion temperature and species concentration. However, when scaled up to the pilot or industrial coal combustors, the turbulent effect is non-negligible as it can influence the heat/mass transfer and chemical reaction kinetics.

This work aims to make preliminary efforts on investigating the turbulence effect on the ignition behaviors of coal particles. A swirl-stabilized tubular burner was then specially developed. The ignition delay time of dispersed coal particles in the

tubular swirl burner and that in the flat-flame Hencken burner was especially compared and discussed.

2. Experimental set-up

One kind of high-volatile lignite was particularly used in this experiment. The proximate and ultimate analyses of the coal sample are presented in Table 1.

Table 1 Proximate and ultimate analysis of Hulunbel lignite

Fuel type	Hulunbel lignite
Proximate analysis (on a dry basis)	
Fixed Carbon (%)	49.1
Volatile (%)	38.8
Ash(%)	12.1
Ultimate analysis (on a dry-ash-free basis)	
Carbon (%)	74.05
Hydrogen (%)	4.17
Oxygen* (%)	20.47
Nitrogen (%)	1.00
Sulfur (%)	0.31

A schematic of the experimental set-up is shown in Fig. 1. The specially designed $CH_4/O_2/N_2$ swirl-stabilized tubular burner consists of four tangential slits, a central jet tube at the bottom and a quartz tube. The tangential slit is 2 mm in width and 12 mm in height. The swirl-stabilized tubular flame is confined by the quartz tube of 30 mm in diameter and 100 mm in length, which allows for optical diagnostics. The swirl number *S*, defined as the ratio of axial flux of angular momentum to the axial flux of linear momentum, can be determined by the geometry of the burner, as depicted in Eq. 1. Here, D_0 is the tube diameter, D_e is approximately determined by subtracting the slit width from the burner diameter, and A_T is the total cross-sectional area of the injection slits. In our current configuration, the swirl number is fixed at 7.36.

$$S_w = \frac{\pi D_e D_0}{4A_T}. \tag{1}$$

A particle feeder, based on the principle of de-agglomeration via high-frequency vibration, was utilized to offer a well-dispersed coal stream with a steady flow rate of 0.07 g/min. Coal particles, carried by N_2 (about 300 mL/min), were injected into the burner through the central jet tube with an inner diameter of 2 mm at the bottom of the burner. A digital single lens reflex (DSLR) camera was used as RGB pyrometry for temperature measurement, as well as for detecting the coal combustion behaviors. Two typical ambient temperatures, 1500 K and 1700 K, as well as three oxygen mole fraction, 0.1, 0.15, and 0.2 were chosen as the experimental conditions. The gas flow rates under different conditions are shown in Table 2.

Table 2. Gas flow rates under different conditions

T (K)	O_2	CH_4 (L/min)	O_2 (L/min)	N_2 (L/min)
1500	0.2	2.95	17.41	37.24
	0.15	2.94	14.52	40.15
	0.1	2.93	11.62	43.05
1700	0.2	3.53	18.58	35.49
	0.15	3.52	15.68	38.40
	0.1	3.51	12.78	41.31

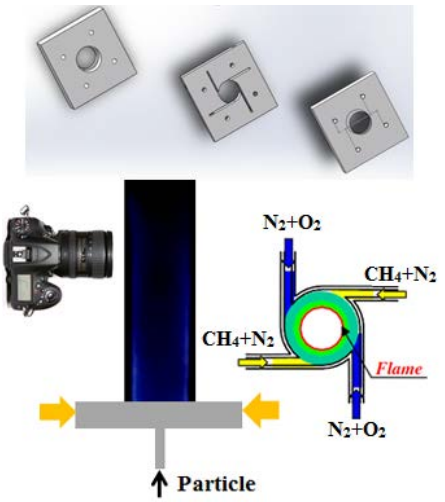

Figure 1. Schematics of the swirl burner set-up and the RGB pyrometry

3. Results and discussion

3.1 Temperature and velocity field of the tubular swirl burner

CFD simulation is carried out in a three-dimensional geometry of the realistic swirl-stabilized tubular burner configuration to predict the inner temperature and velocity profile. The simulation results, as well as the measured temperature profile by RGB pyrometry is shown in Fig 2. Fig. 2(a) illustrates that the temperature profile in the burner has a relatively uniform distribution close to the designed experimental conditions in both the radial and axial direction. Fig. 2(b) further shows that in the axial direction, the temperature remains constant in the region about 2 cm above the slit outlet. Therefore, we select the temperature-constant region as the combustion ambience for the coal particles. Fig. 2(c) indicates that the axial velocity reaches peak at the position near the tube rim. However, in the central regime of the tube, the mean axial velocity is negative, which implies a characteristic recirculation zone along the centerline as expected for the swirl structure. The time-averaged radial turbulence intensity at 5 cm above the slit

outlet is shown in Fig. 2(d). An average of about 85% relative turbulence intensity is found, exactly in the high turbulence regime (commonly recognized as >10%). In general, the tubular swirl burner can provide a uniform temperature and species ambience, as well as a high turbulent field for investigation of coal particle combustion.

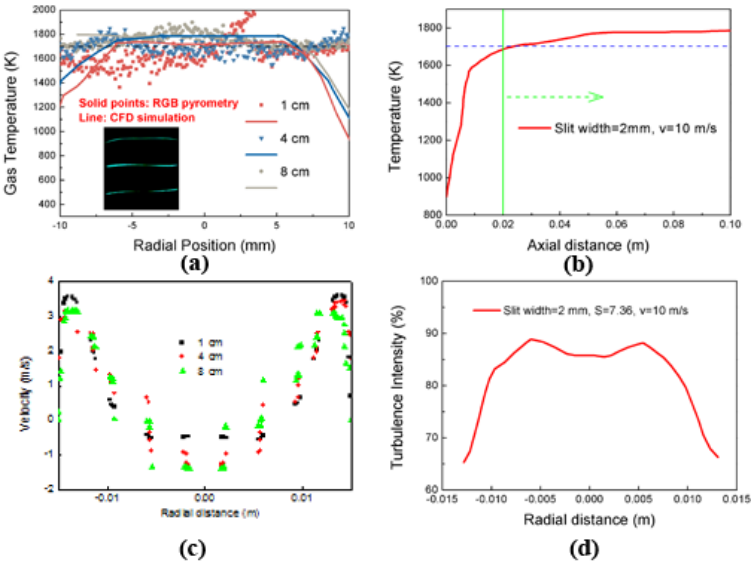

Figure 2. Temperature and velocity profile of the swirl burner

3.2 Ignition of coal particles in the swirl burner

The coal particles were injected into the high temperature ambience through the central tube. The coal combustion behavior was recorded by a digital camera. Figure 3(a) shows the recorded combustion behaviors of coal particles in different ambiences (exposure time: 1/10 s). It can be seen, in relatively high oxygen cases, the particle tracks are quite clear with bright luminosity, while as the oxygen mole fraction decreases, the luminosity intensity decreases and the particle trajectory becomes less distinct. Instead, the gas phase combustion becomes prominent in low oxygen conditions. To better quantitatively characterize the ignition process, we then select the 10% percent of the maximum intensity signal as the ignition position based on our previous study in Hencken burner [4]. It is challenging to obtain the particle residence time from experimental measurement in a 3-D framework in the tubular swirl burner, we therefore approximately get the particle residence time from CFD simulation. Figure 3(b) shows the axial position as a function of particle residence time. The ignition delay time in different ambiences can thus be determined, as shown in Fig. 3(c). It can be seen, the ignition delay time in these two high temperature conditions, 1500 K and 1700 K, quite approach in the swirl burner. Notably, when compared with the results obtained on the flat-

flame burner, the ignition delay time in the swirl burner shows little dependence on the oxygen mole fraction. Moreover, under the conditions with the same ambient temperature, different ignition behaviors are found in different burners when the oxygen mole fraction varies. In ambiences with higher oxygen mole fraction (*e.g.*, 0.15 and 0.2), the ignition delay time is rather comparable in both the laminar and turbulent ambience. While in low oxygen ambience, the ignition delay time in the swirl burner with strong turbulence is found to be much lower than that in the laminar flow field.

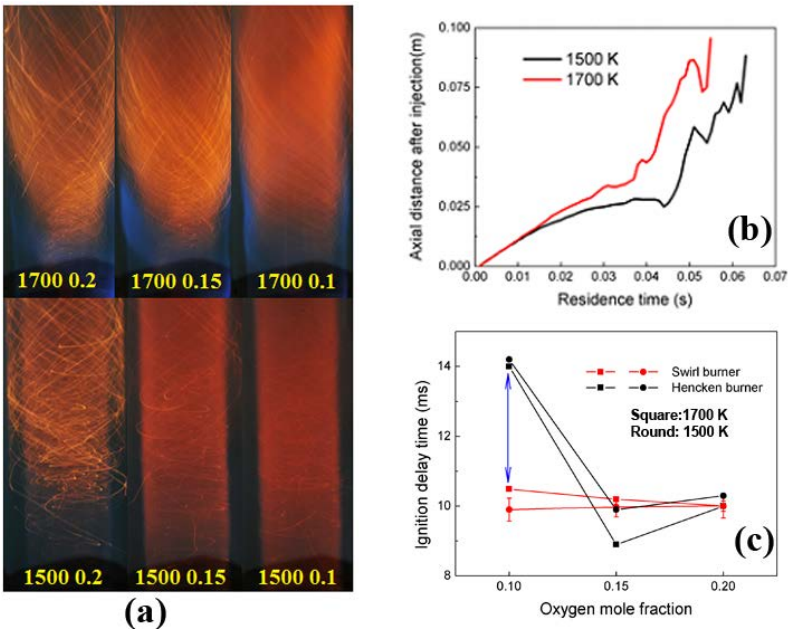

Figure 3. (a) Combustion behaviors of coal particles in the swirl burner; (b) Particle residence time as a function of axial displacement; (c) comparison of ignition delay time in different ambiences time

Based on our previous work [4], in 1500 K and 1700 K with sufficient oxygen (i.e. >0.15), the ignition process is dominated by the hetero-triggered hetero-homogeneous joint mode. The particle temperature history plays the crucial role in the ignition process. It is reasonable to believe that the ignition delay time changes little in these cases due to the similar particle temperature history in different ambiences. However, in lower oxygen ambiences (i.e. 0.1), the homogeneous ignition becomes prominent and even dominant. This is due to the bulk consumption of oxygen in the gas phase before it can reach the particle surface, which is also termed as ‘‘volatile barrier effect’’. When changing from the laminar flow ambience to the turbulent ambience, the strong turbulence enables enhanced species transport surrounding the particle surface. The released volatile can be quickly swept from the particle surface. The rapid mix of the volatile species with

the surrounding gas can accelerate the gas phase ignition. Moreover, the partial pressure of O_2 in the particle surface is also higher than that in the laminar ambience due to the reduced diffusion resistance, which also promotes the particle surface temperature increment. Therefore, compared with that in the laminar ambience, the ignition delay time of coal particles in the tubular swirl burner is much lower. Further quantitative correlation between the ignition delay time with the turbulence intensity need to be explored.

4. Conclusion

This paper makes preliminary efforts to investigate of turbulence effect on the ignition behavior of coal particles in a specially-designed tubular swirl burner. Combined with the CFD simulation, the ignition delay time of coal particles under conditions with different ambient temperature and oxygen mole fraction was estimated. Compared with the results in the flat-flame Hencken burner, the turbulence effect on the ignition delay time in different ignition modes was specially discussed.

In ambiences with higher oxygen mole fraction (*e.g.*, 0.15 and 0.2), the ignition delay time is rather comparable in both the laminar and turbulent ambience due to the similar particle temperature history. While in low oxygen ambience, the ignition delay time in the swirl burner with strong turbulence is found to be much lower than that in the laminar flow field due to the weakened volatile barrier effect.

Reference

[1] Toftegaard MB, Brix J, Jensen PA, Glarborg P, Jensen AD. ‘‘Oxy-fuel combustion of solid fuels’’.*Progress in Energy and Combustion Science*. 36(5): 581-625 (2010).

[2] Riaza J, Khatami R, Levendis YA,Álvarez , Gil MV, Pevida C, Rubiera F, Pis J J. Combustion of single biomass particles in air and in oxy-fuel conditions. *Combust. Flame* 161:1096-1108 (2014).

[3] Khatami R, Stivers C, Joshi K, Levendis YA, Sarofim AF. Combustion behavior of single particles from three different coal ranks and from sugar cane bagasse in O_2/N_2 and O_2/CO_2 atmospheres. *Combust. Flame* 159:1253-1271 (2012).

[4] Yuan Y, Li S, Li G, Wu N, Yao Q. The transition of heterogeneous–homogeneous ignitions of dispersed coal particle streams. *Combust. Flame* 161:2458–2468 (2014).

[5] Simões G, Magalhães D, Rabaçal M, Costa M. Effect of gas temperature and oxygen concentration on single particle ignition behavior of biomass fuels. *Proc. Combust. Inst* 36:2235-2242 (2017).

[6] Molina A, Shaddix CR. Ignition and devolatilization of pulverized bituminous coal particles during oxygen/carbon dioxide coal combustion. *Proc. Combust. Inst* 31:1905-1912 (2007).

A NOVEL METHOD TO COUPLE DEM AND CFD TO SIMULATE TRANSPORT PHENOMENA IN SOLID BIOMASS FUEL BEDS

F. Buß*, S. Wirtz* and V. Scherer*
buss@leat.rub.de
* Department of Energy Plant Technology, Ruhr-University Bochum,
Universitätsstraße 150, 44801 Bochum

Abstract
A new coupled DEM/CFD concept for the simulation of the transport processes in agitated fuel beds of thermally thick objects is presented. In contrast to other approaches, where a static interface between the fuel bed and the freeboard atop is predefined, the proposed method allows a continuous transition from the dense fuel bed, with a CFD mesh resolving the voids between the objects, to the freeboard, where much coarser meshes are sufficient. Momentum, heat and mass exchange at the interfaces to the fuel objects are calculated using wall functions, eliminating the requirement of shape specific correlations. Thermochemical source terms are determined by modeling conduction, drying and devolatilization within each fuel object in 3D. Local adaption of the effective viscosity accounts for different flow regimes; partial or full obstructions of the cell volumes are handled dynamically. First results show advantages of this concept especially for the simulation of agitated fuel beds.

Introduction and background

For fine fuel particles in the sub-mm range, the so called Euler-Lagrange description, where a representative number of material points associated with individual particle properties is numerically tracked trough a reacting flow field, is the method of choice. This is valid since the actual particles are small with respect to the control volumes (CFD-cells) and only marginally influencing the flow field. Additionally, the individual particles are either far apart or collision can be described in a statistic manner, since particles collide only occasionally. Here, the interaction with the fluid phase can be safely modeled in a cell averaged fashion (many particles per CFD-cell) and particles do not displace a considerable amount of fluid. For larger fuel particles like solid biomass the situation is different, because the particles (further denoted as fuel objects), typically extend over the range of several CFD-cells. In these cases, the movement of the fuel objects is more or less controlled by the mechanical interaction among the fuel objects. Under these conditions the Discrete Element Method (DEM) provides an appropriate time resolved solution of the mechanical interaction and the resulting movement of the fuel objects. A challenging aspect evolves, if the interface between the fuel bed passed by combustion air and the freeboard atop is not stationary (as in [1]). This results in regions sparsely populated and

zones highly loaded with solids, both required to coexist and move across the same computational domain. One solution is the so called "porous media" DEM/CFD approach [2], where the DEM solution is tightly coupled with the CFD-solver and continuously updates the positions and velocities of the solid material. Semi-empirical models are used (for pressure loss, heat and mass transfer) but require averaging of the source terms across the CFD-cells. Although detailed information on the thermophysical/-chemical processes inside the bulk of objects (sub-grid models, e.g. individual temperatures of objects) can be readily obtained, averaging across the CFD-cells filters the higher frequency part of this data. Unfortunately, these details strongly affect the conversion processes [6]. At this point the requirement of a finer mesh resolution (at least in the region populated by the solids) becomes obvious. In consequence, this results in CFD-cells fully covered by fuel objects where the porosity is zero, which cannot be handled by the current implementations of porous zone models. Immersed boundary methods [3] may be considered as an alternative to calculate details in the fuel bed, but reach their limits, especially when direct mechanical contact of fuel objects becomes relevant. Zambra et. al. [4] proposed a different approach, where the CFD-domain is modified "manually" at positions of solid objects to mimic their physical presence in the flow field. In the current work, this idea is coupled with the Discrete Element Method, which enables the dynamic calculation of the interaction (momentum, heat and mass transfer) of large numbers of arbitrarily moving objects, even of varying shape, within a flow field defined on a stationary mesh. This method is applied to a test case where movement of the solid fuel objects through stoking occurs during the conversion process, to demonstrate the capabilities of this approach.

Solid object definition and transfer processes at the interfaces

The fuel considered here is pelletized straw, which is approximated as a bulk of spherocylinders of constant size in the DEM simulation. This is a reasonable assumption, since the pellets contain up to 8 wt % ash and form a stable sintered matrix during conversion. The internal volume of the pellets is discretized with a tetrahedral finite volume mesh to allow simulation of the internal transport processes and to provide interface elements to the surrounding fluid phase. The CFD-domain defined in FLUENT consists of a three-dimensional finite volume mesh and requires (in areas where fuel objects may exist) a cell size smaller than the smallest object size. Since the CFD-cells and the details of their geometries are initially imported to the DEM code, the contact detection algorithm of the DEM continuously determines the CFD-cells fully contained in the object volume (blue) and the cells containing the interface of the two phases (green), as exemplified in fig 1a. A cross-sectional view of the straw pellet combustor targeted in this work is shown in fig 1.b and 1.c. The solid fuel objects (and the solid burner bowl components, blue), the fluid cells containing pellet surface elements (green) and the cells containing fluid only (red) are indicated. The fuel bed is considered either in a static state (fig 1b) or in a dynamic state when stoked (fig 1c) by vertical movement of the inner and outer cylinder.

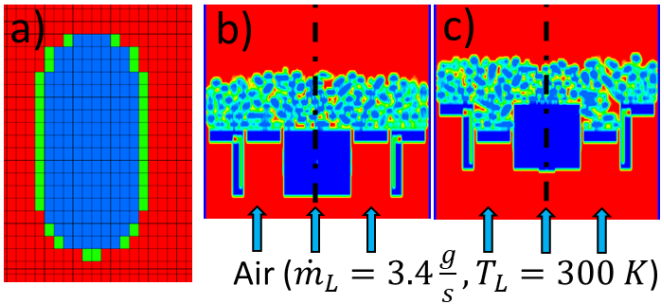

Figure1. Representation of a single particle (a), a fixed fuel bed (b) and a stoked fuel bed (c) in the CFD-Domain

Turbulent wall boundary conditions (which default to the laminar condition if the wall distance becomes small) are applied at each surface element of the respective DEM-object and collocated in the CFD-cell involved. Accordingly, $\overrightarrow{U_{Psf}}$ the velocity of the cell center closest to the respective surface element is determined from equation 1:

$$\vec{U}_{Psf} = \frac{\vec{U}_\tau \, \nu}{y_P \, {C_\mu}^{0.25} \, k^{0.5}} \cdot U^* \tag{1}$$

With the friction velocity

$$U_\tau = \vec{U}_{Fsf} - \left(\vec{U}_{Fsf} \cdot \vec{F}_n\right) \cdot \vec{F}_n \tag{2}$$

Here $\vec{U}_{Fsf}$ is the velocity vector of the closest fluid cell and $\vec{F}_n$ is the normal vector of the particle surface element. U^* and C_μ are defined as in [5]. y_P is the distance from the particle surface to the CFD-cell center, ν is the dynamic viscosity and k is the turbulent kinetic energy. Heat and mass transfer from the particle surface elements follows Reynolds analogy. For further explanations we refer to [6]. Sources for the turbulent kinetic energy and values for the turbulent dissipation rate are calculated accordingly. Finally, the CFD-cells fully covered by the fuel objects are modified such that they are no longer passed by the flow (setting the transported values and the transport coefficients accordingly). This results in an acceleration of the fluid around the solid objects and automatically creates a pressure drop satisfying momentum conservation.

Treatment of the viscous terms

In the test case considered (fig. 1b, c), the essentially laminar flow in the fuel bed and the turbulent flow field in the freeboard atop are required to be solved simultaneously and within the same domain. This requires an adaptive treatment of the viscous terms in the Navier-Stokes equations. As proposed in [7] the effective viscosity entering the equation is modified according to the local conditions (VLES), ranging from laminar in the void of the bulk to fully turbulent in the freeboard. As a first step

and in order to verify the applicability of the proposed approach, numerical results from a LES simulation of two side-by-side spheres [8] were compared to a corresponding simulation using the new approach on a coarser mesh. Figure 2 compares the time averaged velocity fields of the two methods, indicating a reasonable conformance.

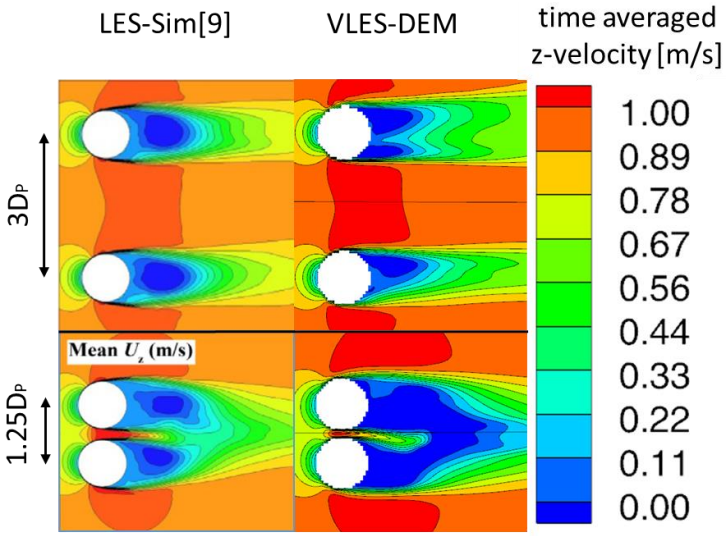

Figure2. Comparison of the LES and VLES-DEM approach

Processes within the fuel objects

As a prerequisite to describe drying and pyrolysis within the thermally thick fuel objects, the temporal development of the temperature is determined by solving Fourier's Law within the particle (simultaneously for all objects involved). Drying of the particle is modeled with a latent heat and mass sink term for each particle cell with T>373.15 K and YH2O>0.0 as in equation 5 and 6:

$$Q_{lt} = m_{Cell} c_{P,cell} (T_{Cell} - T_{vap}) \tag{5}$$

$$dm_{H2O} = \frac{Q_{lt}}{h_{lt}} \tag{6}$$

Devolatilization is modeled using a macro kinetic one-step Arrhenius behavior:

$$dm_{vol} = k_{vol} e^{\frac{-E_1}{RT}} dt \tag{7}$$

Coefficients($k_{vol} = 4.017\text{e}-7$ [kg/s] ,$E_1 = 23791$[J/kgK]) for the devolatilization rate were obtained from experiments with straw pellets (D=7 mm, moist.=7.2 [wg %], vol.=71.5 [wg%], ash=7.7 [wg%] (raw)) as performed by [9]. Char combustion is accounted for a described in [2].

Results and Discussion

Figure 3 illustrates snapshots of the results obtained from the simulation. A horizontal cross sectional view through the top layer of the fuel bed is depicted. The first row shows results from a stationary fuel bed while the second row shows the respective results when stoking is applied.

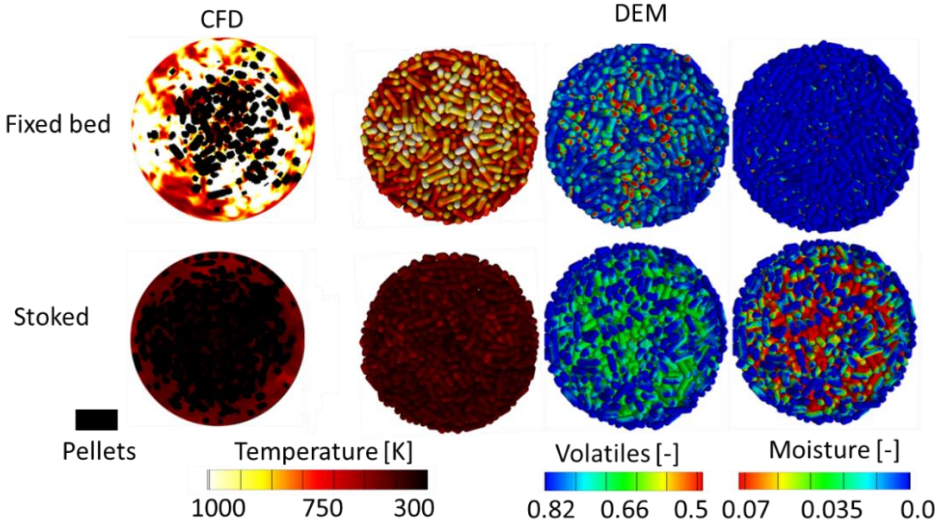

Figure3. Profiles of the fluid (T, left) and solid fuel objects (T, vol., moist., right)

The leftmost image presents the gas phase temperatures, whereas the next three images visualize pellet temperatures, the remaining volatile and the moisture content after 100 seconds of operation (still in an early conversion stage: char combustion already initiated due to radiative heat transfer by electrically heated walls (1000 K) above the fuel bed, but prior to gas flame ignition in the freeboard; passed by air of 300 K). The temperature distributions in the fixed bed show distinct local variations of the temperature level, both for the gas phase and the solid phase. If stoking is applied, temperatures are overall lower, indicating the effect of homogenization, resulting in a significant decreased conversion.

Conclusion

A new CFD/DEM approach for the simulation of stoked solid fuel beds, describing the flow through the fuel layer and the freeboard simultaneously and within one joint computational domain, has been presented. Local transfer processes within the fuel objects can be considered with the spatial resolution required, thus the approach is applicable to thermally thick and complex shaped fuel objects. Although a mesh fine enough to resolve the void space between the objects is required, the new procedure avoids tedious and error prone immersed boundary interpolations or continuous time consuming re-meshing. An approach adapting the effective viscosity to the local requirements is applied and shows promising results. The approach described can be combined with different gas phase reaction models, an aspect not discussed here.

Nomenclature

C_μ	Model constant [-]	U	Velocity [m/s]	*H2O*	Moisture
D	Diameter [mm]	Y	Mass fraction	*lt*	Latent heat
$\vec{F}_n$	Surface normal	y_C	Distance to cell center	*P*	Particle
h	Enthalpy [J/kg]	ν	Kin. viscosity[m²/s]	*sf*	Surface
k	Turb. kin. energy [m²/s²]			*Vol*	Volatile
m	Mass [kg]	subscripts		τ	Shear stress
Q	Energy [J]	*cell*	Cell value		
R	Gas constant [J/kmol K]	*F*	Fluid		

References

[1] F. Wissing, S. Wirtz, V. Scherer, Simulating municipal solid waste incineration with a DEM / CFD method – Influences of waste properties , grate and furnace design, Fuel. 206 (2017) 638–656. doi:10.1016/j.fuel.2017.06.037.

[2] J. Wiese, F. Wissing, D. Höhner, S. Wirtz, V. Scherer, U. Ley, et al., DEM / CFD modeling of the fuel conversion in a pellet stove, Fuel Process. Technol. 152 (2016) 223–239. doi:10.1016/j.fuproc.2016.06.005.

[3] R. Mittal, G. Iaccarino, Immersed boundary methods, Annu. Rev. Fluid Mech. 37 (2005) 239–261. doi:10.1146/annurev.fluid.37.061903.175743.

[4] C.E. Zambra, C. Rosales, N.O. Moraga, M. Ragazzi, Self-heating in a bioreactor : Coupling of heat and mass transfer with turbulent convection, Int. J. Heat Mass Transf. 54 (2011) 5077–5086. doi:10.1016/j.ijheatmasstransfer.2011.07.025.

[5] B.E. Launder, D.B. Spalding, The numerical Computation of Turbulent Flows, Comput. Methods Appl. Mech. Eng. 3 (1974) 269–289.

[6] ANSYS FLUENT Theory Guide, (2011) 120–126.

[7] H.A.N. Xingsi, Y.E. Taohong, C. Yiliang, Calibration of a new very large eddy simulation (VLES) methodology for turbulent fl ow simulation, Sci China-PhysMech Astron. 55 (2012) 1905–1914.

[8] S. Li, J. Yang, Q. Wang, Large eddy simulation of flow and heat transfer past two side-by-side spheres, Appl. Therm. Eng. 121 (2017) 810–819. doi:10.1016/j.applthermaleng.2017.04.065.

[9] J. Behling, *Untersuchungen zum thermischen Umsetzungsverhalten von makroskopi- schen Einzelpartikeln aus Holz*, PhD-Thesis, Bochum, 2017.

Acknowledgement

The IGF-Project 19114 N of the DVV e. V. was funded by the German Federation of Industrial Research Associations (AiF) on behalf of the German Federal Ministry of Economics and Energy.

Thermoanalytical and XPS surface characterization of oxidized chars

F. Cerciello*, O. Senneca*, A. Coppola, P. Salatino****
francesca.cerciello@unina.it
*Istituto di Ricerche sulla Combustione, C.N.R., Naples, Italy
**DICMAPI Università degli Studi di Napoli Federico II, Napoli, Italy

Abstract
The chemical nature of the carbon–oxygen complexes on the surface of solid carbons was investigated with reference to a char from medium-rank coal (South African). Chars have been pre-oxidized in air at temperature 573 K ≤ T ≤1073 K. The carbon oxides that populate the char surface and their evolution have then been investigated combining thermal analysis with core-level XPS Spectra, acquired at high-resolution using Synchrotron radiation. TPDs show that the amount of surface oxides is maximum after exposure to oxygen at 723 K, in correspondence to a carbon conversion degree of ≈ 20%. It decreases for higher temperature of oxidation and carbon burnoff. XPS show formation of epoxy functionalities at low temperature and their evolution into more stable oxides (carbonyl and ether-hydroxy) afterwords. The relative abundance of carbonyl/epoxy and ether-hydroxyl/epoxy on the carbon surface is in fact maximum for an oxidation temperature of 723 K and carbon burnoff of ≈ 20%. Results are analysed in the light of the semi-lumped kinetic models of carbon oxidation with a focus on the role and nature of surface oxides as intermediates in carbon gasification.

1. Introduction

The mechanism of carbon oxidation is a subject that, after extensive literature published [1-11], still raises great interest in a variety of research fields such as carbon combustion, oxidation of carbon-based materials, self-oxidation and safety issues in storage of carbons. Various reaction mechanisms and kinetic models have been proposed to explain the characteristics of consumption of O_2, and formation of oxidation products in the gas and solid phases [1,4,6].
In the four-step mechanism proposed by Haynes [6] (eq.1), oxygen is firstly chemisorbed (non dissociatively) on a free carbon active site forming oxygen-carbon complexes (step 1) which can further on be released as CO and CO_2 (step 4).
The mechanism introduces the so called "switch over reaction" which describes the evolution of *C-O* complex from a less stable to a more stable one under the action of molecular oxygen (step 2). Alternatively, metastable oxides can be rearranged or isomerized into more energetically favourable forms (step 3). In the Haynes' scheme all the reaction steps produce CO and CO_2,

$C_f^* + O_2 \xrightarrow{1} C(O)^{\#}$ formation of '*metastable*' surface oxides

$$C(O)^{\#}+O_2 \xrightarrow{2} C(O)+CO,CO_2 \quad \text{oxygen-driven complex switch-over}$$
$$C(O)^{\#} \xrightarrow{3} C(O)+CO,CO_2 \quad \text{rearrangement of } C(O)^{\#} \text{ into stable complexes}$$
$$C(O) \xrightarrow{4} C_f^{*}+CO,CO_2 \quad \text{desorption into CO,CO}_2 \qquad (1)$$

Larciprete et al. [7-8] employed high resolution XPS spectroscopy (HR-XPS) with ab initio calculations and found that in the early stages of oxidation, epoxy is the dominant surface species, while ethers and C=O bonds become more abundant in the later stages of oxidation. Furthermore, they suggested that aligned epoxy groups tend to unzip into ethers due to the cumulative cleaving force exerted on the underlying C–C bonds. They found also that ether-epoxy pairs attract the diffusing epoxides and convert in lactone-ether pairs promoting the desorption of CO-CO_2.
The role of epoxy interaction with surface oxides has been pointed out also by Montoya at al. [9] investigating the effect of neighbouring surface oxygen groups on the desorption of the CO molecule from carbonyl. They found different possible and energetically feasible CO desorption pathways as a consequence of surface oxides interactions.
Recently, Senneca et al. [10-11] underlined the key role of epoxy groups as metastable intermediates in the heterogeneous oxidation of coal, and investigated the thermicity of reactions occurring during oxidation (600-800 K) and during TPD experiments of char coal. Thermoanalytical methods (DTG, DSC, TPD) were used to identify the key reactive steps (chemisorption, structural rearrangement and switch-over of surface oxides, desorption) and their energetics.
In the present study, temperature programmed desorption experiments are supported by X-ray photoelectron spectroscopy (XPS) of oxidized char samples in order to highlight the distribution of functional groups formed upon coal char oxidation at different temperatures.

2. Experimental description

2.1 Oxidation and Desorption treatments in Thermobalance

South African char was used for the present study. Char samples were subjected to pre-oxidation treatments at 573 K $\leq$ T $\leq$973 K for times ranging from 10 to 45 minutes and Temperature Programmed Desorption (TPD) with analysis of evolved gas. Experiments were performed using NETSCH 409 CD apparatus connected with a NDIR CO and CO_2 analyser (ABBAO2020 Uras 14). In the pre-oxidation step the sample (20 mg) was heated to T_{ox} at the heating rate of 20 K/min in N_2 (250 mL/min) and held at this temperature for 5 min before switch in a flow of synthetic air (250 mL/min) for a time t_{ox}. The TPD experiment was performed heating the sample from up 473 K to 1573 K in nitrogen at the heating rate of 20 K/min and was held at temperature for 40 min. TPD gas evolution was worked out to obtain the CO-CO_2 released as a function of time/temperature. The amount of CO and CO_2 released has been normalized for $w_{0.}$

2.1 Samples preparation for XPS

Oxidation treatments of char in the form of slabs were performed by heating up in electric oven under a flux of air to the temperatures 573 K ≤ T_{ox} ≤ 1073 K. The treatments were carried out for t_{ox} ranging from 1 to 120 min. For comparison, isothermal combustion tests were carried out at the same combustion temperature T_{ox}. In this case, the sample was loaded in the TGA (Netzsch STA 409CD) in and heated up to T_{ox} in a flow of nitrogen (200 mL/min) at the heating rate of 20 K/min. Once the desidered temperature was reached, the gas was switched over from nitrogen to air and the sample was held at T_{ox} for time t_{ox}. This procedure allows to estimate the carbon burnoff level.

2.2 Spectra acquisition of oxidized char samples

The XPS experiments were performed in the ultra high vacuum chamber (UHV) (base pressure 8×10^{-11} mbar) of the SuperESCA beamline at the Elettra synchrotron radiation facility (Trieste, Italy). Samples were in the form of slab of about 6 mm of diameter.

C1s and *O1s* core level spectra were measured at photon energies of 400 and 650 eV, with energy resolutions of 80 and 150 meV, respectively. For each spectrum the binding energy position was calibrated by measuring the Fermi level of the Au reference sample.

To separate the contribution to the intensity of the inelastically scattered electrons and make a comparison of the individual spectra possible, the Shirley background was removed from each of them. Background subtraction was performed with the software *IGOR Pro* version 6.12A. Spectra were fitted, after background removal, with Doniach−Sunjic function convoluted with Gaussians [12]. Band assignment was carried out following the procedure used in [10-11].

3. Results

The following graph in Fig.1A shows as example the deconvolution of the *O1s* spectrum of the char oxidized at 573K. To highlight the influence of oxidation temperature on the nature of functional groups, the bar graph histogram in Fig.2A reports the calculated relative intensities of the components of the *O1s* according to eq.2. The intensity of each component of the *O1s* spectrum has been normalized for the Oxygen/Carbon content of the samples as detected by the XPS measurements. This procedure allows to take into account the different oxidation degrees. The qualitative analysis of the *O1s* spectra was carried out to better visualize and interpret the evolution of the carbon-oxygen functionalities during the oxidation process.

$$\%Intensity\ O_i = \frac{Area_{\ o_i}}{\sum_i Area_{o_i}} \cdot \left(\frac{\sum_i Area_{o_i}}{\sum_i Area_{Ci}}\right) .100;\ \frac{\sum_i Area_{o_i}}{\sum_i Area_{C_i}} \cong \frac{[O]}{[C]} \qquad (2)$$

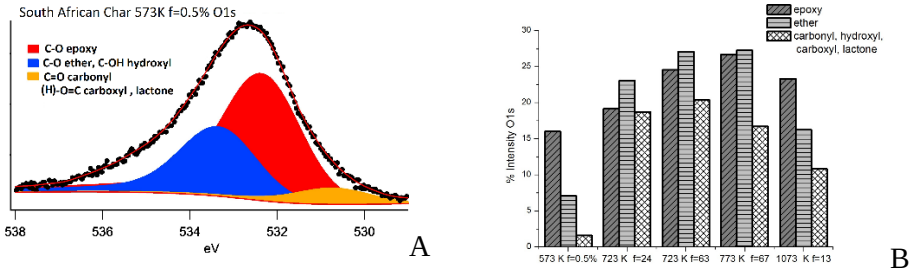

Figure 1. A) Oxygen functionalities obtained by deconvolution of O1s spectrum of char samples oxidized at 573 K. B) Intensities of the components of the *O1s* spectra of the different samples. The carbon burnoff level *%f* is also reported.

As can be seen from the *O1s* spectrum of the char oxidized at 573K, the main component, at about 532.2 eV, is due to epoxy groups. It follows that more than 15% of the oxygen present on the char surface is in the form of epoxides. The remained oxygen forms ethers-hydroxyls (7%), and carbonyls (2%). Their components are at 533.4 and 530.8 eV respectively.
Upon oxidation at 723-773 K the *O1s* spectrum clearly shows that extensive uptake of oxygen is taking place. In fact, a sharp rise in the intensity of the *O1s* signal is evident. An increase in the ratio of the intensity for all the species is observed. Reasonably, rearrangement of epoxides towards ether and carbonyl groups is the predominant event taking place on the surface of this sample. However, at 773 K, the *O1s* spectrum does not show further chemisorption of oxygen compared oxidation at 723 K. In particular the peak of ethers (27%) almost equals that of epoxy component (26%) with a decrease of the component at 530.8 eV (17%). Results suggest that structural rearrangement of epoxides towards ethers and carbonyls upon extensive oxidation promotes also the desorption of labile species. Upon oxidation at 1073 K the *O1s* spectrum still reveals the existence of the main component with epoxy group as predominant species, followed by ether and carbonyl component. Reasonably, due to the high temperature, desorption of labile species is the predominant event taking place on the surface of this sample.

Fig.2A-B show the ratio of ether-hydroxyl (533.4 eV) /epoxy (532 eV) and carbonyl-carboxyl (530.8 eV) /epoxy (532 eV) estimated from *O1s* spectra deconvolution. Fig.2C reports the total amount of gas released $(wCO+CO_2)/w_0$ in the TPD experiments as function of pre-oxidation temperature. Notably the value of carbon conversion reached on the pre-oxidation step is also reported.

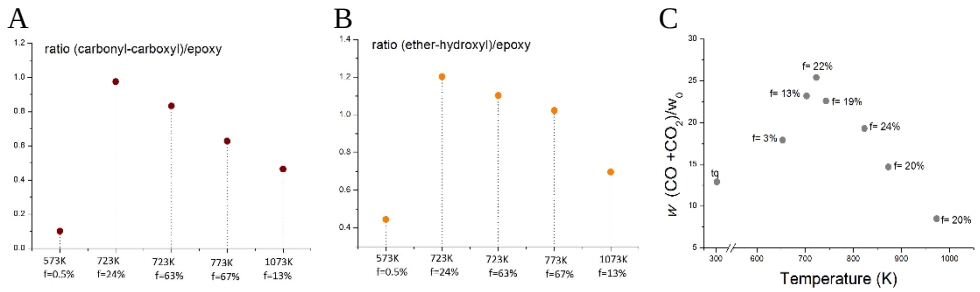

Figure 2. A) Ratio of (ether-hydroxyl)/epoxy and B) ratio of (carbonyl-carboxyl) /epoxy estimated from *O1s* spectra deconvolution. C) Gas released in TPDs as function of pre-oxidation temperature of char samples. The carbon burnoff level *%f* is also reported.

The plot in Fig 2C shows a progressive increase of surface oxide complexes with temperature of oxidation, up to 723 K, and with conversion, up to ≈ 20% In the experiments at higher oxidation temperature roughly same carbon burnoff level is reached but the percentage of total gas released decreases. Notably, similar results have been suggested by the plots in Fig 2A-B. In fact, the plots show an increasing ratio of (ether-hydroxyl)/epoxy and (carbonyl-carboxyl)/epoxy from 573 to 723 K (reaching carbon burnoff of 24%), followed by a decrease for higher carbon burnoff and high temperature. This result confirms the high interaction between carbonyl/epoxy and ether-hydroxyl/epoxy groups upon oxidation at mild temperature and could explain the origin but also the different percentage of CO/CO_2 in TPDs.

4. Discussion and Conclusion

Correlating thermoanalytical and structural (XPS) characterization, suggests the effect of temperature of oxidation on the nature of the carbon–oxygen complexes. In particular, deconvolution of the *O1s* spectra provides valuable clues on epoxidation as being the prevalent type of oxygen functionalization when oxidation is performed at low temperature (early stage of oxidation). TPDs show that the amount of surface oxides is maximum after exposure to oxygen at 723 K, in correspondence to a carbon conversion degree of ≈ 20%. At the same time, *O1s* spectra show a more pronounced increase in the number of ether and carbonyl bonds. Experimental results are in substantial agreement with semiglobal reaction scheme that was assumed as the reference [11] and provide additional insight into the role of the individual reaction steps. Altogether TPD and XPS results suggest that the "metastable" oxides may prevailingly consist of epoxy functionalities, whereas the more stable oxides would be composed by ether and carbonyl moieties. At higher temperatures, and upon extensive oxidation (in particular: T≈ 723 K, $f \approx 20$), "metastable" surface oxides (epoxy) evolve into more stable carbon-oxygen complexes (ether, carbonyl). Results underline the importance of evolution of the "metastable" oxides into more stable

oxides by complex-switch-over driven by molecular oxygen, and their interaction as being the reason of the enhanced CO-CO_2 released.

References

[1] Hurt, R.H., Calo, J.M., "Semi-global intrinsic kinetics for char combustion modelling", *Combust. Flame.* 125:1138-1149 (2001).

[2] Du, Z., Sarofim, A.F., Longwell, J.P., "Kinetic Measurement and Modeling of Carbon Oxidation", *Energy Fuels.* 5:214-221 (1991).

[3] Wang, H., Dlugogorski, B.Z., Kennedy, E.M., "Analysis of the mechanism of the low-temperature oxidation of coal", *Combust. Flam.* 134:107–117 (2003).

[4] Wang, H., Dlugogorski, B.Z., Kennedy, E.M., "Coal oxidation at low temperatures: oxygen consumption, oxidation products, reaction mechanism and kinetic modelling". *Prog. Energy Combust. Sci.* 29:487–513 (2003).

[5] Zhuang, Q., Kyotani, T., Tomita, A., "Dynamics of Surface Oxygen Complexes during Carbon Gasification with Oxygen". *Energy Fuels* 9:630-634 (1995).

[6] Lear, A.E., Brown, T.C., Haynes, B.S., "Formation of metastable oxide complexes during the oxidation of carbons at low temperatures". *Twenty-Third Symposium (International) on Combustion/The Combustion Institute* 23:1191–1197 (1991).

[7] Larciprete, R., Fabris, S., Sun, T., Lacovig, P., Baraldi, A., Lizzit, S., "Dual Path Mechanism in the Thermal Reduction of Graphene Oxide". *J. Am. Chem. Soc.* 133:17315–17321 (2011).

[8] Larciprete, R., Lacovig, P., Gardonio, S., Baraldi, A., Lizzit, S., "Atomic Oxygen on Graphite: Chemical Characterization and Thermal Reduction". *J. Phys. Chem.* 116:9900−9908 (2012).

[9] Montoya, A., Truong, T., Mondragon, F., Truong, T.N., "CO Desorption from Oxygen Species on Carbonaceous Surface: 1. Effects of the Local Structure of the Active Site and the Surface Coverage". *J. Phys. Chem. A* 105:6757–6764 (2001).

[10] Levi, G., Senneca, O., Causà, M., Salatino, P., Lacovig, P., Lizzit, S., "Probing the chemical nature of surface oxides during coal char oxidation by high-resolution XPS". *Carbon* 90:181–196 (2015).

[11] Levi, G., Causà, M., Lacovig, P., Salatino, P., Senneca, O., "Mechanism and thermochemistry of coal char oxidation and desorption of surface oxides". *Energy Fuels* 31:2308–2316 (2017).

[12] Doniach, S., Šunjić, M, "Many-electron singularity in X-ray photoemission and X-ray line spectra from metals". *J. Phys. C: Solid State Phys.* 3:285-291 (1970).

EXPERIMENTAL AND NUMERICAL STUDY OF WOODCHIPS COMBUSTION IN AN UNDERFEED STOKER BOILER

G. Caposciutti*, S. Patronelli, F. Barontini**, M. Antonelli*, U. Desideri*, L. Tognotti**, C. Galletti****
chiara.galletti@unipi.it
*Dipartimento di Ingegneria dell'Energia, dei Sistemi, del Territorio e delle Costruzioni, Università di Pisa, Università di Pisa, Italy
**Dipartimento di Ingegneria Civile e Industriale, Università di Pisa Italy

Abstract
Temperature and gas composition measurements are performed in different locations above the fire pit of a small fixed bed boiler fed with biomass woodchips. These experimental data show a large spatial variation of the values, thus suggesting that the any biomass bed model, to be eventually coupled with the freeboard numerical model, should be able to take into account such variability. Hence a numerical model of the boiler is developed by treating the biomass bed region as porous domain with sources and sinks of energy and chemical species.

Introduction
Biomass is an attractive alternative to fossil fuels for energy production because it is a widely available, renewable and CO_2-neutral energy source. Among the available technologies, small boilers are the widespread option for distributed generation; however, the design of these systems should be improved to increase the process sustainability by rising efficiency and reducing pollutant emissions. For instance, it has been shown how the process performances are affected strongly by the thermal input, air distribution and excess (e.g. [1] [2]).
Logically this goal needs a comprehensive investigation about the effect of boiler configuration and operating condition on combustion efficiency and emissions. In this scenario, computational fluid dynamics (CFD) may represent a useful design and optimization tool. However, the numerical modeling of biomass boilers is computationally very demanding and affected by many uncertainties because the presence of an unsteady multiphase turbulent combustion process. Indeed, the granular biomass phase is generally not included into the CFD simulation, which instead models just the gas phase in the combustion chamber (freeboard). The biomass bed is taken into account by means of proper boundary conditions to the CFD model, i.e. set to the interface between the biomass bed and the freeboard. Such boundary conditions may be obtained empirically or by using off-line bed models. The latter assimilate the biomass bed to a single of a series of interconnected perfectly stirred reactors (PSR), in which biomass conversion processes (drying, devolatilization and char oxidation) occur [3][4]. However. a recent work has shown

how this approach is affected by high uncertainty related to the estimation of the inlet turbulence conditions which determine the turbulent mixing of volatile species and thus reaction rates [5].
In this work, temperature and chemical species are measured in different locations above the fire pit of a small fixed bed boiler fed with woodchips. Then, a numerical model is proposed by treating the biomass bed as a porous domain with sources and sinks of energy and chemical species. With this approach, the distribution of primary air can be well taken into account.

Experimental setup

The underfeed-stoker boiler has a nominal power of 140 kW and is sited at the Biomass to Energy Research Center (CRIBE) of the University of Pisa. The system was modified to fully operate with biomass, which is fed by means of a screw conveyor. Primary air is injected through 68 rectangular nozzles placed laterally with respect to the fire pit, while secondary air is fed through a manifold constituted by 7 circular pipes as shown in Figure 1a. The boiler operates slightly under pressure (20 Pa). Flue gases pass through a gas to oil heat exchanger that ultimately provides hat to CRIBE facilities [2].
The boiler was equipped with a measuring system to monitor: flue gas composition (O_2, CO, CO_2, NOx), inlet air temperature as well as the flue gas and oil temperatures upstream and downstream of the heat exchanger. The thermocouple for the flue gas upstream of the heat exchanger was equipped with a shielded cap to minimize the radiative effects [2]. Moreover, temperature and gas composition are acquired at different locations above the fire pit. The idea is to characterize the release of volatiles products. To this purpose, 6 thermocouples were placed above the biomass bed in the positions indicated in Figure 1b, i.e., 3 on the central line (L) and 3 on the lateral side (H). In addition, a movable steel suction probe allows sampling the gas above the bed. Particularly, the probe is L-shaped, and can both slide and rotate to reach all desired locations as depicted in Figure 1. The sampled gases are analyzed by means of a micro-gas chromatograph and a FTIR to provide CO_2, CO, H_2, CH_4, C_2H_6, C_2H_4 and C_2H_2 [2].
The experimental campaigns were performed by using different thermal inputs, air excesses, secondary to primary air flow ratios, i.e. λ, as well as types of biomass, in order to investigate the effect of operating conditions on the boiler performance. In this work, the test with poplar woodchips with average diameter d_p =13 mm is considered. The biomass ultimate and proximate analyses are reported in Table 1. The total and primary air flow rates were 0.10 and 0.065 kg/s respectively (λ = 0.6), whereas the biomass flow rate was estimated to be approximately 0.033 kg/s.

Table 1. Ultimate and proximate analysis of poplar woodchips.

C	H	O	N	Moisture	VM	FC	Ash	LHV
[% daf]	[% daf]	[% daf]	[% daf]	[%]	[% dry]	[% dry]	[% dry]	[MJ/kg]
49.84	6.06	43.63	0.47	9.84	84.89	13.33	1.78	18.41

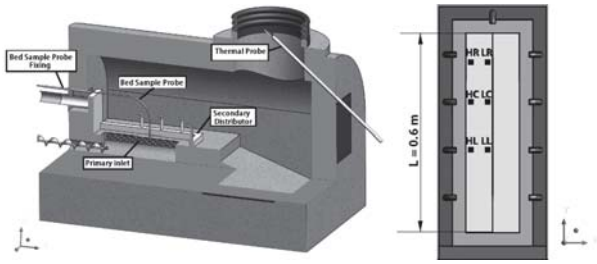

Figure 1. Scheme of (a) boiler and (b) fire pit with sampling locations.

Numerical Model

The numerical model considers a single-phase turbulent reactive flow in two different domains: a fluid domain for the freeboard and a porous domain for the biomass bed. Both domains are discretized through fully structured grid (800k and 10k cells, respectively). The freeboard grid was refined near the nozzles and generated by O-grid (Figure 2). Steady state RANS equations were solved with ANSYS Fluent 17 by means of a pressure-based solver, second upwind interpolation and SIMPLE algorithm for pressure-velocity coupling [6].

Two approaches were used to estimate the volatiles evolution in the freeboard. In approach #1, volatiles were treated as a pseudo-component, whose formula was derived from the biomass proximate and ultimate analysis. In this case the volatile oxidation was considered with a two-step global reaction scheme, assuming infinitely fast chemistry through the Eddy Dissipation Model.

$$C_{1.02}H_{2.04}O_{0.96}N_{0.00113} + 0.53\ O_2 \rightarrow 1.02\ CO + 1.02\ H_2O + 0.0056\ N_2 \quad (1)$$

$$CO + 0.5\ O_2 \rightarrow CO_2 \quad (2)$$

The approach #2, instead, follows the work of Neves et al. [7] and characterizes the devolatilization products by means of seven volatile species (tar, H_2, H_2O, CO, CO_2, CH_4 and other light hydrocarbons) and dry ash-free char. The composition is estimated through semi-empirical correlations [7]. In this case, the turbulence-chemistry interaction is handled with the Eddy Dissipation Concept (EDC). Due to the large computational efforts, the DRM19 reduced mechanism was used instead of a detailed one; to do this, tar was represented as CH_2O.

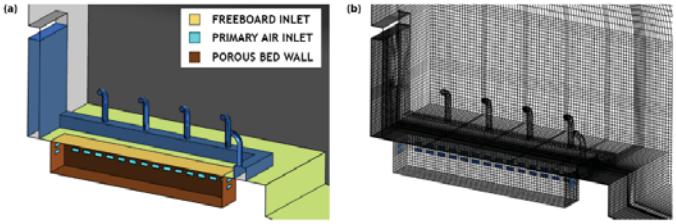

Figure 2: Detailed of porous bed with primary air inlet (a) and grid (b).

Reynolds stresses were determined by means of the k-ε model, while the radiative heat transfer equation was solved with the P1 model and WSGG method use.
The biomass bed is modeled as a porous media, thus estimating pressure drops by means of the Ergun equation:

$$\frac{|\Delta P|}{l} = \frac{1}{\alpha} u_\infty + \frac{1}{2} \rho C_2 {u_\infty}^2 \quad (3)$$

with $\alpha = \frac{{d_p}^2}{150} \frac{\epsilon^3}{(1-\epsilon)^2}$ and $C_2 = \frac{3.5}{d_p} \frac{(1-\epsilon)}{\epsilon^3}$, where ϵ is the void fraction ($\epsilon = 0.5$) and d_p is the average particle diameter.
Volumetric sources and sinks of energy and chemical species were then assigned to the porous domain though a User Define Function, in order to account for drying, devolatilization and char oxidation. Such sources/sinks were estimated from energy and mass balances; basically, there are positive sources of volatiles, H_2O, CO, CO_2 and energy, and a negative source (sink) for O_2, that is consumed during char oxidation. The energy balance takes into account the radiative heat transfer with the freeboard and the boiler walls; such transfer was determined through an iterative procedure [6]. The sources/sinks were assigned non-uniformly along the porous volume because it was observed that the screw conveyor is unable to push the biomass up to the opposite edge of the fire pit. Hence full sources/sinks were set until 85% of fire pit length, while they linearly go to zero in the remaining distance.

Results

The distribution of temperature in different longitudinal sections of the boiler and in the longitudinal mid-plane are shown in Figure 3 and Figure 4, respectively, as predicted with #1 and #2 approaches. The former well matches the outlet experimental temperature, which is 687 K, whereas the predicted one (independently on the void fraction) is 693 K. The agreement concerning major chemical species is also good, e.g. measured and predicted O_2 mass fractions in the flue gas are 0.18 and 0.20, respectively. This is satisfactory, especially considering the many uncertainties (e.g. biomass flow rate) which affect the model.

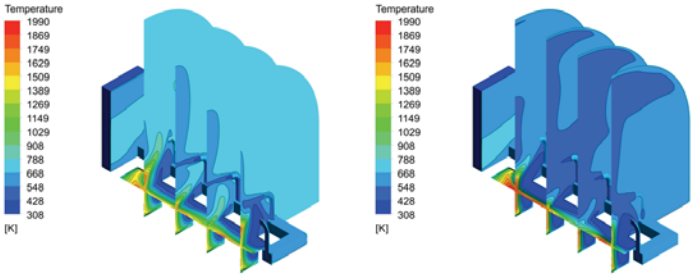

(a) (b)

Figure 3: Distribution of temperature in transversal cross section of the boiler predicted for (a) approach #1 and (b) approach #2.

The effect of secondary air injection on the resulting flame above the bed is well evident. The secondary air, on one hand, increases turbulent mixing and hence improves reactions; however, on the other hand, it carries a cold flow. As a result, the temperature distribution along the longitudinal boiler mid-plane (Figure 4) shows the presence of a cold zone above the fuel bed, approximately at the center, while high temperature zones are pushed toward the fuel bed edges. Approach #2 shows lower temperatures, probably due to the strong assumption in the representation of tar. The comparison between experimental and predicted temperature measurements above the fire pit for different locations is provided in Figure 5 for the two models. The first two temperature near the center (Figure 5a) are reasonably predicted by approach #1, whereas the last temperature is strongly overestimated by both models; as mentioned above this may be partly imputed to fact that the screw conveyor was unable to well distribute the biomass up to the opposite edge of the fire pit. Lateral temperatures (Figure 5b) indicate an underestimation of measurements, suggesting probably an erroneous estimation of the porous domain parameters. As for chemical species, the matching between experiments and predictions should be improved. The comparison between measured and predicted CO_2 is provided in Figure 7 and indicates a large underestimation with both approaches in positions near the center.

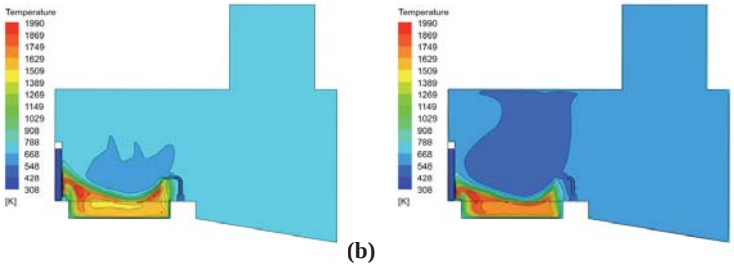

(a) **(b)**

Figure 4: Distribution of temperature in the boiler longitudinal mid-plane predicted for (a) approach #1 and (b) approach #2.

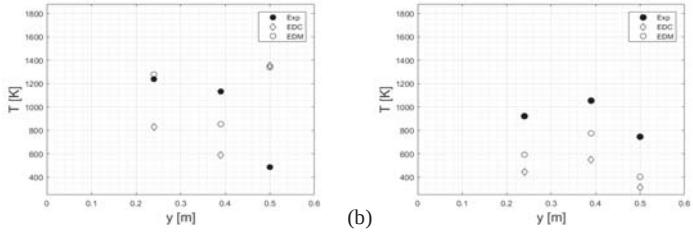

(a) (b)

Figure 6: Comparison between experimental and predicted temperatures: (a) HL, HC, HR (b) LL, LC, LR.

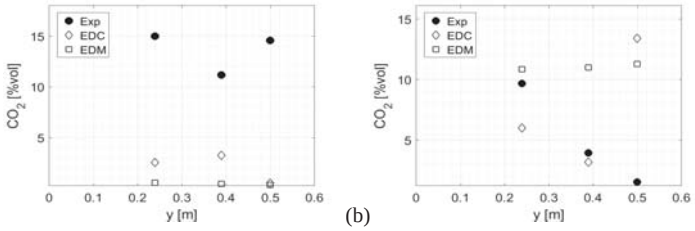

Figure 7: Comparison between experimental and predicted CO_2 molar fractions: (a) HL, HC, HR (b) LL, LC, LR.

Conclusion

A large variation of temperature and chemical species was measured just above the fire pit of a small fixed bed boiler fed with woodchips. This suggests that biomass bed models based on a single or a series of PSR are either inadequate or difficult to be set. Instead, representing the biomass bed with a porous region with source/sinks of energy and chemical species may involve reasonable computational resources still taking into account the flow distribution induced by the primary air. A preliminary reduced kinetic model was implemented, however further efforts are needed to better represent volatiles species and incorporate proper oxidation schemes.

References

[1] Wiinikka, H., Gebart, R., "The influence of air distribution rate on particle emissions in fxed bed combustion of biomass", *Comb. Sci. Technol.* 177:1747-1766 (2005).

[2] Caposciutti, G. Barontini, F. Antonelli, M. Tognotti, L., Desideri, U., "Experimental investigation on the air excess and air displacement influence on early stage and complete combustion gaseous emissions of a small scale fixed bed biomass boiler", *Appl. Energy* 216, 576–587 (2018).

[3] Yin, C., Rosendahl, L.S., Kær, K., Clausen, S., Hvid, S.L., Hille, T., "Mathematical Modeling and Experimental Study of Biomass Combustion in a Thermal 108 MW Grate-Fired Boiler", *Energy Fuels* 22:1380–1390 (2008).

[4] Galletti, C., Giomo, V., Giorgetti, S., Leoni, P., Tognotti, L., "Biomass furnace for externally fired gas turbine: Development and validation of the numerical model", *Appl. Therm. Eng.* 96,: 372–384 (2016).

[5] Patronelli, S., Caposciutti, G., Barontini, F., Galletti, C., Antonelli, M., Desideri, U., Tognotti, L., "Experimental and numerical investigation of a small-scale fixed-bed biomass boiler", *Chem. Eng. Trans*. 57:187-192 (2017).

[6] S. Patronelli, Antonelli, M., Tognotti, L., Galletti, C., "Combustion of wood-chips in a small-scale fixed-bed boiler: Validation of the numerical model through in-flame measurements", *Fuel* 221:128–137 (2018).

[7] Neves, D., Thunman, H., Matos A., Tarelho, L., Gómez-Barea, A., "Characterization and prediction of biomass pyrolysis products", *Prog. Energy Combust. Sci*. 37:611–630 (2011).

Fluidized Bed Combustion of Pelletized Sewage Sludge in a Pilot Scale Reactor

A. Cammarota, F. Cammarota, R. Chirone, G. Ruoppolo, R. Solimene, M. Urciuolo
m.urciuolo@irc.cnr.it
Istituto di Ricerche sulla Combustione Consiglio Nazionale delle Ricerche, Piazzale V. Tecchio 80, 80125 Napoli (ITALY)

Abstract
Thermal conversion of sewage sludge is a viable route to reduce the amount of waste to dispose. A pilot scale bubbling fluidized bed combustor (FBC370) was used to investigate the combustion of dried and pelletized sewage sludge particles. An experimental campaign was carried out to study gaseous and particulate emissions and stable thermal regimes during the combustion of dried and pelletized sewage sludge in the thermal power ranging from 45 to 65 kW_{th}. The results show that, under the experimental conditions investigated, a stable and efficient combustion behavior was obtained in terms of low emissions of unburnt species, but a train of cleaning processes is necessary to reduce gaseous and particulate emissions. A two stage de-dusting system for the capture of fine and ultrafine particles and the proper units for the abatement of the NOx, SO_2 and HCl produced in high concentrations are needed. The temperature profile in the post-combustion zone and stable combustion conditions are critical for the formation of dioxins.

Introduction

Thermal conversion of sewage sludge derived from the treatment of urban wastewaters remains the most viable technological pathway to reduce the huge produced volumes of this waste and to overcame the severe legal restrictions of other disposal options [1-3]. Fluidized bed combustion stems out as one of the most feasible technology to dispose sewage sludge, entailing large reduction of the sludge volume and thermal destruction of the toxic organic constituents [4-6]. However, the low calorific value, the possible generation of pollutants (e.g., based on sulphur, chlorine, nitrogen) and the complex management of the produced bottom and fly ash enables critical the pretreatment of the native material. Drying and palletization of sewage sludge could be beneficial to reduce ash management issues, to mitigate particulate emissions and to improve the axial and transversal distribution of heat release along the combustor [7,8]. A pilot scale bubbling fluidized bed combustor (FBC370) was used to investigate the combustion of dried and pelletized sewage sludge particles. An experimental campaign was carried out using the FBC370 to study gaseous and particulate emissions and stable thermal regimes during the combustion of dried and pelletized sewage sludge.

Experimental

Fig. 1 shows the schematic representation of the pilot-scale FBC used for the experimental campaign of combustion of pelletized sludge, details of the plant are given elsewhere [9].

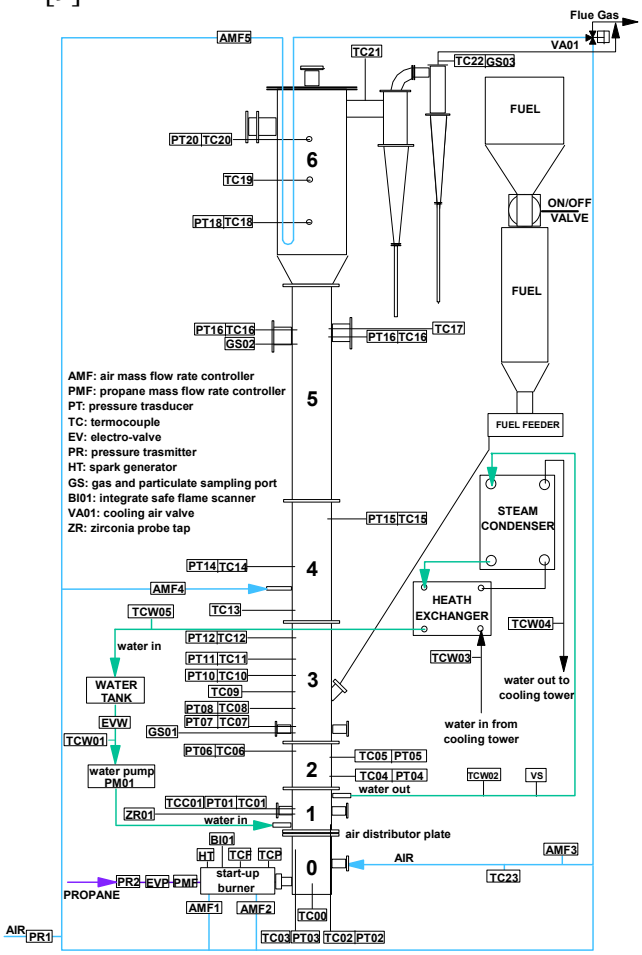

Figure 1. Experimental apparatus

The AISI 310 stainless steel fluidization column had a circular section (370 mm ID) for almost all its height (5.05 m) whereas the upper part of freeboard was characterized by ID of 700 mm and height of 1.85 m (total height of 6.9 m). The reactor is equipped with several access ports for measurements of temperature, pressure, and gas concentration along the axis and with two cyclones in series having medium and high efficiency, in sequence, for flue gas de-dusting and for particulate characterization. A probe was installed at the exit of the second cyclone for gas sampling. An on-line gas analyzer measurement system consisting of a set of ABB

AO2020 gas analyzers is used to monitor the concentration of O_2, CO, CO_2, SO_2, NO, NO_2 and TOC. A data acquisition and control unit is used to process signals from the pressure transducers, the thermocouples and the on-line gas analyzers. Particle size distribution of the elutriated fine particles collected by the two cyclones was evaluated by means of a laser light scattering particle size analyzer, Malvern Instruments Mastersizer 2000. Proximate and ultimate analysis of the fuel and the elutriated fine have been carried out by LECO CHN 628, LECO CS144 and LECO TG701.The inorganic elemental analysis of bed material before and after combustion tests was accomplished by ICP-MS using an Agilent 7500 CE instrument after dissolving the fuel samples by means of microwave-assisted acid digestion according to US-EPA 3051 and 3052 methods. Specific sampling lines were devoted to collect heavy metals, dioxins and ultrafine particles.

Figure 2. Picture of pelletized sludge pellets

Pelletized sewage sludge particles and their main properties are reported in figure 2 and Table 1, respectively. Silica sand in the size range 0.8–1.2 mm was used as bed material and initial bed inventory was kept constant at 40 kg.

Table 1. Main properties of the sludge pellets

Proximate analysis, %$_{wt,\ ar}$		*Metals composition, mg/kg$_{ar}$*			
Moisture	12.1	Al	6932	Na	428
Volatile matter	57.4	B	55	Ni	68
Fixed carbon	9.3	Ba	130	P	14960
Ash	21.2	Ca	13780	Pb	69
Heating value, MJ/kg$_{fuel,\ ar}$		Co	3.6	Se	3
HHV (measured)	13484	Cr	81	Si	2544
Ultimate analysis, %$_{wt,\ ar}$		Cu	294	Sn	18
C	34.6	Fe	26710	Sr	70
H	4.9	Hg	3	Ti	202
N	5.9	K	2019	V	15
S	0.8	Mg	3597	Zn	586
Cl	0.6	Mn	247	Zr	3
O (by diff.)	19.8	Mo	6		
Moisture	12.1				
Ash	21.2				

The moisture content of the fuel is 12% (table 1) and the concentration of the ash is higher than 20%$_{wt}$. A not negligible amount of S and Cl is present in the fuel. The more abundant element in the ashes are Fe, Ca and P. The Ca, Fe and Al concentration is probably associated to the stabilization and flocculation stages of sewage sludge, whereas P is related to the nature of the fuel itself.

Results and Discussion

Table 2 reports operating conditions, particulate and gaseous emissions and combustion efficiency measured during the combustion tests.

Table 2. Main operating parameters and results of the experimental tests

Fuel	Sludge Pellets		
Test #	1	2	3
Operating parameters			
F_{fuel}, kg/h	13.6	16.9	18.6
Power, kW_{th}	47.7	59.4	65.4
Air flow rate, Nm^3/h	62.4	87	95.5
Ug(@ bed T), m/s	0.67	0.91	1.01
T_{bed}, K	867	838	847
Air excess, %	22	36	35
$\eta_{comb.}$, %	98.4	99.8	99.8
Flue gas composition			
O_2, %	4.1	5.78	5.44
CO_2,%	14.24	12.94	13.04
CO, ppm	110	114	15
SO_2, ppm	1300	1229	1040
NO, ppm	901	420	1654
NO_2, ppm	36	8	186
TOC, mg C/Nm^3	7	13	2
PCDD, PCDF (T.E.Q.), ng/Nm^3	18.1	0.064	1.0
HCl, mg/Nm^3	1.2	17	10.3
Ash after cyclones, mg/Nm^3	834	136	79
Ash collected at the cyclones			
I° Cyclone ash, g/h	1533	707	2656
Carbon I° Cyclone, g/h	68.1	3.7	13.5
II° Cyclone ash, g/h	27.6	83.9	96.0
Carbon II° Cyclone, g/h	2.6	1.0	1.1
Total ash concentration, mg/Nm^3	25777	9333	29628

It is worth to note that the experiments were carried out at the same bed temperature,

but at three different thermal power, from about 48 up to 65 kW_{th}. The emissions of particulate, NO, SO_2 and HCl are above the law limits in all the cases and highlight the need of a further de-dusting system and other abatement devices for gaseous pollutant species. Significant differences can be observed comparing the test #1 and the other two, #2 and #3, as regard the combustion efficiency and the PCDD and PCDF emissions at the exhaust. This behavior could be explained considering the axial temperature profiles during the steady state thermal regimes for three tests, reported in figure 3.

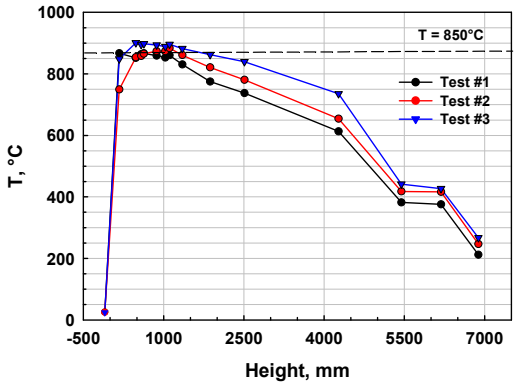

Figure 3. Axial temperature profiles during the steady state thermal regimes

The analysis of the figure shows that during the test #1, the temperature profile has never exceeded the 850 °C threshold, comporting: i) a minor combustion efficiency, 98.4% for test #1 vs 99.8% for both #2 and #3 tests; ii) a very high value of dioxin emissions, i.e. an order of magnitude larger than the emission related to the tests #2 and #3.

As regards the particulate emissions, the amount of fine particles collected from the second cyclone (table 2) is much lower than that collected by the first cyclone and, therefore, the particle size distribution of the particles collected from the first cyclone can be considered, with good approximation, that of the particulate emitted in the its complex.

Table 3. Sauter mean diameter (D_{32}) and volumetric mean diameter (D_{43}) of the particles collected a the cyclones during the tests.

Diameter	#1 I°Cycl.	#2 I°Cycl.	#3 I°Cycl.	#1 II°Cycl.	#2 II°Cycl.	#3 II°Cycl.
D_{32}, µm	12.1	10.6	16.7	3.5	3.0	5.6
D_{43}, µm	31.3	34.0	39.4	7.3	6.8	10.9

The values of the average diameters on a volumetric basis, D_{43}, and the average

surface/volume diameters, D_{32}, of the powders captured in the two cyclones during the experimental tests (Table 3) shows that the first cyclone mainly captures relatively coarse particles, in the range of tens of microns; the second cyclone captures mainly finer particles, in the order of 3-6 microns. The size of fine particles collected by the cyclones increases, as expected, with fluidization velocity, which increases the carry-over capacity of the fluidizing gas stream.

Conclusions

Combustion of pelletized sludge pellets was studied performing experimental measurements using a pilot fluidized bed combustor. More specifically, three tests have been carried out at a thermal power ranging from 45 to 65 kW_{th}. The results show that a stable and efficient combustion behavior was obtained in terms of low emissions of unburnt species, but a train of cleaning processes is necessary to reduce gaseous and particulate emissions. A two stage de-dusting system for the capture of fine and ultrafine particles and the proper units for the abatement of the NOx, SO_2 and HCl produced in high concentrations are needed. The temperature profile in the post-combustion zone and stable combustion conditions are critical for the formation of dioxins.

References

[1] Dichtl, N., Rogge, S., Bauerfeld, K., “Novel strategies in sewage sludge treatment”, Clean 35 (5): 473–479 (2007)

[2] Singh, R.P., Agrawal, M., “Potential benefits and risks of land application of sewage sludge”, Waste Manage. 28: 347–358 (2008)

[3] Werther, J., Ogada, T., “Sewage sludge combustion”, Prog. Energy Combust. Sci. 25:55-116 (1999)

[4] Petersen, I., Werther, J., “Experimental investigation and modeling of gasification of sewage sludge in the circulating fluidized bed”, Chem. Eng. Process. 44: 717–736 (2005)

[5] Hartman, M., Svoboda, K., Pohoel, M., Trnka, O., “Combustion of dried sewage sludge in a fluidized-bed reactor”, Ind. Eng. Chem. Res. 44: 3432–3441 (2005)

[6] Mullen, J.F., “Consider fluid-bed incineration for hazardous waste destruction”, Chem. Eng. Prog. 88, 50–58 (1992)

[7] Cammarota, A., Chirone, R., Salatino, P., Scala, F., Urciuolo, M., “Attrition phenomena during fluidized bed combustion of granulated and mechanically dewatered sewage sludges”, *Proc. Combust. Inst.* 30: 3017–3024 (2005)

[8] Urciuolo, M., Solimene, R., Chirone, R., Salatino, P., “Fluidized bed combustion and fragmentation of wet sewage sludge”, Exp. Therm. Fluid Sci. 43: 97–104 (2012)

[9] Solimene, R., Cammarota, A., Chirone, R., Leoni, P., Rossi, N., Salatino, P., “Combustion of lignin-rich residues with coal in a pilot-scale bubbling fluidized bed reactor”, Powder Technology 316: 718-724 (2017)

ENTRAINED FLOW GASIFICATION: EXPERIMENTS AND MATHEMATICAL MODELLING BASED ON RANS

M. Dammann*, M. Mancini, S. Fleck***, R. Weber**, T. Kolb*,*****
maximilian.dammann@kit.edu
*Karlsruhe Institute of Technology (KIT), Engler-Bunte-Institute, Division of Fuel Technology (EBI ceb), Engler-Bunte-Ring 3, 76131 Karlsruhe, Germany
**Clausthal University of Technology, Institute for Energy Process Engineering and Fuel Technology (IEVB), Agricolastrasse 4, 38678 Clausthal-Zellerfeld, Germany
***Karlsruhe Institute of Technology (KIT), Institute for Technical Chemistry (ITC), Herrmann-von-Helmholtz-Platz 1, 76344 Eggenstein-Leopoldshafen, Germany

Abstract
Interdisciplinary research has been conducted in the frame of the Helmholtz Virtual Institute for Gasification Technology (HVIGasTech) [1-4]. The main objective is to develop a validated numerical simulation tool for describing the entrained flow gasification of biomass (cf. bioliq® process [5]). This paper presents work-in-progress and reports the recent experimental and numerical results for the entrained flow gasification of model fuels (ethylene glycol, 90 % ethylene glycol + 10 % wood-char) under atmospheric conditions. Three experimental campaigns have been carried out at the Research Entrained flow GAsifier (REGA). Radial profiles of gas phase composition (CH_4, CO, CO_2, H_2) and temperature have been measured at burner distances of 300 mm and 680 mm. In parallel to the experimental campaigns, RANS based simulations have been performed using ANSYS Fluent. Turbulence-chemistry interaction has generally been described by the Eddy Dissipation Concept (EDC). EDC has been used in combination with two global reaction mechanisms for the entrained flow gasification of ethylene glycol: the HVI1 mechanism and the extended Jones-Lindstedt mechanism [3]. Devolatilisation and the heterogeneous reactions of wood-char with CO_2 and H_2O are computed using kinetics derived from measurements [6, 7]. The numerical results for the entrained flow gasification of ethylene glycol show good agreement with the measured data. In particular, the model based on EDC and the HVI1 mechanism predicts the gas composition well. Gas temperatures are slightly overpredicted. The numerical results for the gasification of slurry deviate from the experimental results concerning the gas phase composition. Further research needs to be carried out to close this gap.

1. Introduction
Entrained flow gasification (EFG) is one of the most promising gasification technologies and considers the conversion of low-rank fuels into high quality

syngas. To improve the knowledge of the gasification of biomass-based suspension fuels, the bioliq® process [5] has been realised at Karlsruhe Institute of Technology (KIT). Research on EFG was initiated in the frame of the Helmholtz Virtual Institute for Gasification Technology (HVIGasTech) [1-4]. The research is in particular based on a two-step approach: i) experiments and simulations at atmospheric conditions for improving and validating the sub-models used in the simulations; ii) experiments and simulations at high-pressure conditions for developing a numerical model for operation and scale-up of the entrained flow gasifier of the bioliq® process.

Experimental data from entrained flow-gasifiers is mainly available for the gas phase composition and temperature at the outlet of several gasifiers (see e.g. Chen et al. [8]). Radial profiles of gas phase composition and temperature were measured at the entrained flow gasifier of Brigham Young University (BYU), which was operated with coal at atmospheric conditions (see e.g. Brown et al. [9]).

Many studies on the mathematical modelling and simulation of EFG have been carried out in the last decades. Starting with one-dimensional models due to the limited computer resources at that time (see e.g. Wen [10]), CFD and RANS based models (see e.g. Marklund et al. [11]) are nowadays state of the art in the modelling of EFG in various geometries (e.g. two-stage up-flow, one-stage down-flow) and at various operating conditions. Such models are mainly based on two-equation turbulence models (e.g. standard k-ε, SST k-ω) and global reaction mechanisms (Westbrook and Dryer [12], Jones and Lindstedt [13]) for the homogeneous kinetics. For the heterogeneous kinetics, the reactions of the fuel (generally coal) with CO_2, H_2, H_2O and O_2 are considered. Their reaction rates and the reaction rate of the devolatilisation process have usually been based on literature data or on measurements (see e.g. Brown et al. [9]). Radiation has often been calculated using discrete-ordinates method, P1 model or discrete transfer radiation model.

To the best of the authors' knowledge, no mathematical model is available which describes the EFG of biomass-based fuels and which has been validated using gas phase compositions and temperatures measured inside a gasifier. This paper provides an overview of the current status of the experiments at the atmospheric Research Entrained flow GAsifier (REGA) and of the corresponding mathematical modelling.

2. Experiments

The REGA consists of a ceramic tube with an inner diameter of 280 mm and a length of 3000 mm. The heat loss of the system is minimized by electric heating of the reactor walls. The fuel (ethylene glycol or 90 % ethylene glycol + 10 % wood-char) is atomised using a twin-fluid external mixing atomiser and oxygen enriched air as gasification medium. A movable burner construction and flanges along the reactor axis allow measurements at a large continuous range of burner distances. Usually, radial profiles of gas phase composition and temperature are measured at

burner distances of 300 mm and 680 mm. The gas phase composition is determined as dry mole fractions of CH_4, CO, CO_2, H_2 and O_2 using standard gas analysers and a µGC. Radial profiles of the gas phase temperatures are measured with type B double bead thermocouples with bead diameters of 300 µm and 1500 µm, which allow temperature correction by taking into account radiation. Further details concerning the test rig and the analytical equipment are given in Fleck et al. [2].
To improve the sub-models, several experimental gasification campaigns have been carried out under atmospheric operating conditions. In the first two campaigns, glycol was used as model fuel in order to exclude the impact of wood-char and to investigate the gasification at higher and lower adiabatic temperatures. For the third campaign, wood-char has been added and a similar adiabatic temperature has been selected as in the second campaign. Table 1 gives an overview of the experimental conditions.

Table 1. Experimental conditions of three gasification campaigns.

Campaign	Mass flow rate in kg/h			Adiabatic Temperature in K
	Fuel	O_2	Air	
REGA-glycol-T1	12.56	7.11	9.04	2273
REGA-glycol-T2	12.42	6.54	3.76	1973
REGA-slurry1-T2	12.45	6.99	3.66	2041

3. Mathematical modelling

The numerical model is based on the software package ANSYS Fluent and a two-dimensional, axis-symmetric geometry of the REGA. Assuming a steady-state, the continuity equation, the momentum equations, the energy equation and a certain number of species equations have in particular been solved for the gas phase using a finite volume solver on an unstructured mesh. Additionally, equations according to the selected turbulence model and the selected radiation model have been solved. For describing turbulence, the standard k-ε model or the Reynolds stress equation model (RSM) has been applied by default while the SST k-ω model and the realizable k-ε model have also been tested. Consequently, the model is based on RANS (although all flow variables are Favre averaged). Radiation is taken into account by solving the radiative transfer equation by the discrete-ordinates method in 4x8x8 = 256 directions. Due to the use of unstructured meshes, pixelation of 4x4 is also applied for reducing the control-angle overhang. The absorption coefficient is assumed to be constant. Its value of $0.53\ m^{-1}$ has been calculated based on spectral line-by-line calculations using HITEMP-2010 and on a mean beam length. Detailed information about calculating the absorption coefficient and other material properties can be found in Mancini et al. [3].
The boundary conditions for the gas phase at inlet are defined by the mass flow rates given in Table 1 and temperatures measured near the atomiser (316 K; 317 K;

309 K). Additionally, the mass flow rates of purge nitrogen flow (0.64 kg/h; 0 kg/h; 0 kg/h) and the mass flow rates of infiltration air derived from balancing (1.93 kg/h; 0.59 kg/h; 0.69 kg/h) were considered. The boundary conditions at the wall are based on the no-slip condition, the linear law of the wall due to wall distances $y^+ < 5$ and an refractory temperature of 1200 °C in combination with a one-dimensional thermal resistance for the refractory with a depth of 50 mm.
The disperse phase is calculated using the Lagrange approach and the discrete phase model available in ANSYS Fluent and assuming an injection near the atomiser. The injection properties are based on measurements [2] and the total mass flow rate of the fuel given in Table 1. If glycol is used as fuel (REGA-glycol-T1, REGA-glycol-T2), the disperse phase at injection consists of liquid droplets containing ethylene glycol. If slurry is applied as fuel (REGA-slurry1-T2), the disperse phase at injection is modelled by a solid particle surrounded by a liquid layer. Material properties of liquid and solid phase are calculated using appropriate temperature dependent functions or proper constant values.
The reactions in the gas phase are described by the Eddy Dissipation Concept (EDC) in combination with a global reaction mechanism. Based on an extended version of the Jones-Lindstedt mechanism (eJL; see Mancini et al. [3]), the HVI1 mechanism has been developed consisting of six reactions [3]. These reactions describe the thermal decomposition of the evaporated fuel, the reaction with O_2 and reforming/gasification [3]. The reaction rates are based on comparisons with other reaction mechanisms (including the extended version of the Jones-Lindstedt mechanism and the GRI mechanism [14]). For the solid phase, the reaction rates for the devolatilisation and for the heterogeneous reactions with CO_2 and H_2O have been implemented based on the latest results of the collaborative research in the frame of HVIGasTech [6, 7].

4. Results

Figure 1 compares the impact of the global reaction mechanism on the temperature profiles and composition profiles at 300 mm and 680 mm. Obviously, both the HVI1 mechanism and the eJL mechanism reproduce the experimental data at 680 mm while the HVI1 mechanism predicts the experimental data at 300 mm better than the eJL mechanism. The temperature profiles are slightly overpredicted by both mechanisms.
Figure 2 shows the experimental and numerical results of the campaigns REGA-glycol-T2 and REGA-slurry1-T2. The numerical results have been computed using the HVI1 mechanism. For the gasification of glycol, the numerical results agree well with the experimental data. This is, however, only partially true for the gasification of slurry. The reasons for the deviations are still under investigation. To this end, experiments and simulations of one further campaign (70 % ethylene glycol + 30 % wood-char; REGA-slurry2-T2) are already on-going.
The numerical results were produced using RSM (REGA-glycol-T1) or standard k-ε model (REGA-glycol-T2, REGA-slurry1-T2) due to lower computing time.

Sensitivity analysis has shown that the choice of the RANS turbulence model has only a small influence on temperature and composition.

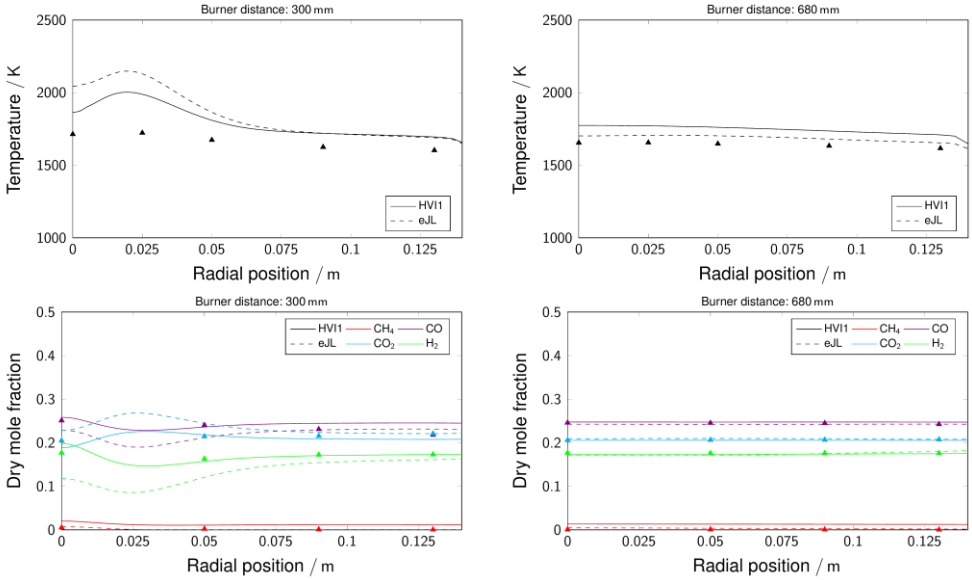

Figure 1. Comparison of experimental and numerical results of REGA-glycol-T1 campaign (as reported in Mancini et al. [3]).

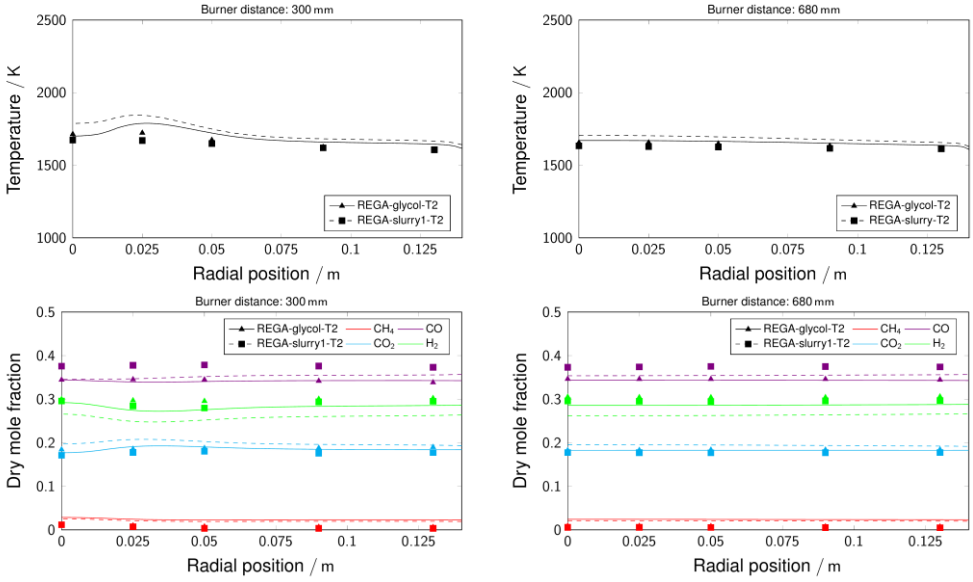

Figure 2. Comparison of experimental and numerical results of REGA-glycol-T2 campaign and REGA-slurry1-T2 campaign.

References

[1] Kolb, T., Aigner, M., Kneer, R., Müller, M., Weber, R., Djordjevic, N., "Tackling the challenges in modelling entrained-flow gasification of low-grade feedstock", *J. Energy Inst.* 89: 485-503 (2016)

[2] Fleck, S., Santo, U., Hotz, C., Jakobs, T., Eckel, G., Mancini, M., Weber, R., Kolb, T., "Entrained flow gasification. Part 1: Gasification of glycol in an atmospheric-pressure experimental rig", *Fuel* 217: 306-319 (2018)

[3] Mancini, M., Alberti, M., Dammann, M., Santo, U., Weber, R., Kolb, T., Eckel, G., "Entrained flow gasification. Part 2: Mathematical modeling of the gasifier using RANS method", accepted, *Fuel* (2018)

[4] Eckel, G., Le Clercq, P.C., Kathrotia, T., Sänger, A., Fleck, S., Mancini, M., Kolb, T., Aigner, M., "Entrained flow gasification. Part 3: Insight into the reactor near-field by Large Eddy Simulation with detailed chemistry", accepted, *Fuel* (2018).

[5] Dahmen, N., Abeln, J., Eberhard, M., Kolb, T., Leibold, H., Sauer, J., Stapf, D., Zimmerlin, B., "The bioliq process for producing synthetic transportation fuels", *WIREs Energy Environment* (2016)

[6] Kreitzberg, T., Haustein, H.D., Gövert, B., Kneer, R., "Investigation of gasification reaction of pulverized char under N_2/CO_2 atmosphere in a small-scale fluidized bed reactor", *J. Energy Res. Technol.* 138: 42207 (2016)

[7] Stoesser, P., Schneider, C., Kreitzberg, T., Kneer, R., Kolb, T., "On the influence of different experimental systems on measured heterogeneous gasification kinetics", *Appl. Energy* 211: 582-589 (2018)

[8] Chen, C., Horio, M., Kojima, T., "Numerical simulation of entrained flow coal gasifiers. Part I: modeling of coal gasification in an entrained flow gasifier", *Chem. Eng. Sci.* 55: 3861-3874 (2000)

[9] Brown, B., Smoot, L.D., Smith, P.J., Hedman, P.O., "Measurement and prediction of entrained-flow gasification processes", *AlChE J.* 34: 435-446 (1988)

[10] Wen, C.Y., Chaung, T.Z., "Entrainment coal gasification modeling", *Ind. Eng. Chem. Proc. Des. Dev.* 18: 684-695 (1979)

[11] Marklund, M., Tegman, R., Gebart, R., "CFD modelling of black liquor gasification: Identification of important model parameters", *Fuel* 86: 1918-1926 (2007)

[12] Westbrook, C.K., Dryer, F.L., "Simplified reaction mechanisms for the oxidation of hydrocarbon fuels in flames", *Combust. Sci. Technol.* 27: 31-43 (1981)

[13] Jones, W.P., Lindstedt, R.P., "Global reaction schemes for hydrocarbon combustion", *Combust. Flame* 73: 233-249 (1988)

[14] Smith, G.P., Golden, D.M., Frenklach, M., Moriarty, N.W., Eiteneer, B., Goldenberg, M., Bowman, C.T., Hanson, R.K., Song, S., William, J., Gardiner, C., Lissianski, V.V., Qin, Z., "GRI mechanism 3.0", Tech. Rep., Sandia National Laboratories

Food Waste Gasification through Hydrothermal Carbonization Pre-treatment

A. N. Izaharuddin[a], M. C. Paul[a*], S. Theppitak[b], X. Dai[b], Kunio Yoshikawa[b]

[a] Systems, Power & Energy Research Division, School of Engineering, University of Glasgow, Glasgow G12 8QQ, UK
[b]School of Environment and Society, Tokyo Institute Technology, Yokohama 226-8502, Japan
*Manosh.Paul@glasgow.ac.uk; a.binti-izaharuddin.1@research.gla.ac.uk; yoshikawa.k.aa@m.titech.ac.jp

Abstract

Non-recyclable wastes promise great potential for the development of new and robust Waste-to-Energy (WtE) technology. Most of these wastes consist of the vital energy contents which could potentially be converted to various forms of useful energy through advanced thermochemical processes such as gasification, thus helping to reduce landfill of wastes. In gasification technology, syngas (synthesis gas) as the energy source is produced, which mainly includes hydrogen (H_2), carbon monoxide (CO), carbon dioxide (CO_2) and methane (CH_4) contents. Food waste has a great potential in the energy field as a feedstock and it has the advantage in recovering energy since there is the high energy content help to reduce landfill. The equilibrium model of food waste gasification initially is developed by fixing the value of temperature at 1023K – 1173K with moisture content of 0% - 40% and equivalence ratio of 0.2 – 0.4, by using air as a gasifying agent. Secondly, mass and energy balance equations are solved to calculate the gasification temperature thorugh an iterative procedure. For this research, food waste has been collected and the ultimate and proximate analyses performed, and the data then fed into a gasification equilibrium model to compare the syngas production between non-pre-treatment and hydrothermal carbonisation (HTC) pre-treatment food waste.

Introduction

Food waste refers to appropriate food for a human that discarded whether it is kept after expiry date or not. Usually, these foods are thrown away because it has spoiled and for some other reasons such as oversupply due to markets or the consumer shopping habits [1]. The Waste & Resources Action Programme

(WRAP) and the Department for Environment Food & Rural Affairs reported that a total of 15 million tonnes of food and drink was wasted in the food chain in 2013 which is equivalent to around one-third of the 41 million tonnes of food that is bought annually in the UK [2, 3]. Ko et al. [4] performed an experimental work on food waste gasification by using a fluidized bed with steam. This thermal method converts waste to carbonized solid to produce synthesis gas.

Japanese Government has introduced the efforts of recycling and reducing food waste in an enactment of food waste recycling law in 2000 [5]. Tanaka et al. [6] has identified the basic characteristics of food waste and food ash on steam gasification to design gasifier. Furthermore, this study reported the effects of the highly efficient system in producing hydrogen by adding alkali components in food ash. Additionally, calcium oxide in an ash can absorb CO_2 generated in steam gasification. Ahmed and Gupta [7] has studied both pyrolysis and gasification of food waste, and reported gasification is a preferable process based on the syngas characteristics and char kinetics. Based on previous study, food waste gasification has high potential in the renewable energy field.

Hydrothermal carbonisation (HTC) pre-treatment is a treatment of feedstock (food waste) to convert into char before proceed for gasification. HTC is operated at a mild temperature of up to 524K. Additionally, water is used as a solvent and also as the catalyst [8]. To compare the syngas production of food waste between without pre-treatment and pre-treatment, the experimental work has been done through hydrothermal carbonization (HTC) pre-treatment. An equilibrium model of food waste gasification is developed and verified with other studies. The model is then used to examine the syngas production from gasification of feedstock under both the pre- and non-pre-treatment conditions.

Equilibrium model

Equilibrium model is developed based on the global reaction of gasification as shown below.

$$CxHyOz + wH_2O + mO_2 + 3.76mN_2 \rightarrow x_1H_2 + x_2CO + x_3CO_2 + x_4H_2O + x_5CH_4 + 3.76mN_2 \quad (1)$$

In gasification, several reactions occurred, such as the Boudouard reaction, water-gas reaction, water-gas shift reaction and methanation reaction. There are 5 unknowns in this global equation (x_1, x_2, x_3, x_4, and x_5), so need to have 5 equations in a gasification process to determine the value of unknowns which include mass balance and equilibrium constant. The equations include carbon balance, hydrogen balance, oxygen balance, an equilibrium constant for methane formation in equation (2) and an equilibrium constant for water-gas shift reaction in equation (3). Equilibrium constant equations to find k_1 and k_2 are based on the methanation

and the water-gas shift reactions, according to Buekens and Schoeters [9], Zainal et al. [10], and Jarungthammachote and Dutta [11].

$$k_1 = \frac{(nCH_4)(n_{total})}{(nH_2)^2} \quad (2)$$

$$k_2 = \frac{(nCO_2)(nH_2)}{(nCO)\ (nH_2O)} \quad (3)$$

The equilibrium model of gasification is initially fixed at 0 – 40% moisture content, 1023-1173K temperature and 0.2 – 0.4 equivalence ratio. After that, mass and energy balance of gasification is calculated to find the gasification temperature by iteration.

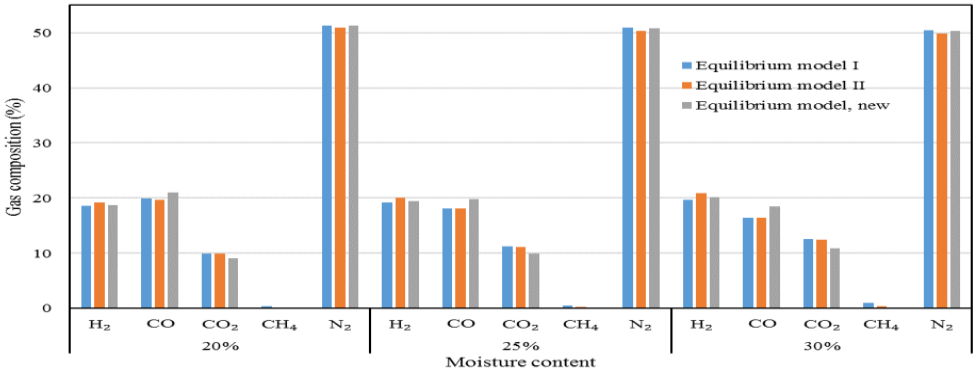

Figure 1. Comparison between Jarungthammachote and Dutta, 2007 [11], equilibrium model at fixed temperature and a new equilibrium model with iteration temperature

Figure 1 shows the comparison of equilibrium model by using solid waste feedstock. From this figure, it shows the gas composition has not so much different between the models, so that the new model can be used for further research, which food waste feedstock. For equilibrium model II, the fixed temperature is 1100K. At MC 20%, the new temperature is 1331.6K, at MC 25% is 1307K and at MC 30% is 1281K. The new CO production is highest between other models, because of temperature increased which effect on the water-gas shift reaction equilibrium constant. For this research, the food waste has been collected to examine the ultimate and proximate analysis, which then run in the equilibrium model that has been developed.

Figure 2. Mixed food waste: as received (left) and after drying (right)

The food waste has been collected and dried for 24 hours as shown in **Figure 2**.

Table 1. Ultimate analysis (dry basis) and proximate analysis of food waste

Ultimate analysis (%)		**Proximate analysis (%)**	
Carbon	58.08	Moisture content	0.96
Hydrogen	8.29	Volatile matter	83.44
Oxygen	30.34	Fixed carbon	14.01
Nitrogen	4.33	Ash	1.59
Sulfur	0.7		

Table 1 shows the ultimate analysis and proximate analysis of dried food waste as a without pre-treatment feedstock sample.

Hydrothermal Carbonization (HTC) pre-treatment

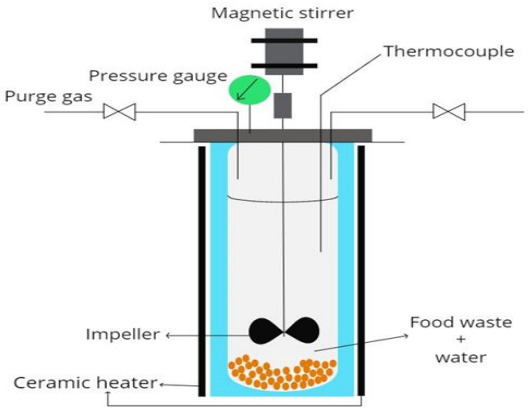

Figure 3. Schematic diagram of hydrothermal autoclave for food waste

Figure 3 shows the schematic of hydrothermal autoclave, which has been used for pre-treatment of food waste. The ratio of food waste to water is 1:5, in which food waste is constant for 40g, while water is constant at 200g. Argon gas is used to purge the gas into hydrothermal autoclave, the water bath is used to recycle the water in the autoclave and the autoclave is heated until the targeted temperature. Once the temperature is reached at the targeted temperature, 30 minutes residence time is started before the cooling process until the temperature reached about 343K. Then, the product is filtered by using vacuum pump, which the solid part is dried for 24 hours at 378K. The operated temperature of food waste hydrothermal at 453K, 473K and 493K.

Table 2. Ultimate and proximate analysis of food waste hydrothermal pre-treatment

Ultimate Analysis (%)				**Proximate Analysis (%)**			
Sample	**I**	**II**	**III**		**I**	**II**	**III**
C	67.29	68.04	70.22	**MC**	0.32	0.70	0.70
H	9.87	9.32	9.45	**VM**	87.20	85.08	83.09
O	18.33	17.43	15.89	**FC**	11.28	13.48	15.73
N	3.66	4.09	3.51	**Ash**	1.20	0.74	0.47
S	0.55	0.74	0.71				

Table 2 shows the ultimate and proximate analysis of food waste for hydrothermal pre-treatment at temperature 453K for sample I, 473K for sample II and 493K for sample III. The fixed carbon increased with increasing temperature.

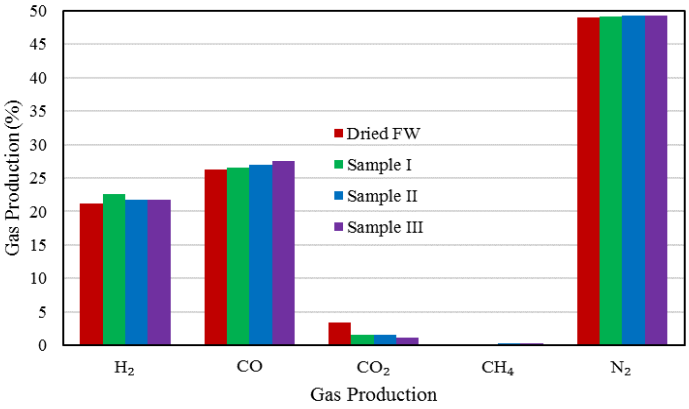

Figure 4: Gas production (%) comparison between dried food waste and hydrothermal conditions sample of food waste

Figure 4 shows the gas production of food waste gasification, which comparison

between dried food waste and hydrothermal pre-treatment conditions sample, which sample I is at 463K, sample II at 473K and sample III at 493K. The equivalence ratio for this comparison is constant at 0.34. Through the comparison, H_2 and CO production of hydrothermal conditions shows higher than fried food waste (without pre-treatment). In hydrothermal condition has more carbon than without pre-treatment which could produce more CO through Boudouard reaction and water-gas reaction. Furthermore, H_2 content in pre-treatment sample has higher than without pre-treatment to produce more H_2 which is produced by water-gas shift reaction as well as to reduce CO_2 production.

Conclusion

In conclusion, hydrothermal pre-treatment of food waste is a preferable process to produce more quality char to enhance in food waste gasification. This is shown in ultimate analysis of food waste and the result of gas composition through food waste gasification equilibrium model.

w	Amount of water per kmol biomass
m	Amount of air per kmol biomass
x_1,x_2,x_3,x_4, x_5	The coefficients of product
k_1, k_2	Equilibrium constants
MC	Moisture content
VM	Volatile matter
FC	Fixed carbon

References

[1] FAO, *Food wastage footprint*, in *Impacts on natural resources*. 2013, Food and Agriculture Organization of the United Nations

[2] WRAP, *Estimates of Food and Packaging Waste in the UK Grocery Retail and Hospitality Supply Chains*. 2015, Waste and Resources Action Programme

[3] DEFRA, *Digest of waste and resource statistics-2016 Edition*. 2016, Department for Environment Food and Rural Affairs.

[4] Ko, M.K., et al., *Gasification of food waste with steam in fluidized bed.* Korean Journal of Chemical Engineering, 2001. **18**(6): p. 961-964.

[5] MEGJ, *Sweeping Policy Reform Towards A 'Sound Material- Cycle Society' Starting From Japan and Spreading Over the Entire Globe: The '3R' Loop Connecting Japan With Other Countries* 2006, Ministry of the Environment Government of Japan

[6] Tanaka, M., et al., *Basic characteristics of food waste and food ash on steam gasification.* Industrial & Engineering Chemistry Research, 2008. **47**(7): p. 2414-2419.

[7] Ahmed, I.I. and A.K. Gupta, *Pyrolysis and gasification of food waste: Syngas characteristics and char gasification kinetics.* Applied Energy, 2010. **87**(1): p. 101-108.

[8] Hrncic, M.K., G. Kravanja, and Z. Knez, *Hydrothermal treatment of biomass for energy and chemicals.* Energy, 2016. **116**: p. 1312-1322.

[9] Buekens, A.G. and J.G. Schoeters, *Modelling of Biomass Gasification* in *Fundamentals of Thermochemical Biomass Conversion*, R.P. Overend, T.A. Milne, and L.K. Mudge, Editors. 1985, Elsevier Applied Science Publishers London and New York

[10] Zainal, Z.A., et al., *Prediction of performance of a downdraft gasifier using equilibrium modeling for different biomass materials.* Energy Conversion and Management, 2001. **42**(12): p. 1499-1515.

[11] Jarungthammachote, S. and A. Dutta, *Thermodynamic equilibrium model and second law analysis of a downdraft waste gasifier.* Energy, 2007. **32**(9): p. 1660-1669.

PARTICLE-WALL IMPACT EXPERIMENTS FOR ENTRAINED-FLOW BIOMASS GASIFIERS

M. Troiano*, F. Montagnaro, R. Solimene***, P. Salatino***
maurizio.troiano@unina.it
*Dipartimento di Ingegneria Chimica, dei Materiali e della Produzione Industriale, Università degli Studi di Napoli Federico II, Piazzale V. Tecchio 80, 80125 Napoli (Italy)
**Dipartimento di Scienze Chimiche, Università degli Studi di Napoli Federico II, Complesso Universitario di Monte Sant'Angelo, 80126 Napoli (Italy)
***Istituto di Ricerche sulla Combustione, Consiglio Nazionale delle Ricerche, Piazzale V. Tecchio 80, 80125 Napoli (Italy)

Abstract
Particle–wall interaction phenomena relevant to entrained-flow biomass gasifiers have been investigated. The dynamics of char and ash particles as they are impacted onto a flat surface in hot conditions has been characterized by means of high speed imaging and tracking. Two types of biomass have been investigated, i.e. wood chips and corn stover. Particle–wall collisions were described in terms of normal, tangential and global coefficients of restitution. The influence of carbon conversion and impact velocity on the dynamical pattern of rebound and deposition has been investigated. The results indicate that the global restitution coefficient for char and ash particles is well below 1, suggesting that some plastic deformation occurs upon impacts. Furthermore, ash of wood chips is not prone to form a slag layer, while ash of corn stover extensively contributes to formation of ash deposits and melts. The dissipation of momentum associated with particle impact promotes the establishment of a dense-dispersed phase in the near-wall zone of entrained-flow slagging gasifiers.

1. Introduction
The use of biomass represents one important element toward a sustainable energy production in the near-future, allowing a substantial reduction of net CO_2 emissions, while providing energy reliably and weather-independent. Gasification is a very efficient way of converting the chemical energy embedded in biomass and one of the best alternatives for deriving energy and basic chemicals from waste carbonaceous solids [1]. In entrained-flow gasifiers (EFG), fine particles react with gaseous oxidants within a short residence time (in the order of a few seconds). Most industrial EFGs operate at high temperatures (slagging mode) to guarantee a tar-free syngas and high carbon conversion [2]. The ash behaviour plays a key role in the performance of EFGs. Above the softening point, ash becomes sticky and agglomerates causing blockage of the bottom bed at the discharge or fouling of the heat exchange equipment. Once above the slagging temperature, ash has a fully liquid behaviour and it is easily drained from the bottom of the gasifier and

quenched as vitrified slag. The slag layer results in a molten protective coating and reduces wear and heat loss at the wall, contributing to increase the cold gas efficiency of the gasifier. However, uncontrolled build-up of the slag layer can cause refractory corrosion and plugging. The rate of ash deposition under inertial conditions depends on ash stickiness and properties of the surface against which the particles are impacted. Furthermore, for coal particles, the effective ash stickiness depends on its residual carbon content. Empirical methods, such as slagging indices, ash sticking temperatures and viscosity models, initially proposed for coal, are used for biomass to determine particle sticking criteria [2]. Further studies on ash formation, deposition and char/slag interaction are still needed.
The performance of slagging EFG may be critically affected by the fate of char/ash particles as they interact with the wall slag layer. Montagnaro and Salatino [3] proposed a phenomenological model which considers the establishment of a particle segregated phase in the near-wall region of the gasifier. This annular phase is characterized by a longer residence time than the average gas space-time, a feature beneficial to enhanced carbon conversion. Further studies confirmed the soundness of this phenomenological framework [4]. The recent literature has investigated particle–wall interactions in terms of a coefficient of restitution (the ratio between the rebound and the impact velocities), as it critically affects the boundary condition for particle–wall collisions in the context of multiphase flow modelling of the gasifier. The restitution coefficient of normal and oblique impacts at room and hot temperature conditions has been investigated to simulate the different patterns of particle–surface collision relevant to coal EFG [5–8]. No data are available for the rebound characteristics of biomass particles. The aim of the present study is to characterize the impact-deposition-rebound dynamical patterns of biomass particles in terms of coefficient of restitution during non-orthogonal particle–wall impacts. Experiments were carried out with batches of wood chips and corn stover particles pre-gasified to different degrees of carbon conversion, while varying the impact velocity.

2. Methodology

The characterization of the rebound behaviour of particles in EF slagging gasifiers is not trivial. Non-spherical char particles at different carbon burn-off are impacted onto confining walls covered by either a dry refractory material or a slag layer. Furthermore, the particle stickiness deeply affects the interaction behaviour as a consequence of the variation of particle mechanical properties with temperature and residual carbon content. In this study impact tests were carried out to evaluate the rebound/deposition behaviour of biomass particles upon collision with a planar surface. Two types of biomass fuels were considered, wood chips (woody biomass) and corn stover (straw from agricultural and herbaceous biomass). The particle–wall collisions are characterized in terms of a restitution coefficient ε, defined as the ratio between the rebound and the impact velocity. The restitution coefficient embodies phenomena like elasto–plastic deformation, viscoelastic behaviour of

solid materials, surface contact forces and particle–wall friction. It is useful to define a normal, tangential and global coefficient of restitution, ε_n, ε_t, and ε_g, respectively as:

$$\varepsilon_n = \frac{-v_{n,r}}{v_{n,i}}; \quad \varepsilon_t = \frac{v_{t,r}}{v_{t,i}}; \qquad \varepsilon_g = \frac{v_r}{v_i} = \sqrt{\frac{v_{n,r}^2}{\frac{v_{n,i}^2}{sin^2\,\alpha_i}} + \frac{v_{t,r}^2}{\frac{v_{t,i}^2}{cos^2\,\alpha_i}}} = \sqrt{\varepsilon_n^2\,sin^2\,\alpha_i + \varepsilon_t^2\,cos^2\,\alpha_i} \qquad (1)$$

where v_n and v_t represent the components of the velocity in the normal and tangential directions, respectively, while the subscripts i and r are referred to the impacting and rebound phase, respectively. ε_g tends to ε_n for large impact angles ($\alpha_i \rightarrow 90°$) and to ε_t for small impact angles ($\alpha_i \rightarrow 0°$).

3. Experimental

Particle–wall micromechanical interactions were investigated by means of the experimental apparatus shown in Fig. 1. The test rig consisted of a Carbolite vertical tubular furnace equipped with a PID system for temperature control, an alumina tube (1.5 m-height and 0.056 m-ID) inserted in the furnace and a hot impact chamber connected to the alumina tube at the bottom of the upper vertical furnace. The impact chamber was designed and built-up to guarantee the desired temperature and to enable direct optical access to the impact zone. The optical access was ensured by a quartz window, sandwiched by refractory slabs to ensure a good insulation. Three shielded R-type thermocouples were used to monitor the gas temperature: in the alumina tube, in the pre-impact zone and close to the target.

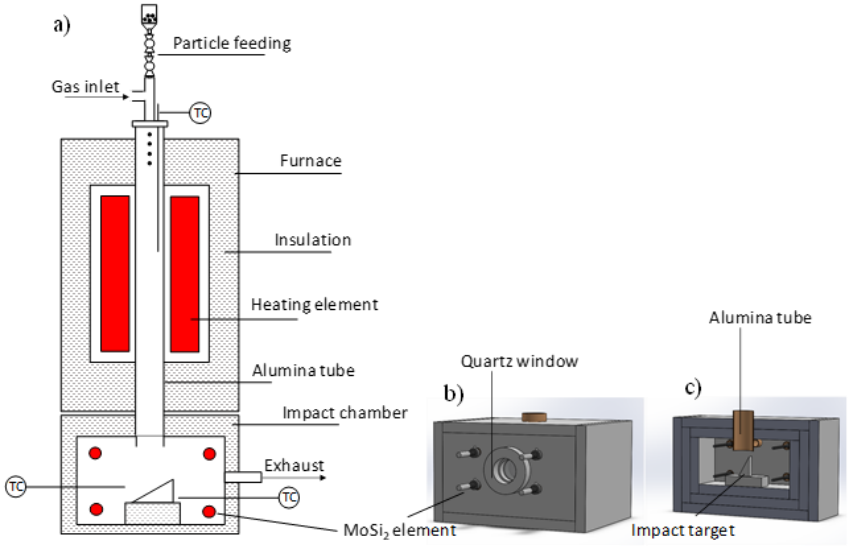

Figure 1. Experimental test rig. a) Outline of the apparatus; b) Impact furnace; c) Section of the impact furnace.

Batches of micron-sized particles (150–180 μm) were fed at the top of the alumina tube by means of two on/off valves, and entrained along the tube by a stream of nitrogen fed at the top of the furnace at ambient temperature. The particles are entrained by the mainstream gas flow along the reactor. The particle impact velocity was controlled by regulating the main nitrogen flow rate. When the particles left the tube, they impacted on a target plate located in the impact chamber about 0.05 m below the tube (Fig. 1b-c)). The target was shaped to establish particle impact angles around 60° with respect to the horizontal [6]. Particle velocities before and after the impact were determined experimentally by image analysis, hence the restitution coefficient was calculated. Details of the image post-processing technique are reported elsewhere [7,8]. Two types of biomass were investigated, i.e. wood chips and corn stover. Table 1 reports proximate and ultimate analyses for the two fuels. Ash mineral analysis was also carried out. The ratio of species which form low-melting compounds (Si+P+K-based, wt %) to the species with high fusion temperature (Ca+Mg-based, wt %) was 0.7 for wood chips and 4.7 for corn stover. To investigate the effect of carbon conversion, impact experiments were carried out in nitrogen environment using particles pre-converted at different degrees of carbon burn-off. Raw particles were sieved in the range d_p=165±15 μm and pyrolyzed in a vertical tubular furnace at 750°C in nitrogen. After pyrolysis, char particles underwent CO_2 gasification at 900°C for different reaction times to obtain char particles with different residual carbon content.

Table 1. Proximate and ultimate analyses of wood chips and corn stover.

	Wood chips		**Corn stover**	
Proximate analysis	***As-received (wt%)***	***Dry (wt%)***	***As-received (wt%)***	***Dry (wt%)***
Moisture	15.3	0.0	9.3	0.0
Volatile Matter	63.9	75.4	69.8	77.0
Ash	1.7	2.0	4.0	4.4
Fixed Carbon	19.1	22.6	16.9	18.6
Ultimate analysis	***As-received (wt%)***	***Dry (wt%)***	***As-received (wt%)***	***Dry (wt%)***
Carbon	44.2	53.3	42.8	49.4
Hydrogen	6.42	7.7	6.1	7.1
Nitrogen	0.4	0.5	0.5	0.6
Sulphur	0.1	0.1	0.1	0.1
Chlorine	0.1	0.1	0.2	0.2
Ash	1.7	2.0	4.0	4.4
Moisture	15.3	0.0	9.3	0.0
Oxygen	31.8	36.3	37.0	38.2
HHV (MJ kg^{-1})	**–**	**21.1**	**–**	**17.8**

The experimental tests aimed at characterizing the phenomenology of particle–wall interaction in terms of restitution coefficients. Experiments were performed in hot conditions (1400 °C) using as target material the raw refractory that was coated with a high temperature cement and then polished. The rebound characteristics of char particles with different residual carbon content (X_C=0.28, 0.45, 0.9 for wood chips and X_C=0.12, 0.5, 0.9 for corn stover) and of ash particles were investigated. Coefficients of restitution and deposition efficiency were measured at fixed impact angle (60°) while varying the particle impact velocity (0.3–2.3 m s^{-1}).

4. Results and discussion

Experimental data for the coefficient of restitution are reported as values averaged over multiple tests (symbols). Bars corresponding to the standard error are also reported. To ensure experimental reproducibility, each point is the average of at least 30 measurements. The rebound characteristics of char particles at different degrees of carbon conversion and ash particles are hereby reported and discussed. The effect of the global impact velocity $v_{g,i}$ on the global restitution coefficient ε_g is shown in Fig. 2a) and b) for wood chips and corn stover, respectively. The values of ε_g are always smaller than unity, suggesting that plastic deformations occur as the mechanical properties change with increasing temperature. For both the biomass types, ε_g is nearly constant with the impact velocity and it decreases for ash particles. This result highlights that for both the biomasses the char/slag transition occurs only when all the carbon is consumed, i.e. for a carbon conversion equal to 100%, while for Illinois coal particles enhanced deposition was recorded when carbon conversion reached a value around 90% [8]. For wood chips particles (Fig. 2a)) the global coefficient of restitution is around 0.35 for char particles and around 0.2 for ash particles, while for corn stover (Fig. 2b)) it is around 0.3 for char and lower than 0.05 for ash.

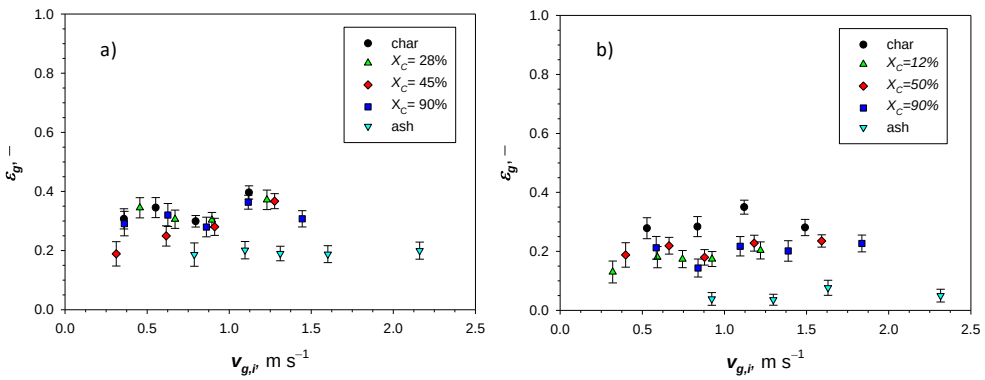

Figure 2. Effect of the global impact velocity on the global coefficient of restitution for char with different carbon conversion and ash particles of a) wood chips; b) corn stover. Operating conditions: T=1400°C, α_i=60±10°.

These results highlight that wood chips ash is not prone to form extensive deposits and a stable molten layer on the wall upon the impact. It is possible to relate the slagging tendency of wood chips char and ash to the ratio of species which are likely to form low-melting compounds (Si+P+K-based, wt %) to the species with high fusion temperature (Ca+Mg-based, wt %). In terms of the corresponding oxides, this ratio is around 0.7 for wood chips ash, consistent with limited tendency to slagging reported also in the literature [9]. The formation of high-temperature melting compounds, such as CaO, and the lack of Ca silicates which have a relatively low melting temperature [9] are responsible for this behaviour. On the contrary, corn stover ash particles, characterized by a different ash composition, display much larger propensity to deposition and formation of a stable molten layer, as confirmed by the high ratio (Si+P+K)/(Ca+Mg) which is about 4.6.

References

[1] Tijmensen, M.J.A., Faaij, A.P.C., Hamelinck, C.N., van Hardeveld, M.R.M., "Exploration of the possibilities for production of Fischer Tropsch liquids and power via biomass gasification", *Biomass Bioenergy* 23: 129–152 (2002).

[2] Higman, C., van der Burgt, M., *Gasification 2nd edition*, Gulf Professional Publishing, 2008.

[3] Montagnaro, F., Salatino, P., "Analysis of char-slag interaction and near-wall particle segregation in entrained-flow gasification of coal", *Combust. Flame* 157: 874–883 (2010).

[4] Troiano, M., Salatino, P., Solimene, R., Montagnaro, F., "Wall effects in entrained particle-laden flows: the role of particle stickiness on solid segregation and build-up of wall deposits", *Powder Technol.* 266: 282–291 (2014).

[5] Dong, M., Li, S., Xie, J., Han, J., "Experimental studies on the normal impact of fly ash particles with planar surfaces", *Energies* 6: 3245-3262 (2013).

[6] Gibson, L.M., Gopalan, B., Pisupati, S.V., Shadle, L.J., "Image analysis measurements of particle coefficient of restitution for coal gasification applications", *Powder Technol*. 247:30-43 (2013).

[7] Troiano, M., Solimene, R., Salatino, P., Montagnaro, F., "Multiphase flow patterns in entrained-flow slagging gasifiers: physical modelling of particle–wall impact at near-ambient conditions", *Fuel Process. Technol.* 141: 106-116 (2016).

[8] Troiano, M., Santagata, T., Montagnaro, F., Salatino, P., Solimene, R., "Impact experiments of char and ash particles relevant to entrained-flow coal gasifiers", *Fuel* 202: 665-674 (2017).

[9] Vassilev, S.V., Baxter, D., Andersen, L.K., Vassileva, C.G., "An overview of the chemical composition of biomass", *Fuel* 89: 913-933 (2010).

DETAILED DEM SIMULATION OF PARTICLE-WALL INTERACTIONS UNDER COAL GASIFIER CONDITIONS

D.M. Balice*, F. S. Marra, F. Montagnaro*, P. Salatino*****
marra@irc.cnr.it
*Dipartimento di Scienze Chimiche,
Università degli Studi di Napoli Federico II, Napoli, Italy
**Istituto di Ricerche sulla Combustione – CNR, Napoli, Italy
***Dipartimento di Ingegneria Chimica, dei Materiali e della Produzione Industriale,
Università degli Studi di Napoli Federico II, Napoli, Italy

Abstract
Detailed DEM simulations of a simplified configuration, aiming at reproducing the conditions encountered by char and ash particles near the walls of a reactor during gasification, have been performed. A large number of parameters related to material properties and operative conditions were investigated. Results allowed to identify the parameters most affecting the effective conversion rates of entrained flow coal gasifiers.

Introduction
The entrained flow gasification is one of the main technologies for converting solid fuels into energy and basic chemicals. The process returns a product, the syn-gas, a gaseous mixture composed of H_2 and CO plus by-products, and a residue, the slag which, in the investigated process conditions (1900K, 30bar), is a viscous fluid that runs along the internal walls of the reactor and essentially consists of molten ash.
Although the entrained flow gasification is a widely used technology in the industrial field, the design and the sizing of the gasification reactors still present uncertainty points [1]. In particular, the description of the dynamics of the particles flow, as a result of their interaction with the gas flow and with the gasifier walls, as well as their self-interactions, is largely incomplete [2]. Several attempts to model, by means of computational simulations or theoretical studies, the particle-wall interactions are present in the literature [3]. However, most of these works adopt simplified models for the solid particle phase that are already the result of assumptions on the particle behavior in gasifiers, as the assumption of a critical viscosity discriminating the adherence and the consequent inclusion of impacting particles in the slag layer [4], leading to approximations that invalidate the design of the plants [5].
It was observed that the fate of char particles during gasification when they interact with a wall has a significant role in determining the final gasification degree depending on the coverage by slag, the presence of adhered particles on the surface and, not less important, the establishment of a dense-dispersed particle phase in the proximity of the wall [6]. Indeed, the buildup of a zone near the wall, where the

particles segregate and accumulate as a result of interaction with the wall, causes a lengthening of the average residence times of the char particles in the gasifier, which benefits the degree of conversion.
These interactions have been investigated by this research group, both in a phenomenological way [7] and by modeling analysis [8]. The present work aims to extend the modeling studies and to establish, through detailed DEM simulations, the most influencing mechanical and rheological properties of the particles (mainly determined by the progress of the reaction) and the role of the process variables (in particular the variation of the feeding flux of particles and the flow of oxidizing gas), to identify the conditions influencing the build-up and structure of the dense-dispersed phase near the wall. This information is essential to establish the effective average residence time of the particles in the gasifier.

Model setup
The particle and wall properties have been modeled assuming sticky and non-sticky limits: wall portions and particles covered by an exposed slag surface layer (characterized by a low restitution coefficient and the possibility of forming "liquid bridge") are considered as sticky, and wall portions not covered by slag or particles not sufficiently warm and converted as not sticky.

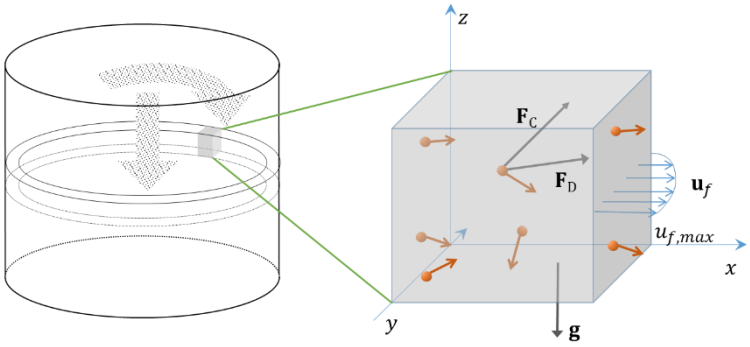

Figure 1. Geometrical setup of the computational domain.

The modeling analysis was carried out using an open-source software named LIGGGHTS [9], a very efficient and parallel DEM solver suitable to face the considerable computational effort required by this complex model. Several submodels were selected to describe in detail particle-particle and particle-wall collisions, starting with the soft-sphere model from the Hertzian theory. Submodels for rolling friction, cohesion and the possibility of formation of liquid bridge were included. The resulting model is computationally very demanding, requiring to greatly simplify the computational domain while keeping the particle phase fully described as single lagrangian elements. A very small portion of a cylindrical reactor, adjacent to the confining wall, as illustrated in Fig. 1, is considered. To further simplify the setup, the domain is represented by a hexahedron. Proper centrifugal forces are added to represent the effect of the curvature of the wall. Periodic

conditions are assigned along the x and z direction. All particles move under the action of this body force and of the drag forces determined by a fictitious gas flow field with prescribed velocity profile, null at the wall, and then having only v_x not null, with a maximum at a fixed distance from the wall.

Results

A parametric investigation was first conducted to establish the mechanical properties of particle most influencing the dynamic behavior of the system. Starting from the injection of a fixed number of particles randomly dispersed in the domain, the system evolves with all particles remaining in the domain and eventually reaches a statistically asymptotic behavior, characterized by a certain level of total kinetic energy, as shown in Fig. 2.

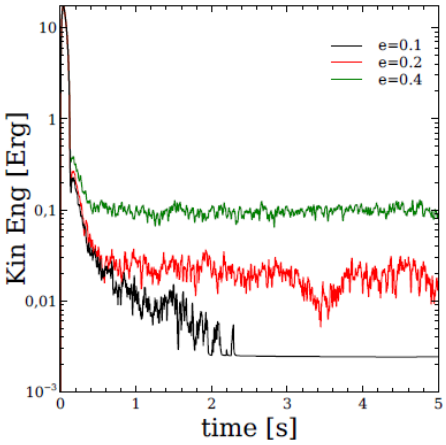

Figure 2. Total kinetic energy of particles versus time at different $\boldsymbol{e}$. $\boldsymbol{N_p = 7500}$.

This analysis confirmed the prominent role of the normal coefficient of restitution e with respect to other material relevant properties, like the Young's modulus, the friction coefficient and the rolling friction coefficient. Following the findings reported in [7], this parameter has then been varied between 0.4 (for not sticky particle) and 0.1 (for sticky particles). It is evident that the asymptotic state is an equilibrium between the kinetic energy gained under the action of the forces acting on the particles and the energy dissipated by collisions. The important feature of the system is the distribution of residence times that the particles realize in the domain upon their stratification structure is stabilized. These are reported in Fig. 3 for the same condition of Fig. 2. It is found that a roughly bimodal profile is realized, with the two main peaks separating apart by reducing e: a layer of particles with short residence time forms on top of the layer of particles almost lying on the walls. The time required to establish this structure (see Fig. 2) reduces with increasing e and becomes of order of magnitude comparable with the average residence time of coal particles in swirled gasification reactors.

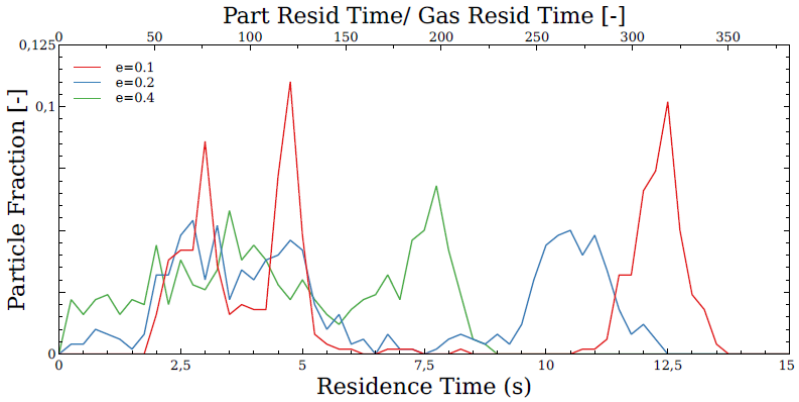

Figure 3. Distribution of particle fractions versus residence times for $\boldsymbol{N_p = 7500}$ and $\boldsymbol{v_{max} = 40}$ cm/s.

Two operative parameters were found to mostly influence this dynamics: the particle number density and the gas flow velocity. The corresponding profiles of total kinetic energy versus time are reported in Fig. 4.

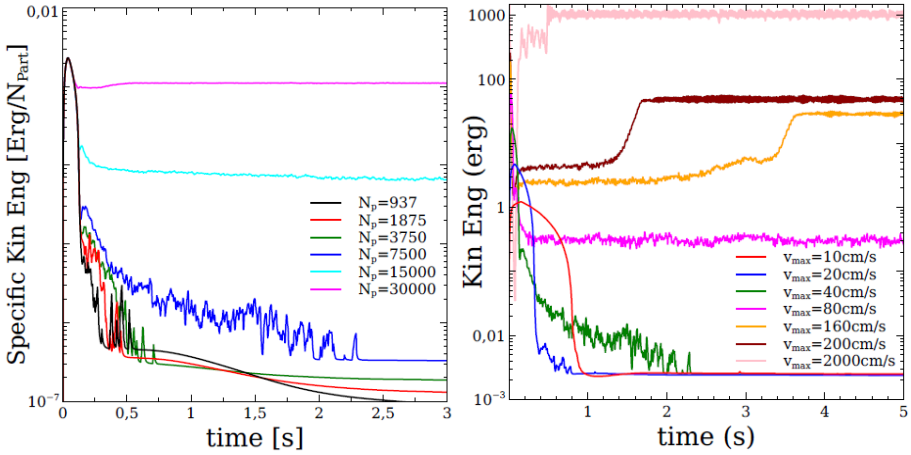

Figure 4. Total kinetic energy vs. time. On the left at varying the total particle number with0 $v_{max} = 40$ cm/s; on the right at varying the gas flow maximum velocity with $N_p = 7500$ and $e = 0.1$.

Even if different patterns are found varying these parameters, it arises that both the increasing of flow velocity and increasing of particles number act towards the increasing of total kinetic energy. The observation of the distribution of particles residence times reported in Fig. 5 reveals that a critical value exists (respectively $N_p = 15000$ and $v_{max} = 80$ cm/s) beyond which a large portion of particles has a very short residence time (less than 1 s), meaning that, if real char particles are

considered, their conversion would be significantly limited. Conversely, at the lowest particle number and gas flow velocities, a large portion of particles results practically deposited on the reactor wall, indicating that if real char or ash particles are considered, they will be promptly engulfed in the slag, again limiting the char conversion.

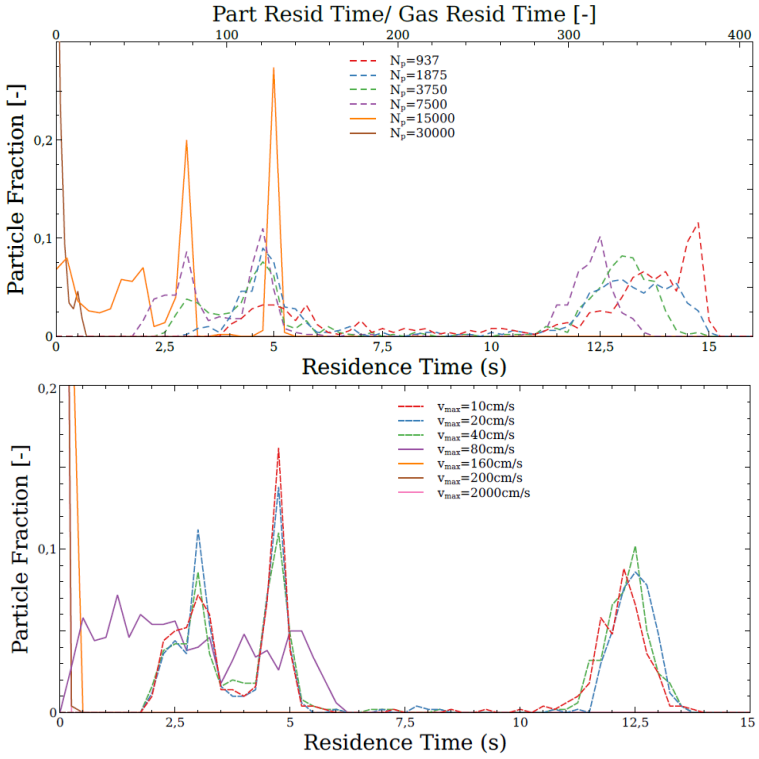

Figure 5. Distribution of particle fractions versus residence times. On top at varying $\boldsymbol{N_p}$ and $\boldsymbol{v_{max}} = \mathbf{40}$ cm/s. On bottom at varying $\boldsymbol{v_{max}}$ and $\boldsymbol{N_p} = \mathbf{7500}$.

Notably, in all cases the distribution of residence times is roughly bimodal, meaning that in any case the segregation and formation of a dense-dispersed phase is likely to establish on top of a surface covered by particles.

Conclusions

Results of simulations show that, among the mechanical and rheological properties investigated, the restitution coefficient alone is able to describe the variations of the particle and wall properties, causing major changes in the dynamic behavior of the particle phase.

An even greater effect on this behavior is given by the operating process conditions, expressed in terms of number density of particles flow and intensity of the bulk flow velocity of the gaseous phase. The formation of the segregated particle phase,

hypothesized by the reported studies, was reproduced by the present model. Several dynamic regimes have been observed indicating the limits of optimal conditions for operation of entrained flow gasifiers.
The results of this analysis have been further elaborated (here not shown for the sake of brevity) with reference to a kinetic gasification model [10], and considering the variation of residence times according to the different operating conditions as obtained from the modeling analysis. This allowed to obtain relations between: operating conditions, residence time, characteristic reaction time, Damköhler number, degree of gasification.

[1] Montagnaro, F. and Salatino, P. "Analysis of Char–slag Interaction and Near-Wall Particle Segregation in Entrained-Flow Gasification of Coal." *Comb. Flame* 157: 874–83. (2010).
[2] Marra, F.S., Tretola, G., Troiano, M., Montagnaro, F. Salatino,P., "Coal Particles as Discrete Elements: the Role of Collisions in Entrained-Flow Slagging Gasifiers", MFIP17 - *14th International Conference on Multiphase Flow in Industrial Plants*, Desenzano del Garda, September 13-15, 2017.
[3] Chen, L., Yong, S.Z., Ghoniem, A.F. "Modeling the Slag Behavior in Three Dimensional CFD Simulation of a Vertically-Oriented Oxy-Coal Combustor." *Fuel Proc. Tech.* 112: 106–17 (2013).
[4] Seggiani, M. "Modelling and Simulation of Time Varying Slag Flow in a Prenflo Entrained-Flow Gasifier." *Fuel* 77: 1611–1621 (1998).
[5] Balakrishnan, S., Nagarajan, R. and Karthick, K. "Mechanistic Modeling, Numerical Simulation and Validation of Slag-Layer Growth in a Coal-Fired Boiler." *Energy* 81: 462–70 (2015).
[6] F.S. Marra, M. Troiano, F. Montagnaro, P. Salatino, R. Solimene, International Journal of Multiphase Flow, 91, 2017, 142-154.
[7] Troiano, M., Santagata, T., Montagnaro, F., Salatino, P. and Solimene, R. "Impact Experiments of Char and Ash Particles Relevant to Entrained-Flow Coal Gasifiers." *Fuel* 202 (August): 665–74 (2017).
[8] Marra, F.S., Tretola, G., Balice, D.M., Montagnaro, F., Salatino, P. "Effects of Soft-Sphere Model Parameters in the Simulation Of Slagging Gasifiers" *Proc. 40th Meeting of the Italian Section of the Comb. Inst.*, 2017, Rome, Italy.
[9] Kloss, C., Goniva, C., Hager, A., Amberger, S. and Pirker, S. "Models, Algorithms and Validation for Opensource DEM and CFD–DEM." *Prog. Comp. Fluid Dyn., Int. J.* 12: 140–152 (2012).
[10] Liu, G.-S. and Niksa, S. "Coal Conversion Submodels for Design Applications at Elevated Pressures. Part II. Char Gasification." Prog. En. Comb. Sci. 30: 679–717 (2004).

UNSTEADY THREE-DIMENSIONAL SIMULATION OF A FLUIDIZED BED FOR BIOMASS GASIFICATION

Muhammad Ali Uzair*, Sergio Camporeale*, Francesco Fornarelli*, Paolo Oresta*
muhammadali.uzair@poliba.it
*Department DMMM, Polytechnic of Bari, Via Orabona 4, 70125, Bari, Italy

Abstract
CFD simulation study has been performed on a lab-scale cold-flow bubbling fluidized bed using the two-fluid Eulerian-Eulerian model considering a 2D and a 3D approach. The simulation results have been compared to experiments of Deza et al. (DOI: 10.1115/1.4000257) considering pressure drop, bed height and void fraction profiles over different heights of the bed. Grid Independence study shows that a grid size equivalent to ten times particle diameter is enough for grid independent results. Although 2D simulations are able to predict qualitatively the hydrodynamics of bubbling fluidized bed successfully, 3D simulations have been vital in understanding the hydrodynamics of fluidized bed and in explaining small discrepancies in simulation results due to particle shape and sphericity.

Introduction
The application of gas-solid fluidized beds to biomass gasification systems comes from their superior mixing properties that lead to nearly isothermal conditions and higher heat and mass transfer between the different phases as well as the bed and immersed objects [1]. A proper understanding of the complex hydrodynamics of gas-fluidized beds is required for design and optimization of fluidized bed system parameters. These complex hydrodynamics are still difficult to quantify owing to difficulty in obtaining sufficient experimental data. Computational Fluid Dynamics CFD can bring a much-desired contribution in connecting externally accessible observations from experiments with the intrinsic phenomenon. For this matter, CFD is the platform extensively being used to complement the design of fluidized beds.

Two main CFD approaches namely Lagrangian and Eulerian can be used to model the gas-solid flows- the former being more realistic yet expensive in terms of computational time. Eulerian approach considers both solid and gas phases as inter-penetrating continuum. Conservation equations of mass, momentum and energy are solved for each phase. These equations are enclosed by Kinetic Theory of Granular Flow KTFG [2]. Lagrangian approach considers gas phase as continuum but tracks the solid phase on particle level according to Newton's law of motion.

The present study is based on Eulerian approach considering a lab-scale size glass bead bubbling fluidized bed. A grid independence and validation study has been conducted between three 2D meshes and one 3D mesh and the results compared with the experimental results of Deza et al. [3].

Geometry

One fine 2D geometry (grid size ~5 times particle diameter D_p), two coarse 2D (grid size ~10 and ~15 times D_p) and one 3D geometries (grid size ~10 times D_p) are constructed and meshed in a commercial meshing software POINTWISE.

The geometries represent the experimental setup of Deza et Al. [3]. The experimental setup consists of a 0.095 m internal diameter (ID), 0.40 m high acrylic tube. Other details of the experimental setup can be found in the afore mentioned research article. The height of the domains is 0.40 m and the bed height is 0.10 m for all simulations (Figure 1). The diameter of 3D cylinder is 0.095 m and the cross-section of 2D rectangular geometry is 0.095 m. 2D geometries are meshed with square cells and 3D geometry with predominantly cubical cells. The grid resolution and time step size are chosen to satisfy Courant-Friedrichs-Lewy CFL condition.

$$CFL = (V_{max}\Delta t)/\Delta x_{min} \leq 1.0 \quad (1)$$

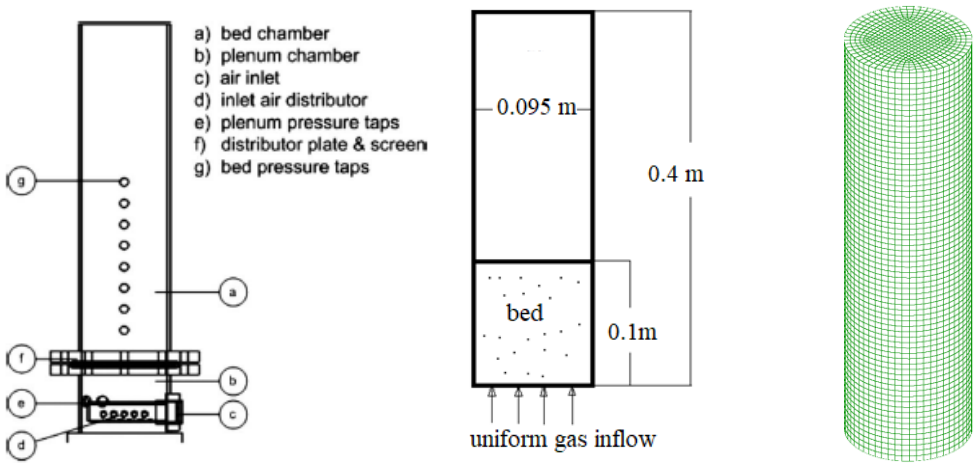

Figure 1. From left to right: schematic of the experimental setup of Deza et al. [3], 2D plane and 3D geometry of grid size ~ 10 times D_p

Initial and Boundary conditions:

The initial settle bed depth is set at 0.10 m for simulations and initial solid volume fraction at 0.627 in the bed and zero in the freeboard assuming only gas. Particle sphericity ψ was taken as 1.0 and particle-particle coefficient of restitution e as 0.95. Walls are modelled no-slip boundary condition for gas phase and partial slip for solid phase. The distributor plate having uniformly distributed holes

characterizes the gas inlet of a fluidized bed to ensure a nearly uniform flow. Therefore, a uniform inlet gas velocity (velocity inlet) of 0.258 m/s corresponding to a minimum fluidization velocity U_{mf} of 0.199 m/s is employed at the bottom of the bed and ambient pressure (pressure outlet) at the exit. Gidaspow's drag model [1] for dense granular phases is used, which is a combination of Ergun and Wen-Yu equations.

Numerical Approach:
All simulations are conducted on commercial software package ANSYS FLUENT 17.2. Flow equations are discretised by Finite-volume technique which are solved by phase coupled SIMPLE (Semi-Implicit Method for Pressure Linked Equations) [4]. The details of governing flow equations for gas-solid flow for fluidized bed are given by Gidaspow [2] .Second-order upwind scheme is chosen for spatial discretization. Second-order upwind scheme resolves bubbles boundaries by better determining voidage differences, while first-order upwind scheme is unable to resolve bubble boundaries due to numerical diffusion [5]. Quadratic Upstream Interpolation for Convective Kinematics (QUICK scheme) is used for volume fraction. A small time-step size of 0.0001 s based on CFL condition is chosen considering the convergence issues, accuracy and simulation time. Time-averaging was performed excluding first five seconds of the simulations (i.e. from 5 s to 40 s) to avoid unsteady conditions in the start of simulations to affect the results.

Table 1. Glass bead bed properties

Property	Value
Particle diameter D_p (m)	5.5×10^{-4}
Particle density ρ_p (kg/m^3)	2600
Minimum fluidization velocity U_{mf} (m/s)	0.199
Inlet gas velocity U_g (m/s)	0.258
Restitution coefficient *e*	0.95
Initial bed void fraction	0.373
Sphericity of particles ψ	1.00

Results and Discussion
Time-averaged values of simulated void fraction at heights (z = 0.04 m, 0.08m) are compared with experimental values in Figure 2. All simulations capture almost the same void fraction within 5% variation at height z = 0.04 m. The differences become evident at height of 0.08 m, where coarse grids under-predict the void fraction compared to the finer grid but capture the same phenomenon.
Also from figure 3, it can be seen that 2D simulations cannot represent the fluidization phenomenon of a 3D system as 2D simulations predict bubbles smaller in size and greater in number compared to 3D simulations.

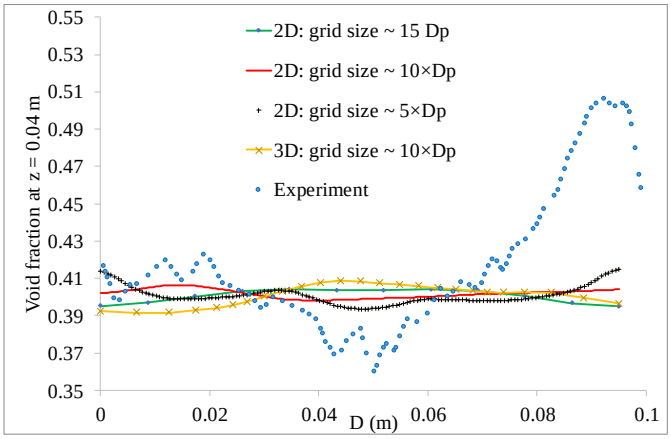

(a)

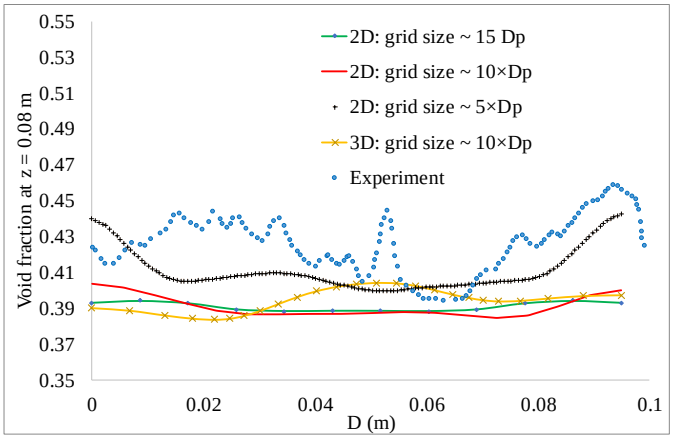

(b)

Figure 2. Comparison of time-averaged void fraction profiles a) at bed height z = 0.04 m b) at bed height z = 0.08 m

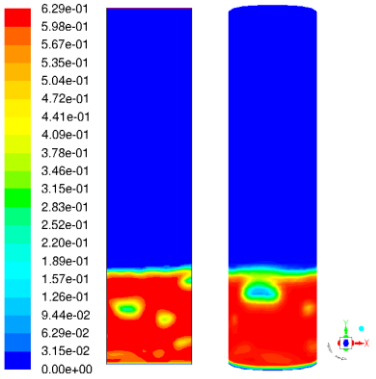

Figure 3. Instantaneous contours of bubbles from; left: 2D simulation (at 8.53 s), right: 3D simulations (at 10.92 s)

Pressure Drop Prediction:

Pressure drop estimated values from the grid study are compared with the measured pressure drop from the experiments at superficial air velocity of 0.258 m/s (Figure 4). 2D simulations are in good agreement with the experimental results. As the grid resolution becomes finer, the pressure drop is very slightly over estimated. It can also be noted that 3D simulation overpredicts the pressured drop compared to 2D simulations, which can be attributed to presence of wall effects in the third direction which is absent in 2D geometries. Also, experiments have regions close to inlet and near the walls where the material doesn't fluidize leading to slightly lower pressure drop owing to incomplete fluidization.

Another aspect to consider is the sphericity of the particles. An ideal sphericity of 1 for glass beads was considered in the simulations. When particles are not perfectly spherical, they allow for more space in between them and hence the higher volume fraction of air in the bed. This leads to lower mass of the bed compared to ideally spherical particles for the same bed height. Therefore, bed comprising non-spherical particles have lesser pressure drop and require low minimum fluidization velocity to fluidize the bed.

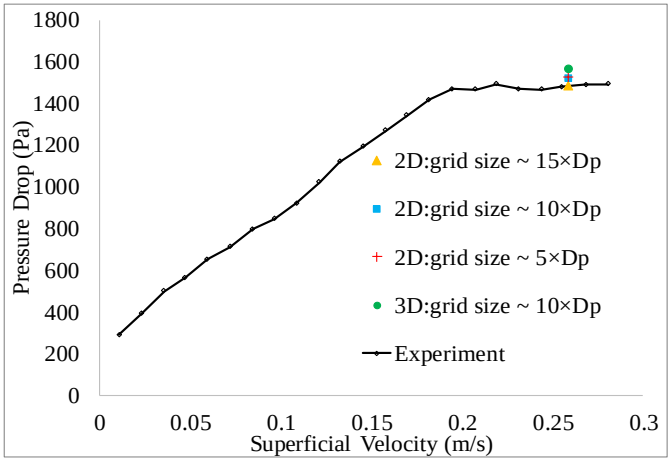

Figure 4. Pressure Drop vs superficial air velocity

Bed Expansion Prediction:

Average expanded bed height from experiments is 0.112 m, while simulations slightly under-predict the bed height when time-averaged void fraction across the bed is compared with the spatially averaged experimental data (Figure 5). All simulations show typical trend of uniform average void fraction throughout the bed and a sharp rise in the free-board. Lower void fraction predictions by simulations along the bed height are a consequence of assumption of ideal sphericity, leading to lower void fraction compared to non-spherical particles.

Influence of sphericity factor is also evident in bed expansion, as non-spherical particles result in lower mass of bed and more bed expansion.

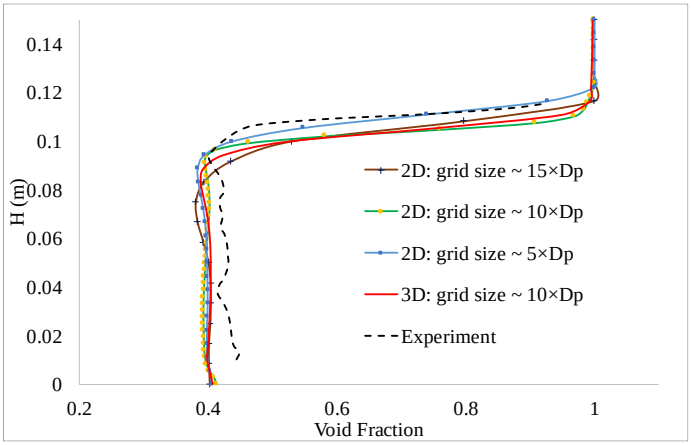

Figure 5. Comparison of time-averaged void fraction profiles from simulations with the experimental results

Conclusion:

In this work, grid resolution study has been reported for numerical simulations of glass beads bubbling fluidized bed. Grid independence was achieved with a grid size of order of minimum ten times particle diameter. While 2D simulations predicted more accurately the pressure drop, 3D simulations were in closer proximity of theoretical pressure drop. Similar is the case for bed expansion prediction. The differences call for a detailed parametric study e.g. quantification of bubble characteristics and effect of inlet geometry, sphericity of particles and coefficient of restitution on hydrodynamics of gas-solid fluidized beds.

References

[1] D. Gidaspow, *Multiphase flow and fluidization: continuum and kinetic theory descriptions*. Academic press, 1994.

[2] Jianmin, Ding, and D. Gidaspow, "A bubbling fluidization model using kinetic theory of granular flow," *AIChE J.*, vol. 36, no. 4, pp. 523–538, 1990.

[3] M. Deza, N. P. Franka, T. J. Heindel, and F. Battaglia, "CFD Modeling and X-Ray Imaging of Biomass in a Fluidized Bed," *J. Fluids Eng.*, vol. 131, no. 11, p. 111303, 2009.

[4] S. Patankar, *Numerical Heat Transfer and Fluid Flow*. Hemisphere Publishing Corporation, 1980.

[5] I. Hulme *et al.*, "Article CFD Modeling and Validation of Bubble Properties for a Bubbling Fluidized Bed CFD Modeling and Validation of Bubble Properties for a Bubbling," *Ind. Eng. Chem. Res.*, vol. 44, no. 12, pp. 4254–4266, 2005.

Reactivity of biochar gasification in atmospheres of steam, carbon dioxide and their mixtures

T. Kreitzberg, S. Pielsticker, O. Hatzfeld, R. Kneer
kreitzberg@wsa.rwth-aachen.de
Institute of Heat and Mass Transfer (WSA), RWTH Aachen University
Augustinerbach 6, D-52056 Aachen, Germany

Abstract
In this work conversion rates of biogenic char particles stemming from beech wood are measured with a lab-scale fluidized bed reactor in combination with FTIR-exhaust gas analysis at different gas atmospheres containing CO_2, H_2O and mixtures of both gases. The observed reaction rates are compared for all three gas atmospheres in a temperature range from 800 °C to 1000 °C to investigate the governing mechanism behind the gasification reactions in mixtures of CO_2 and H_2O.

Introduction

Heterogeneous reaction kinetics of carbon with carbon dioxide (Boudouard reaction) and carbon with steam (heterogeneous water gas reaction) are studied by a variety of research groups around the globe. Since these reactions are understood to be the slowest in gasification processes limiting the overall efficiency, precise knowledge on the related reaction rates is mandatory for the design and dimensioning of technical apparatuses. In this context, experimentally verified kinetic models of gasification reactions are required for implementation in pertinent CFD simulations.

A big share of experimental investigations focusing on the two above mentioned gasification reactions are conducted in gas atmospheres consisting either of one pure reacting gas (CO_2 or H_2O) or dilutions of them in an inert balance gas (e.g. in N_2 or Ar). Studies where particles are exposed to mixtures of both CO_2 and H_2O at the same time are scarce and reveal inconsistent outcomes regarding the governing mechanism of gasification: Some studies propose an additive mechanism between the two separate reactions of CO_2 and H_2O gasification, resulting in higher overall observed reaction rates. Other studies suggest an inhibitive or competitive mechanism, where observed reactivities lie below the sum of the two single reactions. A review of *Roberts and Harris* [1] gives a summary about the findings from different research groups concerning this issue and underlines the discrepancy of the reported mechanisms.

In this paper, a kinetic study of wood char particles is undertaken regarding gasification reactions in atmospheres containing CO_2, H_2O and mixtures of both gases in a small-scale fluidized bed reactor. The concentrations of the released product gases are continuously measured by FTIR-spectrometry and serve as a

basis for the calculation of particle conversion rates. By fitting model predictions to these conversion profiles, kinetic parameters are derived and compared for the different reacting atmospheres.

Experimental

A small-scale fluidized bed reactor (FBR) has been designed to implement the concept of a well stirred reactor approximating uniform distributions of thermodynamic state variables as well as of reacting species. Small batches of pulverized solid fuel are supplied to a fluidized bed consisting of alumina particles while simultaneously analyzing the exhaust gas. The experimental set-up is completed by a gas feeding system, including thermal mass flow controllers and a Fourier transform infrared spectrometer (FTIR) for product gas analysis.

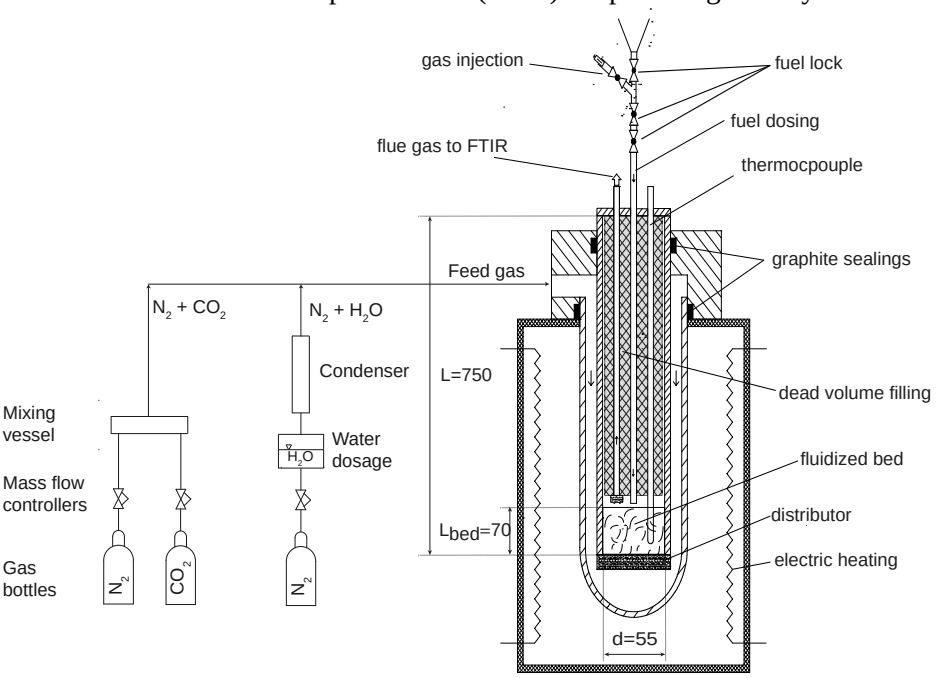

Figure 1. Scheme of the fluidized bed reactor (dimensions in mm)

The employed feed gas system is adapted depending on the type of experiment conducted:

For CO_2 gasification experiments, nitrogen and CO_2 are fed from separate gas bottles into the reactor. The flow of each component is regulated by thermal mass flow controllers. The resulting CO_2 concentration is adjusted by the ratio of the entering nitrogen and carbon dioxide streams.

For gasification experiments containing H_2O and mixtures of H_2O and CO_2 a controlled nitrogen stream is bubbled through a heated water trap; thus, the N_2 gas flow gets enriched with water vapor. This water dosage unit is followed by a

condenser to cool down the N_2/H_2O mixture. In this way, the gas is cooled to the dew point temperature corresponding to the target steam concentration. Excess water is condensed and fed back to the water dosage unit. By these means, a saturated N_2/H_2O gas mixture is obtained which serves as the feed gas for H_2O gasification experiments. CO_2 is added to this stream to achieve a desired gas mixture consisting of equal amounts of CO_2 and H_2O.

The gas enters the inner reactor pipe through a porous distributor plate made from sintered silica glass and fluidizes the bed particles. All ceramic parts of the reactor are located in an electrically heated furnace which can be heated up to 1553 K. Gaseous reaction products are captured just above the fluidized bed by an exhaust pipe. A ceramic filter, which is mounted to the lower pipe end, prevents entrainment of small particles. The exhaust gas is fed into the FTIR-gas analyzer through a sampling line and a filter. A Gasmet DX-2000 FTIR spectrometer is employed for real-time gas analysis, sampling at 0.56 Hz. More detail on construction, operation and error analysis is given elsewhere [2–4].

In this work a biogenic char made from beech wood chips pyrolyzed in a screw reactor under pure nitrogen atmosphere with a residence time of 5 minutes at 773 K is investigated. Table 1 gives an overview of the proximate and ultimate analysis results for the fuel: The char mainly consists of carbon (> 80 wt.-%) with a remaining volatile content of 23.3 wt.-%.

Table 1. Fuel properties based on ultimate and proximate analysis for investigated beech wood char particles (mesh size: 125–160 µm)

Ultimate analysis	**C (daf)**	**H (daf)**	**N (daf)**	**S (daf)**	**O (daf)**
	81.2 %	3.3 %	0.3 %	0.0 %	12.1 %
Proximate analysis	**Moisture (raw)**		**Ash (dry)**		**Volatiles (daf)**
	3.6 %		3.1 %		23.3 %

Evaluation procedure

The establishment of kinetic parameters is based on a carbon species balance around the reactor. The dimensionless carbon conversion rate dX/dt can be derived experimentally from the temporal concentrations of the reactor exhaust gas species discharging the reacted carbon from the reactor - namely CO_2 and CO (cf. eq. 1). It can also be computed by a model approach, which can be interpreted using the characteristic reaction rate r_0 as an adjustable fit-parameter (cf. eq. 2). This characteristic reaction rate is determined iteratively by fitting the model prediction to the experimental data. A detailed overview of all steps of the employed evaluation routine is given in [4].

$$\frac{\mathrm{d}X_{\mathrm{exp}}}{\mathrm{d}t} = \frac{M_{\mathrm{c}}}{m_{\mathrm{c}}} \cdot \Delta C \cdot \dot{n}_{\mathrm{out}} \tag{1}$$

$$\frac{\mathrm{d}X_{\mathrm{mod}}}{\mathrm{d}t} = (1 - X) \cdot r_0 \tag{2}$$

Where M_C is the molar weight of carbon and m_C represents the total captured carbon mass in the exhaust gas flow. The molar change in carbon due to reaction is symbolized by ΔC and the molar gas flow leaving the reactor by $\dot{n}_{\mathrm{out}}$. Depending on the type of experiment conducted (CO_2, H_2O or CO_2/H_2O gasification) the balance yields different expressions for both of the factors $\dot{n}_{\mathrm{out}}$ and ΔC (cf. [3]).

Results

Three sets of experiments have been conducted under different gas atmospheres:

1. 20 vol.-% CO_2 in N_2
2. 20 vol.-% H_2O in N_2
3. 20 vol.-% H_2O + 20 vol.-% CO_2 in N_2

For all three sets, temperature has been varied from 800 °C to 1000 °C. Reacting conditions regarding temperature, particle size and reactant partial pressure have been chosen to ensure that particles react under regime I, which means that no significant mass transfer limitations (e.g. pore diffusion or external diffusion) are expected. After performing the evaluation routine described above, the determined characteristic reaction rate r_0 is plotted against the reciprocal temperature in Figure 2. Marker symbols specify the mean value of at least 5 repeated single measurements with error bars showing their standard deviation. The diagram exhibits linear profiles for all three reaction types, indicating that in the investigated range of temperature a typical exponential temperature dependency is found.

Focusing first on the experiments conducted in environments containing either CO_2 or H_2O (blue triangles, black squares) ratios of both reactions are close to unity (r_{H2O}/r_{CO2} = 0.95) at 800 °C. With increasing temperature rates start to diverge, reaching a ratio of r_{H2O}/r_{CO2} = 1.56 at 1000 °C. This trend is due the higher activation energy of the H_2O gasification reaction compared to CO_2 gasification, which is directly proportional to the slope of the continuous black line. The calculated activation energies are $E_{A,H2O}$ = 230 kJ/mol and $E_{A,CO2}$ = 202 kJ/mol.

Comparing the determined rates in mixtures of CO_2 and H_2O (red circles) to the two single reactions it can be concluded that the rates in mixed atmospheres clearly lie above the others for low temperatures (T < 900 °C) and are in between them for higher temperatures (T > 900 °C). Furthermore, the rates in mixed atmospheres are lower than the sum of the two individual reactions for the investigated conditions, leaving no evidence for an additive reaction mechanism (cf. dashed line in

Figure 2). This finding suggests a competitive behavior between the two reactions. However, an extrapolation of the continuous lines in Figure 2 suggest, that an additive behavior of the rates might be observable for even lower temperatures at around 700 °C. The slope of the mixed gasification reaction is almost identical to the one of CO_2 gasification which leads to a similar activation energy of $E_{A,mix}$ = 196 kJ/mol.

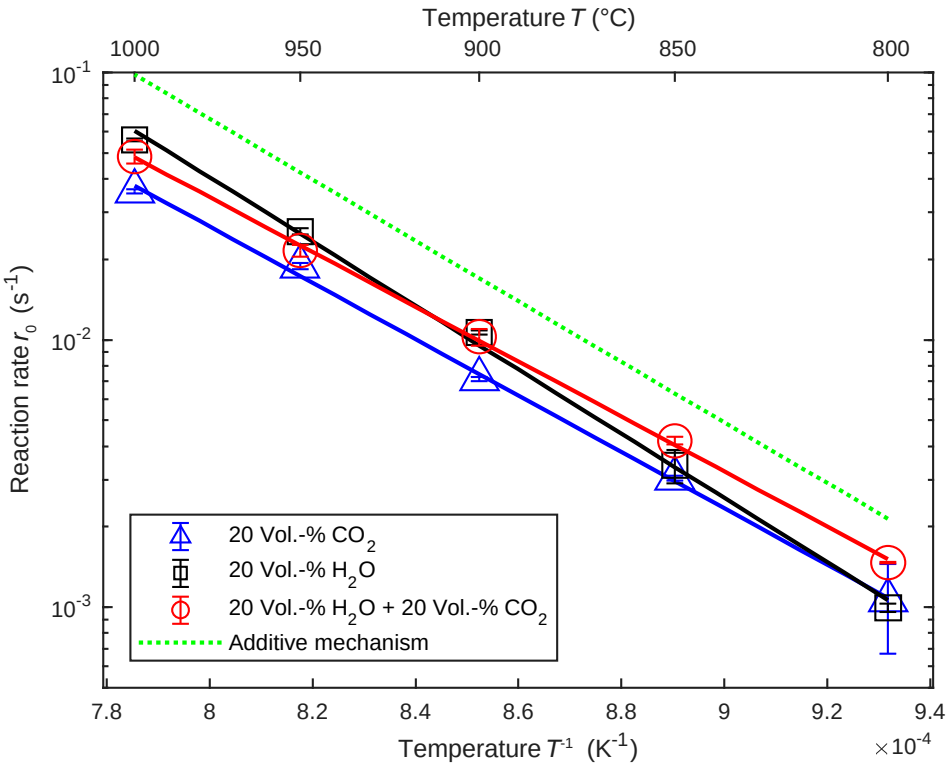

Figure 2. Reaction rates of biochar particles measured under different gas atmospheres in the fluidized bed reactor plotted against reciprocal temperature. Symbols give mean values of repeated experiments, continuous lines represent linear regressions.

Conclusions

This study has investigated the gasification of biochar particles and has underlined an inhibitive/competitive reaction mechanism regarding the reactivity in mixtures of CO_2 and H_2O. It has been shown that rates in mixtures of both reacting gases are above the two single reactions for low temperatures (T < 900 °C) and are in corridor between the two reactions at higher temperatures (T > 900°C).

Acknowledgements
The authors would like to thank the German Research Foundation (DFG) for funding Stefan Pielsticker and Thobias Kreitzberg within the SFB/Transregio 129 "Oxyflame".

References

[1] Roberts, D. G., Harris, D. J., "Char Gasification Kinetics in Mixtures of CO_2 and H_2O: The Role of Partial Pressure in Determining the Extent of Competitive Inhibition", *Energy & Fuels* 28: 7643–7648 (2014).

[2] Pielsticker, S., Gövert, B., Kreitzberg, T., Habermehl, M., Hatzfeld, O., Kneer, R., "Simultaneous investigation into the yields of 22 pyrolysis gases from coal and biomass in a small-scale fluidized bed reactor", *Fuel* 190: 420–434 (2017).

[3] Pielsticker, S., Gövert, B., Kreitzberg, T., Habermehl, M., Hatzfeld, O., Kneer, R., "Development of a rapidly responding fluidized bed reactor by theoretical and experimental evaluation of combustion reactions", *Fuel* 223 available online (2018).

[4] Gövert, B., Pielsticker, S., Kreitzberg, T., Habermehl, M., Hatzfeld, O., Kneer, R., "Measurement of reaction rates for pulverized fuel combustion in air and oxyfuel atmosphere using a novel fluidized bed reactor setup", *Fuel* 201: 81–92 (2017).

AN ASSESSMENT OF CARBON OXIDATION MECHANISM BY DYNAMIC OXIDATION/DESORPTION IN A LOOPING REACTOR

A. Coppola*, O. Senneca, F. Cerciello**, P. Salatino***
o.senneca@irc.cnr.it
*Dipartimento di Ingegneria Chimica, dei Materiali e della Produzione Industriale, Università degli Studi di Napoli Federico II, Piazzale V. Tecchio 80, 80125 Napoli, Italy
**Istituto di Ricerche sulla Combustione, Consiglio Nazionale delle Ricerche, Piazzale V. Tecchio 80, 80125 Napoli, Italy

Abstract
The mechanism of carbon oxidation by oxygen has been scrutinized by means of dynamic experiments consisting of cyclic oxidation of solid carbon at low-moderate temperature (200-300°C) followed by desorption of surface oxides at high temperature (700-800°C). The rapid shift between oxidation and desorption conditions is accomplished thanks to a purposely designed reactor consisting of a dual fluidized bed configuration equipped with a rapid transfer line that enables fast pneumatic conveying of the solid sample from one reactor to the other while keeping distinct reaction conditions in the two reactors. Results are analysed with a specific focus on the role and nature of surface oxides as intermediates in carbon gasification. The existence of surface oxides of different chemical nature and stability provides the starting point to elaborate a tentative mechanistic frame of the experiment. The key features of the phenomenology, namely the oxidation rate and the CO/CO_2 ratio in the evolved gasification products, are interpreted in the light of the relative abundance and stability of "edge" oxides and epoxy moieties generated by carbon oxidation.

1. Introduction

Modelling the kinetics and mechanisms of carbon combustion has been accomplished with lumped and semi-lumped models of increasing complexity. The three-step mechanism proposed by Hurt and Calo [1] (eq.1) introduces the so called "switch over reaction" which describes the evolution of C-O complex from a less stable one to a more stable under the action of molecular oxygen with release of CO_2:

$$C_f + O_2 \xrightarrow{1} 2C(O) \quad (1.a)$$

$$C(O) + O_2 \xrightarrow{2} C(O) + CO_2 \quad (1.b)$$

$$C(O) \xrightarrow{3} CO \quad (1.c)$$

The three steps mechanism of Hurt and Calo has been included in the CBK model and was able to fit a large set of experimental data of coal combustion mainly in EFR.

Haynes and co-workers [2] further extended the model into a four-step kinetic mechanism (eq.2):

$$C_f + O_2 \xrightarrow{1} C(O)^{\#} \quad (2.a)$$

$$C(O)^{\#} + O_2 \xrightarrow{2} C(O) + CO_2, CO \quad (2.b)$$

$$C(O)^{\#} \xrightarrow{3} C(O) + CO_2, CO \quad (2.c)$$

$$C(O) \xrightarrow{4} C_f + CO_2, CO \quad (2.d)$$

which, based on experimental evidence, considered the formation of a "metastable" ($C(O)^{\#}$) surface oxide which can undergo complex switch-over in the presence of oxygen, as already described in the previous three step scheme, but can also be rearranged into more energetically favourable forms. Other two differences between the semi-lumped schemes of Hurt and Calo [1] and Haynes et al. [2] deserve mention. The first difference lies in the mechanism of chemisorption, which is dissociative for Hurt and Calo and non-dissociative for Haynes and coworkers. Radovic [3] and Larciprete et al. [4-5] showed, thanks to ab initio quantum chemistry calculations of graphene oxidation, that both paths of formation of carbon-oxygen complexes are possible. On carbene-type edge sites, O_2 chemisorption is non-dissociative and leads to direct CO_2 formation [3]. Alternatively, O atoms bond in bridge position over the C−C bonds, forming epoxy groups [4-5]. This species, which can be roughly identified with the metastable carbon-oxygen complexes, may undergo surface diffusion and unzipping steps and finally CO_2 formation. In Haynes and coworkers' scheme all the reaction steps produce CO and CO_2, whereas in Hurt and Calo's model CO_2 mainly comes from the switch over reaction, and CO from the desorption step, accordingly the CO/CO_2 ratio in the combustion products would derive from the relative rate of the second and third reaction steps.

In the present study the mechanism of carbon-oxygen interaction is scrutinized by performing dynamic oxidation in a purposely designed reactor that enables periodic exposure of a solid fuel sample to different reaction environments and temperatures with minimum transfer and heat up/cooling time. This technique may offer a valuable tool for the assessment of the mechanism of interaction of solid carbon with oxygen. Studies in this field are helpful not only in view of applications to innovative technologies of stationary combustion or gasification [6], but also to shed light on the dynamical patterns of carbon chemisorption/desorption under alternating oxidizing conditions, relevant to "looping combustion" of carbon [7-8].

2. Experimental description

In order to investigate the carbon-oxygen mechanisms under fast dynamic conditions the experimental campaign has been carried out in a novel lab-scale apparatus, named Twin Beds (TB), consisting of two identical fluidized beds which can be operated separately in batch mode. The main feature of TB is that the two reactors are connected to each other by a duct which is partially immersed in both beds. The duct, equipped with valves, enables the fast pneumatic conveying of the char sample

from one reactor to the other and vice-versa. The Twin Beds apparatus is depicted in Fig.1. A detailed description of the TB system can be found elsewhere [9].

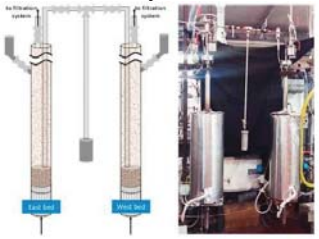

Figure 1. Twin fluidized bed apparatus.

Tests have been carried out with samples of a South African char (400-1000μm) obtained by devolatilization in a fluidized bed at 850°C for 5 min of mm-sized coal particles. Char properties are given in the Table 1. Silica sand (900-1000μm) in both reactors was used as a ballast in order to avoid significant bed temperature variations due to chemical reactions and solid conveying. For our purposes, the two reactors were employed as an Oxidizer and a Desorber respectively. Several oxidation/desorption cycles were carried out varying the oxidation temperature values between 200 and 300°C and the desorption temperature values between 700 and 800°C. Each test is labeled with the acronym O_x-D_y where the O_x and D_y indicate the oxidation and the desorption steps with their relative operating temperatures in °C, respectively.

Table 1. Proximate and ultimate analysis of the coal char

Moisture raw wt%	**Volatiles** wt%	**Fixed Carbon** wt%	**C** dry, wt%	**H** dry, wt%	**N** dry, wt%	**S** dry, wt%	**O** dry, wt%	**Ash** dry, wt%
3.34	7.04	69.17	71.92	1.37	0.52	0.02	4.26	20.45

For each test (O_x-D_y), three oxidation-desorption cycles were carried out and the concentration of CO and CO_2 in the exhaust was monitored by means of NDIR analyzer throughout.

3. Results

Fig. 2 reports the typical outcome of a dynamic oxidation experiment, namely the time-series of CO and CO_2 concentration measured at the exhaust of the TB reactor during 3 oxidation/desorption cycles. Profiles in Fig. 2 correspond to O_{200}-D_{700} test conditions. During the desorption step a large amount of CO_2 was released, and several peaks appear in CO and CO_2 profiles in the early stages of desorption, which suggest the presence of different superficial –C(O) complexes. As soon as air is fed to the oxidizer an abrupt release of CO and CO_2 occurs. The origin of these very high

peaks under dynamic conditions is not clear. A possible explanation may be the formation of reactive sites (C_f and/or –C(O)) during dynamic desorption at 700°C, that are stable enough not to be desorbed during the desorption step, but reactive enough to undergo switch-over in the subsequent oxidation stage, in the presence of oxygen, despite the fairly low temperature of the oxidation step.

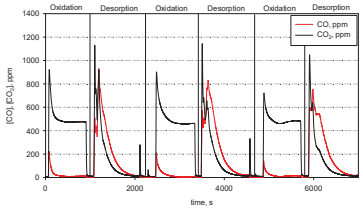

Figure 2. Time series of CO and CO_2 concentrations at the exhaust during the oxidation/desorption cycles.

Table 2 reports the CO/CO_2 ratios obtained during oxidation and desorption steps in different experiments.

Table 2. Average moles of CO and CO_2 released per Kmole of carbon loaded and CO/CO_2 molar ratio during the oxidation/desorption cycles.

	CO/C	**CO_2/C**	**CO/CO_2**
O_{200}-D_{700}	0.0047	0.0130	0.3602
	0.0314	0.0219	1.4344
O_{250}-D_{700}	0.0136	0.0374	0.3640
	0.0547	0.0318	1.7198
O_{300}-D_{700}	0.0269	0.0863	0.3120
	0.1037	0.0439	2.3633
O_{200}-D_{800}	0.0037	0.0069	0.5312
	0.0368	0.0246	1.4928

It is interesting to note that, despite the fact that the amount of $CO+CO_2$ increases with the oxidation temperature, the CO/CO_2 ratio remains almost unchanged. On the contrary, in the desorption stage the CO/CO_2 ratio increases from the value of 1.4 of O_{200}-D_{700} to the value of 2.4 for O_{300}-D_{700}. This suggests that the nature and/or amount of surface oxides which are formed during the oxidation stages have a strong influence on the subsequent desorption steps. Moreover, when the temperature of the desorption step is increased, while keeping the oxidation temperature fixed at 200°C, the release of CO and CO_2 during the subsequent oxidation steps appears to be enhanced. Data of CO and CO_2 produced during each cycle of Oxidation/Desorption have been further worked out to calculate the moles of oxygen uptaken during the

oxidation steps. A rough indication on the rate of oxygen uptake is obtained by dividing the total amount of oxygen uptaken during the oxidation step by the duration of the oxidation stage (20 min. A linear trend is obtained accounting for an activation energy in the order of E= 30 kJ/mol. The value is comparable with the value of E=25 kJ/mol suggested for the chemisorption reaction by Hurt and Calo [1].

4. Discussion and Conclusion

In this study a novel Twin Beds reactor has been used to perform dynamic oxidation of carbon, consisting of periodic oxidation/desorption cycles on a bituminous coal char. The key findings of the present experimental campaign can be summarized in the following statements:

a) the extent (and rate) of oxygen uptake during the oxidation step increases with oxidation temperature, and is well correlated by an Arrhenius-like law with an activation energy of the chemisorption step (E= 30 kJ/mol). This activation energy is fairly smaller than typical activation energies found when the combustion rate of similar carbons is correlated according to single-step kinetic models (E= 120 kJ/mol);

b) the CO/CO_2 ratio during a given oxidation or desorption step is not constant;

c) the CO/CO_2 ratio in the products of the oxidation step is barely influenced by the oxidation temperature, whereas it is affected by changes in the temperature of the desorption step;

d) the CO/CO_2 ratio in the desorption step is heavily affected by the temperature of the oxidation step, but barely affected by the desorption temperature.

Understanding these features requires consideration of the nature of the different surface carbon-oxygen groups that are formed in the oxidation processes and their possible interaction with the adjacent carbon sites. In particular, the CO/CO_2 ratio provides an indication of the alternative paths along which carbon gasification occurs, and may be helpful to track the prevailing path to carbon conversion.

The following tentative mechanism can be offered to explain the recorded phenomenology. Oxidation at mild temperature yields surface oxides to an extent and rate that depend on oxidation temperature according to an Arrhenius-type law. The moderate activation energy suggests that the prevailing moiety of surface oxide formed during early oxidation is the “metastable” epoxy, which may eventually act as oxygen “donor”. The rate of oxygen uptake might be at least partly controlled by surface diffusion (spill over) of mobile epoxy over the polyaromatic basal domains. Results of previous studies [10-11] suggest that increasing oxidation temperature (from 200 to 300 °C) should result in a larger fractional content of “edge” oxides (ether, carbonyl, lactone) as compared to the epoxy. As reaction conditions are switched to the desorption stage, the much higher temperature promotes the formation of further stable edge oxides at the expenses of epoxy. Edge oxides eventually undergo decomposition either as CO or, by interaction with neighboring mobile epoxy and unzipping, as CO_2

It may be inferred that the CO/CO_2 ratio observed during the desorption step reflects

the relative abundance of edge versus epoxy sites established during the previous oxidation stage: the higher the oxidation temperature (from 200 to 300°C), the larger the edge vs epoxy fractional content, the larger the CO/CO_2 ratio (from 1.43 to 2.36). The release of CO_2 and, to a lesser extent, of CO during the early oxidation stages might instead be related to decomposition of surface oxides that have survived the previous desorption step, as their stability is undermined by direct interaction with molecular oxygen (complex switch-over) or with newly formed neighbouring surface oxides. Further investigation is in progress to fully assess the dynamics of epoxy and different types of edge oxides and to provide a quantitative mechanistic frame for carbon oxidation and combustion.

References

[1] Hurt, R.H., Calo, J.M., "Semi-global intrinsic kinetics for char combustion modelling", *Combust. Flame.* 125:1138-1149 (2001).

[2] Lear, A.E., Brown, T.C., Haynes, B.S., "Formation of metastable oxide complexes during the oxidation of carbons at low temperatures", *Twenty-Third Symposium (International) on Combustion/The Combustion Institute.* 23: 1191–1197 (1991).

[3] Radovic, L.R., "Active Sites in Graphene and the Mechanism of CO_2 Formation in Carbon Oxidation", *J. Am. Chem. Soc.* 131: 17166–17175 (2009).

[4] Larciprete, R., Fabris, S., Sun, T., Lacovig, P., Baraldi, A., Lizzit. S., "Dual Path Mechanism in the Thermal Reduction of Graphene Oxide", *J. Am. Chem. Soc.* 133: 17315–17321 (2011).

[5] Larciprete, R., Lacovig, P., Gardonio, S., Baraldi, A., Lizzit. S., "Atomic Oxygen on Graphite: Chemical Characterization and Thermal Reduction", *J. Phys. Chem.* 116: 9900−9908 (2012).

[6] Pielsticker, S., Heuer, S., Senneca, O., Cerciello, F., Salatino, P., Cortese, L., Göver,t B., Hatzfeld, O., Schiemann, M., Scherer, V., Kneer, R., "Comparison of pyrolysis test rigs for oxy-fuel conditions", *Fuel Proces. Technol.* 156:461-472 (2017).

[7] Salatino,P., Senneca, O., Int. Patent application WO2010/026259A2 (2010)

[8] Salatino, P., Senneca, O., "Preliminary assessment of a concept of looping combustion of carbon", *Ind. Eng. Chem. Res.* 48:102-109(2009).

[9] Coppola, A., Scala, F., Gargiulo, L., Salatino, P., "A twin-bed test reactor for characterization of calcium looping sorbents", *Powder Technol*. 316:585–591(2017).

[10] Levi, G., Senneca, O., Causà, M., Salatino, P., Lacovig, P., Lizzit, S., "Probing the chemical nature of surface oxides during coal char oxidation by high-resolution XPS", *Carbon* 90**,** 181–196 (2015).

[11] Levi, G., Causà, M., Lacovig, P., Salatino, P., Senneca, O., "Mechanism and thermochemistry of coal char oxidation and desorption of surface oxides", *Energy Fuels* 31 (3), 2308–2316 (2017).

Progress and Challenges in Flow Field Studies of 40 - 60 kW_{th} Pulverized Coal Flames

D. Zabrodiec*, J. Hees, A. Massmayer, O. Hatzfeld, R. Kneer
zabrodiec@wsa.rwth-aachen.de
*Institute of Heat and Mass Transfer, RWTH Aachen University, Augustinerbach 6, 52056 Aachen, Germany

Abstract

The present poster is dedicated to report recent results from experimental studies upon flow fields from pulverized coal (PC) swirl flames and associated challenges. Studied flames are confined within a cylindrical down-fired combustion chamber operating under conventional air and oxy-fuel combustion modes. To study the flow fields inside the combustion chamber a non-intrusive laser Doppler velocimetry (LDV) system has been gradually improved in order to maximize tracer-particle count rates and to minimize the error associated to particle slip. LDV measurements showed better results when compared against particle image velocimetry (PIV) measurements, as the LDV system utilized features an improved data collection in flame regions with high particle number density and strong background radiation. Measured two-component velocity profiles are presented and provide information about mean velocity values and turbulent fluctuation of the particles in the flow at different locations in the combustion chamber. Six studied cases were taken employing two different burners with similar geometries. Three cases correspond to 60 kW_{th} flames with similar stoichiometric ratios under air and oxy-fuel combusting modes. The other three correspond to 40 kW_{th} oxy-fuel flames with identical inlet velocities but varied oxygen concentration in the oxidizer mixture. Presented data is intended to generate a new extended database of experimental data for the validation of numerical models. Also, measurement results show that the structure of the flame and the intensity of the inner recirculation zone (IRZ) can be modified and enhanced by changes in momentum and viscosity of the combusting gases introduced by different reactant mixtures (i.e. by increasing oxygen concentration in oxy-fuel) under similar stoichiometric ratios or under similar inlet gas velocities. This is highly relevant as it can contribute to optimizing boiler retrofitting processes and to the general understanding of the behavior of pulverized coal swirl flames. More detailed validation data is available upon request.

Introduction

The usage of coal for industrial and thermal conversion processes comprises a wide range of mayor applications. Although pulverized coal combustion has been

studied now for several decades, new interest has risen since the possibility emerged to retrofit existing large-scale boilers and combustors with technologies, such as oxy-fuel combustion, which can enable carbon capture and sequestration (CCS) [1]. Given technical limitations of the past, the study and analysis of coal furnaces and combustors has relied largely on empirical studies which were mostly limited to the observed relationships given by the parametric variation of inputs and the resulting outputs (such as the complex flow fields and chemical reactions) of different combustor and burner configurations. Fortunately, recent advances in computational performance, modeling and experimental diagnostic techniques allow the conduction of much detailed simulations and a deeper characterization of phenomena such as turbulent multi-phase reacting flows.

This work presents results based on laser Doppler velocimetry (LDV) flow field measurements. LDV is an optical, non-intrusive measurement technique commonly used for the characterization of flow fields. The quality of the LDV measurements relies strongly on the presence of suitable flow tracer particles in the flow and adequate optical access to the studied flow. Unfortunately, in the case of coal-fired combustors, the fuel employed is composed of polydisperse, non-spherical solid particles acting as flow tracers and also the optical access to the flows is usually difficult (or impossible). In order to address these two problems, the chosen combustor possesses a simplified geometry with suitable optical access and is capable of reproducing all the highly coupled multiscale phenomena present in industrial scale flames. The employed LDV measurement system has been modified in order to be able to work with polydisperse flow tracers and to improve the accuracy of the velocity measurements. The objective of this work is to present experimental results with unprecedented level of detail for self-sustained PC swirling flames and to comment on the challenges found when attempting to perform LDV measurements on these flames. Shown results are based on measurements conducted upon 60 kW_{th} and 40 kW_{th} Rheinish Lignite flames under conventional atmospheric and oxy-fuel combustion modes with oxygen contents between 21% and 33% in volume in the reactant.

Experimental setup

Experiments were conducted at the combustion test facility of the Institute of Heat and Mass Transfer, RWTH Aachen University, which consist of a vertically down-fired cylindrical combustion chamber, equipped with electrically heated ceramic inner walls [2]. For the present work two swirl burners were employed (Figure 1). The first burner, shown in Figure 1a, was used to generate all 60 kW_{th} studied flames [2]. The second burner (Figure 1b) was employed for all 40 kW_{th} flames [3,4]. Both burners are composed of two annular concentric nozzles: the primary nozzle (PN, Figure 1), which is responsible for delivering an axial annular jet around a bluff body, this jet is a mixture of coal particles and a carrier gas. The

secondary nozzle (SN, Figure 1) generates an annular swirled jet and is the main

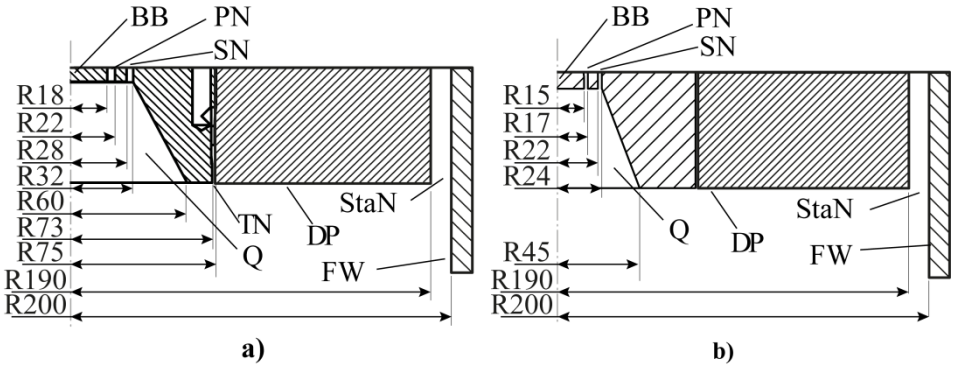

Figure 1. The two employed swirl burners, a) 60 kW_{th} and b) 40 kW_{th}, mounted at the top of the asymmetrical combustion chamber, main burner features are shown: central bluff body (BB), primary nozzle (PN), secondary nozzle (SN), tertiary nozzle (TN), burner quarl (Q), staging-flow nozzle (StaN), dump plane (DP) and the combustion chamber walls (FW). Also, the relevant radial dimensions R are presented, in mm.

inlet for oxidant gas. Additional oxidant is delivered through the tertiary and the staging nozzle (TN and StaN in Figure 1).

The LDV diagnostic system is mounted at observation port no. 1 (P1) of the combustion chamber (see Figure 2), the entire integrated sending-receiving optic system (A) can be traversed along the radius of the combustion chamber in order to compose point-based measurement profiles. Different measurement profiles at different axial distances from the burner can also be obtained by moving the burner along the axis of the combustion chamber [2].

The 2D-LDV system has been specially designed and optimized to deliver maximum laser power to the measurement volume and to be able to optically generate a small (Ø150 μm) measurement volume (D in Figure 2) at distances larger than 1.5 m from the collecting optics. By combining high laser power and adequate optics the problem of tracer particle size polydispersity can be addressed, the error in velocity measurement introduced by the slipping particles is reduced by increasing the detectability of small particles and decreasing the weight of large coal particles on the statistical evaluation of the turbulent flow [2].

Present results were obtained from a set of six different operating conditions, three for each burner, keeping in both cases the thermal output of the flames constant (same fuel mass flow provided), also only Rhenish lignite was employed. For the case of the 60 kW_{th} flames the composition of the oxidant was varied from

conventional atmospheric conditions to two oxy-fuel conditions with 21 and 25 vol.% of O_2 in pure CO_2 respectively while keeping the oxygen-fuel ratio $\lambda_L = 0.8$ constant [2]. The remaining three conditions were obtained with the 40 kW_{th} burner keeping the inlet velocities constant between oxy-fuel oxidant mixtures (25, 27 and 33 vol.% O_2 content.). Lignite fuel particles had a typical median diameter of D_{50} = 29 µm with a size distribution spanning from D_{10} = 5 µm to D_{90} = 132 µm.

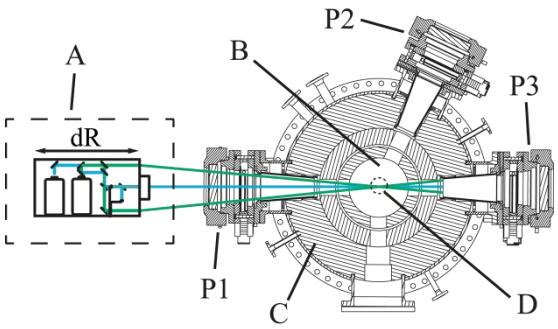

Figure 2. Cross-section of the combustion chamber at the measurement level showing the measurement ports (P1-P3) and the schematic layout of the 2D-LDV integrated sending-receiver optical system (A), active cross section of the combustion chamber (B), the ceramic insulation layer (C) and the location of the radially traversed (dR) LDV measurement volume (D).

Measurement results

Figure 3 shows measured radial profiles from three lignite 60 kW_{th} flames under the same stoichiometric conditions ($\lambda_L = 0.8$) for air flame (Fig. 3a) and two oxy-fuel conditions (Fig. b and c) with 21 and 25 vol.% O_2 content. Each of the six subfigures showing profiles for eight relative distances to the burner. Higher mean velocity values are measured for both oxy-fuel cases than in the conventional air case, possibly attributed to the higher momentum and smaller dynamic viscosity compared to the air case [2].

In an analogous way, Figure 4 shows measured radial profiles from three lignite 40 kW_{th} oxy-fuel flames (different λ_L). The three operating conditions have identical volume flows for the oxidant (same inlet velocity) but increasing O_2 contents: 23, 27 and 33 vol.% in the oxidizer. Although profiles show very similar trends, a reciprocal relationship following the increased O_2 has been observed. The peak velocity values at the swirling jet increase with increasing O_2 content but the opposite occurs with the velocities at the internal recirculation zone.

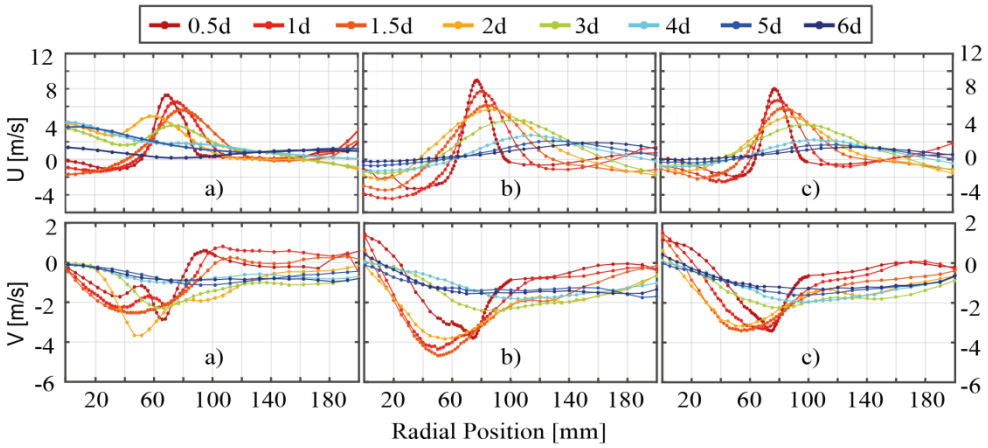

Figure 3. Mean axial (U) and tangential (V) velocity profiles of 60 kW_{th} (lignite, $\lambda_L = 0.8$), for: a) air case, b) 21/79 O_2/CO_2 vol.% c) 25/75 O_2/CO_2 vol.% at eight relative positions from the DP, shown as factors of the SN diameter d = 64 mm [2]

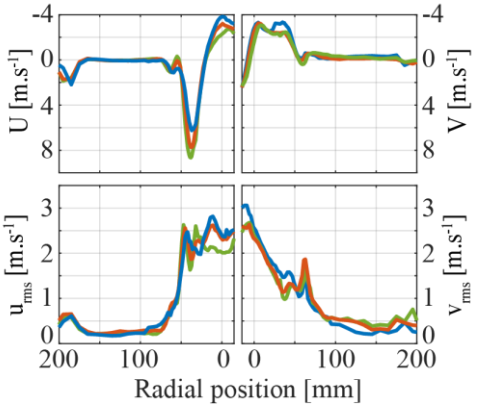

Figure 4. Mean axial (U) and tangential (V) velocity profiles and respective (RMS) values of particle velocity fluctuations of 40 kW_{th} Lignite flames at 24 mm from the DP with same inlet velocities and oxidant mixtures: 23/77 O_2/CO_2 vol.%, 27/73 O_2/CO_2 vol.% and 33/67 O_2/CO_2 vol.%

Conclusions

The improved LDV system provides highly detailed velocity measurements of flow fields of PC swirl flames under different mixture conditions. Also information about the local velocity fluctuations of the particles in the flow (RMS) is provided. The combined approach of higher laser power and smaller measurement volume

size result in much higher accuracy of the measurements as i.e. data rates have increased by a factor of 10 or more and the velocity histograms show smooth characteristics in comparison to the discontinuous character associated to flow with high particle slip.
Additional seeding has also been tested, but no significant improvement in measured velocities or data rates have been observed. Possibly attributed to the high mass ratio between coal particles and additional seeding present in the flow. More detailed information about the polydispersity issues in the flow and further measurement results will be shown on the poster.

Acknowledgements

This work has been financed by the German Research Foundation (DFG) within the framework of the SFB/TRR 129 ‘‘Oxyflame”.

Nomenclature

D_{10}	*Biggest particle size for 10% of the cumulative mass*
D_{50}	*Mass median diameter of coal particles (50%)*
D_{90}	*Biggest particle size for 90% of the cumulative mass*
λ_L	*stoichiometric ratio*

References

[1] Chen, L., Yong, S.Z., Ghoniem, A., “Oxy-fuel combustion of pulverized coal: Characterization, fundamentals, stabilization and CFD modeling”, *Prog. in Ener. and Comb. Sci.* 38:156–214 (2012)

[2] Zabrodiec, D., Becker, L., Hees, J., Massmeyer, Habermehl, M., Dreizler, A., Kneer, R., “Detailed Analysis of the Velocity Fields from 60 kW Swirl-Stabilized Coal Flames in CO_2/O_2- and N_2/O_2-Atmospheres by Means of Laser Doppler Velocimetry and Particle Image Velocimetry”, *Comb. Sci. and Tech.* 189:1751–1775 (2017)

[3] Becker L. G., Kosaka H., Böhm B., Doost S., Knappstein R., Habermehl M., Kneer R., Janicka J., Dreizler A., “Experimental investigation of flame stabilization inside the quarl of an oxyfuel swirl burner”, *Fuel,* 201:124–135 (2017)

[4] Toporov D., Bocian P., Heil P., Kellermann A., Stadler H., Tschunko S., Förster M., Kneer R., “Detailed investigation of a pulverized fuel swirl flame in CO_2/O_2 atmosphere”, Comb. and Flame 155: 605–618 (2008)

SESSION III

Fuel and biofuel processing and upgrading

ON TORREFACTION OF AGRO-INDUSTRIAL RESIDUES: FROM LOW-VALUE WASTES TO HIGH-QUALITY ENERGY CARRIERS

Paola Brachi*, Riccardo Chirone*, Francesco Miccio, Michele Miccio***, Giovanna Ruoppolo***

p.brachi@irc.cnr.it

*Institute for Research on Combustion, National Research Council, Napoli, Italy,
**Institute of Science and Technology for Ceramics (ISTEC-CNR), Faenza (RA), Italy
***Department of Industrial Engineering, University of Salerno, Fisciano (SA), Italy

Abstract

The torrefaction treatment, which is a technically feasible method for converting any lignocellulosic material into a high-energy density, hydrophobic, compactable, easily grindable, and biochemically stable coal-like solid, suitable for commercial and residential combustion and gasification applications, has been adopted to valorize wastes from agro-industrial activities. A review on the activities carried out by our research group will be reported. In particular, the role played by the main process variables (i.e., torrefaction temperature and reaction time) on the properties of the solid products (e.g., elemental composition, calorific value, ash content, etc.) and the process performances in terms of mass yield, energy yield and energy densification index has been evaluated. The effect of the reactor configuration (fixed bed vs. fluidized bed reactor) has also been investigated. Findings of this research work are useful to provide some guidelines for optimizing the process operating conditions yielding high quality energy carriers from low-value agro-industrial residues.

Introduction

The concept of exploiting wastes from agro-industrial activities to produce energy by thermo-chemical route is not new [1]. However, the high costs associated with handling, storing, and processing such feedstocks, characterized by low heating value, high moisture content, hygroscopic behavior, and putrescible nature, have, to date, hampered the development in this sector [2].

Over the past 10 years, a lot of attention has been devoted to the torrefaction process as suitable option to overcome the above-mentioned barriers. Torrefaction is a relatively new thermochemical treatment where biomass is heated (typically < 50 °C/min) in an inert environment up to a temperature of about 200-300 °C for a relatively long reactor residence time (from 30 min to 120 min, depending on the

specific feedstock) [3]. During the process, a combustible gas ('torgas') consisting of different organic compounds is also produced in addition to the torrefied solid.
In a properly designed and operated torrefaction system the torgas may be combusted in a burner and the flue gas used to directly or indirectly (via heat exchangers supply) supply the process heat demand which basically consists of the energy needed for biomass the pre-drying heating, drying, post-drying heating and torrefaction. Whether or not auto-thermal operation is conceivable for any specific case depends on the moisture content of the incoming biomass feedstock and the severity of the torrefaction settings [4]. In particular, the larger is the moisture content in the incoming biomass, the higher is the amount of torgas required to achieve auto-thermal operation, and consequently, the lower are the mass and the energy yields of the solid product [4]. Therefore, an economic optimum between biomass properties and energy yield is typically sought. Thanks to the torrefaction pre-treatment technology, the following advantages can be achieved: a. to convert any hydrophilic lignocellulosic raw materials into a hydrophobic solid, which can be stored outdoors; b. to decrease the biological activity of biomass, thus preventing loss of quality and off-gas emissions; c. to realize a sort of standardization of chemical properties of the various kinds of biomass; d. to produce a solid product having a higher energy content with respect to the raw biomass reducing the transportation costs. In this paper, a summary of the research activities performed in the field of torrefaction by our research group is presented. These activities, in particular, began performing a preliminary screening of the agro-industrial residues that are largely available in Campania region (Italy).

Experimental

Agro-industrial residues such as tomato processing residues [2,4-7], olive mill residues [2,8,9] and orange peels [10, 11] were selected as biomass feedstocks for torrefaction studies. The main chemical and physical properties of the selected agro-industrial residues were analyzed before and after the torrefaction treatment by means of a TGA 701 LECO thermogravimetric analyzer, CHN 2000 LECO analyzer, a Parr Model 6200 calorimeter. A new laboratory scale experimental set-up was purposely designed and built for torrefaction tests (see Fig. 1). It consists of a gas supply unit, a gas heating system, a torrefaction unit, a tor-gas treatment unit, where the volatile stream is split into a liquid and a gas phase, and a data acquisition system. The apparatus and the experimental technique are already described elsewhere [2].

Results

The results obtained showed that the torrefaction treatment of agro-industrial residues is a promising pre-treatment route for upgrading their properties as a fuel [2, 4, 8, 10]. In particular, for all the investigated residues, the torrefaction treatment led to a significant improvement of their chemical and physical properties (see data in Fig.2 relative to the specific case of tomato peels). More specifically, it was found that the hydrogen-to-carbon (H/C) and oxygen-to-carbon ratio (up to approximately

40 % for the biomass torrefied at 285 °C and 30 min) decrease with increasing torrefaction temperature, as can be seen in Fig. 2a showing the Van Krevelen plot (i.e., a diagram obtained by plotting the data from ultimate analysis in term of H/C-ratio versus O/C-ratio, daf basis) for parent and torrefied tomato peels.

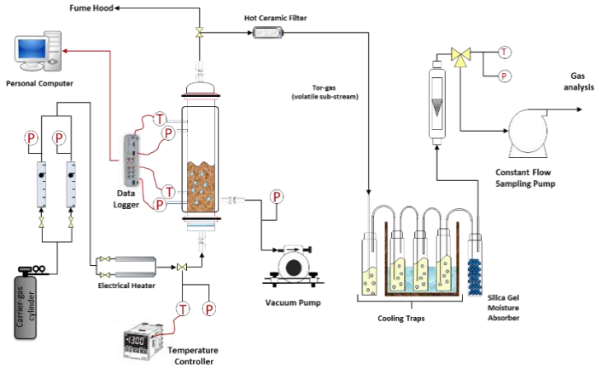

Figure 1. Schematic of the fluidized bed experimental apparatus used for torrefaction tests

Again, results show that higher temperatures and longer holding times lead to a significant increase in the calorific value (by a factor of 1.2 for the biomass treated at 285 °C and 30 min, see Fig.2b) and an improved hydrophobicity of the torrefied tomato peels with respect to the parent ones (see Fig 2c), while maintaining the mass yield (approximately between 75 and 94 %, daf) and energy yield (approximately 90 and 96 %, daf, see Fig. 2d) at satisfactory levels. The effect of the reaction temperature was overall more pronounced than that of the holding time within the tested conditions. Outcomes of our research activities also highlighted that fluidized-bed torrefaction concept is particularly suitable to cope with the exothermicity associated with the thermal degradation of agro-industrial residues, which have the tendency to carbonize easily during torrefaction. In fact, due to the high heat transfer rate and large thermal inertia within the dense bed of sand, this technology was able to ensure a uniform and consistent quality of the solid product (Fig. 3), which is generally difficult to obtain in other torrefaction reactors [2, 5]. The non-uniform color of torrefied tomato peels (TPs) arising from fixed bed reactor torrefaction tests (Fig. 3) was interpreted as evidence of the non-uniform temperature profile inside the packed bed reactors, while the presence of dark-black particles was considered to be the result of the occurrence of hot spots in the reactor as a consequence of the combined effect of the exothermic decomposition reactions of TPs and low heat-transfer coefficients in packed bed [5].

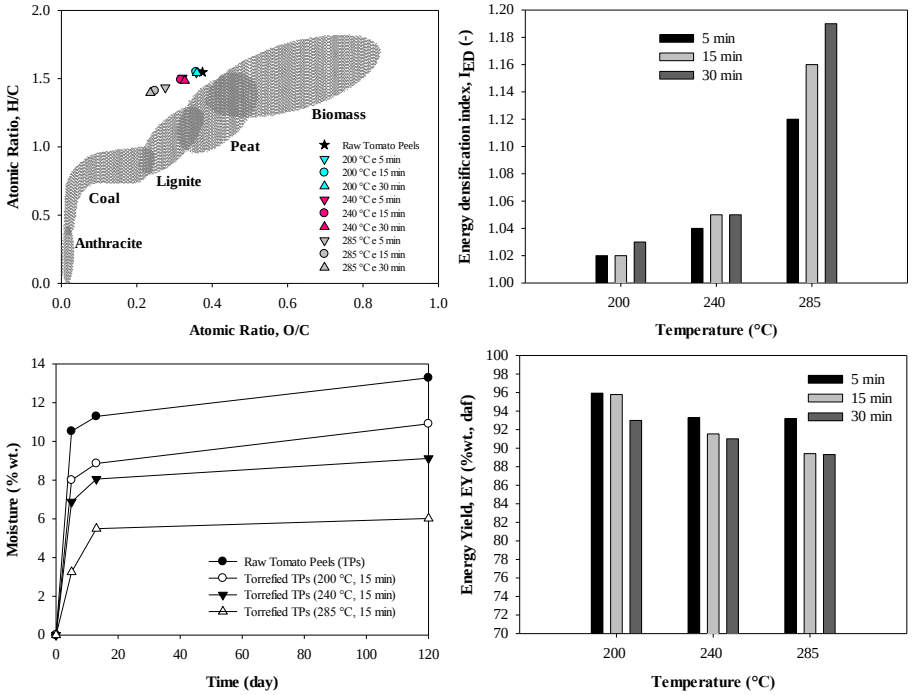

Figure 2. Van Krevelen diagram (a), energy yield (b), energy densification index (c) and (d) equilibrium moisture content (EMC at 80 % relative humidity and ambient temperature.) of raw and torrefied tomato peels from fluidized bed torrefaction tests.

However, the use of fluidized bed reactor is restricted by the need to ensure a proper fluidization behavior and mixing of the bed components; if the operating conditions are not opportunely chosen, several undesired phenomena can occur, which include in-bed channelling, small and/or big lump formation (i.e., localized accumulation of biomass particles), and bed cracks, thus worsening the thermochemical performances of the fluidized bed technology [2, 10]. For this purpose, ad hoc studies aimed at investigating the fluidization and segregation behavior of poly-disperse binary mixtures consisting of small and dense inert particles (Coarse Ticino sand (CS), fine quartz sand (FS), fine alumina powder (FA), coarse alumina spheres (CA)) mixed with less dense and coarse pieces of biomass fuels (orange peel, OP) has been also carried in order to determine the maximum batch loading, i.e. the critical value of the biomass weight fraction in the bed (XB) beyond which the fluidization quality deteriorate (e.g., channelling, irreversible segregation, slugging, see Fig. 4). The main results of this activity show that the bed components' density difference prevails over the size difference in determining the mixing/segregation behavior of binary fluidized bed and that the velocities of minimum and complete fluidization increase with the increase of the biomass weight fraction in the bed [10].

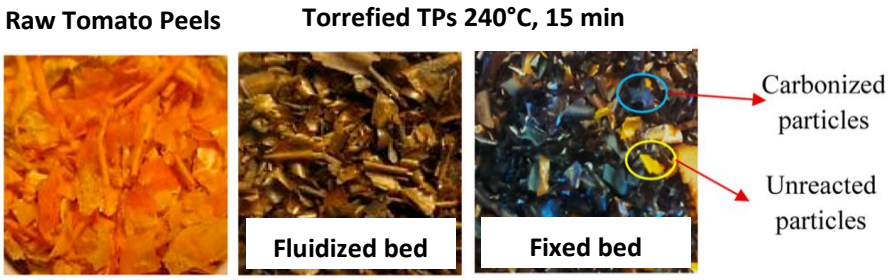

Figure 3. Solid product homogeneity and color change during torrefaction of tomato peels (TPs) in fluidized bed and fixed bed [5].

Finally, outcomes of our research activities suggest that the thermal integration of a torrefaction unit with any other plant making process heat available for the treatment of high moisture agro-industrial residues may be the best option to achieve an acceptable energy efficiency. A full integration between the mass and energy flows of torrefaction and gasification processes appears a promising option and hence deserves further analysis [4].

Figure 4. Segregation and slug phenomena in : a. FS/OP (XB = 6.1 %wt); b. CS/OP (XB = 7.1 %wt.); c. CA/OP (XB = 18.4 %wt.); and d. FA/OP (XB = 20.7%wt.) binary mixtures at high fluidization number (Ug/Umf).

Conclusions

Fluidized bed batch torrefaction tests performed in this research work at a lab-scale with different biomass types (e.g., tomato peels, olive husks and orange peels) have highlighted that, due to the large thermal inertia and the high heat transfer rate within a dense bed of granular solid, the fluidized bed torrefaction concept offers a viable solution to cope with the exothermicity associated with the thermal degradation of non-woody biomass, providing an even product quality that is generally difficult to attain in many other conventional laboratory scale systems (i.e., ovens and fixed beds reactors both directly and indirectly heated).

Moreover, the efficient heat transfer rate to the biomass particles within the dense bed of granular solid offers a viable option to shorten the reaction time, typically ranging from 15 to 120 minutes depending on the specific feedstock, technology and

temperature, down to 5-15 min, which may beneficial for industrial application. In addition, outcomes of a study focused on the segregation and the fluidization behavior of polydisperse binary mixtures in a cold flow fluidization column highlighted that replacing sand with lower density materials, such as porous alumina, results in an improvement of the fluidized bed operability through a remarkable increase in the maximum allowed biomass-to-inert ratio in the bed, namely the biomass weight fraction that still ensures an acceptable quality of fluidization without undesired segregation phenomena.

References

[1] Brito, P., Rodrigues, F., Calado, L., Oliveira, A., "Thermal gasification of agro-industrial residues. WIT transactions on ecology and the environment", *Waste Manage. Environ. VI* 163:95-102 (2012).
[2] Brachi, P, 2016. "Fluidized bed torrefaction of agro-industrial residues: the case study of residues from Campania region, Italy". Ph.D. Thesis. ISBN 8878970735.
[3] Bergman, P.C.A., Kiel, J.H.A., Torrefaction for biomass upgrading. ECN Report No.: ECN-RX-05-180 (2005), Energy Research Centre of The Netherlands. Available online at: https://www.ecn.nl/docs/library/report/2005/rx05180.pdf.
[4] Brachi, P., Chirone, R., Miccio, F., Miccio, M., Ruoppolo, G., "Mass and Energy Balances for a Stand-alone Tomato Peels Torrefaction Plant", Proc. *XXXIX Meeting of the Italian Section of the Combustion Institute",* 4 - 16 June, 2016, Napoli, Italy.
[5] Brachi, P., Miccio, F., Miccio, M., Ruoppolo, G., "Torrefaction of Tomato Peel Residues in a Fluidized Bed of Inert Particles and a Fixed-Bed Reactor". *Energy Fuels* 30:4858-4868 (2016).
[6] Brachi, P., Miccio, F., Miccio, M., Ruoppolo, G.,"Pseudo-component thermal decomposition kinetics of tomato peels via isoconversional methods". *Fuel Process. Technol.* 154:243-250 (2016).
[7] Brachi, P., Chirone, R., Miccio, F., Miccio, M., Ruoppolo, G., "Entrained-flow gasification of torrefied tomato peels: Combining torrefaction experiments with chemical equilibrium modeling for gasification" *Fuel* 220:744–753 (2018).
[8] Brachi, P., Miccio, F., Miccio, M., Ruoppolo, G. "Isoconversional kinetic analysis of olive pomace under torrefaction operating conditions". *Fuel Process. Technol.* 130:147–154 (2015).
[9] Brachi, P., Miccio, F., Ruoppolo, G., Miccio, M., "Pressurized steam torrefaction of biomass: focus on solid, liquid, and gas phase distributions" *Ind. Eng. Chem. Res.* 56:12163-12173 (2017).
[10] Brachi, P., Chirone, R., Miccio, F., Miccio, M., Ruoppolo, G., "Segregation and Fluidization Behavior of Poly-disperse Mixtures of Biomass and Inert Particles". *Chem Eng Trans.* 57:811-816 (2017).
[11] Brachi, P., Chirone, R., Miccio, F., Miccio, M., Ruoppolo, G. , "Valorization of orange peel residues via fluidized bed torrefaction: comparison between different bed materials", Proceedings, Proc. 23nd International Conference of Fluidized Bed Conversion, 13 -17 May, 2018, Seoul, Korea.

TORREFACTION OF A LIGNIN-RICH RESIDUE IN A SOLAR FLUIDIZED BED REACTOR

C. Tregambi*, F. Montagnaro, P. Salatino*, R. Solimene*****
claudio.tregambi@unina.it
*Dipartimento di Ingegneria Chimica, dei Materiali e della Produzione Industriale, Università degli Studi di Napoli Federico II, Piazzale V. Tecchio 80, 80125 Napoli (Italy).
**Dipartimento di Scienze Chimiche, Università degli Studi di Napoli Federico II, Complesso Universitario di Monte Sant'Angelo, 80126 Napoli (Italy).
*** Istituto di Ricerche sulla Combustione, Consiglio Nazionale delle Ricerche, Piazzale V. Tecchio 80, 80125 Napoli (Italy).

Abstract
The thermochemical conversion of solar power to energy carriers provides an attractive pathway to energy storage. The present study aims at demonstrating the solar-driven thermochemical processing of a lignin-rich residue derived from a second-generation bioethanol production process. The influence of operational conditions on the quality of the torrefied biomass has been assessed.

Introduction

Concentrating Solar Power (CSP) may effectively be exploited in solar-driven thermochemical processes aimed at the production of solar fuels and chemicals [1]. A pathway currently being explored is aimed at upgrading the properties of conventional/alternative solid fuels by means of pyrolysis, gasification and torrefaction processes driven by solar energy [2–4]. More into detail, torrefaction is a thermal treatment of biomass performed at temperature in the 200–300 °C range under an inert atmosphere. It aims at maximizing the yield in solid char and at upgrading its properties for subsequent utilization. Torrefied solid products are sterilized and stabilized, feature a higher heating value as a consequence of the reduction of H/C and O/C ratios and of the H_2O content, and display enhanced grindability [5–6]. Biomass torrefaction can be conveniently performed in Fluidized Bed (FB) solar reactors. However, the chemical-physical properties of torrefied materials are quite sensitive to the reaction temperature and care must be paid to thorough control peak temperatures in the bed under highly concentrated solar flux [7]. In this work, a waste biomass material consisting of a lignin-rich residue derived from a second-generation bioethanol production process [8] was torrefied in both a conventional FB reactor and a directly irradiated FB reactor. Chemical-physical analyses were performed on the product materials in order to investigate changes in the elemental composition and volatile matter content as a function of the reaction temperature. The influence of operational conditions on the quality of the torrefied biomass has been assessed, with a close-up on the possible role of uncontrolled particle overheating under high-flux conditions.

Experimental Apparatus

Two different FB reactors were used in this work, one to perform the tests under solar simulated heating conditions (solar tests), the other to perform the tests under conventional (i.e. electrical) heating conditions (non-solar tests).

The first FB reactor (solar tests) is depicted in Figure 1-a. It has both bed internal diameter and height equal to roughly 0.1 m. The freeboard is conically shaped and hosts at its upper extremity a transparent window. The FB surface is exposed to a 12 kW_{el} simulated solar furnace made by an array of three short-arc Xe-lamps coupled with elliptical reflectors. Each Xe-lamp has a dimmer to reduce the power by a multiplicative factor of 0.75 or 0.50. For low-temperature processes, the use of a single Xe-lamp is sufficient. In this condition, the peak flux and the total power on the FB surface are of roughly 1200 kW m^{-2} and 1 kW_{th}. Two semi-cylindrical radiant heaters surround the FB to both heat and insulate the reaction chamber. A gas preheater is also provided. Two mass flow controllers supply the air and N_2 required for the reactor operation. Concerning the diagnostic tools, two K-type thermocouples are located inside the FB to measure the inner temperatures: one 0.05 m above the distribution grid and 0.05 m from the reactor wall, and the other at 0.01 m under the bed surface and 0.01 m from the reactor wall.

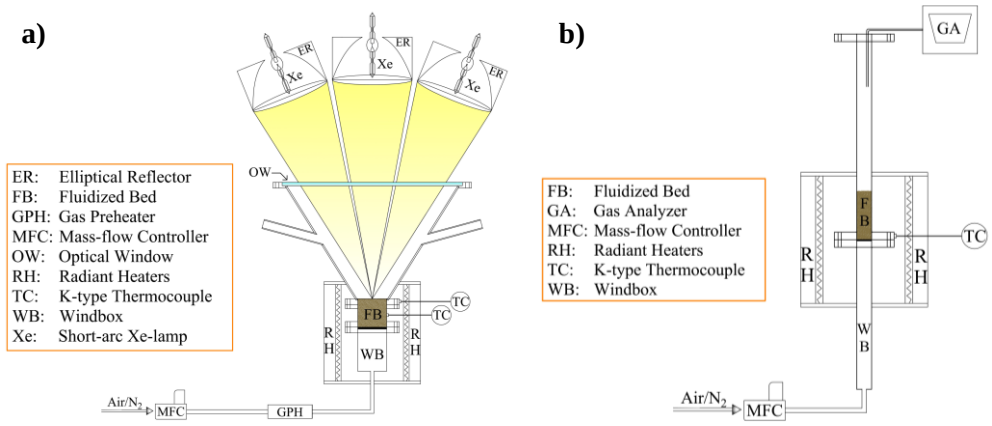

Figure 1. Outline of the reactor used for the solar (a) and non-solar (b) tests.

The second reactor (non-solar tests) is depicted in Figure 1-b. It has an internal diameter of 0.04 m and an overall height of about 1.4 m. The first part of the reactor, 0.6 m long, represents the windbox, whereas the second part of the reactor, 0.8 m long, consists of the reaction plus freeboard zone. Gas leaves the system at the top of the reactor. Two semi-cylindrical radiant heaters in ceramic fiber, driven by an ON/OFF PID controller, surround both the windbox and the reaction zones for a length of 0.3 m each. Two mass flow controllers supply the air and N_2 required for the reactor operation. Concerning the diagnostic tools, a single K-type thermocouple is located inside the FB reactor to measure the bulk bed temperature. An Advance Optima ABB AO2020 gas analyzer was used to monitor the

concentration of CO, CO_2, CH_4 and H_2 at the exhaust. The gas collection is realized through a probe made of a 6 mm stainless steel pipe inserted for approximately 0.1 m from the top of the reactor. A bubble column and a filter between the reactor and the analyzer remove the condensable gases and the entrained solid particles.

Materials

The materials used for the experimental tests were an inert silica sand (0.4–0.6 mm) and the waste biomass material consisting of a lignin-rich residue [8]. The waste biomass was pelletized into cylindrical pellets (diameter: 6 mm, length: 5–20 mm). The chemical properties of the pelletized material, as obtained from proximate and elemental analyses, are summarized in Table 1. The Higher Heating Value (HHV), estimated with a bomb calorimeter, is reported too. Only a small reduction in the water content was observed as a consequence of the pelletization process.

Table 1. Main chemical properties of the pelletized waste biomass residue. M=Moisture, V=Volatile, FC=Fixed C, A=Ash. HHV is on a dry ash-free basis.

Proximate analysis, as received [$\%_{wt}$]				**Elemental analysis, dry basis [$\%_{wt}$]**				**Elemental ratios [–]**		**HHV [MJ/kg]**
M	**V**	**FC**	**A**	**C**	**H**	**N**	**O**	**H/C**	**O/C**	
57.6	25.9	9.4	7.0	47.6	5.3	1.6	38.5	0.112	0.810	23.4

Experimental Procedure

Solar and non-solar torrefaction tests were performed on the pelletized biomass samples at different temperatures (250 °C, 275 °C, 300 °C) and for a fixed reaction time (30 min, a typical reaction time for torrefaction processes). The inlet gas velocity was always kept at 0.4 m s^{-1} and the fluidizing gas was pure N_2 (99.999%).

During a typical solar test, the reactor was charged with about 850 g of sand and heated up to the scheduled temperature by using the electric gas preheater and a single Xe-lamp. Once the scheduled temperature was reached, a sample of roughly 20 g of pellets was fed to the system and the reaction was carried out for the pre-set time of 30 min. When the process was completed, the Xe-lamp was powered off and the system was cooled down as fast as possible. Finally, the bed was discharged and the torrefied pellets were recovered. The fraction of heat provided by the gas preheater was far low or even negligible (it was powered off for the test at 250 °C, while gas were preheated up to 100 °C for the test at 300 °C).

During a typical non-solar test, the reactor was initially charged with about 150 g of sand. The reactor was then heated up to the scheduled temperature by using the radiant heaters. Once the scheduled temperature was reached, a sample of roughly 15 g of pellets was fed to the system and the reaction was carried out for the pre-set time of 30 min. When the process was completed, the reactor was cooled down and the pellets were removed and collected. During these non-solar tests, exhaust gases were continuously sampled and analyzed. This was instead not possible during the

solar test as a consequence of a strong dilution effect of the exhaust gas (similar quantity of pellets were fed to the two reactors despite the different reactor ID).
Pellets recovered from both the solar and non-solar tests were grinded and subjected to proximate and elemental analyses. HHV values were estimated too.

Results: In-Bed Temperature and Concentration-Time Series of Exhaust Gas
Analysis of the temperature profiles showed a good temperature control for both solar and non-solar tests. Altogether, the following mean values were obtained: 250 ± 4 °C, 275 ± 3 °C and 301 ± 4 °C (solar tests) and 251 ± 1 °C, 278 ± 3 °C and 303 ± 2 °C (non-solar tests).
Figures 2-a and 2-b report the time-series of the concentration of CO, CO_2, CH_4 and H_2 obtained at the exhaust gas during the non-solar torrefaction tests. It can be observed that the major non-condensable gaseous species released, among the detectable ones, were CO and CO_2. More into detail, the CO and CO_2 peak values raised from about 70 to 425 ppm and from 400 to 1800 ppm, respectively, when the torrefaction temperature was increased from 250 to 300 °C.

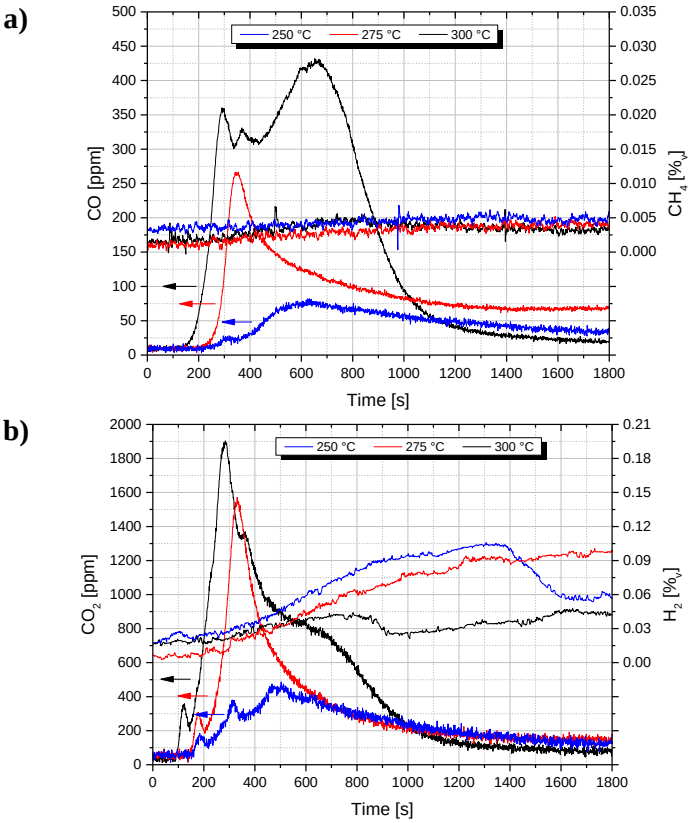

Figure 2. Time series of the concentration of CO and CH_4 (a) and CO_2 and H_2 (b) at the exhaust gas during the three non-solar torrefaction tests.

It is also interesting to observe that the production of CO and CO_2 became evident at longer time from the pellet feeding as the torrefaction temperature was decreased, probably owing to a slower reaction rate of the process. CH_4 concentration remains practically constant for the whole duration of the tests. The H_2 profile shows instead a peak, but its shape is less smooth and defined with respect to the one of CO and CO_2.

Results: Chemical-Physical Analyses on the Torrefied Residue

Table 2 reports the results of the proximate and elemental analyses performed on the torrefied residues, as well as the HHV values (dry ash-free basis) estimated with the bomb calorimeter. In both solar and non-solar tests, the proximate analyses highlight a decrease in the volatile fraction and an increase in the fixed C and ash content, as the torrefaction temperature increases and with respect to the unprocessed material. Moreover, the moisture content becomes negligible in all the samples. On the other side, the elemental analyses highlight a reduction in both the H/C and O/C ratios when increasing the torrefaction temperature as expected from the application of more severe reaction conditions. Lastly, the HHV values of the torrefied pellets show an increasing trend with the torrefaction temperature and, even more important, the values obtained are always higher than the one of the untorrefied material. It is important to underline that, in order to disclose the higher HHV values of the torrefied pellets, it was necessary to evaluate the HHV values on an ash-free basis. Indeed, as a result of the intimate mixing between the inert sand and the biomass pellets in the FB reactor, some sand particles were encapsulated in the torrefied pellets at the end of the torrefaction tests. This can be easily observed by looking at a picture of the torrefied pellets (Figure 3). As a consequence of this phenomenon, the ash content in the torrefied pellets increases more than it would have been resulted from the sole torrefaction process.

Table 2. Main chemical properties of the torrefied pellets.

T [°C]	Proximate analysis [$\%_{wt}$]				Elemental analysis [$\%_{wt}$]				Elemental Ratios [–]		HHV [MJ/kg]
	M	V	FC	A	C	H	N	O	H/C	O/C	
250	2.5	46.9	23.3	27.3	42.2	4.4	1.5	24.5	0.103	0.58	25.7
275	2.3	40.0	26.7	31.0	46.1	4.3	1.6	17.0	0.094	0.37	25.9
300	3.0	31.4	31.7	33.9	49.5	3.9	1.7	11.0	0.079	0.22	28.9
250	3.1	37.4	31.6	27.9	47.1	4.1	1.6	19.2	0.088	0.41	26.5
275	3.1	32.3	32.0	32.6	47.3	3.6	1.4	15.1	0.075	0.32	29.4
300	3.1	28.3	35.3	33.3	48.2	3.4	1.6	13.5	0.071	0.28	30.5

Interesting results are highlighted when comparing the data between solar and non-solar tests performed at the same operating temperature. For each of the temperature values investigated, the solar tests produce a more severe torrefied

product as it can be easily inferred by the volatile fraction or by the H/C and O/C ratios. This phenomenon is probably a result of the higher temperature values that are achieved on the FB surface following the high concentrated beam impinging on the bed surface [7]. Visual observation of the bed surface showed that the pellets tend to segregate to the top of bed during the torrefaction. This evidence, coupled to the dark colour of the pellets (which makes them good absorber of the impinging light), corroborates the previous argument in explaining the more severe torrefaction conditions experienced during the solar tests.

Figure 3. Pellets of the lignin-rich biogenic waste after torrefaction.

References

[1] Prieto, C., Cooper, P., Fernández, A.I., Cabeza, L.F., "Review of technology: Thermochemical energy storage for concentrated solar power plants", *Renew. Sust. Energ. Rev.* 60: 909–929 (2016)

[2] Gokon, N., Izawa, T., Kodama, T., "Steam gasification of coal cokes by internally circulating fluidized-bed reactor by concentrated Xe-light radiation for solar syngas production", *Energy* 79: 264–272 (2015)

[3] Zeng, K., Gauthier, D., Minh, D.P., Weiss-Hortala, E., Nzihou, A., Flamant, G., "Characterization of solar fuels obtained from beech wood solar pyrolysis", *Fuel* 188: 285–293 (2017)

[4] Cellatoğlu, N., İlkan, M., "Solar torrefaction of solid olive mill residue" *Bioresources* 11: 10087–10098 (2016)

[5] Wen, J.L., Sun, S.L., Yuan, T.Q., Xu, F., Sun, R.C., "Understanding the chemical and structural transformations of lignin macromolecule during torrefaction", *Appl. Energ.* 121: 1–9 (2014)

[6] Chen, W.H., Kuo, P.C., "Torrefaction and co-torrefaction characterization of hemicellulose, cellulose and lignin as well as torrefaction of some basic constituents in biomass", *Energy* 36: 803–811 (2011)

[7] Tregambi, C., Chirone, R., Montagnaro, F., Salatino, P., Solimene, R., "Heat transfer in directly irradiated fluidized bed", *Sol. Energy* 129: 85–100 (2016)

[8] Solimene, R., Cammarota, A., Chirone, R., Leoni, P., Rossi, N., Salatino, P., "Combustion of lignin-rich residues with coal in a pilot-scale bubbling fluidized bed reactor", *Powder Technol.* 316: 718–724 (2017)

Improving the catalytic performance of Ni(Ru)/MgO in the conversion of ethanol to butanol by dispersion on γ-Al_2O_3 pellets.

J. Apuzzo*, S. Cimino*, L. Lisi*,
j.apuzzo@irc.cnr.it
*Istituto di Ricerche sulla Combustione, CNR, Napoli, Italy

Abstract
Nickel or ruthenium have been dispersed on commercial γ-Al_2O_3 pellets promoted with magnesium oxide for use as catalysts in the upgrade of bio-ethanol into butanol as possible higher alcohol additive into gasoline. Interactions between MgO and Al_2O_3 as well as between the active metal and the composite Mg/Al substrate have been investigated by XRD, SEM/EDX, N_2 physisorption, H_2-TPR, CO_2-TPD. The conversion of ethanol into butanol has been investigated at 350-400°C under diluted ethanol feed conditions in order to define properties promoting high butanol yields.

Introduction
The use of fuels from renewable resources offers some environmental advantages as the reduction of greenhouse gas emissions. Bio-ethanol is widely used as a fuel additive but it requires modifications of engines and can be added to gasoline in a limited amount [1] due to its water solubility, corrosivity and low calorific value [1]. On the contrary, n-butanol can be burned in the existing engines and can be transported via the existing gasoline pipelines [2]. Bio-butanol can be produced by biomass fermentation using *Clostridium* microorganisms (Acetone Butanol Ethanol or ABE fermentation) [2, 3]. The fraction of ethanol produced in this process could be upgraded to butanol via catalytic routes [1-5]. The main process to increase the carbon number of alcohols is called Guerbet reaction. Results of a preliminary screening of nickel or ruthenium dispersed on different supports (hydroxyhapatite, Al_2O_3 and MgO) as powder catalysts suggested that metal-promoted MgO provided the best butanol yields compared to the other supports [5]. The basic properties of MgO and its high surface area, both properties further improved by metal dispersion, were identified as key-features for good butanol productivity.
The preliminary screening carried out on powder catalysts for a lab-scale rig [5], was followed by the scale-up of the MgO-based catalysts into a structured form (pellets) to be used in a larger scale rig. Thus, the preparation, characterization and the performance in the Guerbet reaction of Ni and Ru on MgO-coated γ-Al_2O_3 pellets have been investigated comparing results with those obtained using pure MgO pellets and powder MgO with the same fraction of dispersed metal.

Materials and methods

Pure MgO pellets were supplied by Harshaw (BET area=13 m^2/g). MgO/γ-Al_2O_3 pellets were prepared by incipient wetness impregnation of NORPRO γ-Al_2O_3 pellets supplied by Saint-Gobain (BET area=169 m^2/g) with a solution of $Mg(NO_3)_2 \cdot 6H_2O$ to obtain about 15%MgO. After drying at 120°C pellets were calcined 2h at 600°. A fraction of these pellets was further calcined 2h at 900°C.
Nickel was dispersed by incipient wetness impregnation starting from a solution of $Ni(NO_3) \cdot 6H_2O$ whereas ruthenium was dispersed from a 1.4 % ruthenium (III) nitrosyl nitrate solution. The nominal loading of metal in the catalysts is 1wt %.
Hereafter, the composite pellets will be labelled as MeMg/Al, with Me representing the active metal (Ni or Ru).
XRD analysis was performed on powder samples with a Bruker D2 Phaser diffractometer. BET specific surface area and pore size distribution measurements were performed with a Quantachrome Autosorb 1-C by N_2 adsorption at 77 K after degassing samples for 2h at 150°C. Scanning electron microscopy (SEM) was carried out on pellet cross section with a FEI Inspect instrument equipped with an energy dispersive X-ray (EDX) probe. Temperature programmed reduction (TPR) and CO_2 TPD experiments were carried out with a Micromeritics AutoChem 2020 equipped with a TC detector on catalysts and supports pre-treated in air at 600°C heating the sample at 10 °C min^{-1} up to 900°C under H_2/N_2 mixture for TPR and under He flow for TPD after adsorption of CO_2 at room temperature.
Catalytic tests were carried out at 350-400°C in a lab-scale fixed bed reactor loaded with 1 g catalyst feeding a 3% vol. ethanol/N_2 mixture, as described in [5]. Reactants and products were analysed by an online GC (Hewlett Packard 1540A) equipped with FI detector and a ZB-WAX*plus* column. Percentage butanol yield was expressed as butanol produced/ethanol reacted x 100 (vol./vol.).

Results and discussion

XRD analysis of MeMg/Al showed that γ-alumina structure was preserved in MgO-coated pellets and, in addition to the signals of γ-Al_2O_3, the main signals of periclase MgO phase at 42.7° and 62.3° [JCPDS 78-0430] were detected for Mg/Al sample calcined at 600°C. These two signals almost disappear for Mg/Al pellets calcined at 900°C, indication of possible migration of Mg^{2+} into alumina lattice. The same occurred for MeMg/Al pellets, suggesting the formation of an amorphous solid solution with metal incorporation into MgO. The values of BET surface area indicate that, as expected, MgO deposition onto alumina slightly decreases its original surface area, which is also reduced by exposure to the higher calcination temperature.
TPD of CO_2 was used as fingerprint to evaluate the MgO exposure on alumina pellets through the comparison with the distribution of basic sites typical of magnesia or alumina. On the basis of TPD results it was assessed that the calcination of Mg/Al at 900°C promoted the formation of an alumina-like structure, whereas pellets calcined at 600°C showed basic sites typical of MgO indicating an effective coverage with a magnesia layer.

The dispersion of metals represented a crucial step in the preparation of pellets due to the possible poor penetration of the metal inside the pellet core. White pure MgO pellets turned into green pellets after Ni impregnation, as shown in Figure 1 (left). Nevertheless, the pellet consists of an external thin green layer and a white inner core according to an *egg shell* Ni distribution, as shown in Figure 1 (right).

Figure 1. Picture of MgO and Ni/MgO pellets (left) and corresponding cross section of a Ni/MgO pellet (right).

The same was observed for Ni/Mg/Al pellets showing a very uniform distribution of Mg on alumina in contrast to Ni which was confined on the external surface although in a thicker layer than on pure MgO pellets. This phenomenon, also observed by others [6], can be attributed to the precipitation of $Ni(OH)_2$ from the nitrate solution at the first contact with the very basic MgO surface which is more rapid than penetration of nickel nitrate inside the pellet. A limited penetration depth was observed for Ru as well.

In order to promote metal penetration, an attempt to modify the preparation procedure was done. Ni and Mg were simultaneously impregnated on γ-Al_2O_3 pellets from their nitrate precursors in order to hinder the contact between Ni^{2+} and preformed MgO layer. This procedure led to a very homogeneous distribution of Ni across the whole pellet as detected by SEM/EDX analysis.

In Table 1 butanol yield obtained in the catalytic tests carried out at 350 or 400°C for all catalysts investigated is reported and compared with the results recorded over a Ni/MgO powdered catalyst under identical operating conditions.

All catalysts activate ethanol and produce butanol in addition to acetaldehyde, ethylene and traces of crotonaldehyde. Ni/MgO pellets provide butanol yield slightly lower than that obtained over Ni/MgO powder, likely ascribable to the lower surface area of the pellets with the same composition and to the bad Ni distribution inside the pellets. Mg/Al pellets calcined at 600°C have a good intrinsic activity towards butanol production, in contrast with Mg/Al pellets calcined at 900°C which, despite of the very high ethanol conversion (almost doubled with respect to the material calcined at 600°C), produce a low amount of butanol. This catalytic behavior, already observed for alumina [5], confirms that the high calcination temperature promotes the formation of a surface aluminate phase. Therefore, these results show

that ethanol mostly contact a MgO layer for Mg/Al pellets calcined at 600°C whilst an alumina-like surface for those calcined at 900°C.
The addition of nickel strongly improves butanol yield at both temperatures for an ethanol conversion very close to that obtained over the parent Mg/Al pellets (about 40% at 400°C). The enhanced performance is not completely assignable to the increase of surface area but should also involve a synergic effect of the Ni-Mg mixture. Addition of ruthenium provides an even higher butanol yield for similar ethanol conversion. On the other hand, notwithstanding the very good dispersion of Ni in the co-impregnated catalyst, its performance is very similar to that of Mg/Al pellets. A TPR analysis carried out on the co-precipitated catalyst indicated that a highly more reducible nickel is present on this sample in contrast with the hardly reducible metal in close contact with MgO obtained through the two steps preparation. In other words, nickel interacts with alumina rather than with MgO when the impregnating solution contains both Mg^{2+} and Ni^{2+}.
Finally, the comparison between performances of Ni/MgO and Ni/Mg/Al pellets highlights the importance of MgO dispersion. The higher butanol yield obtained with Ni/Mg/Al pellets compared to Ni/MgO pellets is in agreement with the increase of surface area.

Table 1. Butanol yield for the different catalysts (1g catalyst, 3 l h^{-1} 3% $EtOH/N_2$)

Catalyst	**BET surface area (m^2 g^{-1})**	**Butanol yield (%)**	
		350°C	*400°C*
MgO powder	75	-	4.03
Ni/MgO	29	-	3.45
Mg/Al pellets calc. 600°C	141	0.63	1.97
Mg/Al pellets calc. 900°C	127	0.46	0.73
Ni/Mg/Al	144	4.55	6.36
Ni/Mg/Al co-impr.	128	0.98	1.68
Ru/MgO/Al	125	5.76	-

Conclusion

Nickel and ruthenium supported on MgO-coated γ-alumina pellets were prepared, characterized and tested for the catalytic conversion of ethanol into butanol. The preparation conditions were investigated defining those providing pellets keeping or improving performance of powder catalyst with the same formulation.
Calcination of MgO-coated pellets at 600°C allows the formation a well dispersed MgO layer on the alumina pellet for the subsequent metal addition.
The formation of the solid solution between active metal (Ni or Ru) and MgO is responsible for a good butanol production, much higher than that obtained using corresponding powder catalysts with the same composition, despite of the low MgO load in the reactor.

Acknowledgments

The present work has been done in the framework of the H2020-LCE-2015 Waste2Fuels project (Sustainable production of next generation biofuels from waste streams - Waste2Fuels. GA - 654623), funded by the European Union's Horizon 2020 Research and Innovation Programme.

References

[1] Earley J. H., Bourne R. A., Watson M. J., Poliakoff M., "Continuous catalytic upgrading of ethanol to *n*-butanol and $>C_4$ products over Cu/CeO_2 catalysts in supercritical CO_2", *Green Chem.* 17:3018–3025 (2015).

[2] Sun J., Wang Y., "Recent Advances in Catalytic Conversion of Ethanol to Chemicals", *ACS Catal.* 4:1078−1090 (2014).

[3] Ndou A. S., Plint N., Coville N. J., "Dimerisation of ethanol to butanol over solid-base catalysts", *Appl. Catal. A Gen.* 251:337–345 (2003).

[4] Tsuchida T., Kuboa J., Yoshioka T., Sakuma S., Takeguchi T., Ueda W., "Reaction of ethanol over hydroxyapatite affected by Ca/P ratio of catalyst", *J. Catal*. 259:183-189 (2008).

[5] Cimino, S., Lisi, L., Romanucci S., "Catalysts for conversion of ethanol to butanol: effect of acid-base and redox properties", *Catal. Today*, 304:58-63 (2018).

[6] Takehira K., Kawabata T., Shishido T., Murakami K., Ohi T., Shoro D., Honda M., Takaki K., "Mechanism of reconstitution of hydrotalcite leading to eggshell-type Ni loading on Mg–Al mixed oxide", *J. Catal.* 231:92–104 (2005).

INTEGRATION OF ENZYMATIC PROCESSES FOR DELIGNIFICATION AND HYDROLYSIS OF AGRO-FOOD WASTES

S. Niglio*, A. Procentese, M.E. Russo**, F. Raganati*, A. Marzocchella***

alessandra.procentese@irc.cnr.it

* Dipartimento di Ingegneria Chimica, dei Materiali e della Produzione Industriale - Università degli Studi di Napoli Federico II, P.le V. Tecchio 80, 80125 Napoli (Italy)

** Istituto di Ricerche sulla Combustione– Consiglio Nazionale delle Ricerche, P.le V. Tecchio 80, 80125 Napoli (Italy)

Abstract

Among next generation bio-fuels, bio-butanol produced by the Acetone-Butanol-Ethanol (ABE) fermentation [1] can be obtained from renewable carbon sources such as agro-food wastes. This biorefinery approach will beneficiate of both the advanced fermentation technologies for butanol production and of the exploitation of resources different from food-feed crops. Maximization of the sugar yield and reduction of the operating costs of the biomass pretreatment/hydrolysis process are among the main aims of the current research. The present study proposes an attempt of integration between two enzymatic steps of biomass delignification and hydrolysis that may offer effective and costs saving alternative to the conventional mechanical/physical pretreatments and acid hydrolysis of biomass. Bubble column has been adopted as lab-scale reactor with pneumatic mixing to perform tests on laccase lignin degradation and sequential cellulose hydrolysis by commercial cellulase cocktail using apple pomace residues as substrate.

Introduction

The production of next-generation biofuels from biogenic residues and wastes by a combination of thermochemical and biochemical pathways is an option for the production of drop-in biofuels and alternative renewable fuels dedicated to the energy and transport areas. Production of bio-butanol from ABE fermentation [1] can be obtained using agro-food wastes as feedstock [2, 3]. Effective delignification and cellulose hydrolysis is a crucial issue in the field of biorefinery process development. It is strongly related to the maximization of sugar yields and concentration in the hydrolysate that should be obtained with energy and water saving strategies to favor efficient feedstock utilization and high bio-fuel yield in the fermentation step. Novel pretreatments for biomass delignification try to obtain reduction of lignin content that should promote cellulose hydrolysis by enhanced accessibility of cellulose by the hydrolytic enzymes (cellulases and hemicellulases). Among these diluted acid or basic hydrolysis [4], ultrasounds or microwaves assisted processes [5], green-solvents extraction [6] and enzymatic

delignification [7] have been recently studied. Main advantages are related to the use of environmental friendly solvents (e.g. deep eutectic solvents) and catalysts (e.g. enzymes) and low production of compounds (hydroxymethylfurfural) that inhibit microbial growth in the fermentation step and are largely produced by conventional pretreatments such as steam explosion. Drawbacks related to these novel pretreatments come out of the large use of water, the need of recycling solvents and enzymes and of reaching competitive sugar yields with respect to conventional pretreatments. Moreover, other issues are related to the development of the enzymatic hydrolysis of cellulose and include: handling and effective mixing of high solid content (up to 15%wt) slurries made by not spherical, swelling solids having widespread particle size distribution; ensuring efficient liquid-solid mass transfer; limiting energy consumption required for mixing; recycling the enzyme through effective confinement/ reuse strategies. The present contribution reports a first attempt to develop an integrated enzymatic delignification and hydrolysis process of agro-food wastes that address few of the above mentioned issues, in particular, water and energy saving through integration of two enzymatic pretreatment/hydrolysis processes and pneumatic mixing.

Methods

Materials

Apple pomace (AP) samples were provided by the Instituto Tecnològico Agrario Castilla y Leòn in the framework of the research project "Waste2Fuels" [2]. The biomass was oven dried at 50 °C until a constant weight was achieved. Dry AP was sieved in the range 500-1000 µm, samples were collected and stored in sealed plastic bags at room temperature until used. Salts for liquid buffers and any other reagent were supplied by SigmaAldrich® (Merck KGaA, Darmstadt, Germany).

Bioreactor

The bioreactor (Fig. 1) was a cylindrical glass (Pirex®) column (0.4 m height, 0.034 m ID) and was equipped with a water jacket connected to a thermostatic bath (Julabo Italia s.r.l.). Agitation of the suspension in the column was provided by the gas bubbles. Air flow rate was controlled with a rotameter in the range 0 - 120 NL/h. The gas hold-up (εG) in the column was assessed according to Eq. (1):

$$\varepsilon_G = \frac{H - H_0}{H} \quad (1)$$

where H_0 and H are the height of the stagnant and mixed by a fixed gas flow rate liquid-solid suspension, respectively. The effects of the liquid temperature (28-50°C) and biomass loading (0-15%wt) on gas hold-up were analysed.

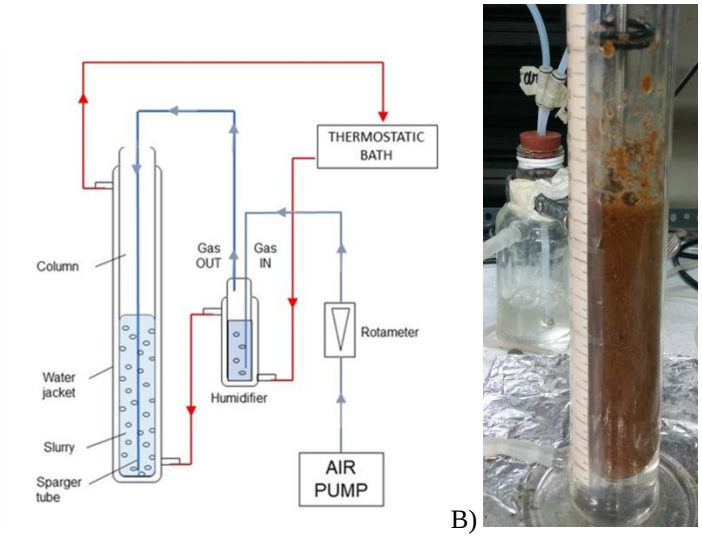

Figure 1. A) Scheme of the lab-scale apparatus; B) detail of the glass column with AP slurry during laccase catalyzed delignification.

Delignification and cellulose hydrolysis in the bubble column

Laccases (166U/mL) were kindly provided by Biopox s.r.l. (Napoli, Italy). Before pretreatment, AP samples were soaked in the 0.1 M Sodium citrate buffer (pH 5). The delignification tests were carried out for 24 h in the above mentioned buffer at 28°C. Air flow rate and laccase concentration were set at 20 NL/h and 10U/g of raw dry biomass, respectively. The hydrolysis of cellulose in the biomass pretreated with laccase was accomplished using the commercial cocktail of hydrolytic enzymes CellicCTec2® (Novozymes, Denmark) in 0.1 M Sodium citrate buffer (pH 4.8) at 50 °C with 1 FPU/g cellulose. Samples were taken after 72 h, inactivated at 95 °C for 5 min, then centrifuged and filtered (0.22 μm) for the analysis of sugars content. The effect of the process integration mode was investigated. In particular, two operation modes were adopted: single batch of liquid buffer with sequential addition of the enzymes; sequential laccase and cellulase catalysed processes with both enzyme and buffer replacement. In both cases the temperature was increased from 28°C (delignification) to 50°C (cellulose hydrolysis). Moreover, air distribution mode (porous stone sparger vs 4mm ID tubing) and biomass loading (5-10%wt) were also changed according to the observation on pneumatic mixing of the AP suspension. At the end of reaction, the slurry was filtered and the liquid was analysed for reducing sugars and phenolic content

Analytical methods

The composition of AP before and after laccase pretreatment was determined two steps of acid hydrolysis [9]. Glucose, xylose and arabinose concentrations in the hydrolysed liquid samples were assessed by means of HPLC (Agilent 1260 Infinity

HPLC system) and refractive index detection using a Rezex RHM-Monosaccharide H+ 8 µm, 300 x 7.8 mm column (Phenomenex), and 5 mM of H_2SO_4 as mobile phase (0.6 mL/min). Sugars in the liquid after enzymatic hydrolysis were quantified by means of 3,5-dinitrosalicylic acid (DNS) method [10].
The liquid fractions after pretreatment of AP were analyzed to reveal the concentration of phenolic compounds via colorimetric assay using Folin-Denis reagent [11]. Total phenolic content was expressed as mg Gallic Acid Equivalents (GAE) per gram of pretreated CSS.

Results
Integrated enzymatic delignification and hydrolysis tests were performed according to the described procedure and results are reported in Table 1. The use of porous gas sparger for long lasting tests did not provide stable and vigorous mixing of the solids, thus the BL was limited at 5%wt. Gas supplementing the 4 mm ID tubing gave turbulent bubble regime that provided effective mixing of the AP suspension up to 10%wt. This allowed a larger sugar concentration with an almost similar sugar yield with respect to the case of 5%wt suspension with porous sparger. The concentration of phenolic compounds was not affected by both bubbling regime and BL. The integration strategies adopted showed that the same sugar concentration and yield were obtained with both a single liquid batch (no buffer replacement between laccase pretreatment and cellulase hydrolysis) and two sequential liquid batches (buffer replacement).

Table 1. Sugars concentration and yield after pretreatment/hydrolysis of AP in bubble column reactor.

Air supply	Porous sparger		4 mm tubing	
Buffer replacement	N	Y	N	Y
Biomass loading (%wt)	5		10	
Air flow rate (NL/h)	20			
Sugar concentration (g/L)	14.2	14.2	30.4	29
Sugar yield (% g/g_glucan)	69.4	69.2	74.2	70.5
Sugar yield (% g/g_raw biomass)	28.4	28.3	30.4	28.9
Phenolic compounds (mg/graw)	3.51	2.5	3.5	2.7

The gas hold up analysis was accomplished supplementing the gas through the 4 mm ID tube. Figure 2 shows the results on gas holdup in the bubble column filled

with AP suspension at different air flow rates, biomass loading (BL) and temperatures. In the absence of solids, the gas hold-up slightly decreases by increasing temperature from 28 to 50°C, accordingly not significant temperature effects are reported in the literature [12]. The opposite temperature effect was observed in the presence of AP at BL between 5 and 15%wt. Moreover, gas hold up slightly decreased at increasing BL at 28°C, this effect is still less evident at 50°C. Effect of solids reported in the literature is both increase and decrease of gas hold-up [13]. This phenomenon is related to the composition of the liquid phase. In this case AP tends to release soluble sugars in the liquid that may affect surface tension and consequently average bubble size.

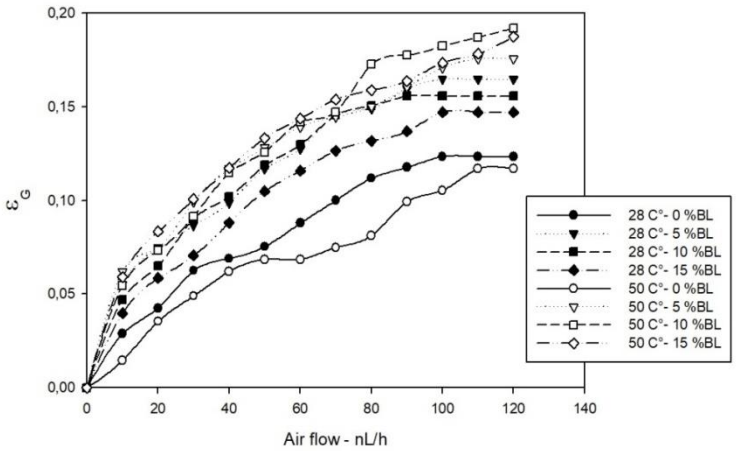

Figure 2. Gas hold-ups versus air flow rate at different temperatures and AP biomass loadings (BL).

Conclusions

The reported results showed that possible effective mixing of biomass suspension at high solid loading can be achieved with turbulent bubble regimes. Moreover, the attempt of integrating two enzymatic pretreatments (delignification and cellulose hydrolysis) has been successfully accomplished at lab scale. The main advantage of such strategy is the possibility to reduce water consumption if sequential addition of enzymes is accomplished or, alternatively, to recover phenolic compounds produced by the laccase catalysed delignification for further valorization of such by-products and replace the liquid buffer with the solution containing hydrolytic enzymes. Further experiments will be accomplished to optimize both the delignification and the hydrolysis enzymatic processes in the bubble column for sugar yields maximization.

Acknowledgments

The present work has been performed as part of the H2020-LCE-2015

Waste2Fuels project (Sustainable production of next generation biofuels from waste streams - Waste2Fuels. GA - 654623), funded by the European Union's Horizon 2020 Research and Innovation Programme. Alessandra Piscitelli and Simona Giacobbe are gratefully acknowledged for discussion on the use of laccase.

References

[1] Raganati, F., Procentese, A., Olivieri, G., Russo, M.E., Gotz, P., Salatino, P., Marzocchella, A., "Butanol production by Clostridium acetobutylicum in a series of packed bed biofilm reactors" *Chem. Eng. Sc.*, 152: 678-688. (2016)

[2] www.waste2fuels.eu

[3] https://ec.europa.eu/inea/en/horizon-2020/projects/h2020-energy/biofuels/waste2fuels

[4] Procentese, A., Raganati, F., Olivieri, G., Russo, M.E., Marzocchella, A., "Pre-treatment and enzymatic hydrolysis of lettuce residues as feedstock for bio-butanol production", *Biomass Bioenerg.*, 96:172-179 (2017)

[5] Niglio, S., Procentese, A., Russo, M.E., Sannia, G., Marzocchella, A., "Ultrasound-assisted Dilute Acid Pretreatment of Coffee Silverskin for Biorefinery Applications", *Chem. Eng. Transact.* 57: 109-114 (2017)

[6] Procentese, A., Raganati, F., Olivieri, G., Russo, M.E., Rehmann, L., Marzocchella, A., "Low-energy biomass pretreatment with deep eutectic solvents for bio-butanol production", *Biores. Technol.*, 243: 464-473, (2017)

[7] Avanthi, A., Banerjee, R., "A strategic laccase mediated lignin degradation of lignocellulosic feedstocks for ethanol production", *Ind. Crops Prod.*, 92: 174-185 (2016)

[8] Andey, B. and Baker, J., "Measurement of cellulase activities" NREL Technical Report, NREL/TP -510-42628 (2008).

[9] Sluiter, A., Hames, B., Ruiz, R., Scarlata, C., Sluiter, J., Templeton, D., Crocker, D., "Determination of structural carbohydrates and lignin in biomass" NREL Technical Report, NREL/TP-510-42618, 2008.

[10] Wood, I., P., Elliston, A., Ryden, P., Bancroft, I., Roberts, I., N., Waldron, K., T., "Rapid quantification of reducing sugars in biomass hydrolysates: Improving the speed and precision of the dinitrosalicylic acid assay" *Biomass Bioenerg*, 44: 117-121 (2012).

[11] Rattanachitthawat, S., Suwannalert, P., Riengrojpitak, S., Chaiyasut, C., Pantuwatana, S., **"**Phenolic content and antioxidant activities in red unpolished Thai rice prevents oxidative stress in rats" *J Med. Plants Res.* 4: 796-801, (2010).

[12] Kantarci, N., Borak, F., Ulgen, K., O., "Bubble column reactor" *Proc. Biochem.*, 40: 2263-2283 (2005).

[13] Krishna, R., De Stewart, J., W., A., Ellenberg, J., Martina, G., B., Maretto, C., "Gas holdup in slurry bubble columns: effect of column diameter and slurry concentrations" *AIChE J*, 48: 889-911 (1997)

SOLAR THERMOCHEMICAL CO_2 SPLITTING OVER $La_{0.6}Sr_{0.4}MnO_3$ PEROVSKITES

G. Luciani*, C. Imparato*, G. Landi, A. Aronne*, A. Di Benedetto***
landi@irc.cnr.it
*Dipartimento di Ingegneria Chimica, dei Materiali e della Produzione Industriale, Università degli Studi di Napoli Federico II, P.le Tecchio 80 - 80125 Napoli (Italy)
**Istituto di Ricerche sulla Combustione, Consiglio Nazionale delle Ricerche (CNR), P.le Tecchio 80 - 80125 Napoli (Italy)

Abstract
The effect of Fe and Mn content in mixed perovskites ($La_{0.6}Sr_{0.4}Mn_{1-x}Fe_xO_{3-\delta}$) on the performance of solar thermochemical CO_2 splitting is studied.
Catalyst were tested by thermogravimetric analysis (TGA) and activity tests in a lab-scale reactor.
On increasing the Fe content the temperature at which reduction is activated decreases. Conversely, the oxidation step is favored by high Mn content.
Results show that for optimizing both reduction and oxidation step bi-functional systems with two active sites are needed. One site should enhance the self-reduction activity, the other should enhance the oxidation reaction.

Introduction
Thermochemical splitting cycles can be divided into low (LT) and high (HT) temperature cycles [1].
The features required to good materials for solar thermochemical splitting cycles are mainly a high oxygen desorption at temperature as low as possible, fast CO production in CO_2 streams and structure stability.
Several material have been proposed, including volatile and non-volatile oxides, the latter classified into stoichiometric and non-stoichiometric oxides [2-3]. Among all these materials, the best candidates are non-stoichiometric oxides.
The main issue is to design a catalyst which is able to activate both the reduction and the oxidation step, at low temperature [4-5].
Perovskites (ABO_3) can have several compositions by changing the type and amount of A and/or B cations [6].
Among all the compositions investigated, $LaMnO_3$ has received a great interest as splitting material, showing good redox properties during reduction/oxidation cycles as well as favorable thermodynamics [7].
Up to now, few works have been developed to study the effect of the partial substitution of A and B cations. In this work, we propose a novel strategy for the

preparation of materials active in the solar thermochemical CO_2 splitting based on the partial substitution of Mn with Fe in the $La_{0.6}Sr_{0.4}MnO_3$ perovskite.

Methods

2.1 Materials preparation

Perovskites $La_{0.6}Sr_{0.4}Mn_{1-x}Fe_xO_3$ ($0 \leq x \leq 1$) with variable Mn/Fe molar ratios (x) were prepared according to the following procedure. Aqueous solutions were prepared by stoichiometric amounts of manganese (II) nitrate tetrahydrate, strontium nitrate, lanthanum nitrate hydrate and iron (III) nitrate nonahydrate in bi-distilled water and stirred for 3 h. Solutions were heated in a MW oven (CEM SAM-155) up to the formation of a homogeneous gel. The obtained gel was calcined at 1400°C for 4h.
In Table 1 the general formulas of the samples are given.

Table 1 – Prepared materials and their corresponding labels

Sample	Label
$La_{0.6}Sr_{0.4}MnO_3$	LSM
$La_{0.6}Sr_{0.4}Mn_{0.8}Fe_{0.2}O_3$	LSMF-0.2
$La_{0.6}Sr_{0.4}Mn_{0.6}Fe_{0.4}O_3$	LSMF-0.4
$La_{0.6}Sr_{0.4}Mn_{0.4}Fe_{0.6}O_3$	LSMF-0.6
$La_{0.6}Sr_{0.4}FeO_3$	LSF

2.2 TG analysis

TG analysis was performed in a TGA/DSC TA Instrument Q600SDT. 30 mg sample was placed in an alumina crucible. Each sample was pre-treated in air at 1200°C (heating rate: 20°C/min) in order to remove the chemisorbed CO_2 [8] and then cooled down to room temperature. After a 1 h purging under a nitrogen flow, the sample was heated up to 1350°C (heating rate: 20°C/min) under a nitrogen flow (0.1 l(STP)/min) and kept for 20 min at 1350°C. Then it was cooled down to 1000°C and the atmosphere was switched to CO_2, followed by an isothermal step at 1000°C for 50 min (oxidation step).

Results and Discussion

In Figure 1 the weight loss (a) and the corresponding derivatives (b) are shown.
LSF is the most reducible catalyst, showing both the lowest reduction temperature and the highest O_2 production.
For the samples with x= 0.4 and x = 0.6 reduction starts at higher temperatures than LSM. However, LSMF samples show a lower temperature reduction phenomenon, more evident by increasing the iron content.
In Table 2 the amount of O_2 released is given as calculated for all the samples investigated.
The largest oxygen production is obtained on the LSF sample.

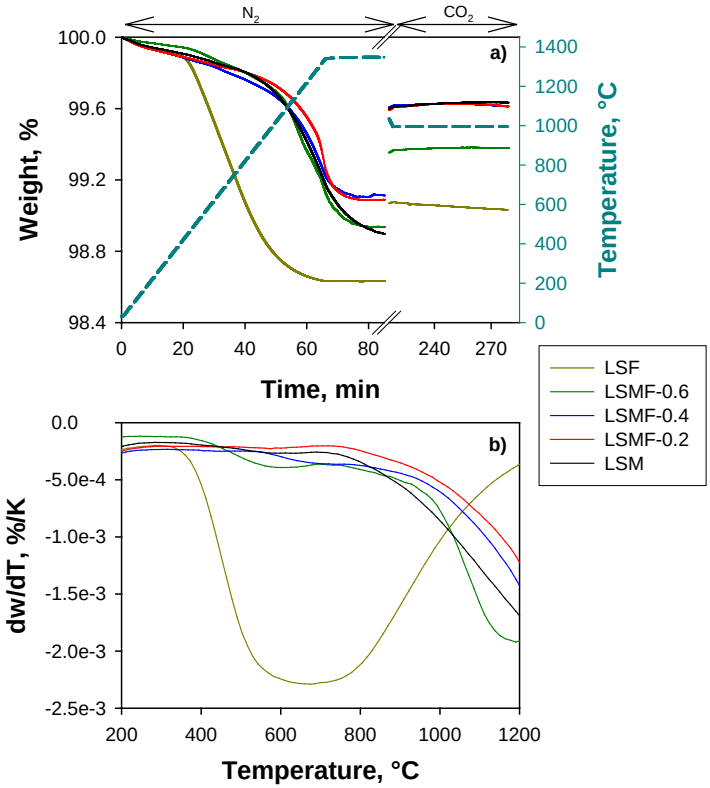

Figure 1. a) Weight losses of LSMF-x samples as a function of the time during TGA in N_2 and subsequent weight increases under pure CO_2; b) weight loss derivatives as a function of temperature during TGA in N_2.

Table 2 – O_2 evolution and CO production as measured in TGA

Sample	O_2 production, µmol/g	CO production, µmol/g	Re-oxidation degree
LSM	348.8	469.1	67.2%
LSMF-0.2	286.0	329.9	57.7%
LSMF-0.4	280.0	317.5	56.7%
LSMF-0.6	333.2	277.2	41.6%
LSF	427.3	250.6	29.3%

CO production shows a progressive decrease as Fe^{3+} ions are substituted to Mn^{3+}/Mn^{4+} species in the B sites of ABO_3 perovskite structure.

Accordingly, in CO_2 atmosphere mixed perovskites show re-oxidation properties intermediate between those of the reference samples.

Conclusions

We prepared perovskites with La and Sr as A cations (La/Sr = 1.5) and with Mn (very active towards splitting reactions as $La_xSr_{1-x}MnO_3$) and Fe (showing good self-reduction properties as $La_xSr_{1-x}FeO_3$) as B cations, studying the effect of the Mn/Fe ratio on morphological, structural and redox catalytic properties.

TG analysis showed that both starting reduction temperature and produced oxygen amount through self-reduction follow a non-monotonic trend with the iron content. This could be related to a preferential substitution of Mn^{4+} with Fe.

From CO_2 splitting tests in TG it follows that all samples show only partial re-oxidations, but with significant CO productions, that progressively decrease with Fe content.

The obtained results suggest that structural features as well as reduction/oxidation properties can be tuned by opportunely changing the nature and amount of B cations.

References

[1] Rao, C.N.R., Dey, S., 2015. Generation of H2 and CO by solar thermochemical splitting of H2O and CO2 by employing metal oxides. J. Solid State Chem. 242, 107–115.

[2] Fu, Y., Li, S., Zhang, J., Sun, Y., 2016. Effective Macroporous Core-Shell Structure of Alumina-Supported Spinel Ferrite for Carbon Dioxide Splitting Based on Chemical Looping. Energy Technol. 4, 1349–1357.

[3] Scheffe, J.R., Steinfeld, A., 2014. Oxygen exchange materials for solar thermochemical splitting of H2O and CO2: A review. Mater. Today 17, 341–348.

[4] Miller, J.E., McDaniel, A.H., Allendorf, M.D., 2014. Considerations in the Design of Materials for Solar-Driven Fuel Production Using Metal-Oxide Thermochemical Cycles. Adv. Energy Mater. 4, 1300469.

[5] Jiang, Q., Tong, J., Zhou, G., Jiang, Z., Li, Z., Li, C., 2014. Thermochemical CO2 splitting reaction with supported LaxA1−xFeyB1−yO3 (A=Sr, Ce, B=Co, Mn; 0⩽x, y⩽1) perovskite oxides. Sol. Energy 103, 425–437.

[6] Royer, S., Duprez, D., Can, F., Courtois, X., Batiot-Dupeyrat, C., Laassiri, S., Alamdari, H., 2014. Perovskites as Substitutes of Noble Metals for Heterogeneous Catalysis: Dream or Reality. Chem. Rev. 114, 10292–10368.

[7] Scheffe, J.R., Weibel, D., Steinfeld, A., 2013. Lanthanum–Strontium–Manganese Perovskites as Redox Materials for Solar Thermochemical Splitting of H 2 O and CO 2. Energy & Fuels 27, 4250–4257.

[8] Di Benedetto, A., Barbato, P.S., Landi, G., 2013. Effect of CO_2 on the Methane Combustion over a Perovskyte Catalyst at High Pressure. Energy & Fuels 27, 6017–6023.

Process modelling of an innovative Power to LNG demonstration plant

E. A. Morosanu, S. Bensaid*, R. Pirone

* samir.bensaid@polito.it
Department of Applied Science and Technology (DISAT), Politecnico di Torino, Corso Duca degli Abruzzi 24, 10129 Torino, Italy

Abstract
The continuous increase of electricity production from renewable energy sources (RES) introduces the intrinsic fluctuating characteristic of RES in the electric power grid, causing non-trivial grid management issues (e.g. grid congestion). In this work, an innovative power to liquefied methane concept was developed and process simulations for a 200 kW_{el} demonstration plant were carried out. The proposed concept is based on water electrolysis to produce hydrogen, CO_2 capture from air using solid adsorption materials, catalytic CO_2 methanation, gas separation and a single mixed refrigerant (SMR) liquefaction process.
The gas separation unit produces an exhaust stream, rich in hydrogen and carbon dioxide but also in methane, that is recycled to the methanation unit inlet. A thermodynamic analysis excluded the possibility of carbon deposition formation in the methanation reactor due to methane recirculation. The gas separation system was designed using a combination of temperature swing adsorption techniques (stream dehumidification) and membrane separation (CO_2 separation). After a screening of different polyimide type membranes, a two-stage layout was selected and dimensioned. Subsequently the liquefaction unit was developed optimizing the SMR composition and pressures to minimize the total work required. Hence, the minimum work required for the liquefaction resulted being 0,57 kWh_{el}/kg_{LNG}.
Finally, the thermal integration was performed to minimize the external heat requirement. The heat produced by the electrolyser and methanation unit is greater than the thermal energy requirement by the CO_2 capturing unit during desorption. A process efficiency up to 52,6% (electric to chemical) resulted from the study.

Introduction
As the increase in the adoption of renewable energy sources (RES) for electricity production grows also the electric grid management gets more and more complicated. This is caused by the fluctuating and intermittent production characteristic that RES have making balancing the electric grid a challenging issue. There are a few technologies that can tackle with this issue: flywheels, supercapacitors, batteries, compressed air storage, pumped hydroelectric storage, power-to-gas (PtG) and power-to-liquid.
The PtG technology received in the past years a lot of attention since it appears to

be a promising solution in converting excess renewable electricity in a gaseous energy carrier. In PtG water is converted into hydrogen using electricity in a water electrolysis process. Since hydrogen does not have a transportation and distribution infrastructure it is further converted into methane by means of the Sabatier reaction (1). The CO_2 required to perform this reaction can be obtained from biogas upgrading plants or even captured from air.

$$CO_2 + 4H_2 \rightleftharpoons CH_4 + 2H_2O \qquad \Delta H_{298K} = -164{,}9\ kJ/mol \tag{1}$$

The produced methane has the same proprieties as natural gas and can then be injected in the natural gas grid and the product gas is called substitute or synthetic natural gas. In case grid injection is not feasible the produced gas can be liquefied obtaining liquefied natural gas (LNG). LNG has received a lot of interest in the past years as new applications have been studied (i.e. heavy trucks and light-duty freight/passengers vehicles [1] and marine transportation [2]).
In this work we focus on the process simulation of a novel demo plant that uses CO_2 captured from air and produces liquefied gas equivalent to LNG.

Process description and simulation model overview

Renewable electricity is used to produce hydrogen through water electrolyzer for which different technologies are available: alkaline electrolysis cells (AEC), proton exchange membrane electrolysis cells (PEMEC) and solid oxide electrolysis cells (SOEC). For this simulation an alkaline electrolyzer was used since it is the most mature and low capital cost technology even though it has a slightly lower efficiency with respect to PEMEC. The AEC unit used in the demo has a power consumption of 4,9 $kWh_{el}/Nm^3_{H_2}$ (including all the utilities) and this translates to a module efficiency of 71,7% HHV basis (60,7% LHV basis). The demo plant's electrolyzer module can be fed with up to 200 kW of electricity allowing for the evaluation of hydrogen flowrate and heat production.
CO_2 capture from air is a challenging process since the mean concentration is 400 ppm. Carbon dioxide is captured by moving air through an adsorption material that traps the CO_2 inside. When the material is saturated the desorption phase is performed using heat and afterwards the cycle is restarted. The sorption material is generally functionalised with amine groups for a better selectivity towards carbon dioxide. The specific energy requirements for a CO_2 capture unit were taken from the datasheet of a commercially available collector and these are as follows: 300 kW_{el}/ton_{CO_2} and 2000 kWh_{th}/ton_{CO_2}. The obtained carbon dioxide is then mixed with the hydrogen coming from the electrolyzer.
The CO_2 and H_2 blend stream is mixed with the recycle stream and the CO_2 and H_2 ratio is maintained at reaction stoichiometric ratio of 4. This stream is fed to the methanation reactor where the highly exothermic methanation reaction occurs. Different reactor configurations were considered: series of adiabatic reactors with intercooling, an adiabatic and an isothermal with intercooling and two isothermal reactors with intercooling. However, none of these solutions would manage to

reach the required purity to the liquefaction unit and a purification unit will be needed. Hence, a refrigerated reactor that still can guarantee CO_2 conversions ≥95% was used in the simulation.
The methanation outlet stream is made of water, methane, hydrogen and carbon dioxide. In order to be able to liquefy methane, the stream has to have a CO_2 concentration below 50 ppm and a water concentration below 1 ppm to avoid freezing in the condenser. Hence, a gas separation unit is required: steam condensation by cooling the stream, temperature swing adsorption (TSA) to remove the water vapor residue, membrane gas separation unit to lower hydrogen and carbon dioxide in the stream and finally a polishing TSA to lower CO_2 and H_2O content to the required concentration. The membrane gas separation unit was simulated using a shortcut method for a hollow fiber module in countercurrent [3] while the TSA modules were commercially available units.
At this point the stream is fed to the liquefaction unit and the hydrogen rich boil-off stream is recycled to the process. The liquefaction technology chosen is the single mixed refrigerant (SMR) solution. The composition of the refrigerant and pressure were optimized using the genetic algorithm [4] to minimize the energy demand keeping the constraint of the minimum temperature approach between cold and hot streams equal to 3 °C.
Finally, a thermodynamic analysis was performed to investigate if recycling methane to the reactor inlet could cause the formation of carbon deposition.
In Figure 1 the block flow diagram of the process is reported with preliminary mass and energy balance.

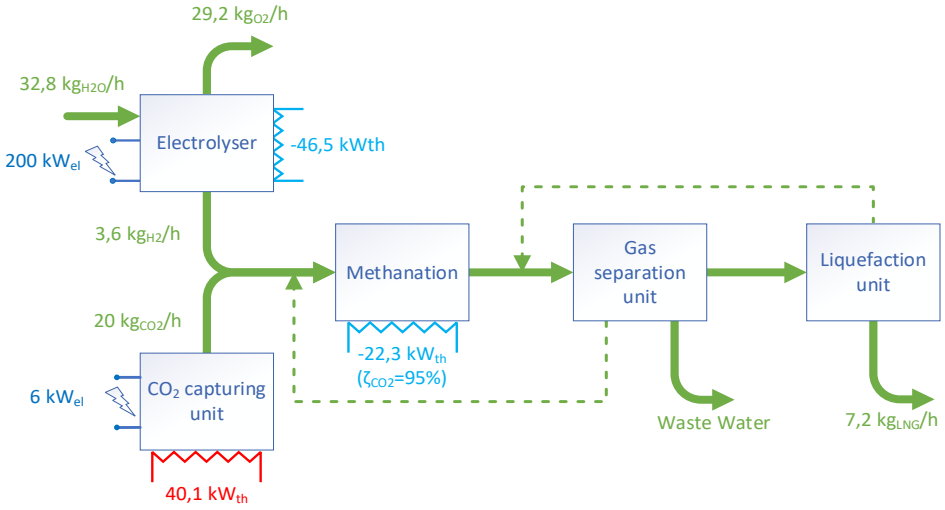

Figure 1. Block flow diagram with preliminary mass and energy balance

Results and discussion

The target for the demo plant in terms of electricity to the electrolyser was set equal to 200 kW, resulting in a total hydrogen production of 3,6 kg_{H2}/h (41,3

Nm^3_{H2}/h). The CO_2 inlet flow was calculated by keeping the stoichiometric ratio (H_2/CO_2=4), including also the non-stoichiometric recycle stream. A CO_2 flow rate of 20 kg_{CO2}/h (10,3 Nm^3_{CO2}/h) resulted from the simulation. The carbon dioxide capturing unit energy requirements are 6,0 kW of electricity and 40,1 kW of heat. After mixing the H_2, CO_2 and recycle the resulting stream is heated to 280 °C; the calculated duty of the heat exchanger is 5,3 kW. Since the reactor is cooled the 21,9 kW of heat produced by the methanation reaction are removed. About 60% of the methanation outlet stream is made of water vapor, the majority of which (97,8%) is separated in a water-cooled condenser that cools the stream to 40°C resulting in a duty of the condenser of 14,8 kW. The stream is then sent to the drying module to complete the operation. The dried stream is then compressed to 13 bar,a and sent to a membrane gas separation system. The most used membrane type in CO_2 gas separation is the glassy polymer category thanks to their selectivity, excellent thin film forming, good mechanical properties and higher permeability to low molecular weight species [5]. After the screening of numerous membranes, we concluded that a single module is not able to perform the wanted separation with reasonable cut ratio. Therefore, a two-stage membrane separation unit was implemented with the permeate of the first stage (rich in H_2 and CO_2) recycled to the methanation unit and the permeate of the second stage (rich in methane) recycled to the first stage inlet. The optimized configuration was obtained with two modules using the membrane in Table 1 with 20 m^2 of active area each.

Table 1. Membrane permeability

	Permeability (barrer[a])			*Ideal selectivity*	
	H_2	CO_2	CH_4	H_2/CH_4	CO_2/CH_4
TBDA1-6FDA-PI [6]	253	155	3,3	76,7	46,9

[a] $1\ barrer = 1 \times 10^{-10}\ cm^3_{STD}\ cm\ s^{-1}\ cm^{-2}\ cm^{-1}_{Hg}$

At this point, the SMR liquefaction process was simulated and optimized. The pressure of the lamination was set to 3,4 bar and the optimized composition and pressure are reported in Table 2.

Table 2: Refrigerant composition, pressures and performance

Refrigerant composition (%.mol)							*Pressure*	*Refrigerant flow*	*Required work*
N_2	CH_4	C_2H_6	C_2H_4	C_3H_8	C_3H_6	Iso-pentane	bar	$\frac{kg_{REF}}{kg_{LNG}}$	$\frac{kWh}{kg_{LNG}}$
12,0	42,1	-	17,9	13,7	-	14,3	32,6	7,9	0,57

Next the thermodynamic analysis on the reactive system excluded the possibility of carbon deposition in the ranges of temperature and pressure of the methanation unit (280-500 °C and 4-10 bar).

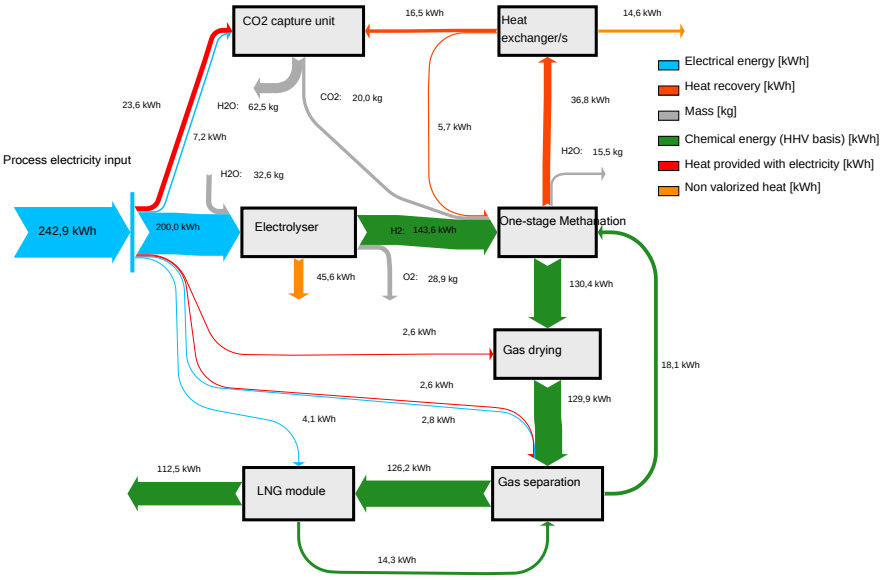

Figure 2. Energy and mass balance Sankey diagram for the optimized system

Finally, the heat integration analysis was performed. The electrolyser heat is not useful since it is generated at a low temperature of (75-80 °C) hence no heat recovery is feasible for the plant needs. Since the methanation reaction is highly exothermic part of the produced heat is supplied to the feed stream, to meet the required temperature at the reactor inlet of 280 °C, while the remaining part is sent to the CO_2 capturing unit. In Figure 2 the Sankey diagram for the energy and mass balance is reported for stationary operation at nominal capacity. By using this system integration layout ~41% of the heat required by the CO_2 capturing unit is coming from excess heat produced by the methanation reactor.

Conclusions

A concept to produce synthetic LNG using hydrogen generated from excess renewable electricity and carbon dioxide captured from air was analysed in this study. Process simulations of the concept were performed including optimisation of single units and whole plant by including thermal integration. The simulation model accounted for the efficiency of commercially available technologies (i.e. electrolysis and CO_2 capture).

A thermodynamic analysis focused on the methanation reactor excluded the carbon formation in the range of possible operating. Subsequently, a membrane gas separation system was developed: screening of different membranes and choosing the appropriate module layout. A two-stage membrane system resulted adequate for the stream purification. Besides this, choosing the appropriate separation system would give the possibility for the produced gas to be injected into the

natural gas grid or undergo liquefaction allowing for a flexible operation. Afterwards, the optimization of the SMR liquefaction system confirmed that the tested refrigerant compositions can be used. Among the several considered mixtures, the ethylene-propane refrigerant gave the lowest energy consumption of 0,57 kWh/kg_{LNG}.
Finally, after heat recovery an overall plant efficiency of 46,3% electrical to chemical conversion was calculated for the demo plant. However, the use of an electrolysis system operating at slightly higher temperature would allow to recover the produced heat and use it in the carbon dioxide capturing unit and the two TSA modules. This would allow to reach an electrical to chemical efficiency of 52,6%.

References

[1] LNG Blue Corridors Consortium, “LNG Blue Corridors,” 2013. [Online]. Available: http://lngbc.eu/. [Accessed: 03-Apr-2017].
[2] International Gas Union, “Enabling clean marine transport,” 2017.
[3] T. Pettersen and K. M. Lien, “A new robust design model for gas separating membrane modules, based on analogy with counter-current heat exchangers,” *Comput. Chem. Eng.*, vol. 18, no. 5, pp. 427–439, May 1994.
[4] L. Cao, J. Liu, and X. Xu, “Robustness analysis of the mixed refrigerant composition employed in the single mixed refrigerant (SMR) liquefied natural gas (LNG) process,” *Appl. Therm. Eng.*, vol. 93, pp. 1155–1163, 2016.
[5] J. K. Adewole, A. L. Ahmad, S. Ismail, and C. P. Leo, “Current challenges in membrane separation of CO2 from natural gas: A review,” *Int. J. Greenh. Gas Control*, vol. 17, pp. 46–65, Sep. 2013.
[6] Z. Wang, D. Wang, F. Zhang, and J. Jin, “Tröger’s Base-Based Microporous Polyimide Membranes for High-Performance Gas Separation,” *ACS Macro Lett.*, vol. 3, no. 7, pp. 597–601, Jul. 2014.

Acknowledgement

This project has received funding from the European Union's Horizon 2020 research and innovation program under grant agreement 691797 – Store and GO (Innovative large-scale energy STORagE Technologies & Power-to-Gas concepts after Optimization) project (http://storeandgo.info/).

TORREFACTION OF HEAVY METALS CONTAMINATED BIOMASSES

C.M. Grottola*, P. Giudicianni*, F. Stanzione*, J.B. Michel, R. Ragucci***

cm.grottola@irc.cnr.it

* Istituto di Ricerche sulla Combustione - C.N.R., Napoli – Italy

**HEIG-VD – Haute Ecole d'Ingenierie et de Gestion du Canton de Vaud– Switzerland

Abstract

Biomass for energy production has been extensively studied in recent years. In order to overcome some constraints imposed by the chemico-physical properties of the biomass, several pre-treatments were proposed. Torrefaction is one of the most interesting one since torrefied biomass holds a wide range of advantages over raw biomass suche as the increase of the calorific value, both on mass and volumetric basis. The process raises some concerns when biomass from phytoremediation and wood from demolition and construction activities are used as feedstock, since they could contain potential toxic elements (PTEs). During the torrefaction treatment, the fate of PTEs should be controlled in order to avoid their release in the gas phase and evaluate the extent of their concentration in the torrefied biomass. Herein, torrefaction tests on *Populus* nigra L. branches from phytoremediation, and demolition wood were conducted at three temperatures. For each temperature, biomasses have been holding at the final temperature for different residence time, namely 15 min for 250 °C, 10 for 270 °C and 5 min for 300 °C. The energetic content of the torrefied biomasses was evaluated; the fate of PTEs (Cd, Pb and Zn) as a function of the temperature was studied and their mobility in the torrefied biomasses was investigated and compared to the mobility in the raw biomass.

Introduction

Torrefaction is gaining attention thanks to the advantages that the process offers as a pretreatment of vegetal residues intended for energy production. The mild thermal treatment lowers the moisture content and removes volatiles oxygenated compounds thus increasing the calorific value on both mass and volumetric base. The treatment also induces physical and chemical transformations that make the torrefied material recalcitrant, hydrophobic and easy to be grinded thus increasing the energetic sustainability of the operational activities connected to the storage, transportation and use in coal based power plants [1]. However, the environmental sustainability of the torrefaction of lignocellulosic waste such as wood from demolition and construction activities (DW) and plants grown on contaminated land needs to be addressed due to the high content of potentially toxic elements (PTEs) that may affect the quality of the gas and of the solid residue. At authors knowledge, few studies addressed this issue, the most relevant being those from Bert et al and Edo et al **[**2; 3]. These studies were conducted at relativel y low

temperature, namely 290°C for [2] and 220 °C in [3]. In both cases the results suggested that torrefaction can reduce the potential formation of the pollutants compounds due to the lower chlorine content achieved in the chars, compared to that in the feedstocks. The determination of the amount, recovery and mobility of PTEs in torrefaction products was not estimated. In this study torrefaction of *Populus* nigra L. branches (PN-B) from phytoremediation, and demolition wood (DW) was studied with a special focus on the fate of PTEs (Cd, Pb and Zn) as a function of the temperature. Three torrefaction temperatures were investigated (250, 270 and 300 °C). The energetic properties of the torrefied biomasses were evaluated and the concentration of PTEs in the torrefied biomasses was evaluated as well as their mobility. Leaching tests in water and in a EDTA-NH4 solution were performed in order to study the water solubility and the bioavaialability of PTEs in the torrefied biomass with respect to the raw materials [4; 5].

Experimental

Torrefaction tests

The torrefaction experiments were conducted in the SOLO furnace, available at laboratory of Haute Ecole d'Ingenierie et de Gestion du Canton de Vaud (HEIG-VD) in Switzerland. The tests were carried out under oxygen-limited conditions, at constant heating rate (10 °C/min), at 250 °C for 15 min; 270 °C for 10 min and 300 °C for 5 min. The cross section of the furnace is shown in Fig. 1. The cylindrical reactor is divided into two concentric and connected zones. In the internal cylindrical section the container with the biomass was positioned, whereas in the external section the recirculation of the exhausted gases evolving during the torrefaction test occurs.

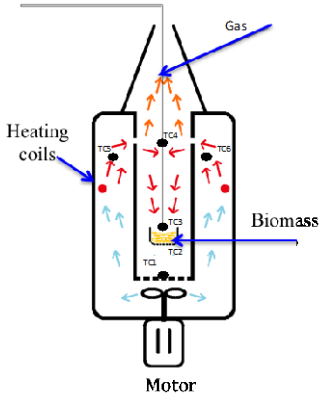

Figure 1. Cross section of the SOLO furnace.

The volatiles produced in the reaction unit entered the condensation device, which consists of two pyrex condensers where condensable volatiles condense. At the condenser's outlet, a flask was allocated for the collection of the liquid products. The non-condensing gases were fed to the analytical system for on-line

characterization (Horiba Mexa 7170D). Temperature of the sample and of the reaction environment was monitored constantly through six K-type thermo-couples ($TC_{n:1,6}$) as reported in Fig.1

Materials characterization

The PN-B was collected from phytoremediation tests conducted in Litorale Domitio - Agro Aversano NIPS (South Italy, Campania region) in the framework of the European LIFE Project ECOREMED ((LIFE11/ENV/IT/275 – ECOREMED, 2016), whereas the DW was provided from the HEIG-VD. The material was grinded and the sieved fraction, in the 400–600 m size range, was recovered for the characterization and for the torrefaction tests. For the raw and torrefied materials the proximate and the elemental analysis were performed and HHV were measured. The CHNS content were measured using Analyseur Flash 2000 (Thermo Scientific) according to ISO 16948:2015. Moisture content was measured through the Sartorius Moisture Analyzer (Model MA35) according to ISO18134-3. Carbolite AFF 1100 furnace was used for the determination of ash content according to ISO 1171/2015 and volatile fraction content was measured following the ISO 18123:2015 procedure. The fixed carbon content was calculated as the amount needed to complete the mass balance. The calorific value was determined using a bomb calorimeter (Oxygen Combustion Vessel 110 - Parr Instrument Company) according to EN14918. Ash composition was determined by dissolving the biomass samples via microwave-assisted acid digestion based on US-EPA Methods 3051 and 3052. The results of ICP/MS analysis were used for the calculation of the ion recovery in the torrefied material. The results were reported in terms of content of the inorganic species and of ion recovery in the torrefied biomass. The first is intended as mass of ion per mass of char and is used to calculate the ion recovery by multiplying it by torrefied yield and dividing by the mass of ions in the raw biomass. The metals mobility was determined through leaching test on biomass and corresponding torrefied materials using water and EDTA-NH_4 solution, as reported in [4]. The amount of heavy metals in the leached was estimated on the basis of the PTEs recovered in the torrefied biomasses. The Ion Release was the ratio between the amount PTEs released in the leachate and the amount of PTEs in the torrified material. The energy yield, energy content, and energy density were calculated on dry basis by Eqs. (1) and (2).
In the equations "*t*" stands for torrefied material and "*f* "for feedstock.

$$\text{Energy content} = \text{Weight}\,(f\,;\,t) * HHV\,(f\,;\,t) \quad (1)$$

$$\text{Energy yield} = (\text{Energy content}\,(t)) \,/\, (\text{Energy content}\,(f)) * 100 \quad (2)$$

Results and discussion

In this section, the results of characterization of untreated and torrefied DW and PN-B obtained at different temperature are discussed. The effect of the torrefaction temperature on the solid is shown in Table 1. It should be noted that even though the origin of the waste was different, the results of the both elemental and

proximate analysis were comparable except for the ash and the nitrogen content. The biomass from phytoremediation was richer in ash than the DW. Whereas, the higher nitrogen content of DW compared to PB-N could be attributed to adhesives used in the production of timber goods (such as particle boards) that end up in the DW waste wood stream [6]. As expected, for both the PN-B and DW, the mass yield decreased with the torrefaction temperature, but, despite of the similar results obtained from the elemental and proximate analysis, at each temperature the mass loss was higher for PN-B then DW. At the highest torrefaction temperature (300 °C), the mass yield of the torrefied was 64.0 and 80.5 for PN-B and DW respectively. As expected, the volatiles content of both the torrefied feedstocks decreased with the temperature, whereas fixed carbon content increased. According to the higher mass loss observed for PN-B the fixed carbon content is highest for the corresponding material torrefied at 270 and 300 °C. The fixed carbon content of torrefied DW and even more in PB-N was greatly enhanced and was comparable to that of coal [7]. At increasing torrefaction temperature, for both the feedstocks an increase in elemental carbon and a drop in elemental oxygen and hydrogen were observed in agreement with the literature [1]. This is due to the breaking of the weak C–O and C–H bonds in the hemicellulose matrix responsible of the release of volatile species and permanent gases (mainly CO and CO_2) [8] rich in oxygen and hydrogen, thus causing the de-oxygenation of the torrefied biomass. At each temperature H/C ratio, similar in both the feedstocks was always higher for torrefied DW denoting the devolatilization of a greater amount of compounds containing saturated C-H bonds. The thermal behavior of elemental nitrogen was different in the two feedstocks revealing a different chemical nature of the N-compounds in PN-B and DW. Nitrogen content always increased with the torrefaction temperature for DW sample, whereas a not clear trend was observed for PN-B.

Table 1. Characterization and energy properties of untreated and torrefied DW and PB-N obtained at 250 °C, 270 °C, and 300 °C.

	moisture	volatiles	fixed carbon	ash	C	H	N	S	O	O/C	H/C	HHV	Energy content	Mass yield	Energy yield
	wt % as recieved		wt % db		wt % daf					mol/mol		MJ/Kg	MJ	db %	%
DW	1.10	80.20	18.30	1.50	47.70	6.10	2.13	0.00	42.57	0.67	1.53	19.25	1.68	100.00	100.00
DW 250	1.30	71.79	25.50	2.75	50.02	5.79	2.42	0.00	39.02	0.59	1.39	19.29	1.48	87.92	88.10
DW 270	1.40	71.90	25.97	2.09	53.04	5.79	3.05	0.00	36.03	0.51	1.31	21.51	1.64	85.55	95.60
DW 300	1.30	70.30	27.97	1.77	54.42	5.84	3.45	0.00	34.53	0.48	1.29	22.55	1.66	80.47	94.26
	moisture	volatiles	fixed carbon	ash	C	H	N	S	O	O/C	H/C	HHV	Energy content	Mass yield	Energy yield
	wt % as received		wt % db		wt % daf					mol/mol		MJ/Kg	MJ	db %	%
PN-B	7.00	77.00	18.20	4.80	47.12	5.87	0.74	0.00	41.47	0.66	1.49	19.90	1.60	100.00	100.00
PN-B 250	1.20	69.10	25.75	5.15	51.40	5.40	1.00	0.00	38.00	0.55	1.26	20.80	1.25	74.62	78.14
PN-B 270	1.50	67.90	27.20	4.93	51.80	5.20	0.80	0.00	37.30	0.54	1.21	21.50	1.22	70.19	75.77
PN-B 300	1.60	62.54	31.67	5.79	54.20	5.10	0.90	0.00	34.00	0.47	1.13	23.30	1.20	63.98	74.96

The HHVs of torrefied solids were remarkably improved at increasing torrefaction temperature, being always slightly higher for PN-B. In the whole temperature range, the energy content of the DW torrefied was higher than torrefied PN-B. However, it should be noted that the energy yield was always lower for PN-B due

to the higher devolatilization. Moreover, in the case of DW the energy yield has a non-monotonous trend with the temperature, showing a maximum at 270 °C. On the contrary, it decreased with the temperature for PN-B. The concentration of the detected heavy metals, namely Cd, Pb Cu, and Zn was reported in Table 2 for the raw biomasses and the corresponding torrefied materials. Their concentration increased with the torrefaction temperature for both the feedstocks and the ion recovery for all the torrefied materials was always equal to 1, thus it can be inferred that condensable and gas phase evolving from the torrefaction tests was free of heavy metals. In order to investigate the effect of torrefaction on the mobility of the heavy metals retained in the solid residue two leaching tests were performed, respectively in water and in a EDTA-NH4 solution.

Table 2. ICP/MS analysis of untreated and torrefied DW and PB-N obtained at 250 °C, 270 °C, 300 °C.

	Cd	Cu	Pb	Zn
		mg/Kg		
DW	0.14 (6)	6.4 (6)	39.65 (55)	142.4 (62)
DW250	0.17 (19)	8.35 (5)	51.7 (10)	185 (7)
DW270	0.18 (4)	8.54 (26)	52.9 (17)	188 (15)
DW300	0.2 (2)	8.78 (7)	54.12 (71)	195.45 (7)
	Cd	Cu	Pb	Zn
		mg/Kg		
PN-B	2.16 (4)	8.23 (17)	60.3 (4.8)	50 (8.9)
PN-B 250	2.58 (3.4)	9.65 (0.3)	70.43 (10)	61 (0.6)
PN-B 270	2.63 (1.8)	9.76 (4.3)	72.34 (3.2)	65.39 (4)
PN-B 300	3.21 (3.5)	11.45 (5)	89 (4.6)	73.24 (0.1)

The higher ion release in water was observed for Zn followed by Cu>Cd>Pb, and their mobility decreased with the torrefaction temperature. Leaching with EDTA-NH4 was more severe, and all the metals were released from the raw materials. Temperature hadn't any effect on the PTEs mobility up to 300 °C, when part of the metals retained in the char are immobilized in the solid matrix even in more severe leaching conditions. It is likely that in acid condition, the acid groups, associated with lignin, hemicellulose, and extractives, were easily removed together with the associated inorganic elements [5].

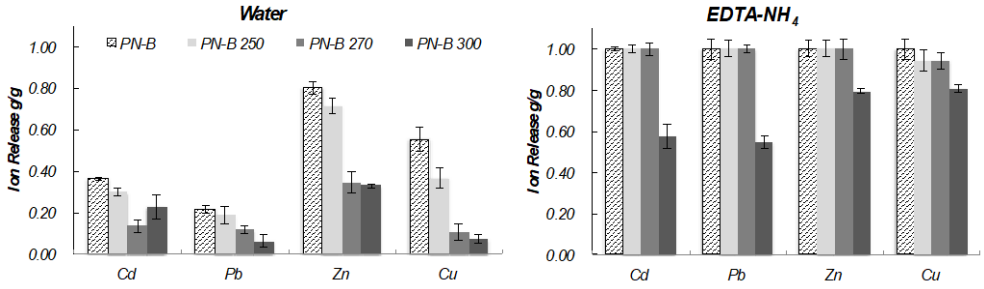

Figure 2. Heavy metals ion release in water (left) and EDTA-NH4 leaching solution (right).

Conclusion

Torrefaction of woody waste (demolition wood and biomass from soil phytoremediation) was studied with the aim of evaluating the energetic properties of the torrefied material and the fate of heavy metals during the pre-treatment. It was found that increasing the torrefaction temperature the energy properties of both torrefied biomasses were improved. In particular, the study revealed that demolition wood has a high potential as for its energy content as well as energy yield. Some concerns arise for its high nitrogen content compared to PN-B both in the raw and in the torrefied materials. For both the feedstocks, PTEs were retained in the torrefied biomasses up to 300 °C allowi.ng the production of a heavy metals free vapor phase fuel. The higher the temperature, the lower the PTEs release by water leaching, thus increasing the safety of the material storage in open areas.

References

[1] Tumuluru, J. S., Sokhansanj, S., Hess, J. R., Wright, C. T., & Boardman, R. D., "A review on biomass torrefaction process and product properties for energy applications", Ind Biotechnol. 7(5): 384-401 (2011)

[2] Bert, V., Allemon, J., Sajet, P., Dieu, S., Papin, A., Collet, S., & Raventos, C., "Torrefaction and pyrolysis of metal-enriched poplars from phytotechnologies: Effect of temperature and biomass chlorine content on metal distribution in end-products and valorization options", Biomass Bioenergy, 96: 1-11 (2017)

[3] Edo, M., Skoglund, N., Gao, Q., Persson, P. E., & Jansson, S., "Fate of metals and emissions of organic pollutants from torrefaction of waste wood, MSW, and RDF", Waste Manag. 68: 646-652 (2017).

[4] Gonsalvesh, L., Yperman, J., Carleer, R., Mench, M., Herzig, R., & Vangronsveld, J., "Valorisation of heavy metals enriched tobacco biomass through slow pyrolysis and steam activation" J Chem Technol Biotechnol, 91(6): 1585-1595 (2016)

[5] Wigley, T., Yip, A. C., & Pang, S., "The use of demineralisation and torrefaction to improve the properties of biomass intended as a feedstock for fast pyrolysis", J Anal Appl Pyrolysis. 113: 296-306 (2015)

[6] Jermer, J., Ekvall, A., & Tullin, C., "Inventory of contaminants in waste wood", Värmeforsk Service AB, Report. 732: 6-64 (2001)

[7] Rago, Y. P., Surroop, D., & Mohee, R., "Assessing the potential of biofuel (biochar) production from food wastes through thermal treatment", Bioresour Technol. 248: 258-264 (2018)

[8] Giudicianni, P., Gargiulo, V., Grottola, C. M., Alfè, M., & Ragucci, R., "Effect of alkali metal ions presence on the products of xylan steam assisted slow pyrolysis", Fuel. 216: 36-43 (2018)

A PRELIMINARY STUDY OF FLUIDIZED BED SORPTION-ENHANCED METHANATION BY CaO

A. Coppola*, F. Massa*, P. Salatino*,, F. Scala*,****
coppola@irc.cnr.it
*Dipartimento di Ingegneria Chimica, dei Materiali e della Produzione Industriale, Università degli Studi di Napoli Federico II, P.le Vincenzo Tecchio 80, 80125 Napoli, Italy
**Istituto di Ricerche sulla Combustione, Consiglio Nazionale delle Ricerche, Piazzale Vincenzo Tecchio 80, 80125 Napoli, Italy

Abstract
The unceasing concern for climate change, closely related to the exploitation of fossil fuels, pushes the scientific community to develop new technologies for CO_2 utilization. Moreover, the growth and diffusion of solar energy requires new energy storage systems that put solar fuels at the forefront. Methane seems to be a suitable energy vector which could both store solar energy and use fossil fuel derived CO_2. Moreover, methane has the main advantage of an already existing supply and storage infrastructure. The methanation reaction from hydrogen and carbon dioxide (or monoxide) is generally carried out in staged adiabatic fixed beds operated at high pressure in order to overcome the limitations due to chemical equilibrium. The sorption enhanced methanation concept is based on the employment of a sorbent which is able to capture *in situ* the H_2O produced during the reaction, in order to shift equilibrium towards the formation of methane. In this work CaO, derived from natural limestone, is tested as sorbent material for H_2O capture in an innovative configuration for the sorption enhanced methanation based on the concept of chemical looping in dual interconnected fluidized bed systems. The experimental campaign was focused on the study of the sorbent performance in terms of hydration and dehydration cycles at different operating conditions. The results showed that CaO has good capacity to capture and release steam in the temperature range of interest for methanation. Unfortunately, even at the lowest temperatures tested, the sorbent is affected by the presence of CO_2 that worsen its performance in terms of H_2O capture capacity.

Introduction
Methane is an important energy carrier for many sectors such as industry, household and transportation. The largest source of methane is represented by fossil resources (natural gas), but the growing debate on the utilization of fossil fuels in the framework of climate change has stimulated a growing interest towards catalytic and biological paths to production of methane [1-3]. In particular, the catalytic methanation reaction ($4H_2+CO_2=CH_4+2H_2O$ or $3H_2+CO=CH_4+H_2O$),

discovered by Sabatier and Senders in 1902 [4], assumes an important role when combined with the concepts of chemical storage, solar fuels and utilization of CO_2. Methane could be considered as the final product for the storage of solar energy, initially converted into hydrogen by water splitting with photochemical or thermochemical processes [5]. Unlike hydrogen, the main advantage of methane is the current existence of a well-developed distribution and storage infrastructure in many countries, and its massive utilization in the automotive, household and industrial sectors. Furthermore, methane benefits from a relatively large public acceptance. In addition, methanation could be considered as a process for the utilization of CO_2 coming from fossil fuels in the framework of Carbon Capture and Utilization (CCU) technologies [6]. The conventional methanation process typically requires a cascade of adiabatic fixed bed reactors with intermediate cooling steps and recycles [1,7] and high operational pressure to yield a product matching the specification for injection in the natural gas infrastructure. Borgschulte et al. [8] and Walspurger et al. [9] studied the possibility to improve the methanation process by the application of the concept of Sorption-Enhanced Methanation (SEM), where the steam generated by the reaction is continuously removed from the gas phase in the catalytic bed by adding a suitable sorbent material, e.g. a zeolite. In this preliminary study a novel configuration for SEM based on the technology of dual interconnected fluidized beds is investigated. The concept is based on a chemical looping reactor arrangement where the catalytic methanation occurs simultaneously with the hydration of the sorbent in one reactor (methanator/hydrator), so as to drive the equilibrium towards product formation, while the regeneration of the sorbent takes place in another reactor (dehydrator). The material tested as sorbent was CaO from natural limestone.

Experimental

The sorbent was CaO obtained by calcination of a German limestone named EnBW: the material was prepared in a lab-scale fluidized bed (40mm-ID) at 850°C with air and a fluidization velocity of 0.5m/s for 20min. The experimental apparatus used for the tests (called Twin Beds) consists of two identical lab-scale bubbling beds of silica sand, acting as thermal ballast, operated batch-wise and connected by a rapid solids transfer line. This system is an *ad hoc* device used to study looping processes, and a complete description is reported elsewhere [10]. The two reactors were employed as hydrator and dehydrator respectively. The experimental campaign was aimed at evaluating the suitability of CaO to capture and release water at different temperatures and reaction environments.

The main operated conditions were: hydration with 10% steam (balance air) and dehydration in nitrogen or in air. A preliminary sensitivity analysis on temperature was first carried out fixing the hydration temperature at 250°C and varying the dehydration temperature at 350, 400 and 450°C in nitrogen (named H25A-D35N, H25A-D40N, H25A-D45N), and subsequently fixing the dehydration temperature at 400°C and varying the hydration one at 200, 250 and 300°C (named H20A-

D40N, H25A-D40N, H30A-D40N). The progress of hydration and dehydration reactions was followed during the tests by measuring the concentration of steam at the outlet by means of a humidity sensor. The H_2O capture capacity of the material was evaluated after each cycle for 4 complete cycles, while the fluidization velocity was fixed at 0.5m/s. The time of each hydration or dehydration step was fixed at 15 min. After each test the exhaust material was analyzed by a thermogravimetric device (LECO-TGA701) to evaluate the amount of CO_2 captured during the hydration stages.
Another set of tests was carried out fixing the temperature of both hydration and dehydration at 200 and 400°C respectively, and using air (instead of nitrogen) as fluidizing gas during the dehydration stages, in order to investigate possible detrimental effect of the CO_2 (contained in the air) on the sorbent performance: these tests were named H20A-D40A.
Finally, the effect of high levels of CO_2 was also studied during the hydration stage introducing CO_2, at different concentrations, together with steam. Two different levels of CO_2 were employed: 1 and 10% by volume (balance air), keeping fixed the fluidization velocity (0.5m/s). The temperatures of the two stages were again maintained fixed at 200°C for hydration and 400°C for dehydration. These conditions produced the tests named H20A1C-D40N and H20A10C-D40N. In Table 1 all the investigated conditions are summarized.

Table 1. Main operating conditions of the hydration/dehydration tests.

	Temperature	Fluidizing gas		
		H_2O	CO_2	Balance
H25A-D35N	250/350 (°C)*	10/0 (%vol)	400/0 (ppm)	Air/Nitrogen
H25A-D40N	250/400 (°C)			
H25A-D45N	250/450 (°C)			
H20A-D40N	200/400 (°C)			
H30A-D40N	300/400 (°C)			
H20A-D40A	200/400 (°C)		400/400 (ppm)	Air/Air
H20A1C-D40N	200/400 (°C)		1/0 (%vol)	Air/Nitrogen
H20A10C-D40N	200/400 (°C)		10/0 (%vol)	

*the first value (250) refers to the hydration stage, the second one (350) to the deydration stage. This notation is valid for all couples of values in the table.

Results and Discussion
Figure 1 shows the measured H_2O capture capacity of CaO, expressed as gram of H_2O captured per gram of initial sorbent, as a function of the cycle number at different temperature of dehydration (fig.1A) and hydration (fig.1B). Generally, capture capacity seems to increase with the dehydration temperature after the first cycle, with a maximum around the 2^{nd}-3^{rd} cycle for H25A-D40N and H25A-D45N, while the value remains nearly constant for H25A-D35N (fig.1A). This behavior may be explained by the fact that different dehydration temperatures could alter the microstructure of the CaO (hence the pores) with consequent variation in sorbent capacity. On the contrary, during the first cycles the capture capacity decreases with hydration temperature (fig.1B). This trend is probably due to the increasing

role of carbonation by CO_2 (present in air) at higher hydration temperatures. Apparently, the effect of the hydration temperature vanishes after 4 cycles.

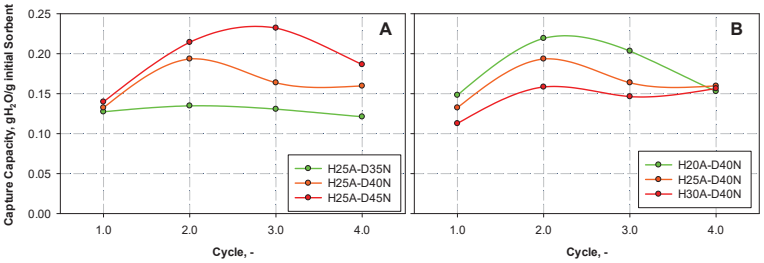

Figure 1. H_2O capture capacity of the sorbent along cycles: effect of the dehydration temperature (A) and of the hydration temperature (B).

When nitrogen was substituted by air during the dehydration stage, the presence of additional CO_2 determined a detrimental effect which increased with the number of cycles. This is showed in Figure 2A where the H_2O capture capacity measured in tests H20A-D40N (in black) and H20A-D40A (in blue) are compared. It is clear, just after the first cycle, that there is a difference between the values of the two tests (as expected) and this is mainly due to the additional carbonation of CaO during the dehydration stages. Despite the CO_2, the curve still shows an increase of hydration capacity after the first cycle, demonstrating that the phenomenon related to the microstructural change after the first dehydration is still active.
The effect of a high concentration of CO_2 during the hydration stage is shown in Figure 2B. The red curve refers to the test with CO_2 at 1% (H20A1C-D40N), and a negative effect with respect to the black curve (H20A-D40N), where CO_2 was not added, is clearly visible. The increase of the hydration capacity (after the first dehydration) is still present, but to a reduced extent. The decrease of the hydration capacity was about 67% for the first cycle, about 75% for the fourth.

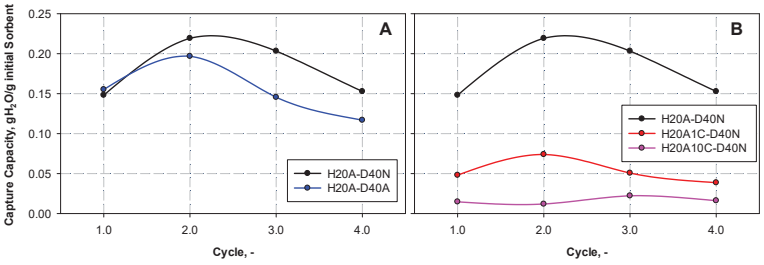

Figure 2. H_2O capture capacity of the sorbent along cycles: effect of the presence of low (A) and high (B) levels of CO_2 during the hydration stages.

When the percentage of CO_2 was increased at 10% (pink curve - H20A10C-D40N), the hydration capacity of CaO decreased further, and the maximum observed in all the other conditions disappeared. The curve is practically flat with a value of the hydration capture which is around 0.016g H2O/g of sorbent. This probably means that the carbonation process is so prominent to limit the microstructural effects after the first dehydration.

However, the sole carbonation does not completely explain the observed detrimental effect on the hydration capture; in fact, from the analysis (by thermogravimetry) on the exhaust sorbents H20A-D40N and H20A10C-D40N the carbonation degrees were measured to be about 11.7 and 12.6% by mass respectively, which are not dramatically different. This seems to indicate the presence of an additional effect caused by CO_2. For this reason, a specific test was conceived where the first two cycles were carried out under H20A10C-D40N conditions (with the presence of 10% CO_2 during the hydration stage), while the third and the fourth cycle were operated under H20A-D40N conditions (in absence of additional CO_2 during the hydration stage). Figure 3 shows the measured H_2O capture capacity during this 'hybrid' test. It is possible to note that for the first two cycles the capture capacity showed values similar to those obtained for the test H20A10C-D40N (see Fig.2B), but when the additional CO_2 to the hydrator was turned off (from the third cycle) an increase of the H_2O capacity occurred. This behavior cannot be explained only with the carbonation reaction, since this reaction is irreversible at the operating temperatures employed in the tests, and a permanent decrease of the H_2O capacity should have been observed. Possibly, an additional inhibition effect by CO_2 to the hydration reaction takes place under the conditions investigated, but further investigation is clearly necessary to explain this effect.

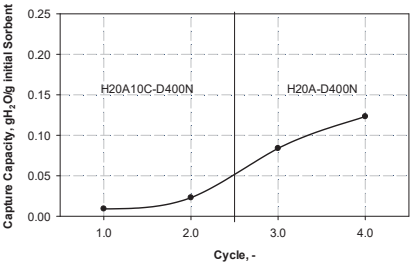

Figure 3. H_2O capture capacity of the sorbent along cycles: effect of the variable presence of CO_2 during the hydration stage.

Conclusions

CaO showed good H_2O capture capacity in the temperature range of interest for catalytic methanation. Cyclic hydration/dehydration tests demonstrated the potential of *in situ* steam uptake in a dual fluidized bed chemical looping reactor.

Important results were obtained as to the competition between CO_2 and H_2O for the sorbent, which may negatively impact selective H_2O capture in the presence of CO_2. However, the mechanism of the inhibition by CO_2 of the H_2O capture is not completely clear and deserves deeper studies. Moreover, further tests are necessary to measure the attrition tendency of the CaO particles under these conditions.
These results encourage the use of CaO for SEM with CO, while suggest the need to search for alternative more selective sorbents for methanation with CO_2.

Acknowledgments
The authors thank Mr. Alfonso Iovane and Mr. Salvatore Piccolo for their help in carrying out experimental tests.

References

[1] Seifert, A.H., Rittmann, S., Herwig, C., "Analysis of process related factors to increase volumetric productivity and quality of biomethane with Methanothermobacter marburgensis", *Appl. Energy* 132: 155–162 (2014).
[2] Götz, M., Lefebvre, J., Mörs, F., McDaniel Koch, A., Graf, F., Bajohr, S., et al., "Renewable Power-to-Gas: A technological and economic review", *Renew. Energy* 85: 1371-1390 (2015).
[3] Rönsch, S., Schneider, J., Matthischke, S., Schlüter, M., et al., "Review on methanation – From fundamentals to current projects", *Fuel* 166: 276–296 (2016).
[4] Sabatier, P., Senderens, J-B., "New methane synthesis", *J. Chem. Soc.* 82: 333-337 (1902).
[5] Smestad, G.P., Steinfeld. A., "Review: Photochemical and Thermochemical Production of Solar Fuels from H_2O and CO_2 Using Metal Oxide Catalysts", *Ind. Eng. Chem. Res.* 51: 11828−11840 (2012).
[6] Cuéllar-Franca, R.M., Azapagic, A., "Carbon capture, storage and utilisation technologies: A critical analysis and comparison of their life cycle environmental impacts", *Journal of CO_2 Utilization* 9: 82–102 (2015).
[7] Twigg, M.V., *Catalyst Handbook*, second ed., Manson Publishing Ltd., London, 1996.
[8] Borgschulte, A., Gallandat, N., Probst, B., Suter, R., Callini, E., Ferri, D., Arroyo, Y., Erni, R., Geerlings, H., Züttel, A., "Sorption enhanced CO_2 methanation", *Phys. Chem. Chem. Phys.* 15: 9620-9625 (2013).
[9] Walspurger, S., Elzinga, G.D., Dijkstra, J.W., Saric, M., Haije, W.G., "Sorption enhanced methanation for substitute natural gas production: Experimental results and thermodynamic considerations", *Chem. Eng. J.* 242: 379–386 (2014).
[10] Coppola, A., Scala, F., Gargiulo, L., Salatino, P., "A twin-bed test reactor for characterization of calcium looping sorbents", *Powder Technol.* 316: 585-591 (2017).

SESSION IV

Soot, nanoparticles and PAH

OXIDATION BEHAVIOR AND RAMAN SPECTROSCOPIC ANALYSIS OF DIESEL SOOT AND PROPANE SOOT

C. Zöllner, D. Brüggemann
lttt@uni-bayreuth.de
Department of Engineering Thermodynamics and Transport Processes,
Bayreuth Engine Research Center (BERC),
University of Bayreuth, Universitätsstraße 30, 95447 Bayreuth, Germany

Abstract
Particulate filters are effective devices to remove particulate matter (PM) from the engine exhaust and to meet the strict emission standards. As the deposition of the PM inside the filter results in an increase of backpressure which has a negative impact on the engine performance and fuel consumption, the filter has to be regenerated periodically by oxidation of the PM. However, this regeneration behavior is influenced by the characteristics of the deposited and accumulated soot. The thermal control of the regeneration process poses a challenge that might become more important in the future because of lower exhaust temperatures due to more efficient combustion and hybridization.
In this study, propane and diesel soot were collected on quartz filters and compared via optical and analytical measurement techniques. This includes the investigation of the structure and the reactivity via Raman spectroscopy and Thermogravimetric Analysis (TGA). The results from the Raman spectroscopy give information on the structural order and also on the organic content of the soot. These values were coupled with the kinetic parameters of the TGA determined with an Arrhenius-type equation and with the detected value for the volatile organic fraction (VOF).
Considering the propane soot, the results show a good correlation between the reaction rate constant and the structural order whereas the activation energy does not show a common trend. Furthermore, the determined VOF fluorescence and the Raman signal show a good accordance. Moreover, the relation between structural order and the reaction rate constant of diesel soot fits very well. However, a correlation between the Raman fluorescence and the VOF was not observed.
The studies on diesel soot properties will be extended to soot that is deposited inside the particulate filters to investigate the influences of engine operating parameters.

Introduction
To meet the strict emission standards for vehicles and engines additional exhaust aftertreatment systems are necessary. Especially particulate filters are unavoidable because they capture particles from the engine exhaust to comply with the limits.

The most frequently used variant for this purpose is the wall-flow filter. The particles are deposited inside the porous walls and on the inner side of the filter channels. As more particles are trapped in the filter, the exhaust backpressure increases, resulting in a lower engine performance and higher fuel consumption. For this reason, the filter has to be regenerated periodically by oxidizing the deposited particulate matter (PM). This oxidation process should proceed with little fuel penalty, low temperature rise and high regeneration efficiency. However, the regeneration strongly depends on the characteristics of the deposited soot. A decisive factor is the nanostructure of the soot. Concerning that issue, the engine operating parameters play a crucial role [1]. Incomplete regeneration processes cause a change in the nanostructure and the size distribution of the primary particles in the deposited soot layer. Under the influence of high temperatures, the deposited soot changes from a largely amorphous structure to a polyaromatic structure with higher order. The increased structural order can ultimately have a negative impact on reactivity. In addition, the resistance of the soot structure also changes with higher order and the diffusion behavior of oxidative gases is influenced [2].

Furthermore, it is well known that diesel particulates contain, beside the elemental carbon, organic compounds, ashes like metal oxides and sulphuric components which have been reduced since the introduction of low sulphur fuel. The components of the volatile organic fraction (VOF) mainly occur due to the incomplete combustion and consist of different groups of hydrocarbons like polycyclic aromatic hydrocarbons (PAH). Collura et al. [3] found that raw soot is non-porous, but the thermal decomposition of the adsorbed organic fraction in an inert atmosphere, leads to a more porous structure of the soot, deriving in an increase in the specific surface area.

Within this study basic investigations on the properties of propane soot and diesel soot samples collected on tissue quartz filters were done. The propane soot is free of contamination whereby the applicability of the measurement techniques for further investigations can be proven. The linkage between the structure and the VOF of the diesel soot and the oxidation behavior gives useful information for the regeneration process of particulate filters.

Experimental

Soot production was carried out with two different aggregates. On the one hand a miniCAST aerosol generator (Model 6204C, Jing Ltd) was used for the generation of contamination free and reproducible soot samples by combusting propane. The soot samples differ in the C:O-flame ratio that was adjusted during propane combustion. On the other hand a modern four-cylinder diesel engine (model OM 651 from Daimler AG) was applied for the studies of diesel soot. The engine was operated at the test bench with a water-cooled eddy-current brake. The experiments were conducted with standard diesel fuel according to DIN 590 that may contain up to 7 % by volume of fatty acid methyl ester. During soot sampling, the engine

was driven in a steady state engine mode. For generation of different soot samples, five different steady state engine operating parameters (OP 1 – OP 5) were chosen which differ in exhaust mass flow and the particle size distribution. Soot samples were collected on standard tissue quartz membrane filters (Pall Corporation). The filters were preconditioned in a muffle oven at 850 °C and in a drying oven at 200 °C. For the sampling procedure, the filters were placed in a heated and modified filter holder (Pall Corporation) and integrated into a bypass stream of the exhaust gas flow. The flow through the filter holder was controlled with a vacuum pump to guarantee isokinetic soot sampling. The target particulate mass on the filter was about 5 mg. This technique of soot sampling was applied at the exhaust line of the miniCAST aerosol generator and of the production diesel engine.
The PM collected on these filters was used for reactivity studies with Thermogravimetric analysis (TGA) and Raman spectroscopy for the investigation of the nanostructured order and the fluorescence.
TGA was carried out with the thermogravimetric analyzer Netzsch 209 F1 Libra. In the first step, the sample was heated in inert atmosphere to 550 °C to evaporate the organic fraction of the soot. The mass loss of the sample at the end of the inert phase was used for quantification of the content of VOF. Before the gas flow was switched to oxidative atmosphere, the temperature was either kept constant at 550 °C or was increased to 600 °C. Those two temperature levels were chosen for isothermal soot oxidation. The oxidative atmosphere consisted of 5 vol.-% oxygen and 95 vol.-% nitrogen. The mass loss curve obtained during the isothermal soot oxidation was used to determine the kinetic parameters with an Arrhenius-type equation with first order reaction kinetics:

$$k_c = A \cdot e^{\left(\frac{-E_A}{R \cdot T}\right)} \quad (1)$$

with the reaction rate constant k_c in [$Pa^{-1}s^{-1}$], the pre-exponential factor or frequency factor A in [$Pa^{-1}s^{-1}$] and the activation energy E_A in [kJ/mol].
The structural properties of the soot samples on the tissue quartz filters were analysed via Raman spectroscopy. Raman spectra of carbon blacks typically have the G band at about 1600 cm^{-1} and the D band at about 1350 cm^{-1}. Raman spectra were recorded with a setup consisting of a Nd:YVO4 laser (Verdi V-5, Coherent) with a wavelength of 532 nm, a spectrometer (Holospec f / 1.8i, Kaiser Optical Systems) and an ICCD camera (PI-Max 4, Princeton Instruments). However, the simplest way to compare different soot samples is the evaluation of the intensities of the two characteristic bands.

Results and Discussion

Figure 1 depicts the relation between the I_D/I_G-ratio out of Raman signal intensities and the results of the kinetic parameters for propane soot samples with different flame C:O-ratios. The intensity-ratio I_D/I_G decreases with increasing flame C:O-ratio. According to Ferrari and Robertson [4] the value of this I_D/I_G-ratio strongly

depends on the soot nanostructure and amorphous carbon structures show an increasing I_D/I_G-ratio with increasing order. As a consequence a higher structural order for the PM samples with lower flame C:O-ratio could be suggested. Furthermore, the values for the reaction rate constant are lower for oxidation of soot with lower C:O-flame ratios. This indicates that the highly ordered soot tends to be less reactive, providing that a lower reactivity means that soot tends to oxidize more slowly. A clear correlation between the intensity ratio and the activation energy is not visible.

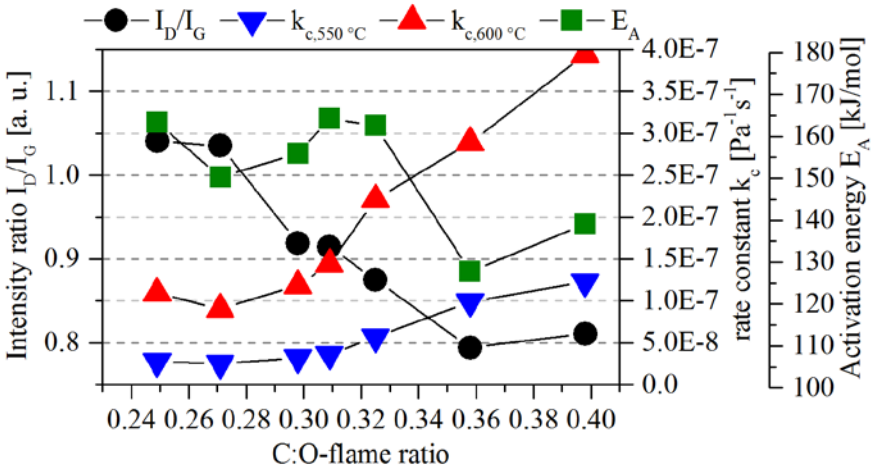

Figure 1. Correlation between Raman intensity ratio and kinetic parameters of oxidation of propane soot

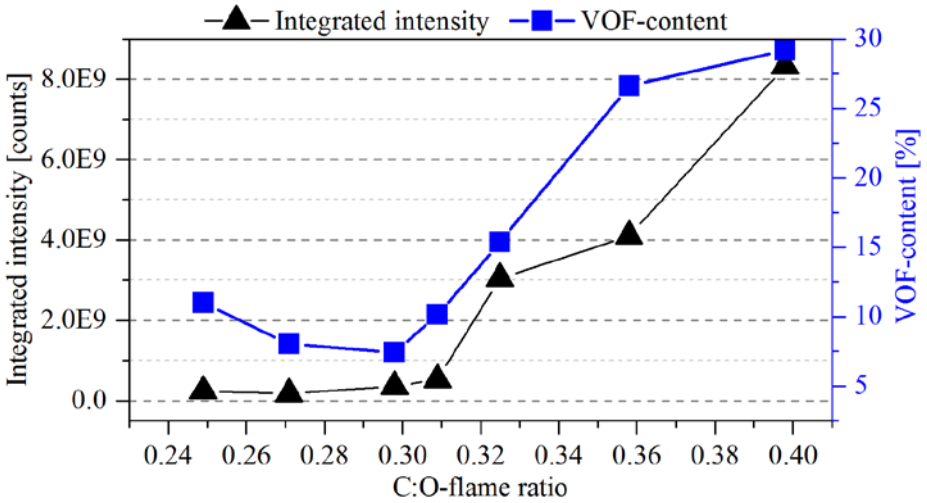

Figure 2. Integrated intensity of Raman signal and VOF of propane soot

Figure 2 gives the integrated intensity and the VOF of the different propane soot samples with different C:O-flame ratios. The integrated intensity is the value for the area under the raw Raman spectra. Higher values for this superposing scattering are typical for fluorescence effects. The VOF reflects the value for the mass loss after the inert phase during the TGA. It is evident that there is a clear correlation between the increasing fluorescence background and the higher content of the VOF. As the organic content in the soot increases with increasing C:O-flame ratio due to more formation of PAH, those fluorescence effects might occur from the mentioned organic compounds inside the soot [5]. Comparing the reaction rate constant and the VOF in figures 1 and 2, it is visible that the rate constant shows higher values for soot with more volatile compounds. This is in conformity with other publications who found out that the evaporation of the organic fraction might increase the soot porosity and therefore the active surface area [3].
Figure 3 describes the relation between the intensity ratio I_D/I_G and the kinetic parameters for the diesel soot samples that were collected during different steady state engine operating conditions (OP 1 – OP 5). Similar to propane soot the results show a good correlation between the intensity ratio and reaction rate constants for isothermal soot oxidation with 550 °C and 600 °C indicating a good correlation between reactivity and soot structure. With the exception of one engine operating parameter (OP 5) the activation energy seems to increase with decreasing reaction rate constant. The mean particle diameter of the soot increases from OP 1 to OP 5. This results in a different active surface area which might be the main factor for the influence on the oxidation behavior. A larger specific surface area leads to a higher reactivity.

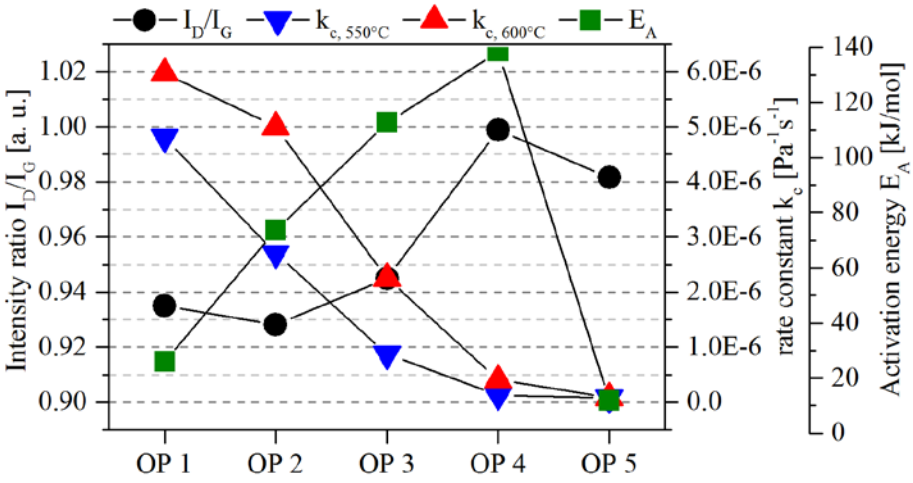

Figure 3. Correlation between Raman intensity ratio and kinetic parameters of oxidation of diesel soot

The relation between the integrated intensity and the VOF is shown in figure 4. It is visible that the two parameters do not correlate directly. Furthermore, it has to be

mentioned that the general differences of the integrated intensities are not as clear as it is the case for propane soot. However, there is a correlation between the higher values for the VOF and the higher reaction rate constant in figure 3.

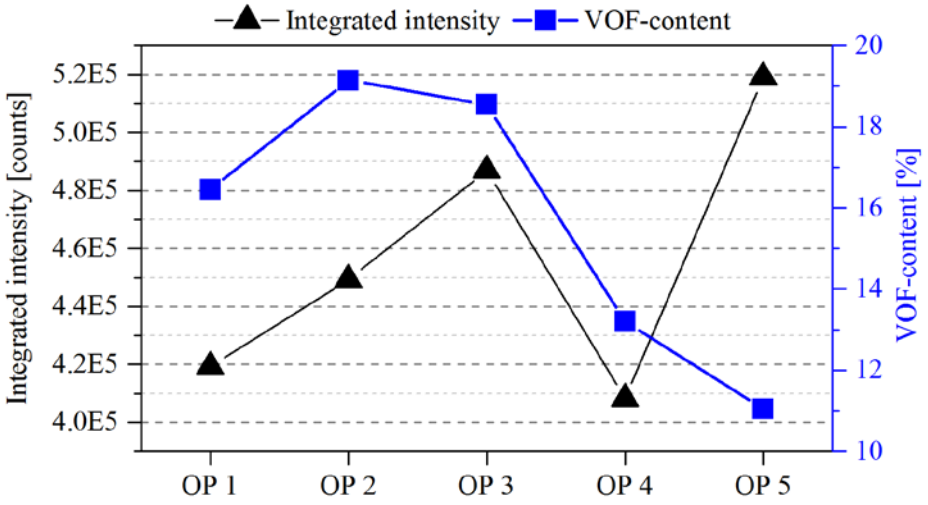

Figure 4. Integrated intensity of Raman signal and VOF of diesel soot

Outlook

Further studies will focus on the different properties of soot that is deposited inside the particulate filters after loading at the engine test bench. This includes differences in axial and radial direction of the filter and differences that result from various engine conditions.

Acknowledgments

This study was financially supported by the German Research Foundation (DFG) under grant no. BR 1713/17-1.

References

[1] W. Mühlbauer, C. Zöllner, S. Lehmann, S. Lorenz, and D. Brüggemann, "Correlations between physicochemical properties of emitted diesel particulate matter and its reactivity," Combustion and Flame **167**, 39–51 (2016).
[2] H. L. Fang and M. J. Lance, "Influence of Soot Surface Changes on DPF Regeneration," SAE Technical Paper 2004-01-3043 (2004).
[3] S. Collura, N. Chaoui, B. Azambre, G. Finqueneisel, O. Heintz, A. Krzton, A. Koch, and J. V. Weber, "Influence of the soluble organic fraction on the thermal behaviour, texture and surface chemistry of diesel exhaust soot," Carbon **43**, 605–613 (2005).
[4] A. C. Ferrari and J. Robertson, "Interpretation of Raman spectra of disordered and amorphous carbon," Phys. Rev. B **61**, 14095–14107 (2000).

[5] M. Schnaiter, M. Gimmler, I. Llamas, C. Linke, C. Jäger, and H. Mutschke, "Strong spectral dependence of light absorption by organic carbon particles formed by propane combustion," Atmos. Chem. Phys. **6**, 2981–2990 (2006).

Experimental investigation of soot oxidation under well-controlled conditions in a high-temperature flow-reactor

T. Bierkandt*, P. Oßwald*, M. Köhler*
thomas.bierkandt@dlr.de
*German Aerospace Center (DLR), Institute of Combustion Technology, Germany

Abstract
A new setup is presented to study the oxidation of soot by molecular oxygen (O_2) in a flow reactor from 750–1150 K at atmospheric pressure. A laminar, premixed ethylene/air-flame with an equivalence ratio of 1.85 serves as the soot source and sampled flame gases with freshly produced soot are introduced highly diluted with nitrogen into the reactor, which is typically used to study the reaction kinetics of generic and technical fuels. Soot oxidation is then investigated under well-controlled conditions during continuously temperature-ramping with 6145 ppm of O_2. Soot particles are characterized before and after oxidation by electrical mobility technique. Additional information about molecular flame species is obtained simultaneously by molecular-beam mass spectrometry. Only a few oxygenated species are formed during the oxidation process, while all hydrocarbon species are sampled directly from the flame, but show partly different oxidation behavior. Particle size distributions (PSDs) for a large temperature range and for two different inlet size distributions provide insights into soot oxidation kinetics. Particle sizes vary distinctly for the two investigated sampling positions and soot oxidation starts at different temperatures, but is clearly separated from flame species oxidation, which starts prior to soot oxidation at lower temperatures. Complete oxidation of soot particles is achieved at high temperatures for both sampling positions. Calculation of soot oxidation rates by O_2 and comparison with the Nagle-Strickland-Constable (NSC) equation indicates that our investigated flame-sampled soot is more reactive than graphitized soot. The presented dataset may help to validate existing soot models.

Introduction
Soot is formed by coagulation and growth of polycyclic aromatic hydrocarbons during incomplete combustion. Besides understanding the formation of soot, the kinetics of soot oxidation by molecular oxygen (O_2) and hydroxyl radicals (OH) is of crucial importance because of the high uncertainties of soot oxidation rates in existing soot models [1]. The NSC equation derives from measurements of oxidation rates of heated carbon rods by O_2 for temperatures from 900–2000°C and was later extended to 2400°C [2]. Vander Wal and Tomasek [3] have studied the soot oxidation by adding different soot aerosols obtained from pyrolysis into a

laminar flame and analyzing changes in particle diameter by transmission electron microscopy. In a recent study, Camacho et al. [4] have measured PSDs for the oxidation of nascent soot from ethylene, *n*-heptane, and toluene flames by O_2 from 1000–7800 ppm in a flow reactor for 950, 1000, and 1050 K. Oxidation rates from [3] and [4] were higher than predicted by the NSC equation. Here, we have studied the oxidation of soot produced from a C_2H_4/air-flame in a flow reactor for a wide temperature range.

Experiment

A laminar, premixed ethylene-air-flame at atmospheric pressure with an equivalence ratio $\Phi = 1.85$ and a total flow rate of 10 slm (1.14 slm C_2H_4, 8.86 slm air) is used as the soot source. The flame is stabilized on a McKenna burner with a water-cooled, porous bronze matrix (6 cm in diameter). To prevent flame-flickering a stainless-steel plate is placed 30 mm above the burner surface and the whole burner setup is also sideways enclosed. Additionally, a high co-flow of air (4 slm) shields the flame from the surrounded air. Flame gases and soot particles are sampled by a standard Dekati diluter based on ejection dilution, i.e., a high stream of N_2 (20 slm) flows around the ejector nozzle behind the sampling tube, which causes a pressure drop and gases at the tip of the sampling nozzle are sucked in and directly diluted. The nozzle of the diluter is made from stainless steel with an opening diameter of 4.5 mm and is introduced into the center of the flame at two different positions. First sampling position is directly above the burner with a distance of 5 mm from the burner surface to the center of the sampling nozzle. The second sampling position is at a height above the burner (HAB) of 25 mm in the exhaust gas region. A flow rate of 0.39 slm of sampled flame gases was measured by calibration with argon flowing through the burner matrix. This gives a dilution factor of 52.85 in our setup. The high dilution minimizes diffusion loss effects of sampled particles. For the soot oxidation process, O_2 (180 mg/min) is added together with N_2 behind the ejector nozzle. Nitrogen is preheated to 180°C and the diluter is also heated to 120°C to prevent condensation. Gas flows are precisely metered by Coriolis (C_2H_4, O_2, and N_2) and thermal mass flow controllers (air).

The sampled aerosol should be quickly transferred to the reactor to minimize changes in PSD. Therefore, the outlet of the diluter is connected by a flexible stainless steel line (950 mm in length, 16 mm in diameter) to the reactor inlet which is heated to 80°C. Depending on the aerosol temperature, the transfer time is no longer than 0.5 s. All gases are also premixed before entering the reactor. There is a 4-way cross mounted at the reactor inlet to measure continuously stable flame gases by quadrupole mass spectrometry (QMS) and the PSD at the beginning and the end of the temperature-ramping by scanning mobility particle sizer (SMPS). At the outlet of the reactor, the molecular gas phase composition is measured continuously by molecular-beam mass spectrometry (MBMS) and the PSD by SMPS. The temperature inside the reactor is varied between 750–1150 K. Soot experiments starts at the high temperature where total oxidation is achieved and

temperature then decreases with a cooling rate of 200 K/h. The high-temperature flow reactor is coupled to the MBMS and is typically used for investigation of technical fuels. The reactor and the MBMS are described in detail elsewhere [5, 6]. Briefly, the oven has three temperature zones with total heated length of 1000 mm, but all zones are set to same temperature for our experiment. To prevent emerging of particles at higher temperatures, the ceramic tube was replaced by a quartz tube. This limits the maximum temperature to 1350 K. Total length of the used quartz tube is 1500 mm with inner diameter of 43 mm. The residence time of the particles inside the heated length is approx. 1–1.5 s depending on the studied temperature for the soot oxidation. Gases are sampled at the outlet of the reactor by a quartz nozzle (opening diameter < 50 µm) to determine the molecular gas phase composition by MBMS. Sampled molecules are ionized by electron impact ionization (11.4 eV) and separated in the reflectron time-of-flight mass spectrometer (Kaesdorf) with the high mass resolution of 3000.

The measurement of stable flame gases (H_2, H_2O, C_2H_2, and CO_2) and the diluent gas (N_2) with the QMS at the inlet of the reactor allows of monitoring the initial gas phase composition and ensures the long-term stability during the soot oxidation experiments. If the sampling nozzle starts clogging, signal intensity of sampled flame gases (e.g., acetylene or CO_2) will drop while stability of the dilution gas shows general stability of the sampling process. For the flame with $\Phi = 1.85$, the signal intensities of the flame gases decrease slightly over time.

Because it is necessary to use nitrogen as diluent gas for the SMPS, detection of CO is not possible neither with QMS (R = 300) or MBMS (R = 3000). The used SMPS (TSI, Model 3938) with the electrostatic classifier (TSI, Model 3082) consists of four parts. The impactor at the inlet of the SMPS is 0.071 cm in diameter and removes very large particles. The adjusted inlet flow is 1.5 L/min. An X-ray source is used as neutralizer to make sure that all particles have a uniform and known bipolar charge distribution. All particles will be positively-charged. The differential mobility analyzer (DMA, TSI, Model 3085A) classifies the positively-charged particles in an electric field depending on their electrical mobility. By applying different voltages, certain particle size classes will pass the DMA and all particles are considered as monodisperse in size. A PSD of 1.5–150 mm can be measured depending on the sheath gas flow. A condensation particle counter (CPC) is connected to the outlet of the DMA to determine the particle concentration. SMPS scan time was 120 s.

Results and discussion

Complete soot oxidation series were measured three times for both sampling positions and good reproducibility is achieved. The sampling process of flame gases and soot particles is also stable enough for continuously temperature-ramping for the adjusted Φ of the flame. Addition of O_2 to the aerosol does not change the initial PSD and all measured particles are generated in the flame as measurements with a HEPA filter have shown. The signal from the SMPS was nearly zero with

the HEPA filter between the reactor inlet and the diluter indicating that no particles are released from the reactor at higher temperatures as observed for ceramic materials.

Figure 1 shows measured PSDs before (inlet) and behind (outlet) the reactor for the two sampling positions. All measured PSDs are log-normal or close to log-normal distributions. Sampling at 5 mm gives a small distribution with median mobility diameter of 12 nm while the higher sampling position at 25 mm provides a larger distribution with median mobility diameter of 28.5 nm. The PSD changes from unimodal to bimodal at the reactor inlet when vary the sampling position from 5 to 25 mm. A similar observation was also done by Stirn et al. [7] for an ethylene/air flame with $\Phi = 1.9$ where this transition was observed at a HAB of 14 mm. PSD also changes from bimodal to unimodal when passing the reactor at pyrolytic conditions and high temperatures. At room temperature the PSD stays bimodal at the reactor outlet. We also observed that the absolute concentration of the soot particles (without any oxidation process) is smaller at the reactor outlet in comparison to the inlet. For the small distributions, a significant particle loss has to be stated when passing the reactor (up to 60%). At the high sampling position, the particle loss is only 15%. Median diameter changes only slightly for both positions. A loss of sampling efficiency of approx. 20% must be also stated over time. Camacho et al. [4] investigated the oxidation of nascent soot from laminar flames in a flow reactor with shorter residence times (0.20–0.22 s) and did not mentioned a particle loss.

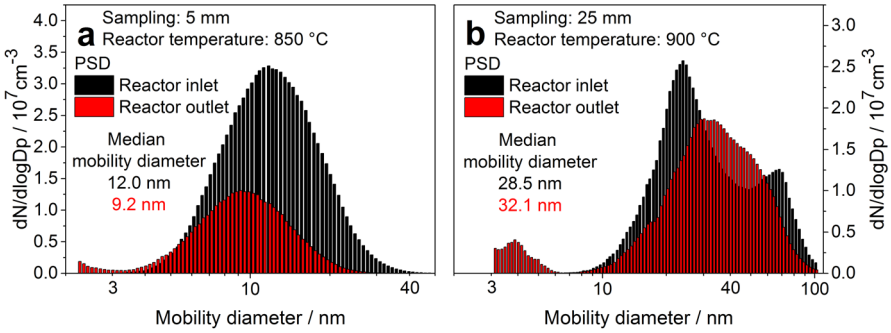

Figure 1. PSDs at the reactor inlet (black) and outlet (red) for two sampling positions (5 and 25 mm) in the flame with $\Phi = 1.85$.

PSDs of the soot oxidation with 6145 ppm O_2 for both sampling positions (5 and 25 mm) are shown in Figure 2 as function of the oven temperature. Oxidation of small soot particles starts at lower temperatures (approx. 940 K), while it is 990 K for the larger particles. All soot particles are almost oxidized above 1100 K. PSD shifted to smaller diameter when soot oxidation starts which can be clearly seen for the large distribution. Soot oxidation rates ω for the oxidation of soot by O_2 can be calculated based on a simple shrinking sphere model according to equation (1).

$$\frac{dm}{t} = \omega \cdot A \qquad (1) \qquad \omega = \frac{\rho}{2} \cdot \frac{dD}{t} \qquad (2)$$

Soot oxidation takes place at the particle surface A and is expressed as mass loss dm over time t. If the density of the soot ρ is constant, the soot oxidation rate ω can also be expressed by equation (2) considering the change of the particle diameter dD over time. For our experiment, t is the residence time of the particles in the heated length of the reactor where the oxidation takes place and dD is the difference of the initial median mobility diameter of the PSD at the inlet of the reactor and the median mobility diameter of the PSD at the outlet of the reactor. Soot density was estimated to be 1.8 g/cm^3, which is a typical value for soot between nascent soot [4] and amorphous carbon [3]. Figure 3 shows the calculated oxidation rates in comparison to the NSC equation for the oxidation of graphitized soot from [2]. Our results show that the investigated soot is more reactive than graphitized soot similar to the results of Camacho et al. [4] who studied nascent soot.

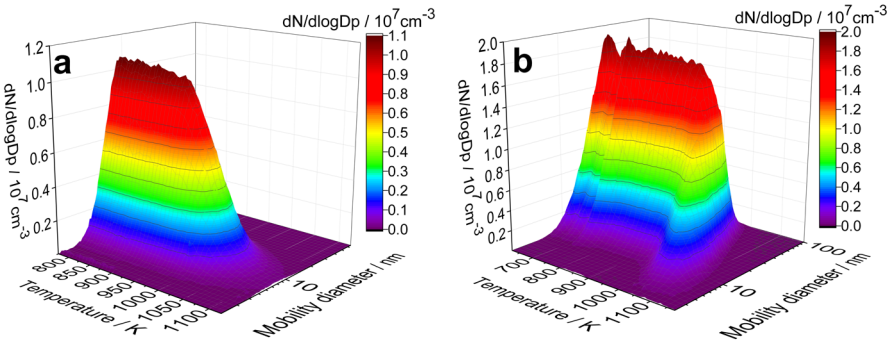

Figure 2. PSDs of the soot oxidation experiments in the temperature range of 750–1200 K and for sampling positions of 5 mm (left) and 25 mm (right).

Mole fraction profiles of small combustion intermediates were measured by MBMS and some of them are shown in Figure 3 in comparison with the total number concentration of soot particles for sampling at 25 mm. All detectable hydrocarbons have a mole fraction profile showing typical fuel behavior (e.g., C_2H_2, C_6H_6) and are directly sampled from the flame, while oxygenated species like CH_2O or CH_2CO are intermediates formed within the oxidation process. The lower sampling position is in the reaction zone of the flame where combustion intermediates are formed and mole fraction of sampled acetylene is significantly higher as at 25 mm. As a result, intermediates which are formed during the oxidation process in the reactor like formaldehyde are also observed in higher concentrations. One of the species with highest observed mass in detectable amounts was $C_{10}H_8$. Largest observed oxygenated species was on m/z = 94 and can be related to phenol. Soot oxidation is clearly separated from the flame species

oxidation and starts at higher temperatures. It was also observed that some sampled flame species have different oxidation behavior, e.g., oxidation of C_2H_2 starts a little earlier than oxidation of C_6H_6.

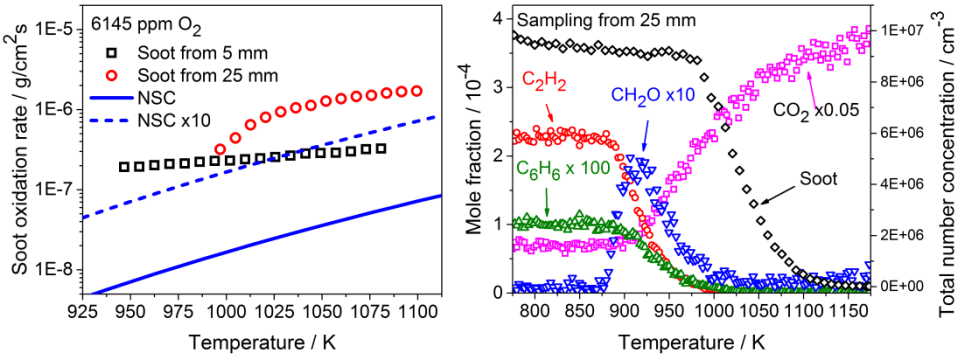

Figure 3. Soot oxidation rates in comparison with the NSC equation (left) and mole fraction profiles of molecular gas phase species in comparison with total number concentration of soot particles (right).

Conclusions

A laminar, premixed ethylene/air-flame was used as a soot source to investigate the oxidation of soot particles under well-controlled conditions between 750–1150 K and at atmospheric pressure. The flame with an equivalence ratio of 1.85 gives a reproducible data set for soot oxidation at two sampling positions including PSDs and species mole fractions. Small soot oxidation products (e.g., formaldehyde, ketene) and sampled molecules from the flame (e.g., acetylene, benzene) were quantified by MBMS. Calculated soot oxidation rates show that our investigated soot is more reactive than graphitized soot. The presented dataset for the oxidation of soot obtained from two different flame positions and for a wide temperature range may help to validate existing soot models.

Acknowledgements

The authors gratefully acknowledge funding from the European Union within the SOPRANO H2020 project under Grant Agreement No 690724.

References

[1] H. Guo, P.M. Anderson, P.B. Sunderland, Fuel, 172 (2016) 248-252.
[2] J.R. Walls, R.F. Strickland-Constable, Carbon, 1 (1964) 333-338.
[3] R.L. Vander Wal, A.J. Tomasek, Combust. Flame, 134 (2003) 1-9.
[4] J. Camacho, Y. Tao, H. Wang, Proc. Combust. Inst., 35 (2015) 1887-1894.
[5] P. Oßwald, M. Köhler, Rev. Sci. Instrum., 86 (2015) 105109.
[6] M. Köhler, P. Oßwald, D. Krüger, R. Whitside, J. Vis. Exp., (2018) e56965.
[7] R. Stirn, T.G. Baquet, S. Kanjarkar, W. Meier, K.P. Geigle, H.H. Grotheer, C. Wahl, M. Aigner, Combust. Sci. Technol., 181 (2009) 329-349.

SECONDARY TAR REACTIONS AND SOOT FORMATION IN PYROLYSIS OF COAL

C. Russo*, O.Senneca*, F. Cerciello*, F. Stanzione*, L. Cortese*, A. Ciajolo*, S. Heuer, V. Scherer**, B. Apicella***

c.russo@irc.cnr.it

* Istituto di Ricerche sulla Combustione, IRC-CNR, P.le Tecchio 80, 80125 Napoli (ITALY)

** Department of Energy Plant Technology, Ruhr-Universität Bochum, Universitätsstr. 150, 44780 Bochum (GERMANY)

Abstract

In the present work fast pyrolysis of coal in N_2 and CO_2 atmospheres was studied using two different systems: a drop tube reactor (DTR) and a heated strip reactor (HSR). The two systems allow comparable particles heating rates with different temperature of the gas phase. The tars produced in the two systems have been analyzed with the aim to study the role of gas tar reactions in soot inception.

It was found that in DTR, where volatiles react in a hot atmosphere, polycyclic aromatic hydrocarbons (PAH) formation and growth is larger than in the HSR, where the volatile species are quickly quenched.

The results provide evidence that secondary reactions of the tar are a source of PAH, which in turn, can be soot precursors, even in pyrolytic conditions. Also soot formation is highly limited in the HSR system, confirming the role of tar in soot formation mechanism. The effect of CO_2 is not straightforward and varies according to pyrolysis time and temperature.

Introduction

Coal pyrolysis is the first step in coal combustion and gasification. Although coal pyrolysis occurs on a time scale (up to several hundreds of milliseconds) much shorter than the subsequent char oxidation process (0.5 to 2 seconds for pulverized coal), it has a huge impact on the overall combustion efficiency and pollutant production in industrial furnaces. Coal pyrolysis has been studied extensively for more than a century. However, due to complexity of the chemistry and of transportation phenomena involved, no general mechanism is universally accepted, nor all observations can be accounted for by any single model [1].

Recent work from a collaboration of Bochum and Naples addressed the influence of environment gas atmosphere (N_2 and CO_2) on the early products of fast pyrolysis in a DTR at 1573 K of a high volatile bituminous coal [2]. As regards the char, it was found that the CO_2-char exhibited a lower reactivity compared to the N_2-char. Moreover, in CO_2 atmosphere the amount of submicronic fraction of carbon particulate, referred to as soot, was found to be up to four times as much as upon N_2 experiments [3]. Beside the larger formation of soot, relevant differences

in terms of combustion reactivity, size distribution and chemical structure of the residual carbon particulate produced in CO_2 environment with respect to N_2 environment were observed [2].
The present paper reports data on the tar produced in the fast pyrolysis of the same coal in a DTR and also in a heated strip reactor (HSR). In the DTR particles heat up and pyrolyze in a hot gas environment. Differently, in the HSR the particles heat up on a hot carbon foil, the surrounding gaseous environment being at nearly ambient temperature. As a consequence, volatile pyrolysis products are released in a hot environment in the DTR and in a cold environment in the HSR, determining different paths of volatile matter evolution.

Experimental

Experiments have been carried out on Colombian Coal (CC) whose properties are reported in [2]. Samples have been pyrolyzed in atmospheres of N_2 and CO_2 using gases of chromatographic grade in two different reactors, namely a drop tube reactor and a heated strip reactor, which are shortly described in the following. The experimental conditions of the pyrolysis experiments are summarized in Table 1.

Table 1. Summary of the process conditions.

Reactor type	**HSR**	**DTR**
Location	Naples	Bochum
Process type	Batch	Continuous
Reactor temperature (K)	1573-2073 (strip)	1573 (wall)
Gas	N_2/CO_2	N_2/CO_2
Particle heating rate	$1\text{-}2\cdot10^5$ K/s	$\approx 3\cdot10^4$ K/s
Residence time (s)	3	0.050-0.13

DTR: The reactor was designed for high heating rate and short residence times, comparable to devolatilization conditions of pulverized fuel boilers. The fuel particles are fed through a water-cooled injection tube to avoid preterm exposure to heat or reaction atmosphere. A microwave-based plasma source is used to heat the gases to a pre-selected temperature. The volume flow rate (process and feed gas flow) has been set to (49+1) l/min in all experiments. The reactor tube is a 320 mm long electrically heated Al_2O_3 pipe (i.d.= 50 mm). The wall temperature has been set to 1573 K. Due to the thermal conditions, particles are heated up rapidly by radiation and convection with maximum heating rates in the order of $3\cdot10^4$ K/s. An oil-cooled probe was used to sample and quench reaction products. The exhaust gases pass through a Pyrex glass tube, where the tar condenses. A more detailed description of the system is given in Refs. [2,3].
HSR: The reactor is a special heated grid device, where the usual metal grid used as the sample holder is replaced by a pyrolytic graphite foil thermally stabilized for use up to 2773 K [4]. The apparatus is enclosed in a stainless-steel vessel which can be pressurized up to 12 bar. The temperature of the grid is set by changing the

value of the voltage at the two extremes of the strip. Due to the very high heating rate of the HSR, the strip can be considered isothermal for the entire duration of the test. About 100 mg of particles have been laid on the strip. The reactor is flushed with the test gas (either N_2 or CO_2) for 10 min with a high flow rate to remove any oxygen traces. After flushing, the pressure was increased to 2 bar. The strip has then been heated up to 1573-2073 K and the total reaction time is 3 s. Due to the very small particle size, the coal particles are quickly heated up by contact with the strip and radiation from the reactor cover and can be considered isothermal with the strip. Details on equipment and heating rate profiles is provided in [4]. A Pyrex glass support was positioned over the strip to intercept ejected volatiles. The bridge did not heat up being nearly transparent to thermal radiation, therefore, tars condensed as soon as they impact on in.

Products analysis: The tar samples were recovered by washing the glass tube placed downstream of the DTR and the glass support located above the HSR with acetone in ultrasonic bath. The acetone volume was reduced to 0.5 ml under vacuum for analysis by gas chromatography-mass spectrometry (GC-MS). Acetone was unable to dissolve all the material deposited on the glass tube (DTR) and on the glass support (HSR) and the insoluble fraction was dissolved in N-methyl pyrrolidinone (NMP) and named “heavy tar”. The heavy tar was characterized by Size Exclusion Chromatography (SEC) for obtaining a molecular weight (MW) distribution and by UV-visible absorption for having information on the aromatic moieties.

The soot and char samples were recovered from the solid samples collected at the filter in DTR and from the sample holder/strip at the end of the experiment by a separation procedure involving dispersion in ethanol by ultrasonic mixing, followed by settling and decanting. The procedure produces top and bottom products constituted by coarse (char) and fine particle (soot) fractions, respectively as verified by SEM and granulometry [5].

Analytical techniques: *Gas chromatography-mass spectrometry (GC-MS).* The GC-MS employed is an AGILENT GC 7890 - MSD 5975C. In the GC, a HP-35 (length 30 m, i.d. 250 μm, film 0.25 μm) column is mounted. Sample injection was done in splitless mode at 300 °C with a gas flow of 1 ml/min (STP). The temperature program consists of four isothermal steps: 323 K (5 min), constant heating for 30 min to 473 K (5 min), constant heating for 1.75 min to 543 K (5 min) and finally, constant heating for 6 min to 573 K (15 min). The transfer line between the GC and the MS is held at 573 K. The mass spectrometer operated in electron ionization mode, and m/z was scanned from 50 to 400. The concentration of aromatics, oxo-compounds and aliphatics is quantified using response factors calculated from the analysis of a standard samples of known concentrations (PAH mixture with MW up to 300 Da supplied by Supelco EPA 525 PAH mix; C16 and phenol sample from Sigma Aldrich).

Size Exclusion Chromatography (SEC). The SEC analysis of heavy tar samples was carried out on a HPLC system HP1050 series by elution with NMP on a Jordi

Gel DVB Solid Bead column 300x7.8mm for the MW determination in the 2,000-400,000,000 Da range (i.e. up to nm). The online detection of species eluted from the SEC column used a HP1050 UV-Visible diode array detector that measured the absorbance signal at a fixed absorption wavelength (350 nm).
UV- visible absorption. UV-Vis spectra of the samples, dissolved in N-methyl pyrrolidone (NMP), were measured on an HP 8453 Diode Array spectrophotometer using 1 cm quartz cuvettes.

Results
Fig. 1 reports the results of GC-MS analysis on HSR and DTR tars. The classes of species reported in figure are: light aliphatics (C7-C20), heavy aliphatics (C20-C30), oxygenated compounds (oxy) and PAH with different ring numbers (from 2 up to >5).

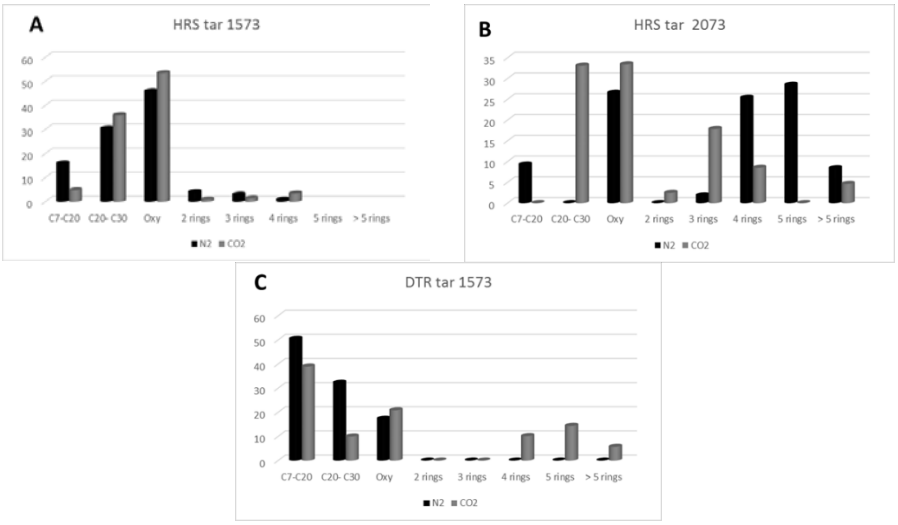

Figure 1. GC-MS analysis of tars collected in N_2 and CO_2 environment in HSR at 1573 K (a) and 2073 K (b), and in DTR at 1573 K (c).

It can be observed that the oxygenated compounds are the most abundant class in HSR system at 1573K whereas they are lower than aliphatics and comparable with PAH in the case of DTR system. Oxygenated compounds are comparable with heavy aliphatics in primary tar generated at 2073 K.
It can be assumed that the low temperature of the gas phase in the HSR limits the occurrence of secondary reactions of tar. This allows the formation of oxygenated species, limits cracking of heavy aliphatics in smaller aliphatics and, even more, their fragmentation in small hydrocarbons which participate in a series of H-abstraction, C_2H_2-addition steps to form benzenoid [6] and PAH of successively larger ring number, as in fuel-rich combustion [7]. By contrast, in DTR, the high temperature of the gas phase allows secondary reactions of tar and, as consequence,

the small aliphatics and heavy PAH, mainly unsubstituted, including cata-annelated and peri-fused species, are more abundant.
The observation of Fig.1 suggests also a role of CO_2 in HSR at higher temperature and in DTR. Indeed, in HSR at 1573K the compositional distribution of tar is very similar in N_2 and CO_2, whereas at 2073K in CO_2 the composition presents less small aliphatics and less heavy PAH, suggesting an inhibition of aromatic growth by CO_2. By contrast, in DTR the CO_2 largely promotes PAH and heavy PAH formation with respect to N_2, which is consistent with the larger soot formation found in previous work [3]. The effect of CO_2 on char properties in dependence of the operative conditions is discussed in a companion paper [8].
The heavy tar, which is insoluble in acetone and therefore not analyzable by GC-MS, was dissolved in NMP and analyzed by SEC (Fig.2A) and UV-visible spectroscopy (Fig.2B).
From Fig.2A it is observable that in HSR system the MW distribution of heavy tar is very similar with both the temperatures and environment gases. It reveals for all the samples a bimodality in MW range going from 100 up to 6*10^7 u and only in the case of HSR at 1573K in CO_2 (Fig.2A) it is observable a slight decrease of the higher MW range. In DTR (Fig.2c) the distribution is essentially monomodal in the same MW range, with a shoulder shifter at higher MW with respect to HSR tar.

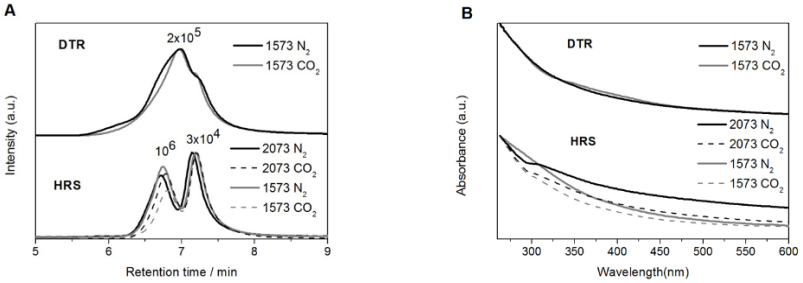

Figure 2. A) Normalized SEC profiles and B) Normalized Absorption spectra of heavy tars collected in N_2 and CO_2 in HSR and in DTR.

The UV-visible spectra of heavy tar of all samples reported in Fig.2B appear structure-less indicating the presence of aromatic moieties with bigger extension with respect to GC-MS PAH (up to 7 rings). They appear very similar among them regardless the temperature and the system, and the only notable difference is represented by HSR 2073 N_2 tar which shows a slope change and intensity increase of the spectrum after 300 nm. This feature suggests a heavier and more aromatic structure.

Conclusions

In the present work experiments in a HSR and a DTR allowed to investigate the effect of particles temperature, heating time, gaseous atmosphere and gas phase temperature on the tars produced from pyrolysis of Colombian Coal.

The results provide evidence that secondary reactions of the tar have a predominant role in formation of large PAH and soot inception. It is well known in literature that the degradation route rapidly increases with temperature along with aromatic growths [9]. The aromatic growth has a key role in soot formation [7], and, therefore, the much higher amount of soot formed from DTR with respect to HSR system confirms the hypothesis that soot from fast pyrolysis is formed from secondary reactions of tar [3 and references therein].

Acknowledgments
This work has been partially financed by the German Research Foundation (DFG) within the framework of the SFB/Transregio 129 "Oxyflame". We acknowledge Ruhr-University Bochum (RUB) Research School for awarding O. Senneca with an International Visiting Professor Grant (VIP_4_2016_02).

References

[1] Solomon, P.R., Fletcher T.H., Pugmire R.J., "Progress in coal pyrolysis" *Fuel*, 72(5):587-597 (1993).
[2] Heuer, S., Senneca, O., Wütscher, A., Düdder, H., Schiemann, M, Muhler, M., Scherer, V., 'Effects of oxy-fuel conditions on the products of pyrolysis in a drop tube reactor'. *Fuel Process. Technol*. 150:41–49 (2016).
[3] Senneca, O., Apicella, B., Heuer, S., Schiemann, M., Scherer, Stanzione, F., V., Ciajolo, A., Russo, C., 'Effects of CO_2 on submicronic carbon particulate (soot) formed during coal pyrolysis in a drop tube reactor'. *Combust. Flame* 172:302-308 (2016).
[4] Senneca, O., Allouis, C., Chirone, R., Russo, S., "Set up of an experimental apparatus for the study of fragmentation of solid fuels upon severe heating", *Experimental Thermal and Fluid Science*, 34:366-372 (2010).
[5] Apicella, B., Senneca, O., Russo, C., Heuer, S., Cortese, L., Cerciello, F., Scherer, V., Schiemann, M., Ciajolo, A., "Separation and characterization of carbonaceous particulate (soot and char) produced from fast pyrolysis of coal in inert and CO_2 atmospheres", *Fuel* 201:118-123 (2017).
[6] Ledesma, E.B., Kalish, M.A., Nelson, P.F., Wornat, M.J., Mackie, J.C., "Formation and fate of PAH during the pyrolysis and fuel-rich combustion of coal primary tar", *Fuel*, 79:1801–1814 (2000).
[7] D'Anna, A., Sirignano, M., Kent, J., "A model of particle nucleation in premixed ethylene flames" *Combust. Flame*, 157: 2106–2115 (2010).
[8] Senneca, O., Apicella, B., Russo, C., Cerciello, F., Ciajolo, A., Salatino, P., Wütscher, A., Muhler, M., Scherer, V., "Effects of CO2 on pyrolysis of walnut shells at high temperature and heating rate in a HSR", submitted to the *Proceedings of the Joint meeting of the German and Italian sections of the Combustion Institute*, 23-26 May, Sorrento, Italy.

[9] Barnard, J.A., *Flame and combustion*, United States,1985.

Deconvolution of soot particle size distributions

H. Mätzing*, P. Vlavakis, M. Sentko**, A. Loukou**, B. Stelzner**, D. Trimis** and D. Stapf***

corresponding author e-mail: hartmut.maetzing@kit.edu
*KIT, Institute for Technical Chemistry (ITC), D-76344 Eggenstein-Leopoldshafen, Germany
**KIT, Engler-Bunte-Institute (EBI-VBT), D-76131 Karlsruhe, Germany

Abstract
Soot particle size distributions are usually reported in single mode form which may be a crude approximation to the measurements. In this paper, soot particle size distributions were measured in premixed CH_4/O_2/Ar flames by SMPS. Up to five lognormal modes were fitted to the experimental results by nonlinear least squares regression. The multimode size distributions give a much better representation of the experimental data than single mode size distributions. Fitting 1 – 3 peaks to the size distributions increases the accuracy of data representation, while fitting more peaks does not optimize the precision further. The data fits include some extrapolation beyond the size limits of the experimental data ($d_P \approx 5$ - 60 nm). This type of data evaluation was performed for measurements at several heights above the burner. With increasing height above the burner, peaks with large modal particle diameters are found to become more and more important, while the peak widths are close to the limit of self-preserving distributions. This report appears to be the first attempt to examine measured soot particle size distributions with ultimate precision. The technique allows representing the evolution of different particle modes as well as the evolution of the soot volume fractions in these modes. Future perspectives are to obtain more insight into the coagulation kinetics of soot particles.

Introduction
The production of high purity syngas during the partial oxidation of methane has been studied for many years [1,2]. It requires high equivalence ratios and, flame stabilization is achieved by enhanced flame temperatures (preheated feed gas, little N_2 or Ar). Under such oxy-fuel conditions, flame temperatures are often found to be superadiabatic [3,4]. The soot formation in such flames has been studied recently using an SMPS technique [5]. The standard data evaluation implies a single peak representation of the measured particle size distributions. However, the results obtained for these flames clearly indicate the presence of several particle modes superimposing each other. As a follow-up to the aforementioned work, the present data evaluation focuses particularly on the multimode nature of these size distributions. This novel post processing of the measured particle size distributions is not contradictory to the previous evaluation [5], rather it gives extended, supplementary information about the soot formation in these flames.

There are numerous reports on soot particle size distributions measured in flat flames. Dual mode size distributions have been detected by mass spectrometry recently and have been characterized quantitatively [6]. SMPS techniques have also been reported frequently [e.g. 7-9]. By visual inspection, the SMPS results often show (or at least indicate) the presence of several peaks, either because they have a distinctive global minimum or just because they look distorted. Some authors fitted two superimposed lognormal distributions to their experimental results [9,10], however, until so far, there have been no attempts to investigate the multimodal nature of such soot particle size distributions in detail.
In this paper, up to five lognormal modes are fitted to the measured particle size distributions using the method of nonlinear least squares regression by Differential Evolution (DE). In this way, it is possible to monitor the history of various particle modes and to investigate the evolution of the soot volume fractions in these modes.

Theory
Soot particle size distributions are represented by lognormal distributions usually. If this assumption is accepted for all individual modes of multimode distributions also, the deconvolution can be a laborious task, because it requires a nonlinear regression. Previous deconvolution methods are listed in [11] and recently, it has been shown that Differential Evolution (DE) is a powerful and fast method to perform this type of peak deconvolution [11]. Lognormal size distributions are characterized by three parameters, the modal diameter d_{P0}, the total number density N_0 and the distribution width $\log \sigma_g$ (or $\ln \sigma_g$) and here, a summation is performed over 1 … imax distributions:

$$\frac{d\,N}{d\log\,d_P} = \sum_{i=1}^{imax} \frac{N_{0,i}}{\sqrt{2\,\pi}\cdot \log\,\sigma_{g,i}} \cdot \; exp\left\{-0.5 \cdot \frac{log^2\,d_P/\,d_{P0,i}}{log^2\,\sigma_{g,i}}\right\} \qquad (1)$$

The soot volume fractions $f_{v,i}$ of each peak are calculated from the third moments of the number distributions [12]:

$$f_{v,i} = \frac{1}{6}\pi\,N_{0,i}\cdot d_{P0,i}^3 \cdot exp(ln^2 10 \cdot {}^9\!/_2 \cdot log^2\,\sigma_{g,i}) \qquad (2)$$

The DE fitting process starts with two arbitrary (random) population vectors for the provided diameters, generates a mutant vector therefrom and mixes the parameters of a mutant and a solution vector to obtain trial populations. Depending on fit quality, the trial solution is accepted or rejected and the iteration starts again until successive solutions converge and predefined quality criteria are reached (minimum sum of squared errors etc.). In this way, good fits to both differentiable and discontinuous functions can be obtained comparatively fast [13,14].
In this work, the F77 code provided by Mishra [15] was adapted to the problem type considered here. The final code, Fit4LogNorms, provides an interactive user

interface for data input and output. Input values are the particle diameters d_P [nm or μm], the measured number densities d N/dlog d_P [cm^{-3} or m^{-3}] and several control parameters, e.g.

- the numerical ranges within which to search d_{P0}, N_0 and log σ_g
- minimum required differences between adjacent peaks (ΔN_0, Δd_{P0} and $\Delta \log \sigma_g$); they are used to detect occasional peak identities.

Fit4LogNorms was tested against literature data [11] and against additional artificial test cases. In particular, Fit4LogNorms was found to give reliable results for incomplete (truncated) size distributions, as they are often found experimentally due to instrumental or other limitations [7-11]. Special care was taken for the treatment of sparse datasets which have not a sufficient number of data points to perform a reliable fit. In these cases, Fit4LogNorms offers the possibility to enlarge the sample size by Bezier interpolation. As described above, the fitting procedure is a purely mathematical tool and, it does not imply any assumptions about the physical processes behind (soot mass growth, particle coagulation).

Experimental

The measurements are part of a larger project described elsewhere [5], investigating the soot formation in fuel-rich methane flames at constant equivalence ratio Φ = 2.6, but at different temperatures. Here we report only results for the coldest flame (x_{CH4} = 0.342, x_{O2} = 0.264, x_{Ar} = 0.394). The flame was stabilized on a 30 mm i.d. heat-flux burner with a burner plate temperature of 160 °C. The cold gas velocity was 11.1 cm/sec (corresponding to the flame velocity as derived by the heat-flux burner method [3]) and the flame was not shielded against surrounding air. The flame temperatures were measured with an S-type (Pt–Rh) thermocouple (wire thickness 100 μm) and corrected for radiation losses. The accuracy is better than ± 200 K [5]. Soot sampling and instant dilution were performed along the central flame axis through the pinhole of a stainless steel pipe. Size measurements were performed with an SMPS system (TSI model 3938) which was operated with a soft X-ray Neutralizer (TSI model 3088), a nano DMA (TSI model 3085A) and a condensation particle counter (CPC, TSI model 3776). In a standard procedure, the total number density and the soot volume fraction were obtained by summing up over all size intervals Δlog d_P. The resulting data have been corrected for flame dilution and for diffusion losses in the transport line from the probe orifice until the SMPS inlet and within the SMPS system [5]. The evaluated median particle diameter divides the size distribution into two halves of 0.5 ΣN_i.

Results and Discussion

According to the previous standard data evaluation, the average size d_P of the soot particles and the soot volume fraction f_v were found to increase with increasing height above the burner (HAB), while the total soot particle number density was decreasing [5]. These findings are confirmed by the present data evaluation and, for the particular flame (at Φ = 2.6), the extended data evaluation is demonstrated here.

The flame and its temperature profile are shown in Figs. 1 and 2. Close to the main reaction zone, the maximum temperature was ~ 1950 K, which is ~ 250 K above the adiabatic value [3,4].

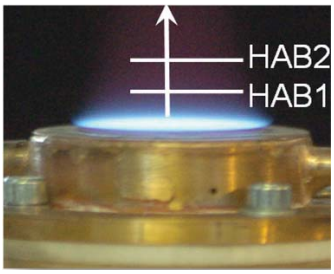

Figure 1. Heat-flux burner, sooting flame.

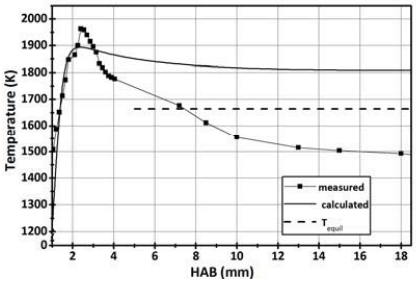

Figure 2. Flame temperature profile.

Fig. 3 shows measured and fitted size distributions at HAB = 10 mm. The single peak fit does not represent the data points precisely. The triple peak fit represents the data points much better and, it extrapolates into the very small size range, beyond the limit of reliable measurements [5]. A particle inception mode around $d_P \approx 2$ nm is not unlikely at high flame temperatures [6,16]. With increasing peak number, the sum of squared errors decreases (Fig. 4), hence the fit quality is improved. The same fitting procedure was performed at several HAB. At low HAB, the resulting total particle number density is higher than the SMPS result because of the extrapolation mentioned above (Fig. 3). The coagulation rate constants of the coagulation modes are in the range $d(1/N)/dt = 6 - 12 \cdot 10^{-9}$ cm^3/sec, which is reasonable. A comparison of the particle size as determined by the SMPS and by the fitting procedure is shown in Fig. 5. The size distribution widths are in the range $\log \sigma_g = 0.15 - 0.19$, close to the self-preserving limit (~ 0.13). The total soot volume fractions differ by up to ± 30% (Fig. 6). This is

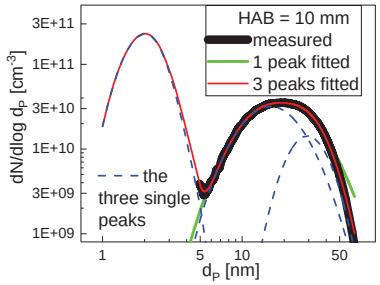

Figure 3. Three peak fitting example.

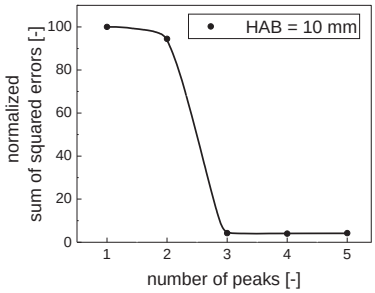

Figure 4. Fit error vs. peak number.

because at low HAB, the peak fits give a smaller amount of large particles, while at high HAB, they give larger particle sizes.

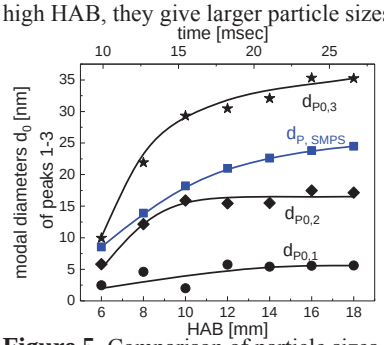

Figure 5. Comparison of particle sizes.

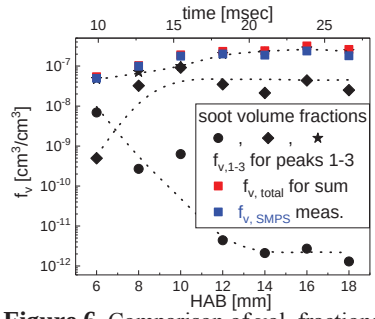

Figure 6. Comparison of vol. fractions.

Conclusions

A novel peak fitting method has been used to evaluate soot particle size distributions in flat, premixed $CH_4/O_2/Ar$ flames measured by SMPS. The experimental results can be represented very precisely by superposition of three lognormal modes. Even more peaks do not improve the fit precision further. Also, the procedure helps to make plausible estimates of the particle inception mode which is difficult to detect by SMPS. Therefore, the resulting total particle number densities turn out to be significantly higher than determined by SMPS at low HAB (the SMPS intrinsically employs the single peak assumption). This may also help to quantify diffusion losses during the SMPS measurement in the future. The total soot particle volume fractions agree within a ± 30% range. The novel peak fitting method can also be applied to other types of size distributions and, it will also allow better insight into the particle coagulation kinetics in the future.

Acknowledgements

The authors gratefully acknowledge the financial support by Federal Ministry of Food and Agriculture in the project "Formation of soot particles and catalytic filter regeneration for application of biomass fuels in direct-injection spark-ignition engines" (project number: 22040811) and the Helmholtz Association of German Research Centres (HGF).

References

[1] Baukal, C.E., *Oxygen-Enhanced Combustion*, CRC Press, Boca Raton,1998.
[2] Smith, H.C., Pineda, D.I., Ellzey, J.L., "Syngas production from burner-stabilized methane/air flames: The effect of preheated reactants", *Combust. Flame* 160: 557-564 (2013).
[3] Sentko, M., Weis, C., Harth, S., Habisreuther, P., Zarzalis, N., Trimis, D., "Temperature dependency of the laminar burning velocity of fuel-rich

methane oxygen measurements", *Proc. European Combustion Meeting 2015*, Budapest, Hungary, Paper P3-44, March 30–April 2, 2015, (ISBN 978-963-12-1257-0).

[4] Stelzner, B., Weis, C., Habisreuther, P., Zarzalis, N., Trimis, D., "Super-adiabatic flame temperatures in premixed methane flames: A comparison between oxy-fuel and conventional air combustion", *Fuel* 201: 148–55 (2017), doi:10.1016/j.fuel.2017.01.025.

[5] Vlavakis, P., Sentko, M., Loukou, A., Stelzner, B., Trimis D., "Soot formation in premixed fuel-rich oxygen-enhanced methane flames", submitted to Fuel, Dec 2017, manuscript number: JFUE-D-17-04934.

[6] Mätzing, H., Baumann, W., Bockhorn, H., Paur, H.-R., Seifert, H., "Detection of electrically charged soot particles in laminar premixed flames", *Combust. Flame* 159: 1082-1089 (2012).

[7] Zhao, B., Yang, Z., Li, Z., Johnston, M.V., Wang, H., "Particle size distribution function of incipient soot in laminar premixed ethylene flames: effect of flame temperature", *Proc. Comb. Inst.* 30: 1441-1448 (2005).

[8] Maricq, M.M., "Coagulation dynamics of fractal-like soot aggregates", *Aerosol Sci.* 159: 1082-1089 (2012).

[9] Gu, C., Lin, H., Camacho, J., Lin, B., Shao, C., Li, R., Gu, H., Guan, B., Huang, Z., Wang, H., "Particle size distribution of nascent soot in lightly and heavily sooting premixed ethylene flames", *Combust. Flame* 165: 177-187 (2016).

[10] Camacho, J., Singh, A.V., Wang, W., Shan, R., Yapp, E.K.Y., Chen, D., Kraft, M., Wang, H., "Soot particle size distributions in premixed stretch-stabilized flat ethylene–oxygen–argon flames", *Proc. Comb. Inst.* 36: 1001-1009 (2017).

[11] Alderliesten, M., "Mean Particle Diameters. Part VIII. Computer program to decompose mixtures of (truncated) lognormal particle size distributions using differential evolution to generate starting values for nonlinear least squares", *Part. Part. Syst. Charact.* 33: 675-697 (2016).

[12] Herdan, G., Smith, M.L., Hardwick, W.H., Connor, P., *Small particle statistics: an account of statistical methods for the investigation of finely divided materials,* Butterworths, London, 1960.

[13] Price, K.V., Storn, R.M., Lampinen, J.A., *Differential Evolution, A Practical Approach to Global Optimization*, Springer-Verlag, 2005.

[14] DE homepage, http://www1.icsi.berkeley.edu/~storn/code.html (accessed Feb 2018).

[15] Mishra, S.K. (2007), "NLINLS: a Differential Evolution based nonlinear least squares Fortran77 program", http://mpra.ub.uni-muenchen.de/4949/.

[16] Tang, Q., Cai, R., You, X., Jiang, J., "Nascent soot particle size distributions down to 1 nm from a laminar premixed burner-stabilized stagnation ethylene flame", *Proc. Comb. Inst.* 36: 993-1000 (2017).

HOW TO VALIDATE NUMERICAL RESULTS ON PRIMARY PARTICLE DIAMETER TO EXPERIMENTAL DATA FROM LAMINAR SOOTING FLAMES

A. Bodor*, A. Cuoci*, B. Franzelli**
agneslivia.bodor@polimi.it
* Department of Chemistry, Materials, and Chemical Eng., Politecnico di Milano (Italy)
** Laboratoire EM2C CNRS, CentraleSupélec, Université Paris-Saclay, Chatenay-Malabry (France)

Abstract
Combustion generated soot particles have harmful effects on human health and our environment. An important aspect is to accurately determine the surface area of the particle population, which can be estimated from the particle size distribution (PSD) and morphology. Experimental investigations showed that large particles are aggregates constituted of several small primary particles [1]. Therefore, the determination of the primary particle size distribution (PPSD) is essential for the characterization of soot population.
On the one side, sectional methods can be used to numerically predict the particle population of sooting flames. However, most of models assumes that large particles are spherical for all sections [2] or aggregates constituted of primary particles of identical size for all sections [3-5]. These strong assumptions can affect the results' quality and the validity of the models themselves. On the other side, Time Resolved Laser Induced Incandescence (TiRe-LII) is a powerful, non-intrusive experimental method, which exploits the fact that the temporal decay of the LII signal is related to the primary particle diameter d_p. Information on the PPSD can then be derived once the PPSD shape is presumed [6]. The general approach is to assume log-normal distribution, but Transmission Electron Microscopy measurements showed that this assumption may be not always valid [7].
In this context, the comparison of numerical results on the PPSD with experiments is extremely complex due to the strong assumptions underlying the numerical models and the fact that TiRE-LII technique does not measure directly the PPSD. In this work, we propose a new way to compare numerical to experimental data on PPSD. First, we improved our existing CFD code to obtain the mean size of the primary particles for each section, based on what proposed in [4]. Second, the TiRe-LII signal is reconstructed from the numerical PPSD and compared directly to the measured signal [8] to avoid any potential errors due to a presumed PPSD shape. This approach is applied to the investigation of an ethylene laminar-coflow

diffusion flame [9], which is a target of the ISF workshop [10], and potential sources of errors are discussed.

Improving the sectional model: the primary particle transport equation

The discrete sectional approach of Saggese et al. [3] is considered here. Gas phase is described with 197 gaseous species. The solid phase is described by 20 mass sections (BIN) with 3 H/C subsections for small particles (from BIN_5 to BIN_{12}) and 2 H/C subsections for big particles (from BIN_{13} to BIN_{20}). In the original model, small particles are considered by construction as spherical, whereas big particles are supposed to be aggregates whose primary particles size is identical for all sections and equal to the last spherical particle (~10 nm diameter) [3, 11]. In the improved approach, called transport equation (TE) model in the following, the particle morphology is not prescribed *a priori* for a given BIN, but it is obtained from the transport equation for the primary particle number of each section [14]:

$$\frac{\partial}{\partial t}(\rho\rho_{PBi}) + \nabla(\rho\rho_{PBi}\boldsymbol{v}) = -\nabla(\rho\rho_{PBi}\boldsymbol{V_i}) + \sum_r \Omega_{r,i}(Y_0, \dots, Y_{12}, \rho_{PB0}, \dots, \rho_{PB12}) \qquad (1)$$

where ρ is the density, ρ_{PBi} is the primary particle density of BIN_i type, $\boldsymbol{v}$ is the velocity, $\boldsymbol{V_i}$ is the diffusion velocity of BIN_i [12] and $\Omega_{r,i}$ is the BIN_i type primary particle source term of reaction r, Y_i is the species mass fraction of BIN_j. Fick's diffusion was neglected as previous studies showed that only thermal diffusion plays a significant role for soot particles. It should be noticed that in the TE model, the biggest possible d_p value is 64 nm, i.e. the diameter of a spherical particle belonging to BIN_{20}.

The effect of particle collision on d_p is described in the TE approach by the model of Lahaye et al. [13]. Small particles coalescence and form spherical particles, whereas a pure aggregation occurs between big particles. The collision of a small with a big particle leads to the coalescence of the first one on the second one. In practice, primary particle growth of big particles occurs only through surface growth processes (additional mass is uniformly distributed among the primary particles) or coalescence with small spherical particles. For a general reaction:

$$\sum_{i=12}^{20} \nu_i BIN_i + \sum_{s=1}^{N_s} \nu_s X_s => \sum_{i=12}^{20} \mu_i BIN_i + \sum_{s=1}^{N_s} \mu_s X_s \qquad (2)$$

the source term for primary particles based on the above considerations will be:

$$\Omega_{r,i} = \left(\frac{\mu_i M_i}{\sum_{k=12}^{20} \mu_k M_k} \sum_{k=12}^{20} \frac{\nu_k M_k \rho_{PBk}}{Y_k} - \frac{\nu_i M_i \rho_{PBi}}{Y_i} \right) \cdot R_r \qquad (3)$$

where ν_i is the stoichiometric coefficient for reaction r, X_s are the non-aggregate species s, N_s is the number of non-aggregate species, M_i is the molecular mass of BIN_i and R_r is the reaction rate of reaction r. It should be noticed that, at this stage, the TE model is used as a post-processing reconstruction method to obtain the mean primary particles size for each BIN and, consequently, the PPSD.

LII signal reconstruction method

The LII signals reconstruction is based on the relations derived by Hofman et al. [14], where the contribution by a particle with d_p diameter to LII signal is given by:

$$S_{LII} = 2\pi^2 hc^2 d_p^2 \int_{\lambda_1}^{\lambda_2} \frac{\Omega(\lambda)\varepsilon(\lambda)}{\lambda^5[exp(hc/\lambda k_B T_p)-1]} d\lambda \quad (4)$$

where h is the Planck constant, Ω the spectral response function of the detection system, and ε the spectral emissivity of soot. The integral boundaries λ_1 and λ_2 are defined by the detection bandpass. Experimental related parameters were chosen based on reference measurements [8]. The particle temperature can be derived from the energy balance, whereas the particle mass based on the mass loss due to vaporization. The detailed expression of the energy terms can be found in [14].
The total LII signal is reconstructed by summing the LII contribution of each single primary particle for each section, calculated from the gaseous and solid fields obtained in our numerical simulation. Therefore, the aggregate shielding effect is here neglected.

Numerical setup

The numerical simulation reproduces the flame investigated with LII at EM2C [8] on the burned designed at Yale [9]. The flame is fed by an 80% ethylene - 20% nitrogen mixture, which is injected through an inner tube of diameter of 3.9 mm with 0.38 mm wall thickness. An air co-flow is injected through an external tube of 50 mm diameter. The bulk velocity of both inner and outer streams was set to 35 cm/s with parabolic and uniform velocity profiles, respectively. Temperature is set to the ambient value of 293 K and atmospheric pressure was prescribed.The simulation solves the usual conservation equations for mass, momentum, energy, and species with the laminarSMOKE framework [12], which has been extended with the TE post-processing tool to solve the primary particle number transport equation. The simulation was performed with an axisymmetric assumption on a 2D structured mesh, refined in the flame area. A second-order, centered spatial discretization scheme was adopted. The transport equations of species are solved through the operator-splitting approach.
BIN_5 to BIN_7 will not be considered in the reconstruction of soot volume fraction f_v, d_p and LII signals, since the smallest particles may be not captured by the experimental LII measurements due to sublimation effects [15].

Comparison of numerical and experimental results

Numerical results for the soot volume fraction are compared to experiments [8] in Figure 1a. The calculated and experimentally measured f_v are qualitatively similar, since higher values were detected in the wings of the flame. However, it should be noticed that results have been normalized by their maximum (1.2 ppm and 4.8 ppm for numerical and experimental results) and that the predicted soot region is shorter that the experimental one.

On Figure 1b the mean d_p derived from the experimental LII signal with a lognormal PPSD assumption [8] is compared to the numerical solutions. Three models are here considered: the original model, the TE approach, and a further post-processing approach where all particles are consider as spherical (SP). As expected, the original, TE and SP models predict the smallest, the intermediate and the biggest values of d_p, respectively. In particular, with the spherical assumption d_p reaches higher values than the other two models, especially in the post flame region where oxidation quickly removes small particles. The original model provides an almost constant d_p value everywhere. The TE and SP models greatly improve the qualitative agreement with the experiments: larger d_p values are observed on the wings. However, d_p values in the wings are still largely underestimated by simulations. This may have many causes: the underestimation of f_v can possibly affect the d_p prediction; the maximum predictable d_p value is smaller than the highest experimentally observed value; the experimental d_p value may be affected by the post-processing procedure.

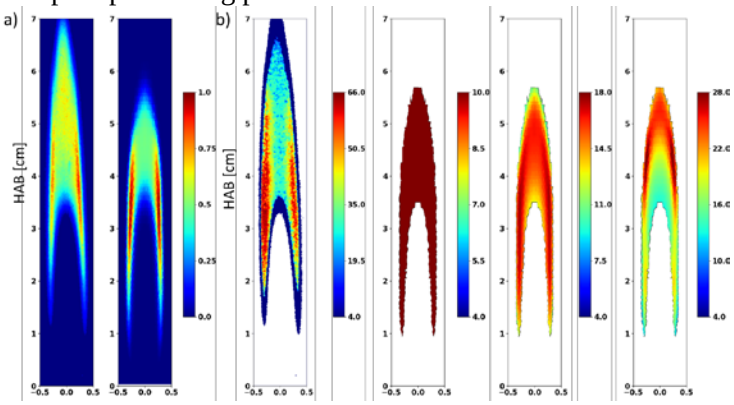

Figure 1. a) Experimental (left) and numerical (right) normalized soot volume fraction; b) Experimental (left), numerical (TE) (center) and numerical (Sp) (right) mean d_p [nm].

To clarify this last point, the experimentally captured and the numerically reconstructed LII signals at 6 different times are shown on Figure 2 normalized by the signal at 0 ns. The numerical LII signals have much faster decay until 50 ns, almost one order of magnitude faster decays are reached within this time compared to the experiment. This seems to indicate that the discrepancies on d_p are most probably due to the underprediction of large primary particle presence and/or an underestimation of their diameter size in the numerical simulations. In addition, a lower spatial inhomogeneity of d_p is observed in the simulations compared to experiments. The TE model predicts slower signal decay than the original model due to the presence of larger primary particles and less spatial uniformity due to the varying PPSD for big particles, which is in better agreement with the experimental observations. The better agreement of results from the SP model with experiments indicate that the presence of even larger particles would be required. The direct comparison on LII signals allows concluding that the discrepancies among

experiments and simulations observed in this case are not due to the use of a presumed PPSD shape for the TiRe-LII signal post-processing, but to some accuracy limits of the numerical model.

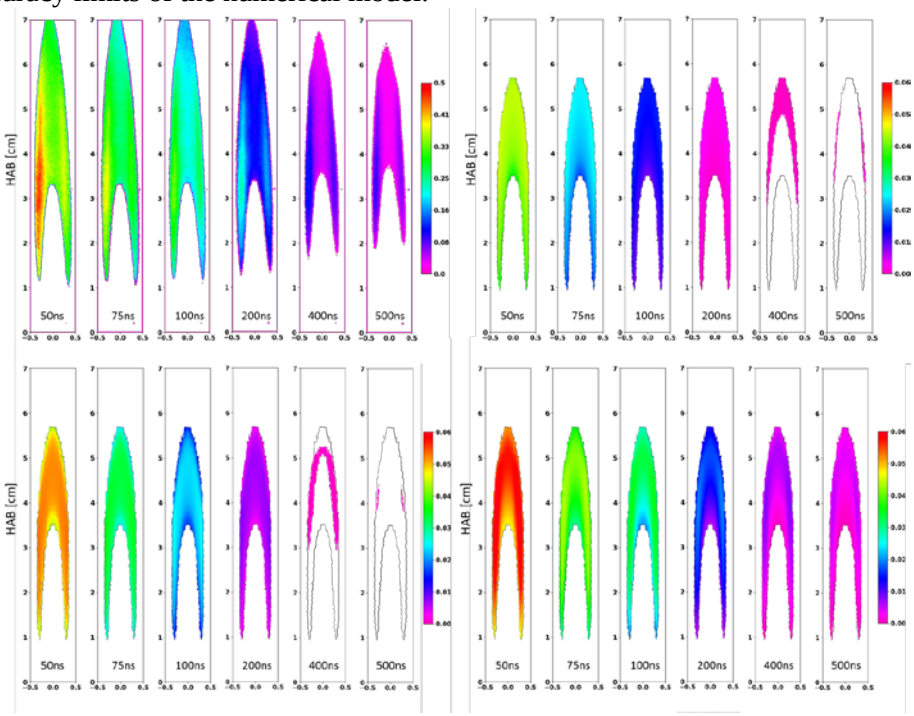

Figure 2. LII signal at six different delay times. Experiment data (top left) are compared to numerical calculations with the original model (top right), with the TE model (bottom left) and the SP approach (bottom right).

Conclusions

A new validation approach of numerically calculated primary particle size distribution with TiRe-LII experiments was presented and applied on an ethylene co-flow laminar flame. The numerical simulation used the sectional soot model with detailed gas and solid phase chemistry. The model was improved by introducing an additional transport equation for the primary particle density in each section. Results on d_p were qualitatively improved by the new model. LII decay signals were calculated based on numerical results from the original model, the improved one, and by assuming sphericity for all soot particles. Simulations were compared to the experimental LII signal. The simulated signals showed a much faster decay in the first 50 ns than the experiments and lower inhomogeneity in space. This implies that the predicted contribution of large particles to the particle population is not high enough relatively to the small ones and/or that the predicted largest particles are not big enough. The proposed approach to compare numerical and experimental data on PPSD seems a promising procedure for a pertinent validation of numerical data.

Acknowledgements
This project has received funding from the European Union's Horizon 2020 research and innovation programme under the Marie Sklodowska-Curie Grant Agreement No 643134.

References

[1] Sorensen, C.M., Feke, G.D., "The Morphology of Macroscopic Soot" *Aerosol Sci. Technol.* 25: 328–337 (1996)
[2] Blacha, T., Di Domenico, M., Gerlinger, P., Aigner, M.m "Soot predictions in premixed and non-premixed laminar flames using a sectional approach for PAHs and soot" *Combust. Flame* 159: 181–193 (2012)
[3] Saggese, C., et al. "Kinetic modeling of particle size distribution of soot in a premixed burner-stabilized stagnation ethylene flame" *Combust. Flame* 162: 3356–3369 (2015)
[4] Veshkini, A., "Understanding Soot Particle Growth Chemistry and Particle Sizing Using a Novel Soot Growth and Formation Model", PhD Thesis University of Toronto (2015)
[5] Rodrigues, P., Franzelli, B., Vicquelin, R., Gicquel, O., Darabiha, N., "Unsteady dynamics of PAH and soot particles in laminar counterflow diffusion flames" *Proc. Combust. Inst*. 36: 927–934 (2017)
[6] Daun, K.J., Stagg, B. J., Liu, F., Smallwood, G.J., Snelling, D.R. "Determining aerosol particle size distributions using time-resolved laser-induced incandescence" *Appl. Phys. B Lasers Opt.* 87: 363–372 (2007)
[7] Kempema, N.J., Long, M.B., "Combined optical and TEM investigations for a detailed characterization of soot aggregate properties in a laminar coflow diffusion flame" *Combust. Flame* 164: 373–385 (2016)
[8] Franzelli, B., et al. "Multi-diagnostic soot measurements in a laminar diffusion flame to assess the ISF database consistency" *Proc. Combust. Inst.*, submitted (2018)
[9] Smooke, M.D., et al. "Investigation of the transition from lightly sooting towards heavily sooting co-flow ethylene diffusion flames" *Combust. Theory Model.* 8: 593–606 (2004)
[10] http://www.adelaide.edu.au/cet/isfworkshop/, updated in 2016
[11] Saggese, C., "Detailed Kinetic Modeling of Soot Formation in Combustion Processes" PhD Thesis, Politecnico di Milano (2014)
[12] Cuoci, A., Frassoldati, A., Faravelli, T., Ranzi, E., "Numerical modeling of laminar flames with detailed kinetics based on the operator-splitting method" *Energy and Fuels* 27: 7730–7753 (2013)
[13] Lahaye, J., "Particulate carbon from gas phase" Carbon, 30: 309–314 (1992)
[14] Hofmann, M., Kock, B., Schulz, C., http://web.liisim.com/, updated in 2007
[15] Cenker, E., Bruneaux, G., Dreier, T., Schulz, C., "Determination of small soot particles in the presence of large ones from time-resolved laser-induced incandescence" *Appl. Phys. B Lasers Opt.* 118: 169–183 (2015)

SOOT MODELING OF ETHYLENE COUNTERFLOW DIFFUSION FLAMES

W. Pejpichestakul[1,2], A. Frassoldati[1], A. Parente[2], T. Faravelli[1*]
tiziano.faravelli@polimi.it
[1]Politecnico di Milano – Dip. CMIC – p.zza L. Da Vinci, 32 – 20133 Milano – Italy
[2]Université Libre de Bruxelles, Ecole Polytechnique de Bruxelles, Aero-Thermo-Mechanical Laboratory, Avenue F.D Roosevelt, 50 - CP 165/41, 1050 Brussels, Belgium

Abstract
Combustion-generated nanoparticles cause detrimental effects to not only health and environment but also combustion efficiency. A detailed kinetic mechanism employing a discrete sectional model is validated using experimental data obtained in laminar counterflow diffusion flames of ethylene/oxygen/nitrogen (Hwang and Chung, 2001). Two configurations, named Soot formation (SF) and soot formation/oxidation (SFO) flames, are modeled using one-dimensional simulation. Radiative heat losses reduce the maximum flame temperature in the range of 20-60 K and therefore reduce soot volume fraction by ~10%. The model predictions accounting for the radiation effects are quite satisfactory. In SFO flames, the difference of maximum soot volume fraction between the experiment and model is less than 30%. In SF flames, the most considerable discrepancy is observed at the most sooting flame ($x_{O,o}$ = 0.28) in which the model underpredicts the soot volume fraction by a factor of two. In these conditions, the soot particles are not able to reach the stagnation plane as observed in the experiments. This suggests that transport properties of soot particles may require further attention. The effect of soot oxidation shows that the model neglecting oxidation of soot significantly increases soot volume fraction in SFO flames by two folds while SF flames are only marginally affected. Also, the absence of soot oxidation leads to the presence of soot particles in the oxidizer zone where they are not observed experimentally. The successful predictions using the soot model including soot oxidation in SFO flames demonstrate that the reaction rates of the processes involved in soot growth and oxidation are appropriate.

Introduction
Combustion-generated nanoparticles are well-known for their adverse effects on health and environment. In practical applications, the presence of soot particles leads the radiative heat losses and consequently lowers the combustion efficiency [1]. Polycyclic aromatic hydrocarbons (PAHs) are widely accepted as soot precursors, and acetylene plays an essential role in the soot growth processes through the sequential HACA (hydrogen abstraction and acetylene addition) mechanism [2]. In addition, condensation of PAHs and gaseous species on soot particle contributes the soot growth. On the contrary, the oxidations of particles

compete with the soot growth. The oxidation processes include the burnout at the surface of particles mainly by OH radical, and the oxidation-induced fragmentation which is the internal burning induced by the penetration of oxygen molecules into particles [3].

Particulate formation and oxidation have been extensively studied in the past two decades particularly in premixed planar laminar flames. In practical combustors, however, the soot evolution becomes extremely complex due to the interactions between chemistry and turbulence flow environment. To achieve a better understanding of soot formation in turbulent flames, laminar counterflow diffusion flame configuration is a good candidate because of its well-defined boundary conditions that can simplify as one-dimensional simulations and its relevance to flamelet model which is often adopted to model practical industrial scale applications [4].

In this work, detailed kinetic modeling of soot formation in atmospheric laminar counterflow diffusion ethylene/oxygen/nitrogen flames has been performed and compared with the experimental studies by Hwang and Chung (2001) [5]. The validation includes soot formation (SF) and soot formation/oxidation (SFO) flames. The inlet velocities are 19.5 cm/s. For SF flames, the fuel inlet was pure ethylene while oxygen mole fraction of the oxidizer inlet ($x_{O,o}$) was varied from 0.2 to 0.28. For SFO flames, the oxidizer inlet is 90% oxygen in nitrogen while the mole fraction of oxygen in the fuel inlet ($x_{F,o}$) was varied from 0.23 to 0.28.

Model Description and Numerical Simulations

The high temperature gas-phase mechanism consists of 300 species and over 8000 reactions. It implements a C_0-C_3 core mechanism obtained from the H_2/O_2 and C_1/C_2 subsets from Metcalfe et al. [6], C_3 from Burke et al. [7], and heavier fuels from Ranzi et al. [8]. The model describes the pyrolysis and oxidation of wide range hydrocarbon fuels and includes the formation of PAHs up to pyrene. The thermochemical properties were obtained from the ATcT database of Rusic [9] or Burcat's database [10]. For some species that were not available in the aforementioned databases, the thermochemical properties were adopted from group additivity method [11].

A soot model based on a discrete sectional approach is coupled to the gas-phase mechanism to model the evolution from gas-phase to solid particles. The model includes the discretization large PAH and soot particles into 20 sections, considered as lumped-pseudo species called "BINs", with a constant discretization spacing factor of two in terms of carbon atoms. Three hydrogenation levels are considered for each BIN as sub-sections, labeled "A", "B" and "C", which varies from 0.8 for BIN1A to 0.05 for BIN25C. The complete soot mechanism used in this work (POLIMI1800s) has been extensively validated against laminar premixed flames of different fuels in wide range operating conditions which is discussed elsewhere [12]. The successive kinetic mechanism consists of approximately 400

species and 25,000 reactions. Further details of the soot kinetics model are available in [13,14].

All numerical simulations were performed using OpenSMOKE++ suite program by Cuoci et al. [15]. Laminar counterflow diffusion flames 1-D simulations were performed using the mixture-average diffusion coefficient and including thermal diffusion (Soret effect) in species transport equations. Radiative heat losses were accounted using optically thin approximation [16,17]. Solution gradient and curvature coefficients of 0.05 and 0.5 were assigned to ensure the smoothness of the calculated profiles.

Results and Discussions

Figure 1 shows the effects of radiative heat losses on the predicted flame temperatures. The yellow shaded areas represent the sooting region of the two flames. As expected, the radiative heat losses reduce the maximum temperature of all flames in the range of 25-60 K.

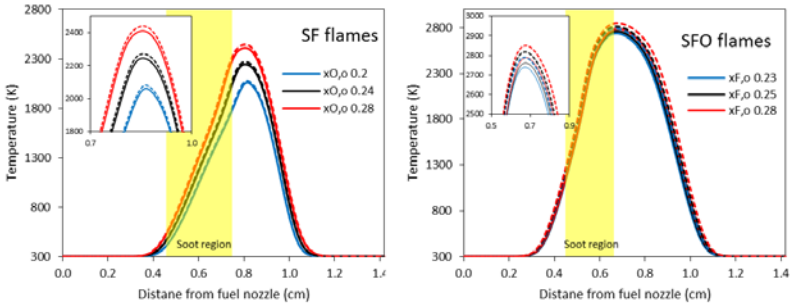

Figure 1. Calculated temperature profiles of SF flames (left panel) and SFO flames (right panel). Dashed lines: model neglecting radiative heat losses. Solid lines: model including radiative heat losses.

Figure 2 shows the comparison of the soot volume fractions profiles between experimental data and model predictions. The model predictions are obtained both including and the neglecting radiative heat losses. The lower temperature reduces soot formation in all flames by approximately 10%. However, the model predictions including radiative heat losses still provide good agreement with the experimental data. It can reproduce the qualitative trends of soot volume fraction peaks that are slightly shifted towards oxidizer zone with the increased oxygen content. Specifically, the model predictions of SFO flames are quite satisfactory, with the discrepancy in maximum soot volume fraction between the model and measurement of less than 30%. The largest differences are observed for SF flames in particular the xO,o = 0.28 flame, the most sooting flame, where the model underpredicts the soot volume fraction by less than a factor of two. In SF flames, the model is not able to capture the particle stagnation plane location well which is resulting from the convection/diffusion of particles towards the stagnation

plane. This suggests the transport properties of soot particles should be investigated further, in particular thermophoresis, which plays a major role in these conditions [18].

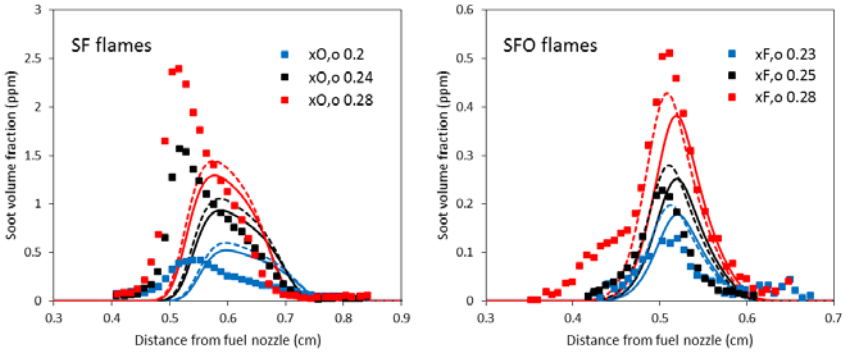

Figure 2. Comparison of soot volume fraction profiles between experimental data (symbol) and model (lines) of SF flames (left panel) and SFO flames (right panel). Dashed lines: model neglecting radiative heat losses. Solid lines: model including radiative heat losses.

To highlight the effect of soot oxidation, Figure 3 shows the effect of soot oxidation on the predicted soot volume fraction in comparison with the measurements. As expected, in SF flames, soot oxidation has marginal effects, since soot particles are pushed away from the sooting region of the flames and are convected towards fuel region. On the contrary, in SFO flames, the removal of particle oxidation increases soot volume fraction drastically by approximately 50%. Additionally, the soot particles are able to form and diffuse towards the oxidizing zone where soot particles are not observed experimentally. The successful predictions using the complete soot model in SFO flames demonstrate that the reaction rates of the processes involved in soot growth and oxidation are appropriate.

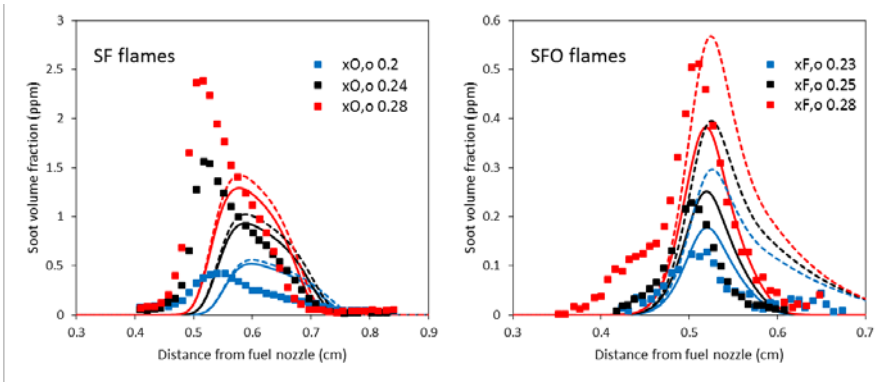

Figure 3. Comparison of soot volume fraction profiles between experimental data

(symbol) and model (lines) of SF flames (left panel) and SFO flames (right panel). Dashed lines: model neglecting soot oxidation. Solid lines: model including soot oxidation.

Conclusions

This work contains the validation of a detailed kinetic mechanism employing a discrete sectional soot model using experimental results from two different laminar counterflow diffusion ethylene flames configurations. Soot formation (SF) and soot formation/oxidation (SFO) flames at different oxygen content have been analyzed. All numerical simulations are performed using one-dimensional simulations considering radiative heat losses.

The inclusion of radiative heat losses lowers the maximum temperature by 25-60 K. The reduction of temperature leads to a lower soot volume fractions in all flames by 10%. Model predictions accounting for radiative heat losses provide good agreement with the experimental data in particular for SFO flames. The difference of maximum soot volume fraction between the experiment and model is less than 30%. In SF flames, the largest discrepancy in soot formation is observed at the most sooting flame conditions ($x_{O,o} = 0.28$) in which the model underpredicts the soot volume fraction by a factor of two. The underprediction of soot volume fraction is evident close to the stagnation plane. These discrepancies show that that the convection and diffusion of particles away from the flame is insufficient. This suggests that transport properties and particularly thermophoresis of soot particles may require further attention.

The effect of soot oxidation is also demonstrated. The model neglecting oxidation of soot significantly increases total soot volume fraction in SFO flames by two folds. On the contrary, SF flames are only slightly affected by soot oxidation. In addition, the absence of soot oxidation leads to the presence of soot particles in the oxidizer zone of SFO flames, where they are not observed experimentally. The successful predictions using the soot model including soot oxidation in SFO flames demonstrate that the reaction rates adopted in this model to describe the processes involved in soot growth and oxidation are appropriate.

Acknowledgement

This project has received funding from the European Union's Horizon 2020 research and innovation programme under the Marie Sklodowska-Curie grant agreement No 643134.

References

[1] Bockhorn, H., D'Anna, A., Sarofim, A.F., Wang, H., "Combustion generated fine carbonaceous particles", 2007

[2] Wang, H., Frenklach, M., "A detailed kinetic modeling study of aromatics formation, growth and oxidation in laminar premixed ethylene and acetylene flames, Combust. Flame". 2180: 173–221 (1997)

[3] Ghiassi, H., Toth, P., Jaramillo, I.C., Lighty, J.S., “Soot oxidation-induced fragmentation: Part 1: The relationship between soot nanostructure and oxidation-induced fragmentation”, Combust. Flame. 163: 179–187 (2016)

[4] Chrigui, M., Gounder, J., Sadiki, A., Masri, A.R., Janicka, J., “Partially premixed reacting acetone spray using LES and FGM tabulated chemistry”, Combust. Flame. 159: 2718–2741 (2012)

[5] Hwang, J.Y., Chung, S.H., “Growth of soot particles in counterflow diffusion flames of ethylene”, Combust. Flame. 125: 752–762 (2001)

[6] Metcalfe, W.K., Burke, S.M., Ahmed, S.S., Curran, H.J., "A hierarchical and comparative kinetic modeling study of C1- C2hydrocarbon and oxygenated fuels”, Int. J. Chem. Kinet. 45: 638–675 (2013)

[7] Burke, S.M., Burke, U., Mc Donagh, R., & Curran, H.J., “An experimental and modeling study of propene oxidation. Part 2: Ignition delay time and flame speed measurements”, Combust. Flame. 162: 296–314 (2015)

[8] Ranzi, E., Frassoldati, A., Grana, R., Cuoci, A., Faravelli, T., Kelley, A.P., Law, C.K., “Hierarchical and comparative kinetic modeling of laminar flame speeds of hydrocarbon and oxygenated fuels”, Prog. Energy Combust. Sci. 38: 468–501 (2012)

[9] Ruscic, B., “Active Thermochemical Tables: Sequential Bond Dissociation Enthalpies of Methane, Ethane, and Methanol and the Related Thermochemistry”, J. Phys. Chem. A. 119: 7810–7837 (2015)

[10] Goos, E., Burcat, A., Ruscic, B., BurcatThermo, (2016). http://garfield.chem.elte.hu/Burcat/burcat.html (accessed May 1, 2017).

[11] Benson, S. W., “Thermochemical Kinetics”, Wiley, New York, 1976.

[12] Pejpichestakul, W., Ranzi, E., Pelucchi, M., Frassoldati, A., Cuoci, A., Parente, A., Faravelli, T., “Soot effect on intermediate pahs concentration in premixed laminar flames”, Proc. Combust. Inst. Submitted (2018)

[13] Saggese, C., Ferrario, S., Camacho, J., Cuoci, A., Frassoldati, A., Ranzi, E., Wang, H., Faravelli, T., “Kinetic modeling of particle size distribution of soot in a premixed burner-stabilized stagnation ethylene flame”, Combust. Flame. 162: 3356–3369 (2015)

[14] Pejpichetsakul, W., Frassoldati, A., Parente, A., Faravelli, T., “Kinetic modeling of soot formation in premixed burner-stabilized stagnation ethylene flames at heavily sooting condition”, Tenth Mediterr. Combust. Symp., Naples, Italy, 2017.

[15] Cuoci, A., Frassoldati, A., Faravelli, T., Ranzi, E., “OpenSMOKE++: An object-oriented framework for the numerical modeling of reactive systems with detailed kinetic mechanisms”, Comput. Phys. Commun. 192: 237–264 (2015)

[16] Grosshandler, W.L., “RADCAL: A Narrow-band Model for Radiation Calculations in a Combustion Environment”, NIST Tech. Note 1402. (1993)

[17] Sazhin, S., “An approximation for the absorption coefficient of soot in a

radiating gas", Fluent Eur. Ltd. (1994)

[18] Stagni, A., Cuoci, A., Frassoldati, A., Ranzi, E., Faravelli, T., "Numerical investigation of soot formation from microgravity droplet combustion using heterogeneous chemistry", Combust. Flame. 189: 393–406 (2018)

FLAME AEROSOL SYNTHESIS OF TIO_2 NANOPARTICLE COATINGS WITH ADVANCED ANTIBACTERIAL AND HYDROPHILIC PROPERTIES

G. De Falco*, C. Almini*, R. Ciardiello*, M. Commodo, P. Del Gaudio***, P. Minutolo**, A. Porta***, A. D'Anna***
gianluigi.defalco@unina.it
* Dipartimento di Ingegneria Chimica, dei Materiali e della Produzione Industriale - Università degli Studi di Napoli Federico II, P.le Tecchio 80, 80125, Napoli, Italy
** Istituto di Ricerche sulla Combustione - CNR, P.le Tecchio 80, 80125, Napoli, Italy
*** Dipartimento di Farmacia (DIFARMA) - Università di Salerno, Via Giovanni Paolo II 132, 84084 Fisciano (Salerno), Italy

Abstract
In this work, the production of thin coating layers of TiO_2 nanoparticles by aerosol flame synthesis and direct thermophoretic deposition is reported. Three different flame reactor configurations were designed in order to study the effect of particle size on the performances of coating layers. The wetting behavior was investigated by water contact angle analysis, showing that titania coating layers are characterized by a high photoinduced hydrophilicity. Measurements of the inhibition of *Staphylococcus aureus* biofilm formation revealed a high antibacterial activity from TiO_2 nanoparticle films. Hydrophilic character and bactericidal effect are found to be mainly dependent on the dimension of primary particles composing the coating layers. The optimal synthesis conditions have been identified to produce a self-cleaning and self-disinfecting coating layer material, with a nearly superhydrophilicity and a high antibacterial activity, both activated by normal ordinary solar light radiation in standard room illumination conditions.

Introduction
Nanomaterials and their assemblage into functional devices and coatings are currently playing an increasing role in several fields, spanning from energy production and environment to biomedicine and biotechnology [1-2]. Flame synthesis of nanomaterials is characterized by a proven scalability, a fast processing time and an ease of manufacturing and collection [3]. In addition, nanostructured films and coatings of flame synthesized nanoparticles are produced in a single-step process by placing a cold substrate downstream the flame synthesis burner, on which nanoparticles are deposited by thermophoresis [4]. A relevant field of application of functional nanoparticle coatings is biomedicine. Nanomaterials characterized by an antimicrobial activity can be used as coatings with the aim to fight the proliferation of potentially pathogenic microorganisms as fungi and bacteria, since they possess the capability to inhibit microbial growth [5].

Among several antimicrobial nano-crystalline materials, titanium dioxide (TiO_2, titania) is the most harmless to environment and human health [6].
In this work, thin coatings of titania nanoparticles synthesized in flame were produced from a single step procedure by direct thermophoretic deposition on surfaces. Particle and coating properties were characterized using Differential Mobility Analyzer (DMA) and Raman spectroscopy. In addition, the hydrophilic/hydrophobic characteristics of the coatings were also investigated. Inhibition of biofilm formation was evaluated against Staphylococcus aureus bacterium as a function of nanoparticle size and coating morphology.

Experimental
TiO_2 nanoparticles were synthesized in an Aerosol Flame Synthesis (AFS) system, coupled to a thermophoretic deposition device made of a rotating circular aluminum disk. A detailed description of both the AFS system and the deposition system, as well as a scheme of the experimental set-up, can be found in previous works [7]. The flame reactor was obtained from premixed ethylene/air laminar flame doped with a solution of titanium tetraisopropoxide (TTIP, Aldrich, 97%) dissolved into ethanol (ACS reagent, ≥99.5%). In order to study the effect of particle dimension and coating morphology on the antimicrobial performances, three different flame reactor configurations, reported in Table 1, were investigated. Coatings were obtained using a disk rotating speed of 600 rpm, positioned at different height above the burner (HAB), corresponding to different particle residence times in the flame reactor. Circular substrates (diameter=16 mm, height=3 mm) made of aluminum alloy AA2024 were used.

Table 1. Summary of flame conditions.

Flame	TTIP, % mol	Φ	Disk HAB, cm
A	0.030	0.89	11
B	0.030	0.89	16
C	0.059	0.94	11

A dimensional characterization of the synthesized nanoparticles was made on-line by measuring number particle size distributions (PSDs) using a TapCon 3/150 Wien Type Differential Mobility Analyzer (DMA). Raman spectra were acquired using a Horiba XploRA Raman Microscope System (excitation wavelength λ=532 nm). The hydrophilic/hydrophobic properties were investigated by static contact angle measurements, following a previously described protocol [8].
Antimicrobial activity was investigated by testing the inhibition of biofilm formation of a Gram positive bacterium, *Staphylococcus aureus* (ATCC 6538), under ordinary light radiation in standard room illumination conditions. Bacteria cells (108 cellule/mL) were suspended in Mueller-Hinton Broth (MHB), aliquoted in a 12-wells plate (1.5 ml/well) containing the aluminum substrates and incubated

overnight at 37 °C. Aluminum substrates were moved in a new 12-well plate and washed three times with phosphate-buffered saline (PBS) to remove non adherent cells. SEM images of the samples were then acquired using a Carl Zeiss EVO MA 10 microscope with a secondary electron detector (Carl Zeiss SMT Ltd., Cambridge, UK). Finally, the biofilm mass was quantified by counting the number of bacterial colonies from SEM images using the image processing software ImageJ®.

Results and Discussion

The number distributions of particle diameter measured by DMA are shown in Fig. 1 (left panel), together with their best fit obtained by a lognormal distribution function or a sum of two lognormal distributions. From the fitting procedure, the mean particle diameter was found to increase from $<D_p>$ = 2.6 nm for Flame A, to $<D_p>$ = 3.1 nm for Flame B, due to the increase in particle residence time in the flames. On the other hand, the increase of both TTIP concentration and particle residence time in Flame C condition resulted in a bi-modal PSD with the first mode characterized by $<D_p>$ = 2.4 nm, while the second mode is characterized by $<D_p>$ = 10.5 nm. Fig. 1 (right panel) reports the normalized size distributions in mass. It can be assumed that the prevailing mass contribution to the TiO_2 coatings on the substrates is given by particles with a mean dimension of 4.5 nm (Flame A), 7 nm (Flame B) and 18 nm (Flame C).

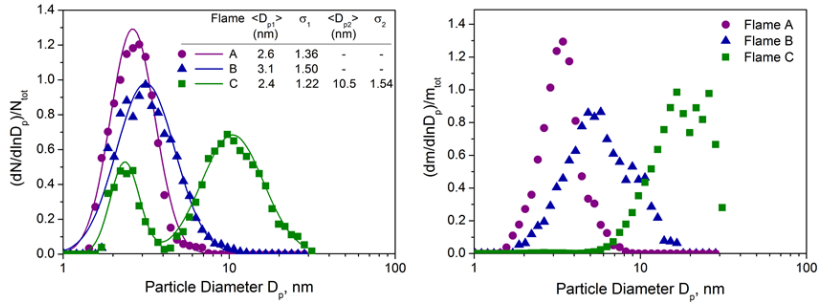

Figure 1. Left panel: Normalized number PSDs, $(dN/dlnDp)/N_{tot}$; symbols are experimental DMA data, lines are best lognormal fits of data. Right panel: Normalized size distributions in mass, $(dm/dlnDp)/m_{tot}$.

The phase composition of as-deposited coating layers was determined using Raman spectroscopy. The acquired spectra are presented in Fig. 2, showing the presence of five Raman scattering peaks, corresponding to the Raman bands assigned to the allowed modes of anatase phase TiO_2 [9], thus confirming that coatings were made of pure anatase particles. In this study, flame reactors were operated in fuel-lean conditions in order to promote the formation of anatase (the most photoactive phase of titania), which is favored in oxygen-rich environments [10].

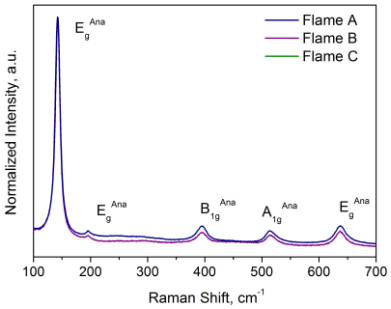

Figure 2. Raman spectra of TiO_2 nanoparticle coating layers.

The wettability of the coatings was investigated by water contact angle analysis and the results are reported in Fig. 3. Measurements performed under ordinary light radiation in standard room illumination conditions indicate that all the three coating layers were able to decrease the contact angle with respect to the bare aluminum substrate (62±3°). Particularly, the coatings produced in Flame A and Flame B possess a nearly super-hydrophilic behavior, with θ of about 10±3° and 10±3° respectively, while the angle measured for Flame C (33±3°) is larger. The high hydrophilicity of TiO_2 thin films has been demonstrated to be mainly caused by a photoinduced process [11]. This was confirmed by measuring the contact angles on deactivated TiO_2 samples, obtained by placing for 70 hours the coated substrates in the dark (Fig. 3, red bars). The values of θ without UV-visible radiation increased up to about 50° for all the samples.

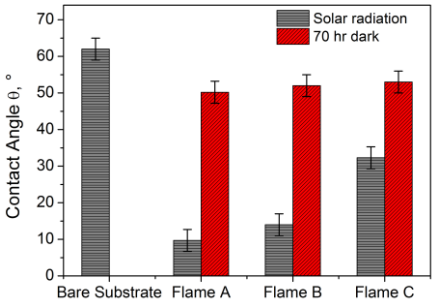

Figure 3. Water contact angles measured under ordinary room light (gray bars) and after 70 hours of dark storage (red bars).

Antimicrobial activity of nano-TiO_2 layers was characterized by evaluating the extent of *Staphylococcus aureus* biofilm formation by SEM analysis of the samples exposed to bacteria colonies. Obtained SEM images are reported in Fig. 4. The bare aluminum substrate, which represents the positive control, showed the presence of a stable and mature biofilm of *S. aureus* cells. On the other hand, it is possible to observe a clear decrease of the number of adherent *S. aureus* cells on

TiO_2-coated substrates. All the coating layers are characterized by a remarkable antibacterial activity under ordinary room light, which is higher for Flame B and Flame C coatings with respect to Flame A coating.

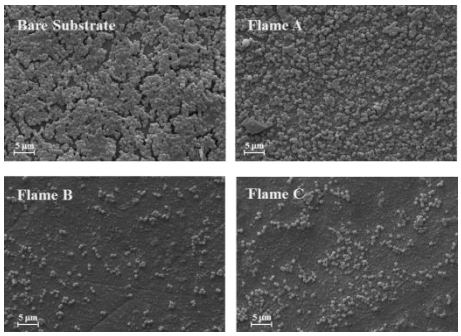

Figure 4. SEM microphotographs of *Staphylococcus aureus* biofilm on uncoated aluminum substrates and TiO_2 coated aluminum substrates.

From SEM images, the highest efficacy against *S. aureus* biofilm was measured on Flame B and Flame C coating layers, which were able to inhibit 82% and 80% of biofilm formation respectively, while *S. aureus* inhibition on Flame A coating was measured to be about 54%. Those results are reported in terms of percentage of biofilm formation relative to the positive control, i.e., the bare aluminum substrate, on which 100% of bacterium biofilm is formed. The measured trend of the antimicrobial activity is likely to be related to the size of particles composing the coating layers, suggesting the existence of an optimal size range for the maximum antibacterial efficiency [12]. However, further work is needed to isolate the effect of primary particle size from the effect of film properties on both hydrophilicity behavior and antimicrobial activity in our coating layers.

Conclusions

The use of a highly controllable and tunable technique for the production of a nanostructured TiO_2 coating film on aluminum substrates has been reported. This method, based on the combination of aerosol flame synthesis and direct termophoretic deposition, provides a fine control over particle size and crystalline phase, as well as film morphology. Nano-titania layers showed a high hydrophilic character and high antimicrobial activity against *Staphylococcus aureus* biofilm formation under ordinary light radiation in standard room illumination conditions. Both hydrophilicity and antimicrobial activity have been seen to depend on the dimension of primary particles composing the coating layers. Flame B coating layers possess the highest bactericidal activity, together with an almost superhydrophilic character, both photoactivated even under ordinary light radiation in standard room illumination conditions. The combination of such properties, taking place simultaneously on the same surface, widen the application as an

excellent self-cleaning and self-disinfecting coating materials for the sanitization of environmentally contaminated surfaces in indoor and outdoor buildings [13].

References

[1] S. Li, Y. Ren, P. Biswas, S.D. Tse, Flame aerosol synthesis of nanostructured materials and functional devices: Processing, modeling, and diagnostics, *Prog. Energy Combust. Sci.* 55 (2016) 1-59.

[2] W.Y. Teoh, R. Amal, L. Mädler, Flame spray pyrolysis: An enabling technology for nanoparticles design and fabrication, *Nanoscale* 2 (2010) 1324–1347.

[3] P. Roth, Particle synthesis in flames, *Proc. Combust. Inst.* 31 (2007) 1773–1788.

[4] L. Mädler, A. Roessler, S. E. Pratsinis, T. Sahm, A. Gurlo, N. Barsan, U. Weimar, Direct formation of highly porous gas-sensing films by in situ thermophoretic deposition of flame-made Pt/SnO_2 nanoparticles, *Sens. Actuators B Chem.* 114 (2006) 283-295.

[5] J.T. Seil, T.J. Webster, Antimicrobial applications of nanotechnology: methods and literature, *Int. J. Nanomedicine* 7 (2012) 2767–2781.

[6] C. McCracken, P.K. Dutta, W. J. Waldman, Critical assessment of toxicological effects of ingested nanoparticles, *Environ. Sci.: Nano* 3 (2016) 256–282.

[7] G. De Falco, A. Porta, A.M. Petrone, P. Del Gaudio, A. El Hassanin, M. Commodo, P. Minutolo, A. Squillace, A. D'Anna, *Environ. Sci.: Nano* 4 (2017) 1095-1107.

[8] M. Commodo, G. De Falco, R. Larciprete, A. D'Anna, P. Minutolo, On the hydrophilic/hydrophobic character of carbonaceous nanoparticles formed in laminar premixed flames, *Exp. Therm. Fluid. Sci.* 73 (2015) 56-63.

[9] A.G. Ilie, M. Scarisoareanu, I. Morjan, E. Dutu, M. Badiceanu, I. Mihailescu, Principal component analysis of Raman spectra for TiO2 nanoparticle characterization, *Appl. Surf. Sci.* 417 (2017) 93-103.

[10] Y.K. Kho, W.Y. Teoh, L. Mädler, R. Amal, Dopant-free, polymorphic design of TiO2 nanocrystals by flame aerosol synthesis, *Chem. Eng. Sci.* 66 (2011) 2409-2416.

[11] Z. Zhang, C.-C. Wang, R. Zakaria, J.Y. Ying, Role of particle size in nanocrystalline TiO_2-based photocatalysts, *J. Phys. Chem. B* 102 (1998) 10871-10878.

[12] Z. Zhang, C.-C. Wang, R. Zakaria, J.Y. Ying, Role of particle size in nanocrystalline TiO_2-based photocatalysts, *J. Phys. Chem. B* 102 (1998) 10871-10878.

[13] B. Jalvo, M. Faraldos, A. Bahamonde, R. Rosa, Antimicrobial and antibiofilm efficacy of self-cleaning surfaces functionalized by TiO_2 photocatalytic nanoparticles against Staphylococcus aureus and Pseudomonas putida, *J. Hazard. Mater.* 340 (2017) 160-170.

THE IMPACT OF TEMPERATURE AND FLAME CHEMISTRY ON THE DEGRADATION OF METAL OXIDE NANOPARTICLES

N. Teuscher, W. Baumann, M. Hauser, J. Mahl, H.-R. Paur, D. Stapf
nadine.teuscher@kit.edu
Institute for Technical Chemistry, Karlsruhe Institute of Technology, 76344 Eggenstein-Leopoldshafen, Germany

Abstract
The behavior of CeO_2 nanoparticles at high temperatures is investigated experimentally. This is of importance for the design of combustion processes with the purpose of incineration of nanoparticle containing end-of-life products. For this purpose a McKenna burner and a tube furnace are used to distinguish between temperature and flame chemistry effects. Flame temperatures were measured via thermocouples and corrected for radiation losses. The particle size distribution of the Ceria nanoparticles was measured via mobility particle sizer. Key result is that by passing the flame front an additional nanoparticle peak is forming. This effect increases with increasing temperature. Nanoparticles degrade and reform at temperatures below the bulk material melting temperature. The experiments in the tube furnace showed that this effect is not only temperature driven but also dependent on the humidity of the system. Therefore the conclusion is made that metal oxide nanoparticles are able to react in the presence of water vapor at high temperatures, forming new nanoparticles. Further perspective is to obtain a better understanding about the mechanism of nanoparticle behavior in flames

Introduction
The amount of consumer products containing engineered nanomaterials is constantly growing. Cosmetics, plastics, paints, fuel catalysts, UV-coatings, textiles and electronics are only a few product groups in which nanoparticles like Titania, Ceria and CNTs are used to improve their properties. As these products reach their end of life they often end up in the waste incineration. Until now only few data are published concerning a possible release of nanoparticles (NP) into the environment [1]. At Karlsruhe Institute of Technology (KIT) the NP behavior is analyzed in lab-scale flames as well as in semi-technical investigations at a 2.5 MW combustion chamber. In addition, large-scale investigations are performed at an industrial hazardous waste incineration plant in the chemical industry. In this paper the focus lies on the basic investigations concerning nanoparticle behavior in combustion processes.

Experimental

For this purpose a suspension consisting of Ceria nanoparticles and deionized water is added to a burner and a furnace and the change in particle size distribution and morphology is detected downstream. The used temperature in both systems is similar and the comparison of the results allows a differentiation between flame chemistry and temperature effect.

The used Ceria suspension (Cerium(IV) oxide) is commercially available at Alfa Aesar (NanoTek CE 6082) and is specified as 18 m.-% Ceria in H_2O. The producer declares the primary particle size to be approximately 30 nm. The melting temperature of the bulk material is around 2400 °C and the bulk density is 7.3 g/cm³.

For this study a McKenna burner was used, which provides a laminar premixed flame. The burner was operated with an Ethylene/Air-mixture and the flame is stabilized on a porous bronze plate. The burner is considered to be one-dimensional, therefore the flame properties only change with one coordinate, the height above burner (HaB). The laminar flame speed v_L is supposed to be higher than the velocity of the cold gases v_{cold}, otherwise the flame would lift off.

Through a centered tube in the middle of the porous plate it is possible to add gases or sprayed liquids. In this case a cerium dioxide suspension with a concentration of 4 g/l in deionized water was sprayed in the centered tube via an atomizer. The cold gas velocity of the Ehtylene/Air flame was varied at a constant stoichiometry, resulting in a change of the real flame temperature. The temperature profiles were recorded over the cross section of the burner plate in different heights above the burner.

The temperature was measured via a thin wired type S thermocouple and the measurement was corrected for radiation losses according to [2]. The thermocouple was fixed on a movable mounting which allows a positioning in all 3 axes, *see* Figure 1. The radial temperature profile was measured by traversing the mounting of the thermocouple along the burner surface in 5 mm steps and pivoting the thermocouple into the flame for about 15 s. The axial temperature profile was measured respectively by traversing the mounting of the thermocouple perpendicular to the burner surface.

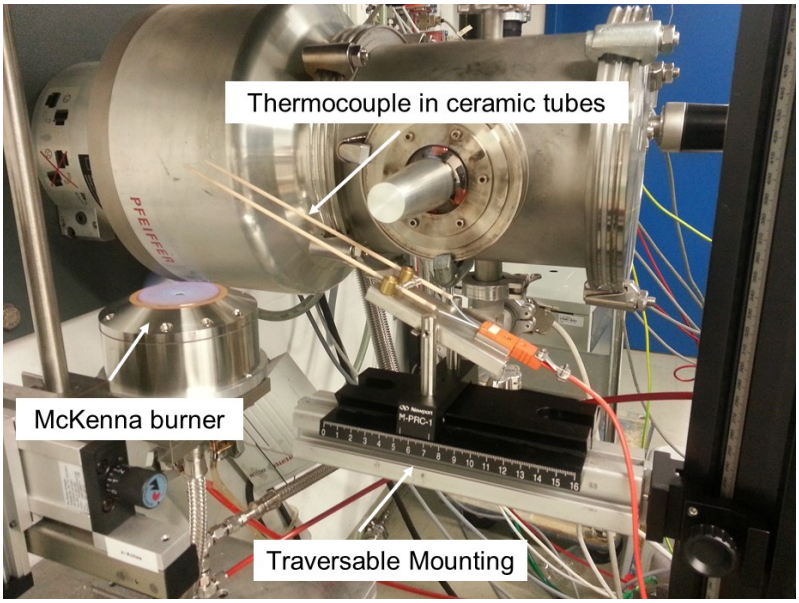

Figure 1. Image of the set up for temperature measurement.

The burner was operated under non-sooting conditions only. The size distribution of the aerosol downstream of the burner was measured with a scanning mobility particle sizer (SMPS+C, Grimm) by sampling in different heights above the burner. In addition to the McKenna burner a tube furnace (Gero HTRH 100-600/18 with temperature controller Eurotherm Type 2408) was used. This furnace can reach up to 1800 °C. The tube material was Al_2O_3 with a heated length of 600 mm and an inner diameter of 30 mm. Either Air or Nitrogen can be used as carrier gas for the sprayed nanoparticle suspension. Additionally the humidity of the carrier gas could be varied via a bubbler system to adjust a similar water-content compared to the flue gas of the flame.

Results

In Figure 2 the measured and corrected temperature in dependence of cold gas velocity is shown. For this diagram the average temperature over the burner surface in 15 mm height above burner was used. The temperature increases with cold gas velocity while the corrected values are about 50 to 100 °C higher than the measured values.

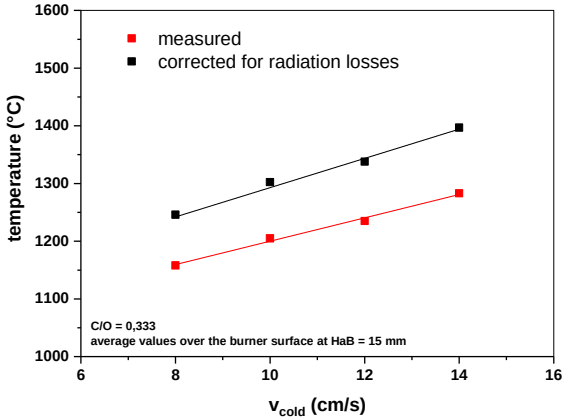

Figure 2. Temperature measurement at an Ethylene/Air flame (λ = 1) in dependence of cold gas velocity.

The flame parameters cold gas velocity and stoichiometry can change the flame temperature and their influence on the morphology, size distribution, sintering behavior, or new particle formation is investigated in different heights above the burner (HAB).

The size distributions for different cold gas velocities are shown in Figure 3 for CeO_2 nanoparticle injection. The red squares belong to the lowest cold gas velocity and therefore the lowest temperature and refer to the right axis. With increasing cold gas velocity and flame temperature a new particle mode around 10 nm starts to form. Because of the scaling it can't be seen easily that the original peak around 100 nm is still there, but shifted to smaller diameters due to sintering of the agglomerates.

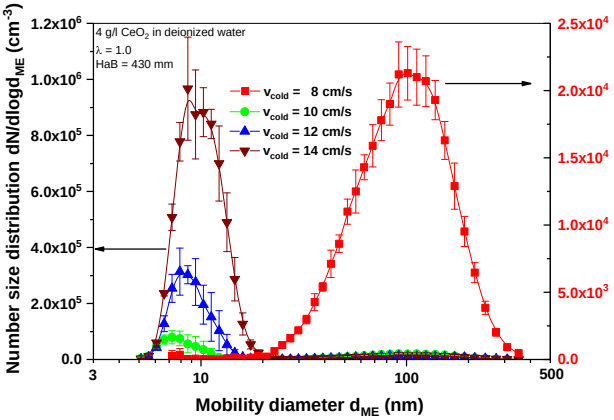

Figure 3. Number size distributions of CeO_2 in dependence of cold gas velocity.

Additionally TEM pictures were taken, *see* Figure 4, to compare the aerosol with and without passing the flame. The original aerosol (without flame) shows typical

angular Ceria agglomerates, whereas the aerosol with flame consists of sintered agglomerates and small single particles.

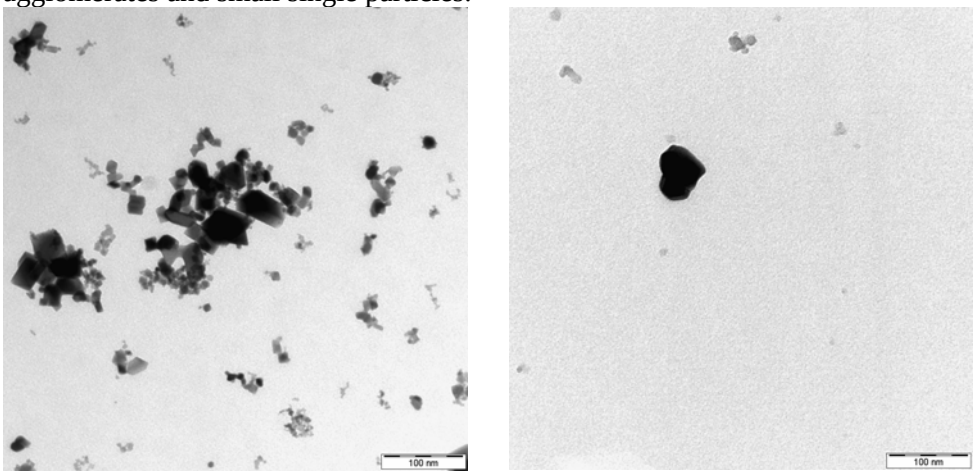

Figure 4. TEM images of CeO_2, left: upstream of the burner, right: downstream of the burner.

If the seen effect was only temperature driven it should lead to the same results by using a furnace with comparable temperature instead of a burner. This investigations have been performed, *see* Figure 5 and Figure 6, and only in case of adding water to the carrier gas flow the formation of a new particle peak can be observed.

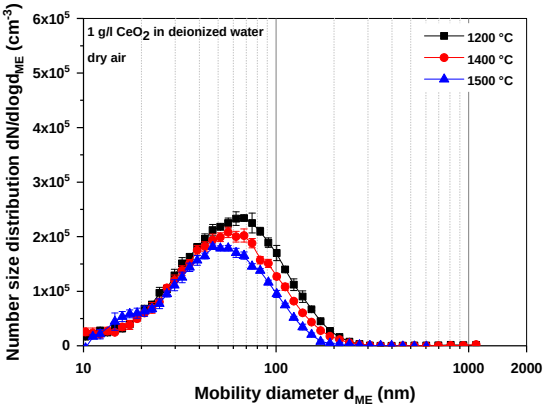

Figure 5. Number size distributions of CeO_2 passing a tube furnace at different temperatures, with dry air as carrier gas.

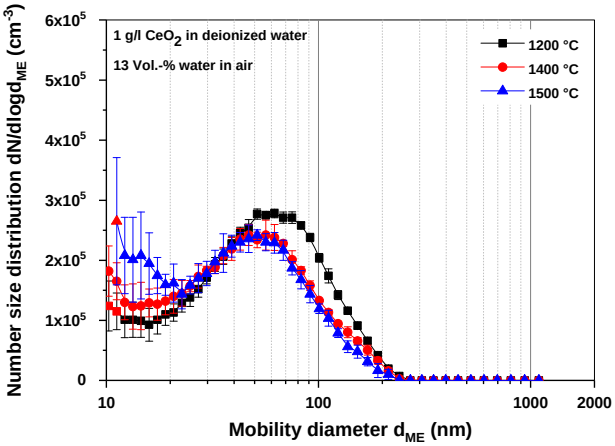

Figure 6. Number size distributions of CeO_2 passing a tube furnace at different temperatures, with humid air as carrier gas.

Limited literature studies indicate that it is possible for metal oxides to form hydroxides or oxyhydroxides in the presence of water vapor at high temperatures [3, 4].

Summary

Nowadays engineered nanoparticles are used in many products and at the end of their life cycle they often end up in the waste incineration. Therefore deeper knowledge about the behavior of nanoparticles in thermal treatment is necessary. Basic investigations in a flame show a sintering of metal oxides. With increasing flame temperature the formation of a new particle mode around 10 nm was observed. This formation is not only temperature driven but also dependent on the gaseous components in the flame, especially on the presence of water vapor.

References

[1] Baumann, W., Teuscher, N., Hauser, M., Gehrmann, J., Paur, H.-R., Stapf, D., Behaviour of engineered nanoparticles in a lab-scale flame and combustion chamber. *Energy Procedia* 2017, *120*, 705–712.

[2] Shaddix, C. R., in:, *Proceedings of the 33rd National Heat Transfer Conference: August 15 - 17, Albuquerque, New Mexico* 1999.

[3] Courcot, E., Rebillat, F., Teyssandier, F., Louchet-Pouillerie, C., Stability of rare earth oxides in a moist environment at high temperatures—Experimental and thermodynamic studies. Part I: The way to assess thermodynamic parameters from volatilisation rates. *Journal of the European Ceramic Society* 2010, *30*, 1903–1909.

[4] Nguyen, Q. N., Bauschlicher, C. W., Myers, D. L., Jacobson, N. S., Opila, E. J., Computational and Experimental Study of Thermodynamics of the Reaction of Titania and Water at High Temperatures. *The journal of physical chemistry. A* 2017, *121*, 9508–9517.

EELS AND HRTEM OF ETHYLENE SOOT

B. Apicella*, A. Tregrossi*, A. Ciajolo*, J. Abrahamson, R.L. Vander Wal**, C. Russo***
apicella@irc.cnr.it
* Istituto di Ricerche sulla Combustione - C.N.R.,
P.le Tecchio 80, 80125 Napoli, Italy
** The EMS Energy Institute & Leone Department of Energy & Mineral Engineering, The Pennsylvania State University, University Park, PA 16802, United States

Abstract
Soot nanostructure was analyzed in fuel-rich premixed laminar C_2H_4/O_2 flames at a constant C/O ratio of 0.8 and different maximum temperatures, namely 1620K and 1690K, obtained using different cold gas velocity. Bulk properties of soot as H/C ratio and reactivity were investigated, along with morphological, nanostructural and chemical features (using TEM, HRTEM, EELS).
It was found that dehydrogenation and aromatization of soot occurring along the flames, are favoured at higher flame temperatures. Nevertheless, soot from the two flames reach a final nanostructure rather similar, independently on the temperature conditions at least in the 1620-1690K range.

Introduction
The dependence of soot bulk properties and its structure at nanometric scale upon soot formation conditions is a way for inferring soot formation mechanism [1,2] as well as to foresee their possible effects on environment [3]. Indeed, the implications are significant, as variation of the soot nanostructure would impact its physical properties and chemical reactivity and therefore its toxicological impact, its feasibility as a new material precursor, the efficiency of its abatement, etc..
In the present work, Transmission Electron Microscopy (TEM), High Resolution TEM (HRTEM) and electron energy loss spectroscopy (EELS) were applied to soot probed along two ethylene flames from the inception phase up to the burnout region in order to follow the transformations of soot nanostructures at different flame temperature. The coupling also with important bulk properties, as H/C ratio and reactivity, allowed deeply investigating all the processes involved in soot inception and growth and their relation with operative parameters of the flame.

Experimental
Samples: Soot specimens were sampled by means of a stainless-steel water-cooled probe (i.d.= 2mm) in rich premixed C_2H_4/O_2 flames produced at atmospheric pressure on water-cooled sintered-bronze McKenna (Holthuis & Associates) burner (d = 60 mm) at a constant mixture composition (C/O=0.8) and different cold-gas flow velocities (3 and 4 cm/s) as shown in Table 1, where flame operative

conditions are reported. Temperatures were measured by a fast-response, silica-coated, 25-µm Pt/Pt-13%Rh thermocouple with a bead size of 50 µm. A fast insertion procedure was used to prevent massive soot deposition on the thermocouple bead. Temperature data were corrected for radiation losses.
Carbon particulate material collected on the probe walls, on the teflon filter, and in an ice-cooled trap placed in the sampling line were extracted by dichloromethane (DCM) to separate soot from the organic compounds, soluble in DCM. More details on the combustion system and sampling are given elsewhere [4].
The H/C ratios and TGA of soot were measured by a Perkin-Elmer 2400 CHNSO elemental analyzer and a Perkin Elmer Pyris 1 thermogravimetric analyzer, respectively.
For TEM, HRTEM and EELS analysis, the soot samples were dispersed in ethanol by ultrasonic agitation and dropped onto a carbon lacey grid.
Methods:
HR-TEM - A 200 kV field emission TEM (FEI®TALOS) was used to take high-resolution bright field images. Images reported in this work were acquired at a nominal instrument magnification of 500,000×. All images were acquired using an objective aperture size of 70 µm and an exposure time between 0.5 and 1 s. Typically 10 aggregates or more from at least five locations were surveyed to establish the consistency of the observations and ensure accurate representations. Quantification of the HRTEM images by lattice fringe analysis provides several statistical metrics describing the nanostructure order. The parameters extracted from the skeleton images are denoted as fringe length, and fringe tortuosity. [5]
EELS - Measurements were taken in TEM mode on FEI® Titan transmission electron microscopes [2] to evaluate carbon hybridization (sp^2/sp^3). For the quantitative analysis of EELS spectra an appropriate standard sample is required [6,7]. In this work a multifaceted polyhedral carbon (made from graphitization heat treatment of carbon black) was selected as the calibration standard because it is free of orientation effects due to its spherical geometry, thereby it can be assumed constituted of 100% sp^2 (i.e. 1:3 $\pi^*:\sigma^*$).

Table 1. Operating conditions of ethylene flames

	LT-E	**HT-E**
C/O ratio	0.8	0.8
Ethylene, vol %	44.44	44.44
Oxygen, vol %	55.56	55.56
Cold gas velocity, cm/s	3	4
Temperature, K	1620	1690

Results
The temperature profiles of the two ethylene flames at v=3 cm/sec and v=4 cm/sec, in the following indicated with the label LT-E and HT-E, respectively, are reported in Fig.1a. For LT-E the maximum flame temperature is 1620 K and is located at

2.5mm of height above burner (HAB), whereas the maximum flame temperature for HT-E is 1690K and is located at 1.8mm HAB. The temperature rises linearly up to the peak values, where ethylene and O_2 are disappearing and both CO and CO_2 are produced with maximum rates.
An earlier soot inception (lower HAB) and a lower soot concentration are observed for the HT-E flame, as shown in Fig.1b, where soot concentration profiles are reported for the two flames. This feature indicates the lower sooting tendency of ethylene in higher temperature conditions in agreement with the bell-shaped profile of soot yield as a function of temperature [8].

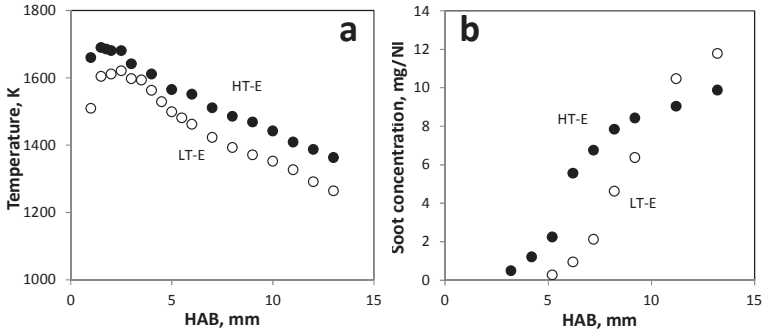

Fig. 1 Temperature (a) and soot concentration profiles (b) measured along the axis of LT-E and HT-E flames.

TG analysis of soot was performed by heating it from 30 to 900 °C in air flow (30 ml* min^{-1}) in order to obtain insights about soot oxidation reactivity that is related to its morphology and composition.
The temperature of the maximum combustion rate of soot (i.e. the temperature to which the maximum weight loss occurs) along the flame axis is reported in Fig. 2.

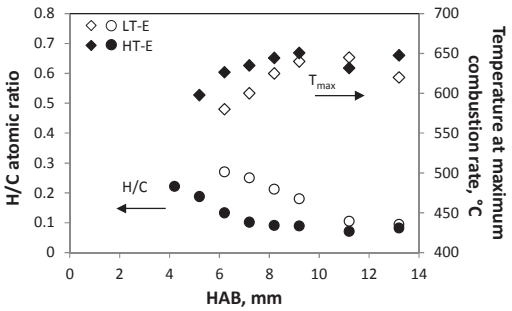

Fig. 2 Temperatures of the maximum combustion rate and H/C atomic ratio of soot formed along LT-E and HT-E flames.

The higher the maximum combustion temperature, the lower is the oxidation reactivity. Overall, soot exhibits an increase of the maximum combustion temperature, from 580 to 650°C, along the flame, indicating the decrease of soot oxidation reactivity during the soot formation/maturation process. After then, the oxidation reactivity of soot remains rather constant in the post-oxidation flame region. It is noteworthy that the oxidation reactivity of LT-E soot is higher with respect to the HT-E soot along the flame, but reaches similar values at the end of soot maturation region.
The H/C atomic ratio, also reported in Fig. 2, slightly decreases as soot ages along the flame axis, tracing the progressive dehydrogenation/carbonization of soot . The H/C of the HT-E soot is lower along the flame with respect to the LT-E soot, indicating the occurrence of a higher degree of dehydrogenation. Thus, looking at the bulk properties, soot formed in higher temperature conditions appears to be initially less hydrogenated and less reactive with respect to the lower temperature flame, reaching similar properties at the final maturation stage.
TEM, HRTEM and EELS techniques have been applied to soot sampled in LT-E and HT-E flames at three different HAB, representative of the different phases of soot evolution, namely the soot inception (nascent soot), the maximum soot formation rate (young soot) and the postflame (mature soot). In previous works [1,2], the nanostructure of the early sampled soot was found very similar to that of the young soot, therefore the sampling point of nascent has been slightly downshifted (0.5 mm) looking for the "true" nascent soot. Actually, it has been observed that at this sampling point soot particles are very rich in organic carbon as shown in Table 2, where the organic carbon/soot ratio is reported and required long sampling times for recovering measurable amounts of soot.

Table 2- Mean structural parameters measured by HRTEM and sp^2 content measured by EELS analysis of soot sampled along the two ethylene flames.

	LT-E				HT-E			
Soot sample	**sp^2 (%)**	**L (nm)**	**τ (nm)**	**Organic carbon/ soot (mass ratio)**	**sp^2 (%)**	**L (nm)**	**τ (nm)**	**Organic carbon/ soot (mass ratio)**
Nascent (*amorphous -like*)	95.7 (*80.3*)	0.86	1.28	17.73	89.7	0.87	1.27	3.82
Young	95.0	0.85	1.31	4.85	93.3	0.78	1.53	1.14
Mature	95.7	0.84	1.25	0.63	96.0	0.83	1.40	0.34

Fig. 3 reports the TEM images at the same resolution (100 nm) of nascent and mature ethylene soot of the two flames. The presence of large coalesced structures, with just few primary particles, features the LT-E nascent soot, as can be seen in

Fig. 3a. Some spherules can be also visualized, but it is not possible to evaluate the size of the few primary particles detected. The HT-E nascent soot presents much more spherule aggregates, even if some coalescent amorphous-like material is still noticeable, as visualized in Fig. 3c. In both the flames, these coalesced structures disappeared with increasing HAB and chain-like spherule aggregates become predominant in mature soot (Figs. 3b and 3d).
From EELS, the percentage of sp^2 bonds with respect to the total (sp^2+sp^3) chemical bonds in soot particles, i.e. their aromaticity degree, was calculated and reported in Table 2 for the two flames. From HRTEM, nanostructural parameters as the fringe length (L) and tortuosity (τ, obtained dividing the fringe length to the Euclidean distance between the two ends) have been evaluated and also reported in Table 2.

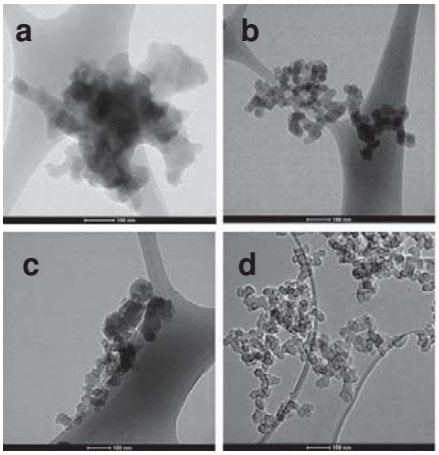

FIG:3- TEM images of LT-E (pre-nascent (a), and mature (b)) and HT-E soot (pre-nascent (c), and mature (d)).

The observation of the nanostructural and chemical parameters indicate that most of the differences regards the nascent soot. Specifically, the nascent HT-E soot presents a lower amount of sp^2 with respect to young and mature soot. Nascent LT-E soot, present two components morphologically different: a fraction completely unstructured, amorphous-like, where the sp^2 percentage is very low, around 80% (Table 2, value in brackets) and a more structured fraction with a higher $\%sp^2$, similar to the other more aged soot. These findings are in agreement with the observation on the TEM images above described and reported in Fig.3.
In the case of nascent soot, the first particles are formed in an environment very rich of organic carbon, especially in the case of LT-E flame, as shown in Table 2. Nascent soot presents a nanostructure still very similar to amorphous tarry carbon, even if soot particles were deprived of the organic compounds (organic carbon) by

DCM extraction before the microscopic analysis. Therefore, also from morphological, nanostructural and chemical point of view, the soot produced in the low temperature flame, in addition to be formed later, undergoes a slightly slower path of transformation from amorphous-like material up to the well structured, mainly sp^2 bonded mature soot. Nevertheless, HT-E and LT-E soot in the post-flame region present very similar bulk properties and nanostructural features.

Final remarks

In the present work TEM and HRTEM analysis have been coupled to EELS analysis to give an overall vision of the soot multi-scale organization during the soot formation and growth in ethylene flames at different temperatures. Bulk proprieties as H/C ratio and reactivity were also investigated.

It was found that freshly generated particles formed at soot inception (nascent soot) are more hydrogenated, reactive and less aromatic than aged soot and these features are enhanced at higher flame temperature.

Soot formed in the high temperature flame, in addition to present an earlier inception with respect to the low temperature flame, undergoes enhanced dehydrogenation and aromatization processes, even if it reaches a final nanostructure in the post-flame region rather similar to those of soot formed in lower temperature conditions.

References

[1] Apicella B., Pré P., Alfè M., Ciajolo A., Gargiulo V., Russo C., Tregrossi A., Deldique D., Rouzaud J. N., "Soot nanostructure evolution in premixed flames by High Resolution Electron Transmission Microscopy (HRTEM)" *Proc. Combust. Inst*. 35: 1895-1902 (2015).

[2] Apicella B., Ciajolo A., Tregrossi A., Abrahamson J., Vander Wal R.L., Russo C., "HRTEM and EELS investigation of flame-formed soot nanostructure", *Fuel* 225C: 218-224 (2018).

[3] T. J. Grahame, R. R. Klemm, R.B. Schlesinger, *J. Air Waste Manage. Assoc.* 64 (6): 620-660 (2014).

[4] Apicella, B., Barbella, R., Ciajolo, A., Tregrossi A. "Formation of low- and high-molecular-weight hydrocarbon species in sooting ethylene flames". *Combust. Sci. Technol.*, 174: 309–324 (2002).

[5] Yehliu, K., Vander Wal, R.L., Boehman, A.L., "Development of an HRTEM image analysis method to quantify carbon nanostructure". *Combust. Flame,* 158: 1837–1851 (2011).

[6] Williams, D. B., Carter, C. B., *Transmission electron microscopy*, 2nd ed.; Springer, 2009.

[7] Egerton, R. F., *Electron energy-loss spectroscopy in the electron microscope*, 3rd ed., Springer, 2011.

[8] H. Bohm et al., "The influence of pressure and temperature on soot formation in premixed flames" *Proc. Combust. Inst*. 22: 403–411(1988).

SOOT PREDICTION IN A MODEL AERO ENGINE COMBUSTOR WITH MULTIPHYSICS APPROACH

S. Paccati*, D. Bertini*, S. Puggelli*, L. Mazzei*, A. Andreini*
simone.paccati@htc.de.unifi.it
*Department of Industrial Engineering
University of Florence
50139, via S. Marta 3, Florence, Italy

Abstract
The main objective of this paper is the assessment of a new multiphysics approach (THERM3D) where reactive CFD, radiation and heat conduction calculations are computed sequentially with a separate solver in a dedicated framework. Therefore, a set of numerical analyses performed on a high pressure test rig are reported. In this context, the importance of taking into account radiative phenomena in order to correctly predict reactive flow fields and pollutant emission in sooting flames is highlighted. Particularly, soot formation and oxidation largely depend on temperature field, leading to an indirect coupling with radiative emissions, showing great differences on soot distribution and emission, due to different rates of formation and oxidation of soot parcels, when radiative calculation is not computed.

Test case
The investigated test case is the DLR-FIRST combustor [1,2]. The rig consists of a combustion chamber of square section, surrounded by a stainless steel pressure housing, as shown in Figure 1. Both are equipped with four quartz windows which provide optical access to the internal reactive flow.

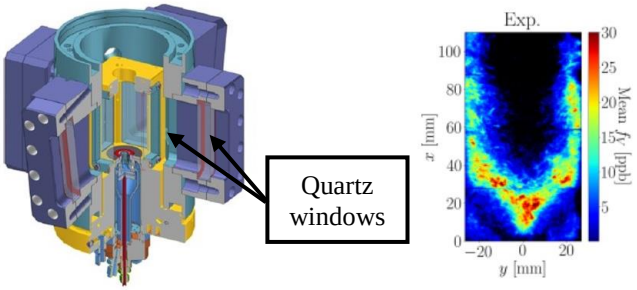

Figure 1. Test case design and soot volume fraction experimental map (adapted from [2,3]).

Air is supplied to the combustion chamber by means of an annular swirled nozzle which enclose the gas fuel injection (Ethylene, C_2H_4). The gap between the chamber and the pressure housing is fed by air to ensure the cooling of combustion chamber

windows. For more information regarding the rig, the reader is addressed to [1] and references therein. Several cases at high pressure have been investigated in [1]. In Table 1, the conditions of the considered operating point are reported.

Table 1. Considered operating point.

P [bar]	Φ [-]	$P_{primary}$ [kW]	$Q_{air,c}$ [slm]	$Q_{air,r}$ [slm]	Q_{fuel} [slm]	Q_{oxi} [slm]	$Q_{air,c}$/ $Q_{air,r}$ [-]	Q_{oxi}/ Q_{air} [-]
3	1.2	32.2	140.8	328.5	39.3	187.4	0.3	0.4

Experimental measurements include gas temperature using Coherent Anti-Stokes Raman Spectroscopy (CARS) [3], time averaged soot distributions and instantaneous soot volume fraction maps [1].

Description of the methodology (THERM3D)

In this work, a new in-house multiphysics tool developed in ANSYS Fluent framework is presented. The main feature of this methodology is to compute three different simulations to solve reactive CFD, radiation and heat conduction in a sequentially manner [4]. As shown in Figure 2, the exchange of specific source terms in the conservation equations and the use of proper boundary conditions allow to take into account interactions among the simulations, according to [5, 6, 7].

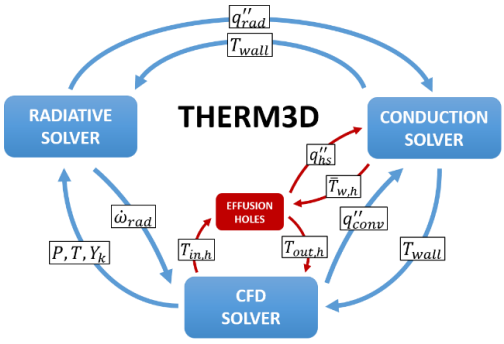

Figure 2. Schematic representation of the THERM3D methodology [4].

Considering the different characteristic scales and the different computed equations, each simulation is performed with the most suitable mesh and numerical setup for the considered physical phenomena, leading to a decrease of the computational time of the entire simulation.

Numerical setup

The results of four different simulations are reported in this work. Firstly, THERM3D (T3DR case) and CHT (CHTR case) solutions were computed together with a flametube calculation (FTR case) without solid domain, employing the

radiation model. Then, a THERM3D without radiative calculation was performed (T3D case) to highlight the weight of radiation in this coupled problem.
All simulations were computed with the commercial code ANSYS Fluent v17.1 using a RANS approach and the realizable k-ε model [8] was considered to take into account turbulence effects. Figure 3 shows the employed computational domain together with boundary conditions assumed for gas phase. Top-hat profiles were adopted for velocity, temperature, mixture fraction and progress variable at inlets, whereas a static pressure was imposed at flametube outlet, according to data reported in Table 1. All walls were treated as smooth with a no-slip condition for velocity. Particularly, quartz windows were considered as transparent to radiation. A constant temperature (313 K) and HTC (121 W/m^2K) value was applied on the cold side of the quartz windows for T3DR and CHTR cases, using the method explained in [9]. A uniform temperature of 900 K was imposed at gas-solid interface for FTR calculation.

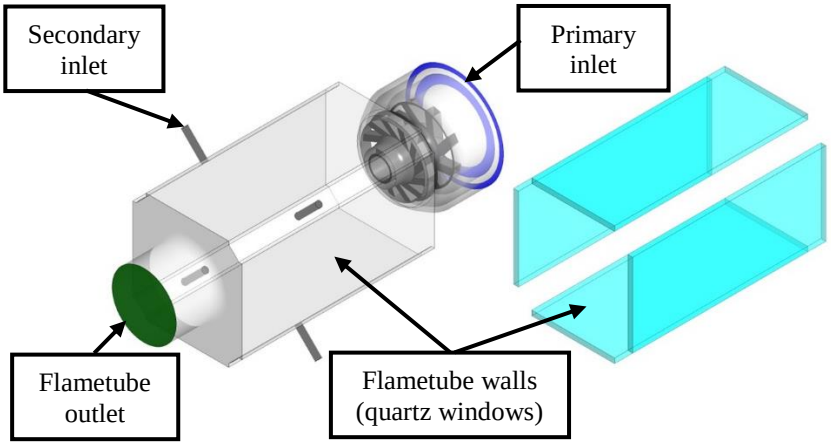

Figure 3. Flametube and solid computational domain.

A tetrahedral mesh of 14M elements with three prismatic layers close to the wall was employed for the gas phase simulation whereas heat conduction calculation within solid framework was performed in a hexahedral mesh of 600k elements. Instead, a coarser tetrahedral mesh of 2.6M elements was employed for radiative calculation with THERM3D approach as a result of a previous mesh sensitivity that is not reported for the sake of brevity. Meshes were created in ANSYS Meshing with a global size of 1.15 mm for the reactive gas phase, considering a refinement at injector burner with a sizing of 0.2 mm.
Regarding combustion modelling, the Flamelet Generated Manifold (FGM) was adopted to describe the reactive flow behavior and the flame characteristics [10]. In order to take into account soot formation within the combustor, two additional transport equations for radical nuclei concentration and soot mass fraction were solved according to Moss-Brooks model [11].
The radiative thermal loads are computed by solving the Radiative Transfer Equation

(RTE) in a frozen gas phase solution together with temperature distributions at walls, using Discrete Ordinate (DO) model [12]. RTE solution is parallelly performed in a proper and coarser mesh to balance accuracy and CPU efforts.

Results

Results of the simulated operating condition are here highlighted. First of all, a comparison between temperature fields of each simulation is reported. Then, the significant impact of radiative phenomena on soot emission is evaluated.

Figure 4 shows computed temperature distributions in a plane through the centerline of the combustor. Considering radiative calculation, it is possible to observe a great agreement between T3DR and CHTR approach, whereas slight differences can be noted with FTR solution near the walls, due to the different boundary conditions, and so temperature distributions, at gas-solid interface. When radiation is not computed (T3D), the absence of heat dispersion related to radiative emissions leads to a temperature increase, especially close to swirler outlet and quartz windows.

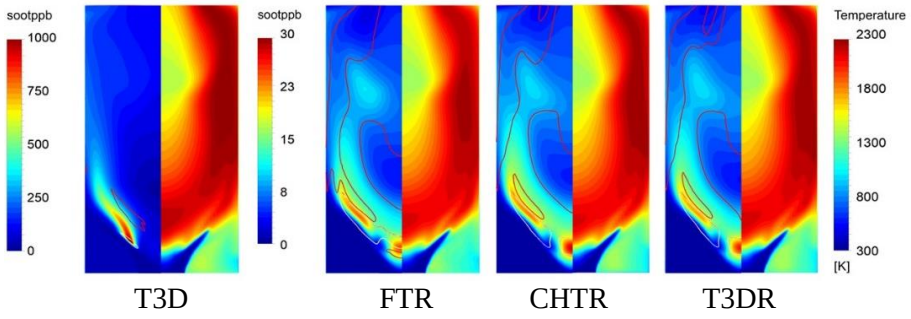

Figure 4. Temperature and soot volume fractions distributions in a plane through the centerline of the combustor.

This fact is also confirmed by a quantitative comparison with experimental data, as shown in Figure 5, where temperature profiles along the centerline of the combustion chamber are reported. A general good agreement can be appreciated with an under-prediction of about 60 K in the first part of the combustor, whereas it is possible to note an over-prediction of about 100 K at 80 mm downstream of swirler outlet, probably due to the employed steady approach.

Considering soot formation, soot volume fraction fields are also reported in Figure 4. The white line is the iso-contour at 15% of soot mass source maximum value (related to soot formation) while the red line is the iso-contour at 15% of its minimum value (related to soot oxidation). Great differences can be observed in terms of values and distributions when radiation is not computed.

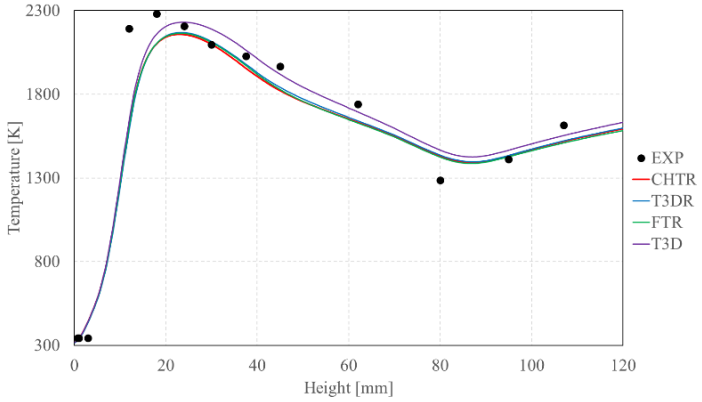

Figure 5. Temperature profiles along the centerline of the combustor.

Consequently, radiative phenomena have a strong impact on soot emissions, related to the non-linear dependence on the temperature of the source terms of soot model equations [11]. While in T3D case soot formation and oxidation are focused in small regions next to swirler outlet, a more uniform distribution of soot oxidation can be observed when radiative calculation is computed.

Nomenclature

P	Power [kW]
Q	Volume flow rate [slm]
p	Pressure [bar]

Acronyms

CFD	Computational Fluid Dynamics
HTC	Heat Transfer Coefficient
RANS	Reynolds Averaged Navier Stokes

Greek

Φ	Equivalence ratio [-]

Subscripts

c	central
r	ring

References

[1] Geigle, K.P., Hadef, R., and Meier, W., "Soot formation and flame characterization of an aeroengine model combustor burning ethylene at elevated pressure", *J. Eng. Gas Turbines Power* 136: 021505–1–021505–7 (2014).

[2] Geigle, K. P., O'Loughlin, W., Hadef, R., & Meier, W., "Visualization of soot

inception in turbulent pressurized flames by simultaneous measurement of laser-induced fluorescence of polycyclic aromatic hydrocarbons and laser-induced incandescence, and correlation to OH distributions". *Appl. Phys. B*, 119: 717–730 (2015).

[3] Geigle, K. P., Köhler, M., O'Loughlin, W., & Meier, W., "Investigation of soot formation in pressurized swirl flames by laser measurements of temperature, flame structures and soot concentrations", *Proceedings of the Combustion Institute*, 35: 3373-3380 (2015).

[4] Bertini, D., Mazzei, L., Puggelli, S., Andreini, A., Facchini, B., Bellocci, L., Santoriello, A., "Numerical and experimental investigation on an effusion-cooled lean burn aeronautical combustor: Temperature profiles and emissions", *Proceedings of GT2018 ASME TURBO EXPO 2018: Power for Land, Sea & Air*, Lillestrøm, Norway, number GT2018-76779.

[5] Berger, S., Richard, S., Staffelbach, G., Duchaine, F., & Gicquel, L., "Aerothermal prediction of an aeronautical combustion chamber based on the coupling of large eddy simulation, solid conduction and radiation solvers". *In ASME Turbo Expo 2015: Turbine Technical Conference and Exposition*, pp. V05AT10A007-V05AT10A007 (2015).

[6] Duchaine, F., Corpron, A., Pons, L., Moureau, V., Nicoud, F., & Poinsot, T., "Development and assessment of a coupled strategy for conjugate heat transfer with large eddy simulation: application to a cooled turbine blade", *International Journal of Heat and Fluid Flow*, 30: 1129-1141 (2009).

[7] Berger, S., Richard, S., Duchaine, F., Staffelbach, G., & Gicquel, L. Y. M., "On the sensitivity of a helicopter combustor wall temperature to convective and radiative thermal loads", *Applied Thermal Engineering*, 103: 1450-1459 (2016).

[8] Shih, T. H., Liou, W. W., Shabbir, A., Yang, Z., & Zhu, J., "A new k-ε eddy viscosity model for high reynolds number turbulent flows", *Computers & Fluids*, 24: 227-238 (1995).

[9] Rodrigues, P., Gicquel, O., Darabiha, N., Geigle, K. P., Vicquelin, R., "Assessment of external heat transfer modeling of a laboratory-scale combustor inside a pressure-housing environment", *Proceedings of GT2018 ASME TURBO EXPO 2018: Turbomachinery Technical Conference & Exposition*, Oslo, Norway, number GT2018-76579.

[10] Van Oijen, J. A., "Flamelet-generated manifolds: development and application to premixed laminar flames", Technische Universiteit Eindhoven, Eindhoven (2002).

[11] Brookes, S. J., & Moss, J. B., "Predictions of soot and thermal radiation properties in confined turbulent jet diffusion flames", *Combustion and Flame*, 116: 486-503 (1999).

[12] Murthy, J. Y., & Mathur, S. R., "Finite volume method for radiative heat transfer using unstructured meshes", *Journal of thermophysics and heat transfer*, 12: 313-321 (1998).

MODELLING OF SOLAR RADIATION ON SOOT FORMATION IN DIFFUSION FLAME

M. Sirignano, A. D'Anna
mariano.sirignano@unina.it
Università degli Studi di Napoli Federico II, DICMAPI, P. le Tecchio, 80, 80125, Napoli (Italia)

Abstract
The coupling of solar thermal energy with existing energy conversion technologies is fundamental to enlarge the field of applicability and lower the costs of renewable energy sources. Traditional combustion technologies have been coupled with solar energy mainly by heating up the fuel/oxidizer stream and recently high flux radiation technology has been tested to heat up directly a flame. This latter setup has the advantage of relative compactness, minimizing the heat losses, and to use the high absorption coefficient of combustion by-products present in flame such as soot particles. In fact, soot particles formed in flame are responsible for more than 90% of the total radiation flux and thus it is also responsible for the majority of the solar radiation adsorbed. The solar thermal radiation has been already tested in these conditions and an increase of the flame temperature and soot volume fraction inside the flame have been found, but with an even reduced soot emission from the flame. The lack of modelling studies did not allow to fully understand the effect of solar radiation and just some hypotheses have been formulated. In this work, we use our detailed model of soot formation and oxidation to simulate the behaviors of a coflowing diffusion ethylene flame with and without the exposure to a concentrated solar radiation. Modelling data are compared with experimental data reported in the literature. Our model is able to reproduce the effect of radiation both matching the temperature and soot volume fraction increase. On the other hand, the model gives the possibility to evaluate the effect of solar radiation on flame heating and soot formation and oxidation. Our model is a reliable tool to evaluate the effect of solar radiation for future experimental setup designs and device analysis.

Introduction
The use of solar thermal energy in combination with other source of energy, in particular with traditional technologies based on fossil and renewable fuels, are receiving increasing interest [1]. This combination helps reducing the net emission of greenhouse gases and thus reducing the impact of energy conversion on climate. On the other hand, it gives also the possibility to readily use, even partially, the solar energy with much lower cost and applicability on larger scale.
The use of the energy from the interaction of solar radiation with available and retrofitted technologies has been various and by different approach. Most of the

concepts are based on the possibility to use the solar thermal energy to heat air that can be used directly as combustion oxidizer [2] or for heating water [3]; alternatively, it is possible to use the solar radiation to obtain low-temperature modification of service fluids such in the regeneration of exhausted solvents [4].
One of the most interesting approach integrates the solar receiver and the traditional conversion energy technology in a single structure. This reduces the impact of having separate devices, minimizing the dispersions and reducing the costs and the applicability. A group of researchers of the University of Adelaide (Australia) chaired by prof. Gus Nathan proposed the fully integration of a combustion device and a solar receiver, with a direct irradiation to the flame [1]. This approach is promising, but it has to be fully tested in order to understand the implications of high radiation flux on the flame structure, on the major combustion by-products and finally on particles formed. In fact, the radiation can influence the flame due to absorption of the solar radiation by species produced in combustion, a local increasing of temperature with all the implications on the flame structure and combustion-formed products.
The effect of high flux radiation on a flame has been studied firstly by Medwell et al. [5]: they adopted a laser to irradiate a small portion (close to the tip) of a laminar coflow diffusion ethylene flame by using a single coherent radiation at 10.6 μm. Beside of the limitation of the experimental setup, some effects have been observed: the solar radiation increased the local soot volume fraction, moving the soot formation zone to the outer zone of the flame. Successively Dong et al. [6] adopted a different irradiation system and an experimental setup to measure soot volume fraction and temperature simultaneously by-using optical technique. A complex system of reflectors and concentrators produces a heat flux of 0.27 MW/m^2 from a metal halide lamp which approximates quite well the solar spectrum. The radiation was centered on the axis of a diffusion flame; thus the heat flux was considered uniform. Planar laser induced incandescence (PLII) and two-line atomic fluorescence was used to detect soot volume fraction and temperature, respectively and not intrusively. The irradiation induced an increase of temperature and of soot volume fraction by 50% with a translation towards upstream region and an increase of soot burnout.
The present work aims to use a well-established Multi-Sectional model to simulate the effect of radiation flux on the same diffusion ethylene flame investigated by Dong et al. [6]. The model will allow to better understand the phenomena that lead the changes in the combustion features and thus to better design future experiments and devices.

Numerical Method

A Multi-Sectional method is used for the modelling of aromatic growth and particle inception [7-10]. It is based on a previously developed kinetic mechanism of particle formation with a single discretization of the particle phase in terms of C atoms with a fixed H/C ratio. A successive discretization has been introduced to

take into account variable H/C ratios. The upper and the lower limit of this discretization are fixed by physical constraints. H/C ratio can reach 0 a bottom limit value, e.g. structures containing just C-atoms, on the other hand H/C ratio equal to 1 representing the value of benzene. The present model also distinguishes between different particle structures based on their state of aggregation, i.e. high molecular mass aromatic molecules (Molecules), clusters of molecules (Clusters) and agglomerates of particles (Aggregates) [7-10]. This allows to follow not only the mass of the formed particles, but also their hydrogen content and internal structure. Oxidation-induced fragmentation is also considered. Oxygen is considered the only species able to not react on the surface and diffuse towards the points of contact of the primary particles causing internal oxidation and subsequent particle fragmentation.

A coflowing diffusion ethylene flame is simulated with and without solar irradiation. The burner is well described in many experimental and numerical papers: a central fuel pipe with (ID=10.5 mm and OD=12.6 mm) is surrounded by an annular co-flow (ID 97.7=mm and OD 101.5 mm). the velocity was kept uniform at the exit for both streams. Pure ethylene (0.184 STLPM) was used as fuel, while purified air was used in the coflow (127.7 STLPM). The radiation flux was simulated by changing the radiation absorption coefficient used for the soot. Soot is considered the only absorption/emitting species which is consistent with experimental and numerical findings. The soot coefficients were chosen in order to match the maximum temperature measured by Dong et al. [6].

Results and Discussion

Figure 1 shows the contour plots for the temperature and total particle volume fraction. The effect of lamp radiation has a significant effect on both fields as indicated also by the experimental data [6]. In particular, the temperature (Fig 1 – left panel) increases in the whole field. However, it is worth to remind that soot particles are considered the only species able to absorb and remit the radiation, beside the natural incandesce of the flame. In fact, the largest increase in temperature can be noticed close to the zones where the particle concentration is higher.

Still looking at Fig 1 (right panel), it is possible to see how the soot volume fraction increases in terms of peak value but does not change significantly in terms of shape. A small shift toward the burner and the inner part of the flame is observed.

The experimental and modelling results of the radially integrated volume fraction are reported in Fig.2. This parameter reflects the global evolution of the particles along the flame axis. Lamp radiation (0.27MW/m^2) increases the formation of the particles; however, modelling results also show a slight over prediction for the non-irradiated condition in the first part of the flame. In all the cases particles are completely oxidized at the end of the flame as also suggested by the contour plot.

Consequently, the burnout rate must be higher in the irradiated case due to the

large amount of particles to be oxidized. Usually the increase of volume fraction is linked with a decrease of temperature (due to large radiation losses); the locally decreased temperature is linked with the smoking behavior of the flame. In the irradiated case presented here, the net effect between the lamp radiation and increased soot radiation losses is that the temperature is higher and thus the oxidation process is fast enough to compensate for the increase of the volume fraction. This effect has to be considered in the future design of the experiment: if the lamp radiation in some conditions is not able to overcome the increased radiation losses the flame could turn into a smoking one with evident consequences on the feasibility of the process itself.

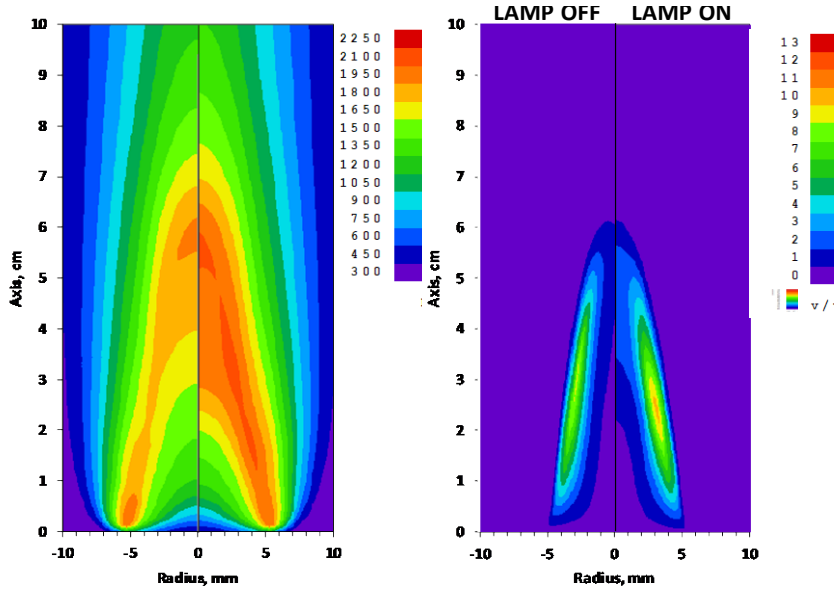

Figure 1. Contour plot of temperature (left panel) and total volume fraction of particles (right panel) with (left side of each panel) and without (right side of each panel) considering radiation of the lamp.

In Fig.3 the contour plot of the modelled OH molar faction is reported. It is possible to see how the lamp radiation has a consequence the increase of OH radical concentration which is responsible for particle oxidation. The role of O_2 has been found to be quite important as well but this latter is less affected the lamp radiation. The OH on the contrary shows a significant increase, up to 50%, when the lamp is on. This increase has to be linked with the increased temperature: hence the increased oxidation rate is linked to increased temperature both directly by increasing the oxidation kinetic constant and indirectly by increasing the OH concentration. The combination of these two effects are promising looking at the possibility to use the setup in heavily sooting conditions where the increase of the particle volume fraction could otherwise lead to a smoking flame.

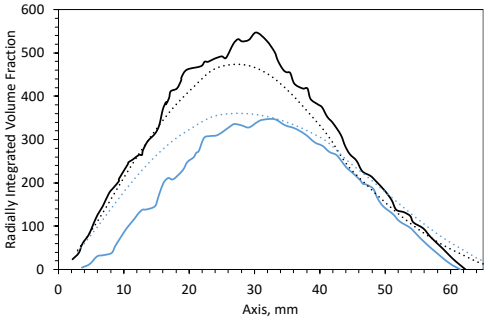

Figure 2. Radially Integrated Volume Fraction of particles with (black) and without (blue) considering radiation of the lamp experimental data [6] are reported as continuous line; modelling as dotted lines.

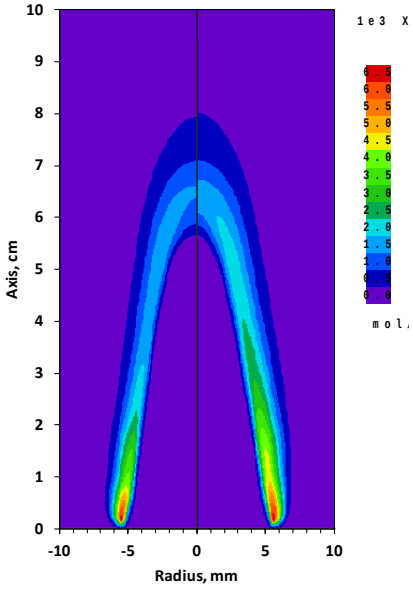

Figure 3. Contour plot of OH molar fraction with (left side of panel) and without (right side of panel) considering radiation of the lamp.

Conclusions

A Multi-Sectional Method has been adopted to simulate the effect of a concentrated solar radiation on a diffusion laminar flame behaviours. The experimental results available in literature are fairly reproduced by numerical simulation in terms of increasing temperature and particle volume fraction when solar radiation is considered. Also the model is able to reproduce the burn out of the particles in both conditions. Modelling analysis allowed to punctually evaluate

the impact of solar radiation on the flame and on particle formation. The temperature and the volume fraction of the particles mainly responsible for absorption/emission phenomenon simultaneously increased due to solar radiation. This suggests that the increased emitted radiation from particles due to higher volume fraction was mitigated and overwhelmed by the lamp radiation. The net effect of increasing the temperature allowed to have an efficient global oxidation rate for particles by combining a direct effect on kinetic constant of oxidation rate and an indirect effect by increasing OH radical concentration, the oxidizing species The model represents a reliable tool for the future design of the experiments and for the possible evaluation of the impact of reactor parameters on lamp-soot interaction.

References

[1] Nathan G.J., Battye D.L., Ashman P.J., Economic evaluation of a novel fuel-saver hybrid combining a solar receiver with a combustor for a solar power tower. Appl. Energy, 113 (2014), pp. 1235–1243

[2] Costerg P., Garcia P., Soler R, Gagnepain B, Ferriere A, Flamant G., Solar field efficiency and electricity generation estimations for a hybrid solar gas turbine project in France. J. Solar Energy Eng., 130 (2008), pp. 1–3

[3] Ying Y., Hu E.J., Thermodynamic advantages of using solar energy in the regenerative Rankine power plant. Appl. Therm. Eng., 19 (1999), pp. 1173–1180

[4] Mokhtar, M., Ali, M.T., Khalilpour, R., Abbas, A., Shah, N., Al Hajaj, A., P. Armstrong, M. Chiesa, Sgouridis, S., Solar-assisted post-combustion carbon capture feasibility study. Appl. Energy, 92 (2012), pp. 668–676.

[5] Medwell P.R., Nathan G.J., Chan Q.N., Alwahabi Z.T., Dally B.B., The influence on the soot distribution within a laminar flame of radiation at fluxes of relevance to concentrated solar radiation Combust. Flame, 158 (2011), pp. 1814–1821

[6] Dong X., Sun Z., Gu D., Ashman P.J., Alwahabi Z.T., Dally B.B., Nathan, G.J., The influence of high flux broadband irradiation on soot concentration and temperature of a sooty flame. Combustion and Flame, (2016) 171, 103-111.

[7] Sirignano M., Kent J., D'Anna A., Detailed modeling of size distribution functions and hydrogen content in combustion-formed particles, Combust. Flame 157: 1211–1219 (2010).

[8] D'Anna A., Sirignano M., Kent J., A model of particle nucleation in premixed ethylene flames, Combustion and Flame, (2010) 157:2106-2115

[9] Sirignano, M., Kent, J., D'Anna, A. "Modeling formation and oxidation of soot in nonpremixed flames", Energy Fuels 27: 2303–2315 (2013).

[10] Sirignano M., Kent J., D'Anna A., "Further experimental and modelling evidences of soot fragmentation in flames", Proc. Combust. Inst. 35: 1779–1786 (2015).

STUDY OF SOOT PARTICLES NANOSTRUCTURE EVOLUTION IN A LAMINAR PREMIXED FLAME BY RAMAN AND EPR SPECTROSCOPY

F. Picca*, M. Di Serio*, G. De Falco*, M. Commodo, G. Vitiello*, G. D'Errico***, P. Minutolo**, A. D'Anna***

francesca.picca@unina.it; commodo@irc.cnr.it

* Dipartimento di Ingegneria Chimica, dei Materiali e della Produzione Industriale - Università degli Studi di Napoli Federico II, P.le Tecchio 80, 80125, Napoli, Italy

** Istituto di Ricerche sulla Combustione - CNR, P.le Tecchio 80, 80125, Napoli, Italy

*** Dipartimento di Scienze Chimiche - Università degli Studi di Napoli Federico II, Complesso Monte S. Angelo, 80126, Napoli, Italy

Abstract

In this study the physicochemical evolution of soot particles in a laminar premixed flame has been investigated. The evolution of the particle size distribution as function of the different heights above the burner has been explored in conjunction with changes of particle chemical/physical properties retrieved by Raman and Electron Paramagnetic Resonance spectroscopy. In addition, the results obtained by Raman spectroscopy on flame formed soot particles were compared to those obtained by analyzing some standard carbon-based materials such as commercial carbon black, activated carbon, disordered graphite and highly oriented pyrolytic graphite.

Introduction

Soot formation results from the incomplete combustion of hydrocarbons. These carbonaceous particles have been the object of numerous studies over the decades in various research areas because of thei r negative effects on human health, climate change, and the environment [1,2]. Soot can be defined as a mixture of particles and aggregates composed prevalently by aromatic carbon compounds, thus mainly presenting sp^2 carbons. Despite the great efforts in understanding the mechanism of soot formation in combustion and several advances achieved in the last years, the complete understanding of this process has not reached yet.

In fuel-rich flames, the incomplete oxidation of the fuel molecules results on the formation of gas-phase products, close to the flame front, which later recombine forming benzene, naphthalene and other larger polycyclic aromatic hydrocarbons (PAHs). In order to describe the soot formation process is fundamental to understand the structure of the PAH compounds acting as building blocks of the soot particles. Indeed, once formed, these aromatic structures begin to assemble into just-nucleated particles or clusters, whose size is usually of the order of few

nanometers, i.e., 2-3 nm [3]. Only at higher residence times, i.e., at increased height above the burner (HABs), the particle growth process due to coagulation/coalescence and surface mass addition lead to the formation of a second mode centered at larger diameters in the particle size distribution (PSD) [3, 4].The aim of this research has been to move a step forward in the understanding of this complex process, by analyzing the physicochemical transformation of soot particles during the aging process in the flame. In this work the initial evolution of carbon nanoparticles in a laminar premixed flame has been investigated in term of particle size by on-line differential mobility analysis (DMA), and in term of chemical/structural properties by Raman and Electron Paramagnetic Resonance spectroscopies.

Experimental

A premixed laminar ethylene-air flame was stabilized on a water cooled sintered bronze McKenna burner. Ethylene was chosen as fuel being one of the main products of the decomposition of any hydrocarbons. The cold gas stream velocity was 9.8 m/s and the carbon to oxygen (C/O) atomic ratio was set at 0.67, corresponding to a flame equivalence ratio Φ of 2.01.

PSDs, were measured online by a DMA system. To this purpose, flame products were sampled through an orifice (ID = 0.2 mm, thickness = 0.5 mm) into the turbulent flow dilution probe with 1 cm outer diameter, positioned horizontally, using N_2 as diluent ensuring a dilution ratio, DR, of $3*10^3$. Such sampling procedure was adopted to prevent particle coagulation and to quench chemical reactions, thus preventing particle mass growth within the sampling line [4-6].

Off-line analyses were performed on the particles sampled with a tubular probe (similar to the one used for PSDs measurements) and were collected on quartz filters (Whatman QM-A Quartz Microfiber Filters, with diameter of 47 mm) placed on-line in a filter holder. Total sampling time for each filter was 7 hours. Particles collected on the Quartz filters were first analyzed by Raman spectroscopy using a Horiba XploRA Raman microscope system equipped with a 100×objective (NA0.9, Olympus). The laser source was a frequency doubled Nd:YAG laser (λ = 532 nm) and an infrared laser (λ = 785 nm). The power of the excitation laser beam, the exposure time and the other instrumental parameters were opportunely adjusted to avoid structural changes of the sample due to thermal decomposition and to ensure the best resolution. Spectra were obtained with a laser beam power of 1%, and an accumulation-exposure time of 5 cycles of 30 s each. For each sample, 10 spots were randomly selected and averaged to obtain statistically relevant Raman spectra. Finally, all the spectra were baseline corrected and normalized to the maximum of the G-peak, around 1600 cm^{-1}. In addition, Raman spectra of commercially available carbon-based material have been also measured. These include: carbon black, activated carbon, disordered graphite and, highly oriented pyrolytic graphite, HOPG.

EPR spectroscopy experiments of soot particles collected on the quartz filters were

carried out by means of X-band (9 GHz) Bruker Elexys E-500 spectrometer (Bruker, Rheinstetten, Germany), equipped with a super-high sensitivity probe head. Defined sections of quartz filters were coaxially inserted in a standard 8 mm quartz sample tube and the measurements were performed at 25 °C. The instrumental settings were as follows: sweep width, 100 G; resolution, 1024 points; modulation frequency, 100 kHz; modulation amplitude, 1.0 G. EPR spectra were recorded at an attenuation value of 15 dB and 128 scans were accumulated to improve the signal-to-noise ratio. The *g*-factor values were evaluated by means an internal standard (Mg/MnO) [7] which was inserted in the quartz tube co-axially with the samples.

Results

Particle size distributions measured by DMA along the flame axis are reported in Fig.1. PSDs are plotted in terms of volume diameter, d_P, [7]. PSD evolves from unimodal to bimodal by increasing the HABs.

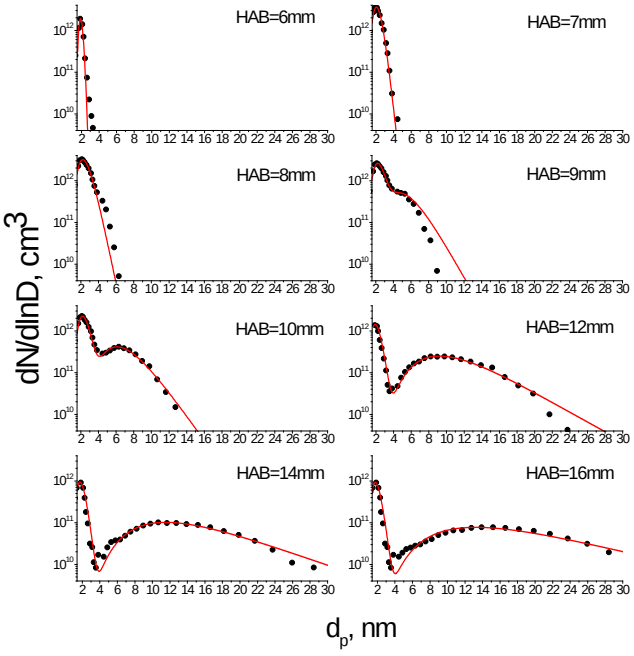

Figure 1. Evolution of the PSD as a function of HAB. Black dots represent the measurement data, red lines are the sum of the log-normal fits.

Lognormal distribution functions are usually used to fit particles distributions: one function is sufficient to fit PSDs from 6 to 8 mm above the burner, while two lognormal functions are required to fit the PSDs at higher HABs, i.e. from 9 to 16 mm.

Further information on the physicochemical evolution of soot particles in laminar

premixed flame were obtained by Raman spectroscopy. Indeed, Raman scattering is as a remarkable and powerful tool for gaining chemical, structural and electronic information of many carbon-based materials. The Raman spectra of soot collected at HABs, obtained by using two different excitation wavelengths, i.e., λ = 532 nm and λ = 785 nm are shown in Fig 2. Spectra are acquired in the first order Raman region of 1000 – 2000 cm^{-1}. All the measured spectra present the typical characteristics of any disordered carbonaceous materials for which a thorough description is reported elsewhere [8,9]. Briefly: two main bands are commonly present, one centred at about 1600 cm^{-1} named G band, the other centred at about 1350 cm^{-1} and named D band.

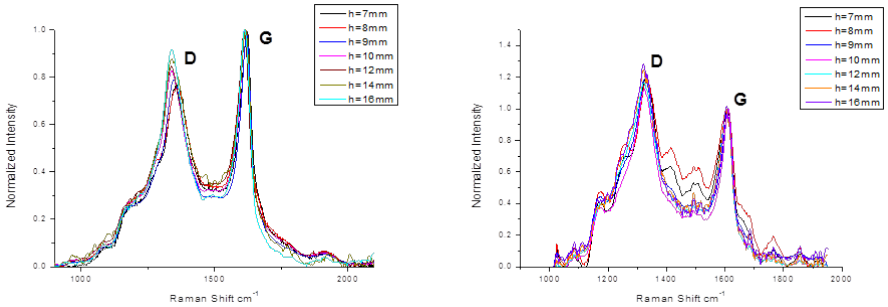

Figure 2. Raman spectra at several heights above the burner. On the left, collected spectra at 532nm;on the right, collected spectra at 785nm. The data have been normalized on the G peak after subtracting the photoluminescence background

The high sensitivity of the technique, in probing chemical/structural information of carbon materials, lies in the fact that the presence of defects in the sp^2 aromatic network allows the activation of the Raman D mode at ~1350 cm^{-1}, prohibited in the perfect hexagonal lattice [8, 9] Conversely, the G band, at ~1600 cm^{-1}, which is due to every sp^2 bond, is mostly insensitive to defects only presenting small changes in width and position of the maximum as function of the different carbon structures. It is worth noticing that although D and G bands represent the most prominent features in the first order spectrum of soot and other amorphous carbon materials, the presence of other Raman lines can be also taken into account [10] each characteristics of specific disorder origin in the carbon matrix [9-11]. However, because of the superposition of these lines, the Raman spectrum needs to be fitted with a multiple-line function to evidence each contribution. This will be part of future work. The major differences in the spectra changing HABs consist in changes in the relative intensity of the D and G peak and in the band position.
In Fig 3 the trends of these parameters are reported in detail. Fig. 3a and Fig. 3b report the D-peak and G-peak position, respectively Pos(D) and Pos(G), obtained from the Raman spectra of soot collected at different HABs in comparison to that of standard carbon materials such as activated carbon (AC), carbon black (CB), defected graphite (DG) and HOPG.

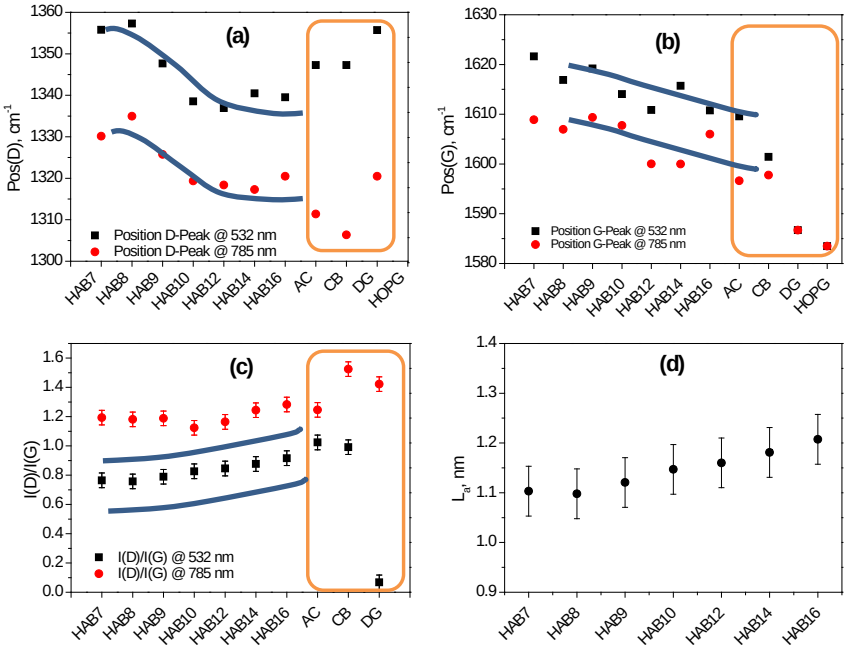

Figure 3. Position D-peak, Pos(D), (a); Position G-peak, Pos(G), (b); I(D)/I(G) ratio (c) from the Raman spectra of soot particles collected at several HABs and other standard carbon materials.

It is observable a decrease of the position of the two bands as the soot particle aging proceeds, almost approaching the values obtained for the AC and CB. For the G band this trend is consistent with graphitization process as also reported by Ferrari and Robertson [8] investigating amorphous carbon materials. The shift of D line is generally consequent to strain or doping in the lattice [12]. In the case of the particles here examined strain could be caused by the non-perfect planarity of the aromatic units. The trend of Fig. 3a is consistent with the increase of bending of the aromatic islands in the particles when particle aging proceeds at increasing HABs. Although not directly comparable to soot particles, the trend observed for the carbon standards follows the same tendency with the position of the D band of AC and BC shifted towards lower wavenumber (larger strain) respect to the graphite. Other source of strain/doping such as electrical charges and/or Oxygen atom are less likely. The change in the chemical/structural properties of the different soot particles can be also observed by considering the relative intensity of the D and G band, i.e., I(D)/I(G). It is well known that this ratio is related to the average size of the aromatic units or clusters forming the carbon materials, L_a [8]. For graphite and nano-graphite the intensity ratio I(D)/I(G) has been shown to be inversely proportional to L_a [13]. Such functional dependence has been successively verified

up to a minimum L_a, of about 2-3 nm, where I(D)/I(G) reaches a maximum value [9]. When L_a further decreases, I(D)/I(G) decreases to zero. For flame-generated soot particles the low-L_a regime, i.e., L_a < 2-3 nm, usually applies [13], for which the following empirical expression has been found to correlate L_a with the relative intensity of the Raman bands [8]:

$$L_a^2(\mathrm{nm}^2) = 5.4 \cdot 10^{-2} \cdot E_L^4(\mathrm{eV}^4) \frac{I(D)}{I(G)} \quad (1)$$

where E_L is the energy of the incident photon. The results obtained for the different soot particles are reported in Fig. 3d, in which an increase of L_a as function of HAB is observable.
EPR spectra of soot collected at different HABs are reported in Figure 4.

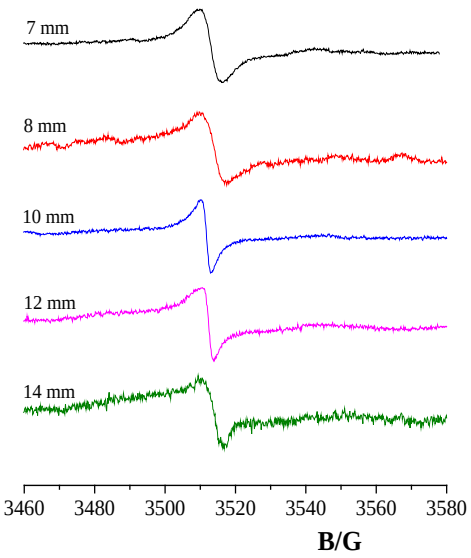

Figure 4. EPR spectra of soot particles on quartz filters collected at different HABs.

All spectra show a single peak at *g*-factor = 2.0024-2.0028 (as reported in Table 1), typical of very persistent carbon-centered radicals with the single electron localized on a carbon atom, aliphatic or aromatic [14]. However, a closer inspection of Figure 4 indicates that the spectra at lower (7 and 8 mm) and higher (14 mm) HABs reveal a significantly broad signal. This evidence is associated to the presence and superposition of multiple paramagnetic species into the soot particles [14, 15]. This difference in these line shapes was quantitatively corroborated by the determination of signal amplitude, ΔB, which is also inversely related to the mean distance between the radical centres. In our case, EPR analysis shows that the ΔB value for the soot samples obtained at lower and higher HABs was significantly

larger than those obtained at other HABs (see Table 1). Since soot is principally composed of carbon and the spectral width ΔB of soot resulting from electron spin-spin interactions is usually ~2 G [16], the reported variations in ΔB values are a clear confirmation of the presence of multiple radical species, indicating different chemical and structural organization properties of soot particles produced at different HABs.

Table 1. EPR spectral parameters of soot particles collected at different HABs.

HAB	***g-factor***	***ΔB (G)***
7 mm	2.0026 ± 0.003	6.5 ± 0.2
8 mm	2.0027 ± 0.003	7.1 ± 0.2
9 mm	2.0024 ± 0.003	2.7 ± 0.2
10 mm	2.0024 ± 0.003	3.1 ± 0.2
12 mm	2.0026 ± 0.003	4.0 ± 0.2
14 mm	2.0025 ± 0.003	6.8 ± 0.2
16 mm	2.0025 ± 0.003	6.6 ± 0.2

Conclusions

In this work, the physicochemical evolution of soot particles in a laminar remixed flame has been investigated. PSDs measurements coupled to Raman and EPR spectroscopy analysis have been performed. As the residence time in flame increases, the PSD change from unimodal to bimodal. In addition to the particle size, the soot evolution in flame also includes chemical/structural modifications. Indeed, the analysis of the measured Raman spectra shows that the two main peaks, the D and G bands, change in terms of relative intensity and band position. Using standard carbon materials as reference, the position and intensity of D and G were used as an index of a structural change. The results showed an evolution of the soot particles toward a more ordered structure during the growing process. Finally, the EPR data shows the presence and superposition of multiple paramagnetic species characteristics of carbon radicals. In addition, the reported variations in ΔB values indicate different chemical and structural organization properties of soot particles produced collected at different HABs.

References

[1] De Falco, G., Terlizzi, M., Sirignano, M., et al., “Human peripheral blood mononuclear cells (PBMCs) from smokers release higher levels of IL-1-like cytokines after exposure to combustion-generated ultrafine particles”, *Scientific Reports*, 7: 43016, (2017).

[2] Bond, T.C., Doherty, S.J., Fahey, D.W., et al., “Bounding the role of black carbon in the climate system: A scientific assessment”, *Journal of Geophysical Research: Atmospheres*, 118: 5380-5552 (2013).

[3] M. Commodo, G. De Falco, P. Minutolo, A. D'Anna, "Structure and size of soot nanoparticles in laminar premixed flames at different equivalence ratios", *Fuel*, 216: 456-462 (2018).

[4] B. Zhao, Z. Yang, Z. Li, H. Wang, A.S. Wexler, M. Balthasar, M. Kraft, Measurement and numerical simulation of soot particle size distribution functions in a laminar premixed ethylene oxygen-argon flame, *Combust. Flame*, 133: 173–188 (2003).

[5] F. Carbone, M. Attoui, A. Gomez, Challenges of measuring nascent soot in flames as evidenced by high resolution differential mobility analysis, *Aerosol Sci. Tech.*, 50: 740–757 (2016).

[6] Commodo, M., De Falco, G., Bruno, A., Borriello, C., Minutolo, P., D'Anna, A., "Physicochemical evolution of nascent soot particles in a laminar premixed flame: from nucleation to early growth", *Combust. Flame* 162: 3854–3863 (2015).

[7] Yordanov, N.D., Lubenova, S., "Effect of dielectric constants, sample containers dimensions and frequency of magnetic field modulation on the quantitative EPR response", *Analytica Chimica Acta*, 403, 305-313 (2000).

[8] Ferrari, A.C., Robertson, J., "Resonant Raman spectroscopy of disordered, amorphous, and diamondlike carbon", Phys. Rev. B, 64: 075414 (2001).

[9] Sadezky, A., Muckenhuber, H., Grothe, H., Niessner, R., Pöschl U., "Raman microspectroscopy of soot and related carbonaceous materials: Spectral analysis and structural information", *Carbon*, 43: 1731-17422005.

[10] Herdman, J.D., Connelly, B.C., Smooke, et al., "A comparison of Raman signatures and laser-induced incandescence with direct numerical simulation of soot growth in non-premixed ethylene/air flames", *Carbon*, 49, 5298–5311 (2011).

[11] Commodo, M., De Falco, G., Minutolo, P., D'Anna, A., "Structure and size of soot nanoparticles in laminar premixed flames at different equivalence ratios", *Fuel*, 216: 456-462 (2018).

[12] Ferrari and Basko, "Raman spectroscopy as a versatile tool for studying the properties of graphene", *Nature Nanotechnology*, 8:235–246 (2013)

[13] Tuinstra,F. and Koenig, J.L, "Raman spectrum of graphite", *The Journal of chemical physics*, 53:1126-1130 (1970).

[14] Valavanidis, A., Iliopoulos, N., Gotsis, G., Fiotakis, K., "Persistent free radicals, heavy metals and PAHs generated in particulate soot emissions and residue ash from controlled combustion of common types of plastic", *J. Hazar. Mater.*, 156*:* 277-284 (2008).

[15] Herring, P., Khachatryan, L., Lomnicki, S., Dellinger, B., "Paramagnetic centers in particulate formed from the oxidative pyrolysis of 1-methylnaphtalene in the presence of Fe(III)2O3 nanoparticles", *Combust. Flame*, 160: 2996-3003 (2013).

[16] Ingram, D.J.E., "Free radicals as studied by electron spin resonance". London: Butterworths Scientific Publications, 210 (1958).

SESSION V

Internal combustion engines

EXPERIMENTAL INVESTIGATION OF DIFFERENT COMBUSTION MODES IN A SINGLE-CYLINDER DUAL-FUEL CI ENGINE

M. Korkmaz*, B. Jochim, J. Beeckmann, H. Pitsch
m.korkmaz@itv.rwth-aachen.de
*Institute for Combustion Technology, RWTH Aachen University, Templergraben 64, 52056 Aachen, GER.

ABSTRACT

In this study, the effects of different diesel injection strategies on methane / diesel-dual-fuel (DDF) combustion are experimentally investigated. In order to enhance the fundamental understanding of the in-cylinder process, the impact of DDF key control parameters, i.e. injection timing, injection duration, and substitution rate (80 – 90 %) on the combustion phasing and pollutant formation is examined, while engine speed, global equivalence ratio, and injection pressure are held constant. The results reveal regimes that show different dependencies between injection timing of diesel fuel and combustion phasing. It was found that early injection timings lead to reduced NO_x, THC, and soot emissions at simultaneously improved thermal efficiencies. The increase in thermal efficiency has been further investigated by analyzing the engine losses with a 0D thermodynamic engine model, indicating that early injection timings reduce non-ideal combustion losses. To summarize, this study shows that diesel-dual-fuel operation is a promising combustion mode to counteract the drawbacks of compression ignition engine.

INTRODUCTION

Compression ignition (CI) engines have higher efficiencies than spark ignition (SI) engines, caused by high compression ratios and avoided throttling losses [1, 3]. However, the non-premixed combustion process in CI engines can lead to high emissions of nitric oxides (NO_x) and particulate matter (PM). For reduction of those emissions, exhaust-after-treatment devices are required for modern CI engines, which can increase fuel consumption and costs [4, 6]. To reduce the engine-out emissions and the operating costs, while ensuring high levels of overall engine efficiency, advanced combustion strategies are required [3, 4, 6]. One of those strategies is the diesel-dual-fuel (DDF) concept. By employing two fuels with different auto-ignition characteristics, e.g. port fuel injection of a low-reactivity fuel (natural gas) and direct injection of a high-reactivity fuel (diesel), it is possible to reduce the engine-out emissions while keeping high thermal efficiencies.
Depending on the injection timing of the high reactivity fuel, two different

combustion modes – reactivity-controlled compression ignition (RCCI) and dual-fuel (DF) – can occur [7]. In RCCI mode, the diesel fuel is injected very early during the compression stroke and a stratification in reactivity is generated within the combustion chamber. In DF mode, the diesel fuel is injected close to TDC yielding a compression ignition that is used to initiate a propagating flame front like in SI engines [7]. In this work, in-cylinder fuel blending with premixed methane / air-mixture and direct injection of diesel fuel is investigated. Methane is chosen as a supplement to diesel fuel, due to its benefits like higher knock resistance, cleaner combustion, availability, and higher auto-ignition temperature [8].

EXPERIMENTAL SETUP

The experiments in this study were conducted in a modified single-cylinder research engine (SCE) that is based on a DV6 TED4 production engine. For the DDF investigations, the compression ratio is reduced from 17.4:1 to 15.1:1 and the piston bowl geometry is changed from a re-entrant type to a flat piston bowl geometry. The relevant engine and injector parameters are listed in Table 1 and a schematic test bench layout is illustrated in Figure 1.
The air supply is ensured by an external unit consisting of three EATON M62 compressors with inter-coolers. Auxiliary systems for heating or cooling oil, water, air, and fuel are applied to the test bench in order to maintain well-defined conditions. The load is represented by a DC motor (speed-controlled) equipped with a torque meter. For controlling the engine (i.e. intake pressure, exhaust pressure, injection timing, duration, cylinder pressure, etc.), a customized engine control unit (ECU) is used. The exhaust gas was collected using a heated probe and emissions data including NO_x, THC, CO, CO_2, O_2, and soot are metered in the appropriate analyzers. Simultaneous measurements of the air-fuel-ratio (AFR) and the external EGR-rate are performed by the EGR 5230 module. The single cylinder engine is equipped with a piezoelectric pressure transducer (mounted via a glow plug adapter) in conjunction with the charge amplifier. Hereby, reliable thermodynamic data determination is ensured. The analysis of in-cylinder parameters, e.g., indicated mean effective pressure of the high-pressure process ($IMEP_{HP}$), combustion phasing (CA50), and heat release rate (HRR) were evaluated in a thermodynamic real-time analysis module (TRA) for 100 consecutive cycles.

Table 1 Engine and injector specifications.

Quantity	Value	Unit
Displaced volume	390	ccm
Stroke / Bore	88.3 / 75	mm
Compression Ratio	15.1:1	-
Number of Cylinders	1	-
Swirl Number	1.386	-
Nozzle (#/∅)	6/142	-/µm

Figure 1 Schematic of the test bench layout.

Experimental Results

In this section, the experimental results are presented in the following order:

- CA50 as a function of start of energizing (SOE) and substitution rate (SR)
- In-cylinder data for early and late branch

Figure 2 summarizes the results for variations in SOE for SR ranging from 80 to 90 %. Starting at -15 °CA aTDC, the SOE is advanced up to -55 °CA aTDC with an increment of approx. 3 °CA. The engine speed, equivalence ratio, injection pressure, and methane mass flow are held constant. Furthermore, different dependencies between CA50 and SOE as well as between CA50 and the amount of injected diesel fuel are revealed in Figure 2. For describing the process characteristics, e.g. for the 2.2 mg/stroke case (SR= 90 %), the depicted curve is divided into three areas. In the interval from -15 °CA aTDC to -30 °CA aTDC, the local sensitivity is found to be positiv $\frac{\partial CA50}{\partial SOE} > 0$, i.e. an advancement of SOE leads to an advancement of CA50. This area is referred to as late branch and is designated with injection timings closer to TDC. Further advancement of SOE results in $\frac{\partial CA50}{\partial SOE} = 0$, which is referred to as reversal point and characterized by the earliest CA50, i.e. 7 °CA aTDC, that is achieved. For injection timings beyond the reversal point, i.e. earlier than -35 °CA aTDC, the combustion is retarded and a sign-inversion of the local sensitivity, i.e. $\frac{\partial CA50}{\partial SOE} < 0$, is observed, which is referred to as early branch (cf. Figure 2).

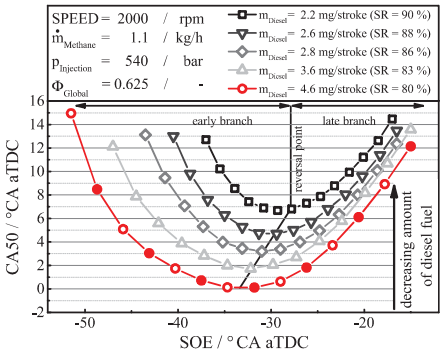

Figure 2 CA50 as function of injection timings and substitution rates, engine speed, equivalence ratio, injection pressure, and methane mass flow are held constant.

The retarding of CA50 on the early branch can be explained by changing ratios of chemical and mixing time scales. For early diesel injection timings more, time is available for premixing prior to ignition due to long ignition delays at lower temperatures and pressures. Hence, leaner local fuel-air mixture are present, which delays the ignition even further [9]. In order to get more detailed understanding of the combustion process, the in-cylinder data, i.e. cylinder pressure and heat release rate (HRR) for the late (left) and early branch (right), is given for a constant SR of 80 % in Figure 3. For the late branch, the injection timings -15 °, -18 °, and -26 °CA aTDC are shown, while for the early branch the injection timings -38 °, -43 °, and -49 °CA aTDC are depicted (filled circles in Figure 2). For both cases the reversal point that occurs at an injection timing of -32 °CA aTDC is included

On the late branch, an increase in combustion pressure is observed for advanced injection timings with a maximum cylinder pressure of 130 bar, that is achieved in the reversal point curve. On the contrary, if the injection timings are advanced for the early branch - starting at the reversal point - the maximum cylinder pressure decreases. Interestingly, the rate of change in pressure is smoother for the early branch compared to the late branch. The decrease in the cylinder peak pressure for the early branch can be explained by the increased ignition delay times caused by leaner mixtures. Longer ignition delay times can shift the combustion towards the expansion stroke [8]. The HRR profiles clearly visualize the different combustion modes. For the late branch, a process similar to conventional diesel combustion, consisting of a rapid pre-mixed combustion close to TDC and a pronounced non-premixed combustion tail, is observed. The characteristic of the HRR can be divided in three parts. First, the ignition of the diesel fuel is observed (peak in the HRR), followed by the ignition of the methane air mixture in the vicinity of the diesel spray (reduced HRR) that finally result in a propagating premixed flame [10]. The contribution of the different parts to the accumulated heat release changes with

varying injection timings, e.g. for an advancement of the late injection timings the peak in HRR increases, while a decrease in the combustion tail is determined. The maximum HRR peak is achieved in the reversal point, while the occurrence of pre-combustion is detected. The pre-combustion is observed for all injection timings on the early branch. Furthermore, with earlier injection timings on the early branch a remarkable change in shape of the HRR is noticed. The previously mentioned characteristic combustion parts are no longer visible, which might be related to the more homogenized diesel-methane-air mixture that result in predominantly premixed flame combustion. The described dependencies are observed for all considered SR in this work. However, the CA50 shifts towards earlier timings with increasing diesel mass and the position of the earliest CA50 moves towards earlier injection timings, which is related to the increased time to promote a lean mixture (cf. Figure 2). To summarize, the indicated efficiency is influenced by CA50 and the SR, while SR has a stronger impact. Highest efficiencies (approx. 48.5 %) are achieved for CA50 close to TDC, on the early branch, and for the lowest SR. A retarding combustion to later CA50 leads to a decrease in the efficiency.

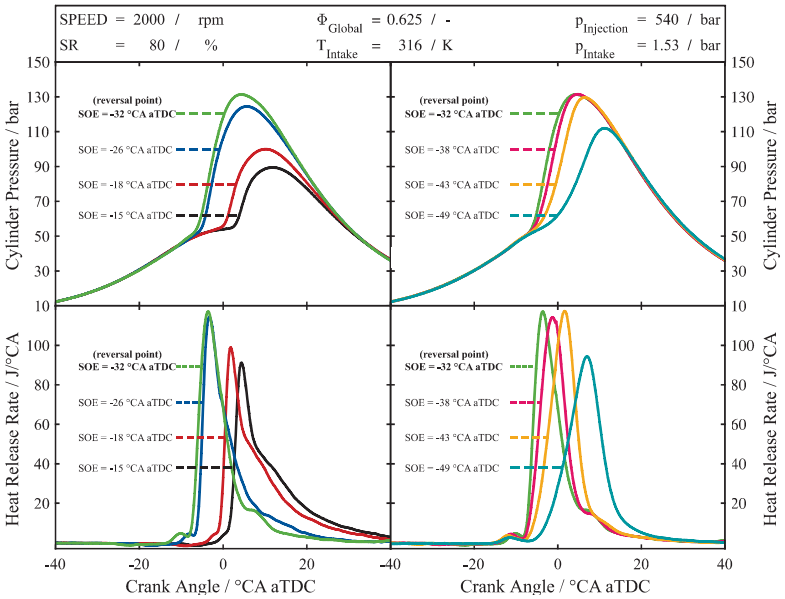

Figure 3 In-cylinder data, i.e. cylinder pressure and HRR, for different injection timings on the late branch (left) and on the early branch (right). Additionally, the reversal point is shown for both injection timings.

Summary and Conclusion

In this work, the effects of different diesel injection strategies on methane / diesel-dual-fuel (DDF) combustion have been experimentally investigated in a compression ignition engine. The engine has been operated with premixed gas / air charge and direct injection of diesel fuel. Variations in injection timings, injected fuel mass, and substitution rates have been conducted and evaluated. The results revealed different dependencies between combustion phasing and the injection timing of the diesel fuel. The in-cylinder pressure and heat release rates have been analyzed in more detail for a single substitution rate. For injection timings close to TDC, a process like the conventional diesel combustion process, consisting of a rapid pre-mixed combustion close to TDC and a pronounced combustion tail, were detected. In contrary, for early injection timings, a remarkable change in the shape of the HRR was noticed, which indicate the combustion of a more homogenized diesel-methane-air mixture with predominantly premixed combustion.
Overall, the highest indicated efficiencies were achieved for early injection timings and low substitution rates.

References

[1] J. B. Heywood, *Internal Combustion Engine Fundementals*, Internat., vol. 21. New York: McGraw-Hill, 1988.
[2] R. Stone, *Introduction to Internal Combustion Engines*. Palgrave, 2012.
[3] J. E. Dec, “Advanced compression-ignition engines - Understanding the in-cylinder processes,” *Proc. Combust. Inst.*, vol. 32 II, no. 2, pp. 2727–2742, 2009.
[4] D. Splitter, M. Wissink, S. Kokjohn, and R. D. Reitz, “Effect of Compression Ratio and Piston Geometry on RCCI Load Limits and Efficiency,” in *SAE International Journal of Engines*, 2012.
[5] D. E. Nieman, A. B. Dempsey, and R. D. Reitz, “Heavy-Duty RCCI Operation Using Natural Gas and Diesel,” *SAE Int. J. Engines*, vol. 5, no. 2, pp. 2012-01–0379, Apr. 2012.
[6] M. Wissink and R. Reitz, “Exploring the Role of Reactivity Gradients in Direct Dual Fuel Stratification,” *SAE Int. J. Engines*, vol. 9, no. 2, pp. 2016-01–0774, Apr. 2016.
[7] M. Boot, *Biofuels from lignocellulosic biomass: innovation beyond bioethanol*. WILEY-VCH Verlag GmbH & Co. KGaA, 2016.
[8] L. Wei and P. Geng, “A review on natural gas/diesel dual fuel combustion, emissions and performance,” *Fuel Process. Technol.*, vol. 142, pp. 264–278, Feb. 2016.
[9] S. Martin, M. Foulonneau, S. Turki, and M. Ihadjadene, “Open Data: Barriers, risks and opportunities,” *Proc. Eur. Conf. e-Government, ECEG*, pp. 301–309, Nov. 2013.
[10] F. Konigsson, P. Stalhammar, and H.-E. \aSngstr\arm, “Combustion Modes in a Diesel-CNG Dual Fuel Engine,” in *SAE Paper*, 2011, no. 2011-01–1962, pp. 2387–2398.

Study of liquid and vapour phases of a GDI spray

A. Montanaro*, L. Allocca*
a.montanaro@im.cnr.it
*Istituto Motori, National Research Council, Italy

Abstract
Gasoline direct injection (GDI) systems have become dominant in passenger cars due to their flexibility in managing and advantages in the fuel economy. With the increasingly stringent emissions regulations and concurrent requirements for enhanced engine thermal efficiency, a comprehensive characterization of the fuel spray behavior has become essential. Characteristics of free and impingement spray fueled with iso-octane were investigated by a hybrid Mie scattering and schlieren optical technique with a direct injection gasoline injector, from the Engine Combustion Network (ECN). The experiments provided the spatial distribution and time-resolved evolution of the free, as well as the post-impingement spray characteristics under various operating conditions. A customized algorithm, able to catch the contours of both liquid and vapour/atomized phase, was used to extract the diffusion and evaporation parameters that characterized the fuel spray. Aim of this study is a detailed understanding of a GDI spray evolution under engine-like conditions, by studying both the liquid and the vapour phases as the ambient and injection conditions vary in a controlled environment.

Intoduction
The greater control on the in-cylinder air-to-fuel ratio gives gasoline direct injection (GDI) engines the possibility to operate at higher compression ratios with respect to port fuel injection (PFI) ones, hence to achieve different charge characteristics depending on the specific load or speed, as the homogeneous mode for stoichiometric operation or stratified mixtures for lean overall operation. Since liquid fuel is directly injected into the combustion chamber, the fuel spray characteristics strongly influence the process of fuel-air mixing and combustion [1]. One important challenge for the GDI technology is that while it is essential to have a more uniform in-cylinder fuel distribution for better preparation of the combustion, the time available for fuel atomization and air mixing is very limited. Therefore, rapid atomization and vaporization of fuel spray are highly desirable. A key feature for better atomization is the fuel injection pressure. A higher injection pressure facilitates a higher degree of fuel atomization and vaporization but, at the same time, create an over-penetrating spray, so optimization is required [2]. Due to the short distance between the injector nozzle and the piston head/cylinder walls, one of the major drawbacks of the GDI systems is the impingement of liquid fuel on the combustion chamber wall that produces an increasing of HC emissions and soot

formation due to the fuel film deposits on the piston head. In this work, both free evolution and spray-wall interaction of a GDI spray were investigated at several operative conditions in a constant volume vessel by two synchronized optical techniques, schlieren for the vapour and Mie scattering for the liquid phase, working in alternative and quasi-simultaneous mode.

Experimental Methods

The tests were performed in a constant volume combustion vessel optically accessible by three quartz windows allowing the admittance to the investigated area. Iso-octane was fueled by a solenoid-activated eight-hole direct-injection gasoline injector from the Engine Combustion Network (ECN) effort on gasoline sprays (Spray G). More details on the adopted injector were reported in [3, 4]. The injector was located on the top of the vessel in a holder including a jacket for the temperature setting of the nozzle nose and connected to a chiller for fluxing a cooling liquid. The fuel was supplied through a common rail system, heated by an electrical resistance and controlled in temperature by a J-type thermocouple located in the rail. Both the injector and the fuel temperature were kept at 363 K. An optical setup of simultaneous Mie scattering and schlieren imaging techniques was applied for the spray-wall interaction test by using a Photron Fastcam SA4 high-speed camera to acquire the liquid/vapour spray at 25,000 fps by a 90 mm lens with f-stop 1-2.8. A homemade algorithm for image-processing was performed using a customized procedure developed under MATLAB platform to treat the batch and to outline the contours of the images. Further specifications on the adopted hybrid optical setup as well as on the image processing procedure were reported in [5].

Results and Discussion

In the first part of the work will be studied the liquid and vapor envelopes of free sprays as function of the injection pressure, the ambient temperature, and the backpressure in the vessel, through the measurements of the axial penetration and cone angle. The changes in the spray structure and the vaporization processes for non- and flash-boiling multi-hole sprays were investigated over a broad range of ambient conditions using Mie scattering and schlieren optical techniques. The tests were carried out at the injection pressure (p_{inj}) of 10.0 MPa and five consecutive measures were acquired per each injection condition for an evaluation of the jet spreads. Fuel spray images were acquired at ambient temperatures (T_{amb}) ranging from 333 to 573 K. Four ambient pressures (N_2), corresponding to densities (ρ_{amb}) of 0.2, 0.5, 1.0, and 3.5 kg/m^3, were investigated for each ambient temperature. Figure 1 summarizes the conditions evaluated. At the fixed time of 720 μs from the start of injection, contours of the liquid and vapor phases of the spray, superimposed to the schlieren images, are shown. Each row reports a different ambient gas density while it is possible to evaluate the ambient temperature effect along the vertical direction. The inner (blue) contours were derived from the Mie scattering images and represent the liquid phase. The outer (red) contours were derived from the schlieren images

and include the liquid core and vapor phase. The effect of the gas density is manifest: reduction of the axial penetration and a slight contraction of the spray cone angle. At the ambient temperature of 333 K, the vapor phase of the edge was slightly larger than that of the liquid phase, which suggests that the vaporization occurred along the perimeter of the spray plume. Flash boiling conditions (last column in Figure 1) occur when the ratio of the ambient to the saturation pressure is lower than 1. The individual spray plumes are observed to collapse toward the spray centerline with vortexes observed all along the spray edges. The spray collapses into a single solid-cone plume with a longer spray tip and a narrowed spray cone. The vapor quantity increases at higher rate with decreasing ambient /saturation pressure ratio during flash boiling conditions, due to a combination of prompt thermodynamic phase transition and an enhanced atomization process [6]. In addition, at reducing of the gas density, the liquid phase captured by Mie scattering is not as dense as that at the non-flash boiling conditions. For flare flash-boiling conditions, the distribution of liquid phase is more uniform and symmetric along the spray axis while the vapor boundary is mostly found in the lower part of the spray plume. Finally, at the highest ambient temperature (573 K), individual plumes are no longer discernible and a strong reduction of the liquid phase is detectable due to the quasi-complete vaporization of the injected mass.

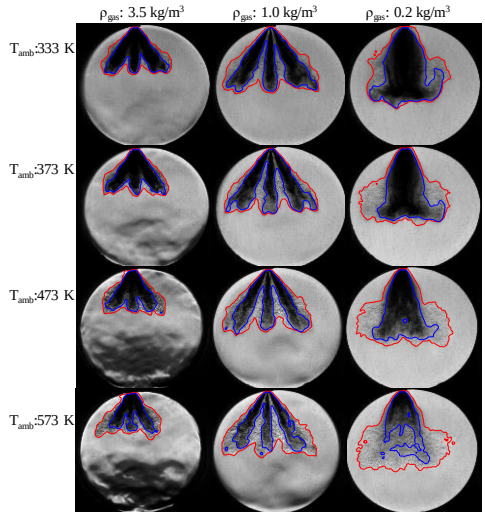

Figure 1. Liquid and vapor envelopes for different ambient conditions

Figure 2 depicts the schlieren axial penetration profiles versus the time after the injection for different gas densities, at the ambient temperature of 373 K. The penetration was extracted by selecting the farthest point of the spray contour along the axis of the nozzle. The profiles show a quite regular growth with the time and a well-scaled behavior with respect to the gas density. They decrease with increasing of the ambient pressure due to the increase of the resultant drag force. The lowest density case provides a higher penetration and thinner sprays. The reason of this is

mainly attributed to the effects of flashing conditions that promote the development of spray collapse, which increase penetration and reduce the total spray angle.

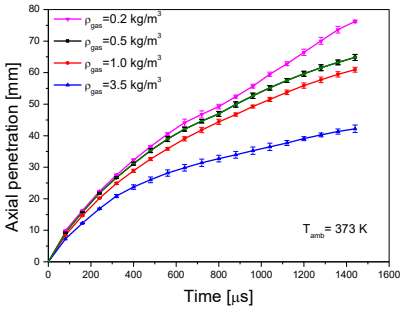

Figure 2. Effect of the gas density on the axial penetration

The spray characterization was completed by studying the interaction of the fuel with a heated flat wall under engine-like conditions, observing both the liquid and the vapour phases as the surface temperature varied (room to 573 K). Characterization of the spray impingement on a wall was made by introducing an 80 mm in diameter aluminum flat plate into the vessel positioned 21 mm downstream the injector tip facing orthogonal to the injector axis. The same hybrid optical setup as well as the images processing procedure described before were used for investigating the liquid phase from Mie scattering images while the corresponding schlieren ones were employed to visualize the vapour phase. The test conditions for the spray-wall interaction experiments are listed in Table 1.

Table 1. Test conditions

Ambient gas temperature [K]	Ambient gas density [kg/m^3]	Ambient gas composition	Ambient gas velocity [m/s]	Fuel injection pressure [MPa]	Fuel	Fuel temperature [K]	Energizing time [μs]	Distance between injector tip to impinging surface [mm]	Wall temperature [K]
293	1.12	100% N_2	0	5, 10, 20	Iso-octane	363	680	21	293, 373, 473, 573

Figure 3 reports an impacting spray sequence at different wall temperatures (from 293 to 573 K) from Mie scattering (on the top) and schlieren (on the bottom) optical technique. The imagines refer at the time step of 480 μs after the impact and injection pressure is 20.0 MPa. For each column the effects of the wall temperature can be evaluated on liquid phase from Mie scattering images and on both liquid and vapour from schlieren ones. The impinging spray images showed an intact liquid core coming from the nozzle and flowing along the surface of the wall. Its maximum elongation in radial direction, as function of the time from the impact, was called "liquid width" and we referred to it as the intact liquid core. The impinged spray height (thickness) is considered as the maximum height in the perpendicular direction with respect to the impinged wall. The liquid core is surrounded by an area composed of fuel vapour mixed to liquid ligaments and droplets more or less finely atomized. It extends itself on the plate beyond the "liquid width" and the "liquid thickness" and we refer to it as "vapor width" and "vapor thickness".

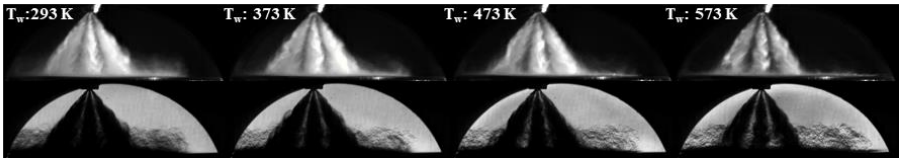

Figure 3. Impacting spray images for different wall temperatures

After the impingement, the fuel develops on the wall in regular and quasi-symmetrical mode on both sides with respect to the injector axis. Vortexes are formed at the jet periphery due to the interaction with the wall and the ambient gas. The slipping/rebounding fluid shows a double structure: denser and impenetrable to the schlieren light beam close to the wall, indicative of predominance of a dense liquid phase, lighter and almost transparent upper the plate, symptomatic of vapour generated by the heating with the wall. The increment of the wall temperature has an effect on both the liquid, with much dispersed droplets, and the vapour phases. It determines a shift of the impact regime from deposition towards rebound or thermal break-up, thus leading to enhanced vaporization. The growth of the mixed area, overhanging the liquid portion (dark part immediately on the wall), appears evident when the temperature increases. More, the higher is the temperature of the wall the stronger the characteristic vortexes of the vapor phase appear. The fuel vaporization is encouraged mainly by two factors: the impact that contributes to the breaking of the droplets thus facilitating the evaporation process and the heat transferred to the droplets from the wall giving a contribution to the latent heat of vaporization and determining the secondary evaporation of the droplets. As consequence of the vaporization process, a strong reduction of the liquid thickness comes out by looking at the Mie scattering images when increasing the wall temperature from room value to 573 K. Figure 4 depicts the liquid width (on the left) and thickness (on the right) profiles versus time as function of different wall temperatures at injection pressure of 20.0 MPa.

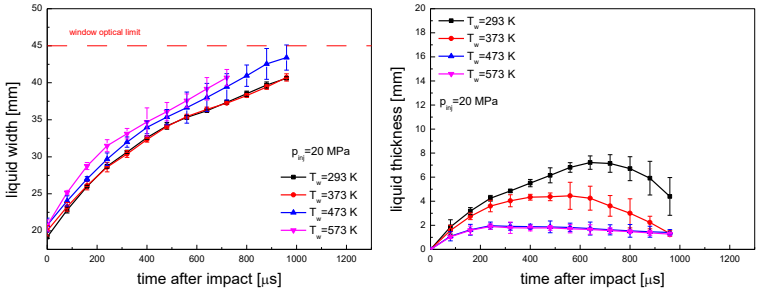

Figure 4. Liquid width and thickness profiles at different wall temperatures

The increment of the wall temperature from 293 to 373 K doesn't produce any effect on liquid width in fact the curves (black and red respectively) overlap for all the entire injection process. For temperatures higher than vaporization value of the iso-

octane (372 K), the curves show a well-scaled trend of liquid length with respect the wall temperature, the higher is the temperature and the faster the fuel slipping results. Vice versa, the liquid thickness shows an inverse trend with respect the wall temperature with a strongest rebound at room value (black line). At wall temperatures of 473 and 573 K the trend is still of increasing versus the time from the impact only up to 200 μs with a quick tendency to saturate towards a stable value, around 2 mm, indicating a faster fuel evaporation.

Conclusions

Mie-scattering and schlieren images techniques were coupled in a quasi-simultaneous timing for studying both the liquid and the vapour phases from a multi-hole GDI injector. The experiments provided the spatial distribution and time-resolved evolution of the free, as well as the post-impingement spray characteristics under various operating conditions. The effects of both ambient temperature and density were evaluated on the free spray morphology under conventional and flashing conditions. More, the spray-wall interaction was studied and the separate behaviour of both liquid and vapour phases was investigated as function of different wall temperatures. The combined optical technique has proven to be well suitable to capture the peculiarities of the diverse thermodynamic phases of the fuel and sensitive to the governing parameters. Finally, the data generated will be used to support the validation of spray-wall interaction models and to support the combustion system developments. For future works, wall-film characteristics, wall temperature and heat flux measurements in the spray-wall test will be further investigated.

References

[1] Parrish, S., "Evaluation of Liquid and Vapor Penetration of Sprays from a Multi-Hole Gasoline Fuel Injector Operating Under Engine-Like Conditions," SAE Int. J. Engines 7(2):2014, doi:10.4271/2014-01-1409.

[2] Zhao, F., Lai, M.C., Harrington, D.L., “Automotive Spark-Ignited Direct-Injection Gasoline Engines,” Progress in Energy Combustion Science, vol. 25, no. 5, pp. 437-562, 1999

[3] https://ecn.sandia.gov/gasoline-spray-combustion/

[4] Moulai, M., Grover, R., Parrish, S., and Schmidt, D., "Internal and Near-Nozzle Flow in a Multi-Hole Gasoline Injector Under Flashing and Non-Flashing Conditions," SAE Technical Paper 2015-01-0944, 2015, doi:10.4271/2015-01-0944

[5] Montanaro, A., Allocca, L., and Lazzaro, M., "Iso-Octane Spray from a GDI Multi-Hole Injector under Non- and Flash Boiling Conditions," SAE Technical Paper 2017-01-2319, 2017, https://doi.org/10.4271/2017-01-2319.

[6] Zeng W., Xu M., Zhang G., Zhang Y., Cleary David J., “Atomization and Vaporization for Flash-boiling Multi-Hole Sprays with Alcohol Fuels”, Fuel 95 (2012) 287–297

Particle Formation and Emissions from Dual Fueled CNG DI and Gasoline PFI SI Research Engine

F. Catapano, S. Di Iorio, P. Sementa, B. M. Vaglieco
Istituto Motori CNR
b.m.vaglieco@im.cnr.it

Abstract
Compressed natural gas (CNG) is considered as cleaner fuel compared to gasoline and has emerged as an alternative transport fuel in view of its abundant availability. CNG has been implemented in transport sector globally. PM and NO_x emissions were reduced, nevertheless, recent studies highlighted the presence of ultrafine particle emissions at the exhaust. The present study deals of the effect of CNG on particle formation and emissions when it was direct injected and when it was dual fueled with gasoline. In this latter case, the CNG was direct injected and the gasoline port fuel injected. Measurements were performed in cylinder and at the exhaust of a single cylinder SI research engine similar to modern commercial engine for passenger cars. The in-cylinder formation process of particles was evaluated by high spatial and temporal resolution optical measurements based on 2D chemiluminescence measurements from UV to visible. Two "ad hoc" filters, at 310 and 431 nm, were used to detect two representative radical species that influence the in-cylinder pollutants formation and oxidation. In particular, OH* and CH* spatial distribution were measurement to evaluate the local air fuel ratio in the cylinder too. Simultaneously, the exhaust emissions were characterized and the particle size distribution function was measured by an Engine Exhaust Particle Sizer in the range from 5.6 to 560 nm. The local air fuel ratio spatial distribution was strongly correlated to oxidation and particle emissions.

Introduction
Currently, the possible fuel depletion as well as the growing concerns on environmental issues prompt to the use of more environmentally friendly fuel for urban vehicles. The use of gaseous fuels can be considered a right choice also as transition for next future of internal combustion engines and the retrofitting of old cars too as an alternative to reduce air pollutant emissions in congested towns. The use of methane was encouraged over time especially in countries where there was lack fossil resource or where there was abundance natural gas resources. Recently, several studies on greenhouse gas intensity of natural gas, whose main component is methane, have shown that natural gas reduces GHG emissions from passenger cars on a Well-to-Wheel (WtW) basis by 23% compared with petrol and by 7% compared with diesel. Moreover, on the heavy-duty application, benefits compared to diesel are of 16% for compressed natural gas (CNG) and up to 15% for liquid natural gas (LNG). Also in the maritime sector, overall WtW benefits are up to

21% compared to conventional Heavy-Fuel-Oil (HFO) fuels [1]. The CNG properties make it suitable for the use in the spark ignition engines. It has a high-octane number, and hence high auto-ignition temperature and anti-knocking property. Then, spark ignition engines fueled with CNG can run at higher compression ratios, thus producing higher thermal efficiencies. It mixes uniformly with air, resulting in efficient combustion and a substantial reduction of the emissions at the exhaust [2-4]. On the other hand, the slow burning velocity, the poor lean-burn capability and the air displacement, lead to large cycle-by-cycle variations, lower engine power output and large fuel consumption [5].

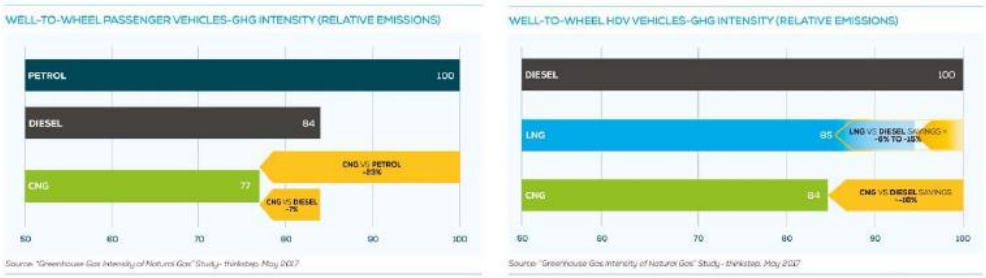

Figure 1-WTW Passenger vehicle relative emission using gaseous and fossil fuels [1]

The combustion of gaseous fuels is cleaner than liquid fuels. It can reduce the NO_x and PM, several studies indicated that particle concentration levels emitted from CNG fueled engines are lower than gasoline the port fuel injection (PFI) SI engines [5, 6], as well as contributing to the reduction of CO_2 emissions, due to the low carbon-to-hydrogen ratio. Nevertheless, recent studies highlighted the presence of ultrafine particle at the exhaust of CNG engines. To overcome these phenomena, different injection strategies based on simultaneous use of CNG direct injected (DI) and gasoline in the duct were proposed and evaluated. Moreover, the phenomena that induced their formation were evaluated by simultaneous in-cylinder optical measurements and conventional one.

Experimental Apparatus and Procedures

An optically accessible four-valve single cylinder research engine (Figure 2) was used. The engine was equipped with the prototype GDI cylinder head of a 250 cc engine widely used in Europe, it is provided with a hole between the two intake valves for the direct injection system. The head is characterized by pent-roof chamber engine mounted on an elongated piston. The engine reached a maximum speed of 5000 rpm. It was modified to run fueled with CNG and gasoline both simultaneously (Dual Fuel configuration) and not. The CNG was supplied by a pressurized bottle using a pressure regulators typically set to 8 bar directly in to the combustion chamber. A Synerject strata injector in house modified was used for the gaseous fuel. For the liquid fuel injection in the intake port was used a commercial injector with 3 holes. It is a commercial injector for the real reference

engine. For the DI was used a Magneti Marelli prototypal 6-holes injector. Further details on the experimental procedure can be retrieved in [5,6].
The head of engine had a centrally located spark plug and a quartz pressure transducer flush-installed in the combustion chamber to measure the in-cylinder pressure. A crankshaft encoder with a resolution of 0.1 crank angle degree (CAD) was used to trigger the pressure measurements. The in-cylinder pressure, the rate of chemical energy release and the related parameters were evaluated on an individual cycle basis and/or averaged on 400 cycles [5, 6].
The design of this engine utilizes a classic extended piston with piston-crown window similar to that originally introduced by Bowditch in 1961 [7]. This is of relatively high importance for this study, given that the design did not allow any lubricant droplets to enter the combustion chamber (i.e. the optically accessible part of the engine features self-lubricating Teflon-bronze piston rings); therefore, no contribution that could have originated from the oil interfere with the formation of particulate.

Optical Apparatus

Natural flame emission passed through the sapphire window fitted in the piston crown and was reflected toward the optical detection assembly by an UV-enhanced mirror inclined at 45°. The combustion process was followed by means of the 2D UV-visible digital imaging techniques. A CCD camera with sensitivity only in the visible range was used. It was equipped with a 50 mm focal length, f/3.8 Nikon lens. Moreover, CH* and OH* measurements were performed by using a dichroic filter, two band pass filters and two ICCD cameras equipped with a F/3.8 UV Nikon objectives with 105 mm focal length. The dichroic filter is a pass-through of the UV light from 230 to 360 nm the luminosity was forwarded in the direction of the first ICCD by means a 310 nm band pass filter to detect the OH* luminosity; at the same time the light above 360 nm is reflected towards the second ICCD camera. In this case a band pass filter centred at 431 nm was used to detect the CH* luminosity. The ICCD has an array size of 1024x1024 pixels with a pixel size of 19x19 μm^2 and 16-bit dynamic range digitization at 100 kHz. More details are reported in ref. [5.6].

Procedures

Two injection systems were used both simultaneously and separately to perform the PFI, the DI and the dual fuel (DF). In PFI configuration, the engine was fueled with gasoline (GPFI). In DI configuration, the engine was fueled with gasoline (GDI) and CNG (CNGDI). For DF configuration, the gasoline and CNG were separately injected. The gasoline was port fuel injected and the CNG direct injected (DF). The DF ratio was defined on energy basis. The 20% of the total energy was given by the combustion of port injected gasoline. The remaining 80% of the energy supply was due to the combustion of the CNG. More details are reported in ref. [5.6].The engine was equipped with a programmable system for the injection

and ignition management. In particular, the duration of injection (DOI) was properly set to obtain stoichiometric equivalence ratio and lambda 1.3. The start of spark (SOS) and the end of injection (EOI) was chosen to optimize the combustion considering the coefficient of variation of the indicated mean effective pressure (IMEP) and the exhaust emissions. Moreover, for DI the EOI was properly chosen to reproduce a stratified combustion. The gasoline injection pressure was fixed at 100 bar for DI and 3.5 bar for PFI, the injection pressure was 8 bar for the CNG.
Engine was operated at 2000 rpm-full load, chosen as representative of the urban driving condition in the New European Driving Cycle (NEDC). All the tests were carried out at stoichiometric and lean conditions. The air fuel ratio was measured by a linear lambda sensor at exhaust.

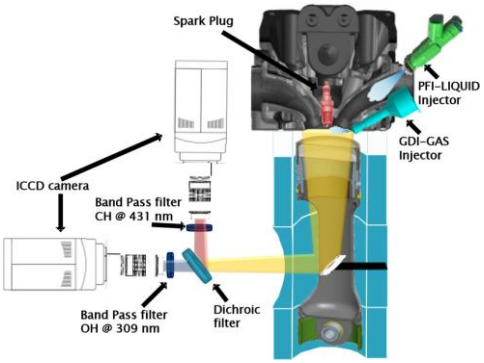

Figure 2. Experimental apparatus for optical investigations and a detail of head view with the injectors used

Exhaust Measurements

An opacimeter was used for evaluating the exhaust gas opacity. Particle number and size distributions were measured with an Engine Exhaust Particle Sizer 3090 by electrical mobility methods. It measures particle sizes from 5.6 to 560 nm with a sizing resolution of 32 channels. Before entering the EEPS, the sample of exhaust gas was taken by a 1.5 m long line heated at 150°C and it was diluted with the Dekati® Engine Exhaust Diluter, a Particle Measurement Program compliant conditioning system. Steady-state measurements of CO, CO_2, UHC and NO_x were detected. Moreover, Methane HC emissions were measured with a HP 5890 gas chromatography.

Experimental Results

The effect of dual fueling on engine combustion and performance were evaluated by the indicated data and the IMEP at two different air-fuel ratios. Figure 3 shows the in cylinder pressure and rate of heat release (ROHR) for all the injection strategies and fuels in stoichiometric condition.

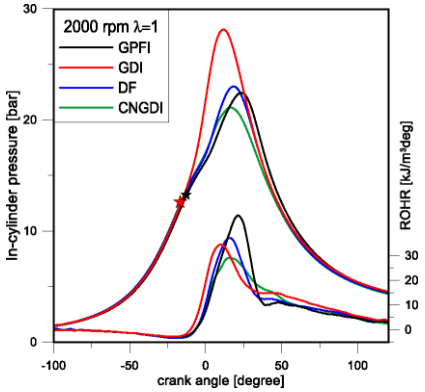

Figure 3. In-cylinder pressure and rate of heat release for all injection strategies at 2000 rpm in stoichiometric condition

The GDI configuration has the highest in-cylinder pressure than the other configurations. This can be ascribed to the stratification of the charge that results in a faster combustion that evolves closer to the TDC lowering the heat transfer through the cylinder wall so increasing the in-cylinder pressure. The positive effect of the charge stratification is less evident for CNGDI, for which the pressure curve was lower and the combustion is slower than GPFI as well. In this case, the beneficial effect of the stratification is counteracted by the CNG properties such as the slow flame propagation and the higher diffusivity. When CNG was dual fueled, the pressure was higher and more advanced than CNGDI and GPFI, indicating that the gasoline improves the CNG combustion better exploiting all the advantages of the charge stratification. Nonetheless, for CNGDI, despite the same SOS the combustion evolution is closer to that of GPFI, suggesting that the better charge stratification of GDI plays an important role, resulting in an improved kernel formation and flame propagation as observed from optical measurements too [6]. From the analysis of the ROHR can be distinguished a fast main combustion phase subsequently the spark and a much slower combustion phase, occurring late in the expansion stroke. Moreover, the flame front sweeps the combustion chamber, burning the air/fuel mixture in a quite premixed combustion [6]. At the end of the main combustion phase, the ROHR shows a diffusive combustion phase. The charge stratification of the GDI is also evident looking at the sharp increase of the ROHR during the first combustion phase. At the same time, the more evident diffusive phase, ascribable to the combustion of the liquid fuel, evidenced a bad evaporation and the fuel impingement that are typical issues of the charge stratification. CNGDI is characterized by a slow combustion. When dual fueled, the combustion is accelerated, as evidenced by the sharper ROHR, even if it is slower than the GDI. Nevertheless, the diffusive phase is quite lower with respect to GDI configuration because the direct injected fuel is the CNG leading to the reduction of the typical drawbacks of the charge stratification evidenced in the GDI. Moreover, despite the same ignition timing of GPFI, the DF combustion is

slightly advanced suggesting a more favorable kernel formation. This can be due to the combined effect of the combustion of gasoline as well as the ignition of gaseous fuel in the immediate vicinity of the combustion center of the gasoline combustion as observed in a previous paper [5, 6].

Figure 4 depicts the particle size distribution functions (PSDF) for all the engine injection configurations. For GDI the PSDF shows a strong accumulation mode centered around 80 nm in both stoichiometric and lean conditions. GPFI shows a bimodal size distribution where the weight of the nucleation is stronger in stoichiometric condition and comparable to the accumulation mode in lean condition. The accumulation mode is lower of about 1 order of magnitude with respect to the GDI and it is shifted towards smaller diameter in both stoichiometric and lean conditions. For CNGDI, the PSDF has a strong nucleation mode peaked around 10nm in both the operating conditions. A weak accumulation mode is observed. It is interesting noting that in lean condition, the emissions of particle smaller than 10 nm are larger than that in GDI. For DF, the PSDF is quite similar to that of GPFI. A strong nucleation mode can be observed both in stoichiometric and lean conditions. Nevertheless, for both the stoichiometric and lean conditions, the DF has a lower particle number concentration than GPFI and the curve is shifted toward smaller diameter. Moreover, a slightly larger emission of particles smaller than 10 nm with respect to GPFI is observed in lean condition.

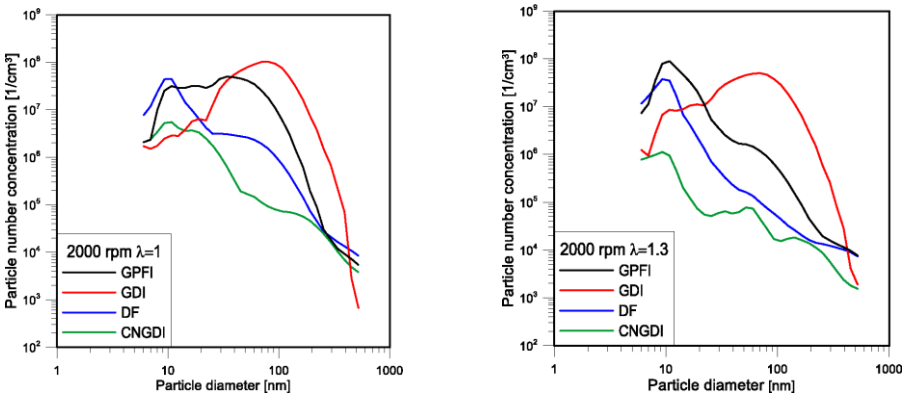

Figure 4. Particle size distribution functions for all the injection configurations in stoichiometric (left) and lean (right) condition.

For a comprehensive analysis of the effect of CNG and dual fuel on particle emissions, the combustion process was analysed by in cylinder optical techniques for detailing the formation and oxidation processes occurring in the combustion chamber with high spatial and temporal resolution. The optical analysis allows valuable information not only on combustion evolution but also on pollutant formation.

To better analyse the combustion process, natural flame chemiluminescence was

detected by 2D-digital imaging measurements performed in the visible range. Measurements in the UV range were carried out as well. In particular, narrow band pass filters at wavelengths typical of OH* (λ=310 nm) and CH* (λ=431 nm), respectively, were used. As known by literature, OH* is the main oxidant of soot and CH* is a flame front marker because it exists only in a narrow layer of the reaction zone taking part in the decomposition process of the fuel molecules in hydrocarbon flames. Furthermore, OH* and CH* can provide information also on the equivalence ratio. The local AFR can be evaluated from OH* and CH* chemiluminescence emissions from the following empirical equation for liquid and gaseous fuels [5]:

$$AFR=0.894-0.26 \ln (I_{OH}/I_{CH} -0.597) \quad (1)$$

$$AFR=0.599-0.314 \ln (I_{OH}/I_{CH} -0.344) \quad (2)$$

where I=Emission Intensity of OH* and CH* measured at ambient pressure.
Figure 5 depicts the images of the emissions of the natural flame, of the OH* and CH* radicals detected during the combustion process in stoichiometric condition, and the correspondent lambda spatial distribution for the GPFI, CNGDI and DF configurations.

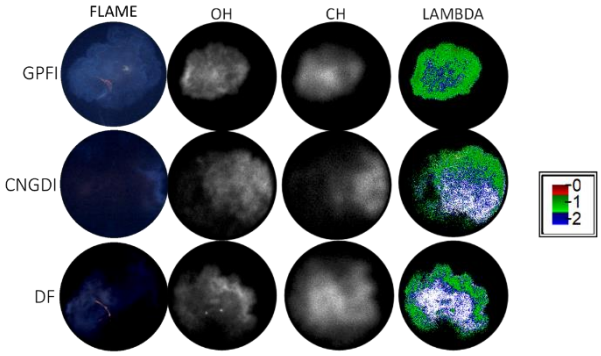

Figure 5. Flame, OH* and CH* emissions and Lambda spatial distribution at typical crank angles of the combustion process in stoichiometric condition

In GPFI the presence of a diffusive flame, characterized by a yellow-orange flame mainly due to thermal radiation of hot soot particles [5-7], in correspondence of the intake valve is well recognizable by the natural flame chemiluminescence. In PFISI engines, in fact, despite the high temperature of the valves, liquid fuel can deposit on the valves surface during the fuel injection forming a liquid film that burns in a diffusive way. In DF, a weak flame is recognizable close to the intake valve. The lower luminosity is due to the lower amount of gasoline and indicates a lower soot production. For GNGDI, weak luminous and not localized flames, where nuclei soot particle is formed, are observed. These can be due to the presence of rich zone likely due to the presence of lube oil passing through the valve stem seals. In real engines, it is still not entirely clear which mechanism is the main contributor to oil consumption due to the complexity of the phenomenon. It is controlled by engine

architecture and by the design of four salient escape routes: the piston rings, the turbocharger seals, the valve stem seals, and the positive crankcase ventilation system. In the optical engine, unlubricated Teflon-Bronze rings are used then lube oil may reach the combustion chamber only by the valve stem seals. It is important noting that, looking at the particle emissions, a small leak through the exhaust valve generates more particulate matter emissions than a far larger leak through the inlet valve, simply because, in the former case the oil is oxidized less effectively [6].
The chemiluminescence emission @ 431 nm is lower with respect to the signal at 310 nm. Nevertheless, they show a similar behaviour.
The analysis of the local lambda values shows for CNGDI and DF a more heterogeneous mixture. The central region of the flame, in fact, rapidly becomes lean indicating a fast decomposition of the fuel molecules. In DF combustion, the turbulence due to the gas direct injection coupled with the lower carbon content of the gas enhance the gasoline vaporization reducing the flame rich region so reducing the formation of soot. At the same time, the larger presence of lean region results in an improved oxidation process.

Conclusions

The CNG-gasoline dual fuel combustion was characterized in a SI 4-stroke small engine. The thermodynamic analysis suggests that under dual fuel operating mode the quality of the gaseous fuel combustion was improved by the liquid fuel supplementary addition. Gasoline favors the propagation of the flame front, resulting in an improvement of the combustion.

Moreover, the beneficial effect of CNG in terms of particle emissions reduction is ascribable to the low particle formation due to the gaseous properties, such as no C-C bound, probably most of the particles measured for CNGDI condition are due to leaking of the lubricating oil through the valves. When the CNG is dual fuelled with gasoline the particle emissions are quite lower than GPFI because of the lower contribution of gasoline injected in the intake duct. DF weak flame is recognizable close to the intake valve. The lower luminosity can be ascribed to the lower amount of gasoline and indicates a lower soot production.
The combined analysis of optical and particle exhaust measurements highlights that the use of direct injection of CNG both in the conventional and the dual fuel configuration, in which gasoline was injected in the intake duct, leads to soot formation and particle emissions. Nevertheless, the mean diameter detected at exhaust is smaller than 20 nm. The use of “ad-hoc” after treatment should be carried out to better evaluate the dual-fuel engine efficiency.

References

1. http://ngvemissionsstudy.eu/
2. Korakianitis, T., Namasivayam, A. M. and Crookes, R. J. (2011). Natural-gas fueled spark-ignition (SI) and compression-ignition (CI) engine performance

and emissions. Prog. Energ. Combust., 37, 89-112.
3. Aslam, M.U., Masjuki, H.H., Kalam, M.A., Abdesselam, H., Mahlia, T.M.I., Amalina, M.A.,(2006). An experimental investigation of CNG as an alternative fuel for a retrofitted gasoline vehicle. Fuel 85, 717–724.
4. Huang, X., Wang, Y. Xing, Z., Du, K. (2016) Emission factors of air pollutants from CNG-gasoline bi-fuel vehicles: Part II. CO, HC and NOx Science of the Total Environment, 565 698–705.
5. Di Iorio, S., Sementa, P., and Vaglieco, B., M., (2013) Experimental Investigation of a Methane-Gasoline Dual-Fuel Combustion in a Small Displacement Optical Engine, SAE Technical Paper 2013-24-0046, 2013, doi:10.4271/2013-24-0046.
6. Catapano, F., Di Iorio, S., Sementa, P., and Vaglieco, B., M., (2017) "Particle Formation and Emissions in an Optical Small Displacement SI Engine Dual Fueled with CNG DI and Gasoline PFI," SAE Technical Paper 2017-24-0092, 2017, doi:10.4271/2017-24-0092.
7. Ladommatos, N. and Zhao, H., "Engine Combustion Instrumentation and Diagnostics," (Warrendale, SAE International, 2001), doi:10.4271/R-264, 2001.

MODELING VIRTUAL FUELS FOR HCCI-LIKE INTERNAL COMBUSTION ENGINES DEVELOPMENT

Paolo Miceli*, Debora Fino*, Marco Chiodi**
paolo.miceli@polito.it
*Politecnico di Torino, Corso Duca degli Abruzzi 24, 10129 Torino
**FKFS, Pfaffenwaldring 12, 70569 Stuttgart

Abstract
Efficiency and cleanliness of internal combustion engines can be easily improved with better *after-design agents* like cleaner lubricants and fuels, tribo-coatings and innovative materials or complex exhaust after-treatment systems, but it is above all a matter of well-planned design from the beginning of engine development itself.
The rush for the *zero-emission vehicle* sets on the table the old chimaera of automotive engineers: the HCCI combustion engine. This particular engine has very high efficiency and produces neither PM nor NOx but, however, for its development, it cannot be simulated trustfully and completely with current virtual tools yet (because of the complexity of that kind of combustion) nor tested on real benches (because of the that kind of combustion is still hard to control).
Supported by *QuickSim©*, a Virtual Engine (VE) used in FKFS/IVK for series/motorsport/educational purposes, a better description of the combustion characteristics of gasoline surrogates has been developed by means of Virtual Reactors (VR), as far as flame speed and ignition point are concerned, and the results are presented in this work, as extract from the PhD final work of the author. [1]
This way, innovative combustions can be investigated and developed involving also unconventional fuels and following operations at real test benches where slight differences among traditional gasolines do affect tests results.

Background
All possible strategies aimed to improve the efficiency of an engine would increase its specific power output and, above all, automatically lower its specific pollutant emissions. These strategies can involve friction and vibrations reduction, like less/lighter moving components and better lubrication, better *breathing* and higher compression ratios, faster combustions, particular scavenging timings, smart thermal managements, hybridization and so on. [2]
Nowadays, efficiency means cleanliness rather than performances and, besides the aforementioned technologies, innovative working cycles are arising, like those characterized by Low Temperature Combustion (LTC), which allows cleaner combustions, in a generic engine, in lean operation modes.

There are indeed particular engine designs, working with LTC principles, called Homogeneous Charge Compression Ignition (HCCI) [3], where a homogenous mixture – as in gasoline-like Spark Ignited cycles (SI) - is compressed and induced to auto-ignition – as in Diesel Compression Ignition cycle (CI).
In HCCI operating mode, as far as emission are concerned, the mixture is too lean to allow soot formation and the temperatures are not sufficiently high to produce nitrogen oxides. This way, emissions of the most harmful engine pollutants are limited (or avoided) at the root.

From a thermodynamics point of view, rapid homogenous combustions, lean mixtures and high compression ratios lead to very high overall efficiencies. [4]
However, working with HCCI cycles is not that easy, because a lean mixture is usually hotter than a rich one (no heat spent by unburned fuel vaporizing): to keep combustion temperature under control, the mixture has to be homogeneous in the whole chamber. Furthermore, the control of fuel auto-ignition and flame propagation are crucial to master these applications.

These last two properties, characteristic of a given fuel, are the reason of the absence of HCCI-like engines on the market, despite their clear advantages. In fact, the development of all those technologies aimed to control auto-ignition and flame propagation (or flame speed) pass thorough deep investigations and experimentation on engine proof stands but the effects of uncontrolled combustions may lead to tragic failures, with dramatic increase of development costs and efforts.
More than ever, VE gained a central role in HCCI-like engines development, exploring all possible design variations with no worries about expensive prototypes and rig damaging.

QuickSim©, a virtual engine developed in FKFS, is a well-known tool for internal combustion engines development, used since years for series, motorsport and educational purposes that is already been involved in successful research activities about HCCI combustion. [5]
Being HCCI combustion strongly fuel-dependent, the most important models in these kinds of simulations are those regarding flame speed, auto-ignition timings and thermodynamics properties of fuels. The next question about HCCI-like combustion is how gasoline/fuel recipe may help or hinder these applications.

The current set of fuel models equipping QuickSim© is not suitable to investigate unconventional fuels neither to discriminate among gasoline recipes differences so this would be a nice occasion to develop new and better gasoline surrogates with this software. This way, this VE could follow, and even predict, the real combustion behavior of different fuels even in HCCI modes, which may differ only for slight changes in their recipes, that can be noticed at the proof stand and discriminate if a test is successful or not.

Modeling approach

Actually, QuickSim© uses a smart mechanism that may discretely trigger gasoline ignition [6]. A *generic* gasoline. For the Flame Speed description, QuickSim© uses a model proposed by Gülder in 1984, about a generic RON90 gasoline. [7]
To overcome these limitations, two VR has been set with CANTERA© in order to evaluate the behavior of gasoline surrogates ranging temperature, lambda, pressure and dilution (indicated as *cold EGR*). [8][9][10]
Auto-ignition VR is set as a 0-D constant volume bomb reactor. Flame Speed VR is a 1-D, grid-based reactor, which is of course time-dependent and requires way more calculation times then the other VR.

Selection of a suitable thermokinetics mechanism is as crucial as the design of the VE. The requirements are the following: a good set of mid-temperature reactions, a high number of low-temperature ones, the presence of all the chemical species which the surrogates are made of and, of course, a good balance between description and calculation times needed; the mechanism proposed by Fandakov (2017) has been chosen. [11]

Auto-ignition

The recipe of a gasoline however, is more complicated than PRF/TRF surrogates (Primary Reference Fuel and Toluene Reference Fuel, respectively) and this limitation is evident more than ever in HCCI-like development where, at the real proof stand, light differences between several fuels can discriminate between successful tests or tragic failures.
These applications need new fuels virtual surrogates, capable of a better description than PRF/TRF but, after all, still simple enough to be evaluated by VR in acceptable calculation times.

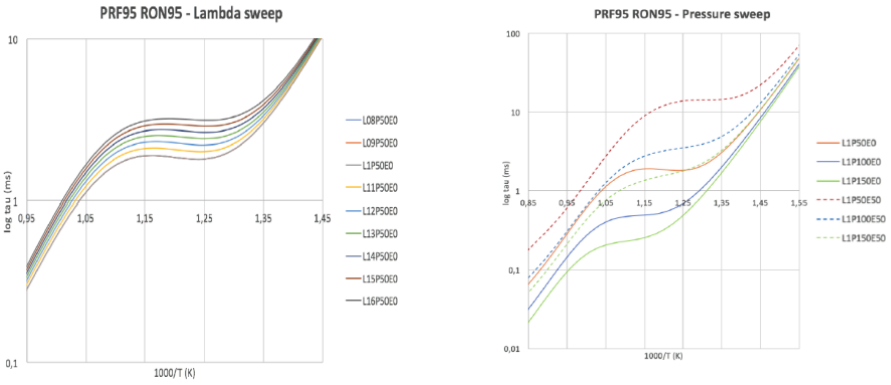

Figure 1. The effects of lambda and pressure sweeps on auto-ignition timings of PRF95. L is lambda, P is pressure (bar) and E is cold EGR (%). [1]

Comparing several recipes of real gasolines, six families of components have been recognized and, for each of them, their effects and main representatives have been screened until a new gasoline surrogate, made by six components, has been proposed and evaluated in the VR (see **Table 1**). In Figure 2 the behaviors of traditional surrogates, like PRF and TRF, and the new proposed surrogate, *MRF (Modeling Reference Fuel)*, are depicted. Of course, the *recipe* of MRF is closer than the others to the real fuel chosen as reference, despite all surrogates have the same RON 95 basis.

Table 1. Comparison between traditional RON surrogates (PRF), ultra-RON surrogates (TRF) and the proposed, more descriptive, six-components gasoline surrogate (MRF), suitable for unconventional combustion modeling. [1]

	PRF	**TRF**	**MRF**
Paraffines	n-Heptane	n-Heptane	n-Heptane
Isoparaffines	iso-Octane	iso-Octane	iso-Octane
Aromatics	-	Toluene	Toluene
Naphtenes	-	-	cycle-Hexane
Olefines	-	-	iso-Octene
Oxygenated	-	-	Ethanol

The Negative Temperature Coefficient (NTC) region is still present in MRF but less wide and, consequently, less decisive in affecting combustion control and behavior. In general, but particularly in HCCI applications, an accurate description of NTC phenomena is crucial in combustion control and the traditional fuel surrogates show NTC regions wider than they actually are, adding uncertainty to VE's control.

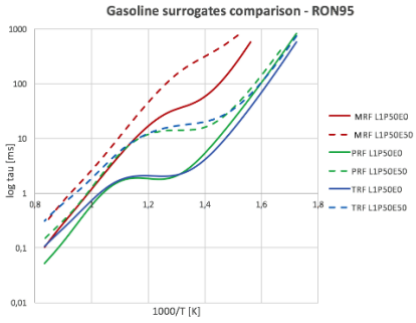

Figure 2. Comparison between auto-ignition profile of PRF, TRF and the new six-components gasoline surrogate MRF, all RON95 grade; with (dashed) and without (solid) cold EGR effect, cause of auto-ignition delay. L is lambda, P is pressure (bar) and E is cold EGR (%) [1]

Flame speed

Comparing CANTERA©'s VR and old Gülder's flame speeds, it seems that Gülder offers higher peak values (see Figure 3); this is not acceptable in HCCI investigations since high flame speeds could be source of misinterpretations in QuickSim© and lead to inexistent knocking and detonation phenomena. Moreover, Gülder is not able to calculate the flame speed when EGR is over about 40%, limiting the opportunities of investigation. The flame speed by Gülder is not suitable for HCCI unconventional combustions. In turn, the VR approach offers lower peak temperatures, the possibility to range operating conditions to support VE operations, the capability to blend gasolines with ethanol and water, and it well fits the initial request from QuickSim© for a fast, reliable and flexible flame speed model.

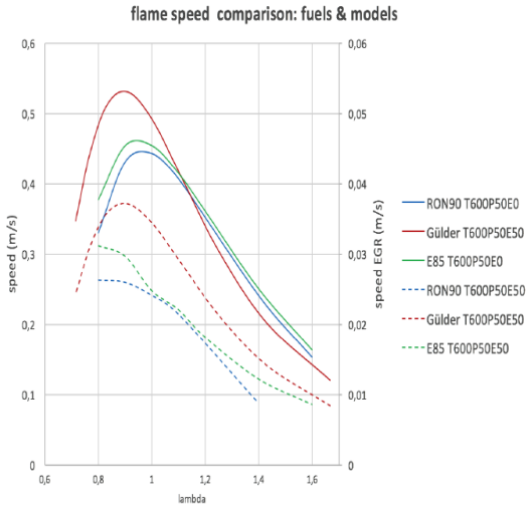

Figure 3. Differences of flame speed between TRF40, E85-TRF40 and Gülder RON90 gasoline. Of course, TRF40 is as knocking resistant as PRF90. L is lambda, P is pressure (bar) and E is cold EGR (%). [1]

Outlook

Two virtual reactors for auto-ignition (0D) and flame speed (1D), coupled with a smart thermokinetics mechanism, have been set with CANTERA©, allowing the development of a new six-components gasoline surrogate, able in turn to retrace real fuels more precisely than traditional three components surrogates, like PRF and TRF. Data collecting in 4-D look-up tables and VE implementation is still on going, but the study about HCCI combustion (and even the ideal HCCI fuel) has already led to encouraging results, achieving engine settings for a regular and controlled HCCI combustion at the test bench. Yet, using a commercial gasoline. Ethanol blends and pure ethanol are meant to be tested as soon as the VE is finally ready to fully use these new fuels descriptions [1].

Nomenclature

CI	Compression Ignition
FKFS	Forschungsinstitut für Kraftfahrwesen und Fahrzeugmotoren Stuttgart
HCCI	Homogeneous Charge Compression Ignition
LTC	Low Temperature Combustion
MRF	Modeling Reference Fuel
NOx	Nitrogen Oxides
NTC	Negative Temperature Coefficient
PM	Particulate Matter
PRF	Primary Reference Fuel
SI	Spark Ignition
TRF	Toluene Reference Fuel
VE	Virtual Engine
VR	Virtual Reactor

References

[1] Miceli, P., *A multifunctional approach to the reduction of internal combustion engines emissions*, PhD thesis, Polytechnic University of Turin, March 2018

[2] Heywood, J.B., *Internal Combustion Engine Fundamentals*, McGraw-Hill, 1988.

[3] Saxena, S., Bedoya, I., "Fundamental phenomena affecting low temperature combustion and HCCI engines, high load limits and strategies for extending these limits", *Progr. in Energy and Combustion Science 39(5)*, 2013

[4] Hairuddin, A. A., Wandel, A., Yusaf, T.F., "An Introduction to a Homogeneous Charge Compression Ignition Engine", *Jou. of Mech. Eng. and Sci.* 7, 2014

[5] Chiodi, M., Kaechele, A., Bargende, M., Wichelhaus, D. et al., "Development of an Innovative Combustion Process: Spark-Assisted Compression Ignition" *SAE Int. J. Engines 10(5)*, 2017

[6] Chiodi, M., *An Innovative 3D-CFD-Approach towards Virtual Development of Internal Combustion Engines*, Vieweg+Teubner Verlag, Springer Fachmedien Wiesbaden GmbH 2011

[7] Gülder, Ö., "Correlations of laminar combustion data for alternative S.I. engine fuels", *SAE Technical Paper #841000*, 1984

[8] Goodwin, *Cantera: An object- oriented software toolkit for chemical kinetics, thermodynamics, and transport processes*, Version 2.3.0, 2017

[9] Hann, S., Urban, L., Grill, M., and Bargende, M., "Influence of Binary CNG Substitute Composition on the Prediction of Burn Rate, Engine Knock and Cycle-to-Cycle Variations," *SAE Int. J. Engines 10(2)*, 2017

[10] Urban, L., Grill, M., Hann, S., and Bargende, M., "Simulation of Autoignition, Knock and Combustion for Methane-Based Fuels", *SAE Technical Paper 2017-01-2186*, 2017

[11] Fandakov, A., Grill, M., Bargende, M., and Kulzer, A., "Two-Stage Ignition Occurrence in the End Gas and Modeling Its Influence on Engine Knock," *SAE Int. J. Engines 10(4)*, 2017

Experimental Study on Global and Local Turbulent Premixed Flame Characteristics of Alcohols

J. Trabold*,, S. Walther*, S. Hartl*,***, A. Dreizler*, D. Geyer***

trabold@rsm.tu-darmstadt.de
*Thermodynamics, University of Applied Sciences, Darmstadt, Germany
** Reactive Flows and Diagnostics (RSM), TU Darmstadt, Germany
*** Simulation of reactive Thermo-Fluid Systems (STFS), TU Darmstadt

Abstract

Turbulent premixed flame characteristics are significant in technically relevant combustion processes. The here investigated fuels, belonging to the group of alcohols, are situated among the currently discussed biogenic fuels, which shall contribute to the emission reduction within the traffic sector. The aim of this experimental study is to discuss local and global flame characteristics to identify differences of the alcohols methanol, ethanol, 2-propanol and 2-butanol. The well-studied fuel methane is used as reference. All flames are stabilized on the novel Temperature Controlled Piloted Jet Burner (TCPJB), which incorporates an annular pilot flame and an air coflow. First, blow off Reynolds numbers for the different fuels are compared. Secondly, comparisons of CL images reveal differences in the global appearance of the flames. To detect the flame front and subsequently calculate the flame surface density (Σ) for varying bulk Reynolds (bulk Re) and equivalence ratios (ϕ), Planar Laser Induced Fluorescence (PLIF) of the OH molecule is used. The OH-PLIF images reveal significant differences between the fuels in the magnitude and distribution of Σ.

Introduction

In order to receive predictive modeling approaches for technical applications, turbulent combustion processes have to be assessed in detail, which requires comprehensive experimental data sets. Additionally, the potential of renewable energy sources is a central social issue and a topic of current research. In this contest, the turbulence-chemistry interaction and the local and global flame characteristics for fuels that are more complex than the widely investigated methane need to be investigated.

Velocity fields, spatially and temporarily resolved quantitative data of main species concentrations and temperature (Raman/Rayleigh scattering), as well as detailed information on the flame structure (e.g. OH-PLIF), are required for a more detailed understanding of flame-chemistry interaction and model validation. Effects of fuel variations on premixed flame structures were recently investigated by [1] for different C1 - C8 hydrocarbons using flame luminescence. [2] studied the flame structure of premixed flames of the alkanes methane, ethane and propane, stabilized

on a piloted Bunsen burner employing particle image velocimetry and Mie scattering. Still, detailed investigations on turbulent premixed flames of alcohol fuels in the gaseous phase are sparse and to the knowledge of the authors, a systematic analysis of global and local flame characteristics on the variation of liquid fuels is yet to be conducted.

The novel TCPJB was particularly developed to allow for the stabilization of gaseous and pre-vaporized liquid fuels over a wide range of equivalence ratios ϕ, mixture temperatures and bulk velocities. Within this work, the CL was captured to discuss flame appearance and to quantify global flame parameters, such as the flame height. Further, PLIF experiments were performed to obtain the flame surface density Σ. Flames were fueled by the four lowest chain-length alcohols methanol (CH_3OH), ethanol (C_2H_5OH), 2-propanol (C_3H_7OH) and 2-butanol (C_4H_9OH) were investigated at equivalence ratios ϕ varying from lean (ϕ=0.6) to rich (ϕ=1.5) conditions and operated at different bulk Reynolds numbers (bulk *Re*). Methane (CH_4) flames, at the same range of conditions, were employed to explore differences to a well-known gaseous fuel.

The capability to assess and describe the global and local flame structure of alcohols by means of the bulk blow-off Reynolds number, CL and the flame surface density gives a significant advance for understanding complex combustion processes for complex and alternative fuels.

Experimental Methodology

TCPJB System

A gear pump and Coriolis type mass flow controllers (MFCs, Bronkhorst, accuracy of 0.1 % FS) were employed to control the flow rate of the liquid fuels. The liquids were continuously vaporized over an evaporation matrix (ADrop, DV4), of which the temperature was limited to 573 K, to avoid thermal fuel decomposition. Further, the air flow was metered by a MFC and supplied to a temperature-controlled gas heater. Subsequently, the vaporized fuel and the heated air were mixed in a high shear static mixer. A second gas heater (ADrop NH3) was employed for bulk flows exceeding the thermal power of the first heater. Heated hoses between the gas heater/vaporizer system and the burner prevented partial condensation of the gaseous air/fuel mixture at cold spots. For the same reason, all flow conducting parts were temperature controlled by custom designed heating elements. An illustration of the burner nozzle section is given Fig. 1. The TCPJB consists of a central jet (inner diameter of D_i = 11.4 mm), surrounded by a co-annular pilot flame (D_i = 31.0 mm) and a homogeneous coflow (D_i = 260 mm) at 0.3 m/s air. The stainless steel tube temperature was controlled by three nozzle heaters (brown) up to 45 mm upstream of the burner exit. Thermocouples (type K) incorporated in the heating elements in

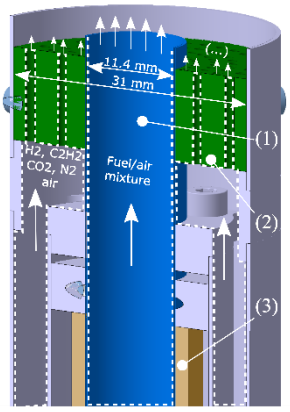

Figure 1. TCPJB jet and pilot area.

combination with PID controllers allowed for a temperature precision of about ±1 K up to temperatures of more than 400 K at the nozzle exit. As pilot flame, a co-annular slot, consisting of four rings holding 36 circular evenly distributed holes each, is utilized. Gas mixtures supplied to the pilot consisted of the five gases air, hydrogen, acetylene, carbon dioxide and nitrogen at ambient temperature. The gas composition was selected to match the C/H and C/O atom ratio, as well as the adiabatic temperature of the respective fuel/air mixture in the central jet at an equivalence ratio of $\phi = 0.7$. A constant pilot bulk velocity of $u_p = 1.0$ m/s was employed throughout all fuels.

Chemiluminescence imaging

Temporally averaged CL of the flames were captured using a Nikon D5600 and an 18-35 mm F1.8 Sigma lens at 31 mm with a pixel resolution of approximately 335 µm/pixel. The three major emitters in hydrocarbon flames within the sensitivity range of the experimental setup are CH* emitting around 431 nm, the Swan bands of C_2*, emitting between 430 nm and 650 nm, as well as the broadband emitting CO_2* [3]. Note that the experimental setup is insensitive in the wavelength region around 307 nm, where OH* radiates.

OH-PLIF imaging

OH-PLIF was used to image flame structures of the jet at six different axial positions. The laser beam emitted from a pulsed UV laser system at 283 nm and was formed into a 28 mm high and 0.2 mm thick sheet to excite the Q1(6) transition in the A-X (1-0) band. The OH fluorescence signal of a 24 x 32 mm^2 area was imaged onto a CCD camera (Imager E-lite, LaVision) using Intensified Relay Optics (High-speed IRO, LaVision). The pixel resolution of the detection system was 23 µm/pixel.

In a first step of data post-processing, images were background corrected. Next, the laser sheet intensity distribution was normalized using an in-situ averaged sheet profile [4]. The flame front was deduced to generate a binary burned/unburned image by tracking the highest gradient of OH [5]. Splines were fitted to recover the flame front. To deduce flame surface densities Σ as a measure of the mean reaction rate [6], flame lengths were determined in quadratic control areas. The size of the control areas was set to 0.2 x 0.2 mm^2. This was smaller than 20% of the smallest observed flame brush thickness (near the nozzle), but larger than the reaction zone thickness, as recommended by [7]. At fixed axial positions, cross sections of Σ are evaluated. Furthermore, Σ was integrated in radial direction to receive an axial distribution of Σ.

Laminar burning velocities

An in-house flame solver [8] was used to simulate one-dimensional adiabatic steady laminar premixed flames. The methane flames are modelled using the GRI30 mechanism by [9]. For methanol and ethanol the recently developed ELTE mechanism by [10] is used and for 2-propanol and 2-butanol the POLIMI/CRECK mechanism was chosen [11].

Results and Discussion

To explore global flame characteristics, CL images taken at lean, stoichiometric and rich conditions and at bulk *Re* of 18.000 are shown in Fig. 2.

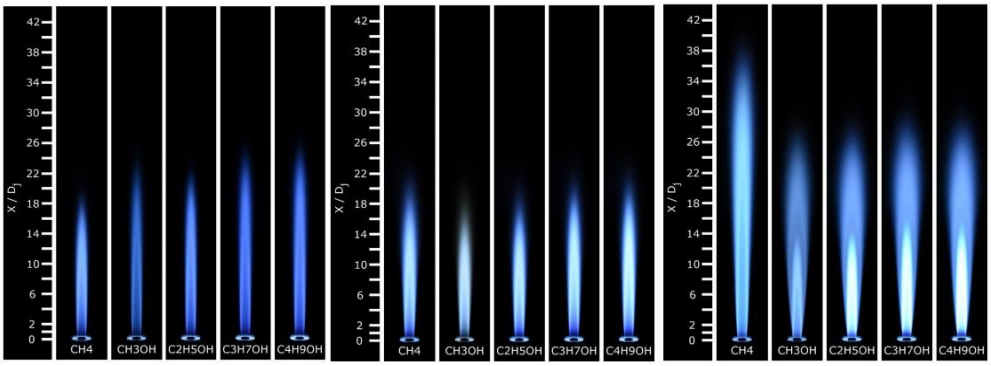

Figure 2. CL at bulk *Re* of 18000 and equivalence ratios ϕ of 0.8, 1.0, 1.5 (left to right).

At lean conditions (ϕ = 0.80), all flames are bluish, indicating mainly emissions from CH*. The luminosity is, over all axial positions, largest in the methane flame, which is in line with the largest CH mole fraction being located in stoichiometric methane flames [3]. At stoichiometric conditions, the flames appear more greenish for all fuels, which is due to C_2* emissions. At rich conditions (ϕ=1.5), a remarkable difference in between the alcohols and methane is visible. All alcohol flames show a bright, more greenish flame region, implying mostly C_2* emissions originating at rich conditions at lower axial distances, followed by a bluish flame region further downstream. The intensity of the CL within this lower axial region increases from methanol to 2-propanol, as the length of the C-chain in the molecules increases. Thus, a gain in the global fuel consumption rate in the lower axial region of the alcohol fueled rich flame is illustrated [1]. CH* emissions seem to be more prominent in the downstream flame region, as the color and the intensity substantially changes.

Fig. 3 shows the bulk Reynolds numbers *Re* at blow-off, the laminar burning velocities s_L and the normalized bulk velocities in dependency on the equivalence ratio ϕ. With respect to the blow off *Re*, all flames investigated show an increasing stability from lean towards rich conditions. *Re* of about 30000 and higher were reached at stoichiometric conditions and up to 60000 at rich conditions for the present pilot flame conditions. This demonstrates that the TCPJB configuration is well suited to study turbulence-chemistry interaction at technically relevant conditions. Further, global flame characteristics can be explored in dependency on s_L and the turbulent burning velocity. For lean conditions, the methane/air flames can be stabilized at higher bulk *Re* of the jet than the four alcohols. In contrast, flames based on the alcohol/air mixtures are more stable at rich conditions. Here, the stability of the flames is decreasing towards the one with the largest chain length. It is worth mentioning that methanol and ethanol show steeper gradients in stability than 2-propanol and 2-butanol.

The impact of s_L on the flame stability is illustrated in Fig. 3 c) by relating the bulk velocity at the nozzle exit at blow-off u_{bulk} to s_L. Alcohol fuels are grouped together at smaller u_{bulk}/s_L, while methane can withstand a larger u_{bulk}/s_L ratio in the present flow configuration. The difference in u_{bulk}/s_L is notably smaller within the alcohols than in between methane and the alcohols, revealing an impact of the fuel group on the flame stability. Fuels with the largest s_L showed the lowest stability. Further parameters relevant for flame stability will have to be investigated to address these impacts in more detail.

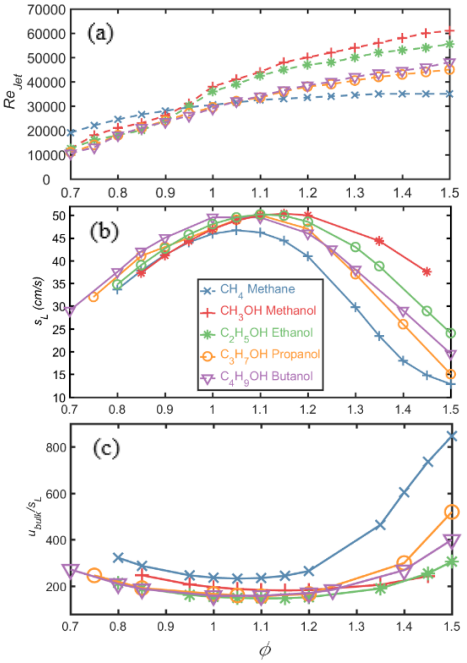

Figure 3. (a) Reynolds number at blow-off, (b) laminar burning velocity s_L and (c) normalized bulk velocity u_{bulk}/s_L over ϕ.

Lastly, the flame surface density Σ of flames with bulk Reynolds numbers of Re=18000 and equivalence ratios of ϕ=1.05 are discussed using results of OH PLIF measurements. Fig. 4 a) to c) show the evolution of Σ at three axial locations. At around x/D=1 (4a), the profile of Σ exhibits two distinct peaks, resulting from the plane of observation intersecting the flame centrally. At this location, Σ values are at maximum because flame intermittency is lowest. Further downstream, at x/D=5 (4b), the Σ profiles widen due to an increased flame brush thickness. Approaching the flame tip, the two peaks merge at around x/D=10 (4c). The integral of Σ along the radial direction is shown in Fig. 4 d), indicating the axial progression of mean reaction rates. Whereas methanol and ethanol flames reach their maximum at around x/D=7.5, methane, 2-propanol and 2-butanol peak around x/D=10. The gradient of Σ in axial direction is slightly larger for the alcohols, both up- and downstream the maximum peak. However, it should be considered that the methane flame was operated without preheating, using inlet temperatures of 293 K.

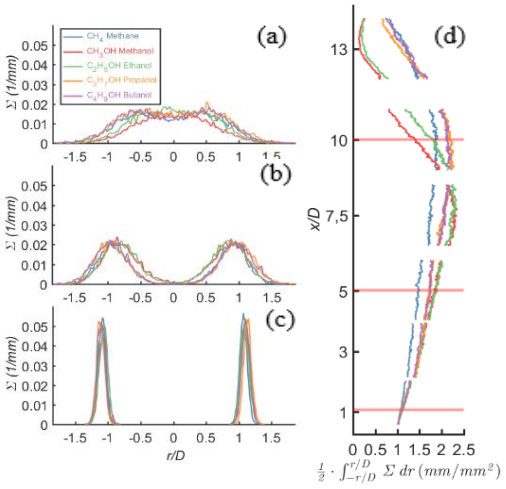

Figure 4. Radial distribution of flame surface density Σ at three heights ((a) to (c)) and integral Σ (d).

This reduces s_L (36.3 m/s instead of 46.7 m/s at 343 K) and reactivity is accordingly lower.

Conclusion

This experimental study discusses local and global flame characteristics of the alcohols methanol, ethanol, 2-propanol and 2-butanol. Significant differences between the fuels were found in the blow off Reynolds number, chemiluminescence images and the flame surface density. This serves as a indicator that flame stability, size and turbulence of the TCPJB flames are strongly dependent on the fuel type. In near future, experimental data will be analyzed with regards to influences of thermo-diffusive and hydrodynamic instabilities. Further, combined Raman- and Rayleigh measurements shall yield even more detail on the turbulence-chemistry interaction of alcohol flames, particularly of Ethanol.

Acknowledgements

We gratefully acknowledge financial support by the Deutsche Forschungsgemeinschaft (DFG) through GE 2523/2-1 and DR 374/17-1. A. Dreizler was financially supported by the Gottfried Wilhelm Leibniz-Preis (DFG). D. Geyer was financially supported by the ZFE of the Darmstadt University of Applied Sciences.

References

[1] Carbone, F., et al., “Comparative behavior of piloted turbulent premixed jet flames of C1-C8 hydrocarbons“, *Combustion and Flame*, 180:88-101 (2017).
[2] Tamadonfar, P. and Ö. L. Gülder "Experimental investigation of the inner structure of premixed turbulent methane/air flames in the thin reaction zones regime", *Comb. and Flame* 162(1):115-128 (2015).
[3] Kathrotia, T., et al. "Experimental and numerical study of chemiluminescent species in low-pressure flames", *Applied Physics B*, 107(3):571-584 (2012).
[4] Peterson, B. et al., “Early flame propagation in a SI engine measured with quasi 4D-diagnostics”, *Proc. Comb. Inst.*, 35:3829-3837 (2015).
[5] Nauert, A., „Laseroptische Untersuchungen an verdrallten Vormisch-flammen“, Technische Universität Darmstadt (2008).
[6] Bray, K. N. C., “Studies of the Turbulent Burning Velocity”, *Proceedings of the Royal Society A*, 431(1882):315-335 (1990).
[7] Donbar, J. and Driscol, J., “Reaction Zone Structure in Turbulent Nonpremixed Jet Flames - From CH-OH PLIF Images”, *Comb. and Flame*, 122:1–19 (2000).
[8] Zschutschke, A., et al.: “Universal Laminar Flame Solver (ULF)”, https://figshare.com/articles/ULF_code_pdf/5119855/2 (2017).
[9] Smith, G., P., et al., GRI30, in http://www.me.berkeley.edu/gri_mech/
[10] Olm, C., et al., ELTE, “Development of an Ethanol Combustion Mechanism Based on a Hierarchical Optimization Approach”, *International Journal of Chemical Kinetics*, 48:423-441 (2016).
[11] Frassoldati, R., et al., CRECK, *Comb. and Flame*, 159:2295-2311 (2012).

Analysis of engine control parameters effect to minimize GHG emissions in a dual fuel NG/Diesel light duty engine

C. Beatrice, V. Fraioli, C. Guido, P. Napolitano
c.guido@im.cnr.it
Istituto Motori CNR - Viale Marconi n°8, 80125 Napoli, ITALY

Abstract
In the present work, a 2.0L Euro 5 compliant diesel engine, equipped with an advanced electronic combustion control system, has been set up to operate in Dual Fuel (DF) Diesel- Natural Gas (NG) DF mode. An experimental campaign has been devoted to the engine optimization, in order to assess the achievable reduction of unburned hydrocarbon emissions, keeping the peculiar benefits of DF combustion.
A thorough analysis of the effects of many engine control parameters (e.g. NG substitution ratio, diesel pilot injection strategies, EGR, *etc.*) on DF engine performance was performed. Combustion timing and EGR- displayed a strong potential on Total Hydro-Carbon (THC) emissions control (represented for more than 90% by CH_4), exhibiting wider margins of engine recalibration, in comparison with the use of a standard Diesel calibration also in DF mode.

Introduction
The use of natural gas (NG) as fuel for internal combustion engines traces back to 30s [1] and the interest in its adoption is still increasing, due to well-known reasons, mainly linked to the environmental benefits in terms of particulate and carbon dioxide emissions reduction, to the availability of NG resources and in view of a desirable energy sources diversification [2]. In this respect, the Diesel-NG Dual Fuel (DF) concept can represent an opportunity to extend the NG use to Diesel architectures in the passenger cars' sector [3].
The DF combustion concept foresees the contemporary use of NG (or alternative high octane index fuels like biogas, ethanol, gasoline etc.) and Diesel fuel. The last one should be used to ignite NG, which would not burn spontaneously in absence of an ignition source. The most common solution consists in a port fuel injection (PFI) of NG, as easily adoptable for aftermarket Diesel engine modifications. In some cases, DF concept has proven to be not only viable, but also industrially appealing, as HD engines (e.g. trucks and buses) in DF version are effectively produced by manufacturers [2], applied to various engine classes, architectures and fuels combinations.
In this framework, a general agreement appears to be reached on the DF concept applicability to CI engines and the generic potential of this combustion mode for CO_2, NOx and soot reduction. On the other hand, the release of high amounts of

unburned methane, mainly at low engine loads, with correlated efficiency issues, is still widely recognized as an important limit for its practical application to light duty engines. Moreover, it turned out that, at low engine load, the extent of Diesel substitution is limited, due to unacceptably high methane emission levels [4].
Goal of the present paper was to assess the effect of critical engine parameters and evaluate the potentiality of a proper engine calibration in GHGs reduction, for a practical application of the DF concept to an existing Diesel architecture. In other words, the main scope of the parametric study was to minimize unburned gaseous, keeping the typical advantages of DF configuration in terms of CO_2, PM and NOx reduction.
A multi-cylinder automotive Diesel engine, Euro5 compliant, and equipped with an advanced electronic control system, named CLCC (Closed Loop Combustion Control), able to automatically adapt combustion phasing and engine torque to target values, was suitably modified to work in DF mode with NG PFI system. The considered architecture can be considered as representative of a significant share of the current EU fleet. The use of the CLCC system implies that the modification of a single parameter can determine the contemporary automatic adjustment of other parameters, to guarantee a prescribed target of engine torque and combustion phasing. This approach allows performing a consistent comparison among the various tested conditions, always keeping fixed the engine operating point. So, it is possible to evaluate the actual response of a real system to the parameterization, thus quantifying the attainable potentialities of a subsequent engine recalibration in terms of DF combustion optimization.

Methodology
The research activity started with a first engine characterization in transient operative condition, with a flat DF calibration map at constant energy substitution ratio (SRe) of 50% (except at idle), whose results have been published in [5]. This first calibration was chosen to carry out a “picture” of the engine behavior in DF mode during the NEDC homologation cycles. Then the experimental campaign addressed the analysis of the engine performance and emissions in steady-state conditions, varying the NG substitution ratio, trying to achieve the maximum gas substitution without the onset of critical functional conditions (mainly in terms of excessive THC emissions). In that paper, it was highlighted the potentialities and issues related to the DF application to a Euro 5 nominal diesel calibration, keeping the same values of all the engine control parameters apart from the gas substitution.
The present work describes the subsequent phase of the research, in which the engine response to crucial calibration parameters has been investigated, carrying out the identification and quantification of the potentialities of these parameters in the exploitation of DF benefits, in view of an optimized DF calibration.
The work was split in two phases. The first regarded the analysis of the SRe variation effects on engine performance and emissions, to obtain an optimal NG injection map. To this aim, the methodology, summarized in the next, was

followed.

An experimental campaign was designed to identify the emissions and engine performance trends, varying the SRe within a predefined domain.

A data fitting procedure allowed modeling every detected trend by means of 2nd order polynomials for each engine Operating Point (OP), thus obtaining the engine "surface response" to SRe variation.

A consolidated estimation procedure [6] was adopted to predict the engine behavior over the homologation driving cycle (NEDC), starting from emissions and performance values, for each OP, resulting from the implemented engine model.

Solving a multi-objective optimization problem, the optimal map of gas substitution ratio was identified, among various SRe combinations. The target was to minimize THC emissions, preserving the benefits of DF configuration in terms of CO_2, NOx, PM emissions, combustion efficiency and noise, at most matching the correspondent values of the conventional diesel mode.

In the second research phase, once fixed the optimized SRe values for each OP, the effects of other fundamental engine calibration parameters on DF combustion were analyzed. In the present study, the percentage of the premixed NG was quantified on an energy basis (SRe) according to the following formula:

$$SRe = \frac{m_{NG} \cdot LHV_{NG}}{m_{NG} \cdot LHV_{NG} + m_d \cdot LHV_d} \cdot 100\ [\%] \qquad (1)$$

Where m_{NG} and m_d are the mass flow rates of NG and diesel fuel, while LHV_{NG} and LHV_d represent the lower heating values of NG and diesel fuel, respectively.

Experimental Set Up

The engine employed in the experimental activity was a Euro 5 four-cylinder 2L diesel engine equipped with a close coupled DOC+DPF, whose characteristics are reported in [5]. The engine is equipped with pressure sensor glow plug from BERU. The engine Electronic Control Unit (ECU) is able to automatically adapt cylinder per cylinder and cycle per cycle the desired targets of 50% of the fuel mass burnt (MBF50%) and of the Indicated Mean Effective Pressure (IMEP), by the direct control of the Start Of main Injection (SOImain) and main injection Energizing Time (ETmain) [5].

The engine was coupled with a variable frequency fast response dynamometer and fully instrumented for emission analysis of the gaseous species (CO2, CO, THC, CH4, O_2 and NOx) and the particulate (mass of dry soot and mass of particulate) [5]. The engine was properly adapted in DF configuration, by means of an automotive NG Port Fuel Injection (PFI) retrofit system.

Results and discussion

Phase 1: Engine response vs SRe and SRe map optimization

In order to define a more suitable SRe map in the whole engine working area, the engine response to different SRe values was investigated. Six steady-state OP,

selected as the most representative of the engine behavior during the European homologation cycle (NEDC), were tested. The engine speed and load (rpm x bar BMEP) will be used in the text to schematically denote the tested engine points, as follow: 1500x2, 1500x5, 2000x2, 2000x5, 2000x10, 2500x8.
The choice of the SRe values domain was done on the basis of the previous results [5], which have clearly shown the upper limit of SRe in terms of engine emissions and performance. Then a proper SRe parametrization was performed in order to find the optimal value in each OP. At 1500x2 and 2000x2 test points, unacceptable CH_4 emissions were observed for SRe values higher than 40-45%, so no further SRe increment was possible. Then, the analysis of the engine behavior varying the SRe, will refer only to the four test points 1500x5, 2000x5, 2000x10, and 2500x8.
The best set of SRe values, for each OP, were obtained solving the multi-objective scalar problem, capable of providing the optimized combination, giving lowest THC and CO2 emissions levels, without penalties in NOx and PM emissions. In this way, the optimized SRe map for the whole engine working area was identified.
Table 1 reports the SRe optimal values selected for the six operative conditions. As expected, high SRe levels could be only achieved at high engine load, while at low and medium engine load it was not possible to exceed, within the prescribed constraints, values around 40% and 65% respectively.

Table 1. SRe optimized values at different operative points.

	1500	1500	2000	2000	2000	2500
SRe [%]	**39**	**66**	**40**	**63**	**82**	**68**

Phase 2: Engine response vs SRe and SRe map optimization
Once fixed the optimized SRe map, a pre-screening of the DF engine behavior varying some ECU Diesel parameters was performed, in order to identify the most effective ones in terms of DF configuration optimization. Their effect is discussed in the present section in the following order:
1. MBF50 - Engine combustion phasing, in terms of crank angle degree corresponding to the 50% of the fuel mass burned fraction;
2. Qpil - Diesel quantity of pilot injection, in a Pilot+Main pattern;
3. Prail - Diesel injection pressure;
4. DT - Dwell time between pilot and main Diesel injection event;
5. EGR - Exhaust gas recirculation rate.

The preliminary investigation highlighted that other controlling parameters (like air swirl ratio, air boost pressure, *etc*.) display a minor effect on the DF engine behavior, therefore, their effects are not reported here.
The optimization of DF configuration at high load appears less critical, due to the possibility to employ high SRe levels without excessive penalty in THC emissions. For this reason, the present analysis is focused on the OP namely 1500x2, 1500x5, 2000x2 and 2000x5.
A complete characterization has been carried out in terms of combustion analysis,

engine performance, fuel consumption and emissions. For sake of brevity, in the following sections the effects of MBF50 and EGR on THC emission are analyzed, resulted as the most meaningful parameters.

MBF50%

On the left plot of Figure 1, the engine out THC emissions over the MBF50 sweep. The higher slope of the curves clearly shows that the MBF50 has a higher influence on THC emissions at low loads. Conversely, at 1500x5 and 2000x5, the trends are less pronounced, so evidencing that MBF50 phasing is a less effective way to reduce THC. As visible in the plot on the right of Figure 5, reporting the measured pressure profiles (Pcyl) and the rate of the heat release (R.o.H.R.) at 1500x2 and 1500x5 over the MBF50% sweep, the combustion event occurs at higher pressure levels and high cylinder temperatures, enhancing the CH4 post-oxidation.

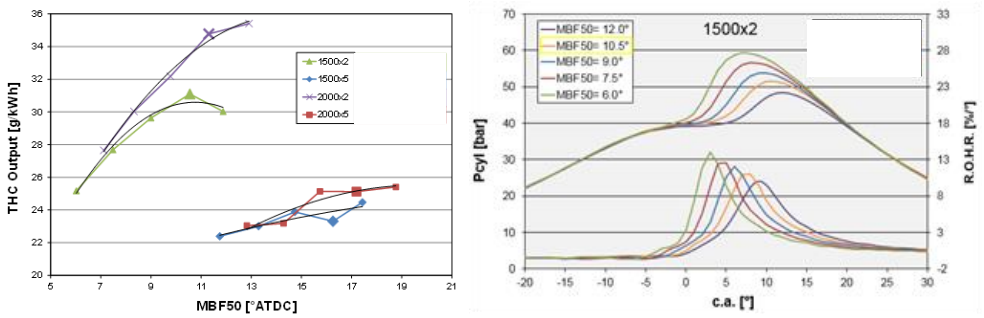

Figure 1. THC vs MBF50 at 1500x2, 1500x5, 2000x2 and 2000x5, on the left. Cylinder pressure and RoHR vs MBF50 at 1500x2.

EGR

Figure 2 reports THC versus EGR sweep for all OPs: as evident, a significant abatement of THC emissions occurred increasing EGR, in all Ops, more marked at low loads. Such result has to be partly ascribed to the lower exhaust flow rate corresponding to the increased EGR, an analogous trend was maintained in terms of raw ppm THC values too.

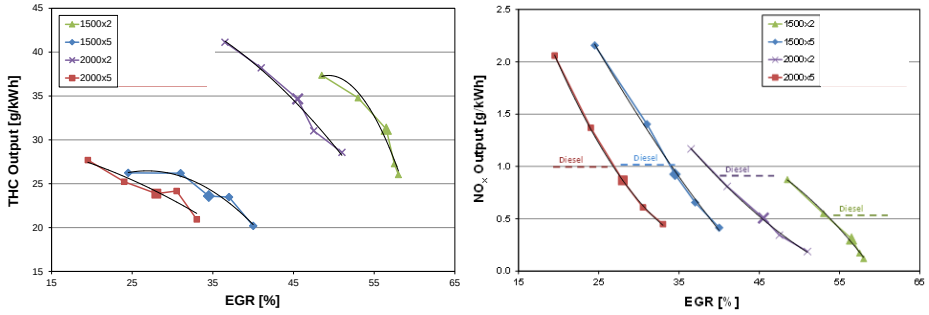

Figure 2. THC vs EGR at 1500x2, 1500x5, 2000x2 and 2000x5, on the left. NOx vs EGR at same OPs, on the right.

According to the CLCC strategy, keeping fixed the MBF50, the SOI_{main} and SOI_{pil} events were advanced as EGR was increased, determining a combustion process at higher cylinder thermodynamic temperatures and a longer premixing phase of diesel fuel in the methane-air charge. Such effects promote a better oxidation of the premixed air-CH4 charge. The expected benefits of EGR on NOx emissions can be observed in the right plot of Figure 2. At the highest EGR level, Euro 6 level were approached without the use of an after-treatment system, and also soot emission were well below the correspondent Diesel one.

Summary

The present study evidenced that the optimization of the DF engine calibration offers a wide margin for THC control. The benefits on THC emissions can be obtained without detrimental effects on the overall engine performance and the other regulated pollutant emissions. It is worth to highlight that, in view of a general GHGs emission reduction, the presented investigation showed how the mentioned advantages on exhaust methane can be reached keeping the typical DF benefits on CO_2. Among the investigated parameters, MBF50 and EGR displayed a very strong potential. The observed tendencies suggest the possibility to combine these parameters, to contemporarily mitigate THC and NOx emissions.

References

1. Sonia, Y., "An empirical analysis on the adoption of alternative fuel vehicles: The case of natural gas vehicles", *Energy Policy*, 35: 11 (2007).
2. Sahoo, B. B., Sahoo, N., Saha, U. K., "Effect of engine parameters and type of gaseous fuel on the performance of dual-fuel gas diesel engines—A critical review", *Renewable and Sustainable Energy Reviews*, 13: 6–7 (2009).
3. Korakianitis T, *et al*., "Natural-gas fueled spark-ignition (SI) and compression-ignition (CI) engine performance and emissions", *Progress in Energy and Combustion Science*, 37: 1 (2011).
4. Garcia, P. and Tunestal, P., "Experimental Investigation on NG-Diesel Combustion Modes under Highly Diluted Conditions on a Light Duty Diesel Engine with Focus on Injection Strategy," *SAE Int. J. Engines* 8(5): 2177-2187 (2015).
5. Napolitano, P. *et al*., "Application of a Dual Fuel Diesel-NG Configuration in a Euro 5 Automotive Diesel Engine", *SAE Paper 2017-01-0769*, 2017.
6. Arrigoni, S., *et al*. "Development of an integrated methodology for the design and optimization of charging and EGR circuits in modern diesel engines based on 1D-CFD engine modelling". *Engine process simulation and turbocharging*. 3rd conference, Berlin; May 2011. ISBN-10: 3816930735.

Acknowledgments
Authors would like to thank Mr. Alessio Schiavone and Mr. Roberto Maniscalco for their technical assistance in the engine testing.

EXERGO-ECONOMIC ANALYSIS OF AN HCCI-ENGINE POLYGENERATION SYSTEM

D. Schröder*, A. Güngör, R. Hegner*, B. Atakan***
dominik.schroeder@uni-due.de
*Institute for Combustion and Gas Dynamics - Thermodynamics,
University of Duisburg-Essen, 47048 Duisburg, Germany
**Ege University, Faculty of Engineering, Department of Mechanical Engineering, 35100 Bornova, Izmir - Turkey

Abstract
Fuel rich combustion processes in engines can also be used for the production of base chemicals like syngas together with work and heat. In this work, such an HCCI engine polygeneration system, which was previously modeled in python/cantera, with respect to kinetics and thermodynamics, is now investigated by conducting an exergo-economic analysis including a global sensitivity analysis. It was found that the systems product costs depend strongly on certain device costs, interest rate, operating hours and lifetime, although the exhaust gas recirculation rate primarily determines the product costs. The highest exergy destruction rate and therefore the highest costs caused through this, occur in the HCCI engine with about 46 % of the total exergy destruction. The analysis indicates that, for lowering the product costs, the investment costs of the hydrogen membrane and the shift reactor should be reduced or substituted for a different, cheaper hydrogen separation technology and the lifetime and operating hours of the system should be increased. It was found that the hydrogen costs per kg have a reasonable range of 2.6 to 10.4 €/kg.

Introduction
In order to reduce the emissions of carbon dioxide, the consumption of finite fossil fuel resources and to stabilize the grid that is increasingly affected by volatile renewable energy systems, a more flexible energy system is needed. If a facility, e.g. a chemical plant, has an additional need for chemicals a partial oxidation in gas engines could provide, the efficiency and flexibility would improve even more. In earlier studies therefore a polygeneration process concept with HCCI engines that produces heat, power and chemicals by partial oxidation has been studied to compare this concept to the conventional, separate production on a thermodynamic basis. It was found that the exergetic efficiency of an HCCI engine polygeneration process producing acetylene is more than 20% higher than a separate production [5]. Most often economic reasons are essential for building certain devices. Therefore, beside the thermodynamic and kinetic analysis of the polygeneration system this study has been conducted to do a exergo-economic research. The results help to determine in which part of the system it is important to improve the exergy effiency due to high costs that are generated by the exergy destruction and where it is less important in

order to reduce the costs of the final products. Due to the uncertainty in costs, that are needed for the analysis, the global sensitivity of the prices on the different estimated costs is applied.

Process concept

The investigated polygeneration energy system [5] mainly consists of an HCCI engine, a watergas-shift reactor, a hydrogen membrane reformer and several shell and tube heat exchangers and hydrogen compressors to produce hydrogen in addition to power, heating water and process steam. The systems process flow diagram is shown in figure 1.

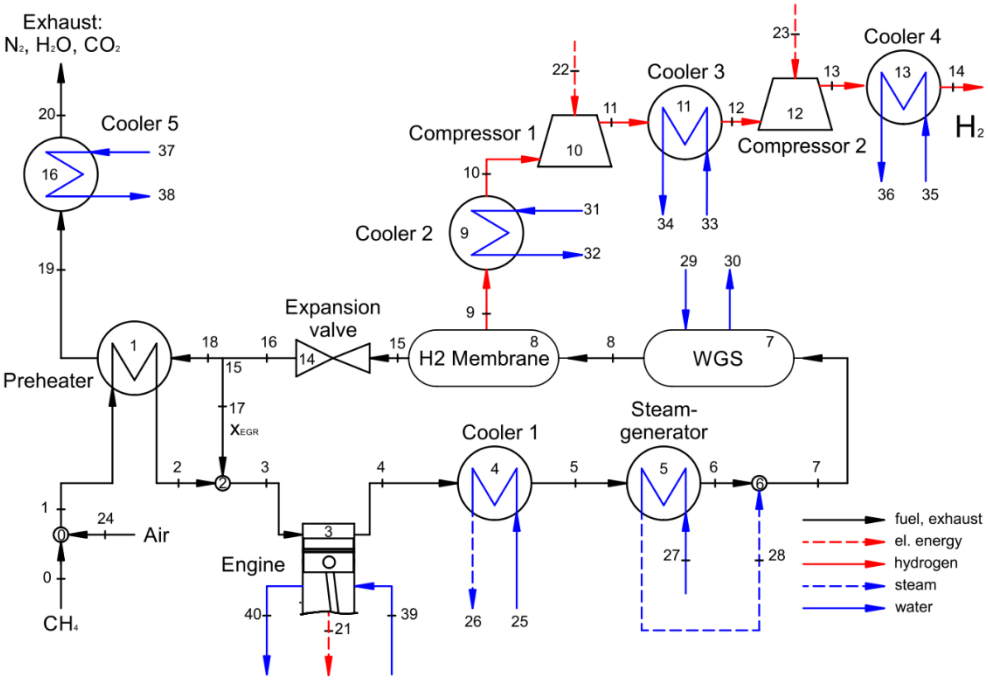

Figure 1. Process flow diagram of the polygeneration process.

To achieve ignition with neat, relatively inert methane as fuel, a preheater using the exergy from the exhaust gas to heat the air-fuel mixture and an exhaust gas recirculation (EGR) to increase the temperature und number of reactive radicals in the intake are used. For further information on the system and its components it is referred to previous work of Hegner et al. [5].

Exergo-economic analysis

The main principle of exergo-economic analyses is defining the costs of an energy flow i as the product of the specific exergy costs c_i and the exergy flow $\dot{E}_i$ according to (1). To calculate the specific exergy costs of the products, cost balances (2) for

each component k are conducted that lead to a linear equation system [2].

$$\dot{C}_i = c_i * \dot{E}_i \quad (1)$$

$$\sum \dot{C}_{F,i} + \dot{Z}_k = \sum \dot{C}_{P,i} + \dot{C}_{L,k} \quad (2)$$

The total device costs per time unit $\dot{Z}_k$ are defined as the sum of the total investment costs and the total operating and maintenance costs per time unit. For these costs the time value of money and the salvage value of the devices are considered [1]. The device investment costs are established by using the purchased equipment costs method from Turton et al. for known device costs [8]. Subsequently the maximum device costs of all EGR ratios x_{EGR} are used for the calculations. The chosen financial parameters for the analysis are shown in table 1.

Table 1. Financial parameters

Description	Symbol	Value	Unit
Lifetime	T	15	a
Operating hours	τ	7920	h/a
Interest rate	i	0.1	-
Salvage value factor	Ω	0.05	-
Op. & maint. factor	Φ	0.03	-
Air exergy costs	c_{air}	7.2	€/MWh
Methane exergy costs	c_{CH4}	17.9	€/MWh
Water exergy costs	c_{water}	86.0	€/MWh
Electricity costs	c_{el}	42.0	€/MWh

For devices with n exiting flows $n-1$ auxiliary relations are required to solve the cost balances [2]. Based on the extraction method [6] the engines electrical energy costs are maximized and the water costs are kept constant to charge all costs to the exhaust gas. The cost balance equations (2) do not take exergy losses into account even though they are very important when correlating exergy flows with cost flows. Therefore, the costs of exergy destruction $\dot{C}_{D,k}$ are calculated corresponding to [2] with the assumption that the exergy destruction $\dot{E}_{D,k}$ is independent on the specific fuel costs $c_{F,k}$ (3).

$$\dot{C}_{D,k} = c_{F,k} * \dot{E}_{D,k} \quad (3)$$

To distinguish the increase of the specific product costs by the device costs from the exergy related exergy destruction and exergy loss costs, Bejan et al. [2] defines the

exergo-economic factor f_k as the ratio of the non-exergy-related cost increase to the total cost increase (4). If the value is low, the cost increase is mainly caused by exergy-loss-related costs and thus the exergetic efficiency of the device should be improved even if it increases the device costs. On the contrary the device costs should be lowered if the factor has a high value at the expense of the exergetic efficiency.

$$f_k = \frac{\dot{Z}_k}{\dot{Z}_k + c_{F,k} * (\dot{E}_{D,k} + \dot{E}_{L,k})} \tag{4}$$

In addition to the constant financial parameters a global sensitivity analysis is conducted to determine the influence of changing device costs, fuel costs and financial parameters on the final product costs using the Sobol method [7]. The sensitivity of an input parameter describes the part of uncertainty of the results the input parameter is accountable for. If only one parameter is varied and therefore there is no interdependency with other parameters the result is called the first order sensitivity. In this work, the first order sensitivity and the total sensitivity is regarded. The latter is the sum of all sensitivities (of all orders) of the investigated input parameter and thus gives the information how significant the sensitivities of higher orders are.

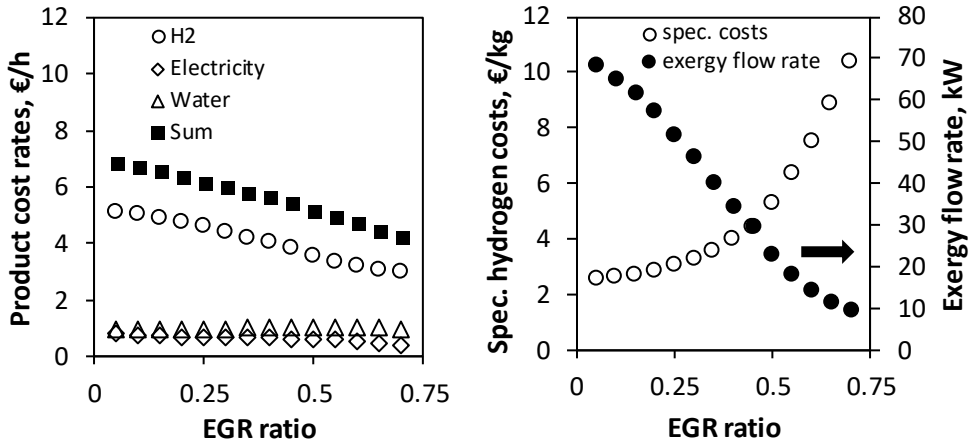

Figure 2. Product costs per hour (left figure) and hydrogen costs per kg (open symbols, left scale, right figure) and exergy flow rates (filled dots, right scale, right figure) as a function of EGR ratio.

Results and discussion

For the given constant financial parameters, figure 2 shows the product costs per hour of H_2, electricity and water. Since hydrogen was chosen as the main product, and thus charged with all costs of the exhaust gas flowing into the H_2 membrane and the device costs of the membrane itself, the hydrogen costs represent 68 – 75 % of

the total product costs. Due to the decreasing exergy flows with increasing EGR ratios, the H_2 costs per kg rise strongly. The effect of the decreasing exergy flows on the product costs with maximum device costs is shown in figure 2. The hydrogen costs per kg rise gradually with EGR ratios at 0.5 and above, leading to four times higher hydrogen costs compared to the lowest EGR ratio (0.05). For this reason, high EGR ratios should be avoided or reduced to small periods per year which limits the flexibility of the polygeneration systems according to the financial parameters. Table 2 shows the results for the sensitivity analyses for EGR ratios of 0.05 and 0.7 where the first order sensitivity S_1 is larger than 0.03. It is found that only four parameters have non-negligible sensitivities: the interest rate, lifetime, operating hours and the device costs of the hydrogen membrane (it has the highest investment costs of all devices). Depending on the demand for the products, it can be desirable to increase the operating hours per year by running the system at higher EGR ratios for this additional period instead of shutting it down completely.

Table 2. Sensitivity analysis results for $S_1 > 0.03$

EGR ratio	0.05		0.7	
Sensitivity parameter	S_1	S_{T1}	S_1	S_{T1}
H_2 membrane costs $\dot{Z}_8$	0.1784	0.1831	0.1971	0.2025
Interest rate i	0.2011	0.2079	0.1986	0.2058
Lifetime T	0.2051	0.2134	0.2031	0.2117
Operating hours t	0.3800	0.3835	0.3760	0.3797

As it can be seen in table 3, the engine, the hydrogen membrane and the water gas-shift reactor cause the highest exergy destruction rates with about 12 % for the reactor and the membrane and 46 % for the engine.

Table 3. Most impact of exergo-economic factors for $x_{EGR} = 0.05$.

Device	$\dot{E}_{D,k}$	$y_{D,k}$	f_k	$\dot{C}_{D,k}$
	W	%	%	€/h
3) Engine	10883.6	46.46	85.8	0.211
7) Water gas-shift reactor	2883.6	12.31	79.3	0.087
8) H_2 membrane	2875.5	12.28	95.6	0.086
14) Expansion valve	1087.0	4.64	50.5	0.000

The hydrogen costs increase by the hydrogen membrane is mainly caused by its high investment costs and not by the exergy destruction as the exergo-economic factor f_k has a high value of 95.6 %. The engine and the reactor have a greater amount of exergy destruction costs with 85.8 % and 79.3 % being caused by the device costs.

In contrary the expansion valve has a relatively high exergy destruction, but because its investment costs are low there is no effect on the product costs.

Conclusion

An exergo-economic analysis of the polygeneration engine system helps to determine in which case an improvement of the exergetic efficiency is reasonable and in which case non-exergy-related parameters, e.g. investment costs, are limiting. To reduce the product costs – especially the H_2 costs – of the investigated HCCI polygeneration system the investment costs of the hydrogen membrane and the water gas-shift reactor should be reduced or substituted by a different, cheaper H_2 separation technology. The H_2 costs per kg for the given financial parameters have a reasonable range of 2.6 to 10.4 €/kg, compared to about 4.2 to 5.67 €/kg when using a separate water electrolysis [3] or hydrogen membrane reformer [4]. In further investigations these results shall be compared to an exergo-economic analysis of distinct processes: a CHP plant and a separate hydrogen production.

Acknowledgements

Financial support of this work by the Deutsche Forschungsgemeinschaft within the framework of the DFG research unit FOR 1993 ‘Multi-functional conversion of chemical species and energy’ (AT24/13-2) is gratefully acknowledged.

References

[1] Balli, O., Aras, H., Hepbasli, A., “Exergoeconomic analysis of a combined heat and power (CHP) system”, *International Journal of Energy Research*. 32: 273-289 (2008).

[2] Bejan, A., Tsatsaronis, G., Moran, M., *Thermal Design & Optimization*, John Wiley & Sons, 1996, pp 405-460.

[3] Buxbaum, R., REB Research & Consulting, “Electrolysis Hydrogen Costs and Membrane Reformer Hydrogen Costs”, 2010.

[4] Dittmar, B., *Entwicklung eines technischen H_2-Membranreaktors*, Karlsruhe Institute of Technology, 2014.

[5] Hegner R., Atakan B., “A polygeneration process concept for HCCI-engines – Modeling product gas purification and exergy losses”, *International Journal of Hydrogen Energy*. 42: 1287-1297 (2016).

[6] Oliveira Junior, Silvio de, *Exergy. Production, Cost and Renewability*, Springer, 2013, pp 42-44.

[7] Saltelli, A., Ratto, M., Andres, T., Campolongo, F., Cariboni, J., Gatelli, D., Saisana, M., Tarantola, S., *Global Sensitivity Analysis. The Primer*, John Wiley & Sons, 2008, pp. 1-51.

[8] Turton, R., Bailie, R. C., Whiting, W. B., Shaeiwitz, J. A., Bhattacharyya, D., *Analysis, Synthesis and Design of Chemical Processes*, Pearson Education, 2009, pp. 185-187.

A COMPUTATIONALLY AEFFICIENT COMBUSTION PROGRESS VARIABLE (CPV) APPROACH FOR ENGINE APPLICATIONS

Adina Werner[1]*, Corinna Netzer[1], Harry Lehtiniemi[2], Anders Borg[2,4], Andrea Matrisciano[2,4], Lars Seidel[3], Fabian Mauss[1]**

[1]Brandenburg University of Technology, Cottbus, Germany
[2]LOGE AB, Lund, Sweden
[3]LOGE Deutschland GmbH, Cottbus, Germany
[4]Chalmers University of Technology, Gothenburg, Sweden
e-mail of corresponding author
*Adina.Werner@b-tu.de
**harry.lehtiniemi@logesoft.com

Abstract

The use of complex reaction schemes is accompanied by high computational cost in 3D CFD simulations but is especially important to predict emissions. A possible solution to this dilemma is the use of tabulated chemistry. The approach presented herein combines pretabulted chemistry look-up tables and the calculation of the combustion progress based on chemical enthalpy. This work includes the comparison between the combustion progress variable (CPV) model and an on-line chemistry solver applying a reduced *n*-heptane mechanism and the emission prediction for different EGR amounts applying the CPV model and a *n*-decane/*α*-methyl-naphthalene mechanism. The simulations show in general a good agreement between on-line and CPV model. Also, the soot and NO_x emissions are reasonable. The gain in CPU time depends on the mechanism size but is at least of factor 2 for mechanisms of about 50 species.

Introduction

The main target in modern Computational Fluid Dynamic (CFD) simulations of internal combustion engine combustionis predictive simulations. In order to reach this goal, the use of detailed chemistry schemes are indispensable. Detailed chemistry schemes are especially important for the prediction of emissions as nitrogen oxides (NO_x), soot and unburned hydrocarbons. Today there are more and more complex detailed chemistry schemes available in literature, c.f. [1] and references therein. In general, with more complex schemes including more species, more accurate results can be obtained. The biggest disadvantage of those complex schemes is the high demand of computational cost due to the high number of transported scalars and the chemistry solver. To overcome these problems tabulated chemistry approaches have been proposed.

The idea of our approach is to use the chemical enthalpy h_{298} as progress variable as

for transient flamelet models and cell local Conditional Moment Closure [2] and apply to the Well-Stirred Reactor (WSR) combustion model [3, 4]. The WSR model is chosen for simplicity, to treat the chemical source term without consideration of any turbulence fluctuations. The benefit of this approach is that the mechanism size will not affect the CFD run-time, since all combustion chemistry is pretabulated and the number of scalars to transport will be the same regardless of the chemical mechanism.

Methodology

To validate the presented tabulated chemistry approach, the prediction of the CPV model is compared to the prediction of a WSR on-line chemistry solver [5]. The same approach was introduced and discussed for the Stochastic Reactor Model (SRM) in [6] [7].

The Combustion Progress Variable (CPV) model

The base for this approach forms the assumption that a progress variable *C* can be used for the reconstruction of the thermo-chemical state on the whole reaction trajectory. The reaction progress variable *C* is defined as function of the chemical enthalpy h_{298} as it was suggested in [8]:

$$C = \frac{h_{298} - h_{298,0}}{h_{298,eq} - h_{298,0}} \tag{1}$$

In the model the chemistry is solved using constant pressure reactors [5] and stored in a look-up table (CPV table). The look-up parameters are pressure *p*, unburned temperature T_u, equivalence ratio ϕ, reaction progress *C* and the EGR amount $Y_{EGR.}$ The generated table and look-up replaces the chemistry solver in the CFD code. For this additional transport equations for the mixture fraction *Z*, h_{298} and the tabulated species Y_α are introduced.

$$\frac{\partial \bar{\rho}\tilde{Z}}{\partial t} + \nabla \cdot \left(\bar{\rho}\tilde{\boldsymbol{v}}\tilde{Z}\right) - \nabla \cdot \left(\bar{\rho} D_t \nabla \tilde{Z}\right) = \overline{\rho\dot{\omega}_S} \tag{2}$$

$$\frac{\partial \bar{\rho}\tilde{h}_{298}}{\partial t} + \nabla \cdot \left(\bar{\rho}\tilde{\boldsymbol{v}}\tilde{h}_{298}\right) - \nabla \cdot \left(\bar{\rho} D_t \nabla \tilde{h}_{298}\right) = \overline{\rho\dot{\omega}_{S,h298}} + \overline{\rho\dot{\omega}_{chem,h298}} \tag{3}$$

$$\frac{\partial \bar{\rho}\tilde{Y}_\alpha}{\partial t} + \nabla \cdot \left(\bar{\rho}\tilde{\boldsymbol{v}}\tilde{Y}_\alpha\right) - \nabla \cdot \left(\bar{\rho} D_t \nabla \tilde{Y}_\alpha\right) = \overline{\rho\dot{\omega}_S}\delta_{\alpha\beta} + \overline{\rho\dot{\omega}}_\alpha \tag{4}$$

Those equations are transported and solved by the CFD code (Converge [9]), except for $\overline{\rho\dot{\omega}_S}$, $\overline{\rho\dot{\omega}_{S,h298}}$, $\overline{\rho\dot{\omega}_{chem,h298}}$ and $\overline{\rho\dot{\omega}}_\alpha$ which are the source terms from the CPV model. Only 9 CPV species are transported and used to calculate the thermodynamics of the gas phase. To predict NO_x and soot, corresponding source terms can be stored in the CPV table and used later in the CFD simulation. For NO_x prediction the thermal NO model is applied. Soot is predicted by the Method of

Moments [10] using two moments: M_0 (number density) and M_1 (soot mass). Their sources can be calibrated by adjusting the parameters for nucleation, surface growth, fragmentation, oxidation by O_2 and by OH. The soot model is based on [11] and described in [12].

Reaction schemes

Two different reaction schemes are analyzed: first, a reduced *n*-heptane mechanism from [13], which includes 56 species and 206 reactions. *n*-heptane is still a widely used simple surrogate to model commercial Diesel and is therefore used to compare the tabulated versus on-line combustion prediction. Second, a more complex *n*-decane/*α*-methyl-naphthalene mechanism [5] to predict emissions. The surrogate consists 75 mass% *n*-decane and 25 mass% *α*-methyl-naphthalene. This reaction scheme has 189 species and 2483 reactions. Table 1 shows the used ranges to generate the look-up tables.

Table 1. CPV table ranges.

	reduced *n*-heptane		***n*-decane/ *α*-methyl-naphthalene**	
Property	Range	Grid points	Range	Grid points
EGR [%]	0.0 – 50.0	6	0.0 – 50.0	6
Equivalence ratio [-]	0.1 - 10.0	38	0.1 - 4.0	20
Pressure [bar]	1.0 - 200.0	24	1.0 - 200.0	17
Unburnt temperature [K]	300.0 - 1500.0	89	300.0 - 1500.0	22

Engine case

For this study a diesel engine sector case is used (137 mm bore, 165 mm stroke and 263 mm connecting rod). The engine operates at 1600 rpm and the fuel is injected as single injection at 9° CA bTDC. The EGR amount is set to 4 %, 15 % and30 %.

Results and Discussion

Figure 1 shows the comparison between 4% and 30% EGR amount predicted using the n-heptane mechanism. The decreasing maximum pressure and lower temperatures are well captured by the CPV approach. The heat release (HR) rate indicates that the CPV cases ignites earlier than the on-line chemistry cases. Further, the premixed peak of the CPV case for 4% EGR is recognizable higher than the other premixed peaks. The reason for that can be understood considering Figure 2 that shows 3D post-processing. In the upper row the ignition of the on-line case applying 30% EGR in the bottom row the corresponding CPV prediction is shown. The overall temperature pattern is close except for the ignition. The CPV case ignites earlier and around the whole injection cone, whereas the on-line solution shows a clear lift-off. The reason of the early ignition is because of the use of 9 species for the

thermodynamics in the CPV model only. The injected mass can either be assigned to *n*-heptane or to small hydrocarbons as C_2H_4, whereas in the on-line calculation several possible decomposition pathways with different contribution to the thermodynamic state are available.

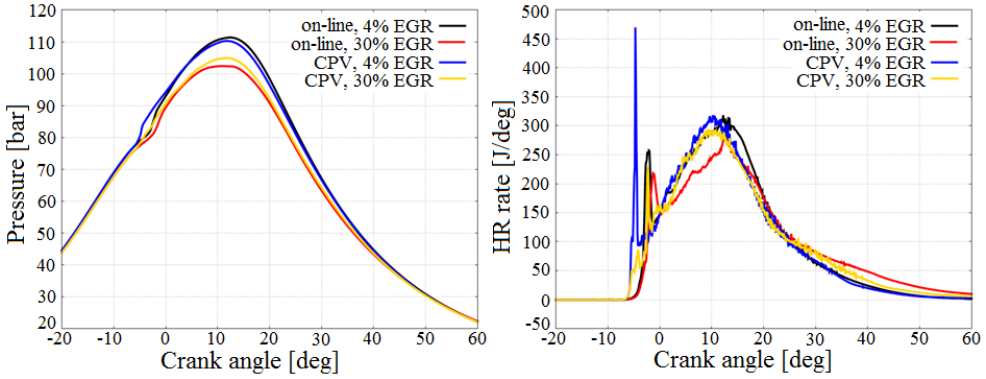

Figure 1. Pressure and HR rate comparison between CPV and on-line chemistry.

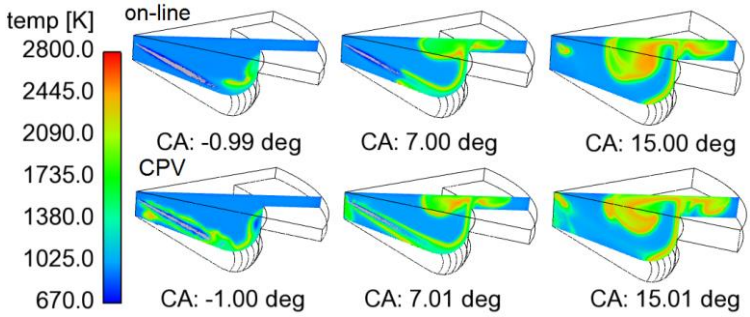

Figure 2. Temperature profiles from on-line and CPV cases with 30% EGR.

Figure 3 shows the emission prediction for three different EGR amounts using the *n*-decane/*α*-methyl-naphthalene mechanism and the CPV model. The soot number density is predicted to have about the same maximum for all three EGR cases. After the maximum the soot number density decrease while at exhaust valve opening (EVO) the value with 30% EGR is the highest, with 4% EGR the lowest. This soot mass shows the same trend at EVO. A low EGR amount leads first to a higher soot formation rate, but because of the higher temperatures and available oxygen and hydroxyl radicals, the soot is oxidized during expansion. As a result the soot number density and the soot mass are the lowest at EVO. The lower soot production by lower EGR amounts results on the other hand in a higher NOx production, as shown in the figure 3. The trends in soot and NO_x formation are physical plausible.

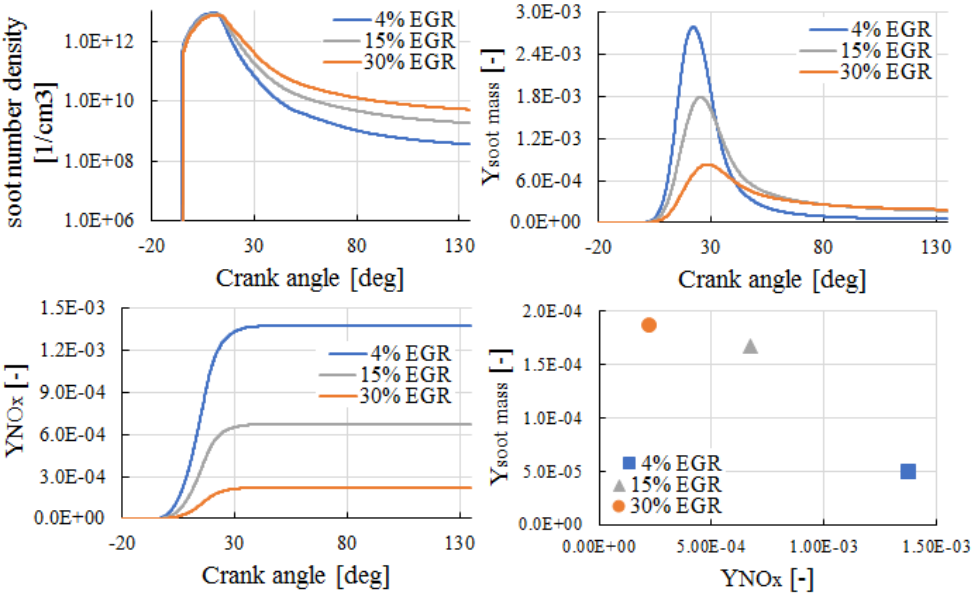

Figure 3. CPVDiesel results with different EGR amounts.

The on-line simulation with the reduced *n*-heptane mechanism has a wall-clock time of 36.7 h on 32 cores (AMD OPTERON from 2008). The use of the CPV model decreases the CPU times to 15.7 for the reduced *n*-heptane mechanism and to 17.2 h for the bigger *n*-decane/α-methyl-naphthalene mechanism. Even though the species number is increased and additionally the soot and NO_x model are applied, the CPU time is the same than for the smaller reaction schemes, due to the tabulated approach.

Conclusion

The combustion prediction using the CPV approach agrees good and reasonable with the on-line chemistry solver. Also, the emission prediction is plausible. The CPV tables are applicable over a wide range of operating conditions.

The use of CPV model results in CPU times, which are for small reaction schemes twice as fast and higher CPU depending on the mechanism size. Additionally, the emission prediction is free of CPU costs.

Future steps will include updates in treatment of the species for thermodynamics and the improvement of the vaporization handling. Further a comparison to experiments for combustion and emission will be carried out.

Nomenclature

C	reaction progress variable
D_t	diffusion constant
h_{298}	current chemical enthalpy in the cell
$h_{298,0}$	enthalpy of formation at standard state

$h_{298,eq}$ chemical enthalpy in equilibrium
p pressure
T_u unburned temperature
t time
Y mass fraction
Z mixture fraction
Φ equivalence ratio
δ_{ii} Kronecker delta
v velocity
ρ density
$\dot{\omega}$ source term

References

[1] Lu, T., Law, C. K., "Toward accommodating realistic fuel chemistry in large-scale computations", *Prog. Energ. Combust.* 35(2):192-215 (2009).
[2] Lehtiniemi, H., Borg, A., Mauss, F., "Combustion Modeling of Diesel Sprays", *SAE Technical Paper*: 2016-01-0592 (2016).
[3] Vishwanathan, G., Reitz, R. D., "Development of a practical soot modeling approach and its application to low-temperature diesel combustion", *Combust. Sci. Technol.* 182:1050-1082 (2010).
[4] Pang, K. M., Jangi, M., Bai, X.-S. and Schramm, J., "Evaluation and optimization of phenomenological multi-step soot model for spray combustion under diesel engine-like conditions", *Combust. Theor. Model.* 19(3):279-308 (2015).
[5] LOGE AB, www.logesoft.com, 2018.
[6] Matrisciano, A., Franken, T., Perlman, C., Borg, A. et al.., "Development of a Computationally Efficient Progress Variable Approach for a Direct Injection Stochastic Reactor Model", *SAE Technical Paper*: 2011-01-0512 (2017).
[7] Matrisciano, A., Borg, A., Perlman, C., Lehtiniemi, H. et al.., "Soot Source Term Tabulation Strategy for Diesel Engine Simulations with SRM", *SAE Technical Paper*: 2015-24-2400 (2015).
[8] Lehtiniemi, H., Mauss, F., Balthasar, M., Magnusson, I., "Modeling diesel spray ignition using detailed chemistry with a progress variable approach", *Comb. Sci. and Tech.* 178: 1977-1997 (2006).
[9] Richards, K.J., Senecal, P.K., and Pomraning, E., "CONVERGE (v2.3), Convergent Science, Inc., Madison, WI," 2016.
[10] Frenklach, M., Harris, S. J., "Aerosol dynamics modelling using the method of moments" *J. Colloid Interface Sci.118*:252–261 (1987).
[11] Mauß, F., *Entwicklung eines kinetischen Modells der Rußbildung mit schneller Polymerisation.* PhD thesis, RWTH Aachen, (1998).
[12] Pasternak, M., Mauss, F., Perlman, C., Lehtiniemi, H., "Aspects of 0D and 3D Modeling of Soot Formation for Diesel Engines", *Combust. Sci. Technol.* 186:10-11, 1517-1535 (2014).
[13] Seidel, L., Netzer, C., Hilbig, M., Mauss, F. et al., "Systematic Reduction of Detailed Chemical Reaction Mechanisms for Engine Applications", *J. Eng. Gas Turbine Power 139(9)*:GTP-17-1030 (2017).

SESSION VI

Reaction kinetics

A COMPREHENSIVE DETAILED KINETIC MECHANISM FOR THE SIMULATION OF GASOLINE FUELS

M. Mehl[1*], K. Zhang[1], S.W. Wagnon[1], G. Kukkadapu[1], C.K. Westbrook[1], W.J. Pitz[1], Y. Zhang[2], H.J. Curran[2], M.J. Al Rashidi[3], N. Atef[3], S.M. Sarathy[3]

[*]Corresponding Author Email: mehl6@llnl.gov, marco.mehl@polimi.it
[1]Lawrence Livermore National Laboratory, Livermore, USA
[2]Combustion Chemistry Centre, National University of Ireland, Galway, Ireland
[3]Clean Combustion Research Center (CCRC), King Abdullah University of Science and Technology (KAUST), Thuwal, Saudi Arabia

Abstract
This work presents a recently compiled comprehensive model for gasoline fuels resulting from the collaboration of three research groups: LLNL, NUI Galway and KAUST. In the past 5 years new fundamental calculations led to significant improvements in the fidelity of detailed kinetic models of important surrogate components (e.g. n-heptane, iso-octane, toluene…) improving predictions of the combustion behavior of pure components and mixtures. By extending the newly adopted reaction rate rules, mechanisms for components that were not included in the previous LLNL gasoline were developed (e.g. polyalkylated aromatics, cycloalkanes, components from bio-logical sources…). The major features of this updated and extended model are presented together with validation comparisons, examples of applications and future directions.
Keywords: Detailed kinetics, transportation fuels, fuel surrogates

Introduction

Thanks to the increasing accessibility to high performance computing, it is becoming common practice for industry to incorporate detailed kinetic calculations in the design of combustion systems.
Compared to semi-empirical and highly reduced models, detailed kinetics allows extrapolating predictions to a wide range of conditions. Furthermore, it enables to simulate different fuel compositions, a powerful feature when the focus is the study of candidate fuel components under consideration for future engine applications.
This work presents a detailed kinetic mechanism for transportation fuels developed through the cooperative effort of LLNL, NUI Galway and KAUST combustion teams. In the current model, compared to the previously published LLNL gasoline model, the number of available fuel components is expanded significantly, and a broad range of distillation temperatures and structures are covered. Particular relevance is given to oxygenate components in the gasoline boiling range and their blending behavior.

The kinetic mechanism: general features

The kinetic mechanism here presented is based on principles of hierarchy, self-consistency and modularity. The mechanism core is the recent extensively validated base chemistry compiled by the NUI Galway combustion group, the AramcoMech 2.0. The AramcoMech 2.0 covers the combustion chemistry of C0 to C4 hydrogen/carbon compounds as well as ethanol, methanol and dimethyl ether. Compared to its previous version (AramcoMech 1.3), this mechanism incorporates updated rates emerging from extensive studies on the chemistry of small olefins (e.g. [1]). These updates impacted positively predictions at high temperature conditions, where large fuel molecules rapidly decompose into C2-C4 unsaturated species (e.g. high temperature ignition, flame speed and structure...).

The C0-C4 mechanism has been extended to lager alkanes up to C7 species. Long chain saturated species are characterized by low temperature oxidation pathways leading to degenerate chain branching. While this chemistry has been the subject of investigations for decades, it is only in recent years that quantomechanic calculations provided more precise estimates of the reaction rates involved in the process. The recent studies by Bugler et al, and Zhang et al. [2-4] carried of a critical review of these recent fundamentally calculated rates and validated self-consistent comprehensive models based on them. Adopting the same principles, a collaborative effort involving NUI Galway, LLNL and KAUST carried out a comprehensive study on iso-octane and updates based on recently calculated reaction rates have been proposed [5].

Beside saturated species, the mechanism here discussed features a recently updated toluene model based on the work by Zhang et al. Contrarily to most of the kinetic mechanisms available for toluene, Zhang experimental and modeling work focused on the reactivity of toluene in blends, allowing to probe the reactivity of the aromatic component in the low temperature region (650K-950K), where the pure component is too refractory to be tested rapid compression machines [6]. In this work, Zhang's mechanism underwent minor updates to correct transcription errors affecting the original version.

Mixtures of primary reference fuels (n-heptane and iso-octane) and toluene are often used within the engine community to mimic the reactivity of gasoline fuels but typically fail to reproduce physical and chemical properties such as distillation curve, density, sooting tendency or H/C ratio. A better characterization of the fuel can be achieved through the use of more complex mixtures including olefins, naphthenes and oxygenates. The mechanism here discussed expands the possibility of modelers by including the detailed oxidation chemistry of C6 linear olefins, diisobutylene [7] and cycloalkanes from C5 to C7 [8].

A number of mechanism for oxygenated species were also included. The previously published mechanisms for higher alcohols (C3-C5 isomers) were merged with the gasoline portion of the mechanism and revalidated against older predictions. The previously published mechanism for small esters was thoroughly revised and updated using recently calculated reaction rates from quantomechanic calculations.

Finally, validation targets for ethyl and methyl acetate were expanded to include ignition delay time data.
A detailed kinetic model for anisole, an oxygenated aromatic considered to be representative of bio oils derived from fast pyrolysis, has been developed and incorporated in the model. Further details on this mechanism are available in a paper by Wagnon et al. [9].
Finally, in order to provide NOx formation predictions and capture NO sensitization effects for engine combustion application, the detailed kinetic model for gas phase nitrogen reactions from Politecnico di Milano [10] was added to the mechanism.
Comprehensively, this detailed kinetic model covering a number of gasoline components, together with the bio-derived fuel components, includes about 2300 species and 10000 reactions.

The kinetic mechanism: selected validation comparisons
The significant updates introduced in the gasoline mechanism led to improved agreement with literature and newly collected experimental data.
Figure 1a and 1b respectively compare the simulated ignition delay times (solid lines) of n-heptane and iso-octane against literature experimental data (symbols). Results obtained with the previously published kinetic mechanism are presented with a dashed line.

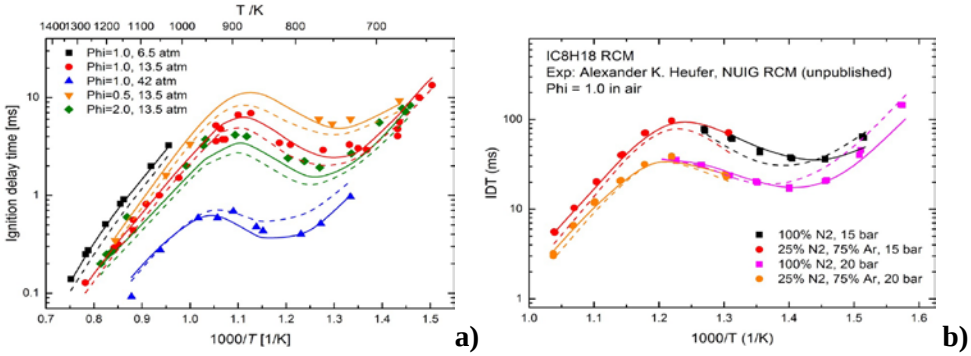

Figure 1. Predicted ignition delay times of PRFs (a: n-heptane, b: iso-octane) versus measurements (n-heptane data are from Ciezky and Adomeit, 1993). Dashed lines show predictions obtained with the 2011 LLNL mechanism.

It can be noticed how the new mechanism exhibits an improved pressure dependence predicting a significantly enhanced reactivity at 40 atm and longer ignition delay times at 3-15 atm.. These changes can be attributed to the new rates adopted for the low temperature chemistry and updates in the thermochemical properties, which were calculated in THERM using a revised version of the group contribution database. These changes have important implication in the simulation of engine combustion where the in-cylinder pressure at top dead center easily exceeds 25atm, a pressure condition for which the two models respond similarly.

Another important element covered by the mechanism validation was the study of fuel component mixtures. Beside validation on pure components, great emphasis was given to the study of binary and multicomponent blends, an effective way to investigate the reactivity of refractory fuels such as aromatics in the low temperature region.
Figure 2 shows the calculated ignition profiles obtained for a 50/50 by mole mixture of toluene and n-heptane. Solid lines indicate predictions obtained with the current model, symbols are recent experimental data collected in the NUI Galway RCM. Dashed lines indicate calculations obtained using the previously published mechanism. Once more the mechanism captures correctly the experimental trends exhibiting an improved pressure dependence (mostly due to the changes in the n-heptane chemistry).

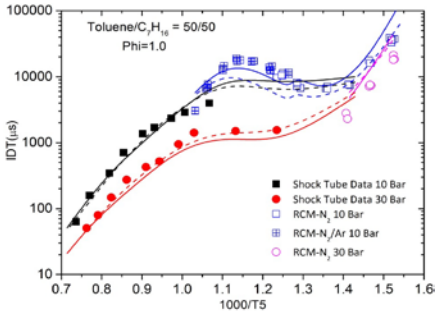

Figure 2. Predicted ignition delay times of a n-heptane/toluene blend. Dashed lines shows predictions obtained with the 2011 LLNL mechanism

Applying the kinetic mechanism to octane number estimates
An interesting application of the described kinetic mechanism is the evaluation of the blending behavior for a variety of fuels containing oxygenate compounds. This effort fit within the scope of the Co-Optima effort carried out by nine US National laboratories, including LLNL, and supports the computational and experimental search for more efficient combustion strategies for automotive application where fuel and engines are considered as a whole system subject to optimization. The methods used to estimate the octane numbers of mixtures from their ignition delay times in constant volume calculations is described in Mehl et al. [11].
In this work, the original correlations have been reformulated using a broader set of mixtures as training set.
The updated kinetic model and correlations were used to explore the blending behavior of some oxygenate components of interest in a 4 component base fuel mimicking the composition of a high octane BOB (before oxygenate blending) with a RON of 91.
Increasing fractions of oxygenate components were added to the base fuel and, using the correlations, their RON and sensitivities (not discussed here) were estimated. The same blends were independently tested in a standard CFR engine to meas-

ure their octane numbers [12]. Figure 3 shows the predicted RONs (solid lines) and measured ones across a wide region of blending ratio.
The model captures the relative effectiveness in increasing the antiknock performances of most of the considered fuel additives and, even more interestingly, replicates correctly the synergistic (e.g. methanol) vs antagonistic (n-butanol) blending behavior of different fuels, noticeable through the convexity of the presented curves. Similar tests have been successfully carried out for other fuel components and demonstrates how the presented model can be effectively applied to the study of complex blends and compositional effects in engines.

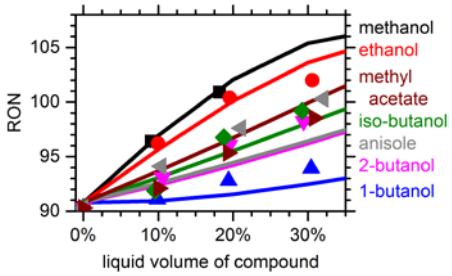

Figure 3. RON predictions for blends including increasing amount of oxygenate species (lines) vs experiments (symbols)

Conclusions

This work presents a comprehensive model for transportation fuels resulting from a multi-year collaboration of three combustion research groups (LLNL, NUI Galway and KAUST). The model discussed in the paper includes the most recent mechanisms by these groups for fuel components ranging from natural gas to diesel. The mechanism features rates obtained through extensive critical reviews of current fundamental calculations and provides predictions showing improved agreement with literature data. New experimental data were also obtained to validate the model at less investigated conditions. Thanks to the large number of components included in the mechanism, this comprehensive model allows to investigate the blending behavior of an unprecedented variety of fuels.

Acknowledgements

The portion of this work performed at LLNL was supported by the U.S. Department of Energy (DOE), Office of Energy Efficiency and Renewable Energy (EERE), Vehicle Technology Office (VTO) under contract no. DE-AC52-07NA27344

References

[1] C-W. Zhou, Y. Li, E. O'Connor, K.P. Somers, S. Thion, C. Keesee, O. Mathieu, E.L. Petersen, T. A. DeVerter, M.A. Oehlschlaeger, G. Kukkadapu, C-J. Sung, M. Alrefae, F. Khaled, A. Farooq, P. Dirrenberger, P-A. Glaude, F. Battin-Leclerc, J.

Santner, Y. Ju, T. Held, F.M. Haas, F.L. Dryer, H.J. Curran, A Comprehensive experimental and modeling study of isobutene oxidation, Combust. Flame 167 (2016) 353–379.
[2] J. Bugler, B. Marks, O. Mathieu, R. Archuleta, A. Camou, C. Grégoire, K.A. Heufer, E.L. Petersen, H.J. Curran, An Ignition Delay Time and Chemical Kinetic Modelling Study of the Pentane Isomers, Combustion and Flame 163 (2016) 138-156.
[3] K. Zhang, C. Banyon, C. Togbé, P. Dagaut, J. Bugler, H.J. Curran, An experimental and kinetic modeling study of n-hexane oxidation, Combustion and Flame 162 (2015) 4194–4207.
[4] K. Zhang, C. Banyon, J. Bugler, H.J. Curran, A. Rodriguez, O. Herbinet, F. Battin-Leclerc, C. B'Chir, K.A. Heufer, An updated experimental and kinetic modeling study of n-heptane oxidation Combustion and Flame 172 (2016) 116–135.
[5] N. Atef, G. Kukkadapu, S.Y. Mohamed, M. Al Rashidi, C. Banyon, M. Mehl, A. Heufer, E.F. Nasir, A. Alfazazia, A.K. Das, C.K. Westbrook, W.J. Pitz, T. Lu, A. Farooq, C-J. Sung, H.J. Curran, S.M. Sarathy, A Comprehensive iso-Octane Combustion Model with Improved Thermochemistry and Chemical Kinetics Combustion and Flame 178 (2017) 111–134.
[6] Y. Zhang, Kieran P. Somers, Marco Mehl, William J. Pitz, Roger F. Cracknell, Henry J. Curran, Probing the antagonistic effect of toluene as a component in surrogate fuel models at low temperatures and high pressures. A case study of toluene/dimethyl ether mixtures, Proceedings of the Combustion Institute 36 (2017) 413-421.
[7] W. Metcalfe, W. J. Pitz, H. J. Curran, J. P. Orme, J. M. Simmie, C. K. Westbrook
The Development of a Detailed Chemical Kinetic Mechanism for Diisobutylene and Comparison to Shock Tube Ignition Times, Proc. Combust. Inst. 31 (2007) 377–384.
[8] M.J. Al Rashidi, S. Thion, C. Togbé, G. Dayma, M. Mehl, P. Dagaut, W.J. Pitz, J. Zádor, S. M Sarathy, Elucidating reactivity regimes in cyclopentane oxidation: Jet stirred reactor experiments, computational chemistry, and kinetic modeling, Proceedings of the Combustion Institute 36 (2017) 469–477.
[9] Wagnon S. W., Thion,S., Nilsson E. J. K., Mehl M., Zhang K., Serenyel Z., Konnov A., Dagaut P. Dayma G., Pitz W. J., Experimental and modeling studies of a biofuel surrogate compound: laminar burning velocities and jet-stirred reactor measurements of anisole, Combustion and Flame 189 (2018) 325-336
[10] T. Faravelli, A.Frassoldati and E. Ranzi, Kinetic modeling of the interactions between NO and hydrocarbons in the oxidation of hydrocarbons at low temperatures, Combustion and Flame 132 (2003) 188 – 207.
[11] M. Mehl, J.Y. Chen , W.J. Pitz, S.M. Sarathy, C.K. Westbrook, An Approach for Formulating Surrogates for Gasoline with Application Toward a Reduced Surrogate Mechanism for CFD Engine Modeling, *Energy and Fuels* 25 (2011) 5215-*5223*.

[12] R.L. McCormick, G.M. Fioroni, L. Fouts, J. Yanowitz, E. Polikarpov, K. Albrecht, D.J. Gaspar, J. Gladden, A. George, Selection Criteria and Screening of Potential Biomass-Derived Streams as Fuel Blendstocks for Advanced Spark-Ignition Engines, SAE Technical Paper No. 2017-01-0868 (2017).

DRG AND GQL REDUCTION METHODS FOR A H2/AIR AUTO-IGNITION PROBLEM

C.Yu*, F. Minuzzi, V.Bykov*, U.Maas***
viatcheslav.bykov@kit.edu
*Institute of Technical Thermodynamics, Karlsruhe Institute of Technology (KIT)
**Graduate Program in Applied Mathematics, Federal University of Rio Grande do Sul

Abstract
Two advanced reduction methods for systems of chemical kinetics, Global Quasi-linearization (GQL) and Directed Relation Graph (DRG), are implemented to reduce a homogeneous combustion system. In this work, the auto-ignition process of H2-air system is considered for a wide range of system parameters and initial conditions. Results based on GQL and DRG reduced chemistry are compared.

Introduction

The interest in the numerical simulation of combustion processes has grown considerably during the last decade due to strict regulations with respect to pollutant formation and efficiency of combustion processes. An auto-ignition problem represents one of the most important and studied topics in combustion theory used for combustion mechanisms development and for their validation [1]. In order to accurately model the auto-ignition a large number of different elementary reactions between many species has to be accounted for. Vastly different characteristic time-scales induced by elementary reactions due to the non-linearity of elementary reaction rates result in stiffness of the governing system of ODEs [1] [2]. Both high dimensionality of such systems and their stiffness lead to an extreme complexity and high computational load with respect to the CPU time and memory storage required to treat combustion systems numerically. Therefore, there is a need to reduce these detailed mechanisms.

At present, significant progress in developing model reduction methodology has been made in a number of studies. It was originated by the Quasi-Steady state Approximation (QSSA) [3] and Partial Equilibrium Approximation (PEA) [4] approaches. The methods treat either species in quasi-steady state or elementary reactions in partial equilibrium [1] [5]. A very transparent example of such approaches is the Directed Relation Graph (DRG) [8], which is used in the current study. All these methods eliminate species and, hence, the resulted reduced models compute only some of the species, thus, reducing the dimension of governing equation systems [1].

Other model reduction approaches use low-dimensional invariant manifolds, namely, the Intrinsic Low-Dimensional Manifold (ILDM) method [6], the Global Quasi-linearization (GQL) approach [7], the Computational Singular Perturbation (CSP) method [9], which allow to keep information about all species involved and

nevertheless reduce the dimension of kinetic models.
In this work, two model reduction techniques, that belong to these different groups: the GQL method and the DRG method, are investigated and compared. The GQL method explores globally the multiple time-scale hierarchy of the system and the reduction algorithm follows the fast and slow invariant manifold concepts [7], while the DRG is based on the construction of skeletal mechanisms, aiming to remove those species having negligible influence on the important species [8].

Mathematical Model
In this work, auto-ignition processes are described by a pure homogeneous systems of ODEs. The mathematical model can be expressed in a general vector form:

$$\frac{d\boldsymbol{\psi}}{dt} = \mathbf{F}(\boldsymbol{\psi}), \quad \boldsymbol{\psi} \in R^n \tag{1}$$

Here ψ is the n-dimensional thermos-kinetic state vector $\boldsymbol{\psi} = \left(h, p, \frac{w_1}{M_1}, \frac{w_1}{M_1}, \cdots, \frac{w_{ns}}{M_{ns}}\right)^T$, where h is the enthalpy, p the pressure and w_i and M_i the mass fractions and molar masses of species. $\mathbf{F}(\boldsymbol{\psi})$ is the n-dimensional vector of thermo-kinetic source term[4].

Global Quasi-linearization (GQL)
The Global Quasi-linearization (GQL) approach stems from the singular perturbation theory and aims at the appropriate approximation of the low-dimensional manifold describing the system dynamic generically [7] [10]. The GQL is based on an assumption that the system dynamic can be decomposed and a small "hidden" parameter of the system determining the main disparity of time-scales exists [7] [11]. According to this assumption, the vector field $\mathbf{F}(\boldsymbol{\psi})$ can be globally linearly approximated [7]:

$$\mathbf{F}(\boldsymbol{\psi}) \cong \mathbf{T}_{\mathrm{GQL}} \cdot \boldsymbol{\psi} \tag{2}$$

The Eq. (2) shows that within the GQL approach we look for a linear mapping $\mathbf{T}_{\mathrm{GQL}}$ that transforms some thermo-kinetic state vectors $\boldsymbol{\psi}$ to the vector field of source term $\mathbf{F}(\boldsymbol{\psi})$. Once this mapping is found we can follow the main idea of ILDM method [6] and a time-scale separation can implemented to yield the eigenvalue decomposition of the GQL matrix $\mathbf{T}_{\mathrm{GQL}}$ identifying the fast and slow invariant subspaces:

$$\mathbf{T}_{\mathrm{GQL}} = \begin{pmatrix} Z_s & Z_f \end{pmatrix} \cdot \begin{pmatrix} N_s & 0 \\ 0 & N_f \end{pmatrix} \cdot \begin{pmatrix} \tilde{Z}_s \\ \tilde{Z}_f \end{pmatrix}, \tag{3}$$

here N_s and N_f denote the diagonal matrices of the two groups of eigenvalues on the diagonal, and Z_s and Z_f the relevant base of slow and fast eigenspaces. Then, similar to the assumption of the ILDM method [6], the fast relaxed processes define an approximation of the low-dimensional slow manifold within the thermo-kinetic system state space as $\tilde{Z}_f \cdot \mathbf{F}(\boldsymbol{\psi}) = 0$. Then, the implementation scheme of

the GQL approach can be applied to solve the fast and slow subsystems. For the fast subsystem, one can solve [11]:

$$\begin{cases} \dfrac{d\boldsymbol{\psi}}{dt} = Z_f \cdot \tilde{Z}_f \cdot \mathbf{F}(\boldsymbol{\psi}) \\ \tilde{Z}_s \cdot \psi = \tilde{Z}_s \cdot \psi_0 \end{cases}, \tag{4}$$

and the slow subsystem governs the system dynamics on the low-dimensional slow manifolds [11]:

$$\begin{cases} \dfrac{d\boldsymbol{\psi}}{dt} = Z_s \cdot \tilde{Z}_s \cdot \mathbf{F}(\boldsymbol{\psi}) \\ \tilde{Z}_f \cdot \mathbf{F}(\boldsymbol{\psi}) = 0 \end{cases}. \tag{5}$$

Directed Relation Graph (DRG)

The empirical Directed Relation Graph (DRG) approach, developed by Lu and Law in 2005 [8], is a reduction method for the construction of skeletal mechanisms. The aim of the method is to efficiently resolve the species coupling, such that those who have a little or none influence on the important species can be removed.

The DRG is applied to identify the unimportant species and remove the elementary reactions that are not associated with them, using an empirical criterion. Accordingly, the contribution of species B in the production/consumption rate of species A can be quantified through the normalized index r_{AB} [12], given by

$$r_{\mathrm{AB}} = \frac{\sum_{i=1}^{n_r} |\nu_{A,i} \cdot \dot{\omega}_i \cdot \delta_{B,i}|}{\sum_{i=1}^{n_r} |\nu_{A,i} \cdot \dot{\omega}_i|} \tag{6}$$

where $\nu_{A,i}$ is the stoichiometric coefficient of A in reaction I, $\dot{\omega}_i$ is the reaction rate and $\delta_{B,i}$ is

$$\delta_{B,i} = \begin{cases} 1, & \text{if the i}^{\text{th}} \text{ elementary reaction involves species B} \\ 0, & \text{otherwise} \end{cases} \tag{7}$$

The terms in the denominator of Eq.(6) measure the contribution of reactions to the production/consumption of species A, and the terms in the numerator are those from the denominator involving species B only [12].

Defining a threshold limit value ε ($0 < \varepsilon < 1$), and if index r_{AB} is larger compared to this threshold, then removing species B, can induce error in the production of species A, so that species B must be maintained in the skeletal mechanism. Usually, species A are chosen as those who have some desirable chemical attributes that the reduced mechanism should reproduce [13]. The resulting skeletal mechanism obtained has errors according to the user-specified threshold ε for the conditions under which it is developed [8]. Therefore, mechanisms with different levels of accuracy can be obtained by assigning different values for ε.

From a practical point of view, the index r_{AB} defines an error estimate in predicting

species A if B is neglected. Therefore, consumption and production reactions must be considered altogether [13].

Results and Discussion

As a test example, the hydrogen-air system represents a simple combustion system but still sufficient for comparison of these two approaches: GQL and DRG. The detailed chemical kinetic model [4] consists of 9 species (including the inert gas N_2 but NO_x formation is not taken into account).

For DRG calculation applied in this work the following procedures are conducted: first, the target species, which will play the role as A species in the index r_{AB}, are defined, consisting of H_2, O_2 and H_2O. The detailed mechanism is used to simulate an ideal gas reactor and to estimate ignition delay times. For each time step, the DRG is applied using concentrations and temperature from the reactor calculations, and the species with the index greater than the threshold are retained and stored. The final set of species consists in the union of the specie's set from each time step of the reactor calculation. The reactions containing only those species then are selected to be in the skeletal mechanism. Note that the DRG calculation is problem dependent. Therefore, if one only focuses on high temperature range or normal pressures, DRG calculation shows that H_2O_2 can be removed. In this case, one obtains skeletal mechanism with 13 elementary reactions and 8 species (without H_2O_2). However, since H_2O_2 plays important roles in high pressures [4], if one should obtain a satisfactory accuracy over a wider range including high pressures, H_2O_2 should be considered as well and, in this case, all species should be retained in the reduced skeletal model.

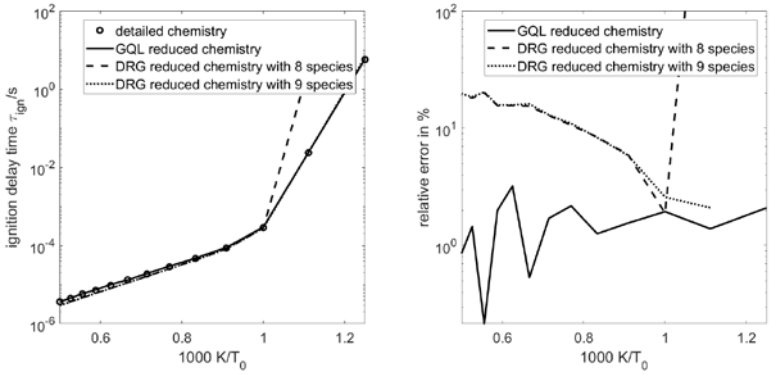

Figure 1. Dependence of the ignition delay time on the initial temperature at p_0=1bar and $\Phi = 1.0$.

The GQL approach for hydrogen-air system has been discussed in [10], where a 4-dimension (4D) reduced model was achieved by using the low-dimensional manifold concept. At present the system (5) represents the reduced model, where the manifold in an implicit form is taken into account and it comprises a reduced model. The system is integrated as a system of Differential and Algebraic

Equations (DEAs). Then, the solution of the system (5) is compared to the solution of the system (1).

The figures illustrate the performance of both approaches and show the dependence of the ignition delay time on the initial temperatures (Fig. 1) and initial pressures (Fig. 2). At first, one can see for the studied range that the GQL reduced model (solid lines) can predict the ignition delay time very well with relative errors less than 2%. The DRG method performs as following. If H_2O_2 was not considered (dashed lines), then relative errors are relatively large at low temperatures (T_0 <1000 K) and at high pressures (p_0 >10 bar). However, if H_2O_2 is considered (point lines), then relative errors remain rather small (less than 15%) for the whole studied range. It should be emphasized that the hydrogen mechanism is already a small mechanism (19 reversible elementary reactions) and all species are strongly coupled. As it is shown by the results outlined, the GQL can predict the auto-ignition processes for a wide range of initial conditions with less number of reduced dimension and more accurately. The DRG, on the other hand, has the advantage of being represented by the skeletal mechanisms, which can be straightforwardly implemented.

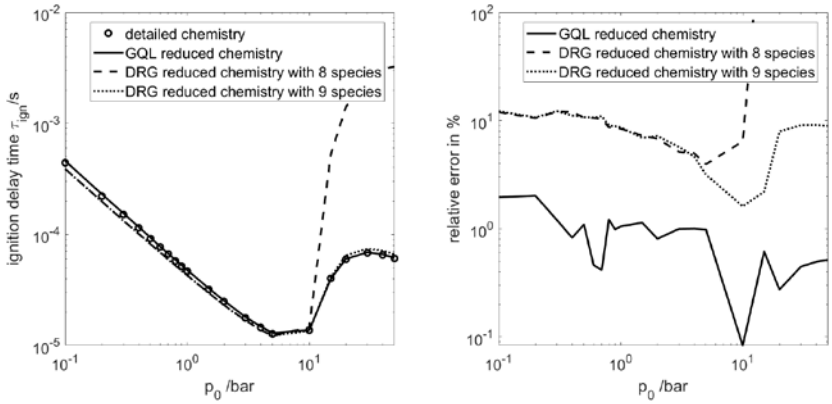

Figure 2. Dependence of the ignition delay time on the initial pressure at T_0=1200 K and $\Phi = 1.0$.

Conclusion

The Global Quasi-linearization (GQL) and Direct Relation Graph (DRG) methods were discussed and their performance was compared for the auto-ignition problem of hydrogen-air system. The results of the comparison were validated in a very wide range of initial conditions ($800 \leq T_0 \leq 2000$ K, $0.1 \leq p_0 \leq 50$ bar). It was shown that for the whole considered range, the relative errors by using the 4D GQL reduced chemistry were often less than 2%. For the DRG method, since hydrogen mechanism is already small, all species are strongly coupled and the only specie that could be withdrawn from the detailed mechanism to obtain the least number of species and elementary reactions is the H_2O_2. But in this case, the results will show less accuracy for high pressures and low temperatures. However, for large

mechanisms, DRG will produce a higher reduction in the dimension of the resulting skeletal mechanisms.

Acknowledgement
Financial support by the German Research Foundation (DFG) within the project SFB/TRR 150 is gratefully acknowledged. F. Minuzzi is supported by CAPES – Brazil under the grant No. 88881.132868/2016-01.

Reference

[1] T. Echekki and E. Mastorakos, Turbulent combustion modeling: Advances, new trends and perspectives, Springer Science & Business Media, 2010.

[2] C. K. Law, Combustion Physics, Cambridge university press, 2010.

[3] M. Bodenstein, "Eine Theorie der photochemischen Reaktionsgeschwindigkeiten," *Zeitschrift für physikalische Chemie,* vol. 85, pp. 329-397, 1913.

[4] J. Warnatz, U. Maas and R. W. Dibble, Combustion: Physical and Chemical Fundamentals, Modeling and Simulation, Experiments, Pollutant Formation, Berlin: Springer-Verlag, 2000.

[5] T. Turanyi and A. S. Tomlin, Analysis of Kinetic Reaction Mechanisms, Springer, 2014.

[6] U. Maas and S. B. Pope, "Simplifying chemical kinetics: intrinsic low-dimensinal manifolds in composition space," *Combustion and Flame,* vol. 88, no. 3, pp. 239-264, 1992.

[7] V. Bykov, V. Gol'dshtein and U. Maas, "Simple global reduction technique based on decomposition approach," *Combustion Theory and Modelling,* vol. 12, no. 2, pp. 389-405, 2008.

[8] T. Lu and C. Law, "A directed relation graph method for mechanism reduction," *Proceeding of the Combustion Institute,* vol. 30, pp. 1333-1341, 2005.

[9] S. Lam and D. Goussis, "The CSP method for simplifying kinetics," *Int.J.Chem.Kinetics,* vol. 26, pp. 461-486, 1994.

[10] C. Yu, V. Bykov and U. Maas, "Global quasi-linearization (GQL) versus QSSA for a hydrogen-air auto-ignition problem," *Physical chemistry chemical physics,* no. DOI: 10.1039/c7cp07213a.

[11] V. Bykov, V. Gol'dshtein and U. Maas, "Global Quasi Linearization (GQL) for the automatic reduction of chemical kinetics," in *3th European Combustion Meeting,* 2007.

[12] T. Lu and C. Law, "Linear time reduction of large kinetic mechanisms with directed relation graph: n-Heptane and iso-octane," *Combustion and Flame,* vol. 144, pp. 24-36, 2006.

[13] P. Pepiot-Desjardins and H. Pitsch, "An efficient error-propagation-based reduction method for large chemical kinetic mechanisms," *Combustion and Flame,* vol. 154, pp. 67-81, 2008.

DEVELOPMENT OF A MECHANISM FOR DUAL FUEL COMBUSTION

S. Schuh*, J. Frühhaber, F. Winter***
sebastian.schuh@tuwien.ac.at
* Institute of Chemical, Environmental & Bioscience Engineering,
Technische Universität Wien, Getreidemarkt 9/166, 1060 Vienna, Austria
** Institute for Powertrains and Automotive Technology,
Technische Universität Wien, Getreidemarkt 9/315, 1060 Vienna, Austria

Abstract
The pollutant emission limit requirements for marine engines and engines used in heavy-duty vehicles like railways and trucks, becoming stricter and more difficult to meet. The operation of engines in dual fuel mode, using the fuels natural gas and diesel, offers the possibility to significantly reduce pollutant emissions. In the development process of a new engine, simulation tools can reduce the required engine test bench time and therefore lower the total development costs. The reaction mechanism used for the simulation must therefore be able to correctly describe both the combustion of natural gas and diesel. In this study, n-heptane was chosen as diesel surrogate, a mixture of methane and propane considered natural gas. As basic mechanism, the Complete San Diego Mechanism with the heptane and nitrogen chemistry add-on was used. In order to reduce the deviation between the simulation results and the experimental values, an optimization of the reaction mechanism was performed. With a sensitivity analysis, influential reactions were identified and adapted by adjusting the Arrhenius parameters to improve the prediction accuracy of the simulation.

Introduction
In the transport sector, whether on land or on water, engines with a self-ignition concept play the dominant role due to their proven economy, rugged durability and reliability [1]. However, compared to gasoline engines, the increased emission of nitric oxides is one of the major drawbacks of diesel engines. In the case of operating the engine with heavy oil, a high proportion of sulfur compounds is additionally added to the exhaust gas. Due to the more stringent environmental directives such as Eurocode 5 and 6 for motor vehicles in Europe or the Tier II and III standards for maritime large engines, more sophisticated engine concepts are needed, or additional technologies such as selective catalytic reduction have to be applied to meet the limits. An approach to reduce the emission of pollutants from self-igniting engines is the operation in the dual fuel mode. Here, a gas-air mixture is directed into the combustion chamber and ignited by the injection of a diesel pilot jet. Compared to a conventional diesel engine, the NOx and SOx fraction can be reduced significantly [2]. To further optimize the efficiency of the engine and to keep the

emission of pollutants as low as possible, it is highly necessary to know and understand the processes in the combustion chamber precisely. Since the experimental investigation on an engine test stand is associated with high costs and a high time expenditure, it is desirable to develop a theoretical model for the simulation of the dual fuel combustion processes. Due to the injection of a diesel jet into a gas-air mixture in the dual fuel combustion process, the simulation tool must be able to accurately reflect the ignition and combustion kinetics in the diesel-poor as well as diesel-rich ranges. Furthermore, the knocking behavior must be correctly predicted. Diesel fuel is a complex mixture of thousands of hydrocarbon compounds with carbon numbers between 6 and 28 [3]. A consideration of every species would lead to an unmanageable calculation time. To ensure calculability, n-heptane was used as diesel surrogate in this study. The second fuel, natural gas, was substituted by a mixture of methane and propane.

Basic reaction mechanism

The basic mechanism is composed of the Complete San Diego Mechanism and the heptane and nitrogen chemistry add-on [4]. In order to assess the predictive accuracy of the mechanism, experimental data for gas mixtures, as well as gas-n-heptane mixtures were used for validation. Pachler et al. [5] investigated the ignition delay time of methane-propane mixtures with the composition 100 mol% methane and 0 mol% propane, 95 mol% methane and 5 mol% propane and 70 mol% methane and 30 mol% propane at a pressure of 100 bar and a λ-value of 1.9. In the study of Herzler et al. [6], the ignition behavior of a methane-n-heptane mixture with 95 mol% methane and 5 mol% n-heptane at a pressure of 30 bar and a λ-value of 0.5 was investigated. Figure 1 shows a comparison between experimental data, measured with a rapid compression machine and a shock tube, and the ignition delay time calculated with the basic mechanism. All simulations have been performed with the software LOGEresearch v1.10 [7]. The ignition delay time for pure methane is reproduced well by the mechanism in its basic configuration. Increasing the amount of propane leads to a reduction of the ignition delay time. As can be seen, the reducing effect of the propane addition [8] is overestimated, leading to a significant deviation between the experimental and calculated results for a mixture of 70 mol% methane and 30 mol% propane. In the case of the methane-n-heptane mixture, basically, a good approximation of the simulation results to the experimental data is already evident. However, for a temperature lower than 770 K and in the temperature range 950 to 1100 K, the ignition delay time is overestimated. Between 760 and 900 K, as well as for temperatures higher than 1100 K, the calculated ignition delay time is too short.

Reaction selection

In order to determine the reactions, which have a significant influence on the ignition delay time, the individual reactions were investigated with respect to their sensitivity

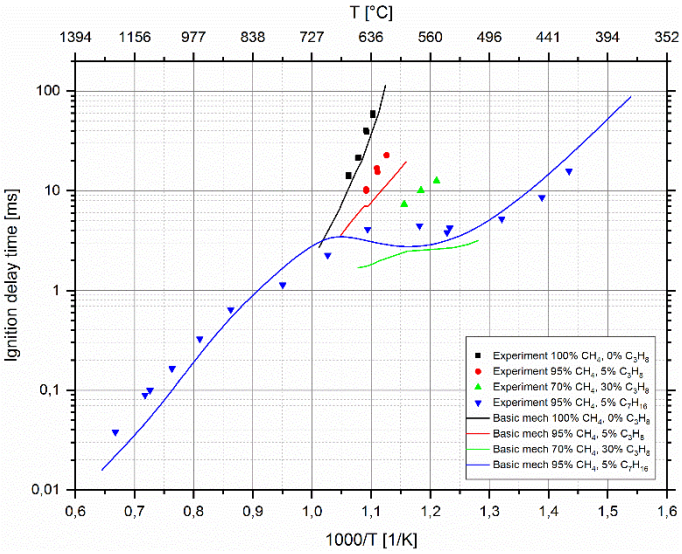

Figure 1. Measured and calculated ignition delay time of methane-propane mixtures with a mol% mixing ratio of 100 to 0, 95 to 5 and 70 to 30, as well as a methane-n-heptane mixture with a mol% mixing ratio of 95 to 5.

on the ignition process. Due to the fact, that the concentration of CH-radicals shows a sharp increase shortly before the ignition event as presented in Figure 2, they can be used as an ignition trigger. Therefore, the elementary reactions of the mechanism were investigated concerning their influence on the formation of CH-radical. Based on this analysis, 12 of 354 reactions have been selected for optimizing the mechanism.

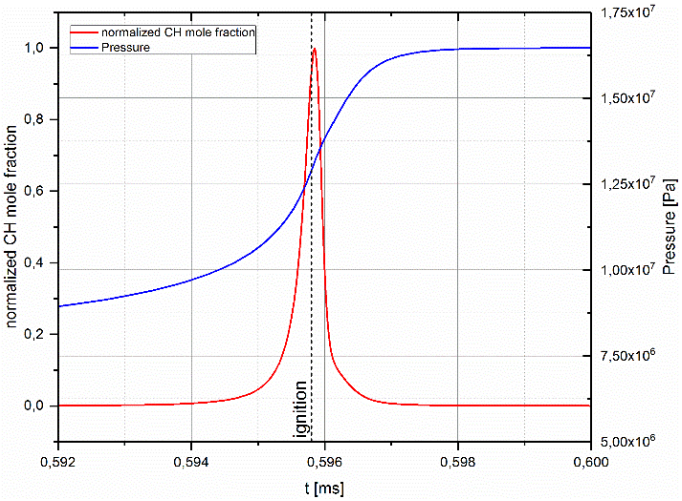

Figure 2. Normalized mole fraction of CH-radicals during the ignition process.

Reaction adaption

The reaction rate coefficients of the elementary reactions are calculated using the extended Arrhenius approach

$$k = A \cdot T^{\beta} \cdot e^{\frac{-E_A}{R \cdot T}} \quad (1)$$

with the frequency factor A, the temperature T, the temperature exponent β, the universal gas constant R and the activation energy E_A. By adapting the Arrhenius parameters of the 12 selected reactions, the mechanism was optimized. The adaptation of the reaction 233 will be described in the following exemplary. The reaction and the associated Arrhenius parameters in the basic configuration are shown in Table 1.

Table 1. Arrhenius parameter overview of reaction 233 in its basic configuration.

Reaction 233	A [-]	β [-]	E_A $[kJ/mol]$
$C_3H_8 + OH \rightarrow nC_3H_7 + H_2O$	$1 \cdot 10^{10}$	1	6.69

The reaction 233 shows a significant influence on the mechanism's underestimating behavior on the ignition delay time when adding propane. The faster this reaction takes place, the shorter is the total ignition delay time. The adaptation of the reaction was carried out by a reduction of the reaction rate constant. The reduction was not uniform, but increased with decreasing temperature. Figure 3 shows the temperature-dependent reaction rate coefficient of reaction 233 in its basic and adapted configuration. The other 11 selected reactions were adjusted in the same or similar way.

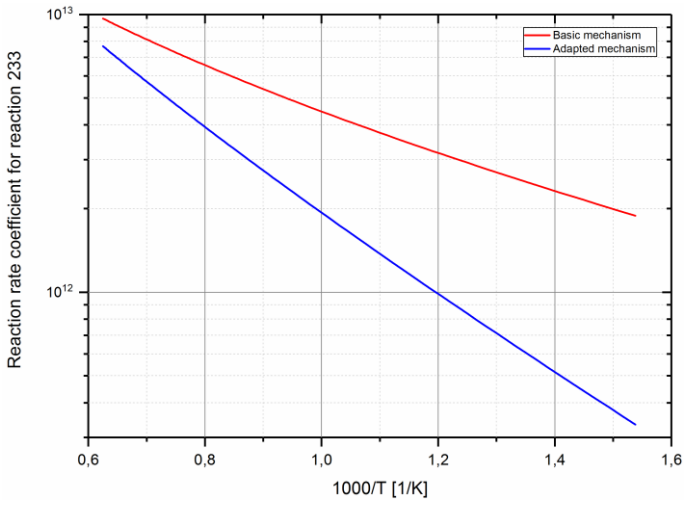

Figure 3. Temperature-dependent reaction rate coefficient of reaction 233.

Optimized mechanism

The impact of the mechanism adaptation is shown in Figure 4. In addition to the simulation result with the new mechanism and the experimental data, the simulation result of the basic mechanism is shown for comparative purposes.

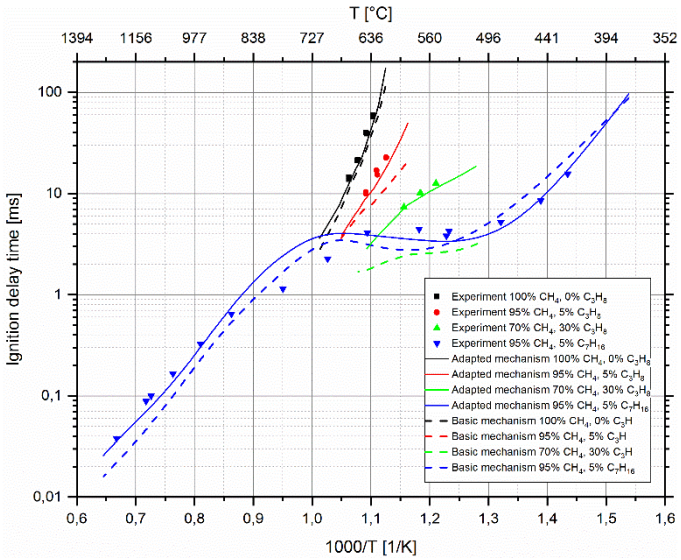

Figure 4. Comparison of experimental data and simulation results using the basic and adapted reaction mechanism.

As a result of the mechanism adaptation, the influence of propane addition on the ignition delay time is reproduced well. In the case of the methane-n-heptane mixture, a good approximation of the simulation results to the experimental values is evident both in the temperature range 700 to 900 K and in 1150 to 1500 K. In the temperature range 900 to 1050 K, an overestimation of the ignition delay time is obvious, where further adaption of the mechanism is necessary.

Conclusion

In this study, the optimization of a mechanism for simulation of a dual fuel combustion process was presented. The basic mechanism is composed of a mechanism for natural gas and a n-heptane mechanism. Comparison of the simulation results with experimental data from a rapid compression machine and a shock tube showed a wrong assessment of the propane influence on the ignition delay time. With a sensitivity analysis, reactions with a significant influence on the rate of the reaction process were identified and adapted by changing the corresponding Arrhenius parameter. With the optimized mechanism, the propane influence on the ignition delay time is reproduced well. For the methane-n-heptane mixture, the simulation shows a good approximation to the experimental values over a large temperature range. Between 900 to 1150 K, however, the ignition delay time is still

overestimated and indicates potential for further optimization.

Acknowledgement
We would like to show our gratitude to the Austrian Research Promotion Agency (FFG) for funding this work (project number 850690). Further thanks go to LOGE AB for providing the simulation software LOGEresearch v1.10.

References

[1] Wright, G., *Fundamentals of Medium/Heavy Duty Diesel Engines*. Jones & Bartlett Learning, 2015.
[2] Schlick, H., "Potentials and challenges of gas and dual-fuel engines for marine application," *5th CIMAC CASCADES*, Busan, South Korea, 2014.
[3] Fischer, M., *Modellierung der Multikomponenten-Verdampfung im homogenisierten dieselmotorischen Brennverfahren*. Cuvillier Verlag Göttingen, 2006.
[4] "Chemical-Kinetic Mechanisms for Combustion Applications," San Diego Mechanism web page, Mechanical and Aerospace Engineering (Combustion Research), University of California at San Diego (http://combustion.ucsd.edu).
[5] Pachler, R. F., Ramalingam, A. K., Heufer, K. A. Winter, F., "Reduction and validation of a chemical kinetic mechanism including necessity analysis and investigation of CH4/C3H8 oxidation at pressures up to 120 bar using a rapid compression machine", *Fuel* 172:139-145 (2016).
[6] Herzler, J., Fikri, M., Welz, O., Schulz, C., "High-pressure shock-tube study of the ignition of fuel-rich CH4/air and CH4/additive/air mixtures over a wide temperature range," *7th European Combustion Meeting*, Budapest, Hungaria, 2015.
[7] LOGEresearch v1.10 (http://www.logesoft.com.)
[8] Schuh, S., Winter, F., "Comparing the Influence of Propane and n-Heptane Addition on Methane Ignition," *8th Europena Combustion Meeting*, Dubrovnik, Croatia, 2017.

Insights into Oxidation Behavior of Potential Gasoline Additives: 2-Methylfuran and 2-Methyltetrahydrofuran

R. Tripathi*, U. Burke, A. K. Ramalingam**, C. Lee**, R. X. Fernandes**, K. A. Heufer**, S. M. Sarathy***, H. Pitsch***
r.tripathi@itv.rwth-aachen.de
*Institute for Combustion Technology, RWTH Aachen University, Germany
**Physico Chemical Fundamentals of Combustion, RWTH Aachen University, Germany
***King Abdullah University of Science and Technology, Clean Combustion Research Center, Thuwal, Saudi Arabia

Abstract
Ignition behavior of an unsaturated cyclic ether, 2-methylfuran (2-MF) and its blend with *n*-heptane (50/50 molar %) have been investigated in the present work. Two different experimental facilities shock tube and rapid compression machine were employed to measure the ignition delays for stoichiometric 2-MF/air and 2-MF/*n*-heptane/air mixtures at pressures of 10 and 20 bar, and temperatures between 650 K to 1200 K. A detailed chemical kinetic model including relevant high- and low-temperature oxidation chemistry for these fuels were formulated and utilized to back the experimental findings. A comparison of the ignition behavior of 2-MF with its saturated counterpart, 2-Methyltetrahydrofuran (2-MTHF) is further presented, and the impacts of unsaturation in the cyclic ether ring on fuel ignition characteristics are analyzed.

Introduction
Due to their superior physico-chemical properties [1] and possible production pathways from ligno-cellulosic biomass [2], various furans are identified as potential additives for spark-ignition (SI) engines. 2-MF is one of such candidates, which can be blended with gasoline without the risk of current engine design alterations [3]. The gasoline/2-MF blend offers several advantages such as reduction in hydrocarbon (HC) and carbon monoxide (CO) emissions [3] and high knock resistance [4]. A strong interest in this mono-alkylated unsaturated cyclic ether (2-MF) as a gasoline additive has resulted in many combustion studies [5-10]. These studies involve measurement of its various combustion properties in a variety of reactors [5-8]. Also, its combustion behavior has been investigated theoretically with the help of detailed chemical kinetic models [7-9] and quantum mechanical calculations [10].

Despite extensive research on its combustion behavior [5-10], the chemical kinetics of 2-MF oxidation at lower combustion temperatures are not well known. There remains a need to characterize the combustion behavior of 2-MF at low temperatures because phenomena such as knock in SI engines and ignition in compression ignition (CI) engines are influenced by low-temperature oxidation reactions. 2-MF is a stable unsaturated compound, and that limits its reactivity at low temperatures, but practical engine applications would blend 2-MF with a hydrocarbon base fuel. The presence of more reactive species (*n*-alkanes) in blends could initiate the oxidation of 2-MF at low temperatures.
With this motivation, the main objective of this study is to investigate the ignition behavior of pure 2-MF as well as its blend with *n*-heptane, both experimentally and numerically. In order to shed light on the effect of saturated and unsaturated cyclic ether rings on the ignition delay time, the ignition behavior of 2-MF is compared with its saturated counterpart, 2-methyltetrahydrofuran (2-MTHF), with the help of the present study and literature sources.

Kinetic model development

The proposed chemical kinetic model, consisting of 883 species and 7872 reactions (forward and backward counted separately), was built hierarchically upon the C_0-C_4 base model of Blanquart et al. [11]. A sub-model of *n*-heptane, along with the C_5 and C_6 chemistry, was taken from the most recent optimized *n*-dodecane model of Cai et al. [12]. Regarding 2-MF specific reactions, a high-temperature specific sub-model was adopted from the 2,5-dimethylfuran (2,5-DMF) mechanism of Somers et al. [13]. The rate constants for several high-temperature specific reactions were revised based on the theoretical study of Somers et al. [9] and Tran et al. [8]. Additionally, a low-temperature specific sub-model of 2-MF was developed as a part of this research work and combined with the base mechanism. The main reaction pathways considered in the low-temperature specific 2-MF sub-model are as follows:

- A set of co-oxidation reactions between intermediate species formed in the oxidation of 2-MF and the species of *n*-heptane were included in the current model. The rate coefficients of these co-oxidation reactions were estimated on the basis of co-oxidation reactions of toluene and *n*-Heptane, explained in the work of Andrae et al. [14].
- Through his theoretical calculations, Davis et al. [10] revealed that the formed adduct, after addition of OH to 2-MF, can further decompose via hydrogen migration (HM), concerted elimination (CE), Waddington elimination (WE), and Waddington concerted elimination (WCE) reactions. In order to investigate the nature of radical addition to 2-MF all the proposed pathways of 2-MF/OH adducts, dominantly formed at α sites of the 2-MF ring were taken into account.

- In order to assess the importance of low-temperature specific chemistry, reaction of predominantly formed 2-MF radical with O_2 was incorporated. Rate parameters for this reaction were adopted from the quantum calculation work of Tran et al. [8].

Experimental results and model validation

Figures 1a and 1b present the experimental results obtained in rapid compression machine (RCM) and shock tubes (STs) for pure 2-MF and the 2-MF/*n*-heptane blend, respectively. Note that a detailed description of the RCM used for the low-temperature measurements, has been described in detail previously [15]. In order to assess the facility-to-facility variation in the shock tube (ST) experimental data, ST measurements were carried out at the same conditions in two different facilities, PCFC RWTH Aachen ST facility and SWL RWTH Aachen ST facility. A detailed description on design features of both STs has been provided in previous studies [16-17].

Fig. 1a presents numerically computed ignition delays compared to the newly measured ignition delay results of stoichiometric 2-MF/oxidizer/diluent mixtures at P = 20 bar, the ST ignition delays measured by Uygun et al. [6] at P = 40 bar, and those measured by Sudholt et al. [5] at a pressure of 20 bar in an RCM. Numerical simulations at constant volume are shown as line plots, while simulations including ST and RCM facility effects are represented by dotted lines. The newly measured RCM data set matches well with the data set of Sudholt et al. [5]. The predicted ignition delays compare well with the experimental values with the exception of those below 890 K (1.12 1/K). Both ST and RCM data sets are over predicted by the model at lower temperature regimes.

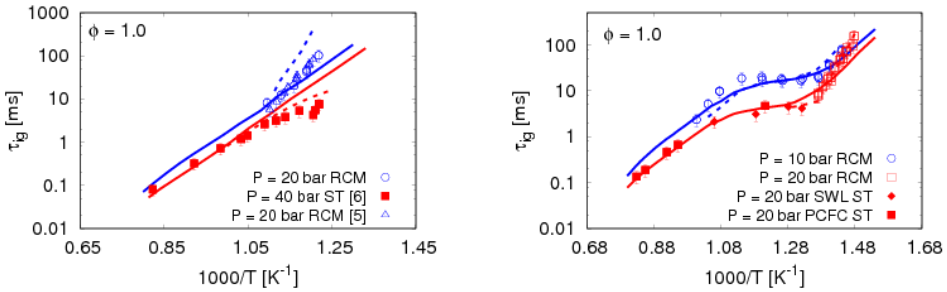

(a) **(b)**

Figure 1. Ignition delay times in RCM and in ST. Figure (a) pure 2-MF; (b) 2-MF/*n*-heptane blend.

Figure 1b shows the measured and the calculated ignition delays of 2-MF/*n*-heptane blends at pressures of 10 bar and 20 bar. It should be noted that due to non-ideal bursting of diaphragms in ST, a pressure rise was observed for longer ignition

delay times. This rate of pressure change (dp/dt) is different for both ST facilities, 5 %/ms and 8 %/ms for SWL and PCFC, respectively. It can be seen from Fig. 1b that experimental measurements from both the facilities agree very well; furthermore, SWL ST measurements are at lower temperatures, hence longer ignition delays, in comparison to the PCFC ST measurements. Since the pressure rise mainly occurs for longer ignition delays, numerical simulations for ST data were performed using the observed dp/dt of 5 % in SWL ST. The model accurately predicts the ST and the RCM ignition delay data at the pressure of 20 bar. However, data points obtained in the RCM at the pressure of 10 bar are under-predicted in the temperature range of 833 - 926 K (1.20 – 1.08 1/K). Unlike pure 2-MF, the blend of 2-MF/*n*-heptane exhibits a negative temperature coefficient (NTC), which is reproduced by the model as well.

Comparison with saturated mono-alkyl furan, 2-methyltetrahydrofuran

In order to see the effect of saturated and unsaturated cyclic ether ring on ignition delay time, ignition delays of 2-MF are compared with those of 2-MTHF [18-19] in Fig. 2. 2-MTHF is saturated counterpart of 2-MF and has only one structural difference that is the absence of double bonds in the cyclic ring. Yet, a higher reactivity of 2-MTHF compared with 2-MF is evident from Fig. 2. The ignition delay times of 2-MF and 2-MTHF are consistent with their cetane numbers, calculated by Sudholt et al. [1], which are representative of temperatures of 788 to 841 K at a pressure of 21.1 bar [20]. The reported cetane number of 2-MF (8.9) is much less than that of 2-MTHF (22.0), and hence its reactivity is lower at these conditions.

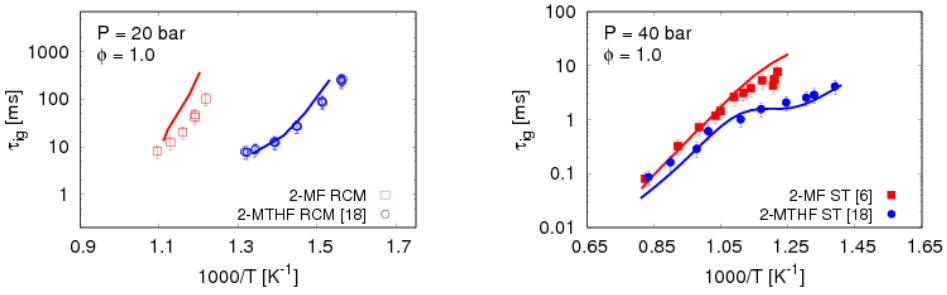

Figure 2. Comparison between 2-MF and 2-MTHF ignition delays. Figure (a) in RCM at 20 bar; (b) in ST at 40 bar.

In order to assess the impact of the fuel's molecular structure on the reactivity, a comparative reaction path analysis of 2-MF and 2-MTHF was performed (Fig. 3). It can be seen from Fig. 3 that due to presence of a stable unsaturated ring in 2-MF, H-abstraction from the ring carbons are restricted, and methyl side chain is the

main site for the abstraction reactions. Also, a large amount of the 2-MF is decomposed by its addition reactions with OH radical. Comparatively, in 2-MTHF, abstraction mainly takes place at α-ring carbon sites. The resulting fuel radical in 2-MF further reacts with HO_2 and leads to the formation of one OH radical. However, 2-MTHF fuel radicals either undergo ß-scission reaction or O_2 addition reaction. 2-MTHF and O_2 adducts mainly lead to low temperature degenerate branching pathways, which results in its higher reactivity.

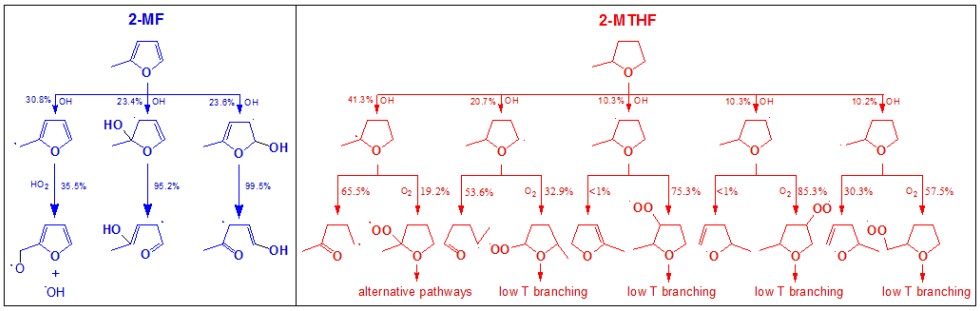

Figure 3. Comparison between main reaction pathways of 2-MF with those of 2-MTHF at 20 bar, 750 K, $\phi = 1$, and at 30 % fuel consumption.

Conclusions

This work presents a chemical kinetic investigation on the oxidation of 2-MF and its blend with *n*-heptane. A detailed chemical kinetic model was developed based on the literature understanding of furan chemistry. Low- to high-temperature ignition delay measurements were performed in RCM and STs. Overall a satisfactory agreement between experiments and numerical simulations has been observed. In comparison to 2-MTHF, the unsaturated ring structure in 2-MF results in inhibited fuel reactivity, hence longer ignition delay times.

References

[1] Christensen, E., Yanowitz, J. et al., "Renewable oxygenate blending effects on gasoline properties", *Energy Fuels* 25: 4723-4733 (2011).

[2] Mascal, M., Nikitin, E.B., "Direct high-yield conversion of cellulose into biofuel", *Angewandte Chemie* 120: 8042-8044 (2008).

[3] Wei, H., Feng, D. et al., "Experimental investigation on the combustion and emissions characteristics of 2-methylfuran gasoline blend fuel in spark-ignition engine", *Applied Energy* 132: 317-324 (2014).

[4] Singh, E., Shankar, V.S.B. et al., "2-Methylfuran: A bio-derived octane booster for spark-ignition engines", *submitted to Fuel.*

[5] Sudholt, A., Lee, C. et al., "Ignition characteristics of saturated and unsaturated furans", *Combust. Flame* 171: 133-136 (2016).

[6] Uygun, Y., Ishihara, S. et al., "A high pressure ignition delay time study of

2-methylfuran and tetrahydrofuran in shock tubes", *Combust. Flame* 161: 2519-2530 (2014).

[7] Somers, K.P., Simmie, J.M. et al., "A high temperature and atmospheric pressure experimental and detailed chemical kinetic modelling study of 2-methylfuran oxidation", *Proc. Combust. Inst.* 34: 225-232 (2013).

[8] Tran, L.S., Wang, Z. et al., "Comparative experimental and modeling study of the low to moderate-temperature oxidation chemistry of 2,5-dimethylfuran, 2-methylfuran, and furan", *Combust. Flame* 181: 251-269 (2017).

[9] Somers, K.P., Simmie, J.M. et al., "The pyrolysis of 2-methylfuran: A quantum chemical, statistical rate theory and kinetic modelling study", *Phys. Chem. Chem. Phys.* 16: 5349-5367 (2014).

[10] Davis, A.C., Sarathy, S.M., "Computational study of the combustion and atmospheric decomposition of 2-methylfuran", *J. Phys. Chem. A* 117: 7670-7685 (2013).

[11] Blanquart, G., Pepiot-Desjardins, P. et al., "Chemical mechanism for high temperature combustion of engine relevant fuels with emphasis on soot precursors", *Combust. Flame* 156: 588-607 (2009).

[12] Cai, L., Pitsch, H. et al., "Optimized reaction mechanism rate rules for ignition of normal alkanes", *Combust. Flame* 173: 468-482 (2016).

[13] Somers, K.P., Simmie, J.M. et al., "A comprehensive experimental and detailed chemical kinetic modelling study of 2,5-dimethylfuran pyrolysis and oxidation", *Combust. Flame* 160: 2291-2318 (2013).

[14] Andrae, J.C.G., Brinck, T. et al., "HCCI experiments with toluene reference fuels modeled by a semidetailed chemical kinetic model", *Combust. Flame* 155: 696-712 (2008).

[15] Lee, C., Vranckx, S. et al., "Zeitschrift fur physikalische chemie-international journal of research in physical chemistry & chemical physics", *Z. Phys. Chem.* 226: 1-27 (2011).

[16] Heufer, K.A., Olivier, H., "Determination of ignition delay times of different hydrocarbons in a new high pressure shock tube", *Shock Waves* 20: 307-316 (2010).

[17] Zhang, K., Banyon, C. et al., "An updated experimental and kinetic modeling study of *n*-heptane oxidation", *Combust. Flame* 172: 116-135 (2016).

[18] Tripathi, R., Lee, C. et al., *Proc. Combust. Inst.* 36: 587–595 (2017).

[19] Tripathi, R., Ramalingam, A.K. et al., "Unraveling the high reactivity of 3-methyltetrahydrofuran over 2-methyltetrahydrofuran through kinetic modeling and experiments", submitted to *Proc. Combust. Inst.*.

[20] Sudholt, A., Cai, L. et al., "Ignition characteristics of a bio-derived class of saturated and unsaturated furans for engine applications", *Proc. Combust. Inst.* 35: 2957-2965 (2015).

DEVELOPMENT OF A KINETIC MECHANISM FOR NO_x FUEL INTERACTION

Krishna Prasad Shrestha[*], Lars Seidel[**], Fabian Mauß[*], Thomas Zeuch[***]
Corresponding author: Krishna Prasad Shrestha, E-mail: shrestha@b-tu.de

* Thermodynamics and Thermal Process Engineering, Brandenburg University of Technology, Siemens-Halske-Ring 8, 03046 Cottbus, Germany
** Lund Combustion Engineering, LOGE Deutschland GmbH, Burger Chaussee 25, 03044 Cottbus, Germany
*** Institut für Physikalische Chemie, Georg-August-Universität, Tammannstr. 6, D-37077 Göttingen, Germany

Abstract

This work introduces a newly developed reaction mechanism to predict fuel/NO_x interaction in freely propagating, burner stabilized premixed flames, shock tubes, jet stirred reactors and plug flow reactors experiments. The study focuses on pure ammonia as fuel as well as H_2, H_2/CO, CH_4 doped with NO, NO_2 and N_2O. The kinetic scheme also focuses on the formation and consumption of nitrogen oxides at different experimental conditions. It is found that the doping with N_2O has almost no sensitivity on the H_2 chemistry, while small amount of NO_2 is enough to change the pressure dependence of H_2 auto ignition. The experiments with N_2O still show the significant influence of the chain breaking reaction $H+O_2(+M)\leftrightharpoons HO_2(+M)$ on the H_2 ignition delay times, resulting in the crossing lines for the ignition delay times, which are moved at higher pressure to higher temperature. The concentration of HO_2 is decisive for the active reaction pathway in shock tube oxidation as well as in jet stirred and flow reactor. Reaction $NO+HO_2\leftrightharpoons NO_2+OH$ and $NO_2+H\leftrightharpoons NO+OH$ are very important because they strongly influence the inter conversion process of NO and NO_2 in jet stirred reactor and flow reactor for cases studied herein. The formation of NO in burner stabilized premixed flames is shown to demonstrate the capability of the mechanism to be integrated into mechanisms for hydrocarbon oxidation.

Introduction

Several NO_x formation mechanisms have been developed in recent years, often dedicated to particular conditions of interest. Unlike hydrocarbons, there are not enough experimental or modelling studies for nitrogen related chemistry available. Still today we lack reliable rate parameter values, thermochemistry data and a sufficient experimental data base for validating NO_x model. To support the engine development process by simulations, detailed mechanisms for the oxidation of ammonia (NH3) and the formation and the reduction of NO_x are needed. This highly motivates the development of a detailed kinetic model in this work. The objective of our work is to develop the reliable kinetic model validated over a wide range of experimental data, i.e. laminar flame speeds, ignition delay times, speciation in jet stirred reactors (JSR), in plug flow reactors (PFR) and in burner stabilized flames (BSF) for pure fuels and mixtures. An updated kinetic mechanism for the H_2 and C_1 system along with NO_x formation and consumption has been developed on the basis of an extensive literature review, including wide set of experimental data. The kinetic model has been developed on a hierarchical basis: first H_2 combustion, than H_2/CO and NH_3, NO, NO_2, N_2O and their mixtures. Further model is extended to include C_1 chemistry higher than CO.

H_2/CO/NH_3/NO_x Kinetic model and validation

The detailed chemical kinetic mechanism of H_2 and CO is developed and validated extensively. The reaction rate parameter in this subset of mechanism in mostly based on the recommendations of Baulch et al. [1] and the uncertainty boundaries proposed by the authors. We refer Baulch et al. [1] because it is a comprehensive source, which provides reaction rate constants with their uncertainties. Alongside a NH_3/NO_x mechanism is developed. Ammonia is discussed as a carbon-free alternative fuel produced by overpower from alternative

energy system [2]. Ammonia was also discussed as an internal measure in Diesel engines to recycle NO to form N_2. Most recently there has been various experimental studies on the NH_3 and H_2-NH_3 oxidation due to which the development and validation of NO_x model can be improved. The two key parameters for NH_3 combustion, laminar flame speed (see Fig 1 (a)) and ignition delay time (see Fig 1 (b)) are compared against the developed model. All simulations were performed using LOGEsoft 1.08.00 [3].

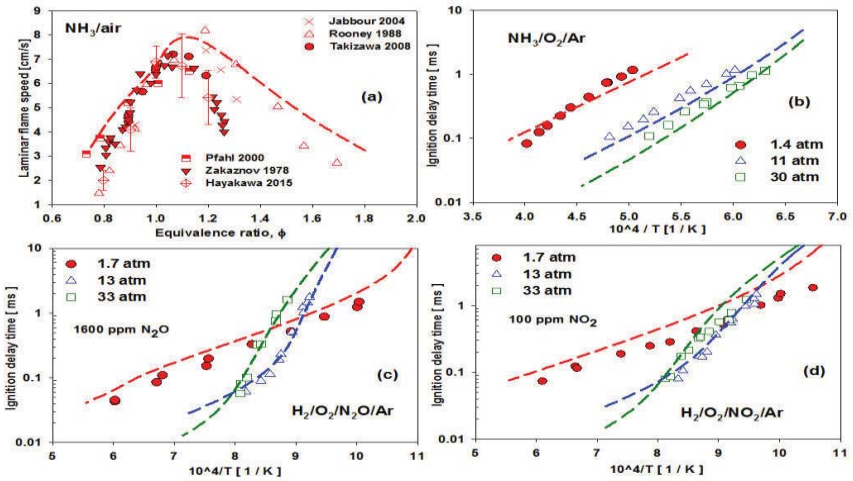

Figure 1. Comparison between model prediction and measurements. Symbols: Experimental data. Lines: model prediction. (a) laminar flame speed of NH_3/air at 298 K , 1 atm [3–7]; (b) ignition delay time of $NH_3/O_2/Ar$(99%),Φ=1.0 [9]; (c)H_2/N_2O(1600 ppm)/O_2/N_2 [11] and (d) H_2/NO_2(100 ppm)/O_2/N_2 [12] in shock tube respectively.

To develop the $H_2/CO/NH_3/NO_x$ model various fuel mixtures at different conditions have been studied and validated against the wide set of experimental data available from literature. The laminar flame speed of NH_3/air mixture (at 298 K, 1atm, Fig. 1(a)) is very low compared to hydrocarbons and may not be well suited for internal combustion engines. As can be seen from Fig. 1 there is large discrepancies within the experimental data from literature which suggest that more accurate and reliable experimental data for ammonia laminar flame speed is required. However, the low laminar flame speed of NH_3 can be increased by the addition of H_2 as it is done for hydrocarbons which will promote the formation of H, O and OH radicals. The present model shows good agreement with published experimental data for NH_3/H_2/air laminar flame speed (not shown here).

Speciation of the NH_3-H_2 (Fig. 2 (c)), NH_3-H_2-NO (Fig. 2 (d)), NH_3-NO, H_2-N_2O and CO-N_2O system was studied in burner stabilized flames. Oxidation of H_2 in presence of NO and NO_2, H_2-CO system doped with NO was studied in JSRs. Further flow reactor experimental targets of H_2 oxidation in presence of NO and CO oxidation in presence of NO and NO_2 was also considered for model development and validation. In NH_3 and NH_3-H_2 flames NO formation is mainly controlled by $N+O_2 \rightleftharpoons NO+O$ and $N+OH \rightleftharpoons NO + H$ reactions. NH_3 subsequently decomposes to the Amidogen radical (NH_2) which, decomposes to the Imidogen radical (NH). Both are very reactive species and their reactions with H, O, OH, NO control the overall reactivity of the system. Overall good agreement between the model prediction and experimental data is observed. With the available published experimental data for the H_2-N_2O (Fig. 1(c)) and H_2-NO_2 (Fig. 1(d)) system in shock tubes the model was validated. H_2 oxidation in JSRs in presence of NO and NO_2 was also investigated (see Fig. 2 (a, b)). The conversion of NO to NO_2 is explained by the chain propagation reaction $NO+HO_2 \leftrightharpoons NO_2+OH$, which is accelerating the H_2 chemistry. As can be seen the highest NO_2 concentration occurs at 790 K. At

higher temperature the reaction progress of the H_2 oxidation reaches higher values, and NO_2 is reduced to NO via reaction $NO_2+H \leftrightharpoons NO+OH$. It was found that in H_2-NO/NO_2 and CO-NO/NO_2 system reaction $NO+HO_2 \leftrightharpoons NO_2+OH$ and $NO_2+H \leftrightharpoons NO+OH$ are very important for inter conversion between NO and NO_2.

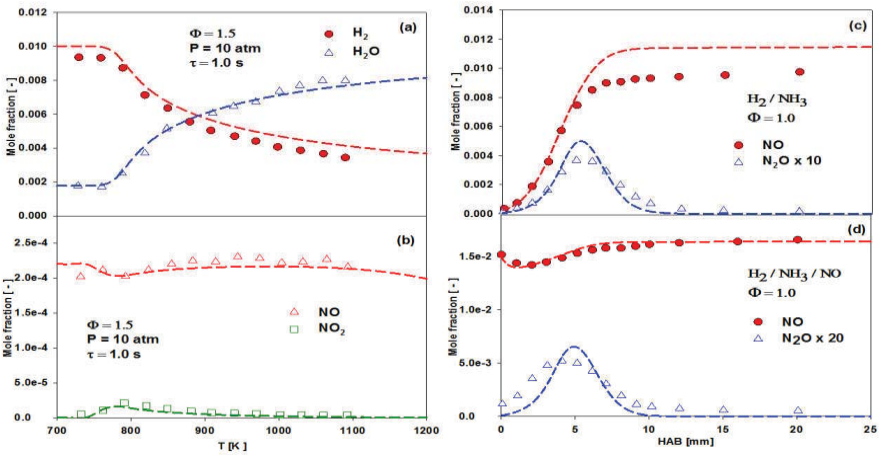

Figure 2. Comparison between experimental data and model prediction from this work. (a,b) H_2(0.01)/O_2(0.00333)/NO(220 ppm)/N_2 oxidation in JSR at Φ = 1.5, p = 10 am and τ = 1.0 s, symbols measurements from [10]. (c,d) Species profile comparison between measurements and model prediction(imposing experimental temperature profile) in burner stabilized premixed flame at 4.6 kPa, (c) NH_3(0.03)/H_2 (0.209)/O_2 (0.127)/Ar (0.634); (d) NH_3 (0.015)/H_2 (0.2315)/NO (0.015)/O_2 (0.1195)/Ar (0.6190), symbols measurements from [13].

C_1 – NO_x Kinetic model and validation

The model for H_2/CO/NH_3/NO_x was extended to include C_1 fuel chemistry. The updated model includes methane, methanol and formaldehyde as fuels and was validated against a wide set of experimental data available from literature.

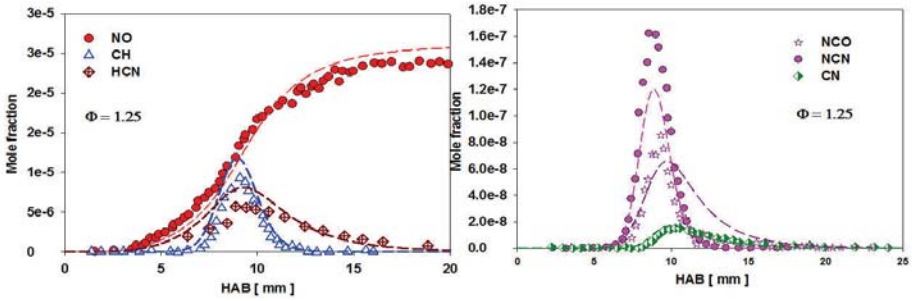

Figure 3. Speciation in premixed CH_4/O_2/N_2 flame at p = 5.3 kPa; T = 273.15 K; Φ=1.25. Symbols: measurements from Lamoureux et al. 2016 [20], lines: present model prediction imposing experimental temperature profile.

Special attention was paid for the formation and consumption of NO. In flames prompt-NO formation (see Fig. 3) results from the reaction between CH and N_2 yielding Cyanonitrene (NCN) and H. The NCN radicals reacts with H and O atoms yielding HCN+N and CN+NO, respectively. Beside NO profile other radicals (CH, NCN, CN, HCN and NCO) which are important in nitrogen chemistry (see Fig. 3) are also taken into consideration for the model development and validation.

The sensitivity of thermochemistry on NO_x prediction was investigated, especially for the NCN radical for which the enthalpy values reported in the literature varies by more than 10 kJ/mol (see Fig. 4(a) and Fig. 4(b)). Finally based on our study we choose the NCN thermochemistry from the theoretical study by Goos et.al. 2013 [14]. It was found that the rate parameter for the two main reactions ($CH + N_2 \rightleftharpoons NCN + H$ and $NCN + H \rightleftharpoons HCN + N$) are important for the NO_x prediction in flames which was reviewed based on the experimental and theoretical study from literature [15–19]. The product branching ratio of the reaction NCN + H is also important which subsequently effects the NO_x prediction.

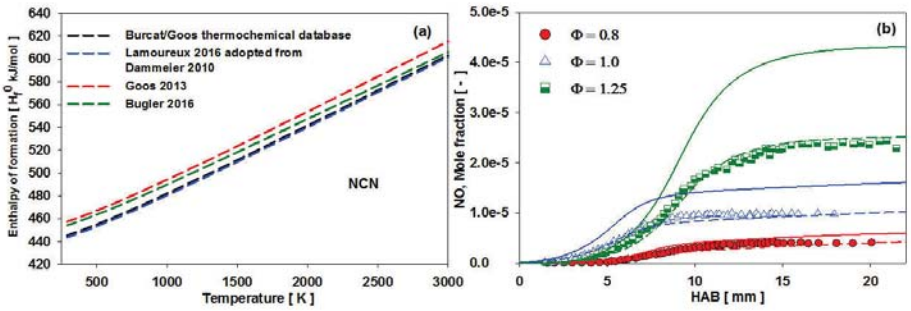

Figure 4. (a), NCN Enthalpy comparison between different authors; black [21]:HF298=445.7 kJ/mol, blue [20]:HF298=444.1 kJ/mol, red [14]:HF298=457.8 kJ/mol and green [22]: HF298=454.52 kJ/mol. (b), Effect of NCN thermochemistry on NO prediction in $CH_4/O_2/N_2$ low pressure burner stabilized flame at p= 5.3 kPa, T=273 K at different equivalence ratio. Symbols: measurements from [20]. Continuous lines: prediction using the NCN thermochemistry of Lamoureux et.al. 2016 (HF298=444.1 kJ/mol) [20]; dash lines: prediction using NCN thermochemistry of Goos et.al. 2013 (HF298=457.8 kJ/mol) [14].

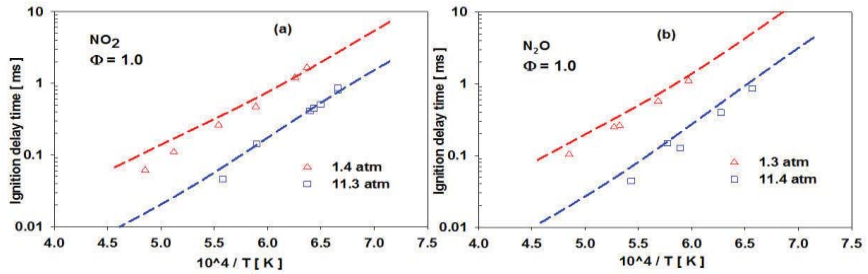

Figure 5. Ignition delay time comparison between experimental data from [27] and model prediction from this work. (a) CH_4 (0.83%)/O_2 (1.67%)/NO_2 (0.1383%)/Ar (b) CH_4 (0.83%)/O_2 (1.67%)/N_2O (0.1383%)/Ar.

Ignition delay time of CH_4/NO_2 and CH_4/N_2O mixtures in shock tube experiments (see Fig. 5) have also taken into account as model development target. In addition experiments dedicated to CH_4 oxidation in presence of NO in JSR [23] were also considered and model is well able to predict consumption and formation of NO_x.

Methanol oxidation in presence of NO in a JSR [24, 25] was also investigated and model performs well at those condition, too. Further experiments dedicated to HCN oxidation in a JSR [26] are also considered in model development targets.

Conclusion

In this work we developed a $H_2/C_1/NH_3/NO_x$ kinetic model which is validated over a wide range of experimental targets for pure fuels and mixtures. Overall there is a good agreement between the model prediction and measurements for broader range of experimental conditions obtained from published literature. We showed that the $H_2/CO/NH_3/NOx$ model was successfully extended to include C_1 chemistry and in future works this model can be further extended to include higher hydrocarbon. It was found that effect of NCN thermochemistry on prompt NO formation in premixed flames is significant. More accurate and reliable thermochemistry of NCN and other nitrogen related species are required to enhance the current understanding of NO_x chemistry and improve kinetic models. Rate parameters of reactions related to nitrogen chemistry are limited, future work should be dedicated for more reliable rate constant values at combustion condition from both experimental and theoretical side.

References

[1] Baulch, D.L., Bowman, C.T., Cobos, C.J., Cox, R.A., Just, T., Kerr, J.A., Pilling, M.J., Stocker, D., Troe, J., Walker, R.W., Warnatz, J., "Evaluated Kinetic Data for Combustion Modeling : Supplement II Evaluated Kinetic Data for Combustion Modeling : Supplement II", *J. Phys. Chem. Ref. Data* 34: 757-1397, (2005).

[2] https://www.asme.org/engineering-topics/articles/sustainability/the-ammonia-economy.

[3] http://logesoft.com/loge-software/.

[4] Ronney, P.D., "Effect of Chemistry and Transport Properties on Near-Limit Flames at Microgravity", *Combust. Sci. Technol.* 59: 123–141 (1988).

[5] Takizawa, K., Takahashi, A., Tokuhashi, K., Kondo, S., Sekiya, A., "Burning velocity measurements of nitrogen-containing compounds", *J. Hazard. Mater*. 155: 144–152 (2008).

[6] Pfahl, U.J., Ross, M.C., Shepherd, J.E., Pasamehmetoglu, K.O., Unal, C., "Flammability limits, ignition energy, and flame speeds in H2-CH4-NH3- N2O-O2-N2 mixtures", *Combust. Flame*. 123: 140–158 (2000).

[7] Zakaznov, V.F., Kursheva, L.A., Fedina, Z.I., "Determination of normal flame velocity and critical diameter of flame extinction in ammonia-air mixture", *Combust. Explos. Shock Waves*. 14: 710–713 (1978).

[8] Hayakawa, A., Goto, T., Mimoto, R., Arakawa, Y., Kudo, T., Kobayashi, H., "Laminar burning velocity and Markstein length of ammonia/air premixed flames at various pressures", *Fuel*. 159: 98–106 (2015).

[9] Mathieu, O., Petersen, E.L., "Experimental and modeling study on the high-temperature oxidation of Ammonia and related NOx chemistry", *Combust. Flame.* 162: 554–570 (2015).

[10] Dayma, G., Dagaut, P. , "Effects of air contamination on the combustion of hydrogen — effect of NO and NO2 addition on hydrogen ignition and oxidation kinetics", *Combust. Sci. Technol*. 178: 1999–2024 (2006).

[11] Mathieu, O., Levacque, A., Petersen, E.L. , "Effects of N2O addition on the ignition of H2-O 2 mixtures: Experimental and detailed kinetic modeling study", Int. J. Hydrogen Energy. 37: 15393–

15405 (2012).

[12] Mathieu, O., Levacque, A., Petersen, E.L. , “Effects of NO2addition on hydrogen ignition behind reflected shock waves”, *Proc. Combust. Inst*. 34: 633–640 (2013).

[13] Bian, J., Vandooren, J., Van Tiggelen, P.J. , “Experimental study of the formation of nitrous and nitric oxides in H2-O2-Ar flames seeded with NO and/or NH3”, *Twenty third Symp. Combust*. 379–386 (1990).

[14] Goos, E., Sickfeld, C., Mauss, F., Seidel, L., Ruscic, B., Burcat, A., Zeuch, T. , “Prompt NO formation in flames: The influence of NCN thermochemistry”, *Proc. Combust. Inst*. 34: 657–666 (2013).

[15] Tian, Z., Li, Y., Zhang, L., Glarborg, P., Qi, F. , “An experimental and kinetic modeling study of premixed NH3/CH4/O2/Ar flames at low pressure”, *Combust. Flame*. 156: 1413–1426 (2009).

[16] El Bakali, A., Pillier, L., Desgroux, P., Lefort, B., Gasnot, L., Pauwels, J.F., Da Costa, I. , “NO prediction in natural gas flames using GDF-Kin®3.0 mechanism NCN and HCN contribution to prompt-NO formation”, *Fuel*. 85: 896–909 (2006).

[17] Vasudevan, V., Hanson, R.K., Bowman, C.T., Golden, D.M., Davidson, D.F. , “Shock tube study of the reaction of CH with N2: overall rate and branching ratio”, *J. Phys. Chem. A*. 111: 11818–11830 (2007).

[18] Faßheber, N., Dammeier, J., Friedrichs, G. , “Direct measurements of the total rate constant of the reaction NCN + H and implications for the product branching ratio and the enthalpy of formation of NCN”, *Phys. Chem. Chem. Phys*. 16: 11647–11657 (2014).

[19] Harding, L.B., Klippenstein, S.J., Miller, J.A. , “Kinetics of CH + N2 revisited with multireference methods”, *J. Phys. Chem. A*. 112: 522–532 (2008).

[20] Lamoureux, N., Merhubi, H. El, Pillier, L., de Persis, S., Desgroux, P. , “Modeling of NO formation in low pressure premixed flames”, *Combust. Flame*. 163: 557–575 (2016).

[21] Burcat, A., Branko, R. , “Third millennium ideal gas and condensed phase thermochemical database for combustion with updates from active thermochemical tables”, *Tech. Rep*. ANL-05/20, ANL-05/20 TAE 960 (2005).

[22] Bugler, J., Somers, K.P., Simmie, J.M., Güthe, F., Curran, H.J. , “Modeling Nitrogen Species as Pollutants: Thermochemical Influences”, *J. Phys. Chem. A.* 120: 7192–7197 (2016).

[23] Dagaut, P., Nicolle, A. , “Experimental study and detailed kinetic modeling of the effect of exhaust gas on fuel combustion: Mutual sensitization of the oxidation of nitric oxide and methane over extended temperature and pressure ranges”, *Combust. Flame*. 140: 161–171 (2005).

[24] Moréac, G., Dagaut, P., Roesler, J.F., Cathonnet, M. , “Nitric oxide interactions with hydrocarbon oxidation in a jet-stirred reactor at 10 atm”, *Combust. Flame*. 145: 512–520 (2006).

[25] Dayma, G., Ali, K.H., Dagaut, P. , “Experimental and detailed kinetic modeling study of the high pressure oxidation of methanol sensitized by nitric oxide and nitrogen dioxide”, *Proc. Combust. Inst*. 31: 411–418 (2007).

[26] Dagaut, P., Glarborg, P., Alzueta, M.U. , “The oxidation of hydrogen cyanide and related chemistry”, *Prog. Energy Combust. Sci*. 34: 1–46 (2008).

[27] Mathieu, O., Pemelton, J.M., Bourque, G., Petersen, E.L. , “Shock-induced ignition of methane sensitized by NO2 and N2O”, *Combust. Flame*. 162: 3053–3070 (2015).

COMPARISON OF DIFFERENT DIAGNOSTIC TECHNIQUES FOR THE ASSESSMENT OF COAL PYROLYSIS RATE

S. Krusch*, V. Scherer*, R. Solimene, G. Ruoppolo**, F. Cerciello**, S. Pielsticker***, R. Kneer***, K. Schlögel***, O. Senneca****
krusch@leat.rub.de
*Department of Energy Plant Technology, Ruhr-University, Bochum, Germany
**Istituto di Ricerche sulla Combustione, C.N.R., Naples, Italy
*** Institute of Heat and Mass Transfer, RWTH Aachen, Aachen, Germany

Abstract and Introduction

Simulation of fluidized bed combustion by commercial tools such as Barracuda or other CFD codes requires suitable kinetic models. Notably in fluidized bed reactors pyrolysis takes place with high heating rate in the temperature range of 800–900 °C and with coarse particle sizes (up to 10 mm). Therefore, intrinsic kinetics must be combined with modeling of heat and mass transfer.

Intrinsic kinetics can be obtained by conventional TGA analysis at low heating rate (2–20 K/min) and with small particle size (in the order of 100 μm). Recently a fluidized bed reactor purposely designed for operation with small particle size in combination with FTIR gas analysis has been used in Aachen to measure pyrolysis kinetics with high particle heating rate compatible with fluidized bed conditions [1]. Another innovative method to assess the rates of pyrolysis under fluidized bed conditions has been proposed by Solimene [2] in Naples and relies on the measurement of time resolved pressure.

In the present work these different methodologies have been used for a German bituminous coal “Auguste Victoria” to obtain pyrolysis behavior over a broad range of operating conditions. Results show that for the two fluidized bed test rigs, using larger particle sizes, transport limitations become important. As expected, for this regime the reactions rates become lower the larger the particle size.

Experimental description

The work was carried out on a German bituminous coal “Auguste Victoria” (AV). Ultimate and proximate analysis are reported in Table 1 and ash analysis in Table 2. The experimental conditions are given in Table 3.

Table 1. Coal analysis

Ultimate Analysis [wt.-%, dry]	
Carbon	79.36
Hydrogen	4.81
Nitrogen	1.85
Sulphur	1.08
Oxygen (Rest)	5.37
Proximate [wt.-%, raw]	
Ash	7.29
Volatile Matter	27.01
Fixed Carbon (Rest)	62.46
Moisture	3.24
Calorific Analysis [MJ/kg, dry]	
LHV	31.2

Table 2. Ash analysis

Ash	**[wt.-%] of ash**
SiO_2	51.0
Al_2O_3	27.3
Fe_2O_3	8.7
CaO	2.2
MgO	1.1
SrO	0.09
BaO	0.14
Na_2O	1.28
K_2O	4.7
MnO	0.04
TiO_2	1.1
SO_3	1.78
P_2O_5	0.61

Table 3. Experimental conditions of different tests

Reactor	**Particle size range [µm]**	**Temperature [°C]**
Fluidized bed with FTIR gas analysis	125–160	500; 600; 700; 800
Fluidized bed with pressure measurement	200–600; 600–850; 1,000–1,400; 1,400–2,800	700; 750; 800; 850
TGA	94–112	up to 850

TGA

TGA experiments were carried out in a Netzsch STA 409 CD thermo balance in a flow of nitrogen of 250 ml/min. Before the pyrolysis tests the samples of about 20 mg were dehumidified in the TGA for 10 min at 100 °C. Afterwards the samples were heated up to 850 °C with constant heating rates of 2, 5, 10 and 20 K/min. The samples were finally held at 850 °C for additional 30 min.

Mass loss data has been worked out to calculate:

conversion degree $f(t) = \frac{m_0 - m(t)}{m_0 - m_{Char}}$ and conversion rate $R = \frac{df}{dt}$.

Fig. 1 compares the pyrolysis rate profile obtained from mass loss with the results of gas analysis. It can be observed that the main peak of mass loss (indicated by arrow 1 in Fig. 1) is not balanced by the net release rate of CH_4, CO, CO_2 and H_2. The difference in mass loss rate and net gas release rate can be traced back to the

formation of heavier volatile compounds in the main stage of pyrolysis (primary pyrolysis) not detected by the gas analyzers. At higher temperature a second and modest event of pyrolysis (indicated by arrow 2 in Fig. 1), which can be regarded as a secondary pyrolysis stage, occurs with formation of CH_4, CO_2 and H_2. Here, the release of heavier volatiles seems to be negligible because mass loss rate and net release rate of CH_4, CO, CO_2 and H_2 match well with each other.

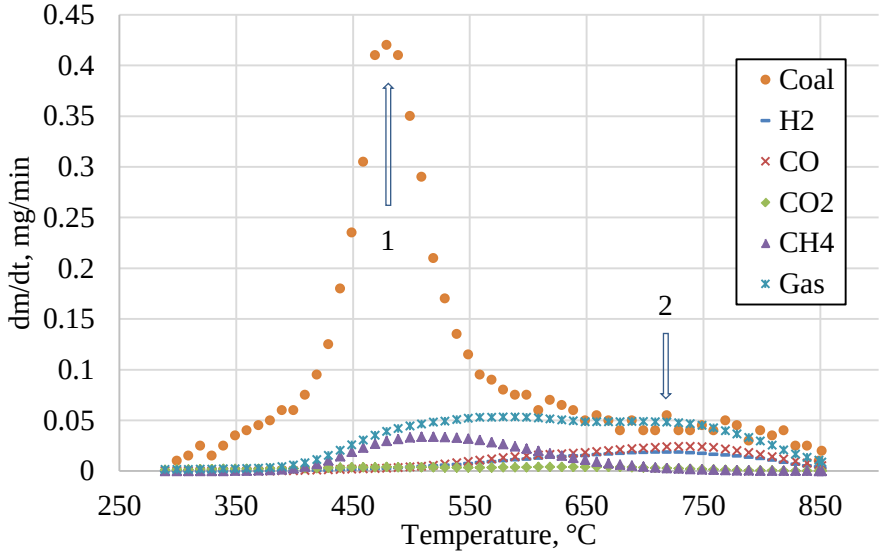

Figure 1. Mass loss rate of coal compared to measured species in the TG

Primary pyrolysis has been modeled by a power law kinetic expression:

$$R = \frac{df}{dt} = k_0 \exp\left(\frac{E_a}{R_u T}\right) \cdot (1-f)^n \quad (1)$$

The kinetic parameters obtained by Kissinger [3] and Friedman [4] methods are reported in Table 4:

Table 4. Kinetic data from TG analysis

	E_A/R_u [K]	k_0 [1/s]	n
Primary pyrolysis	2.9E+04	1.4E+15	6.8

Naples' fluidized bed with pressure measurement

Experiments have been carried out in a 17 mm inner diameter fluidized bed reactor (Figure 2, left) described in detail in [2]. A high-precision piezo resistive electronic pressure transducer has been used to measure the pressure increase due to released gases.

Quartz sand with a size range of 300–400 µm was used as bed material with an inventory of 13 g, which corresponds to a static bed height of about 40 mm.

The nitrogen gas flow for all experiments was 39.2 l_N/h, which corresponds to a superficial velocity of 0.18 m/s at 850 °C. The batch-wise fuel mass fed into the reactor is about 50 mg. Typical heating rates are in the order of 10^4 K/s.
Assuming ideal gas law, the mass balance on the nitrogen and volatiles leads to

$$V_R \frac{dP}{dt} + K_P P(P - P_{ATM}) = R_G T_R \left(\frac{\dot{m}_0}{M_{gas}} + \frac{\dot{m}_v(t)}{M_{vol}} \right), \quad (2)$$

where V_R is the reactor volume, $\dot{m}_0$ is the mass flow rate of the nitrogen and $\dot{m}_{vol}(t)$ is the mass flow rate of the emitted volatiles. M_{gas} is the molar mass of nitrogen and M_{vol} the molar mass of the volatiles. K_P is the linear constant between flowrate and pressure difference in the reactor to the surrounding [2]. Equation 2 can be solved for $\frac{\dot{m}_v(t)}{M_{vol}}$, the molar mass flow of the volatiles, based on the measurement data. A typical result is shown in Fig. 2, right. The negative values for molar mass flow occur for the moment in time when the coal is added to the reactor. These negative values are excluded from further data analysis.
The rate of pyrolysis has been calculated as $0.95/t_{95}$, where t_{95} is the time required to attain 95 % devolatilization. Further details on data analysis can be found in [2].

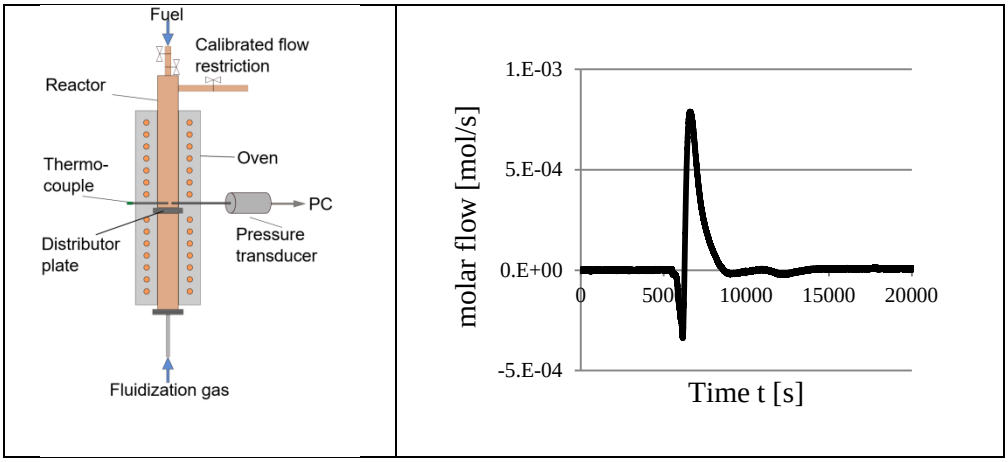

Figure 2. Scheme of the fluidized bed reactor (left) and molar mass flow rate of volatiles based on results of pressure measurements (right)

Aachen's fluidized bed with FTIR gas analysis

A small-scale fluidized bed reactor (Fig. 3, left) with a diameter of d = 55 mm was used, which is described in detail in [1]. Al_2O_3 particles (d_{50}=116 µm) are used as bed material with a static bed height of about 70 mm. Volume flow was 300 l_N/h, which corresponds to a superficial velocity of 0.16 m/s at 800 °C. Fuel samples (30 mg at 400 °C and 15 mg at 500 to 800 °C) were supplied to the reactor in batches. Particle transport from the fuel lock to the bed was forced with a gas flush (10 ml N_2) to achieve fast heating rates of approximately 10^4 K/s [1].

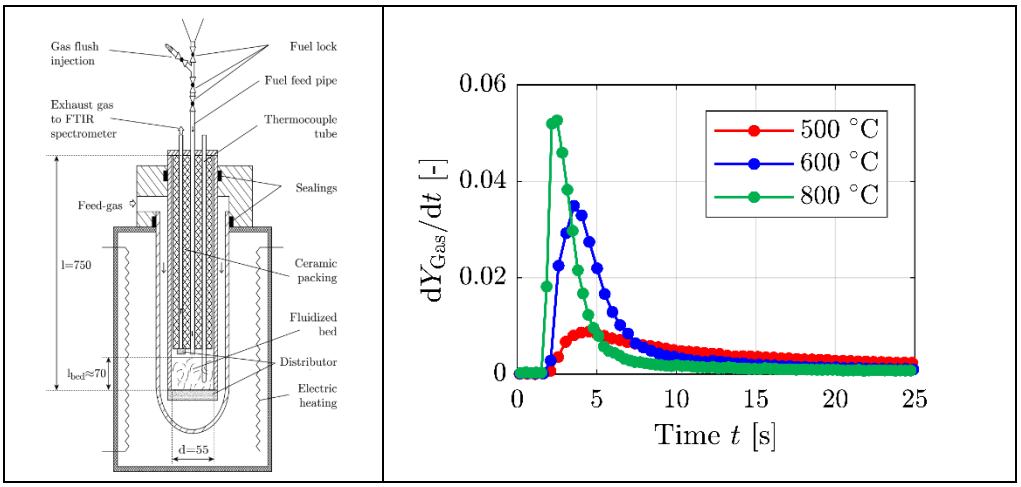

Figure 3. Scheme of the fluidized bed reactor (dimensions in mm) (left) and mass release rate of volatiles based on gas analysis (right)

Product gases were captured just above the bed and then transported to an FTIR spectrometer. The sampling line was heated to 453 K to avoid condensation of H_2O and tar components. Time dependent gas concentrations $c_i(t)$ were measured with an Agilent Cary 670 FTIR spectrometer and a sampling frequency of 10 Hz. More detail on construction, operation and error analysis is given elsewhere [1,5].
FTIR gas concentrations c_i of 21 different gas species (including CO, CO_2, $C_xH_yO_z$, SO_2 and NO_x) have been worked out to obtain:

$$\frac{\mathrm{d}Y_{\mathrm{Gas,exp}}}{\mathrm{d}t} = \frac{\rho_{\mathrm{N_2}} \cdot \dot{V}_{\mathrm{N_2}}}{m_{\mathrm{F}} \cdot M_{\mathrm{N_2}}} \cdot \frac{\sum_{i=1}^{n} c_{\mathrm{i}}(t) \cdot M_{\mathrm{i}}}{1 - \sum_{i=1}^{n} c_{\mathrm{i}}(t)} \tag{3}$$

Herein m_{F} is the injected fuel mass, $\dot{V}_{\mathrm{N_2}}$ the fluidizing volume flow of nitrogen, $\rho_{\mathrm{N_2}}$ the density and M_{i} the molar mass of each measured species. Results for $\mathrm{d}Y_{\mathrm{Gas}}/\mathrm{d}t$ at 500, 600 and 800 °C are depicted in Fig. 3 (right). Reaction rate is derived by fitting the experimental results to a 2-step model including primary and secondary pyrolysis. Details about underlying equations can be found in [5].

Comparison of the data and Summary

Results for reaction rate *R* obtained with the different techniques are compared in the Arrhenius plot of Fig. 4. Note that the reaction kinetics measured in Aachen from FTIR analysis refer to particle size of 125–160 µm, intermediate between the size used in the TGA (94–112 µm) and in the fluidized bed experiments carried out in Naples (200-2,800 µm). Around 900 K Aachen results are in good agreement with the ones obtained from TGA and allow stretching the Arrhenius plot up to 1000 K. At still higher temperature the slope of the Arrhenius plot decreases suggesting the onset of heat transfer limitation. The pressure-based rates measured

in Naples' fluidized bed were obtained with larger particles size. Here pyrolysis rate appears lower the larger the particle size, confirming the dominance of heat transfer limitations on the rate of pyrolysis. However, the rates are consistent with the Aachen data, keeping in mind the lower particle size used for the Aachen FTIR experiments.

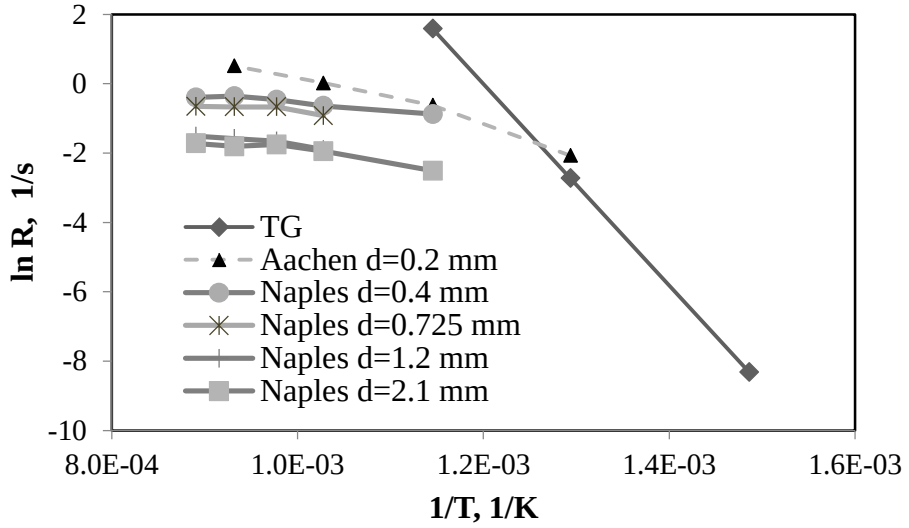

Figure 4. Evaluated reaction rate for the tests in an Arrhenius plot

Acknowledgement
A part of the work has been financed by the German Research Foundation (DFG) within the framework of the SFB/Transregio 129 "Oxyflame".

References

[1] Pielsticker, S., Gövert B., Kreitzberg, T., Habermehl, M., Hatzfeld, O., Kneer, R., "Simultaneous investigation into the yields of 22 pyrolysis gases from coal and biomass in a small-scale fluidized bed reactor", *Fuel* 190: 420–434 (2017).

[2] Solimene, R., Chirone, R., & Salatino, P. "Characterization of the devolatilization rate of solid fuels in fluidized beds by time-resolved pressure measurements", *AIChE Journal* 58(2): 632–645 (2012).

[3] Kissinger, H. E. "Reaction kinetics in differential thermal analysis", *Analytical chemistry*, 29(11): 1702–1706 (1957).

[4] Friedman, H. L., "New methods for evaluating kinetic parameters from thermal analysis data", *J. Polym. Sci.:* Part C 6 183 (1963).

[5] Pielsticker, S., Schlögel, K., Kreitzberg, T., Hatzfeld, O., Kneer, R., "Measurement of beech wood pyrolysis kinetics in a fluidized bed reactor", *Joint Meeting of the German and Italian Sections of the Combustion Institute*, Sorrento, Italy (2018)

Plug-flow reactor study of the partial oxidation of methane and natural gas at ultra-rich conditions

D. Kaczmarek, T. Kasper, B. Atakan
Institute for Combustion and Gas Dynamics - Thermodynamics,
University of Duisburg-Essen, 47048 Duisburg, Germany
dennis.kaczmarek@uni-due.de

Abstract
The homogenous partial oxidation of fuel-rich CH_4/O_2, $CH_4/C_2H_6/C_3H_8/O_2$ as well as $CH_4/C_2H_6/C_3H_8/H_2/O_2$ mixtures is investigated in a plug-flow reactor at intermediate temperatures ($473 \leq T \leq 973$ K) and a pressure of 6 bar. Experiments are carried out at equivalence ratios (Φ) of 2, 10 and 20. Product species are analyzed by time-of-flight molecular-beam mass spectrometry. The experimental results are further compared with simulations, using a reaction mechanism from the literature. It was found that under the investigated conditions, the onset temperature for CH_4 oxidation is above 773 K. In case of the neat CH_4 mixtures and equivalence ratios of 10 and 20, even at the highest investigated temperature CH_4 conversion is very low ranging from 3 % to nearly 0 %. Due to the higher reactive species content in the natural gas (NG) mixtures, conversion of CH_4 can be raised to 13 % and 10 % with respect to these equivalence ratios. But, the reaction onset temperature is not influenced by the presence of these species. After the oxidation takes place, useful chemicals like synthesis gas (H_2/CO), C_2H_4, C_2H_6 or CH_3OH are formed. Whereas synthesis gas and C_2H_4 are preferentially formed at higher temperatures, CH_3OH formation is limited to the temperature range between 773 and 973 K. Caused by the increased CH_4 conversion in the case of the NG mixtures, much higher yields of all products can be reached at higher Φ. Comparing experiments with simulations it can be noticed that the reactivity of the mixtures is slightly overestimated by the model, shown by higher CH_4 conversion as well as higher product yields. In summary, the addition of small amounts of C_2H_6 or C_3H_8 into CH_4/O_2 mixtures is a good way to initiate CH_4 conversion even at very high Φ. However, the addition of H_2 does not alter the product spectrum.

Introduction
Homogenous partial oxidation in internal combustion engines could be an exergetically viable alternative to normal combustion because it involves the production of useful chemicals while providing work and heat at the same time. The fuel used could be CH_4 as a major component of NG or NG itself, since it will continue to play a major role in the energy sector in the near future and will also be sufficiently available. In addition, the growth of renewable energies requires an expansion of the power grid and new options for storing fluctuating electricity from renewable sources. Here, power-to-gas, i.e. the conversion of renewable electricity

into hydrogen (H_2) and the direct seasonal storage capacity and distribution in existing natural gas infrastructure, can make an important contribution to the transformation of the energy system. To investigate the impact of H_2 addition into NG during these reactions, fuel-rich diluted CH_4/O_2 as well as $CH_4/C_2H_6/C_3H_8$ and $CH_4/C_2H_6/C_3H_8/H_2$ mixtures are investigated at different temperatures in a plug-flow reactor. Product species are analyzed by time-of-flight molecular-beam mass spectrometry. The data are compared to model results with the intention to validate the used reaction mechanism for the uncommon reaction conditions.

Experimental setup

The investigated flow conditions are shown in table 1. A low volume flow of 280 sccm (standard conditions: 273.15 K, 1 atm) is used to ensure compliance with a plug-flow assumption and the high dilution is used to avoid or reduce temperature changes due to exothermal reactions. Details of the experimental setup can be found in [1, 2].

Table 1. Flow conditions

CH_4	O_2	C_2H_6	C_3H_8	H_2	Ar	Φ
[Mol%]						[-]
5.00	5.00	-	-	-	90	2
4.32	5.20	0.43	0.048	-	90	2
4.27	5.16	0.43	0.047	0.095	90	2
8.33	1.67	-	-	-	90	10
7.40	1.78	0.74	0.082	-	90	10
7.27	1.76	0.73	0.081	0.162	90	10
9.09	0.91	-	-	-	90	20
8.12	0.98	0.81	0.090	-	90	20
7.97	0.96	0.80	0.089	0.177	90	20

Important features of the current setup are summarized below. The flow reactor consists of an inert quartz tube with an inner diameter of 6 mm. It is surrounded by a stainless-steel tube for safety reasons. To prevent catalytic reactions with stainless-steel the gap between the quartz and the stainless-steel tube is sealed with teflon tape at both ends. The reactor is heated by a temperature regulated heating tape. A homogeneous temperature profile with deviations below $\Delta T = \pm 5$ K, and an isothermal reaction zone of 45 cm at an overall reactor length of 65 cm is confirmed prior to the experiments with similar gas flows as a function of the set temperature of the heating tape. Gas flows are metered by calibrated mass flow controllers. The reactor pressure is regulated manually with a heated needle valve at the reactor outlet. The reactor is coupled to a time-of-flight mass spectrometer (ToF-MS) for

online measurements. In a differentially pumped three-stage extraction, a gas sample is extracted from the reactor at 6 bar and directed into the ToF-MS with a mass resolution of m/Δm=2500 at a pressure of 10^{-7} mbar. The gases are ionized by electron impact at 18 eV kinetic energy to avoid excessive fragmentation. Uncertainties in the mole fractions of detected species have been calculated by means of the gaussian error propagation law, taking all main error sources into account and are estimated to be around 10 %.

Modeling

In order to validate reaction mechanisms for the atypical reaction conditions of polygeneration processes, the experimental results are compared with simulations. A plug-flow reactor model is used with a fixed temperature profile and constrained pressure for simulations in the Chemical Workbench Ver. 4.1 [3]. The reaction mechanism of Burke et al. [4] is used for the simulations, as it is based on a mechanism, which has been widely validated for several fuels.

Results and discussion

The following figures show the CH_4 conversion as well as yields of CO, H_2 and C_2H_4 as a function of temperature and equivalence ratio. The yields are calculated by dividing the amount of C atoms in the product i by the initial amount of C atoms in the mixture. Symbols represent experimental data and lines simulations. The different mixtures are marked by different colors. From figure 2 it is obvious that the conversion of CH_4 starts around 773 K for all mixtures. If Φ is increased from 2 to 20 the conversion of CH_4 decreases rapidly from 50 % to nearly 0 %. Also at Φ = 10 the conversion is very low (< 4 %).

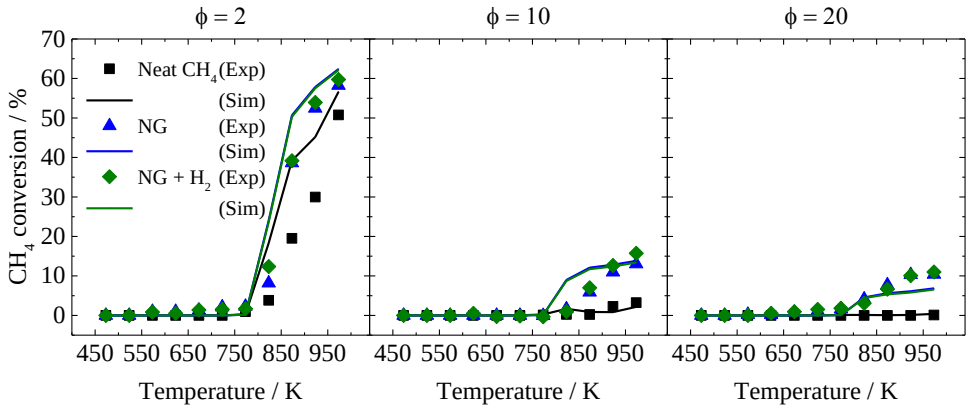

Figure 2. CH_4 conversion as a function of temperature for all investigated mixtures (Symbols: experiment, lines: simulations, NG: natural gas)

In the NG mixtures, much more CH_4 is converted, as more radicals are formed at temperatures above 773 K, mainly from C_2H_6 oxidation. The initiation reaction is

the reaction of C_2H_6 with O_2 forming an ethyl radical (C_2H_5) and a hydroperoxyl radical (HO_2). HO_2 reacts with CH_4, C_2H_6 and C_3H_8 forming the respective alkyl radical and hydrogen peroxide (H_2O_2), which will finally decompose to two OH radicals. As the most important reaction with respect to CH_4 conversion is the H-abstraction by OH radicals to methyl radicals (CH_3) and water (H_2O) [5], the consumption of CH_4 is enhanced. This is confirmed by global reaction flow analyses for all mixtures at these conditions using the reaction mechanism of Burke et al. [4]. So even at $\Phi = 20$, 10 % CH_4 is converted at temperatures above 873 K. H_2 addition into the NG mixture, however, does not influence the oxidation process. The general trends are predicted well by the model, whereas the CH_4 conversion is slightly overestimated for all mixtures at $\Phi = 2$ and 10 in the temperature range between 773 K and 923 K and underestimated at $\Phi = 20$ at temperatures higher than 873 K. Two of the main products are CO and H_2, both presented in figure 3. In this figure, the CO yield was multiplied by a factor of 4 and 9 for the $\Phi = 10$ and 20 cases, respectively.

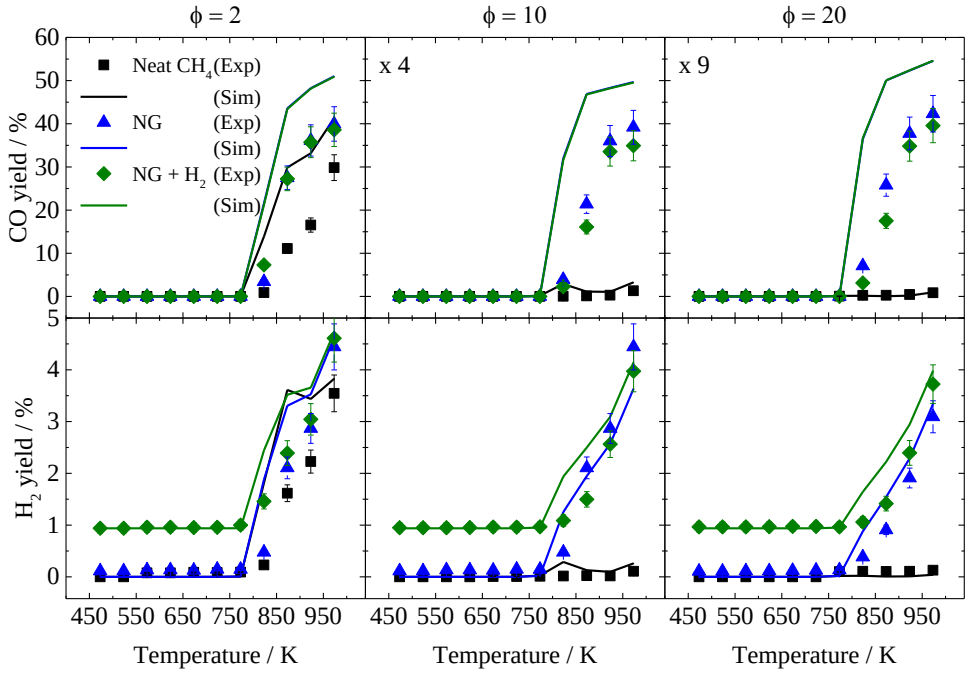

Figure 3. Yields of synthesis gas as a function of temperature (Symbols: experiment, lines: simulations, NG: natural gas)

It can be noted that the formation of CO and H_2 increase with rising temperature and that the highest CO yields can be achieved at $\Phi = 2$. For H_2, yields of 4 – 5 % can be observed at 973 K for all NG mixtures as well as the neat CH_4 mixture at $\Phi = 2$. As less CH_4 is converted at $\Phi = 10$ and 20, compared to $\Phi = 2$, it can be concluded that

the most H_2 is formed out of C_2H_6 and C_3H_8 oxidation, as up to 80 % of these reactants are converted at 973 K. All H_2 containing mixtures show the same behavior as NG mixtures without H_2 with the difference that the H_2 yields start at 1 %, as this is the amount which is in the mixture. At temperatures higher than 773 K, the H_2 yields are similar in both mixtures. Comparing experimental results with simulations it is seen that the model predicts a higher reactivity of all mixtures, since predicted yields are almost always higher than experimental ones.
C_2H_4 is produced in all NG experiments mainly at high Φ (see figure 4).

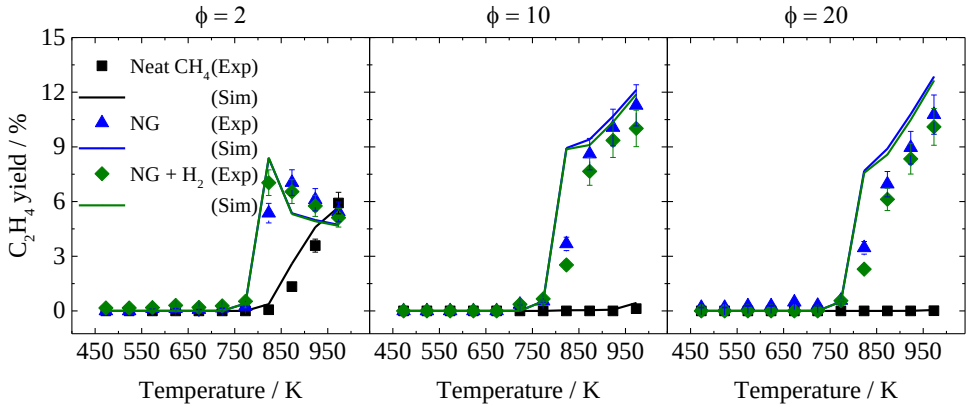

Figure 4. Yields of C_2H_4 as a function of temperature (Symbols: experiment, lines: simulations, NG: natural gas)

Regarding the neat CH_4 mixture, C_2H_4 is only formed at Φ = 2 because of the negligible conversion of CH_4 at higher Φ. The maximum yield of C_2H_4 with up to 12 % is observed at the highest investigated temperature (973 K) at both Φ = 10 and 20. But, considering the low CH_4 conversion at these equivalence ratios, it is obvious that C_2H_4 mainly comes from C_2H_6 and C_3H_8 oxidation. At Φ = 2 the maximum yields are about 7 and 6 % for the NG and neat CH_4 mixture, respectively. In case of the NG mixture the maximum can be found at 773 K with slightly decreasing yields at rising temperatures, whereas in the neat CH_4 case a linear increase of the yield can be noticed from 773 K to 973 K. The reason for the higher yields at lower temperatures is that there is a direct route towards C_2H_4 in the reaction network of the NG mixtures. As mentioned before, the initiation reaction regarding NG mixtures yields C_2H_5. This radical reacts with O_2, finally forming C_2H_4 and HO_2. In the neat CH_4 mixture, first of all C_2H_6 is formed by the recombination of two CH_3 radicals. C_2H_5 is then formed by H-abstraction from C_2H_6 by CH_3, OH or HO_2 radicals. Finally, C_2H_4 is formed by the same reaction as in the NG mixture. Therefore, more steps are necessary to produce C_2H_4 out of neat CH_4, which explains the higher yields in the NG experiments. The decrease in the C_2H_4 yields at temperatures above 773 K can be explained by the reaction of C_2H_4 with OH radicals forming an ethenyl radical (C_2H_3) and H_2O. With respect to the reaction flow analysis this reaction becomes

more important at higher temperatures at $\Phi = 2$. Both the trends and the yields are in good agreement to the model predictions

Apart from the shown products, also oxygenated species like methanol (CH_3OH) and formaldehyde (CH_2O) are formed as well as hydrocarbons like C_3H_6 or even C_4- and C_5-species. The maximum CH_3OH yields are found to be around 0.4 % at $\Phi = 2$ and a temperature of 823 K. For C_3H_6, yields of 0.4 % (neat CH_4, $\Phi = 2$) and 1 % (all NG mixtures) can be observed, whereas the maximum shifts towards higher temperatures with rising Φ.

Conclusion

In this study, the homogenous partial oxidation of CH_4 and NG mixtures as well as H_2 doped NG mixtures was investigated in a plug-flow reactor at temperatures between 473 and 973 K and a pressure of 6 bar. It could be observed that the CH_4 conversion can be significantly enhanced if higher reactive species like C_2H_6 and C_3H_8 are present in the mixture. At very high Φ (10 and 20), CH_4 conversion was negligible small in case of the neat CH_4 mixture and was increased to more than 10 % in case of the NG mixtures. As a result of that much higher product yields of synthesis gas, C_2H_4, CH_3OH or C_3H_6, for example, can be obtained with NG at these Φ, compared to neat CH_4. The addition of H_2 into the NG mixture did not alter the product composition in any case. Furthermore, the initiation reactions as well as the reaction pathway towards C_2H_4 have been analyzed by performing global reaction flow analyses with the reaction mechanism of Burke et al. [4]. Simulations, conducted with this mechanism, showed reasonable agreements with the general trends of the yields. Nevertheless, some discrepancies could be observed as well, which corroborate the need for better kinetics models for these uncommon reaction conditions.

References

[1] Sen, F., Shu, B., Kasper, T., Herzler, J., Welz, O., Fikri, M., Atakan, B., Schulz, C., “Shock-tube and plug-flow reactor study of the oxidation of fuel-rich CH4/O2 mixtures enhanced with additives”, *Combust. Flame 169*: 307-320 (2016).

[2] Kaczmarek, D., Kasper, T., Atakan, B., “An Experimental Investigation of the Partial Oxidation of Methane: the Influence of N-Heptane Addition”, *ECM 2017, 8th European Combustion Meeting*, Dubrovnik, Croatia (2017).

[3] Chemical Workbench® 4.1, Kintech Laboratory.

[4] Burke, U., Somers, K. P., O’Toole, P., Zinner, C. M., Marquet, N., Bourque, G., Petersen, E. L., Metcalfe, W. L., Serinyel, Z., Curran, H. J., “An ignition delay and kinetic modeling study of methane, dimethyl ether, and their mixtures at high pressures”, *Combust Flame 162*: 315-330 (2015).

[5] Dagaut, P., Boettner, J.-C., Cathonnet, M., “Methane Oxidation: Experimental and Kinetic Modeling Study”, *Comb. Sci. and Tech.* 77: 127-148 (1991).

Advancement on heat transfer modelling of oxidation processes in Jet Stirred Flow Reactors

L. Acampora*, M. Lubrano Lavadera*, P. Sabia*, R. Ragucci*, M. de Joannon*, F.S. Marra*
marra@irc.cnr.it
*Istituto di Ricerche sulla Combustione – CNR, Napoli, Italy

Abstract
The paper investigates the role of the heat transfer in Jet-Stirred Flow Reactor (JSFR). Through the parametric continuation analysis of a lean and very diluted hydrogen/oxygen/diluent mixture in a non-adiabatic PSR and the experimental studies on JSFR, the paper demonstrates that some classical global heat transfer correlations for this class of system are not adequate to achieve quantitatively correct predictions.

Introduction

The current environmental challenges are driving the development of new combustion concepts. However, despite the progresses in the application of these concepts to practical systems, unresolved issues on the stabilization, auto-ignition, and structure of the reaction zone remain. Hence, large-scale implementation of advanced combustion processes is hampered by the risks associated with adopting relatively unknown new techniques. Indeed, combustion processes of hydrocarbons and related compounds can evolve with complex dynamic behaviors, originating from non-linear dependence of relevant variables [1]. Moreover, in open systems, by contrast to chemical reactions in closed vessels, multiple permanent/oscillatory stationary states can be achieved [2]. Conditions at which a transition from one state to another occurs in response to a continuous change in control parameters identify critical phenomena such as discontinuous jumps, or bifurcations [3], which are undesirable during combustion.

Therefore, it is important to establish these conditions and to understand both the factors that govern the stability of stationary states and those that give oscillations. In addition, since most chemical kinetic models have been validated at higher temperatures and low dilution, there is a need of optimal experiments to restrict uncertainties for low temperatures and high dilution conditions. These targets become fundamental because of the uncertainty of the kinetic models available in the literature to reproduce the oxidation behavior even of standard fuels in the presence of high dilution levels. Therefore, the ability to simulate each different dynamic behavior of reacting systems and its parametric range of existence can be used as an auxiliary, yet stringent, test of kinetic mechanisms [4].

A formidable tool for the observation of the dynamic variety is undoubtedly the Perfectly (also known as Well) Stirred Reactor (PSR). With such system, steady

states and sustained oscillations may both be preserved indefinitely. Jumps from one state to another and regions of multi-stability can be found [3].
PSR systems have been successfully applied to the oxidation of hydrocarbons and oxygenates [5]. However, most of these studies have been concerned with kinetic and mechanistic aspects only. But none of the overall phenomena under discussion arises solely from kinetics. Heat release and heat dissipation rates are integral to the development of events. In non-adiabatic conditions the heat loss brings about a decoupling of the fixed relationship between concentration and temperature. The two variables can change independently of each other and both must be specified to fully characterize the system. With this extra degree of freedom different patterns of behavior, including sustained oscillations, can result [1].
The main purpose of this paper is to investigate the importance of the heat loss in this simple thermo-kinetic system at low temperatures in lean and very diluted conditions. Particularly, the significance of the heat transfer coefficient model in the numerical analysis of the PSR is evaluated. To these ends both numerical and experimental study are carried out. The hydrogen is adopted as reference fuel in order to simplify the analysis by reducing the complexity of the kinetic aspects.

Experimental and numerical tools

The experiments were carried out in a spherical quartz Jet-Stirred Flow Reactor (JSFR) of 1.13e-4 m^3. Uniform temperatures and concentrations of reactants are achieved within the reactor by jet stirring. The reaction vessel and pre-heating assembly are located within two electrically heated recirculating-air ovens bounded by refractory walls. An electronic control of the ovens gives temperatures that are uniform to within ± 5 K over the vessel external surface and constant in time to within ± 0.5 K. The two ovens temperatures (then the reactor wall temperature) are monitored continuously by two Nicrosil-Nisil thermocouples.
Hydrogen, oxygen and diluent are each drawn separately from cylinders and filters that retain particulate impurities. Precise control of gaseous flow rates is achieved by means of thermal mass flow controllers upstream of the vessel. The reactants are pre-heated separately before flowing into the vessel.
Inlet temperature T_{in}, pressure P, residence time τ, and the reactant mixture composition define the control parameters. The reactant pressure in the vessel is measured continuously by means of a pressure transducer connected to the outlet from the vessel. For this series of experiments P was maintained at 111457.5 Pa.
The vessel is washed with nitrogen before use. Normally, an initial condition is set which represents the displacement of a non-reactive gas from the vessel by the reactants at the operating pressure and temperature. Once reactants flows have been established to match the required composition, total pressure and mean residence time in the vessel, the fuel is injected. Thermal equilibrium is established after any change of parameters to characterize extents of self-heating correctly at the fixed temperature. Each result is referred to the set pressure, residence time and temperature established prior to reaction taking place.

The temperature inside the reactor is monitored with a Pt/Pt-13% Rh thermocouple by employing a very fine junction (200 μm diameter wire), introduced near the center of the vessel through a horizontal entry arm. The thermocouple response is sufficiently rapid to give faithful record of all temperature changes occurring in the reacting gas. The combined response time for the sampling system and the acquisition is roughly 0.03 s.
When a steady state has been established, the response of the system to large or small, artificially induced, perturbations may be studied by temporarily changing the equivalence ratio (thus inducing a small temperature perturbation) or by momentarily stopping the flow of fuel (a large perturbation). The consequences reveal the nature of the steady state.
Reactants and molecular products compositions during the reaction were measured directly by gas chromatography. Samples for analytical measurements were sent continuously from the reaction vessel directly to a gas chromatograph valve via the exhaust tube without any pumping system. Rapid quenching of the reactant composition was achieved with a water-cooling system. A cold trap upstream of the valve removes readily condensable fractions that might otherwise block the jet.
Chemical analyses of the exhaust gas were undertaken principally to determine the extent of reaction, by monitoring the concentration of oxygen and hydrogen.

Mathematical models
The governing ordinary differential equations of the non-adiabatic, constant pressure PSR can be given as [6]:

$$\frac{dY_i}{dt} = \frac{Y_{i,f} - Y_i}{\tau} + \frac{W_i r_i}{\rho} \quad , \quad i = 1, \dots, N_S$$
$$\frac{dT}{dt} = \sum_{i=1}^{N_S} \frac{Y_{i,f}(h_{i,f} - h_i)}{\tau c_P} - \sum_{i=1}^{N_S} \frac{W_i r_i h_i}{\rho c_P} - \frac{Q}{\rho V} \tag{1}$$

Here t, ρ, T, N_S, c_P refer to time, gas density, temperature, number of species, and mixture constant pressure specific heat, respectively. Y_i, W_i, r_i, and h_i, are the mass fraction, molecular weight, net species production rate and specific enthalpy of the i-th species; the subscript f indicates the feeding (inlet) conditions, $\tau = \rho V / \dot{m}_f$ is the nominal residence time related to the reactor volume (V) and the mass flow rate ($\dot{m}_f$) and $Q = UA(T - T_{env})$ represents the Newtonian-type reactor heat loss depending on global heat transfer coefficient (U), reactor surface (A) and environmental temperature (the temperature of the ovens, T_{env}). The heat-transfer coefficient depends on pressure, temperature, composition and flow rate. Since in JSFR the heat transfer coefficient depends on fluid dynamic conditions generated by gas streams outflowing from nozzles, it is impossible to vary residence time and heat transfer coefficient independently. Heat transfer for JSFR reactors has been firstly studied by David et al. [7]. They developed an empirical correlation for

cylindrical geometry based on Reynolds number evaluated on nozzle conditions (Re_N). Since operative conditions and reactor geometry of interest are different from those of David et al., the appropriate heat transfer correlation for spherical geometry developed by Lignola and Reverchon [8] is adopted in this work:

$$U = 0.89\mathrm{Re}_N{}^{0.683}\mathrm{Pr}^{1/3}\frac{k}{D} \quad (2)$$

where k is the thermal conductivity of the gas mixture, D is the reactor internal diameter and $\mathrm{Pr} = \mu c_p/k$ is the Prandtl number (μ is the dynamic viscosity). In this work, it was assumed that two of the contributions considered in [8], the oven side thermal resistance and the thermal resistance of reactor wall, can be neglected. Therefore, only the reactor side heat transfer coefficient is taken into account.

Three different reaction schemes are adopted to model hydrogen oxidation: the detailed combustion of H_2/O_2 mixtures introduced by Ó Conaire et al. [9]; the optimized kinetic model of H_2/CO combustion proposed by Davis et al. [10]; the detailed mechanism for hydrogen oxidation developed by Politecnico di Milano [11, 12]. Different mechanisms are taken into account in order to isolate the effects depending on heat transfer from those depending on kinetic phenomena.

Results

The effect of the feed mixture temperature (continuation parameter) on the bifurcation behavior of a lean hydrogen/oxygen/diluent mixture (equivalence ratio $\phi = 0.5$) in a non-adiabatic PSR is studied by using the parametric continuation tool introduced in [13, 14]. The hydrogen oxidation is analyzed in very diluted conditions; the mole fraction of the diluent is set to 0.94. Two different diluents are considered: nitrogen and a mixture nitrogen/water (60% N_2 – 40% O_2).

Since the global heat transfer coefficient depends on fluid dynamic conditions generated by gas streams outflowing from nozzles and thus on the diluent choice and on the continuation parameter, it is not assumed constant, but it is computed by the equation (2) at each equilibrium point.

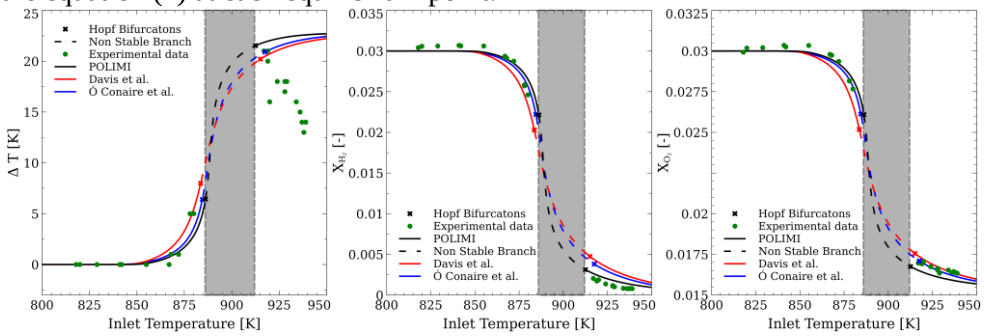

Figure 1. States in the JSFR as function of inlet temperature for the $H_2/O_2/N_2$ mixture. From left to right ΔT and mole fractions of hydrogen and oxygen.

The comparison between experimental data and the parametric continuation

analysis obtained with nitrogen as diluent are reported in Figure 1. The reported temperature increment in the reactor ΔT is defined as the difference between reactor temperature and the feeding mixture temperature.
Figure 1 shows that the predicted mole fractions of the reactants are in very good agreement with experimental data. Furthermore, the Hopf bifurcation points appear to be congruent with the region where an oscillatory behavior is experimentally detected (highlighted in gray in the figure). However, the temperature increment appears to be overestimated by the numerical model for feeding mixture temperature approximately greater than 915 K. Considering that these results are fairly independent from the choice of the reaction mechanism, this discrepancy may suggest that a correct evaluation of the heat transfer is important, and that the heat transfer correlation adopted is not adequate in modeling this system.
These results are partially confirmed by the comparison between experimental and numerical data obtained with nitrogen/water mixture as diluent (Fig.2).

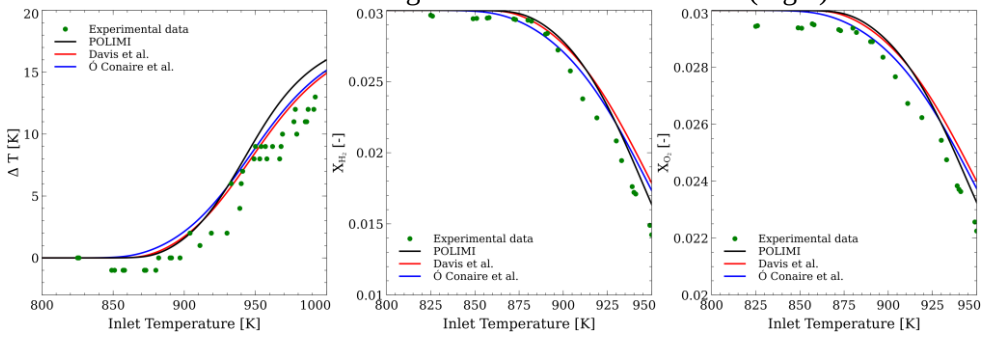

Figure 2. States in the JSFR as function of inlet temperature for the $H_2/O_2/N_2/H_2O$ mixture. From left to right ΔT and mole fractions of hydrogen and oxygen.

Indeed, also in this case the temperature of the reactor appears to be slightly overestimated by numerical analysis especially for the POLIMI mechanism. However, the differences reported in Fig.2 are not as significant as those obtained in the previous case due to the lower ΔT and then to the lower heat transfer rate.

Conclusions

The paper investigates the role of the heat transfer in the JSFR. The importance of this phenomenon is highlighted. Through the parametric continuation analysis of a lean hydrogen/oxygen/diluent mixture in a non-adiabatic PSR and the experimental studies on JSFR, the paper underlines not only that the heat losses must be included in mathematical models but also that classical global heat transfer correlation adopted for this class of system cannot be able to predict some phenomena. Particularly, the results show that there are significant discrepancies in the evaluation of the reactor temperatures when the nitrogen is adopted as diluent. Future works are needed in order to deepen this lack of understanding on heat transfer in JSFR. This aspect appears to be fundamental because JSFR are commonly used to validate reaction mechanisms.

References

[1] Griffiths, J.F., Scott, S.K., "Thermokinetic interactions: Fundamentals of spontaneous ignition and cool flames", *Prog. Energy Comb. Sci.* 13:161-197 (1987).

[2] Gray, P., Scott, S.K., "Archetypal Response Patterns for Open Chemical Systems with Two Components", *Philos. Trans. R. Soc. London, Ser. A* 332(1624): 69-87 (1990).

[3] Gray, P., Griffiths, J.F., Hasko, S.M., "Ignitions, Extinctions and Thermokinetic Oscillations Accompanying the Oxidation of Ethane in an Open System (Continuosly Stirred Tank Reactor)", *Proc. R. Soc. London, Ser. A* 396(1811): 227-255 (1984).

[4] Griffiths, J.F., "Reduced kinetic models and their application to practical combustion systems", *Prog. Energy Comb. Sci.* 21(1): 25-107 (1995).

[5] Simmie, J.M., "Detailed chemical kinetic models for the combustion of hydrocarbon fuels", *Prog. Energy Comb. Sci.* 29(6): 599-634 (2003).

[6] Glarborg, P., Miller, J.A., Kee, R.J., "Kinetic modeling and sensitivity analysis of nitrogen oxide formation in well-stirred reactors", *Comb. Flame* 65: 177-202 (1986).

[7] David, R., Houzelot, J.-L., Villermaux, J., "A novel and simple jet-stirred reactor for homogeneous and heterogeneous reactions with short residence times", *Chem. Eng. Sci.* 34(6): 867-876 (1979).

[8] Lignola, P.G., Reverchon, E., "A Jet Stirred Reactor for Combustion Studies: Design and Characterization", *Comb. Sci. Tech.* 60: 319-333 (1988).

[9] Ó Conaire, M., Curran, H.J., Simmie, J.M., Pitz, W.J., Westbrook, C.K., "A comprehensive modeling study of hydrogen oxidation", *Int. J. Chem. Kinet.* 36(11): 603-622 (2004).

[10] Davis, S.G., Joshi, A.V., Wang, H., Egolfopoulos, F., "An optimized kinetic model of H2/CO combustion", *Proc. Comb. Inst.* 30:1283-1292 (2005).

[11] Frassoldati, A., Faravelli, T., Ranzi, E., "Ignition, Combustion and Flame Structure of Carbon Monoxide/Hydrogen Mixtures. Note 1: Detailed Kinetic Modeling of Syngas Combustion also in Presence of Nitrogen Compounds", *Int. J. Hydrogen Energy*, 32: 3471-3485 (2007).

[12] Cuoci, A., Frassoldati, A., Buzzi Ferraris, G., Faravelli, T., Ranzi, E., "Ignition, Combustion and Flame Structure of Carbon Monoxide/Hydrogen Mixtures. Note 2: fluid Dynamics and Kinetics Aspects of Syngas Combustion", *Int. J. Hydrogen Energy*, 32: 3486-3500 (2007).

[13] Acampora, L., Mancusi, E., Marra, F.S., "Bifurcation analysis of perfectly stirred reactors with large reaction mechanisms", *Chem. Eng. Trans.* 43: 877-882 (2015).

[14] Acampora, L., Marra, F.S., "Numerical strategies for the bifurcation analysis of perfectly stirred reactors with detailed combustion mechanisms", *Comput. Chem. Eng.* 82: 273-282 (2015).

A Comparison of Numerical Frameworks for Modelling Homogenous Reactors and Laminar Flames

R. Langer*, A. Cuoci, L. Cai*, U. Burke***, C. Olm****, H. Curran***, T. Turányi****, H. Pitsch***

r.langer@itv.rwth-aachen.de

*Institute for Combustion Technology, RWTH Aachen University (R. Langer, L. Cai, H. Pitsch)

**Department of Chemistry, Materials, and Chemical Engineering, Politecnico di Milano (A. Cuoci)

***Combustion Chemistry Centre, School of Chemistry, NUI Galway, Ireland (U. Burke, H. Curran)

****Institute of Chemistry, ELTE Eötvös Loránd University (C. Olm, T. Turányi)

Abstract

Five different numerical frameworks with possibilities of modelling homogenous batch reactors and laminar premixed flames are compared in terms of results consistency and performance. The considered projects are Cantera, Chemkin-II, Ansys/Chemkin-PRO, FlameMaster, and OpenSMOKE++. In this study, first, results for homogenous, isochoric, adiabatic batch reactors are compared based on test cases precisely defined in terms of numerical setup and initial conditions. All frameworks provide consistent results. Based on this agreement, the comparison is extended for premixed laminar flames. Very good agreement between Cantera, Ansys/Chemkin-Pro, FlameMaster, and OpenSMOKE++ is achieved given that the same modelling assumptions and a sufficiently accurate numerical setup are chosen by the user. Finally, Cantera, FlameMaster, and OpenSMOKE++ are compared in a process time benchmark for homogenous, isochoric batch reactors.

Introduction

Simulations of homogenous zero-dimensional reactors and one-dimensional laminar flames are the foundation upon which the analysis and the understanding of various combustion processes rest. Numerical frameworks that enable researchers to conduct such simulations are a key tool in the development of complex kinetic models [1]. Simulation results can be analyzed and compared to experimental measurements from various devices such as shock tubes, rapid compression machines, or spherical combustion chambers. Besides the stand-alone application, which usually only allows for simulating relatively simple configurations, implementations of zero- and one-dimensional simulations are often directly or indirectly incorporated to solve complex three-dimensional problems. For example, the same set of equations that describes homogenous, isobaric batch reactors can be solved within a finite rate

chemistry simulation to obtain a new gas phase composition at the end of a time step [2]. An example for an indirect incorporation would be the tabulation and lookup of simulation results as done in the flamelet approach. These examples show that the numerical frameworks for zero-dimensional and one-dimensional configurations are useful in a vast range of applications. Frequently, these applications have specific design, implementation, or feature requirements and it is not surprising that many different frameworks have evolved in the past decades. Researchers concerned with a problem from one of the above-mentioned fields are confronted with the question which of the available software packages, if any, suites their needs. This question cannot be answered universally due to users' specific aims and interests. In this work, we focus on an important prerequisite to make this decision: The consistency of results predicted by some of the most commonly used numerical frameworks. The considered free, open source projects are Cantera [3], Chemkin-II [4], FlameMaster [5], and OpenSMOKE++ [2,6]. Ansys/Chemkin-PRO (Chemkin-Pro) [7] is the only commercial software in the comparison. The presented results are intended not only for the users and developers of the presented programs, but they are also meant to serve as reliable data for the validation of other implementations. Besides accurate and consistent results, the performance in terms of process time can be an important criterion for the choice of software. Here, a comparison is carried out for two specific test cases. Comparability of process time for such a small set of test cases requires sufficiently similar numerical methods, which is given for Cantera, FlameMaster, and OpenSMOKE++ for homogenous, isochoric reactors as discussed below.

Homogeneous, Isochoric, Adiabatic Batch Reactors

The first configuration under investigation is the one for homogenous, isochoric, adiabatic reactors, which can be described by a set of ordinary differential equations (ODE) for the species mass fractions and the temperature [6]. This configuration is important as straightforward extensions for facility effects allow to simulate rapid compression machines and shock tubes. However, in the below defined test cases, such effects where not considered to ensure simple and yet precisely defined conditions for the test cases. Homogenous zero-dimensional reactors are well suited to validate the computation of the reaction kinetics and the thermodynamic species properties. The implementation of this configuration is similar in Cantera, FlameMaster, and OpenSMOKE++. All three frameworks provide the option to make use of the same solver for initial value problems, which is CVODE [8]. Therefore, this test case serves as a starting point for the comparison. The initial conditions for this test case are given in Table 1 and a small kinetic model for hydrogen-air combustion is used [9]. If CVODE is available, the employed relative and absolute tolerances are 3.0e-12 and 3.0e-14, respectively. Chemkin-II and Chemkin-Pro do not provide this option. Instead, a solver for differential algebraic equations (DAE), DASPK [4,7], is integrated. While OpenSMOKE++ integrates multiple ODE- and DAE-solvers [6], only CVODE was used in this study.

The results from all frameworks agree very well. Several species mole fractions and temperature profiles were compared. An illustration of the results is not included as it would not provide further insight due to the very small deviation of the results.

Table 1. Initial conditions for the homogenous, adiabatic, isochoric reactors.

Pressure [bar]	30.0
1000/Temperature [1/K]	0.7 – 1.5
Fuel-Air-Equivalence Ratio [-]	0.7, 1.0, 1.3

Laminar, Freely Propagating, Premixed Flames

As a second test case simulations of premixed, freely propagating, laminar flames are considered. This configuration is chosen not only because of its importance for the simulation of several experimental setups, but also because one-dimensional configurations add another important layer of complexity to the simulation. Besides different numerical methods for solving a set of partial differential equations [6], they also introduce models that account for transport phenomena. To assess the consistency of the results for this configuration, predictions for the laminar burning velocity of methane-air flames are considered over a range of fuel-air-equivalence ratios. In all simulations, the GRI3.0 kinetic model [10] is utilized and radiation is not considered. Conditions of the unburnt mixture are summarized in Table 2.

Table 2. Conditions in the unburned mixture for the premixed, laminar flames.

Pressure [bar]	1.0
Temperature [K]	300.0
Fuel-Air-Equivalence Ratio [-]	0.6 - 1.7

For one-dimensional flames, an important part of the implementation are models that account for transport phenomena. All simulations were conducted using the same mixture-averaged diffusion model and accounting for thermal diffusion, if possible. Note that the current standard version of FlameMaster implements a different thermal diffusion model than Chemkin-II, Chemkin-Pro, and OpenSMOKE++ and the implementation was extended to include the thermal diffusion model identical to the other frameworks. Cantera only allows to account for thermal diffusion, if multi-component diffusion is applied. Therefore, thermal diffusion was not accounted for in the Cantera simulations. The below presented simulations were rerun with FlameMaster and OpenSMOKE++ without thermal diffusion and it was found that the applied model reduces the burning velocity slightly by approximately 1%.

Another important factor for simulations of one-dimensional flames is the utilized grid. An insufficient number of grid points results in a poor prediction of the laminar burning velocity. Therefore, all simulations were run with at least 1200 grid points and central differences, if possible. In tests previously conducted with Cantera, it was found that this number is sufficient whereas increasing the number of grid points

beyond this value does not change the predicted laminar burning velocity significantly.

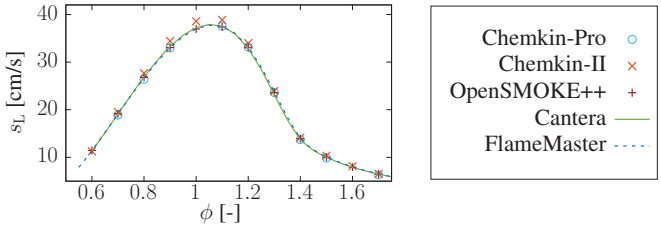

Figure 1. Flame speed of premixed, laminar flames over fuel-air-equivalence ratio.

Fig. 1 shows the predicted laminar burning velocities as a function of the fuel-air-equivalence ratio. The results from Cantera, Chemkin-Pro, FlameMaster and OpenSMOKE++ agree very well. Most of the predicted values deviate less than 0.2 cm/s from one another. Only for slightly rich mixtures, Cantera predicts a laminar burning velocity that is 0.45 cm/s lower than the other predictions. As thermal diffusion was not accounted for, it was expected that the laminar burning velocity would be slightly increased instead. The largest deviation is obtained for Chemkin-II. For near stoichiometric mixtures, the laminar burning velocities predicted by Chemkin-II are up to 1.6 cm/s higher compared to the other frameworks.

Process Time Benchmark

Finally, the performance in terms of process time required for running simulations of homogenous, isochoric, adiabatic batch reactors is compared between Cantera, FlameMaster, and OpenSMOKE++. The terms process or CPU time refer to the amount of time the central processing unit (CPU) requires for processing all instructions of a simulation. The comparability of the measured values is only given, if the numerical method is sufficiently similar. Cantera, FlameMaster, and OpenSMOKE++ all provide the option to run batch reactor simulations with CVODE [8], which means in all simulations identical numerical methods can be applied to conduct the time integration. Within the time integration, it is required to solve a system of nonlinear equations. This is done using a modified Newton method. The corresponding Jacobian evaluation can be done numerically using finite differences or analytically. A numerical evaluation is provided with CVODE and therefore available in all three frameworks. A semi-analytical evaluation of the Jacobian is already implemented in OpenSMOKE++. However, this option is only available with ODE solvers other than CVODE. In Cantera, the Jacobian is always estimated numerically. To demonstrate the impact of the Jacobian estimation, the current version of FlameMaster is extended to include analytical derivatives.

All benchmark simulations were done on an Intel Xeon CPU (E5-2650 v4 @ 2.20GHz). All frameworks were compiled with the Intel compilers. Cantera and

FlameMaster were linked against the multi-threaded version of math kernel library (MKL). OpenSMOKE++ was linked against the sequential MKL. For all test cases, the relative and absolute tolerances for CVODE are 1.0e-9 and 1.0e-16, respectively.

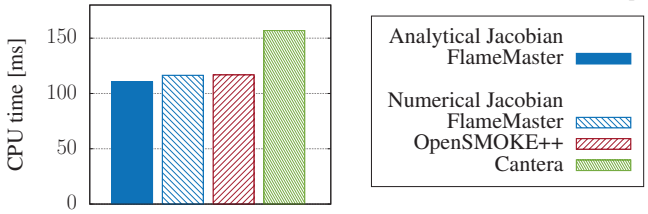

Figure 2. CPU time for simulations of isochoric reactors using a small model [10].

In the first benchmark, a stoichiometric methane-air mixture in a homogenous, isochoric batch reactor is simulated for two seconds using the GRI3.0 kinetic model [10]. The initial pressure and temperature are 30 bar and 1000 K, respectively. Fig. 2 shows that the measured CPU times are similar for all implementations. The CPU time required by FlameMaster with the analytical Jacobian evaluation is virtually the same as with the numerical evaluation.

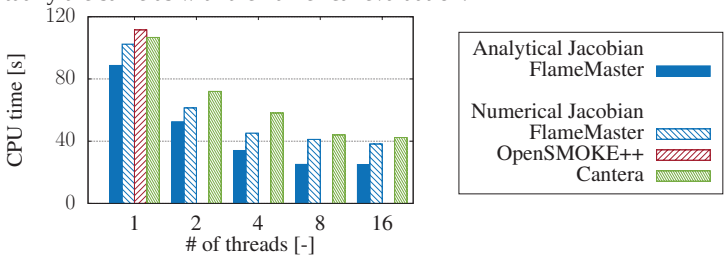

Figure 3. CPU time for simulations of isochoric reactors with a large model [1].

In the second benchmark, an isochoric reactor with a stoichiometric decane-air mixture at 30 bar and 1000 K is simulated for two seconds. The kinetic model consists of 1692 species and 5804 reactions [1]. The CPU times are shown in Fig. 3. Again, for all three frameworks, the CPU time is similar with a numerical Jacobian evaluation. The performance of FlameMaster is slightly improved with the analytical Jacobian evaluation. As Cantera and FlameMaster were linked against the multithreaded MKL, the simulations were also executed with up to 16 threads. The CPU time is clearly decreased with an increasing number of threads. The observed, significant speed up results solely from the parallelized solution of the linear system within the MKL and the remaining computation is still executed sequentially. This emphasizes the importance of the linear solver. Note that OpenSMOKE++ and the extended version of FlameMaster used here implement options for solving sparse linear systems, which are more appropriate for this test case. With these options, the CPU time for sequential execution is reduced significantly by up to a factor of 7.

Conclusions

Simulation results predicted by five commonly used numerical frameworks were compared for two representative configurations. Cantera, Chemkin-Pro, FlameMaster, and OpenSMOKE++ predict consistent results for both configurations. While the Chemkin-II results are consistent with the other frameworks for isochoric batch reactors, the predicted burning velocities for near stoichiometric conditions are slightly larger. A process time benchmark showed that the considered frameworks provide similar performance. The CPU time for the simulation of large mechanisms can be reduced with sparse or parallelized dense linear solvers.

Acknowledgment

This project has received funding from the European Research Council (ERC) under the European Union's Horizon 2020 research and innovation programme (Grant Agreement No 695747).

References

[1] Cai, L., Pitsch, H., Mohamed, S., Raman, V., Bugler, Curran, H., Sarathy, S., "Optimized reaction mechanism rate rules for ignition of normal alkanes", *Combust. Flame.* 173: 468-482 (2016)

[2] Cuoci, A., Frassoldati, A., Faravelli, T., Ranzi, E., "Numerical Modeling of Laminar Flames with Detailed Kinetics Based on the Operator-Splitting Method", *Energy Fuels*. 27: 7730-7753 (2013)

[3] Goodwin, D., Moffat, H., Speth, R. "Cantera: An object- oriented software toolkit for chemical kinetics, thermodynamics, and transport processes.", http://www.cantera.org, Version 2.3.0 (2017)

[4] Kee, R., Rupley, F., Miller, J., "Chemkin-II: A Fortran chemical kinetics package for the analysis of gas-phase chemical kinetics", (1989)

[5] Pitsch, H., FlameMaster, a C++ computer program for 0D combustion and 1D laminar flame calculations.

[6] Cuoci, A., Frassoldati, A., Faravelli, T., Ranzi E., "OpenSMOKE++: An object-oriented frame- work for the numerical modeling of reactive systems with detailed kinetic mechanisms", *Comput. Phys. Commun.* 192: 237-264 (2015)

[7] ANSYS® Academic Research Chemical Kinetics, Chemkin-PRO, Rel. 19.0

[8] Hindmarsh, A., Brown, P., Grant, K., Lee, S., Serban, R., Shumaker, D., Woodward, C., "SUNDIALS: Suite of Nonlinear and Differential/Algebraic Equation Solvers", *ACM Trans. Math. Softw.* 31: 363-396 (2005)

[9] Hong, Z., Davidson, D., Hanson, R., "An improved H2/O2 mechanism based on recent shock tube/laser absorption measurements", *Combust. Flame.* 158: 633-644 (2010)

[10] Smith, G., Golden, D., Frenklach, M., Moriarty, N., Eiteneer, B., Goldenberg, M., Bowman, C., Hanson, R., Song, S., Gardiner Jr., W., Lissianski, V., Qin, Z., http://www.me.berkeley.edu/gri_mech/

INVESTIGATION OF S_2 + AIR COMBUSTION

N. Sebbar*, T. Zirwes, P. Habisreuther*, H. Bockhorn*, D. Trimis***
nadia.sebbar@kit.edu
*Karlsruhe Institute of Technology (KIT), Engler-Bunte-Institute, Combustion Technology, Engler-Bunte Ring 7, D-76131 Karlsruhe, Germany
**Karlsruhe Institute of Technology (KIT), Steinbuch Center for Computing, Hermann-von-Helmholtz-Platz 1, 76344 Eggenstein-Leopoldshafen

Abstract

This study comprises burning velocity calculations for the combustion of S_2 with air for a wide range of air/fuel ratios. The reaction mechanism used in the flame simulations considers S/N/O reactions. Sensitivity analysis of the computed results is performed to evaluate crucial reaction steps. The results show high sensitivity of the burning velocity to the rate coefficient of the reaction $S + O_2 \rightarrow SO + O$. Flame simulations have been performed on the basis of different rate constants for this reaction. Using rate coefficients from literature the calculations exhibit a unusual high burning velocity in the order of 350 cm s^{-1} at T_0 = 373 K and no influence of the nitrogen-sulphur reactions on the flame behavior.

Introduction

Sulphur on one hand is used on a megaton scale in industrial production process of sulphuric acid. On the other hand, heat generated from sulphur combustion may be used for generation of electricity in closed cycles where, e.g. solar heat is applied to recover elemental sulphur from the combustion products [1]. Experimental and numerical studies on combustion of sulphur combined with hydrogen and hydrocarbons have been performed and detailed C/H/O/S reaction mechanisms are reported in the literature [2, 3, 4, 5, 6]. Still, relatively little research on the combustion and behaviour of pure sulphur are available in the literature.

In the present study burning velocity calculations for the combustion of S_2 with air for a wide range of air/fuel ratios are performed. The simulations use mechanism comprising 27 reactions between the species of the S/N/O-system. The nitrogen reactions are taken from [7, 8] and the GRI [9] mechanism. The impact of the different rate coefficients on laminar burning velocities were analyzed and compared. Different rate parameters from literature and re-estimated values for the determinant reaction $S + O_2 \rightarrow SO + O$ are used. The effect of N_2 and O_2 on the combustion of sulphur is examined, as well as that of temperature and pressure.

Results and Discussion

1. Mechanism

In a previous study [8], a reaction mechanism involving only sulphur and oxygen species was developed. This mechanism, encompassing 11 reactions, is extracted

from a detailed combustion mechanism developed in [7]. In the present work, reactions involving nitrogen and sulphur reactions are added. The N/S/O-reactions are taken from the original mechanism in [7] and completed with N/O reactions from the GRI-mechanism [9]. The N/S/O reaction mechanism encompassing 27-reactions is listed in Table 1.

Table 1. N/S/O mechanism extracted from [7] and GRI [9].

Reactions from [7] A (mole-cm-sec-K), T_A (Kelvin)	$k = A \cdot T^b \cdot \exp(-T_A/T)$		
	A	b	T_A
1. $S + O_2 \leftrightarrow SO + O$	5.20E+06	1.8	-600.0
2. $S_2 + M \leftrightarrow 2S + M$	4.80E+13	0.0	38800.0
3. $S_2 + O \leftrightarrow SO + S$	1.00E+13	0.0	0.0
4. $SO_3 + O \leftrightarrow SO_2 + O_2$	2.00E+12	0.0	10000.0
5. $SO_3 + SO \leftrightarrow 2SO_2$	1.00E+12	0.0	5000.0
6. $SO + O(+M) \leftrightarrow SO_2 (+M)$	3.20E+13	0.0	0.0
7. $SO_2+O(+M) \leftrightarrow SO_3 (+M)$	9.20E+10	0.0	1200.0
8. $SO + M \leftrightarrow S + O + M$	4.00E+14	0.0	54000.0
9. $SO + O_2 \leftrightarrow SO_2 + O$	7.60E+03	2.4	1500.0
10. $2SO \leftrightarrow SO_2 + S$	2.00E+12	0.0	2000.0
11. $SO_3 + S \leftrightarrow SO + SO_2$	5.12E+11	0.0	0.0
12. $S + NO \leftrightarrow SN + O$	1.00E+12	0.5	17500.6
13. $N + SO \leftrightarrow NO + S$	6.31E+11	0.5	1010.3
14. $SN + NO \leftrightarrow N_2 + SO$	1.81E+10	0.0	0.0
15. $SN + O_2 \leftrightarrow SO + NO$	3.00E+08	0.0	0.0
16. $SN + NO_2 \leftrightarrow S + NO + NO$	4.07E+15	-1.0	0.0
17. $N + SN \leftrightarrow N_2 + S$	6.30E+11	0.5	0.0
18. $SO_2 + NO_2 \leftrightarrow NO + SO_3$	4.25E-19	8.9	3797.2
19. $SO + NO_2 \leftrightarrow SO_2 + NO$	8.43E+12	0.0	0.0
20. $SN + O \leftrightarrow SO + N$	6.31E+11	0.5	4030.6
Reactions from GRI [9]			
21. $N + NO \leftrightarrow N_2 + O$	2.70E+13	0.0	178.7
22. $N + O_2 \leftrightarrow NO + O$	9.00E+09	1.0	3271.3
23. $N_2O + O \leftrightarrow N_2 + O_2$	1.40E+12	0.0	5440.4
24. $N_2O + O \leftrightarrow 2NO$	2.90E+13	0.0	11650.7
25. $N_2O(+M) \leftrightarrow N_2 + O(+M)$	7.91E+10	0.0	28193.3
26. $NO + O \leftrightarrow NO_2$	1.06E+20	-1.4	0.0
27. $NO_2 + O \leftrightarrow NO + O_2$	3.90E+12	0.0	-120.8

2. Laminar burning velocities

Laminar burning velocities S_L have been calculated as a function of the air/fuel ratio λ. Figure 1 (left) illustrates results at normal pressure (P = 1 atm) for two temperatures of the incoming mixture T_0 = 373 and T_0 = 423 K and the effect of

pressure at T_0 = 373 K (right). The air/S_2 ratio has been varied in the range 0.2 < λ < 3.0. The airl/fuel ratio is based on the stoichiometry of reaction $S_2 + 2O_2 \leftrightarrow 2SO_2$ and the mechanism listed in Table 1 has been used.

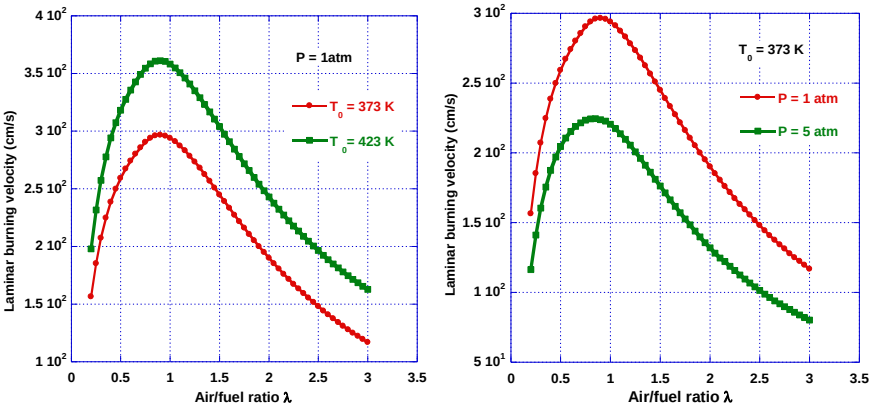

Figure 1. Laminar burning velocity for S_2/air calculated at two temperatures, T_0 = 373 K and T_0 = 423 K (left) and at two pressures P = 1 atm and 5 atm (right).

The calculations show that the highest burning velocity for the combustion of S_2 is obtained under slightly rich conditions. As expected from 0.2 < λ < 1.0 (rich region) the flame speed increases to attain a maximum near 300 cm s^{-1} at λ = 0.85 and T_0 = 373 K and then decreases. The burning velocity profile obtained at higher temperature, namely T_0 = 423 K, is significantly above the T_0 = 373 K curve and its maximum reaches about 360 cm s^{-1} at λ = 0.90. The results show the expected decrease of the laminar burning velocity with pressure.

The results exhibit unusual high burning velocities values, which are unfortunately difficult to confirm since no experimental data are available. In [10] values for S_L for combustion of H_2S are reported which are lower by about a factor of 1/10.

3. Sensitivity analysis

In order to identify the reactions having most impact on the burning velocity and to characterize the effect of nitrogen species in the S/N/O-system, sensitivity analysis was performed at stoichiometric air/fuel ratio, λ = 1.0. The sensitivity coefficients reflect a relative change of the model response, caused by a relative change of the rate coefficient of a specific reaction.

Figure 2 demonstrates that reaction $S + O_2 \rightarrow SO + O$ is one of the determinant steps in the oxidation of S_2. At 1 atm and T_0 = 373 K all other reactions exhibit a significant lower impact on S_L at stoichiometric mixture composition. Figure 2 reveals also that none of the reactions involving nitrogen (reactions 12 to 27) has even a small impact on the flame velocity. New reactions involving the interaction of nitrogen species with sulphur and oxygen species are being developed and will be reported in a near future.

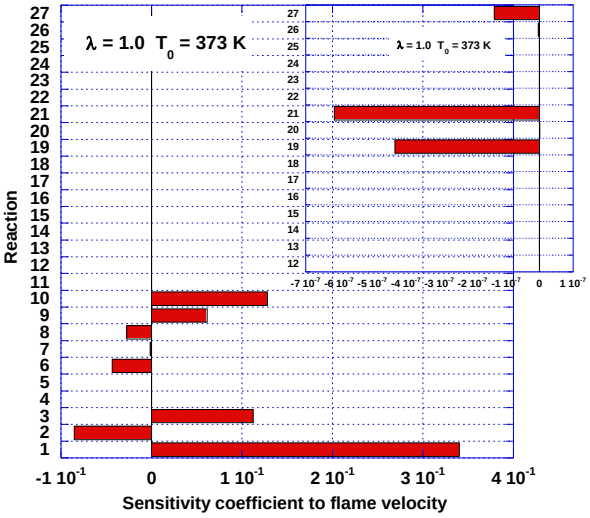

Figure 2: Sensitivity coefficients with respect to the burning velocity at stoichiometric conditions (λ = 1), T_0 = 373 K and P = 1 atm.

4. Rate coefficients from literature

Since reaction (1) turned out to be the crucial and determinant step for the combustion of S_2 with air, the rate coefficient of this reaction was re-evaluated with quantum chemistry methods [8] and has been employed in the numerical simulations. The results are compared with simulations including different rate coefficient reported in the literature [7, 11, 3]. The rate parameters of reaction (1) as well as are those reported in the literature are listed in Table 2 along with the corresponding references.

Table 2. *Rate coefficients for reaction (1) from literature and own work for the flame calculations.*

Reaction	$k = A\,T^b \exp(-T_A/T)$		
	A	b	T_A
$S + O_2 \longrightarrow SO + O$ [7] basic mechanism	5.20E+06	1.8	-600.0
$S + O_2 \longrightarrow SO + O$ [11] Titova	6.32E+11	0.5	0.0
$S + O_2 \longrightarrow SO + O$ [3] Glarborg	5.40E+05	2.11	-729.7
$S + O_2 \rightarrow SO + O$ *singlet* [8]	2.69E+10	0.15	5358.8
$S + O_2 \rightarrow SO + O$ *triplet* [8]	1.09E+11	0.15	2369.4.

A (mole-cm^3-sec-K), T_A (Kelvin)

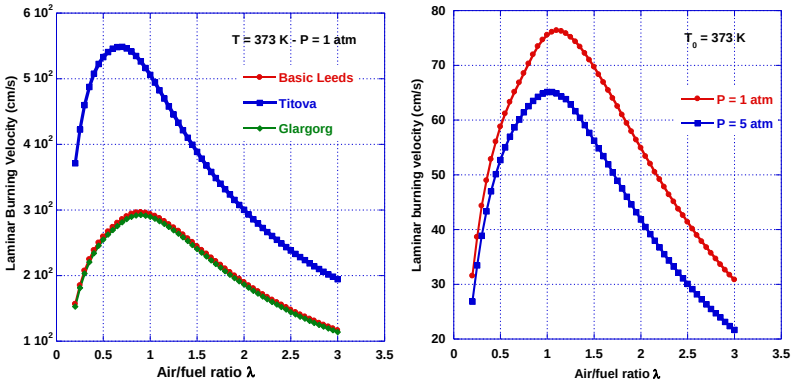

Figure 3. *Laminar burning velocity for S_2/air calculated with different rate coefficients for reaction (1), T_0 = 373 K and P = 1 atm, left. Laminar burning velocity for rate coefficient from [8], P = 1 and 5 atm, right.*

The burning velocities obtained at T_0 = 373 K and P = 1 atm, with different rate coefficients are compared in Figure 3. Over all, the behavior of the burning velocity is similar for the rate coefficients from [3] and [7]. It appears that the burning velocity calculated with the rate coefficient from [11] is by far faster than the others. This is easily understandable with its pre-exponential factor of 6.32×10^{11} which is five orders of magnitude higher than that from [7]. Because of the pre-exponential factor of 5.40×10^{5}, the burning velocity obtained with the rate coefficient from [3] is slightly below that obtained with the rate coefficient from [7] (5.20×10^{6}). The burning velocity profiles obtained with the re-estimated rate parameters for reaction (1) from [8] are plotted at T_0 = 373K, and two pressures P = 1 and P = 5 atm in Figure 3, right. The results demonstrate that, apparently, the use of the re-estimated rate parameters considerably slows down the burning velocity by almost a factor of 1/10.

5. Species profiles

Figure 4 gives mole fraction profiles of SN (left) and NO (right) at λ = 2.5, 1.0 and 0.25. The calculated profiles exhibit that both SN and NO formation is strongly favored under stoichiometric conditions. This is in agreement with the flame temperature which at λ = 1.0 attains a maximum value. At λ = 0.25, SN formation is significantly lower but still observable, whereas NO formation at rich and lean conditions is negligible.

Acknowledgements
The results presented have been obtained within the framework of the PEGASUS project. This project has received funding from the European Union's Horizon 2020 research and innovation program under grant agreement No 727540".

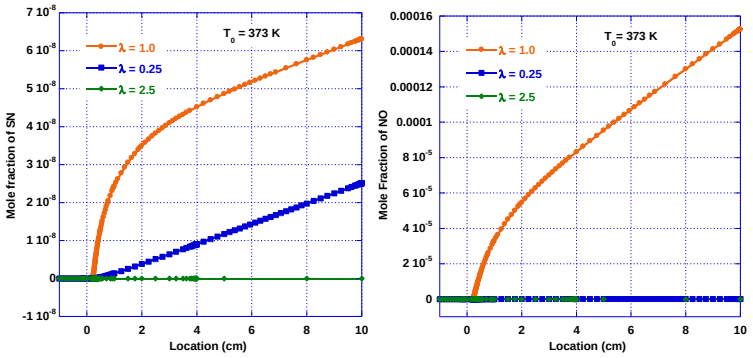

Figure 4. Mole fraction profiles of SN and NO for λ = 2.5, 1.0 and 0.25

References

[1] PEGASUS (H2020-LCE-2016-2017): *Renewable Power Generation by Solar Particle Receiver Driven Sulphur Storage Cycle. Horizon 2020. Competitive Low-Carbon Energy* (2016).

[2] Giménez-López, J. ; Martínez, M.; Millera, A.; Bilbao, R. ; Alzueta, M.: *Combustion and Flame* 158, 48–56 (2011)

[3] Glarborg, P.; Marshall, P.: *Int. J. Chem. Kinet*. 45, 429–439 (2013).

[4] Song, Y. ; Hashemi, H. ; Munkholt Christensen, J. ; Zou, C. ; Haynes, B.S.; Marshall, P. ; Glarborg, P.: *Int J Chem Kinet* 1–16 (2016).

[5] Mueller, M. A. ; Yetter, R. A.; Dryer, F. L.: *Int J Chem Kinet* 32: 317–339, (2000).

[6] Zhang, Y.; Yang, H.; Zhou, J.; Wang, Z.; Liu, J.; Cen K.: *Applied Energy* 130, 396–402 (2014).

[7] Hughes, K. J.; Blitz, M. A.; Pilling, M. J.; S. H. Robertson, S. H. *Proceedings of the Combustion Institute* **2002**, *29*, 2431–2437.

[8] Sebbar, N.; Zirwes, T.; Habisreuther, P.; Bozzelli, J.W.; Bockhorn, H.; Trimis, D. Special issue of the SMARTCATs COST Action. Submitted to *Energy and Fuels*.

[9] Smith, G. P.; Golden, D. M.; Frenklach, M.; Moriarty, N. W.; Eiteneer, B.; Goldenberg, M.; Bowman, C. T.; Hanson, R. K.; Song, S.; Gardiner, Jr., W. C.; Lissianski, V. V.; Qin, Z. http://www.me.berkeley.edu/gri_mech/

[10] Vervisch, L.; Labegorre, B.: *Proc. of the European Combustion Meeting 2003*, Orléans, France, paper 216.

[11] Savel'ev, A. M.; Starik, A. M.; Titova, N. S. *Combustion, Explosion, and Shock Waves*, **2002**, *38*, (6) 609-621.

SESSION VII

Formation and control of pollutants and greenhouse gases

Calcium looping with air pollution control residues from municipal solid waste incinerators: a preliminary screening

A. Dal Pozzo*, A. Armutlulu, M. Rekhtina**, C.R. Müller**, V. Cozzani***

alessandro.dalpozzo3@unibo.it

* Dipartimento di Ingegneria Civile, Chimica, Ambientale e dei Materiali, Alma Mater Studiorum – Università di Bologna, Via Terracini 28, 40131 Bologna (Italy)

** Department of Mechanical and Process Engineering, ETH Zürich, Leonhardstrasse 21, 8092 Zürich (Switzerland)

Abstract

Acid gases such as HCl and SO_2 are typical pollutants generated by waste combustion and their removal by means of dry neutralization processes generates so-called air pollution control (APC) residues, whose fate is to be sent to disposal, in absence of commercially viable valorization routes. When the reactant used in dry neutralization is slaked lime, the residues contain fly ash, unreacted calcium hydroxide and the products of its reaction with HCl and SO_2. Given the high Ca content of APC residues, the present study explored the possibility to use these waste materials as CO_2 sorbents in the calcium looping process. Samples collected in three waste-to-energy plants were tested in a thermogravimetric analyzer over multiple carbonation/calcination cycles, comparing their performance to that of virgin slaked lime. The CO_2 carrying capacity of residues resulted inferior to that of virgin lime, since the amount of calcium available for carbonation in the residues is lower than in the fresh material, but in terms of CaO conversion the carbonation performance over 20 cycles was comparable. Furthermore, the evolution of CO_2 uptake upon cycling showed a peculiar trend, with a temporary increase of performance occurring during cycling. This phenomenon was attributed to the possible role of the chlorinated phase in the residues in promoting CO_2 sorption during the diffusion-controlled stage of reaction. The findings of this preliminary screening provide a useful basis for the planning of further investigations on the suitability of APC residues for calcium looping applications.

Introduction

CO_2 capture and storage is a technological option aimed at mitigating the emissions of carbon dioxide from large-scale sources, such as thermoelectric power stations, cement manufacturing sites and steelmaking plants. An emerging approach for CO_2 capture is the so-called calcium looping, CaL [1], based on the reversible reaction between calcium oxide (CaO) and carbon dioxide to form calcium carbonate ($CaCO_3$). The regenerable CaO is provided by natural materials, such as limestone

or dolomite. In the CaL process, the sorbent adsorbs CO_2 from a flue gas stream in a carbonator vessel operated at 650-700 °C and releases it in a calciner vessel operated at 950 °C, thus generating a CO_2-rich gas stream suitable for geological storage. Various bench scale and pilot scale investigation campaigns have already demonstrated the feasibility of the process [2].
In order to reduce the consumption of natural resources, several investigators have recently proposed the use of Ca-rich waste materials (*e.g.* lime mud [3] or carbide slag [4]) as feedstock for the process.
Air pollution control residues from dry acid gas removal are a class of waste materials containing a relevant calcium fraction. They are generated as solid products of the neutralization of acid gases (HCl, SO_2), characteristic pollutants emitted by waste incineration, by means of the injection of a powdered reactant such as slaked lime, $Ca(OH)_2$:

$$Ca(OH)_2 + HCl = CaOHCl + H_2O \quad (1)$$
$$Ca(OH)_2 + SO_2 = CaSO_3 + H_2O \quad (2)$$
$$Ca(OH)_2 + CO_2 = CaCO_3 + H_2O \quad (3)$$

According to reactions 1-3, the residues, referenced in the following as calcium-based waste (CBW), contain CaOHCl and $CaSO_3$ derived from the abatement of acid gases, and $CaCO_3$ derived from the undesired reaction with the CO_2 present in the flue gas. In addition, a relevant fraction of the residues is still formed by unreacted $Ca(OH)_2$, because at the typical operating temperatures of dry acid gas removal (150-180 °C) the complete conversion of the reactant is hindered by diffusional limitations [5].
After the acid gas removal stage, CBWs are typically separated from the flue gas in the same fabric filter where also the fly ash generated by waste combustion are captured. Therefore, CBWs are mixed together with an ash fraction containing harmful micro-pollutants (*e.g.* heavy metals) and, as such, are generally classified as hazardous waste throughout Europe. To date, no commercial valorization option is available. “Once-through” gas-solid carbonation has been proposed as a stabilization method to reduce the leaching potential of CBWs [6]. Here, it is proposed to expose the CBWs to repeated carbonation/calcination cycles in order to valorize the residual sorption capacity of the residues in a CaL scheme. The results of a preliminary investigation of the CO_2 uptake potential of CBWs in TGA are presented.

Experimental section
CBW samples generated by the dry sorbent injection of slaked lime were collected at three Italian waste-to-energy plants. A sample of the commercial slaked lime before injection (provided by the same supplier to the three plants) was collected and used as reference of the virgin material before reaction with acid gases.
The elemental composition of the samples was determined according to the UNI

EN ISO 11885:2009 protocol, while scanning electron microscope (SEM) imaging was employed to visualize their morphology. Thermogravimetric runs, carried out in a TGA-Q500 (TA Instruments), were used to gather quantitative information on the relative abundance of $Ca(OH)_2$, $CaCO_3$ and CaOHCl in the CBW samples, thanks to the different decomposition temperature of the compounds.
The carbonation performance of the CBW samples was also tested in TGA, following the subsequent thermal program: i) pre-calcination in N_2 by heating the sample up to 800 °C at a rate of 50 °C/min; ii) 20 min carbonation in 60 vol.% CO_2, after cooling the sample to 700 °C at a rate of 50 °C/min; iii) 10 min regeneration of the sample via calcination in N_2 after heating the sample to 900 °C at a rate of 50 °C/min. Steps ii) and iii) were repeated 20 times in order to test the cyclic performance of samples. A platinum pan and an amount of sample of ~ 20 mg were used in the experiments.

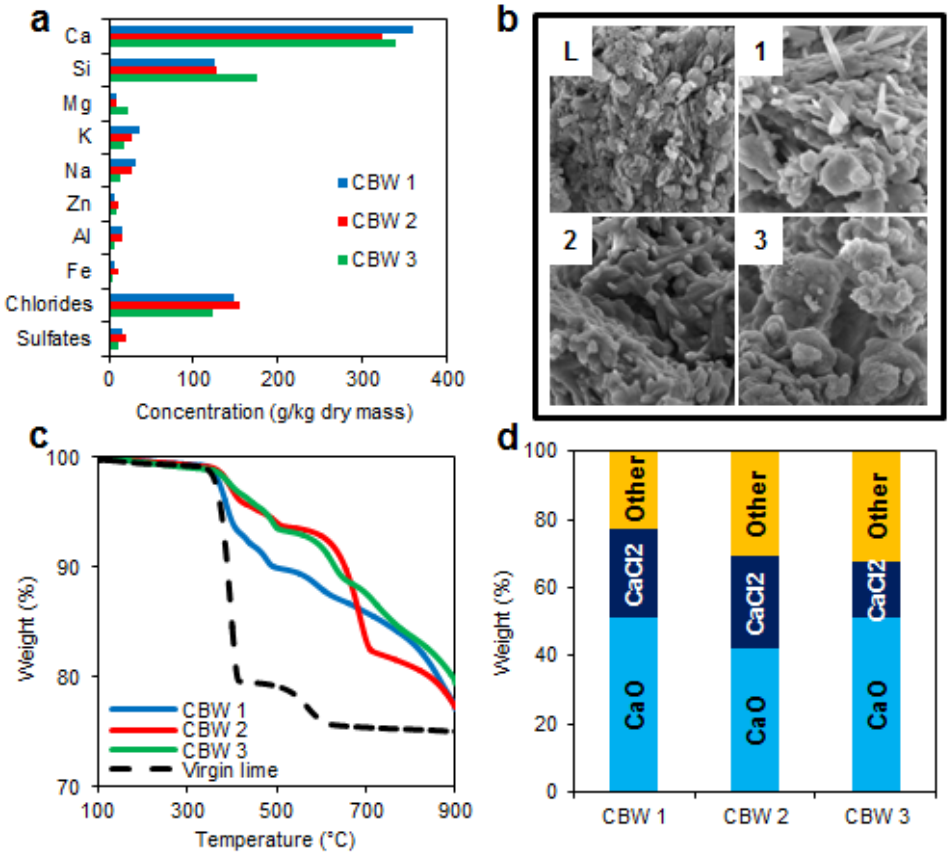

Figure 1. Characterization of the CBW samples. a) concentration of the main components in the "as received" samples; b) SEM micrographs of the virgin lime (L) and the three CBW samples; c) thermal decomposition of the samples; d) composition of the CBW samples after pre-calcination at 800 °C.

Results and discussion

The CBW samples analyzed in the study were characterized as summarized in Figure 1. Regarding their elemental composition (Fig. 1a), calcium is unsurprisingly the most abundant element in CBWs, but a variety of other elements, which are the major components of the fly ash fraction, are present. Chlorides and sulfates derive from the capture of HCl and SO_2. Chlorides are an order of magnitude more abundant than sulfates, as a consequence of the higher concentration of HCl in the flue gas of waste incinerators. The SEM images in Fig. 1b illustrate the morphology of the samples. The flat and roughly hexagonal nanograins of $Ca(OH)_2$ which populate the micrograph of the commercial virgin lime are visible also in the CBW samples, confirming the presence of unreacted $Ca(OH)_2$, although mixed with carbonate layers and laminar crystals of the chlorinated phase. TGA was employed to quantitatively investigate the composition of samples (Fig. 1c), since the main compounds in the CBWs decompose at different temperature ranges [7]:

$$Ca(OH)_2 = CaO + H_2O \quad [350\text{-}400°C] \quad (4)$$

$$2\,CaOHCl = CaO + CaCl_2 + H_2O \quad [450\text{-}550°C] \quad (5)$$

$$CaCO_3 = CaCO_3 + CO_2 \quad [> 600°C] \quad (6)$$

Considering the occurrence of reactions 4-6 during heating, the composition of the calcined samples was estimated as shown in Fig. 1d, where the fraction labelled "other" includes the fly ash fraction and the sulfated phase.

Only the CaO fraction was assumed to take part in carbonation. Hence, the carbonation performance of the calcined CBW samples, exposed to repeated carbonation/calcination cycles, was expressed in terms of conversion of the CaO fraction (Fig. 2a). The absolute CO_2 uptake in terms of g of adsorbed CO_2 per g of sample is reported for selected cycles in Fig. 2b.

While, as expected, the CO_2 carrying capacity of the virgin lime declines monotonically upon cycling, the CBW samples exhibit a more complex evolution of CO_2 uptake over cycles. Although their uptake in absolute terms remains always lower than the virgin material (see Fig. 2b), the CBWs show an abrupt decline of CO_2 capture in the first 3 cycles and then a recovery of performance, which results in a conversion of CaO higher than that of the virgin lime. This happens with different intensities and lasts for a different number of cycles for the three samples: the upward trend of CO_2 uptake is in cycles 8-12 for CBW 1, 5-6 and 10-19 for CBW 2, and 4-6 for CBW 3. After this phase is finished, the CO_2 carrying capacity of the samples undergoes an eventual steady decay of performance comparable to that of virgin lime.

An insight on the characteristic behavior of the Ca-based residues can be obtained by comparing how the kinetics of CO_2 uptake changes upon cycling for sample CBW 1 and for the virgin lime (Fig. 3). For both sorbents, carbonation occurs according to two well-distinguished reaction stages: i) a fast regime controlled by

the chemical reaction rate in the first minute of reaction, followed by ii) a slow regime in which sorbent conversion is hindered by diffusional limitations. For the virgin lime (Fig. 3a), the CO_2 capture taking place in both the fast and slow stages of reaction progressively decreases with cycle number. Conversely, for CBW 1 (Fig. 3b), while the CO_2 uptake during the fast kinetically-controlled stage steadily declines upon cycling, the uptake during the following slow diffusion-controlled phase first increases (compare curves at cycle 5 and 10) and then decreases (compare curves at cycle 10 and 15) with cycle number. This produces the complex evolution of CaO conversion upon cycling presented in Figure 2. The increased performance during the diffusion-controlled stage of carbonation might be ascribed to the presence of the $CaCl_2$ phase, in agreement with experimental evidence pointing out the effect of doping with chloride salts in enhancing the reactivity of limestone during the slow reaction stage [8].

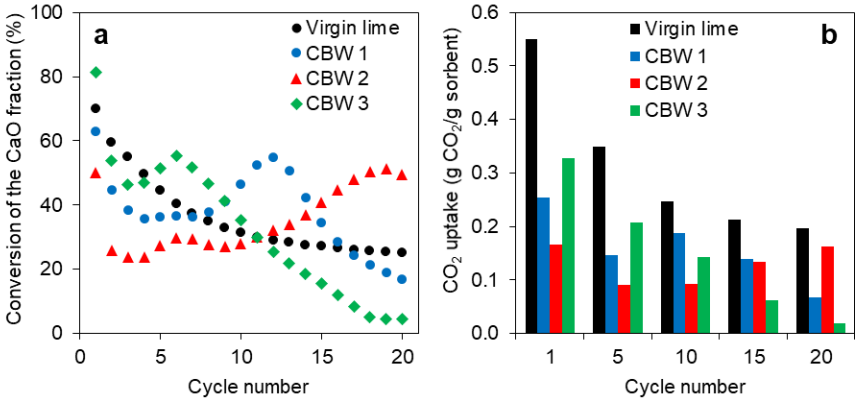

Figure 2. a) Conversion of available CaO over 20 cycles and b) CO_2 uptake at selected cycles for the three calcined CBW samples, compared to virgin lime.

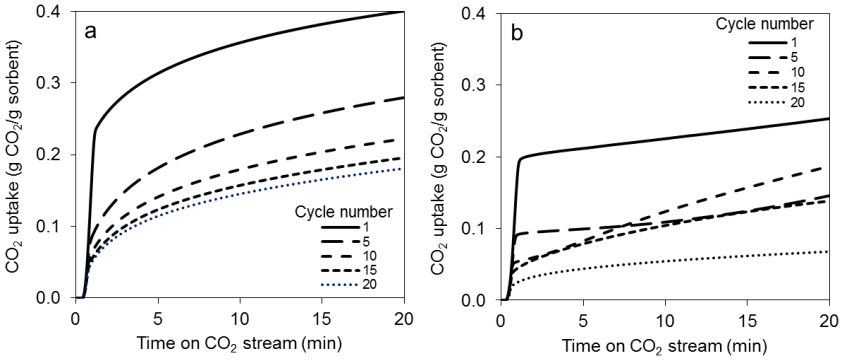

Figure 3. CO_2 uptake curve during different cycles for: a) virgin lime, b) CBW 1. Partially adapted from [9].

This preliminary analysis evidenced the potential of Ca-based APC residues as CO_2 sorbents for CaL applications. The relevant Ca content of the residues can be carbonated to a significant extent, achieving an appreciable CO_2 uptake, although expectedly lower than that of the virgin material. Nonetheless, an important share of CO_2 uptake (*e.g.* ranging from 21% in cycle 1 to 74% in cycle 10 for sample CBW 1, Fig. 3b) takes place during the diffusion-controlled stage and, as such, could not be completely exploited in the short residence times of typical CaL fluidized bed operation. Further tests, aimed at assessing the behavior of residues in harsher calcination conditions, closer to those of the industrial application, and at evaluating the resistance of residues to attrition, could contribute to give a complete picture of the suitability of CBWs for the CaL process.

References

[1] Abanades, J.C., Arias, B., Lyngfelt, A., Mattisson, T., Wiley, D.E., Li, H., Ho, M.T., Mangano, E., Brandani, S. Emerging CO_2 capture systems. *Int. J. Greenhouse Gas Control* 40: 126-166 (2015)

[2] Hanak, D.P., Anthony, E.J., Manovic, V. A review of developments in pilot-plant testing and modelling of calcium looping process for CO_2 capture from power generation systems. *Energy Environ. Sci.* 8: 2199-2249 (2015)

[3] Li, Y., Sun, R., Liu, C., Liu, H., Lu, C. CO_2 capture by carbide slag from chlor-alkali plant in calcination/carbonation cycles. *Int. J. Greenhouse Gas Control* 9: 117-123 (2012)

[4] Sun, R.; Li, Y.; Liu, C.; Xie, X.; Lu, C. Utilization of lime mud from paper mill as CO_2 sorbent in calcium looping process. *Chem. Eng. J.* 221: 124-132 (2013)

[5] Antonioni, G., Dal Pozzo, A., Guglielmi, D., Tugnoli, A., Cozzani, V. Enhanced modelling of heterogeneous gas-solid reactions in acid gas removal dry processes. *Chem. Eng. Sci.* 148: 140-154 (2016)

[6] Baciocchi, R., Costa, G., Di Bartolomeo, E., Polettini, A., Pomi, R. The effects of accelerated carbonation on CO_2 uptake and metal release from incineration APC residues. *Waste Manage.* 29: 2994-3003 (2009)

[7] Dal Pozzo, A., Moricone, R., Antonioni, G., Tugnoli, A., Cozzani, V. Hydrogen Chloride Removal from Flue Gas by Low-Temperature Reaction with Calcium Hydroxide. *Energy Fuels* 32: 747-756 (2018)

[8] Al-Jeboori, M.J., Fennell, P.S., Nguyen, M., Feng, K. Effects of Different Dopants and Doping Procedures on the Reactivity of CaO-based Sorbents for CO_2 Capture. *Energy Fuels* 26: 6584-6594 (2012)

[9] Dal Pozzo, A., Armutlulu, A., Rekhtina, M., Müller, C.R., Cozzani, V. CO_2 Uptake Potential of Ca-based Air Pollution Control (APC) Residues over Repeated Carbonation/Calcination Cycles. *Energy Fuels*, in press. DOI: 10.1021/acs.energyfuels.8b00391

EMBEDDING GRAPHENE-LIKE LAYERS IN HYBRID METAL ORGANIC FRAMEWORKS: THE EFFECT ON CO_2 CAPTURE

Michela Alfè*, Riccardo Rea, Valentina Gargiulo*, Matteo Minelli****
Luciana Lisi*, Maria Grazia De Angelis**
alfe@irc.cnr.it
* Istituto di Ricerche sulla Combustione (IRC-CNR), P.le Tecchio 80, 80125 Napoli, Italy
** Dipartimento di Ingegneria Civile Chimica Ambientale e dei Materiali, Alma Mater Studiorum-Università di Bologna, Via Terracini 28, 40131, Bologna, Italy

Abstract
A new class of metal organic framework was designed and characterized for CO_2 capture strategy also evaluating selectivity toward CO_2/N_2 mixtures. The adsorption measurements were performed under static conditions with a pressure decay technique. In this study, HKUST-1 (or $Cu_3(BTC)_2$) was used as benchmark MOF material. The HKUST-1 framework was modified by enclosing Zn^{2+} and a small amount (5 wt. %) of graphene-like layers (GL), a new-concept graphene related material (GRM), and the effect of such modifications on the microstructure and CO_2 capture performance was studied. The modified HKUST-1 samples showed a different gas adsorption behavior, that depends on the chemical structure and on the material microtexture. The best performing samples in terms of CO_2 uptake contain either a small amount of Zn^{2+} (< 0.5 wt. %) or GL layers.

Introduction
Actions aimed to carbon capturing and sequestration (CCS) are still considered as a priority task to mitigate the consequent drawbacks on global warming due to fossil fuels combustion [1]. A possible approach, in which huge efforts of dedicated scientific research are currently focused, is the development of innovative materials able to capture CO_2 more efficiently in operating conditions typical of a flue gas [2,3]. Metal-organic frameworks (MOFs), also known as coordination polymers, have attracted intense research interest as novel functional materials. In particular, the combined favorable properties of large surface area, permanent porosity and tunable pore size/functionality, have enabled metal-organic frameworks (MOFs) as ideal candidates for CO_2 capture in post-combustion configuration [4]. The chemical structure of MOFs is based on metal centers (nodes) coordinated by organic linkers, to form a regular crystalline structure characterized by cages where the gas molecules are entrapped. By varying the chemical composition (metal centers and linkers), the size of the pores and the separation performance of such structures can be properly tuned [5].
HKUST-1, formed by Cu centers coordinated by organic benzene tricarboxylate (BTC) linkers (Cu_3 $(BTC)_2$) is a benchmark material conventionally used as

reference for MOF functional characterization. In this work, starting from HKUST-1, a new class of MOF was produced by intercalating, in the framework self-assembling stage, carbonaceous graphene-like layers (GL) with the aim to induce modifications to the structure and porosity distribution [6]. The effect of the partial replacement of Cu centers with Zn centers [7] and of the simultaneous presence of Zn centers and GL layers were also investigated.
The microtexture of the modified HKUST-1 was characterized and CO_2, N_2 adsorption isotherms at 35 °C and pressures up to 25 bar were acquired by using a manometric technique [8].

Experimental section

Sample preparation. HKUST-1 and MGL, namely HKUST-1 in which GL are embedded (5 wt. %) were prepared in accordance with the synthetic route described in [6]. Zinc-doped MOFs were synthetized by applying the same solvothermal procedures adopted for HKUST-1 and MGL, also including a variable amount of zinc nitrate hexahydrate (15 and 50 % of the total Cu and Zn salts amount) in order to accomplish the target Zn^{2+} content (0.3 and 5 wt. %).
Material characterization. The quantitative determination of the metals (Cu and Zn) was measured by an Agilent ICP-MS 7500ce spectrometer following the procedure reported in [6]. BET specific surface area (SA) and pore size distribution of the samples were evaluated using a Quantachrome Autosorb 1-C by N_2 adsorption at 77 K. The samples were outgassed under vacuum at 110 °C before the analysis. Data of the adsorption branch of the complete isotherm were processed according to NLDFT method to evaluate the pore size distribution and pore volume. X-ray diffraction (XRD) analyses were carried out using a Philips PW1710 diffractometer operating between 5 °2θ and 60 °2θ with a Cu Kα radiation (λ = 1.54056). Scanning electron microscopy (SEM) was performed on a FEI Inspect™ S50 Scanning Electron Microscope. SEM was performed on the powdered sample, previously dried and sputter coated with a thin layer of gold to avoid charging.
Gas adsorption measurements. The experimental apparatus used to measure the N_2 and CO_2 gas isotherms was a pressure decay apparatus with fixed volume equipment, whose details have been reported elsewhere [8]. As the samples were in powders, they have been stored in an appropriate aluminum case to avoid the dispersion in the apparatus during the test. To evaluate the materials sorption capacity at the different pressure investigated, a mass balance has been used, using the Peng Robinson EOS [9] to describe the gas behavior. The samples before adsorption tests were kept under vacuum at 80°C for 8 hours in order to remove any trace of water and other gases adsorbed in the materials.

Result and discussion

The metal contents in the samples are reported in Table 1. As expected on the basis of previous literature findings [7], the actual incorporation of Zn^{2+} is very low and

reaches only the 5 wt.% when the nominal amount of zinc salt used during the synthetic process is 50 wt. % respect the copper salt. This result is consistent with the different coordination properties of Zn^{2+} compared to Cu^{2+} [7]. Coherently, the Cu^{2+} content decreases in presence of Zn^{2+}.

Sample	Zn (wt.%)	Cu (wt.%)	SA (m^2/g)	Total pore volume (cm^3g^{-1})	Micro-pore volume (cm^3g^{-1})	Meso-pore volume (cm^3g^{-1})
HKUST-1	0	37.4	2277	0.99	0.87	0.12
MGL	0	37.1	2100	1.01	0.80	0.21
MZn15	0.2	37.6	2203	0.85	0.83	0.02
MZn50	5.3	28.7	1509	0.64	0.46	0.18
MZn15GL	0.3	35.2	2503	1.12	0.96	0.16
MZn50GL	5.1	27.6	1670	0.84	0.62	0.22

Table 1. Metal contents and textural properties

In Table 1 the textural properties of all samples evaluated from N_2 adsorption isotherms at 77 K are also reported. All the samples exhibit high surface areas and high pore volumes, with a high contribution of micropores volume. The intercalation with GL layers or the presence of low amounts of Zn^{2+} (< 0.5%) do not correspond to a considerable change in textural properties. On the contrary, a considerable decrease of surface area and pore volume was detected only for the two samples containing the higher amount of Zn^{2+}. This last result was in accordance with literature and again correlated to the coordination properties of Zn^{2+} [7].

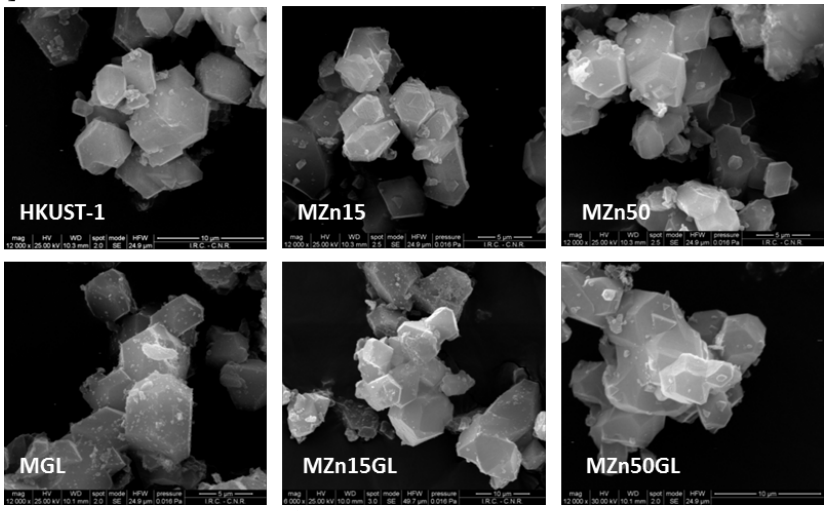

Figure 1. SEM images.

The SEM images of all the investigated samples are reported in Fig. 1. HKUST-1

is made up by typical octahedral crystals of different sizes with relatively smooth surface, in accordance with literature [10]. The incorporation of GL in MGL does not affect the formation of octahedral crystals [6] as well as the incorporation of Zn^{2+} even at higher load (5 wt. %).

The sample crystallinity was confirmed by the X-ray diffraction analysis (Figure 2).

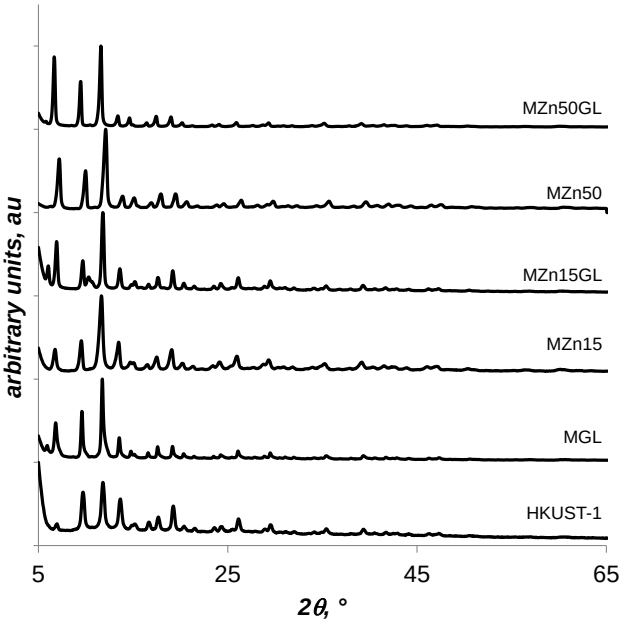

Figure 2. XRD patterns.

The diffraction pattern of the MGL is similar to that of HKUST-1 [10,11] indicating that the crystallinity of HKUST-1 crystals is preserved even in presence of GL during the self-assembling process [6]. Similarly, the diffraction patterns of the zinc doped MOFs are very similar to that of HKUST-1 indicating that the CuBTC phase dominates over the ZnBTC phase.
In Figure 3 the CO_2 and N_2 adsorption isotherms of the samples are reported. The CO_2 isotherms are concave curves towards the pressure axis indicating a favorable interaction between the CO_2 and the frameworks. The MZn15GL, MZn50 and MZn50GL samples exhibits a significantly lower CO_2 sorption capacity compared to HKUST-1, MGL, and MZn15. The highest CO_2 uptake were detected for HKUST-1 and MGL, while it decreases with the increasing of Zn^{2+} content.
All the samples exhibit a quasi-linear N_2 adsorption isotherms in the pressure range explored, that is limited to 7 bar for this gas for operative reasons. In all cases, the adsorption of N_2 is very low. These preliminary results indicate that these materials are selective for CO_2 in CO_2/N_2 mixtures.

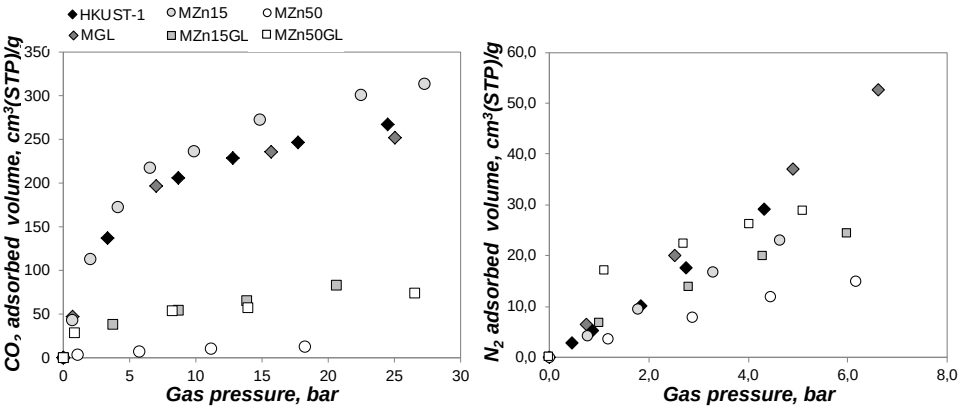

Figure 3. CO_2 and N_2 adsorption isotherms of the samples at 35 °C

Remarks and Conclusions

A novel class of hybrid Cu/Zn/GRM MOFs was produced starting from the benchmark HKUST-1 by varying the Zn^{2+} loading and incorporating conductive GL layers into the framework. It was shown that the incorporation of Zn^{2+} up to 5 wt.% does not affect drastically the morphology and the characteristic crystallinity of pristine HKUST-1 as well as a 5 wt.% incorporation of GL. The surface area does not significantly decrease when a 0.3 wt.% of Zn is enclosed, while it drops for a higher amount (5 wt.%). Interestingly, a further incorporation of GL enhances the MOF SA for both the Zn loading.

As concern the CO_2 capture, pristine HKUST-1, MGL and MZn15 exhibit the highest and comparable performances (around 125 mg_{CO2}/g at 1 bar). The CO_2 sorption performance dramatically drops when a 5 wt.% of Zn^{2+} is enclosed in the framework, that is in line with the SA decrease (from 2203 to 1509 m^2/g passing from MZn15 to MZn50). An intermediate behavior is exhibited when GL is also enclosed: irrespective of the highest SA, the CO_2 uptake of MZn15GL is lower. In the case of MZn50GL the slightly higher CO_2 detected with respect to MZn50 is ascribable to the higher SA. The unexpected behavior of MZn15GL could be due to a different polarity of the framework pores, driven by the GL presence.

Overall the modified HKUST-1 samples exhibited good CO_2 adsorption and very low N_2 adsorption capacity indicating a selectivity toward CO_2 over N_2 and thus their potentiality for application in CO_2 capture strategies.

Acknowledgments

The authors thank Mr. Fernando Stanzione for ICP-MS measurements and Mr. Luciano Cortese for SEM and XRD analyses. The financial support of Piano Annuale della Ricerca Mise-CNR under the project "Sistemi elettrochimici per l'accumulo di energia" was kindly acknowledged.

References

[1] Nanda, S., Reddy, S.N., Mitra, S.K., Kozinski, J.A. "The progressive routes for carbon capture and sequestration", *Energy Sci. Eng.* 4(2):99–122 (2016).

[2] D'Alessandro, D.M., Smit, B., Long, J.R. "Carbon dioxide capture: prospects for new materials", *Angew. Chem. Int.* 49:6058–6082 (2012).

[3] Smit, B. "Carbon Capture and Storage: introductory Lecture", *Faraday Discuss*.192:9-25 (2016).

[4] Sumida, K., Rogow, D.L., Mason, J.A., McDonald, T.M., Bloch, E.D., Herm, Z.R., Bae, T.-H., Long, J.R. "Carbon Dioxide Capture in Metal–Organic Frameworks", *Chem. Rev*. 112:724-781 (2012).

[5] Stock N., Biswas S. "Synthesis of Metal-Organic Frameworks (MOFs): Routes to Various MOF Topologies, Morphologies, and Composites", *Chem. Rev*. 112:933-969 (2012).

[6] Alfe, M., Gargiulo, V., Lisi, L., Di Capua, R. "Synthesis and characterization of conductive copper-based metal-organic framework/graphene-like composites", *Mater. Chem. Phys*. 147:744-750 (2014).

[7] Gul-E-Noor, F., Jee, B., Mendt, M., Himsl, D., Pöppl, A. "Formation of Mixed Metal $Cu_{3-x}Zn_x(btc)_2$ Frameworks with Different Zinc Contents: Incorporation of Zn^{2+} into the Metal–Organic Framework Structure as Studied by Solid-State NMR", *J. Phys. Chem. C* 116(39):20866-20873 (2012).

[8] Ferrari, M. C., Galizia, M., De Angelis, M. G., Sarti, G. C. "Gas and Vapor Transport in Mixed Matrix Membranes Based on Amorphous", *Ind. Eng. Chem. Res.* 49:11920-11935 (2010).

[9] Peng, D. Y., Robinson, D. B. "A New Two-Constant Equation of State", *Ind. Eng. Chem. Fundam.* 15:59-64 (1976).

[10] Biemmi, E., Christian, S., Stock, N., Bein, T., "High-throughput screening of synthesis parameters in the formation of the metal-organic frameworks MOF-5 and HKUST-1", *Micropor. Mesopor. Mat*. 117(1–2): 111–117 (2009).

[11] Chui, S.S.Y. Lo, S.M.F., Charmant, J.P.H., Orpen, A.G., Williams, I.D., "A Chemically Functionalizable Nanoporous Material $[Cu_3(TMA)_2(H_2O)_3]_n$" *Science*, 283:1148-1150 (1999).

Thermodynamic and kinetic study of CO_2 adsorption on a fine activated carbon in a sound assisted fluidized bed

F. Raganati, R. Chirone and P. Ammendola
federica.raganati@irc.cnr.it
Istituto di Ricerche sulla Combustione (IRC)-CNR, Piazzale Tecchio 80, 80125 Naples, Italy

Abstract
This work is focused on the investigation of the mechanism (isotherm), nature/strength (thermodynamics) and rate (kinetics) of CO_2 adsorption on a commercial activated carbon in a sound assisted fluidized bed. Langmuir and Freundlich equations were used to model the CO_2 adsorption isotherm in the low pressure region (i.e. typical of a combustion flue gas). Then, adsorption behaviour was elucidated by energy function such as standard Gibbs free energy, enthalpy and entropy. The isosteric heat of adsorption was also evaluated. Finally, this study also presented a kinetic analysis of CO_2 adsorption, from which CO_2 binding on activated carbon was deduced to follow pseudo-first order kinetic.

Introduction
Among all the available CO_2 capture technology, in the framework of CO_2 capture and storage (CCS) post-combustion approaches, adsorption is one of the most promising one, avoiding the weaknesses of aqueous amine systems and offering potential energy savings with lower capital and operating costs [1]. However, the success of this approach depends on the design of highly specific CO_2 adsorbent materials [2]. In this framework, fine particles have the greatest potential since they can be easily tailored and/or functionalized on the surface with different ligands to induce significant changes in their physical and chemical properties [2]. Besides, also common and commercially available adsorbent materials (such as activated carbons and zeolites) are generally in the form of fine powders. According to the literature, the activated carbons are among the most appropriate sorbents for CO_2 separation/capture [1]. With reference to the reactor configuration, Raganati et al. [3,4] demonstrated the viability of sound assisted fluidization technology in processing, handling and testing sorbents in the form of free-flowing fine powders. The same Authors [5–7] also showed that sound assisted fluidized beds may be feasible for temperature swing adsorption (TSA) processes by remarkably enhancing the CO_2 adsorption on fine sorbents due to the enhancement of the fluidization quality and gas–solid contact. However, before the design of an adsorption equipment, the investigation of both equilibrium and kinetics is necessary. Thermodynamic data only provide information about the final state of a system (i.e. the equilibrium adsorption capacity), whereas kinetics deals with how the system

changes in time, with particular attention to the rates of these changes. In this work, a commercially available fine activated carbon was tested as a low cost CO_2 adsorbent in a sound assisted fluidized bed apparatus in order to maximize its CO_2 adsorption capacity and kinetics. In particular, the previous research was furthered into the investigation of the mechanism (isotherm), nature/strength (thermodynamics) and rate (kinetics) of CO_2 adsorption on a commercial activated carbon in a sound assisted fluidized bed. Langmuir and Freundlich models were used to describe the CO_2 adsorption isotherm in the low pressure region typical of a combustion flue gas. Moreover, the most important thermodynamic properties. Then, the CO_2 adsorption kinetics was also evaluated.

Experimental

An activated carbon DARCO FGD (Norit) was used as adsorbent material. Detailed information on its chemico-physical and fluid-dynamic characterization are reported elsewhere [8,4]. Briefly, it is a submicronic powder (0.39 μm) [8,4], i.e. it belongs to the C group of Geldart's classification. It has a large BET surface area (1060 m^2 g^{-1}) and by a broad pore size distribution characterized by the presence of both mesopores and micropores. Its CO_2 equilibrium (i.e., saturation) adsorption capacity and dynamic column breakthrough measurements were performed in a laboratory scale sound assisted fluidized bed apparatus [8]. More detailed information about the system can be found elsewhere [8,4]. All the CO_2 adsorption tests were performed under sound-assisted fluidization conditions (140 dB–80 Hz, corresponding to the best fluidization quality of the activated carbon [8,4]). Different inlet CO_2 concentrations (1-15%vol. in N_2) and temperatures (18-130 °C) were tested.

Adsorption thermodynamics

The experimental adsorption isotherm data were modelled by fitting them to Langmuir and Freundlich isotherm models (Table 1). The validity of these models was evaluated by the coefficient of regression, R^2.

Table 1. Isotherm Equations

Langmuir	**Freundlich**
$q_e = \left(q_s K_L P_{CO_2}\right)/\left(1 + K_L P_{CO_2}\right)$	$q_e = k_F {P_{CO_2}}^{1/n}$
• q_s (mmol g^{-1}), maximum-monolayer adsorption capacity • K_L (atm^{-1}), Langmuir adsorption constant	• k_F (mmol g^{-1} atm^{-1}/n), Freundlich isotherm constant • n (-), heterogeneity factor
P_{CO2} (atm) equilibrium pressure of the gas adsorbed q_e (mmol g^{-1}), equilibrium adsorption capacity	

The Langmuir model [9] is the simplest theoretical one to describe monolayer adsorption onto the homogeneous surface. K_L is a measure of how strong an

adsorbate molecule is attracted onto a surface. The Freundlich model describes multilayer adsorption, i.e. the adsorption energy exponentially decreases as the number of available adsorption sites reduces and the strength of bonds is not homogeneous [10]. As k_F increases, the adsorption capacity of adsorbent for a given adsorbate will increase too. The n parameter indicates type of the adsorption process, whether the adsorption is a chemical process ($n < 1$) or a physical process ($n > 1$) [10]. 1/n (dimensionless; $0 < n < 10$) is the Freundlich intensity parameter, which indicates the magnitude of the adsorption driving force or surface heterogeneity [10]. Moreover, values of 1/n less than 1 represent a favorable adsorption [10].
In general, the negative/positive value of the enthalpy change (ΔH^0) determines whether a process is exothermic or endothermic, respectively. Generally, for absolute physical adsorption $|\Delta H^0| < 20$ kJ mol^{-1}, while for chemisorption $|\Delta H^0| = 80$ - 200 kJ mol^{-1} [11]. With reference to Gibbs free energy change ΔG^0, a process is defined as a spontaneous process if $\Delta G^0 < 0$, otherwise ($\Delta G^0 > 0$), it will be non-feasible and non-spontaneous. The value of the entropy change (ΔS^0) indicates whether the organization of the adsorbate at the solid/gaseous interface during the adsorption process becomes less random ($\Delta S^0 < 0$) or more random ($\Delta S^0 > 0$). As widely reported in literature [11], the thermodynamic laws, combined with the experimental data obtained from the Langmuir isotherms, can be used to determine ΔG^0. ΔH^0 and ΔS^0 can be determined from the slope and intercept of the plot of ln K_L against 1/T according to the well-known van't Hoff equation [1]. Another important thermodynamic parameter is the isosteric heat of adsorption (Q_{st}) defined as the heat of adsorption determined at constant amount of adsorbate adsorbed and it represents the strength of adsorbate–adsorbent interaction [12]. Q_{st} value can be determined from the slopes of the straight lines after plotting ln P_{CO2} against 1/T at at a given q_e, according to the well-known Clausius–Clapeyron equation [12].

Adsorption kinetics

Pseudo-first pseudo-first order model is able to represent the reversible interaction between adsorbent and adsorbate, which is more suitable to predict the CO_2 adsorption behavior on physical adsorbents, such as activated carbons [13]. Pseudo-first order kinetics model assumes that the rate of adsorption is proportional to the number of available free active sites on the adsorbent surface. This pseudo-first-order rate equation is:

$$q_t = q_e\left[1 - exp\left(-k_{ft}\right)\right] \quad (1)$$

where q_t is the amount of CO_2 adsorbed per mass of sorbent at any time, and k_f is the rate constant of first-order sorption. The validity of this kinetic model was evaluated by R^2 and Δq (%). Also the activation Energy (E_a) was evaluated by applying the well-known Arrhenius equation, once the kinetic constant is known.

Results - Adsorption thermodynamics

The adsorption isotherms obtained at different temperatures are reported in Fig. 1. Obviously, the adsorption capacity increased with increasing P_{CO2}, in agreement with

P_{CO2} being the thermodynamic driving force of the adsorption process. On the contrary, as expected, an increase in adsorption temperature led to a reduction in the amount of adsorbed CO_2, in agreement with the exothermicity of adsorption process. The experimental data were fitted by both Langmuir (Fig. 1a) and Freundlich (Fig. 1b) models. Fig. 1 shows that both Langmuir and Freundlich models predicted well the results, showing good agreement with the experimental adsorption isotherms. However, R^2 is larger for the Freundlich (0.999) model than it is for the Langmuir model (0.989), thus indicating a heterogeneous surface binding, i.e. the activated carbon surface exhibits a non-uniform distribution of adsorption energy [10]. With reference to Langmuir fitting, q_s (0.51-0.27 mmol g^{-1}) and K_L (30.06 – 3.76 atm^{-1}) values decreased with the temperature rising from 18 to 130°C, which confirms that the CO_2 adsorption on the activated carbon is an exothermic process. With reference to the Freundlich model, n varied from 2.52 to 1.16 passing from 18to 130°C, i.e. it is always larger than 1, thus confirming that CO_2 adsorption on the activated carbon is a physisorption. Finally, besides n, also k_F (0.93-0.51 mmol g^{-1} $atm^{-1/n}$) decreased with increase of temperature, thus confirming that adsorption is favorable at low temperatures [11].

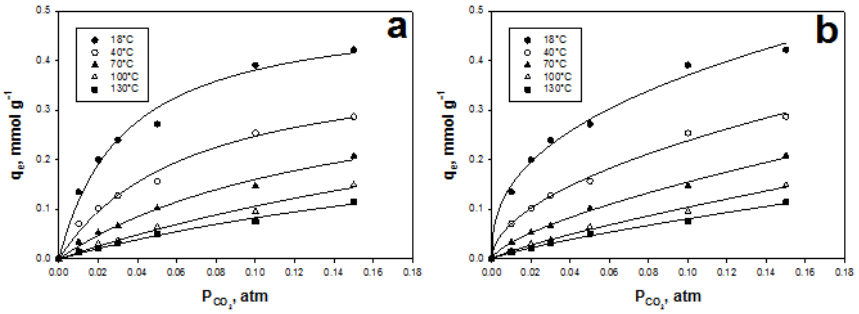

Figure 1. Adsorption isotherms of CO2 on the activated carbon at different temperatures fitted by (a) Langmuir and (b) Freundlich models.

ΔG^0 varied from -3.57 to -1.93 kJ mol^{-1} passing from 18 to 130°C. This means that the CO_2 adsorption process on the activated carbon occurs favorably and spontaneously and that the adsorption feasibility decreases at higher temperatures [11]. The value obtained for ΔH^0 was -7.98 kJ mol^{-1}, thus confirming that the adsorption process is exothermic in nature and that it is physical in nature [11]. The value obtained for ΔS^0 was -0.02 kJ mol^{-1}, thus suggesting that the disorder and randomness of the system decrease during the adsorption process [11]. The values of Q_{st} (< 18 kJ mol^{-1}) of adsorption for the activated carbon were smaller than 80 kJ/mol, which also indicates that CO_2 adsorption is physical in nature [11]. Q_{st} decreased from 16.60 kJ/mol to 5.33 kJ/mol when adsorption capacity of CO2 increased from 0.05 mmol g^{-1} to 0.5 mmol g^{-1}. This may be due to heterogeneity of adsorption sites and also to variation in adsorbate-adsorbent interactions followed by adsorbate-adsorbate interactions [12].

Results - Adsorption kinetics

The experimental data were fitted to the pseudo-first order model. Table 2 shows the obtained values of the kinetic constants along with the associated errors. Pseudo-first order kinetic model provided a good correlation for the adsorption of CO_2 on the activated carbon at all the investigated adsorption temperatures, as confirmed by R^2 being close to 1. These results are in agreement with earlier reports available in literature, suggesting that the pseudo-first order kinetic model is applicable at low CO_2 partial pressures, as typical of post-combustion operating conditions [13]. k_f increases with the temperature increasing in agreement with the fact that high temperatures are generally beneficial to the reaction rate. The value obtained for the activation energy (7.13 kJ mol^{-1}) is positive and relatively small, which means that an increase of temperature leads to an increase of the reaction rate and that adsorption is physical in nature.

Table 2. Values of the pseudo-first order kinetic model parameters and fitting comparison.

T °C	q_e mmol g^{-1}	k_f min^{-1}	R^2 -
18	0.387	0.110	0.999
40	0.253	0.189	0.999
70	0.146	0.334	0.998
100	0.096	0.552	0.997
130	0.074	0.700	0.966

Conclusion

With reference to the CO_2 adsorption thermodynamics, the obtained results revealed that Freundlich model was more suitable to describe CO_2 adsorption than Langmuir one, thus indicating the heterogeneity of CO_2 adsorption on the activated carbon surface. The values of 1/n were below 1 at all the experimental temperatures indicating that the activated carbon have high adsorption intensity for CO_2. The thermodynamic analysis showed that CO_2 adsorption on the activated carbon is spontaneous ($\Delta G^0 < 0$), exothermic ($\Delta H^0 < 0$) and physical in nature (magnitude of $\Delta H^0 < 20$ kJ mol-1,). The isosteric heat of adsorption decreased with increase in surface loading indicating again that the activated carbon is characterized by energetically heterogeneous surface and there may be some lateral interactions between the adsorbed CO_2 molecules. Finally, the adsorption kinetics of CO_2 on the activated carbon was successfully described using a pseudo-first order kinetic model, which accurately fit the experimental data at all the investigated adsorption temperatures. Furthermore, the calculated kinetic coefficients were used to evaluate the activation energy of the CO_2 adsorption process by using a linearized Arrhenius type equation, which further confirmed the physical nature of the process.

References

[1] Plaza, M. G., García, S., Rubiera, F., Pis, J. J., and Pevida, C., "Post-combustion CO2 capture with a commercial activated carbon: Comparison of different regeneration strategies", *Chem. Eng. J.* 163: 41–47 (2010).

[2] D'Alessandro, D. M., Smit, B., and Long, J. R., "Carbon Dioxide Capture: Prospects for New Materials", *Angew. Chemie Int. Ed.* 49: 6058–6082 (2010).

[3] Raganati, F., Ammendola, P., and Chirone, R., "CO2 capture performances of fine solid sorbents in a sound-assisted fluidized bed", *Powder Technol.* 268: 347–356 (2014).

[4] Raganati, F., Ammendola, P., and Chirone, R., "Role of Acoustic Fields in Promoting the Gas-Solid Contact in a Fluidized Bed of Fine Particles", *KONA Powder Part. J.* 32: 23–40 (2015).

[5] Raganati, F., Ammendola, P., and Chirone, R., "Effect of acoustic field on CO2 desorption in a fluidized bed of fine activated carbon", *Particuology* 23: 8–15 (2015).

[6] Ammendola, P., Raganati, F., and Chirone, R., "Effect of operating conditions on the CO2 recovery from a fine activated carbon by means of TSA in a fluidized bed assisted by acoustic fields", *Fuel Process. Technol.* 134: 494–501 (2015).

[7] Raganati, F., Ammendola, P., and Chirone, R., "On improving the CO2 recovery efficiency of a conventional TSA process in a sound assisted fluidized bed by separating heating and purging", *Sep. Purif. Technol.* 167: 24–31 (2016).

[8] Raganati, F., Ammendola, P., and Chirone, R., "CO2 adsorption on fine activated carbon in a sound assisted fluidized bed: Effect of sound intensity and frequency, CO2 partial pressure and fluidization velocity", *Appl. Energy* 113: 1269–1282 (2014).

[9] Langmuir, I., "The constitution and fundamental properties of solids and liquids. Part I. Solids", *J. Am. Chem. Soc.* 38: 2221–2295 (1916).

[10] Freundlich, M. F., "Over the adsorption in solution", *J. Phys. Chem.* 57: 355–471 (1906).

[11] Adelodun, A. A., Ngila, J. C., Kim, D.-G., and Jo, Y.-M., "Isotherm, Thermodynamic and Kinetic Studies of Selective CO2 Adsorption on Chemically Modified Carbon Surfaces", *Aerosol Air Qual. Res.* 16: 3312–3329 (2016).

[12] Sircar, S., Mohr, R., Ristic, C., and Rao, M. B., "Isosteric Heat of Adsorption: Theory and Experiment", *J. Phys. Chem. B* 103: 6539–6546 (1999).

[13] Serna-Guerrero, R., and Sayari, A., "Modeling adsorption of CO2 on amine-functionalized mesoporous silica. 2: Kinetics and breakthrough curves", *Chem. Eng. J.* 161: 182–190 (2010).

PRELIMINARY CHARACTERIZATION OF THE EMISSIONS FROM SCENTED TEA-LIGHT CANDLES

E. Oddo, M. Derudi
marco.derudi@polimi.it
Politecnico di Milano, Dip. di Chimica, Materiali e Ingegneria Chimica "G. Natta", Milano, Italy

Abstract
In recent years, scented candles have grown in popularity as indoor fragrance products, thus increasing the safety concern related to the air pollutants in candles emissions. Among the different types of candles, scented tea-lights are probably the most widespread, but few studies are present in literature regarding their emissions. Therefore, this preliminary study aims to characterize the emissions of several volatile and semi-volatile compounds from burning of scented tea-light candles. A laboratory-scale test chamber has been used for this purpose, as it can provide reproducible and realistic burning conditions. Emissions in terms of CO, SO_2, NOx as well as short chain aldehydes, volatile organic compounds and particulate matter have been evaluated for all candles. In addition, raw materials in terms of both waxes and wicks have been analyzed to evaluate the content of heavy metals and sulfur. As a result, all tested samples showed low emissions of CO, SO_2 and NOx. All candles emitted formaldehyde and acetaldehyde, the emission of the latter being very low. PM emissions were low and mainly dominated by ultrafine particles in the range of 0.3-0.5 μm. Analysis of the waxes and wicks revealed no traces of heavy metals and low content of sulfur.

Introduction
Both indoor and outdoor sources can affect the concentration and composition of pollutants in indoor air. There is usually more information available on emissions characteristics, such as emission factors or emission rates, of outdoor pollutants sources than of indoor ones [1]. However, the assessment and quantification of emissions from indoor sources is very important for assessing the possible human exposure to pollutants and relate the measured emission values to the regulatory guidelines. Combustion processes are among the main indoor pollutant sources, releasing gaseous pollutants and fine particles in indoor environments. In recent years there has been an increase in the use of scented candles and, consequently, of the concern about possible human health effects due to the exposure to their emissions. In fact, burning of candles can release a wide variety of chemicals, including short chain aldehyde (SCA), polycyclic aromatic hydrocarbons (PAHs) and volatile organic compounds (VOCs) [2,3]. Candles can also be source of

ultrafine particles [4]. Tea-light candles are among the most widespread types of candles, due to their low price and high availability; however, very few studies regarding tea-lights are available in the literature and are focused on volatile organic compounds [5] and odorous volatile organic compounds [6]. Therefore, this preliminary work focused on the characterization of the emissions from scented tea-lights burning in a lab-scale test chamber. The emissions of SCA, VOCs and PM of all scented candles were measured to evaluate the emission factors, which have also been compared to the few data available in the literature. Measurements have been carried out for an unscented sample as well, to estimate the possible influence of fragrances and dyes to the emissions. In addition, the raw materials of all candles were analyzed to evaluate the concentration of heavy metals and Sulfur as well as the thermal stability. This may provide further insights regarding the relation between wax composition and pollutants emission.

Experimental setup

The selected tea-light candles are mainly composed of paraffin, molded in a cylindrical shape and surrounded by an aluminum shell. Candles have an average weight of 12 g. Selection criteria were based on providing variety of both fragrances and countries. All candles tested in the study are shown in Table 1.

Table 1. Main features of the candles investigated in the present study.

Candle	Fragrance	Color	Country
A	-	White	Poland
B	Vanilla	Brown	China
C	Jazmin	Green	Spain
D	Fruit Cake	Yellow	Poland
E	Winter Warm	Crimson	Belgium

Experimental tests were conducted in the test chamber depicted in Figure 1. The chamber is conceived to assure reproducible and realistic burning conditions and to sample the exhausts easily [7,8]. It exhibits a total volume of about 175 L. The chamber is equipped with an air sparger at the bottom to supply the air in laminar conditions; for all experiments pre-cleaned air, passed through a charcoal trap, has been used. The air flow rate was adjusted to reach realistic burning conditions. For all experiments three candles were burnt simultaneously; each candle was weighted before and after the test and the corresponding burning time was recorded.

Materials and methods

Sampling of the exhausts was carried out according, when possible, to the European Standard EN 16738:2015 [9]. Before entering the chamber, candles are weighted and burnt for 20 minutes, to ensure stable combustion. Main combustion products (CO_2, CO, NOx e SO_2) were measured with an on-line gas analyzer

(Horiba PG-250) and CO concentration was used as a marker of steady-state conditions during the experiments. In steady-state, exhausts were collected and analyzed for evaluation of SCA, VOCs and PM.

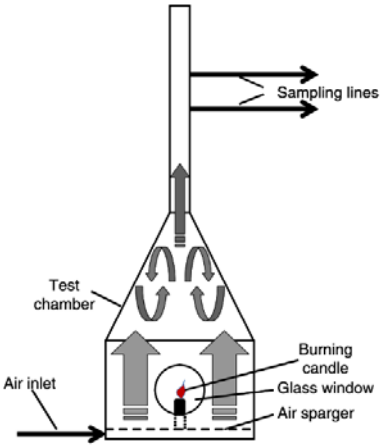

Figure 1. Schematic of the combustion chamber with arrows roughly representing air patterns [8].

Aldehydes were sampled according to the DNPH (2,4-dinitrophenylhydrazine) method: sampling of 60 min through the DNPH cartridge with a sampling flow of about 1.5 L min^{-1}; then, the cartridge was eluted with acetonitrile and analyzed through HPLC (Hypersil Gold C18 column, 5 µm, 250 mm, detector UV@360 nm). VOCs were sampled for 240 min at 50 mL min^{-1} using a charcoal cartridge (Carbotrap 349); the content was desorbed thermally and analyzed through GC/MS (Restek column Rxi-5Sil-MS, 5 µm). PM was measured using an OPC (Lighthouse model 3016-IAQ), to evaluate the time-averaged particles concentration (sampling of 30 s at 2.8 L min^{-1}) according to six dimensional classes (0.3, 0.5, 1, 2.5, 5 and 10 µm). In addition, characterization of the raw materials was carried out through a TGA/DTA (heating rate of 1 °C min^{-1} until 90 °C and 5 °C min^{-1} until 500 °C), using Nitrogen as carrier gas (flowrate of 100 NmL min^{-1}). Waxes and wicks were also mineralized to be analyzed through ICP/OES to evaluate their content of sulfur and heavy metals (especially Pb and Ni).

Results and discussion

TG analysis revealed similar behaviors for all tested candles. All candles are made up of low-melting wax, with an average melting point of 45 °C, and evidenced a good thermal stability, as shown by the TG plot of sample C in Figure 2. Elemental analysis revealed no significant amount of Pb or Ni; traces of Sulfur were found in the waxes, with values in the range of 20-50 µg g^{-1}.

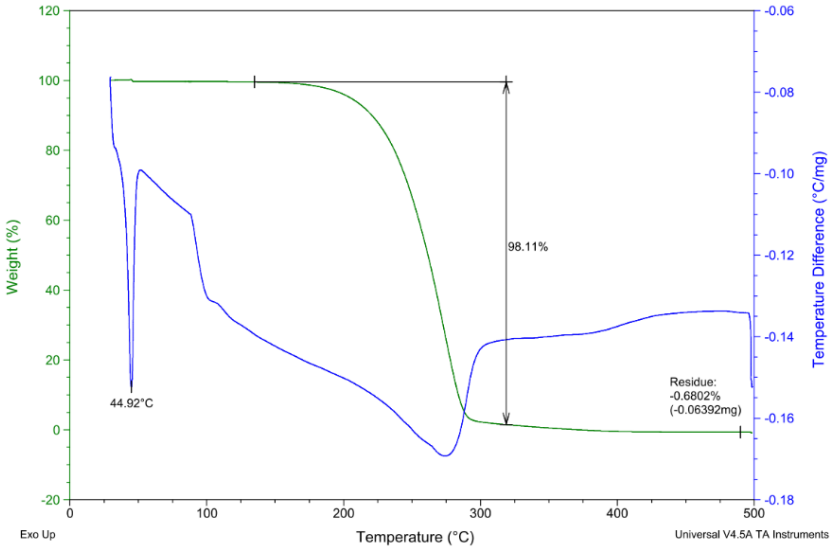

Figure 2. Results of TG analysis of sample C.

Candles were weighted before and after each test and the resulting average burning rate was compared to the burning rate of the same candle in air. Average burning rates and normalized mass loss differences with respect to the reference values are reported in Table 2. All mass loss values fall inside the ±15% region, as prescribed by the European Standard EN 16738:2015 [9].

Table 2. Average burning rate (g h^{-1}) inside the chamber and normalized mass loss difference (% by weight) between burning rate inside and outside the chamber.

Candle	Avg. Burning Rate	Norm. Mass Loss Diff.
A	2.43	+ 0.4
B	1.91	- 4.3
C	2.28	+ 2.2
D	2.92	- 1.8
E	3.10	+ 3.8

Gaseous measurements showed presence of CO, NOx and SO_2 in the exhausts. Concentration of CO ranges from 9 to 14 ppm and is similar for all samples (air exchange rate of 2 h^{-1}). NOx emissions are even lower, ranging from 2 to 5 ppm, and are closely linked to the burning rate. SO_2 emissions always fall in the range 2-3.5 ppm, independently of the burning rate. Sampling and analysis of SCA showed that formaldehyde and acetaldehyde are present in the exhausts for all samples, as shown in Table 3. Unscented candle A evidenced factors similar to the other specimens, contrarily to what was found for other types of candles [7].

Table 3. Emission factors of light aldehydes (μg g^{-1}) for all tested samples.

Candle	Formaldehyde	Acetaldehyde
A	2.56	0.41
B	3.84	0.68
C	2.97	0.86
D	6.09	1.34
E	4.33	0.62

Conversely, VOCs concentrations were always close to or below the quantification limit. Measurements with the OPC were used to compute PM emission factors, which are proposed in Table 4.

Table 4. Emission factors of PM (μg g^{-1}) for all investigated samples, according to six dimensional classes (μm).

Candle	0.3-0.5	0.5-1	1-2.5	2.5-5	5-10	> 10
A	0.42	0.16	0.11	0.12	0.01	<0.01
B	0.51	0.18	0.18	0.23	<0.01	<0.01
C	0.03	0.01	0.03	0.06	<0.01	<0.01
D	0.34	0.15	0.11	0.10	<0.01	0.01
E	0.33	0.13	0.10	0.12	<0.01	0.01

PM factors are at least one order of magnitude lower than those of formaldehyde. Again, emissions from candle A are comparable to the ones from scented samples. Ultrafine particles (0.3-0.5 μm) usually represent half of the distribution, while factors in the ranges 0.5-1, 1-2.5 and 2.5-5 μm are comparable. As an example, Figure 4 proposes the relative abundance of the different classes for candle A.

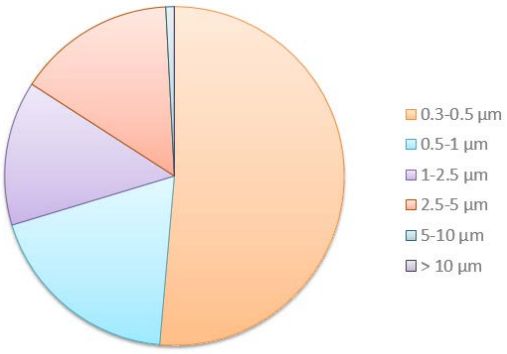

Figure 4. Graphical representation of the estimated abundance of size fractions in PM emissions for candle A.

Table 5. Comparison among emission factors (in μg g^{-1}) from different studies.

Pollutant	This study (max. value)	Uhde and Schultz [5]	Derudi et al. [7][1],[8][2]
Formaldehyde	6.09	6.5	2.91[1]
Acetaldehyde	0.86	3.0	1.12[1]
PM2.5	0.87	-	3.29[2]

The estimated emission factors have been compared to the few information available in literature regarding tea-lights [5] and to some previous works [7,8], as summarized in Table 5. Emission factors for aldehydes are comparable to the ones obtained by Uhde and Schultz [5] for a tea-light paraffin candle and to the one by Derudi et al. [7], while acetaldehyde and PM are lower of one order of magnitude.

Conclusions

Raw materials analysis showed rather homogeneous, low-melting materials, with traces of Sulfur and free of heavy metals. Measurements in the test chamber revealed that scented tea-lights can be source of several air pollutants, mainly formaldehyde and PM, especially ultrafine particles. A comparison with data available in literature showed that emissions from different type of candles can be rather different. This clearly evidences the need for simple and cheap methodologies to measure emissions from scented tea-light candles to foresee the possible exposure of people to harmful compounds in indoor environments.

References

[1] Cattaneo A., Fermo P., Urso P., Perrone M.G., Piazzalunga A., Tarlassi J., Carrer P. and Cavallo D.M., *Environ. Pollut.* 218: 16-25 (2016)
[2] Lee S.C and Wang B., *Atmos. Environ.* 40: 2128-2138 (2006)
[3] Orecchio S., "Polycyclic aromatic hydrocarbons (PAHs) in indoor emission from decorative candles", *Atmos. Environ.* 45: 1888-1895 (2011)
[4] Pagels J., Wierzbicka A., Fors E., Isaxon C., Dahl A., Gudmundsson A., Swietlicki E. and Bohgard M., *J. Aerosol Sci.* 40: 193-208 (2009)
[5] Uhde E. and Schulz N., "Impact of room fragrance products on indoor air quality", *Atmos. Environ.* 106: 492-502 (2015)
[6] Bartsch J., Uhde E. and Salthammer T., *Anal. Chim. Acta* 904: 98-106 (2016)
[7] Derudi M., Gelosa S., Sliepcevich A., Cattaneo A., Rota R., Cavallo D. and Nano G., *Atmos. Environ.* 55: 257-262 (2012)
[8] Derudi M., Gelosa S., Sliepcevich A., Cattaneo A., Cavallo D., Rota R. and Nano G., *Environ. Sci. Pollut. Res.* 21: 4320-4330 (2014)
[9] EN 16738:2015, Emission safety of combustible air fresheners - Test methods (2015)

COMPARISON BEHAVIOUR OF COMMERCIAL ACTIVATED CARBON AND COAL-DERIVERED CHAR IN HOT SYNGAS CLEANING

F. PARRILLO[1], G. RUOPPOLO[2], U. ARENA[1]

[1] *Department of Environmental, Biological and Pharmaceutical Sciences and Technologies, University of Campania "Luigi Vanvitelli", via A. Vivaldi 43, 81100 Caserta, Italy.*

[2] *Combustion Research Institute, National Research Council-CNR, P.le Tecchio 80, 80125 Naples, Italy.*

Abstract

This study aims at investigating and comparing the performances provided by a coal-derived char and a commercial activated carbon as catalysts for tar conversion. The char has been specifically produced in our facilities by steam activation of a Colombian coal's granulates, carried out at 900°C for 100 minutes. The activated carbon, named Norit RB4W, has been selected among those available on the market for utilization at temperature higher than 700°C.

Naphthalene has been used as tar model compound. The influence of temperature (in the range 750-900°C) on the initial naphthalene conversion and the evolution of the naphthalene conversion with time at 750°C have been investigated. A correlation between the changes in the internal structure and the observed activity has been observed. In particular, for both the adsorbents the reduction of activity is associated to a decrease of the total specific pore surface.

Introduction

The gasification of a solid fuel (biomass, waste, coal) produces a syngas consisting of some major compounds (CO, CO_2, H_2, H_2O, CH_4, and N_2). The produced fuel gas can be burned to produce electricity or further processed to manufacture chemicals and liquid or gaseous fuels. The obtained syngas generally contains a not negligible amount of tars, a mixture of heavy hydrocarbons condensing at temperatures below 400°C, which can strongly limit the number of possible final applications [1]. One of the most promising options for removal of tars is their adsorption on the surface of activated carbons or chars [2-8]. These adsorbents appear attractive for their low cost and the extraordinary physical adsorption capability, which is sometime coupled with a catalytic action for the tar cracking reactions.

The activated chars generally show high resistance to poisoning and can be produced within the gasification process [3]. On the other hand, there is a lack of knowledge about the parameters involved in their catalytic activity. Some authors report that tar conversion depends on the amount and the nature of the char surface available for tar cracking reaction [9]. Other researchers attribute the high activity of char to the presence of oxygenated surface groups and alkali and alkaline earth metallic (AAEM) species distributed over its surface [8-10].

The physico-chemical properties of activated chars depend on different parameters, such as the composition of the parent material, activating agent and reaction temperature [11]. Steam activation produces chars with higher mesopore volume while CO_2 activation produces higher micropore volume [10-12]. It has been also reported that their activity changes during the tar conversion [5, 9] due to the evolution of the pore size distribution and the concentration of active groups on the surface, as consequence of a balance between the rate of carbon conversion and that of soot deposition.
This study investigated the decomposition of naphthalene (model tar compound) over a char and a commercial activated carbon, with a special attention to the evolution of the pore size distribution and the surface during the conversion of naphthalene.

Materials and characterization

A commercial activate carbon (Norit RB4W) and a homemade char (Char 100) have been used. The char has been prepared by devolatising a Colombian coal at 900°C in a bubbling fluidized bed, and a successive steam activation at 900°C for 100 min. The adsorbents have the characteristics reported in Table 1.

Table 1. Proximate and ultimate analyses of Norit RB4W and Char 100

	Norit RB4W	Char 100
Proximate Analysis (d.b.)		
Volatile matter	6.34	4.33
Fixed Carbon	84.65	89.74
Ash	9.01	5.93
Ultimate Analysis (as received)		
Carbon	82.42	91.22
Hydrogen	0.2	0.48
Nitrogen	0.55	1.89
Oxygen	7.82	0.48
Ash	9.01	5.93

Experimental apparatus and test procedure

Naphthalene conversion tests have been carried out in the experimental apparatus reported in Figure 2, having four different sections: feeding system, reactor, sampling/cleaning device and gas analyser. Further details can be found elsewhere [13]

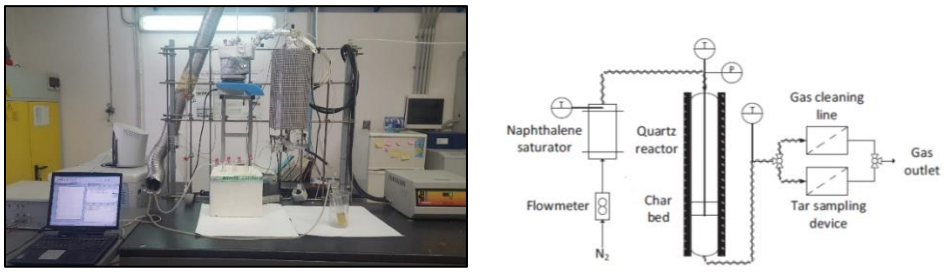

Figure 2. Photo and scheme of the experimental apparatus used for the naphthalene conversion tests

The gas at the exit of the cleaning section is analysed by means of a micro-GC with a TCD for the online determination of short chain hydrocarbons (from acetylene to benzene) and molecular hydrogen. The off-line determination of the naphthalene concentration in the isopropanol sample has been performed by using a gas chromatography coupled with mass analysis.

Two kinds of tests have been carried out. In the first set of experiences, the initial conversion of naphthalene has been measured. A known amount of solid naphthalene has been deposited within two glass impingers (about 20 g each) immersed in oil at 65°C. The reactor, with the sample inside, has been heated at 750°C, 800°C or 900°C in pure nitrogen stream. When system reaches the steady state, the nitrogen flow has been driven through the naphthalene saturator to the reactor (naphthalene concentration 22 mg/NL). After five minutes of stabilization, naphthalene has been sampled for two minutes. Then, the reactor has been purged and cooled down with pure nitrogen. A nitrogen flow has been used to obtain a residence time of 0.15 s, using a bed of 3 cm height: the related flow rates were 0.49 NL/min at 750°C, 0.47 NL/min at 800°C, and 0.43 NL/min at 900°C.

In the second kind of experiences, the evolution with time of the naphthalene conversion and the internal structure of the char samples have been studied. To achieve this, the same conditions as first set of tests have been used, but the test duration has been varied between 5 and 310 minutes. Various gas samples have been taken during the tests to measure the naphthalene concentration in the exit gas at different times.

Results and discussion

Figure 3 presents the naphthalene conversion as measured after five minutes of test (i.e. initial conversion), the two different materials at different temperature for a gas residence time of 0.15 s.

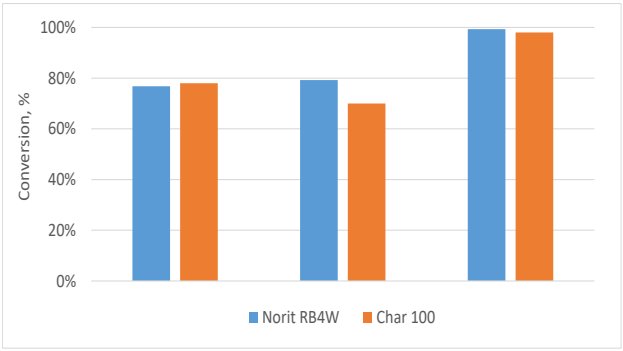

Figure 3. Naphthalene conversion obtained with Norit and Char-100 at 750°C, 800 °C and 900 °C for a gas residence time of 0.15 s.

The results show that in the range 750°C-800°C the temperature does not have a significant influence on the naphthalene conversion. A further increase of temperature improves the naphthalene conversion up to the 100%, in agreement with results obtained in a previous study [13]. The initial activity of the Char 100 is slight lower than that obtained for the commercial activated carbon whatever the reaction temperature adopted.
Figure 4 reports the evolution of the naphthalene conversion for Norit RB4W and Char 100 obtained at 750 °C for a gas residence time of 0.15 s.

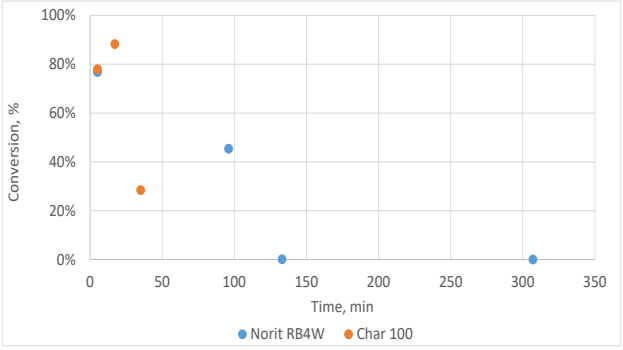

Figure 4. Evolution of the naphthalene conversion for Norit and Char 100 at 750 °C and gas residence time of 0.15 s.

The conversion efficiency of the commercial activated carbon is higher than that of char whatever is the adopted length of the reaction; moreover a longer deactivation time is observed for the commercial sample. According to a high naphthalene conversion, a higher amount of hydrogen (not here reported for brevity) is produced using the Norit RB4W.

Table 2. Naphthalene conversion obtained on Norit and Char-100 at 750°C, 800 °C and 900 °C for a gas residence time of 0.15 s.

Sample	Time, min	Specific Surface Area, m^2/g	Micropore Area, m^2/g	Mesopore Area, m^2/g
Char 100	0	388	329	59
	5	357	284	73
	231	16	2.6	13.4
Norit RB4W	0	958	866	92
	5	993	586	407
	307	74.8	33.6	41.2

The porosimetric analysis of the samples (fresh, after five minutes and at the end of the test) are reported in Table 2. It is possible to observe that the amount of mesopores initially present in the Norit RB4W is enhanced in the first five minute. During the test, a progressive reduction of the specific surface area occurs up to the complete deactivation of the sample. This can be explained with the mechanism of "soot deposition" from tar cracking. Further studies are required to assess the role of the presence of oxygenated surface groups and alkali and alkaline earth metallic (AAEM) species since the deactivation occurs for different value of the final surface area for the two samples.

Conclusions

The decomposition of naphthalene (model tar compound) under the same experimental conditions over a char produced in laboratory (char 100) from coal and a commercial activated carbon (Norit RB4W) has been investigated. The adsorbents have been characterized by ultimate, proximate and porosimetric analysis.

The increasing of temperature influences the activity especially for temperature higher than 800°C. The Norit RB4W shows better performance than Char 100 in terms of both higher initial conversion and slower deactivation. The activity decrease for both samples is associated to the reduction of the amount of mesopore even if further studies are required to elucidate the role of oxygenated surface groups and alkali and alkaline earth metallic (AAEM) species.

References

[1] Li, C., Suzuki, K., "Tar property, analysis, reforming mechanism and model for biomass gasification, An overview", Reew. Sust. Ener. Rev. 13: 594–604 (2009).

[2] Abu el-Rub Z., Bramer E.A., Brem G., "Experimental comparison of biomass chars with other catalysts for tar reduction", Fuel 87: 2243-2252 (2008).

[3] Hosokai S., Norinaga K., Kimura T., Nakano M., Li C.Z., Hayashi J.I., "Reforming of volatiles from the biomass pyrolysis over charcoal in a sequence of coke deposition and steam gasification of coke", Energ. Fuel. 25:5387-5393 (2011).
[4] Fuentes-Cano D., Gómez-Barea A., Nilsson S., Ollero P., "Decomposition kinetics of model tar compounds over chars with different internal structure to model hot tar removal in biomass gasification", Chem. Eng. J. 228:223-1233 (2013).
[5] Di Gregorio F., Parrillo F., Cammarota F., Salzano E. and Arena U., "Removal of naphthalene by activated carbons from hot gas", Chem. Eng. J. 291:244-253 (2016).
[6] Nestler F., Burhenne L., Amtenbrink M.J., Aicher T., "Catalytic decomposition of biomass tars: The impact of wood char surface characteristics on the catalytic performance for naphthalene removal", Fuel Process. Technol. 145:31-41 (2016).
[7] Morgalla M., Lin L., Strand M., "Decomposition of benzene using char aerosol particles dispersed in a high-temperature filter", Energ. 118:1345-1352 (2017).
[8] Feng D., Zhao Y., Zhang Y., Sun S., Meng S., Guo Y., Huang Y., "Effects of K and Ca on reforming of model tar compounds with pyrolysis biochars under H_2O or CO_2", Chem. Eng. J. 306:422-432 (2016).
[9] Moliner R., Suelves I., Lazaro M., Moreno O., "Thermocatalytic decomposition of methane over activated carbons: influence of textural properties and surface chemistry", Int. J. Hydrogen. Energ. 30: 293-300 (2005).
[10] Wang Y., Chen X., Yang S., He X., Chen Z., Zhang S., "Effect of steam concentration on char reactivity and structure in the presence/absence of oxygen using Shengli brown coal", Fuel Process. Technol. 135:174-179 (2015).
[11] Guizani C., Jeguirim M., Gadiou R., Escudero Sanz F.J., Salvador S., "Biomass char gasification by H_2O, CO_2 and their mixture: Evolution of chemical, textural and structural properties of the chars", Energ. 112:133- 145 (2016).
[12] Rodríguez-Reinoso F., Molina-Sabio M., González M.T. "The use of steam and carbon dioxide as activating agents in the preparation of activated carbons", Carbon 33:15-23 (1995).
[13] Cano D.F., Parrillo F., Ruoppolo G., Gomez Barea A., Arena U., "The influence of the char internal structure and composition during heterogeneous naphthalene conversion", Fuel Process. Technol. 172: 125-132 (2018).

Insights into the mechanism of H_2S reactive adsorption over ZnO–CuO dispersed onto activated carbon

G. de Falco[*/], F. Montagnaro[**], M. Balsamo[***], A. Erto[***], F.A. Deorsola[****], L. Lisi[*], S. Cimino[*]**
stefano.cimino@cnr.it
*Istituto di Ricerche sulla Combustione, CNR, Napoli, Italy
**Dipartimento di Scienze Chimiche, Università degli Studi di Napoli Federico II, Italy
*** Dipartimento di Ingegneria Chimica, dei Materiali e della Produzione Industriale, Università degli Studi di Napoli Federico II, Italy
**** Dipartimento di Scienza Applicata e Tecnologia, Politecnico di Torino, Italy

Abstract
The kinetics of products formation during adsorption at low temperature of gaseous H_2S onto zinc and/or copper oxides supported on activated carbon is dealt in this work. Sorbents with a fixed total metal content and variable Zn:Cu ratios were prepared by impregnation of a commercial activated carbon. H_2S (100 and 3000 ppmv in N_2) removal tests were run under dynamic conditions at 30 °C. Raw and spent sorbents were characterized via N_2 porosimetry at –196 °C to determine BET surface area and pore size distribution. XPS and TPD tests performed on partially converted and spent sorbents allowed the speciation of adsorbed sulphur species.

Introduction

Hydrogen sulphide is a noxious compound occurring in different gaseous fuel streams such as natural gas and biogas [1]. The removal of H_2S from gaseous phase via adsorption offers numerous advantages related to the operating flexibility of this purification technology generally coupled with low costs. Nowadays, research efforts are devoted to develop sorbents based on metal oxides, hydroxides and carbonates supported onto high surface area substrates (e.g. mesoporous alumina, activated carbons) capable to efficiently capture H_2S at room temperature [2]. Activated carbons (AC) are widely applied as support for the removal of H_2S due to their favourable properties including high surface area and the presence of numerous functional groups that can remarkably influence the capture process [3]. The selection of optimal sorbents for H_2S capture requires a proper identification of the products formed during reactive adsorption. Most literature studies highlight that the reaction between metal oxides and H_2S leads to the formation of metal sulphides [4]. Nonetheless, different compounds can be formed onto supported metal oxides as function of both substrate microstructural properties/surface chemistry and adopted operating conditions of the adsorption process. For example, our research group recently observed the formation of $CuSO_4$ and $ZnSO_4$ after saturation with H_2S of ZnO and CuO supported on a commercial activated carbon [5]. This work extends

the previous investigation focusing on the synergistic effect of the mixed metals in the active phase and on the identification of products formed during various stages of the H_2S adsorption process.

Materials and methods

Hybrid adsorbents based on ZnO–CuO highly dispersed onto commercial AC (Darco G40, Norit) were produced by incipient wetness impregnation using aqueous solutions of metal nitrates, followed by heat treatment at 250 °C under N_2 flow [5]. The nominal loading of metals (Zn+Cu) in functionalized sorbents was set to 10% wt., whereas the relative content of Zn and Cu was varied. The specific surface area (S_{BET}) and pore size distribution (PSD) of sorbents were determined by N_2 adsorption at –196 °C with a Quantachrome Autosorb 1-C apparatus. X-ray photoelectron spectroscopy (XPS) analysis was carried out on saturated sorbents using a XPS PHI 5000 Versa probe instrument; assignation of XPS signals was based on the NIST spectral database. Dynamic adsorption tests at 100 ppmv H_2S in dry N_2 (20 SL h^{-1}) were carried out at 30 °C in a fixed-bed reactor using 20–80 mg of sorbent (particle size range 125–200 μm) mixed with quartz. A continuous analyzer (ABB Optima Advance Limas 11 UV) was used for the simultaneous measurement of H_2S (0–300 ppmv) and SO_2 (0–100 ppmv) concentrations. Some specific H_2S adsorption tests at higher concentration (3000 ppmv) were carried out in a lab-scale plant presented elsewhere [5]. H_2S specific adsorption capacity ω_{ads} [mmol g^{-1}] was determined either at the break-point ($C^{out}_{H_2S}(t)/C^{in}_{H_2S}$=0.02) and at saturation ($C^{out}_{H_2S}(t)/C^{in}_{H_2S}$=0.99). Temperature programmed desorption (TPD) tests were carried out in the same lab-scale plant: the sorbents (just after the adsorption test, without being exposed to air) were treated under a flow of 20 SL h^{-1} of high purity N_2 and heated at 10 °C min^{-1} up to a maximum of 620 °C. The specific amount of sulphur desorbed during TPD tests (and obtained by integration of H_2S and SO_2 concentration profiles) was termed ω^{TPD}_{des}.

Results and discussion

Table 1 reports the S_{BET} values of fresh and spent sorbents after capture tests with $C^{in}_{H_2S}$=3000 ppmv at T=30 °C. Figure 1 shows the PSD determined for raw and spent Zn/AC, $Cu_{0.5}Zn_{0.5}$/AC sorbents and for the pristine activated carbon. Results for raw sorbents confirm that the preparation technique allowed obtaining a high dispersion of the metal oxides onto the support, thus largely preserving the PSD of the raw AC. However, it is clear that the active phase composition affects the sorbent PSD. In particular, Zn/AC sorbent displayed a prevailing loss of porosity with respect to the AC substrate in the region of micropores smaller than 10 Å. On the other hand, $Cu_{0.5}Zn_{0.5}$/AC sorbent showed a micropore size distribution rather similar to the one retrieved for raw AC, whereas a minor reduction of mesoporosity in the size range 26–33 Å was detected. The PSD of Cu/AC (not shown) and AC raw overlapped in the micropore size range, but the deposition of CuO resulted in a more evident

reduction of mesoporosity with respect to $Cu_{0.5}Zn_{0.5}$ sample. Therefore, it can be argued that ZnO and CuO phases showed a different tendency to be preferentially dispersed onto the surface of micro- and meso-pores, respectively.

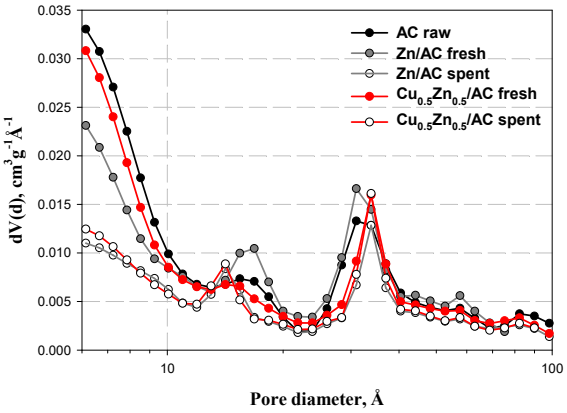

Figure 1. Pore size distributions of raw AC, Zn/AC and $Cu_{0.5}Zn_{0.5}$/AC before and after saturation with $C_{H_2S}^{in}$=3000 ppmv in N_2, T=30 °C.

After saturation with H_2S, all of the spent sorbents experienced a significant reduction of surface area and porosity due to the formation and accumulation of different S-bearing compounds. More specifically, among the saturated sorbents, the Zn-containing materials displayed an evident and similar loss of BET surface area (–40%) down to ca. 330 $m^2\ g^{-1}$ that was mainly due to the occlusion of micropores. Furthermore, Zn-rich sorbents also showed signs of partial occlusion of their smallest mesopores (Fig. 1). On the other hand, the spent Cu/AC material retained a higher value of S_{BET} (426 $m^2\ g^{-1}$). Table 1 compares the performance of H_2S capture of the tested sorbents, in terms of ω_{ads}, for tests carried out at $C_{H_2S}^{in}$=100 and 3000 ppmv and T=30 °C. For both H_2S inlet concentration levels, raw AC is characterized by low H_2S adsorption capacity. The functionalization treatment by single, and particularly by composite Zn and Cu oxides, resulted into a significant increase in ω_{ads}, confirming the existence of a clear optimum of the performances for the $Cu_{0.5}Zn_{0.5}$/AC sorbent (i.e. with equimolar Cu and Zn content). TPD of spent sorbents were carried out in order to investigate the species formed after H_2S adsorption and to study the sorbents regenerability. All the functionalized spent sorbents released about the 40% of ω_{ads} in the form of SO_2 deriving mainly from thermal decomposition of $ZnSO_4$ and $CuSO_4$ [5]; no H_2S was released during TPD tests. The remaining fraction of captured sulphur can be imputed to both Cu and Zn sulphides, that decompose to temperature higher than 1000 °C in inert atmospheres [6], and to elemental or organic S, not detected by the analyzer. XPS analysis was conducted on a spent $Cu_{0.5}Zn_{0.5}$/AC sorbent after recovery in air under ambient conditions: deconvolution of signals in the range 160–172 eV allowed the identification of S-containing compounds (Figure 2).

Table 1. Main parameters of the sorbents under investigation. Values of S_{BET} after saturation with $C_{H_2S}^{in}$=3000 ppmv in N_2, T=30 °C are reported in brackets.

Sorbent	S_{BET} [$m^2\ g^{-1}$]	$C_{H_2S}^{in}$ [ppmv]	$C_{H_2S}^{out}/C_{H_2S}^{in}$ [–]	ω_{ads} [mmol g^{-1}]	ω_{des}^{TPD} [mmol g^{-1}]
AC raw	641	100	0.02	–	–
		100	0.99	0.08	0.08
	(604)	3000	0.99	0.20	0.20
Zn/AC	558	100	0.02	0.21	0.21
		100	0.99	0.73	0.29
	(330)	3000	0.99	0.97	0.41
$Cu_{0.05}Zn_{0.95}$/AC	520	100	0.02	0.22	0.22
		100	0.99	0.88	0.34
	(327)	3000	0.99	1.28	0.58
$Cu_{0.5}Zn_{0.5}$/AC	570	100	0.02	0.40	0.27
		100	0.99	1.00	0.39
	(327)	3000	0.99	1.46	0.59
Cu/AC	559	100	0.02	0.22	0.15
		100	0.99	0.88	0.33
	(426)	3000	0.99	1.36	–

The predominant form of surface S-species was copper and zinc sulfates with their characteristic S $2p_{3/2}$ and $2p_{1/2}$ lines respectively centered at 168.83 eV and 170.01 eV. A minor presence of Zn sulphide was also identified with S $2p_{3/2}$ and $2p_{1/2}$ lines at 162.11 eV and 163.29 eV, respectively. Interestingly, the S $2p_{3/2}$ and S $2p_{1/2}$ peaks observed at BE=164.02 eV and 165.20 eV are representative of sulphur directly adsorbed on activated carbon as they can be ascribed to the occurrence of some elemental sulphur as well as to organic sulphur compounds, such as sulphide (C-S-C), thiol (C-S-H), thiophene (C_4S-H) and disulphide (C-S-S-C).

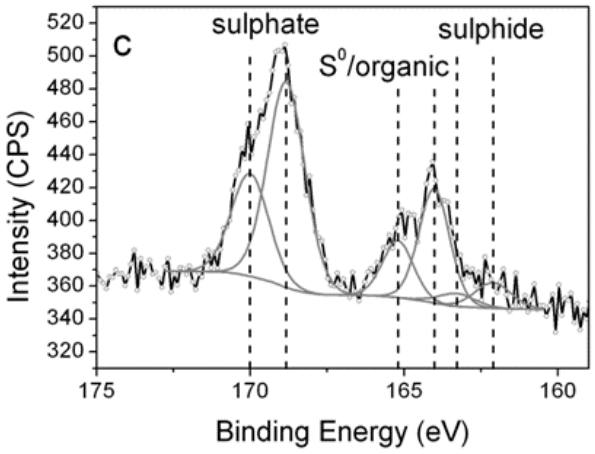

Figure 2. XPS analysis on a saturated $Cu_{0.5}Zn_{0.5}$/AC sorbent ($C_{H_2S}^{in}$=3000 ppmv in N_2, T=30 °C) recovered in air, showing the 2p spectral region of S.

The TPD investigation was extended to materials previously undergoing adsorption only up to the breakpoint ($C_{H_2S}^{in}$=100 ppmv) in order to obtain deeper insights into the type of S-based species early formed during the H_2S capture process and into the role of copper. Notably, for Zn/AC and $Cu_{0.05}Zn_{0.95}$/AC (Zn-rich sorbents), all of the H_2S adsorbed up to the breakpoint was stored as $ZnSO_4$ and released as SO_2 during the following TPD ($\omega_{des}^{TPD}=\omega_{ads}$, Table1). On the contrary, $Cu_{0.5}Zn_{0.5}$/AC and Cu/AC, adsorbed more H_2S up to the breakpoint but $\omega_{des}^{TPD}=0.7\omega_{ads}$, due to the formation of species that cannot be desorbed (i.e. copper and zinc sulphides) or detected (i.e. elemental S).
Deconvolution of TPD profiles of the spent sorbents up to breakpoint (not reported) indicated that the degree of conversion of ZnO to $ZnSO_4$ increased progressively from 10.1% up to 21.0%, moving from Zn/AC to $Cu_{0.5}Zn_{0.5}$/AC. Therefore, copper substitution promoted the ZnO conversion to $ZnSO_4$ mainly in the first stages of the capture process, likely due to a sacrificial role of copper as oxygen donor to accelerate the formation of zinc sulphate.

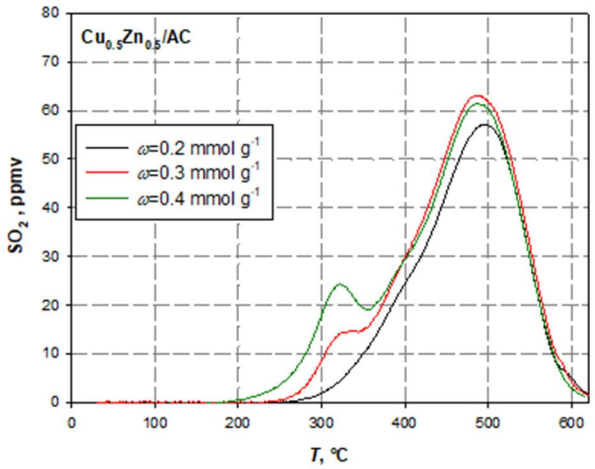

Figure 3. SO_2 release during TPD tests from $Cu_{0.5}Zn_{0.5}$/AC after adsorption carried out at different sulphur loadings (corresponding to different process times).

Moreover, TPD tests performed for $Cu_{0.5}Zn_{0.5}$/AC with increasing S loadings (corresponding to adsorption tests of increasing durations) suggest that $ZnSO_4$ formed at a faster rate with respect to $CuSO_4$. In fact the SO_2 peak related to $ZnSO_4$ decomposition did not experience any substantial modification, whereas the intensity of the $CuSO_4$-deriving peak of SO_2 emission increased progressively as shown in Figure 3.
Altogether the results indicate that, for the best performing sorbent with equimolar Cu:Zn content, $ZnSO_4$ was formed at a faster rate with respect to $CuSO_4$ with copper likely acting as oxygen donor/structural promoter enabling a faster conversion rate and a higher utilization factor of the ZnO phase. On the other hand, the final degree

of conversion of both Zn and Cu oxides to form their sulphates was equivalent and most probably limited by oxygen availability on the sorbent.

Conclusion

Sorbents for the deep removal of H_2S from gas streams at room temperature were prepared by dispersing mixed oxides (ZnO–CuO) onto a commercial granulated activated carbon, at fixed total metal loading of 10% wt. Pore size distribution analysis indicated that Zn and Cu oxides have a different tendency to be preferentially dispersed onto the surface of micro- and meso-pores, respectively. The sorbent with an equimolar amount of Cu and Zn ($Cu_{0.5}Zn_{0.5}$/AC) outperformed both counterparts containing 100% Zn or Cu in terms of H_2S adsorption capacity both at the breakpoint and at saturation, discovering an evident synergic effect between the two metal oxides.

XPS and TPD analysis of saturated sorbents demonstrated that metal sulphides, commonly recognized in the literature as the main reaction products from metal oxides, started to be formed with slow overall kinetics after the corresponding sulphates, probably due to the lack of oxygen available from the sorbent.

In particular copper substitution promoted the ZnO conversion to $ZnSO_4$ mainly in the early stages of the capture process, likely due to a sacrificial role of copper oxide as oxygen donor to accelerate the formation of zinc sulphate. Considering the large increase in the molar volumes of zinc and copper sulphates with respect to their corresponding oxides as well as sulphides, micropores (partially) clogged during adsorption thus slowing down the overall capture kinetics due to increased intraparticle diffusion limitations or even inhibiting direct access to the unreacted active phase.

References

[1] Stirling, D., *The Sulfur Problem: Cleaning up Industrial Feedstocks*, Royal Society of Chemistry, 2000.

[2] Yang, H., Tatarchuk, B., “Novel-doped zinc oxide sorbents for low. temperature regenerable desulfurization applications”, *AIChE J.* 56:2898–2904 (2010).

[3] Bandosz, T.J., “On the adsorption/oxidation of hydrogen sulfide on activated carbons at ambient temperatures”, *J. Colloid Interf. Sci.* 246:1–20 (2002).

[4] Carnes, C.L., Klabunde, K.J., “Unique chemical reactivities of nanocrystalline metal oxides toward hydrogen sulfide”, *Chem. Mater.* 14:1806–1811 (2002).

[5] Balsamo, M., Cimino, S., de Falco, G., Erto, A., Lisi, L., “ZnO-CuO supported on activated carbon for H_2S removal at room temperature”, *Chem. Eng. J.* 304:399–407 (2016).

[6] Nguyen-Thanh, D., Bandosz, T.J., “Activated carbons with metal containing bentonite binders as adsorbents of hydrogen sulfide”, *Carbon* 43:359–367 (2005).

THE INFLUENCE OF H_2O AND SO_2 ON CO_2 UPTAKE IN FLUIDIZED BED CALCIUM LOOPING

A. Coppola*, F. Montagnaro, A. Esposito**, F. Scala*,***, P. Salatino*,*****

coppola@irc.cnr.it

*Dipartimento di Ingegneria Chimica, dei Materiali e della Produzione Industriale, Università degli Studi di Napoli Federico II, Piazzale V. Tecchio 80, 80125 Napoli, Italy
**Dipartimento di Scienze Chimiche, Università degli Studi di Napoli Federico II, Complesso Universitario di Monte Sant'Angelo, 80126 Napoli, Italy
***Istituto di Ricerche sulla Combustione, Consiglio Nazionale delle Ricerche, Piazzale Vincenzo Tecchio 80, 80125 Napoli, Italy

Abstract

The effect of steam and sulfur dioxide on CO_2 capture during calcium looping was studied in a novel lab-scale twin fluidized bed device. Tests were carried out under typical calcium looping operating conditions with or without the presence of H_2O and/or SO_2 during the carbonation stage. Carbonation was carried out at 650°C in presence of 15% CO_2, 10% steam (when present) and by investigating two SO_2 levels, representative of either raw (1500ppm) or pre-desulfurised (75ppm) typical flue gas derived from coal combustion. The sorbent used was a reactive German limestone. Its performance was evaluated in terms of CO_2 capture capacity and sulfur uptake. Results demonstrated the beneficial effect of H_2O and the detrimental effect of SO_2 on the CO_2 capture capacity. When both species were simultaneously present in the gas, steam was still able to enhance the CO_2 capture capacity even outweighing the negative effect of SO_2 at low SO_2 concentrations. A clear relationship between the degree of Ca carbonation and sulfation was observed. Microstructural porosimetric characterizations aided in explaining the observed trends.

Introduction

Calcium Looping (Ca-L) is one of the most interesting technologies for the post-combustion capture of CO_2 produced by fossil fuels in power plants. This process is based on the reversible carbonation of Ca-based sorbents, such as those derived from natural limestone [1-3]. In particular Ca-L consists of a chemical looping process, which entails the utilization of two reactors (a carbonator and a calciner) in a dual interconnected fluidized bed configuration. In the carbonator, the flue gas coming from the power plant is depleted of CO_2 due to the reaction with CaO. This reaction takes place at a temperature of about 600–650°C and yields calcium carbonate. Eventually the $CaCO_3$ coming from the carbonator is processed in another reactor (the calciner) where calcination occurs at a temperature of 900–950°C, producing CaO and an almost pure stream of CO_2 ready for transportation, and storage or utilization.

The main limit of the Ca-L technology is represented by the occurrence of high temperature sintering of the sorbent (especially during the calcination stage) with a consequent decay of the CO_2 capture capacity over iterated cycles. Sorbent deactivation, together with the inevitable sorbent loss by attrition in the fluidized bed system [1,4], implies the necessity of a make-up stream of fresh sorbent to compensate that leaving the plant in the purge and fly ash streams. Another important issue consists in the possible presence of SO_2 in the flue gas which has a negative effect on the performance, since it reacts irreversibly with CaO according to the sulfation reaction, thus decreasing the amount of available sorbent for CO_2 capture [5,6].
The presence of steam in the flue gas, hence in the carbonation stage, has been acknowledged to improve the performance of the sorbent in terms of its CO_2 capture capacity. Studies show that most likely steam is able to increase the diffusion of CO_2 through the sorbent pores [7-9]. These aspects concerning the effect of SO_2 and H_2O have important consequences on the design of the Ca-L system, and so deserve further consideration [10].
The aim of this study was to scrutinize the effect of steam in presence of SO_2 and their mutual interaction in Ca-L tests carried out in a novel lab-scale twin fluidized bed reactor. Two different SO_2 levels were investigated: a low one, to simulate a typical concentration of a previously desulfurized flue gas; a high one, to verify possible simultaneous flue gas decarbonation and desulfurization in the same device. The effect of steam and SO_2 was evaluated in terms of CO_2 capture capacity of the sorbent material. Finally, a characterization of the microstructure of the exhaust sorbent was carried out to assess the relationship between operating conditions and structural changes of sorbent particles.

Experimental

The experimental campaign was carried out in a lab-scale electrically-heated apparatus, purposely designed for chemical looping tests. The apparatus, named Twin Beds, consists of two identical bubbling fluidized beds employed as calciner and carbonator, respectively. A detailed description of the Twin Beds system can be found elsewhere [11]. The material used for the present tests is a German limestone named EnBW, substantially pure in $CaCO_3$ and characterized by good properties in terms of sintering resistance [1]. The tests simulated the Ca-L process for ten complete cycles of calcination/carbonation, plus an 11^{th} calcination stage. For all tests, the calcination conditions were set up at temperature of 940°C with fluidization velocity of 0.5m/s and CO_2 concentration of 70% by volume (balance air) to represent oxy-combustion conditions inside the calciner. In the carbonation stage, the temperature was 650°C, the fluidization velocity 0.5m/s and the CO_2 concentration was set up to the value of 15% by volume in order to represent a typical combustion flue gas. In order to evaluate the effect of the presence of SO_2 and steam during the carbonation stage, six different carbonation conditions were investigated. A base case, called DRY, was used as benchmark where only CO_2 and air were present (no steam, no SO_2). In STECAR (STEam CARbonation) tests

the effect of steam was studied adding a steam concentration of 10% (by volume), a typical value in flue gas. DSP (Dry Sulfur Poor) and DSR (Dry Sulfur Rich) tests were characterized by the presence of SO_2 (without steam) at two different concentration levels: 75ppm for DSP (a typical concentration of a desulfurized flue gas), 1500ppm for DSR (to simulate a Ca-L process with in situ simultaneous desulfurization). The two other conditions investigated the combined effect of steam and SO_2: SCSP (Steam Carbonation Sulfur Poor) and SCSR (Steam Carbonation Sulfur Rich). In both tests the steam concentration was 10% by volume, while the SO_2 concentration was 75ppm for SCSP and 1500ppm for SCSR. Each test was repeated three times to reduce the experimental error. A summary of the operating conditions is reported in Table 1.

Table 1. Operating conditions of the Ca-L tests.

	Calcination	*Carbonation*					
Temperature, °C	940	650					
Test duration, min	20	15					
Fluidization velocity, m/s	0.5	0.5					
Gas composition (balance air)		DRY	STECAR	DSP	DSR	SCSP	SCSR
CO_2, %vol	70	15					
H_2O, %vol	0	0	10	0	0	10	10
SO_2, ppm	0	0	0	75	1500	75	1500

During the carbonation stage the CO_2 concentration was measured by a NDIR analyzer, sampling the outlet gas from the carbonator, and the amount of captured CO_2 in each cycle was calculated by time-integration of the outlet CO_2 profile. The CO_2 capture capacity (ξ) was assessed as the grams of captured CO_2 per gram of initial sorbent. A chemical titration technique, based on the use of phenolphthalein, hydrogen chloride and sodium hydroxide, allowed to determine, on a sorbent sample retrieved from the system at the end of the eleventh calcination (DSP, DSR, SCSP and SCSR cases), the relative amounts of CaO, $CaCO_3$ and $CaSO_4$. This, in turn, made possible the evaluation of χ_{CS}, the degree of calcium conversion to calcium sulfate defined as the ratio between the moles of $CaSO_4$ and the total moles of Ca in the sample ($CaO+CaCO_3+CaSO_4$). Finally, selected samples of exhaust sorbent were characterized by means of N_2 porosimetry carried out in a Quantachrome Autosorb instrument for the analysis of micro- and meso-porosity (the pore size range 0.6–17nm was investigated).

Results and Discussion

In Figure 1 the experimental value of ξ is reported as a function of the number of carbonation cycles for the six investigated operating conditions (see Table 1). As expected, for all the tests ξ decreased along the ten cycles approaching a fairly constant value after approximately the seventh cycle. For the base case DRY, ξ

resulted 0.20g/g for the first cycle (expressed as average value) and, due to sintering, decayed down to 0.052g/g in the tenth cycle, thus highlighting an overall loss of sorbent capture capacity of about 75%. The addition of steam in the carbonation stage (STECAR) improved ξ with respect to the base case, in particular after the 2nd cycle. The asymptotic value of ξ for STECAR was 0.06 g/g, an increase of about 15% over the DRY condition.

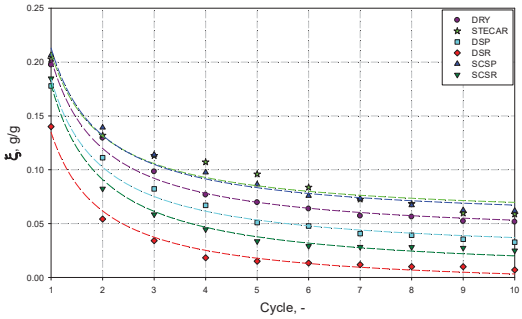

Figure 1. CO_2 capture capacity as a function of the number of cycles under different operating conditions.

As expected, the presence of SO_2 during carbonation (DSP, DSR) produced a stronger decline of ξ because of the simultaneous sulfation reaction which irreversibly subtracted free CaO forming calcium sulfate. In detail, under DSP conditions ([SO_2]=75ppm) ξ passed from an initial value of 0.18g/g down to a final value of 0.033g/g representing here a 36% decrease with respect to the DRY case (the overall loss of capture capacity was about 82%). The results clearly showed that this detrimental effect increased with the SO_2 concentration. In fact, when the SO_2 concentration was 1500ppm (DSR), ξ fell down reaching an asymptotic value of about 0.007g/g, corresponding to an 86% decrease with respect to the base case. The overall loss of capture capacity under DSR conditions was 95%. It is interesting to note that the negative effect of SO_2 was counterbalanced by the addition of steam. As a matter of fact, at low SO_2 concentration (SCSP) the ξ values were similar to those for STECAR. The beneficial effect of steam appeared to outweigh the detrimental effect of SO_2 in this condition. Also, at higher SO_2 concentration (SCSR) it is possible to observe an improvement of ξ with respect to the corresponding case without steam (DSR). In particular, the asymptotic ξ value stabilized to 0.025g/g revealing an increase of about 250% over the DSR conditions. Altogether, conditions with steam (STECAR), also allowing for a reduced sulfur amount (SCSP), improved the performance with respect to the base (DRY) case. When either sulfur in a reduced amount without steam (DSP), or sulfur in a high amount with steam (SCSR), or sulfur in a high amount without steam (DSR) was present in the carbonation atmosphere, the sorbent performance progressively worsened. The following final values of the degree of calcium

sulfation χ_{CS} were obtained: 3.4% (SCSP), 7.4% (DSP), 18.2% (SCSR) and 27.7% (DSR). Higher degrees of calcium sulfation corresponded to lower CO_2 capture capacities. Namely, χ_{CS} was higher when the SO_2 concentration was increased, and in absence of water vapor at fixed [SO_2], the vapor orienteering the reactivity of CaO toward CO_2. These values quantify the irreversible loss of CaO (sulfated) with respect to CO_2 capture, and are useful to correctly design the make-up flow rate of fresh sorbent needed to compensate for loss of reactivity by sintering, loss of reactivity by concurrent sulfation, and loss of material by elutriation.

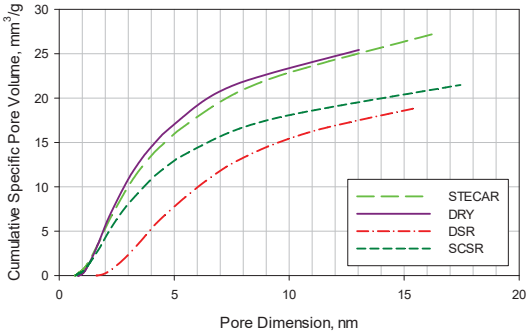

Figure 2. Cumulative pore undersize distribution for the sorbent after the 11th calcination.

Figure 2 reports the porosity of selected exhaust materials, in terms of cumulative specific pore volume as a function of the pore diameter. The same ranking (STECAR>DRY>SCSR>DSR) as the one observed for the CO_2 capture capacity can be recognized in terms of the overall value of micro+mesoporosity. Data confirm (STECAR vs. DRY) that steam can accelerate sintering of the material only at higher temperatures than those of interest here, so showing only the positive effect on ξ likely related to an improvement of CO_2 diffusion into the sorbent pore structure. The introduction of a high SO_2 concentration (without steam) during the carbonation stage (DSR) determines a significant reduction of the total porosity which involves the whole pore population. This effect should be related to pores clogging after Ca sulfation (cf. Figure 4). The addition of steam in presence of a high SO_2 concentration has the important role to partially preserve the porosity of the sorbent (SCSR vs. DSR) by improving the diffusion of SO_2 (i.e. by limiting pores clogging and allowing for a better utilization of the pore surface).
Competitive uptake of acidic gases is favorable to SO_2. Steam exerts a beneficial effect on CO_2 uptake, that can be large to the point of compensating the detrimental effect of SO_2 when the concentration of the latter is small. This may be the case of flue gases that are desulfurized prior to Ca looping.

Acknowledgments
Dr. Luciana Lisi, Mr. Andrea Bizzarro are gratefully acknowledged for their help in carrying out porosimetric characterizations. The authors thank Prof. Mauro Iuliano and Dr. Gaetano De Tommaso (UNINA) for their support in the chemical titration technique, and Mr. Cuono Ruggiero (UNINA) for his help in carrying out experimental tests.

References

[1] Coppola, A., Scala, F., Salatino, P., Montagnaro, F., "Fluidized bed calcium looping cycles for CO_2 capture under oxy-firing calcination conditions: Part 1. Assessment of six limestones", *Chem. Eng. J.* 231: 537–543 (2013).
[2] Erans, M., Manovic, V., Anthony, E.J., "Calcium looping sorbents for CO_2 capture", *Appl. Energy* 180:722–742 (2016).
[3] Salaudeen, S.A., Acharya, B., Dutta, A., "CaO-based CO_2 sorbents: A review on screening, enhancement, cyclic stability, regeneration and kinetics modelling", *J. CO_2 Util*. 23: 179–199 (2018).
[4] Xiao, G., Grace, J.R., Lim, C.J., "Evolution of Limestone Particle Size Distribution in an Air-Jet Attrition Apparatus", *Ind. Eng. Chem. Res*. 53: 15845–15851 (2014).
[5] Coppola, A., Montagnaro, F., Salatino, P., Scala, F., "Fluidized bed calcium looping: The effect of SO_2 on sorbent attrition and CO_2 capture capacity", *Chem. Eng. J.* 207–208: 445–449 (2012).
[6] Luo, C., Zheng, Y., Yin, J., Qin, C., Ding, N., Zheng, C., Feng, B., "Effect of sulfation during oxy-fuel calcination stage in calcium looping on CO_2 capture performance of CaO-based sorbents", *Energy Fuel.* 27: 1008–1014 (2013).
[7] Coppola, A., Allocca, M., Montagnaro, F., Scala, F., Salatino, P., "The effect of steam on CO_2 uptake and sorbent attrition in fluidised bed calcium looping: The influence of process conditions and sorbent properties", *Sep. Purif. Technol.* 189: 101–107 (2017).
[8] Zhang, L., Zhang, B., Yang, Z., Guo, M., "The Role of Water on the Performance of Calcium Oxide-Based Sorbents for Carbon Dioxide Capture: A Review", *Energy Technol.* 3: 10–19 (2015).
[9] Fan, Y., Yao, J.G., Zhang, Z., Sceats, M., Zhuo, Y., Li, L., Maitland, G.C., Fennell, P.S., "Pressurized calcium looping in the presence of steam in a spout-fluidized-bed reactor with DFT analysis", *Fuel Process. Technol.* 169: 24–41 (2018).
[10] Champagne, S., Lu, D.Y., Symonds, R.T., Macchi, A., Anthony, E.J., "The effect of steam addition to the calciner in a calcium looping pilot plant", *Powder Technol.* 290: 114–123 (2016).
[11] Coppola, A., Scala, F., Gargiulo, L., Salatino, P., "A twin-bed test reactor for characterization of calcium looping sorbents", *Powder Technol.* 316: 585–591 (2017).

CO_2 ADSORPTION DATA ON DIFFERENT SORBENTS UNDER DYNAMIC CONDITIONS: AN OVERVIEW

V. Gargiulo, M. Alfè, F. Raganati, P. Ammendola, R. Chirone
gargiulo@irc.cnr.it
Istituto di Ricerche sulla Combustione IRC-CNR, P.le V. Tecchio 80, 80125 Napoli

Abstract
CO_2 adsorption on solid sorbents under dynamic conditions is driven by a number of factors, among them textural features (pore volumes, pore size distribution, surface area…), the surface chemistry (polarity, active site, unsaturated coordinative sites…) and the overall active sites accessibility. Depending on the strength of the interaction with CO_2 (chemisorption or physisorption), solid sorbents are broadly divided in two groups, although of course a sharp distinction between the two phenomena (in many cases concurrent) is not possible. Starting from CO_2 adsorption data acquired in dynamic conditions in a lab-scale fixed-bed reactor or in a fluidized-bed reactor on commercial and ad-hoc synthetized sorbents, a first attempt to correlate adsorption capacities and materials textural properties or relevant adsorption parameters (breakthrough times, $\Delta\tau$...) was here reported. Typical conditions of post-combustion CO_2 capture were selected. Literature data available on CO_2 uptake acquired on solid sorbent under experimental conditions comparable to those considered in this work were also included.

Introduction

Adsorption on a solid matrix is a well-assessed approach for the capture and separation of CO_2 from gas exhausts [1]. An ideal adsorbent for CO2 capture: i) should exhibit high selectivity toward CO_2 over N_2 and other exhaust components (CO, NH_3 and light hydrocarbons (i.e. CH_4)), ii) should exhibit low heat of adsorption for an easy regeneration, iii) should exhibit hydrophobic character in order to be less sensitive to moisture conditions iv) should be produced via inexpensive and low-energy consumption methods and by using renewable resources as precursors, v) should exhibit flexible morphologies, pore structures and functionalities, and vi) should exhibit good mechanical properties to undergo repeated adsorption-desorption cycles [1].

It has been proven that adsorption capacity and selectivity toward CO_2 are strongly dependent on the porous structure and chemical surface of the adsorbent. Solid sorbents are conventionally classified on the basis of the kind of interaction that takes place between CO_2 and the material: physical interaction (physisorption) and chemical interaction (chemisorption). Typical materials acting as physisorbent are porous carbonaceous materials, zeolites, alumina, silica gels, and some metal

organic frameworks (MOFs). Chemisorbents are usually porous materials incorporating basic sites (alkaline carbonates and amino groups) capable of strongly interacting with acidic CO_2. Solid sorbents whose mechanism of CO_2 adsorption lies between chemisorption and physisorption are highly desirable for post-combustion capture purposes since they accomplish both easy regeneration and sufficient selectivity toward CO_2.
With reference to the reactor configurations, adsorption/desorption operations can be performed in either fixed-bed or fluidized bed reactors. However, before the design of an adsorption equipment, the investigation of both equilibrium and kinetics is necessary. The use of fixed bed set-up is a reliable way to perform a rapid screening of the solid sorbents performances in small amounts (about hundreds of mg), achieving more realistic fluid-dynamic conditions compared to thermogravimetric analysis.
With the aim to discriminate between the variety of factors that govern CO_2 uptake on solid sorbents under dynamic conditions, in this work, CO_2 adsorption data acquired in a lab-scale fixed-bed reactor on commercial and ad-hoc synthesized materials were used to correlate adsorption capacities and materials textural properties and relevant adsorption parameters (breakthrough times, $\Delta\tau$...).

Experimental section

Materials. The sorbents reported in this work are listed in Table 1. With the exception of commercial materials (AC, zeolites, tuff), most of them were the object of previous papers where the detailed synthesis are reported [2-5].
Rice husk (RH) derived materials were produced as follows: carbonized rice husk (cRH) was obtained by carbonization of RH in an auger furnace in the 500° - 800°C temperature range for 3 hours; cRH-NH_4OH was obtained by treating cRH suspended in de-ionized water with 10 mL 28% ammonia solution for 1 h at 90° C under stirring; cRH-NaOH was obtained with the same procedure used for cRH-NH_4OH but using a 5M solution of NaOH instead of ammonia solution. cRH-NH_4OH and cRH-NaOH were recovered by centrifugation and washed more times with distilled water. At the end of the purification procedure, the samples were dried at 100 °C. cRH-nFM was synthetized adapting the procedure proposed by [6] for magnetite nanoparticle synthesis: 2.6 g of $FeCl_3 \cdot 6H_2O$ and 2.7 g $FeSO_4 \cdot 7H_2O$ were dissolved in 60 mL of distilled water, mixed with a water suspension containing 10 g of cRH and then the resulting suspension mixed with 60 ml of NaOH 5M for 2 h at 80 °C under stirring. After that time, 5 ml 25% (w/w) etramethylammonium hydroxide was added to stabilize magnetite nanoparticles. The suspension was then cooled to room temperature and the dark brown solid was recovered by filtration and washed with water to remove all traces of unreacted salts and sodium hydroxide. The sample was dried at 100 °C.
Textural properties characterization. The BET specific surface areas (SA) of the samples were measured by Ar adsorption at 87 K using a Quantachrome Autosorb 1 apparatus. The samples were outgassed under vacuum at 120 °C before the

analysis. Adsorption/desorption data were processed in accordance with the BJH model to evaluate the pore size distribution and the pore volume.

CO_2 adsorption tests. The CO_2 uptakes of the materials have been evaluated in a lab-scale fixed bed or fluidized bed reactor described elsewhere [2-5,7,8]. The breakthrough curves (i.e. C/C_0 versus time, where C and C_0 are the CO_2 concentration in the effluent and feed stream, respectively) have been worked out to evaluate:

i) the CO_2 adsorbed per unit mass of adsorbent, m_{ads}, calculated by integrating the breakthrough curves;

ii) the breakthrough time, t_b, or breakpoint, which is the time it takes for CO_2 to reach the 5% of the inlet concentration at the adsorption column outlet;

iii) the time parameter $\Delta\tau = t_{70}-t_{10}$, t_{70} (with t_{10} and t_{70} being the time for which CO_2 reach 70% and 10% of the inlet concentration at the adsorption column outlet) which is related to the slope of the linear part of the sigmoid (the smaller this parameter is, the steeper the breakthrough curve and consequently the faster the adsorption kinetics will be);

iv) the fraction of bed utilized at breakpoint, W, namely the ratio between the CO_2 adsorbed until the breakpoint and that adsorbed until saturation.

Results

The materials listed in Table 1 belong to different categories: carbon-based materials derived from thermochemical conversion processes (carbon black, carbonized rice husk…) used as obtained and/or post-processed (thermally or chemically activated, covered and/or embedded in active layers or functionalized with amine groups…), MOF, zeolites, and activated carbons. Such great variability in the nature and the properties of the materials allowed to obtain a very rich array of data and offered the possibility to take into account the different types of CO_2-material interactions, namely almost pure physisorption, physisorption+chemisorption and almost pure chemisorption.

The most of the adsorption data reported in Table 1 refers to measurements performed by the authors in lab-scale reactors (fixed-bed or fluidized bed) with a CO_2 inlet concentration between 3-10%, typical of post-combustion. In the Table literature data acquired in similar experimental conditions (fixed-bed, CO_2 concentration 4-10%) were also reported to enlarge and validate the correlations outputs reported in the following.

As first and more immediate correlation between adsorption capacities and materials textural properties, we reported m_{ads} vs surface area estimated through BET equation (Figure 1). This representation allows the comparison of data from different sorbents without constraints related to experimental conditions (reactor configuration, sorbent amount). Sorbents are gathered into three groups corresponding to the three main CO_2-material interactions: pure physisorption, physisorption+chemisorption, chemisorption. The materials falling in the

physisorption regime were of different types: pure carbon-based materials (activated carbon, carbon black), zeolite and MOF.

	Sample	mads $mg_{CO2}\ g^{-1}$	tb, s	Δτ, s	W, %	SA $m^2\ g^{-1}$	Total pore volume $cm^3\ g^{-1}$	Micropores volume $cm^3\ g^{-1}$	Mesopores volume $cm^3\ g^{-1}$	pCO_2	Reactor	Ref
chemisorption	HKUST-1 (Zn)	13,86	10,00	13,00	29,22	20	0,0068	0,0000	0,0068	3	*	[5]
	MIL-96 (Al)	21,66	15,00	27,00	36,41	51	0,0047	0,0180	0,0029	3	*	[5]
	MIL-100 (Fe)	7,71	2,00	10,00	13,58	1105	0,7400	0,6000	0,1400	3	*	[5]
	CBox–NH2	12,80	1,00	16,00	n.a.	30	0,0044	0,0005	0,0039	3	*	[3]
	CB–IL	27,30	18,00	22,00	n.a.	36	0,0055	0,0019	0,0036	3	*	[3]
	CBox–IL	9,90	6,00	16,00	n.a.	40	0,0127	0,0057	0,0070	3	*	[3]
phys+chem	HKUST-1 (Cu)	22,88	n.a.	n.a.	n.a.	680	0,6600	n.a.	n.a.	5	**	[7]
	FM	10,87	4,00	11,00	16,13	154	0,0472	0,0089	0,0383	3	*	[2]
	CB–FM-1	11,10	15,00	15,00	n.a.	160	0,0534	0,0179	0,0355	3	*	[2]
	CB–FM-2	16,10	25,00	19,00	n.a.	148	0,0405	0,0159	0,0246	3	*	[2]
	CB–FM-3	16,50	24,00	16,00	n.a.	157	0,0359	0,0098	0,0261	3	*	[2]
	CB–FM-4	14,90	27,00	18,00	n.a.	157	0,0338	0,0088	0,0250	3	*	[2]
	CB–FM-5	7,20	3,00	19,00	n.a.	145	0,0312	0,0105	0,0207	3	*	[2]
	CBox–FM	8,00	1,00	19,00	n.a.	248	0,0531	0,0181	0,0350	3	*	[3]
	RH-nFM	15,55	12,00	n.a.	n.a.	271	n.a.	n.a.	n.a.	3	*	this work
	C-700	19,34	n.a.	n.a.	n.a.	463	0,4800	n.a.	n.a.	10	*	[11]
	SBA-APTSgrafted	13,55	n.a.	n.a.	n.a.	230	n.a.	n.a.	n.a.	4	*	[10]
physisorption	CB	6,50	2,00	n.a.	n.a.	143	0,1750	0,0050	0,1700	3	*	[2]
	Cbox	8,81	8,00	11,00	38,80	277	0,5700	0,3600	0,2100	3	*	[3]
	CNT	16	n.a.	n.a.	n.a.	394	0,63	n.a.	n.a.	5	*	[12]
	GAC Filtrasorb 400	14	n.a.	n.a.	n.a.	954	0,48	n.a.	n.a.	5	*	[12]
	RH	11,26	8,00	15,00	30,76	105	0,0640	0,0410	0,0230	3	*	this work
	RH_NaOH	15,28	14,00	20,00	38,78	431	0,3750	0,1700	0,2050	3	*	this work
	RH_NH4OH	12,04	10,00	14,00	n.a.	180	0,0640	0,0410	0,0230	3	*	this work
	Cbox_annealed	11,12	14,00	8,00	58,19	464	0,9000	0,5800	0,3200	3	*	this work
	AC Norit	10,56	n.a.	n.a.	n.a.	1060	1,3400	n.a.	n.a.	3	**	[7]
	Zeolite 13X	10,12	4,00	n.a.	n.a.	960	0,4100	n.a.	n.a.	3	*	[3]
	Zeolite Na-Y/NH4-Y	8,36	n.a.	n.a.	n.a.	756	0,4000	n.a.	n.a.	10	**	[7]
	TUFF	1,54	12,00	11,00	n.a.	141	n.a.	n.a.	n.a.	5	*	[9]
	Zeolite CBV100	13	n.a.	n.a.	n.a.	788	0,35	n.a.	n.a.	5	*	[12]
	SIFSIX-3-Zn	104,4	n.a.	n.a.	n.a.	250	n.a.	n.a.	n.a.	10	*	[13]
	SIFSIX-2-Cu-i	55	n.a.	n.a.	n.a.	735	0,26	n.a.	n.a.	10	*	[13]

* fixed bed ** fluidized bed

Table 1. CO_2 uptake and textural properties

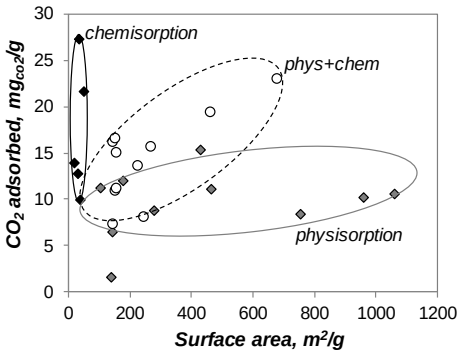

Figure 1. Plots of m_{ads} vs surface area

All of them were characterized by low m_{ads} (< 15 mg/g) even if some of them exhibited high surface areas as zeolite and MIL-100 Fe (up to 1100 m^2/g).The

materials falling in combined physisorption+chemisorption regime containing basic functional groups and/or active coating (magnetite coated carbon-based materials, activated carbon containing N, …) as well as a not negligible surface area and total pore volumes. All of them were characterized by higher CO_2 uptake (between 5 and 20 mg/g). The sorbents active for physisorption+chemisorption partially overlap, in the plot at lower SA, with sorbents exhibiting almost pure physisorption interaction with CO_2. The materials falling in the chemisorption regime were those containing basic groups able to interact with the acidic CO_2 molecules: these materials exhibited high m_{ads} (up to 28 mg/g) and quite low surface areas (< 50 m^2/g). Similar graphical representations have been obtained by reporting the adsorption capacities as a function of pore volumes (total pore volume, micropore volume and mesopore volume) not reported here for lack of room.

Another attempt of correlation was performed by reporting the m_{ads} as a function of the breakthrough time. For this correlation only data acquired under the same experimental conditions (fixed-bed, CO_2 inlet pressure 3 %) were considered.

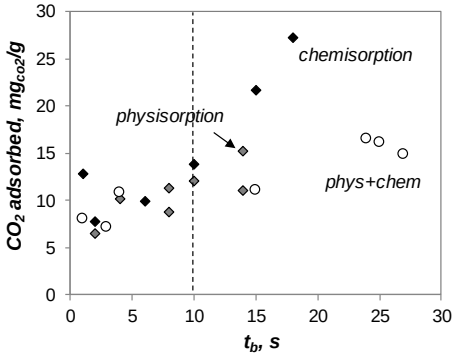

Figure 2. Plot of m_{ads} as a function of the breakthrough time.

t_b together with the m_{ads}, could be considered an useful single metric for ranking adsorbents, since, for practical purposes, a high value of t_b is highly desirable because it reduces the frequency of sorbent regeneration. On the basis on the available data and as a very preliminary outcome, Figure 2 indicates that materials acting in the chemisorption+physisorption regime exhibit higher breakthrough times for a quite limited CO_2 uptake. The materials falling in the almost pure physisorption regime overall exhibited the lowest t_b while an intermediate trend is discernible for chemisorbents. A focused experimental campaign is planned to shed light into possible t_b and m_{ads} correlations.

Conclusions

CO_2 adsorption data acquired in dynamic conditions in a lab-scale fixed-bed reactor or in a fluidized-bed reactor on commercial and ad-hoc synthetized sorbents were used to tentatively correlate adsorption capacities and materials textural

properties or relevant adsorption parameters. The correlation of m_{ads} vs surface area gathered the sorbents into three groups corresponding to the three main CO_2-material interactions: pure physisorption, physisorption+chemisorption, and chemisorption. The correlation of m_{ads} vs t_b indicates that higher t_b values are exhibited by sorbents falling in the chemisorption+physisorption regime, the lower t_b value for materials falling in the almost pure physisorption regime while an intermediate trend is discernible in the case of chemisorbents.

Acknowledgements
The authors thank Prof. M. Jumabayev from al-Farabi Kazakh National University for providing carbonized rice husk and Dr. Paola Giudicianni for BET analyses. The financial support of Piano Annuale della Ricerca Mise-CNR was kindly acknowledged.

References

[1] D'Alessandro, D.M., Smit, B., Long, J.R., *Angew. Chem. Int.* 49:6058–6082 (2012).
[2] Alfè, M., Ammendola, P., Gargiulo, V., Raganati, F., Chirone, R., *Proc. Comb. Inst*. 35:2801–2809 (2015)
[3] Gargiulo, V., Alfe, M., Ammendola, P., Raganati, F., Chirone, R., *Appl. Surf. Sci.* 360: 329–337 (2016).
[4] Raganati, F., Gargiulo, V., Ammendola, P., Alfè, M., Chirone, R., *Chem. Eng. J*. 239: 75–86 (2014).
[5] Gargiulo, V., Alfè, M., Raganati, F., Lisi, L., Chirone, R., Ammendola, P., *Fuel* 222: 319-326 (2018)
[6] Utkan, G., Sayar, F., Batat, P., Ide, S., Kriechbaurnd, M. Piskin, E., *J. Colloid Interface Sci.* 353:372–379(2011)
[7] Raganati, F., Ammendola, P., Chirone, R., *Powder Tech.* 268: 347-356 (2014)
[8] Ammendola, P., Raganati, F., Chirone, R., *Chem. Eng. J*. 322:302-313 (2017).
[9] Ammendola, P., Raganati, F., Chirone, R., Miccio, F., *Energ. Proc.* 114: 46-52 (2017).
[10] Chang, A.C.C., Chuang, S.S.C., Gray, M., Soong, Y., *Energy Fuels* 17:468–473 (2003).
[11] Goel, C., Kaur, H., Bhunia, H., and Bajpai, P. K., *J. CO_2 Util.* 16: 50–63 (2016).
[12] Lu, C., Bai, H., Wu, B., Su, F., Hwang, J.F., *Energy Fuels* 22: 3050-3056 (2008).
[13] Nugent, P., Belmabkhout, Y., Burd, S. D., Cairns, A. J., Luebke, R., Forrest, K., Pham, T., Ma, S., Space, B., Wojtas, L., Eddaoudi, M., Zaworotko, M. J., *Nature letter* 495:80-84 (2013)

A DESCRIPTIVE MODEL FOR A PILOT-SCALE WET ELECTROSTATIC SCRUBBER

M. Esposito[*, **], C. Carotenuto [***], A. Lancia[*], M. Giavazzi[**], E. Di Benedetto[*], F. Di Natale[*]
Francesco.dinatale@unina.it

* Dipartimento di Ingegneria Chimica, dei Materiali e della Produzione Industriale, Università degli studi di Napoli Federico II, P.le V. Tecchio 80, 80125 Napoli, Italy.
** Boldrocchi Srl., Viale Trento e Trieste 93, 20046 Biassono MB (Italy)
***Dipartimento di Ingegneria, Università della Campania "L. Vanvitelli", Via Roma 29, 81031, Aversa (CE), Italy.

Abstract
This paper reports the preliminary results of a modelling study of a pilot scale wet electrostatic scrubber, aimed to provide accurate design and operating tools to sustain process scale up. The model comprises a CFD analysis of the scrubber (including spray pattern estimation), performed with a commercial software, and a proprietary post-processing model for the calculation of particle depletion inside the unit. Starting from a set of available experimental data, a descriptive approach was used to fit particle efficiency results by tuning the information on particle charge distribution with a single-parameter binomial function. The descriptive model provides results consistent with theoretical models for particle charging and with corona current measurements and demonstrates the importance of introducing suitably estimation of particle charge distribution to improve our capacity of describing scrubbing phenomena.

Introduction
Wet electrostatic scrubbing (WES) is an emerging technique to reduce particles number in polluted gas streams and its application to marine and industrial fields is under scrutiny. This technique is particularly suitable for soot particles that are hardly captured by conventional systems based on hydrodynamic forces or by filtration media. A WES unit consists in contacting the particle-laden gas with an electrified spray (ES) in a suitably designed scrubber. In most cases, the gas is exposed to a corona source (PCU) before entering the spray chamber.
In recent times, our research group performed a large number of experimental tests on pilot scale wet electrostatic scrubbers, within the framework of the EU Research project DEECON and industrial cooperation with the Vessel Technical Service (IT) and the Boldrocchi Ecologia (IT). Experiments can be interpreted by following two approaches. The most rigorous one includes calculation of particles trajectories inside the scrubber taking into account the interactions with each of the scrubbing droplets and their relative motion. The broad number of particles and droplets to be tracked makes this approach unfeasible. A good description of the data may come from the use of stochastic approach, similar to those adopted for atmospheric

scavenging and suitably adopted to account the physics of electric interactions between particles and droplets. Although unable to address some points of the phenomena (i.e. the effect of temperature and humidity gradients or the occurrence of the elastic rebound phenomena), this approach was successfully adopted to describe laboratory scale tests at ambient temperature, when droplets and particles size, charge, velocity and volumetric concentration can be suitably controlled and measured [1]. The core of a stochastic model is the assessment of a scavenging coefficient $\lambda(d_p, D, q_D, q_P, U, T, P, RH)$, which embodies all the interactions between a droplet of size D and charge q_D and a particle of size d_p and charge q_p, moving with a relative velocity U inside a gas of temperature (T) and pressure (P). According to Di Natale et al. [2] the rate of depletion of particles exposed for t seconds to a WES process is given by:

$$ln\left[\frac{n(d_p)}{n_0(d_p)}\right] = -\int_0^\infty \lambda\left(D, d_p, q_p, U, q_D\right) N \psi_j(D) rtd(t) dD \cdot t \qquad (1)$$

Where N (1/m^3) is the total number concentration of droplets $n(d_p)$ (1/m^3) is the concentration of particles of size d_p (m) and $\psi(D)$ is the size distribution of the droplets in a differential volume Using a Lagrangian approach, if $n_0(d_p)$ particles enter the scrubber, their concentration progressively reduce along their travel in the vessel according to the droplets they interact with. Therefore, an accurate tracking of particles trajectories, droplet concentration and size distribution inside the scrubber is mandatory to proficiently apply the model. Commercial CFD models provide reliable tools to estimate these information. As from Eq.(1), also the information pertaining to droplets and particle charge are required. However, while experiments allow determining a reasonable value of droplets charge according to their size [1-4], the assessment of particle charge is much more complex [5-7].

In many industrial applications, particles are charged by unipolar corona. Corona charging is a complex process in which particles acquire charge due to the deposition of gas ions on their surface. The amount of charge that can be deposited over a particle depends on its size, to the electric field, E (V/m), and the ion concentration, N_i (1/m^{-3}) it is exposed to and to the time of exposure, t_r (s).

Since corona charger generate non-uniform distributions of E and N_i and the velocity field of particles is non-uniform as well, particles of the same size and physical properties entering the corona charger in different positions, are charged in different ways. The charger geometry highly influences particle charging.

The absence of precise information on the actual charge distribution of particles of generic size d_p is the main hindrance to the application of stochastic models to describe experiments on pilot scale wet electrostatic scrubbing.

To this end, this work presents a numerical modelling of a pilot scale wet electrostatic scrubber used to treat soot particles from an open gasoline flame in a gas stream of up to 220 kg/h, using water as scrubbing media. The experimental tests and the adopted setup were presented in Di Natale et al. [4].

A thermo-fluid-dynamic numerical model was applied to estimate the trajectories and the velocities of sprayed droplets (including their evaporation) and the gas streamlines inside the WES reactor. The model also allows estimating the number of droplets that collide with the WES walls, for which is assumed that they lose their capacity to further capture particles.
These information, together with the value of gas temperature and humidity inside the WES are used as the starting points of a proprietary program in Matlab® for modelling particle scrubbing. This model assumes that particles charge are distributed according to a binomial function:

$$y_k(d_p) = \binom{k_{max}}{k} p^k (1-p)^{k_{max}-k} \quad (3)$$

Where $y_k(d_p)$ is the fraction of particles of size d_p having k elemental charges, varied within 1 and k_{max}, and p is the binomial shape factor varying with d_p. The particle scrubbing model was developed to fit experimental data on the particles capture in the different operating conditions [4], using p is best-fitting parameter.

Methodology

The thermo-hydrodynamic modelling of the scrubber includes simulations of the gas and the sprayed phases and assumes that, due to their small sizes (<450 nm), particles trajectories follow the gas streamlines. The CFD model was developed in ANSYS FLUENT 15.0® starting from the mechanical drawings of the WES setup. The CFD model uses a standard k-ε model for gas phase and Discrete Particle Model for tracking of the sprayed droplets, whose size distribution, velocity and spray angle are defined by the user. The scrubber was meshed in 3D with tetrahedral volumes, using 1949886 cells with mean size from 5 to 10 mm, having element quality of 0.21 and average aspect ratio of 1.83. Rossetti [5] reports the details of CFD meshing and simulations.
The software also allows tracking the streamlines of the gas entering the computational domain. For our scopes, the inflow surface of the unit was divided in 200 equal sectors and the gas streamlines starting from them are tracked. The mathematical model for particle capture based on Eq.(1) was applied as follows:

1. For each particle size d_p, a number of k_{max}=100 possible charges are distributed according to Eq.(3). The concentration of particles having charge $q_{p,k}(d_p)$, $n_{0k}(d_p)$, is obtained by multiplying $n_0(d_p)$ with the k-th term of Eq.(3).
2. Each gas streamline is labeled with the index i=1…200.
3. To each of the 200 inlet cells is associated a concentration of particles equal to $n_{0,i}(d_p)=n_0(d_p)/200$, being $n_0(d_p)$ the number of particles entering the scrubber during the generic test.
4. The reactor is divided in j=1…J subvolumes and, from the spray tracking are derived: i) the concentration of droplets in each volume N_j, and their size distribution, $\psi_j(D)$ and ii) their relative velocity respect to the gas, $U_j(D)$. Each droplet size is associated to a net charge q_D, determined from the values of the

spray charge reported in Di Natale et al. [4]. The mean values of temperature, humidity and pressure are also registered.

5. For the *i*-th streamline, the residence times, $t_{i,j}$, in the subvolume *j* is determined.
6. When a streamline enter a subvolume *j*, coming from the subvolume *j*-1 with a concentration $n_{i,j-1,k}(d_p)$, the particle concentration leaving volume are:

$$ln\left[\frac{n_{i,j,k}(d_p)}{n_{i,j-1,k}(d_p)}\right] = \int_0^\infty \lambda\left(D, d_p, q_{p,k}, U_{i,j}, q_D\right) N_j \psi_j(D) t_{i,j} dD \quad (3)$$

7. At the scrubber exit (subvolume *J*) the concentration of particles of size d_p is:

$$n(d_p) = \sum_{i=1}^{I} \sum_{k=1}^{k_{max}} n_{i,J,k}\left(d_p\right) \quad (4)$$

8. The shape factor *p* is determined, for each particle size, by best fitting of the model removal efficiency with the corresponding experimental value, i.e:

$$\eta_{exp}\left(d_p\right) = 1 - \frac{n(d_p)}{n_0(d_p)} \quad (6)$$

Results and discussion

Four operating conditions were investigated, corresponding to fixed electric potential of the electrified nozzle, 15 kV, and liquid flow rate, 195 kg/h, and two potential of the corona charging unit (13 and 15 kV) and two gas flow rates (170 and 222 kg/h). To improve robustness of experimental data, only particles in the range 100-300 nm, which represent >95% of the total particles number and for which the experimental error is well below 5% were considered.

Figure 1 reports the value of the shape factor *p* of the binomial distribution as a function of the particles diameter as obtained by best fitting of experimental data.

The shape factor *p* increases with the particles diameter in a similar way for all the cases considered. It is worth noticing that higher values of *p* imply both a higher mean and a higher standard deviation of the distribution, but the trend shown here led to the conditions that the larger the particles, the higher the mean charge and the narrow is the charge distribution (data not shown). This is consistent with the physical observation [6,7] that smaller particles, with their higher Brownian diffusion and the lower tendency to reach their saturation time, are less prone to leave the corona charger unit with a uniform number of deposited charge compared to larger particles. Besides, the model indicates that higher V_{PCU} and lower residence times in the corona charger lead to slightly higher values of *p*. This is consistent with the large difference between operating potentials (>13 kV) and onset corona potential (about 5 kV).

To compare the results of the descriptive model with the theoretical models available in literature, we run the model imposing a particle charge level equal to that calculating from theoretical models as reported by Jaworek et al. [7]. The details of calculation are reported in Rossetti [5].

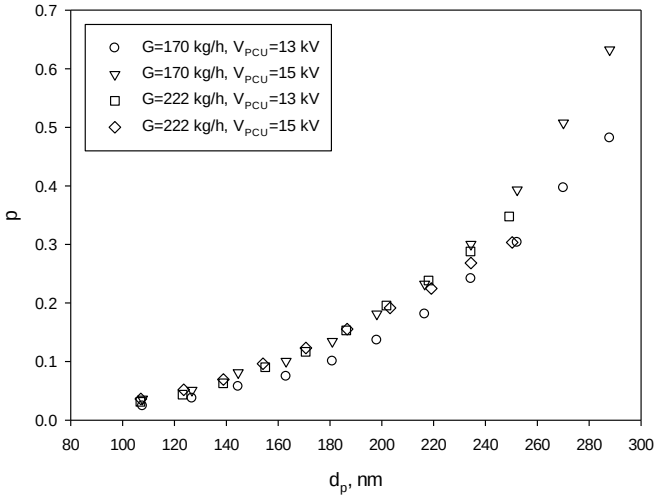

Figure 1. Value of the shape factor *p* of the binomial distribution as a function of the particle diameter and parametric with the V_{PCU} and *G*.

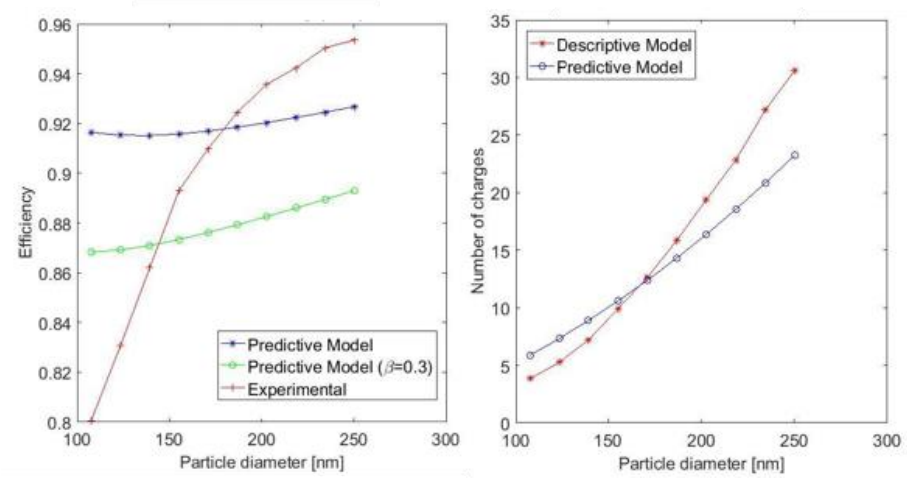

Figure 2. Comparison between predictive and descriptive model for particle capturing and corona charging in the WES for V_{PCU}=15kV and *G*= 222 kg/h.

Figure 2 shows a sample result in terms of calculated removal efficiency and mean particle charge. The removal efficiency calculated from the theoretical particle charging model deviates from the experimental evidences and overestimates the total removal efficiency by about 5 percent points. To fit the actual value of the total removal efficiency, theoretical particles charges have to be corrected by a multiplying factor β=0.3. On the other hand, comparing the theoretical predictive

model with the results of our best fitting analysis in terms of particles mean charges, the results are consistent and the factor β is not needed. Besides, the descriptive model provided a reliable estimation (within 5%) of the charged aerosol current obtained from experiments and from predictive models. Similar result are obtained for the other experimental cases.
These results led to conclude that the scarce capacity of the predictive model to describe experiments is mostly related to the absence on information on the actual particle charge distribution, which is actually assumed to be a Dirac's function.

Conclusion

Our research group is developing modelling tools to better design and operate WES units for submicron and ultrafine particle capture from flue gases. The most critical hindrance to this goal is the absence of detailed information of particle charging. To fill this gap, this study proposes the use of a stochastic model for particle scrubbing and a CFD code for WES thermo-hydrodynamic simulation to infer data on particle charge distribution from experimental data. This approach provided a reliable estimation of mean particle charge together with an excellent and consistent description of the available experimental data. This interesting result suggest the extension of the study to a wider set of experiments and to coupling with existing theoretical models.

References

[1] D'Addio L., Carotenuto C., Balachandran W., Lancia A., Di Natale F., Experimental analysis on the capture of submicron particles (PM0.5) by wet electrostatic scrubbing, Chem. Eng. Sci. 106:222-230 (2014)
[2] Di Natale, F., Carotenuto, C., D'Addio, L., Lancia, A., Effect of gas temperature on the capture of charged particles by oppositely charged water droplets, Aerosol Sci. & Tech., 50(2):110-117 (2016)
[3] Krupa A., Jaworek A., Sobczyk A.T., Marchewicz A., Szudyga M., Antes T., Charged spray generation for gas cleaning applications, Journal of Electrostatics 71(3): 260-264 (2013)
[4] Di Natale F., Carotenuto C., D'Addio L., Jaworek A., Krupa A., Szudyga M., Lancia A., Capture of fine and ultrafine particles in a wet electrostatic scrubber, J. Env. Chem. Eng., 3(1):349-356 (2015)
[5] Rossetti C., Numerical modelling of a wet electrostatic scrubber for submicron particle capture, M.Sc. Th. in Chem.Eng., Univ. of Naples, 2016.
[6] Hinds, W. C., Aerosol Technology, 2nd Ed., Wiley & Sons, 1999, New York.
[7] Jaworek A., Krupa A., Sobczyk A.T., Marchewicz A., Szudyga M., Antes T., Balachandran W., Di Natale F., Carotenuto C., Submicron particles removal by charged sprays. Fundamentals, Journal Elect., 71(3):345-350 (2013).

SESSION VIII

Detonations, Explosions and Supersonic Combustion

Spray and Droplets

SHOCKLESS FLAME ACCELERATION AND DDT IN OPEN CHANNELS DRIVEN BY HYDRAULIC RESISTANCE

M. Kuznetsov*, J. Yanez, V. Bykov
*E-mail:kuznetsov@kit.edu
Karlsruhe Institute of Technology 76131 Karlsruhe, Germany

Abstract
Hydrogen-air and hydrogen-oxygen deflagrations with end venting in obstructed and smooth tubes with an ignition from open end are studied experimentally and numerically. A shockless transition from laminar to sonic flame propagation regime is reported. Hydrogen-air mixtures with 10-13% vol. of hydrogen and stoichiometric hydrogen-oxygen mixtures were ignited from open end of the tube at the interface between fuel and the ambient air. Different venting ratios of the tube (the ratio of orifice area to the tube cross-section) from 10% to 100% were selected. In all cases, the flame initially propagates without acceleration at a velocity close to the laminar flame speed. The flame configuration excludes most of conventionally acknowledged phenomena of the DDT, namely, volumetric explosions, igniting shock and shock waves interactions. However, after an induction period, of the order of 1 sec, the flame accelerates more than 100 times, within a period of 3-30 ms, until the steady-state flame propagation regime or detonation is established. The mechanism of such rapid acceleration is investigated both numerically and analytically. A one dimensional reduced description was suggested and analyzed to model the process of the flame acceleration. The study of the over simplified model reveals that the hydrodynamic resistance of the tube behind the flame causes sudden flame acceleration and governs initial stage of the DDT.

Introduction
The criteria to predict the flame propagation regimes in tubular configurations have developed in [1-2]. Following those authors, the expected regimes will be dependent on the tube geometry, and specifically, on the configuration of the obstacles. The propagation could be classified as *slow* sub-sonic, *fast* sonic (choked) and *quasi-detonations* (due to the strong pressure loss in the baffles, the Chapman-Jouguet propagation velocity is not reached in obstructed tubes).
Fast and *quasi-detonations* regimes may be suppressed by the use of venting orifices. The effect of the lateral venting on flame acceleration and DDT was experimentally investigated [3-4]. It was found that the amount of reactive mixture necessary for the development of sonic flames or DDT grows with an enlargement of the venting surface. A comparison between end- and side-vented explosions in tubes showed a higher efficiency of the end opening reducing the combustion pressure [5]. In such

configurations, a prolonged quasi-laminar propagation phase is followed by a sudden and violent shockless flame acceleration that culminates when the sonic regime is reached. The main mechanism causing this sudden acceleration of flames was the hydraulic resistance [6-8]. Due to the friction forces, a quasi-laminar deflagration wave cannot reach a stationary regime. Nevertheless, the parameters controlling the de/acceleration and the form in which this occurs remains unclear. In order to improve current understanding of the phenomenon, the authors have carried out the analysis presented in this article by combining experimental, numerical and analytical approaches to the problem.

Description of experiments and numerical simulations

The experiments were performed in the DRIVER facility, which is an obstructed shock tube with a total length of 12.2 m and an internal diameter of 174 mm. Inside the tube, ring shape obstacles were positioned in a regular manner and spaced by a tube diameter accounting for a blockage ratio equal to 0.6. Hydrogen-air mixtures with 10, 11.3 and 13 vol. %H2 at ambient conditions were ignited at the open end, directly at the interface between the inflammable mixture and the surrounding air. The instrumentation included photo diodes and pressure gauges installed along the channel. The venting ratio α of the orifice was varied from fully closed to completely open cross-section.

Numerical simulations of the experiments for venting ratios 0%, 40% and 100%, were carried out with the combustion code COM3D [9] in order to provide an enhanced comprehension of the test and analyze the mechanism of the flame acceleration in presence of end venting. The simulations has several implications. Specifically, the Kolmogorov and Taylor turbulent micro-scales, the boundary layers and the laminar flame thickness remain unresolved. To overcome those restrictions, the KYLCOM combustion model [10], specifically designed for under-resolved calculations, and the standard k-ε turbulence model were utilized.

Experimental/numerical results. Analysis of the acceleration mechanism

Figure 1 left displays a comparison of the flame propagation obtained from the results of simulations and experiments. In the closed channel, the flame accelerates immediately after reaching the first obstacle generating an additional flow motion which steepens into the shock wave. The turbulent flow ahead of the flame created by the thermal expansion of the products supports the flame acceleration within a relatively short time after ignition (~0.1 s). Beyond the run-up distance, of about 1.3 m, the flame reaches the sonic regime and propagates further with a steady velocity of 540 m/s (close to speed of sound in products) and with pressure from 6 to 11 bar. In the presence of venting, combustion products are discharged to the atmosphere through the end orifice and do not support the flame acceleration. Two regions with different propagation regimes, slow and fast, can be clearly identified. Initially, the flame propagates in a quasi-laminar regime with a stationary velocity of ~3.5 m/s. The experimental records show that during this phase no significant pressure and,

therefore, no relevant flow motion (generating turbulence) appears ahead of the flame. Nevertheless, around 1 s after the ignition, the flame suddenly accelerates from the quasi-laminar to the fast sonic regime within an interval of 3-30 ms (50 ms in the calculations). After the acceleration, the sonic flame propagates until the end of tube with a constant velocity of ~540 m/s (both experiments and simulations) creating peaks of pressure of 6-11 bar.

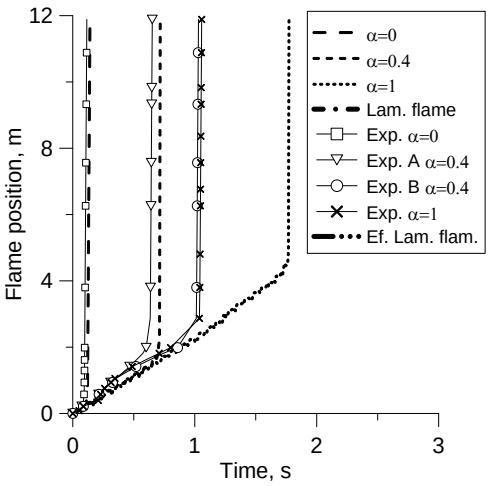

Figure 1. Flame position: calculations (dashed line); experiments (thin solid line). Venting ratio α is indicated.

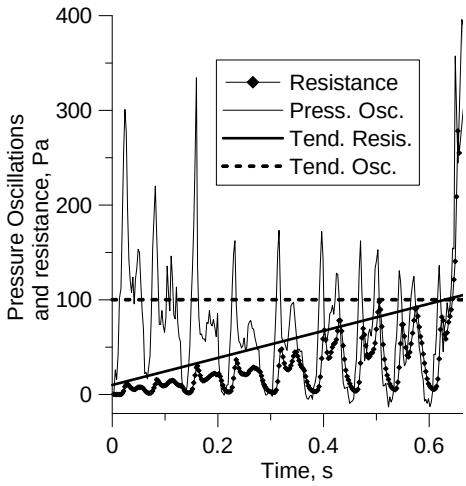

Figure 2. Pressure oscillations and resistance obtained for the case α=0.4

While the flame penetrates in the tube, the combustion products are discharged to the atmosphere through the vent. The hydrodynamic resistance to the flow was expressed as $F=-2c_D\rho u^2/d$, where c_D is the drag force coefficient [6]. The results of the numerical experiments carried out with diverse flow velocities in the range 1-30 m/s allow approximating c_D with the value 0.12. Therefore the total *loss of momentum* can be estimated as $\Delta P=\int F dx$ where integration is taken until the flame front position and the opening of the tube. For the propagation of the flame in the laminar regime the obstacles produce a change in the total surface of the flame and thus the total reaction rate. Within the congested region, cyclic pressure oscillations (Figure 2) and velocity of product discharge will appear. Nevertheless, it is important to underline that no shock waves develop during the entire quasi-laminar regime.

Figure 2 shows how pressure variations slightly compress and decompress the part of the tube filled by the reactants. This area can be understood as a close cylinder, or a *drum*, in which the flame actuates as an oscillating piston. In order to study the compression/decompression cycle of the reactants the one dimensional Euler's equations of continuity and impulse may be used to model the phenomenon. By taking into account the observations performed during the numerical experiments, the oscillations inside the reactants resulted to be mainly of the first harmonic. The

wave equation may thus be simplified to

$$\ddot{p} + \left(0.5 \cdot \pi \cdot \frac{c}{L - x_f}\right)^2 \cdot p = 0 \quad (1)$$

where L is the total length of the tube, c is the local sound velocity in the fresh mixture.

The resistance of the products grows linearly as the flame penetrates inside the tube (see Figure 2, thick line (trend)). When the resistance (about 100 Pa) is comparable with the pressure peaks created by the flame, the products have difficulties to be discharged and a part of them are accumulated inside the tube. The reactants receive an enhanced compression and thus an increased compression-decompression cycle is triggered. Some significant flow appears ahead of the flame. The burning rate, the compression of the reactants and the hydrodynamic resistance are thus enhanced. Next compression-decompression cycle, will drive the flame to a very intense acceleration that will ultimately finish in the fast sonic regime or even detonations.

One dimensional reduced model

In the following 1D model a coarse tube is considered to simplify the model and make it treatable analytically. The effect of the obstacles is taken into account as an enhanced hydrodynamic resistance. Two separate regions of the tube are considered. In the so-called products region, between the flame and the discharge orifice the flow is assumed to be uncompressible. For the reactants, region between the flame and the closed end of the tube, the velocity is considered to be small and the term $u \cdot (grad\ u)$ can therefore be neglected during the initial flame acceleration stage.

With these considerations, the one dimensional equation of the momentum conservation, $(\rho u)_t+(\rho u^2)_x+p_x=F$, can be simplified for the region of the products (between the flame and the discharge orifice) to be

$$\rho u_t + p_x = F. \quad (1)$$

Taking into account the open end and propagation of the flame in the laminar regime, and considering the reactants as uncompressible, the velocity of the products can be defined as $u=-(\sigma-1)\dot{x}_f$ with σ expansion ratio. Operating and integrating between the open end of the tube and the position of the flame

$$\rho(\sigma-1)x_f\ddot{x}_f = P - \rho\sigma(\sigma-1)(\dot{x}_f - S_L) + 2c_D\rho(\sigma-1)^2\dot{x}_f x_f/d \quad (3)$$

This equation contains p_f, the pressure at the flame position in the products side, as a free parameter that can be closed with the equation (1) obtained in the reactants area. The increment of pressure between both sides, in the case of a stationary flame front can be estimated applying Rankine-Hugoniot conditions $\Delta p = \rho\sigma(\sigma-1)\dot{x}_f^2$. The formulation can be re-written considering over-pressure, P, instead of pressure to obtain $P=p_f^+-\sigma(\sigma-1)S_L^2-p_0$. This equation can be coupled with the equation (1) to close the system. The result of this problem are shown in Fig. 3. There is a good agreement of the results obtained with the one dimensional simplification it has to be underlined that the validity of the analysis is restricted to the initiation stage of the flame acceleration.

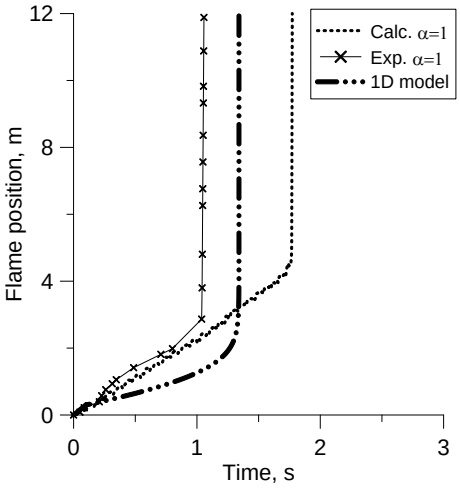

Figure 3. Flame position. Comparison of calculations experiments and one dimensional model.

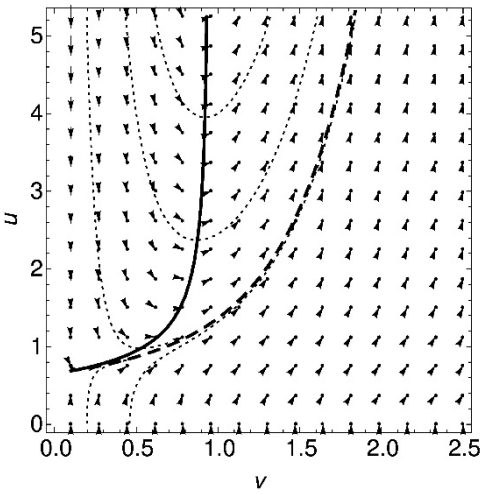

Figure 4. Phase portrait $(x, \dot{x})=(v,u)$: isoclines of the reaction velocity (solid line); streamlines of the vector field (arrows); solution trajectory (dashed)

The most important observation about the system initial behavior, namely, the role of the system isocline of the flame speed equation can be analyzed studying the points $\mathring{u}=0$ that naturally fulfill

$$u^2 = 2d\, S_L^2 c_D \sigma(\sigma-1)/\left(2c_D(\sigma-1)\left(d\,\sigma-2vc_D(\sigma-1)\right)\right) \tag{4}$$

Figure 4 right shows this locus with solid black line that near the origin represents a stable attractor, all trajectories starting nearby converges (fast) to the lower branch of the isocline and follow the detailed solution. Moreover, right after crossing the isocline the system solution trajectories changes the character (speeding up instead of decreasing for initial point above the curve), this make the border line which is asymptotically given by

$$x_f^* = d\,\sigma/\left(2c_D(\sigma-1)\right) = 0.94 \tag{5}$$

a very important and crucial property defining the critical behavior. It explains the transition phenomena in terms of the phase plane.

One clearly sees that if the initial point is on the right from this curve $v=d\sigma/(2c_D(\sigma-1))$ the vector field demonstrates the exponential increase of the flame speed as a function of the flame distance. Additionally, the form of the isocline dependence on the system parameters and variables (4) predicts the sensitivity of the critical phenomena on the initial pressure perturbation with respect to time (critical time equal $t_f^*=1.24$) but the sensitivity is lower with respect to the space. The found asymptotic of the equation physically means that the flame starts rapidly accelerating whenever the pressure jump (drop of the pressure - work of the pressure force) less or equals to the work of the friction forces,

$$\Delta p = \int_0^{x^*_f} F\left(u(t,s)\right) ds \Rightarrow x^*_f = d\,\sigma / \left(2c_D\left(\sigma - 1\right)\right) \quad (6)$$

Thus, when the work of the friction force starts dominate, the pressure in the reaction front increases triggering the flame acceleration due to the cumulative effect of the pressure diffusion. It is very important to note that there no regular singularity (reaching infinity in final time or space as a reaction front position) was observed in the solution of the governing equations, just very smooth and exponential (although hyper-geometric) growth of the system solution was found to take place. This confirms, explains and fully justifies an irregular *shockless* character of the flame acceleration observed in the experiments.

References

[1] Dorofeev, S.B., Sidorov, V.P., Kuznetsov, M.S., Matsukov, I.D., Alekseev, V.I., "Effect of scale on the onset of detonations", *Shock Waves*, 10:137-149 (2000)

[2] Dorofeev, S.B., Kuznetsov, M.S., Alekseev, V.I., Efimenko, A.A., Breitung, W. "Evaluation of limits for the effective flame acceleration in hydrogen mixtures". *J. Loss Prev. Proc. Ind.*, 14:583-589 (2001)

[3] Ciccarelli, G., Boccio, J., Ginsberg, T., Finfrock, C., Gerlach, L., Tagava, H., Malliakos, A., The effect of lateral venting on deflagration-to-detonation transition in hydrogen–air steam mixtures at various initial temperatures. NUREG/CR-6524. Washington, DC: US NRC 1998

[4] Alekseev, V. I., Kuznetsov, M. S., Yankin, Yu. G., Dorofeev, S. B., "Experimental study of flame acceleration and the deflagration-to-detonation transition under conditions of transverse venting", *J. Loss Prev. Proc. Ind.*, 146:591-596 (2001)

[5] Alexiou, A., Andrews, G.E., Phylaktou, H. A, "Comparison between End-Vented and Side-Vented Gas Explosions in Large L/D Vessels, Process Safety and Environmental Protection, 75: 1:9-13 (1997)

[6] Brailovsky, I., Sivashinsky, G.I., "Hydraulic resistance as a mechanism for deflagration-to-detonation transition", *Comb. Flame*, 122: 492-499 (2000)

[7] Bykov, V., Goldfarb, I., Goldshtein, V., Kagan, L., Sivashinsky, G., *Comb. Theory Modelling*, 8: 413-421 (2004)

[8] Sivashinsky, G.I., Combustion in Hydraulically Resisted Flows, *Rev. R. Acad. Cien. Serie A Mat.*, 2001(2) 173-186 (2007)

[9] Scholtyssek, W., Efimenko, A., Kuznetsov, M., "Integral large scale experiments on hydrogen combustion for severe accident code validation", FIKS-1999-00004, 344, 2000

[10] Yanez, J., Kotchourko, A., Lelyakin, A., "Kylcom model for the calcula- tion of under resolved hydrogen combustion problems", in: Bradley, D., Makhviladze, G., Molkov, V. (Eds.), *Proc. Sixth International Seminar on Fire and Explosions Hazards*, Research publishing, 2011, p. 137-149.

CHANGE IN FLAME GEOMETRY OF AN ETHANOL SPRAY FLAME BY VARYING THE INJECTION FREQUENCY

F. C. C. Galeazzo[1,]*, N. K. Fukumasu*, J. A. Denev **, G. C. Krieger Filho*

[1]flavio.galeazzo@usp.br

* Laboratory of Thermal and Environmental Engineering (LETE) of the Polytechnic School of the University of São Paulo, Av. Prof. Mello Moraes, 2231, São Paulo, Brazil

** Karlsruhe Institute of Technology, Steinbuch Centre for Computing, Hermann-von-Helmholtz-Platz 1, 76344 Eggenstein-Leopoldshafen, Germany

Abstract

Turbulent swirl flames using fuels sprays are found in many combustion systems. The use of a pulsed spray injection allows the realization of different flames types using the same burner, as sprays with different characteristics can be produced. Two different flame types have been studied experimentally and numerically: a burner-attached and a lifted flame.

Large-eddy simulations using Lagrangian particles to represent the spray and a combined presumed PDF and tabulated chemistry approach to model the turbulent combustion were able to represent the different flame types satisfactorily.

The numerical results have been used to investigate the phenomena leading to the different flame geometries, showing that the burner-attached flame is caused by a destructive interaction between the spray droplets and the central recirculation zone (CRZ). In the case of a lifted flame, the CRZ remains preserved.

Introduction

Turbulent swirl flames using liquid fuels in the form of spray are found in many combustion systems, such as gas turbine combustors and industrial furnaces. Due to the dynamics of fuel droplets, spray flames exhibit a broad distribution of air-fuel mixtures. Premixing occurs between the swirl flow and surrounding air, while fuel vapor is supplied by the evaporating droplets, continuously changing the local stoichiometry.

The use of a pulsed spray injection allows the active control of the interaction between the droplets and the swirling flow, making possible the realization of flames with different characteristics using the same burner [1]. With the operating conditions used in the current study, two different flame types are generated: a burner-attached and a lifted flame.

The objective of the present work is to verify if the proposed numerical models are able to represent the different flame types observed experimentally. A second objective is the use of numerical results to investigate the phenomena leading to the

different flame geometries.

Experimental setup

The test bench consists of an open burner comprising a swirl-type flame stabilizer and an automotive fuel injector, as shown in Figure 1. The swirler has ten vanes, with variable angle α between 17.7° and 43° relative to the axial direction, an axial length of 15.5 mm, an inner diameter of 17.5 mm and an outer diameter (D) of 40.0 mm. The geometric swirl number S is 0.62, calculated as the area averaged tangent of α. This swirl number promotes the appearance of central recirculation zone (CRZ) and precessing vortex core (PVC) structures [2].

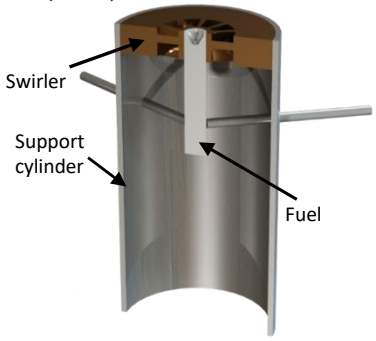

Figure 1. Schematic cross-section of the burner comprising a swirl-type flame stabilizer and an automotive fuel injector.

A solenoid fuel injector (pn: 0280150747 from BOSCH GmbH) is used to produce the pulsed fuel spray, in which a Pulse Width Modulated signal (PWM) is applied to specify both the injection frequency (fi) and the duty cycle (dc) of the valve. The duty cycle defines the duration of fuel injection per cycle (ti), as described in more detail in [1]. Two conditions have been selected to be compared with simulations, with injection frequencies of 100 Hz (ESF100) and 400 Hz (ESF400). The duty cycles have been adjusted to allow the same fuel mass flow for both injection frequencies (see Table 1). The droplet diameter distribution has been measured using the Phase Doppler Interferometry (PDI) technique and reported in ref. [1].

Table 1. Boundary conditions of the simulations.

	ESF100	ESF400
Air flow	6.6 ± 0.7 g/s	
Air temperature	27 ± 3° C	
Ethanol flow	438 ± 6 mg/s	
Ethanol temperature	35 ± 3°C	
Injection frequency	100 Hz	400 Hz
Injection time per cycle	2.90 ms	1.47 ms
Spray angle	0°	31° - 61°

Liquid anhydrous ethanol (99.6% by volume) is used as fuel. The boundary conditions used in the current experiments are listed in Table 1. The thermal power of the flame is 60.2 kW, and the Reynolds number, calculated with the bulk velocity and the hydraulic diameter of the swirler vanes, is Re = 3878. At this Reynolds number, the flow produced by the swirler is turbulent, mainly induced by the strong shear layer created by the swirling flow.
The time-resolved Particle Image Velocimetry (PIV) technique was applied to measure the air flow in isothermal conditions [1]. The visible-range chemiluminescence was used as the indicator of the flame geometry. It has been recorded using a simple digital imaging system.

Numerical setup
Simulations using the LES (Large Eddy Simulation) methodology have been performed with the software OpenFOAM version 2.3.1 [3]. The computational domain has a diameter of 16 D and extends 6 D upstream and 15 D downstream of the swirler, and was discretized using the finite volume method, with 1.8 million hexahedral elements. Figure 2 shows the computational domain with the orientation axis and a detail of the computational grid of the swirler.

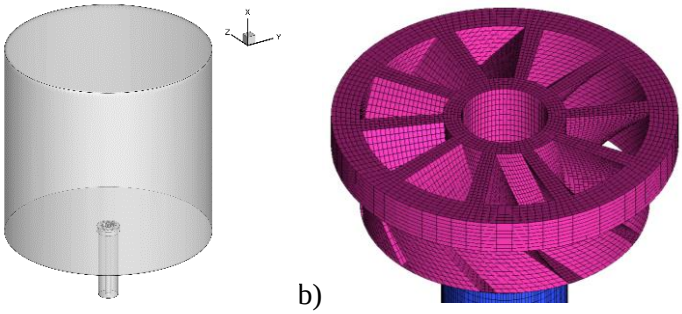

a) b)

Figure 2. Computational domain with orientation axis (a) and detail of the computational grid of the swirler (b).

The dynamic version of the Smagorinsky subgrid-scale model (SSG) was employed in the simulations [4], [5]. The modeling of the ethanol spray was based on the technique of Lagrangian particle tracking, The initial droplet diameter distribution was modeled using an ensemble of Gaussian distribution functions, reproducing the distribution determined experimentally [1]. The different spray angles observed for different injection frequencies are implemented in the simulations (see Table 1).
The turbulent combustion is modeled using a combined presumed PDF and tabulated chemistry approach, and is an extension of the model used by Prathap *et al.* [6] and Eiberger *et al.* [7]. In the Joint Probability Density Function (JPDF) model, four independent variables are used to define the thermodynamical state of the system: the mean values and variances of the mixture fraction f and reaction progress variable c. Employing a beta-PDF distribution, the marginal PDFs of f and c are

calculated, and the joint probability is defined, assuming a statistical independence between them. As the flame in this study burns lifted and is not confined by side walls, the heat losses are mainly due to the heat of evaporation of the ethanol spray, which is small and therefore neglected in the current simulations.
A detailed ethanol combustion mechanism [8] (37 species and 167 reactions) is used to solve premixed laminar flames covering the entire spectrum of mixture fractions. To allow the visualization of the chemiluminescence, a reaction mechanism for the OH* species has been added [9] (1 species and 11 reactions), which is one of the responsible species for the visible-range chemiluminescence.

Results

For the simulation of the isothermal flow, the mean values were collected in 3 s of physical time. Figure 3a shows results of the mean axial velocity at selected axial positions. The main features of the mean flow are reproduced satisfactorily, with the position and size of the central recirculation zone (CRZ) reproduced well. The intensity of the CRZ, however, is underpredicted. Simulations with more refined grids are being prepared to resolve the CRZ correctly.

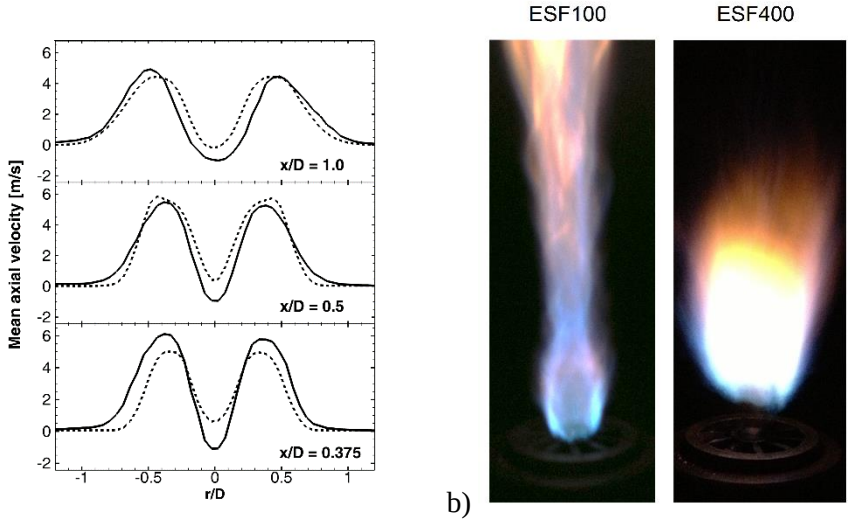

Figure 3. Line plots of the mean axial velocity of the isothermal flow at selected axial positions. Experiment, solid line; LES, dashed line (a) and visible-range chemiluminescence of cases ESF100 and ESF400 (b).

Figure 3b shows photographs of the visible-range chemiluminescence of the studied flames. The light intensity threshold was kept constant, allowing a direct comparison between the images. Different flame geometries are observed, depending on the injection frequency: the flame ESF100 has a more elongated and narrow shape, burning attached to the swirler; while the flame ESF400 is shorter and wider. In the flame ESF400 is also possible to identify a region close to the burner that does not present spontaneous chemiluminescence, suggesting the formation of a lifted flame.

Figure 4 shows the volume rendering of the mean OH* mass fraction for the LES of flames ESF100 and ESF400. The comparison of the predicted flame geometries with the experimental data from Figure 3b is very good, showing that the proposed numerical model is able to capture the mechanism leading to the different flame geometries. The flame ESF400 burns lifted in the LES, as the experiments have suggested.

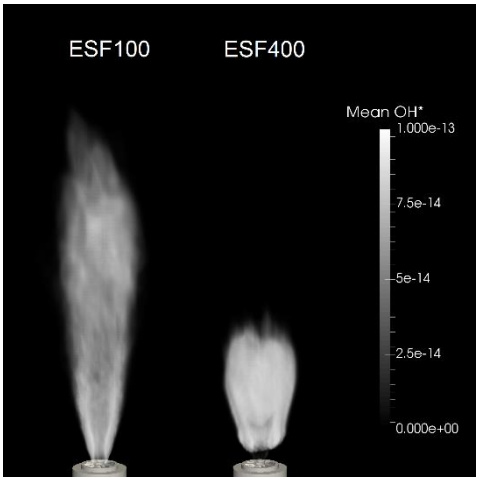

Figure 4. Volume rendering of the mean OH* mass fraction for the simulations ESF100 and ESF400.

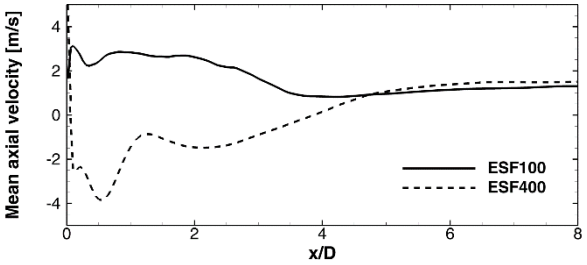

Figure 5. Line plots of the mean axial velocity at the centerline for the simulations ESF100 and ESF400.

The very different flame geometries can be explained by the interaction of the spray droplets with the CRZ. The spray angle of ESF100 is mainly axial, which promotes a destructive interaction with the CRZ, as the droplets have positive axial velocity while the CRZ has negative axial velocities at the centerline. On the other hand, the broader spray angle of ESF400 disturbs only slightly the CRZ, allowing a typical swirl flame to stabilize. Figure 5 presents the mean axial velocity at the centerline for both simulations, showing that the CRZ of ESF100 is effectively destroyed by the spray droplets, exhibiting only positive axial velocities, while the CRZ of ESF400 remains preserved.

Conclusion

Turbulent swirl flames with pulsed ethanol spray injection have been studied experimentally and numerically. The employed simulation methodology was able to represent the different flame types satisfactorily. More refine numerical grids are needed to resolve the CRZ correctly.

The fuel injector produces different spray spatial distributions depending on the injection frequency, which has an important impact on the formation of the central recirculation zone (CRZ). In the case with a mainly axial spray (ESF100), the CRZ is destroyed by the interaction with the droplets and a burner-attached flame develops. On the other hand, the case with a broader spatial distribution of the spray (ESF400) shows an active CRZ and the stabilization of a typical swirl flame.

Acknowledgments

This work was supported by the São Paulo Research Foundation (FAPESP), grant number 2013/50238-3.

References

[1] N. K. Fukumasu, J. I. Yanagihara, and G. C. Krieger Filho, “Influence of fuel injection frequency on droplet dispersion in ethanol pulsed spray flames,” *Appl. Therm. Eng.*, vol. 81, pp. 198–209, 2015.

[2] N. Syred, “A review of oscillation mechanisms and the role of the precessing vortex core (PVC) in swirl combustion systems,” *Prog. Energy Combust. Sci.*, vol. 32, no. 2, pp. 93–161, 2006.

[3] H. G. Weller, G. Tabor, H. Jasak, and C. Fureby, “A tensorial approach to computational continuum mechanics using object-oriented techniques,” *Comput. Phys.*, vol. 12, no. 6, pp. 620–631, 1998.

[4] M. Germano, U. Piomelli, P. Moin, and W. H. Cabot, “A dynamic subgrid-scale eddy viscosity model,” *Phys. Fluids A Fluid Dyn.*, vol. 3, no. 7, p. 1760, 1991.

[5] D. K. Lilly, “A proposed modification of the Germano subgrid-scale closure method,” *Phys. Fluids A Fluid Dyn.*, vol. 4, no. 3, p. 633, 1992.

[6] C. Prathap, F. C. C. Galeazzo, P. Kasabov, P. Habisreuther, N. Zarzalis, C. Beck, W. Krebs, and B. Wegner, “Analysis of NOX Formation in an Axially Staged Combustion System at Elevated Pressure Conditions,” *J. Eng. Gas Turbines Power*, vol. 134, no. 3, p. 31507, 2012.

[7] F. Eiberger, P. Habisreuther, N. Zarzalis, and F. Turrini, “Evaluation of the Turbulence Radiation Interaction and the Validity of the Optically Thin Fluid Approximation in a High Turbulent Premixed Methane Flame,” in *ASME Turbo Expo 2015: Turbine Technical Conference and Exposition*, 2015, p. V05CT17A006.

[8] M. J. E. Demétrio, “Análise de mecanismos cinéticos para a combustão de etanol,” Universidade Federal de Santa Catarina, 2013.

[9] T. Kathrotia, U. Riedel, A. Seipel, K. Moshammer, and A. Brockhinke, “Experimental and numerical study of chemiluminescent species in low-pressure flames,” *Appl. Phys. B Lasers Opt.*, vol. 107, no. 3, pp. 571–584, 2012.

An experimental investigation of emulsification effect on Heavy Fuel Oil droplet combustion

Paolo Guida*, William.L.Roberts*
paolo.guida@kaust.edu.sa
* Clean Combustion Research Centre, King Abdullah University of Science and Technology, 23955-6900 Thuwal, Saudi Arabia.

Abstract
The purpose of this study is to investigate the burning behavior of Heavy Fuel Oil/Water emulsified droplets with a single suspended droplet experiment. In the suspended droplet experiment, the droplet is suspended on a fine thermocouple wire and exposed to a hot environment until the evaporation, or eventual combustion process is completed. The whole experiment is recorded with a high speed camera. This experiment permits to measure the evolution of the droplet size and the liquid phase temperature in time. The emulsions are prepared using a supersonic homogenizer and a commercial surfactant. Three samples with different water percentage were analyzed. Particular effort is dedicated to micro-explosions that are of key importance in the spray combustion.

Introduction
Heavy Fuel Oil (HFO) is a widely used fuel, in particular in marine engines and power generation technologies [1]. The HFO combustion has a very significant environmental impact, this is why several technologies have been developed to reduce the amount of pollutants this process generates. The use of an emulsified fuel is one of the possible alternatives to reduce the emissions of pollutants.
This solution has been previously studied in previous works [2].
Since in every application this fuel burns in the form of a spray, a better understanding of the droplet combustion is necessary.
The suspended droplet technique was used for this purpose. The experiment consists in suspending a droplet on a fine thermocouple wire and successively exposing it in a hot environment to observe its evaporation and eventual combustion. Three different samples were compared with pure HFO to explore the influence of the emulsification process on the combustion characteristics and the relevant parameters.

Preparation of the emulsified fuel
The HFO sample was collected from Shuaibah power plant in Saudi Arabia. The HFO in Saudi Arabia has an asphaltene content range between 7 w% to 15 w% (weight percentage) and sulfur content of 3 w% to 4 w%. Physical and chemical properties of the fuel used in this work can be found in the work of Elbaz et al [1].
A commercial surfactant was used as an emulsifying agent to prepare the water in oil emulsion. Three samples were made containing 5±0.1, 8±0.1 and 14±0.1 vol% (volume percentage). The w/o emulsified fuel was prepared dripping water and the

emulsifying agent into the raw fuel, and mixing the solution using a supersonic homogenizer (Hielscher UP400S 400) at the frequency of 12 kHz for 20 minutes. The experiments were done 3 days after the preparation of the samples and the stability of the mixture was tested two times using a centrifuge. The initial amount of water was respectively 5, 10 and 20 vol% for the three samples and no further separation was observed after the first centrifuge.

Suspended droplet experimental setup

Preheated air co-flow by an inline heater (Sylvania heater, F074719, 8000 Watt) goes upwards through a ceramic honeycomb from the bottom of a hinged tube furnace (Lindberg/blue, HTF55000 series) through quartz tube (134 mm inner diameter and 750 mm length). The co-flow air is assumed to be uniform after that and can be controlled with flow rate up to 130 l/min. Once the temperature profile inside the electrical furnace reaches required values, HFO droplet is suspended on a fine thermocouple wire (Type S, 75 µm diameter, Omega P10R-003). The thermocouple is inserted inside a two-hole ceramic tube and connected to a computer for data processing and temperature readings. The droplet is positioned into the preheated electrical furnace by a 3D mechanism through an air cooling channel. This channel will keep the droplet temperature low until the burning point inside the furnace is reached. High speed camera (LaVision, Imager HS) is used to record the whole HFO droplet combustion process and a data acquisition card to read the temperature history inside the droplet from the thermocouple.

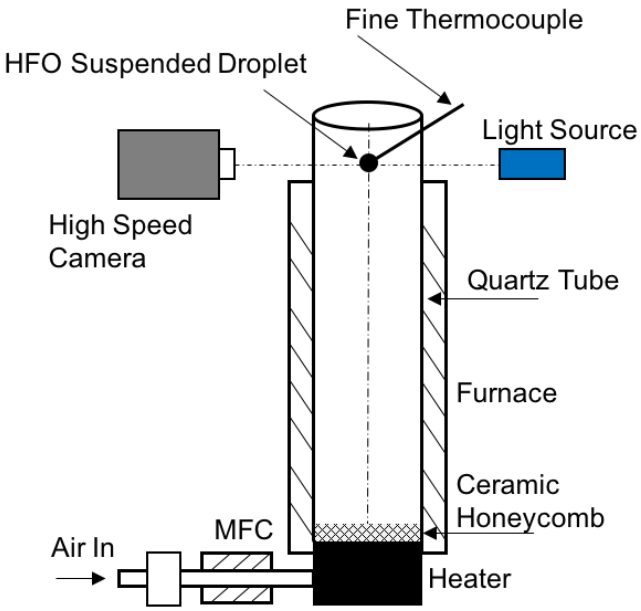

Figure 1. Experimental setup**.**

Combustion behavior of the raw fuel

Figure 2 shows the liquid phase temperature history for a single suspended HFO droplet with no water addition. It is possible to divide the combustion in several steps as in [4]. Initially the temperature rises and the most volatile species evaporate forming a vapor cloud around the droplet. During the first step, the droplet size oscillates as a consequence of the differential evaporation of the various species. It is typical of multicomponent fuel to present a disruptive behavior called micro-explosion. This phenomenon causes a secondary atomization process that suddenly enhance the surface area leading a faster evaporation.

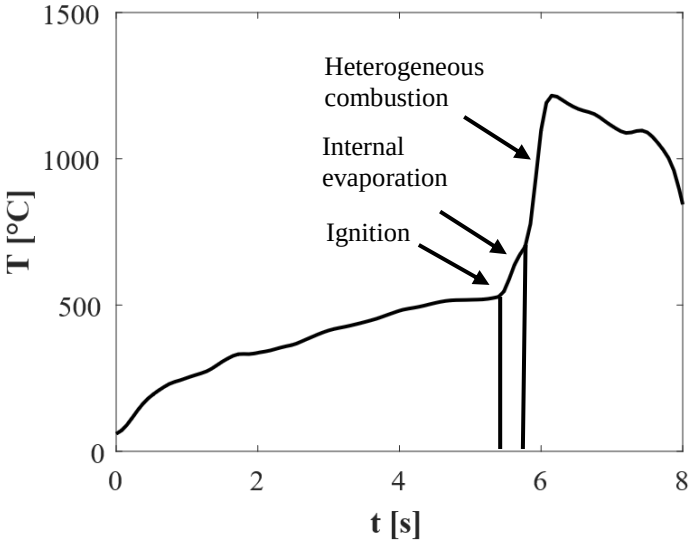

Figure 2. Distinctive combustion stages of HFO.

The second step consists in the ignition of the cloud that surround the droplet. The formation of the flame around the droplet generates a rapid increase of the liquid temperature that coincides with a faster nucleation and, as a consequence, more frequent micro-explosions. At the end of this step the liquid phase does not surround the thermocouple, but a carbonaceous residue remains on the junction. This residue is exposed to the air flux leading the heterogeneous combustion, with consequent temperature increment above 1200 °C.

Emulsion influence

Figure 3 shows how the normalized squared diameter evolves in time for the 4 samples. The peaks in the initial part of the graph can be associated with the micro-explosive behavior of the fuel, while, those at the end, correspond with the massive internal evaporation and consequent consumption of the liquid phase (for the emulsified fuel) or cenosphere formation (for the pure sample). The increment of the droplet size at the beginning is much more consistent for the emulsified fuel. In

particular, for the 14 vol% sample (d) the oscillation of the size is remarkable and it is direct consequence of the fact that the volatility of the water is much higher than the average volatility of the species that form the heavy fuel oil. At the end of this phenomenon the size of the droplet is much smaller and the reduction of size randomly changes among the different runs. A more stable evaporation process follows the initial micro-explosions until the combustion takes place.

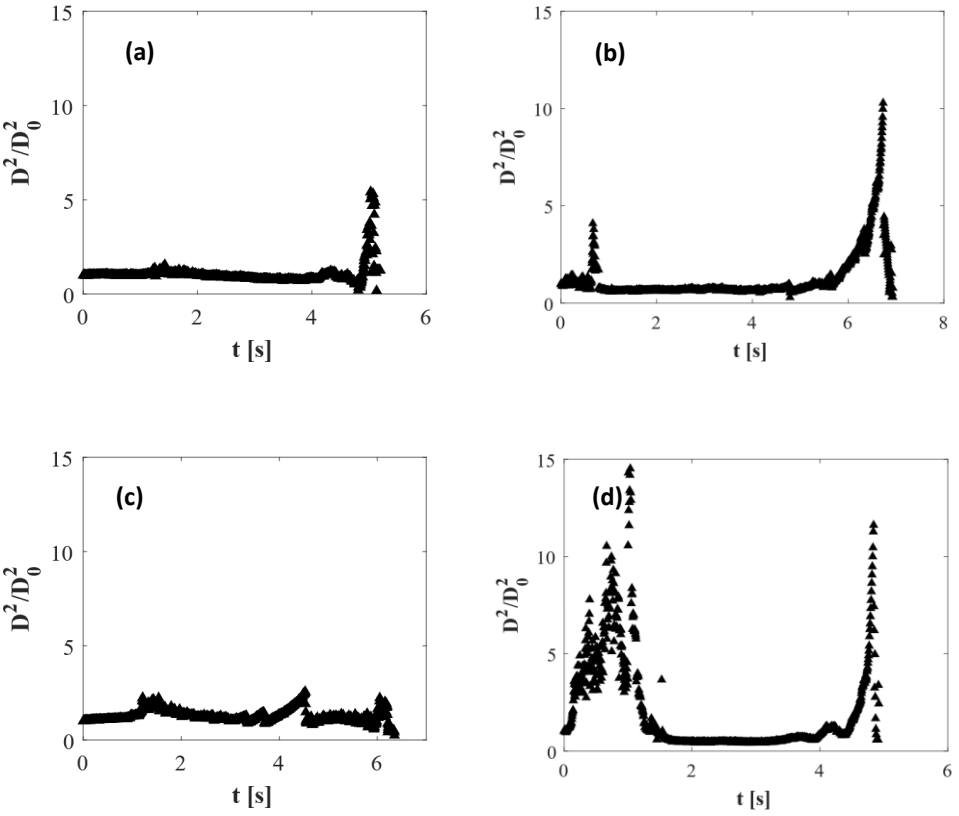

Figure 3. Normalized squared diameter profile for the raw sample (a), 5 vol% (b), 8 vol% (c) and 14 vol% (d). The droplet diameter for the cases is 1.15±0.05 mm.

The temperature profile in Figure 4 shows the liquid phase temperature history for four droplets with different w/o percentage. The temperature grows regularly for the raw sample while as the water percentage increases it becomes more unstable, The ignition delay time (IDT), that is defined as the time occurs from the entrance to the ignition, is higher for the raw sample with respect to the 8 and 14 vol% samples. This trend can be justified considering the reduced size of the droplet after the initial micro-explosions. The 5 vol% sample, vice-versa, presents a higher IDT,

this finding appears reasonable considering the droplet size of this sample, after the micro-explosions, is not as influenced as in the previous cases.

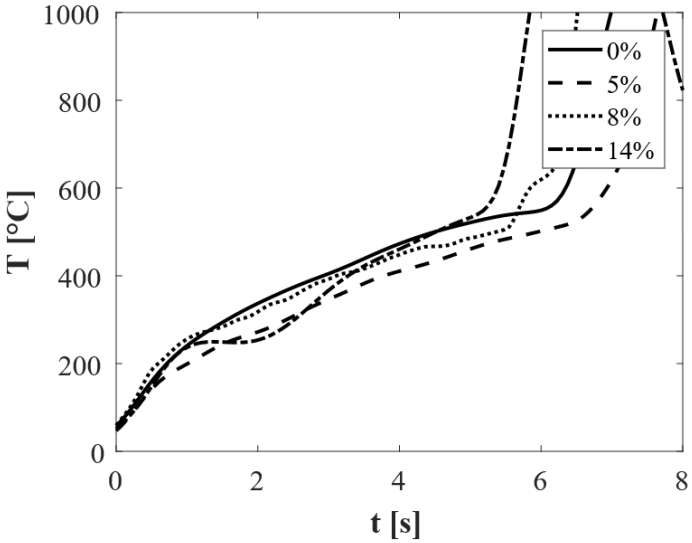

Figure 4. Liquid phase temperature for the raw sample (a), 5 vol% (b), 8 vol% (c) and 14 vol% (d). The droplet diameter for the cases is 1.41±0.05 mm.

A sequence of the 5 vol% combustion is present in Figure 5. In the first three pictures it is possible to observe that the droplet size increases extremely even in absence of flame. The fourth picture shows the water bubbles that grow as a consequence of the high temperature. A similar trend was observed by [3]. Once the bubble growth reaches the limits and the surface tension is not high enough to sustain the pressure, the water leaves the droplet as vapour and the rest of the fluid that remains on the thermocouple burns until its full consumption. No traces of cenosphere is present for the emulsified fuel but some ashes are released.

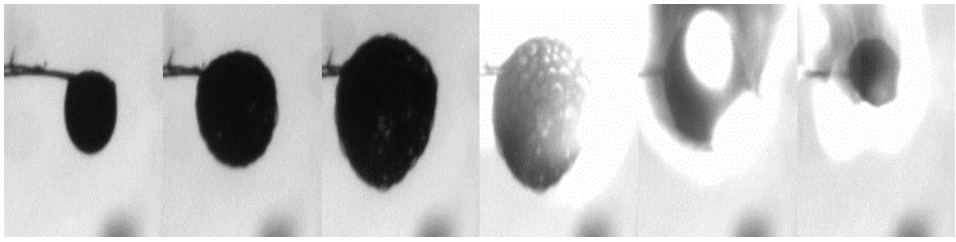

Figure 5. A sequence of the 5 vol% sample combustion.

Conclusions and Outlooks

An experimental analysis on the single emulsified droplet combustion was performed in order to extend the knowledge of this phenomenon.
The main steps of the combustion process were identified and the differences between the various w/o percentages were explored.
One of the most important finding is that the ignition delay time is not directly proportional to the amount of water in the fuel. The IDT mainly depends,in fact, on the micro-explosions intensity and frequency that can lead to unpredictable trends.
To enhance the understanding of this phenomenon more experiments are in progress. A wider amount of data permits to identify a statistical trend.
Previous researches [5] moreover suggest an influence of the asphaltene percentage on the emulsified fuel combustion. This topic is currently under investigation.
The effect of the emulsion mixing procedure is another key aspect to explore, in particular, the photomicrografy technique permits to measure the size of the micro-droplets of water inside the mixture and estimate how this factor influences the droplet stability. Two more different experiments are actually in progress at KAUST, the falling droplet experiment, that permits to avoid the influence of the thermocouple on the droplet combustion and the spray combustion which gives a more general view of the problem.

Acknowledgment

Research reported in this publication was supported by the Saudi Electricity Company (SEC) in collaboration with the Clean Combustion Research Center (CCRC) at King Abdullah University of Science and Technology (KAUST).

References

[1] A. G. N. H. A.-H. E. S. M. S. a. W. L. R. A. M. Elbaz, «TG/DTG, FT-ICR Mass Spectrometry, and NMR Spectroscopy Study of Heavy Fuel Oil,» *Energy Fuels,* p. 7825–7835, 2015.

[2] R.-B. R. AntonioDiego-Marin, «An experimental study of the effect of water content on combustion of heavy fuel oil/water emulsion droplets,» *Combustion and Flame,* vol. 126, n. 4, pp. 1845-1855, 2001.

[3] Y. S. T. H. Y. M. H. A. T. M. Hirotatsu Watanabe, «An experimental investigation of the breakup characteristics of secondary atomization of emulsified fuel droplet,» *Energy,* vol. 35, pp. 806-813, 2010.

[4] G. M.Ikegami, «Distinctive combustion stages of single heavy oil droplet under microgravity,» *Fuel,* vol. 82, n. 3, pp. 293-304, 2003.

[5] M.T.JacquesJ.B.JordanA.WilliamsL.Hadley-Coates, «The combustion of water-in-oil emulsions and the influence of asphaltene content,» *Symposium on Combustion,* vol. 16, n. 1, pp. 307-319, 1977.

A CFD FRAMEWORK FOR EVAPORATING FUEL DROPLETS IN A GRAVITY FIELD

A.E. Saufi, A. Cuoci, A. Frassoldati, T. Faravelli
abdessamade.saufi@polimi.it
Dip. Chimica, Materiali e Ingegneria Chimica, Politecnico di Milano, 20133 Milano, Italy

Abstract
A comprehensive CFD model for the simulation of evaporating droplets under gravity conditions is here presented. The model is based on the Volume Of Fluid (VOF) methodology [1], which allows an accurate tracking of the gas-liquid interface with excellent mass conservation properties. The whole flow and temperature field are given by a single momentum and energy equation valid for both phases. Three numerical simulations are presented: an assessment of mass conservation of the CFD code and a comparison between the absence and the presence of a gravity field in the evaporation of a n-heptane droplet. A final section on the presence of internal recirculation in the liquid phase is also presented.

Introduction

The high energy density of liquid fuels is exploited nowadays in many engineering applications such as internal combustion engines, industrial burners and sprays. In these systems the fuel is used after a proper atomization, in order to minimize pollution problems and increase the efficiency. The study of the complex interacting phenomena occurring among this large amount of droplets is essential, but still too complex to be handled. In order to simplify the problem, isolated droplets are usually studied, both from an experimental and numerical point of view. Numerous analyses can be found on isolated droplets evaporation and combustion [3], and they can be divided in two main areas. The first in which microgravity conditions are imposed. The FLEX campaign [3] showed many phenomena regarding isolated droplets in microgravity conditions and the mathematical modeling of these systems it is still a wide and interesting area of research. The microgravity condition allows a relatively simple modeling, since 1D geometry is established and because many effects such as surface tension, natural convection and droplet deformation can be easily neglected. However, in most of the engineering applications these phenomena are important and they often control the physics of the problem; the presence of forced or natural convection heavily affects the evaporation rate, as well as the droplet deformation which locally modifies the droplet surface [4]. This is why most of the experiments are done in gravity conditions, which also allow much cheaper experimental devices. The drawback is that in this case the mathematical modeling is more complicated. The droplet has now a 3D geometry, its shape and curvature depend on surface tension. Moreover, the liquid and gas phase velocity field has to be calculated in order to

account for external convection and internal liquid recirculations, which are known to be key phenomena for a correct modeling of droplets [5].
In this work a multiphase CFD model has been developed, exploiting the VOF methodology to dynamically track the liquid interface. This method is a one-fluid approach, widely known for its simplicity, robustness and mass conservation properties. The liquid volume fraction is tracked by a function α, while the interface is advected geometrically [6]. A single equation of motion is written for the whole flow field, modeling therefore a single fluid with step physical properties. This methodology has been successfully implemented to model bubbles growth, liquid films [2] and it is widely used in naval engineering problems.
The main drawback in VOF approach is the modeling of surface tension driven flows. Small droplets (~1-2 mm diameter) have a very large interface curvature, whose value is needed to compute the surface tension force. The numerical evaluation of curvature from α step-function is a numerical challenge and errors in this calculation form unphysical velocities around the interface called parasitic currents, which can easily propagate [9]. Many ways have been proposed to reduce this problem [8], but none of them is able to completely eliminate the parasitic currents, in particular for such small droplets. In order to overcome this problem, a small spherical fiber is place inside the droplet and a centripetal force directed towards its center has been imposed, in order to keep it strongly held to the fiber even when gravity is present. In this system surface tension is not needed anymore and it can be neglected, eliminating parasitic currents directly from their source.

Mathematical modeling
The governing equations for the multiphase CFD model are here presented. The VOF methodology has been used, where a step function α tracks the liquid volume fraction. The solver is based on the OpenFOAM 4.x framework.
The transport equation for α is here reported:

$$\frac{\partial \alpha}{\partial t} + \nabla \cdot (\alpha \vec{v}) = -\frac{\dot{m}}{\rho_L} \tag{1}$$

The liquid volume fraction has a negative source term because of evaporation. The transport properties (thermal conductivity, viscosity and diffusion coefficients) are weighted by the α function. The momentum equation describes the whole flow field:

$$\frac{\partial \rho \vec{v}}{\partial t} + \nabla \cdot (\rho \vec{v} \vec{v}) = \nabla \cdot \mu (\nabla \vec{v} + \nabla \vec{v}^{\mathrm{T}}) - \nabla p + \rho \vec{g} \tag{2}$$

while the energy equation provides the temperature field:

$$\rho C_p \left(\frac{\partial T}{\partial t} + \nabla \cdot (\vec{v} T) \right) = \nabla \cdot (k \nabla T) - \dot{m} \Delta h_{ev} \tag{3}$$

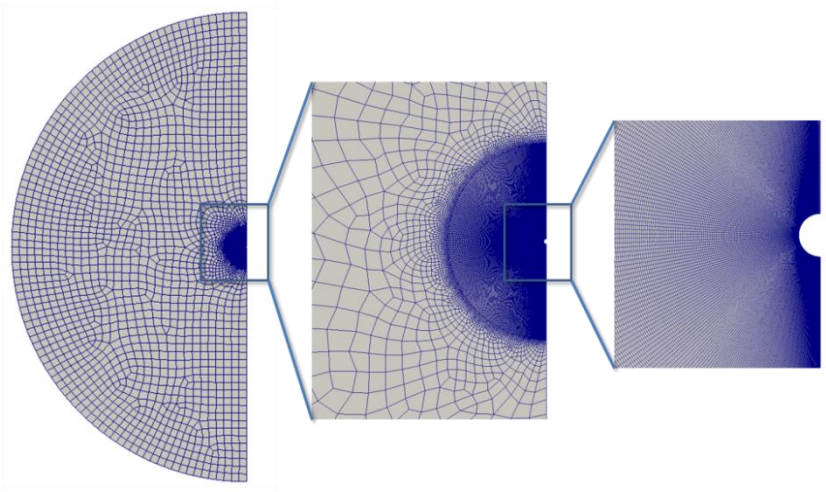

Figure 1: Computational mesh in three different levels of detail. Global geometry (left figure) and fiber (right figure).

Concerning the species transport, the equation is written only for the saturated mass fraction following the approach proposed by Banerjee [10]. The equilibrium vapor mass fraction at the interface is computed through ideal thermodynamics and from the interface is diffused into the gas phase. It is extremely important to correctly model the species diffusion since the evaporating flux is not obtained by semi-empirical laws [2], but it directly depends on the mass fraction gradient at the liquid-gas interface:

$$\dot{m} = -\frac{\rho \mathfrak{D}_i \nabla \omega_i}{1 - \omega_i} \nabla \alpha \tag{4}$$

Where the term $1 - \omega_i$ accounts for the Stefan flow induced by evaporation. The α gradient describes the interface surface per unit volume [4] and forces evaporation to happen only at the interface (where the gradient is different from zero). Equation (4) also accounts for the cooling of the surface when evaporation occurs.
All the transport properties for liquid and gas phases are given by the OpenSMOKE++ library [11], developed at Politecnico di Milano.

Setup of the numerical simulation
The computational mesh describes an axisymmetric domain (Figure 1), where only a 5° angle of a global spherical geometry is accounted for. The domain diameter is 50 mm, while the liquid droplet (placed at the center of the domain) diameter is 1

mm. Inside the droplet a spherical fiber (d = 0.1 mm) is placed. The mesh is made by 110,000 cells, chosen by a sensitivity analysis on the cells size. The time step is controlled by the Courant number (< 1) .
The initial droplet diameter is 1 mm for all the simulations and the fuel is n-heptane.

Monocomponent droplet evaporation

In this work three simulations are presented: the first one is done in microgravity conditions, only to verify the correct mass conservation of the code. A fixed mass flux $\dot{m}$ is imposed and the diameter behavior in time given by the CFD code is compared with the simple analytical solution $D(t) = \sqrt[3]{D_0^3 - \frac{6\dot{m}}{\rho\pi}t}$

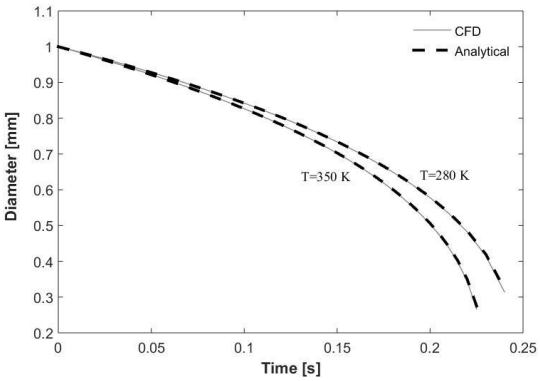

Figure 2: Diameter vs. time plot for two different temperatures. CFD results vs. analytical solution.

The results are shown in Figure 2 showing a good agreement with the given analytical solution. This is a key simulation in order to assess if the source term in equation (1) is correctly implemented. This has been done for two temperatures (T = 350 K and T = 280 K) to verify the effect of the consequent difference in the liquid density. The other two simulations concern the diffusion controlled evaporation of a liquid droplet of n-heptane in microgravity and in gravity conditions. In Figure 3 we can see the liquid volume fraction field α, the fuel mass fraction and the velocity field for the two simulations. Differently from the 1D codes, the CFD simulation can provide an immediate visualization of the vapor cloud which is formed around the droplet during the evaporation. When gravity is present, an important velocity field is formed because of the high density difference between the air and the released heptane vapor which heavily modifies the cloud shape around the droplet.

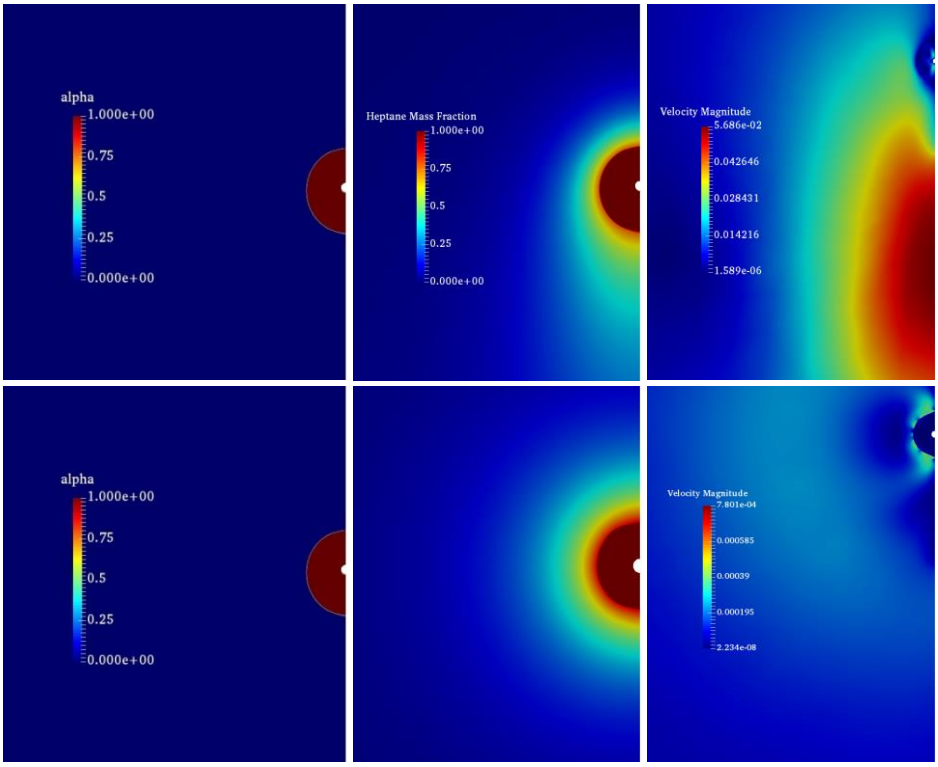

Figure 3: Liquid volume fraction α (left), fuel mass fraction (middle) and velocity field (right). Simulations in gravity (top) and microgravity (bottom) conditions.

Internal liquid recirculations

1D codes for the modeling of droplets evaporation usually suffer from an under estimation of the heat transfer from the gas to the liquid phase [3]. This is because 1D model cannot predict the internal recirculations, caused by temperature or concentration gradients and by the shear stress on the liquid surface given by the external gas motion. In the presented model the liquid velocity field is naturally included in the solution of Equation (2), as can be seen in Figure 4. The net effect of this velocity field is the higher internal mixing which enhances heat and mass transfer.

Conclusions and future developments

A three-dimensional CFD model for the evaporation of fuel droplets has been developed. The VOF method has been used to track the liquid interface and it is coupled with the solution of a velocity, temperature and concentration field. The presence of gravity induces natural convection around the droplet modifying the vapor cloud shape. The external gas flow also causes internal recirculation in the liquid phase, because of the external applied shear stress.

Future developments concern the validation of the evaporative model with experimental data and the activation of gas-phase reactions.

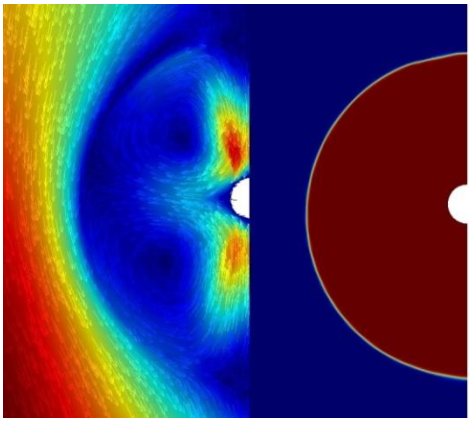

Figure 4: Liquid volume fraction α (right) and velocity field [0-2 cm/s] inside and outside the droplet during the evaporation (left).

References

[1] Hirt C.W., Nichols B.D., "VOF Method for the Dynamics of Free Boundaries", *Journal Of Computational Physics* 39, 201-225 (1981)

[2] Nabil M., Rattner S. A., " A framework for two-phase flow simulations with thermally driven phase change" *SoftwareX* 5, 216-226 (2016)

[3] Cuoci A. et. al. "Autoignition and burning rates of fuel droplets under microgravity" *Comb. and Flame* 143, 211-226 (2005)

[4] Soh G.Y., Yeoh G.H., Timchenko V. "An algorithm to calculate interfacial area for multiphase mass transfer through the VOF method" *Int. Journal of Heat and Mass transfer* 100, 573-581 (2016)

[5] Jaeheon S., Hong I., C. Suk-Ho "A computational study of droplet evaporation with fuel vapor jet ejection induced by localized heat sources" *Physics of Fluids* 27, (2015)

[6] Roenby J., Bredmose H., Jasak H. "A computational method for sharp interface advection" *Royal Society Open Science* (2016)

[8] Cummins S.J. et.al. "Estimating curvature from volume fractions" *Computers and structures* 83, 425-434 (2005)

[9] Raeini A.Q. et. al. "Modelling two-phase flow in porous media at the pore scale using VOF method" *Journal of Comp. Physics* 231, 5653-5668 (2012)

[10] Banerjee R. "An algorithm to determine the mass transfer rate from a pure liquid surface using the VOF multiphase model" *Int. Journal Engine Research* (2004)

[11] Cuoci et. al. "OpenSMOKE++: An object-oriented framework for the numerical modeling of reactive systems with detailed kinetic mechanisms "*Computer Physics Communications* 192, 237-264 (2015)

EXPERIMENTAL AND NUMERICAL EVALUATIONS ON THE CHARACTERISTICS OF VENTED METHANE EXPLOSION

LUO Zhen-min[a]*, SU Bin[a], WANG Tao[a], CHENG Fang-ming[a], ZHAO Jing-yu[a]
zmluo@xust.edu.cn
[a] School of safety science & Engineering, Xi'an University of Science and Technology, 58, Yanta Mid. Rd., Xi'an 710054, Shaanxi, PR China

Abstract
In order to provide the reference for the prevention of methane explosion accidents in the pipeline, coal mine tunnel or other closed space, the relative experiments and simulations were carried out. In this paper, explosion characteristics and flame propagation characteristics of methane in pipeline and coal mine tunnel are studied by using an explosion test system, combined with FLACS code, under different venting conditions. The numerical simulation results of methane explosion are basically consistent with the physical experiment. Which indicates the numerical simulation for methane explosion is. The results show that explosion parameters (pressure, temperature and product concentration) of methane at five volume fractions have the same change trend. Nevertheless, the explosion intension of 10.0% methane is the largest and that of 9.5% methane is relatively weak, followed by 11.0% methane, 8.0% methane and 7.0% methane respectively. Under different venting conditions, the pressure and temperature of methane explosion are the highest in the pipeline without a vent, followed by the pipeline where ignition and vent position is in each end. Whereas those are the lowest in the pipeline with ignition and venting position at the same end. There is no significant effect on product concentration of methane explosion under three venting conditions. For coal mine tunnel, it is indicated that the maximum explosion pressure at the airproof wall in return airway with the branch roadway at 50m from goaf is significantly decreased while that in intake airway doesn't change overwhelmingly. In addition, when the branch roadway is longer or its section is larger, the peak pressure of airproof wall would decrease slightly.

Experiment

(1) Experiment system

The experiment system consists of a flammable gas explosion limits test device and a high-speed video camera, as shown in Figs.1 and 2.

(2)Experimental results and analysis

The flame propagations of methane explosion were recorded by a high-speed video camera as shown in Fig.3. There are three stages when methane explosion

happened, the forward propagation, the back propagation and the turbulent forward propagation.

Fig.1 Explosion reaction tube

a. Camera body b.Camera lens

Fig.2 High-speed video camera

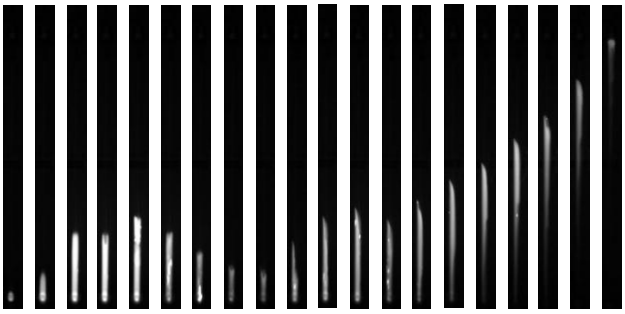

Fig.3 The process of flame propagation of 9.5% methane explosion in the pipeline

The interval of two pictures obtained by the high-speed camera with a working speed 1000 fra/s is 1 ms. In order to analyze quantitatively, the data of the pictures were calculated according to the principle of similarity to obtain the propagation velocity and the displacement of the flame front. The calculation formula is shown as following.

$$\frac{S_g}{H_g} = \frac{S_p}{H_p} \tag{1}$$

$$V = \frac{S_g}{\Delta T} \tag{2}$$

where S_g is the displacement of the flame front in the pipeline, S_p is the displacement of the flame front in the picture, H_g represents the length of the pipe in

the picture, H_p represents the size of the picture, V is the velocity of flame propagation and is the time interval of two pictures.

The relationship between the flame propagation velocities and time is as shown in Fig.4. With the process of methane explosion going on, the amount of heat given out continued to accumulate and turbulence intensity was increased by the effect of the pipe wall. Meanwhile, the flame front was deformed and the velocity of flame propagation increased to the first peak quickly. As the top of reaction pipe is closed, the reflection and superposition happened when the pressure propagated to the top of the pipe. Then, the unburned gas was compressed and the flame propagated to the maximum promptly with the effect of explosion vent. Additionally, the flame propagation velocity fluctuated on the time axis until the flame propagation speed was reduced to 0 m/s. Compared with 7.5% and 11.0% methane, 9.5% is the theoretical equivalent concentration of methane combustion in the air in which methane reacts with air completely. The explosive power is the largest and the reaction rate is the fastest at that concentration. That's why the flame propagation velocity of 9.5% methane is larger than the other two concentrations no matter forward or back propagation.

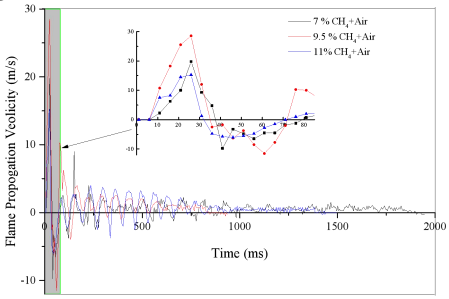

Fig.4 Flame propagation velocities of different methane mole fractions

Numerical simulation in the pipeline

(1) Comparative analysis of numerical simulation and experiment results

The explosion of methane at different concentrations in the pipeline is simulated by Flacs software. Fig.5 and Fig.6 illustrate the varieties of product concentration field and flame propagation velocity of methane explosion respectively. The distribution of product concentration field from Fig.5 is essentially in agreement with the flame propagation of methane explosion in Fig.3. The product concentration field with ellipse initially propagated to the end of closed pipe. Then it started to sag because of pressure release. With the flame propagation, the product concentration field showed "tulip". Finally, the "tulip" disappeared gradually and the front of product concentration field presented triangle. Compared with experimental results, the flame propagation velocity simulated by Flacs software is roughly consistent. The error is caused by the condition where energy does not suffer a loss in the ideal state. Therefore, the flame propagation time simulated by Flacs software is significantly shorter than that in the experiment and there is no obvious fluctuation

in the flame propagation velocity later. In summary, the results simulated by the software agree with experimental results essentially.

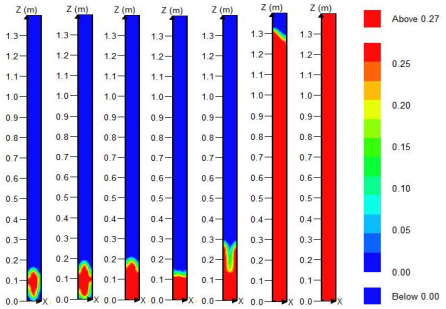

Fig.5 Distribution of product concentration field

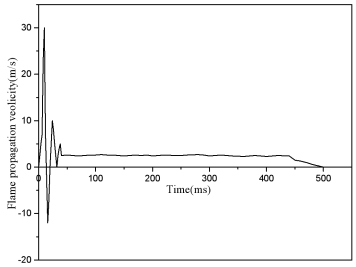

Fig.6 Flame propagation velocities of 9.5 methane

(2) Methane explosion in the pipeline under different venting conditions

Fig.7 shows the variation of methane explosion pressure at the center of the pipeline with time under three venting modes. Under the condition where ignition and vent position is at the same end of the pipeline, the center pressure of pipeline hit the highest quickly, then fluctuated continuously until decreased to 0 m/s. When ignition and vent position is at each end of the pipeline, the pressure rose initially to the maximum and then dropped to the negative pressure. Additionally, the pressure continued to increase to the peak value without a vent in the pipeline. On the whole, the explosion pressure of methane (9.5%, 10%, 11%) reached the peak quickly while that of methane (7%, 8%) had obvious delay to hit the maximum.

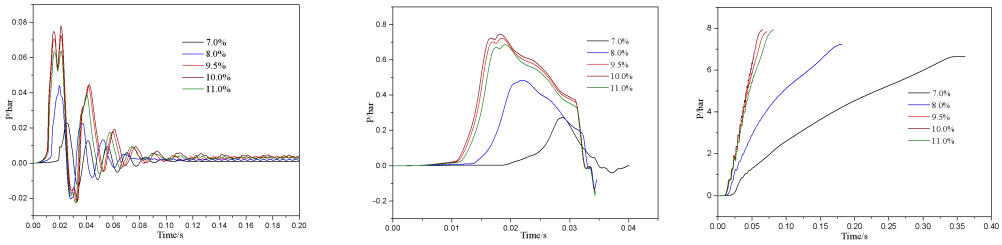

ignition and vent at the same end ignition and vent at each end no venting

Fig.7 Variation of methane explosion pressure at the center of the pipeline

The variation of the pipeline center temperature with time under three venting modes is as shown in Fig.8 in which the change trends are roughly identical. When ignition and vent position is at the same end of the pipeline, the pipeline center temperature heaved up in great swells at about 0.2s, then remained unchanged. Under the condition where ignition and vent position is at each end of the pipeline, the pipeline center temperature reached the peak more quickly, then had a fluctuation within a narrow range and dropped to a certain value. Without venting

condition in the pipeline, the temperature of pipeline center rose rapidly at first and then had a slight increase. In addition, 7% and 8% methane lagged behind the other three concentrations in time, which is similar to methane explosion pressure.

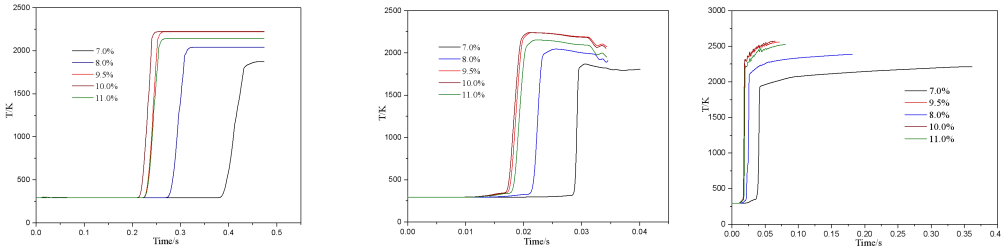

ignition and vent at the same end ignition and vent at each end no venting

Fig.8 Variation of temperature at the center of the pipeline

The variation of product concentration at the center of the pipeline is as shown in Fig.9 in which the change trends are roughly identical under three venting modes. The product concentration rapidly increased initially, and then kept the maximum value unchanged. The order of time to reach the maximum product concentration is $t_{10\%}<t_{9.5\%}<t_{11\%}<t_{8\%}<t_{7\%}$. Furthermore, compared with the other three concentrations, 7% and 8% methane had a significant delay to reach the maximum product concentration. The time to reach the maximum in the pipeline with ignition and vent at each end or without vent is shorter than that under the other condition. However, the venting condition has no obvious influence on the product concentration of methane explosion.

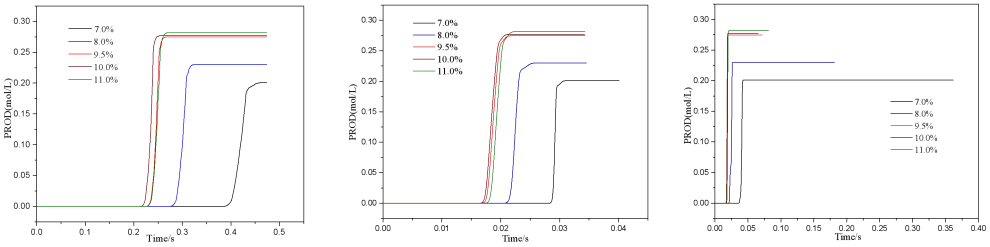

ignition and vent at the same end ignition and vent at each end no venting

Fig.9 Variation of product concentration at the center of the pipeline

Numerical simulation in coal mine tunnel

Fig.10 shows the variation of the maximum explosion pressure at the airproof wall with the distance between goaf and branch roadway. It is noted that the pressure corresponding to 0 m means the pressure of sensor where intake and return airways are without branch roadway. As illustrated in Fig.10, with the increase of the distance from 50m to 400m, the maximum explosion pressure in return airway increases to 22.41 bar gradually, then decreases to 18.18 bar with Faster rate. Compared to the pressure of return airway without branch roadway, it shows a

relatively lower pressure when the distance between goaf and branch roadway is 50m and the pressure decreases by 29.4%. However, the pressure in intake airway presents a small fluctuation trend, only to rise to 7.05 bar at 400m. Therefore, it is obvious to decrease the maximum explosion pressure in return airway with the branch roadway at 50m from goaf while that in intake airway doesn't change significantly.

Fig.11 displays the change of pressures at the airproof wall with different sectional dimensions of the branch roadway. Compared with the condition without branch roadway, the pressure peak of airproof with the branch roadway has a significant decline in return airway, while it has a slight rise in intake airway. In addition, explosion propagation time is longer in the tunnel with branch roadway than that without branch roadway (0*0 represents the tunnel without branch roadway). And there are more pressure peaks appearing in the tunnel with branch roadway, contrasting with only one peak in the tunnel without branch roadway. But the secondary pressure peak is smaller than the first peak. This can be explained that the part of explosion propagation is shared by the branch roadway in which the decreasing overpressure propagates to the tunnel conversely. By comparing different sectional dimensions of the branch roadway, the larger section of the branch roadway indicates the lower peak pressure to some extend.

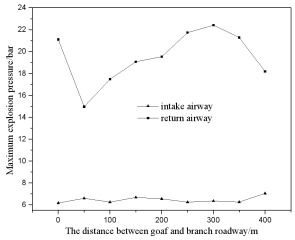

Fig.10 Pressures with different distances

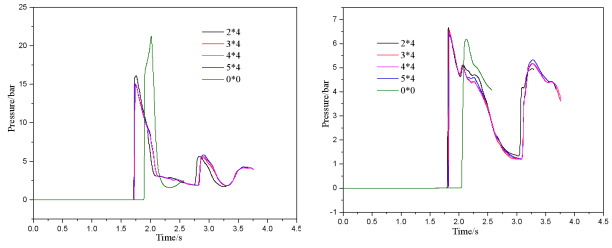

Fig.11 Pressures with different sectional dimensions of branch roadway

Fig.12 displays the viration of pressures at the airproof wall with different lengths of the branch roadway. Obviously, the longer the branch roadway is the lower the peak pressure changes. Nevertheless, the peak pressure varies slightly whatever the length of branch roadway is.

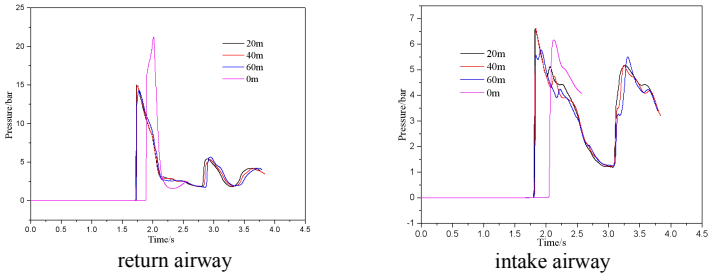

Fig.12 Pressures with different lengths of the branch roadway

FLASH POINT OF BINARY MIXTURES

V. Di Sarli*, R. Sanchirico*, A. Di Benedetto**
valeria.disarli@irc.cnr.it
*Istituto di Ricerche sulla Combustione, Consiglio Nazionale delle Ricerche (CNR), P.le Tecchio 80 - 80125 Napoli (Italy)
**Dipartimento di Ingegneria Chimica, dei Materiali e della Produzione Industriale, Università degli Studi di Napoli Federico II, P.le Tecchio 80 - 80125 Napoli (Italy)

Abstract
A model for calculating the Flash Point (FP) of binary mixtures was developed and applied to ethanol/n-octane mixtures. The non-ideality of the mixture was taken into account. This non-ideality leads to values of FP lower than those of the pure components.
The effect of pressure on the FP was also quantified. It has been found that, at pressure lower than 1 atm, the FP significantly decreases. This suggests that, when dealing with industrial processes operated under such pressure conditions, the FP present on the material safety data sheet is not conservative, being measured at 1 atm.

Introduction
For the design of prevention and mitigation measures in the process industries involving flammable substances, reliable safety data are required. One of the most relevant safety parameters for liquids is the Flash Point (FP) [1].
In the literature, FP data of pure substances are largely available, whereas FP data of mixtures are rather scarce as they are dependent on composition.
The FP of ideal mixtures may be calculated starting from the definition of FP and then using Raoult's law. When the mixture deviates from the ideal behavior, the effect of non-ideality has to be taken into account in order to correctly predict the FP [2].
It is also worth noting that in the material safety data sheets, the FP of pure substances is measured at atmospheric pressure. However, in several processes, the operating pressure is different from 1 atm.
In conclusion, there is a substantial lack of FP data for (non-ideal) mixtures and under non-atmospheric pressure conditions.
In this work, a model was developed for predicting the FP of non-ideal mixtures and quantifying the effect of pressure on this safety parameter. Calculations were performed for ethanol/n-octane mixtures.

Methods
Calculations of the FP of ethanol/n-octane mixtures were performed by means of a model based on Le Chatelier's rule for the Lower Flammability Limit (LFL):

$$\sum_i \frac{\gamma_i \cdot x_i \cdot P_i^o(T)}{P \cdot (LFL_i/100)} = 1 \quad (1)$$

In Eq. (1), γ_i, x_i, $P_i°$ and LFL_i are the activity coefficient, the liquid molar fraction, the vapor pressure, and the flammability limit, respectively, of the pure component i, and P is the total pressure. γ_i takes into account the intermolecular forces that give rise to a non-ideal behavior during the evaporation process. The values of the activity coefficients were calculated according to the nonrandom two-liquid (NRTL) equation [3]. The variation of Pi° with temperature (T) was estimated by using the Antoine equation.

Results and Discussion

In Figure 1, the results of FP calculations for ethanol/n-octane mixtures are plotted versus the ethanol molar fraction. The values of FP obtained as linear combination of the values of FP of the pure components are also shown. Finally, the horizontal line represents the lowest value of FP between those of the pure components (FP_{min}).

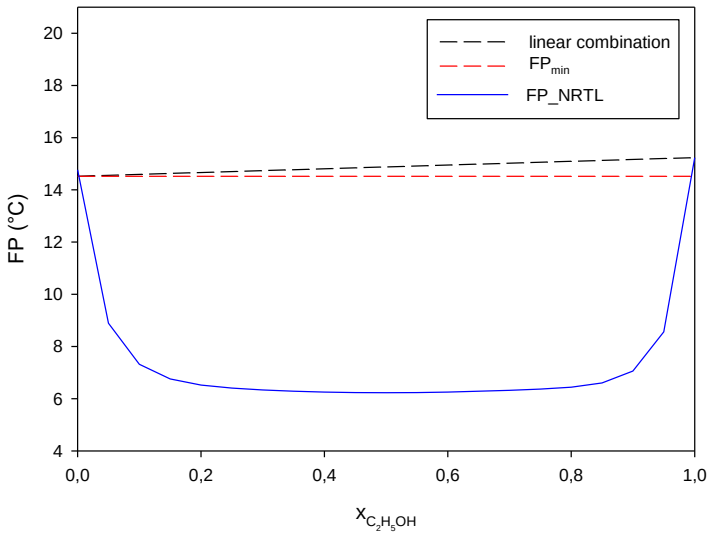

Figure 1. Ethanol/n-octane: Computed values of Flash Point (FP) as a function of ethanol molar fraction (total pressure, P, equal to 1 atm).

The model predicts values of FP lower than FP_{min} over almost the whole range of mixture compositions. This synergistic behavior has to be attributed to the intermolecular forces that increase the volatility of the mixture with respect to that

of the pure components.
From a safety point of view, these findings highlight that, for non-ideal mixtures such as ethanol/n-octane mixtures, measurements/calculations of the FP at different liquid compositions are absolutely necessary, given that the lowest value of FP between those of the pure substances cannot be considered as the most conservative value.
The effect of pressure on the FP of ethanol/n-octane mixtures was also quantified. In Figure 2, the calculated values of FP are plotted versus the ethanol molar fraction as obtained at (total) pressure varying from 0.4 bar up to 10 bar.

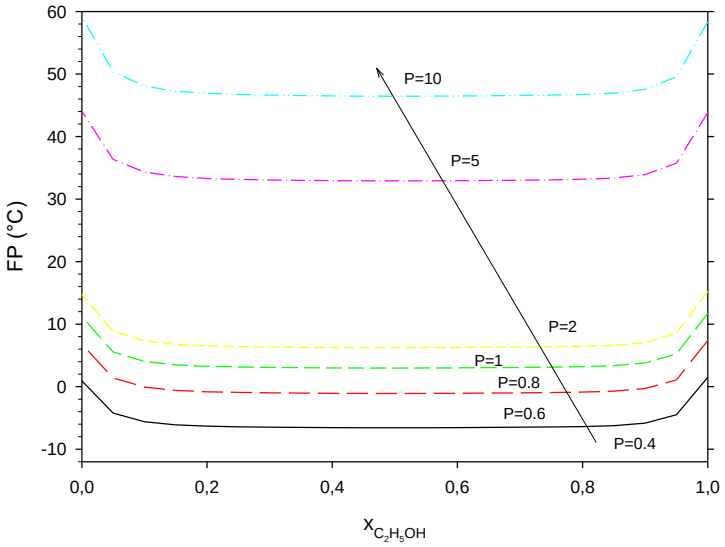

Figure 2. Ethanol/n-octane: Computed values of Flash Point (FP) as a function of ethanol molar fraction at different (total) pressures.

The FP significantly decreases with decreasing pressure from 10 atm to 0.4 atm. In particular, in going from 1 atm to 0.4 atm, it decreases of about 10 °C. This means that, when dealing with industrial processes operated at pressure lower than 1 atm, the FP present on the material safety data sheet is not conservative, being measured at 1 atm.

Conclusions

A model for calculating the Flash Point (FP) of binary mixtures was developed and applied to ethanol/n-octane mixtures. The non-ideality of the mixture was taken into account.
Results have shown that the values of FP are lower than the lowest value of FP between those of the pure liquids over almost the whole range of mixture compositions. This synergistic behavior has been attributed to the intermolecular

forces that increase the volatility of the mixture with respect to that of the pure components.

The effect of pressure on the FP of ethanol/n-octane mixtures was also quantified. It has been found that, in going from 1 atm to 0.4 atm, the FP decreases of about 10 °C. This means that, when dealing with industrial processes operated at pressure lower than 1 atm, the FP present on the material safety data sheet is not conservative, being measured at 1 atm.

References

[1] Crowl, D.A., Louvar, J.F., *Chemical Process Safety: Fundamentals with Applications*, Prentice Hall, 2002 (2nd edition), pp. 230-232.

[2] Liaw, H.-J., Chiu, Y.-Y., "The prediction of the flash point for binary aqueous-organic solutions", *Journal of Hazardous Materials* 101:83-106 (2003).

[3] Renon, H., Prausnitz, J.M., "Local compositions in thermodynamic excess functions for liquid mixtures", *AIChE Journal* 14:135-144 (1968).

EXPERIMENTTAL STUDY ON THE EFFECTS OF CRUDE OIL ON SPONTANEOUS COMBUSTION: A CASE STUFY

J. Deng*, S.X. Fan*, K. Wang*, Y.N. Zhang*, C.P. Wang*, J.Y. Zhao*
fanxust@yeah.net
* School of Safety Science and Engineering, Xi'an University of Science and Technology (XUST), Xi'an 710054, PR China

Abstract

An investigation of the effects of crude oil on the physicochemical structure and spontaneous combustion characteristics of coal is important for safe production in coal mines. In this study, the 4 coal samples with different crude oil contents were prepared. Their pore structure was characterized by the low-pressure N_2 adsorption (LP-N_2A). The spontaneous combustion propensity of coal samples was investigated using the low-temperature oxidation experiment. The Pore structure analysis revealed that the coal samples with higher content oil appeared lower porosity, smaller pore volume and specific surface area. Moreover, the addition of crude oil would hinder the absorption of O_2 and the interactions between molecules of O_2 and coal surface. The low-temperature oxidation experiment indicated that with increasing content of crude oil in coal sample, activation energy (E_a) rose gradually, while the oxygen consumption rates, oxidizing gases production and heat release intensity decreased slowly. Therefore, CO was not the indictor to the coal self-ignition, the shape increase in the plots of CO and CO/CO_2 versus were recommended to evaluate the risk of coal spontaneous combustion.

Introduction

Underground coal fires caused by self-heating represents a challenging hazard for coal industries worldwide, which have greatly threatened the mining industry. Statistics show that more than 100 working faces were closed every year in state-owned coal mines, due to the spontaneous combustion of residual coal in gob area. To retard underground coal fires efficiently, many novel methods, materials and relevant equipment have been developed and applied in the field. However, the above measures cannot be employed in all the coalmines, because of the difference of the geological conditions, mining technologies, and characteristics of coal.

The coal-bearing strata in the Huangling coalfield mainly include the middle Jurassic Yan'an Formation. The Yan'an formation consists of 2 main coal seams: No.3 and No.4 coal seams, with abundant coal reserves. Fine sandstone upper the No.3 coal seam and medium sandstone upper the No.4 coal seam partially contained the crude oil, which affected the spontaneous combustion characteristics of coal seam severely. However, little attention has been devoted to the impact

mechanism of the crude oil on self-heating properties of coal.

It has been acknowledged that the oxidation of coal at low temperature is a complicated reaction sequence, which is mainly caused by the interactions between molecules of O_2 and particular active sites on the coal surface . It consists of multiple steps, involving the absorption of O_2, the generation of intermediate carbon-oxygen compounds, as well as the decomposition of these unstable solid oxygenated intermediates to gaseous products and stable solid products, along with the heat release. In addition, some specific sites on the surface of aromatic rings and aliphatic groups would react with the molecules of O_2 directly, resulting in the formation of gaseous products. The entire low-temperature oxidation process is an irreversible exothermic reaction, during which the heat released from the oxidation reaction increase the temperature conversely and further to promote the reaction.

Numerous previous papers have revealed that any factors influenced the above multiple steps would affect the oxidation of coal and release of the heat, involving the pore-fracture system, metamorphism, mineral composition, moisture content, particle size, air velocity, temperature, and the partial pressure of oxygen . Pore-fracture system in coal offers plenty of channels and storage sites for the O_2 transportation and absorption, which plays a significant role in the development of coal spontaneous combustion. The occurrence of crude oil was considered to affect the pore structure significantly, and eventually affect the spontaneous combustion characteristics and some representative parameters, the indicator gases, oxygen consumption rate, and the CO generation rate.

In this study, four coal samples with the different crude oil contents were selected for the low-pressure N_2 adsorption (LP-N_2A) and low-temperature oxidation experiment. Subsequently, on the basis of the experimental results, the effects of crude oil on the pore characteristic, the representative parameters of spontaneous combustion of coal were systemically investigated. The research results might enable us to better understand the impact mechanism and offer practical references for the prevention of spontaneous combustion of oil-bearing coal seam.

2. Samples and experimental methods

2.1 *Sample preparation*

The fresh coal samples were directly collected from the No. 410 coalface in Huangling No.2 Mine, Shaanxi, China. The crude oil was collected through the gas drainage borehole from overlying rock strata. The coals were milled and sieved into 8 size fractions: 0.048-0.075mm, 0.075-0.18mm, 0.18-0.38mm and 0-0.9mm, 0.9-3.0 mm, 3.0-5.0mm, 5.0-7.0mm, and 7.0-10.0mm. Subsequently, the crude oil were added into the 8 size fractions coals in the proportion of 5% (Sample 2#), 10% (Sample 3#), and 15% (Sample 4#), respectively. The coal sample without crude oil was Sample 1#.

The coals of size ranging from 0.075 to 0.18mm were used for proximate and ultimate analysis, the results is listed in Table 1. Moreover, the coals in the 0.18-

0.38mm size fractions were used to perform the pore characterization by low-pressure N_2 adsorption (LP-N_2A). Next, the coal sample used for the low-temperature oxidation experiment was prepared by mixing the other 5 size range of sample. The amount of each size fraction was 200g.

Table 1. Proximate and ultimate analyses of the raw coal used in the experiments.

Proximate,%				Ultimate,%					Coal forming period
M_{ad}	A_d	V_{daf}	FC_d	C	H	O	N	S	
2.70	17.11	33.75	46.44	84.62	4.96	8.95	1.21	0.23	Jurassic

2.2 *Experimental methods*

Pore structures characterization of the coal samples, including the specific surface area (SSA), pore volume, pore size distribution (PSD), was tested using a Micrometritics ASAP 2020 system. After completion of degassing, the nitrogen adsorption-desorption isotherms of 4 coal sample were collected at a temperature of 77.35 K with a relative pressure (p/p_0) range of 0.01-0.99.

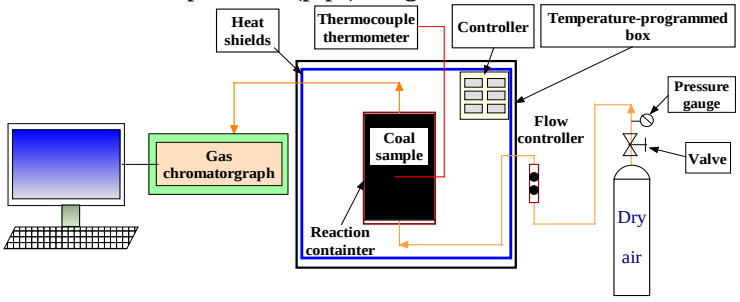

Fig. 1 The experimental testing system of programming temperature-control box

The low-temperature oxidation experiment of coal was conducted using self-designed temperature-programmed experimental system (TPES), as shown in Fig. 1. The device consists of SP-3430 gas chromatograph, a programmable temperature-control box, a flow controller, a dry air supply cylinder, a thermocouple, and a reaction container.

3. Results and discussion

3.1 *Pore structures characterization*

The specific surface area and pore volume of coal samples calculated from the adsorption isotherms are shown in Table 2. The data obtained shows that a large variation in specific surface area and pore volume within different coal samples. The SSA computed using BET and BJH methods range from 0.2190 to 2.5140 m^2/g, 0.1868 to 2.5243 m^2/g, respectively. The SSA of sample 1# is approximately 12 times as large as that of sample 4#. Concerning the pore volume, there was a remarkable reduction in BJH volume from $9.080\times10^{-3}cm^3/g$ (Sample 1#) to $0.525\times10^{-3}cm^3/g$ (Sample 4#). The total volume also significantly decreased from $9.248\times10^{-3}cm^3/g$ to $0.541\times10^{-3}cm^3/g$ under the effects of crude oil. The results indicated that SSA was mainly dominated by micropores and mesopores, which

was consistent with the previous literature.

Table 2. Pore structure characterization of coal samples.

Coal sample	Specific surface Area		Pore volume	
	BET SSA (m^2/g)	BJH SSA (m^2/g)	BJH volume ($\times10^{-3}cm^3/g$)	Total volume ($\times10^{-3}cm^3/g$)
1#	2.5104	2.5243	9.080	9.248
2#	0.3071	0.3244	0.591	0.634
3#	0.2841	0.2635	0.548	0.567
4#	0.2190	0.1868	0.525	0.541

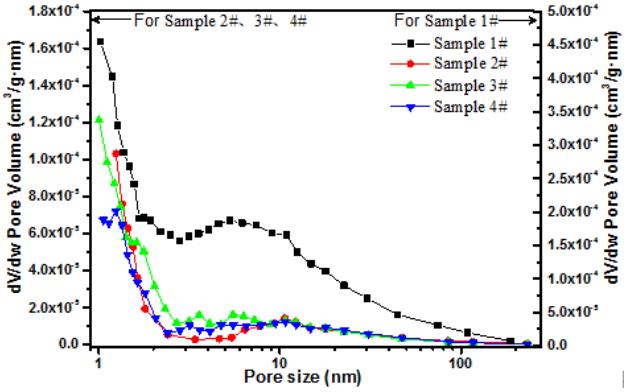

Figure 2. Pore size distribution of 4 Coal samples

The pore size distributions (PSD) of coal samples are shown in Fig.2. The experimental results indicate that all the studied samples display the multimodal pore size distribution, with the major peaks between 1.0 nm and 2.0nm. For Sample 1#, the dominate mesopore size is between 4nm and 10nm. Whereas, for Samples 2#、3# 4#, the dominate mesopore size mainly exists in the range of 7~12nm. Compared with the PSD of Sample 1#, a remarkable decrease were observed for the distribution peaks of the coal samples bearing crude oil when the pore diameter was less than 20 nm. This indicated that a large number of mesopores and micropores were covered by the crude oil, which would hinder the absorption of O_2 in low-temperature oxidation of coal.

3.2 *Low-temperature oxidation experiment*

$$V_{CO}^{0}(T)=\frac{V_{O_2}^{0}(T)\cdot(C_{CO}^{b}-C_{CO}^{a})}{C_{O_2}^{a}\cdot[1-e^{-\frac{V_{O_2}^{0}(T)\cdot H\cdot(z_b-z_a)}{Q_e\cdot C_{O_2}^{0}}}]} \quad (1)$$

The production rate of CO can be calculated according to Eq. (1). The CO concentration and CO production rate was plotted in Fig. 3. As shown in the Fig. 3, the CO concentration and CO production rate both increased exponentially with the increasing temperature. Clearly, the coal samples with the higher crude oil content

had the slower generation rate, in accordance with changing laws of O_2 consumption rate.

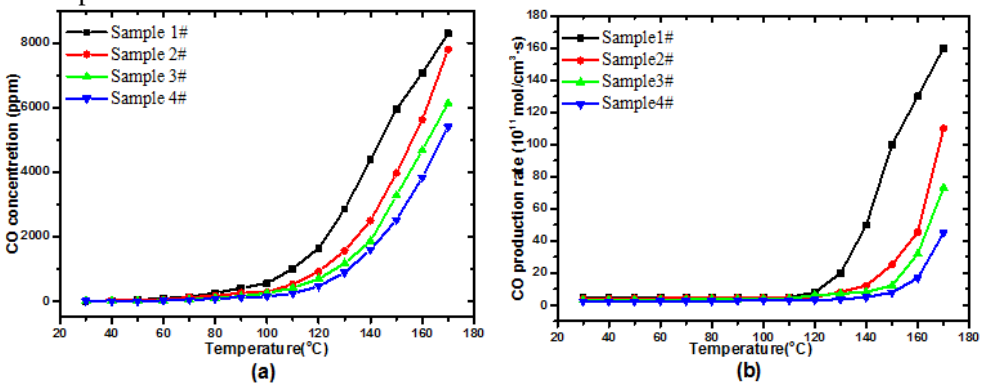

Figure 3. CO concentration and CO production rate for 4 coal samples

$$\ln(c_i) = -\frac{E_a}{R}\cdot\frac{1}{T} + \ln\left(\frac{A\cdot S\cdot L\cdot \eta\cdot C_{O_2}^{n}}{k\cdot v_g}\right) \tag{2}$$

Table 3. Activation energy of 4 coal samples in the low-temperature process.

Coal sample	Crude oil content (%)	Slope	Activation Energy (kJ/mol)	R^2
1#	0%	-3577.917	29.74	0.99584
2#	5%	-3672.602	30.54	0.99174
3#	10%	-3958.948	32.91	0.99618
4#	15%	-4173.216	34.70	0.99072

Table. 3 presents the activation energy of 4 coal samples obtained by the Eq. (2). Obviously, the activation energy of Sample 1# was 29.74 kJ/mol, whereas the activation energy of the oily coal samples had the slightly higher activation energy, 30.54 kJ/mol (Sample 2#), 32.91kJ/mol (Sample 3#) and 34.70kJ/mol (Sample 4#). Moreover, the activation energy of samples increased with the increasing crude oil content. The higher value of activation energy indicated that the oily coal had the lower oxidation reactivity. In conclusion, the addition of crude oil lowered the sensitivity to oxygen of coal samples and inhibited the reaction of coal and oxygen.

4. Conclusions

In this paper, the effects of crude oil on the spontaneous combustion characteristics of weakly caking coal in Huangling No.2 Mine were investigated using LP-N_2A and low-temperature oxidation experiments. The following conclusions can be drawn as follows:

1. The coal samples with higher content oil appeared lower porosity, smaller pore volume and specific surface area.

2. With increasing content of crude oil in coal sample, activation energy (E_a) rose gradually, while the oxygen consumption rates, oxidizing gases production and heat release intensity decreased slowly.

3. CO cannot be used the indictor to the coal self-ignition, the shape increase in the plots of CO and CO/CO_2 versus were recommended to evaluate the risk of coal spontaneous combustion.

References

[1] Deng, Jun, Qingwei Li, Yang Xiao, and Hu Wen. "The Effect of Oxygen Concentration on the Non-Isothermal Combustion of Coal." *Thermochimica Acta* 653 (2017): 106-15.

[2] Deng, Jun, Yang Xiao, Qingwei Li, Junhui Lu, and Hu Wen. "Experimental Studies of Spontaneous Combustion and Anaerobic Cooling of Coal." *Fuel* 157 (2015): 261-69.

[3] Deng, Jun, Jingyu Zhao, Yanni Zhang, Anchi Huang, Xiangrong Liu, Xiaowei Zhai, and Caiping Wang. "Thermal Analysis of Spontaneous Combustion Behavior of Partially Oxidized Coal." *Process Safety and Environmental Protection* 104 (2016): 218-24.

[4] Hu, Wen, Xu Jingcai, and Ge lingmei. "Experimental Simulation and Numerical Analysis of Coal Spontaneous Combustion Process at Low Temperature." *Jouranl of Coal Science & Engineering (CHINA)* 7, no. 2 (2001): 61~66.

[5] Song, Zeyang, and Claudia Kuenzer. "Coal Fires in China over the Last Decade: A Comprehensive Review." *International Journal of Coal Geology* 133 (2014): 72-99.

[6] Su, Hetao, Fubao Zhou, Jinshi Li, and Haining Qi. "Effects of Oxygen Supply on Low-Temperature Oxidation of Coal: A Case Study of Jurassic Coal in Yima, China." *Fuel* 202 (2017): 446-54.

[7] Wang, Haihui, Bogdan Z. Dlugogorski, and Eric M. Kennedy. "Coal Oxidation at Low Temperatures: Oxygen Consumption, Oxidation Products, Reaction Mechanism and Kinetic Modelling." *Progress in Energy and Combustion Science* 29, no. 6 (2003): 487-513.

[8] Wen, Hu, Zhijin Yu, Jun Deng, and Xiaowei Zhai. "Spontaneous Ignition Characteristics of Coal in a Large-Scale Furnace: An Experimental and Numerical Investigation." *Applied Thermal Engineering* 114 (2017): 583-92.

[9] Wen, Hu, Zhijin Yu, Shixing Fan, Xiaowei Zhai, and Wenyong Liu. "Prediction of Spontaneous Combustion Potential of Coal in the Gob Area Using Co Extreme Concentration: A Case Study." *Combustion Science and Technology* 189, no. 10 (2017): 1713-27.

[10] Xia, Tongqiang, Fubao Zhou, Feng Gao, Jianhong Kang, Jishan Liu, and Jianguo Wang. "Simulation of Coal Self-Heating Processes in Underground Methane-Rich Coal Seams." *International Journal of Coal Geology* 141-

142 (2015): 1-12.

SESSION IX

Laminar flames

EXPERIMENTAL INVESTIGATION OF FUEL-SPECIFIC SPECIES FORMATION IN BLENDED PREMIXED FLAMES

Julia Wullenkord[1], Meirong Zeng[1,2], Maurin Salamanca[1,3], Isabelle Graf[1], Steffen Schmitt[1], Lena Ruwe[1], Katharina Kohse-Höinghaus[1]
julia.wullenkord@uni-bielefeld.de
[1]Department of Chemistry, Bielefeld University, Bielefeld, Germany
[2]National Synchrotron Radiation Laboratory, University of Science and Technology of China, Hefei, P. R. China
[3]Department of Chemical Engineering and Biotechnology, University of Cambridge, Cambridge, United Kingdom

Abstract
To contribute to the understanding of fuel-structure-dependent influences on chemical pathways and pollutant formation in combustion, low-pressure flames burning hydrocarbon-oxygenated fuel mixtures were investigated with electron-ionization molecular-beam mass spectrometry. The chosen fuel blends – selected combinations of branched and unbranched hydrocarbons and oxygenated fuels – represent a wide span of different chain lengths, branching degree, and structural motives. Two sets of experiments were conducted to investigate the influence of the molecular structure on the species composition in the flames of such mixtures. In one series, *n*-heptane (C_7H_{16}) and iso-octane (C_8H_{18}) were blended with either dimethyl ether, DME, (C_2H_6O) or diethyl ether, DEE ($C_4H_{10}O$) [1]. The second experiment was devoted to mixtures of ethene (C_2H_4), 1-butene (1-C_4H_8), and isobutene (i-C_4H_8) that were blended with esters of different unsaturation degree, namely methyl crotonate, MC ($C_5H_8O_2$) and methyl butanoate, MB, ($C_5H_{10}O_2$) [2]. While the respective pool of intermediates in the blends typically consists of species also detected in the pure flames, a strong dependence is noted of the amounts of various intermediates and products – including undesired pollutants – on the individual fuels' decomposition pathways.

Introduction
The energy demand in transportation is still mainly met by fossil-fuel combustion. To reduce the fossil fuel share, to decrease harmful emissions of carbon dioxide, soot, and unregulated pollutants, and to adjust the fuel characteristics to various operation conditions, blending strategies are being applied. Adding oxygenated compounds to petroleum-based fuels leads to an altered intermediate species pool as well as a different spectrum of exhaust products. While the combustion reactions of many individual fuels in flames have been studied in detail, often providing numerous experimental species profiles in combination with the development and

critical testing of kinetic models, similar work on fuel mixtures has remained scarcer, especially for blends of conventional and biogenic fuels. In the present study, iso-octane and *n*-heptane, representatives of primary reference fuels, as well as three C_2-C_4 hydrocarbon fuels, namely 1-butene, isobutene, and ethene, were chosen as well-studied base fuels in an investigation of laminar premixed low-pressure flames burning fuel mixtures. The two alkane fuels were blended with DME and DEE, while MC and MB were added to the alkene fuels, resulting in a total of 25 flames of pure fuels and their combinations that permitted to study effects of the specific fuel structure on the combustion chemistry.

Experimental Method and Kinetic Modeling

Fuel-rich laminar premixed low-pressure (4 kPa) flames were chosen as a simplified laboratory system and stabilized on a movable, water-cooled (333 K) flat bronze matrix burner. Argon dilution was chosen to provide a good standoff distance of the mixture flames (0.50 for *n*-heptane-, iso-octane-, and ethene-based and 0.25 for butene-based flames). Analyses were performed with a time-of-flight molecular-beam mass spectrometer using electron ionization to enable the simultaneous detection of almost all stable and radical species. The mass resolution ($m/\Delta m$~4000) allowed for the simultaneous separation and detection of all species based on their elemental composition of C/H/O. To support the data interpretation, the experiments were complemented by kinetic modelling. For the simulation of the combustion behavior of the first set of blends, namely iso-octane, *n*-heptane, DME, and DEE, we used the mixture model of [1] that combines the mechanism from Pitsch and collaborators [3] and the sub-mechanisms for DME and DEE from AramcoMech2.0 [4] and Tran et al. [5]. Exploratory modelling of the flames blended with small methyl esters was performed with the model of Yang et al. [6,7] that was chosen because it already includes basic mechanisms of the studied fuels.

Experimental Results

Small ether addition to n-heptane and iso-octane base fuels

Effects of DME or DEE addition in flames of the linear or branched alkanes *n*-heptane or iso-octane were studied in 8 hydrocarbon/oxygenated fuel mixture flames (in ratios of 1:1 and 1:4 in either fuel combination) and pure flames of each fuel. It was found that the addition of DME and DEE, where species with more than 4 carbon atoms can only be formed from recombination reactions of smaller species, decreases the mole fractions of C_4-C_9 species compared to mole fractions detected in flames of the pure hydrocarbon fuels. In contrast, the mole fractions of several C_1-C_3 species were seen to increase. As an example, blending with DME or DEE has a significant effect on the formation of formaldehyde (CH_2O), known as a typical oxygenated pollutant from fuel combustion. Mole fractions of CH_2O in all 12 flames are displayed in Fig. 1.

For the two base fuels, the CH_2O production is, not surprisingly, promoted with increasing DME or DEE fractions, since it is a primary product in the fuel-specific reactions of both DME and DEE.

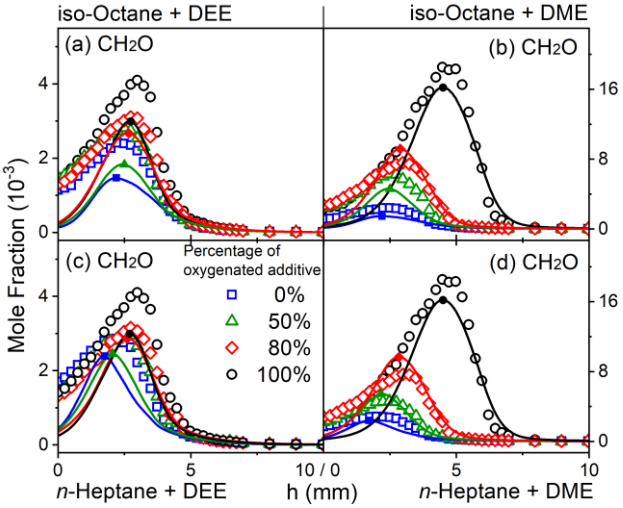

Figure 1. CH_2O mole fractions for the pure fuels and fuel combinations of iso-octane, *n*-heptane, DME and DEE, and model predictions (mixture model [1]). Adapted from [1] with permission from Elsevier/The Combustion Institute.

The stronger CH_2O increase in flames blended with DME can be reasonably explained by the reaction sequence DME → CH_3OCH_2 → CH_2O + CH_3, which is one of the dominant pathways in DME combustion. The produced CH_3 can then additionally contribute to CH_2O formation. In DEE decomposition, CH_2O is mainly a product of a three-step reaction sequence of DEE → $CH_3CH_2OCH_2CH_2$ → CH_3CH_2O → CH_2O involving a less important consumption pathway of DEE [1]. These experimental trends are also satisfactorily captured by the simulation (compare Fig. 1). Further experimental results for hydrocarbon intermediate species are provided in Fig. 2 where their maximum mole fractions are displayed logarithmically; symbols indicate the prediction of the model. Different tendencies can be observed in the mixture flames. For example, methane (CH_4) mostly increases with DME or DEE blending since it is mainly produced from the CH_3 radical, which is abundantly formed from both additives. Ethene (C_2H_4) and propane (C_3H_8) mole fractions are higher in the mixture flames with DEE than for the pure iso-octane flame, with an opposite trend observed for the iso-octane/DME mixture flames. C_3H_8 increases upon blending with DEE, since it is mainly produced from recombination of C_2H_5 and CH_3, both key intermediates from DEE. C_2H_4 is also a direct decomposition product of *n*-heptane and therefore lower in the *n*-heptane/DEE mixture flame.

Mole fractions of species with higher carbon numbers, here exemplarily shown for C_4H_6 (calibrated as 1,3-butadiene) and C_6H_6 (calibrated as benzene), were found to

be lower in the mixture flames than in the pure flames, with a stronger effect on iso-octane blends. For further inspection, experimental and simulated mole fraction profiles of C_6H_6 are displayed in Fig. 3 for all 12 flames.

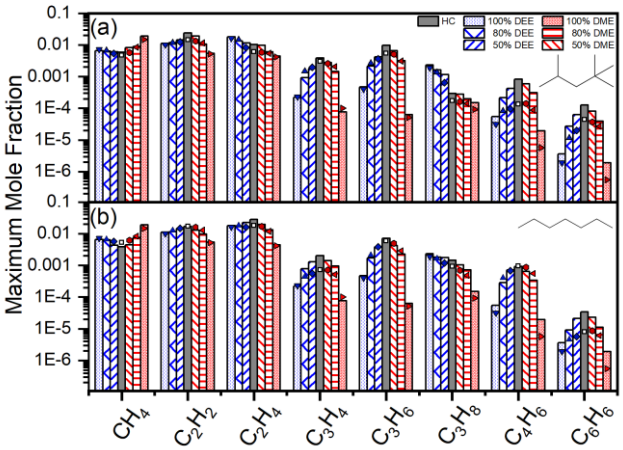

Figure 2. Maximum mole fractions (logarithmic scale) of selected hydrocarbon species for the pure fuels and fuel combinations of iso-octane, *n*-heptane, DME and DEE; experiment: bars, model: symbols (mixture model [1]).

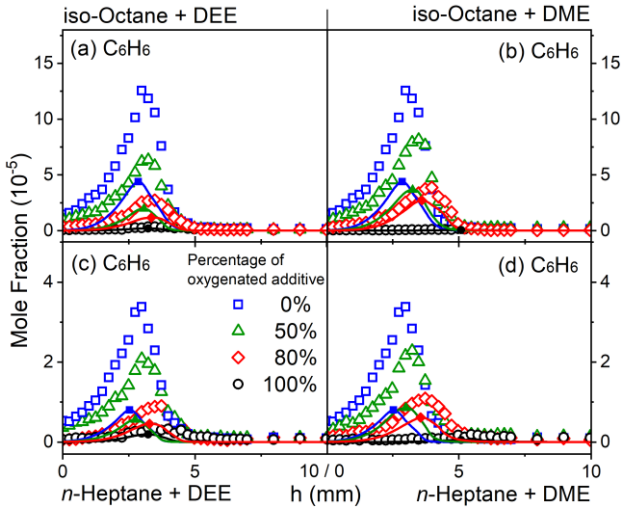

Figure 3. C_6H_6 mole fractions for the pure fuels and fuel combinations of iso-octane, *n*-heptane, DME and DEE, and model predictions (mixture model [1]). Adapted from [1] with permission from Elsevier/The Combustion Institute.

Simulations with the mixture model only qualitatively reproduce the experimental trends upon DME and DEE addition, and the benzene mole fractions are typically

under-predicted by at least a factor of two. The mole fractions of C_3H_3 (not shown here), known as a major benzene precursor, are also seen to decrease upon ether addition in both iso-octane and *n*-heptane flames. It is therefore reasonable that C_6H_6 shows the same tendency. It should be noted that the C_6H_6 mole fraction is significantly higher for the branched fuel iso-octane than for *n*-heptane.

Small methyl ester addition to three C_2-C_4 hydrocarbon base fuels

To investigate effects of methyl ester addition to alkenes, methyl crotonate (MC) and methyl butanoate (MB) were added to ethene, 1-butene, and isobutene [2]. The base fuels represent differences in chain length or branching degree, and MC and MB exhibit different unsaturation degrees, an important characteristic of biodiesel compounds. A total of 13 premixed hydrocarbon/oxygenated fuel flames were investigated (with mixtures in ratios of 1:1 in either fuel combination) [2]. Generally, the results showed changes in the formation of intermediate species upon ester addition to depend strongly on the molecular fuel and/or additive structure. Overall, partial replacement of all base fuels by either MB or MC leads to higher mole fractions of formaldehyde and methanol. Formaldehyde can easily be formed by a β-scission from both methyl ester fuel radicals. Hence, the effect of the base fuel is more important for CH_2O formation. Methanol can be formed by MC via CH_3O radicals by H-abstraction at the weakest C–H bond located at the terminal methyl group of the ester side chain, which is not equally preferred in MB. Therefore, MC addition leads to higher methanol formation. Besides the influence on small oxygenated species, MB and MC addition to the hydrocarbon base fuels significantly affects the pool of C_3-C_6 hydrocarbon species. Not surprisingly, their formation in ethene-based mixture flames is increased. For the butene flames, however, where C_3 species are abundantly present, ester addition decreases the C_3 pool. Highest reduction was found for C_3H_6 in the 1-butene and for C_3H_4 in the isobutene flame. A decrease was noted in C_4-C_6 species for ester addition to the butenes. For example, 1-butene can easily form C_4H_6, and subsequent dehydrogenation can yield significant amounts of C_4H_4. Ester addition reduces the contribution of these reactions. Reduction tendencies in C_5 and C_6 species are more prominent for MB addition. Contrarily, addition of the esters to ethene increases C_5 and C_6 species significantly, especially for MC. Most trends are reasonably well captured by the model [6,7], although absolute mole fraction may differ [2].

Conclusion

The influence of small ether and ester additives on alkane and alkene fuels was investigated in two series of premixed low-pressure flames, including those in [1,2]. Species profiles were obtained with molecular-beam mass spectrometry for 25 flames of the pure fuels and their respective combinations. With a set of about 800 mole fraction profiles, the experiments permit reliable inspection of possible differences in the reaction pathways. In general, the respective pool of intermediates in the blends typically consists of species also detected in the pure flames.

Experimentally observed trends could be correlated to the altered species pool induced by the strong dependence on the individual fuels' decomposition pathways. The experimental data were further compared to simulations by kinetic models, mostly revealing reasonable to good agreement of the experimentally obtained trends.

Acknowledgement
The Bielefeld authors gratefully acknowledge the partial support by Deutsche Forschungsgemeinschaft under contract KO 1363/31-1.

Disclaimer
This paper contains work-in-progress and is not intended to be an archival publication.

References
[1] Zeng, M., Wullenkord, J., Graf, I., Kohse-Höinghaus, K., "Influence of dimethyl ether and diethyl ether addition on the flame structure and pollutant formation in premixed iso-octane flames", *Combust. Flame* 184: 41–54 (2017).

[2] Salamanca, M., Wullenkord, J., Graf, I., Schmitt, S., Ruwe, L., Kohse-Höinghaus, K., "Experimental investigation of the joint combustion behavior of two small methyl esters with three C_2-C_4 hydrocarbon base fuels in laminar premixed low-pressure flames, submitted to *Proc. Combust. Inst.* 37.

[3] Cai, L., Pitsch, H., "Optimized chemical mechanism for combustion of gasoline surrogate fuels", *Combust. Flame* 162: 1623–1637 (2015).

[4] Zhou, C.W., Li, Y., O'Connor, E., Somers, K.P., Thion, S., Keesee, C., Mathieu, O., Petersen, E.L., DeVerter, T.A., Oehlschlaeger, M.A., Kukkadapu, G., Sung, C.J., Alrefae, M., Khaled, F., Farooq, A., Dirrenberger, P., Glaude, P.A., Battin-Leclerc, F., Santner, J., Ju, Y., Held, T., Haas, F.M., Dryer, F.L., Curran, H.J., "A comprehensive experimental and modeling study of isobutene oxidation", *Combust. Flame* 167: 353–379 (2016).

[5] Tran, L.-S., Pieper, J., Carstensen, H.-H., Zhao, H., Graf, I., Ju, Y., Qi, F., Kohse-Höinghaus, K., "Experimental and kinetic modeling study of diethyl ether flames", *Proc. Combust. Inst.* 36: 1165–1173 (2017).

[6] Yang, B., Westbrook, C.K., Cool, T.A., Hansen, N., Kohse-Höinghaus, K., "Fuel-specific influences on the composition of reaction intermediates in premixed flames of three $C_5H_{10}O_2$ ester isomers", *Phys. Chem. Chem. Phys.* 13: 6901–6913 (2011).

[7] Yang, B., Westbrook, C.K., Cool, T.A., Hansen, N., Kohse-Höinghaus, K., "Photoionization mass spectrometry and modeling study of premixed flames of three unsaturated $C_5H_8O_2$ esters", *Proc. Combust. Inst.* 34: 443–451 (2013).

A numerical study on the effect of temperature and composition on the flammability of sour gas

G. Pio*, V. Palma, E. Salzano***

Gianmaria.pio@unibo.it

* Dipartimento di Ingegneria Civile, Chimica, Ambientale e dei Materiali, Università di Bologna, via Terracini 28, 40131 Bologna (IT)

** Dipartimento di Ingegneria Industriale, Università di Salerno, via Giovanni Paolo II 132, 84084 Fisciano, Salerno (IT)

Abstract

The growing research interest in Natural Gas reported in the recent years is due to its large availability as a fuel, and its potential applications in several chemical syntheses, starting from the methane steam reforming. To this aim, the extraction of oil and gas resources, either onshore or offshore, is hardly meeting the global energy needs and new fields are continuously explored. On the other hand, existing and new projects may involve specific geographical areas where the hydrocarbon extraction meets severe safety challenges due to the presence of Hydrogen Sulphide (H_2S) in the extracted hydrocarbons (sour gas). Indeed, the combined effect of flammability and toxicity of such gases has the critical potential to increase the hazard level in the industrial installation, thus aggravating the consequences for human and assets.

In this work a numerical procedure suitable for the evaluation of fundamental parameters such as Laminar Burning Velocity (S_U) and Flammability Limits (FLs) was presented and successfully applied to CH_4 - H_2S – Air mixture (Sour gas), based on fully validated detailed kinetic model and Limiting Burning Velocity ($S_{U,Lim}$) theory. The effect of initial temperature, equivalence ratio and H_2S content was evaluated by varying the data within the ranges, respectively: 250 K – 325 K; 0.4 – 2.5; and 0.75 %v – 15 %v.

It was found that even for larger amount of H_2S, and for all investigated temperatures, an almost negligible variation in S_U is observed, however with a slight reduction for lean conditions and a small increase for rich conditions. Results show also that the addition of H_2S has a strong relevance on $S_{U,Lim}$ values, hence on flammability limits. These phenomena lead to small variation of Lower Flammability Limit but large differences in the Upper Flammability Limit for the given mixture.

Introduction

The potential substitution of oil-based mixtures with Methane (CH_4) as a fuel or as raw material for chemical synthesis has strongly increased the demand of this fuel in the recent years. That has forced the exploration and the exploitation of Natural Gas reservoirs in isolated regions (stranded gas), where climate conditions can vary from very low temperature (as in the Arctic region, in several Russian areas close to polar circle or even in the Caspian area) to very high temperature (as in the case of Indian Ocean, Persian Gulf, Red Sea or Arabic sea). In many cases, however, the presence of non-alkanes compounds and more specifically Hydrogen Sulfide (H_2S), could raise severe safety issue and strong deviation from the ideality of pure Methane gas, due to its flammability and toxicity hazards. Similar issues can be found in biogas, where the presence of Sulphur has to be kept into account.

In this framework, the estimation of crucial factors for reactivity and safety analysis, such as Laminar Burning Velocity (S_U), Lower Flammability Limit (LFL) and Upper Flammability Limit (UFL), under different ambient conditions and composition represents a fundamental step for further scientific and technological development.

Here, the effect of initial temperature and composition on the S_U of $CH_4 – H_2S –$ Air mixtures (Sour Gas) were evaluated by using detailed kinetic model including both hydrocarbons and Sulphur compounds chemistry [1] The LFL and UFL were estimated by means of Limiting Laminar Burning Velocity ($S_{U,Lim}$) theory [2].

Materials and Methods

The numerical analysis was performed by implementing the Chemkin-based code suitable for the premixed laminar flames estimation. The simulation parameters ratio, slope and curve were equal to 3, 0.07 and 0.14, respectively, in order to optimize the simulation time and costs required and number of point in the output files (around 200-250) without affecting the accuracy of obtained results. Moreover, the relative error criteria (RTol) and absolute error criteria (ATol) were kept constant at $1.0 \cdot 10^{-9}$ and $1.0 \cdot 10^{-14}$ for steady-state problem and $1.0 \cdot 10^{-5}$ and $1.0 \cdot 10^{-14}$ for time stepping problem (used by the code as first attempt solution), respectively.

The detailed kinetic model used in this study is based on the light hydrocarbons reactions ($<C_4$) reported by the University of California at San Diego (UCSD) mechanism [3] and Sulphur compound chemical model developed by Leeds University [4], fully validated and selected among the other detailed kinetic model considered in previous works [1][5], by applying a statistical analysis on the comparison with existing S_U data retrieved from the current literature.

For the sake of simplicity, the Natural Gas was modeled as pure CH_4. Three binary mixtures representing typical Sour Gas compositions were studied: Mix 1) CH_4: 99.25 %v; H_2S: 0.75 %v; Mix 2) CH_4: 98.50 %v; H_2S: 1.50 %v; Mix 3) CH_4: 85.00 %v; H_2S: 15.00 %v. The unburned gas initial temperature was changed within the

interval 250 K – 325 K and the equivalence ratio (φ), as defined in the Equation 1, from 0.4 to 2.5.

$$\varphi = \sum \frac{\frac{Fuel}{Oxidant}}{\left(\frac{Fuel}{Oxidant}\right)_{st}} \quad (1)$$

where st stands for stoichiometric conditions, calculated by considering the complete combustion of the fuel, i.e. the reaction forming H_2O and CO_2 for CH_4 case and H_2O and SO_2 for H_2S.
Once the S_U was estimated in all the studied conditions, the Flammability Limits are evaluated by using the Limiting Laminar Burning Velocity ($S_{U,Lim}$) theory, defining the Flammability Limits as the composition such that the Laminar Burning Velocity is equal to a threshold value depending by gaseous mixtures and initial conditions, as calculated in the Equation 2.

$$S_{U,Lim} = \sqrt[3]{2\alpha g \frac{\rho_b}{\rho_u}} \quad (2)$$

where ρ_u and ρ_b are the unburned and burned gas density, respectively, α is the effective diffusivity and g the gravitational acceleration.

Results and discussion
Figure 1 shows the effect of equivalence ratio on the estimated values of Laminar Burning Velocity at initial temperature equal to 300 K for all the analyzed mixtures, being considered as reference temperature for further analysis.

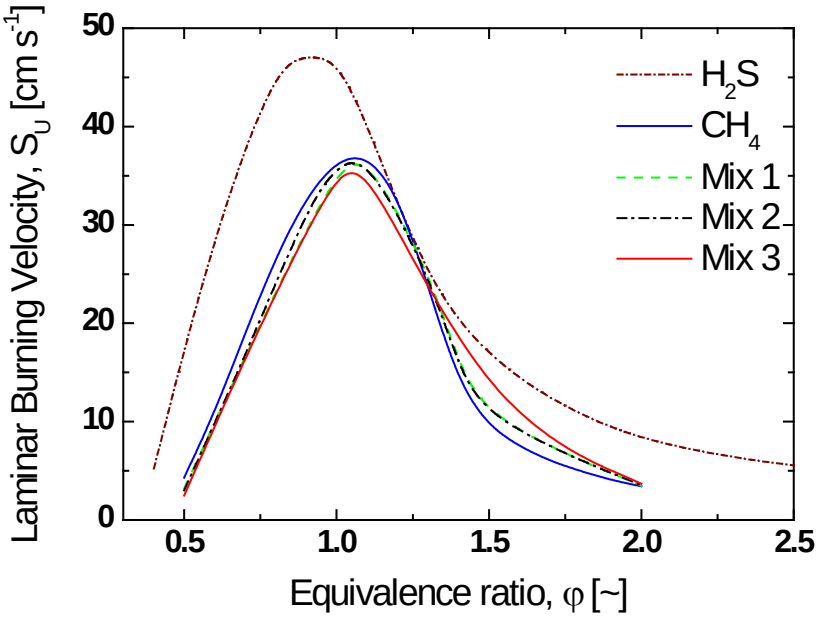

Figure 1. The Laminar Burning Velocity of CH_4-H_2S-Air mixtures at 300 K as a function of equivalence ratio φ and H_2S content.

Noteworthy, H_2S – Air mixtures shows a fundamental burning velocity, i.e. the maximum value of the S_U curve respect to the equivalence ratio, at stoichiometric composition whereas pure CH_4, and the three mixtures, as for many hydrocarbons, it shows a slight shift toward richer conditions (usually within the range 1.05 – 1.10), leading to different shapes for the pure fuels curves. This observation suggests the existence of a more efficient mechanism for the heat transfer for the pure H_2S case, being the fundamental burning velocity shifting mainly due to heat transfer mechanisms [6].

Additional conclusion can be drawn by analyzing lean and rich conditions separately. More specifically, it is relevant to report that the presence of H_2S reduces the S_U, although slightly, in lean and near stoichiometric conditions even if the H_2S – Air mixtures show larger values of S_U with respect to the pure CH_4 – Air mixture. These results are in contrast with the common correlation for the fuels additivity of the laminar burning velocity (e.g. Le Chatelier's rule). However, it should be due to the differences in the stoichiometry of the complete combustion reactions considered in the equivalence ratio definition. An additional explanation of the highlighted behavior should be represented by the reduced availability of H atoms with respect to the pure CH_4 case with the same O_2 concentration, leading to the reduction of the $H + O_2 \leftrightarrow O + OH$ reaction rate, which is considered as the

ruling reaction in the combustion system and the most relevant in the S_U determination.

This hypothesis complies with the results reported for the rich conditions, where the opposite trend is observed, i.e. the more H_2S content, the more S_U is estimated, being oxygen the limiting reagent in the aforementioned reaction. In order to evaluate the effect of initial temperature, the S_U of studied mixtures with respect to the equivalence ratio was shown at 250 K only (Figure 2). Additional data at 275 K are not reported here for the sake of brevity.

Quite clearly, the S_U decreases for all investigated mixtures if reducing the initial temperature. However, it is important to notice that effect of temperature on S_U are strongly dependent on the gaseous composition.

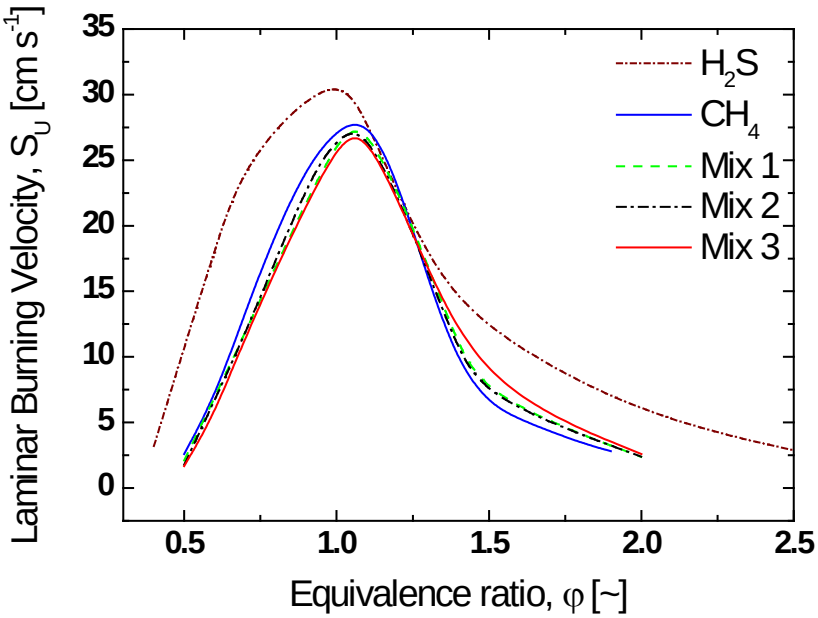

Figure 2. The Laminar Burning Velocity of CH_4-H_2S-Air mixtures at 250 K as a function of equivalence ratio φ and H_2S content.

In order to make a quantitative analysis on the coupled effect of temperature and composition additional calculations are required. To this regard, the exponential trend (Equation 3) is considered the best predictive correlation due to the simplicity, accuracy and range of applicability, as reported by Akram and coworkers (2012) [7].

$$S_U = S_{U,T^\circ} \cdot \left(\frac{T}{T_0}\right)^{\alpha} \quad (2)$$

where T_0 is the reference temperature, equal to 300 K in this study, S_{U,T° is the Laminar Burning Velocity at T_0 and α is the temperature exponent, which depends on the mixture composition. It is important to highlight that the variation between the obtained results for ternary mixtures and CH_4 – Air mixtures are negligible even at high concentration of H_2S (Mix 3) and these values are always lower than the one regarding H_2S – Air mixture, up to 30% at extremely lean and extremely rich conditions. The $S_{U,Lim}$ has been calculated by using the thermodynamic and transport coefficient data of the database of the used kinetic model. Hence, the Flammability Limits were estimated for all the studied mixtures and temperature (Table 1).

Table 1. Flammability limits in terms of %v/v as a function of initial temperature for different H_2S content.

	LFL [%v]				UFL [%v]			
T^{IN}	325 K	300 K	275 K	250 K	325 K	300 K	275 K	250 K
Pure CH_4	4.90	4.99	5.03	5.08	16.70	16.63	15.50	14.31
Mix 1	4.81	4.95	5.02	5.09	17.51	17.38	17.10	16.66
Mix 2	4.82	4.92	5.01	5.11	17.62	17.39	17.13	16.68
Mix 3	4.79	4.90	5.03	5.15	19.62	19.07	18.60	17.91
Pure H_2S	4.42	4.60	4.95	5.30	35.60	35.00	33.02	30.00

As expected, the LFL decrease almost linearly with respect to the initial temperature, whereas a parabolic trend is observed for UFL, thus suggesting the increased complexity of the phenomena occurring at rich conditions with respect to the lean conditions. Moreover, it is possible to conclude that by increasing the H_2S content, which is in principle more reactive, an enlargement of the flammability range is obtained, as expected. That is however in contrast with the calculated trend for S_U. Eventually, it should be considered that additional data, both experimental and numerical on the oxidation of H_2S in various process conditions, should be beneficial to improve the quality and accuracy of the performed analysis [7].

References

[1] Pio, G., Palma, V., Salzano, E., "Evaluation of kinetic model for the oxidative decomposition of H_2S", Proc. 40th Meeting of the Italian Section of the Combustion Institute, Rome, Italy, paper V-4, pp 50.

[2] Hertzberg, M., The Theory of Flammability Limits: Conductive-convective Wall Losses and Thermal Quenching, U.S. Department of the Interior, Bureau of Mines, 1984, p. 14.

[3] University of California at San Diego, "Chemical-Kinetic Mechanisms

for Combustion Applications.", (2017), Available online: http://web.eng.ucsd.edu/mae/groups/combustion/mechanism.html.

[4] Leeds University, "Sulphur mechanism. Version 5.2," (2005).

[5] Pio, G., Barba, D., Palma, V., Salzano, E., "Analysis of Detailed Kinetic Models for the Oxidation of Butene Isomers", Proc. ISCRE25, Florence, Italy, accepted.

[5] Xu C., Konnov, A.A., "Validation and analysis of detailed kinetic models for ethylene combustion," *Energy*, 43, 19–29 (2012).

[6] Akram, M., Saxena, P., Kumar, S., "Laminar Burning Velocity of Methane−Air Mixtures at Elevated Temperatures" *Energy & Fuels*, 5509–5518, (2012).

[7] Barba D., Cammarota F., Vaiano V., Salzano E., Palma V., Experimental and numerical analysis of the oxidative decomposition of H2S, Fuel, 198, 68-75 (2017).

NON-LINEAR EVOLUTION OF THERMODIFFUSIVELY UNSTABLE LEAN PREMIXED HYDROGEN FLAMES

L. Berger*[c], K. Kleinheinz*, A. Attili*, H. Pitsch*
[c]Corresponding author: l.berger@itv.rwth-aachen.de
*Institute for Combustion Technology, RWTH Aachen, Templergraben 64, 52064 Aachen, Germanny

Abstract
The characteristic patterns of thermodiffusively unstable lean premixed hydrogen flames are studied in several large-scale simulations conducting a parameter variation with respect to the thermal expansion ratio of the flame. This enables a systematic separation of the influence of the thermodiffusive and Darrieus-Landau instabilities on the flame front's evolution. A detailed chemical mechanism is employed and the variation of the thermal expansion ratio is obtained by a modification of the equation of state. For all simulations, the flame front corrugation possesses two characteristic length scales. In particular, flames without thermal expansion also feature both length scales, suggesting that both length scales originate from the thermodiffusive instability. Additionally, the size of the largest characteristic length scale is found to increase with the thermal expansion ratio.

Introduction
Recently, the interest in hydrogen combustion has increased as it represents a promising candidate for carbon-free energy carriers in future energy systems. In order to store an energy excess, hydrogen can be generated by the electrolysis of water and in times of demand, it can be electrified again by burning it in gas turbines. However, hydrogen combustion significantly differs from conventional combustion of hydrocarbons since it is prone to combustion instabilities. In particular, lean, premixed hydrogen combustion is susceptible to thermodiffusive and Darrieus-Landau instabilities. Thermodiffusive instabilities arise from the low Lewis number of hydrogen, which induces a strong disparity between the molecular and thermal fluxes entering and leaving the flame front. Depending on the Lewis number, this disparity can either stabilize or destabilize the flame front. The Darrieus-Landau instability is induced by the thermal expansion of the gas during combustion, which is always destabilizing. These instabilities have been studied by Matalon and Matkowsky [1], Pelce and Clavin [2], and Frankel and Sivashinsky [3], among others. As typical flame configurations always involve thermal expansion, thermodiffusively unstable flames are always accompanied by Darrieus-Landau instabilities. Thus, separately studying the impact of the thermodiffusive instability on the flame front evolution becomes difficult. In this work, we performed large-

scale Direct Numerical Simulations (DNS), for which the equation of state is modified such that a separation of the thermodiffusive and Darrieus-Landau instability is possible, enabling a rigorous analysis of the former.

Configuration

The simulation configuration comprises an initially planar, premixed, lean hydrogen/air flame that burns in a rectangular two-dimensional domain towards an inlet as shown in Fig. 1. The simulation domain is periodic in crosswise direction and the inlet velocity of the unburnt mixture is chosen such that the flame is stabilized sufficiently long within the simulation domain. The initially planar flame is perturbed by a harmonic wave to trigger the flame instabilities. All simulations feature an equivalence ratio of $\phi = 0.4$ and an unburnt temperature of $T_u = 298K$. Five different simulations have been conducted, in which the thermal expansion ratio ρ_u/ρ_b is varied from 1 to 4.42 by modifying the equation of state (c.f. section Governing Equations). All computational domains comprise a length of 200 laminar flame thicknesses in the streamwise and crosswise directions. If not stated differently, all quantities are normalized by the laminar flame thickness l_F or the laminar flame speed s_L of the corresponding unstretched premixed flame. Since the long-term behavior of the various flames is studied, simulations are run for at least 300 flame times. The constant density case is run for 1400 flame times.

Governing Equations & Numerical Framework

The governing equations of the DNS are given by the reacting Navier-Stokes equations in the low-Mach limit [4]. Chemical reactions are modeled by the mechanism of Hong et al. [5], which contains 9 species and 46 reactions. Species diffusivities are determined imposing constant, non-unity Lewis numbers, which are the same for all simulations. A detailed description of the employed numerical methods can be found in Ref. [6] and simulations similar to those conducted in this study are described in Ref. [7]. For all cases, the laminar flame thickness is resolved by ten grid points and timesteps between $3\mu s$ and $6\mu s$ are used. The imposed resolution yields numerical meshes of 2048 x 2048 grid points.

The equation of state has been modified by a scaling factor α with the objective to vary the flames' thermal expansion ratio. The resulting equation of state yields

$$\rho = \alpha \left(\frac{p}{RT} - \rho_u \right) + \rho_u, \quad (1)$$

where ρ, p, R, T represent the density, the pressure, the ideal gas constant divided by the mean molar mass of the fluid, and the temperature, respectively. ρ_u refers to the density of the unburnt mixture. The coefficient α is used to control the thermal expansion. It is varied among the different simulations between $\alpha = 0$, for which the density is constant, and $\alpha = 1$, for which the equation of state of an ideal gas is obtained. The case $\alpha = 1$ is referred to as reference case and is characterized by a thermal expansion ratio of ρ_u/ρ_b = 4.42.

Results and Discussion

In Fig. 1, characteristic snapshots of the flames are shown for four of the five conducted simulations. The simulation domains are cropped in streamwise direction to fit all flames, but their full width is shown. For the reference case, Berger et al. [7] proved that the flame dynamics become independent of the domain size if the width of the computation domain comprises at least 100 l_F. Similarly to their study, all flames in Fig. 1 reveal two characteristic length scales. First, a small wrinkling scale that periodically recurs along the flame front is identified, which, for the reference case, has been shown by Berger et al. [7] to be equal to the most unstable wave length of the dispersion relation. Second, a characteristic large structure always appears, which is marked in Fig. 1 and will be referred to as flame finger. These flame fingers periodically arise from the flame front and propagate towards the inlet. Except for the constant density case, these fingers are found to feature a tilting behavior in their propagation movement towards the inlet such that they tilt laterally and eventually collide with a different part of the flame. According to Berger et al. [7], this tilting behavior is a consequence of the deflection of the streamlines at a flame finger's tip. The displacement speed of the flame finger is found to be symmetric with respect to its tip, but as soon as a finger tilts laterally the flow field normal to the flame front becomes asymmetric such that the tilting behavior is amplified. In the constant density case the velocity is constant in the entire domain, so this mechanism does not apply and consequently no tilting behavior is observed. However, in the constant density case, the flame fingers can still move laterally just without tilting, which still enables an interaction among themselves, e.g., merging of two flame fingers. Thus, flame fingers are found to exist also for the constant density case, where Darrieus-Landau instabilities are suppressed. Consequently, their existence needs to originate from the thermodiffusive instability. A visual inspection of Fig. 1 suggests that an increasing thermal expansion ratio of the flame amplifies the size of the flame fingers. Movies of the temporal evolution of all cases will be shown at the conference.

In the following, the impact of the instabilities on the flame front corrugations is assessed by means of the consumption speed. It is defined as

$$s_{cons} = \frac{1}{L\rho_u Y_{H_2,u}} \int \dot{\omega}_{H_2} dx\, dy, \tag{2}$$

where L is the domain size in crosswise direction, $Y_{H_2,u}$ is the unburnt mass fraction of hydrogen and $\dot{\omega}_{H_2}$ represents the source term of hydrogen due to chemical reactions. Fig. 2 shows the time-averaged consumption speed with respect to the thermal expansion ratio ρ_u/ρ_b. The standard deviation of the temporal fluctuations is described by the respective error bar. If neglecting the constant density case, an increasing thermal expansion ratio always leads to an increasing consumption speed. Since the consumption speed depends on the ratio of the largest to the smallest characteristic length scale of the flame front corrugations [8], the range of length

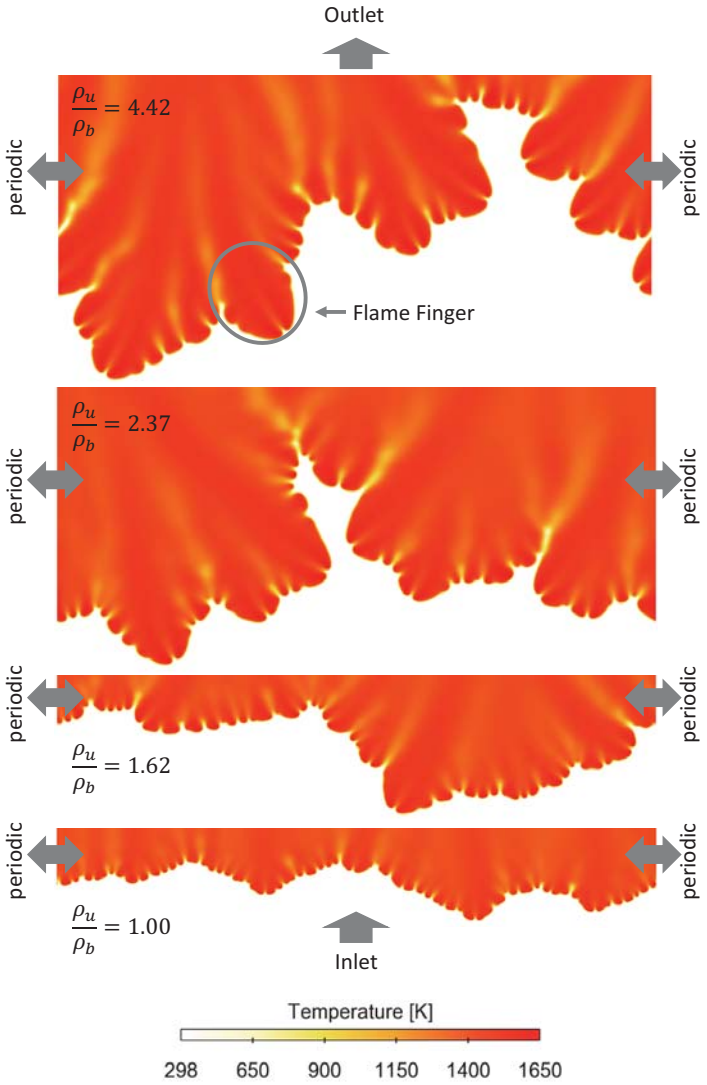

Figure 1. Thermodiffusively unstable premixed, lean hydrogen/air flames at $\phi = 0.4$ and $T_u = 298K$ for varying thermal expansion ratios. The simulation domains are cropped in streamwise direction to fit four of the five flames.

scales of the flame front wrinkles is found to increase with increasing thermal expansion ratio. Assuming the smallest length scale remains constant with respect to the laminar flame thickness, Fig. 2 quantifies that the size of the flame fingers is amplified by the thermal expansion ratio. However, the assumption of a constant smallest length scale still needs to be proven as well as the differing behavior of the constant density case requires further investigation.

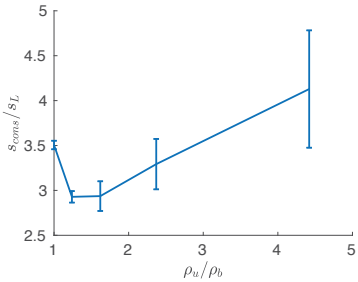

Figure 2. Consumptions speed versus thermal expansion ratio.

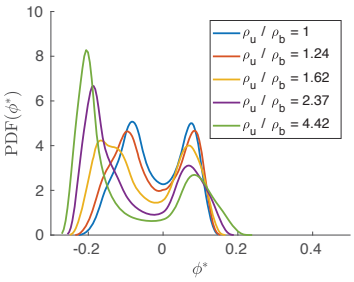

Figure 3. PDF of the local mixture fraction variation expressed by ϕ^*.

In a second step, the intrinsic flame instabilities are assessed by means of the local variations of the composition of the mixture along the flame front. For thermodiffusively unstable flames, a flame front segment that is convexly curved towards the unburnt contains richer mixtures due to the differential diffusion of hydrogen. This induces a local acceleration of the flame and vice versa for concavely curved flame front segments. The local stoichiometry of the flame is determined by the local mixture fraction [9,10]

$$Z = \left(\frac{Z_H}{\nu_{H_2} M_{H_2}} - \frac{Z_O - Y_{O_2,Air}}{\nu_{O_2} M_{O_2}}\right) \Big/ \left(\frac{1}{\nu_{H_2} M_{H_2}} + \frac{Y_{O_2,Air}}{\nu_{O_2} M_{O_2}}\right), \quad (3)$$

where Z_k refers to the element mass fraction of element k, $Y_{O_2,Air}$ is the mass fraction of O_2 in air, the molecular weight of species k is denoted by M_k, and $\nu_{H_2} = 1$ and $\nu_{O_2} = 0.5$ are the stoichiometric coefficients. For convenience, the mixture fraction is expressed in terms of a local equivalence ratio ϕ_{loc} according to

$$\phi_{loc} = \frac{Z}{1-Z} \cdot \frac{1-Z_{st}}{Z_{st}}, \quad (4)$$

where $Z_{st} = 0.028$ is the stoichiometric mixture fraction. Fig. 3 shows the time-averaged PDF of the normalized local equivalence ratio $\phi^* = (\phi_{loc} - \phi_{ref})/\phi_{ref}$ along the flame front. The flame front is defined by the isoline of 1000 K and ϕ_{ref} refers to ϕ_{loc} of an unstretched premixed flame at 1000 K. The PDFs of all cases possess two distinct peaks, which reflect the differential diffusion of hydrogen that leads to leaner and richer mixtures along the flame front. The local equivalence ratio fluctuates up to 25% along the flame front. The variations of local stoichiometry are found to become more pronounced with increasing thermal expansion ratio. For

increasing thermal expansion ratio, the lean peak moves to even leaner mixtures and less flame front segments exist that possess a stoichiometry characteristic of the unstretched flame ($\phi^* = 0$). Thus, differential diffusion and hence thermodiffusive instabilities are enhanced by the thermal expansion of the flame.

Conclusion

Five large-scale DNS have been conducted for a reference flame at an equivalence ratio of $\phi = 0.4$ and an unburnt temperature of $T_u = 298K$. A parameter variation with respect to the thermal expansion ratio of the flame enables a rigorous separation of the influence of the thermodiffusive and Darrieus-Landau instabilities on the flame front's evolution. In agreement with previous studies, two characteristic length scales of the flame front corrugations have been identified, which consistently appear throughout all simulations. Both scales are found to originate from the thermodiffusive instability. Additionally, the largest scale appears to grow when the thermal expansion ratio increases.

Acknowledgement

Generous support of the Deutsche Forschungsgemeinschaft (DFG) under grant number PI 368/9-1 for L. B. is gratefully acknowledged. A. A. and H. P. gratefully acknowledge generous support of the European Research Council (ERC) under the European Union's Horizon 2020 research and innovation program (grant agreement No. 695747). Computational resources have been provided by the Gauss Centre for Supercomputing/Leibniz Supercomputing Centre in Munich.

References

[1] M. Matalon, B. J. Matkowsky, J. Fluid Mech. 124 (1982) 239–259.
[2] P. Pelce, P. Clavin, J. Fluid Mech. 124 (1982) 219–237.
[3] M. L. Frankel, G. I. Sivashinsky, Combust. Sci. Technol. 29 (1982) 207–224.
[4] A. Tomboulides, J. Lee, S. Orszag, J. Scientif. Comput. 12 (1997) 139–167.
[5] Z. Hong, D. F. Davidson, R. K. Hanson, Combust. Flame 158 (2011) 633–644.
[6] O. Desjardins, G. Blanquart, G. Balarac, H. Pitsch, J. Comput. Phys. 227 (2008) 7125–7159.
[7] L. Berger, K. Kleinheinz, A. Attili, H.Pitsch, Proc. Comb. Inst. 37, submitted
[8] O. Chatakonda, E. R. Hawkes, A. J. Aspden, A. R. Kerstein, H. Kolla, J. H. Chen, Combustion and Flame 160 (2013) 2422–2433.
[9] A. R. Masri, R. W. Bilger, Proc. Comb. Inst. 21 (1988) 1511-1520.
[10] N. Peters, Cambridge University Press, Cambridge, 2000.

FLAME FOLDING AND WRINKLING FACTOR FOR 2D AND 3D HYDROGEN-AIR FLAMES

M. Kuznetsov*, N. Chaumeix, J. Yanez*, S. Tengah***
e-mail: kuznetsov@kit.edu
* Karlsruhe Institute of Technology,
Hermann-von-Helmholtz Platz 1, 76344, Eggenstein-Leopoldshafen, Germany
** CNRS – ICARE, 1C, avenue de la recherche scientifique,
45071 Orléans, Cedex 2, France

Abstract
An experimental study and theoretical analysis of laminar flame propagation in spherical 3D- and planar 2D-geometries for hydrogen-air mixtures was carried out in order to investigate an effect of flame instability, a flame structure and a mechanism of initial quasi-laminar flame acceleration prior turbulent flame acceleration and DDT. The theory of laminar flames and theoretical analysis based on solution of Sivashinsky-Michelson equation was performed to explain the experimental results. It was theoretically found, that the burning velocity increased by the factor of 1.2-1.6 due to the flame instability. This value was found to be exactly proportional to the flame area amplification and well confirmed by current experimental data in 2D- and 3D-geometries. Such a flame wrinkling leads to primary flame acceleration remaining the flame of laminar structure in general.

Introduction

Promptly after ignition, the surface of the flame wrinkles due to the Darrieus–Landau and the thermo-diffusive instability [1, 2]. A 2D - planar geometry has an advantage that independent of the boundary layer effect in transversal direction the structure of the flame instability in a radial direction will be freely developed and clearly distinguished. In 3D-geometry, internal flame structure is not visible from outside even with a schlieren system. In order to measure the wrinkling of the flame surface a schlieren imaging system and a laser tomography can be used.

Theory

The enormous potential of Sivashinsky equation [3] for the reproduction and modeling of the different flames instabilities has been demonstrated in [4-5]. The influence of different instabilities as Darrieus-Landau, thermo-diffusive and Rayleigh-Taylor on flame shape and dynamics of the flame for different hydrogen-air mixture has been investigated in [6] utilizing the Michelson method [4] and taking into account Lewis number *Le* and Zeldovich number β. The surface (Fig.1) obtained by numerical integration of Sivashinsky equation shows the dynamics of flame profile as heat map in which the local position of the flame relative to its average position is represented.

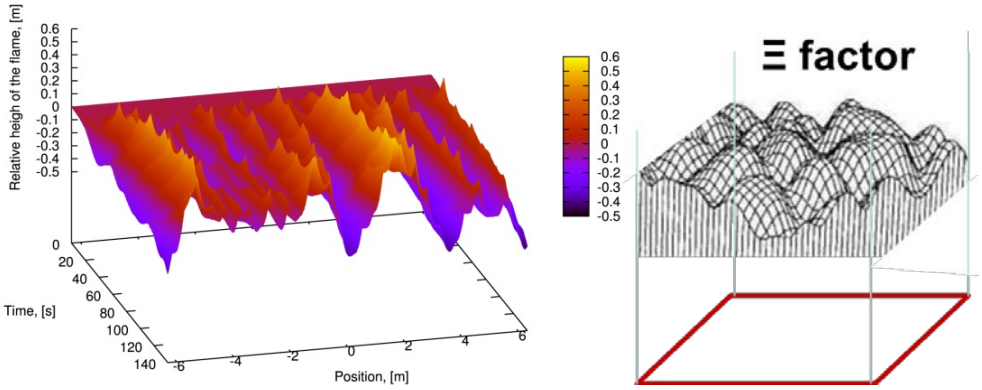

Figure 1. Results of the integration of the one dimensional Sivashinsky equation. Color scale is the position of the flame relative to the average position.

The ratio of real flame surface to planar one is defined by wrinkling factor Ξ. Effective flame velocity S_e accounts the enhancement wrinkling factor Ξ due to flame instability as follows $S_e = \Xi \cdot S_L$. So that the wrinkling factor Ξ is one of the major properties of flame behavior, responsible for potential flame acceleration. The wrinkling factors obtained in [6] by solving Sivashinsky equation for different hydrogen-air mixtures is very close to the ratio S_e/S_L (Table 1).

Table 1. Example of a table.

$[H_2]$ Vol. %	Ξ	S_L [m/s]	S_e [m/s]	S_e/S_L
8	1.34	0.06	0.09	1.49
9	1.33	0.08	0.12	1.50
10	1.34	0.11	0.17	1.58
12	1.34	0.19	0.28	1.48
15	1.38	0.34	0.54	1.58
20	1.46	0.9	1.43	1.59
25	1.52	1.6	2.95	1.84
30	1.49	2.19	3.84	1.75
40	1.42	2.88	4.87	1.69
50	1.4	2.59	4.23	1.63
60	1.38	1.86	2.91	1.56

Dynamics of the wrinkling factor demonstrated two different behaviors [6]. For very lean mixtures, up to 12 % vol H_2 an initial plateau exists, representing a regime in which the thermo-diffusive instability accounts for the most of the excess of surface. This regime is followed by a more or less fast transition that culminates in a regime in which larger surface wrinkling factor due to Darrieus-Landau instability is reached. For richer mixtures above 12 % vol H_2 the transition to

saturation is fast and has no visible transient to the final stage led by Darrieus-Landau instability. Another interesting fact is the almost similar value Ξ = (1.33÷1.52) that the surface wrinkling factor finally reaches for all the concentrations of H_2 (Table 1).

Objectives

The main purpose of the current work is to experimentally investigate the effect of instabilities on the hydrogen flame behavior in a planar 2D- and a spherical 3D-geometry. The main interest of this work is to investigate how the flame instability affects dynamics of the flame propagation and whether the flame acceleration would occur in such configurations leading to the transition from deflagration to detonation (DDT).

Experimental details

2D-experiments were performed a thin layer of H_2 – air mixtures with a center ignition. The experimental facility consists of two glass plates assembly, hydrogen-air intake and exhaust system, an ignition system, an optical schlieren system combined with a high speed camera, data acquisition and control system.

The glass plate assembly was made of two transparent Quartz plates with spacers placed in between to keep parallel gaps of 2, 4 and 6 mm. Experiments were carried out in a squared frame with dimensions of 500 x 500 mm. The mixture within the glass plate assembly was ignited in the center using a spark electrode igniter. The exposure time of a test mixture was set about 30s prior ignition to eliminate the effect of initial turbulent motion. The spark energy was less than 10 mJ. Hydrogen-air mixtures in the range 10-50% H_2 were investigated in the current work. Mass flow rate controllers were used to inject premixed composition directly into the gap. The mixture was isolated around the peripheral sides by a weak plastic foil (~5 mkm). The weakness of the foil provides simultaneous opening to the ambient atmosphere at the perimeter to keep constant combustion pressure of 1 bar. All experiments were performed at ambient conditions of 1 bar and 293 K.

Experimental results and discussions

Figure 2 shows a sequence of flame contours at different times for a very lean mixture of 14%H2 in air. The thermo-diffusion and Darrieus–Landau instabilities lead to the development of a double-mode cellular structure of the flame surface. The primary thermo-diffusion instability appears almost immediately after the ignition, leading to quite random, relatively small-size mode of cellular structure. Then, the large-size mode of very regular cellular structure due to Darrieus–Landau instability develops with a growing cell size similar to the flower petals. Since the Markstein number becomes positive for hydrogen-air mixtures above 20%H2 it changes the sensitivity of the flame to thermo-diffusion instability. In Fig. 3, very smooth flame surface can be seen for mixtures with 30 and 50% H2 in air at the initial stage of the process. Only after a flame radius of the order of 10-15 cm, the

cellularity of the flame surface appears due to Landau-Darrieus instability. The wrinkling factor $\Xi = P/P_m$ (Fig.2, right) was evaluated as a ratio of real flame area A (proportional to the perimeter P) to the mean value $P_m = 2(\pi \cdot A)^{1/2}$. The maximum value Ξ_{max} = 1.7 is very close to theoretical one for lean mixtures. Very close values in the range 1.4-1.7 were found for all tested lean hydrogen-air mixtures from 10 to 20%H2. For mixtures with positive Markstein number, the saturated value of wrinkling factor has not reached because of limited space of the system.

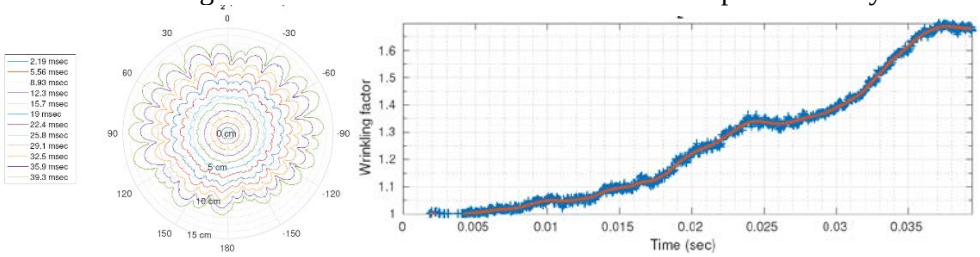

Figure 2. Flame dynamics and wrinkling factor for lean H_2 – air mixture (14% H_2 in air) in a 6-mm gap layer

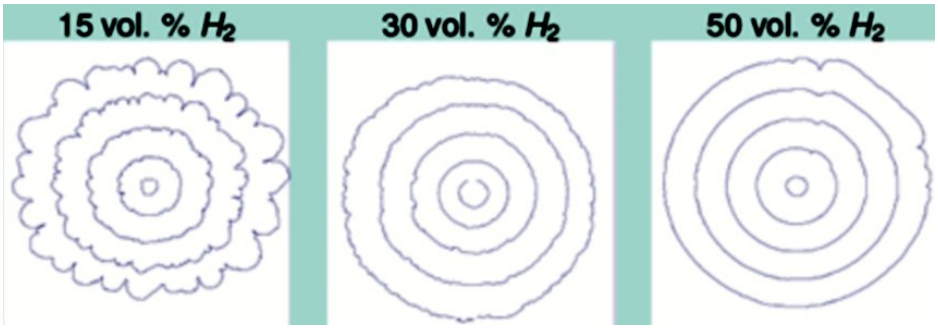

Figure 3. Flame propagation for lean H_2 – air mixture (15, 30 and 50% H_2 in air) in a 6-mm gap layer

Very similar flame structure for 3D-geometry was experimentally obtained using laser tomography [7]. The winkled flame structure, amplification (wrinkling) factor of the surface, AF_{Surf} and the speed, AF_{Speed}, from paper [7] are plotted as a function of the radius of the flame for four different molar fraction of hydrogen in air in Figure 4. The maximum values for flame surface wrinkling factor AF_{Surf} =1.4-1.6 is very close to that for 2D-geometry (ses Fig. 2). Approaching to stoichiometric mixture, the surface wrinkling factor establishes in the range 1.2-1.4.

The flame front velocity was calculated by taking the difference between the instantaneous radius of the flame front, r_f and igniter position, r_o divided by the actual time difference. The stretch-free laminar burning velocity were obtained by linear extrapolation of a plot of the laminar burning velocity S_L as a function of the stretch rate K (Fig. 5). The laminar burning velocity S_L is first calculated by dividing the flame front velocity S_F by the expansion factor σ and stretch rate K.

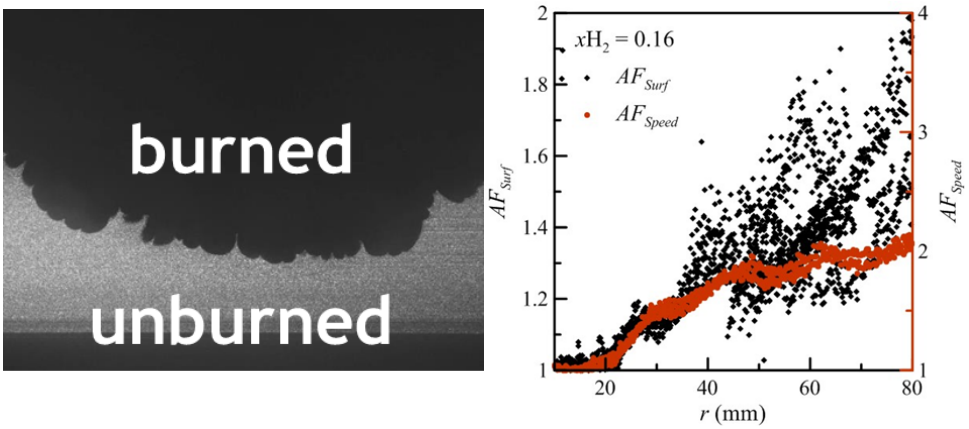

Figure 4. Laminar burning velocity as a function of stretch rate K for H_2 – air mixtures: 2D case current work (left); 3D case Chaumeix et al. [7] (left).

Assuming a linear correlation, the influence of the flame front stretch on the laminar flame speed can be specified by Markstein length L_M:

$$S_L(K) = S_{L,s} - L_M \cdot K \tag{1}$$

where $S_L = S_f/\sigma$, and $S_{L,s}$ are the stretched and free of stretch laminar flame velocities, A is the visible flame area for flame radius r_f and a layer thickness h, $A = 2\pi r_f h$, K is the stretch rate calculated for 2D-planar case as follows

$$K = \frac{1}{A}\frac{dA}{dt} = \frac{1}{r_f}\frac{dr_f}{dt} \tag{2}$$

The stretch rate in a planar geometry (Eq. 2) is two times smaller compared to a spherical 3D-geometry [7].

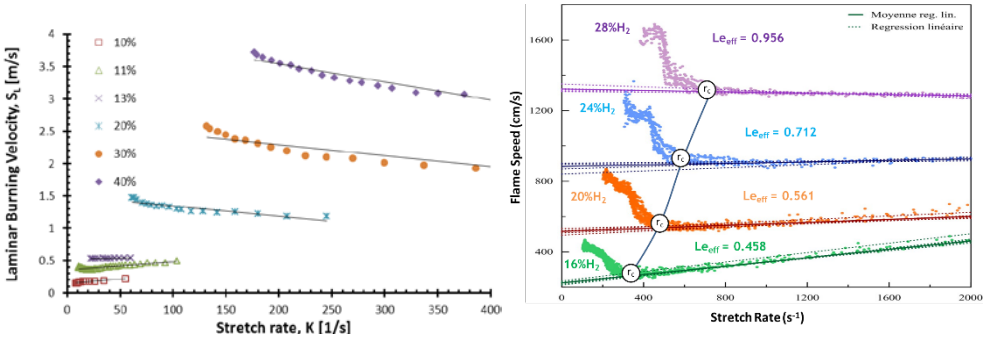

Figure 5. Laminar burning velocity as a function of stretch rate K for H_2 – air mixtures: 2D case current work (left); 3D case Chaumeix et al. [7] (left).

The linear extrapolation of the curve (Fig. 5) represents the stretch-free laminar burning velocity $S_{L,s}$ as the y-intercept of the line fit, whereas the slope of the line

gives the Markstein length, L_m. Figure 5 (left) shows the relationship between laminar burning velocity S_L and the stretch rate K for different H_2 – air mixtures for a peripherally open planar configuration at a gap size 6 mm. Right plot shows the same dependence for 3D case [7]. A critical flame radius r_c in Fig. r when the flame velocity abruptly increases corresponds to the moment when the Darrieus–Landau instability appears producing well developed regular cellular structure.

Conclusions

Hydrogen flame behavior in two-dimensional geometry was experimentally investigated. Hydrogen combustions of H2 – air mixtures were carried out within the gap between two transparent quartz plates spaced by 2, 4 and 6 mm.

To analyze the influence of flame instabilities, the stretch-free laminar burning velocity of the flame and Markstein length were determined via post-processing of optical measurement. Negative Markstein lengths were obtained for lean H2 – air mixtures (< 15% H2). The results also show that the laminar burning velocity strongly depends on H2 concentration and gap size.

The appearance of the cellular structure for H2 – air mixtures was found as a result of two main intrinsic instabilities of the flame, thermal – diffusive instability and hydrodynamic instability, namely Landau – Darrieus instability. Wrinkling of the flame due to the flame instability and enhanced flame area result in a flame velocity amplification factor Ξ = 1.2-1.5, which is the same as found by derivation of the Sivashinsky eqation in [6]

References

[1] Darrieus, G., “Propagation d’un front de flamme”, Communication présentée à La Technique Moderne. (1938)

[2] Landau, L.D., “On the theory of slow combustion”, *Acta Physicochim URSS* 19: 77–85 (1944)

[3] Sivashinsky, G., “Nonlinear analysis of hydrodynamic instability in laminar flames—I. Derivation of basic equations”, *Acta astronautica*, 4: 1177–1206 (1977)

[4] Michelson, D., Sivashinsky, G., “Nonlinear analysis of hydrodynamic instability in laminar flames—II. Numerical experiments”, *Acta astronautica*, 4: 1207–1221 (1977)

[5] Sivashinsky, G., “On the intrinsic dynamics of premixed flames”, *Phil. Trans. Roy. Soc. A, London*, 332(1624): 135–148 (1990)

[6] Yanez, J., Kuznetsov, M., “An analysis of flame instabilities for hydrogen–air mixtures based on Sivashinsky equation”, *Physics Letters A*, 380(33):2549-2560 (2016)

[7] Goulier, J., N’Guessan, K., Idir, M., Chaumeix, N., “Tomographic visualization of thermo-diffusive instabilities of lean hydrogen/air mixtures”, *Proc. 26th ICDERS*, July 30-August 4, 2017, Boston, MA (2017)

The effect of equivalence ratio variation on the flame structures of laminar low-pressure tetramethylsilane/hydrogen flames

Y. Karakaya, T. Kasper
Mass Spectrometry in Reactive Flows-Thermodynamics, IVG
University of Duisburg-Essen, 47057 Duisburg, Germany
yasin.karakaya@uni-due.de

Abstract
This paper investigates the decomposition of tetramethylsilane (TMS) and the formation of key intermediates, which form silicon oxide clusters in laminar premixed low-pressure tetramethylsilane flames using Molecular-Beam Mass Spectrometry (MBMS). The flame-based particle synthesis strongly depends on the pressure, temperature and precursor. In this work, the flame conditions are changed to control the formation of the monomers and consequently influence the formation of silicon oxide cluster, which are considered as precursors for solid nanoparticles. The measurements show that TMS reacts with flame radicals (H, O and OH), oxygen and water, and forms $Si(OH)_4$ as the most stable intermediate at high flame temperatures. In addition, SiO_2 and HSiO, $(CH_3)_3Si(CH_2)OO$, $(CH_3)_3SiO$, $(CH_3)_2Si(OH)$, $(CH_3)Si(OH)_2$, $Si(OH)_3$ are found as the most abundant intermediates in these flames. Small silicon containing clusters with the structure $Si_xO_yH_z$ could also be detected. These are most likely formed in reactions of $Si(OH)_4$. The small clusters lead to subsequent growth of silica nanoparticles. The influence of the flame conditions on the most stable intermediates and silicon oxide clusters and their reaction pathways are investigated systematically for equivalence ratios of Φ=0.8–1.2 for the first time. This work results an extensive database consisting of gas-phase species and small clusters formed during the synthesis of silica nanoparticles. This data base is needed for future reaction mechanism development and validation.

Introduction
Every year, millions of tons of silicon oxide nanoparticles are produced in flame reactors for a variety of applications in medical technology and pharmaceutical industry. The synthesis in a flame reactor is particularly attractive since it produces high-purity nanoparticles at scalable production rates in a continuous gas-phase synthesis process. Laminar low-pressure flames stabilized on model burners are valuable tools for the investigation of combustion kinetics [1]. It is the aim of this work to extend the established technique of Molecular-Beam Mass Spectrometry (MBMS) to the investigation of the decomposition of tetramethylsilane (TMS) and cluster growth in flat, premixed, laminar low-pressure H_2/O_2/Ar-flames. The influence of the flame conditions on the decomposition products of TMS is

investigated systematically. Experimentally determined species concentrations in model flames are needed to validate kinetic reaction mechanisms of these processes.

Experimental setup

Time-of-flight mass spectrometric in-situ measurements on model-flames are used to get a fundamental understanding of the combustion and synthesis processes. The reacting gases of the low-pressure flame (30 mbar) are sampled at different positions in the flame reactor, transferred to and analyzed by a time-of-flight mass spectrometer (Resolution = $m/\Delta m$ = 2400, Company Kaesdorf, Munich). The reacting gases expand through a quartz sampling-nozzle into an intermediate low-pressure chamber (10^{-4} mbar) and form a molecular-beam, which is guided into an electron ionization chamber. The ionized molecules pass ion-optical devices and finally reach the spectrometer (10^{-7} mbar). The recorded mass spectra allow an exact and simultaneous identification of species existing in the sampled gas at different positions along the centreline of the model flames and give an insight into the initial reaction pathways in the early stage of gas-phase synthesis of nanoparticles. The focus of this study is on the decomposition of the precursor and the formation of the first gas-phase species and small clusters. Nanoparticles were outside of the detection range of the mass spectrometer in this study. Tetramethylsilane (sigma-Aldrich, purity of 99 %) was metered with a syringe pump (Landgraf Laborsysteme) with an accuracy of ± 2 % referred to the delivered volume and evaporated in a home-built evaporator at 333.15 K. Calibrated mass flow controllers regulate the gas flow with an accuracy of ± 5 %.

Results and discussion

In this study, the influence of equivalence ratio on the decomposition of the commercially available precursor tetramethylsilane (TMS) in oxygen-rich, stoichiometric and fuel-rich hydrogen/oxygen/argon low-pressure flames is investigated for the first time. The mass spectra are used to identify all species in the flames by their accurate masses. After appropriate calibration, the signals strength of each species in the mass spectrum is related to the mole fraction of the species in the flame so that mole fraction changes can be monitored for different positions in the flame and for different flame conditions. Table 1 lists the initial molar gas composition of the flame with addition of 600 ppm TMS and without addition of TMS in a H_2/O_2/Ar-flame. The mole fractions for H_2, O_2, H_2O, CO, CO_2 and Ar are calculated by solving the O-, H-, C- element balance. Figure 1 shows that the profiles of the major species of the pure hydrogen flame are in good agreement with the simulation. The flame structure is simulated with the Chemical Workbench (Kintech Lab Ltd.) [2], using the reaction mechanism of Li et al. [3] and the disturbed temperature profile, which is determined according to the procedure of Struckmeier et al. [1]. The comparison of the species profiles in figure 1 shows that the addition of TMS shifts the species profiles closer to the

burner, which can be explained by its reaction with the flame radicals eg. O, OH, H.

Table 1. Initial molar gas composition of the flame gases with addition of 600 ppm TMS (Flame 1-3) and without addition of TMS (4-6) with an overall volume flow of 2 slm at standard conditions (1013 mbar, 273.15 K).

	Φ	x_{H2}	x_{O2}	x_{Ar}	x_{total}	TMS (ppm in 2lm)
1)	0.8	0.308	0.192	0.5	1	600
2)	1.0	0.334	0.166	0.5	1	600
3)	1.2	0.353	0.147	0.5	1	600
4)	0.8	0.308	0.192	0.5	1	0
5)	1.0	0.334	0.166	0.5	1	0
6)	1.2	0.353	0.147	0.5	1	0

The temperature profiles for the flames 1)-3) were measured with the aid of an Al_2O_3-coated thermocouple and are radiation-corrected. For the measurements of the temperatures by thermocouple we expect an error of ±100K. As expected the maximum temperature within the flame is achieved with stoichiometric flame conditions in the reaction zone. However, higher temperatures are present immediately above the burner under fuel-rich flame conditions, followed by the stoichiometric and fuel-lean flame conditions.

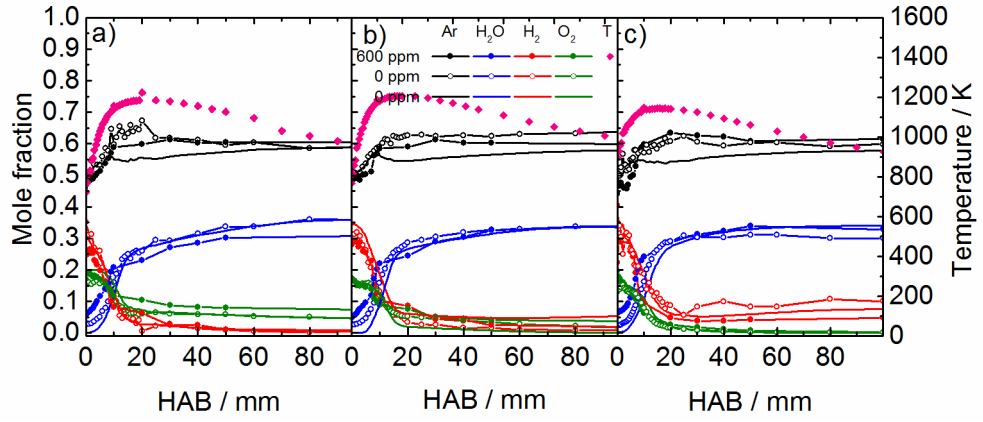

Figure 1. Mole fractions of major species in a) Φ=0.8, b) Φ=1, c) Φ=1.2 with and without addition of 600 ppm TMS (Flame 1-6) and temperature profiles. Symbols represent experimental data and lines simulations.

Figure 2 shows the decomposition of TMS in the flame 1)-3) and the formation of the predominant carbonaceous major decomposition products CO_2 and CO, which do not differ significantly in all flames within the first 8 mm. From the carbon

balance, it becomes clear that the carbon from TMS reacts completely to CO and CO_2. Further carbonaceous intermediates such as e.g. CH_4, HCHO, C_2H_4 and Si-C-O-H species are formed, which are two orders of magnitude smaller.

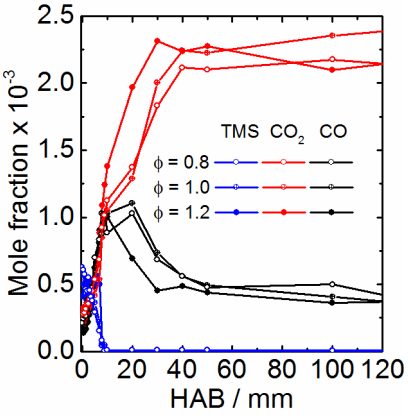

Figure 2. Decomposition of TMS and major carbonaceous species of TMS

For the flames 1)-3) a list of quantified Si-C-O-H and Si-O-H species is compiled. By knowing all the present species along the height of the flame, reaction pathways can be postulated. The decomposition of TMS is initiated by H-abstraction due to reactions with flame radicals such as e.g. O, OH and H and forms $(CH_3)_3Si(CH_2)$. $(CH_3)_3Si(CH_2)$ reacts with oxygen and forms the peroxide $(CH_3)_3Si(CH_2)OO$ very close to the burner in large quantities, which could be measured in all flames (see Figure 3a). In the flames 1)-3) H-abstraction is the predominant reaction step since the peroxide is the predominant silicon-species at the beginning of the reaction zone. As expected, peroxide formation is highest in oxygen-rich flames. From Figure 3a)-3c) it can be seen that with increasing equivalence ratio the mole fraction of the silicon-containing intermediates decreases, and consequently reduces particle formation. The profile shapes of the intermediates reveal that the reaction zone is narrowest under fuel-rich flame conditions. The peroxide $(CH_3)_3Si(CH_2)OO$ decomposes further to $(CH_3)_3SiO$ and HCHO, which are both measured in moderate amounts. Trimethysilanol $(CH_3)_3SiOH$ is formed by a reaction with H_2. This reaction sequence can be repeated until $Si(OH)_4$ is formed. Additionally, the stable $Si(OH)_4$ can be formed by a stepwise substitution of the methyl ligands by hydroxyl groups. Figure 3a)-3c), and Figure 4a), 4b) show that one to four hydroxyl groups are attached to the silicon core and their maximum moves upstream, respectively. In flame-based particle synthesis, two particle formation zones within the flame have already been observed for iron systems. In the first particle formation zone, an easily condensable gaseous species such as e.g. SiO_2 condenses and forms particles. For fuel-rich flames, the gaseous SiO_2 is below the detection limit, while for stoichiometric and oxygen-rich flames a significant amount could be measured (see Figure 4c). Also, the noisy mole

fraction profile of SiO_2 indicates that gaseous SiO_2 may condense to particles early in the flame. The second particle formation zone is at a far distance from the burner at higher temperatures and we expect it is initiated by $Si(OH)_4$.

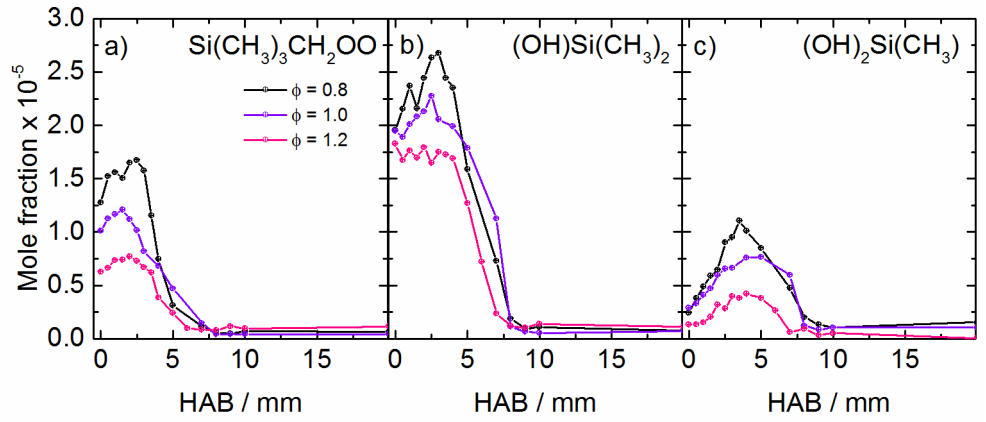

Figure 3. Selected Si-C-O-H decomposition products of TMS in hydrogen-flames

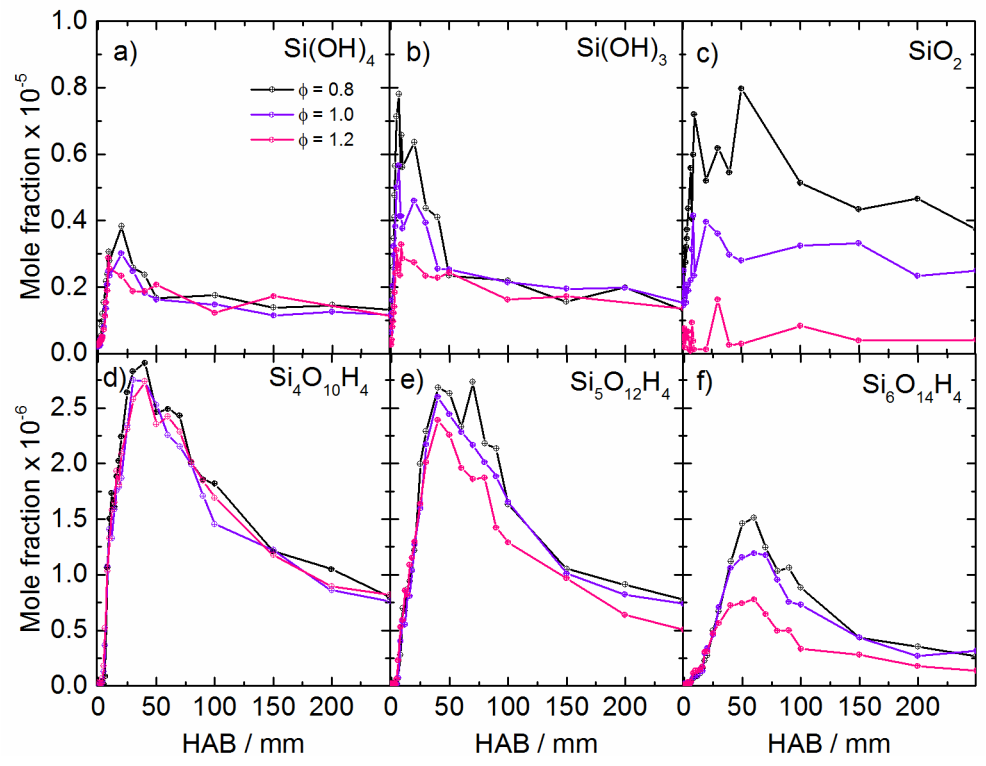

Figure 4. Selected Si-O-H species of TMS in hydrogen flames

Figure 4a) shows the monomer $Si(OH)_4$, which is present in high concentrations at high temperatures and can react further to silicon oxide clusters with the structure $Si_xO_yH_z$ (see Figure 4d)-4f)). While the four- and five- silicon oxide clusters do not differ from each other, the increase in the maximum of the six-core silicon oxide cluster is clearly visible with decreasing equivalence ratio.

Conclusion

This study has shown the effect of changing the equivalence ratio on the flame structures of low-pressure tetramethylsilane/hydrogen flames and the results can be summed as follows: We suggest that the reaction mechanism in the investigated equivalence ratio is similar, because we have shown the existence of the same Si-C-O-H and Si-O-H species for the whole range. The CO/CO_2 ratio does not change significantly in the exhaust. The profiles of the carbonaceous major species reveal that the reaction zone becomes narrower for fuel-rich flame conditions and can thus be controlled by the variation of the equivalence ratio. The noisy mole fraction profile of SiO_2 indicates that gaseous SiO_2 may condense to particles early in the flame (first particle formation zone). For fuel-rich flames, the gaseous SiO_2 is below the detection limit, while for stoichiometric and oxygen-rich flames a significant amount was measured. The second particle formation zone is at a far distance from the burner at higher temperatures and we expect it is initiated by $Si(OH)_4$. While the four- and five-core silicon oxide clusters differ from each other, the increase in the maximum of the six-core silicon oxide clusters is clearly visible with decreasing equivalence ratio.

Acknowledgements

Work was funded by the German Research Foundation DFG within the scope of the Research Unit FOR2284 under contract KA 3871/4-1. Helpful discussions with Burak Atakan and Christof Schulz are gratefully acknowledged.

References

[1] Struckmeier, U., Oßwald, P., Kasper, T., Böhling, L., Heusing M., Köhler, M., Brockhinke, A., Kohse-Höinghaus, K., “Sampling Probe Influences on Temperature and Species Concentrations in Molecular Beam Mass Spectroscopic Investigations of Flat Premixed Low-pressure Flames”, *Z. Phys. Chem.* 223 (2009) 503-537.

[2] *Kintech Laboratory*, Chemical WorkBench® 4.0, available online at http://www.kintechlab.com/products/chemical-workbench/

[3] Li, J., Zhao, Z., Kazakov, A., Dryer, F.L., “An Updated Comprehensive Kinetic Model of Hydrogen Combustion”, *Int. J. Chem. Kinet.* 36 (2004) 566-575.

Numerical and experimental studies of laminar counter-flow diffusion flames using biomass-based gaseous fuels

Marie-Theres Scharl*, Douglas Greenhalgh*, Alba Diéguez Alonso*, Frank Behrendt*
m.scharl@tu-berlin.de
*Department of Energy Process Engineering and Renewable Energy Conversion Technologies, Technische Universität Berlin, Fasanenstr. 89, 10623 Berlin, Germany

Abstract
Further advance in the utilization of biomass-based gaseous fuels in internal combustion engines requires a deeper understanding of the complex combustion chemistry behind, as well as of the coupling of the chemistry with physical phenomena such as turbulence. The former is investigated in the present study combining both experiments with numerical simulations on different types of laminar diffusion flames (sooting and non-sooting).
Laser-based spectroscopy techniques, in particular laser-induced Rayleigh scattering and laser-induced fluorescence, are applied as diagnostic tools, which can provide accurate understanding of temperature distributions, as well as monitoring the flame front through the tracking of intermediate species, such as CH_2O, respectively. Additionally CH* chemiluminescence during the combustion is quantified, as this radical has considerable application in the reaction zone marking, providing a possibility to exactly measure the spatial position the flame.

Methods
The focus here is put on non-premixed product gas mixtures with CH_4 or CH_4 diluted by CO_2, N_2, CO, O_2, and/or H_2 as fuel and air as oxidizer at a wide range of air-fuel ratios. The flow velocities are increased until aerodynamic quenching of the flame occurs. The combustion behaviour at these different flame conditions is studied in a flat-flame counter-flow burner representing an essential element to advance the understanding of the so-called flamelet model of turbulent combustion processes. In correspondence to these experiments, the mentioned flames were numerically simulated by an implicit Fortran code capable of simulating this type of reactive flows [1].
By solving the governing equations for momentum, mass fractions, energy and total mass, temperature and species fraction profiles can be calculated for various strain rates, i.e., flow velocities, finally resulting in a flamelet library to be applied in future work for the numerical simulation of turbulent flames.
Furthermore, based on the simulated species profiles and the incorporation of the Rayleigh cross sections of the major species, together with the imaging system's

possible point spread function to minimize crosstalk background phenomena, a good fit between model and experiment can be established.
This study supports the study of Connelly et al. [2] that models should simulate experiments rather than experiment data being used to estimate quantities such as temperature indirectly (Figure 1).

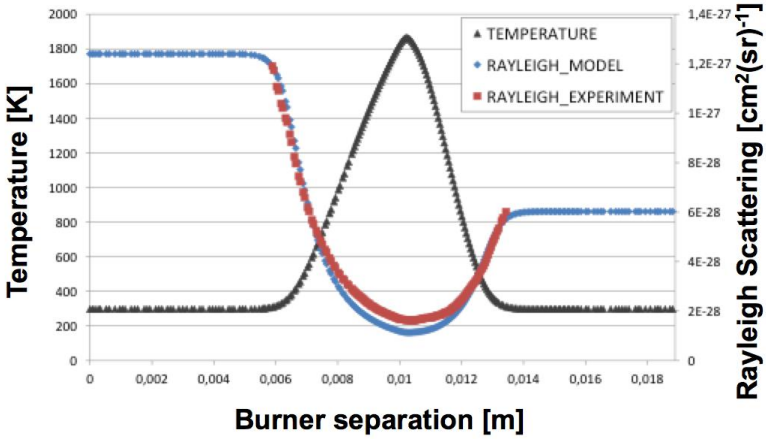

Figure 1. Numerical and experimental Rayleigh signals and temperature profile for non-premixed 40% CH_4 - 40% CO_2 -20% N_2 - air flames

Results

An increase of flow velocities and the thereby finally induced extinction, or straining out, of the diluted flames, are discussed with respect to the changes of the temperature profiles and decreasing peak temperatures both in regards to the corresponding Rayleigh signals as seen in Fig.2.

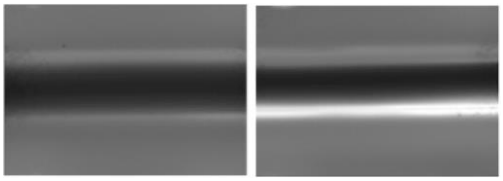

Figure 2. Experimental Rayleigh signal corresponding to temperature fields for diluted non-premixed 40% CH_4 - 60% CO_2 - air flames (top: air side; bottom: fuel side); left figure: $v_{air\ /\ fuel\ sides} = 20 cms^{-1}$, $a = 41{,}1 s^{-1}$; right figure: $v_{air\ /fuel\ sides} = 60 cms^{-1}$, $a = 123{,}1 s^{-1}$

Furthermore, with increasing strain rates a reduction of the flame width and flame shifts, as seen in Fig. 3, and additionally a rise of the CH_2O concentration as well

radicals in the pre-flame region like, e.g., CH_3O, are analysed. A major role plays the choice of the diluent, especially when trying make the flames more resistant to extinction by strain. Also an addition of O_2 to the fuel expanded the flammability of the system markedly with respect to strain.
Additionally the influences of N_2 shroud-flow velocities and diameters and resulting buoyancy effects due to a raise in temperature in the upper burner and a nozzle diameter of d < 25 mm are taken into account. [3]
The position of flames formed in a small burner (d = 24,7 mm) is greatly affected by buoyancy at low strains and increasing temperature, which induces a decrease of the density, at the top nozzle. This buoyancy effect decreases at higher velocities and hence higher strain rates.

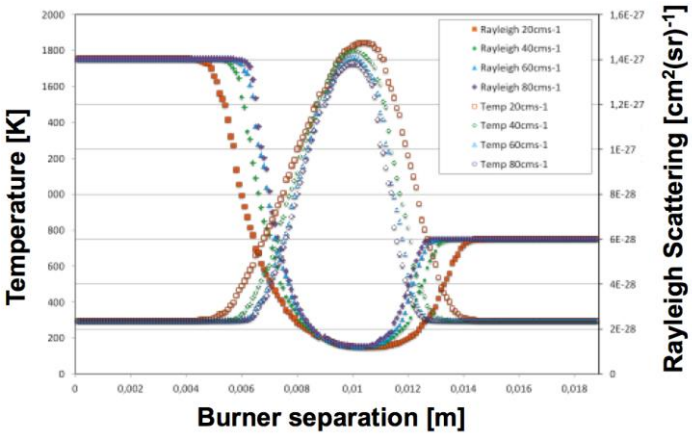

Figure 3. Numerical Rayleigh signals and temperature profiles for diluted non-premixed 40% CH_4 - 60% CO_2 - air flames (left: fuel-side, right: air-side) with increasing velocities on fuel and air sides and therefore strain rates

Conclusions

Due to the higher complexity of biomass-based gas fuels, in comparison to conventional fuels, regarding their composition and also higher heterogeneity depending on the conversion process, feedstock and gasifying agent a detailed characterization of their behaviour during combustion is still needed in order to improve the engine performance in an internal combustion engine, as well as control and reduce emissions.
Measurements of CH* chemiluminescence provide a possibility to advance the analysis of the spatial positions of the differing flames, unifying the evaluation of the reaction zones in both the experimental results and the numerical model. Especially soot precursors like CH_2O and temperature fields, in regards to the production of thermal NO, can therefore be thoroughly quantified.

References

[1] Deutschmann, O., Behrendt, F., Warnatz, J., Modelling and Simulation of Heterogenous Oxidation of Methane on a Platinum Foil, Catalysis Today 21(2-3), 461-470 (1994)

[2] Connelly, B.C., Bennett, B.A.V., Smooke, M.D., Long, M.B., A paradigm shift in the interactions of experiments and computations in combustion research, Proc. Comb. Inst. 32, 879-886 (2009).

[3] Oh, C., Ju Lee, E., Park, J., Effects of the burner diameter on the flame structure and extinction limit of counterflow non-premixed flames, international journal of spray and combustion dynamics (Volume 2, Number 3), 199-218 (2010)

CH_4/AIR-FLAME IMPINGEMENT HEAT TRANSFER TO A CYLINDRICAL SURFACE

P.O. Oketch [*], U. Bergmann[*], B. Atakan[*]
peter.oketch@stud.uni-due.de
[*]Thermodynamics, IVG, Mechanical Engineering, University of Duisburg-Essen, Germany

Abstract
The heat flux of methane/air flames, impinging normal to a cylindrical surface was determined experimentally. Light induced phosphorescence from thermographic phosphors, was used to investigate surface temperatures at the stagnation point from nearly one-dimensional laminar premixed flame burning against a water cooled ceramic tube. The flame heated surface of the ceramic tube was coated with chromium-doped alumina and excited with a green light-emitting diode (LED) to measure the surface temperature. Experiments on the effects of variations in the cold gas velocity (0.1m/s-0.5m/s), equivalence ratio (Φ = 0.85-1.2), separation distance, H (15 – 30 mm) are reported. Stagnation point heat fluxes increased with the increase of the cold gas velocity. At cold gas velocities less than 0.2 m/s, maximum heat fluxes were obtained for fuel-rich mixture conditions, possibly due to air entrainment from the surrounding. While for cold gas velocities greater than 0.2 m/s higher heat fluxes for stoichiometric mixtures were observed, probably due to higher adiabatic flame temperature. Further investigations are under way to study the effects of variation of the separation distance on heat transfer characteristics at different equivalence ratios.

Introduction
The situation of flame impingement heating is majorly encountered in technical applications due to its high heat fluxes. A substantial number of studies have reported the possibility of impinging non-reacting jets to enhance heat transfer in applications ranging from drying of textiles to the cooling of gas turbines blades and combustor walls [1]. The focus of these studies mostly being on jet impingement on flat surfaces. More reviews on the subject may be found in Refs. [2, 3]. Flame impingement on curved surfaces is quite often encountered in industrial applications such as heating and melting of metals and glass. However, reported studies that cover the cylindrical case are limited, most of them concentrate on impingement cooling heat transfer on either concave or convex surfaces and mostly for turbulent flows [4]. The present work extends the investigation on flame impingement heating on curved surfaces for laminar flows. The heat transfer characteristics is investigated for flame impinging normal to a cylindrical surface. This is carried out by measuring the temperatures on the inner and outer surface at the stagnation point of a water cooled ceramic

tube heated by premixed laminar methane/air flame. The inner temperature is measured with a Pt100 thermal resistor while, the outer surface temperature is measured with phosphor thermometry, which depend on luminescence of doped ceramics after exposition to light from a LED [5]. The heat fluxes are calculated using Fourier's law. Effects of variation in the cold gas velocities (0.1 m/s-0.5 m/s), equivalence ratio (0.85-1.2) and separation distance (15 mm-60 mm) are investigated.

Methods

The ceramic tube coated with 1.1 % chromium doped alumina was calibrated in a furnace from room temperature up to 750 K as shown in figure 1. Pflitsch et al. [6] reported that ruby films doped with 1.1 % chromium are most promising for temperature sensor applications, because they show high phosphorescence intensities and long phosphorescence lifetimes.

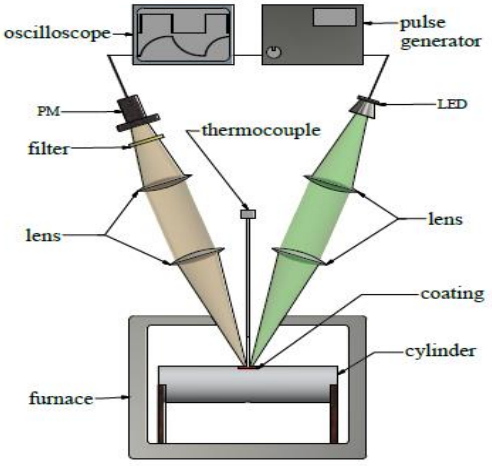

Figure 1. Temperature calibration.

For each temperature, the emission signal of the phosphorescence was recorded and the decay time evaluated by fitting an analytical waveform to the decay curve signal using an algorithm suggested by Brübach et al. [7]. The temperature-dependence of the phosphorescence lifetime was determined only for the outer surface of the ceramic pipe. Figure 3, shows the obtained calibration curve for the phosphorescence lifetime as a function of temperature. To investigate the heat transfer from different flames to the cylindrical surface, another setup, shown in figure 2, was designed, where temperature measurements are only aimed at the stagnation point. A homemade sintered bronzed burner of 30 mm diameter is used to establish a one-dimensional premixed laminar flame, if no cylinder is present. The flame impinges on a water cooled alumina cylinder. For the measurement of the temperature on the flame side, the phosphor coating is excited with a LED array at a wavelength of 532 nm. A fast pulse generator is used to provide the current input for the LED and to control the temporal excitation intensity shape.

The emitted phosphorescence signals from the measurement area are focused with lenses through a band pass filter onto a photomultiplier (PM) tube. The signals are recorded by a digital oscilloscope and then transferred to a personal computer after averaging for 128 pulses.

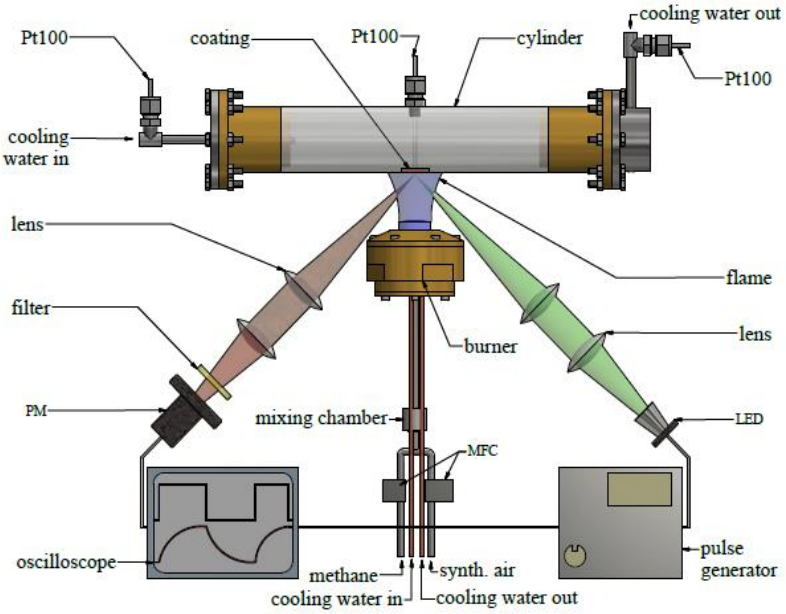

Figure 2. Single flame jet impingement.

A first set of experiments have been conducted to study the effects of variation of cold gas velocity (0.1 m/s–0.5 m/s) on stagnation point heat flux for three equivalence ratios, lean (Φ = 0.85), stoichiometric (Φ = 1.0) and rich (Φ = 1.2) at a separation distance, H = 15mm. This distance is denoted as the axial distance along the burner axis measured from the exit plane of the burner to the target point on the ceramic tube. The second set of experiments is currently underway to investigate the effect of varying, H (15 mm-60 mm) at Φ = 1.0. The flow of the cooling water is kept constant at 20 L/h for all experiments. Methane with 99.5% purity is burnt with synthetic air. Two mass flow controllers (MFC) for volumetric flow rates of 10 and 50 litters/min are used to control the flows of methane and synthetic air respectively.

Results

Temperature dependent lifetime

Figure 3 shows the phosphorescence lifetime as a function of temperature ranging from 2.8 ms at 298 K to 74 µs at 723 K. For the temperature range selected in this study, Seat and Sharp [8] showed that a resolution of 1 K is possible. The lifetimes are decreasing with an increase in temperature. Pflitsch et al. [6] also reported that the lifetimes are decreasing linearly on a logarithmic scale between 290 and 623 K and with a stronger gradient between 623 and 833 K. It was found out that below

623 K, the temperature dependence of the radiative transition is dominating the phosphorescence, while above 623 K the non-radiating energy transfer is rate limiting.

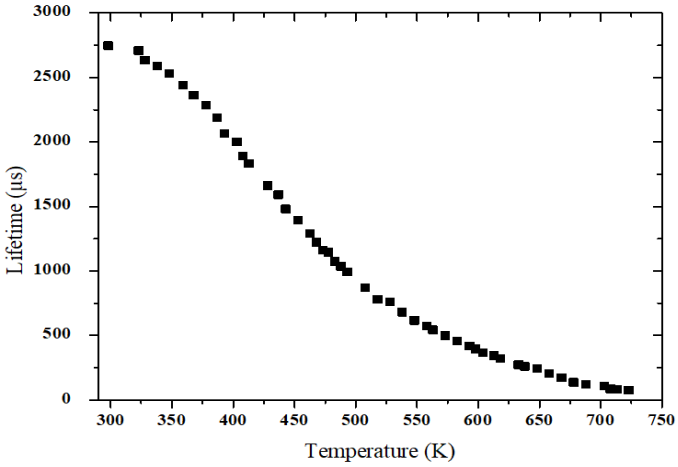

Figure 3. Lifetime of Cr: Al_2O_3 at different temperatures.

A curve was fitted to the calibration curve and used to determine the surface temperatures on the flame side of the ceramic tube.

Effects of equivalence ratio on stagnation point heat fluxes

Heat fluxes at the stagnation point were evaluated with the Fourier's law for one-dimensional steady state conditions.

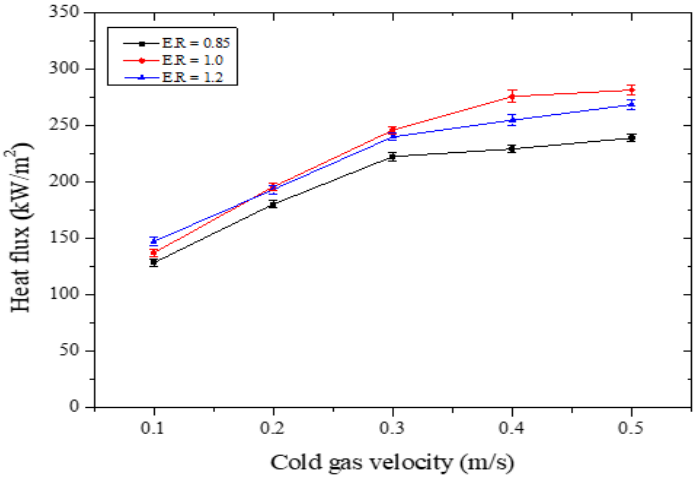

Figure 4. Stagnation heat fluxes at H = 15 mm.

Figure 4 shows the experimental heat fluxes calculated for the equivalence ratios, Φ = 0.85, 1.0 and 1.2 at a separation distance of 15 mm. In all cases heat fluxes increased with increase of cold gas velocity. This increase resulted to increase in convective heating. At cold gas velocities below 0.2 m/s, Φ = 1.2 had the highest

heat flux compared to Φ = 0.85 and 1.0. This was possibly due to the low burning velocity resulting to a larger separation of the flame front from the burner, thus lower heat losses to the burner for Φ =1.2. Also, the initially rich mixtures for Φ = 1.2 possibly becomes nearly stoichiometric due to entrainment of surrounding air. Salem et al. [9] also reported maximum heat fluxes for fuel-rich conditions for mass flux less than 0.3 kg/(sm)^2 for methane/air flames impinging on a flat surface at H = 15 mm. At cold gas velocities above 0.2 m/s, the effects of air entrainment is probably minimal resulting in higher heat fluxes for stoichiomeric as compared to rich and lean conditions. This was attributed to higher adiabatic flame temperature for stoichiomeric as compared to rich and lean conditions.

Effects of separation distance on stagnation point heat fluxes

The distance between the burner and the target surface is important from the perspective of flame stability and heat transfer, more especially when the other operation conditions are fixed or cannot be altered easily. Results are shown in figure 5 for separation distance of 15 mm-30 mm for Φ =1.0

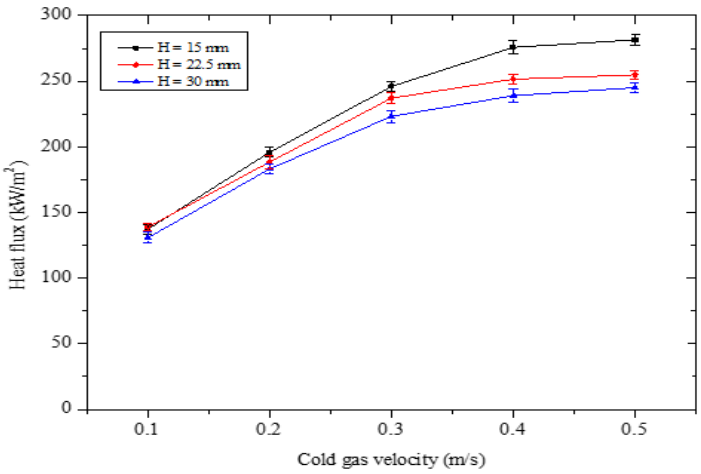

Figure 5. Stagnation heat fluxes at Φ =1.0

The heat flux for the smallest distance is highest, while it is lowest for larger distance. The small separation distance provides very high wall heat fluxes, because of their close proximity to the ceramic tube. Further investigations are being carried out for separation distance larger than 30 mm.

Conclusion

Heat fluxes for laminar premixed methane/air flame impinging on a ceramic tube has been investigated. The surface temperature on the flame side at the stagnation point has been measured with thermographic phosphors. Phosphor thermometry was suitable for these flame measurements, but reduced optical accessibility hindered measurements at separation distances less than 15 mm. The stagnation point heat fluxes increases with increase of cold gas velocity for all the equivalence

ratios and decreases with the increase of the separation distance. For gas velocities below 0.2 m/s fuel-rich conditions has the highest heat fluxes than for stoichiometric and lean, but at gas velocities above 0.2 m/s stoichimetric conditions shows maximal heat fluxes. Throughout the experiments, it is seen that the mechanism of flame stabilization changes from burner to plate stabilized, when the fresh gas velocity approaches the free flame velocity u_{FF}. The heat flux curves tend to increase first quite fast with changing cold gas velocity, which is reduced when approaching u_{FF}.

Acknowledgement
The first author is thankful to the DAAD for sponsoring his fellowship.

References

[1] Cornaro, C., Fleischer, A.S., Rounds, M., Goldstein, R.J., "Jet impingement cooling of a convex semi-cylindrical surface", *Int. J. Therm. Sci*. 40: 890-898 (2001)

[2] Dong, L.L., Cheung, C.S., Leung, C.W., "Heat transfer from an impinging pre-mixed butane/air slot flame jet", *Int. J. Heat and Mass Transfer*. 45: 979-992 (2002)

[3] Kwok, L.C., Cheung, C.S., Leung, C.W., "Heat transfer characteristics of slot and round pre-mixed impinging butane/air flame jet", *Exp. Heat Transfer*. 16: 111-137 (2003)

[4] Chander, S., Ray, A., "Heat transfer characteristics of laminar methane/air flame impinging normal to a cylindrical surface", *Exp. Therm Fluid Sci*. 32: 707-721 (2007)

[5] Atakan, B., Eckert, C., Pflitsch, C., "Light emitting diode excitation of Cr^{3+}: Al_2O_3 as thermographic phosphor: experiments and measurement strategy", *Meas. Sci. Technol*. 20: 075304 (2009)

[6] Pflitsch, C., Siddiqui, R.A., Atakan, B., "Phosphorescence properties of sol-gel derived ruby measured as functions of temperature and Cr3+ content", *Appl. Phys*. A 90: 527-532 (2008)

[7] Brübach, J., Janicka, J., Dreizler, A., "An algorithm for the characterization of multi-exponential decay curves", *Opt. Lasers Eng*.47: 75-79 (2009)

[8] Seat, H. C., Sharp, J. H., "Dedicated temperature sensing with C-axis oriented single-crystal ruby (Cr^{3+}: Al2O3) fibers: Temperature and strain dependences of R-line fluorescence", IEEE Trans. Instr. Meas. 53(1): 140-154 (2004)

[9] Salem, M., Staude, S., Bergmann, U., Atakan, B., "Heat flux measurements in stagnation point methane/air flames with thermographic phosphors", *Exp. Fluids*. 49: 797-807 (2010)

SESSION X

Novel concepts technologies and systems

ON THE INFLUENCE OF THE EFFECTIVE FOCAL LENGTH ON LASER IGNITION WITH A PASSIVELY Q-SWITCHED LASER

M. Bärwinkel, D. Brüggemann
lttt@uni-bayreuth.de
Department of Engineering Thermodynamics and Transport Processes,
Bayreuth Engine Research Center (BERC),
University of Bayreuth, Universitätsstraße 30, 95447 Bayreuth, Germany

Abstract
Under adverse igniting conditions, a reliable ignition can be obtained by passively Q-switched laser ignition systems. The aim of this work is to analyze the effect of the effective focal length on the laser initiated combustion of lean methane/air-mixtures. Experiments are performed in a constant volume combustion chamber. An enhanced combustion behavior can be found for decreased effective focal lengths by igniting a quiescent mixture. However, the shortest focal length does not necessarily lead to the best result. By introducing a flow, the combustion is mainly dominated by the flow. An influence of the effective focal length on the combustion process is observed. Nevertheless, a pulse train ignition can improve the combustion process by choosing the correct pulse spacing.

Introduction

In many applications, a successful ignition is important either due to safety reasons or emission limits. The measures to improve engines like downsizing and lean-mixture combustion impede the ignition process [1–4]. Thus, alternative ignition sources are of growing interest. In particular, laser ignition (LI) is studied with the aim to replace the conventional spark plug in the future. Cryogenic rocket engines [5], aeronautical combustion engines [6], scramjet engines [7], stationary gas turbines [8] but also stationary gas engines [9] and small reciprocating engines [10,11] are potential applications of LI.

The benefits of LI in comparison to the ignition with a conventional spark plug of reciprocating engines have been emphasized by several studies. For example, the following effects have been demonstrated: higher maximum cylinder pressure, earlier pressure rise and a higher rate of heat release [12,13], reduced cyclic variations [10–12], enhanced lean limit and thermal efficiency by multi-point LI [10,14].

A future ignition system has to be robust and cost efficient. Furthermore, the size of the ignition system has to be comparable to a conventional spark plug. In contrast to laboratory bench-top lasers, passively Q-switched lasers (PQL) are able to meet these requirements [4,15]. Laser spark plugs based on Nd:YAG/Cr^{4+}:YAG solid state lasers have been developed by several research groups in the last years

[11,16–18].
A laser ignition system is built up from a laser and one or more lenses to focus the laser beam. Thus, the ignition process can be influenced by the properties of the laser and of the focusing line. The aim of the presented study is to investigate the effect of the laser pulse energy E_{pulse} and the effective focal length f_{eff} of the focusing lenses on the ignition and combustion process of quiescent and flowing lean methane/air-mixtures. The experiments are performed in an optically accessible constant volume combustion chamber at an initial pressure of 10 bar. The net heat release of the combustion is calculated to examine the influence of different pulse energies and effective focal lengths. The results are substantiated with high-speed schlieren records of the ignition and combustion process.

Experimental

The experimental setup is shown in Fig. 1. Ignitions are initiated by a PQL ignition system (1064 nm) pumped longitudinally by a diode laser (808 nm). The laser pulse energy can be varied in the range of 3.0 mJ and 6.2 mJ by changing the coupling efficiency of the pump pulse into the Nd:YAG crystal. The focusing line consists of an expanding and a focusing lens. By varying the lens distance, the effective focal length is modified in the range of 9.6 mm and 24.6 mm. More details about the laser ignition system are given in ref. [19]. The experiments are performed in an optically accessible combustion chamber (CVCC) at an initial pressure of 10 bar. A swirl flow is initiated by injecting a homogeneous methane/air-mixture under high pressure into the CVCC. Flow velocities up to 10.8 m/s are applied in this study.

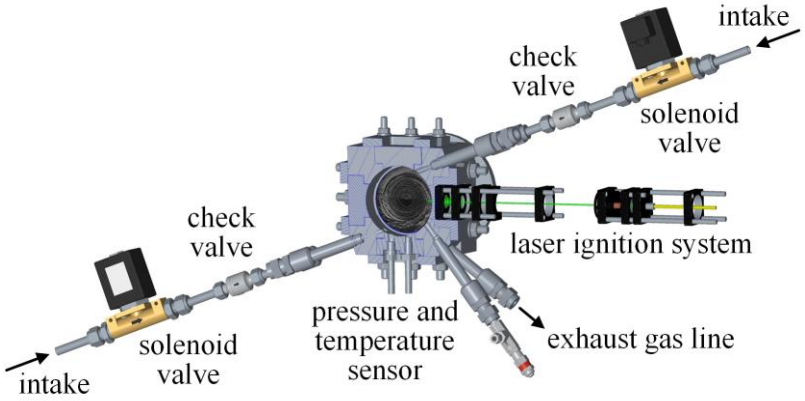

Figure 1: Optically accessible combustion chamber and peripheral equipment for injection of a homogeneous methane/air-mixture.

Ignition of Quiescent Methane/Air-Mixtures

First, quiescent mixtures are ignited in order to analyze the influence of the effective focal length on the ignition and combustion process. Figure 2 summarizes the net heat release curves of the combustion after the ignition with a pulse energy

of 4.7 mJ and different effective focal lengths. A worse combustion behavior can be found for effective focal lengths of 24.6 mm and 19.7 mm. This is attributed to smaller initial flame kernels and a slower flame kernel growth due to a low energy and power density in the focal spot and is proven by simultaneously recorded high-speed schlieren records. However, a significant difference in the net heat release traces of shorter focal lengths is not apparent. Comparable results are achieved by applying pulse energies of 3.0 mJ and 6.2 mJ.

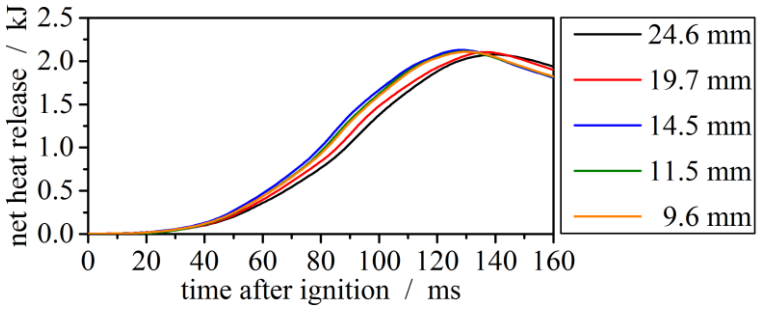

Figure 2: Net heat release after laser ignition of a quiescent methane/air-mixture (λ = 1.4) with different effective focal lengths (E_{pulse} = 4.7 mJ).

Ignition of a flowing methane/air-mixture

In the following, methane/air-mixtures are ignited by single pulses and pulse trains of two and four pulses with a pulse spacing of 100 µs and 200 µs. First, the ignition with a single pulse is discussed.

Single pulse ignition

The effect of different flow velocities on the flame kernel expansion is depicted in Fig. 3. In each case, a mixture with an air/fuel-equivalence ratio λ of 1.4 is ignited by a 4.7 mJ laser pulse and an effective focal length of 14.5 mm. The focused laser beam and the ignition location is indicated by the white triangles (t = 2.5 ms). The flame kernel is moved away from the ignition location by the flow. This effect increases with higher flow velocities. The flame kernel is stretched and is pulled to the center of the combustion chamber due to the lower density compared to the unburned gas. This effect is enhanced by high flow velocities. Moreover, the flame expansion is significantly accelerated by the flow. The flame kernel requires a duration of more than 45 ms to fill the combustion chamber at a flow velocity of 1.8 m/s. By increasing the flow velocity to 10.8 m/s, this time duration can be shortened to 14 ms.

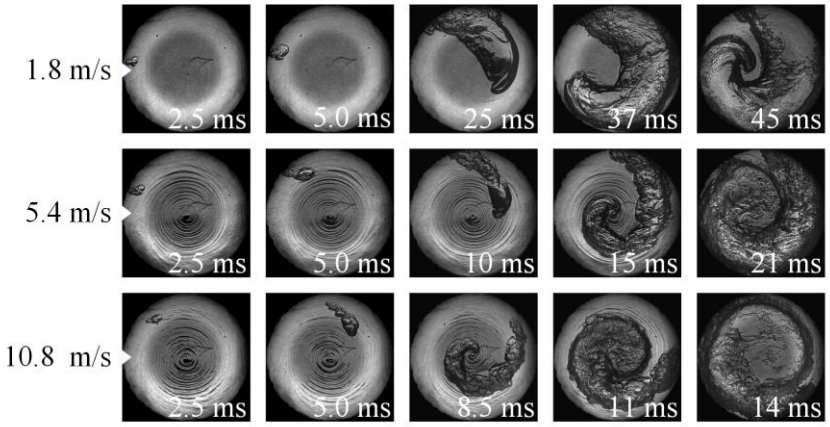

Figure 3: High-speed Schlieren records of the flame kernel expansion after laser ignition of methane/air-mixture (λ = 1.4) with different flow velocities and an effective focal length of 14.5 mm**.**

The effect of the effective focal length on the ignition and combustion of flowing mixtures is described below. The net heat release traces of the combustion of a methane/air-mixture with flow velocities between 1.8 m/s and 10.8 m/s after the ignition with a 4.7 mJ laser pulse and five different focal lengths are displayed in Fig. 4. Assessing the results, an influence of the effective focal length on the combustion process of flowing mixtures cannot be detected. Independently of the flow velocity, no distinct difference between the net heat release traces is found. It seems that even at a flow velocity of 1.8 m/s the combustion process is mainly dominated by the flow. Similarly, this behavior occurs by applying a pulse energy of 3.0 mJ and 6.2 mJ. However, the application of a 3.0 mJ laser pulse leads to longer combustion durations at all tested flow velocities.

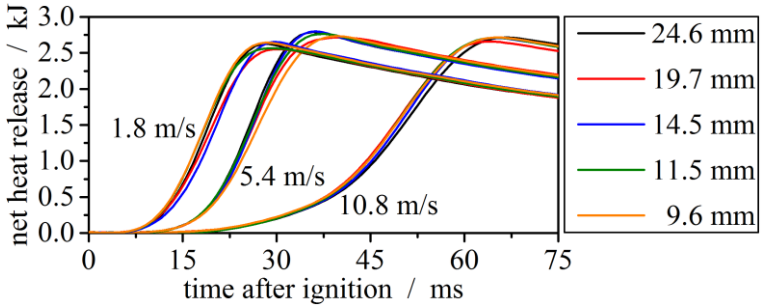

Figure 4: Net heat release after laser ignition of a flowing methane/air-mixture with different effective focal lengths (E_{pulse} = 4.7 mJ).

Pulse train ignition

A PQL emits pulse trains within a single pump pulse by increasing the pump energy. In this study, pulse train ignitions with two and four pulses are compared to a single pulse ignition at a flow velocity of 5.4 m/s. The pulse energy is set to 4.7 mJ and pulse spacing of 100 µs and 200 µs are applied. The net heat release traces of these combustions are given in Fig. 5. For each parameter setting of the pulse trains, ignitions with five different effective focal lengths are performed. As in the case of a single pulse ignition, an influence of the focal length on the combustion process is not apparent. Therefore, all traces of a parameter setting are displayed in the same color in Fig. 5. The results show that the rise of the net heat release trace is increased by a pulse spacing of 100 µs. This suggests a higher heat release rate and a shorter combustion duration. This behavior can be noticed for a pulse train with two and four pulses. However, a higher pulse number does not improve the combustion process. This suggests that the third and fourth laser pulses of the pulse train do not contribute to the ignition process. High-speed schlieren records prove this assumption. Results of pulse train ignitions with a pulse spacing of 200 µs are comparable to single pulse ignitions.

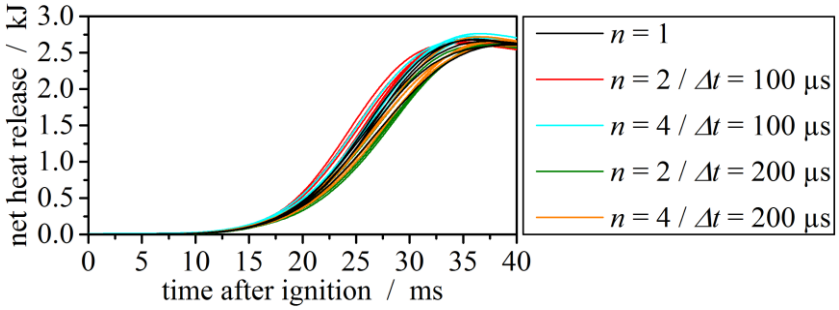

Figure 5: Net heat release after pulse train ignition of a flowing methane/air-mixture (v_s = 5.4 m/s, λ = 1.4) with a 4.7 mJ laser pulse and different number of pulses n and pulse spacing Δt.

Acknowledgments

The authors are grateful for the financial support of the German Research Foundation (DFG) under grant no. BR 1713/13-2. Furthermore, the authors thank Robert Bosch GmbH for the laser ignition system granted as a loan. The authors also thank Lukas Schröder and Markus Stahl for their support with the performance of the experiments.

References

[1] E. Mastorakos, "Ignition of turbulent non-premixed flames," Prog. Energ. Combust. **35**(1), 57–97 (2009).

[2] E. Albin, H. Nawroth, S. Göke, Y. D'Angelo, and C. O. Paschereit, "Experimental investigation of burning velocities of ultra-wet methane-air-steam mixtures," Fuel Process. Technol. **107**, 27–35 (2013).

[3] J. Fuchs, A. Leitner, G. Tinschmann, and C. Trapp, "Concept for High-performance Direct Ignition Gas Engines," MTZ worldwide **74**(5), 18–23 (2013).

[4] G. Dearden and T. Shenton, “Laser ignited engines: progress, challenges and prospects,” Opt. Express **21**(S6), A1113-A1125 (2013).
[5] M. Börner, C. Manfletti, G. Kroupa, and M. Oschwald, “Repetitive laser ignition by optical breakdown of a LOX/H2 rocket combustion chamber with multi-injector head configuration,” CEAS Space J **9**(3), 289–297 (2017).
[6] G. Amiard-Hudebine, G. Tison, and E. Freysz, “Compact nanosecond laser system for the ignition of aeronautic combustion engines,” J. Appl. Phys. **120**(23), 233102 (2016).
[7] S. Brieschenk, S. O’Byrne, and H. Kleine, “Ignition characteristics of laser-ionized fuel injected into a hypersonic crossflow,” Combustion and Flame **161**(4), 1015–1025 (2014).
[8] J. Griffiths, M. Riley, A. Kirk, A. Borman, J. Lawrence, and C. Dowding, “Lean burn limit and time to light characteristics of laser ignition in gas turbines,” Opt. Lasers. Eng. **55**, 262–266 (2014).
[9] D. L. McIntyre, S. D. Woodruff, and J. S. Ontko, “Lean-Burn Stationary Natural Gas Engine Operation With a Prototype Laser Spark Plug,” J. Eng. Gas Turbines Power **132**(7), 72804 (2010).
[10] Z. Kuang, E. Lyon, H. Cheng, V. Page, T. Shenton, and G. Dearden, “Multi-location laser ignition using a spatial light modulator towards improving automotive gasoline engine performance,” Opt. Lasers. Eng. **90**, 275–283 (2017).
[11] N. Pavel, T. Dascalu, G. Salamu, M. Dinca, N. Boicea, and A. Birtas, “Ignition of an automobile engine by high-peak power Nd:YAG/Cr^{4+}:YAG laser-spark devices,” Opt. Express **23**(26), 33028–33037 (2015).
[12] D. K. Srivastava and A. K. Agarwal, “Comparative experimental evaluation of performance, combustion and emissions of laser ignition with conventional spark plug in a compressed natural gas fuelled single cylinder engine,” Fuel **123**, 113–122 (2014).
[13] D. Srivastava and A. K. Agarwal, “Laser Ignition of Single Cylinder Engine and Effects of Ignition Location,” SAE Technical Paper, 2013-01-1631 (2013).
[14] S. Yamaguchi, T. Kashiwazaki, M. Nishioka, E. Takahashi, H. Furutani, H. Kojima, and J. Miyata, “Dual-Point Laser Ignition and its Location Effects on Combustion in Lean-Burn Gas Engine,” SAE Int. J. Engines **8**(3), 1435–1446 (2015).
[15] S. Lorenz, M. Bärwinkel, R. Stäglich, W. Mühlbauer, and D. Brüggemann, “Pulse train ignition with passively Q-switched laser spark plugs,” Int. J. Engine Res. **17**(1), 139–150 (2016).
[16] D. L. McIntyre, S. D. Woodruff, S. W. Richardson, M. H. McMillian, and M. Gautam, “Laser Spark Plug Development,” SAE Technical Paper Series (SAE International, 2007).
[17] M. Tsunekane, T. Inohara, A. Ando, N. Kido, K. Kanehara, and T. Taira, “High Peak Power, Passively Q-switched Microlaser for Ignition of Engines,” IEEE J. Quantum Electron. **46**(2), 277–284 (2010).
[18] G. Kroupa, Franz Georg, and Winkelhofer Ernst, “Novel miniaturized high-energy Nd-YAG laser for spark ignition in internal combustion engines,” Opt. Eng. **48**(1), 14202 (2009).
[19] M. Bärwinkel, S. Lorenz, R. Stäglich, and D. Brüggemann, “Influence of focal point properties on energy transfer and plasma evolution during laser ignition process with a passively q-switched laser,” Opt. Express **24**(14), 15189–15203 (2016).

A LOW POWER LIQUID FUELED BURNER USING A NOVEL ATOMIZATION CONCEPT

T. Müller*[+], A. Goßmann*, J. Kühn*, M. Etzold, B. Stelzner*, N. Zarzalis*, F. Durst**, D. Trimis***

[+] Corresponding author: thomas.mueller9@kit.edu

* Engler-Bunte-Institute - Division of Combustion Technology, Karlsruhe Institute of Technology, 76133 Karlsruhe, Germany

** FMP Technology GmbH, Am Weichselgarten 34, 91058 Erlangen, Germany

Abstract

A previously proposed spray generation concept, promising constant spray quality over a wide range of mass flow rates, were investigated with respect to the application in a low power heating oil burner. The main working principle of this concept is the secondary atomization of a droplet chain impinging on a pin downstream. Through pulse-width modulation (PWM) of the droplet chain generator, a modulation of spray mass flow rate could be achieved without change of spray quality. As the spray generation principle were only investigated with water (w) as liquid, two additional model liquids, glycerine-water mixture (GW) and glycerine-ethanol mixture (GE), are used in this study to determine the influence of liquid properties, especially viscosity and surface tension, on the produced spray, in order to assess the spray quality with fuels like industrial gas oil. Phase-Doppler Anemomentry (PDA) measurements were conducted to examine the influence of liquid properties and operation conditions on Sauter Mean Diameter (SMD). The obtained SMD values are in the range of 10% of primary droplet diameter, which is in good agreement with literature values. A dependence of liquid properties on PWM operation could not be observed. This confirms the assumption of constant spray quality over a wide range of spray flow rates.

Furthermore, a design and first experimental results for a low power burner based on this atomization approach are presented. In contrary to common heating oil burners, atomization and combustion section are spatially separated and a part of the combustion air is used to transport the spray to the combustion section. In the first proof-of-concept tests with this burner design a power variation between 1.25 and 5.1 kW was achieved also fulfilling all normative limits regarding exhaust gas emissions.

Introduction

Due to the reduction of energy consumption in the domestic heating sector (Energy Saving Directive, Germany) there is an increasing demand for low load oil burners. As currently oil burners are limited in load and modulation range due to characteristics of common pressure atomizers used for the fuel preparation, a novel atomization approach is needed for low liquid fuel mass flows.

In the course of the reduction of CO_2 emissions, energy-oriented modernization of buildings is of major importance. As an example, in Germany the Energy Saving Directive limits the allowed heat demand of newly built or renovated buildings and such limits are successively reduced. In this respect, heating boilers at very low burner loads (< 5kW) and with a wide adjustable power range are required, in order to minimize the amount of start-up and shutdown procedures. Commercially available burners at the low load segment are dominated by gas burners, which have no principal low limitation in the fuel supply. On the contrary, oil burners usually utilize pressure atomizers, which need a minimum fuel flow rate for atomization, resulting to a minimum power rate of approx. 5 kW and limited power modulation.

A novel atomizer concept for low liquid mass flows

To close this gap, a novel atomization concept for low load oil burners with a wide adjustable power range were proposed in a previous study [1]. The main working principle of this novel atomization concept is based on a piezo-driven spray generator, which either creates a liquid jet or a monodisperse droplet chain. When the liquid jet impinges on a pin in a certain range of operating conditions, it does not splash and the fuel can be collected and recirculated, while the droplet chain impinging on the pin produces a fine secondary spray. Through triggering of the Plateau-Rayleigh instability via the piezo actuator, hence the disintegration of the liquid jet into a drop chain, the spray generation can be switched-on and -off. Therefore, a wide range of spray flow rates can be realized by pulse-width modulation (PWM). The schematic operation modes are shown in Fig. 1.

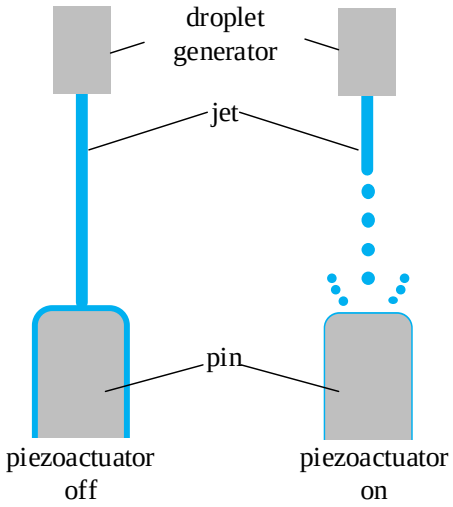

Figure 1. Impinging jet on the pin with no atomization (left) and impinging droplet chain with spray formation (right).

Through PWM drive of the piezo actuator, which is triggering the disintegration of the jet to droplets, a wide turn-down modulation of generated spray volume flow can be achieved. The novel atomization concept holds significant advantages in comparison with pressure atomizers, i.e. good atomization characteristics at low mass flow rates are obtained. Additionally, a wide modulation range with almost constant spray quality is achieved. The function of the spray generator was investigated in detail by Brenn [2,3].

Investigation of the atomization concept

The atomization process was preliminary investigated in non-reactive conditions. The usage of heating oil in this open setup was not possible due to safety and health concerns. Therefore, model liquids have been used to investigate the impact of the liquid properties on the atomization process. The three selected model liquids, water, a binary mixture of glycerine (40 wt.-%) and water and a binary mixture of glycerine (40 wt.-%) and ethanol, differ mainly in surface tension and viscosity. The values of these both liquid properties were chosen to cover the range between water and heating oil. The droplet size distribution was measured along the radial axis from the pin for various operating conditions and different heights above the impingement point using Phase-Doppler-Anemometry (PDA). Close to the pin, the secondary spray shows an SMD of 24 to 25 µm (see Figure 2), which is in good agreement with literature values of around 10% of primary droplet diameter [4,5]. Additional measured SMD at the outlet of the atomization section (see below for design details) confirm that this corresponds to the SMD of the transported spray. The increase in SMD with radial position can therefore only be linked to coagulation in the spray accumulating around the pin and has no influence for our application because there we have constant transport of spray away from the pin.

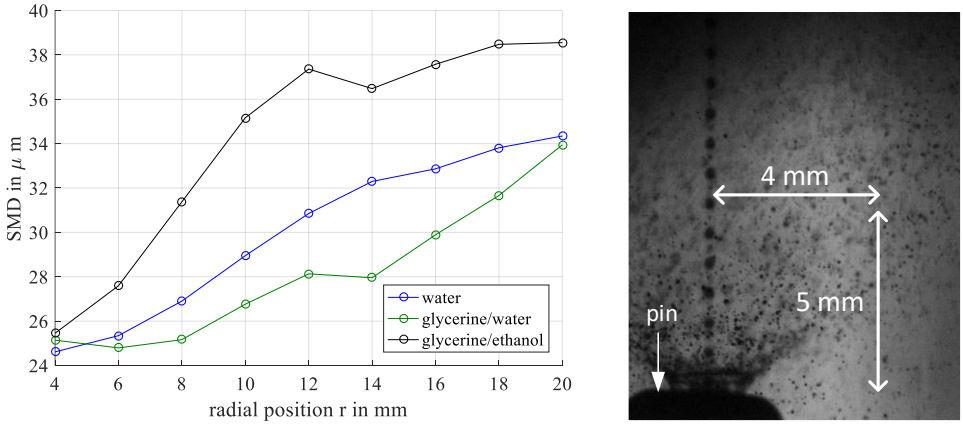

Figure 2. Radial SMD profiles of the three model liquids at a height of 5 mm above the pin tip (left) and camera image of the spray around the pin for water as model fluid (right).

SMD measurements with PWM operation at different PWM frequencies showed no influence of transient PMW operation on spray characteristics. Therefore, the proposed spray generation principle is able to operate at a wide range of spray mass flow rates without any change in spray quality.

Burner concept

The burner was designed with an atomization and combustion section, which are spatially separated. The droplet chain is vertically aligned approaching downwards the pin, where a part of the combustion air is used in horizontal arrangement to transport the fine spray resulting from the secondary atomization after the splashing of droplets on the pin, to the combustion zone. The heating oil, which is not splashed at the impact element (pin) as well as a portion of it forming a wall film is collected and reused. The remaining combustion air is fed after the atomizer section. The schematic of the burner is shown in Fig. 3.

The maximum thermal load is defined by the inlet pressure and the used orifice in the droplet generator under continuous droplet chain conditions (PWM at 100% duty cycle). Flexible turn-down of the thermal load is achieved by applying PWM to the piezo actuator signal. Here, constant operating conditions of the droplet generator in terms of total mass flow or exit velocity, respectively, result in constant spray properties over the complete operating range, since the transported secondary atomization spray is always produced under the same conditions.

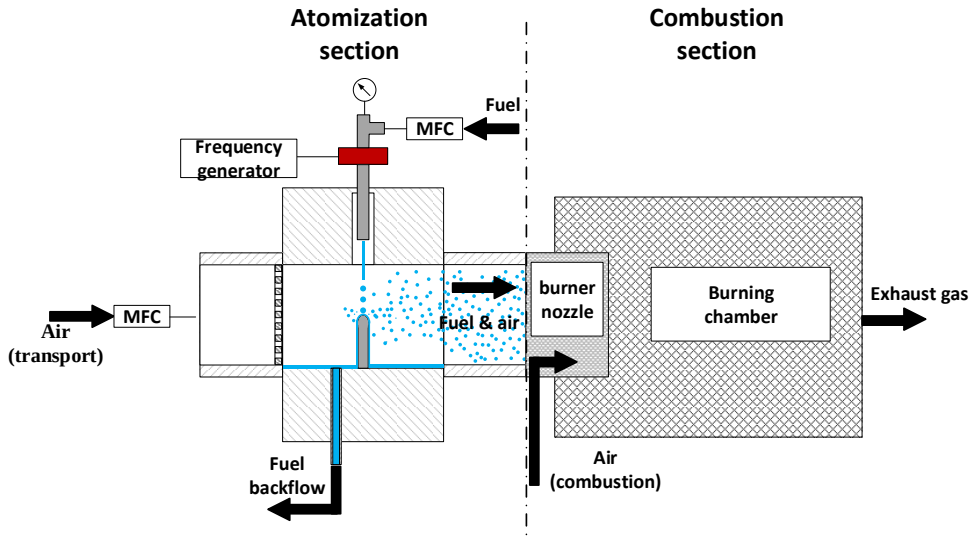

Figure 3. Schematic of the burner concept.

Test rig

The flow diagram of the test rig is shown in Fig. 3. The fuel was supplied from a tank and pressurized by a commercial heating oil pump. The pump was operated in two-line mode, meaning that the pressure at the exit is set and excess oil flows back into the storage tank. The pressurized fuel was fed into a compensation tank and from there to the droplet generator. In between, the mass flow was monitored by a Coriolis flow meter. Moreover, temperature and pressure of the fuel was measured by a thermocouple and a pressure transducer directly in front of the droplet generator. To adjust the flowrate/pressure in the droplet generator a needle valve was mounted between mass flow meter and droplet generator. In addition, the fuel supply line was equipped with a standard oil-burner electrical fuel-preheater.

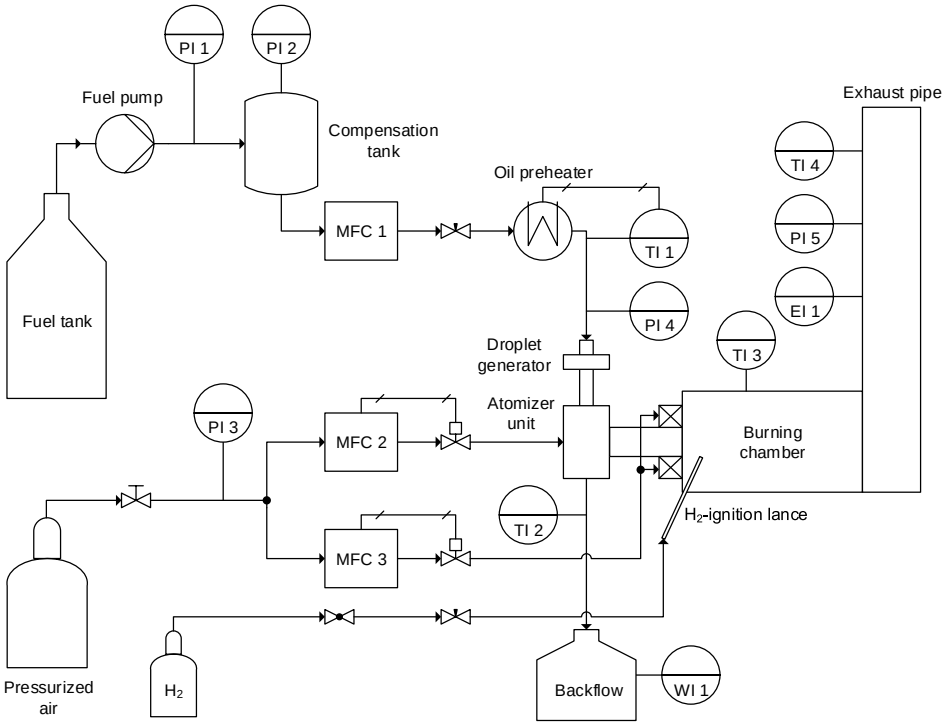

Figure 3. Flow diagram of the test rig.

At the bottom of the atomizer unit, the back flow was collected, flowing into a second tank monitored by a lab scale. Furthermore, the temperature of the back-flowing oil was also controlled by a thermocouple. The combustion and transport air were supplied by pressurized air and their mass flows were separately controlled by two thermal mass flow controllers. For ignition a H_2-lance was mounted in the burning chamber near the nozzle exit. After the burning chamber the exhaust pipe was equipped with a thermocouple, a pressure transducer and an exhaust gas probe, which were placed according to DIN EN 267. The mole fractions of CO and CO_2

were measure with a Non-Dispersive Infrared (NDIR) gas analyzer, whereas the O_2 mole fraction was measured with photochemical sensor. NOx was detected with a chemical luminescence sensor.

Results of the burner test

A first burner prototype was operated in reactive conditions with light fuel oil. There, a maximum thermal load of 5.5 kW was achieved, while a modulation range of 1:5 (down to 1.1 kW) was possible via PWM modulation. The emissions were within the current legislative regulations: the CO- and the NO_X-emissions showed on average of 3 mg/kWh and 95 mg/kWh, respectively. The conversion of the measured emissions over the modulation range into the average ones was performed according to DIN EN 267. An overview of the results is given in Fig. 4. The range of admissible emissions and fuel ratio are marked by a grey background.

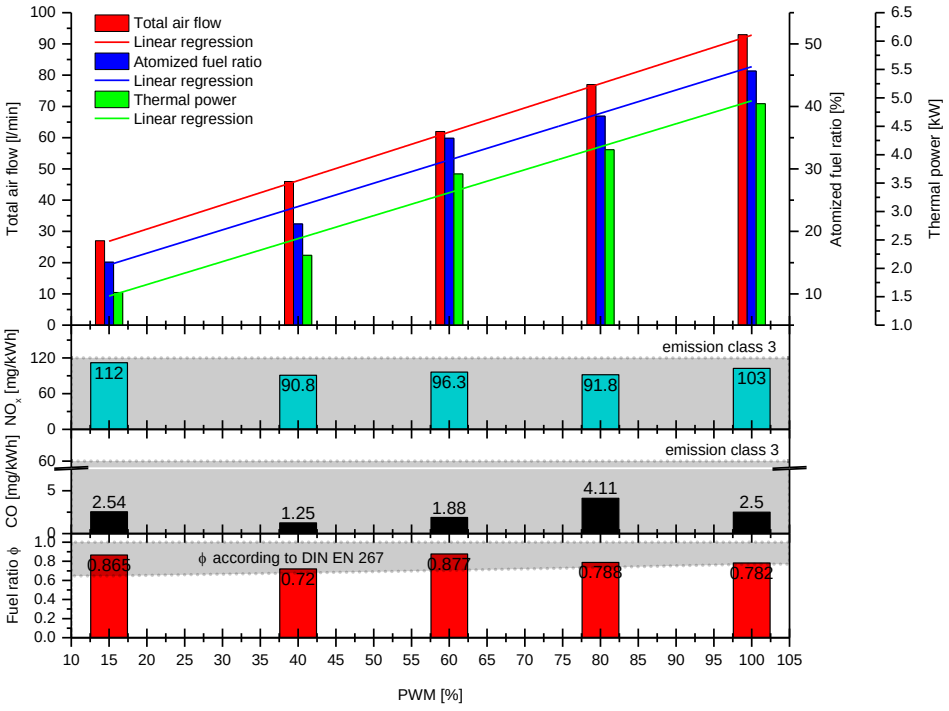

Figure 4. Outcome of the proof-of-concept tests: output power, atomized fuel ratio, total air flow (top); exhaust gas emissions (middle) and air-fuel-equivalence-ratio (bottom) measurements indicating also the standard limit values for exhaust gas emissions and air-fuel-equivalence ratio.

Conclusion and outlook

A novel atomization concept for low liquid fuel mass flows was studied under non-reactive and reactive conditions. The control of the transported atomized fuel mass flow was based on PWM driven piezo actuator signal. In the present study, the atomization process was investigated under non-reactive conditions for three different model fluids..The SMD of the secondary spray was found to be approximately 10% of the size of the monodisperse droplet chain, which is in good agreement with literature values. Spray rate variation with PWM had no influence on spray quality. A first burner prototype was operated with thermal loads in a range of 1 to 5.5 kW. The measured emissions were within the current legislative regulations. Through thorough characterization, a parametrization of the operating parameters can lead to significantly better performance over a wider operating range.

Acknowledgement

The present research work contributes to the AiF German Federation of Industrial Research Associations, which is leading the Central Innovation Programme for small and medium-sized enterprises (project number: ZF4171302AB6). This program is founded by the Federal Ministry for Economic Affairs and Energy and supports the cooperation between research and industry.

References

[1] Etzold, M.; Han, Y.; Durst, F. A novel spray generator for low-energy oil burners. *Int. J. Spray Combust. Dyn.* **2016**, 8 (1), pp. 53–64. DOI: 10.1177/1756827715627065.

[2] Brenn, G.; Durst, F.; Tropea, C. Monodisperse Sprays for Various Purposes-Their production and characterization *Part. Part. Syst. Charact.* **1996**, 13 (3), 179–185. DOI: 10.1002/ppsc.19960130303.

[3] Brenn, G.; Helpiö, T.; Durst, F. A new apparatus for the production of monodisperse sprays at high flow rates *Chemical Engineering Science* **1997**, 52 (2), 237-244. DOI: 10.1016/S0009-2509(96)00397-1.

[4] Yarin, A. L.; Weiss, D. A. Impact of drops on solid surfaces. Self-similar capillary waves, and splashing as a new type of kinematic discontinuity *J. Fluid Mech.* **1995**, 283 (1), 141. DOI: 10.1017/S0022112095002266

[5] Weiss, D. A. Periodischer Aufprall monodisperser Tropfen gleicher Geschwindigkeit auf festen Oberflächen *Mitteilungen aus dem Max-Plank-Institut für Strömungsforschung* **1993**, IV,74.

Assessment of combustion paradigms for modeling a cyclonic burner under MILD Combustion conditions

M. Ferrarotti*, S. Patronelli **, G. Ceriello*,
G. Sorrentino***, C. Galletti **, A. Parente ***
Marco.Ferrarotti@ulb.ac.be

* Service d'Aéro-Thermo-Mécanique, Université Libre de Bruxelles, Bruxelles, Belgium
** Department of Civil and Industrial Engineering, University of Pisa, Italy
*** DICMAPI-Università degli studi di Napoli Federico II, Naples, Italy

Abstract
The development of MILD Combustion systems in several practical applications is hampered by a lack of understanding into such regime and thus novel tools are required compared to conventional combustion systems. In MILD combustion technologies, reactants are diluted with large amounts of burnt reaction products prior to ignition, which enables reactive structure stabilization under diluted conditions, thereby avoiding high-temperature regions that promote enhanced thermal NOx formation. In this background, computational fluid dynamics (CFD) for the prediction of the burner behavior and its optimization, appears essential for a successful introduction of such a concept in some industries. A major issue in the modeling of diluted combustion is the pronounced sensitivity of the reactive structure to the reaction chemistry and therefore detailed kinetic schemes are necessary when a gas mixture is subjected to dilution by hot reaction products.
In order to include detailed chemistry in fluid-dynamics simulations several turbulent combustion models were used and they are represented by the Eddy Dissipation Concept (EDC), PaSR and the Flamelet Generated Manifold (FGM). In particular, this study investigates the combustion characteristics of MILD Combustion in a novel cyclonic lab-scale burner. The numerical computations were performed incorporating turbulent combustion models in RANS simulations in order to determine the effect of several different main parameters such as inlet oxidizer temperature, and mixture composition on models performance.
Therefore, an assessment of models was carried out on the basis of an experimental/numerical comparison by evaluating the temperature inside the burner for a fixed condition. Results suggest that both the modified EDC and PaSR represent promising tool for modeling the complex flame structures of cyclonic MILD burner, although in several conditions they depict some aspects that need to be further investigated.

Introduction
Enhancement of thermal efficiency with fuel flexibility and ultra-low emissions is one of the most challenging area for combustion researchers. Among the new

technologies, MILD combustion [1] seems to be one of the most promising. Such operating conditions feature a process with a distributed reaction zone, relatively uniform temperatures within the combustion chamber, no visible flame, low noise, negligible soot formation and very low NO_x and CO emissions [2]. In recent years, attention has been paid to MILD combustion modeling, due to the very strong coupling between turbulence and chemistry of such a combustion regime. The flue gas entrainment increases the inert content of the fresh mixture so that chemical kinetics become slow enough with time scales comparable to the mixing ones [3]. Therefore, the turbulence/chemistry interaction need to be considered with appropriate and effective turbulent combustion models [4]. The poor knowledge of MILD reaction zones also calls into question the common use of both flamelet-like and non-flamelet-based turbulent combustion models for Reynolds-Averaged Navier-Stokes (RANS) simulations [5] and for Large Eddy Simulations (LES) [6]. The use of CFD tools to understand burner behaviour and to design its optimization appears essential, both for describing turbulent mixing and chemical reactions. Attractive strategies for including detailed chemistry effects using moderate CPU resources are tabulated chemistry techniques. Among such models, there are flamelet generated manifold (FGM) [7] techniques, based on Flamelet approach. In particular, Abtahizadeh et al. [8] showed that Igniting Mixing Layers (IML) type flame is the best option for representing MILD combustion in a jet in hot coflow (JHC) burner.
On the other hand, more complex turbulence/chemistry interaction models have been proposed in literature and successfully applied to MILD. Among them, it is worth to mention the Eddy Dissipation Concept (EDC) [9], which splits every computational cell into two regions: the fine structures, modeled as Perfectly Stirred Reactors (PSR), and the surrounding fluid mixture. Recently, Aminian et al. [10]. have shown the importance of adjusting the fine structure residence time constant (C_τ) simulating MILD combustion. Partially-Stirred Reactor (PaSR) model, originally proposed by Chomiak [11], is an extension of EDC and is characterized by a different definition of the reacting volume fraction, which becomes the ratio between the chemical time scale and the sum of mixing and chemical scales. It has been successfully applied to MILD combustion in the Adelaide Jet in Hot Co-flow (JHC) by Ferrarotti et al. [12]. Although significant progress has been achieved for MILD combustion modeling, there are still important issues concerning the reactive structures, the turbulence-chemistry interaction and the effect of fuel composition, which need to be addressed. The elucidation of the above topics needs high fidelity and comprehensive experimental data to validate the numerical models. In the past, Jet in Hot Coflow (JHC) configuration [13], and the Cabra flame [14] have been conceived to emulate flameless conditions by feeding diluted and hot streams to the burner. The recirculation affects both mixing and chemical timescales so that conceptually these burners are different from JHC and Cabra flames, which act solely on the chemical timescale. Despite the reasonable number of studies in the literature [15], the amount of detailed experimental data available for combustors operating under MILD/Flameless conditions is relatively scarce and limited to few operating

conditions. Based on such considerations, we report some results related to MILD combustion in a novel cyclonic burner [16]. Experiments have been performed in a propane-fired small-scale combustor and include detailed measurements of local mean temperatures. Experimental measurements in terms of temperatures were compared with detailed results of numerical computations in this configuration. This was done for a specific inlet temperature with a fixed mixture composition value. The main aim of the comparison between experimental and numerical data is to assess the considered modeling approaches to understand which method is more useful for prediction/design of MILD burners or which of them needs further modification/tuning.

The cyclonic combustion chamber

Experimental tests were conducted in a lab-scale cyclonic flow reactor. Fig. 1 shows a sketch of the section (a) and the front view (b) of the non-premixed configuration used to investigate the MILD combustion process [16]. It is a prismatic chamber with a square section of 0.2x0.2 m^2 and height of 0.05 m. The burner is fed with two pairs of coaxial oxidant/fuel jets. They are placed in an anti-symmetric configuration thus realizing a centripetal cyclonic flow field with a top-central gas outlet. The main oxidizer flow (N_2/O_2 mixture) is preheated at different temperatures and injected at 38 m/s whereas the fuel stream (N_2/C_3H_8 mixture) is settled at an environmental temperature (T_0=300 K) and 50 m/s. The oxidant injector is located at 0.02 m from the lateral wall and has a diameter of 0.008 m, whereas the fuel injector is at 0.045 m from the wall and has a diameter of 0.0008 m. The feeding configuration is shown in Fig. 1a. The gas exit is located on the top of the chamber.

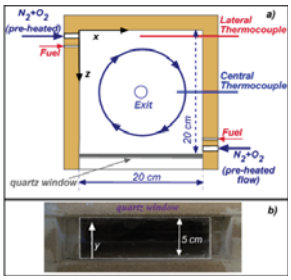

Figure 1. Sketch of the mid-plane section (a) and front view (b) of the cyclonic configuration

The combustor is built using a heat-insulating material (expanded vermiculite) and it is located within an electrically heated ceramic oven. The burner is equipped with two thermocouples (type N) and an optical access (a quartz window) as shown in Fig. 1. The thermocouples are located at the mid-plane and can be moved across the

reactor. The lateral one is placed near the wall (at 0.02 m from the wall) while the central one is placed at the centerline of the combustion chamber (0.1 m from the wall) as depicted in Figure 1a. The uncertainties in the measurements are linked to convective and radiative effects and are ±2% and ±6% in the lateral side and ±1% and ±1.5% for the central one. Further details on the experimental apparatus can be found in previous literature works [17].

Numerical methodology

RANS simulations were carried out with the commercial code Fluent 17.0 by Ansys Inc. The grid was generated with the software Ansys ICEM. The first approach has been a full-hexa mesh. Several attempts with different cells numbers ranging from 400 k to 800 k have been made to test the structured approach. Despite the quite simple chamber's geometry, the structured mesh presented different convergence problems (large fluctuations of residual values and variables instability). It was therefore decided to opt for a polyhedral grid of 200 k cells. A grid independence study was performed using polyhedral grid with a number of cells ranging from 100 k to 400 k. The chosen grid consisted of 200 k polyhedral elements, generated from a 1200 k tetrahedral grid. Reynolds stresses were solved through the RNG k-ε turbulence model with swirl dominated flow corrections to account for the high swirl in the combustor. For turbulence-chemistry interaction, EDC (C_τ=0.4083-1.5) and PaSR were adopted. The mixing time scale of the latter was defined, following Ferrarotti et al. [12], as:

$$\tau_{mix} = C_{mix} \frac{k}{\varepsilon}, \quad (1)$$

where C_{mix} is a mixing constant defined here as 0.1 or 0.01. Instead, the chemical time scale was derived from approximating the Jacobian diagonal terms.

The Discrete Ordinate (DO) radiation model was used, while the radiation properties of the reacting mixture are considered with the Weighted-Sum-of-Grey-Gases (WSGG) model, by using the coefficients proposed by Smith et al. [18]. The GRI 3.0 (35 species, 217 reactions) [19] was used as kinetic scheme. On the other hand, was also assessed the capability of the combustion paradigms based on flamelet-like (FGM) for predicting MILD regime. FGM is a chemistry reduction method, which is based on two assumptions: a n-dimensional composition space can be represented by a lower dimensional manifold; and a turbulent flame is an ensemble of laminar flames [7, 20]. The inclusion of turbulence was made with a presumed $\beta - PDF$ approach. More information about the boundary conditions can be found in [20].

Results and conclusions

The stoichiometric case ($\phi = 1$) was investigated and evaluated numerically with the objective of comparing different combustion model formulations.

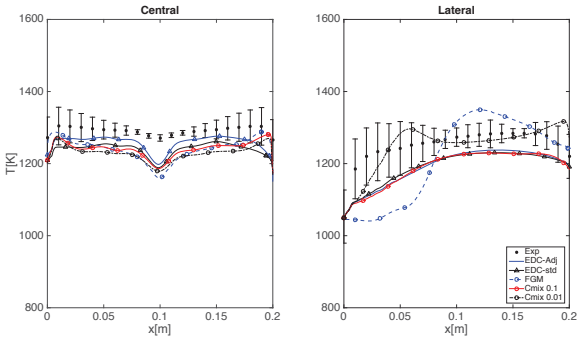

Figure 2. Axial profiles of the measured and predicted temperature profiles with different combustion model (Central and Lateral thermocouples).

All the models provide a satisfactory closure of the energy balance, since the exhausts and wall temperatures are in good agreement with the experimental ones.
Differently from FGM, the EDC and PaSR predicted temperatures show a monotone behavior more similar to the experiments. Indeed, the small increase of temperature along the axial direction is well predicted, especially with PaSR-C_{mix}=0.01. Along the central thermocouple, all the models show a slight under-prediction in the proximity of the center of the burner on the order of maximum 6 % (for FGM). EDC-C_τ=1.5 is the model that best predict the lateral sides of the temperature profile.
All the model depicted some disagreements with respect to experimental data, therefore it will be very important to identify the failure of each model to improve them with respect to the combustion regime.

References

[1] Cavaliere, A., de Joannon, M., "Mild combustion", *Prog. Energy Combust. Sci.* 30: 329-366 (2004).
[2] De Joannon, M., Sorrentino, G., Cavaliere, A., "MILD combustion in diffusion-controlled regimes of hot diluted fuel", *Comb. Flame* 159 :1832-1839 (2012).
[3] Özdemir, I.B., Peters, N., "Characteristics of the reaction zone in a combustor operating at mild combustion", *Exp. fluids* 30 :683-695 (2001).
[4] Frassoldati, A., Sharma, P., Cuoci, A., Faravelli, T., Ranzi, E., "Kinetic and fluid dynamics modeling of methane/hydrogen jet flames in diluted coflow", *Appl. Therm. Eng.* 30: 376-383 (2010).
[5] Galletti, C., Parente, A., Tognotti, L., "Numerical and experimental investigation of a mild combustion burner", *Comb. Flame* 151: 649-664 (2007).
[6] Duwig, C., Stankovic, D., Fuchs, L., Li, G., Gutmark, E., "Experimental and

numerical study of flameless combustion in a model gas turbine combustor", *Comb. Sci. Technol.* 180: 279-295 (2007).

[7] van Oijen, J.A., de Goey, L.P.H., "Modelling of premixed laminar flames using flamelet-generated manifolds", *Combust. Sci. Tech.* 161: 113-137 (2000).

[8] Abtahizadeh, E., de Goey, P., van Oijen, J., "Development of a novel flamelet-based model to include preferential diffusion effects in autoignition of CH4/H2 flames", *Comb. Flame* 162: 4358-4369 (2015).

[9] Magnussen, B.F., "The eddy dissipation concept, a bridge between science and technology", *ECCOMAS thematic conference on computational combustion*, pp 21-24 (2005).

[10] Aminian, J., Galletti, C., Shahhosseini, S., Tognotti, L., "Key modeling issues in prediction of minor species in diluted preheated combustion conditions", *Appl. Therm. Eng.* 31: 3287-3300 (2011).

[11] Chomiak, J., *Combustion: a study in theory, fact and application* Abacus Press/Gorden and Breach Science Publishers, 1990.

[12] Ferrarotti, M., Li, Z., Parente, A., "On the role of mixing models in the simulation of MILD combustion using finite-rate chemistry combustion models", *Proc. Combust. Inst.* (2017), Under review.

[13] Dally, B.B., Karpetis, A.N., Barlow, R.S., "Structure of turbulent non-premixed jet flames in a diluted hot coflow", *Proc. Combust. Inst.* 29: 1147-1154 (2002).

[14] Cabra, R., Chen, J.Y., Dibble, R.W., Karpetis, A.N., Barlow, R.S., "Lifted methane-air jet flames in a vitiated coflow", *Combust. Flame* 143: 491-506 (2005).

[15] Verissimo, A.S., Rocha, A.M.A., Costa, M., "Experimental study on the influence of the thermal input on the reaction zone under flameless oxidation conditions", *Exp. Therm. Fluid Sci.* 44: 75-81 (2013).

[16] Sorrentino, G., Sabia, P., Bozza, P., Ragucci, R., de Joannon, M., "Impact of external operating parameters on the performance of a cyclonic burner with high level of internal recirculation under MILD combustion conditions", *Energy* 137: 1167-1174 (2017).

[17] de Joannon, M., Sabia, P., Sorrentino, G., Bozza, P., Ragucci, R., "Small size burner combustion stabilization by means of strong cyclonic recirculation", *Proc. Comb. Inst.* 36: 3361-3369 (2017).

[18] Smith, T.F., Shen, Z.F., Friedman., J. N., "Evaluation of coefficients for the weighted sum of gray gases model", *J. heat transf.* 104: 602-608 (1982).

[19] Smith, G.P., Golden, D.M., Frenklach, M., Moriarty, N.W., Eiteneer, B., Goldenberg, M., Lissianski, V.V., "GRI-Mech 3.0, 1999", *URL http://www. me. berkeley. edu/gri_mech* (2011).

[20] Sorrentino, G., Göktolga, U., de Joannon, M., van Oijen, J., Cavaliere, A., de Goey, P., "An experimental and numerical study of MILD combustion in a Cyclonic burner", *Enrgy Proced.* 120: 649-656 (2017).

EVALUATION OF FUEL FLEXIBILITY IN A CYCLONIC BURNER.

P. Sabia*, G. Sorrentino, P. Bozza*, R. Ragucci*, M. de Joannon***
g.sorrentino@unina.it
* Istituto di Ricerche sulla Combustione - Consiglio Nazionale delle Ricerche, Napoli, Italy
** DICMaPI - Università degli studi di Napoli Federico II, Napoli, Italy

Abstract
Stabilization of distributed combustion regimes adopting cyclonic flow fields has been proven to be challenging. In fact, the establishment of a toroidal flow field within a combustion chamber may ensure the recirculation of mass and sensible enthalpy required to simultaneously dilute the fresh reactants and increase the temperature above the autoignition one. The combination of reactants dilution and preheating may greatly increase system energy efficiency and lower pollutants production producing very peculiar combustion regime (MILD Combustion). At the same time this strategy can be compromised if the sensible enthalpy is not high enough to promote the auto-ignition process of diluted mixtures. The paper aims at exploiting the performance of a small-size cyclonic burner for a conventional fuel (CH_4) and low calorific fuel (synthetic biogas) or ammonia through the characterization of the process stabilization and pollutant emissions as a function of the mixture equivalence ratio and the nominal thermal power of the inlet mixture (from 2 to 10 kW), with the aim of identifying the optimal operating condition of the system. Results suggest that the system has to be exercised with mixtures with compositions slightly under the stoichiometric conditions for methane or biogas mixtures and in a well identified temperature range to minimize both NOx and CO emission. On the other hand, ammonia/air mixtures have to operate under slightly rich conditions. The burner can be easily exercised also with low calorific fuels or with ammonia-based ones for higher thermal powers according to the low LHV. However, it results that an efficient recirculation of the exhausts produces a robust MILD combustion condition also when low calorific fuels are used.

Introduction
In the consolidated and fast evolving concept of smart energy grid, the leading renewable, alternative energy sources are however integrated with (and supported by) combustion based energy production systems. However, to fit the grid criteria and meet load following requirements, combustion based energy systems at different scales are required to use both fossil and alternative fuels. This latter class includes many fuels produced by means of a wide variety of processes with the general aim of maximizing the renewability of sources and/or find a suitable way of storing the energy excess from renewable sources.
Fuel and power flexibility is not a simple task to pursue in a single combustion

unit. Based on a substantially different combustion regimes, new paradigms of combustion processes, such as MILD combustion [1], give the opportunity to explore the possibility of using a wide palette of fuels in a wide range of power in a single unit. Several configurations have been conceived and studied for practical applications [2,3].
In this framework, the present paper aims to move a further step forward in the knowledge about MILD Combustion application. The results here reported have been obtained using a very simple MILD burner that realizes an internal recirculation scheme. Following the approach already used in previous works from the same research group [4], a systematic experimental study has been carried out to explore the feasibility of fuel and power flexibility. Methane, a surrogating biogas mixture (methane/CO_2) and ammonia have been used as fuels. The combustion effectiveness as a function of thermal power has been evaluated at different equivalence ratio by measuring process temperature and exhaust gas composition.

Experimental setup and methodology
The experimental campaign was carried out in the Laboratory Unit CYclonic (LUCY) burner. It consists of an alumina prismatic (2000 cm^3) chamber mounted inside an AISI 310s stainless case. Several shielded thermocouples (type N) are used to monitor the combustion process inside the burner. Details of the experimental plant can be found elsewhere [5].
Flow rates can be easily changed in a wide range resulting in a nominal thermal power interval from 0.1 up to 10 kW. In all the cases here reported, both the T_{in} and the fuel inlet temperature are kept at environmental temperature.
The exhausts are sampled at the outlet section center by means of a cooled probe and are analyzed through a portable micro-GC analyzer that allows to measure O_2, CO, CH_4 and C_2-species. NO and NO_2 (NO_x) are measured by means of both a flue gas analyzer (TESTO 350) and a ABB analyzer. All the gas concentrations reported in the followings are all normalized to a 15% O_2 in the exhausts.

Results and discussions
The experimental tests were realized, first of all, for methane/air mixtures at ambient conditions (T_{in}=300K, P=1 Atm) by monitoring the temperature and pollutant emissions (CO, NO_X) as a function of the equivalence ratio at two values of the nominal thermal power (4 and 10 kW), as reported in Figure 1.
The equivalence ratio Φ ranged between 0.5 and 1. As shown in previous works [6], such range ensures reasonably low pollutant emissions in the exhausts.
It is possible to note that for P = 10 kW, the temperature increases linearly with Φ, from 1400 K to 1500 K in the considered Φ range. Temperatures are generally higher than the ones recorded at P = 4 kW. For P = 4 kW, the residence time (t) increases with Φ from 0.22 to 0.37s, while for the P = 10 kW, from 0.11 to 0.13s. Because of an increase of system temperatures at higher Φ, t diminishes with Φ,

but as much as Φ increases less air is introduced in the system, thus τ increases.
Figure 1b shows the concentration, normalized at 15% O_2, of CO and NOx, as a function of the equivalence ratio, at fixed power values. In general, it is possible to note that the CO concentration exhibits a non-monotonous trend. At low Φ it is relatively high because of low system temperatures, that does not allow a full conversion of CO to CO_2. As matter of fact, for P = 4 kW and Φ = 0.5, CO value are 166 ppm with a system working temperature equal to 166 ppm. A further decrease of Φ causes a decrease of temperature with an increase of CO with the occurrence of the process extinction. On the contrary, as Φ increases, CO reaches a minimum value and it starts increasing when the equivalence ratio value approaches the stoichiometric condition. For P = 4 kW the minimum CO value occurs around Φ = 0.7, while for P = 10 kW the minimum value occurs at Φ equal to about 0.75.

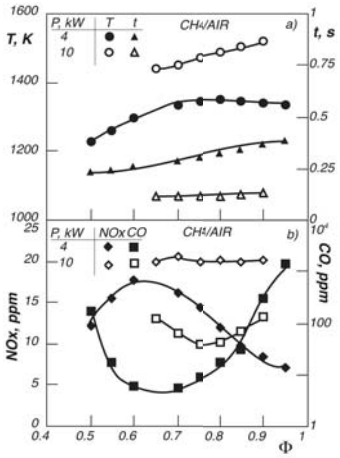

Figure 1. Temperature measurements, characteristic residence time (a) and pollutant emissions (b) for CH_4-air mixtures as a function of Φ for different thermal power values.

The concentration of CO becomes lower than 100 ppm, respectively for 0.55 < Φ < 0.85 for P = 4 kW, and at 0.7 < Φ < 0.85 for P = 10 kW.
NO_x concentrations show a non-monotonous trend at P = 4 kW. In particular, they reach a maximum value of 18 ppm at Φ = 0.6 and then slightly diminishes down to 7 ppm when the mixture composition moves towards the stoichiometric value. This last effect may be correlated to the onset of NO reburning chemistry for temperatures higher than 1200 K [7]. For P = 4 kW, the optimal condition is at Φ = 0.85, while for P= 10 kW it is at Φ = 0.75.
In order to verify the fuel flexibility of the cyclonic burner for small scale

applications, further experimental campaigns were performed with a synthetic mixture (60% CH_4, 40% CO_2 [8], mimicking a fuel with lower LHV.
Similarly to methane/air campaigns reported in previous sections, the experimental tests were realized, for biogas/air mixtures at ambient conditions (T_{in}=300K, P=1 Atm) by monitoring temperature and pollutant emissions (CO, NO_x) as a function of the equivalence ratio (in the same 0.5-1 range) at the same nominal thermal powers (4 and 10 kW).

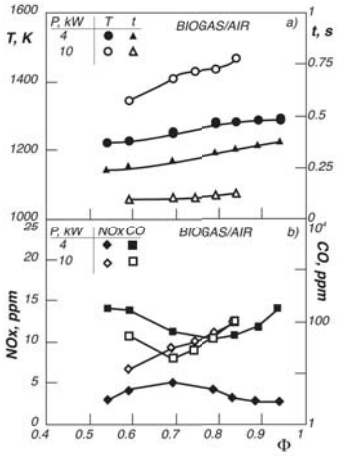

Figure 2. Temperature measurements, characteristic residence time (a) and pollutant emissions (b) for biogas-air mixtures as a function of Φ for different thermal power values.

Temperatures were reported in Figure 2a as a function of the equivalence ratio for biogas-air mixtures. At P = 4 kW, the temperatures profile exhibits a monotonous trend and it increases with Φ, passing from T=1220K at Φ=0.55 to about 1300K at Φ=0.95. They reach higher values for P=10 kW, as expected.
The emissions of main pollutants (CO and NO_x) were reported in Figure 2b, for biogas-air mixtures as a function of the equivalence ratio, on curves parametric in P. CO concentrations show a non-monotonous trend in log-scale in the Φ range considered. The minimum CO value is 50 ppm at Φ = 0.8 for P=4 kW, whereas for P = 10 kW the minimum value is lower and it occurs about at Φ = 0.7. CO emissions are below 100 ppm, respectively for Φ < 0.8 for P = 10 kW, and at 0.65 < Φ < 0.8 for P = 4 kW. On the basis of the showed results it is possible to infer that the reactor performance, in terms of CO emissions, are enhanced for higher values of the thermal power when Φ < 0.8. NO_x concentrations show a non-monotonous trend at P = 4 kW and they are always in the single-digit limit. They reach a maximum value of 6 ppm at Φ = 0.7 and then slightly diminishes up to 3 ppm when the mixture composition moves towards ultra-lean conditions or in the

opposite direction. On the other hand, NO_x emissions for P = 10 kW slightly increase from 6 ppm at Φ=0.6 to 13 ppm at Φ=0.85. They exceed the single-digit value when Φ>0.75.

Finally, experimental tests were realized, for ammonia/air mixtures at ambient conditions (T_{in}=300K, P=1 Atm) by monitoring temperature and pollutant emissions (NO_x) as a function of the equivalence ratio by changing the thermal power from 5 to 10 kW.

As it is possible to note from Figure 3 the process sustainability is ensured when temperature is higher than 1300 K for all P values. On the other hand, the oxidation process is not sustained when the equivalence ratio is lower than 0.7. Results demonstrated the flexibility in terms of fuel of the cyclonic burner also when ammonia is used as fuel, making it implementable in applications such as gas turbines [9].

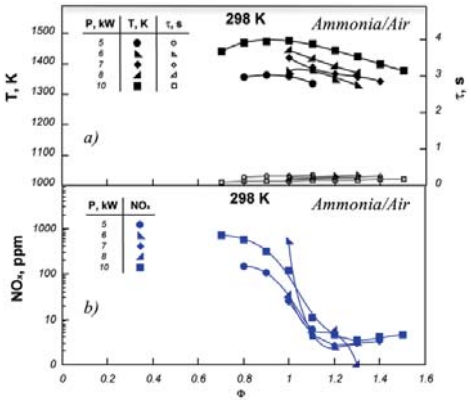

Figure 3. Temperature measurements, characteristic residence time (a) and pollutant emissions (b) for ammonia-air mixtures as a function of Φ for several P values.

In particular, NO_x levels are decreased from high values (up to 1000 ppm at 10 kW) to single digit ones when the equivalence ratio increases from ultra-lean to stoichiometric or slightly rich values.

Conclusions

The experimental results confirmed that the cyclonic burner has shown similar and very good performance for several fuels such as methane, biogas or ammonia.

With respect to the optimal operating conditions, the results have shown that the system has to be exercised with mixtures compositions slightly under the stoichiometric conditions for methane or biogas/air mixtures. In case of the methane/air mixtures the system can be operated with emissions of CO lower than 100 ppm. NO_x emissions can be lowered down to 1 digit values by keeping the

system temperature lower than about 1400 K.
In the case of biogas/air mixtures the optimal equivalence ratio to minimize emissions are slightly lower than the one identified for the methane mixtures. Results have suggested that in this case it is convenient to use higher nominal thermal power to optimize the system in order to contrast the effect of temperature reduction induced by the CO_2 thermal sinking effect. On the other hand, the presence of CO_2 has beneficial effects to contain the NO_x emissions.
Finally, the use of pure ammonia as fuels decreased the operability range of the burner in terms of temperatures and equivalence ratio ranges. Despite that the burner showed very good performance in terms of NO_x when the equivalence ratio is higher than the stoichiometric value.

References

[1] Cavaliere, A., de Joannon, M., "MILD Combustion", *Prog. Energy Combust. Sci.* 30: 329-366 (2004).
[2] Khalil, A. E., Gupta, A. K., "Swirling distributed combustion for clean energy conversion in gas turbine applications", *Applied Energy* 88(11): 3685-3693 (2011).
[3] Reddy, V. M., Katoch, A., Roberts, W. L., Kumar, S., "Experimental and numerical analysis for high intensity swirl based ultra-low emission flameless combustor operating with liquid fuels", *Proc 35th Combustion Institute*, San Francisco, USA, issue (3), pp 3581-3589.
[4] de Joannon, M., Sabia, P., Sorrentino, G., Bozza, P., Ragucci, R., "Small size burner combustion stabilization by means of strong cyclonic recirculation", *Proc 36th Combustion Institute*, Seoul, Korea, issue (3), pp 3361-3369.
[5] Sorrentino, G., Sabia, P., de Joannon, M., Cavaliere, A., Ragucci, R., "The effect of diluent on the sustainability of MILD combustion in a cyclonic burner", *Flow Tur Comb* 96(2): 449-468 (2016).
[6] Sorrentino, G., Sabia, P., Bozza, P., Ragucci, R., de Joannon, M. "Impact of external operating parameters on the performance of a cyclonic burner with high level of internal recirculation under MILD combustion conditions", *Energy* 137: 1167-1174 (2017).
[7] Alzueta, M. U., Bilbao, R., Millera, A., Glarborg, P., Østberg, M., Dam-Johansen, K., "Modeling low-temperature gas reburning. NO x reduction potential and effects of mixing", *Energy & Fuels* 12(2): 329-338 (1998).
[8] Rasi, S., Veijanen, A., Rintala, J., "Trace compounds of biogas from different biogas production plants", *Energy*, 32(8): 1375-1380 (2007).
[9] Kurata, O., Iki, N., Matsunuma, T., Inoue, T., Tsujimura, T., Furutani, H., Hayakawa, A. "Performances and emission characteristics of NH3–air and NH3/CH4–air combustion gas-turbine power generations", *Proc 36th Combustion Institute*, Seoul, Korea, issue (3), pp 3351-3359.

Catalytic Combustion of Methanol over Nano-Structured CeO_2-Pt/Fecralloy Foam Catalysts

S. Cimino*, L. Lisi*, M. Musiani, E. Verlato****
stefano.cimino@cnr.it
*Istituto Ricerche sulla Combustione IRC-CNR, P.le V. Tecchio 80, 80125 Napoli, Italy
**Istituto Chimica della Materia Condensata e di Tecnologie per l'Energia ICMATE-CNR, C.so Stati Uniti 4, 35127, Padova, Italy

Abstract
Pt-based structured catalysts for the low-temperature combustion of methanol were prepared by pulsed electrodeposition, using Fe-Cr-Al alloy (Fecralloy) foam supports. Pt loading and surface area were measured by ICP-MS and cyclic voltammetry, respectively. Although the presence of a CeO_2 film decreased the Pt surface area accessible to electrolyte it enhanced the performance of the catalysts towards methanol combustion, without affecting the activation energy of the process, due to the formation of novel active sites along the Pt-CeO_2 interface of core-shell nanoparticles.

Introduction
Methanol has been proposed as a valuable fuel for Pt-based catalytic burners integrated in fuel cells [1] or mobile thermoelectric power generators [2]. For those applications, catalytic burners are integrated into heat-exchanger reactors which inevitably require a shaping of the catalyst into a structured form [3]. Metallic foams represent a preferred choice to reduce the size of the reactor needed to reach high conversions [4] due to their outstanding heat- and mass-transfer properties. Among them, Fecralloy foams are optimal to design lightweight reactors with low thermal inertia and fast transient response during start-ups [4]. Nevertheless, the deposition of a firmly anchored, homogeneous catalytic active layer over the structured (foam) substrate is not a trivial matter.
In a recent paper, our group has reported on the low/medium-temperature catalytic combustion of methanol on Pt–modified Fecralloy foams prepared by electrodeposition [5]. This simple and straightforward method yielded structured catalysts with stable activity, very low CO emissions and complete selectivity to CO_2. In this work we set out to further improve the performance of the methanol combustion catalysts, through the following actions: (i) diminishing the Pt loading, to enhance the dispersion of the noble metal and its mass activity; (ii) depositing a CeO_2 protecting shell above Pt nanoparticles to favour synergic catalytic effects.

Experimental
Catalysts were prepared by depositing Pt, CeO_2 or both onto Fecralloy foams cylinders with 1.8 cm diameter and 2.3 cm^3 volume (Porvair, 50 pores per linear inch, 0.34 g cm^{-3} apparent density, ca. 95% void volume). Electrodeposition of

either CeO_2 or Pt was carried out in two-compartment cells. The Fecralloy-foam working electrode and a Pt wire counter electrode were placed in the main cell compartment, a Saturated Calomel Electrode (SCE) in the lateral compartment. Platinum was deposited from 0.002 M M H_2PtCl_6 solutions containing 1.0 M NaCl and HCl to yield pH 2.0. Electrolyses were performed by pulsing the working electrode potential between E_1, in the range -0.6 to -1.2 V, inducing Pt electrodeposition, and E_2, variable between 0.1 and -0.1 V. The number of cycles was varied to control the deposition charge and hence the Pt loading. Thereafter, CeO_2 was electrodeposited at constant potential from a 0.100 M $Ce(NO_3)_3$ solution. Cyclic voltammograms aimed at assessing the exposed Pt surface area were recorded using either Pt-Fecralloy or CeO_2-Pt-Fecralloy samples as working electrodes, a Pt wire as counter-electrode and an Hg/HgO/1 M KOH reference electrode using an Autolab PGSTAT 302N potentiostat. SEM images and EDS analyses were obtained with a Zeiss SIGMA instrument, equipped with a field-emission gun. Pt loading was determined by ICP-MS (Thermo Elemental X7-series) after microwave-assisted acid dissolution of samples.
Methanol catalytic combustion tests were performed in a lab scale quartz reactor (d_{inner}=20 mm), operated at nearly atmospheric pressure, by ramping up the temperature with an electric furnace from 50°C to 600°C at 3°C/min. Inlet and outlet temperatures were measured by two K-type thermocouples. A lean methanol in air feed (0.5–2.0 % vol., total flow-rate 40 $Sdm^3\ h^{-1}$) was prepared by mixing two air streams, regulated by independent MFCs, and one of these passed through a methanol saturator. The effluent gas was dried and continuously analyzed with an ABB Advance Optima2020 and a GEIT FLUE GAS, equipped with ND-IR detectors for CO, CO_2, CH_4 and an electro-chemical cell for O_2. In fact the CH_4 detector gave a linear response to methanol, thus it was used to measure its concentration in the feed stream after a specific calibration.
Methanol conversion to CO_2 (yield) was simply defined as the molar ratio between CO_2 formed (outlet) and methanol in the feed. The CO_2 production rate was estimated from low conversion data assuming differential conditions, isothermal plug flow reactor, and constant molar flow.

Results and Discussion

Pt nano-particles formed directly onto Fecralloy foams and consisted of clusters of quasi-cubical particles, deposited with similar surface densities on the struts of outer and inner cells. The number of Pt nuclei per unit surface became larger as E_1 was made more negative, up to reach an asymptotic value around $E_1 \leq$ -1.0 V, and was essentially independent of the number of pulses. The particles dimensions were narrowly distributed, were lower for more negative E_1 potential, and increased with the number of pulses. The Pt loadings (Table 1) were well-below those of catalysts described in [5], and remained unchanged after CeO_2 addition, confirming that Pt nanoparticles were stable under those deposition conditions.

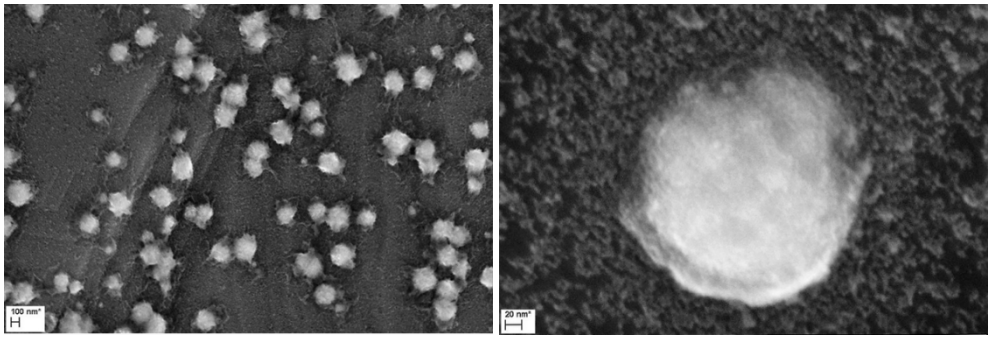

Figure 1. SEM images of CeO_2-Pt-Fecralloy foam catalyst. Pt was deposited from 0.002 M H_2PtCl_6 with E_1 = -0.7 V and 800 pulses. CeO_2 was deposited in 0.100 M $Ce(NO_3)_3$ at -1.2 V with 13 C cm^{-3} deposition charge.

Figure 1 shows SEM images of nano structured CeO_2-Pt-Fecralloy foam catalysts. The formation of Ce-containing deposit, assessed through EDS analyses, occurred both on the Pt particles and on the Fecralloy substrate. The b image, obtained with 500k x magnification, shows that a ca. 20 nm thick, probably discontinuous, oxide skin formed on the Pt particles, producing a sort of core-shell system. A discontinuous CeO_2 layer was visible on the Fecralloy substrate too. Accordingly, the Pt surface area calculated from the H desorption charge ($S_{w,EC}$, Table 1), progressively decreased upon deposition of increasing quantities of CeO_2. In fact, CeO_2-Pt-Fecralloy catalyst used in methanol combustion preserved a residual Pt surface area equal to 30% of the initial one.

Table 1. . Pt loading and Pt surface area and catalytic activity data for the foam catalysys tested for methanol combustion.

System	Pt Load mg cm^{-3}	$S^{Pt}_{w,EC}$ m^2 g^{-1}	E_a kJ mol^{-1}	R_wCO_2 @150°C mmol g_{Pt}^{-1} h^{-1}	S^{Pt}_w m^2 g^{-1}
Fecralloy	-	-	310	-	
CeO_2-Fecralloy	-	-	88.5	-	
Pt-Fecralloy	0.37	16.6	70.4	296	0.12
CeO_2-Pt-Fecralloy	0.37	5.0	70.4	415	0.19
Pt-Fecralloy [ref.5]	5 - 13	12 - 13	69.0	100 - 300	-

Figure 2a presents the results of the lean methanol combustion tests with foam catalysts in terms of the yield to CO_2 as a function of the reaction temperature. Preliminary tests were run with a bare Fecralloy foam and indicated that, under the investigated experimental conditions, the oxidation of methanol started above 375°C with the initial production of CO, followed by the formation of CO_2 only above ca 430 °C.

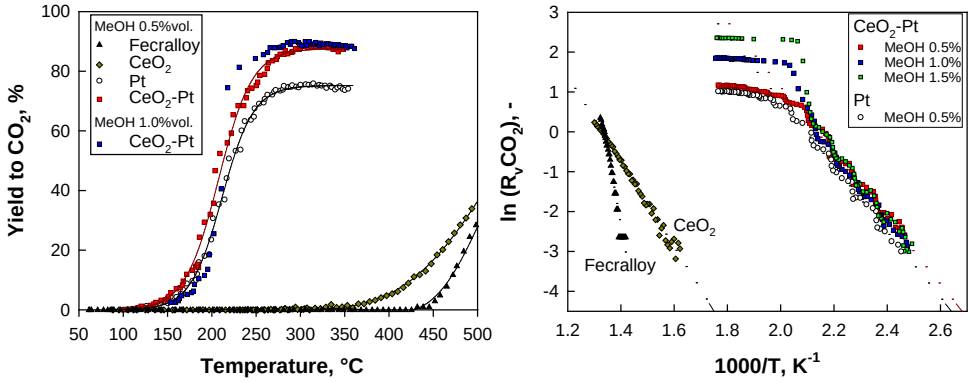

Figure 2. a) Methanol yield to CO_2 as a function of the reaction temperature over Pt-Fecralloy, CeO_2-Pt-Fecralloy, CeO_2-Fecralloy catalysts and a bare Fecralloy foam. b) Corresponding Arrhenius plots for the specific CO_2 production rate per unit volume of foam during methanol combustion. Feed conditions: 40 $Sdm^3\ h^{-1}$, CH_3OH = 0.5 - 1.5 % in air.

The deposition of CeO_2 on the Fecralloy foam induced a limited improvement in the overall methanol oxidation activity of the system, showing some CO_2 formation from ca. 350 °C (Fig. 2a), always accompanied by the production of comparable amounts of CO. In contrast, the Pt-based catalysts displayed a significant activity for methanol total oxidation, despite their rather low noble metal content. CO_2 formation became measurable starting from slightly above 100°C and its yield increased steeply along with the reaction temperature, and eventually reached an asymptotic value above 250 °C. This corresponded to the presence of some unconverted methanol in the exhaust gas leaving the catalyst, whereas no other products were detected.

CeO_2-Pt-Fecralloy catalyst outperformed its Pt-Fecralloy counterpart with identical noble metal loading, both in terms of catalytic activity before light-off as well as in the final CO_2 yield at high temperatures (87.7 % vs. 75.3 %). Moreover, CO formation was never detected in the exhaust gas from the CeO_2-Pt-Fecralloy sample, and remained below 20 ppmv with Pt-Fecralloy system, in good agreement with our previous results on similar foam catalysts with higher Pt-loadings [5]. Reactivity measurements were repeated after having exposed the catalysts to reaction conditions at 600°C (2h), and gave substantially identical results, indicating a good stability of the catalytic activity of Pt-based foams.

As shown in Figure 2a for the case of CeO_2-Pt-Fecralloy, when the inlet concentration of methanol was increased, the CO_2 yield plots shifted slightly towards higher temperatures, indicating a less than linear dependency of the catalytic combustion rate on fuel concentration at low temperature. Analogous results were also found over the Pt-Fecralloy catalyst. Figure 2b presents the Arrhenius plots for the specific CO_2 formation rate over the foam catalysts. Data sets obtained with CeO_2-Pt-Fecralloy in the low temperature region (under kinetic

control) at various inlet methanol concentrations merged into a single line within experimental accuracy, and departed from it above the light-off temperature. The apparent activation energy (E_a, Table 1) was estimated equal to ca 70 kJ mol^{-1}, and it was hardly affected by the addition of CeO_2 as a promoter for Pt or by the noble metal content. Methanol combustion mechanism on Pt-Fecralloy appeared qualitatively insensitive to the addition of CeO_2. On the other hand, the methanol combustion rate ($R_{w,}$ Table 1) at 150°C increased by a factor as large as 1.4, due to the formation of some additional active sites most probably located at the interface between the Pt and CeO_2. As a consequence, the utilization factor of the costly noble metal was significantly enhanced with respect to our previous results with Pt-Fecralloy foams (Table 1).

The asymptotic behaviour of methanol conversion (which is equal to the CO_2 yield) upon light-off suggests the onset of full external mass-transfer control. Indeed, the asymptotic methanol conversion (CO_2 yield) level attained with each foam catalyst was independent of methanol feed concentration. On the other hand, methanol conversion increased to almost 100 % (not shown) when the tests were repeated doubling the contact time at fixed gas velocity, i.e. using two identical catalytic foams in series. Under the assumption of isothermal plug flow behaviour and irreversible reaction, the steady-state mass balance for methanol in the reactor becomes:

$$-\ln(1-x) = \frac{S_v V_{foam} k_m}{Q} \qquad (1)$$

where x represents methanol conversion, S_v is the specific area of the active sites per unit volume of the foam [cm^2 cm^{-3}], V_{foam} is the foam volume [cm^3], k_m is the mass transfer coefficient [cm h^{-1}], and Q is the volumetric flow [cm^3 h^{-1}]. The value of k_m was estimated equal to 30 cm/s at 350 °C with the correlation given by Giani et al. [4], by considering that the approximate diameters of struts (d_s) and pores (d_p) in the Fecralloy foams were respectively 1.0 x 10^{-2} cm and 5.5 x 10^{-2} cm, and the geometric void fraction was 92.2%.

Assuming that k_m was not affected by the addition of the thin CeO_2 overlayer on Pt particles, it was possible to calculate for both catalysts the specific area S_v of those Pt sites that were active after light-off (Table 1). Noteworthy, CeO_2 addition increased the surface area of active sites by as much as 50%, in good agreement with the already reported activity increase before light-off.

Since CeO_2 was added at the final step of preparation after Pt-deposition so that neither metal loading nor its morphology were significantly affected, it can be argued that the increase in the number of available catalytic active sites in CeO_2-Pt-Fecralloy was associated to the formation of novel CeO_2- Pt interface sites that were easily accessible in the nanoparticles with a quasi-core-shell configuration.

Comparing the values of the specific surface area of active Pt sites per gram of metal to the corresponding figures estimated by voltammetric experiments, i.e. comparing $S^{Pt}_{w,EC}$ with S^{Pt}_{w} (Table 1), it is evident that the active sites for methanol catalytic combustion at 350°C were only a small fraction of the total exposed Pt

surface, respectively 0.7% and 3.8% for Pt-Fecralloy and CeO_2-Pt-Fecralloy foams. SEM inspection of used CeO_2-Pt-Fecralloy catalysts showed that there was no Pt particles loss, and that the shape and size of the particles remained unchanged. A change in the morphology of the CeO_2 deposit on Fecralloy, presumably due to crystallization, was detected. These results agree with the observed stable catalytic activity of the samples when they were used in successive methanol combustion tests.

Conclusions

In this work, we have demonstrated how the cathodic deposition of noble metal nanoparticles followed by that of discontinuous oxide layers may be an original and effective way to use electrochemistry for the preparation of active catalysts for low-temperature catalytic combustion processes. Platinum and CeO_2 were deposited, in this order, onto Fecralloy foams to obtain structured catalysts for methanol combustion. The CeO_2-Pt-Fecralloy catalysts were superior to Pt-Fecralloy catalysts with the same noble metal loading. The catalysts were stable and their performance was constant during successive cycles involving temperatures up to 600°C.

The increase in the number of available catalytic active sites in CeO_2-Pt-Fecralloy was associated to the formation of novel CeO_2-Pt interface sites that remained easily accessible in the nanoparticles with a quasi-core-shell configuration.

References

[1] Pasel J., Emonts B., Peters R., Stolten D., “A structured test reactor for the evaporation of methanol on the basis of a catalytic combustion”, Catal. Today 69:193-200 (2001).

[2] Applegate J.R., McNally D., Pearlman H., Bakrania S.D., Platinum Nanoparticle Catalyzed Combustion of a Methanol–Air Mixture”, Energy & Fuels, 27:4014-4020 (2013)

[3] Xiaoding X., Moulijn J.A., “Structured Catalysts and Reactors”, CRC Taylor & Francis, 751-777 (2005).

[4] Giani L., Groppi G., Tronconi E., “Mass-Transfer Characterization of Metallic Foams as Supports for Structured Catalysts”, Ind. Eng. Chem. Res. 44:4993-5002 (2005).

[5] Cimino S., Gambirasi A., Lisi L., Mancino G., Musiani M., Vázquez-Gómez L., Verlato E., “Catalytic combustion of methanol on Pt-Fecralloy foams prepared by electrodeposition”, Chem. Eng. J. 285: 276-285 (2016).

Use of solar energy to sustain limestone calcination for ordinary Portland cement production

C. Tregambi*, R. Solimene, F. Montagnaro***, P. Salatino*, M. Marroccoli****, N. Ibris****, A. Telesca******

antonio.telesca@unibas.it

*Dipartimento di Ingegneria Chimica, dei Materiali e della Produzione Industriale, Università degli Studi di Napoli Federico II, Piazzale V. Tecchio 80, 80125 Napoli, Italia

**Istituto di Ricerche sulla Combustione, Consiglio Nazionale delle Ricerche, Piazzale V. Tecchio 80, 80125 Napoli, Italia

***Dipartimento di Scienze Chimiche, Università degli Studi di Napoli Federico II, Complesso Universitario di Monte Sant'Angelo, 80126 Napoli, Italia

****Scuola di Ingegneria, Università degli Studi della Basilicata, Viale dell'Ateneo Lucano 10, 85100 Potenza, Italia

Abstract

Cement manufacture is one of the most raw materials- and energy-intensive industrial processes; moreover, its contribution to global anthropogenic CO_2 emission is estimated as high as 6%. Most of energy requirement and CO_2 generation are mainly associated with limestone calcination (LC). The use of solar energy as non-carbogenic renewable source for LC was evaluated in this paper; to this end, a directly irradiated fluidised bed (FB) reactor has been employed as limestone precalciner upstream of a cement clinker production kiln. LC was carried out at 940°C in an atmosphere containing about 70% CO_2. The experimental activity was devoted to assess the reactivity of calcinated lime toward the main clay components for the Portland clinker (PCl) production process, as compared to lime from ordinary calcination. Portland cements (obtained by mixing PCls with 5% natural gypsum) were hydrated for periods ranging from 2 to 28 days (water/cement mass ratio=0.5). Parameters as lime saturation factor, burnability, clinker phase composition and cement pastes hydration behaviour were assessed.

Introduction

Cement production is a highly raw-materials as well as energy-intensive manufacturing process and represents one of the World's largest industrial sources of CO_2 emission [1]. Portland cement is the most extensively employed binder obtained by mixing Portland Clinker (PCl) with a few percent of calcium sulphates (mostly natural gypsum, NG); PCl is obtained by heating the "raw meal" (a mix of about 80% of limestone and clay) in a two-step process, namely preheating-calcination and clinkerization, respectively carried out in a stationary apparatus (up to 800°–1000°C) and in a rotary kiln (up to 1400°–1500°C). About 0.87 kg of CO_2, coming from limestone thermal decomposition (around 60% of the total CO_2 emission) and fuel combustion, are released per each kg of PCl produced [2]. The

theoretical heat requirement for PCl manufacture is mainly associated with limestone calcination (LC) [3]. The use of a non-carbogenic renewable energy source for LC could significantly reduce the fuel consumption and provide substantial advantages on both economic and environmental aspects of the process. Solar energy is one of the most important renewable sources of energy. High-temperature thermal energy is efficiently provided by Concentrating Solar Power (CSP); it is a technology employing optical sun-tracking mirrors to focus and concentrate solar energy onto a receiver. The use of directly irradiated Fluidised Bed (FB) as solar receiver/reactor has been widely investigated [4-5]. FB systems feature very favourable thermal properties and provide an ideal environment for gas–solid chemical reactions. However, the bed surface overheating induced by highly concentrated solar radiation could affect the performance of the system due to bed solids sintering and/or degradation [6]. In this paper, the use of a directly irradiated FB reactor as limestone precalciner upstream of a clinker production kiln has been investigated; a commercial Italian limestone (FL), calcined in a directly irradiated solar FB (SFB) reactor, was used together with commercial clay (CL) as kiln feed components (mixture S) for PCl manufacture. A binary mixture (mixture R) composed by FL and CL was employed as reference term.

Experimental

The experimental apparatus used in the present study (Figure 1, left) consists of a FB reactor with both the internal bed diameter and height equal to roughly 0.1 m.

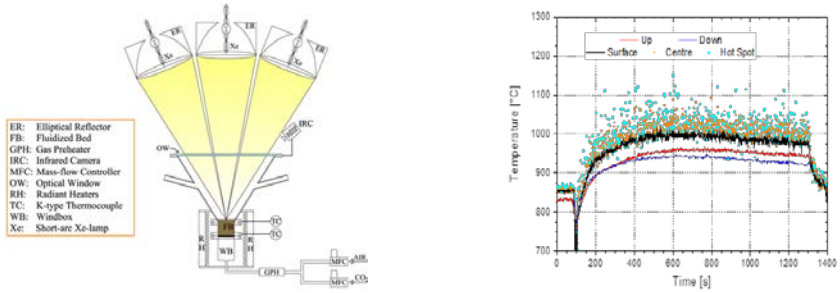

Figure 1. Outline of the experimental apparatus (solar FB) and its ancillary equipment (left). Time series of bed and surface temperature measured during a calcination run (right).

The freeboard is conically shaped with a transparent window on the top. The SFB surface is exposed to a 12 kW_{el} simulated solar furnace made by an array of three short arc Xe-lamps coupled with elliptical reflectors. The peak flux and the total power on the FB surface are equal to about 3000 $kW \cdot m^{-2}$ and 3.2 kW_{th}, respectively. Two semi-cylindrical radiant heaters heat and insulate the reaction chamber. Two mass flow controllers supply the air and CO_2 required for the reactor operation; two K-type thermocouples measure the FB inner temperatures while an IR camera is used to measure the reactor surface temperature. Table 1 reports the density and size range of both an Italian silica sand (SS), acting essentially as thermal flywheel, and FL employed for the tests.

Table 1. Main physical parameters for SS and FL.

Material	Particle density, kg m^{-3}	Size range, μm	u_{mf}^{t} @ 950°C *, m·s^{-1}
SS	2600	850–1000	0.27
FL	2200	420–590	0.07

$^{*}u^{t}_{mf}$ (the theoretical values of minimum fluidisation velocity) evaluated according to the Wen&Yu equation

LC was performed at about 940°C with inlet CO_2 concentration close to 70%v and fluidising gas velocity equal to 0.6 m·s^{-1}. FB reactor was initially charged with SS (about 730g) and heated up to 850°C. Once reached the pre-set conditions, FL (120g) was fed to the reactor and the solar simulator was switched on. LC was prolonged for nearly 20 min; later on, solar simulator was switched off and FB reactor was air cooled to about 20°C to recover the calcined material (SL), used as substitute for FL in mixture S. The major oxides of FL, SL and CL were determined by X-ray fluorescence (XRF) analysis and are indicated in Table 1 together with the loss on ignition (l.o.i.) values. R and S mixtures were conceived to obtain two PCls having the same Lime Saturation Factor [3], LSF, value:

$$LSF = \frac{CaO}{(2.8 \cdot SiO_2 + 1.65 \cdot Al_2O_3 + 0.35 \cdot Fe_2O_3)} \quad (1)$$

where CaO, SiO_2, Al_2O_3 and Fe_2O_3 are the mass fractions of the respective oxides. LSF controls the ratio $3CaO \cdot SiO_2$ to $2CaO \cdot SiO_2$ in PCls, namely the main mineralogical constituents responsible for the technological behavior of hydrated cements. As in modern clinkers LSF values are generally comprised in the range 0.92–0.98, a LSF value equal to 0.93 was here considered.

The burnability of a raw mix for Portland cement manufacture represents the ability of CaO, derived from limestone calcination, to react in the kiln with SiO_2, Al_2O_3 and Fe_2O_3 contained in the clayish material to give the clinker. According to a fixed heating cycle, burnability can be evaluated by the amount of unreacted CaO (free lime) present after a given treatment duration [7]; thus, the test adopted in this investigation, aimed at obtaining a Burnability Index (BI) for both R and S mixtures, was based on the following thermal treatment: (a) first step at 105°C for 120 min; (b) second step at 600°C for 30 min; (c) third step at the final temperature (1350°, 1400°, 1450° or 1500°C) for 15 min. BI is given by the following formula:

$$BI = \frac{3.73(A+B+2C+3D)}{(A-D)^{0.25}} \quad (2)$$

where A, B, C and D are the free lime contents (mass %) in the products burnt at 1350°, 1400°, 1450° and 1500°C, respectively. A relatively low BI value reveals good burnability; more precisely, BI values lower than 60 indicate a very satisfactory behaviour. The free CaO concentration in PCls was measured by the Franke method [8]. The clinkers obtained at 1500°C from both R and S mixtures ($CliR_{15}$ and $CliS_{15}$) were in part characterized by XRF and X-ray diffraction (XRD) analyses, in part mixed with 5% NG and ground in laboratory mill to pass 90 micron-sieve in order to prepare two Portland cements (CEMR and CEMS). Both cements were paste hydrated (water/cement ratio, 0.5 by mass) from 2 to 28 days. XRF, XRD and differential thermal-thermogravimetric, DT-TG, analyses were

utilized for (i) the chemical analysis of FL, SL, CL and NG as well as the synthetic clinkers, (ii) the mineralogical characterization of $CliR_{15}$ and $CliS_{15}$ and (iii) the evaluation of the hydration behaviour of CEMR and CEMS, respectively.

Results and discussion

Figure 1 (right) reports the temperature/time series obtained during the solar calcination test. The blue and red curves refer to the "down" and "up" temperatures, respectively; the black curve refers to the upper surface temperature averaged over the whole FB surface, and the orange circles and the cyan squares refer to a circular area of about 25 mm diameter centered on the FB surface and to the hot spots detected by the IR camera, respectively. The "hot-spot" function of the IR camera shows, for each time instant, the temperature of the pixel size (1 mm diameter) circular area, found on the FB surface, owning the maximum temperature value. The temperature averaged over the whole FB surface (black curve) exhibits indeed a mean value of 984°±15°C corresponding to a mean over-temperature value of roughly 45°C as regards to the temperatures of the bulk bed. The mean temperatures and the related standard deviations are 1008°±25°C for the central area and 1020°±34°C for the hot spots. However, peak temperatures ≥ 1100°C have been detected on the FB surface. The steep decrease in all the temperature values observable at about 100 s is due to the feeding of FL sample.

From Table 2 it can be seen that FL is very rich in $CaCO_3$ while the solar process was successful in achieving almost complete LC (l.o.i.=5% against 43% found for FL sample). These results were confirmed by XRD analysis.

Table 2. Chemical composition for FL, SL, CL and NG mass %.

	CaO	**SiO_2**	**Al_2O_3**	**Fe_2O_3**	**K_2O**	**MgO**	**SO_3**	**l.o.i.[a]**	**Total**
FL	54.40	1.20	0.47	0.10	0.15	0.31	0.24	42.90	99.77
SL	90.17	1.99	0.78	0.17	0.25	0.46	0.35	5.35	99.52
CL	12.20	54.60	10.05	3.70	2.18	0.78	0.56	14.30	98.47
NG	32.10	1.05	0.46	0.41	-	0.27	43.10	21.90	99.29

[a]Loss on ignition at 950°C, according to EN 196-2 Standard for cements.

CL is very rich in silica while CaO and Al_2O_3 were revealed as secondary components; as also stated by DT–TG analysis l.o.i. was equal to about 14%. Application of Eq. (1), for LSF=0.93, was satisfied using the following mass proportions: R mixture (74.25% FL, rest CL); S mixture (63.50% SL, rest CL). For both series the free lime concentration in the synthetic clinkers decreased with the increase of heating temperature (CaO reacts more and more as temperature increases); moreover, satisfactory BI values (calculated according to Eq. (2)) of 20.93 (S-case) and 30.42 (R-case) were obtained. XRF analysis was also carried out on clinkers generated at 1500°C (Table 3). The potential concentration of the four clinkers main mineralogical phases ($3CaO{\cdot}SiO_2$, $2CaO{\cdot}SiO_2$, $3CaO{\cdot}Al_2O_3$, and $4CaO{\cdot}Al_2O_3{\cdot}Fe_2O_3$) was determined according to the Bogue's formulae [9]. From Table 3 (indicating also the phase composition for $CliR_{15}$ and $CliS_{15}$ together with typical values for industrial PCls) it can be observed that there are no significant differences between the two clinkers, whose composition lies in the

Table 3. Chemical and phase composition for $CliR_{15}$, $CliS_{15}$ and common clinkers, mass %.

	$CliR_{15}$	**$CliS_{15}$**	**Common clinkers**
Chemical composition			
CaO	67.34	67.11	62.0–68.0
SiO_2	22.38	22.57	21.0–23.0
Al_2O_3	5.94	5.65	5.5–6.2
Fe_2O_3	2.38	2.47	2.2–3.0
MgO	1.18	1.23	1.1–1.5
SO_3	1.52	1.82	1.3–2.0
Phase composition[a]			
$3CaO{\cdot}SiO_2$	60.78	60.35	58.0–65.0
$2CaO{\cdot}SiO_2$	18.35	19.36	13.0–20.0
$3CaO{\cdot}Al_2O_3$	11.72	10.82	9.0–12.0
$4CaO{\cdot}Al_2O_3{\cdot}Fe_2O_3$	7.25	7.54	7.0–9.0

[a]According to Bogue's formulae.

indicated ranges for commercial materials. The similarity in the mineralogical composition between the traditional and solar clinker has been also confirmed by the XRD patterns (Figure 3). Both cements exhibited a similar hydration behaviour

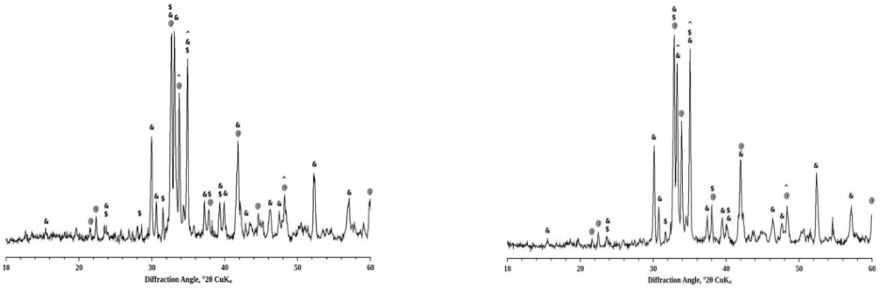

Figure 3. XRD patterns for $CliR_{15}$ (left) and $CliS_{15}$ (right) obtained at 1500°C. Key to symbols: &=$3CaO{\cdot}SiO_2$; $=$2CaO{\cdot}SiO_2$; @=$3CaO{\cdot}Al_2O_3$; ^=$4CaO{\cdot}Al_2O_3{\cdot}Fe_2O_3$.

(Figure 4) in terms of development of the main hydration products, namely calcium silicate hydrates (CSH), ettringite (E), monosulphate (M), and calcium hydroxide, CH, (which also underwent partial carbonation, $CaCO_3$=C). It is recalled here that:

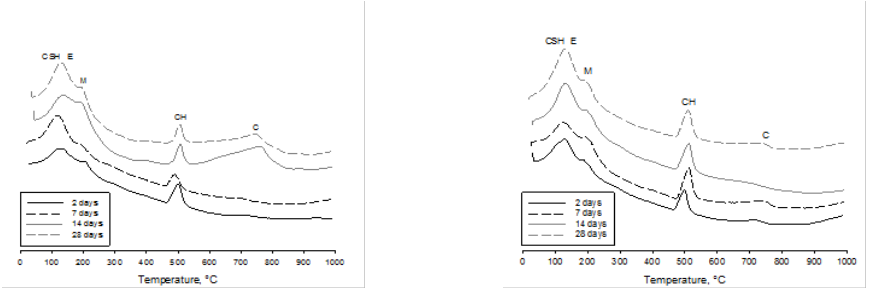

Figure 4. DT curves for CEMR (left) and CEMS (right), hydrated for 2 to 28 days. (CSH=calcium silicate hydrates; E=ettringite; M=monosulphate; CH=$Ca(OH)_2$; C=$CaCO_3$).

i) CSH are the main hydration products of calcium silicates present in the PCls (a process that gives CH as by-product); ii) E can be formed through the hydration of calcium aluminates (CA) with calcium sulphates; iii) M can be regarded as the decomposition product of E.

Conclusions

The use of concentrated solar power as non-carbogenic renewable energy source for limestone calcination in the cement manufacture can allow significant advantages from both economic and environmental points of view. The use of a directly irradiated fluidised bed (FB) reactor represents a practical and robust method to accomplish solar-driven calcination (SDC) of limestone. Laboratory burnability tests revealed that the use of solar CaO in raw meal for Portland clinker does not bring about a reduction in its burnability easiness when compared with a reference non-solar raw meal. A strong similarity in mineralogical composition and hydration behaviour of the related Portland cements was observed. On the whole, the technical feasibility of SDC of limestone in a FB to produce lime usable in the cement clinker production has been demonstrated.

References

[1] Telesca, A., Marroccoli, M., Tomasulo, M., Valenti, G.L., Dieter, H., Montagnaro, F., "Low-CO_2 cements from fluidized bed process wastes and other industrial by-products", *Combust. Sci. Technol.* 188:492–503 (2016).

[2] Telesca, A., Marroccoli, M., Ibris, N., Lupiáñez, C., Díez, L.I., Romeo, L.M., Montagnaro, F., "Use of oxyfuel combustion ash for the production of blended cements: a synergetic solution toward reduction of CO_2 emissions", *Fuel Proc. Technol.* 156:211–220 (2017).

[3] Lea's, *Chemistry of Cement and Concrete*. Peter Hewlett, 5th Edition. Elsevier Science & Technology, 2017, p.1000.

[4] Gokon, N., Izawa, T., Kodama, T., "Steam gasification of coal cokes by internally circulating fluidized-bed reactor by concentrated Xe-light radiation for solar syngas production", *Energy* 79:264–272 (2015).

[5] Tregambi, C., Montagnaro, F., Salatino, P., Solimene, R. "Directly irradiated fluidized bed reactors for thermochemical processing and energy storage: application to calcium looping", *Proc. AIP Conference*, 1850, pp 090007-(1-8).

[6] Tregambi, C., Chirone, R., Montagnaro, F., Salatino, P., Solimene, R., "Heat transfer in directly irradiated fluidized beds", *Solar Energy* 129:85–100 (2016).

[7] Bernardo, G., Marroccoli, M., Nobili, M., Telesca, A., Valenti, G.L., "The use of oil well-derived drilling waste and electric arc furnace slag as alternative raw materials in clinker production", *Res. Cons. Rec.* 52:95−102 (2007).

[8] Horkoss, S., "Reducing the SO_2 emission from a cement kiln", *Int. J. Nat. Soc. Sci.* 1:7–15 (2008).

[9] Bogue, R.H., *The Chemistry of Portland Cement*, 2nd Edition -Reinhold Publishing Corporation, 1955, p. 793.

THE COMBUSTION INSTITUTE
1954

Joint Meeting of the German and Italian Sections of The Combustion Institute

41st Meeting of the Italian Section of The Combustion Institute

Scientific Committee:

Prof. Burak Atakan, Duisburg
Dr. Carlo Beatrice, Naples
Prof. Samir Bensaid, Turin
Prof. Henning Bockhorn, Karlsruhe
Dr. Mario Commodo, Naples
Prof. Francesco Creta, Rome
Prof. Marco Derudi, Milan
Prof. Chiara Galletti, Pisa
Dr. Eugenio Giacomazzi, Rome
Prof. Christian Hasse, Darmstadt
Prof. Heinz Pitsch, Aachen
Prof. Fabrizio Scala, Naples
Prof. Dinosthenis Trimis, Karlsruhe

Local Organizing Committee:

Dr. Barbara Apicella
Dr. Stefano Cimino
Prof. Almerinda Di Benedetto
Prof. Fabio Montagnaro
Dr. Giovanna Ruoppolo
Dr. Osvalda Senneca
Dr. Roberto Solimene
Mr. Antonio Tregrossi

ASICI
Associazione Sezione Italiana del Combustion Institute
P.le V. Tecchio, 80
80125 Napoli – Italia
ASICI website: www.combustion-institute.it
E-mail: secretary@combustioninstitute.it
Telephone: +39 081 7682256

The Combustion Institute Deutsche Sektion e.V.
Tammannstrasse 6
D-37077 Göttingen
Website: http://www.combustioninstitute.de
Office E-mail: jkupfer@gwdg.de
Telephone: +49 551 3933115

ISBN 978-88-88104-22-5